ISSN 1580-3155

Pages 349–682 ■ Year 2020, Vol. 67, No. 2

Slovensko kemijsko društvo
Slovenian Chemical Society

Acta Chimica Slovenica

2

67/2020

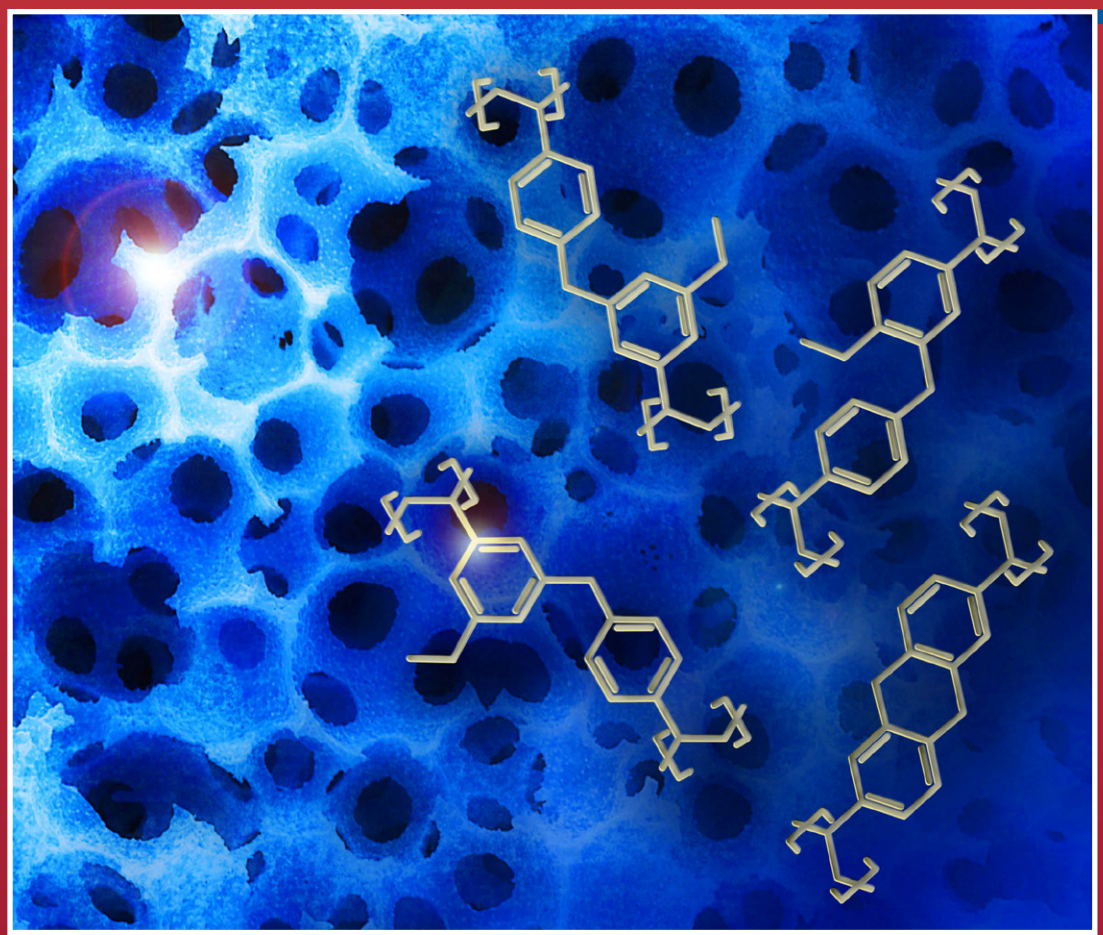

http://acta.chem-soc.si

EDITOR-IN-CHIEF

KSENIJA KOGEJ
University of Ljubjana, Facuty of Chemstry and Chemical Technology, Večna pot 113, SI-1000 Ljubljana, Slovenija
E-mail: ACSi@fkkt.uni-lj.si, Telephone: (+386)-1-479-8538

ASSOCIATE EDITORS

Alen Albreht, *National Institute of Chemistry, Slovenia*
Aleš Berlec, *Jožef Stefan Institute, Slovenia*
Janez Cerkovnik, *University of Ljubljana, Slovenia*
Mirela Dragomir, *Jožef Stefan Institute, Slovenia*
Ksenija Kogej, *University of Ljubljana, Slovenia*
Krištof Kranjc, *University of Ljubljana, Slovenia*
Matjaž Kristl, *University of Maribor, Slovenia*
Franc Perdih, *University of Ljubljana, Slovenia*
Aleš Podgornik, *University of Ljubljana, Slovenia*
Helena Prosen, *University of Ljubljana, Slovenia*

ADMINISTRATIVE ASSISTANT

Marjana Gantar Albreht, *National Institute of Chemistry, Slovenia*

EDITORIAL BOARD

Wolfgang Buchberger, *Johannes Kepler University, Austria*
Alojz Demšar, *University of Ljubljana, Slovenia*
Stanislav Gobec, *University of Ljubljana, Slovenia*
Marko Goličnik, *University of Ljubljana, Slovenia*
Günter Grampp, *Graz University of Technology, Austria*
Wojciech Grochala, *University of Warsaw, Poland*
Danijel Kikelj, *University of Ljubljana*
Janez Košmrlj, *University of Ljubljana, Slovenia*
Blaž Likozar, *National Institute of Chemistry, Slovenia*
Mahesh K. Lakshman, *The City College and The City University of New York, USA*
Janez Mavri, *National Institute of Chemistry, Slovenia*
Friedrich Srienc, *University of Minnesota, USA*
Walter Steiner, *Graz University of Technology, Austria*
Jurij Svete, *University of Ljubljana, Slovenia*
Ivan Švancara, *University of Pardubice, Czech Republic*
Jiri Pinkas, *Masaryk University Brno, Czech Republic*
Gašper Tavčar, *Jožef Stefan Institute, Slovenia*
Christine Wandrey, *EPFL Lausanne, Switzerland*
Ennio Zangrando, *University of Trieste, Italy*

ADVISORY EDITORIAL BOARD

Chairman
Branko Stanovnik, Slovenia

Members
Udo A. Th. Brinkman, The Netherlands
Attilio Cesaro, Italy
Vida Hudnik, Slovenia
Venčeslav Kaučič, Slovenia
Željko Knez, Slovenia
Radovan Komel, Slovenia
Stane Pejovnik, Slovenia
Anton Perdih, Slovenia
Slavko Pečar, Slovenia
Andrej Petrič, Slovenia
Boris Pihlar, Slovenia
Milan Randić, Des Moines, USA
Jože Škerjanc, Slovenia
Miha Tišler, Slovenia
Đurđa Vasić-Rački, Croatia
Marjan Veber, Slovenia
Gorazd Vesnaver, Slovenia
Jure Zupan, Slovenia
Boris Žemva, Slovenia
Majda Žigon, Slovenia

Acta Chimica Slovenica is indexed in: *Academic Search Complete, Central & Eastern European Academic Source, Chemical Abstracts Plus, Chemical Engineering Collection (India), Chemistry Citation Index Expanded, Current Contents (Physical, Chemical and Earth Sciences), Digitalna knjižnica Slovenije (dLib.si), DOAJ, ISI Alerting Services, PubMed, Science Citation Index Expanded, SciFinder (CAS), Scopus and Web of Science.* Impact factor for 2018 is IF = 1.076.

Articles in this journal are published under the Creative Commons Attribution 4.0 International License

Izdaja – Published by:
SLOVENSKO KEMIJSKO DRUŠTVO – SLOVENIAN CHEMICAL SOCIETY
Naslov redakcije in uprave – Address of the Editorial Board and Administration
Hajdrihova 19, SI-1000 Ljubljana, Slovenija
Tel.: (+386)-1-476-0252; Fax: (+386)-1-476-0300; E-mail: chem.soc@ki.si

Slovensko kemijsko društvo
Slovenian Chemical Society

Izdajanje sofinancirajo – Financially supported by:
Slovenian Research Agency, Ljubljana, Slovenia
National Institute of Chemistry, Ljubljana, Slovenia
Jožef Stefan Institute, Ljubljana, Slovenia
Faculty of Chemistry and Chemical Technology, University of Ljubljana, Slovenia
Faculty of Chemistry and Chemical Engineering, University of Maribor, Slovenia
University of Nova Gorica, Nova Gorica, Slovenia

Acta Chimica Slovenica izhaja štirikrat letno v elektronski obliki na spletni strani http://*acta.chem-soc.si*. V primeru posvečenih številk izhaja revija tudi v tiskani obliki v omejenem številu izvodov.
Acta Chimica Slovenica appears quarterly in electronic form on the web site *http://acta.chem-soc.si*. In case of dedicated issues, a limited number of printed copies are issued as well.
Transakcijski račun: 02053-0013322846 Bank Account No.: SI56020530013322846-Nova Ljubljanska banka d. d., Trg republike 2, SI-1520 Ljubljana, Slovenia, SWIFT Code: LJBA SI 2X
Oblikovanje ovitka – Design cover: KULT, oblikovalski studio, Simon KAJTNA, s. p. Grafična priprava za tisk: Majanafin, d. o. o.

Graphical Contents

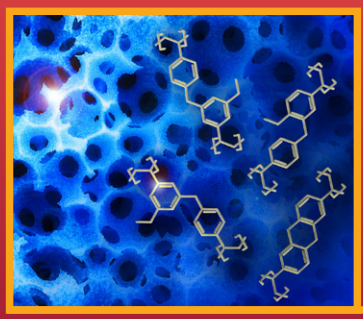

Acta Chimica Slovenica

Year 2020, Vol. 67, No. 2

FEATURE ARTICLE

349–360 Feature Article

Post Polymerisation Hypercrosslinking with Emulsion Templating for Hierarchical and Multi-Level Porous Polymers

Amadeja Koler, Irena Pulko and Peter Krajnc

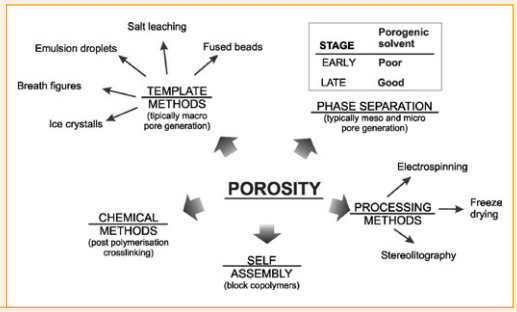

REVIEW

361–374 Applied chemistry

A Review on Recent Progression of Modifications on Titania Morphology and its Photocatalytic Performance

Nor Amira Marfur, Nur Farhana Jaafar, Melati Khairuddean and Norazzizi Nordin

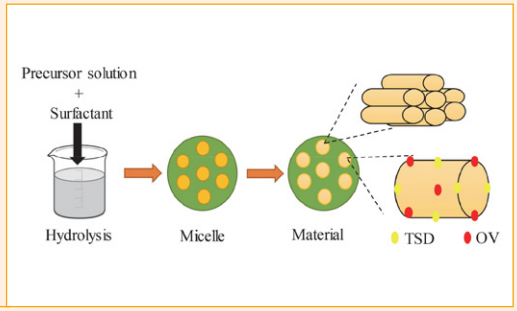

SCIENTIFIC PAPER

375–385 Analytical chemistry

Use of Fe_3O_4 Magnetic Nanoparticles Coated with Polythiophene for Simultaneous Preconcentration of Cu (II), Co (II), Cd (II), Ni (II) and Zn(II) Ions Prior to their Determination by MIS-FAAS

Nilgün Elyas Sodan, Ayşen Höl, Osman Çaylak and Latif Elçi

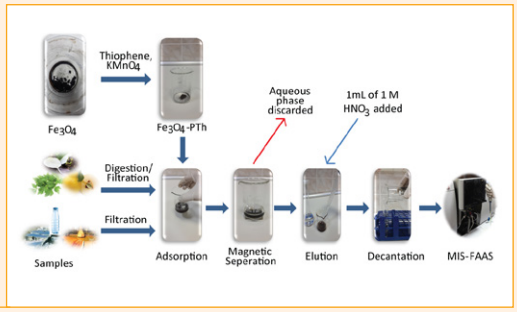

386–395 Biomedical applications

Prediction of Hit-to-Lead Ligand Molecule Interaction with G-Quadruplex DNA from c-Myc Oncogene Promoter Region

Petar M. Mitrasinovic

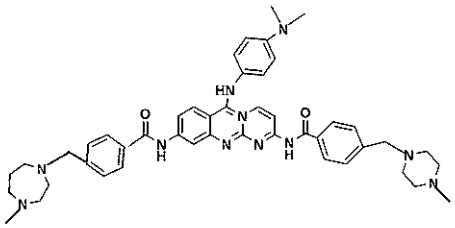

396–402 Analytical chemistry

Electrochemical Quantitative Assessment of Labetalol Hydrochloride in Pure Form and Combined Pharmaceutical Formulations

Maissa Yacoub Salem, Nagiba Yehia Hassan, Yasmin Mohamed Fayez, Samah Abd ELSabour Mohamed and Enas Shabaan Ali

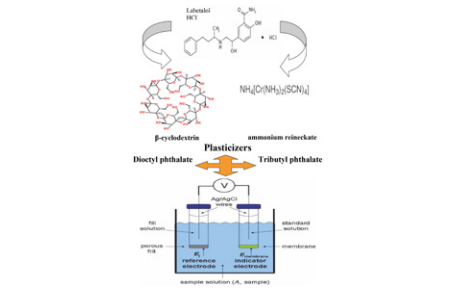

403–414 Organic chemistry

Synthesis of Bi-Heterocyclic Sulfonamides as Tyrosinase Inhibitors: Lineweaver–Burk Plot Evaluation and Computational Ascriptions

Muhammad Athar Abbasi, Zia-ur-Rehman, Aziz-ur-Rehman, Sabahat Zahra Siddiqui, Majid Nazir, Mubashir Hassan, Hussain Raza, Syed Adnan Ali Shah and Sung-Yum Seo

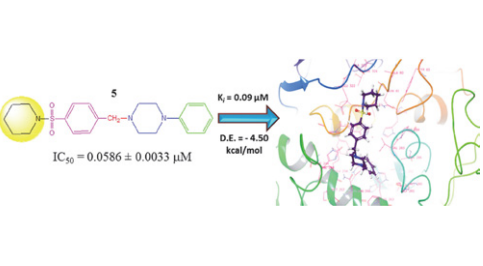

415–420 General chemistry

Specification of Zwitterionic or Non-Zwitterionic Structures of Amphoteric Compounds by Using Ionic Liquids

Leila Sheikhian, Morteza Akhond and Ghodratollah Absalan

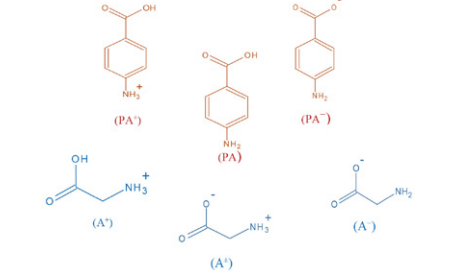

421–434 Organic chemistry

Preparation of Quinoline-2,4-dione Functionalized 1,2,3-Triazol-4-ylmethanols, 1,2,3-Triazole-4-carbaldehydes and 1,2,3-Triazole-4-carboxylic Acids

David Milićević, Roman Kimmel, Damijana Urankar, Andrej Pevec, Janez Košmrlj and Stanislav Kafka

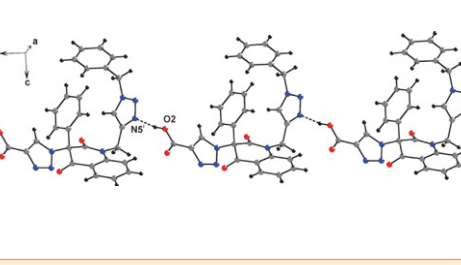

435–444 Chemical education

Demographic Characteristics of Chemistry Teachers in Croatia Affecting the Use of Pre-laboratory Activities in the Classroom

Snježana Smerdel and Meliha Zejnilagić Hajrić

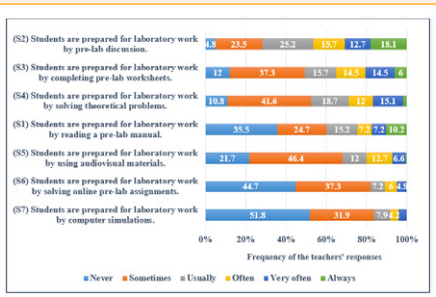

445–461 Applied chemistry

Characterization of Biomolecules with Antibiotic Activity from Endophytic Fungi *Phomopsis Species*

Janko Ignjatović, Nevena Maljurić, Jelena Golubović, Matjaž Ravnikar, Miloš Petković, Nika Savodnik, Borut Štrukelj and Biljana Otašević

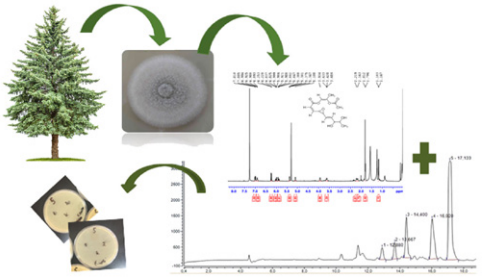

462–468 Biomedical applications

Facile Synthesis of Poly(DMAEMA-co-MPS)-coated Porous Silica Nanocarriers as Dual-targeting Drug Delivery Platform: Experimental and Biological Investigations

Mohammad Hegazy, Pei Zhou, Guangyu Wu, Nadia Taloub, Muhammad Zayed, Xin Huang and Yudong Huang

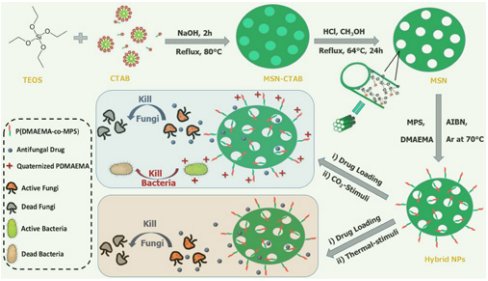

469–475 Materials science

Oxidized Carbon Nanohorns as Novel Sensing Layer for Resistive Humidity Sensor

Bogdan Catalin Serban, Octavian Buiu, Nicolae Dumbravescu, Cornel Cobianu, Viorel Avramescu, Mihai Brezeanu, Marius Bumbac and Cristina Mihaela Nicolescu

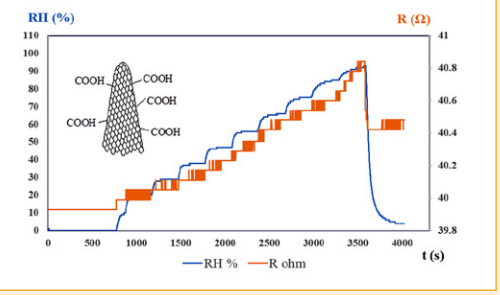

476–486 Materials science

Immobilized VO–Schiff Base Complex on Modified Graphene Oxide Nanosheets as an Efficient and Recyclable Heterogeneous Catalyst in Deep Desulfurization of Model Oil

Maryam Abdi, Abdollah Fallah Shojaei, Mohammad Ghadermazi and Zeinab Moradi-Shoeili

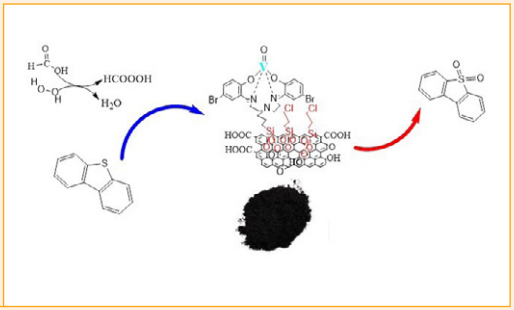

487–495 Inorganic chemistry

Encapsulation of Dirhenium(III) Carboxylates into Zirconium Phosphate

Anastasiia Slipkan, Nataliia Shtemenko, Dina Kytova and Alexander Shtemenko

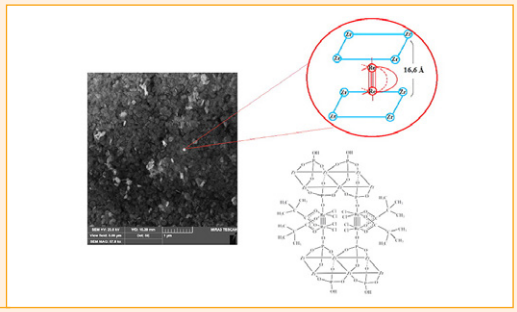

496–506 Biomedical applications

Effective Adsorption of Doxorubicin Hydrochloride on the Green Targeted Nanocomposite

Omid Arjmand, Mehdi Ardjmand, Ali Mohammad Amani and Mohmmad Hasan Eikani

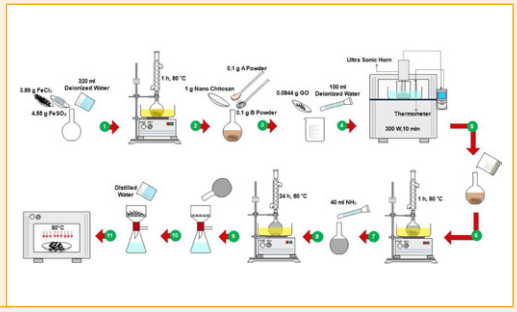

507–515 Inorganic chemistry

Hydrothermal Preparation, Crystal Structure, Photoluminescence and UV-Visible Diffuse Reflectance Spectroscopic Properties of a Novel Mononuclear Zinc Complex

Xiu-Guang Yi, Xiao-Niu Fang, Jin Guo, Jia Li and Zhen-Ping Xie

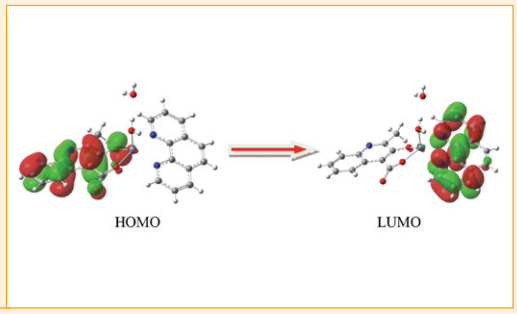

516–521 Inorganic chemistry

Nickel(II) Complex with a Flexidentate Ligand Derived from Acetohydrazide: Synthesis, Structural Characterization and Hirshfeld Surface Analysis

Rasoul Vafazadeh, Zahra Mansouri and Anthony C. Willis

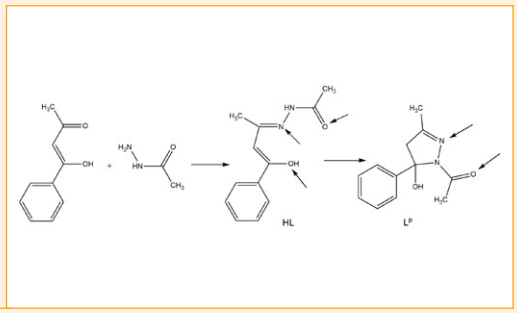

522–529 Materials science

Formation of Cobalt Ferrites Investigated by Transmission and Emission Mössbauer Spectroscopy

Vit Prochazka, Anezka Burvalova, Vlastimil Vrba, Josef Kopp and Petr Novak

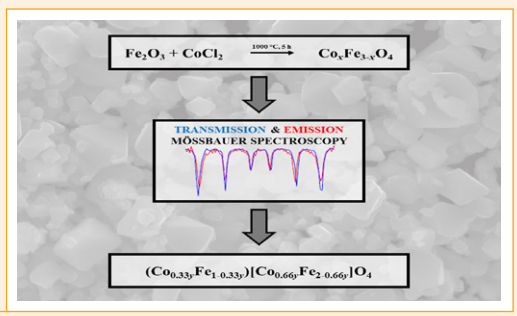

530–536 Analytical chemistry

FT-IR Spectroscopy for the Detection of Diethylene Glycol (DEG) Contaminant in Glycerin-Based Pharmaceutical Products and Food Supplements

Ayman Y. Hammoudeh, Safwan M. Obeidat, Eman Kh. Abboushi and Amal M. Mahmoud

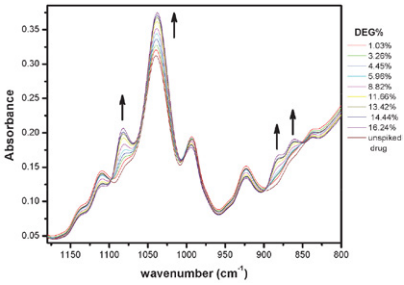

537–550 Chemical, biochemical and environmental engineering

Selective Colorimetric Detection of Mn^{2+} and Cr^{2+} Ions using Silver Nanoparticles Modified with Sodium Dodecyl Sulfonate and β-Cyclodextrin

Maryam Akhondi and Effat Jamalizadeh

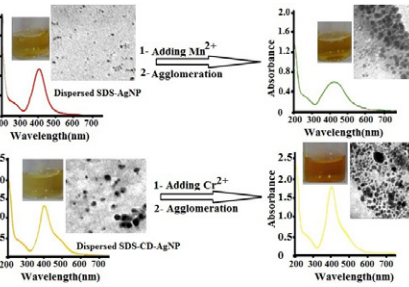

551–559 Inorganic chemistry

Synthesis and Characterization of Cross Linked Acetoguanamine Polymer Complexes: Investigation of their Thermal and Magnetic Properties

Gurkan Guney, Saban Uysal and Ziya Erdem Koc

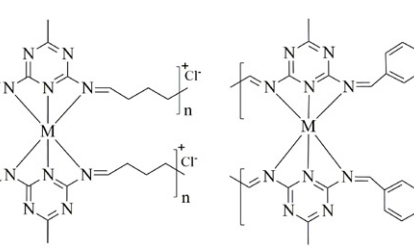

560–569 Organic chemistry

Synthesis and *in vitro* Anticancer Activity of Novel Heterocycles Utilizing Thiophene Incorporated Thioureido Substituent as Precursors

Marwa Abdel-Motaal, Asmaa L. Alanzy and Medhat Asem

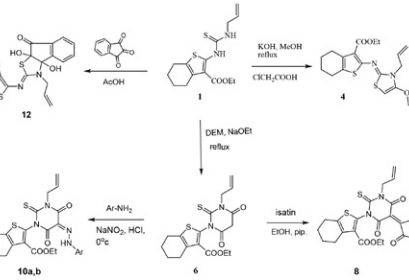

570–580 Physical chemistry

Adsorption Kinetics for CO_2 Capture using Cerium Oxide Impregnated on Activated Carbon

Azizul Hakim Lahuri, Michael Ling Nguang Khai, Afidah Abdul Rahim and Norazzizi Nordin

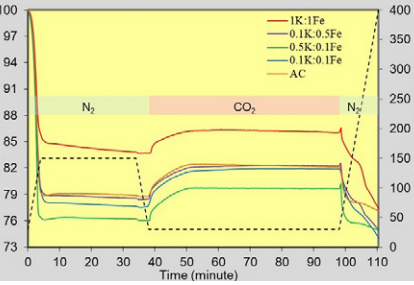

581–585 Inorganic chemistry

Two Zinc(II) Complexes with Similar Hydrazone Ligands: Syntheses, Crystal Structures and Antibacterial Activities

Ya-Li Sang, Xue-Song Lin and Wei-Dong Sun

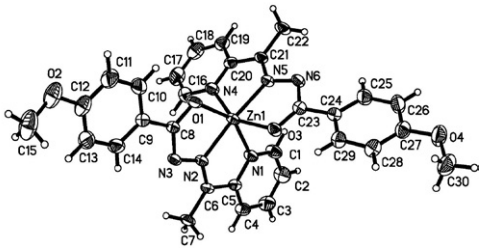

586–593 Organic chemistry

A Simple and Convenient Method for the Synthesis of 1-Methyl-7-arylfuro[3,2-*g*]pteridine-2,4(1*H*,3*H*)-diones and Their Substituted Derivatives

Maxim Stanislavovich Kazunin, Oleksii Yurievich Voskoboynik, Svetlana Valentynivna Shishkina, Oleksii Mykolayovych Antypenko and Sergey Ivanovich Kovalenko

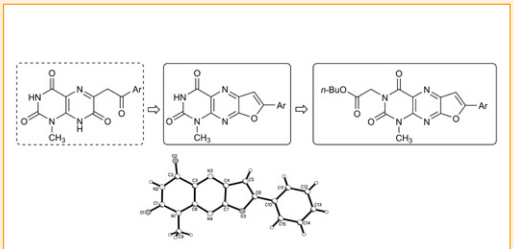

594–601 Inorganic chemistry

Study on the Complex Formation and the Ion-Association of Anionic Chelate of Molybdenum(VI) with Bidentate Ligand and the Cation of 2,3,5-Triphenyl-2*H*-tetrazolium Chloride

Kirila Stojnova, Petya Racheva, Vidka Divarova, Pavel Yanev and Vanya Lekova

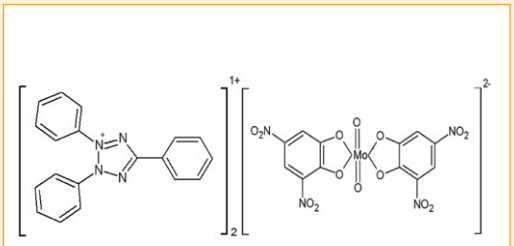

602–608 Chemical, biochemical and environmental engineering

Enhanced Adsorption of Lead (II) Ions from Aqueous Solution by a Chemically Modified Polyurethane

Mangaleshwaran Lakshmipathy, Muthukumaran Chandrasekaran and Rasappan Kulanthasamy

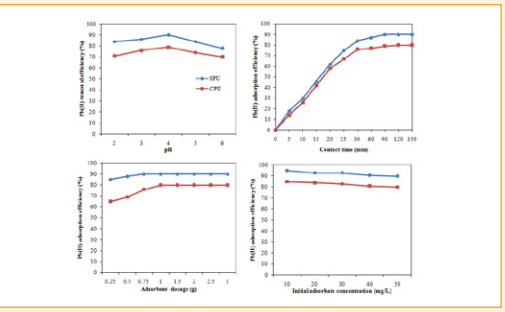

609–621 Physical chemistry

Enhanced Catalytic Degradation of Acid Orange 7 Dye by Peroxymonosulfate on Co_3O_4 Promoted by Bi_2O_3

Vanina Ivanova-Kolcheva, Labrini Sygellou and Maria Stoyanova

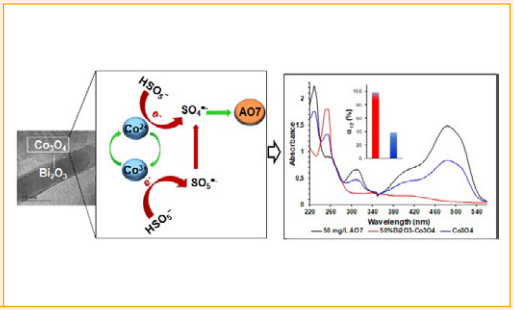

622–628 Inorganic chemistry

Magnetic, Photoluminescent and Semiconductor Properties of a 4*f*-5*d* Bromide Compound

Wen-Tong Chen

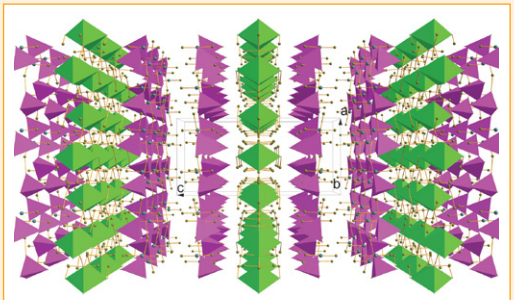

629–637 Physical chemistry

Study of Quinizarin Interaction with SDS Micelles as a Model System for Biological Membranes

Ana Maria Toader, Petruta Oancea and Mirela Enache

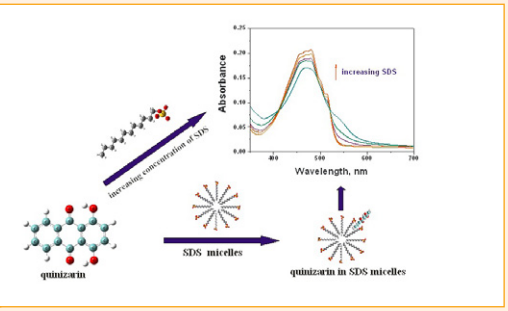

638–643 Inorganic chemistry

***N'*-(2-Hydroxybenzylidene)-3-Methylbenzohydrazide and its Copper(II) Complex: Syntheses, Characterization, Crystal Structures and Biological Activity**

Hui Zhao, Xiang-Peng Tan, Qi-An Peng, Cong-Zhong Shi, Yi-Fei Zhao and Yong-Ming Cui

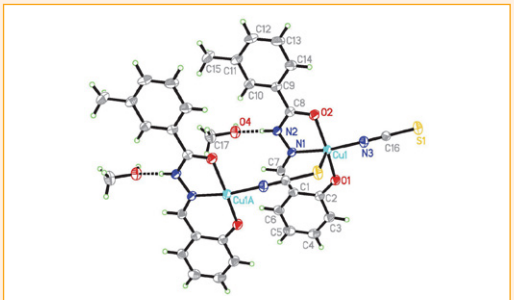

644–650 Inorganic chemistry

Synthesis, X-Ray Crystal Structure of Oxidovanadium(V) Complex Derived from 4-Bromo-*N'*-(2-hydroxybenzylidene)benzohydrazide with Catalytic Epoxidation Property

Qi-An Peng, Xiang-Peng Tan, Yi-Di Wang, Si-Huan Wang, You-Xin Jiang and Yong-Ming Cui

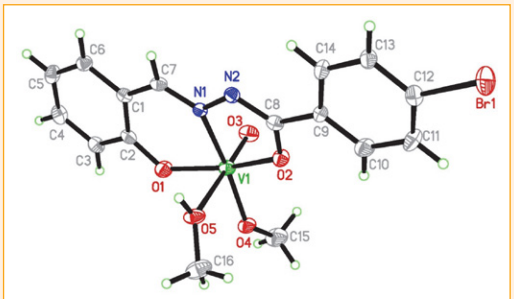

651–665 Chemical, biochemical and environmental engineering

Kinetic Analysis of Poly(ε-caprolactone)/poly(lactic acid) Blends with Low-cost Natural Thermoplastic Starch

Vesna Ocelić Bulatović, Miće Jakić and Dajana Kučić Grgić

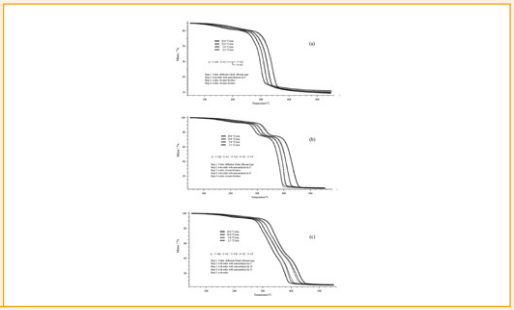

666–673 Biomedical applications

The c.3140-26A>G Variant of the *CFTR* Gene in Homozygous State Causes Mild Cystic Fibrosis – Overview of Longitudinal Clinical Data of the Patient Managed in our CF Center and Review of the Literature

Ana Kotnik Pirš, Uroš Krivec and Katarina Trebušak Podkrajšek

The c.3140-26A>G Variant of the *CFTR* Gene

674–681 Biomedical applications

Active Forces of Myosin Motors May Control Endovesiculation of Red Blood Cells

Samo Penič, Miha Fošnarič, Luka Mesarec, Aleš Iglič and Veronika Kralj-Iglič

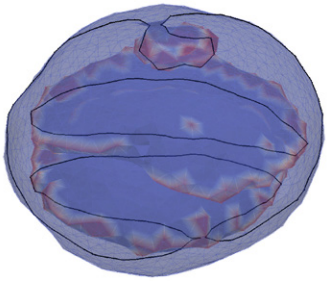

DRUŠTVENE VESTI

S49–S61 Chemical education

Richard Klemen, the First Lecturer of Enzymology at the University of Ljubljana

Marko Dolinar

Feature article

Post Polymerisation Hypercrosslinking with Emulsion Templating for Hierarchical and Multi-Level Porous Polymers

Amadeja Koler,[1] Irena Pulko[2] and Peter Krajnc[1,*]

[1] *University of Maribor, Faculty of Chemistry and Chemical Engineering, PolyOrgLab, Smetanova 17, Maribor, Slovenia*

[2] *Faculty of Polymer Technology, Ozare 19, Slovenj Gradec, Slovenia*

* *Corresponding author: E-mail: peter.krajnc@um.si*

Received: 02-11-2020

Abstract

Porosity in polymers and polymeric materials adds to their functionality due to achieving the desired tailored characteristics porosity offers, such as improved mass transfer through the material, improved accessibility of reactive sites, reduced overall mass, tunable separation properties, etc. Therefore, applications in many fields, e.g. catalysis, separation, solid phase synthesis, adsorption, sensing, biomedical devices etc., drive the development of polymers with controlled morphology in terms of pore size, shape, interconnectivity and pore size distribution. Of particular interest are polymers with distinct bimodal or hierarchical pore distribution as this enables uses in applications where pore sizes on multiple levels are needed. Emulsion templating can be used for the preparation of polymers with included interconnected spherical pores on the micrometre level while post polymerisation crosslinking adds micro porosity. Combined use of both techniques yields multi-level and hierarchically porous materials with great application potential.

Keywords: PolyHIPE; hypercrosslinking; porous polymers; porosity; emulsion templating; hierarchical polymers

1. Introduction

Methods for generation of porosity in polymers can be generally divided into chemical and physical. Among physical methods, various templating can be used while post polymerisation crosslinking and phase separation induced syneresis are examples of chemical methods (Figure 1). According to IUPAC guidelines,[1] pores are referred to as macro (diameters over 50 nm), meso (diameters between 2 and 50 nm) and micro (diameters less than 2 nm). In terms of pore size distribution, it can be statistical however materials with distinct bimodal or hierarchical pore distribution can be prepared meaning that micro and macro pores are present or that pore size distribution follows a hierarchical concept where a multi-level porous material is produced with pore size levels following one after another. Among templating methods, emulsion templating is widely used.[2–7] Both water-in-oil and oil-in-water emulsions can be used for the purpose of macro porosity induction during the polymerisation process. When a high concentration of the droplet phase is used, droplets' shapes become distorted and a dispersion of droplet size is observed (Figure 2). In the case of inclusion of monomers into the continuous phase the polymerisation results in a monolithic porous material, typically with an interconnected porosity which is the result of the shrinkage of continuous phase volume at the sol-gel transition. In the case of uniform packing of monodisperse spherical droplets, the volume of the droplet phase accounts for 74,05% of the total emulsion volume while at random packing this share is lower, namely 64%.[8] Polymers prepared from emulsions with droplet phase volume shares higher than these border values are termed polyHIPEs, following the abbreviation for high internal phase emulsion.[9] The internal topology of so prepared polymeric material features two levels of pores, the primary pores, termed cavities and secondary, interconnecting pores (Figure 3). The size of primary pores follows the size of the droplets prior to polymerisation as demonstrated by a series of experiments containing emulsion aging and room temperature polymerisation initiation with a redox initiation pair.[10] Therefore, the control of emulsion droplet size prior to polymerisation is the main control also for the primary pore size. The main factors controlling emulsion droplet size include emulsion

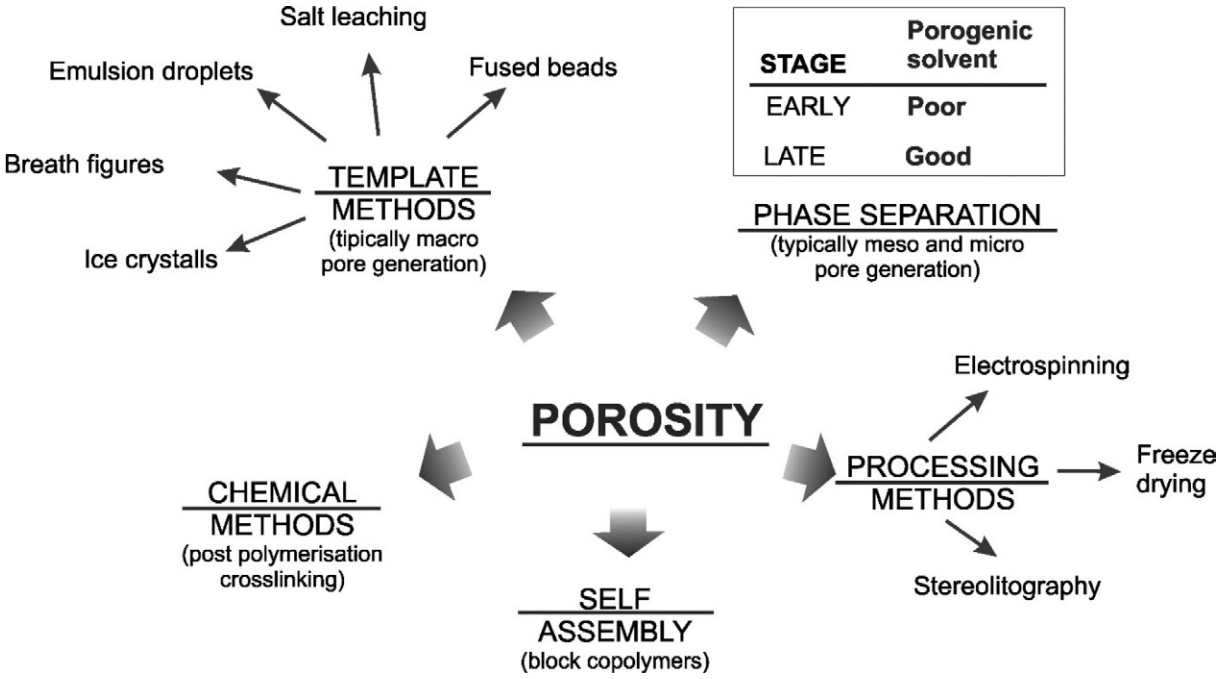

Figure 1: Methods for porosity creation in polymers

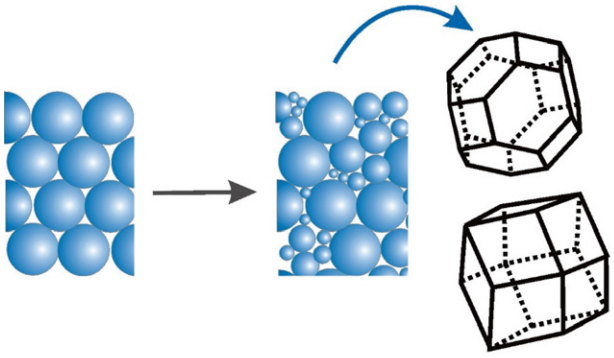

Figure 2: Droplet size and shape change at emulsion concentration

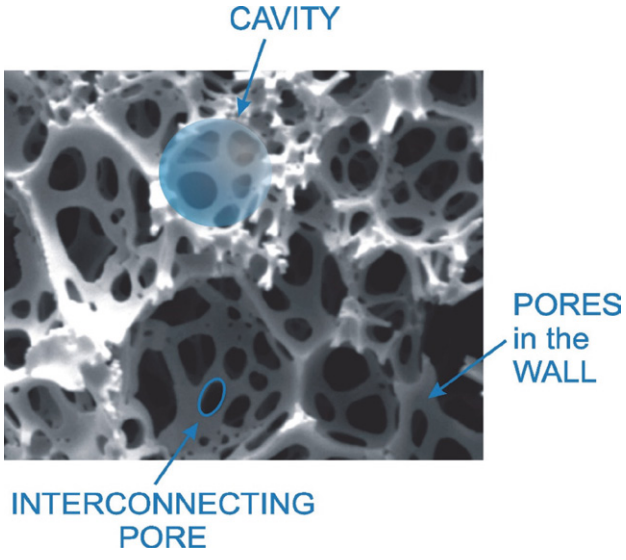

Figure 3: PolyHIPE morphology

stabilization by surfactant molecules and energy input at emulsion preparation.

On the other hand, the frequency and size of interconnecting pores determine the connectivity of porous structure or what could be defined as the *openness* of the structure (Figure 4).[11]

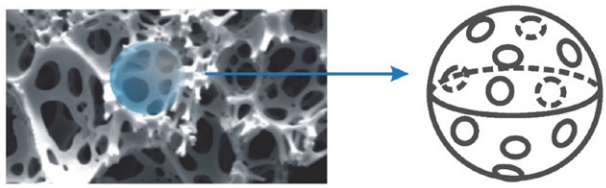

$$O = \frac{\text{Open surface of cavity}}{\text{Surface of cavity}} = \frac{S_O}{S_C}$$

Figure 4: Interconnectivity of porous structure in polyHIPEs

The thickness of the film of continuous phase between the adjacent droplets seems to be the main factor affecting the size and frequency of the interconnecting pores. This is mainly determined by the droplet to continuous phase volume ratio and by the concentration and structure of the surfactant(s). In summary, main factors determining the morphological features of polyHIPEs are volume ratio of droplet/continuous phase, energy input at preparation, and surfactant concentration and structure. Many other variables were considered and their role can be important. This makes a polymerizable HIPE a multi variable system and careful experimental consideration must be involved when planning a particular structure (Figure 5, Table 1).

Table 1: Experimental factors and their effect on HIPE stability and polyHIPE morphology

Experimental factor	Effect on HIPE stability	Effect of polyHIPE morphology
Rate of stirring	Higher rates-increase in stability	Smaller cavities
Time of stirring	Prolonged stirring-increase in stability	Reduced dispersion of cavities
Viscosity	Increase in viscosity-increase in stability	Smaller cavities
Surfactant content	Lowers the interfacial tension	Increase in interconnectivity
Temperature	Increase in temperature-enhances the coalescence, reduces stability	Increase in cavity size, increased dispersion.
stabilizing salts	Enhance the rigidity of the interfacial film-enhances stability. Inhibiting Ostwald ripening.	Reduces cavity size

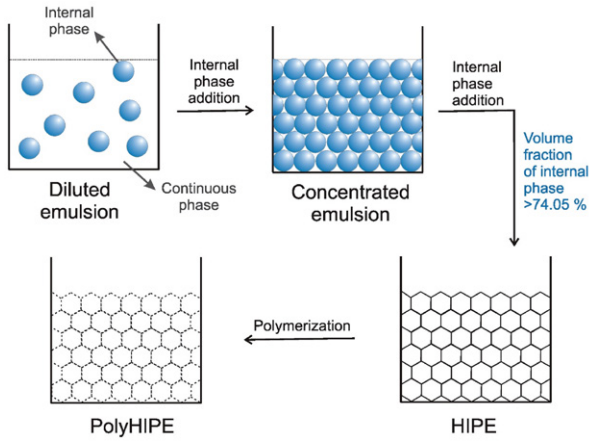

Figure 5: polyHIPE preparation

2. Recent Advances in PolyHIPE Synthesis and Creation of Multi-Level Porosity

While water-in-oil high internal phase emulsions are most commonly used for the preparation of polyHIPE polymers, other emulsion based systems have also been described. Both oil-in-water and oil-in-oil high internal phase emulsions can be applied.[12] For water soluble or hydrophilic monomers, solvents such as hydrocarbons or benzene derivatives were used as the droplet phase. In such manner, polyHIPEs were prepared from acrylic acid,[13] 2-hydroxyethyl methacrylate,[14–18] *N*-isopropyl acrylamide (NiPAAm),[19,20] acrylamide,[21] 1-vinyl-5-aminotetrazole,[22,23] and dimethylaminoethyl methacrylate.[24]

Furthermore, combination of emulsion templating and other porosity induction techniques, have yielded hierarchically porous polymer materials. Sušec et al.[25] and Johnson et al.[26] have demonstrated the principle of applying a high internal phase emulsion within a stereophotolithographic based additive manufacturing setup. With such a system, a three-dimensional object can be built using a lithographic photo polymerizable system. Due to the use of a high internal phase emulsion with photo polymerizable monomers in the continuous phase, the object has an internal polyHIPE structure. Thus, another level of porosity is created using the lithographic process while pores of smaller dimensions are created as a result of emulsion templating. Monomer mixtures particularly suitable for such photo polymerisation were found to be multifunctional thiols and alkenes producing polymer networks via the thiol-ene click reaction.[27]

Another recent example of adding structure complexity is the use of hard sphere templating. Within this approach, spherical particles (typically polymeric) are fused together, to construct a monolithic porous network with interconnected porosity. So constructed material is then impregnated with a monomer mixture, polymerized while the previously constructed template dissolved. Macroporous polymethacrylates prepared in this way have open interconnected porosity and have been used as scaffolds in tissue engineering applications.[28–31] We have shown that a combination of this hard sphere templating and high internal phase emulsion templating can yield polymers with open interconnected and hierarchical porosity which is especially advantageous in biomedical applications such as tissue constructs.[32] Primary monolithic template was formed by sintering polymethyl methacrylate beads and subsequently filled with a high internal phase emulsion containing thiols and alkenes as monomers in the continuous phase (Figure 6). Photopolymerisation yielded hierarchically structured polymer network with open porosity and biodegradability was introduced by the use of thiol monomers with ester groups. (Figure 7) So prepared multi-level porous polymers were successfully applied as scaffolds for human bone cell growth.

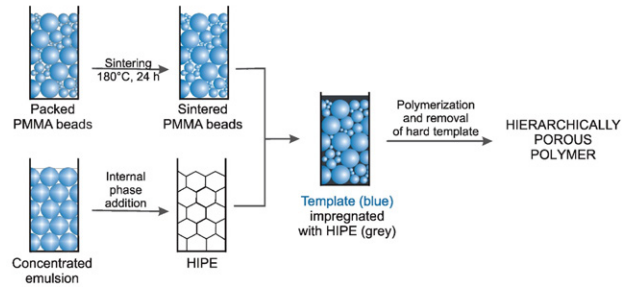

Figure 6: Combination of hard sphere and emulsion templating

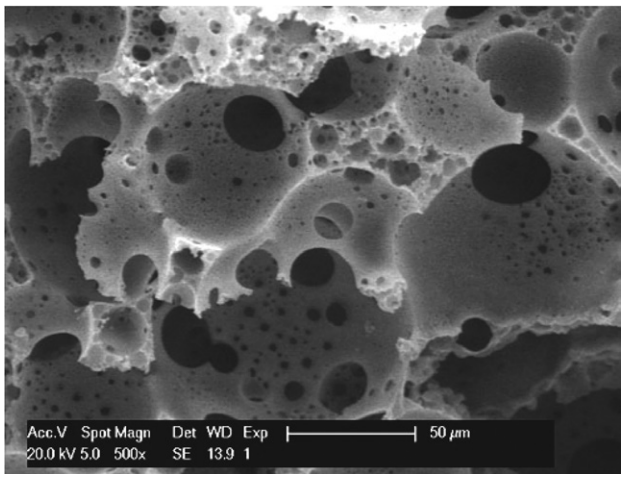

Figure 7: Scanning electron micrograph of hierarchically porous polymer prepared by combining hard sphere and emulsion templating

While electrospinning is in itself a method producing porous fibrous structures from polymer solutions or melts,[33,34] high internal phase emulsion templating has been used in combination with electrospinning to add a level of porosity to the product.[35,36] Using this combination, fibres with bicontinuous morphology were obtained by electrospinning HIPEs consisting of aqueous poly(vinyl alcohol) solutions dispersed within polycaprolactone-in-toluene solutions.[35] Similarly, Dikici et al.[36] used a polycaprolactone barrier membranes to form bilayers by combining electrospinning and emulsion templating techniques and applied them for guided bone regeneration. The electrospunn fibres had a mixture of open and closed cell porous polyHIPE type morphology.

3. Inducing Meso and Micro Porosity Within PolyHIPEs

Due to relatively large pores induced by the droplet phase in polyHIPE preparation, the result is a macroporous material with primary pore sizes typically between 500 nm and 100 μm. Consequently, specific surface areas of polyHIPEs are low, usually below 50 m^2/g. This is the result of the lack of meso and micro porosity. For many applications surface area of the polymer support plays a vital role. Early attempts of improving specific surface areas of polyHIPEs mostly included the addition of porogenic solvents to the monomer containing continuous phase[37] and increasing the crosslinking degree[38] thus producing polyHIPEs with specific surface areas up to 550 m^2/g. Introduction of porogenic solvent into the monomer containing continuous phase induces meso porosity via either early or late phase separation within the gelation process during the polymerisation.[39] Surfactant concentration and structure also affect the surface area of styrene based polyHIPEs.[40] However, both methods, namely adding porogenic solvent and surfactant to the monomer containing continuous phase increase the nominal porosity which results in sacrificing the material mechanical properties in terms of elastic modulus and brittleness. The morphology of polymers prepared by the addition of porogenic solvents include a fused-bead, cauliflower-like features which is not optimal for mechanical properties.[39] Our study comparing materials with fused-bead and polyHIPE morphology showed that polyHIPE structure is superior to fused-bead morphology allowing for the preparation of materials with overall porosities higher than 75%.[32] Combining high porosity with sufficient mechanical stability is an important materials feature with applications in mind. For example, permeable open cellular polyHIPEs for chromatography stationary phases and membranes with significantly higher porosity compared to commercially available monolithic columns facilitate lower back pressures and thus the efficiency of separation.[41–50]

4. Post Polymerisation Crosslinking

In order to avoid the formation of fused bead type morphology within the formulating polymer film of the continuous phase of a high internal phase emulsion, a post polymerisation crosslinking of already formed polyHIPE material can be attempted.

Post polymerisation crosslinking, in this description referred to as hypercrosslinking, is a method of polymer chain crosslinking and the result is the creation of numerous new pores at meso and micro size scale and thus the creation of meso and/or microporous polymer material.[51,52] The porous profile of hypercrosslinked polymers differs from the porous profile of polymers prepared by free radical polymerisation of monomers and crosslinkers. The porosity of polymers prepared by conventional copolymerisation is the result of phase separation during polymerisation in the presence of an inert diluent, which may be either a non-solvent or a thermodynamically good solvent. The non-solvent does not dissolve the growing crosslinked chains, so the network shrinks and precipitates into micro spheres. These non-porous nodules aggregate and agglomerate in a cauliflower-like structure, and the prepared material is macroporous.[53–55] When a good solvent is used, the polymer network swells, but at high crosslinking degrees it can no longer adsorb the diluent. This results in phase separation in the form of micro and macrosyneresis.[56] In the case of macrosyneresis, a macro porous network is formed as the resulting gel decomposes and thus a microgel is formed, which behaves as a continuous phase in the reaction mixture. These particles then agglomerate during the polymerisation to form a macroporous network. While in microsyneresis the diluent is distributed over the gel. The result of the whole texture is a macroporous network with cauliflower-like structure, but

having micro pores due to the primary polymer nodules.[53–55] By using a diluent during radical crosslinking even in the continuous phase of high internal phase emulsions, macroporous materials are obtained. Microsyneresis also introduces micro pores, thus influencing the increase of specific surface area. However, frequently, due to strong capillary forces, the micro pores in polyHIPE collapse during solvent removal.

Unlike traditional crosslinking polymerisation, hypercrosslinked polymers are prepared by post polymerisation crosslinking of long polymer chains in a semi-solution state creating many new bridges. This does not result in phase separation because the polymer chains are distributed throughout the solution and are strongly solvated throughout the hypercrosslinking. A typical example of such process is heating of solvated chloromethylated polystyrene in the presence of a Friedel-Crafts catalyst. This creates new connections by converting chloromethyl groups into methylene bridges that interconnect polymer chains. When the swelling solvent is removed by drying, the additional crosslinking prevents complete collapse of the polymer network and the resulting polymers exhibit extensive microporosity even in the dry state. Initially, the formation of methylene bridges is fast because the mobility of the polymer chains in the swollen polymer is higher than later in the reaction, when the polymer chains are already connected to the newly formed methylene bridges. By introducing new methylene bridges into the network, pores are formed as spaces between highly cross-linked nodules. In further stages of hypercrosslinking, the rigidity of the nodules increases and therefore, after solvent removal, the morphology results in a stable microporous network.[52,57] Hypercrosslinked polymers prepared from gel-type precursors contain only the micro pores. If, on the other hand macroporous polymer is used as the precursor, the product then contains beside the macro pores also micro pores, and a polymer with a bimodal pore distribution is formed. Hypercrosslinked polymers contain a very high density of crosslinks creating micro pores and exhibit high surface areas up to 2000 m^2/g.[58,59] After the removal of the solvent, micro pores remain, which increases compatibility with both polar and non-polar solvents,[60,61] what is extremely important for applications. The chemical nature of the conventionally prepared STY/DVB polymer is very similar to the hypercrosslinked polymers that have many methylene bridges between polymer chains. However, these materials differ crucially in terms of topology and mechanical properties. STY / DVB copolymers are prepared without the addition of solvent, which means that their polymer chains are very densely packed in dry state, due to the strong attraction between them. Under these conditions, the polymers swell in thermodynamically good solvents, since the polymer-polymer interactions are replaced by stronger polymer-solvent interactions. Hypercrosslinked polymers, however, are prepared in the presence of an excess of good solvent, and if the crosslinking rate is high and conformational rigid connections are established, then the polymer chains are not densely packed after removal of the solvent. The final material in the dry state has high free volume and significantly reduced polymer-polymer interactions. It is essential that due to the affinity between the polymer fragments, the rigid structure of the hypercrosslinked polymer causes high inner stresses in the polymer chains of the network. Because of this, the hypercrosslinked materials tend to release inner stresses, which happens when the network is expanded, that is, when it swells. Swelling is possible on contacting any liquid, regardless of thermodynamic affinity with the polymer which means that the hypercrosslinked polymers are compatible with both thermodynamically good and bad solvents.[60,62]

Hypercrosslinking can be achieved by different chemical methods and can be divided into: post polymerisation crosslinking (hypercrosslinking using polystyrene precursors, hypercrosslinking using VBC / DVB precursors), direct one-step polycondensation of functional monomers and hypercrosslinking by the so called *knitting* method.

4. 1. Hypercrosslinking of Polystyrene Precursurs (*Davankov* Resins)

Introduction of hypercrosslinking of polymer chains dates into 70's when hypercrosslinked polystyrene (PS) was demonstrated, using linear PS or gel-type swollen polystyrene-co-divinylbenzene and external crosslinkers in the presence of Lewis acid catalyst and solvents.[63] External crosslinkers create new covalent bonds between polystyrene chains applying the Friedel-Crafts reaction[61,64,65] (Scheme 1). This reaction achieves short and rigid connections and forms a rigid three-dimensional polymer network. Almost all aromatic rings can be consumed in this reaction, which results in a high degree of hypercrosslinking, and consequently in a large number of newly formed links and a high specific surface area of the materials.[51] Typical protocol for hypercrosslinking of linear polystyrene or the STY / DVB copolymer contains introducing a sufficient amount of external crosslinker into the dissolved linear polystyrene or swollen polystyrene network and adding the Lewis acid while cooling the reaction medium to achieve homogeneous distribution of the catalyst before gelation of the mixture. The mixture is then heated, allowing high conversion of the reactive linker groups.[66] As external linkers, chloroalkanes are most commonly used; usually dichloroethane, as it plays two roles - as an external linker and a good solvent for PS.

Chloromethyl ether was used predominantly for the hypercrosslinking of polystyrene, but was replaced by monochlorodimethyl ether,[60,67–69] carbon tetrachloride,[70,71] dichloroxylene,[64,72] 4,4'-bis (chloromethyl)-biphenyl,[64,72] trifunctional tris-(chloromethyl)-mesitylene,[51] 4,4'-bis-chloromethyl-1,4-diphenylbutane,[51] formalde-

hyde dimethyl acetal[71–74] or dichloroethane[51,75,76] and other dichloroalkanes,[76] due to its adverse health effects. It should be noted that the length of the external crosslinker affects the rigidity of the hypercrosslinked material, which also affects the morphology of the material. All the compounds form bridges of a limited conformational mobility in the final network except for diphenylbutane. In this case, the diphenylmethane crosslinker type are most influenced by the rigidity of the structure. Another limitation in mobility is tris-(chloromethyl)-mesitylene because it links three polystyrene chains at one point.

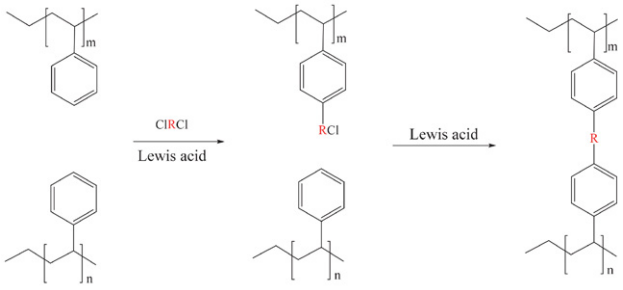

Scheme 1: Post polymerisation hypercrosslinking: Hypercrosslinking using polystyrene precursurs (*Davankov* resins)

When PS with a low degree of initial crosslinking (0.3–2%) is used for hypercrosslinking, intrinsic microporosity is formed. However, if the initial degree of crosslinking is increased, the macroporous network is formed prior to hypercrosslinking, so the final pore distribution is bimodal.[61,77]

Due to their high surface area, good solvent compatibility and good mechanical properties, bimodal porosity and interpenetrating network, hypercrosslinked polystyrenes are often used as adsorbents for gases[78,79] and various organic molecules,[57,80,81] for chromatographic separation,[82–84] or for adsorbents for blood purification.[85]

4. 2. Hypercrosslinking Using Chloromethylated Groups of Vinylbenzyl Chloride

Hypercrosslinking can be performed on polyvinylbenzyl chloride or its copolymers utilizing vinylbenzyl chloride moieties in the polymer chains as internal electrophiles in the Friedel-Crafts reaction, without the addition of external linkers (Scheme 2).[58,61] In this reaction, the chloromethyl groups are converted to methylene bridges and thus new links are created. The aromatic ring which is to be substituted is electron-rich, resulting in a formation of six-membered ring following the cyclization reaction. As with Davankov's type of hypercrosslinking, $FeCl_3$ is most commonly used as a Friedel-Crafts catalyst because it has good solubility in the usual solvents used and does not cause steric hindrance.[58] Due to the similarity of the polystyrene network to VBC / DVB network, the same solvents are used, most commonly DCE. The morphology of polymers hypercrosslinked by this post-polymerisation approach is similar to *Davankov* type resins meaning that hypercrosslinking induces micro pores and results in a significant increase of specific surface area. This was demonstrated by hypercrosslinking several poly (VBC-DVB) copolymers with DVB content between 2% and 20%.[58] The specific surface area of hypercrossliked products depended on the initial crosslinking and reaction time, being highest with lowest initial crosslinking and increasing with reaction time up to 2 hours while further elongation of reaction time had no effect. Decrease in the chloride content of the polymer coincides with the drastic increase in the specific surface area.

The importance of initial crosslinking for efficiency of hypercrosslinking and final porous structure was confirmed in another report.[86] The maximum specific surface area was achieved after hypercrosslinking of polymer containing 2% of DVB (2060 m^2/g). By increasing the DVB amount, a bimodal structure was formed, with well-defined macro and micro pores, while at 7% of DVB the structure was completely micro porous. Increasing the surface area after hypercrosslinking of VBC/DVB polymers at a lower DVB content occurs because the macromolecular chains of the polymer are still very loose and can orient more favorably in the presence of solvent in the hypercrosslinking process, thus forming more methylene bridges than in the case of higher crosslinked poly (VBC / DVB).

One of the most advantageous consequences of hypercrosslinking VBC / DVB polymers is their improved sorption properties. Unlike non-functionalized hypercrosslinked polystyrene, which is a good sorbent due to hydrophobic π-π interactions,[82] functional groups can undoubtedly improve the adsorption properties, which in turn can affect the development of many applications.[87–91]

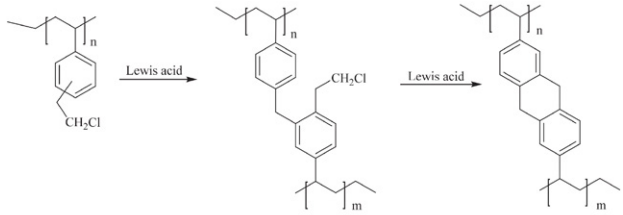

Scheme 2: Post polymerisation hypercrosslinking : Hypercrosslinking using chloromethylated groups of vinylbenzyl chloride

4. 3. Direct Hypercrosslinking Arising from Polycondensation

Hypercrosslinked polymers can also be produced by the direct polycondensation of small molecule monomers without the need to make the precursor crosslinked polymer. However, the synthesis of polymer precursors is

time-consuming and limited functional monomers can be selected to satisfy the combined conditions from reactions of radical polymerisation and Friedel–Crafts alkylation. Similarly to the other hypercrosslinking approaches, these use DCE as a solvent and $FeCl_3$ as a Friedel-Crafts catalysts. The resulting networks can be considered the analogues of the Friedel-Crafts linked PS materials. This direct approach creates microporous organic networks and uses bis(chloromethyl) aromatic monomers such as dichloroxylene,[92] bis(chloromethyl)biphenyl,[75,93] and bis(chloromethyl) anthracene.[75,93] By using Lewis acid as a catalyst, the chloromethylene groups react with adjacent phenyl rings. This results in the formation of rigid methylene bonds between the rings, which in turn produces micro pores and high specific surface areas up to 2000 m^2/g.[93] Due to high specific surface areas hypercrosslinked polymers using polycondensation have good gas adsorption capacity.[75,93–95] The use of *o*-DCX isomers for condensation with *m*-DCX or *p*-DCX has been found to have an adverse effect on the growth of specific surface areas, while *m*-DCX and *p*-DCX provide materials with comparable specific surface areas.[75] For well-defined micro porous polymers, DCX and BCMBP were used as crosslinkers in order to connect heterocyclic (carbazole), metal-doped (ferrocene) and highly rigid (triptycene) building blocks. It was also found that the length of crosslinkers can affect the porosity of the resulting polymer. For example, longer crosslinker molecules affect larger pores, while shorter molecules create micro pores, thereby contributing to an increase in the specific surface area of the polymer.[96] Fluorene derivatives (fluorene, 9,90-spirobi(fluorene), dibenzofuran and dibenzothiophene) were also used as non-functional aromatic precursors, which showed good microstructure in condensation with BCMBP under Friedel-Crafts catalytic conditions. The highest surface area of up to 1800 m^2/g was obtained from dibenzofurane monomers with 10% molar fraction.[95]

Aromatic precursors used in addition to benzene[97,98] were polyaniline,[95] polypyrrole,[94] polythiophene, polyfurane, aniline, carbazole,[99,100] aminobenzene,[101] bishydroxymethyl monomers,[102] and were found to form hypercrosslinked polymers.

4. 4. Knitting Aromatic Compound Polymers Using an External Crosslinker

A special type of one-step polycondensation, however, is the "knitting" method for hypercrosslinking with an external crosslinker-formaldehyde dimethyl acetal FDA, which is more environmentally friendly as it has no dangerous by-products during the Friedel-Crafts reaction. The mechanism of the reaction is proposed as: Lewis acid first complexes with the crosslinking molecule, which reduces the interaction between the methoxyl group and the central carbon atom, and then produces a large number of intermediate carbocations in the DCE (Scheme 3).[98] The carbocations then react with the phenyl ring and the addition of the multi - methoxymethyl groups to the aromatic ring proceeds, releasing methanol. The methoxymethyl groups are then converted to methylene links and reacted with other phenyl rings to form a rigid crosslinked structure.

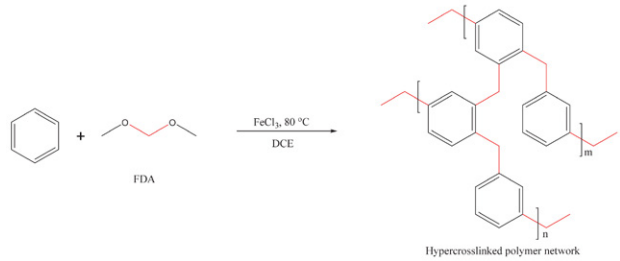

Scheme 3: Typical hypercrosslinking by the knitting method from benzene monomers[98]

Typically, in this one-step approach, the aromatic monomer (including benzene, phenol or chlorobenzene), the crosslinker (FDA) and the catalyst ($FeCl_3$) are dissolved in DCE to complete the condensation.[98] Increasing the FDA crosslinker content of hypercrosslinked materials obtained using tetraphenylmethane blocks also increases the specific surface area up to 1314 m^2/g.[103] Similar approaches using FDA as external crosslinker were shown with different monomers such as aromatic heterocycles,[104,105] hydroxymethylated aromatic molecules,[102] aniline and benzene,[72,97] styrene[105] and tetrahedral monomers,[106,107] among others. The "knitting" method is used for the design and synthesis of microporous polymers based on various rigid aromatic building blocks, including nonhalogenated monomers. 1,4-dimethoxybenzene was also used as an external crosslinker.[108]

5. Hypercrosslinking of PolyHIPEs

Hypercrosslinking of polyHIPE polymers results in rigid polymers with induced meso and microporosity (tertiary pores) in macroporous material which leads to very high specific surface areas due to induction of micro and meso pores. Research so far shows that the morphology of polyHIPEs does not change significantly after hypercrosslinking and the typical open cellular macroporous structure is retained.[59] Rigid connections created during hypercrosslinking make better compatibility with both thermodynamically good and bad solvents and thus better accessibility of reactive sites. As a result, hierarchically porous material is obtained with macro pores that allow convective transfer and reduce back pressure in flow systems, and at the same time with high specific surface area due to the presence of micro and meso pores allowing good accessibility of reactive sites. PolyHIPEs with hierarchical or

bimodal porosity can be very useful in many applications as demonstrated by various research groups.

Schwab et al.[77] synthesized VBC / DVB polyHIPE monoliths, and the DVB molar fraction varied between 2.5 and 40%. Materials were hypercrosslinked by Friedel-Crafts alkylation reaction in the presence of a Lewis base to give monoliths with specific surface areas up to 1200 m^2/g, while maintaining the morphology of precursor polyHIPE. Due to hypercrosslinking, the non-porous walls of polyHIPEs have become highly microporous. Such monolithic VBC based polyHIPE polymers with bimodal structure were proven to be very promising for n-butane storage and the results were comparable to the commercially available Sorbonorit powder. In another report, VBC based polyHIPEs with 2 mol% DVB content were used for controlled hypercrosslinking to leave some unreacted benzyl chloride groups for further binding of methyl amino pyridine. Functionalized hypercrosslinked polyHIPE was used as a very effective nucleophilic catalyst for the alkylation of methylcyclohexanol with acetic anhydride due to its hierarchical porosity and high specific surface area. It was found that after 3 hours, 100% alkylation conversion was achieved using hypercrosslinked polyHIPE-MAP while non hypercrosslinked materials performed significantly worse demonstrating the advantage of the bimodal pore structure with facilitated mass transfer.[59]

In addition to hypercrosslinking styrene type polyHIPEs with an internal crosslinker, Friedel-Crafts reaction with an external crosslinker was used. Crosslinked STY / DVB polyHIPEs were used for hypercrosslinking using formaldehyde dimethyl acetal as the external crosslinker applying the knitting approach. This hypercrosslinking method resulted in polyHIPE monoliths with specific surface areas between up to 595 m^2/g. Due to their extremely hydrophobic surface, the hypercrosslinked STY / DVB polyHIPE materials have shown good absorption capacity for oils, and could be used for oil-spill cleaning.[109]

Knitting type hypercrosslinking was also used to synthesize porous carbon foams, which were produced by carbonizing the STY / DVB hypercrosslinked polyHIPEs. Dimethoxymethane was used as an external crosslinker for hypercrosslinking. It was found that the STY / DVB ratio of polyHIPE precursors is strongly influenced by char yield, micro pore volume and BET surface area of carbonized polyHIPEs.[110]

Silverstein et al. synthesized porous carbons with high specific surface areas and hierarchical porous structure by pyrolysis of hypercrosslinked VBC/DVB polyHIPEs. [111] Hypercrosslinking generated new links which limited the degradation of polyHIPE morphology after pyrolysis. Surface areas of pyrolyzed hypercrosslinked polyHIPEs were as high as 553 m^2/g, which meant less than 40% reduction compared to precursor polymers. Hypercrosslinking via $FeCl_3$ catalysis was further used to synthesize acrylonitrile-DVB polyHIPEs, which were used for pyrolysis to produce nitrogen- and oxygen-codoped carbo-polyHIPEs with interconnected macro pores and micro / mesoporous carbon skeleton.[112] Such carbo-polyHIPE was applied as a solid-state support for Pt and Ru bimetal nanoparticles, which, in turn, demonstrated a remarkable electrocatalytic ability to methanol electrooxidation. The specific surface area of carbo-HIPE was increased to 417 m^2/g after hypercrosslinking, which proved to be important for improving electrocatalytic performance. Silica particle stabilized polyDVB polyHIPE was used as a porous solid acid catalyst for the production of hydroxymethyl furfural from cellulose in the presence of 1-ethyl-3-methyl-imidazolium chloride. For comparison, basic polyDVB was prepared, grafted with a $-SO_3H$ sulfonation process, and PDVB-co-SS polyHIPE, which was also sulfonated. This polymer was then hypercrosslinked and used as a solid state catalyst which, in addition to the macro pores in its skeleton, also had micro pores and, consequently, high specific surface area. Large specific surface area of polyHIPE and super-strong acid sites have been found to be crucial for cellulose conversion.[113] Sevšek et al.[114] synthesized STY/DVB polyHIPE monoliths with high DVB content. The remaining vinyl groups of DVB in STY/DVB monoliths were used for post-polymerisation crosslinking using the radical initiator di-tert-butyl peroxide in toluene and acetonitrile. The surface area in both solvents was found to be much larger after hypercrosslinking (up to 355 m^2/g), and the nitrogen adsorption / desorption method showed an increase in the number of micro pores after hypercrosslinking, which coincides with an increase in specific surface area. Pyridine containing polyHIPE could be hypercrosslinked by the second stage radical crosslinking of remaining vinyl groups.[115] For the purposes of solid state support for catalysts, vinyl pyridine-DVB polyHIPE was prepared. Pyridine ring nitrogen was used for further functionalization – for the Cu (II) coordinate linker. This functionalized polyHIPE has been used as a solid state support for catalysts for a cycloaddition click reaction. Post polymerisation radical treatment (using di-tert-butyl peroxide) increased the specific surface area and created a multi modal porous profile, which was crucial for the success of the cycloaddition reaction.

Hypercrosslinking was demonstrated also on non-styrene-type polyHIPEs. Mezhoud et al.[116] synthesized poly (2-hydroxyethyl methacrylate-co-N,N'-methylenebisacrylamide) polyHIPE and functionalized it with allylamine and propargylamine to create free double bonds that were used for hypercrosslinking with di- or tetra-thiols via thiol-ene click reactions. After the treatment surface areas of up to 1500 m^2/g ware measured. The monoliths were then used for Au-nanoparticle decorated catalytic support to reduce nitrophenol and Eosin Y.

Another similar method is described as *in situ* hypercrosslinking of GMA-based polyHIPEs with multifunctional amines, where the amino-epoxy reaction is running parallel to the polymerisation. The result is a highly porous material with surface areas up to 63 m^2/g

and with good accessibility of reactive sites, but this system has disadvantages in terms of HIPE stability.[117]

6. Conclusion and Outlook

Porous polymers in different formats e.g. particles, monoliths, membranes, have a wide range of application fields; in separation, catalysis, synthesis, purification, in biomedical fields as supports for cell and tissue cultivation etc. Control of pore geometry, interconnectivity and size is of utmost importance for the desired performance. Not only is the control to narrow the pore size distribution important but the possibility to create materials with bimodal and hierarchical pore size distribution is very desired. While there are many methods for creating macroporosity in polymers, either during the polymerisation or after, high internal phase emulsion templating offers easily scalable straightforward technique for the synthesis of polymers with spherical interconnected pores with micrometer dimensions and high pore volume. Polymerisation parameters, droplet phase volume share and surfactants are key factors deciding the final structure. While good control of macroporosity in polyHIPEs is possible, the introduction of meso and microporosity is less trivial. Addition of porogenic solvents into the continuous phase can induce meso and micro porosity however the prevalence of cauliflower-like morphology and increase of pore volume significantly decreases the mechanical properties and is therefore in many cases unpractical. On the other hand, the post polymerisation hypercrosslinking enables the creation of meso and microporosity in already formed macroporous polyHIPEs without sacrificing the mechanical properties or even improving them in many aspects. Improved accessibility of reactive sites in the interior of the bulk of the material, increased surface area and wide solvent compatibility are further advantages of hypercrosslinked polyHIPEs. It is therefore expected that such materials with bimodal and hierarchical pore distribution will play an increasingly important role in various application fields in the future.

List of abbreviations used

BCMBP 4,4'-bis(chloromethyl)biphenyl
BET Brunauer-Emmett-Teller
DCE dichloroethane
DCX dichloroxylene
DVB divinylbenzene
FDA formaldehyde dimethyl acetal
GMA glycidyl methacrylate
HIPE high internal phase emulsion
MAP 4-(N-methylamino)pyridine
NiPAAm N-isopropyl acrylamide
PS polystyrene
STY styrene
SS sodium p-styrene sulfonate
VBC vinylbenzyl chloride

Author biographies

Amadeja Koler is a PhD student in PolyOrgLab at the Faculty of Chemistry and Chemical Engineering, University of Maribor. She studies the preparation of multi-level porous macromolecules. Her research includes the introduction of new reagents for controlled RAFT polymerization as well as colloidal precursor methods for formation od macroporosity and incorporation of hypercrosslinking for microporosity in macroporous materials.

Irena Pulko is a professor of chemistry of materials at the Faculty of Polymer Technology in Slovenj Gradec. She studied for PhD in the PolyOrgLab and in the research groups of Prof. Neil Cameron at Durham University and Prof. Christian Slugovc at Graz University of Technology. Her research includes porous materials and polymer-based materials from renewable resources.

Peter Krajnc runs PolyOrgLab at the Faculty of Chemistry and Chemical Engineering, University of Maribor and is the vice dean at the faculty. He did his PhD in the group of Prof. Marko Zupan at the Faculty of Chemistry and Chemical Technology of the University of Ljubljana. He was a Marie Curie Fellow at the Department of Chemistry, Durham University with Prof. Neil Cameron. His main research interests are synthesis and applications of multi-level porous polymer-based materials.

7. References

1 A. Wilkinson, A. McNaught, *Compendium Of Chemical Terminology ("Gold Book")*, Blackwell Scientific Publications, Oxford, UK, **1997**.
2 M. S. Silverstein, Polymer **2014**, *55*, 304–320. **DOI:**10.1016/j.polymer.2013.08.068
3 M. S. Silverstein, Polymer **2017**, *126*, 261–282. **DOI:**10.1016/j.polymer.2017.07.046
4 Y. Huang, S. H. Kim, L. R. Arriaga, *Adv. Colloid Interface Sci.* **2017**, *247*, 413–425. **DOI:**10.1016/j.cis.2017.07.013
5 B. F. B. Silva, C. Rodríguez-Abreu, N. Vilanova, *Curr. Opin. Colloid Interface Sci.* **2016**, *25*, 98–108. **DOI:**10.1016/j.cocis.2016.07.006
6 N. R. Cameron, Polymer **2005**, *46*, 1439–1449. **DOI:**10.1016/j.polymer.2004.11.097
7 I. Pulko, P. Krajnc, *Encycl. Polym. Sci. Technol.* **2017**, 1–28. **DOI:**10.1002/0471440264.pst653
8 S. Torquato, T. M. Truskett, P. G. Debenedetti, *Phys. Rev. Lett.* **2000**, *84*, 2064–2067. **DOI:**10.1103/PhysRevLett.84.2064

9 D. Barby and Z. Haq, *Low Density Porous Cross-Linked Polymeric Material Sand Their Preparation*, **1986,** EP Pat 60138.

10 S. Kovačič, D. Štefanec, P. Krajnc, *Macromolecules* **2007**, *40*, 8056–8060. **DOI:**10.1021/ma071380c

11 I. Pulko, P. Krajnc, *Macromol. Rapid Commun.* **2012**, *33*, 1731–46. **DOI:**10.1002/marc.201200393

12 E. Kot, N. Shirshova, A. Bismarck, J. H. G. Steinke, *RSC Adv.* **2014**, *4*, 11512-11519. **DOI:**10.1039/C4RA00118D

13 P. Krajnc, D. Štefanec, I. Pulko, *Macromol. Rapid Commun.* **2005**, *26*, 1289–1293. **DOI:**10.1002/marc.200500353

14 S. Kovačič, D. Štefanec, P. Krajnc, *Macromolecules* **2007**, *40*, 8056–8060. **DOI:**10.1021/ma071380c

15 J. Majer, M. Paljevac, E. Žagar, S. Kovačič, P. Krajnc, *React. Funct. Polym.* **2016**, *109*, 99–103. **DOI:**10.1016/j.reactfunctpolym.2016.10.008

16 M. Paljevac, K. Jeřabek, P. Krajnc, *J. Polym. Environ.* **2012**, *20*, 1095–1102. **DOI:**10.1007/s10924-012-0524-4

17 O. Kulygin, M. S. Silverstein, *Soft Matter* **2007**, *3*, 1525–1529. **DOI:**10.1039/b711610a

18 M. Ovadia, M. S. Silverstein, *Polym. Int.* **2016**, *65*, 280–289. **DOI:**10.1002/pi.5052

19 B. H. L. Oh, A. Bismarck, M. B. Chan-Park, *J. Mater. Chem. B* **2015**, *3*, 4118-4122. **DOI:**10.1039/C5TB00303B

20 N. C. Grant, A. I. Cooper, H. Zhang, *ASC Appl. Mater. Interface* **2010**, *2*, 1400–1406. **DOI:**10.1021/am100049r

21 R. Butler, I. Hopkinson, A. I. Cooper, *J. Am. Chem. Soc.* **2003**, *125*, 14473–14481. **DOI:**10.1021/ja037570u

22 F. Audouin, M. Birot, E. Pasquinet, O. Besnard, P. Palmas, D. Poullain, H. Deleuze, *Macromolecules* **2011**, *44*, 4879–4886. **DOI:**10.1021/ma200861j

23 C. Youssef, R. Backov, M. Treguer, M. Birot, H. Deleuze, *J. Polym. Sci. Pt A Polym. Chem.* **2010**, *48*, 2942–2947. **DOI:**10.1002/pola.24075

24 D. Golub, P. Krajnc, *React. Funct. Polym.* **2020**, *149*, 104515-104526. **DOI:**10.1016/j.reactfunctpolym.2020.104515

25 M. Sušec, S. C. Ligon, J. Stampfl, R. Liska, P. Krajnc, *Macromol. Rapid Commun.* **2013**, *34*, 938–943. **DOI:**10.1002/marc.201300016

26 D. W. Johnson, C. Sherborne, M. P. Didsbury, C. Pateman, N. R. Cameron, F. Claeyssens, *Adv. Mater.* **2013**, *25*, 3177–3177. **DOI:**10.1002/adma.201370154

27 C. E. Hoyle, C. N. Bowman, *Polym. Chem.* **2010**, *49*, 1540–1573. **DOI:**10.1002/anie.200903924

28 A. Galperin, K. Smith, N. S. Geisler, J. D. Bryers, B. D. Ratner, *ACS Biomater. Sci.* **2015**, *1*, 593–600. **DOI:**10.1021/acsbiomaterials.5b00133

29 H. B. Ly, L. Halbardier, D. Grande, *Macromol. Symp.* **2016**, *365*, 49–58. **DOI:**10.1002/masy.201650013

30 R. B. Diego, M. P. Olmedilla, A. S. Aroca, J. L. G. Ribelles, M. M. Pradas, G. G. Ferrer, M. S. Sanchez, *J. Mater. Sci.* **2005**, *40*, 4881–4887. **DOI:**10.1007/s10853-005-3885-4

31 T. J. Long, C. C. Sprenger, S. R. Plymate, B. D. Ratner, *Biomaterials* **2014**, *35*, 8164–8174. **DOI:**10.1016/j.biomaterials.2014.04.090

32 M. Paljevac, L. Gradišnik, S. Lipovšek, U. Maver, J. Kotek, P. Krajnc, *Macromol. Biosci.* **2018**, *18*, 1–8. **DOI:**10.1002/mabi.201870003

33 N. Bhardwaj, S. C. Kundu, *Biotechnol. Adv.* **2010**, *28*, 325–347. **DOI:**10.1016/j.biotechadv.2010.01.004

34 L. Wang, A. J. Ryan, *Electrospinning Tissue Regen.* **2011**, 3–33. **DOI:**10.1533/9780857092915.1.3

35 A. Samanta, B. Nandan, R. K. Srivastava, *J. Colloid Interface Sci.* **2016**, *471*, 29-36. **DOI:**10.1016/j.jcis.2016.03.012

36 B. A. Dikici, S. Dikici, G. C. Reilly, S. MacNeil, F. Claeyssens, *Materials.* **2019**, *12*, 2643-2667. **DOI:**10.3390/ma12162643

37 N. R. Cameron, A. Barbetta, *J. Mater. Chem.* **2000**, *10*, 2466–2471. **DOI:**10.1039/b003596n

38 J. M. Williams, A. J. Gray, M. H. Wilkerson, *Langmuir* **1990**, *6*, 437–444. **DOI:**10.1021/la00092a026

39 D. C. Sherrington, P. Hodge, *Synthesis Separations Using Functional Polymers*, Wiley-VCH Verlag GmbH&Co. KGaA, **1988**.

40 A. Barbetta, N. R. Cameron, *Macromolecules* **2004**, *37*, 3202–3213. **DOI:**10.1021/ma035944y

41 S. Huš, M. Kolar, P. Krajnc, *J. Chromatogr. A* **2016**, *1437*, 168–175. **DOI:**10.1016/j.chroma.2016.02.012

42 P. Krajnc, N. Leber, D. Štefanec, S. Kontrec, A. Podgornik, *J. Chromatogr. A* **2005**, *1065*, 69–73. **DOI:**10.1016/j.chroma.2004.10.051

43 S. Jerenec, M. Šimić, A. Savnik, A. Podgornik, M. Kolar, M. Turnšek, P. Krajnc, *React. Funct. Polym.* **2014**, *78*, 32–37. **DOI:**10.1016/j.reactfunctpolym.2014.02.011

44 M. Tebboth, A. Menner, A. Kogelbauer, A. Bismarck, *Curr. Opin. Chem. Eng.* **2014**, *4*, 114–120. **DOI:**10.1016/j.coche.2014.03.001

45 J. Pribyl, B. Fletcher, W. Steckle, K. Taylor-Pashow, T. Shehee, B. Benicewicz, *Anal. Chem.* **2017**, *89*, 5174–5178. **DOI:**10.1021/acs.analchem.7b01153

46 K. M. L. Taylor-Pashow, J. G. Pribyl, *Solvent Extr. Ion Exch.* **2019**, *37*, 1–26. **DOI:**10.1080/07366299.2019.1592924

47 D. Yin, Y. Guan, H. Gu, Y. Jia, Q. Zhang, *RSC Adv.* **2017**, *7*, 7303-7309. **DOI:**10.1039/C6RA27609A

48 J. Majer, P. Kranjc, *Macromol. Symp.* **2010**, *296*, 5–10. **DOI:**10.1002/masy.201051002

49 J. M. Hughes, P. M. Budd, K. Tiede, J. Lewis, *J. Apply. Polym. Sci.* **2014**, *132*, 41229-41237. **DOI:**10.1002/app.41229

50 S. Choudhury, L. Fitzhenry, B. White, D. Connolly, *Materials.* **2016**, *9*, 1–14. **DOI:**10.3390/ma9030212

51 V. A. Davankov, M. P. Tsyurupa, *React. Polym.* **1990**, *13*, 27–42. **DOI:**10.1016/0923-1137(90)90038-6

52 M. P. Tsyurupa, V. A. Davankov, *React. Funct. Polym.* **2002**, *53*, 193–203. **DOI:**10.1016/S1381-5148(02)00173-6

53 O. Okay, *Prog. Polym. Sci.* **2000**, *25*, 711–779. **DOI:**10.1016/S0079-6700(00)00015-0

54 M. P. Tsyurupa, V. A. Davankov, *React. Funct. Polym.* **2006**, *66*, 768–779. **DOI:**10.1016/j.reactfunctpolym.2005.11.004

55 D. C. Sherrington, *Chem. Commun.* **1998**, 2275–2286. **DOI:**10.1039/a803757d

56 K. Dušek, *J. Polym. Sci. Part C Polym. Symp.* **2010**, *16*, 1289–1299. **DOI:**10.1002/polc.5070160307

57 P. Veverka, K. Jeřábek, *React. Funct. Polym.* **2004**, *59*, 71–79. **DOI:**10.1016/j.reactfunctpolym.2003.12.008

58 J. H. Ahn, J. E. Jang, C. G. Oh, S. K. Ihm, J. Cortez, D. C. Sherrington, *Macromolecules* **2006**, *39*, 627–632. **DOI:**10.1021/ma051152n

59 I. Pulko, J. Wall, P. Krajnc, N. R. Cameron, *Chem. Eur. J.* **2010**, *16*, 2350–2354. **DOI:**10.1002/chem.200903043

60 A. V. Pastukhov, M. P. Tsyurupa, V. A. Davankov, *J. Polym. Sci. Pt B Polym. Phys.* **1999**, *37*, 2324–2333. **DOI:**10.1002/(SICI)1099-0488(19990901)37:17<2324::AID-POLB4>3.0.CO;2-B

61 P. Veverka, K. Jeřábek, *React. Funct. Polym.* **1999**, *41*, 21–25. **DOI:**10.1016/S1381-5148(99)00030-9

62 V. A. Davankov, M. P. Tsyurupa, *React. Polym.* **1990**, *13*, 27–42. **DOI:**10.1016/0923-1137(90)90038-6

63 V. Davankov, V. Rogozhin, M. Tsyurupa, *Macronet Polystyrene Structures for Ionites and Method of Producing Same*, **1969,** US Pat 3729457.

64 V. A. Davankov, S. V. Rogoshin, M. P. Tsyurupa, *J Polym Sci Part C, Polym Symp* **1974**, *101*, 95–101.

65 V. A. Davankov, G. I. Timofeeva, M. M. Ilyin, M. P. Tsyurupa, *J. Polym. Sci. Part A Polym. Chem.* **1997**, *35*, 3847–3852. **DOI:**10.1002/(SICI)1099-0518(199712)35:17<3847::AID-POLA23>3.0.CO;2-C

66 V. Davankov, M. Tsyurupa, *Compr. Anal. Chem.* **2011**, *56*, 166–193. **DOI:**10.1016/S0166-526X(11)56006-4

67 M. P. Tsyurupa, Z. K. Blinnikova, Y. A. Davidovich, S. E. Lyubimov, A. V. Naumkin, V. A. Davankov, *React. Funct. Polym.* **2012**, *72*, 973–982. **DOI:**10.1016/j.reactfunctpolym.2011.03.002

68 M. P. Tsyurupa, A. V. Pastukhov, V. A. Davankov, *Dokl. Akad. Nauk* **1997**, *352*, 2324–2333.

69 V. A. Davankov, M. M. Ilyin, M. P. Tsyurupa, G. I. Timofeeva, L. V. Dubrovina, *Macromolecules* **1996**, *29*, 8398–8403. **DOI:**10.1021/ma951673i

70 J. Hradil, E. Králová, Polymer **1998**, *39*, 6041–6048. **DOI:**10.1016/S0032-3861(98)00057-3

71 D. Zhang, L. Tao, J. Ju, Y. Wang, Q. Wang, T. Wang, Polymer **2015**, *60*, 234–240. **DOI:**10.1016/j.polymer.2015.01.053

72 F. Maya, F. Svec, Polymer **2014**, *55*, 340–346. **DOI:**10.1016/j.polymer.2013.08.018

73 T. Ratvijitvech, M. Barrow, A. I. Cooper, D. J. Adams, *Polym. Chem.* **2015**, *6*, 7280–7285. **DOI:**10.1039/C5PY00668F

74 L. Tan, B. Li, X. Yang, W. Wang, B. Tan, Polymer **2015**, *70*, 336–342. **DOI:**10.1016/j.polymer.2015.06.026

75 C. D. Wood, T. Bien, A. Trewin, N. Hongjun, D. Bradshaw, M. J. Rosseinsky, Y. Z. Khimyak, N. L. Campbell, R. Kirk, E. Stöckel, A. I. Cooper, *Chem. Mater.* **2007**, *19*, 2034–2048. **DOI:**10.1021/cm070356a

76 M. Ghafari, J. D. Atkinson, Polymer **2017**, *116*, 278–286. **DOI:**10.1016/j.polymer.2017.03.082

77 M. G. Schwab, I. Senkovska, M. Rose, N. Klein, M. Koch, J. Pahnke, G. Jonschker, B. Schmitz, M. Hirscher, S. Kaskel, *Soft Matter* **2009**, *5*, 1055–1059. **DOI:**10.1039/b815143a

78 Y. Yang, B. Tan, C. D. Wood, *J. Mater. Chem. A* **2016**, *4*, 15072–15080. **DOI:**10.1039/C6TA05226F

79 Q. Liu, B. Xia, J. Huang, B. Liao, H. Liu, B. Ou, L. Chen, Z. Zhou, *Mater. Chem. Phys.* **2017**, *199*, 616–622. **DOI:**10.1016/j.matchemphys.2017.07.032

80 L. D. Belyakova, T. I. Schevchenko, V. A. Davankov, M. P. Tsyurupa, *Adv. Colloid Interface Sci.* **1986**, *25*, 249–266. **DOI:**10.1016/0001-8686(86)80011-2

81 M. P. Tsyurupa, L. A. Maslova, A. I. Andreeva, T. A. Mrachkovskaya, V. A. Davankov, *React. Polym.* **1995**, *25*, 69–78. **DOI:**10.1016/0923-1137(95)00021-A

82 N. A. Penner, P. N. Nesterenko, M. M. Hyin, M. P. Tsyurupa, V. A. Davankov, *Chromatographia* **1999**, *50*, 611–620. **DOI:**10.1007/BF02493669

83 V. Davankov, M. Tsyurupa, M. Ilyin, L. Pavlova, *J. Chromatogr. A* **2002**, *965*, 65–73. **DOI:**10.1016/S0021-9673(01)01583-7

84 V. A. Davankov, C. S. Sychov, M. M. Ilyin, K. O. Sochilina, *J. Chromatogr. A* **2003**, *987*, 67–75. **DOI:**10.1016/S0021-9673(02)01914-3

85 V. Davankov, L. Pavlova, M. Tsyurupa, J. Brady, M. Balsamo, E. Yousha, *J. Chromatogr. B Biomed. Sci. Appl.* **2000**, *739*, 73–80. **DOI:**10.1016/S0378-4347(99)00554-X

86 B. Li, R. Gong, Y. Luo, B. Tan, *Soft Matter* **2011**, *7*, 10910-10916. **DOI:**10.1039/c1sm06113e

87 J. Urban, F. Svec, J. M. J. Fréchet, *J. Chromatogr. A* **2010**, *1217*, 8212–8221. **DOI:**10.1016/j.chroma.2010.10.100

88 J. Urban, F. Svec, J. M. J. Fréchet, *Anal. Chem.* **2010**, *82*, 1621–1623. **DOI:**10.1021/ac100008n

89 Y. Lv, Z. Lin, F. Svec, *Anal. Chem.* **2012**, *84*, 8457–8460. **DOI:**10.1021/ac302438m

90 X. J. Chen, N. P. Dinh, J. Zhao, Y. T. Wang, S. P. Li, F. Svec, *J. Sep. Sci.* **2012**, *35*, 1502–1505. **DOI:**10.1002/jssc.201200138

91 F. Maya, F. Svec, *J. Chromatogr. A* **2013**, *1317*, 32–38. **DOI:**10.1016/j.chroma.2013.07.073

92 Z. K. Blinnikova, I. R. Golding, M. P. Tsyurupa, A. A. Fomkin, A. L. Pulin, V. A. Davankov, *Polym. Sci. - Ser. B* **2018**, *60*, 91–98. **DOI:**10.1134/S1560090418010013

93 C. D. Wood, B. Tan, A. Trewin, F. Su, M. J. Rosseinsky, D. Bradshaw, Y. Sun, L. Zhou, A. I. Cooper, *Adv. Mater.* **2008**, *20*, 1916–1921. **DOI:**10.1002/adma.200702397

94 J. Germain, J. M. J. Fréchet, F. Svec, *Chem. Commun.* **2009**, 1526–1528. **DOI:**10.1039/b821233c

95 M. G. Schwab, A. Lennert, J. Pahnke, G. Jonschker, M. Koch, I. Senkovska, M. Rehahn, S. Kaskel, *J. Mater. Chem.* **2011**, *21*, 2131–2135. **DOI:**10.1039/C0JM03017A

96 D. Chen, S. Gu, Y. Fu, Y. Zhu, C. Liu, G. Li, G. Yu, C. Pan, *Polym. Chem.* **2016**, *7*, 3416–3422. **DOI:**10.1039/C6PY00278A

97 R. Dawson, T. Ratvijitvech, M. Corker, A. Laybourn, Y. Z. Khimyak, A. I. Cooper, D. J. Adams, *Polym. Chem.* **2012**, *3*, 2034–2038. **DOI:**10.1039/c2py20136d

98 B. Li, R. Gong, W. Wang, X. Huang, W. Zhang, H. Li, C. Hu, B. Tan, *Macromolecules* **2011**, *44*, 2410–2414. **DOI:**10.1021/ma200630s

99 L. Pan, Q. Chen, J.-H. Zhu, J.-G. Yu, Y.-J. He, B.-H. Han, *Polym. Chem.* **2015**, *6*, 2478–2487. **DOI:**10.1039/C4PY01797H

100 X. Yang, M. Yu, Y. Zhao, C. Zhang, X. Wang, J. X. Jiang, *RSC*

Adv. **2014**, *4*, 61051–61055. **DOI:**10.1039/C4RA09394A
101 J. Germain, F. Svec, J. M. J. Fre´chet, *Chem. Mater.* **2008**, *20*, 7069–7076. **DOI:**10.1021/cm802157r
102 Y. Luo, S. Zhang, Y. Ma, W. Wang, B. Tan, *Polym. Chem.* **2013**, *4*, 1126–1131. **DOI:**10.1039/C2PY20914D
103 M. L. Errahali M., Gatti G., Tei L., Paul G., Rolla G. A., Canti L., Fraccarollo A., Cossi M., Comotti A., Sozzani P., *J. Phys. Chem.* **2014**, *118*, 28699–28710. **DOI:**10.1021/jp5096695
104 Y. Luo, B. Li, W. Wang, K. Wu, B. Tan, *Adv. Mater.* **2012**, *24*, 5703–5707. **DOI:**10.1002/adma.201202447
105 T. Ratvijitvech, M. Barrow, A. I. Cooper, D. J. Adams, *Polym. Chem.* **2015**, *6*, 7280–7285. **DOI:**10.1039/C5PY00668F
106 S. Yao, X. Yang, M. Yu, Y. Zhang, J. X. Jiang, *J. Mater. Chem. A* **2014**, *2*, 8054–8059. **DOI:**10.1039/C4TA00375F
107 R. Dawson, E. Stöckel, J. R. Holst, D. J. Adams, A. I. Cooper, *Energy Environ. Sci.* **2011**, *4*, 4239–4245. **DOI:**10.1039/c1ee01971f
108 L. Tan, B. Li, X. Yang, W. Wang, B. Tan, Polymer **2015**, *70*, 336–342. **DOI:**10.1016/j.polymer.2015.06.026
109 X. Yang, L. Tan, L. Xia, C. D. Wood, B. Tan, *Macromol. Rapid Commun.* **2005**, *36*, 1553–1558. **DOI:**10.1002/marc.201500235
110 R. T. Woodward, A. Jobbe-Duval, S. Marchesini, D. B. Anthony, C. Petit, A. Bismarck, Polymer **2017**, *115*, 146–153. **DOI:**10.1016/j.polymer.2017.03.042
111 S. Israel, I. Gurevitch, M. S. Silverstein, Polymer **2015**, *72*, 453–463. **DOI:**10.1016/j.polymer.2015.02.055
112 F. Yi, Y. Gao, H. Li, L. Yi, D. Chen, S. Lu, *Electrochim. Acta* **2016**, *211*, 768–776. **DOI:**10.1016/j.electacta.2016.06.092
113 J. Pan, H. Gao, Y. Zhang, J. Zeng, W. Shi, C. Song, Y. Yan, L. Yu, D. Chang, *RSC Adv.* **2014**, *4*, 59175–59184. **DOI:**10.1039/C4RA10383A
114 U. Sevšek, J. Brus, K. Jeřabek, P. Krajnc, Polymer **2014**, *55*, 410–415. **DOI:**10.1016/j.polymer.2013.09.026
115 A. Koler, M. Paljevac, N. Cmager, J. Iskra, M. Kolar, P. Krajnc, Polymer **2017**, *126*, 402–407. **DOI:**10.1016/j.polymer.2017.04.051
116 S. Mezhoud, M. Paljevac, A. Koler, B. Le Droumaguet, D. Grande, P. Krajnc, *React. Funct. Polym.* **2018**, *132*, 51–59. **DOI:**10.1016/j.reactfunctpolym.2018.09.009
117 J. Majer, E. Žagar, P. Krajnc, S. Kovačič, *Colloid Polym. Sci.* **2019**, *297*, 239–247. **DOI:**10.1007/s00396-018-4455-z

Povzetek

Poroznost v polimerih in polimenih materialih je zelo pomembna, saj jim le ta daje posebne funkcionalnosti, kot so izboljšani prenos snovi skozi material, izboljšana dosegljivost reaktivnih mest, znižana skupna masa, prilagojene separacijske lastnosti, itd.. Razvoj na področju polimerov s kontrolirano morfologijo, kar se tiče velikosti in oblike por, povezovalnosti por in njihove porazdelitve velikosti pomembno vpliva na uporabnost teh polimerov na področju katalize, separacije, sinteze na trdni fazi, adsorpcije, senzorjev, biomedicinskih pripomočkov in mnogih drugih. Zlasti so zanimivi polimeri z izrazito bimodalno ali hierarhično porazdelitvijo por, saj to omogoča uporabo v aplikacijah, kjer so potrebne velikosti por na več ravneh. Emulzije lahko uporabimo za pripravo polimerov z vključenimi medsebojno povezanimi sferičnimi porami na mikrometrski ravni, medtem ko postpolimerizacijsko zamreženje vpliva na mikro poroznost. S kombinirano uporabo obeh tehnik dobimo materiale z večnivojsko in hierarhično poroznostjo z velikim potencialom uporabe.

Except when otherwise noted, articles in this journal are published under the terms and conditions of the Creative Commons Attribution 4.0 International License

Review

A Review on Recent Progression of Modifications on Titania Morphology and its Photocatalytic Performance

Nor Amira Marfur,[1] Nur Farhana Jaafar,[1,*] Melati Khairuddean[1] and Norazzizi Nordin[1]

[1] *School of Chemical Sciences, Universiti Sains Malaysia, 11800 USM Penang, Malaysia*

* *Corresponding author: E-mail: nurfarhana@usm.my*
Tel: 604-6533566 Fax: 604-6574854

Received: 04-02-2019

Abstract

Titanium dioxide (TiO_2) has been broadly used as a photocatalyst because it has good stability and performance for degradation of pollutants. On the other hand, its efficiency as photocatalyst is limited since it can only be excited under UV-light radiation and has a rapid electron-hole recombination that occurs during the photodegradation. There are many studies focusing on adjusting the synthesis methods, addition of dopants and modifying the TiO_2 structure to enhance its photocatalytic performance. Among them, synthesis of TiO_2 as porous nanoparticles as one of the strategies in modifying the TiO_2 structure has gained attention due to its benefits for better adsorption and accessibility of various pollutants onto the reactive site of catalyst, thus enhancing the photocatalytic performance. In this review, we recapitulated on modifications of synthesis methods for TiO_2 and their effect on the structure along with the photocatalytic performance. Recent progress for TiO_2 in terms of synthesis approaches, effect of dopants, modified structures, and applications are also briefly discussed in this review.

Keywords: Morphology; titania nanoparticles; porosity; photocatalytic activity.

1. Introduction

Titanium dioxide is classified as a transition metal oxide which exists in anatase, rutile, or brookite crystalline structures.[1–3] Many studies have been done by researchers regarding TiO_2 because it is inexpensive, chemically and thermally stable, eco-friendly, and widely used for different applications such as for the production of dye-sensitised solar cells, sunscreen, and water purification.[4–6] Besides functioning as a catalyst, TiO_2 also acts as an additive, promoter, and transporter during the catalytic reaction.[7–10] The extensive usage of TiO_2 in photocatalytic degradation is due to its capability in mineralisation of organic pollutants such as dye and chlorophenol to less harmful compounds as shown in Fig. 1.[11–14] However, its efficiency as a photocatalyst is limited since it can only be excited under UV-light due to a wide band gap which is around 3.2 eV and high electron-hole recombination rate during photodegradation.[15–17]

The effectiveness of TiO_2 as a photocatalyst can be enhanced by increasing the surface area and its crystallinity, while decreasing the particle size will strongly contribute in reducing the band gap. The band gap energy also can be reduced by pairing with other semiconductors. Apart from that, the generation of abundance site defects such as Ti^{3+} site defects (TSD) and oxygen vacancies (OV) can help function as electron acceptors which inhibit the electron-hole recombination and assist the charge carrier migration.[18] Therefore, there are various modifications on TiO_2 forms such as nanotubes and thin films.[19–21] Recent-

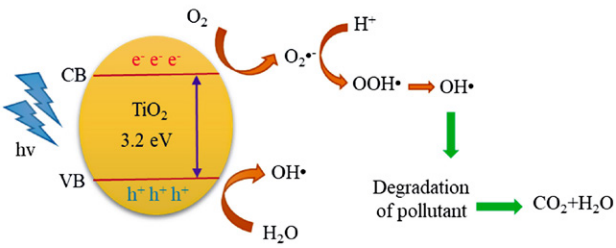

Fig. 1. The schematic diagram of mechanism for photocatalytic degradation using titania.

ly, porous transition metal oxide has also been studied widely since it improves its original properties. This favourable modification gives many benefits for various applications since it can result in varied forms including nanoparticles, fibres, and films besides possessing a consistent large pore pattern which increases surface area, gives an ordered structure and adjustable pore diameter.[22] Mesoporous titania has been intensely studied compared to others due to its diverse applications as a photocatalyst and supercapacitor.[23–26] The first mesoporous TiO_2 was synthesised via a sol-gel approach which yielded hexagonal pores that are particularly organised.[27,28] Afterwards, many methods have been introduced and modified according to the Evaporation-Induced Self-Assembly (EISA) approach using varied titanium precursors or template surfactants to synthesise different morphologies of TiO_2 for specific applications.[29–32]

According to previous studies, organic surfactant is greatly contributing in controlling the size and shape of precursor during the synthesis. It also acts as a soft template and dispersant to form various scales of porous structures such as microporous, mesoporous and microporous with high crystallinity.[33–36] There are several types of surfactants which are anionic, cationic, nonionic, and polymeric fugitive materials used to construct different morphologies of materials while greatly enhancing the surface area, pore volume, and other related properties.[37–44] Organic surfactant acts as a template or SDA (surface directing agent) in preparing porous materials to create the interior part of the building blocks which are pores. The co-existence of chemically bonded hydrophilic (polar) part as well as a hydrophobic (non-polar) hydrocarbon in a molecule of surfactants makes them suitable to be used as SDA. For instance, the presence of cetyl-trimethylammonium bromide (CTAB) which is a cationic surfactant will create a micellar system that contributes as the template to form the interaction with a precursor when the degree of hydration increases. These molecules assemble in the solvent to form micelle and have a high molecular weight. This situation is a primary reaction in preparing highly porous and uniform materials.[45,46]

Therefore, this review will be critically discussing the recent progress for TiO_2 in terms of modification of titania morphology using different surfactants, synthesis methods, the role of dopants and their photocatalytic performance to help other researchers to further the study in this field.

2. Type of Surfactants

Surfactants can be categorised into different groups based on the ions charged at the hydrophilic part. They act as a template to form pores on the metal oxide where the pore size can be controlled by their alkyl chain lengths. For instance, cetyl-trimethylammonium bromide (CTAB) with a longer alkyl chain produces bigger pores compared to *n*-dodecyl-trimethylammonium bromide (DTAB) which has a shorter alkyl chain. The pore morphology of the metal oxide can also be modified by varying the ratio of the reaction mixture and synthesis conditions such as the basic pH of the solution which can produce smaller pores. When the critical micellar concentration of the surfactant is achieved, micelles form and the dispersion effect occurs which produces a more porous material. Besides that, ionic and non-ionic surfactants use different mechanisms to assemble micelles as a template for pore formation. Ionic surfactant has an amphiphilic nature in which micelles can be assembled by electrostatic interactions while non-ionic surfactant involves hydrogen bonding in the formation of metal oxide-surfactant composites for the material framework organisation. However, the strong reactivity between ionic surfactant and material walls makes it difficult to be removed during calcination and may collapse the material structure. Therefore, for certain synthesis conditions, non-ionic surfactant is preferable since it is easier to be removed and only needs much lower temperature during calcination.[47,48] Fig. 2 shows a general micellisation of surfactants that occurs during the synthesis of an intended material.

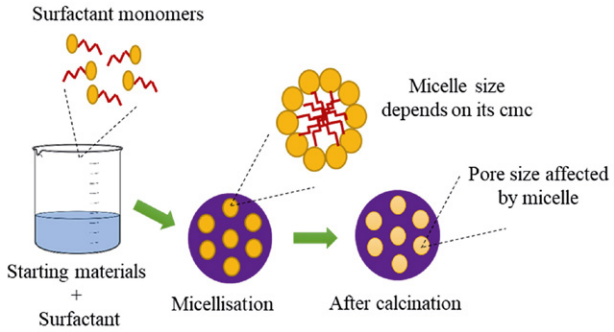

Fig. 2. The general illustration of micellisation of surfactants during synthesis.

2. 1. Anionic and Cationic Surfactants

Generally, anionic and cationic surfactants are classified as detergents or soaps composed of hydrophilic at the end of the chain which either contains cation or anion. Surfactants have remarkable characteristics that allow them to greatly contribute for the generation of intended materials, namely the production of hollow parts by their aggregation behaviour after being calcined. Besides, they can give a significant effect to the extension and particle properties.[49] In addition, the alteration on the concentration plays a significant role during the synthesis. Micelles will start to form when the concentration increases up to a critical micelle concentration (cmc). However, the precipitation will only occur if the concentration of surfactant surpasses the product solubility which can reduce the interaction of the surfactants with other compounds.[38–41,50]

Mohamed et al. had used sodium dodecyl sulphate (SDS) which is an anionic surfactant as a pore forming agent to synthesise a series of TiO_2 nanoparticles using the hydrothermal approach. The usage of SDS was to synthesise titania yielding a high surface area; mesoporous as well as the nanoparticle crystals of anatase TiO_2. Besides that, the pH of the starting material mixture also affected the production of the anatase-rutile phase while preparing these photocatalysts.[40] The framework alteration for inorganic/organic compounds would occur in order to stabilise interlinkage energy by manipulating the morphology of titanium polymer which then modified the local density and interface charge aspects.[39,42]

Casino et al. had synthesised mesoporous TiO_2 nanocrystalline via a facile sol-gel method using an inexpensive titanium oxysulphate starting material with several cationic surfactants which were cetyl-trimethylammonium bromide (CTAB), cetyl-trimethyl-ammonium chloride (CTAC), benzalkonium chloride (BC) and octadecyl-trimethyl-ammonium bromide (C_{18}TAB). Different templates as well as calcination temperatures while producing mesoporous titania nanocrystalline resulted in different features such as chain lengths, counter ions, and morphologies.[51] Addition of surfactant in the starting material mixture produced crystal structures with the anatase phase and smaller grain sizes which agglomerated after a prolonged heat treatment. Generally, bromide counter ions were less hydrated than chloride, thus the micelles formed had more effectual neutralisation charge at their surfaces, considering the effectiveness of micellisation could be affected by the counter ion condensation. Substantial bromide counter ion could also hinder state alteration from anatase to rutile while further stabilising that phase during titania precipitation. In addition, there was the hydrolysis of titanium oxysulphate along with an intermediate compound production firmly attached at the surfactant's hydrophilic group. Therefore, the characteristics of alkyl chain affected the micelles surface charge densities to promote the hydrolysis process. The decrease in micellisation usually could be related to an increment of alkyl chain on the polar group prompted by the molecule hydrophobic feature. Besides that, CTAB greatly contributed in maintaining the anatase and small-scale crystal framework, though after protracted heating that homogenised grains.[52,53] Samples BC-450 and BC-650 exhibited lower degrees of porosity by having low surface area compared to CTAB samples. Calcination step is known for template withdrawal to improve the degree of crystallisation besides influencing the arrangement of mesoporous titania structure.[54]

Li et al. had prepared monodisperse and homogenous mesoporous titania spheres in nano-scale via the sol-gel approach using CTAB as a soft template or pore-forming agent and doped with nitrogen through the hydrothermal approach. Nitrogen doped mesoporous TiO_2 spheres produced had showed significant properties like large surface area, proportionately tiny particles in the anatase phase, along with splendid UV-Vis absorption. Thus, the characteristics could greatly contribute in enhancing the photoactivity of Rhodamine B under visible light.[55]

Jaafar et al. had successfully synthesised mesoporous titania nanoparticles (MTN) via the microwave-assisted method with CTAB as a surfactant for the photodegradation of 2-chlorophenol under visible light. These materials possessed smaller particle sizes, smoother pore structure, as well as more TSD and OV distribution. Increase in microwave power density had highly hydrated the surfactant chains and resulted in better interlinkage with solutions containing titanium ions.[18] In 2017, they had further doped silver into MTN (Ag-MTN) by applying the same method and surfactant which resulted in better photocatalytic performance with lower band gap compared to their previous study. MTN and Ag^0 nanoparticles had created a synergistic effect which reduced the band gap and functioned as an electron acceptor and plasmonic sensitiser, correspondingly.[56] Table 1 shows briefly the synthesis means for varied mesoporous TiO_2 using cationic surfactant as SDA.

2. 2. Non-Ionic Surfactant

Non-ionic surfactant is a compound that will not ionise in aqueous solutions even though it possesses hydrophilic parts. During the synthesis of titania nanoparticles, it plays an important role as macro-/mesoporous template. It is normally utilised to construct nanoscale crystal structures under low calcination temperatures and forms macro-/mesoporous structure which contributes in increasing the mass transport capacity, narrowing channels, and constructing more reachable surface area within the materials.[57]

Table 1. Summary of preparation methods using cationic surfactants as SDA.

Study	Method	Surfactant	Precursor	Cal. Temp. (° C)	Surface area (m^2/g)	Pore Size (nm)	Ref.
Jaafar et al.	Microwave	CTAB	[a] TTIP	600	152.0–187.0	1.50–30.00	57
Jaafar et al.	Microwave	CTAB	[a] TTIP	600	>180.0	11.36	58
Casino et al.	Sol-gel	CTAB	[b] $TiOSO_4$	450	250.0	7.80	55
Li et al.	Sol-gel	CTAB	[c] $Ti(SO_4)_2$	400	84.8	8.80	56

[a] Titanium isopropoxide [b] Titanium(IV) oxysulphate-sulphuric acid hydrate [c] Titanium(IV) sulphide

Besides that, this kind of surfactant can promote interaction between hydrogen and metal oxide while aiding in the production of material-surfactant composites. Other than that, higher specific surface area and smaller pore size might be obtained by increasing the template concentrations up to a specific amount. For instance, different amounts of the Pluronic P-123 (P123) give significant changes in mesoporous titania properties.[43]

Pal et al. had synthesised mesoporous TiO_2 and Fe_3O_4@mesoporous TiO_{2-x} microspheres by combining the surfactant-assisted sol-gel method which used P123 as the template with the inexpensive and eco-friendly spray-drying approach to manufacture gradable mesoporous materials at a large scale. The particle diameter, structure, dispersity, surface area, as well as pore size could be ruled by varying the aspects while pre-hydrolysis and spray-drying reactions took place. In this means of preparation, surfactant was used to form a mesoporous structure. This could be proven by the scanning electron microscope (SEM) results where the as-prepared spheres structure before calcination had shown significantly smooth surfaces in the amorphous state. After calcination and continuing to ultrasonication, amorphous titania was altered into anatase sphere crystals with rougher surfaces and apparent mesopores on the material surfaces.[58]

Smirnova et al. had prepared mesoporous nanosized TiO_2 films modified with several transition metal ions via the sol-gel approach with P123 as SDA. The characterisation results showed that manganese doped into TiO_2 (m-TiO_2) film nanostructures had a mesoporous framework comprised of pore diameters ranging from 2.5 to 6 nm along with specific surface areas of about 147 and 224 m^2/g for titania and manganese doped materials, respectively.[59] Faisal et al. also had synthesised mesoporous titania nanocomposites by the sol-gel technique using Pluronic F127 (F127) as SDA. Simple ultrasonication process was also done to dope NiO_2 at different contents into m-TiO_2 nanocomposites for boosting the percentage degradation of methylene blue under visible light illumination. The outcomes showed that m-TiO_2 nanocomposites had surface area and pore diameter of 106.442 m^2/g and 10 nm, correspondingly, while NiO/m-TiO_2 nanocomposites showed larger surface area which was 111.3 m^2/g. The X-ray diffraction (XRD) analysis also indicated that m-TiO_2 nanocomposites had an anatase structure while NiO/m-TiO_2 nanocomposites had a biphasic anatase-rutile structure. NiO/m-TiO_2 nanoparticles exhibited greatly advanced photoactivity compared to pure mesoporous TiO_2 nanoparticles.[60]

Carlo et al. had synthesised mesoporous titania films (TiMS) via the sol-gel approach with P123 as SDA. This template had a major purpose during the production of grains and enhanced their surface roughness. The result revealed that N719 absorbance normalised to titania film thickness (500 nm) showed TiMS-350 as the most porous sample with the highest dye loading which proved that dye adsorption could be promoted by the coarseness as well as porosity of the material. Thus, the usage of a non-ionic surfactant in TiMS substantially assisted the process while forming compact films with large surface area as well as highly porous.[61] Moreover, the anatase phase revealed in the TiMS-350 indicated that non-ionic surfactant favoured a low calcination temperature.[40]

Samsudin et al. had utilised F127 as SDA in producing mesoporous titania which had an essential function to boost the photoactivity in atrazine degradation. According to the photoluminescence (PL) spectra and X-ray photoelectron spectroscopy (XPS) analysis, mesoporous F127-TiO_2 showed a remarkable increment in terms of particle and crystallite size. Higher surface area along with notably reduced size of anatase crystals have generated barely trapping sites where photogenerated electrons or holes were pairing at the molecular level reaction which could facilitate photocatalytic degradation activity. Moreover, the band gap was narrowed to below 3.2 eV (anatase TiO_2).[62,63] Smirnova et al. also prepared TiO_2, SiO_2, and TiO_2 doped with SiO_2 (TiO_2/SiO_2) mesoporous films via templated sol-gel synthesis using P123 as SDA for the photodegradation of acridine yellow under UV irradiation. Removal of surfactant had left a mesoporous structure with pore sizes around 2 to 4 nm on these mesoporous films. Mesoporous TiO_2 synthesised via this method also possessed a specific surface area of 910 m^2/g.[64]

Geramipour and Oveisi had synthesised multilayer nanocrystalline mesoporous TiO_2 films via layering deposition combined with surfactant-directed sol-gel approach using P123 as a pore template on glass substrates. Field emission scanning electron microscopy (FESEM) analysis revealed that all materials comprised of integrated pore with sizes less than 20 nm in nanoparticles were formed from nanocrystallites clusters. The XRD result also exhibited that anatase nanocrystallites were formed with a particle size of 9.60 nm. Low temperature (250 °C) during the pre-heat treatment of the deposited layers produced totally similar multilayer films with no edged coherence present caused by the intense interlinkage along with adequate dissemination layer by layer.[65]

Islam and Rankin had prepared Ti^{3+} and nitrogen co-doped cubic ordered mesoporous titania thin films using hydrazine technique at different durations and calcination temperatures. During the formation of titania thin films by the sol-gel approach, F127 had been used as SDA. XPS analysis along with UV-Vis absorbance spectra of Ti^{3+}-N-TiO_2 films illustrated that the incorporation of both elements reduced the band gap of titania and resulted in enhancing the photoactivity upon methylene blue under visible light. The optimum calcination conditions for hydrazine treatment in these films were 350 °C and 10 min for high photocatalytic activity.[66]

Islam et al. had prepared cubic ordered mesoporous titania thin films by a surfactant templated sol-gel approach with titanium tetrachloride ($TiCl_4$) as the starting

material and F127 as SDA followed by N_2/Argon plasma treatment for titania doped with nitrogen (N-TiO_2). Thermogravimetric analysis (TGA) measurements had been performed to confirm that the calcination step greatly contributed in removing the template and material weight loss was mainly detected at approximately ~300 °C. The SEM result for TiO_2 films after calcination showed obvious nanopores at the surface while transmission electron microscopy (TEM) result illustrated the presence of pores throughout the material. The mean pore size and wall thickness of titania films were 7 nm and 5.5 nm, correspondingly. The specific surface area of the undoped titania film was 143 m^2/g while for 210 min of N-TiO_2 films, it was 117 m^2/g. Characterisation analysis showed that the introduction of nitrogen into titania films had lowered the band gap from 3.5 eV to 3.0 eV. Therefore, N-TiO_2 films demonstrated better photocatalytic efficiency to degrade methylene blue compared to undoped titania films under visible light.[67]

At first, Dong et al. had synthesised an ordered two-dimensional hexagonal mesoporous anatase crystals-silica nanocomposite by synchronous-assembly of surfactant and inorganic starting material molecules using P123 as the template. The amorphous framework began to crystallise after being calcinated at 350 °C for the withdrawal of SDA. Phase separation took place and anatase nanoscale crystals were arbitrary inserted into amorphous TiO_2 and SiO_2 frameworks. Thus, the materials formed had consistent as well as highly silica dispersal structures. After that, three-dimensional interlinkage mesoporous anatase titania were synthesised through silica extraction technique. The characterisation outcomes showed uniform anatase nanocrystals about 13.0 nm in size and formed a large surface area of around 145 m^2/g. HRTEM image also exhibited that crystals were arbitrarily aligned and linked with the amorphous silica nanoparticles to create "brick-mortar-like" structures. Ink bottle-like structures were produced where almost all crystals were overlapping on the pore partitions, while certain crystals were projected into the mesonecks. The interconnected mesoporous TiO_2 also showed better photocatalytic performance for Acid Red and microcystin-LR compared to the parent sample and commercial TiO_2 (P25) besides being considerably stable and reusable.[68]

Marco-Brown et al. had synthesised mesoporous titania xerogels via a simple and latent scalable technique according to the EISA method using F127 as a structure directing agent. Varying in synthesis parameters such as relative humidity (RH) and temperature have formed catalysts that demonstrated pores with governable pore and channel size dissemination around 3–12 nm, high specific surface area around 125-161 m^2/g and pore volume of about 0.17 to 0.38 cm^3/g. Selected area electron diffraction (SAED) and XRD results also demonstrated the existence of anatase phase in the materials produced. Based on the TEM image, granular products exhibited uniform mesopores which resembled bicontinuous worm-like mesophases. All catalysts revealed type IV isotherms which confirmed the mesoporous structure formation. The adsorption kinetics of gallic acid with the textural aspects indicated that larger pore diameter greatly assisted pollutant molecules to enter the particle pores. The catalysts produced also demonstrated a good performance in terms of recoverable and reusable photocatalysts.[69]

Alagarasi et al. had synthesised stable mesostructured titania via the hydrothermal route using P123 surfactant along with different calcination temperatures. The characterisation outcomes indicated that all materials have a wormhole-like porous framework which had spherical particles with the average size of around 6 to 50 nm. Increase in temperature also led to occurrence of phase transition. Among these catalysts, the sample calcined at 550 °C showed the best photoactivity for 4-chlorophenol due to the co-existence of three crystalline phases of titania

Table 2. Summary of preparation methods using non-ionic surfactants as SDA.

Study	Method	Surfactant	Precursor	Cal. Temp. (° C)	Surface area (m^2/g)	Pore Size (nm)	Ref.
Pal et al.	Sol-gel	P123	[a] TBOT	450	138.00	6.0–7.0	60
Smirnova et al.	Sol-gel	P123	[b] TTIP	400	147.00	2.5–6.0	61
Faisal et al.	Sol-gel	F127	[a] TBOT	450	106.44	10.0	62
Carlo et al.	Sol-gel	P123	[c] $Ti(OCH_3)_4$	350	74.00	5.0–35.0	63
Samsudin et al.	Sol-gel	F127	[b] TTIP	500	38.77	–	64
Smirnova et al.	Sol-gel	P123	[d] $TiC_{12}H_{32}O_4$	500	910.00	2.0-4.0	66
Geramipour & Oveisi	Sol-gel	P123	[b] TTIP	400	–	< 20.0	67
Islam & Rankin	Sol-gel	F127	[e] $TiCl_4$	350	143.00	7.0	68
Islam et al.	Sol-gel	F127	[e] $TiCl_4$	350	143.00	7.0	69
Dong et al.	Synchronous assembly	P123	[b] TTIP	350	145.00	4.7	70
Marco-Brown et al.	Sol-gel	F127	[e] $TiCl_4$	350	125.00–161.00	3.0–12.0	71
Alagarasi et al.	Hydrothermal	P123	[b] TTIP	350	60.00	7.9	72
Faisal et al.	Sol-gel	F127	[a] TBOT	900	85.76	10.0–20.0	65

[a] Tetrabutyl titanate [b] Titanium isopropoxide [c] Titanium(IV) ethoxide [d] Tetrapropyl orthotitanate [e] Titanium tetrachloride

which enhanced the charge segregation through electron hopping mechanism that facilitated the process.[70]

Faisal et al. had synthesised mesoporous $SrTiO_3$ nanocomposites by the sol-gel method using F127 surfactant. Polythiophene (PTh) doped mesoporous $SrTiO_3$ nanocomposites at varied PTh contents were also prepared by *in-situ* oxidative polymerisation means. High-resolution transmission electron microscopy (HRTEM) and FESEM images illustrated the shape of undoped $SrTiO_3$ which showed the production of porous and small spherical nanoparticles with sizes 10–20 nm. The FESEM images also revealed that the PTh-$SrTiO_3$ framework was quite close to the undoped $SrTiO_3$ and possessed type IV isotherm. Undoped $SrTiO_3$ had Brunauer-Emmett-Teller (BET) surface area and total pore volume of 85.76 m^2/g^{-1} and 0.304 cm^3/g, respectively, while BET surface area values of 0.5, 1, and 10 wt% PTh doped $SrTiO_3$ were 118.00 m^2/g, 126.66 m^2/g, and 72.36 m^2/g, correspondingly. The rate of photodegradation for 1% PTh-$SrTiO_3$ nanocomposite was 4.75 times greater than pure PTh or undoped $SrTiO_3$.[63] Table 2 shows a summary of the preparation methods of mesoporous titania using non-ionic surfactant as SDA.

2. 3. Polymers/Polymeric Fugitive Agent (PFA)

Polymeric fugitive agents (PFA) can be grouped as surfactants since they aid in the synthesis of mesoporous titania nanoparticles. Heterogeneous, crack-free and intensifying surface roughness of precursor can be obtained by adding the PFA which leads to superior nanostructures production without being coalesced while the calcination takes place. Previously, various types of PFA such as trehalose dihydrate, polyethylene glycol and hydroxypropyl cellulose have been used to structure mesoporous TiO_2. The addition of various PFA concentrations during the preparation of titania will affect its porosity. The agglomeration of catalyst surfaces could also be prevented due to the steric repulsion of the PFA and reaction solution mixture which leads to the adsorption onto the surface of titania nanoparticle. Maintaining the titania nanoparticles separated by steric repulsions between PFA layers as well as a sufficient thickness of the coating can be obtained with the addition of a sufficient quantity of PFA into the precursor mixture. The probability for the flocculation and coagulation to occur is low since the segregations by van der Waals attractive forces are too weak. Porous structures of titania catalyst are formed due to the presence of the gaps between the particles in films.[71–74]

Yang et al. had synthesised a three-dimensionally ordered macroporous materials of CuO/TiO_2 via a one-step sol-gel method. Before that, monodisperse polystyrene spheres with diameter about 280 nm would be synthesised via emulsifier-free emulsion polymerisation to form colloidal crystal templates which acted as PFA in the sol-gel approach to form a mesoporous structure.[75]

Zhang et al. had created C-doped hollow titania spheres by a simple and cost effective *in-situ* method using monodisperse cationic polystyrene spheres as SDA. After precipitation for titania by the template-assisted sol-gel method was completed, the PFA was separated after calcination at 450 °C. The structure modification of titania into the desired material had enhanced the photocatalytic performance by changing into visible light-activated photocatalyst. The results obtained had indicated that as-synthesised hollow anatase showed outstanding photoactivity in degrading Rhodamine B under visible-light compared to P25 and other titania-based catalysts previously studied.[76]

Study by Liu et al. focused on 3D ordered macro/mesoporous titania inverse opal films which had been synthesised hierarchically using polyethylene glycol (PEG) associated sol-gel means. For the production of macropores, monodispersed PS microspheres were turned into opal frameworks by the self-assembly approach while PEG 2000 mixed with titanium alkoxide starting material was the SDA. SEM and TEM outcomes from this study revealed that the 3D ordered macroporous frameworks comprised of TiO_2 mesoporous structures with hundreds of nanometre spherical air cavities arrayed in an FCC close-packing arrangement. The mesopores' average size was much larger (12 to 25 nm) compared to the same material published in other reports. This photocatalyst had improved the amount of organic dyes to be adsorbed, thus increasing the photoactivity. The introduction of the mesopores into the macropores built by disintegrating PFA in the films had attributed to the enhancement of the photocatalytic process besides enriching the reachable surface area of the material, improving the mass transport, and decreasing the length of the mesopore passages. Increment of PFA content up to 2.1 wt.% had improved the photocatalytic performance of the samples and started to decline with further increase in the PFA content. Thus, an immoderate amount of PFA led to the ruining of framework along with a great drop in photoactivity.[77]

Shao et al. had created carbon-doped TiO_2 single crystal nanorods with cationic polystyrene spheres/titania (CPS/TiO_2) as titania and carbon starting materials by a simple *in-situ* hydrothermal means for degradation of several organic pollutants under visible light. This approach required the usage of CPS as SDA. The titania starting material was successively deposited and the hydrothermal procedure along with the pyrolysis of CPS were under N_2 environment at 450 °C where the SDA would be removed. FESEM analysis clearly showed that TiO_2 nanorods with cubic rod-liked framework had been produced after template removal. This material showed notable photoactivity upon P25, C-doped TiO_2, and blue TiO_{2-X} polycrystal due to the intense synergy between carbon dopant and the single crystal framework.[78] Table 3 shows the brief synthesis means of mesoporous TiO_2 using PFA as SDA.

Table 3. Summary of preparation methods using PFA as SDA.

Study	Method	Surfactant	Precursor	Cal. Temp. (° C)	Surface area (m^2/g)	Pore Size (nm)	Ref.
Shao et al.	Hydrothermal	[a] CPS	[c] TBOT	450	–	–	80
Yang et al.	Sol-gel	Polystyrene	[d] $TiC_8H_{24}O_4$	500	74.00	5 to 35	77
Zhang et al.	Sol-gel	[a] CPS	[e] $TiC_{16}H_{40}O_4$	450	50.27	~ 29	78
Liu et al.	Sol-gel	[b] PEG 2000	[c] TBOT	450	–	12 to 25	79

[a] Cationic polystyrene spheres [b] Polyethylene glycol 2000 [c] Tetrabutyl titanate [d] Tetraethyl orthotitanate [e] Tetrabutyl orthotitanate

3. Synthesis Methods

Generally, self-assembly refers to the building blocks of compound linking via noncovalent bonds like hydrogen bond and van der Waals interaction without exterior interference. This process is usually employed to precursor molecule which will be pre-programmed to enhance its orientation and transformed into a desired supra molecule. EISA approach is a primary means for the formation of desired mesophase compound to further synthesise a mesoporous compound. Amphiphilic surfactants or polymers are usually included in the synthesis procedure since they have hydrophobic and hydrophilic proportions. Beyond the cmc of aqueous solution, surfactants accumulate forming micelle where the hydrophilic parts are exposed to water, thus preserving the hydrophobic parts inside the micelle. Micelles of different structures of mesophase formed are due to self-organisation upon cmc.[32] Therefore, many approaches for the conglomerate of mesoporous titania nanoparticle using a similar concept have been developed to improve the synthesis procedure and the expected outcome.

3. 1. Sol-Gel

The first is sol-gel which is normally used to synthesise ceramic materials at nano-scale by mixing either organic or inorganic precursor and solvents to produce sol which will then form gels. After that, all solvents will be extracted from the gel via drying or the heating process. As for the precursors, they may contain condensed oxide particles or polymeric substances and have metal adjoined by diverse ligands. For instance, methyl alkoxide is one of the frequent precursors used which possesses a metal atom with an organic ligand bound to it. This metaloorganic compound undergoes hydrolysis reaction by reacting with water since hydroxyde ions are present. Afterwards, polycondensation reaction takes place by removing alcohol as well as water molecules from gel and forming xerogel. The process will be continued by heating the xerogel at a certain temperature to form concentrated materials with a better morphology than the original precursor.[9,79–81] Mesoporous materials can be obtained by controlling various parameters such as temperature in the deposition room, withdrawal rate, and relative humidity. Therefore, it is possible to synthesise varying levels of porosity with an ordered structure, commonly mesoporous transition metal oxides via this approach.[82–87]

Previous studies revealed that the sol-gel method can be further modified into sol-gel/co-hydrolysis which resulted in many varieties of morphology with large surface area, specific pore size, and structures suitable for specific applications by controlling the parameters such as dopant concentration. Initially, sol-gel method is time consuming and usually takes about several days to complete. Sol-gel method also has other disadvantages since it involves many chemicals where the precursor needs to be dissolved in chosen solvents and organic reagents with addition of surfactants or SDA that will be removed using heating and calcination processes, plus it needs to be stirred continuously under certain temperature for a long duration which sometimes takes days to complete the experiment.[89,90] Thus, the sol-gel technique needs to go through various modifications including being paired with other synthesis methods and adjusting the solvents ratio to surpass these drawbacks for producing various types of TiO_2 nanostructures.[89–91]

Olsen et al. had synthesised several mesoporous titania doped with Al, La, Si, and Zr at different molar ratios and calcination temperatures using a modified co-hydrolysis method using solvent deficient approach to compare them in terms of their stability and morphology of the materials. Additionally, this modified method provided a fast and facile way to link stabilisers and titanium precursor under a solvent deficient system by not using any SDA. Most of the drawbacks previously mentioned have been overcome through this method since it involved a fast mixing, easy dissolution in a small amount of water which can be recycled and requires a simple apparatus. This method has a high potential to be scaled up to meet industry requirements. This method produced materials with atypical and desirable characteristics, such as high thermal stability, higher surface area, and better pore diameter distributions compared to previous works.[92]

3. 2. Microwave Assisted

Nowadays, microwave oven has become one of the essential utensils and it is easy to find in most kitchens because this modern appliance is cost-effective and requires less energy compared to customary meal preparation means. Currently, the employment of microwaves in material synthesis is considered as an advanced establishment rather than only for preparing meals.[93] Based on the electromagnetic spectrum, microwave radiation has a wave-

length from 1 mm to 1 m with frequency between 0.3 and 300 GHz. Regarding the microwaves for varying purposes, two frequencies which are 0.915 and 2.45 GHz commonly have been set aside by the Federal Devices Fee for microwave heat. Since the processing of new material using microwaves has been discovered, the microwave furnaces with larger range of frequency up to 18 GHz were invented in order to make it a more multipurpose appliance.[94] Miscellaneous techniques were investigated to coalesce the mesoporous titania nanoparticles such as hydrogenation under intense temperature, EISA, plasma treatment, and more.[95–98] Nevertheless, these procedures are harmful to the environment with inconsistent heat dissemination and require a lot of time for the synthesis to complete. However, the speedy and productive reaction proven by the microwaves makes it preferable for the synthesis of porous materials.[99–101]

Particularly, electrical energy will be converted into microwave energy within the reactor and then applied straight onto the substances where the microwave radiation will heat the reactants but not the reaction container itself. In addition, the heating process involves conversion of electromagnetic to thermal energy. Heat can be supplied throughout the sample since microwaves are capable of penetrating the materials and storing energy. This method affects the nucleation without having a direct contact between the reacting chemicals and energy sources which demonstrates that the volumetric heating does not involve the heat diffusion or the wall.[102]

In fact, energy transfer has high possibility to keep constant and heat the condensed substances quickly without being affected by the heat distribution on the surfaces. Therefore, the heating can be uniform throughout the material which usually leads to less formation of byproducts and/or decomposition products, if the machine is well-designed. The microwave energy is capable to increase the heating rate, reduce the kinetics of crystallisation and potentially form new metastable phases.[103] Furthermore, this technique offers a steady and speedy process condition as well as yields better materials surface morphology.[104]

In terms of pressure effect within the reactor, the rise in solvent temperature compared to its respective boiling point is expected. In addition, there are various applications of microwave energy especially for mineral and metal recovery processes like leaching, grinding, spent carbon regeneration, and waste management.[93,94,105,106] Nevertheless, the popularity of using microwave-assisted hydrothermal means in preparing nano-scale materials keeps increasing since it offers a speedy process, volumetric heating capacity, heat selectively, good energy transfer, obtains high purity materials, and good heat distribution throughout the reactants.[105]

Jaafar et al. had prepared mesoporous titania nanoparticles using the microwave approach under varied microwave power densities for photodegradation of 2-chlorophenol. From the result obtained, it was explained that at high power density, heating dispersion consistency has been enhanced with adequate aging to improve the formation between titanium and oxygen bonds and resulted in smaller particle sizes and smoother pore structure. The generation of site defects showed a significant improvement due to condensation while being heated in the microwave which contributes to a separate oxygen surface to produce OV besides reducing the Ti^{4+} to Ti^{3+} sites. Compared to commercial TiO_2, all the prepared catalysts showed smaller band gap and better photocatalytic activity under visible light rather than UV light. Besides that, these site defects function as an electron acceptor which retard the electron-hole from recombining and also aid in migrating the charge carrier. Kinetic studies revealed that adsorption as the dominating process in degradation of the pollutant obeyed a pseudo-first-order Langmuir-Hinshelwood model. In terms of reusability performance, photodegradation process was maintained, even though the fifth cycle ran with only a slight photocatalyst deactivation. Thus, this investigation successfully demonstrated the consistency of heat dispersal in the microwave which contributed in producing mesoporous titania nanoparticles with generous site defects besides being effective when exposed to visible light.[18]

3. 3. Hydrothermal

Hydrothermal or also known as solvothermal is a renowned approach since it can directly synthesise a highly controlled shapes for relatively small crystalline structures up to the micro size.[107] Generally, the synthesis is carried out using autoclave vessel made of steel at high temperature conditions but the crystals agglomerate after reaching the vapour pressure saturation. Therefore, addition of some enhancers, namely stabilising agents is needed to inhibit accumulation.[108,109] Other than that, this technique is mainly applied for heterogeneous process that employs high temperature or pressure with the solvents present or mineralisers in order to dissolve and recrystallise materials.[1,110,111]

Shao et al. had synthesised carbon-doped TiO_2 single crystal nanorods (C-TiO_2) using the hydrothermal method. The C-TiO_2 nanorods showed higher degradation compared to P25, C-doped TiO_2, as well as blue TiO_{2-x} polycrystal due to the synergistic effect between carbon dopant and crystal structure. Previously, it was challenging to assimilate dopant into the TiO_2 crystal lattice because of its high crystallinity. Therefore, a facile hydrothermal approach had been conducted with CPS/TiO_2 as the starting material for titania nanorods and carbon source to enhance the reaction possibility of TiO_2 and C, as well as to increase the possibility of C-TiO_2 single crystal formation. Based on the SEM analysis, the C-TiO_2 single crystal formation via this method had been successfully demonstrated by raising the hydrothermal temperature up to 180 °C. The single crystal nanorods were further confirmed after

being calcined at 450 °C. Besides, energy-dispersive X-ray (EDX) studies which were carried out to verify the elements present in the samples revealed that the specific element signals were distributed throughout the materials.[78]

3. 4. Sonochemical

Sonochemical or sonochemistry is an approach which requires the usage of strong ultrasound around 20 kHz up to 10 MHz during the synthesis procedure and resulting in an acoustic cavitation for the creation, expansion, and collapse of bubbles in the mixture. The implode of a bubble creates a constrained hot spot with conditions of around 4730 °C at 1800 atm with a cooling rate of more than –164.15 °C/s which may be applied to form a well-structured nanomaterial. The effectiveness of this technique can be affected by some factors such as volatile starting materials where it is supposed to be used at the initial reaction site with the vapour contained in the cavitation bubbles.

Previously, Suslick et al. were among the early researchers who managed to synthesise the nanophase of crystalline titania via this method and the modification of this research is still ongoing.[112] In addition, nanoparticles with a better dispersion, larger surface area, good thermal stability, as well as higher phase purity can be obtained via this method. Other than that, the synthesis approach via sonochemical can help in controlling the mineral growth, influencing the distribution of mineral size, controlling the intended morphology, elimination of impurities in the mineral, removing the need to add seed minerals, and improving the separation performance in solid-liquid. Therefore, this approach appears to be one of the efficient means, especially in synthesising the mesoporous compounds since it is not only generating nucleation (sononucleation) which can affect the crystallisation process but also has a good reproducible capability.[113–115]

Swapna et al. had synthesised mesoporous anatase TiO_2 nanopowder via the simple, faster, and inexpensive sol-gel method by ultrasonic irradiation. The application of high intensity ultrasound provided simpler and flexible artificial equipment for nanosized catalysts which cannot be obtained by regular approaches. Several benefits of using ultrasonic irradiation compared to typical methods are improved phase purity, uniform size distribution, and rapid technique. Based on the XRD result, it showed that the mean particle size was around 19 nm with high purity of anatase titania.[116]

Even though mesoporous titania material possesses diverse prospective implementations for its electronic and optical properties, its framework and surface are hard to modify due to its refractory and quick sol-gel reaction. Therefore, Pal et al. had prepared mesoporous titania microspheres by incorporating the sol-gel method along with the spray-drying approach to overcome this limitation by hierarchically fabricating the intended materials at a large scale. Other than that, elements like metal complex or nanoparticles can be doped in the mesoporous TiO_2 microspheres using this method. Fe_3O_4@mesoporous TiO_{2-} x microsphere had also been prepared and showed remarkable selective phosphopeptide-enrichment activity. This coupled method was more favourable due to its simple equipment requirement, fast reaction process, low waste, and abundant products compared to the multistep conventional methods. The diameter of bead, pore size, morphology, monodispersity, and surface area could be tuned by differing the parameters during pre-hydrolysis. Alteration of parameters during spray-drying treatment such as compositions, solvents, aging time, temperature and pressure could also enhance their efficiency. The microspheres synthesised had a range of size from 500 nm to 5 μm with surface area between 150 and 162 m^2/g and average pore size of 4 to 6 nm.[58]

4. Role of Dopants

Surface functionalisation describes the action for surface modification of a material to alter its original properties and characteristic. There are many studies related to surface modification procedures conducted especially for photocatalysts surfaces and addition of dopants which mainly focused on enhancing their optical activity as the main purpose in the modification of titania nanomaterials which can be achieved by altering the activation region from UV to visible. Generally, metals and non-metals usually used as dopants for TiO_2 include non-metallic species, transition metals, rare earth elements, plasmonic photocatalysts, alkali and alkaline earth metals, as well as co-doping of metal and non-metal elements.[117,118] The addition of dopants or coupling with potential elements and compounds will alter the charge-transfer properties between TiO_2 and the overall system where the dopant metal will act as trapper to trap the photogenerated electron besides allowing the interfacial charge-transfer processes to improve their catalytic performance.[117]

4. 1. Metal Dopant

Metal oxide displays distinctive chemical and physical properties due to its composition and multi-structure including specific properties like selective oxidation and electron or ionic separation. These materials also possess the capability to construct different porous mesostructures to be applied for catalysis and energy storage.[80] As an example, during the synthesis of mesoporous titania, transition metals acting as dopants will be added for improving the photodegradation efficiency. Some of the recent examples for metals and metal oxides commonly used to be doped with titania nanoparticles are CuO, Fe_2O_3, SnO, Zn, Ag, Cu, and Nb, as well as common ions such as Co^{2+}, Ni^{2+}, Mn^{3+}, and Cu^{2+}.[119-125]

Generally, transition metal oxides have electrons in the d-orbital compact to nanosized walls, active sites and

bound pore latticeworks.[126] Therefore, the segregation capacity for generation of electrons and holes may be increased due to the creation of heterojunctions and electron moving between conduction bands through the incorporation with other transition metal oxide. The photodegradation will be extended by the electron transfer which will inhibit the electron-hole from recombining. Anatase TiO_2 mostly can absorb UV light that contains energy source in the form of photons since it possesses a large band gap (3.20 eV). However, solar energy only contains about 5% of UV photons while domestic lamps mainly comprise of visible photons. A high recombination rate of electron and hole at the photocatalyst surface also contributes in lowering the photodegradation performance. Hence, the usage of accessible solar energy needs to be maximised since the advanced properties of mesoporous TiO_2 is to produce and segregate hole and electron.[57]

Luna et. al. had revealed that CuO-TiO_2 composite could be produced via common impregnation method to degrade gallic acid under visible light. The incorporation of CuO and TiO_2 in the range of 0–70% revealed that 40% CuO content showed the best performance for degradation of gallic acid under visible light. After the CuO loading, the band gap exhibited a remarkable reduction around 1.04 eV from its original value for titania therefore the photocatalyst could be activated under visible light which might be related to a series injection of charge-carriers. As the band gap has shifted to different electromagnetic radiation, the photodegradation performance under UV light after addition of CuO could no longer show enhancement and only present as impurities or defects on the surface. The production of intermediates like maleic acid after gallic acid degradation took place before reaching mineralisation.[127–130]

Cheng et al. had synthesised TiO_2/Fe_2O_3 through calcination of P25 nanoparticles mix with Fe_3O_4. The result obtained showed that TiO_2/Fe_2O_3 could enhance visible-light activity compared to bare P25 and Fe_2O_3 because of the synergistic effect. Moreover, the result revealed that the coalescence of these two transition metal oxides had promoted movement and segregation of charge carriers which improved photodegradation performance.[131]

4. 2. Non-Metal Dopant

Non-metal dopants occur as separated atoms at the catalyst surface without clustering, unlike transition metals and have the potential to degrade organic pollutants under UV light. Besides, substantial synergistic properties can also be reached by doping with more than one heteroatom. They fundamentally change the surface transfer of charge carriers by providing limited states in the band gap as well as yielding varied surface morphologies. Carbon nanotubes like graphene and fullerene along with nitrogen are some of the examples for non-metal elements with high potential to introduce into TiO_2.[132–136] Basically, carbon usually links with other carbon either by sp^3 or sp^2 covalent bonds which lead to differences in molecular morphologies such as nanotubes. Porous carbons possess properties such as chemical inertness, large surface area, high pore volume, mechanical stability, and low cost to make them suitable as adsorbents, catalyst supports, separation membranes, and more.[137–140]

Li et al. had prepared mesoporous TiO_2/C composite beads through anion-exchange with resin as carbon source which was then used as an adsorbent-photocatalyst to degrade methyl orange under visible light. These composites demonstrated synergistic effect between carbon and titania due to substantial pore size and surface area. Thus, these composites demonstrated better photocatalytic performance compared to TiO_2 alone besides having better absorbance, as well as photocatalytic degradation that could be activated under visible light. In addition, this photocatalyst was easily removed from pollutant due to their bead-like structure which is suitable to be applied for industrial treatment of organic contaminants.[141–143]

Faisal et al. had synthesised mesoporous NiO/TiO_2 composites using varying NiO percentages via a modified sol-gel technique assisted with triblock copolymer, proceeded by a facile ultrasonic approach for better degradation of methylene blue and gemifloxacin mesylate under visible light. The result of XRD analysis illustrated that a biphasic anatase-rutile structure of this catalyst at different NiO percentages was found. The production of extremely small titania nanoparticles and NiO sheet-like framework with particle sizes 10-15 nm and 30-50 nm was sequentially confirmed by the TEM results. Besides, this catalyst had a surface area of 111.3 m^2/g and pore volume of 0.376 cm^3/g. Comparison between this catalyst and its original NiO nanoparticles showed that this catalyst successfully had better degradation upon methylene blue under visible light irradiation resulting from effective charge segregation while the loading of 0.5 wt% NiO into this catalyst exhibited high decomposition upon gemifloxacin mesylate by completing the process after 3 h.[60]

5. Conclusion

Recent advances in science and technology infrastructure especially for semiconductors and nanostructured materials show a remarkable potential to be explored and applied in various applications mainly for the energy, science, and environmental sectors. TiO_2 is one of the transition metal oxides which has been studied widely because it has outstanding electrochemical aspects, is inexpensive, chemically and thermally stable, risk-free, inhibits photo-induced reaction, as well as being widely utilised for varied commercial purposes. Therefore, it is necessary for researchers to keep upgrading the TiO_2 source by modifying the synthesis approaches, adding potential dopants,

and inventing new structures. In this review, we have discussed in detail the information regarding the latest research about modification of titania using different surfactants, synthesis methods, the role of dopants and their effect on titania morphology in terms of crystallinity, porosity, and photocatalytic performance. Thus, these basic information, initial inferences, and expectations are provided for further study.

Acknowledgement

The authors are thankful for the financial support by Ministry of Education Malaysia for Fundamental Research Grant Scheme (203.PKIMIA.6711607) and Universiti Sains Malaysia (USM) for Short Term Grant (304/PKIMIA/6315055).

List of abbreviations

PTh	Polythiophene
BC	Benzalkonium chloride
C-TiO_2	Carbon-doped TiO_2 single crystal nanorods
CPS/TiO_2	Cationic polystyrene spheres/titania
CTAB	Cetyl-trimethylammonium bromide
CTAC	Cetyl-trimethylammonium chloride
P25	Commercial TiO_2
cmc	Critical micelle concentration
Ag-MTN	Silver doped into MTN
EDX	Energy-dispersive X-ray
EISA	Evaporation-induced self-assembly
FESEM	Field emission scanning electron microscopy
HRTEM	High-resolution transmission electron microscopy
m-TiO_2	Manganese doped into TiO_2
TiMS	Mesoporous titania films
MTN	Mesoporous titania nanoparticles
DTAB	n-Dodecyl-trimethylammonium bromide
C_{18}TAB	Octadecyl-trimethyl ammonium bromide
OV	Oxygen vacancies
PL	Photoluminescence
F127	Pluronic F127
P123	Pluronic P123
PEG	Polyethylene glycol
PFA	Polymeric fugitive agents
PTh	Polythiophene
SEM	Scanning electron microscope
SAED	Selected area electron diffraction
SDS	Sodium dodecyl sulphate
SDA	Surface directing agent
TGA	Thermogravimetric analysis
TSD	Ti^{3+} site defects
TEM	Transmission electron microscopy
UV	Ultraviolet
UV-Vis DRS	UV-Vis Diffuse Reflectance Spectroscopy
XRD	X-ray diffraction
XPS	X-ray photoelectron spectroscopy

6. References

1. D. Dambournet, I. Belharouak, K. Amine, *J. Chem. Mater.* **2010,** *22,* 1173–1179. **DOI:**10.1021/cm902613h
2. F. Amano, R. Tosaki, K. Sato, Y. Higuchi, *J. Solid State Chem.* **2018,** *258,* 79–85. **DOI:**10.1016/j.jssc.2017.09.030
3. A. Abbasi, J. J. Sardroodi, *Acta Chim. Slov.* **2016,** *63,* 713–720. **DOI:**10.17344/acsi.2016.2350
4. Z. Zhang, G. Li, Z. Cui, K. Zhang, Y. Feng, S. Meng, *J. Solid State Chem.* **2016,** *237,* 242–247. **DOI:**10.1016/j.jssc.2016.02.005
5. X. Qu, M. Liu, J. Yang, C. Wang, H. Meng, S. Li, L. Shi, F. Du, *J. Solid State Chem.* **2018,** *264,* 77–85. **DOI:**10.1016/j.jssc.2018.05.002
6. N. Veronovski, M. Lesnik, A. Lubej, D. Verhovsek, *Acta Chim. Slov.* **2014,** *61,* 595–600.
7. A. R. Khataee, M. B. Kasiri, *J. Mol. Catal. A Chem.* **2010,** *328,* 8–26. **DOI:**10.1016/j.molcata.2010.05.023
8. D. Chen, L. Cao, F. Huang, P. Imperia, Y. B. Cheng, R. A. Caruso, *J. Am. Chem. Soc.* **2010,** *132,* 4438–4444. **DOI:**10.1021/ja100040p
9. D. Ramimoghadam, S. Bagheri, S. B. A. Hamid, *BioMed Res. Int.* **2014,** *2014.* **DOI:**10.1155/2014/205636
10. S. D. Mo, W. Y. Ching, *J. Phys. Rev. B* **1995,** *51,* 13023–13032. **DOI:**10.1103/PhysRevB.51.13023
11. O. Sacco, V. Vaiano, C. Daniel, W. Navarra, V. Venditto, *Mater. Sci. Semicond. Process.* **2018,** *80,* 104–110. **DOI:**10.1016/j.mssp.2018.02.032
12. T. Okuno, G. Kawamura, H. Muto, A. Matsuda, *J. Solid State Chem.* **2016,** *235,* 132–138. **DOI:**10.1016/j.jssc.2015.12.025
13. T. W. Kim, M. Park, H. Y. Kim, S. J. Park, *J. Solid State Chem.* **2016,** *239,* 91–98. **DOI:**10.1016/j.jssc.2016.04.010
14. X. D. Zhu, Y. L. Zheng, Y. J. Feng, K. N. Sun, *J. Solid State Chem.* **2018,** *258,* 691–694. **DOI:**10.1016/j.jssc.2017.12.001
15. B. Zhao, Y. W. Chen, *J. Phys. Chem. Solids,* **2011,** *72,* 1312–1318. **DOI:**10.1016/j.jpcs.2011.07.025
16. Y. Liu, G. Ji, M. A. Dastageer, L. Zhu, J. Wang, B. Zhang, X. Chang, M. A. Gondal, *RSC Adv.* **2014,** *4,* 56961–56969. **DOI:**10.1039/C4RA10670A
17. X. Qu, D. Xie, L. Gao, L. Cao, F. Du, *J. Mater. Sci.* **2015,** *50,* 21–27. **DOI:**10.1007/s10853-014-8441-7
18. N. F. Jaafar, A. A. Jalil, S. Triwahyono, N. Shamsuddin, *RSC Adv.* **2015,** *5,* 90991–91000. **DOI:**10.1039/C5RA15120A
19. I. Nadeem, Hani Shaker, *Acta Chim. Slov.* **2016,** *63,* 363–368. **DOI:**10.17344/acsi.2016.2337
20. H. Y. Gan, L. E. Leow, S. T. Ong, *Acta Chim. Slov.* **2017,** 64, 144–158. **DOI:**10.17344/acsi.2016.2983
21. W. Gao, M. R. Farahani, M. Imran, *Acta Chim. Slov.* **2017,** 64, 256–260. **DOI:**10.17344/acsi.2016.2947
22. M. Faisal, H. Bouzid, F. A. Harraz, A. A. Ismail, S. A. Al-Sayari, M. S. Al-Assiri, *Surf. Coat. Technol.* **2015,** *263,* 44–53. **DOI:**10.1016/j.surfcoat.2014.12.063
23. N. Wenbin, W. Dengchao, Z. Zhenzhen, H. Zhongjie, Z. Jianwei, *J. Chem. Lett.* **2010,** *39,* 98–99. **DOI:**10.1246/cl.2010.98
24. J. Zhu, W. Mu, L. Su, X. Li, Y. Guo, S. Zhang, Z. Li, *J. Solid State Chem.* **2017,** *248,* 142–149. **DOI:**10.1016/j.jssc.2017.01.028

25. X. An, C. Gao, J. Liao, X. Wu, X. Xie, *Mater. Sci. Semicond. Process.* **2015,** *34,* 162–169. **DOI:**10.1016/j.mssp.2015.02.003
26. Y. Hao, X. Shao, B. Li, L. Hu, T. Wang, *Mater. Sci. Semicond. Process.* **2015,** *40,* 621–630. **DOI:**10.1016/j.mssp.2015.07.026
27. D. M. Antonelli, J. Y. Ying, *Angew. Chem. Int. Ed. Engl.* **1995,** *34,* 2014–2017. **DOI:**10.1002/anie.199520141
28. D. M. Antonelli, J. Y. Ying, *J. Colloid Interface Sci.* **1996,** *1,* 523–529. **DOI:**10.1016/S1359-0294(96)80122-1
29. N. Ulagappan, C. N. R. Rao, *J. Chem. Commun.* **1996,** 1685–1686. **DOI:**10.1039/cc9960001685
30. M. Froba, O. Muth, A. Reller, *J. Solid State Ionics* **1997,** 101–*103,* 249–253. **DOI:**10.1016/S0167-2738(97)84038-6
31. T. E. W. Niessen, J. P. M. Niederer, T. Gjervan, W. F. Holderich, *J. Microporous Mesoporous Mater.* **1998,** *21,* 67–74. **DOI:**10.1016/S1387-1811(97)00049-8
32. C. J. Brinker, *MRS Bull.* **2004,** *29,* 631–640. **DOI:**10.1557/mrs2004.183
33. W. Wu, L. Zhang, X. Zhai, C. Liang, Kaifeng Yu, *Nanomater. Nanotechnol.* **2018,** *8,* 1–8. **DOI:**10.1177/1847980418781973
34. S. S. Pathak, I. C. Pius, R. D. Bhanushali, K. T. Pillai, J. V. Dehadraya, S. K. Mukerjee, *J. Porous Mater.* **2013,** *20,* 753–761. **DOI:**10.1007/s10934-012-9650-6
35. A. P. Lagrow, B. Ingham, M. F. Toney, R. D. Tilley, *J. Phys. Chem. C* **2013,** *117,* 16709–16718. **DOI:**10.1021/jp405314g
36. Y. Du, L. Zhou, Z. Guo, X. Du, J. Lei, *J. Porous Mater.* **2019,** *26,* 1069–1077. **DOI:**10.1007/s10934-018-0701-5
37. T. Kos, A. Anlovar, E. Zagar, Z. C. Orel, M. Zigon, *Acta Chim. Slov.* **2014,** *61,* 497–505.
38. G. Kume, M. Galloti, G. Nunes, *J. Surfact. Deterg.* **2008,** *11,* 1–11. **DOI:**10.1007/s11743-007-1047-1
39. H. Khajuria, J. Ladol, R. Singh, S. Khajuria, H. N. Sheikh, *Acta Chim. Slov.* **2015,** *62,* 849–858. **DOI:**10.17344/acsi.2015.1558
40. M. M. Mohamaed, W. A. Bayoumy, M. Khairy, M. A. Mousa, *J. Microporous Mesoporous Mater.* **2006,** *97,* 66–77. **DOI:**10.1016/j.micromeso.2006.07.028
41. K. C. J. Li, W. Wang, Y. Zhang, X. Wang, H. Su, *Mater. Sci. Semicond. Process.* **2012,** *15,* 20–26. **DOI:**10.1016/j.mssp.2011.05.007
42. D. L. Liao, B. Q. Liao, *J. Photochem. Photobiol. A Chem.* **2007,** *187,* 363–369. **DOI:**10.1016/j.jphotochem.2006.11.003
43. G. Calleja, D. P. Serrano, R. Sanz, P. Pizarro, A. Garcia, *Ind. Eng. Chem. Res.* **2004,** *43,* 2485–2492. **DOI:**10.1021/ie030646a
44. M. M. Mohamaed, W. A. Bayoumy, M. Khairy, M. A. Mousa, *J. Micro. Meso. Mater.* **2007,** *103,* 174–183. **DOI:**10.1016/j.micromeso.2007.01.052
45. J. S. Beck, J. C. Vartuli, W. J. Roth, M. E. Leonowicz, C. T. Kresge, K. D. Schmitt, C. T. W. Chu, D. H. Olson, E. W. Sheppard, S. B. McCullen, J. B. Higgins, J. L. Schlenker, *J. Am. Chem. Soc.* **1992,** *114,* 10834–10843. **DOI:**10.1021/ja00053a020
46. J. S. Beck, J. C. Vartuli, G. J. Kennedy, C. T. Kresge, W. J. Roth, S. E. Schramm, *Chem. Mater.* **1994,** *6,* 1816–1821. **DOI:**10.1021/cm00046a040
47. G. Calleja, D. P. Serrano, R. l. Sanz, P. Pizarro, A. Garcia, *Ind. Eng. Chem. Res.* **2004,** *43,* 2485–2492. **DOI:**10.1021/ie030646a
48. A. M. Putz, S. Cecilia, C. Ianasi, Z. Dudas, K. N. Szekely, J. Plocek, P. Sfarloaga, L. Sacarescu, L. Almasy, *J. Porous Mater.* **2015,** *22,* 321–331. **DOI:***10.1007/s10934-014-9899-z*
49. S. G. Dixit, A. R. Mahadeshwar, S. K. Haram, *Colloids Surf. A: Physicochem. Eng. Aspects* **1998,** *133,* 69–75. **DOI:**10.1016/S0927-7757(97)00126-X
50. N. Kallay, M. Pastuovic, E. Matijevic, *J. Colloids Interface Sci.* **1985,** *106,* 452–458. **DOI:**10.1016/S0021-9797(85)80019-9
51. S. K. Mehta, K. K. Bhasin, R. Chauhan, S. Dham, *Colliod Surf. A: Physicochem. Eng. Aspects* **2005,** *255,* 153–157. **DOI:**10.1016/j.colsurfa.2004.12.038
52. V. K. Aswal, P. S. Goyal, Chem. Phys. Lett. **2003,** *368,* 59–65. **DOI:**10.1016/S0009-2614(02)01833-X
53. H. Shibata, T. Ogura, T. Mukai, T. Ohkubo, H. Sakai, M. Abe, J. Am. Chem. Soc. **2005,** 127, 16396–16397. **DOI:**10.1021/ja0552601
54. S. Casino, F. Di Lupo, C. Francia, A. Tuel, S. Bodoardo, C. Gerbaldi, *J. Alloys Compd.* **2014,** *594,* 114–121. **DOI:**10.1016/j.jallcom.2014.01.111
55. X. Li, P. Liu, Y. Mao, M. Xing, J. Zhang, *App. Catal. B: Environ.* **2015,** *164,* 352–359. **DOI:**10.1016/j.apcatb.2014.09.053
56. N. F. Jaafar, A. A. Jalil, S. Triwahyono, *App. Surf. Sci.* **2017,** *392,* 1068–1077. **DOI:**10.1016/j.apsusc.2016.09.112
57. W. Li, Z. Wu, J. Wang, A.A. Elzatahry, D. Zhao, *J. Chem. Mater.* **2013,** *26,* 287–298. **DOI:**10.1021/cm4014859
58. M. Pal, L. Wan, Y. Zhu, Y. Liu, Y. Liu, W. Gao, Y. Li, G. Zheng, A. A. Elzatahry, A. Alghamdi, Y. Deng, D. Zhao, *J. Colloid Interface Sci.* **2016,** *479,* 150–159. **DOI:**10.1016/j.jcis.2016.06.063
59. N. Smirnova, I. Petrik, V. Vorobets, G. Kolbasov, A. Eremenko, *Nanoscale Res. Lett.* **2017,** *12,* 239. **DOI:**10.1186/s11671-017-2002-3
60. M. Faisal, F. A. Harraz, A. A. Ismail, A. M. El-Toni, S. A. Al-Sayari, A. Al-Hajry, M. S. Al-Assiri, *Ceram. Int.* **2018,** *44,* 7047–7056. **DOI:**10.1016/j.ceramint.2018.01.140
61. G. Di Carlo, G. Calogero, M. Brucale, D. Caschera, T. De Caro, G. Di Marco, G. M. Ingo, *J. Alloys Compd.* **2014,** *609,* 116–124. **DOI:**10.1016/j.jallcom.2014.04.145
62. E. M. Samsudin, S. B. A. Hamid, J. C. Juan, W. J. Basirun, *App. Surf. Sci.* **2015,** *355,* 959–968. **DOI:**10.1016/j.apsusc.2015.07.178
63. M. Faisal, F. A. Harraz, A. A. Ismail, A. M. El-Toni, S. A. Al-Sayari, A. Al-Hajry, M. S. Al-Assiri, *Sep. Purif. Technol.* **2018,** *190,* 33–44. **DOI:**10.1016/j.seppur.2017.08.037
64. N. P. Smirnova, N. I. Surovtseva, T. V. Fesenko, E. M. Demianenko, A. G. Grebenyuk, A. M. Eremenko, *J. Nanostruct. Chem.* **2015,** *5,* 333–346. **DOI:**10.1007/s40097-015-0165-y
65. T. Geramipour, H. Oveisi, *Thin Solid Films* **2016,** 619, 353–358. **DOI:**10.1016/j.tsf.2016.10.030
66. S. Z. Islam, S. E. Rankin, *Mater. Chem. Phys.* **2016,** *182,* 382–393. **DOI:**10.1016/j.matchemphys.2016.07.046
67. S. Z. Islam, A. Reed, D. Y. Kim, S. E. Rankin, *Microporous Mesoporous Mater.* **2016,** *220,* 120–128. **DOI:**10.1016/j.micromeso.2015.08.030
68. W. Dong, Y. Yao, L. Li, Y. Sun, W. Hua, G. Zhuang, D. Zhou, S. Yan, W. Song, *App. Catal. B: Environ.* **2017,** *217,* 293–302. **DOI:**10.1016/j.apcatb.2017.05.083

69. J. L. Marco-Brown, M. A. Blesa, G. J. A. A. Soler-Illia, *Colloids Surf. A: Physicochem. Eng. Aspects,* **2017,** *530,* 93–103. **DOI:**10.1016/j.colsurfa.2017.07.054
70. A. Alagarasi, P. U. Rajalakshmi, K. Shanthi, P. Selvam, *Catal. Today* **2018,** *309,* 202–211. **DOI:**10.1016/j.cattod.2017.08.001
71. F. Chekin, S. Bagheri, S. B. A. Hamid, *J. Sens. Actuators B* **2013,** *177,* 898–903. **DOI:**10.1016/j.snb.2012.12.002
72. V. Nagpal, R. Davis, S. Desu, *J. Mater. Res.* **1995,** *10,* 3068–3078. **DOI:**10.1557/JMR.1995.3068
73. S. J. Bu, Z. G. Jin, X. X. Liu, L. R. Yang, Z. J. Cheng, *J. Eur. Cer. Soc.* **2005,** *25,* 673–679. **DOI:**10.1016/j.jeurceramsoc.2003.12.025
74. T. Miki, K. Nishizawa, K. Suzuki, K. Kato, *J. Mater. Lett.* **2004,** *58,* 2751–2753. **DOI:**10.1016/j.matlet.2004.04.015
75. H. Masai, T. Miyazaki, K. Mibu, Y. Takahashi, T. Fujiwara, *J. Eur. Ceram. Soc.* **2015,** *35,* 2139–2144. **DOI:**10.1016/j.jeurceramsoc.2015.01.013
76. Y. Zhang, Z. Zhao, J. Chen, L. Cheng, J. Chang, W. Sheng, C. Hu, S. Cao, *App. Catal. B: Environ.* **2015,** *165,* 715–722. **DOI:**10.1016/j.apcatb.2014.10.063
77. W. Liu, A. Wang, J. Tang, S. L. Chen, G. Yuan, K. Zhao, C. Li, X. Liu (2015), *Microporous Mesoporous Mater.* **2015,** *204,* 143–148. **DOI:**10.1016/j.micromeso.2014.11.015
78. J. Shao, W. Sheng, M. Wang, S. Li, J. Chen, Y. Zhang, S. Cao, *App. Catal. B: Environ.* **2017,** *209,* 311–319. **DOI:**10.1016/j.apcatb.2017.03.008
79. D. Verhovsek, M. Lesnik, N. Veronovski, Z. Samardzija, K. Zagar, Miran Ceh, *Acta Chim. Slov.* **2014,** *61,* 468–479.
80. N. C. Korosin, N. Bukovec, P. Bukovec, *Acta Chim. Slov.* **2015,** *62,* 304–311. **DOI:**10.17344/acsi.2014.1102
81. B. L. Shinde, L. A. Dhale, V. S. Suryavanshi, K. S. Lohar, *Acta Chim. Slov.* **2017,** *64,* 931–937. **DOI:**10.17344/acsi.2017.3619
82. P. Innocenzi, S. Costacurta, T. Kidchob, L. Malfatti, P. Falcaro, G. Soler-Illia, *J. Sol Gel Methods Mater. Process* **2008,** 105–123. **DOI:**10.1007/978-1-4020-8514-7_7
83. A. Marzec, M. Radecka, W. Maziarz, A. Kusior, Z. Pedzich, *J. Eur. Ceram. Soc.* **2016,** *36,* 2981–2989. **DOI:**10.1016/j.jeurceramsoc.2015.12.046
84. T. Brezesinski, M. Groenewolt, A. Gibaud, N. Pinna, M. Antonietti, B. M. Smarsly, *Adv. Mater.* **2006,** *18,* 2260–2263. **DOI:**10.1002/adma.200600258
85. P. Innocenzi, L. Malfatti, *J. Chem. Soc. Rev.* **2013,** *42,* 4198–4216. **DOI:**10.1039/c3cs35377j
86. L. Mahoney, R. T. Koodali, *J. Mater.* **2014,** *7,* 2697–2746. **DOI:**10.3390/ma7042697
87. D. E. Clark, D. C. Folz, J. K. West, *Mater. Sci. Eng. A* **2000,** *287,* 153–158. **DOI:**10.1016/S0921-5093(00)00768-1
88. K. E. Haque, *Int. J. Miner. Process* **1999,** *57,* 1–24. **DOI:**10.1016/S0301-7516(99)00009-5
89. J. G. Cerrillo, A. N. C. Mendoza, P. M. M. Romero, A. H. Granados, H. Hu, *Mater. Sci. Semicond. Process.* **2017,** *72,* 106–114. **DOI:**10.1016/j.mssp.2017.08.027
90. W. Zhang, X. Pei, J. Chen, H. He, *Mater. Sci. Semicond. Process.* **2015,** *38,* 24–30. **DOI:**10.1016/j.mssp.2015.04.007
91. N. Nithya, G. Bhoopathi, G. Magesh, C. D. N. Kumar, *Mater. Sci. Semicond. Process.* **2018,** *83,* 70–82. **DOI:**10.1016/j.mssp.2018.04.011
92. R. E. Olsen, C. H. Bartholomew, B. Huang, C. Simmons, B.F. Woodfield, *Microporous Mesoporous Mater.* **2014,** *184,* 7–14. **DOI:**10.1016/j.micromeso.2013.09.030
93. E. T. Thostenson, T. W. Chou, *J. Compos. Part A* **1999,** *30,* 1055–1071. **DOI:**10.1016/S1359-835X(99)00020-2
94. P. Lidstrom, J. Tierney, B. Wathey, J. Westman, *J. Tetrahedron* **2001,** *57,* 9225–9283. **DOI:**10.1016/S0040-4020(01)00906-1
95. S. Hoang, S. P. Berglund, N. T. Hahn, A. J. Bard, C. B. Mullins, *J. Amer. Chem. Soc.* **2012,** *134,* 3659–3662. **DOI:**10.1021/ja211369s
96. Z. K. Zhang, M. L. Bai, D. Z. Guo, S. M. Hou, G. M. Zhang, *Chem. Commun.* **2011,** *47,* 8439–8441. **DOI:**10.1039/c1cc12669e
97. Z. Yuan, X. W. Xiao, H. Lv, C. Z. Wen, *J. Phys. Chem. Solids* **2007,** *68,* 1652–1655. **DOI:**10.1016/j.jpcs.2007.04.001
98. G. D. Bromiley, A. A. Shiryaev, *Phys. Chem. Miner.* **2006,** *33,* 426–434. **DOI:**10.1007/s00269-006-0087-9
99. L. Moradi, M. A. Sadegh, *Acta Chim. Slov.* **2017,** *64,* 506–512. **DOI:**10.17344/acsi.2017.3417
100. A. Srinivas, M. Sunitha, K. Raju, B. Ravinder, S. Anusha, T. Rajasri, P. Swapna, D. Sushmitha, D. Swaroopa, G. Nikitha, C. G. Rao, *Acta Chim. Slov.* **2017,** *64,* 319–331. **DOI:**10.17344/acsi.2016.3153
101. L. C. Greiler, H. Haase, B. Mahltig, *Acta Chim. Slov.* **2018,** *65,* 865–874. **DOI:**10.17344/acsi.2018.4513
102. N. H. N. Kamarudin, A. A. Jalil, S. Triwahyono, V. Artika, N. F. M. Salleh, A. H. Karim, N. F. Jaafar, M. R. Sazegar, R. R. Mukti, B. H. Hameed, A. Johari, *J. Colloid Interface Sci.* **2014,** *421,* 6–13. **DOI:**10.1016/j.jcis.2014.01.034
103. S. Komarnenia, R. K. Rajha, H. Katsuki, *Mater. Chem. Phys.* **1999,** *61,* 50–54. **DOI:**10.1016/S0254-0584(99)00113-3
104. M. Shi, L. Kang, Y. Jiang, C. Ma, *Catal. Lett.* **2014,** *144,* 278–284. **DOI:**10.1007/s10562-013-1132-1
105. D. E. Clark, D. C. Folz, J. K. West, *J. Mater. Sci. Eng. A* **2000,** *287,* 153–158. **DOI:**10.1016/S0921-5093(00)00768-1
106. K. E. Haque, *Int. J. Min. Process* **1999,** *57,* 1–24. **DOI:**10.1016/S0301-7516(99)00009-5
107. Z. Bo, R. Dong, C. Jin, Z. Chen, *Mater. Sci. Semicond. Process.* **2017,** *72,* 9–14. **DOI:**10.1016/j.mssp.2017.09.011
108. S. Liu, J. Huang, L. Cao, J. Li, H. Ouyang, X. Tao, C. Liu, *Mater. Sci. Semicond. Process.* **2014,** *25,* 106–111. **DOI:**10.1016/j.mssp.2013.09.021
109. X. Zhang, D. Li, J. Wan, X. Yu, *Mater. Sci. Semicond. Process.* **2016,** *43,* 47–54. **DOI:**10.1016/j.mssp.2015.11.020
110. R. Singh, M. Kumar, H. Khajuria, J. Ladol, H. N. Sheikh, *Acta Chim. Slov.* **2018,** *65,* 319–327. **DOI:**10.17344/acsi.2017.3988
111. K. Pourzare, S. Farhadi, Y. Mansourpanah, *Acta Chim. Slov.* **2017,** *64,* 945–958. **DOI:**10.17344/acsi.2017.3642
112. K. S. Suslick, T. Hyeon, M. Fang, A. A. Cichowlas, *J. Mater. Sci. Eng. A* **1995,** *204,* 186–192. **DOI:**10.1016/0921-5093(95)09958-1

113. A. Gedanken, *J. Ultrason. Sonochem.* **2004,** 1*1,* 47–55. **DOI:**10.1016/j.ultsonch.2004.01.037
114. T.J. Mason, *J. Ultrason. Sonochem.* **2007,** *14,* 476–483. **DOI:**10.1016/j.ultsonch.2006.10.008
115. T. Froschl, U. Hormann, P. Kubiak, G. Kucerova, M. Pfanzelt, C.K. Weiss, R.J. Behm, N. Husing, U. Kaiser, K. Landfesterd, M. Wohlfahrt-Mehrensc, *J. Chem. Soc. Rev.* **2012,** *41,* 5313–5360. **DOI:**10.1039/c2cs35013k
116. M. V. Swapna, K. R. Haridas, *J. Exp. Nanosci.* **2016,** *11,* 540–549. **DOI:**10.1080/17458080.2015.1094189
117. T. Parangi, M. K. Mishra, *Comments Inorg. Chem.* **2019,** *39,* 90–126. **DOI:***10.1080/02603594.2019.1592751*
118. L. Guo, C. Zhang, L. Xu, M. Li, Q. Wang, F. Ye, C. Dan, V. Ji, *J. Eur. Ceram. Soc.* **2017,** *37,* 4163–4169. **DOI:**10.1016/j.jeurceramsoc.2017.04.065
119. W. J. Tseng, P. Lin, *J. Eur. Ceram. Soc.* **2017,** *37,* 5265–5272. **DOI:**10.1016/j.jeurceramsoc.2017.03.040
120. M. Duta, L. Predoana, J. M. Calderon-Moreno S. Preda, M. Anastasescu, A. Marin, I. Dascalu, P. Chesler, C. Hornoiu, M. Zaharescu, P. Osiceanu, M. Gartner, *Mater. Sci. Semicond. Process.* **2016,** *42,* 397–404. **DOI:**10.1016/j.mssp.2015.11.004
121. Y. Wang, J. Tao, X. Wang, Z. Wang, M. Zhang, G. He, Z. Sun, *Ceram. Int.* **2017,** 43, 4866–4872. **DOI:**10.1016/j.ceramint.2016.12.130
122. K. Usha, P. Kumbhakar, B. Mondal, *Mater. Sci. Semicond. Process.* **2016,** *43,* 17–24. **DOI:**10.1016/j.mssp.2015.11.015
123. M. Sreedhar, I. N. Reddy, C. V. Reddy, J. Shim, J. Brijitta, *Mater. Sci. Semicond. Process.* **2018,** *85,* 113–121. **DOI:**10.1016/j.mssp.2018.06.005
124. H. Masai, T. Miyazaki, K. Mibu, Y. Takahashi, T. Fujiwara, *J. Eur. Ceram. Soc.* **2015,** *35,* 2139–2144. **DOI:**10.1016/j.jeurceramsoc.2015.01.013
125. W. Subramonian, T. Y. Wu, S. P. Chai, *J. Environ. Manage.* **2017,** *187,* 298–310. **DOI:**10.1016/j.jenvman.2016.10.024
126. Y. Ren, Z. Ma, P. G. Bruce, *J. Chem. Soc. Rev.* **2012,** *41,* 4909–4927. **DOI:**10.1039/c2cs35086f
127. A. L. Luna, M. A. Valenzuela, C. Colbeau-Justin, P. Vázquez, J. L. Rodriguez, J. R. Avendaño, S. Alfaro, S. Tirado, A. Garduno, J. M. De La Rosa, *App. Catal. A: Gen.* **2016,** *521,* 140–148. **DOI:**10.1016/j.apcata.2015.10.044
128. M. Lei, N. Wang, L. Zhu, Q. Zhou, G. Nie, H. Tang, *App. Catal. B: Environ.* **2016,** *82,* 414–423. **DOI:**10.1016/j.apcatb.2015.09.031
129. B. Li, Y. Hao, B. Zhang, X. Shao, L. Hu, *App. Catal. A: Gen.* **2017,** *531,* 1–12. **DOI:**10.1016/j.apcata.2016.12.002
130. M. Rokhmat, E. Wibowo, Sutisna, Khairurrijal, M. Abdullah, *Procedia Eng.* **2017,** *170,* 72–77. **DOI:**10.1016/j.proeng.2017.03.014
131. L. Cheng, S. Qiu, J. Chen, J. Shao, S. Cao, *Mater. Chem. Phys.* **2017,** *190,* 53–61. **DOI:**10.1016/j.matchemphys.2017.01.001
132. C. H. Park, C. M. Lee, J. W. Choi, G. C. Park, J. H. Joo, *Ceram. Int.* **2018,** *44,* 1641–41645. **DOI:**10.1016/j.ceramint.2017.10.086
133. N. Rozman, L. Skrlep, M. Gaberscek, A. S. Skapin, *Acta Chim. Slov.* **2014,** *61,* 506–516.
134. U. Prah, I. K. Skofic, *Acta Chim. Slov.* **2017,** *64,* 877–887. **DOI:**10.17344/acsi.2017.3497
135. Y. Li, J. Yan, Q. Su, E. Xie, W. Lan, *Mater. Sci. Semicond. Process.* **2014,** *27,* 695–701. **DOI:**10.1016/j.mssp.2014.08.001
136. K. Yu, C. Zhang, Y. Chang, Y. Feng, Z. Yang, T. Yang, L. Lou, S. Liu, *App. Catal. B: Environ.* **2017,** *200,* 514–520. **DOI:**10.1016/j.apcatb.2016.07.049
137. N. R. Khalid, A. Majid, M. B. Tahir, N. A. Niaz, S. Khalid, *Ceram. Int.* **2017,** *3,* 14552–14571. **DOI:**10.1016/j.ceramint.2017.08.143
138. W. Li, Z. Wu, J. Wang, A. A. Elzatahry, D. Zhao, *J. Chem. Mater.* **2014,** *26,* 287–298. **DOI:**10.1021/cm4014859
139. Y. Wan, H. Yang, D. Zhao, *J. Acc. Chem. Res.* **2006,** *39,* 423–432. **DOI:**10.1021/ar050091a
140. Y. Wan, Y. Shi, D. Zhao, *J. Chem. Mater.* **2008,** *20,* 932–945. **DOI:**10.1021/cm7024125
141. X. Li, Y. Jiang, W. Cheng, Y. Li, X. Xu, K. Lin, *Nano-Micro Lett.* **2015,** *7,* 243–254. **DOI:**10.1007/s40820-015-0029-5
142. C. Andriantsiferana, E. F. Mohamed, H. Delmas, *Environ. Technol. (United Kingdom)* **2014,** *35,* 355–363. **DOI:**10.1080/09593330.2013.828094
143. V. R. Posa, V. Annavaram, J. R. Koduru, P. Bobbala, V. Madhavi, A. R. Somala, *J. Exp. Nanosci.* **2016,** *11,* 722–736. **DOI:**10.1080/17458080.2016.1144937

Povzetek

Titanov dioksid (TiO_2) se široko uporablja kot fotokatalizator zaradi svoje dobre stabilnosti in učinkovitosti pri razkroju onesnaževal. Po drugi strani pa je njegova fotokatalitska učinkovitost omejena, ker se vzbudi le pod UV svetlobo in ker med fotorazkrojem prihaja do hitre rekombinacije med elektroni in prazninami. Mnoge raziskave se osredotočajo na uravnavanje metod sinteze, dodatke dopantov in spreminjanje strukture TiO_2 z namenom povečanja fotokatalitske učinkovitosti. Med temi je sinteza TiO_2 v obliki poroznih nanodelcev ena od strategij modificiranja strukture TiO_2, ki je zlasti pritegnila pozornost zaradi svojih prednosti, kot so: boljša adsorpcija in dostopnost različnih onesnaževal do reaktivnih mest na katalizatorju, kar izboljša fotokatalitsko učinkovitost. V tem pregledu literature povzemamo modifikacije sinteznih metod za TiO_2 in njihov učinek na strukturo ter fotokatalitsko učinkovitost. Novejši razvoj na področju TiO_2 glede sinteznih pristopov, učinka dopantov, modificiranih struktur and uporabe je ravno tako predstavljen.

Except when otherwise noted, articles in this journal are published under the terms and conditions of the Creative Commons Attribution 4.0 International License

Scientific paper

Use of Fe_3O_4 Magnetic Nanoparticles Coated with Polythiophene for Simultaneous Preconcentration of Cu (II), Co (II), Cd (II), Ni (II) and Zn(II) Ions Prior to their Determination by MIS-FAAS

Nilgün Elyas Sodan,[1] Ayşen Höl,[1] Osman Çaylak[2] and Latif Elçi[1,*]

[1] *Department of Chemistry, Faculty of Sciences and Arts, Pamukkale University, 20017, Denizli, Turkey*

[2] *Chemistry Department, Vocational School of Technical Sciences, Pamukkale University, 20017, Denizli, Turkey*

* *Corresponding author: E-mail: elci@pau.edu.tr*

Received: 07-29-2018

Abstract

A multielement preconcentration procedure based Fe_3O_4 magnetic nanoparticles coated with polythiophene(Fe_3O_4@PTh MNPs) as a solid phase was reported for Cu(II), Co(II), Cd(II), Ni(II) and Zn(II) ions. Following the preconcentration, the ions were determined by microsample injection system-flame atomic absorption spectrometer (MIS-FAAS). The effect of sample pH, type and volume of eluent, sample volume, extraction time, amount of adsorbent and interfering ions were optimized. The analytes were preconcentrated from 75 to 150 mL of sample solutions buffered to pH 7. The eluent was 1 mL of 1 mol L^{-1} HNO_3 solution. Under optimum conditions, the limits of detection for the analyte ions varied from 1 to 10 μg L^{-1}. The adsorption capacities of Fe_3O_4@PTh was in the range of 2.85 to 9.76 mg g^{-1}. The method was validated by analysis of the certified reference materials. The relative errors and standard deviations were lower than 5%. The developed procedure was applied to various water, soil and some vegetable samples.

Keyword: Fe_3O_4@PTh; heavy metals; preconcentration; water; vegetable; MIS-FAAS

1. Introduction

Large quantities of wastes containing toxic substances are discharged from various industrial plants into environment. Among these toxic substances, heavy metal ions such as Cu(II), Co(II), Cd(II), Ni(II) and Zn(II) have an important place in environmental pollution. These metal ions merge with water and soil to threaten human life and health in food chain.[1] If concentrations in the environment exceed ppm levels, the metal ions exhibit toxic effects. Therefore, the concentrations of these heavy metal ions must be monitored carefully.

Many standard and reference methods have been designed for the determination of heavy metal ions at trace and ultratrace levels. Most commonly flame atomic absorption spectrometry (FAAS) is employed for the determination of trace heavy metals, due to its ease of operation, widespread availability, economical cost, and good precision. With FAAS, however, the direct determination of trace metal ions is difficult, because their concentrations are often lower than the limit of detection of FAAS and matrix problems can be encountered at very low concentrations. These difficulties can be overcome by applying a separation or preconcentration step like cloud point extraction, liquid–liquid extraction, coprecipitation and solid phase extraction, prior to their determinations by FAAS.[2–5]

The methods of solid phase extraction can be specified as disc, column and batch techniques. While these techniques allow working with large volume samples to achieve high preconcentration factor, they have limititations when samples contain insoluble suspending matter in aqueous media.[6] Column techniques are hindered due to slow percolation of samples through the column. In the disc and batch techiques, the solid phase in which the analytes are collected is contaminated with insoluble matters and proper separation does not occur. These limitations can be overcome by processes such as filtration and precipitation prior to preconcentration procedure, but the duration of the analysis is extended further. Magnetic solid

phase extraction technique (MSPE) has recently been suggested by Šafaříková and Šafařík as a new solid phase extraction technique developed for preventing these limitations.[7] Magnetic adsorbents are used in MSPE and they had been initially applied to preconcentration and separation of some organic dyes from various matrices. At MSPE, the small amount of magnetic solid phase where the analytes are adsorbed is effectively separated from the large volume sample solutions by means of a magnetic field. The analytes are eluted from the magnetic adsorbent by the appropriate volumes of eluent. The most commonly used magnetic sorbent is Fe_3O_4 (magnetite) due to its magnetic property. However, as a nanoparticle metal oxide it is not selective and is unstable in complicated matrices, especially at low pHs. Furthermore, metaloxide nanoparticles tend to aggregate in aqueous matrices, which decrease the efficiency of the method.[8,9] So, it is essential to coat its surface to avoid the aggregation and to gain selectivity. Polymer coated magnetic nanoparticles have been synthesized by coating the magnetic nanoparticle with polypyrrole,[10] polyaniline[11] and polythiophene[12,13] for extraction of organic or inorganic compounds from different matrices. Among these, the use of magnetic nanoparticles prepared with polythiophene is limited for magnetic solid phase extraction of trace metal ions.[14–17]

Herein, we prepared Fe_3O_4 magnetic nanoparticles coated with polythiophene (Fe_3O_4@PTh MNPs) as a magnetic solid phase for simultaneous preconcentration/separation of Cu(II), Co (II), Cd(II), Ni(II) and Zn(II) ions from various real samples such as some water, soil and vegetable samples prior to their determinations by MIS-FAAS. The important analytical variables affecting the MSPE procedure were optimized. The binding characteristics of Fe_3O_4@PTh for the analyte ions were evaluated using several adsorption isoterms. The method was validated with analysis of sample spiking analyte and the certified reference materials (CRMs) corresponding to the samples.

2. Experimental

2. 1. Instrumentation and Apparatus

A Perkin Elmer model AAnalyst 700 (Norwalk, CT, USA) flame atomic absorption spectrometer equipped with hollow cathode lamp, an air-acetylene burner and a handmade microsample injection system (MIS) were used for the determination of metal ions. The microsample injection system reported in previous work allows acceptable absorbance to be obtained with a sample volume of 100 μL.[18] The spectral bandwidths were 0.7 nm for copper, cadmium and zinc, and 0.2 nm for cobalt and nickel. The acetylene flow rate and nebulizer flow rate were 2.5 and 10.0 mL min^{-1}, respectively. ATR-IR spectrometer (UATR two model from PerkinElmer) was used for recording ATR-Spectra. An analytical balance (Precisa XB-220A Switzerland), pH meter (WTW pH720, Weilheim, Germany), heating magnetic stirrer (Velp Scientifica ARE, Usmate, Italy), dry air sterilizer (Nuve FN-055, Istanbul, Turkey), mini orbital shaker (VWR, USA) and ultrasonic bath (Ultrasound Bendelin Electronic, Berlin, Germany) were used.

2. 2. Reagents and Standard Solutions

All reagents used in the experiments were of the highest available purity and at least analytical reagent grade. Ultra pure (UP) quality water (resistivity 18.2 MΩ cm^{-1}) obtained from reverse osmosis system (Human Corporation, Seoul, Korea) was used for dilution and preparation of solutions. Nitric acid (65%), perchloric acid (70%), hydrochloric acid (37%), phosphoric acid(85%), acetic acid(glacial), sodium hyroxide, ammonia solution (25%), ethanol and hydrogen peroxide (30%) purchased from Merck, Darmstadt-Germany were used for wet digestion and pH adjustment of sample. Iron(III) chloride hexahydrate, iron(III) sulphate heptahydrate, potassium permanganate, anhydrous acetonitrile and thiophene used for the synthesis of polythiophene-coated Fe_3O_4 nanoparticles were supplied from Sigma-Aldrich, Steinheim-Germany.

Standard stock solutions of Cu(II), Cd(II), Co(II), Ni(II) and Zn(II) as 1000 mg L^{-1} were purchased from LGC, Manchester, USA, and further diluted daily prior to use. The pH of the model solutions was adjusted to pH 2 with $H_2PO_4^-/H_3PO_4$ buffer, pH 4–6 with CH_3COO^-/CH_3COOH buffer, pH 6.5–7.5 with $H_2PO_4^-/HPO_4^{2-}$ buffer and pH 8–10 with NH_4^+/NH_3 buffer solutions. All glasswares used in experiments were kept in 20% (v/v) HNO_3 for at least 24 hours, and rinsed several times with ultra pure water prior to use.

2. 3. Synthesis of Polythiophene-Coated Fe_3O_4 Magnetic Nanoparticles

The synthesis of polythiophene coated Fe_3O_4 magnetic nanoparticles (Fe_3O_4@PTh MNPs) was performed with a small modification of previously published work.[12] Firstly, Fe_3O_4 MNPs was synthesized by co-precipitation method. For this, 8.48 g of $FeCl_3 \cdot 6H_2O$ and 3.15 g of $FeSO_4 \cdot 7H_2O$ were dissolved in 400 mL UP water in a beaker heated at 80 °C, under protection of nitrogen gas, while vigorous stirring the beaker content at 1000 rpm by a magnetic stirrer. Then, 20 mL ammonia solution (25%, v/v) was added dropwise to the solution. The color of solution immediately turned from orange to black. After the mixture was stirred for a further 5 min, the Fe_3O_4 NPs precipitates formed was isolated by magnetic decantation using a neodium magnet and then rinsed several times with 100 mL UP water. The Fe_3O_4 NPs were dried in a vacuum oven at 70 °C for 10 h. The surface of Fe_3O_4 NPs were coated using polythiophene formed by oxidative polymerization of thiophene using $KMnO_4$. To do this, firstly, 1.0 g of dried Fe_3O_4 NPs dispersed in 10 mL anhydrous acetonitrile was sonicated with an ultrasonic bath for 10 min. Then,

1.5 mL of thiophene as the monomer was added to the Fe_3O_4 NPs suspension and then stirred by a magnetic stirrer in a beaker for 15 min. Thereafter, 50 mL of 0.6 mol L^{-1} $KMnO_4$ solution prepared in anhydrous acetonitrile was added drop by drop to the mixture stirred at 500 rpm. The final mixture was stirred for a further 3 h. Finally, synthesized Fe_3O_4@PTh MNPs was rinsed several times with UP water and ethanol, successively, and dried at 70 °C for 5 h under vacuum and then stored in a sealed vial in a desiccator before its use.

Fe_3O_4 surface coating with polythiophene was confirmed by the comparison of ATR-IR spectra of bare Fe_3O_4 (a) and synthesized Fe_3O_4@PTh (b) in Fig. S1. The strong peak at 545 cm^{-1} related to the Fe-O stretching vibration is confirmed the existence of Fe_3O_4 magnetic nanoparticles (Fig. S1a).[19] The peaks at 1561 ve 1419 cm^{-1} are attributed to C = C asymmetric and symmetrical stretching vibration of thiophene ring and the peaks at 700 and 800 cm^{-1} indicate the presence of C-S vibration bond of thiophene ring.[12]

2. 4. Preparation of Samples

The water samples such as tap water from our laboratory, mineral water purchased from a local supermarket, wastewater from Denizli wastewater treatment plant's outlet, thermal water from Pamukkale and hot spring water from Karahayıt, were collected around the city of Denizli, Turkey. The samples were filtered through a cellulose nitrate membrane filter of 0.45 µm pore size (Sartorius, Germany) and 50–150 mL aliquots of the filtered water samples transferred to a 250 mL beaker were buffered to pH 7 using a $H_2PO_4^-/HPO_4^{2-}$ buffer. Then, the general procedure was applied to the prepared water samples.

The general procedure was validated analysing 0.5–2 mL aliquots of BCR 715 Industrial Effluent Wastewater and SPS-WW2 Batch 114 Wastewater as certified reference materials.

By modifying a recent literature,[20,21] 0.5 g of NCS DC 78302 Tibet Soil in a 50 mL beaker were digested for 6 h at 90 °C with 8 mL of aqua regia **(Aqua regia is highly corrosive and must be handled with extreme caution)** and 3 mL of concentrated $HClO_4$. Also, one gram of strawberry leaves was weighed in a small beaker and 4 mL of aqua regia were added. The mixture was heated for 3 h at 85 °C for the digestion of strawberry leaves. The digested residues of strawberry leaves and Tibet Soil were separately diluted to 5 and 10 mL with UP water, respectively and then filtered using the cellulose nitrate membrane filter. The filterates were analyzed by the general procedure described.

Vegetable samples including black radish, parsley and quince were purchased from open bazaar in Denizli, Turkey. The samples were thoroughly washed, first with tap water, followed by rinsing three times with UP water and homogenized using a blender, then dried in an oven at 80 °C for 48 h. The dried plant sample weighing 2.0 g was placed into a beaker and a mixture of 12 mL of concentrated HNO_3 (65%, v/v) and 4 mL of H_2O_2 (30%, v/v) was added to perform the digestion process for 4 h at 130 °C. Following completion of digestion process, the residue was cooled, diluted to 5 mL with UP water and finally filtered through 0.45 µm cellulose nitrate filter paper.[22] The filtrate was analyzed to determine the concentration of various elements using the proposed general procedure.

2. 5. General Procedure

The preconcentration of metal ions with MSPE were performed by batch technique. The preconcentration method was optimized using model solutions containing analytes in known quantities depending on the analyte before application of the method to real samples. Firstly, the model solutions were prepared varying concentration of analytes from 5.0 to 10.0 µg L^{-1} and then they were buffered to pH 7 using a $H_2PO_4^-/HPO_4^{2-}$ buffer. Then, 100 mg of Fe_3O_4@PTh MNPs was separately added into 150 mL of Zn(II) solution, 125 mL of Cu(II), Co(II) and Ni(II) solutions and 75 mL of Cd(II) solution. The mixtures were shaken for 3 mins by hand. Fe_3O_4@PTh MNPs loaded with the analyte ions were separated from the mixtures by a neodymium magnet and the supernatant was discarded. The polythiophene-coated Fe_3O_4 MNPs loaded with copper(II), cobalt(II), cadmium(II), nickel(II) and zinc(II) ions were treated with 1 mL of 1 mol L^{-1} nitric acid for eluation. The obtained mixture was carefully shaken for 3 mins by hand. Then, the effluent including analyte ions was magnetically separated from the Fe_3O_4@PTh MNPs. 100 µL of the effluent was introduced into MIS-FAAS using a micropipette to determine the analytes.

3. Results and Discussion

The analytical variables affecting the MSPE procedure such as pH, type and volume of eluent, volume of sample, extractiom time, Fe_3O_4@PTh amount were optimized using a one-factor-at-a-time approach. All the experimental quantifications were evaluated as the average of at least three replicate measurements.

3. 1. Effect of pH

Researches involve the use of SPE, firstly, the pH of sample solution is examined as most important parameter affecting the extraction efficiency of solid phase. It may change the chemical structure of the adsorbent surface and the analyte. Therefore, the effect of pH on the recoveries of metal ions was investigated in pH range of 2–10 using buffered solutions. The pHs of test solutions containing 50 µg L^{-1} analyte ions were adjusted to pH 2 with $H_2PO_4^-/H_3PO_4$, pH 4–6 with CH_3COO^-/CH_3COOH, pH 6.5–7.5 with $H_2PO_4^-/HPO_4^{2-}$ and pH 8–10 with NH_4^+/NH_3 buffer solutions. The test solutions were analyzed by general proce-

dure above and the calculated recoveries were plotted against pH (Fig. 1). The decrease in recovery values of analytes by the reduction of solution pH from 6.5 to 2 may be explained by the protonation of sulfur groups at functional site of polythiophene.[16] The protonation prevents the coordination of analyte ions by donor sulfur atoms, due to the electrostatic repulsion between the positive charged sorbent and the cationic analytes in acidic solution. On the other hand, because of the increasing hydrolysis and/or formation of ammine complexes of analyte ions at pHs 8 and 10 that were buffered with ammonium/ammonia, a slight decrease in the recovery value of analytes is observed. Around pH 7, because of decreasing protonation of the sulfur atoms and increasing formation of ammine complex of metal ions at pHs in the range of 6.5 and 7.5 that phosphate buffers were used, it can be concluded that more favorable conditions arise for interaction of analyte ions with the sulfur atoms at binding site of Fe_3O_4@PTh MNPs. Therefore, the quantitative recovery values(≥ 95%) are obtained in pH range of 6.5–7.5. As a result, pH 7 was chosen as the optimum working pH for further experiments. Also, the neutral pH was evaluated as an advantage for separation and preconcentration of trace metal ions from natural water samples without chemically pretreating the samples.

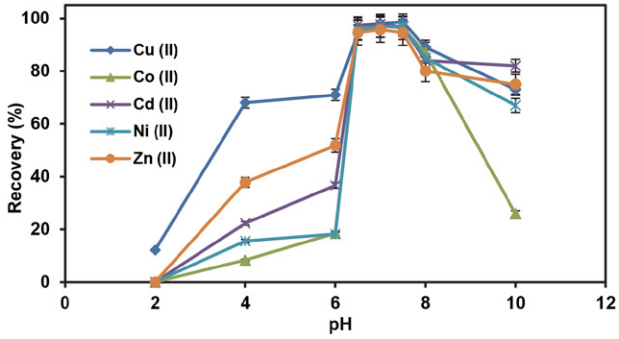

Figure 1. Effect of pH on the recoveries of the analyte ions (sample vol.: 20 mL, eluent vol.: 1 mL, n = 3)

3. 2. Effect of Concentration and Volume of Eluent

In SPE techniques, the volume of the eluent is usually chosen as low as possible to reach greater preconcentration factors along with having ecofriendly properties. It should also be sufficient for the quantitative extraction of the metal ions examined. So, the eluent choice is important. Based on Fig. 1, it was concluded that the recovery values decrease until under 10 % with decreasing pH values of the sample solution from 6.5 to 2.0 and the complex formation of metal ions with the donor atom (S) of Fe_3O_4@PTh will be largely prevented at the more acidic conditions. In this study, nitric acid as eluent was selected instead of hydrochloric acid to prevent the formation of chloro complexes of analyte ions. The concentration and volume of HNO_3 were optimized for analysis. The quantitative recoveries (≥95%) for Cu(II), Co(II), Cd(II), Ni(II) and Zn(II) ions were obtained using 5 mL of HNO_3 solutions in the concentration range of 1–3 mol L^{-1} (Fig. 2). Then, 1.0 mol L^{-1} HNO_3 solutions in range of 1.0–10.0 mL were examined to achieve quantitative recoveries at minimum eluent volume (Table 1). To gain the highest sensitivity with the quantitative recovery values, 1.0 mL of 1.0 mol L^{-1} HNO_3 solution was used as eluent in further experiments.

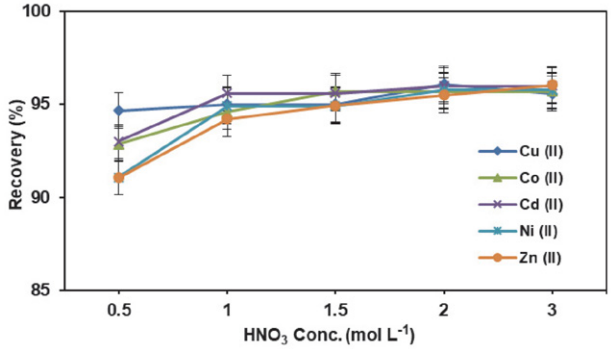

Figure 2. Effect of HNO_3 concentration on elution efficiency of Cu(II), Co(II), Cd(II), Ni(II) and Zn(II) ions from 100 mg of Fe_3O_4@PTh MNPS (eluent vol.: 5.0 mL, n = 3)

Table 1. Effect of eluent volume on recovery of Cu(II), Co(II), Cd(II), Ni(II) and Zn(II) ions (eluent: 1 mol L^{-1} HNO_3, n = 3)

Eluent Volume, mL	Recovery, %				
	Cu(II)	Co(II)	Cd(II)	Ni(II)	Zn(II)
10.0	96 ± 1	97 ± 3	98 ± 1	95 ± 2	96 ± 2
5.0	98 ± 1	96 ± 2	98 ± 1	96 ± 1	95 ± 1
2.5	97 ± 1	96 ± 2	96 ± 1	95 ± 2	96 ± 2
1.0	96 ± 2	95 ± 2	95 ± 1	95 ± 1	95 ± 2

3. 3. Effect of Sample Volume

Sample volume is chosen as large as possible to obtain high preconcentration factor in preconcentration studies. Therefore, the volume of the sample was investigated in the range of 10–200 mL solution, containing 5–10 μg L^{-1} of Cu(II), Co(II), Cd(II), Ni(II) and Zn(II). As shown in Fig. 3, it was found that the analyte ions could be adsorbed quantitatively when sample volumes were less than 150 mL for Zn(II) ions, 125 mL for Cu(II), Co(II) and Ni(II) ions, 75 mL for Cd(II) ions. The eluent volume used was 1 mL and the preconcentration factors (PF) were calculated to be 75 for Cd(II), 125 for Cu(II), Co(II) and Ni(II), and 150 for Zn(II).

3. 4. Effect of Extraction Time

The extraction time including adsorption and desorption times is defined as the minimum time required to

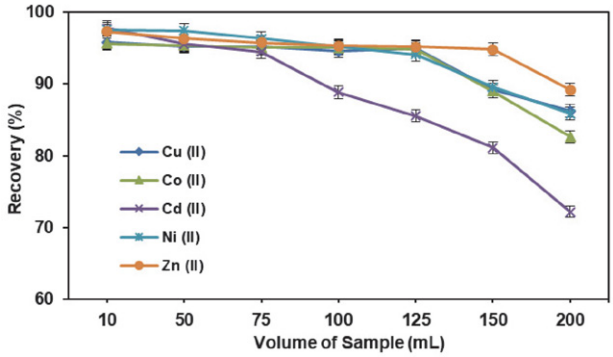

Figure 3. Effect of sample volume on the recovery of the analytes (Eluent vol.:1.0 mL, n = 3)

obtain quantitative extraction efficiency. Therefore, by changing the adsorption and desorption times between 1 and 20 min, the procedure was applied to a 50 mL sample solution containing analytes in the range of 5–10 μg L^{-1} and 100 mg Fe_3O_4@PTh. The results showed that 6 min extraction time as the sum of adsorption time (3 min) and desorption time (3 min) was adequate to access quantitative receovery for all analytes using 1.0 mL of eluent (Figures S2 and S3). It could be concluded that the extraction time is one of the most important advantages of magnetic solid phase extraction technique when compared with other solid phase extraction techniques such as column, filtration and batch.

3. 5. Effect of Fe_3O_4@PTh Amount

To test the effect of Fe_3O_4@PTh amount on recovery of analytes, the preconcentration procedure was applied to a 50 mL of sample solution including analyte ions in the range of 10–20 μg L^{-1} and Fe_3O_4@PTh amount in the range of 30–250 mg. Based on the results depicted in Fig. 4, the recovery values for all the analyte were found to be quantitative(≥95%) using Fe_3O_4@PTh in the range of 100–250 mg. 100 mg of Fe_3O_4@PTh found to be as minimum amount that was preferred to minimize the risk of possible contamination.

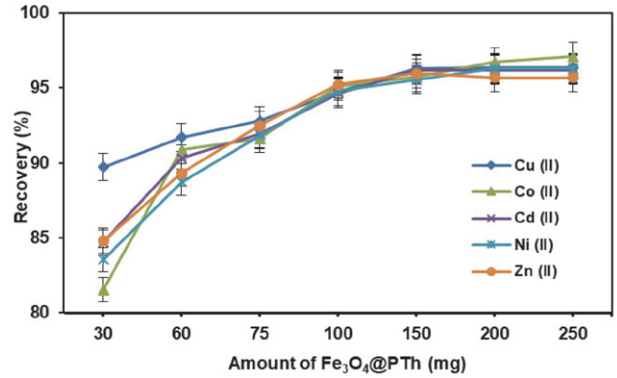

Figure 4. Effect of the amount of the Fe_3O_4@PTh on the recoveries of the analyte ions (n = 3)

Also, to evaluate the possibility of reuse of adsorbent, reusability tests were carried out by consecutive analysis under the optimum conditions. In the second use of Fe_3O_4@PTh, since the recovery values of all analytes are below 5%, it was concluded that the adsorbent can not be used more than once. Probably, on first use, the polythiophene from Fe_3O_4@PTh is stripped during elution that limits its repeated use.

Table 2. Effect of interfering ions on the recoveries of the analyte ions (n = 3)

Interfering ions	Added as	Tolerance limits, mgL^{-1}	Recovery,% Cu(II)	Co(II)	Cd(II)	Ni(II)	Zn(II)
Na^+	NaCl	4000	95 ± 1	95 ± 2	96 ± 1	96 ± 2	96 ± 2
K^+	KCl	5000	94 ± 1	95 ± 2	96 ± 1	95 ± 3	96 ± 1
Mg^{2+}	$MgSO_4$	2000	97 ± 1	94 ± 2	96 ± 1	95 ± 2	94 ± 1
Ca^{2+}	$Ca(NO_3)_2 \cdot 2H_2O$	1000	95 ± 1	95 ± 2	95 ± 1	95 ± 2	95 ± 2
Ba^{2+}	$BaCl_2 \cdot 2H_2O$	800	96 ± 1	95 ± 1	95 ± 2	95 ± 3	95 ± 2
Cl^-	NaCl	6174	95 ± 1	95 ± 2	96 ± 1	96 ± 2	96 ± 2
NO_3^-	$Ca(NO_3)_2 \cdot 2H_2O$	6200	95 ± 1	94 ± 2	94 ± 1	94 ± 2	94 ± 2
CH_3COO^-	$CH_3COONa \cdot 3H_2O$	4500	95 ± 1	94 ± 3	95 ± 2	96 ± 4	94 ± 1
CO_3^{2-}	Na_2CO_3	3500	94 ± 1	94 ± 3	95 ± 1	94 ± 4	94 ± 1
Cu^{2+}	$CuCl_2 \cdot 2H_2O$	600	–	96 ± 2	94 ± 2	94 ± 2	95 ± 2
Pb^{2+}	$Pb(NO_3)_2$	500	96 ± 1	95 ± 2	94 ± 2	94 ± 3	94 ± 2
Ni^+	$Ni(NO_3)_2 \cdot 6H_2O$	400	95 ± 1	94 ± 3	94 ± 1	–	94 ± 2
Cd^{2+}	$Cd(NO_3)_2 \cdot 4H_2O$	500	95 ± 1	94 ± 3	–	94 ± 2	94 ± 2
Co^{2+}	$Co(NO_3)_2 \cdot 6H_2O$	200	95 ± 1	–	95 ± 2	95 ± 2	95 ± 2
Zn^{2+}	$Zn(NO_3)_2 \cdot 6H_2O$	500	95 ± 1	94 ± 2	96 ± 2	94 ± 3	–
Mn^{2+}	$MnSO_4 \cdot H_2O$	300	94 ± 1	94 ± 2	94 ± 2	94 ± 2	94 ± 2
Cr^{3+}	$Cr(NO_3)_3 \cdot 9H_2O$	300	95 ± 1	94 ± 2	94 ± 2	94 ± 3	94 ± 2
Fe^{3+}	$Fe(NO_3)_3 \cdot 9H_2O$	80	94 ± 1	94 ± 2	94 ± 1	94 ± 2	94 ± 1

3. 6. Effect of Interfering Ions

During the application of the method, the selectivity of an adsorbent for an analyte ion can be hampared by interfering ions in the sample matrices. So, the selectivity of Fe_3O_4@PTh towards Cu(II), Co(II), Cd(II), Ni(II) and Zn(II) ions in the presence of some interfering cations and anions was examined. The competitive adsorption effects of analyte ions on each other were also studied (Table 2). 50 mL of test solutions containing 100 μg L^{-1} of the each analyte ions were spiked with varying concentration of probable interfering ions, and then analysed by the proposed general procedure. The eluent volume used was 5.0 mL.

The tolerance limit was defined as the interfering ion concentration causing a deviation higher than 6% on the recovery values of the analyte ions. It was concluded that the proposed procedure could be applied successfully for the magnetic solid phase microextraction of Cu(II), Co(II), Cd(II), Ni(II) and Zn(II) in presence of interfering ion at higher concentration than the concentration of matrix ions in samples. Also, the analytes have no significant interference on each other's extraction.

3. 7. Adsorption Capacity of Fe_3O_4@PTh

The adsorption capacity defined as the amount of adsorbent needed to quantitatively extract analyte ions in a sample solution is one of the important parameters.[23,24] To determine the adsorption capacity of Fe_3O_4@PTh for Cu(II), Co(II), Cd(II), Ni(II) and Zn(II) ions, 50 mL sample solutions containing increasing initial concentrations (C_o) of analyte in the range of 5–500 mg L^{-1} that are buffered to pH 7 were contacted with 100 mg of adsorbent at room temperature for 24 h. The analyte ion concentrations in the supernatant solution diluted at the appropriate ratios were determined by FAAS. The procedure was separately repeated for each analyte ion. The adsorption capacities(Q_m) of Fe_3O_4@PTh MNPs for Cu(II), Co(II), Cd(II), Ni(II) and Zn(II) were found to be 4.59, 4.88, 4.45, 2.85 and 9.76 mg g^{-1}, respectively, using Q_e values corresponding to the plateau in Fig. 5.

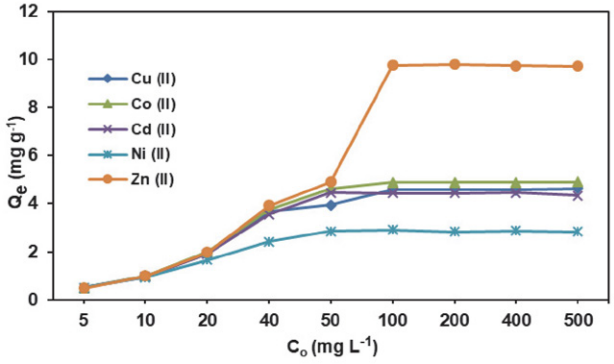

Figure 5. Adsorption capacity of Fe_3O_4@PTh for Cu(II), Co(II), Cd(II), Ni(II) and Zn(II)

The adsorption characteristics of Fe_3O_4@PTh MNPs were investigated using Langmuir, Freundlich, Scatchard, Temkin and Dubinin-Radushkevich isotherms and each isotherm calculation were applied to the experimental data(Table 3). The Langmiur isotherm equation is formulated as Ce/ Qe = 1/(Qm x Kb)+Ce/Qm, where Ce and Qe are equilibrium concentration of analyte ions(mg L^{-1}) in the solution and the solid phase (mg g^{-1}), respectively. The good regression coefficients (R^2 ≥0.9999), R_L values in range of 0 and 1($R_L = 1/(1+K_b C_o)$ and Q_m values obtained from the isotherm close to the experimental adsorption capacities show the compatibility of the experimental data with the Langmuir isotherm. It can be concluded that the analytes on Fe_3O_4@PTh MNPs is favorably adsorbed with a monolayer adsorption process by the sites distribute uniformly.[25,26]

In the Freundlich isotherm equation given as ln Qe = lnKf + (1/n) lnCe, Kf and 1/n are Freundlich constants which corresponds to the adsorption capacity and adsorption intensity or heterogeneity of the adsorbent, respectively. The 1/n<1 and K_f values in Table 3, describe that all the analyte ions are favorably adsorbed by Fe_3O_4@PTh at low concentration.[25] The Scatchard isotherm defines the nature of binding sites and adsorption process. The equation is represented as $Q_e/C_e = Q_m x K_b - Q_e x K_b$, where K_b is the Scatchard isotherm constant. The shape of the isotherm plot explains the type of interaction between analyte ions and adsorbent. A good single linearity of the plot in working range verifies that the binding sites are equivalent and independent sites.[27] The concordance of Scatchard isotherm with experimental data is also supported with Q_m values close to the experimental adsorption capacities, low K_b and good R^2 values in Table 3. The Temkin isotherm given as $Q_e = A x \ln K_T + A x \ln C_e$ ($A = RT/b_T \cdot K_T$ (L g^{-1}) and b_T (J mol^{-1}) is the equilibrium binding constant and change of sorption energy, respectively. The high binding constants and high sorption energies of analytes indicate a strong interaction between the analyte ions and Fe_3O_4@PTh, supporting a chemisorption mechanism. The Dubinin-Raushkevich equation, generally used to distinguish between physical and chemical adsorption, is known as $\ln Qe = \ln Qm - K \varepsilon^2$. ε value is formulated as $\varepsilon = RT\ln(1+1/Ce)$. E(kJ/$mol^{-1}$) calculated from $E = (-2K)^{-1/2}$ is the mean free energy of adsorption per molecule of the adsorbate.[27] If the value of E lies between 8 and 16 kJ mol^{-1}, the adsorption process is a chemisorption, while values of below 8 kJmol^{-1} indicates a physical adsorption process.[28,29] The high adsorption energy values changed from 17.15 to 50.00 kJ mol^{-1} showed that the analytes were chemically adsorbed onto Fe_3O_4@PTh MNPs.

As a result, comparing the isotherms, it can be concluded that the values of R^2 and adsorption capacity obtained from Langmuir, Dubinin-Raushkevich and Scatchard isotherms are good fits to the experimental data. R^2 values of Freundlich and Temkin isotherms are relatively smaller than the others.

Table 3. Langmuir, Freundlich, Scatchard, Temkins and Temkin Dubinin–Radushkevich isotherm parameters for the adsorption of examined metal ions by Fe_3O_4@PTh

Isotherms	Parameters	Cu(II)	Co(II)	Cd(II)	Ni(II)	Zn(II)
Adsorption capacity	Q_m, mg g^{-1}	4.59	4.88	4.45	2.85	9.76
Langmiur	Q_m, mg g^{-1}	4.61	4.89	4.46	2.86	9.75
	K_b, L mg^{-1}	1.50	2.83	1.23	0.87	1.43
	R_L	0.12	0.066	0.14	0.19	0.12
	R^2	0.9999	1.0000	1.0000	0.9999	1.0000
Freundlich	K_f, L g^{-1}	2.13	2.90	1.55	1.22	2.13
	n	6.55	9.86	5.08	4.88	3.41
	R^2	0.9309	0.8714	0.8858	0.8618	0.8738
Scatchard	Q_m, mg g^{-1}	4.59	4.82	4.49	2.87	9.90
	K_b, L mg^{-1}	1.17	5.53	0.76	0.75	0.96
	R^2	0.9782	0.9355	0.9947	0.9696	0.9864
Temkin	K_T, L g^{-1}	13.79	97.89	89.20	96.05	37.60
	b_T, J mol^{-1}	2408	6093	5441	8570	2294
	B	1.0287	0.4066	0.4553	0.2891	1.0799
	R^2	0.9085	0.9204	0.8571	0.8949	0.9566
Dubinin – Radushkevich	q_s, mg g^{-1}	4.59	4.92	4.61	2.88	9.86
	K_{ad}, mol^2 kJ^{-2}	0.0004	0.0002	0.0005	0.0017	0.0004
	E, KJ mol^{-1}	35.36	50.00	31.62	17.15	35.36
	R^2	0.9892	0.9639	0.9935	0.9216	0.9959

3. 8. Method Validation

The method was validated in accordance with the guidelines set out in internationally accepted guidance documents. The validation's parameters, following the recommendations of the IUPAC and others, include limit of detection(LOD) and limit of quantification(LOQ), practical quantitation limit (PQL), linear range, precision, accuracy, selectivity, recovery and uncertainty of measurement.[30–33] The analytical figures of merit are summarized in Table 4. Due to the high experimental enrichment factors calculated

Table 4. Analytical characteristics of the proposed method at the optimum conditions.

Analytical characteristics	Cu(II)	Co(II)	Cd(II)	Ni(II)	Zn(II)
with reconcentration LR, μg L^{-1}	4–80	8–80	3–67	13–80	3–27
RE	y = 3.9579x + 0.0004	y = 3.2959x + 0.0014	y = 7.5124x + 0.0116	y = 3.0898x + 0.0072	y = 20.9775x + 0.0076
R^2	0.9996	0.9951	0.9963	0.9967	0.9994
without preconcentration LR, μg mL^{-1}	0.5–10	0.5–10	0.25–5	0.5–10	0.125-4
RE	y = 0.0325x + 0.0031	y = 0.0270x + 0.0044	y = 0.1039x + 0.0013	y = 0.0258x + 0.0067	y = 0.1454x + 0.0101
R^2	0.9994	0.9968	0.9981	0.9972	0.9985
Enrichment Factor	122	122	72	120	144
Preconcentration Factor	125	125	75	125	150
Error of EF, %	2	2	4	4	4
LOD (n = 16), μg L^{-1}	1.4	3.2	1.1	9.6	1.2
LOQ (n = 16), μg L^{-1}	3.6	5.1	1.9	11.7	2.6
PQL (n = 4), μg L^{-1}	4.0	8.0	3.2	13.2	3.3
Sample Vol., mL	125	125	75	125	150
Eluent Volume, mL	1	1	1	1	1
Consumptive index, mL	1.02	0.61	1.74	1.04	1.04

LR: Linear range; RE: Regression equation; R^2: Regression coefficient; EF: Enrichment Factor

Table 5. Analysis of certified reference materials using present method (n = 3)

Certified reference material		Cu(II)	Co(II)	Cd(II)	Ni(II)	Zn(II)
BCR 715	Certified, mgL^{-1}	0.90 ± 0.14[a]	–	0.040 ± 0.005	1.20 ± 0.09	4.0 ± 0.4
Industrial	Found, mg L^{-1}	0.86 ± 0.02	-	0.038 ± 0.001	1.16 ± 0.03	3.94 ± 0.05
Effluent	Recovery,%	96	–	95	97	99
Wastewater	RSD, %	2.3	–	2.6	2.6	1.3
	$t_{calculated\ value}$	2.65[b]	–	3.50	2.00	1.89
SPS-WW2 Batch	Certified, mgL^{-1}	2.00 ± 0.01	0.300 ± 0.002	0.1000 ± 0.0005	5.000 ± 0.025	3.000 ± 0.015
114 Wastewater	Found, mg L^{-1}	1.93 ± 0.04	0.29 ± 0.01	0.095 ± 0.004	4.84 ± 0.14	2.88 ± 0.06
	Recovery, %	96	97	95	97	96
	RSD, %	2.1	3.3	4.2	2.9	2.1
	$t_{calculated\ value}$	3.25	1.73	2.00	2.00	3.75
Tibet Soil	Certified, μg g^{-1}	24.6 ± 2.8	13.1 ± 1.1	0.081 ± 0.015	31.1 ± 1.6	58.0 ± 6.6
	Found, μg g^{-1}	23.19 ± 0.98	12.55 ± 0.54	0.078 ± 0.003	29.86 ± 0.62	54.98 ± 1.90
	Recovery, %	94	96	96	95	95
	RSD, %	4.2	4.3	3.8	2.1	3.5
	$t_{calculated\ value}$	2.50	1.73	2.00	4.00	3.55
Strawberry Leaves	Certified, μg g^{-1}	10[c]	0.47 ± 0.11	0.17 ± 0.04	2.6 ± 0.7	24 ± 5
	Found, μg g^{-1}	9.09 ± 0.32	0.46 ± 0.02	0.16 ± 0.01	2.51 ± 0.15	22.95 ± 0.48
	Recovery, %	91	97	94	97	96
	RSD, %	3.5	4.3	6.2	6.0	2.1
	$t_{calculated\ value}$	5.01	1.00	2.00	1.00	3.78

[a] Mean ± standard deviation; [b]Student's t-test, $t_{critical}$ = 4.30 at 95% confidence limit(N = 3); [c]not certified, but indicative value

as a ratio of the slopes of the regression equations established with and without the preconcentration, the sensivity of examined analytes determined with FAAS has been improved from trace level(μg mL^{-1}) to ultra trace level(μg L^{-1}), with very low enrichment error(≤ 4%). LOQ values for analytes (out of Ni) ranged from 1.1 to 3.2 μg L^{-1}. The quantitative recovery values (almost 95%) achieved in the analysis of certified reference materials and analyte spiked samples prove the accuracy of the proposed method (Tables 5, 6 and 7). The consumptive index[34] defined as the sample volume(mL) consumed to achieve a unit of EF was found to be quite low in Table 4. It is used to compare preconcentration procedures required different volumes of sample.

The accuracy of the developed procedure for each analyte was confirmed with analysis of the certified reference materials of wastewater (BCR715 and SPS-WW2 Batch 114), soil (NCS DC 78302 Tibet Soil) and plant (LGC7162 Strawberry Leaves). The recoveries and relative standard deviations(RSD,%) were calculated in the ranges of 91-99% and 1.3-6.2%, respectively. The certified and experimental values by applying Student's t-test were compared. The student t-test demonstrated that there is no significant difference between the certified value and the experimental result at the confidence level of 95%.[34] The results are shown in Table 5.

Precision of proposed method was evaluated as repeatability (intraday) and reproducibility (interday). These studies were carried out with analysis of samples spiked with analyte ions on four different days. All the experimental data were evaluated by one way analysis of variance (ANOVA).[35,36] Repeatability and reproducibility as relative standard deviations (RSD %) were in the range of 1.0–7.7% and 1.1–9.2%, respectively. Based on the results given in Table S1, there is no significant difference between the variances.

3. 9. Application of Proposed Method to Real Samples

To assess the applicability of the developed magnetic solid phase preconcentration procedure, it was applied to real samples spiked with analyte. The recoveries and relative standard deviations were obtained in the ranges of 93–97% and 0.7–2.9%, respectively(Table 6).

These recoveries confirm that the method is accurate and selective due to no interference from the sample matrices. The results showed that the actual water samples do not contain the analyte ions being studied (at least below limit of quantification). It was concluded that the proposed method has sufficient efficiency for the water samples including analyte ions at concentration higher than the LOQ values achieved by the proposed procedure.

The method was applied to some salad vegetables purchased from a local market in Denizli, Turkey. EU standards for the permissible levels of Cd(II) and Cu(II) are 0.2 and 20 mg kg^{-1}, respectively.[37] For Zn, permissible levels allowed by both EU standards and UK guidelines is

Table 6. Analysis of various water samples spiked with examined analytes (n = 3)

Ana-lyte	Added µg L^{-1}	Tap water Found[a], µg L^{-1}	R, %	Mineral Water Found[a], µg L^{-1}	R, %	Wastewater Found[a], µg L^{-1}	R, %	Spring Water Found[a], µg L^{-1}	R, %	Thermal Water Found[a], µg L^{-1}	R, %
	0	< BLQ[b]	–	< BLQ	–	< BLQ	–	< BLQ	–	< BLQ	–
Cu	10	9.5 ± 0.3	95	9.6 ± 0.2	96	9.5 ± 0.3	95	9.7 ± 0.3	96	9.7 ± 0.4	97
	20	18.9 ± 0.3	94	19.1 ± 0.3	96	18.8 ± 0.5	94	19.0 ± 0.3	95	19.1 ± 0.4	96
	0	< BLQ	–	< BLQ	–	< BLQ	–	< BLQ	–	< BLQ	–
Co	10	9.4 ± 0.2	94	9.8 ± 0.2	98	9.4 ± 0.2	94	9.4 ± 0.2	94	9.6 ± 0.3	96
	20	18.7 ± 0.3	94	19.4 ± 0.5	97	18.7 ± 0.3	94	8.8 ± 0.2	94	19.0 ± 0.3	95
	0	< BLQ	–	< BLQ	–	< BLQ	–	< BLQ	–	< BLQ	–
Cd	10	9.5 ± 0.2	95	9.7 ± 0.2	97	9.4 ± 0.1	94	9.5 ± 0.2	95	9.4 ± 0.1	94
	20	18.8 ± 0.2	94	19.2 ± 0.1	96	18.6 ± 0.2	93	18.6 ± 0.1	93	18.7 ± 0.1	94
	0	< BLQ	–	< BLQ	–	< BLQ	–	< BLQ	–	< BLQ	–
Ni	20	19.1 ± 0.5	96	19.4 ± 0.5	97	18.7 ± 0.5	94	18.6 ± 0.5	93	19.0 ± 0.4	95
	40	37.7 ± 0.7	94	38.3 ± 0.5	96	37.5 ± 0.4	94	37.2 ± 0.5	93	37.6 ± 0.5	94
	0	< BLQ	–	< BLQ	–	< BLQ	–	< BLQ	–	< BLQ	–
Zn	10	9.5 ± 0.1	95	9.8 ± 0.1	98	9.4 ± 0.1	94	9.4 ± 0.1	94	9.5 ± 0.1	95
	20	18.8 ± 0.2	94	19.3 ± 0.1	96	18.7 ± 0.2	94	18.7 ± 0.1	94	18.6 ± 0.1	93

[a] Mean ± standard deviation, [b] Below limit of quantification

50 mg kg^{-1}.[38–40] Standard concentration levels of Cd, Cr, Cu, Ni and Zn in vegetables are normally <0.5, 0.1–1, 2–20, 1–10 and 5–100 ppm, respectively.[41] Results indicated that the analyte concentrations in all the analysed vegetable samples are lower than the acceptable and the guidelines levels (Table 7). The recoveries were obtained in the ranges of 94–99%. The uncertainty of measurements are based on the uncertainty of calibration standard, calibration curve, adsorbent weighing, sample volume and repeatibility and it is found to be in the range of 1.6–6.3%, depending the analyte(Table S2).[32,35]

3. 10. Comparison with Other Methods

The proposed method was compared to a variety of similiar preconcentration methods reported recently in the literature (Table 8). The method is more favorable than the others, because it has higher enrichment factors, better precision, shorter extraction times (sum of adsorption and desorption times), and mild working conditions due to pH 7. While the LOD of this technique is not better than these other techniques, it does not require the costly equipment. Different experimental conditions used in this study allow extraction of analytes that cannot be extract by the reported method.[14] Another advantage of the method is the ability to simultaneously separate and preconcentrate more trace metals from real samples such as water, soil, fruit leaves and vegetable samples.

4. Conclusion

Using Fe_3O_4@PTh MNPs as magnetic adsorbent, a magnetic solid phase extraction method proposed for

Table 7. Analysis of some salad vegetables spiked with analyte ions (n = 4)

Analyte	Added, µg g^{-1}	Black Radish Root Founded[a], µg g^{-1}	R, %	Parsley Founded[a] µg g^{-1}	R,, %	Quince Founded[a], µg g^{-1}	R, %
Cu(II)	0	0.55 ± 0.03	–	1.87 ± 0.08	–	2.55 ± 0.10	–
	0.5	1.00 ± 0.08	95	2.24 ± 0.06	94	2.90 ± 0.07	95
Co(II)	0	0.65 ± 0.06	–	0.94 ± 0.11	–	0.13 ± 0.02	–
	0.5	1.08 ± 0.07	95	1.36 ± 0.10	94	0.60 ± 0.06	96
Cd(II)	0	0.11 ± 0.01	–	0.24 ± 0.02	–	0.15 ± 0.01	–
	0.4	0.49 ± 0.03	96	0.61 ± 0.04	95	0.52 ± 0.03	94
Ni(II)	0	2.33 ± 0.08	–	1.93 ± 0.12	–	1.13 ± 0.06	–
	0.5	2.80 ± 0.12	99	2.30 ± 0.10	95	1.55 ± 0.10	95
Zn(II)	0	3.00 ± 0.12	–	3.26 ± 0.10	–	2.82 ± 0.07	–
	0.5	3.46 ± 0.11	99	3.58 ± 0.08	95	3.18 ± 0.05	96

[a] Mean ± standard deviation

Table 8. Comparative data from some recent studies based on use of the coated Fe_3O_4

Adsorbent/detection	Analytes	pH	Extraction	EF[b]	LOD, Time[a]	RSD,%	Refs. μg L^{-1}
Polythiophene@Fe_3O_4/ FI-ICP-OES	Cu	4	5 + 6	129	0.5	2.90	14
Polythiophene@Fe_3O_4 ETAAS	Cd	8	10 + 2	200	3.3	4.70	17
Polythionine@Fe_3O_4 / FAAS	Co	8	10 + 5	50	0.3	1.90	42
Carbon@Fe_3O_4/ ICP-MS	Co	5	10 + 5	37.5	0.001	9.40	
	Cd	5		37.5	0.055	6.20	43
	Zn	5		37.5	0.066	8.60	
	Pb	5		37.5	0.11	7.40	
Fe_3O_4@C-TAN/ FAAS	Cu	4	25 + 1	50	1.5	2.60	44
2-((E-2-amino-4,5-dinitrophenylimino)-methyl)-phenol@ SDS-coated Fe_3O_4/ FAAS	Pb	5	1 + –	63.5	0.04	2.8–3.6	45
Fe_3O_4@polythiophene/ FAAS	Cu	7	3 + 3	125	1	2.4	This work
	Co			125	3	2.4	
	Cd			75	1	1.7	
	Ni			125	10	2.3	
	Zn			150	1	1.5	

multielement preconcentration of Cu(II), Co(II), Cd(II), Ni(II) and Zn(II) ions prior to their detemination by MIS-FAAS was successfully established. The method is green, simple, fast, and inexpensive in terms of chemicals, apparatus and manipulation. The method showed high perfomance including excellent accuracy, good precision, quantitative recovery, high enrichment factor and shorter extraction time for the analysis of samples having complex matrices such as waste water, soil and vegetable samples. These results are in accordance with those achieved by analysis of certified reference materials and real samples spiking analyte.

Conflict of Interest

Authors declare that they do not have any conflict of interest with anyone.

Acknowledgments

The financial support of this work by the Scientific Research Projects (SRP) Coordination Unit of Pamukkale University is greatly acknowledged (project number: 2013FBE038)

5. References

1. P. N. Nomngongo, J. C. Ngila, T. A. M. Msagati, B. Moodley, *Phys. Chem. Earth*, **2013**, *66*, 83–88. **DOI:**10.1016/j.pce.2013.08.007
2. S. Candir, I. Narin, M. Soylak, *Talanta*, **2008**, *77*, 289–293. **DOI:**10.1016/j.talanta.2008.06.024
3. A. Hol, A. A. Kartal, A. Akdogan, A. Elçi, T. Arslan, L. Elçi, *Acta Chim. Slov.*, **2015**, *62*, 196–203. **DOI:**10.5740/jaoacint.11-0214
4. M. Soylak, A.Aydin, N. Kizil, *J. AOAC Int.*, **2016**, *99*, 273–78. **DOI:**10.5740/jaoacint.11-0214
5. A. Gundogdu C. Duran, H. B. Senturk, L. Elci and M. Soylak, *Acta Chim. Slov.,* **2007**, *54*, 308–316.
6. M. C. Hennion, *J. Chromatogr. A*, **1999**, *856*, 3–54. **DOI:**10.1016/S0021-9673(99)00832-8
7. M. Šafaříková, I. Šafařík, *J. Magn. Magn. Mater.*, **1999**, *194*, 108–112. **DOI:**10.1016/j.aca.2014.12.022
8. A. Mehdinia, N. Khodaee, A. Jabbari, *Anal. Chim. Act*, **2015**, *868*, 1–9. **DOI:**10.1016/j.aca.2014.12.022
9. X. Pu, Z. Jiang, B. Hu, H. Wang *J. Anal. At. Spectrom.*, **2004**, *19*, 984–989. **DOI:**10.1039/B403389B
10. B. Ebrahimpour, Y. Yamini, S. Seidi, M. Tajik, *Anal. Chim. Acta*, **2015**, *885*, 98–105. **DOI:**10.1016/j.aca.2015.05.025
11. T. Wen, W. Zhu, C. Xue, J. Wu, Q. Han, X. Wang, X. Zhou, H. Jiang, *J. Biosens. Bioelectron.*, **2014**, *56*, 180–185. 3 **DOI:**10.1016/j.bios.2014.01.013
12. E. Tahmasebi, Y. Yamini, M. Moradi, A. Esrafili, *Anal. Chim. Acta*, **2013**, *770*, 68–74. **DOI:**10.1016/j.aca.2013.01.043
13. S. N. A. Baharin, M. N. Sarih, S. Mohamad, *Polymers*, **2016**, *8(5)*, 1–18. **DOI:**10.3390/polym8050117
14. E. Tahmasebi, Y. Yamini, *Microchim. Acta*, **2014**, *181*, 543–551. **DOI:**10.1007/s00604-013–1144-y
15. N. Jalilian, H. Ebrahimzadeh, A. A. Asgharinezhad, K. Molaei, *Microchim. Acta*, **2017**, *184*, 2191–2200. **DOI:**10.1007/s00604-017-2170-y

16. K. Molaei, H. Bagheri, A. A. Asgharinezhad, H. Ebrahimzadeh, M. Shamsipur, *Talanta*, 2017, *167*, 607–616. **DOI:**10.1016/j.talanta.2017.02.066
17. F. Iranzad, M. Gheibi and M. Eftekhari, *Int. J. Environ. Anal. Chem.*, **2018**, *98(1)*, 16–30. **DOI:**10.1080/03067319.2018.1426757
18. J. A. Baig, A. Hol, A. Akdogan, A. A. Kartal, U. Divrikli, T. G. Kazi, L. Elci, *J. Anal. At. Spectrom.*, **2012**, *27*, 1509–1517. **DOI:**10.1039/c2ja30107e
19. D. Maity, D. C. Agrawal, *J. Magn. Magn. Mater.*, **2007**, *308*, 46–55. **DOI:**10.1016/j.jmmm.2006.05.001
20. M. Tüzen, *Microchem. J.*, **2003**, *74*, 289–297. **DOI:**10.1016/S0026-265X(03)00035-3
21. M. Tuzen, M. Soylak, J. Hazard. Mater., 2009, 164, 1428–1432. **DOI:**10.1016/j.jhazmat.2008.09.050
22. H. Altundağ, M. Tuzen, Food Chem. Toxicol., 2011, 49, 2800–2807. **DOI:**10.1016/j.fct.2011.07.064
23. Maquieira, H.A.M. Elmahadi and R. Puchades, Anal. Chim., 1994, *66,* 3632–3638. **DOI:**10.1021/ac00093a016
24. S. Sönmez, U. Divrikli and L. Elci, Talanta, **2010**, 82, 939–94. **DOI:**10.1016/j.talanta.2010.05.062
25. K. R. Eagleton, L. C. Acrivers and T. Vermenlem, Ind. Eng. Chem. Res., **1966**, *5,* 212–223. **DOI:**10.1021/i160018a011
26. Y. Liu, Z. Liu, Y. Wang, J. Dai, J. Gao, J. Xie, et al. Microchim. Acta, **2011**, *172,* 309–317. **DOI:**10.1007/s00604-010-0491–1
27. T. Yordanova, I. Dakova, K. Balashev, I. Karadjova, Microchem. J., **2014**, *113,* 42–47. **DOI:**10.1016/j.microc.2013.11.008
28. S. Kundu, A. K. Gupta, Chem. Eng. J., **2006**, *122 (1–2),* 93–106. **DOI:**10.1016/j.cej.2006.06.002
29. P. Sivakumar, P. N. Palanisamy L. Int. J. Chemtech. Res., **2009**, *1(3),* 502–510.
30. ISO/IEC 17025 General requirements for the competence of testing and calibration laboratories, International Organisation for Standardization, Geneva, **2017**.
31. IEurachem Guide: The Fitness for Purpose of Analytical Methods: A Laboratory Guide to Method Validation and Related Topics, Budapest, Second Edition, **2014**.
32. IEurochem Guides, EURACHEM/CITAC Guide CG 4 Quantifying Uncertainty in Analytical Measurement, Third Edition, **2012**.
33. EPA Region III Quality Assurance, MDL Factsheet, IDL-MDL- PQL: What the "L" is Going On? What Does All This Alphabet Soup Really Mean?, Revision No:2.5., **2016**.
34. P. X. Baliza, L. S. G. Teixeria, V. A. Lemos, Microchem. J., **2009**, *93,* 220–224. **DOI:**10.1016/j.microc.2009.07.009
34. J. N. Miller and J. C. Miller, Statistics and Chemometrics for Analytical Chemistry, 6th Edition, Pearson Education Limited 2000, Harlow, England, 2**010**.
36. A. Akdoğan, G. Buttinger, T. Wenzl, Food Addit. Contam A, **2016**, *33*, 215–224.
37. M. Muchuweti, J. Birkett, E. Chinyanga, R. Zvauya, M. Scrimshaw, J. Lister, Agr. Ecosyst. Environ., **2006**, *112 (1),* 41–48. **DOI:**10.1016/j.agee.2005.04.028
38. EC. Commission Regulation (EC) 466/2001, Setting maximum levels for certain contaminants in foodstuffs. Official J Eur Commun **2001**,77.
39. Union E. Commission Regulation (EC) No. 1881/2006 of 19 December 2006 Setting Maximum Levels for Certain Contaminants in foodstuffs. Off J Eur Union L 364, *5,* **2006**.
40. M. K. Turkdogan, F. Kilicel, K. Kara, I. Tuncer, I. Uygan, Environ. Toxicol. Pharmacol., **2002**, *13,* 175–79. **DOI:**10.1016/S1382-6689(02)00156-4
41. S. E. Manahan, Fundamental of environemental chemistry: Boca Raton: CRC Press, LLC, 2001.
42. S. Shegefti, A. Mehdinia, F. Shemirani, Microchim. Acta, **2016**, *183,* 1963–1970. **DOI:**10.1007/s00604-016–1837-0
43. M. A. Habila, Z. A. ALOthman, A. M. El-Toni, S. A. Al-Tamrah, M. Soylak, J. P. Labis, Microchim. Acta, **2017**, *184,* 2645–2651. **DOI:**10.1007/s00604-017-2283-3
44. A. Samadi, M Amjadi, Microchim. Acta, **2015**, *182,* 257–264. **DOI:**10.1007/s00604-014–1327–1
45. M. Golshekan, S. Shariati, Acta Chim. Slov., **2013**, *60,* 358–367.

Povzetek

V tem delu poročamo o večelementnem predkoncentracijskem postopku za ione Cu (II), Co (II), Cd (II), Ni (II) in Zn (II), ki je osnovan na Fe_3O_4 magnetnih nanodelcih, prevlečenih s politiofenom (Fe_3O_4 @ PTh MNPs) kot trdno fazo. Po predkoncentraciji smo ione določili z vbrizganjem mikro-vzorca v plamenski atomski absorpcijski spektrometer (MIS-FAAS). Optimizirani so bili vplivi pH vzorca, vrste in prostornine eluentov, prostornine vzorca, časa ekstrakcije, količine adsorbenta in motečih ionov. Analite smo predkoncentrirali od 75 na 150 ml in s pufrom uravnali pH na 7. Eluent je bil 1 ml raztopine HNO_3, koncentracije 1 mol L^{-1}. Pod optimalnimi pogoji so se meje zaznavanja ionov analita gibale med 1 in 10 µg L^{-1}. Adsorpcijska zmogljivost Fe_3O_4@PTh je bila v območju od 2,85 do 9,76 mg g^{-1}. Metoda je bila validirana z analizo certificiranih referenčnih materialov. Relativne napake in standardni odkloni so bili nižji od 5 %. Razviti postopek smo uporabili pri različnih vzorcih vode, zemlje in nekaterih rastlin.

Except when otherwise noted, articles in this journal are published under the terms and conditions of the Creative Commons Attribution 4.0 International License

DOI: 10.17344/acsi.2019.5105 *Acta Chim. Slov.* **2020,** *67,* 386–395
creative commons

Scientific paper

Prediction of Hit-to-Lead Ligand Molecule Interaction with G-Quadruplex DNA from c-Myc Oncogene Promoter Region

Petar M. Mitrasinovic*

Center for Biophysical and Chemical Research, Belgrade Institute of Science and Technology, 11060 Belgrade, Serbia

** Corresponding author: E-mail: pmitrasinovic.ist-belgrade.edu.rs@tech-center.com*

Received: 03-02-2019

Abstract

Targeting guanine (G)-rich DNA sequences, folded into non-canonical G-quadruplex (G4) structures, by small ligand molecules is a potential strategy for gene therapy of cancer disease. BRACO-19 has been recently established as a unique (thermodynamically favorable and highly selective) binder, being involved in the external stacking mode of interaction with a G4-DNA formed in the c-Myc oncogene promoter region (P. M. Mitrasinovic, *Croat. Chem. Acta* **2019**, *92*, 43–57). Herein, hit-to-lead ligands are identified using high-throughput virtual screening (HTVS). Search of the Kyoto Encyclopedia of Genes and Genomes (KEGG) databases is performed using the key pharmacophore features of BRACO-19. At the very outset, out of a total of 29,009 entries, 95 hits are extracted and evaluated by docking them in the binding sites of G4. Then, 22 hits are chosen by observing the binding free energies. Consequently, 3 hit-to-lead candidates are selected on the basis of structural criteria. Finally, a lead candidate structure is proposed using analog design and considering both the structural and physicochemical requirements for optimal biological activity and a variety of pharmacological standpoints. Implications of the present study for experimental research are discussed.

Keywords: Anti-cancer drug design; BRACO-19; c-Myc oncogene promoter; G-quadruplex DNA; hit-to-lead ligand

1. Introduction

In addition to forming various canonical duplex structures, highly dynamical DNA macromolecules are able to fold into non-canonical structures, including hairpin, triplex, G-quadruplex, and i-motif. G-quadruplexes (or G-tetraplexes) are secondary structures that form within guanine rich strands of regulatory genomic regions (human telomeres, oncogene promoter regions, immunoglobulin switch regions, ribosomal DNA, some regions of RNA). Even though G4s associate with various conformations and folding energies, and their thermodynamic stabilities are comparable to those of duplex structures, the function of G4s *in vivo* is not fully understood. G4s are hypothesized to participate in important biological phenomena, including telomere maintenance, end-capping and protection, chromosome stability, gene expression, viral integration, and recombination.[1,2] A relevant consequence of G-quadruplex formation in telomeric DNA is the inhibition of telomere elongation by telomerase in cancer cells.[3,4] An increasing number of identified G4-binding proteins means that protein/G4 interactions are associated with important cellular events. Use of small molecules for targeting G4 in order to disrupt protein/G4 recognition emerges as a potential strategy for directing anti-cancer therapy.[5]

G4 structures primarily consist of two or more stacked G-tetrads (or G-quartets) assembled either from a single strand of DNA in an intramolecular (backfolded) way or from two-, three-, or four DNA strands in an intermolecular way. Every single G-tetrad contains four G-G base pairs (bps) linked by Hoogsteen hydrogen bonds. G4s are more compact structures than duplex DNAs and display well-defined binding sites (external stacking, intercalating, and groove/loop).[2,6] Small ligand molecules are expected to be complementary in shape and charge to the biological target. The question of finding ligands that conform to the structural and physicochemical requirements for optimal biological activity is of current relevance. This work is, to some extent, imagined to contribute to the bet-

ter formulation of a daunting challenge – how to design small molecules that can bind selectively to each of the many possible G4 structures.

A G-rich element of repeated sequences with three or four guanine residues (between –137 and –115 bp upstream of the P1 promoter in the c-Myc oncogene) can fold in an intramolecular G4 structure (Figure 1) in order to suppress c-Myc transcription in a silenced form.[7] This element is a potential target for down-regulation of c-Myc overexpression in tumor cells.[8,9] The dynamics of noncovalent interaction between structurally diversified ligand molecules (with a pronounced propensity for the receptor)[9] and the G4 was investigated in a systematic fashion.[10] Among the highest affinity ligands, BRACO-19 (Figure 2), a pure G-quartet binder, was established as a unique – thermodynamically favorable ligand, increasing conformational flexibility of the G4 structure through its stacking mode of interaction.[10] By using the pharmacophore features of BRACO-19 (Figure 2), that is, the structural features of the ligand that are recognized at a receptor site and responsible for the ligand's biological activity, a subtle *in silico* protocol followed by analog design is employed in this work, with the ultimate goal to determine lead candidate structure.

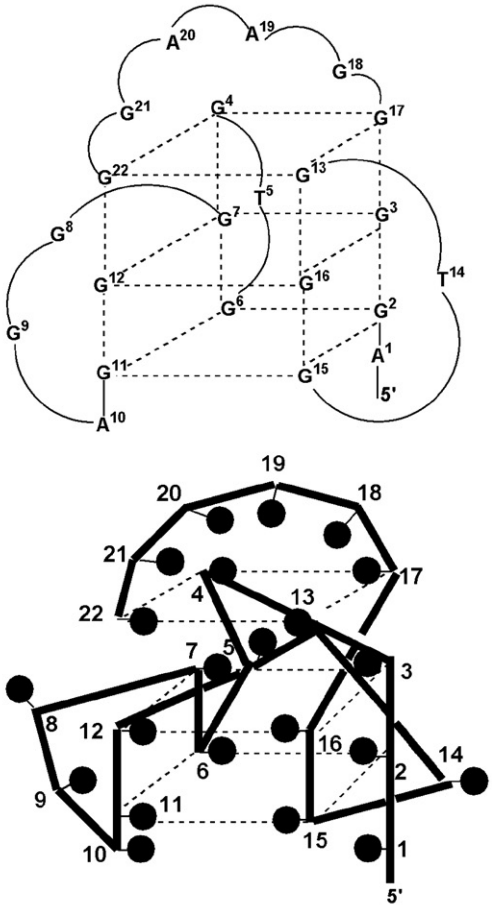

Figure 1. Assembly and topology of G-tetrads in G-quadruplex structure.

2. Methods

Experimental structure of the monomeric parallel-stranded G-quadruplex (Figure 1) was retrieved from the Research Collaboratory for Structural Bioinformatics (RCSB) Protein Data Bank (PDB) in order to obtain the initial coordinates of the target atoms (PDB ID: 2A5P).[11]

The term "pharmacophore" means a spatial arrangement of the essential features of an interaction.[12–14] These features of BRACO-19 (Figure 2) were identified using the interface Pharmit - an online, interactive environment for exploration of chemical space.[15] Features supported by the web server include hydrogen bond acceptors and donors, negative and positive charges, aromatics, and hydrophobic features. For a provided ligand structure as a PDB input, the algorithm searches for these features using tolerance spheres. Structural parts of a compound match if they can be positioned in such a way that their corresponding features are located within these spheres. Some features can have additional constraints, such as size (number of atoms) for hydrophobic features and direction for hydrogen bonds and aromatics.[15]

Hits were generated by searching the Kyoto Encyclopedia of Genes and Genomes (KEGG) databases COMPOUND and DRUG. This search was based upon both the key pharmacophore features of BRACO-19 and SIMCOMP (SIMilar COMPound) – a graph-based method that is implemented in the KEGG system for searching and comparing chemical structures in the databases.[16–18] SIMCOMP provides the atom alignments between two chemical compound graphs and calculates the similarity of two chemical compounds by counting the number of matched atoms in those atom alignments. For all calculations in SIMCOMP, the Global Search was performed and the KEGG Atom Types were chosen as a representation of atoms in order to detect biochemically meaningful features. The KEGG Atom Types are based on the chemical concept of functional groups and 68 atom types (vertex types) are defined for carbon, nitrogen, oxygen, and other atomic species with different environments.[16–18] All the other default options were exploited.

Virtual screening was performed for small molecules (hits) collected from KEGG against G-quadruplex DNA (PDB ID: 2A5P). The Windows platform-based graphical interface Raccoon was used for preparing and automating the AutoDock virtual screening.[19]

Flexible docking of each ligand (hit) in the receptor was performed by AutoDock 4.2.[20,21] Noteworthy is to see into why the particular method was chosen. Docking problem is an exhaustive search problem that includes many degrees of freedom. It means that the use of efficient docking algorithms is critical for finding optimal ligand/receptor configuration and for predicting accurate binding free energy without fetching formal statistical mechanics methods. A fundamental idea underlying AutoDock 4.2 is to calculate the total ligand/receptor binding free energy

by summing distinct, physically interpretable contributions.[22] Scoring functions are calibrated using multivariate regression analysis of a set of ligand/target receptor complexes with respect to experimentally determined structures and binding affinities. The final form of a scoring function depends on the size and quality of the training set. Since scoring functions are derived from diverse ligand/receptor complexes, possible applications are not restricted to a particular set of ligands or a specific receptor. An average level of thermochemical accuracy of 2 kcal mol^{-1} in binding affinity predictions makes empirical scoring acceptable for the structure-based drug (or ligand) design.[23–32] The distinct energetic terms considered throughout this work account for the hydrogen bonding, the van der Waals (vdW) interactions, the electrostatic interactions, the desolvation-mediated ligand/receptor binding, the total internal energy, the torsional potential, and the unbound system's energy respectively.[20] Entropy of ligand interaction is reflected through the loss of degrees of freedom upon binding and is included via the torsional potential being proportional to the number of torsions (sp^3 bonds) in the ligand. The Lamarckian Genetic Algorithm in combination with a grid-based energy evaluation method was employed to calculate grid maps, while atomic potential grid map was computed by AutoGrid4 with a 0.536 Å spacing in a 65Å × 65Å × 65Å (1Å = 10^{-10}m) box centered on the macromolecule. All the other default options were chosen in the AutoDockTools4 for preparing the systems for runs.[21] The lowest energy and physically meaningful (in terms of the spatial orientation of a ligand with respect to the compact binding sites of G4) conformations were extracted from docking experiments. A hit affinity for the receptor was estimated by the total binding free energy ($\Delta G_{binding}$) or the dissociation constant (K_d), taking into account the relation $\Delta G_{binding} = RT \ln(K_d)$ (R = 1.9872 kcal K^{-1} mol^{-1} – the gas constant, T = 300 K – the absolute temperature).

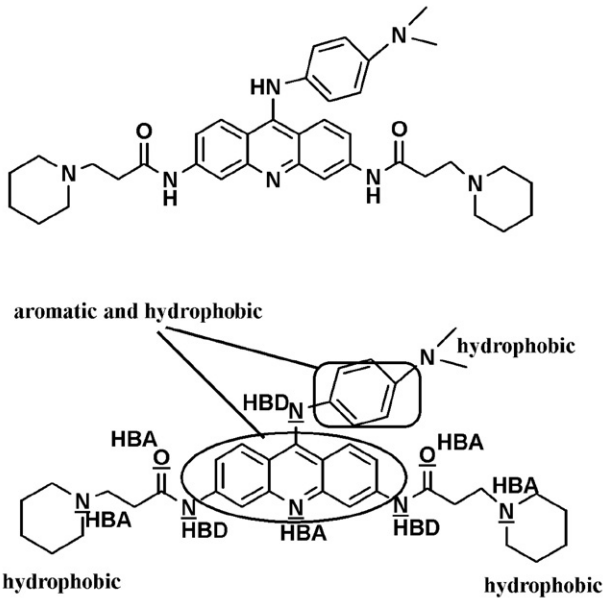

Figure 2. Structure of BRACO-19 and its pharmacophore features. Each underlined atom is hydrogen bond donor (HBD) or hydrogen bond acceptor (HBA).

3. Results and Discussion

Ligand π–π stacking at the end of G-quadruplex can be considered as a preferred mode of interaction according to experimental[9,33] and theoretical[5,10] results. Although nonspecific ligand-groove/loop binding is not inherently stable due to its dependence on a particular topology of the groove/loop,[5,9] the groove/loop is of interest for the structure-based drug design. This recognition motif is a viable site for blocking the interactions between G4 and its binding proteins in aqueous solution.[5] Search for ligands that satisfy the structural and physicochemical requirements for optimal biological activity is currently needed.

From a rigorous biophysical standpoint, the dynamics of interaction of structurally different ligand molecules with the G4 (Figure 1) was recently explored and characterized in a systematic fashion.[10] As a consequence, the highest affinity ligands, being involved in external stacking and groove binding, were observed respectively. Interestingly, BRACO-19 (Figure 2) – a pure G-quartet binder was established to be a unique (thermodynamically favorable) ligand in terms of increasing conformational flexibility of the receptor upon external stacking.[10] The pharmacophore of BRACO-19, which can be defined as a set of structural features in the ligand that is recognized at a receptor site and is responsible for the ligand's biological activity, is a starting point of the present work. The particular set of structural features consists of: i) three aromatic and hydrophobic rings making the core scaffold, ii) two peripheral and hydrophobic hexagons being symmetrically attached to the core scaffold through adequate linkers, iii) three hydrogen-bond donors (HBDs), iv) five hydrogen-bond acceptors (HBAs), and v) a side chain that contains an aromatic and hydrophobic hexagon as well as a hydrophobic region on top of it (Figure 2).

KEGG database search generated hits using the pharmacophore of BRACO-19 as a template. Out of a total of 29,009 entries, 95 hits were extracted, 21 from the database Compound (Table S1, Supplementary Material) and 74 from the database Drug (Table S2, Supplementary Material). Conformations obtained by docking the hit structures in the compact binding sites of G4 were scored and affinities for G4 were evaluated.

The potency of a substance (the concentration required to achieve a defined biological effect) must be significant in order to identify a hit-to-lead. The particular concentration is in the micromolar (10^{-6} M) range for a hit and in the nanomolar (10^{-9} M) range for a lead candidate.[34,35] Affinity issue can be conveniently seen through the total binding free energy ($\Delta G_{binding}$) or the dissociation

constant (K_d), taking into account the relation $\Delta G_{binding}$=RT ln(K_d) (R=1.9872 kcal K^{-1} mol^{-1} – the gas constant, T=300 K – the absolute temperature). The values of $\Delta G_{binding}$ and K_d for the BRACO-19:G4 complex, –6.77 kcal mol^{-1} and 12.01 μM (the footnote a of Table 1), are the references for selecting a hit that is supposed to have a higher affinity for the receptor. Thus, twenty two hits (out of the previous ninety five), which satisfy this criterion, are selected (Figure 3) and their affinity-based ranking is summarized in Table 1.

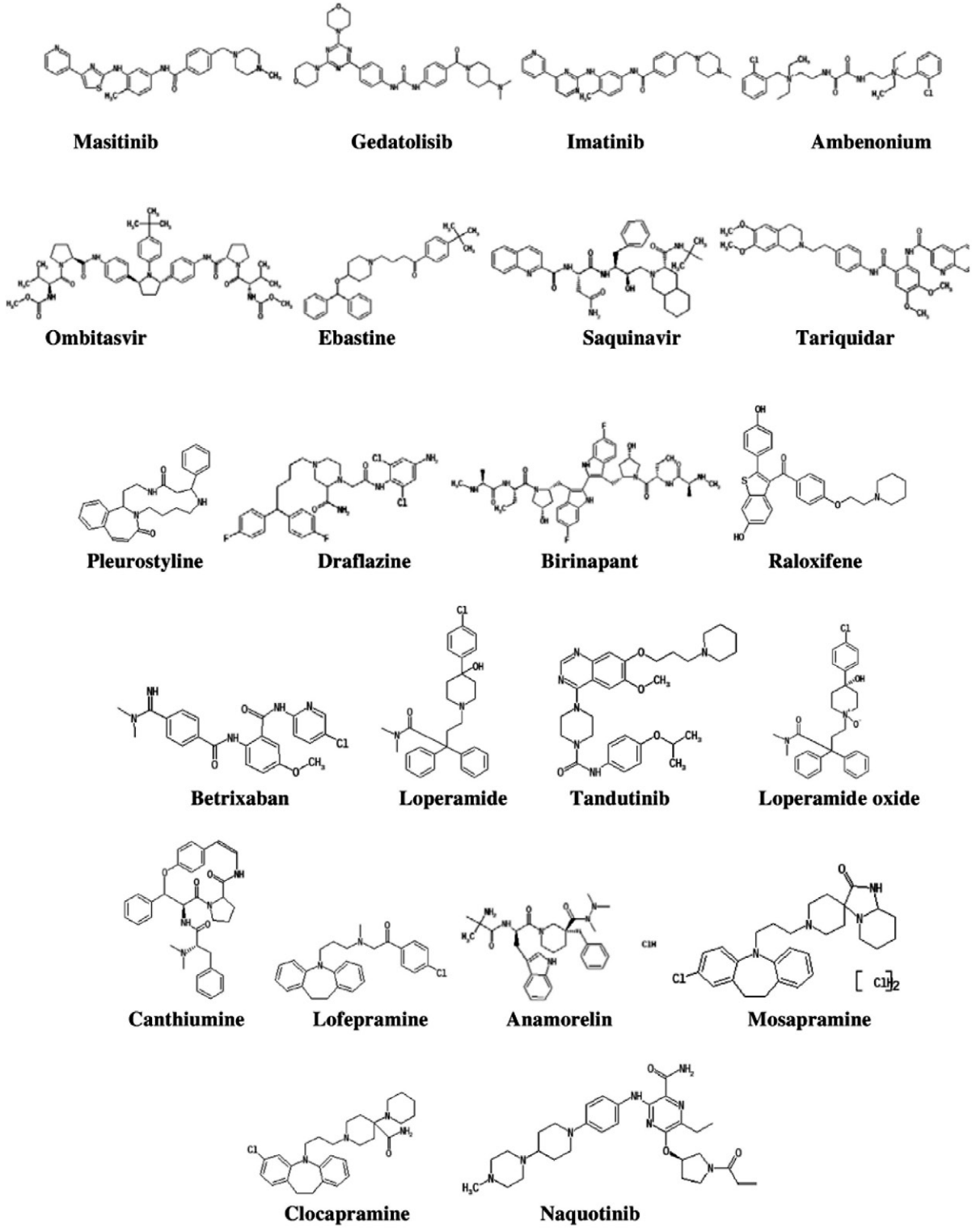

Figure 3. Structures of hit ligand molecules with the most pronounced affinity for the G4-DNA target.

Table 1. Ranking of hits according to the predicted binding free energy

Entry	Ligand name[a]	$\Delta G_{binding}$[b] (kcal mol^{-1})	Dissociation constant[c] K_d (μM)	$\Delta G_{intermolecular}$[d] (kcal mol^{-1})
D10229	Masitinib	–11.85	0.0021	–13.04
D10635	Gedatolisib	–10.50	0.022	–11.69
D08066	Imatinib	–10.36	0.025	–11.56
D01001	Ambenonium	–9.88	0.061	–11.07
D10576	Ombitasvir	–9.82	0.064	–11.90
D01478	Ebastine	–9.48	0.11	–10.97
D00429	Saquinavir	–9.45	0.12	–10.35
D06008	Tariquidar	–9.38	0.13	–10.87
C10612	Pleurostyline	–9.27	0.16	–9.27
D03906	Draflazine	–9.18	0.19	–9.77
D10417	Birinapant	–9.17	0.19	–10.66
C07228	Raloxifene	–8.86	0.32	–10.05
D08873	Betrixaban	–8.84	0.33	–9.73
D08144	Loperamide	–8.68	0.43	–9.57
D06005	Tandutinib	–8.52	0.57	–10.01
D07113	Loperamide oxide	–8.45	0.64	–9.05
C10000	Canthiumine	–8.45	0.64	–8.75
D08856	Anamorelin	–8.32	0.80	–9.21
D08140	Lofepramine	–8.29	0.84	–9.18
D01548	Mosapramine	–8.23	0.92	–8.53
D07718	Clocapramine	–8.21	0.95	–8.21
D10958	Naquotinib	–8.20	0.97	–9.99

[a] Reference values for the BRACO-19:G4 complex are –6.77 kcal mol^{-1}, 12.01 μM, and –9.99 kcal mol^{-1} respectively.
[b] The AutoDock 4.2 score: $\Delta G_{binding} = E_{vdW} + E_{Hbond} + E_{desolvation} + E_{electrostatic} + E_{internal} + E_{torsional} - E_{unbound}$
[c] $\Delta G_{binding} = RT \ln(K_d)$, R – the gas constant (1.9872 kcal K^{-1} mol^{-1}), T – the absolute temperature (300 K), 1 μM = 10^{-6} M.
[d] $\Delta G_{intermolecular} = E_{vdW} + E_{Hbond} + E_{desolvation} + E_{electrostatic}$. The intermolecular energy represents the largest (most negative) contribution to the stability (binding free energy) of the complexes and does not conform to the trend displayed by the values of both $\Delta G_{binding}$ and K_d.

The intermolecular energy (IE), also known as the interaction energy, is a key part of the enthalpy of formation of a molecular complex. In practical energetic analyses, the intermolecular energy is viewed as the largest contribution to the stability (total binding free energy) of a complex. The IE is defined as the sum of distinct energetic terms that account for the van der Waals (vdW) interactions, the hydrogen bonding, the desolvation-mediated receptor-ligand binding, and the electrostatic interactions respectively (the footnote d of Table 1). A numerical inspection of the values given in the last column of Table 1 shows that the key (negative) contribution to $\Delta G_{binding}$ comes from the IE and that the trend of IE values does not conform to the trend displayed by the values of $\Delta G_{binding}$ and K_d separately. The IE of the BRACO-19:G4 complex, –9.99 kcal mol^{-1}, is the reference (the footnote a of Table 1). In comparison to the reference, the hits can be divided into two subgroups: the first one with eleven hits having the IE that is more negative than the reper and the second one with the remaining hits. Thus, the members of the first subgroup are: Masitinib, Gedatolisib, Imatinib, Ambenonium, Ombitasvir, Ebastine, Saquinavir, Tariquidar, Birinapant, Raloxifene, and Tandutinib (Table 1). In other words, as far as affinity issue is concerned, hit-to-lead candidates belong to this subgroup of hits.

In order to further filter out hit-to-lead ligands, it is necessary to invoke some structural arguments. The template structure of BRACO-19 mainly takes part in π–π stacking with the $G^2G^6G^{11}G^{15}$ tetrad by way of its core aromatic scaffold and, therefore, BRACO-19 is considered to be a G-quartet-binding ligand, even though it is involved in several, additional electrostatic interactions with the residues A^1, G^6, G^{11}, and G^{15} by way of its side chains.[10] Since the interaction energy of BRACO-19 is rooted in π–π stacking, any hit-to-lead candidate with a more negative interaction energy is expected to be both primarily associated with external stacking of its core scaffold and more prone than BRACO-19 to electrostatic interactions via its side chain configurations. Fact that the structure of BRACO-19 contains four aromatic and hydrophobic rings (Figure 2) is employed to recruit hit-to-lead candidates from the first subgroup of hits. An inspection of the eleven hit structures (Figure 3) illustrates that the structures of Masitinib, Imatinib and Raloxifene only have four aromatic and hydrophobic rings (Figure 4).

Knowing the structures of hit-to-lead candidates (Figure 4), the question to be raised is: what is a relevant structural basis upon which a lead candidate should rely? Besides observing individual structural and functional features of every single hit-to-lead candidate, a postulate of

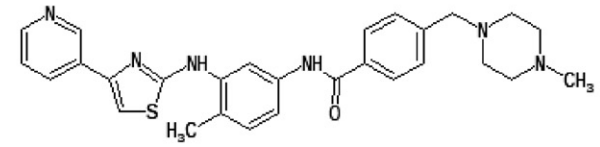

Masitinib

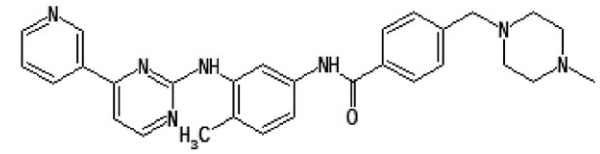

Imatinib

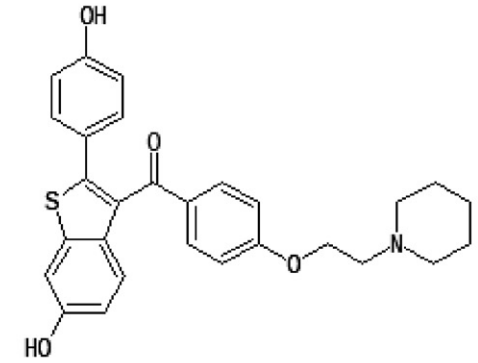

Raloxifene

Figure 4. Structures of hit-to-lead candidates.

outstanding importance is to maintain the structural similarity between a lead candidate and a template structure (BRACO-19) as much as possible.

In contrast to Imatinib, noteworthy is that Masitinib and Raloxifene contain thiophene – a five-membered, sulfur-containing heteroaromatic ring that is often a building block in drugs (Figure 4). Metabolism of thiophene can cause formation of reactive metabolites that may be responsible for drug-induced liver damage. Even though its presence in drugs does not necessarily result in toxic effects, thiophene is seen as a kind of structural alert. For example, tienilic acid – a thiophene-based drug was removed from the market after being both associated with severe cases of immune hepatitis and in use for only several months.[36] BRACO-19 does not contain a thiophene moiety (Figure 2). These observations substantiate the choice of Imatinib as a favorable hit-to-lead candidate. This choice is agreeable with the experimentally detected ability of Imatinib to downregulate telomerase activity and to inhibit proliferation in telomerase-expressing cell lines by targeting various cellular components.[37]

The structural alterations of Imatinib (Figure 4) were needed in order to proceed to the proposal of lead candidate (Figure 5). These steps were guided by the structural and physicochemical requirements for optimal biological activity. To make the core scaffold composed of three fused aromatic rings (as that of BRACO-19, Figure 2), a carbon atom of the bottom methyl group (Figure 4) is replaced by nitrogen and an adjacent N atom is replaced by a C atom. The newly introduced N and C atoms are then bonded and the closure of the intermediate ring is achieved (Figure 5). Also, nitrogen on top of the left-hand side ring is substituted by a C atom and carbon in the central ring is replaced by an N atom (Figure 5). As for the template structure of BRACO-19 (Figure 2), two peripheral and hydrophobic hexagons that are symmetrically attached to the core scaffold through adequate linkers were shown to additionally stabilize an external stacking conformation in the stable regime of molecular dynamics simulation.[10] To mimic this functionality of BRACO-19, a copy of the right-hand side chain of Imatinib (Figure 4) is introduced (Figure 5) by replacing an aromatic ring (Figure 4) that is attached to the left-hand side of the core scaffold. The side chain of BRACO-19, which arises from the middle ring of the core scaffold and contains an aromatic six-membered ring (Figure 2), was found not to interact with the receptor, but its primary role in the binding conformation was to reduce deviations (or distortions) of the stacking portion of the BRACO-19 structure from horizontal planarity.[10] To additionally maintain a clear resemblance of lead candidate to BRACO-19, the particular side chain (as is – without any change) is attached to the intermediate ring of the core scaffold of the modified Imatinib (Figure 5).

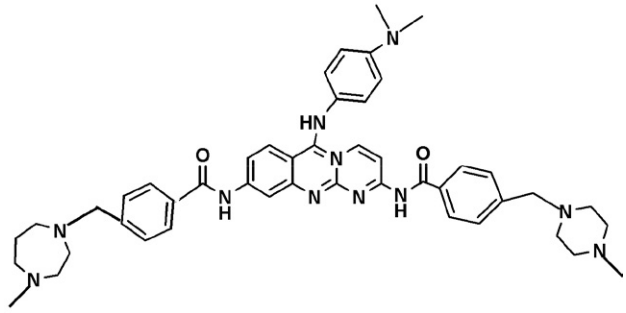

Figure 5. Proposal of lead candidate structure.

As discussed so far, virtual screening resulted in heat-to-lead candidate (Imatinib), while a transition process, from Imatinib to lead candidate, was treated as analog design. The overall protocol was initially imagined to suggest lead candidate that is able to functionally outperform BRACO-19 in binding to the G-quadruplex. To examine the extent of success of this undertaking, proposed lead candidate is docked in the target and obtained binding conformation is contrasted to that of BRACO-19 quantitatively and qualitatively. The values of $\Delta G_{binding}$ and K_d for the lead candidate:G4 complex (–11.29 kcal mol^{-1} and 0.0053 μM) relative to those for the BRACO-19:G4

complex (–6.77 kcal mol^{-1} and 12.01 μM) indicate a stronger affinity of the lead candidate for the receptor in comparison to the reference. A K_d value of 5.3 nm conforms to the requirement of being in the nanomolar (10^{-9} M) range that is relevant for a lead. The intermolecular energy of the lead candidate is estimated to be –13.68 kcal mol^{-1}, which is more negative both than any corresponding value for a hit (Table 1) and than the reference value for BRACO-19 (–9.99 kcal mol^{-1}). To rationalize the origin of the more pronounced complex stability, the mode of interaction between lead candidate and the G4 is observed with respect to the mode of interaction between BRACO-19 and the G4 (Figure 6). The simultaneous external stacking and groove binding of the lead candidate has visible stabilizing advantages over the external stacking of BRACO-19 in forming a complex with the receptor. In this light, it is important to note the extent of conformational flexibility of the core structures of the lead candidate and BRACO-19 (Figure 6). Flexible core scaffold of the lead candidate is an advantage relative to the rigid one of BRACO-19. The conformational flexibility of small molecules proved to be more preferable compared to locking the ligands in a presumed bioactive G4 conformation.[38]

The structural design of optimal groove/loop binders is a challenge, as this mode of interaction is nonspecific and dependent on the particular topology of groove/loop residues. A pure G-quartet-binding mode is hypothesized to be more stable than a multiple-binding mode – two ligands that are involved in external stacking and loop binding respectively.[5] A likely reason for this is that a groove/loop-binding ligand induces loop rearrangement and perturbations to the interactions between the side chains of the other G-quartet-binding ligand and the loop/groove of G-quadruplex. There are indications that a multiple-binding mode increases conformational rigidity of G-quadruplex and decreases conformational flexibility of both G-quartets and backbone.[5] It means that such a mode of interaction, which includes two ligands, would be thermodynamically unfavorable. The present proposal of lead candidate structure, being a G-quartet and groove/loop binder at the same time, is inclined to bypass this kind of glitch. This was accomplished using the following reasoning. Knowing that DNA-groove/ligand recognition is mainly driven by charge-induced phenomena,[39–41] the lead candidate was made more prone than BRACO-19 to electrostatic interactions. While the core aromatic scaffold of BRACO-19 only has one hydrogen-bond acceptor (an N atom, Figure 2), the core aromatic scaffold of lead candidate has three hydrogen-bond acceptors (three N atoms, Figure 5). While two symmetric side changes of BRACO-19 have four HBAs (two N and two O atoms) and two HBDs (two NH groups, Figure 2), two symmetric side changes of lead candidate have six HBAs (four N and two O atoms) and two HBDs (two NH groups, Figure 5). To better conceive this aspect, the mode of interaction of the lead candidate with the receptor is illustrated in Figure 7 containing a molecular surface plot with standard atom colors. The structural basis is an advance in the development of effective ligand molecules that are able to block the interactions of G4 with proteins having G4-groove/loop as binding site. Taking into account both this point and the way in which

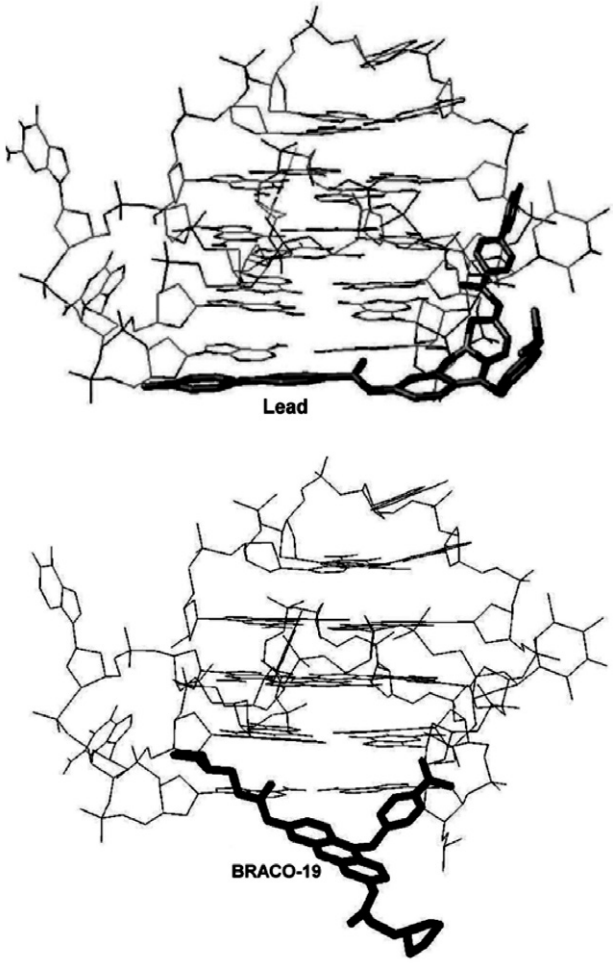

Figure 6. Interaction of lead candidate with G4 through external stacking and groove binding simultaneously versus external stacking of BRACO-19 with G4.

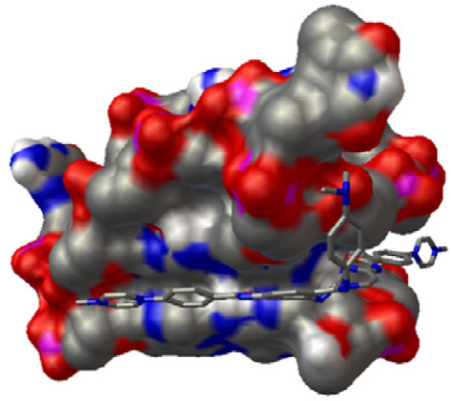

Figure 7. Lead candidate is proposed to interact through external stacking and groove binding with G4 simultaneously.

Table 2. Drug likeness of lead candidate according to Lipinski's Rule of Five[(a)]

Ligand	Number of H-bond donors	Number of H-bond acceptors	Molecular weight (D)	Log*P*[(b)]
Lead	3	10	702.02	0
BRACO-19	3	6	550.01	2.35

[(a)] The Rule of Five got its name from cut-off values that are five or a multiple of five. The rule states that poor absorption or permeation is more likely when: (i) a compound has more than 5 H-bond donors (sum of OHs and NHs), (ii) there are more than 10 H-bond acceptors (sum of Ns and Os), (iii) the molecular weight is over 500 Dalton and (iv) the Log*P* is over 5 (or MLog*P* is over 4.15).[43]
[(b)] Overall hydrophobicity is measured by the partition coefficient *P*. *P* is the water-octanol partition coefficient and is a measure of the equilibrium concentration of solute in octanol divided by the concentration of the same species in water. Log*P* is a measure of hydrophilicity/phobicity of a compound.

Table 3. Predictors of oral bioavailability of lead candidate according to Veber's rules[(a)]

Ligand	Number of torsions	Polar surface area (Å^2)	Number of H-bond donors	Number of H-bond acceptors
Lead	11	60.74	3	10
BRACO-19	13	9.72	3	6

[(a)] Based on measurements in rats for over 1,100 drug candidates, compounds that meet the following criteria may be associated with good oral bioavailability: (i) molecular flexibility reflected through 10 or fewer rotatable bonds – torsions, (ii) polar surface area equal to or less than 140 Å^2, and (iii) a total number of hydrogen-bond donors and acceptors equal to or less than 12.[44]

the lead candidate structure was developed via analog design on top of HTVS, the lead candidate and BRACO-19 can be observed neither like clear structural nor like clear functional analogs. They should rather be placed in between structural and functional analogs.

Virtual screening is an effective method for reducing the initial number of potential candidates. A small molecule with binding affinity to increase the conformational flexibility of an apo (ligand-free) G4 through π–π stacking at the end of G4 can be conceivable as a unique, specific pharmacophore for designing novel lead candidate compounds by high-throughput virtual screening.[6,10] The lead candidate (Figure 5), designed by this approach and aimed to target the c-Myc promoter G4 through external stacking and groove binding simultaneously, would have useful implications for overcoming the challenge of designing specific groove/loop binders. The challenge stems from the dependence of the groove/loop interaction mode on the particular arrangement of residues. Even though the pure quartet-binding mode is more stable than the groove/loop binding mode, groove/loop is a viable binding site that is of interest for the structure-based drug design. The use of grooves/loops offers distinct environments in order to gain specificity among many types of G4s by way of subtle variations of G4 topologies, groove widths, and loop sequences without affecting binding affinity.[42]

The correlation between the structure of a drug candidate and its oral absorption is an important point of consideration when attempting to design novel anti-cancer therapeutics. Empirical recommendations predict drug likeness on the basis of the molecular structure of drug candidate and represent useful guide in drug design process. Lipinski's rule of five (see the footnotes of Table 2)[43] and Veber's rules (see the footnote of Table 3)[44] are used to evaluate the lead candidate with respect to BRACO-19. A close inspection of the data for the lead candidate reveals that molecular weight (MW) is only out of an expected range in Table 2, while both the number of torsions and the total number of hydrogen-bond donors and acceptors are essentially lined up with the upper bounds of suggested ranges in Table 3. The MW of lead candidate is not likely to affect its good absorption as the MW of the reference (BRACO-19), being a highly selective G4-binder that is widely available on the market, is out of range as well (Table 2). An important predictor is *P* – an indicator of hydrophobicity and hydrophilicity. A zero value of log*P* in Table 2 means that the lead candidate is equally hydrophobic and hydrophilic. This is well-correlated with the polar surface area of the lead candidate (60.74 Å^2 in Table 3) that is roughly in middle of the expected range. In contrast, a value of 2.35 for log*P* in Table 2 means that BRACO-19 is substantially (about 224 times) more hydrophobic than hydrophilic, so that its polar surface area (9.72 Å^2 in Table 3) is in a close vicinity of the lower bound of the expected range. These predictions substantiate our fundamental idea to design a lead molecule that is remarkably more susceptible to charge-induced interactions with the receptor (or more specific) than BRACO-19. Further investigations correlating oral bioavailability of the particular molecule in humans and simple molecular property-based rules may be required.[45]

In creating a synthetic route for the development of a ligand molecule, it is necessary to create a molecular entity in which functional groups are correctly positioned in three-dimensional space; this will enable the creation of functional biophoric fragments such as the pharmacoph-

ore. The lead candidate, proposed herein, does not have chiral centers (Figure 5) and it may be eventually synthesized using the small libraries of already-prepared (e.g. by means of a split-mix approach) structural fragments (analogs),[46] even though a potential disadvantage of synthetic libraries is their limited structural diversity. Its atomic composition (Figure 5), presumably, does not interfere with serious side effects. Future research is supposed to see into both pharmacokinetic/dynamic and toxicity profiles *in vitro/in vivo*. The need to know potential targets at the whole genome level means that global genome transcriptome profiling may help in the determination of which genes are affected by a rationally designed G4-interactive small molecule.[47] Consequently, the selectivity and potency of a new G4-preferred compound can be explored using *in vitro* cell assays and *in vivo* models. We believe that this report will inspire modern organic chemists and pharmacists to face new interesting challenges of vital importance with vigor.

4. Conclusions

It has been shown that high-throughput virtual screening in combination with analog design may be an efficient tool for predicting the chemical structure of lead candidate aimed at guiding further steps in a drug design and development process.

A substantial propensity of the lead candidate to stabilize G-quadruplex DNA from the c-Myc oncogene promoter region has been predicted by satisfying the structural and physicochemical requirements for optimal biological activity – by binding to the target through external stacking and groove binding simultaneously. This work has somewhat contributed to the better formulation of a daunting challenge – how to design small molecules that can bind selectively to each of the many possible G4 structures.

It is believed that the present *in silico* study has provided a fruitful ground for the upcoming investigations of pharmacokinetics/pharmacodynamics and toxicity properties *in vitro/in vivo*.

Supplementary Material

Results of the high-throughput virtual screening for hits against G-quadruplex DNA (PDB ID: 2A5P).

5. References

1. E. Ruggiero, S. N. Richter, *Nucl. Acids Res.* **2018**, *46*, 3270–3283. **DOI:**10.1093/nar/gky187
2. N. W. Luedtke, *Chimia* **2009**, *63*, 134–139. **DOI**:10.2533/chimia.2009.134
3. R. J. Harrison, J. Cuesta, G. Chessari, M. A. Read, S. K. Basra, A. P. Reszka, J. Morrell, S. M. Gowan, C. M. Incles, F. A. Tanious, W. D. Wilson, L. R. Kelland, S. Neidle, *J. Med. Chem.* **2003**, *46*, 4463–4476. **DOI:**10.1021/jm0308693
4. J. H. Tan, T. M. Ou, J. Q. Hou, Y. J. Lu, S. L. Huang, J. Y. Wu, Z. S. Huang, K. Y. Wong, L. Q. Gu, *J. Med. Chem.* **2009**, *52*, 2825–2835. **DOI:**10.1021/jm801600m
5. J. Q. Hou, S. B. Chen, J. H. Tan, H. B. Luo, D. Li, L. Q. Gu, Z. H. Huang, *J. Comput. Aided Mol. Des.* **2012**, *26*, 1355–1368. **DOI:**10.1007/s10822-012-9619-1
6. P. M. Mitrasinovic, *J. Biomol. Struct. Dyn.* **2018**, *36*, 2292–2302. **DOI**:10.1080/07391102.2017.1358670
7. D. J. Cashman, R. Buscaglia, M. W. Freyer, J. Dettler, L. H. Hurley, E. A. Lewis, *J. Mol. Model.* **2008**, *14*, 93–101. **DOI**:10.1007/s00894-007-0254-z
8. J. Dai, M. Carver, L. H. Hurley, D. Yang, *J. Am. Chem. Soc.* **2011**, *133*, 17673–17680. **DOI:**10.1021/ja205646q
9. B. J. Chen, Y. L. Wu, Y. Tanaka, W. Zhang, *Int. J. Biol. Sci.* **2014**, *10*, 1084–1096. **DOI**:10.7150/ijbs.10190
10. P. M. Mitrasinovic, *Croat. Chem. Acta* **2019**, *92(1)*, 43–57. **DOI:**10.5562/cca3456
11. A. T. Phan, V. Kuryavyi, H. Y. Gaw, D. J. Patel, *Nat. Chem. Biol.* **2005**, *1*, 167–173. **DOI**:10.1038/nchembio723
12. D. R. Koes, N. A. Pabon, X. Deng, M. A. Phillips, C. J. Camacho, *PLoS ONE* **2015**, *10(8)*, e0134697. **DOI**:10.1371/journal.pone.0134697
13. S. Y. Yang, *Drug Discov. Today* **2010**, *15*, 444–450. **DOI:**10.1016/j.drudis.2010.03.013
14. A. R. Leach, V. J. Gillet, R. A. Lewis, R. Taylor, *J. Med. Chem.***2010**, *53*, 539–558. **DOI:**10.1021/jm900817u
15. J. Sunseri, D. R. Koes, *Nucl. Acids Res.* **2016**, *44*, W442–W448. **DOI**:10.1093/nar/gkw287
16. M. Hattori, N. Tanaka, M. Kanehisa, S. Goto, *Nucleic Acids Res.* **2010**, *38*, W652–W656. **DOI:**10.1093/nar/gkq367
17. M. Hattori, Y. Okuno, S. Goto, M. Kanehisa, *J. Am. Chem. Soc.* **2003**, *125*, 11853–11865. **DOI:**10.1021/jp972635z
18. M. Hattori, Y. Okuno, S. Goto, M. Kanehisa, *Genome Inform.* **2003**, *14,* 144–153. **DOI**:10.11234/gi1990.14.144
19. S. Forli, R. Huey, M. E. Pique, M. F. Sanner, D. S. Goodsell, A. J. Olson, *Nat. Protoc.* **2016**, *11(5)*, 905–919. **DOI:**10.1038/nprot.2016.051
20. G. M. Morris, D. S. Goodsell, R. S. Halliday, R. Huey, W. E. Hart, R. K. Belew, A. J. Olson, *J. Comput. Chem.* **1998**, *19*, 1639–1662. **DOI:**10.1002/(SICI)1096-987X(19981115)19:14<1639::AID-JCC10>3.0.CO;2-B
21. G. M. Morris, R. Huey, W. Lindstrom, M. F. Sanner, R. K. Belew, D. S. Goodsell, A. J. Olson, *J. Comput. Chem.* **2009**, *30*, 2785–2791. **DOI:**10.1002/jcc.21256
22. H. J. Böhm, *J. Comput. Aided Mol. Des.* **1994**, *8*, 243–256. **DOI:**10.1007/BF00126743
23. P. M. Mitrasinovic, *J. Comp. Chem.* **2001**, *22*, 1387–1395. **DOI:**10.1002/jcc.1097
24. A. D. Becke, *J. Chem. Phys.* **2002**, *117*, 6935–6938. **DOI:**10.1063/1.1503772
25. P. M. Mitrasinovic, *Chem. Phys.* **2003**, *286*, 1–13. **DOI:**10.1016/S0301-0104(02)00902-3

26. A. Pavlov, P. M. Mitrasinovic, *Curr. Org. Chem.* **2010**, *14*, 129–138. **DOI:**10.2174/138527210790069866
27. S. Cosconati, S. Forli, A. L. Perryman, R. Harris, D. S. Goodsell, A. J. Olson, *Expert Opin. Drug Discov.* **2010**, *5(6)*, 597–607. **DOI:**10.1517/17460441.2010.484460
28. B. V. Babu, N. K. Konduru, W. Nakanishi, S. Hayashi, P. M. Mitrasinovic, N. Ahmed, *Anti-Cancer Agents Med. Chem.* **2013**, *13*, 307–332. **DOI:**10.2174/1871520611313020017
29. P. M. Mitrasinovic, *Curr. Drug. Targ.* **2013**, *14*, 817–829. **DOI:**10.2174/1389450111314070009
30. P. M. Mitrasinovic, *Med. Chem.* **2014**, *10*, 252–270. **DOI:**10.2174/1573406410031403040143442
31. P. M. Mitrasinovic, *Med. Chem.* **2014**, *10*, 46–58. **DOI:**10.2174/1573406410011312261221 24
32. N. Deng, L. Wickstrom, P. Cieplak, C. Lin, D. Yang, *J. Phys. Chem. B* **2017**, *121(46)*, 10484–10497. **DOI:**10.1021/acs.jpcb.7b09406
33. S. Neidle, *Curr. Opin. Struct. Biol.* **2009**, *19*, 239–250. **DOI:**10.1016/j.sbi.2009.04.001
34. R. Deprez-Poulain, B. Deprez, *Curr. Top. Med. Chem.* **2004**, *4*, 569–580. **DOI:**10.2174/1568026043451168
35. M. Keseru, G. M. Makara, *Drug Discov. Today* **2006**, *11*, 741–748. **DOI:**10.1016/j.drudis.2006.06.016
36. D. Gramec, L. P. Masic, M. S. Dolenc, *Chem. Res. Toxicol.* **2014**, *27*, 1344–1358. **DOI:**10.1021/tx500134g
37. O. Uziel, E. Fenig, J. Nordenberg, E. Beery, H. Reshef, J. Sandbank, M. Birenbaum, M. Bakhanashvili, R. Yerushalmi, D. Luria, M. Lahav, *Br. J. Cancer* **2005**, *92*, 1881–1891. **DOI:**10.1038/sj.bjc.6602592
38. B. Prasad, J. Jamroskovic, S. Bhowmik, R. Kumar, T. Romell, N. Sabouri, E. Chorell, *Chem. Eur. J.* **2018**, *24*, 7926–7938. **DOI:**10.1002/chem.201800078
39. S. Neidle, *Nat. Prod. Rep.* **2001**, *18*, 291–309. **DOI:**10.1039/a705982e
40. P. Pandya, M. M. Islam, G. S. Kumar, B. Jayaram, S. Kumar, *J. Chem. Sci.* **2010**, *122*, 247–257. **DOI:**10.1007/s12039-010-0029-4
41. P. M. Mitrasinovic, *J. Chem. Inf. Model.* **2015**, *55*, 421–433. **DOI:**10.1021/ci5006965
42. S. Asamitsu, T. Bando, H. Sugiyama, *Chem. Eur. J.* **2019**, *25*, 417–430. **DOI:**10.1002/chem.201802691
43. C. A. Lipinski, F. Lombardo, B. W. Dominy, P. J. Feeney, *Adv. Drug Delivery Rev.* **2001**, *46*, 3–26. **DOI:**10.1016/S0169-409X(00)00129-0
44. D. F. Veber, S. R. Johnson, H. Y. Cheng, B. R. Smith, K. W. Ward, K. D. Kopple, *J. Med. Chem.* **2002**, *45*, 2615–2623. **DOI:**10.1021/jm020017n
45. T. Hou, J. Wang, W. Zhang, X. Xu, *J. Chem. Inf. Model.* **2007**, *47*, 460–463. **DOI:**10.1021/ci6003515
46. M. Tassinari, A. Lena, E. Butovskaya, V. Pirota, M. Nadai, M. Freccero, F. Doria, S. N. Richter, *Molecules* **2018**, *23*, 1874. **DOI:**10.3390/molecules23081874
47. C. Marchetti, K. G. Zyner, S. A. Ohnmacht, M. Robson, S. M. Haider, J. P. Morton, G. Marsico, T. Vo, S. Laughlin-Toth, A. A, Ahmed, G. Di Vita, I. Pazitna, M. Gunaratnam, R. J. Besser, A. C. G. Andrade, S. Diocou, J. A. Pike, D. Tannahill, R. B. Pedley, T. R. J. Evans, W. D. Wilson, S. Balasubramanian, S. Neidle, *J. Med. Chem.* **2018**, *61*, 2500–2517. **DOI:**10.1021/acs.jmedchem.7b01781

Povzetek

Ciljanje z gvaninom (G)-bogatih zaporedij DNA, zvitih v ne-kanonične strukture G-kvadrupleksov, z nizkomolekularnimi ligandi, predstavlja potencialno strategijo za gensko terapijo rakavih bolezni. BRACO-19 je bil nedavno potrjen kot edinstven (temodinamsko favoriziran in visoko selektiven) vezalec, ki je vključen v zunanji nalagalni način interakcije z G4-DNA, ki jo tvori promotorska regija c_myc onkogena (P. M. Mitrasinovic, *Croat. Chem. Acta* **2019**, *92*, 43–57). V tem članku smo identificirali spojine vodnice z uporabo visoko-zmogljivostnega virtualnega rešetanja. Izvedeno je bilo iskanje v podatkovni bazi Kyoto Encyclopedia of Genes and Genomes (KEGG) z uporabo ključnih farmakofornih značilnosti BRACO-19. Med skupno 29,009 vnosov je bilo izbranih in ovrednotenih 95 zadetkov z molekulskim sidranjem v vezavno mesto na G4. Potem je bilo izbranih 22 zadetkov z opazovanjem proste vezavne energije. Posledično so bile določene tri kandidatne spojine vodnice na podlagi strukturnih kriterijev. Na koncu je predlagana vodilna kandidatna struktura z uporabo analognega načrtovanja in ob upoštevanju fizikalno-kemijskih zahtev za optimalno biološko aktivnost in nabora farmakoloških vidikov. Obravnavan je tudi pomen študije za eksperimentalne raziskave.

Except when otherwise noted, articles in this journal are published under the terms and conditions of the Creative Commons Attribution 4.0 International License

DOI: 10.17344/acsi.2019.5140 *Acta Chim. Slov.* **2020,** *67,* 396–402
creative commons

Scientific paper

Electrochemical Quantitative Assessment of Labetalol Hydrochloride in Pure Form and Combined Pharmaceutical Formulations

Maissa Yacoub Salem,[1] Nagiba Yehia Hassan,[1] Yasmin Mohamed Fayez,[1] Samah Abd ELSabour Mohamed[2] and Enas Shabaan Ali[2,*]

[1] *Analytical chemistry department- Faculty of Pharmacy, Cairo University. Kasr-El-Aini 11562-Cairo, Egypt*

[2] *National Organization for Drug Control and Research (NODCAR).Giza, Egypt*

* *Corresponding author: E-mail: enas83ali@ gmail.com*
Tel.: +20 1008836585

Received: 04-26-2019

Abstract

This work describes how to utilize the electrochemical technique to determine labetalol hydrochloride (Lab) in pure form and combined pharmaceutical formulation for quality control purposes. Four membrane sensors were developed using two plasticizers, dioctyl phthalate with 2-hydroxypropyl-β-cyclodextrin and ammonium reineckate (RNC) for sensors 1a and 2a, and tributyl phthalate with 2-hydroxypropyl-β-cyclodextrin and ammonium reineckate for sensors 1b and 2b as ionophores in polyvinyl chloride (PVC) matrix. Fast response and stable Nernstian slopes of 59.60, 57.58, 53.00 and 55.00 mV/decade for sensors 1a, 2a, 1b, and 2b, respectively, were obtained by developed sensors within a concentration range 10^{-4} M–10^{-2} M over pH range 2.00–5.10. Developed sensors showed good selectivity for Lab in pure form, in the presence of co-administered drugs, many of interfering ions, and excipients present in pharmaceutical formulation. No remarkable difference was detected upon the statistical comparison between the results of proposed sensors and the official method.

Keywords: Ammonium reineckate; 2-hydroxypropyl-β-cyclodextrin; ion-selective electrode; labetalol hydrochloride; tributyl phthalate; dioctyl phthalate.

1. Introduction

Labetalol hydrochloride (Lab), Fig (1), known chemically as 5-[1-hydroxy-2-[(1-methyl-3-phenylpropyl)-amino]-ethyl]-salicylamide monohydrochloride,[1] is a mixed α- and β-adrenoceptor blocking agent that works by blocking the action of epinephrine on heart and blood vessels. It is considered one of the major therapeutic drugs for the treatment of hypertension either alone or combined with other antihypertensive drugs or diuretics. It is also used to induce hypotension during surgery as Lab reduces blood pressure more rapidly than other α- or β-receptor blockers. Lab is a well-known doping agent in sports and hence has been banned for Olympic players by the International Olympic Committee.[2–4]

Literature survey revealed that various analytical techniques were employed to estimate the concentration of Lab in pharmaceutical preparations, either alone or in combination with hydrochlorothiazide, and in biological fluids. These techniques include spectrofluorimetry,[5–10] chromatography,[11–18] capillary electrophoresis,[19,20] capillary isotachophoresis,[21] NMR spectroscopy,[22] ion-selective electrode using ion-pair complex,[23] and adsorptive voltammetry,[24] methods which in comparison to proposed electrodes require sample manipulation, are affected by various interferences, inappropriate for colored or turbid solutions, and more expensive as they require sophisticated equipment and software for data processing.

Ion-selective electrode (ISE) as a new analytical technique offers an accurate quantitative estimation of active drug substance in pharmaceutical formulation regardless of turbidity or color of sample media due to its relatively high selectivity which is determined by the nature and composition of the membrane materials used in the fabrication of the electrode.[25]

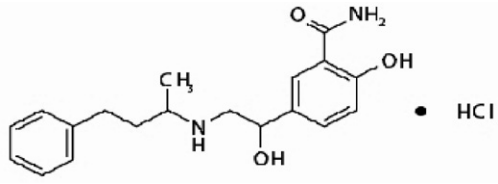

Fig. 1. Chemical structure of labetalol hydrochloride

This work describes the advantage of utilization of ion-selective sensors prepared in PVC matrix using 2-hydroxypropyl-β-cyclodextrin and ammonium reineckate (RNC) with two different plasticizers for the determination of Lab in pure form and combined pharmaceutical formulation having equal efficiency as the previously developed spectrophotometric and HPLC methods,[10,18] with superiority of elimination of sample pretreatment, working over wide pH range, devoid of several preparation steps as in HPLC and being eco-friendly.

2. Experimental

2. 1. Apparatus

- pH meter 3510 pH /mV /°C (Jenway, UK)
- pH glass electrode (Jenway, UK)
- Ag/AgCl double junction reference electrode (Jenway, UK)
- 5-digit electronic balance model XA60/220 (RADWAG, Poland)
- water purification system (Milli Q, France)
- magnetic stirrer: model 34532 (Snijders, Holland)
- thermometer
- sonicator (Falc, Japan)

2. 2. Samples and Pharmaceutical Formulations

- Pure labetalol hydrochloride was kindly supplied by El-debiky Co., Cairo, Egypt. Its purity was found to be 100.48% ± 0.84 according to the official HPLC method.[1]
- Labipress plus® tablets produced by El-debiky Pharmaceutical Company, Cairo, Egypt: Batch No: (141019). Each tablet is labeled to contain 100 mg of labetalol hydrochloride and 25 mg of hydrochlorothiazide.

2. 3. Chemicals and Reagents

All chemicals and reagents used were obtained from Sigma Aldrich.

- 2-hydroxypropyl-β-cyclodextrin (βC), tetrahydrofuran (THF), and ammonium reineckate (RNC)
- polyvinyl chloride (PVC), tributyl phthalate (TBP), and dioctyl phthalate (DOP)
- deionized water
- potassium chloride (KCl)

2. 4. Standard Solutions

- Standard stock solution (10^{-2} M) was prepared by dissolving 364.87 mg of Lab in 100 ml deionized water.
- Serial dilutions from the stock solution were made in deionized water to prepare (10^{-7} M–10^{-3} M) working standard solutions of Lab.

2. 5. Procedures

2. 5. 1. Preparation of Membrane Sensors

(a) Membrane 1a&b

For the preparation of membrane 1a, 0.04 g 2-hydroxypropyl-β-cyclodextrin was mixed with 0.40 g of DOP and 0.19 g of PVC. This mixture was dissolved in 5 ml THF in a 5 cm diameter glass petri dish and covered with filter paper to allow for solvent evaporation at room temperature for 24 h. 0.1 mm thickness master membrane was obtained and used for the construction of the electrode. Membrane 1b was prepared similarly but with the use of TBP instead of DOP.

(b) Membrane 2a&b

For the preparation of membrane 2a, 0.01 g ammonium reineckate (RNC) was mixed with 0.40 g of DOP and 0.19 g of PVC. This mixture was dissolved in 5 ml THF in a 5 cm diameter glass petri dish and covered with filter paper to allow for solvent evaporation at room temperature for 24 h. 0.1 mm thickness master membrane was obtained and used for the construction of the electrode. Membrane 2b was prepared similarly but with the use of TBP instead of DOP.

Disks of about 12 mm diameter were cut from each master membrane with a cork borer and glued to an interchangeable PVC tip (fixed to the end of an electrode glass body) using THF and left to dry for 24 h. Then the prepared electrodes were filled with equal volumes of 10^{-3} M Lab and 10^{-3} M KCl as an internal solution and a 1 mm diameter Ag/AgCl wire was used as an internal reference electrode. Electrodes were soaked in 10^{-3} M aqueous solution of Lab for 24 h for conditioning and kept in the same solution when not in use.

2. 5. 2. Sensors Calibration

Calibration of conditioned sensors was performed by immersing prepared electrodes, in conjunction with the Ag/AgCl reference electrode, into a set of 100 ml beakers containing 50 ml separate aliquots of (10^{-7} M–10^{-2} M) solutions of Lab and allowed to equilibrate under stirring with washing with deionized water between measurements. The potential difference (emf) between each of the prepared membrane sensors (indicator electrode) and Ag/AgCl reference electrode was measured and plotted as a function of the negative logarithm of Lab concentration. Regression equations were calculated for the linear part of the curves and used for the estimation of Lab concentrations.

2. 5. 3. Sensors Selectivity

Potentiometric selectivity coefficient ($K^{Pot.}_{lab,\ interferent}$) was estimated following IUPAC guidelines,[27] using separate solution method (SSM),[26] in which the potential of two separate solutions, A (Lab) and B (interfering ion) at a concentration of 10^{-3} M, was measured by prepared membrane electrode conjugated with reference electrode.

$$\mathrm{Log}K^{Pot.}_{A,B} = [(E_B - E_A) / (2.303\ RT/Z_AF)] + \\ + [1 - (Z_A / Z_B)\ \log[A]$$

Where E_A is the potential measured in 1×10^{-3} M standard Lab solution, E_B is the potential measured in 1×10^{-3} M interfering ion solution, Z_A and Z_B are the charges of Lab and interfering ion, respectively, and $2.303\ RT/Z_AF$ represents the slope of the calibration curve.

2. 5. 4. Application to Pharmaceutical Formulations

Twenty tablets of Labipress plus® tablets were pulverized and the accurate weight of powdered tablets was dissolved in 100 ml deionized water for 15 min to prepare 10^{-2} M solution of Lab. Prepared sensors, conjugated with Ag/AgCl reference electrode, were immersed in the prepared solution. The measured potential was used to estimate the concentration of Lab in solution by substitution in the regression equation of the corresponding electrode.

3. Results and Discussion

3. 1. Sensors Preparation

Ion-selective electrodes' use in quantitative estimation of active drug substances in pharmaceuticals has shown superiority over other analytical techniques because of high selectivity and suitability for the analysis of turbid or colored test solutions over wide ranges of pH and concentrations with high accuracy and fast response.

In the present work, a cationic type of ion exchangers, 2-hydroxypropyl-β-cyclodextrin and ammonium reineckate, was used in electrode preparation based on the fact that Lab in aqueous solution behaves as a cation; also, 2-hydroxypropyl-β-cyclodextrin and ammonium reineckate are physically compatible with PVC polymeric matrix that was used to produce highly stable complexes as PVC has the advantages of chemical inertness and low cost but its use raises a need for a plasticizer.[24]

Dioctyl phthalate and tributyl phthalate were selected as plasticizers because of their chemical asymmetry that results in unique electrical properties as they allow PVC membranes to operate with less energy input than with other plasticizers, relatively non-volatile under heat and maintain flexibility at low temperature combined with a resistance to high temperature.[27]

3. 2. Sensors Calibration and Response Time

IUPAC recommendation data[28] were used for evaluating the electrochemical performance characteristics of proposed sensors, Table 1. Calibration graphs are presented in Fig. 2, showing stability, consistency of potential readings and stability of calibration slopes over 1 month. A fast, stable response was obtained within 10–15 s for sensors 1a, 1b, and 15–20 s for sensors 2a, 2b using concentrations of Lab from 10^{-4} M–10^{-2} M for estimation of the response time of prepared electrodes. The pro-

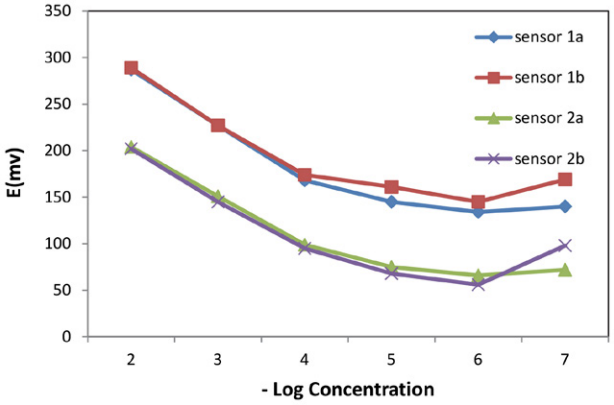

Fig. 2. Profile of the potential in mV versus –log(concentration of Lab) using the investigated sensors.

Table 1. Response characteristics of the investigated sensors.

Parameter	Sensor 1a	Sensor 1b	Sensor 2a	Sensor 2b
Slope (mV/decade)	–59.60	–57.58	–53.00	–55.00
Intercept (mV)	406.40	403.34	310.60	310.60
Correlation coefficient	0.9999	0.9997	0.9999	0.9999
Response time (s)	10–15	10–15	15–20	15–20
Working pH range	2.00–5.10	2.00–5.10	2.00–5.10	2.00–5.10
Concentration range (M)	10^{-4}–10^{-2}	10^{-4}–10^{-2}	10^{-4}–10^{-2}	10^{-4}–10^{-2}
Life span (weeks)	2–4	2–4	2–3	2–3
Average recovery[a] ± SD	100.12 ± 0.27	99.74 ± 0.35	99.83 ± 0.25	99.87 ± 0.52
LOD(M)	4.17×10^{-5}	3.98×10^{-5}	3.98×10^{-5}	3.16×10^{-5}

[a]Average of three determinations

posed sensors displayed good long term potential stability for 2–4 weeks.

3. 3. Effect of pH and Temperature

Conditions affecting the response of ion-selective electrodes were studied to determine the optimum conditions for quantitative measurement. The effect of pH was studied considering both sensor function and chemical form of Lab. It was concluded from Fig. 3–6, that sensors response is fairly steady over pH range 2.00–5.10 where Lab exists in the cationic form and is detectable by the electrodes; outside this pH range, the potentials measured by the electrodes were unstable. The temperature effect was also studied, where the proposed membrane sensors

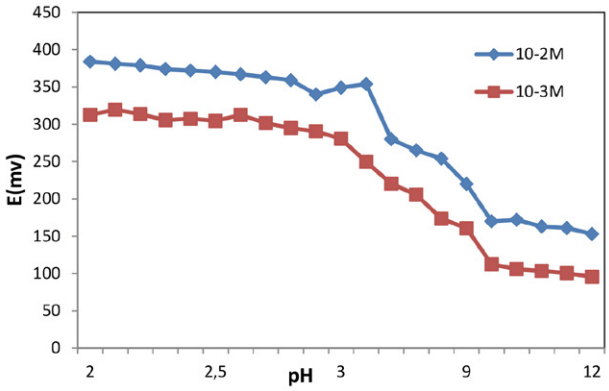

Fig. 3. Effect of pH on the response of Lab sensor 1a

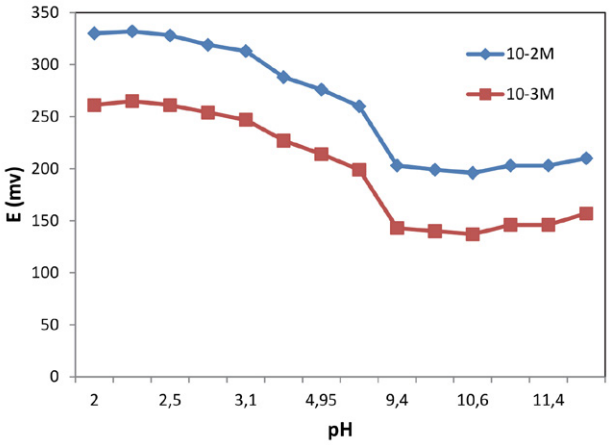

Fig. 4. Effect of pH on the response of Lab sensor 1b

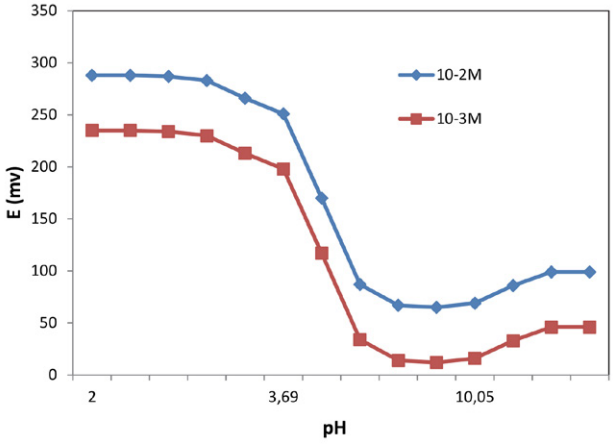

Fig. 5. Effect of pH on the response of Lab sensor 2a

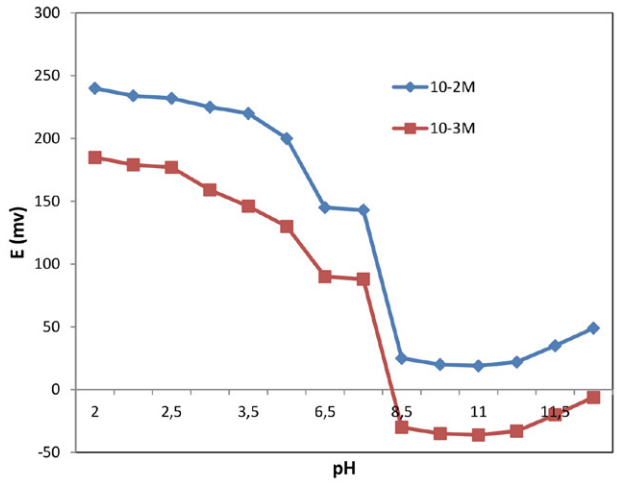

Fig. 6. Effect of pH on the response of Lab sensor 2b

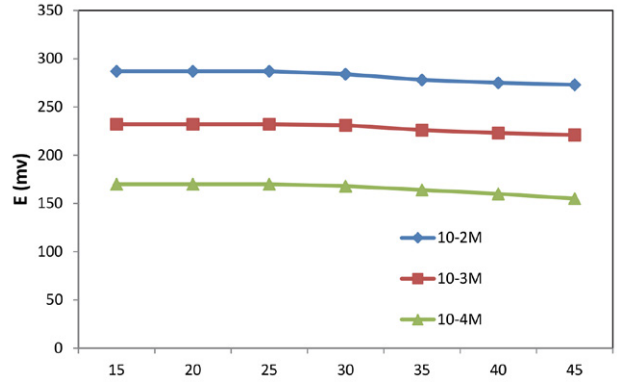

Fig. 7. Effect of temperature on the response of Lab sensor 1a

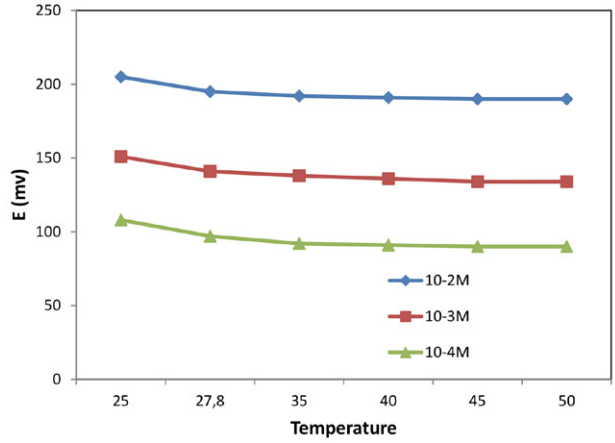

Fig. 8. Effect of temperature on the response of Lab sensor 1b

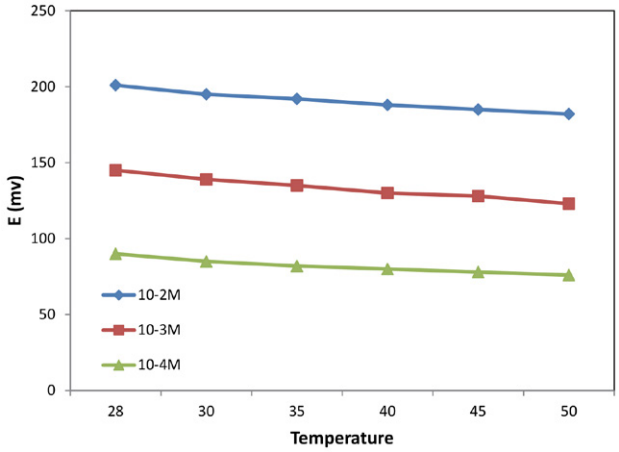

Fig. 9. Effect of temperature on the response of Lab sensor 2a

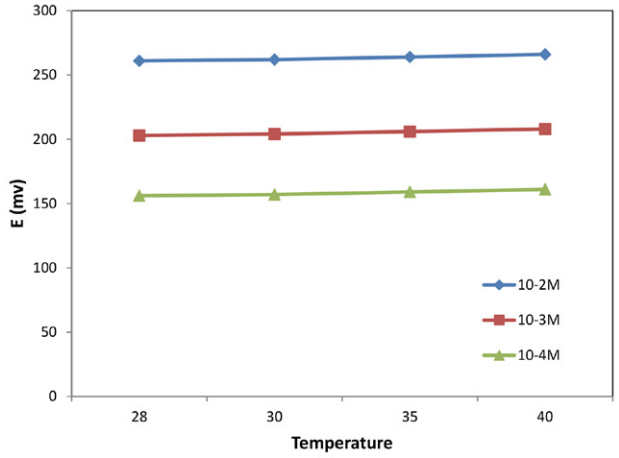

Fig. 10. Effect of temperature on the response of Lab sensor 2b

displayed thermal stability up to 35 °C indicated by a steady potential response, Fig. 7–10.

3. 4. Sensors Selectivity

The potentiometric selectivity coefficient was determined for several excipients, co-administered drugs, and related substances by the proposed sensors. Table 2: the results revealed high selectivity for Lab and that no significant interference was observed.

3. 5. Application to Pharmaceutical Formulations

The proposed sensors were used for determination of Lab in Labipress plus® tablets without pretreatment and no interference was observed from excipients or hydrochlorothiazide as a co-formulated drug, Table 3.

No remarkable difference was detected upon the statistical comparison between results of the proposed electrodes and the official method,[1] for determination of the pure form of Lab, Table 4.

3. 6. Application to Biological Fluids

Trials were made to use the proposed sensors for determination of Lab in biological fluids since Lab is absorbed rapidly after oral administration with peak plasma concentration achieved within 2 h and its bioavailability varies from 10% to over 80% correlating with age. But also approximately 50% of Lab is bound to the plasma proteins which prevented direct determination of Lab in human plasma using proposed sensors.[29] Lab is eliminated mainly by hepatic metabolism with the production of several biologically inactive glucuronides which in turn are excreted in the urine and bile. Approximately 85% of Lab in the blood is removed during a single passage through the liver which also prevented its determination in human urine using proposed sensors.[29]

4. Conclusion

The described sensors displayed fast, selective and accurate potential response for Lab over concentration range (10^{-4} M–10^{-2} M) and have equal efficiency to previously developed methods[10,18] used for quantitative estima-

Table 2. Potentiometric selectivity coefficients of the proposed electrodes using a separate solution method.

Interferents [a]	Selectivity Coefficient			
	Sensor 1a	Sensor 1b	Sensor 2a	Sensor 2b
Hydrochlorothiazide	3.26×10^{-5}	5.62×10^{-5}	2.76×10^{-5}	4.42×10^{-5}
Chlorothiazide	1.76×10^{-4}	4.54×10^{-4}	2.49×10^{-5}	3.95×10^{-5}
Benzothiadiazine	1.59×10^{-5}	3.90×10^{-5}	2.06×10^{-5}	3.17×10^{-5}
KCl	1.90×10^{-4}	3.68×10^{-4}	2.19×10^{-5}	6.31×10^{-5}
NaCl	1.83×10^{-4}	4.49×10^{-4}	3.37×10^{-5}	7.31×10^{-5}
$CuSO_4$	1.31×10^{-3}	3.23×10^{-3}	2.14×10^{-3}	3.66×10^{-3}
Lactose	1.63×10^{-4}	4.08×10^{-4}	2.48×10^{-4}	2.14×10^{-4}
Ammonium dihydrogen phosphate	8.28×10^{-3}	9.06×10^{-3}	8.92×10^{-3}	5.92×10^{-3}
$CaCO_3$	4.87×10^{-4}	3.93×10^{-4}	5.11×10^{-4}	1.43×10^{-6}
Starch	2.49×10^{-4}	3.58×10^{-4}	2.00×10^{-5}	4.33×10^{-5}

[a] Aqueous Solutions of 1×10^{-3} M were used

Table 3. Determination of Lab in Labipress plus® tablets by the proposed sensors

Preparation	Company method [b]	Sensors			
		Sensor 1a	Sensor 1b	Sensor 2a	Sensor 2b
Labipress Plus tablets Each tablet contains 100 mg labetalol HCl, 25 mg hydrochlorothiazide B.N.: 141019	Found [a] ± RD 99.91 ± 0.91	Assay Found [a] ± RD 99.96 ± 0.89	Assay Found [a] ± RD 99.70 ± 1.34	Assay Found [a] ± RD 99.90 ± 0.84	Assay Found [a] ± RD 99.20 ± 0.58

[a]Average of three determinations. [b]HPLC method using C_{18} (250 mm × 4.6 mm, 5 µm) analytical column, with mobile phase acetonitrile:phosphate buffer (pH = 3.5):triethylamine in ratio (40:60:0.1 *v/v/v*) with flow rate 1.0 ml/min at 230 nm.

Table 4. Statistical comparison of results obtained by the proposed sensors and the official method for determination of Lab in pure form.

Items	Offical method[1]	sensor 1a	sensor 1b	sensor 2a	sensor 2b
Mean[a]	100.48	100.12	99.74	99.83	99.87
S.D	0.84	0.27	0.35	0.25	0.52
Variance	0.71	0.07	0.12	0.06	0.27
n	5	3	3	3	3
S.E	0.38	0.16	0.20	0.14	0.30
t-test (2.447)	–	0.87	1.72	1.81	1.26
F-ratio (19.25)	–	10.14	5.92	11.83	2.63

[a] Official HPLC method using C_{18} (200 mm × 4.6 mm, 5 µm) analytical column, with mobile phase methanol:phosphate buffer in the ratio (35:65 *v/v*) with flow rate 1.5 ml/min, 60 °C at 230 nm.[1S]

tion of Lab in pure and combined pharmaceutical formulation and more, they are eco-friendly, require minimum preparations for test measurement and show long term stability in response which suggests their use for quality control purpose as proposed electrodes enable determination of Lab over concentration range that covers its concentration in pharmaceutical formulation with reasonable sensitivity and are easily fabricated in comparison to other membranes.[30]

5. References

1. The United States Pharmacopoeia (USP 40), National Formulary (NF 35), the United States Pharmacopoeial Convention, Rockville, MD, USA. **2017**
2. A. M. Sambrook, R. C. Small, *Anaesth. Intens. Care Med*. **2008**, *9*, 128–131. **DOI:**10.1016/j.mpaic.2008.01.008
3. A. S. Joel, N. Shantaram, C. Naresh, *Int. J. Res. Pharm. Biomed. Sci*. **2013**, *4*, 380–384. **DOI:**10.13179/canchemtrans.2013.01.01.0014
4. P. Lukkari, T. Nyman, M. L. Riekkola, *J. Chromatogr. A*. **1994**, *674*, 241–246. **DOI:**10.1016/0021-9673(94)85229-4
5. D. R. EL-Wasseef, S. M. EL-Ashry, M. A. ABU-EL-Enein, M. A. A. Moustafa. *J. Food Drug. Anal*. **2006**, *14*, 133–140. **DOI**: 10.6227/jfda
6. F. Belal, S. Al-Shaboury, A. S. Al-Tamrah, *J. Pharm. Biomed. Anal.***2002**, *30*, 1191–1196. **DOI:**10.1016/S0731-7085(02)00471-5
7. N. Rahman, S. K. Haque, *Int. J. Biomed. Anal.***2008**, *4*, 140–146.
8. N. Rahman, S. K. Haque, S. M. Hossain, *Can. Chem. Trans*.**2013**, 1(1), 66–77. **DOI:**10.13179/canchemtrans.2013.01.01.0014
9. K. V. Raju, N. Annapurna, D. A. R. Babu, T. S. L. Kethurah, *J. Chem. Pharm. Res.* **2015**, 7(6),399–405
10. M. Y. Salem, N. Y. Hassan, Y. Fayez, S. Abd-Elsabour, E. S. Ali, *J. Curr. Pharm. Anal.* **2018**. **DOI:**10.2174/1573412914666180716161557
11. A. Witek, H. Hopkala, G. Matysik, *Chromatographia*. **1999**, *50*, 41–44. **DOI:**10.1007/BF02493615
12. H. Zhao, H. Li, Z. Qiu, *Chin. J. Chromatogr*, **1999**, *17*, 369–371. **DOI:**10.1046/j.1365-2397.1999.00005.x
13. C. Ceniceros, M. I. Maguregui, R. M. Jimenez, R. M. Alonso, *J. Chromatogr. B*, **1998**, *705*, 97–103. **DOI:**10.1016/S0378-4347(97)00492-1
14. M. Delamoye, C. Duvernewil, F. Paraire, P. de Mazancourt, J. C. Alvarez, *Int. Foren. Sci*, **2004**, *141*, 23–31. **DOI:**10.1016/j.forsciint.2003.12.008
15. A. Changchit, J. Gal, J. A. Zirrolli, *Biolog. Mass. Spectrum*, **1991**, *20*, 751–758. **DOI:**10.1002/bms.1200201202
16. S. Carda-Broch, R. Rapado-Martinez, I. Esteve-Romero, M. C. Garcia-Alverez-Coque, *J .Chromatogr. Sci*, **1999**, *37*, 93–102. **DOI:**10.1093/chromsci/37.4.93
17. C. Karlsson, H. Wikstrom, D. D. Armstrong, P. K. Owens, *J. Chromatogr. A*, **2000,** *897*, 349–363. **DOI:**10.1016/S0021-9673(00)00805-0
18. M. Y. Salem, N. Y. Hassan, Y. Fayez, S. Abd-Elsabour, E. S. Ali, *J. Iran. Chem. Soci.* **2019**.

DOI: org/10.1007/s13738-019-01593-7
19. T. V. Goel, J. G. Nikelly, R. C. Simpson, B. K. Matuszewski, *J. Chromatogr. A*, **2004**, *1027*, 213–221. **DOI:**10.1016/j.chroma.2003.08.082
20. S. L. Tamisier-Karolak, M. A. Stenger, A. Bommart, *Electrophoresis*, **1999**, *20*, 2656–2663. **DOI:**10.1002/(SICI)1522-2683(19990901)20:13<2656::AID-ELPS2656>3.0.CO;2-6
21. S. Jana, P. Jozef, *J .Chromatogr. A*, **1996**, *735*, 403–408. **DOI:**10.1016/0021-9673(95)00722-9
22. M. A. Iorio, A. Mazzeo-Farina, A. Doldo, *J. Pharm. Biomed. Anal*, **1987**, *5*, 1–10. **DOI:**10.1016/0731-7085(87)80002-X
23. E. Gorodkiewicz, P. Falkowski, A. Sankiewicz, Z. Figaszewski, *Central Euro. J. Chem*. **2003**, *1*, 242–259. **DOI:**10.2478/BF02476227
24. A. Radi, Z. El-Sherif, A. Wassel, *Chem. Papers*, **2004**, *58*, 242–246.
25. A. M. El-Kosasy, M. Nebsen, M. K. Abd El-Rahman, M. Y. Salem, M. G. El-Bardicy, *Talanta*, **2011**, *85 (2)*,913–918. **DOI:**10.1016/j.talanta.2011.04.071
26. S. S. Hassan, W. H. Mahmoud, A. H. M. Othman, *Analytica. Chim. Acta*, **1996**, *322*, 39–48. **DOI:**10.1016/0003-2670(96)00223-1
27. J. Murphy, Additives for Plastics Handbook, 2nd Ed, **2001**.
28. IUPAC Analytical Chemistry Division, *Pure Appl. Chem*. **2000**, *72*, 1851.
29. J. J. McNeil, W. J. Louis, *Clin Pharmacokinet*, **1984**, *9(2)*,157–67. **DOI:**10.2165/00003088-198409020-00003
30. J. Gallardo-Gonzalez, A. Saini, A. Baraket, S. Boudjaoui, A. Alcacer,A. Streklas, F. Teixidor, N. Zine, J. Bausells, A. Errachid , *Sens. Actuators. B.*,**2018**, *266*, 823–829. **DOI:**10.1016/j.snb.2018.04.001

Povzetek

Članek opisuje uporabo elektrokemijske tehnike za določanje labetalol hidroklorida (Lab) v čisti obliki in v kombiniranih farmacevtskih pripravkih z namenom kontrole kakovosti. Razvili smo štiri membranske senzorje na osnovi dveh plastifikatorjev, dioktil ftalata z 2-hidroksipropil-β-ciklodekstrinom in amonijevim reinekatom (RNC) za senzorja 1a in 2a, ter tributil ftalata z 2-hidroksipropil-β-ciklodekstrinom in amonijevim reinekatom za senzorja 1b in 2b, ki služita kot ionoforja v matrici polivinil klorida (PVC). Za vse senzorje smo znotraj koncentracijskega območja 10^{-4} M–10^{-2} M in pH-območja 2,00–5,10 ugotovili hiter odgovor in stabilen Nernstov naklon 59,60 mV/dekado za 1a, 57,58 mV/dekado za 2a, 53,00 mV/dekado za 1b in 55,00 mV/dekado za 2b. Razviti senzorji so pokazali dobro selektivnost za Lab v čisti obliki in v prisotnosti drugih zdravil, mnogih interferenčnih ionov ter polnil, prisotnih v farmacevtskih pripravkih. Pri statistični primerjavi rezultatov, dobljenih s predlaganimi senzorji in z uradno metodo, nismo ugotovili znatnih razlik.

Except when otherwise noted, articles in this journal are published under the terms and conditions of the Creative Commons Attribution 4.0 International License

Scientific paper

Synthesis of Bi-Heterocyclic Sulfonamides as Tyrosinase Inhibitors: Lineweaver–Burk Plot Evaluation and Computational Ascriptions

Muhammad Athar Abbasi,[1,*] Zia-ur-Rehman,[1] Aziz-ur-Rehman,[1] Sabahat Zahra Siddiqui,[1] Majid Nazir,[1] Mubashir Hassan,[2] Hussain Raza,[3] Syed Adnan Ali Shah[4] and Sung-Yum Seo[3,*]

[1] *Department of Chemistry, Government College University, Lahore-54000, Pakistan*

[2] *Institute of Molecular Biology and Biotechnology, The University of Lahore, Pakistan*

[3] *College of Natural Sciences, Department of Biological Sciences, Kongju National University, Gongju, 32588, South Korea*

[4] *Faculty of Pharmacy and Atta-ur-Rahman Institute for Natural Products Discovery (AuRIns), Level 9, FF3, Universiti Teknologi MARA, Puncak Alam Campus, 42300 Bandar Puncak Alam, Selangor Darul Ehsan, Malaysia*

** Corresponding author: E-mail: abbasi@gcu.edu.pk Tel: (+92)-42-111000010 Ext. 266*
dnalove@kongju.ac.kr Tel: (+82)-416-8508503

Received: 05-27-2019

Abstract

The designed bi-heterocyclic sulfonamides were synthesized through a two-step protocol and their structures were ascertained by spectral techniques including IR, ^{1}H NMR and ^{13}C NMR along with CHN analysis. The *in vitro* inhibitory effects of these sulfonamides were evaluated against tyrosinase and kinetics mechanism was analyzed by Lineweaver–Burk plots. The binding modes of these molecules were ascribed through molecular docking studies. These synthesized bi-heterocyclic molecules were identified as potent inhibitors relative to the standard (kojic acid) and compound **5** inhibited the tyrosinase non-competitively by forming an enzyme-inhibitor complex. The inhibition constant K_i (0.09 μM) for compound **5** was calculated from Dixon plots. Computational results also displayed that all compounds possessed good binding profile against tyrosinase and interacted with core residues of target protein.

Keywords: Bi-heterocycles; 1-Phenylpiperazine; Sulfonamides; Tyrosinase; Chemical kinetics; Computational study

1. Introduction

Sulfonamides find their wide acceptance as the sulfa drugs across the world and these organic compounds have deep impacts on the biological systems owing to their numerous pharmacological activities. They are widely used to cure the bacterial infections. They find their usage as anti-cancer, anti-microbial, antiviral, anti-inflammatory and anti-tumor agents along with carbonic anhydrase inhibitors.[1] The carbonic anhydrase bustles of sulfonamides possess an appreciated treatment for Alzheimer's disease.[2] They are also used as anti-convulsant, anti-fungal and enzyme inhibitors.[3,4]

The sulfonamides bearing piperazine moiety have enhanced their role as antipsychotic compounds to cure paranoid schizophrenia, mental depression, nausea and as anticonvulsants against electroshock (MES) induced seizures.[5,6] Certain other piperazine derivatives have also antimicrobial and antimalarial potentials.[7,8] Piperdine derivatives have been reported to have anticancer activity.[9] Some sulfonamide based piperidine derivatives have an efficient role as acetylcholinesterase inhibitors. Several other substituted piperidine based derivatives have the potential of inhibition of ureases and α-glucosidases.[10–13]

Tyrosinase (polyphenol oxidase, PPO, E.C.1.14.18.1) which is a copper-containing metalloenzyme, catalyzes two major reactions in the biosynthesis pathway of melanin pigment: the hydroxylation and oxidation of monophenols to *o*-quinones (monophenolase activity) and the oxidation of *o*-diphenols to *o*-quinones (diphenolase acti-

vity).[14] Melanin is an important pigment which is found in the eyes, hair and skin of animals and especially it protects human skin against radiation.[15,16] However, excessive production and hyperpigmentation of melanin is the cause of dermatological disorders such as melasma, ephelides, chloasma, freckles, melanoderma and senile lentigines and can induce inflammation such as eczema, irritant and allergic eczema, contact dermatitis, which can result in critical and emotionally distressing trouble.[17]

Besides the fact that enzymes and their activities are extremely necessary for life, the selective inhibition of critical enzymes is also considerably important for chemotherapeutic intervention in some diseases. Unregulated high enzyme activity results in the formation of reaction products at abnormal levels which can cause specific pathologies. Nowadays, the strategy of selective enzyme inhibition gets attention in modern pharmacy and enzymes have become interesting targets in drug therapies.[18] For this reason, many organic molecules have been synthesized as specific enzyme inhibitors and continue to be synthesized. Modeling methods to ascribe the three-dimensional conformations and interactions of organic molecules with the active sites of enzymes help researchers to design new drug molecules.[19]

Therefore, the objective of the present study was to synthesize some new bi-heterocyclic sulfonamides, to explore their inhibitory potentials against tyrosinase enzyme and ascribe their binding interactions through molecular docking studies.

2. Results and Discussion

The aim of the present research work was to synthesize new biologically active compounds with low toxicity. Indeed, the current need is to introduce pharmacologically active drugs to help in pharmacy against the increasing enzyme inhibition.

2. 1. Chemistry

In our present research work, four bi-heterocyclic sulfonamides were synthesized in two steps and their synthesis is shown in Scheme 1. In the first step, 4-(bromomethyl)benzenesulfonyl chloride (**1**) was reacted with various heterocyclic amines, including piperidine (**2**), morpholine (**6**), 4-methylpiperidine (**9**) and 3,5-dimethylpiperidine (**12**) to obtain respective sulfonamide containing electrophiles, **3**, **7**, **10** and **13**, respectively. In the second step, these newly synthesized electrophiles were coupled with nucleophilic 1-phenylpiperazine (**4**) to acquire the desired bi-heterocyclic sulfonamides **5**, **8**, **11** and **14**. The structures of these derivatives were affirmed by spectral techniques like IR, ^{1}H NMR and ^{13}C NMR, in addition to the CHN analysis data. The spectral data are given in the experimental section. The successful synthesis of targeted bi-heterocyclic sulfonamides was achieved in good yields through a two-step protocol and the structures of these molecules were confirmed through spectral data of IR, ^{1}H NMR and ^{13}C NMR, along with CHN analysis. For the benefit of the reader, the structural characterization of one compound, **5**, is discussed hereby. Its molecular formula, $C_{22}H_{29}N_3O_2S$, was established by CHN analysis and by counting the number of protons in its ^{1}H NMR spectrum. Similarly, the counting of number of carbon resonances in its ^{13}C NMR spectrum also supported this assignment. The salient functional groups in the molecule were identified through absorption bands at ν 2986 (C–H, str. of aromatic ring), 2905 (–CH_2 stretching), 1680 (aromatic C=C stretching), 1382 (S=O), 1115 (C–N–C) cm^{-1}. Two *ortho*-coupled doublets in its ^{1}H NMR spectrum at δ 7.70 (br. d, J = 7.6 Hz, 2H, H-3' and H-5'), and 7.60 (br. d, J = 7.6 Hz, 2H, H-2' and H-6') are typical for a 4-substituted benzenesulfonyl moiety, while a phenyl ring attached with the piperazine unit was rationalized by three signals in the aromatic region at δ 7.20 (br. t, J = 7.2 Hz, 2H, H-3''' and H-5'''), 6.92 (br. d, J = 7.7 Hz, 2H, H-2''' and H-6''') and 6.77 (br. t, J = 6.9 Hz, 1H, H-4'''). The pseudo-symmetrical 1,4-piperazine unit was corroborated by overall two signals in aliphatic region at δ 3.14 (br. s) and 2.87 (br. s) (8H, CH-2", CH-3", CH-5" and CH-6"), while a peculiar singlet at δ 3.63 (s, 2H, CH_2-7') was assignable to a methylene connecting the piperazine heterocycle to the aromatic ring. The presence of a 1-piperidinyl moiety was justified by three signals at δ 3.51–3.46 (m, 4H, CH_2-2 and CH_2-6), 1.53 (br. s, 4H, CH_2-3 and CH_2-5) and 1.35 (br. s, 2H, CH_2-4). The ^{1}H NMR spectrum of this compound is shown in Figures S1 and S2.

The carbon skeleton of this molecule was also fully supported by its ^{13}C NMR spectrum, shown in the Figure S3. The ^{13}C NMR spectrum demonstrated overall fifteen carbon resonances due to some symmetrical duplets in the molecule. The 4-substituted benzenesulfonyl group was characterized by two quaternary and two duplet methine signals at δ 144.16 (C-4'), 134.72 (C-1'), 129.90 (C-2' and C-6') and 127.87 (C-3' and C-5'). The phenyl ring attached to the nitrogen atom of piperazine was obvious by four signals δ 151.43 (C-1'''), 129.37 (C-3''' and 5'''), 119.29 (C-4''') and 115.85 (C-2''' and C-6'''). The pseudo-symmetrical piperazine heterocycle was corroborated by two signals at δ 53.05 (C-3" and C-5") and 47.04 (C-2" and C-6"), while the connecting methylene was rationalized by a signal at δ 61.72 (C-7'). The remaining signals δ 48.67, 48.63 (C-2 and C-6), 25.14 (C-3 and C-5) and 23.32 (C-4) were attributed to a piperidinyl heterocycle in the molecule. Thus, on the basis of the above cumulative evidences, the structure of **5** was confirmed and it was named as 1-phenyl-4-[4-(1-piperidinylsulfonyl)benzyl]piperazine. The structures of other compounds were verified in a similar pattern. The ^{1}H NMR and ^{13}C NMR of all other compounds are shown in supplementary data (Figures S4–S9).

2. 2. Biological Activities (*in vitro*)

2. 2. 1. Enzyme Inhibition Activity

The synthesized bi-heterocyclic sulfonamides, **5**, **8**, **11**, **14**, were screened against tyrosinase and their *in vitro* inhibitory activities are presented in Table 1. These molecules exhibited outstanding potentials, which are evident from their lower IC_{50} (μM) values, relative to standard, kojic acid, having IC_{50} value of 16.8320 ± 1.1600 μM. Although, the experimental activity is cumulative for the whole molecule, however, nevertheless, a partial structure-activity relationship (SAR) was established by analyzing the effect of varying heterocyclic parts on the inhibitory potential. It needs to be mentioned, that except this variation of heterocyclic moiety, all other parts were the same in these molecules. The general structural parts of the inspected compounds are labeled in Fig. 1.

The comparison of inhibitory potential of **5** (IC_{50} = 0.0586 ± 0.0033 μM) and **8** (IC_{50} = 0.4078 ± 0.0151 μM), revealed that the presence of an additional oxygen atom within the heterocyclic ring (4-morpholinyl group) in **8** resulted in a decrease of activity as compared to **5**, in which a simple piperidinyl ring was present. The compound **5** was the most active compound in the series as well. It means, the presence of piperidinyl ring is a credible option for the promising activity of such compounds (Fig. 2).

In compound **11**, a *para*-methyl group was present at the piperidinyl ring (4-methyl-1-piperidinyl), while in **14** two methyl groups were present at the *meta*-positions of this heterocyclic part (Fig. 3). When the inhibitory potential of these two molecules is compared, it was perceived that molecule **14** with two methyl groups in variable heterocyclic part behaved as a slightly better inhibitor. It means when the methyl groups were present in a pseudo-symmetrical manner at 3 and 5 positions (3,5-dimethyl-1-piperidinyl), the compound **14** made some better interactions with the enzyme relative to its mono-methylated analogue **11**.

Table 1. Tyrosinase inhibitory and hemolytic activity of tri-heterocyclic compounds.

Compounds	Varying heterocyclic part	Tyrosinase activity IC_{50} ± SEM (μM)
5	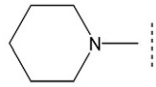	0.0586 ± 0.0033
8	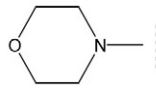	0.4078 ± 0.0151
11	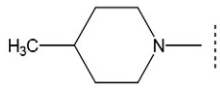	0.1436 ± 0.0056
14	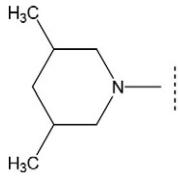	0.0706 ± 0.0013
	Kojic acid	16.8320 ± 1.1600

SEM = Standard error of the mean; values are expressed in mean ± SEM.

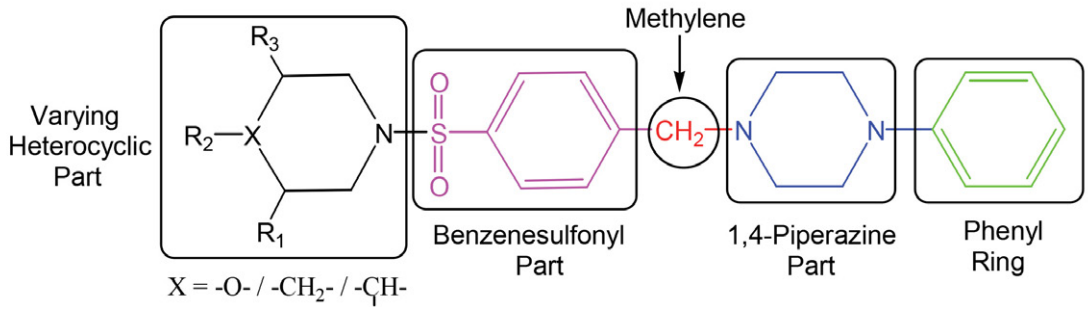

Figure 1. General structural parts of compounds **5**, **8**, **11**, and **14**.

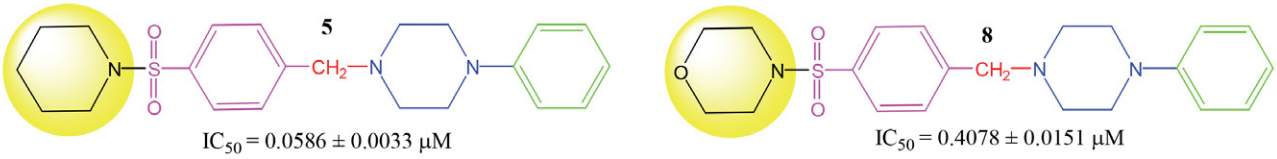

Figure 2. Structure-activity relationship of compounds **5** and **8**.

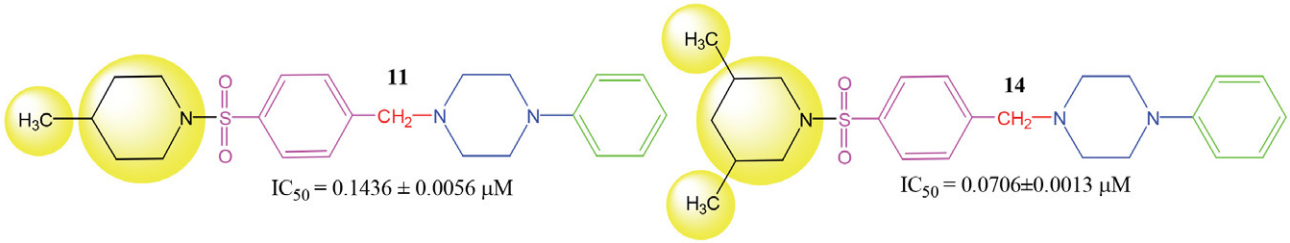

Figure 3. Structure-activity relationship of compounds **11** and **14**.

Moreover, on a closer look, it was also elucidated that compounds **11** and **14** both have substituted piperidinyl ring and possessed slightly lesser inhibitory potentials as compared to **5** in which an un-substituted piperidinyl ring was present. From this, it was conceivable that the presence of any methyl group in this heterocyclic ring may render some steric repulsions and thus tending to retard the interactions of the compound with the enzyme, although to a minor extent. Hence, the presence of an un-substituted piperidinyl ring was the most suited option for the excellent activity of such molecules.

2. 2. 2. Kinetic Analysis

To understand the inhibitory mechanism of these bi-heterocyclic sulfonamides on tyrosinase, kinetic study was performed. Based on our IC_{50} results, the most potent compound **5** was selected to determine the inhibition type and inhibition constant. The kinetic results (Table 2) of the enzyme by the Lineweaver–Burk plot of $1/V$ versus $1/[S]$ in the presence of different inhibitor concentrations gave a series of straight lines (Figure 4a). The result of Lineweaver–Burk plot of **5** showed that this compound intersected within the second quadrant. The analysis showed that V_{max} decreased in new increasing doses of inhibitors, on the other hand, K_m remains the same. This behavior indicated that **5** inhibited the tyrosinase non-competitively to form an enzyme-inhibitor complex. Secondary plot of slope against the concentrations of inhibitor showed enzyme-inhibitor dissociation constant (K_i) (Figure 4b).

2. 2. 3. Mushroom Tyrosinase Structural Assessment

Mushroom tyrosinase, a copper containing protein comprises 391 residues. The detail structure analysis of the target protein showed that it consists of 39% α-helices, 14% β-sheets and 46% coils. The Ramachandran plots and values indicate that 95.90% of protein residues are present in the favored region and 100.0% residues lie in the allowed region. The Ramachandran graph values show good accuracy of phi (φ) and psi (ψ) angles among the coordinates of receptor and most of residues are plunged in the acceptable region. The overall protein structure and Ramachandran graph is shown in Figure 5 (A, B).

2. 2. 4. Computational Docking

2. 2. 4. 1. Glide Energy Evaluation of Synthesized Compounds

Molecular docking examination is the best approach to study the binding conformation of ligands within the

Table 2. Kinetic parameters of the mushroom tyrosinase for L-DOPA activity in the presence of various concentrations of compound 5.

Concentration (μM)	V_{max} (ΔA /Min)	K_m (mM)	Inhibition Type	K_i (μM)
0.00	0.000384	0.2222		
0.0586	7.105673×10^{-5}	0.2222		
0.1172	5.438583×10^{-5}	0.2222	Non-Competitive	0.09
0.2344	3.968313×10^{-5}	0.2222		

Note: V_{max} is the reaction velocity; K_m is the Michaelis–Menten constant; Ki is the EI dissociation constant.

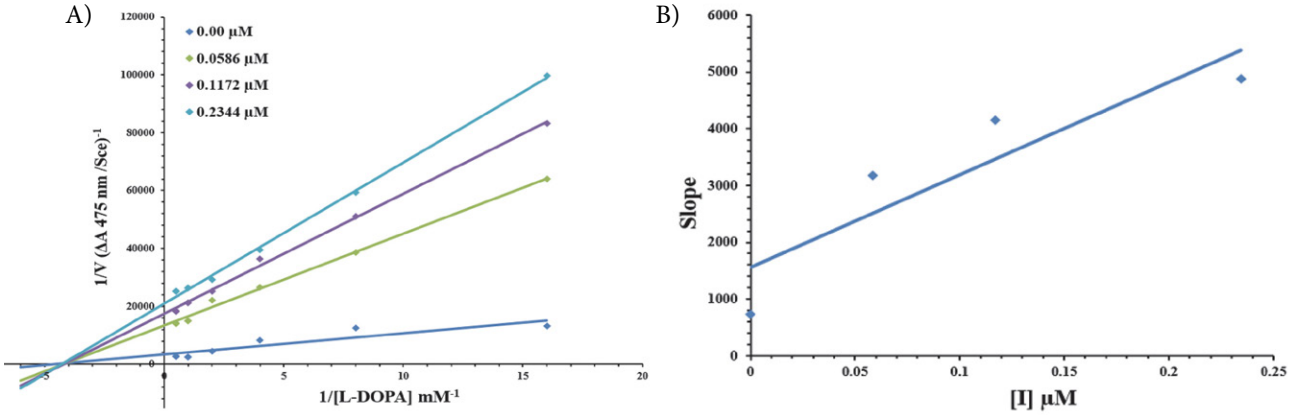

Figure 4. Lineweaver–Burk plots for inhibition of tyrosinase in the presence of compound 5. (a) Concentrations of 5 were 0.00, 0.0586, 0.1172 and 0.2344 µM, respectively. Substrate L-DOPA concentrations were between 0.0625 and 2 mM, respectively. (b) The inset represents the plot of the slope versus inhibitor 5 concentrations to determine inhibition constant. The lines were drawn using linear least squares fit.

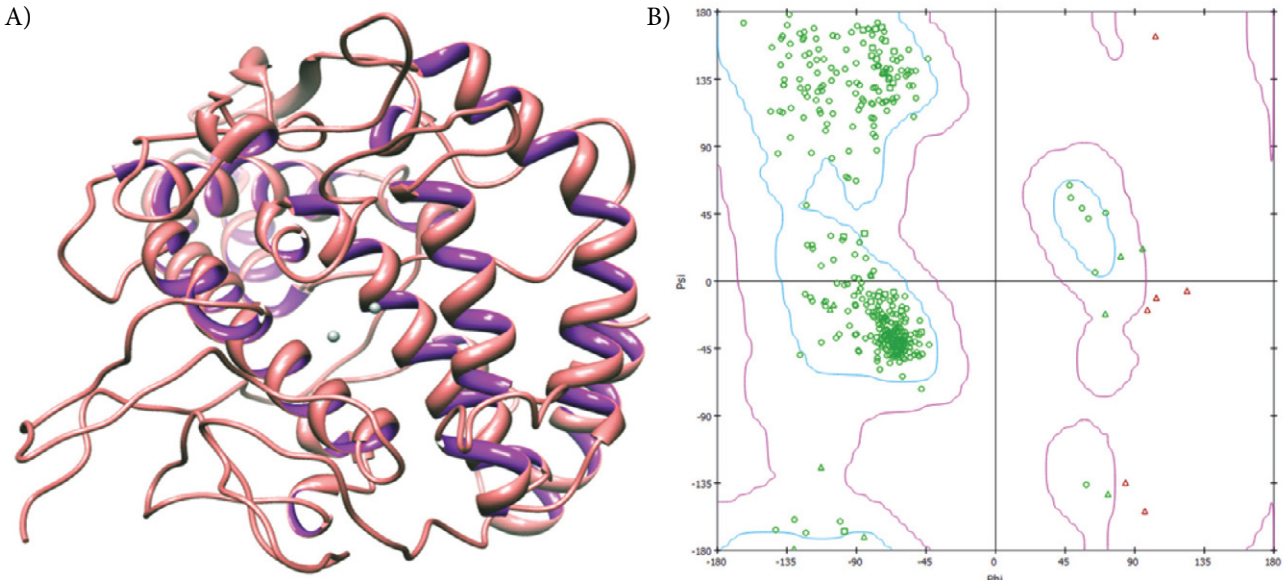

Figure 5. The overall protein structure (A) of tyrosinase and its Ramachandran graph (B).

active region of target proteins.[20,21] To predict the conformational positions of synthesized ligands, compounds **5**, **8**, **11** and **14** were docked against tyrosinase, separately. The generated docked complexes were examined on the basis of glide docking energy values (kcal/mol) and bonding interaction (hydrogen/hydrophobic) pattern. The docking results showed that all the ligands were bound within the active region of the target protein with different conformational poses (Figure 6A). The glide docking energy values fluctuated among all ligands (**5**, **8**, **11** and **14**) and exhibited well docking energy values –4.50, –5.65, –4.89 and –5.81 kcal/mol, respectively. The comparative results show that no big energy value differences were observed (Fig. 6B) as the basic skeleton of ligands was similar in all synthetic compounds with the variation of only one heterocyclic moiety.

2. 2. 4. 2. Ligand-Binding Analysis of Tyrosinase Docked Complexes

It was envisaged that hydrogen bonds and π–π **interactions were observed in 8**, **11** and **14** docking complexes. In **5**–tyrosinase docking no hydrogen bonds were observed, however its binding conformation was quite similar with other ligands docking complexes. In **8**–tyrosinase docking complex three hydrogen bonds were observed at Glu322 and His85. The benzene ring form hydrogen bond with Glu322 having bond length 2.61 Å, whereas the oxygen atoms of benzenesulfonyl part were involved in hydrogen bonding against His85 having bond distances 2.67 Å and 1.99 Å, respectively. In **11**–tyrosinase docking couple of hydrogen bonds were observed between the benzene ring of ligand and tyrosinase residues His85 and Cys83 with bonds length 2.59 Å and 2.46 Å, respectively. Moreover, the com-

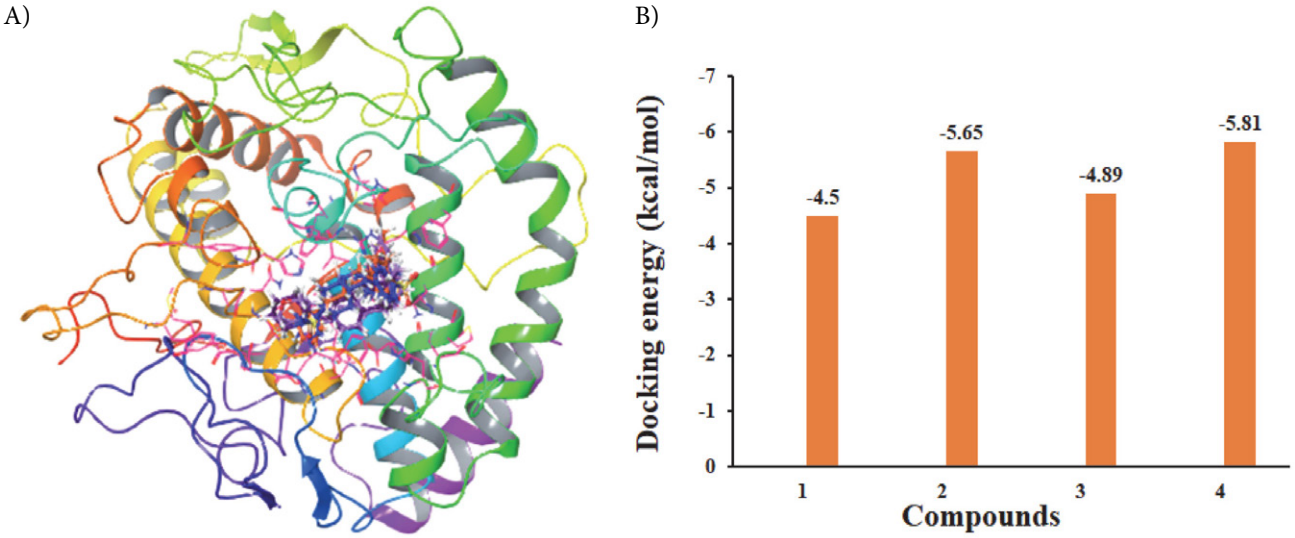

Figure 6. All the tyrosinase docking complexes (A) and their docking energy values (B).

pound **14** also showed two hydrogen bonds against His85 and Cys83 with bond distances 2.61 Å and 2.27 Å, respectively. The 3D and 2D graphical representations of all docking complexes are shown in Figures 7, 8 and 9, respectively.

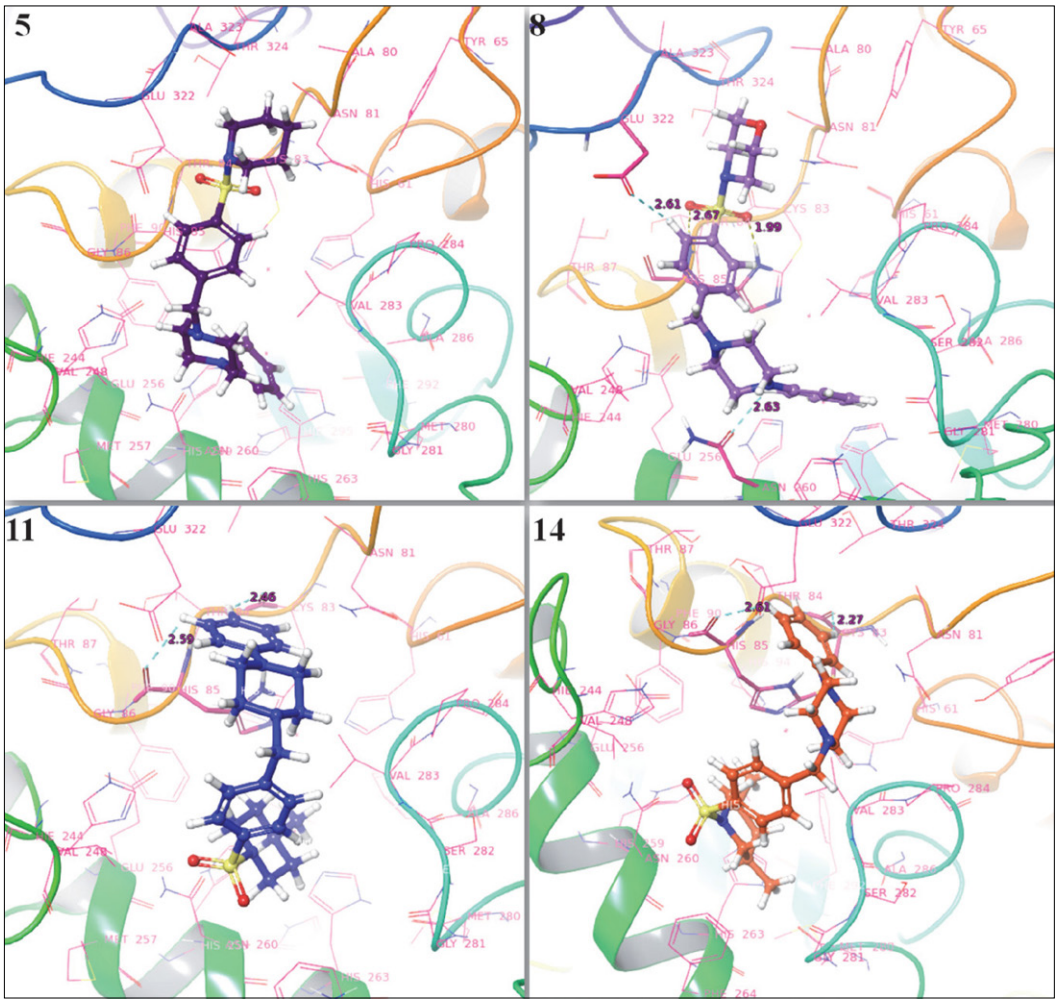

Figure 7. 3D binding interactions of **5**, **8**, **11** and **14** against tyrosinase protein.

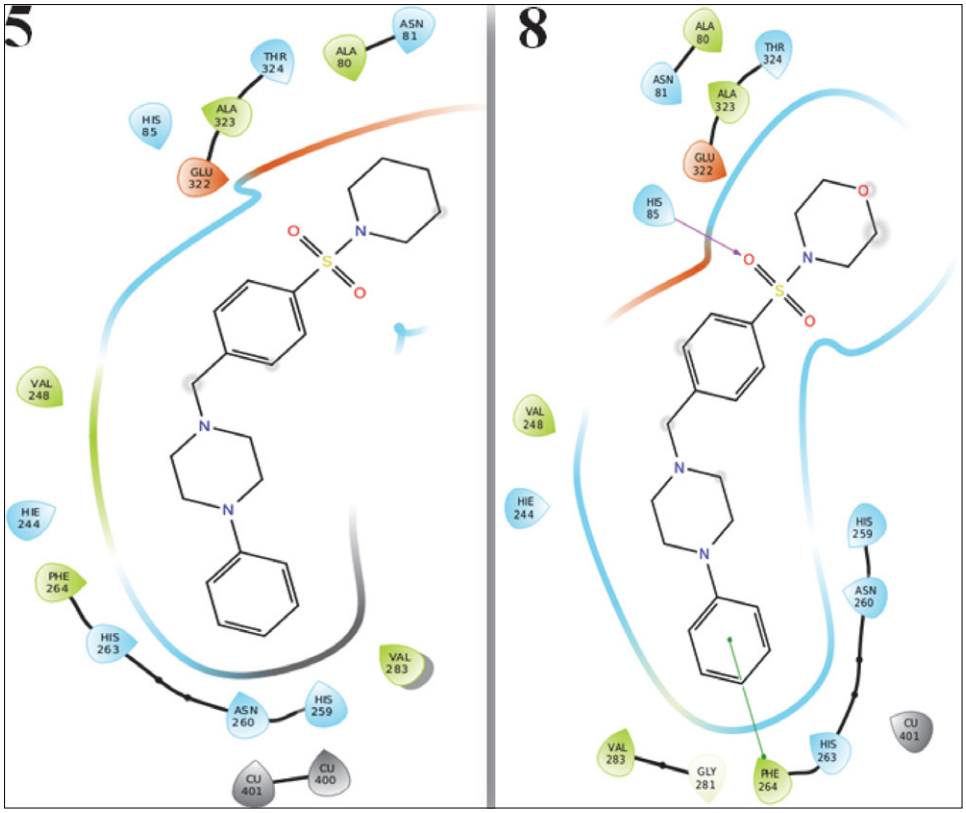

Figure 8. 2D binding interactions of **5** and **8** against tyrosinase protein.

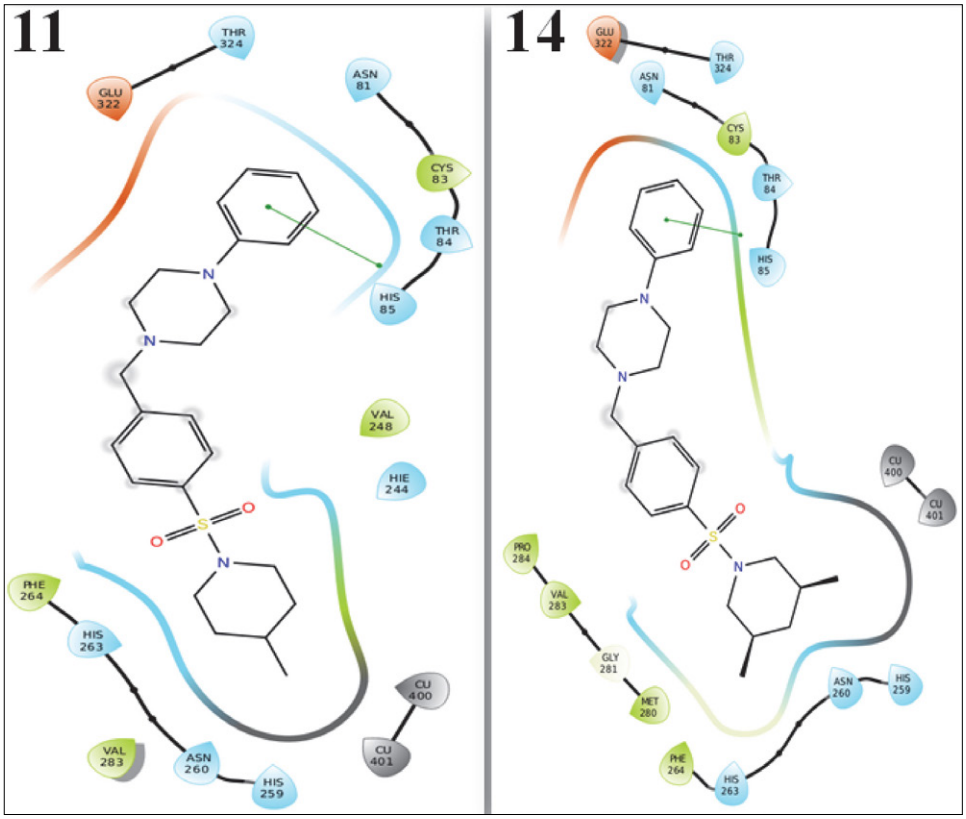

Figure 9. 2D binding interactions of **11** and **14** against tyrosinase protein.

Moreover, computational results also explored the good binding profiles against target protein. All compounds (**5**, **8**, **11**, and **14**) exhibited good docking energy values and bound within active region of the target protein. His85 was common in all docking results. The His85 is copper bonded residue which ensures that our ligands bind within the active region of the target protein. Literature data also ensured the importance of these residues in bonding with other tyrosinase inhibitors which strengthen our docking results.[22,23] The comparative results showed that compound **5** might be considered as a superb template for the designing of new inhibitors against tyrosinase.

3. Experimental

3. 1. General

All the chemicals, along with analytical grade solvents, were purchased from Sigma Aldrich, Alfa Aesar (Germany), or Merck through local suppliers. Pre-coated silica gel Al-plates were used for TLC with ethyl acetate and *n*-hexane as solvent system. Spots were detected by UV_{254}. Gallenkamp apparatus was used to measure melting points in capillary tubes. Elemental analyses were performed on a Foss Heraeus CHN-O-Rapid instrument and were within ± 0.4% of the theoretical values. IR spectra (ν, cm^{-1}) were recorded by KBr pellet method in the Jas-

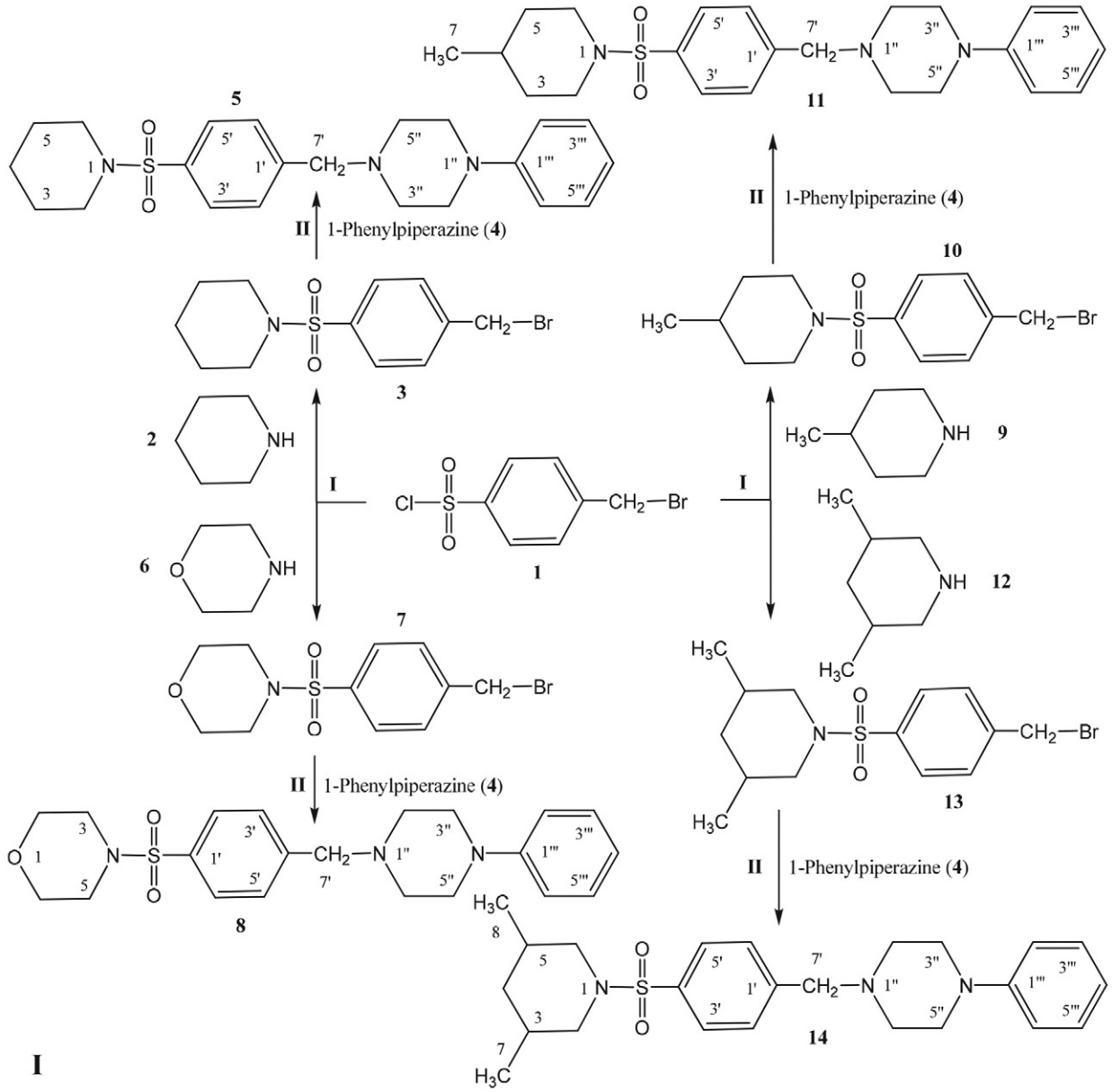

Scheme 1. Outline for the synthesis of 1-phenyl-4-[4-substituted-sulfonyl)benzyl]piperazines (**5**, **8**, **11**, **14**). **Reagents and conditions:** (**I**) 10% Na_2CO_3, pH 9–10, stirring at room temperature for 3–4 h; (**II**) dimethylformamide (DMF), LiH, refluxed for 0.5 h, followed by addition of respective electrophile (one in each reaction) and then refluxing further for 4–5 h.

co-320-A spectrophotometer. ^{1}H NMR spectra (δ, ppm) were recorded at 600 MHz (^{13}C NMR spectra, at 150 MHz) in DMSO-d_6 using Bruker Advance III 600 As-cend spectrometer using BBO probe.

3. 2. Synthesis of 1-{[4-(Bromomethyl)phenyl] sulfonyl}un/substituted-piperidines (3, 10, 13) and 1-{[4-(Bromomethyl)phenyl] sulfonyl}morpholine (7)

The synthesis of 1-{[4-(bromomethyl)phenyl]sulfonyl}un/substituted-piperidines (**3**, **10**, **13**) and 1-{[4-(bromomethyl)phenyl]sulfonyl}morpholine (**7**) was carried out by reaction of respective un/substituted-piperidines (**2**, **9**, **12**) or morpholine (**6**) with 4-(bromomethyl)benzenesulfonyl chloride (**1**) in equimolar quantities (0.001 moles) and shaking manually in 10% aqueous Na_2CO_3 solution. Solid precipitates were formed after 2–3 h, which were filtered and washed with cold distilled water to obtain the desired electrophiles (**3**, **7**, **10**, **13**).

3. 3. General Procedure for the Synthesis of 1-Phenyl-4-[4-(substituted-sulfonyl) benzyl]piperazines (5, 8, 11, 14)

1-Phenylpiperazine (0.2 g, **4**) was added in DMF (5 mL) contained in a 250 mL round bottom flask at room temperature, added one pinch of LiH and stirred for 30 min. Then the respective electrophile from **3**, **7**, **10**, **13** (one in each reaction) was added in equimolar amount and stirred for 4–5 h. The completion of the reaction was monitored by TLC and after its completion, the reaction mixture was quenched with ice cold water (100 mL). Consequently, the respective derivatives (**5**, **8**, **11**, **14**) were collected through filtration in purified form.

1-Phenyl-4-[4-(1-piperidinylsulfonyl)benzyl]piperazine (5)

White crystalline solid; yield: 72%; m.p: 116–117 °C; mol. Formula: $C_{22}H_{29}N_3SO_2$; mol. weight: 399 g/mol; IR (KBr, ν, cm^{-1}) 2986 (C-H, str. of aromatic ring), 2905 (-CH_2 stretching), 1680 (aromatic C=C stretching), 1382 (S=O), 1115 (C-N-C); ^{1}H NMR (600 MHz, DMSO-d_6) δ 7.70 (br. d, J = 7.6 Hz, 2H, H-3' and 5'), 7.60 (br. d, J = 7.6 Hz, 2H, H-2' and 6'), 7.20 (br. t, J = 7.2 Hz, 2H, H-3''' and H-5'''), 6.92 (br. d, J = 7.7 Hz, 2H, H-2''' and H-6'''), 6.77 (br. t, J = 6.9 Hz, 1H, H-4'''), 3.63 (s, 2H, CH_2-7'), 3.51–3.46 (m, 4H, CH_2-2 and CH_2-6), 3.14 (br. s) and 2.87 (br. s) (8H, CH_2-2'', CH_2-3'', CH_2-5'' and CH_2-6''), 1.53 (br. s, 4H, CH_2-3 and CH_2-5), 1.35 (br. s, 2H, CH_2-4); ^{13}C NMR (150 MHz, DMSO-d_6) δ 151.43 (C-1'''), 144.16 (C-4'), 134.72 (C-1'), 129.90 (C-2' and C-6'), 129.37 (C-3''' and C-5'''), 127.87 (C-3' and C-5'), 119.29 (C-4'''), 115.85 (C-2''' and C-6'''), 61.72 (C-7'), 53.05 (C-3'' and C-5''), 48.67 and 48.63 (C-2 and C-6), 47.04 (C-2'' and 6''), 25.14 (C-3 and C-5), 23.32 (C-4); Anal. Calcd. for $C_{12}H_{29}N_3SO_2$ (399.20): C, 66.13; H, 7.32; N, 10.52. Found: C, 66.17; H, 7.25; N, 10.50.

4-({4-[(4-Phenyl-1-piperazinyl)methyl]phenyl}sulfonyl)morpholine (8)

White crystalline solid; yield: 91%; m.p: 176–177 °C; mol. Formula: $C_{21}H_{27}N_3SO_3$; mol. weight: 401 g/mol; IR (KBr, ν, cm^{-1}) 2981 (C-H, str. of aromatic ring), 2901 (-CH_2 stretching), 1678 (aromatic C=C stretching), 1385 (S=O), 1121 (C-N-C); ^{1}H NMR (600 MHz, DMSO-d_6) δ 7.72 (br. d, J = 8.2 Hz, 2H, H-2' and H-6'), 7.64 (br. d, J = 8.2 Hz, 2H, H-3' and H-5'), 7.21 (br. t, J = 7.6 Hz, 2H, H-3''' and H-5'''), 6.93 (br. d, J = 8.1 Hz, 2H, H-2''' and H-6'''), 6.77 (br. t, J = 7.2 Hz, 1H, H-4'''), 3.66 (s, 2H, CH_2-7'), 3.64 (dis. t, J = 4.6 Hz, 4H, CH_2-2 and CH_2-6), 3.15 (dis. t, J = 4.5 Hz) and 2.86 (dis. t, J = 4.4 Hz) (8H, CH_2-2'', CH_2-3'', CH_2-5'' and CH_2-6''), 2.55 (dis. t, J = 4.7 Hz, 4H, CH_2-3 and CH_2-5); ^{13}C NMR (150 MHz, DMSO-d_6) δ 151.46 (C-1'''), 144.72 (C-1'), 133.55 (C-4'), 129.99 (C-3' and C-5'), 129.36 (C-3''' and C-5'''), 128.16 (C-2' and C-6'), 119.27 (C-4'''), 115.85 (C-2''' and C-6'''), 65.76 (C-2 and C-6), 61.72 (C-7'), 53.09 (C-2'' and C-6''), 48.70 (C-3 and C-5), 46.37 (C-3'' and 5''); Anal. Calcd. for $C_{21}H_{27}N_3SO_3$ (401.18): C, 62.82; H, 6.78; N, 10.47. Found: C, 62.78; H, 6.73; N, 10.44.

1-{4-[(4-Methyl-1-piperidinyl)sulfonyl]benzyl}-4-phenylpiperazine (11)

White crystalline solid; yield: 76%; m.p: 81–82 °C; mol. Formula: $C_{23}H_{31}N_3SO_2$; mol. weight: 413 g/mol; IR (KBr, ν, cm^{-1}) 2983 (C-H, str. of aromatic ring), 2900 (-CH_2 stretching), 1676 (aromatic C=C stretching), 1389 (S=O), 1126 (C-N-C); ^{1}H NMR (600 MHz, DMSO-d_6) δ 7.67 (dis. d, J = 7.6 Hz, 2H, H-3' and H-5'), 7.54 (dis. d, J = 7.6 Hz, 2H, H-2' and H-6'), 7.20 (br. s, 2H, H-3''' and H-5'''), 6.92 (dis. d, J = 7.7 Hz, 2H, H-2''' and H-6'''), 6.77 (br. s, 1H, H-4'''), 3.63 (m, 1H, H_e-6), 3.53 (s, 2H, CH_2-7'), 3.38 (br. s, 1H, H_e-2), 3.33 (br. s, 2H, H_a-2 and H_a-6), 3.14 (br. s) and 2.74 (br. s) (8H, CH_2-2'', CH_2-3'', CH_2-5'' and CH_2-6''), 1.62 (m, 2H, H_e-3 and H_e-5), 1.28 (m,1H, H-4), 1.13 (m, 2H, H_a-3 and H_a-5), 0.88 (br. d, J = 7.1 Hz, 3H, CH_3-7); ^{13}C NMR (150 MHz, DMSO-d$_6$) δ 151.44 (C-1'''), 144.94 (C-4'), 134.73 (C-1'), 129.63 (C-2' and C-6'), 129.34 (C-3''' and C-5'''), 127.83 (C-3' and C-5'), 119.25 (C-4'''), 115.84 (C-2''' and C-6'''), 61.74 (C-7'), 53.08 (C-2'' and C-6''), 48.70 (C-3'' and C-5''), 46.48 (C-2 and C-6), 33.27 (C-3 and C-5), 29.75 (C-4), 21.74 (C-7); Anal. Calcd. for $C_{23}H_{31}N_3SO_2$ (413.21): C, 66.79; H, 7.56; N, 10.16. Found: C, 66.75; H, 7.49; N, 10.10.

1-{4-[(3,5-Dimethyl-1-piperidinyl)sulfonyl]benzyl}-4-phenylpiperazine (14)

White crystalline solid; yield: 70%; m.p: 110–111 °C; mol. Formula: $C_{24}H_{33}N_3SO_2$; mol. weight: 427 g/mol; IR (KBr, ν, cm^{-1}) 2990 (C-H, str. of aromatic ring), 2915 (-CH_2 stretching), 1689 (aromatic C=C stretching), 1388

(S=O), 1108 (C-N-C); ^{1}H NMR (600 MHz, DMSO-d_6) δ 7.72 (br. d, J = 7.9 Hz, 2H, H-3' and H-5'), 7.60 (br. d, J = 7.9 Hz, 2H, H-2' and H-6'), 7.20 (br. t, J = 7.7 Hz, 2H, H-3''' and H-5'''), 6.93 (br. d, J = 8.1 Hz, 2H, H-2''' and H-6'''), 6.77 (br. t, J = 7.1 Hz, 1H, H-4'''), 3.64 (s, 2H, CH_2-7'), 3.62–3.60 (m, 4H, CH_2-2 and CH_2-6), 3.15 (br. s) and 2.54 (br. s) (8H, CH_2-2", CH_2-3", CH_2-5" and CH_2-6"), 1.71–1.63 (m, 2H, CH_2-3 and CH_2-5), 0.92 (dis. d, J = 6.7 Hz, 1H, H_e-4), 0.82 (br. d, J = 6.0 Hz, 6H, CH_3-7 and CH_3-8), 0.51 (m, 1H, H_a-4); ^{13}C NMR (150 MHz, DMSO-d_6) δ 151.45 (C-1'''), 144.20 (C-4'), 134.99 (C-1'), 129.90 (C-2' and C-6'), 129.35 (C-3''' and C-5'''), 127.81 (C-3' and C-5'), 119.26 (C-4'''), 115.85 (C-2''' and C-6'''), 61.73 (C-7'), 53.10 (C-2" and C-6"), 52.73 (C-2 and C-6), 48.65 (C-3" and C-5"), 41.09 (C-4), 30.94 (C-3 and C-5), 19.78 (C-7 and 8); Anal. Calcd. for $C_{24}H_{33}N_3SO_2$ (427.23): C, 67.41; H, 7.78; N, 9.83. Found: C, 67.35; H, 7.69; N, 9.77.

3. 4. Biological Activity Assays (*in vitro*)

3. 4. 1. Tyrosinase Inhibitory Activity

The inhibition of mushroom tyrosinase was determined by a modification of the dopachrome method using L-DOPA as the substrate.[24–27] In detail, 140 µL of phosphate buffer (20 mM, pH 6.8), 20 µL of mushroom tyrosinase (30 U/mL) and 20 µL of the inhibitor solution were placed in the wells of a 96-well microplate. After pre-incubation for 10 minutes at room temperature, 20 µL of L-DOPA (3,4-dihydroxyphenylalanine, Sigma Chemical, USA) (0.85 mM) was added and the assay plate was further incubated at 25 °C for 20 minutes. After incubation time, the absorbance was read at 475 nm and the inhibition percentage calculated in relation to the control. Phosphate buffer and kojic acid were tested under the same conditions as negative and positive control, respectively. The amount of inhibition by the test compounds was expressed as the percentage of concentration necessary to achieve 50% inhibition (IC_{50}). Each concentration was analyzed in three independent experiments. IC_{50} values were calculated by nonlinear regression using GraphPad Prism 5.0.

The % inhibition of tyrosinase was calculated as following:

$$\text{Inhibition (\%)} = \frac{\text{B} - \text{S}}{\text{B}} \cdot 100$$

Here, the B and S are the absorbances for the blank and samples.

3. 4. 2. Kinetics Assay

On the basis of IC_{50} results, the most potent molecule, **5**, was selected for kinetic analysis. A series of experiments were performed to determine the inhibition kinetics of **5** by following the already reported methods.[23,28] The inhibitor concentrations for **5** were 0.00, 0.0586, 0.1172 and 0.2344 µM. Substrate L-DOPA concentrations were between 0.0625 to 2 mM in all kinetic studies. Pre-incubation and measurement time was the same as discussed in the mushroom tyrosinase inhibition assay protocol. Maximal initial velocity was determined from the initial linear portion of absorbance up to five minutes after addition of enzyme at a 30 s interval. The inhibition type of the enzyme was assayed by Lineweaver–Burk plots of the inverse of velocities ($1/V$) versus the inverse of substrate concentration 1/[L-DOPA] mM^{-1}. The EI dissociation constant K_i was determined by the secondary plot of $1/V$ versus inhibitors concentrations.

3. 4. 3. Molecular Docking Methodology

3. 4. 3. 1. Retrieval of Tyrosinase in Protein Preparation Wizard

The mushroom tyrosinase structure was retrieved from Protein Data Bank (PDB) (www.rcsb.org) with PDBID 2Y9X[29] in protein preparation wizard. The selected protein structure of tyrosinase was pre-processed and minimized using default parameters in Maestro interface.

3. 4. 3. 2. Grid Generation and Molecular Docking

Prior to molecular docking, the optimized tyrosinase structure was prepared using the "Protein Preparation Wizard" workflow in Schrödinger Suite. Bond orders were assigned and hydrogen atoms were added to the protein. The structure was then minimized to reach the converged root mean square deviation (RMSD) of 0.30 Å with the OPLS_2005 force field. The active site of the enzyme was defined from the co-crystallized ligands from Protein Data Bank and literature data.[30] Furthermore, docking experiment was performed against all synthesized ligands (**5**, **8**, **11** and **14**) sketched by 2D sketcher in Maestro and target protein by using Glide docking protocol.[31] The predicted binding energies (docking scores) and conformational positions of ligands within active region of protein were also performed using Glide experiment. Throughout the docking simulations, both partial flexibility and full flexibility around the active site residues were performed by Glide/SP/XP and induced fit docking (IFD) approaches.[32,33]

4. Conclusion

A structurally unique series of sulfonamides, hybrid with a piperazine, and heterocyclic secondary amines, was synthesized and recognized with very superb tyrosinase inhibition. It was postulated from the SAR studies that molecules particularly bearing un-substituted or symmetrically methylated piperidinyl moiety, generally inhibited the tyrosinase in an excellent manner. So, it was concluded that molecule **5** in particular, and all these bi-heterocyclic sulfonamides in general, can be utilized as leading medicinal scaffolds for the treatment of melanogenesis.

Acknowledgement

The present study was supported by Basic Science Research Program through the National Research Foundation of Korea (NRF) funded by the Ministry of Education (2017R1D1A1B03034948).

5. References

1. V. K. Jain, B. Jain, U. K. Sharma, K. U. Saha, D. Saha, *Int. J. Curr. Pharm. Res*. **2011**, *3*, 66–70.
2. S. Bag, R. Tulsan, A. Sood, H. Cho, H. Redjeb, W. Zhou, H. LeVine III, B. Török, M. Török, *Bioorg. Med. Chem. Lett*. **2015**, *25*, 626–630. **DOI:**10.1016/j.bmcl.2014.12.006
3. M. A. Abbasi, S. Manzoor, Aziz-ur-Rehman, S. Z. Siddiqui, I. Ahmad, R. Malik, M. Ashraf, Qurat-ul-Ain, S. A. A. Shah, *Pak. J. Chem*. **2015**, *5*, 23–29. **DOI:**10.15228/2015.v05.i01.p04
4. J. Winum, A. Scozzafava, J. Montero, C. T. Supuran, *Med. Res. Rev*. **2006**, *26*, 767–792. **DOI:**10.1002/med.20068
5. Antipsychotic piperazine and piperadine derivative, *Expert Opinion on Therapeutic Patents* **1994**, *4*, 281–292. **DOI:**10.1517/13543776.4.3.281
6. H. Marona, A. Gunia, K. Słoczyńska, A. Rapacz, B. Filipek, M. Cegła, W. Opoka, *Acta Pol. Pharm*. **2009**, *66*, 571–578.
7. M. Somashekhar, A. R. Mahesh, *Am. J. Pharm. Res*. **2013**, *3*, 640–645.
8. A. Mendoza, S. Pérez-Silanes, M. Quiliano, A. Pabón, S. Galiano, G. González, G. Garavito, M. Zimic, A. Vaisberg, I. Aldana, A. Monge, E. Deharo, *Exp. Parasitol*. **2011**, *12*, 97–103. **DOI:**10.1016/j.exppara.2011.02.025
9. G. C. L. Ee, C. M. Lim, M. Rahmani, K. Shaari, C. F. J. Bong, *Molecules* **2010**, *15*, 2398–2404. **DOI:**10.3390/molecules15042398
10. H. Sugimoto, Y. Limura, Y. Yamanishi, K. Yamatsu, *Bioorg. Med. Chem. Lett*. **1992**, *2*, 871–876. **DOI:**10.1016/S0960-894X(00)80547-8
11. F. M. Oliveira, L. C. A. Barbosa, V. M. M. Valente, A. J. Demuner, C. R. A. Maltha, A. de J. Oliveros-Bastidas, *J. Pharm. Res*. **2012**, *5*, 5326–5333.
12. L. He, *Bayer. Schering. Pharma*. **1998**, *6*, 132–145.
13. S. A. Shaker, M. I. Marzouk, *Molecules* **2016**, *21*, 155–164. **DOI:**10.3390/molecules21020155
14. C. A. Ramsden, P. A. Riley, *Bioorg. Med. Chem*. **2014**, *22*, 2388–2395. **DOI:**10.1016/j.bmc.2014.02.048
15. Y. J. Zhu, L. Qiu, J. J. Zhou, H. Y. Guo, Y. H. Hu, Z. C. Li, Q. Wang, Q. X. Chen, B. Liu, *J. Enz. Inhib. Med. Chem*. **2010**, *25*, 798–803. **DOI:**10.3109/14756360903476398
16. M. Brenner, V. J. Hearing, *Photochem. Photobiol*. **2008**, *84*, 539–549. **DOI:**10.1111/j.1751-1097.2007.00226.x
17. Y. J. Kim, K. S. Kang, T. Yokozawa, *Food Chem. Toxicol*. **2008**, *7*, 2466–2471.
18. R. A. Copeland, Evaluation of Enzyme Inhibitors in Drug Discovery: A Guide for Medicinal Chemists and Pharmacologists, Published by John Wiley & Sons, Inc., Hoboken, New Jersey, **2005**, *Vol*. 46. ISBN 0-471-68696-4.
19. J. Konc, S. Lešnik, D. Janežič, *J. Cheminform*. **2015**, *7*, article number: 48, 1–8. **DOI:**10.1186/s13321-015-0096-0
20. M. Hassan, Q. Abbas, Z. Ashraf, A. A. Moustafa, S. Y. Seo, *Comput. Biol. Chem*. **2017**, *68*, 131–142. **DOI:**10.1016/j.compbiolchem.2017.02.012
21. M. Hassan, Z. Ashraf, Q. Abbas, H. Raza, S. Y. Seo, *Interdiscip. Sci*. **2018**, *10*, 68–80. **DOI:**10.1007/s12539-016-0171-x
22. A .R. S. Butt, M. A. Abbasi, Aziz-ur-Rehman, S. Z. Siddiqui, H. Raza, M. Hassan, S. A. A. Shah, M. Shahid, S.-Y. Seo, *Bioorg. Chem.* **2019**, *86*, 459–472. **DOI:**10.1016/j.bioorg.2019.01.036
23. F. A. Larik, A. Saeed, P. A. Channar, U. Muqadar, Q. Abbas, M. Hassan, S. Y. Seo, M. Bolte, *Eur. J. Med. Chem*. **2017**, *141*, 273–281. **DOI:**10.1016/j.ejmech.2017.09.059
24. H. Raza, M. A. Abbasi, Aziz-ur-Rehman, S. Z. Siddiqui, M. Hassan, Q. Abbas, H. Hong, S. A. A. Shah, M. Shahid, S-Y Seo, *Bioorg. Chem*. **2020**, *94*, article number: 103445, 1–8. **DOI:**10.1016/j.bioorg.2019.103445
25. Q. Abbas, Z. Ashraf, M. Hassan, H. Nadeem, M. Latif, S. Afzal, S. Y. Seo, *Drug Des. Devel. Ther*. **2017**, *11*, 20–29. **DOI:**10.2147/DDDT.S137550
26. S. Aamer, A. P. Mahesar, P. A. Channar, Q. Abbas, F. A. Larik, M. Hassan, H. Raza, S. Y. Seo, *Bioorg. Chem*. **2017**, *74*, 187–196. **DOI:**10.1016/j.bioorg.2017.08.002
27. Z. Ashraf, M. Rafiq, N. Humaira, H. Mubashir, A. Samina, M. Waseem, A. Khurram, L. Jalifah, *PloS One* **2017**, *12*, e0178069. **DOI:**10.1371/journal.pone.0178069
28. Z. Ashraf, M. Rafiq, S. Y. Seo, M. M. Babar, *Bioorg. Med. Chem*. **2015**, *23*, 5870–5880. **DOI:**10.1016/j.bmc.2015.06.068
29. W. T. Ismaya H. J. Rozeboom, A. Weijn, J. J. Mes, F. Fusetti, H. J. Wichers, B. W. Dijkstra, *Biochemistry* **2011**, *50*, 5477–5486. **DOI:**10.1021/bi200395t
30. M. Hassan, Q. Abbas, H. Raza, A. A. Moustafa, S. S. Seo, *Mol. Biosyst*. **2017**, *13*, 1534–1544. **DOI:**10.1039/C7MB00211D
31. R. A. Friesner, R. B. Murphy, M. P. Repasky, L. L. Frye, J. R. Greenwood, T. A. Halgren, P. C. Sanschagrin, D. T. Mainz, *J. Med. Chem*. **2006**, *49*, 6177–6196. **DOI:**10.1021/jm051256o
32. W. Sherman, T. Day, M. P. Jacobson, R. A. Friesner, R. Farid, *J. Med. Chem*. **2006**, *49*, 534–553. **DOI:**10.1021/jm050540c
33. W. Sherman, H. S. Beard, R. Farid, *Chem. Bio. Drug Des*. **2006**, *67*, 83–94. **DOI:**10.1111/j.1747-0285.2005.00327.x

Povzetek

S pomočjo dvostopenjskega protokola smo sintetizirali načrtovane bi-heterociklične sulfonamide; njihove strukture smo določili s spektroskopskimi tehnikami, vključno z IR, ^{1}H NMR in ^{13}C NMR ter s CHN analizo. *In vitro* inhibitorne učinke teh sulfonamidov smo določili na tirozinazi, mehanizem kinetike pa smo analizirali z Lineweaver–Burkovimi grafi. Vezavni model teh molekul je bil določen s pomočjo študij računskega sidranja. Sintetizirane bi-heterociklične molekule so se izkazale kot učinkoviti inhibitorji glede na standard 5-hidroksi-2-(hidroksimetil)-4*H*-piran-4-on (»kojic acid«); spojina **5** je nekompetitivno inhibirala tirozinazo tako, da je tvorila kompleks encim-inhibitor. Inhibicijsko konstanto K_i (0.09 μM) za spojino **5** smo izračunali iz Dixonovih grafov. Računski rezultati so pokazali, da vse spojine izkazujejo ugoden vezavni profil za tirozinazo in da interagirajo z aminokislinskimi ostanki v jedru tarčnega proteina.

Except when otherwise noted, articles in this journal are published under the terms and conditions of the Creative Commons Attribution 4.0 International License

Scientific paper

Specification of Zwitterionic or Non-Zwitterionic Structures of Amphoteric Compounds by Using Ionic Liquids

Leila Sheikhian,[1,*] Morteza Akhond[2] and Ghodratollah Absalan[2]

[1] *Department of Chemistry, Kazerun Branch, Islamic Azad University, Kazerun, Iran*

[2] *Department of Chemistry, College of Sciences, Shiraz University, Shiraz, 71454, Iran*

** Corresponding author: E-mail: fsheikhian59@gmail.com, sheikhian@kau.ac.ir*
Tel.: +98 7142243930-9, Fax: +98 7142230508

Received: 06-28-2019

Abstract

Some imidazolium-based ionic liquids were used to determine zwitterionic or non-zwitterionic structures of glycine and p-amino benzoic acid, as model amphoteric compounds, in their corresponding isoelectric point. To do this, the partitioning behaviors of both compounds between the ionic liquid and aqueous phase at different pH values were investigated. The results revealed that due to having different pH-dependent chemical structures, each compound showed different partitioning behavior. This observation was considered as a basis for introducing a green technique for understanding the real chemical structures (species), i.e. zwitterionic or non-zwitterionic structures of amphoteric compounds such as amino acids in the aqueous solutions. This study revealed the existence of a non-zwitterionic (neutral) structure for p-amino benzoic acid and a zwitterionic structure for glycine in their corresponding isoelectric points.

Keywords: p-Amino benzoic acid; Glycine; Ionic liquid; Partition coefficient; Zwitterion

1. Introduction

Charge characterization and speciation of amino acids is of interest not only in biological sciences for better understanding of the metabolic processes in tissue membranes but also in analytical chemistry for improving and designing new separation and measurement procedures. Generally, knowing the chemical forms, including the charged structures, of a compound as it really exists in a sample would help revealing its true impact on human or the environment. Speciation analysis plays a unique role in studies of biogeochemical cycles of chemical compound, determination of toxicity as well as ecotoxicity of selected elements, quality control of food products, control of medicines and pharmaceutical products, technological process control, and clinical analysis. For instance, zwitterions, used widely in chemical, biological and medicinal fields, show distinct physicochemical properties relative to ordinary ampholytes, which largely decide their bioavailability and biological activities.[1] Many studies including computational protocols have been done about charge characterization of peptides and proteins (to interpret their mass spectrometry data) [2] as well as amino acids in gas phase.[3-8] However, few studies about the charged structures of amino acids in aqueous phase are available for checking the studies reported by many authors. In 1916, Adams showed that an amino acid might possess a zwitterionic structure, i.e. $^{+}NH_3$–R–COO^{-}, rather than a non-zwitterionic classical structure, i.e. NH_2–R–COOH, in aqueous solutions.[9] However, opposite ideas also were reported.[10] In this regard, in 1930, Harris was able to provide direct evidence through doing many titrations and experiments to show that an amino acid molecule does possess, in preponderant proportion, a zwitterionic rather than a non-zwitterionic classical structure.[11] In a recent study, amino acids were considered as neutral species,[12] while previous studies showed that they can exist in zwitterionic form. So it is necessary to investigate the real amino acid species in aqueous solutions.

Klotz and Gruen performed many experiments and compared the ionization constants of the amino groups in *p*-amino benzoic acid (PABA) and its esteric compounds to reveal that PABA is primarily neutral (i.e. free of any charge) in its isoelectric point (pI = 3.68).[13] Other studies

showed that PABA exists in neutral and not in zwitterionic form in its isoelectric point in aqueous solutions.[14,15] Yet to have further evidence, alternative procedures are required for confirming the above mentioned assumptions such as that presented in this article.

Room temperature ionic liquids (RTILs)[16–18] are known as green solvents and applied in different chemical scopes, such as electrochemistry,[19] batteries and fuel cells investigations,[20,21] chemicals synthesis,[22] catalytic processes,[23] and separation sciences.[24–26] Also, interactions of chemical compounds with ILs can be considered as models of bio-membranes for studying the membrane permeability or structure-activity relationships. It has been reported that the distribution coefficients of ionized forms of solutes in ILs are between one and three orders of magnitude lower than those of the molecular substances.[27,28] So, studying the partitioning behaviors of different compounds, specifically the amphoteric substances, in IL/H_2O system would be a way to obtain information about their different charged species including the zwitterions.

In this work, a simple and efficient methodology is introduced to characterize zwitterionic or non-zwitterionic structure of glycine, as a model amino acid, as well as that of PABA in the isoelectric points by studying their partitioning behaviors between aqueous and ionic liquid phases. The ionic liquids used in this study have imidazolium-based chemical structures: 1-butyl-3-methylimidazolium hexaflorophosphate, [C_4mim][PF_6]; 1-octyl-3-methylimidazolium tetrafloroborate, [C_8mim][BF_4], and 1-octyl-3-methylimidazolium hexaflorophosphate, [C_8mim][PF_6].

2. Experimental

2. 1. Instrument

The UV-Vis absorption spectra were recorded against the solvent blank at room temperature, using Ultrospec 4000 spectrophotometer (Pharmacia Biotech). A Metrohm 780 pH-meter was applied for pH measurements. The NMR spectra were recorded using a Brucker-Advanced DPX/250 (^{1}H NMR 250 MHz and ^{13}C NMR 62.9 MHz) spectrophotometer.

2. 2. Reagents

Ammonium hexafluorophosphate and sodium tetrafluoroborate were purchased from Fluka; 1-bromobutane, 1-bromooctane, 1-methylimidazolium, glycine, *p*-amino benzoic acid (PABA), ninhydrin, and hydrindantin dihydrate were purchased from Merck Chemical Company with the highest available purity and were used without further purification. The ionic liquids (Table1): 1-butyl-3-methylimidazolium hexaflorophosphate, [C_4mim][PF_6]; 1-octyl-3-methylimidazolium tetrafloroborate, [C_8mim][BF_4] and 1-octyl-3-methylimidazolium hexaflorophosphate, [C_8mim][PF_6], were synthesized as described in literature[29,30] and their chemical structures were verified by using NMR spectroscopy. The obtained NMR spectra of ILs were in good agreement with the previously reported spectra[28,29,31,32] and no traces of impurities were observed. Distilled deionized water was used throughout this work.

2. 3. Procedure

Individual aqueous solutions containing 1.0×10^{-3} mol L^{-1} of either glycine or PABA (each with a volume of 500 µl) were brought into contact with 50 µl of IL at room temperature in a stoppered glass test tube. The ionic strengths of aqueous solutions were kept constant using the 0.10 mol L^{-1} KCl solution for all pH values. Each system was vigorously stirred with a magnetic stirrer for 30 minutes and then both phases were carefully separated using a centrifugation device. The partition coefficients of both glycine and PABA between the IL phase and aqueous solution (IL/H_2O system) were calculated according to the following equation: $K_{IL/W} = [(C_i - C_f)V_{aq}]/[C_f V_{IL}]$ where C_i and C_f, respectively, refer to the initial and final concentrations of each compound in aqueous phase; V_{aq} and V_{IL} refer to the aqueous and IL phase volumes, respectively. Final concentration of PABA in the aqueous phase was directly determined by using UV-Vis spectrophotometry. Final concentration of glycine in aqueous phase was determined by ninhydrine method.[33] Generally, in this method the glycine solution is mixed with a solution prepared by dissolving 2.0 g ninhydrin and 0.30 g hydrindantin in 75 mL DMSO and 25 ml of sodium acetate buffer in pH 6.4. The mixture is heated up in a boiling water bath for a period of 5 minutes. Afterward, it is immediately cooled in an ice-bath. The absorbance of the mixture is measured with spectrophotometer at 575 nm.

It is stressed that each point presented on charts in Figures 1 and 2 is the average of triplicate measurement.

3. Results and Discussion

3. 1. Partitioning of Glycine into Imidazolium-Based ILs

As it is shown in Figure 1, comparison at different pHs, partition coefficient of glycine is relatively high in the pH region where its cationic (A^+) and anionic (A^-) species (Table 1) are dominant. However, the *K* value for distribution of glycine between water and [C_8mim][BF_4] is higher (up to $K = 2.0$) at low pH.

Electrostatic interactions of A^+ and A^-, respectively, with the anionic and cationic parts of the studied ILs are responsible for showing this behavior.[30,34] Partition coefficient of the species with net zero-charge (i.e, either a zwitterionic species with both positive and negative charges in

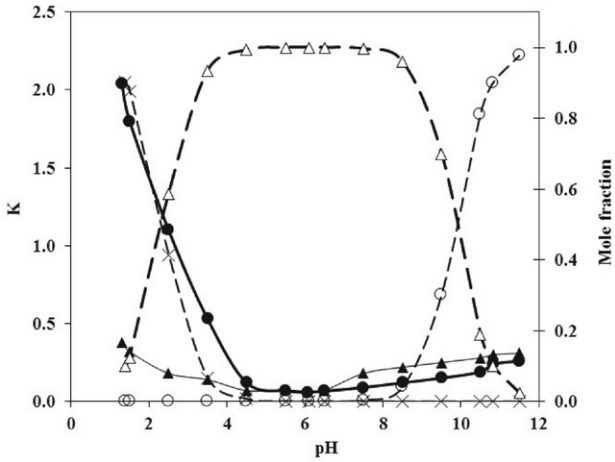

Figure 1. Partition coefficients (*K*) of glycine between water and different ionic liquids: (▲), $[C_4mim][PF_6]$; (●), $[C_8mim][BF_4]$. Mole fraction of various chemical forms of glycine in different pH values: (×), cationic form (A^+); (Δ), zwitterionic form ($A^{\pm}$); (○), anionic form (A^-).

Table 1. Zwitterionic, cationic and anionic chemical structures of Glycine pK1 = 2.35, pK2 = 9.77, pI = 6.06)and p-amino benzoic acid, PABA, (pK1 = 2.49, pK2 = 4.87, pI = 3.68).

	Chemical structure and abbreviation	
	Glycine	PABA
Cationic:	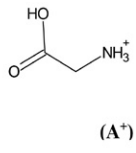 (A^+)	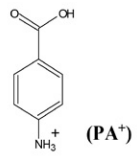 (PA^+)
Zwitterionic:	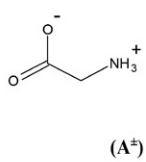 ($A^{\pm}$)	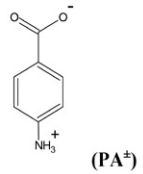 ($PA^{\pm}$)
Neutral:	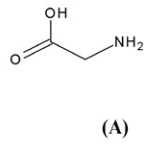 (A)	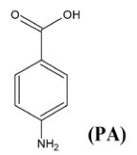 (PA)
Anionic:	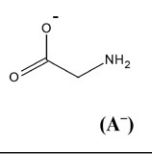 (A^-)	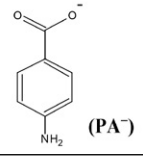 (PA^-)

one molecule, or a neutral species that does not have any charge) of glycine ($A^{\pm}$) is the lowest as a consequence of diminishing of its electrostatic interactions with IL due to the presence of a net zero-charge on the molecule. Moreover, in spite of simultaneous presence of two ionized groups, i.e. $^+NH_3$ and COO^-, the hydrophobicity of glycine molecule decreases so that a lower partition coefficient of its zwitterionic form, $A^{\pm}$, in the pH range 4.0–8.0 is achieved. This behavior showed that the net zero-charge of glycine species at its isoelectric point (pH 6.06) has a zwitterionic (not neutral) structure; because of this, hydrophobicity and consequently its extraction into IL phase is the lowest.

These results show that the number of ionized groups in a molecule is a determining factor for its extraction into the IL phase. Since glycine has two ionized groups ($^+NH_3$ and COO^-) in its isoelectric point, but in acidic or basic conditions has only one of these ionized groups (i.e. $^+NH_3$ or COO^-, respectively, in acidic and basic solutions), partitioning of its zwitterionic form into IL phase is not better compared to its other two forms. These results confirm that glycine has a zwitterionic structure in its isoelectric point which was also already verified by Harris.[11]

If glycine is neutral (instead of being zwitterion) in its isoelectric point, then it will be expected to have a higher partition coefficient due to a more hydrophobic character in comparison to its both cationic (A^+) and anionic forms (A^-).

It is noticeable that charge densities of the ionic constituents of IL phase may affect its extracting ability when it interacts with different forms of an amino acid such as glycine. For instance, the electrostatic interaction of cationic form of glycine (A^+) with the anionic part of an IL, i.e. BF_4^- or PF_6^-, depends on the value of the charge density of these ions. Table 2 provides the calculated charge densities of constituent ions of the ILs used in this study.[34] As it is shown in this table, the charge density of BF_4^- is higher than PF_6^-; also quantum chemical calculations indicated that the effective negative charge in BF_4^- is much higher than in PF_6^-.[35] Therefore, stronger electrostatic interaction between the cationic form of glycine and BF_4^-, and consequently a higher extraction of A^+ into BF_4^--based ILs, is expected as demonstrated in Figure 1.

It has been reported that the presence of water in ionic liquids may have important implications on the properties of room temperature ILs as solvents, such as conductivity, viscosity and diffusivity.[36] The water content of ILs is an important parameter that must be taken into consideration for evaluating the different extraction behaviors of ILs. But, before continuing the following discussion, it should be mentioned that in this text, the water contents of ILs refers to the amount of water that ILs are capable to absorb during their contact time with aqueous phase for a duration of 30 min in all the experiments. In this contact, the ion-pair association between cationic and anionic constituents of an IL is partially disrupted in the presence of water due to the development of H-bonding between water and the anionic part of the IL. For imidazolium-based ILs, it has been reported[37] that water molecules (in the content range of 0.2–1.0 mole water per liter of IL) are mostly in free (not self-associated) state but could bind to the anionic constituent, i.e. PF_6^- or BF_4^-, of the IL. Furthermore, the

bulky cations of ILs containing long alkyl chains can organize water molecules around themselves. These types of ILs undergo hydrophobic hydration in water that is usually known as the formation of more oriented and rigid structures of water surrounding the ILs.[38,39] In this situation, the interaction between anionic and cationic constituents of the IL decreases; however, the electrostatic interactions between cationic form of glycine (A^+) and anionic part of IL enhances. Therefore, the partition coefficients of glycine in the pH values that exists in its cationic form directly depend on the water content of IL.

According to literature,[40] the water contents of ILs decrease in the order of $[C_8mim][BF_4]$ > $[C_4mim][PF_6]$ > $[C_8mim][PF_6]$, which exactly follows the same order found for ILs in the extraction of cationic form of glycine (Figure 1). It is to be noticed that the partition coefficient of glycine, when $[C_8mim][PF_6]$ was used as IL, was so low that it could not be shown in Figure 1.

In brief, both water contents of ILs as well as charge density of their anionic parts make cationic form of glycine to be extracted into IL phase in an order of $[C_8mim][BF_4]$ > $[C_4mim][PF_6]$ > $[C_8mim][PF_6]$, (Figure 1).

At pHs ≥ 7 (Figure 1) where anionic form of glycine (A^-) is dominant, water content and charge density of the cationic form of IL (i.e. the imidazolium ion) could be examined as the possible driving forces for extraction of A^- into the IL phase. It should be noticed again that the partition coefficients, when $[C_8mim][PF_6]$ was used as IL, were so low that they are not shown in this figure. However, the order of ILs for partitioning of A^- could be considered as $[C_4mim][PF_6]$ > $[C_8mim][BF_4]$ > $[C_8mim][PF_6]$ based on data shown in Figure 1. This is in agreement with the order of charge densities of cationic parts of ILs (Table 2). The $[C_4mim][PF_6]$, with both higher charge density in its cationic part and lower water content than $[C_8mim][BF_4]$, has provided higher partitioning for the anionic forms of glycine. This observation shows that charge density of cationic part of ILs is favorable for extraction of glycine. It seems that the extraction of A^- is favored by the water content of the IL when ILs have similar cationic constituents but different water contents.

Extraction of A^- into $[C_8mim][BF_4]$, with a higher water content, was found to be higher than that of $[C_8mim][PF_6]$, which has the least water content. The results obtained for partition coefficients of A^- in different ILs reveal that both charge density of the cationic part of IL and its water content are responsible for the extraction of A^- but they may counteract. As it is shown in Figure 1, the differences in the values of the partition coefficients of A^- in different ILs are not as remarkable as those observed for A^+ in different ILs. It should be mentioned that $[C_4mim][BF_4]$ could not be studied in this work as it is soluble in water.

The order of ILs for partitioning of zwitterionic form of glycine is as follows: $[C_8mim][BF_4]$ > $[C_4mim][PF_6]$ > $[C_8mim][PF_6]$. Polarity and water content of ILs are concluded to be the effective parameters that could explain the above observation. Partition coefficient is more dependent on the charge density of the ionic components of ILs than on its water content (which in a way reflects the polarity of IL). As $[C_8mim][PF_6]$ is a least polar IL with least water content, it is expected that glycine as a polar compound (log*K* in octanol is around −3) would have the smallest *K* in this IL.

Table 2. Chemical structures and charge densities of ionic parts of the ionic liquids used

Ion	Charge density (e/Å^3)
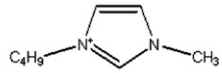 1-Butyl-3-methylimidazolium, $[C_4mim]^+$	0.00541
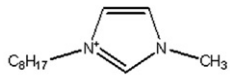 1-Octyl-3-methylimidazolium $[C_8mim]^+$	0.00306
PF_6^-	0.00941
BF_4^-	0.01471

3. 2. Partitioning of p-amino Benzoic Acid Into Imidazolium-Based ILs

Partitioning behavior of PABA between water and imidazolium-based IL phases, at different aqueous pH values, was investigated. As shown in Figure 2, partition coefficient of PABA was the highest at its isoelectric point showing that the hydrophobicity of PABA could be the reason for its higher extraction in the IL phase. This consequently proves that PABA exists in a neutral rather than in a zwitterionic form at its isoelectric point. At pH values higher or lower than the isoelectric pH, ionic forms of PABA (PA^- and PA^+), with lower hydrophobicity than its neutral form (PA), have lower tendency for transporting into the IL phase. Therefore, the electrostatic interactions of PA^- and PA^+ with ILs are the driving forces for extraction of PABA into IL phase. It is remarkable that the extraction of PABA into the studied ILs is in the order of $[C_8mim][BF_4]$ > $[C_4mim][PF_6]$ > $[C_8mim][PF_6]$, which is in agreement with the order of water content of ILs as was mentioned previously. Furthermore, higher ability of BF_4^- than PF_6^- for H-bond formation with –COOH and $–NH_2$ groups[35] of PABA could be another reason for higher extraction of PABA into $[C_8mim][BF_4]$.

Thus hydrophobicity and electrostatic interactions of solutes with ILs are two driving forces for their partitioning into IL phase. It seems that the effect of hydrophobicity is more significant than that of the electrostatic interactions, because an ionic molecule despite of having ability for elec-

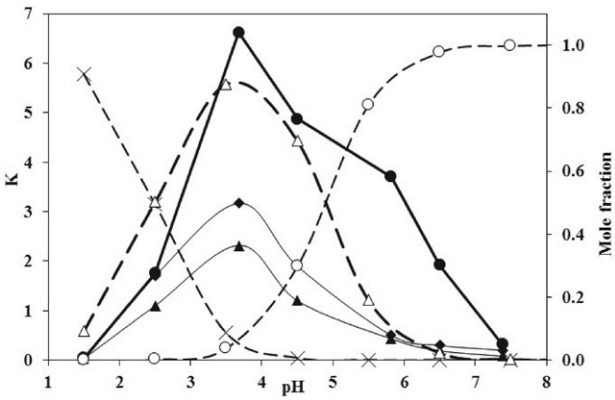

Figure 2. Partition coefficients (K) of PABA between water and different ionic liquids: (▲), $[C_8mim][PF_6]$; (◆), $[C_4mim][PF_6]$; (●) $[C_8mim][BF_4]$. Mole fraction of various chemical forms of PABA at different pH values: (×), cationic form (PA^+); (Δ), neutral form (PA); (○), anionic form (PA^-).

trostatic interactions with ILs, is less hydrophobic than a neutral molecule and its extraction into IL phase is lower.

The partitioning behaviors of either glycine (Figure 1) or PABA (Figure 2) were found to follow a similar pattern in all the studied ILs as is demonstrated by their corresponding curves. This indicates that each of the studied ILs can be utilized for investigating the partitioning behavior of a target amphoteric compound such as glycine and PABA in order to specify either its zwitterionic or non-zwitterionic structures.

It is noticeable that according to previous reports, an ion-exchange mechanism could be proposed for extraction of ionic forms of amphoteric compounds into IL phase.[30,34] So extracted ionic forms of glycine or PABA into IL phase could be as $[RNH_3]^+[BF_4]^-$, $[RNH_3]^+[PF_6]^-$ or $[Rmim]^+[RCO_2]^-$ forms.

4. Conclusion

Partitioning behaviors of glycine and *p*-amino benzoic acid, as two model substances for amphoteric compounds, into imidazolium-based ILs $[C_8mim][BF_4]$, $[C_4mim][PF_6]$, and $[C_8mim][PF_6]$ was studied. The pH-dependent partition coefficients of both compounds revealed the zwitterionic structures of glycine and non-zwitterionic (neutral) structure of *p*-amino benzoic acid in their isoelectric points. Specification of zwitterionic or non-zwitterionic structures of amphoteric compounds through their partitioning between water and IL phases was found to be a simple, fast and reliable method in comparison to the past reported procedures.

Acknowledgments

The authors are grateful to Shiraz University Research Council for financial support of this project.

6. References

1. Z. Yang, Q. Li, G. Yang, *Future Med. Chem.* **2016**, *8,* 2245–2262 **DOI:**10.4155/fmc-2016-0176
2. R. Marchese, R. Gandori, P. Carloni, S. Raugei, PLoS Comput. Biol. **2010**, *6,* 1–11. **DOI:**10.1371/journal.pcbi.1000775
3. T. Wyttenbach, M. Witt, M. T. Bowers, *J. Am. Chem.* Soc. **2000,** *122,* 3458–3464. **DOI:**10.1021/ja992546v
4. W. D. Price, R. A. Jockusch, E. R. Williams, *J. Am. Chem. Soc.* **1997**, *119,* 11988–11989. **DOI:**10.1021/ja9711627
5. R. Wu, T. B. McMahon, *Can. J. Chem.* **2005**, *83,* 1978–1993. **DOI:**10.1139/v05-205
6. R. Wu, T. B. McMahon, *J. Am. Chem.* **2007**, *129,* 4864–4865. **DOI:**10.1021/ja068715a
7. R. WuTerry, B. McMahon, *J. Am. Chem.* **2008**, *130,* 3065–3078. **DOI:**10.1021/ja076685l
8. R. Wu, R. A. Marta, J. K. Martens, K. R. Eldridge, T. B. McMahon, *J. Am. Soc. Mass Spectrom.* **2011**, *22,* 1651–1659. **DOI:**10.1007/s13361-011-0178-9
9. E.Q. Adams, *J. Am. Chem. Soc.* **1916**, *38,* 1503–1510. **DOI:**10.1021/ja02265a008
10. L. Michaelis, *Hydrogen ion concentration*, second ed. London, **1926**.
11. L. J. Harris, *Biochem. J.* **1930**, *24,* 1080–1097. **DOI:**10.1042/bj0241080
12. C. Bretti, O. Giuffrè, G. Lando, S. Sammartano, SpringerPlus, **2016**, *5,* 928–949. **DOI:**10.1186/s40064-016-2568-8
13. I. M. Klotz, D. M. Gruen, *J. Am. Chem. Soc.* **1945**, *67,* 843–846. **DOI:**10.1021/ja01221a044
14. P. H. Bell, R. O. Robin, *J. Am. Chem. Soc.***1942**, *64,* 2905–2917. **DOI:**10.1021/ja01264a055
15. K. Venkateswaran, J. M. Stadlbauer, Z. Wu, H. A. Gillis and D. C. Walker, *J. Phys. Chem.* **1996**, *100,* 3569–3572. **DOI:**10.1021/jp9518320
16. T. Walton, *Chem. Rev.* **1999**, *99,* 2071–2084. **DOI:**10.1021/cr980032t
17. M. Koel, Ionic *liquids in chemical analysis*. Taylor & Francis, Boca Raton, London New York, **2009.** **DOI:**10.1201/9781420046472
18. J. L. Anderson, J. Ding, T. Welton, D.W. Armstrong, *J. Am. Chem. Soc.* **2002**, *124,* 14247–14254. **DOI:**10.1021/ja028156h
19. L. Kong, Q. Chen, X. Shen, G. Zhu, J. Zhu, *J. Colloid. Interface Sci.* **2018**, *532,* 261–271. **DOI:**10.1016/j.jcis.2018.07.135
20. S. Chauque, F.Y. Oliva, O. R. Cámara, R. M. Torresi, *J. Solid State Electrochem.* **2018**, *22,* 3589–3596. **DOI:**10.1007/s10008-018-4078-9
21. V. M. Ortiz–Martínez, A. Ortiz, V. Fernández-Stefanutoc, E. Tojo, M. Colpaert, B. Améduri, I. Ortiz, *Polymer* **2019**, *19,* 121583–121593. **DOI:**10.1016/j.polymer.2019.121583
22. H. Jia, R. Kloepsch, X. He, M. Evertz, S. Nowak, J. Li, M. Winter, T. Placke, *Acta Chim. Slov.* **2016**, *63,* 470–483. **DOI:**10.17344/acsi.2016.2243
23. E. Weiss, B. Dutta, A. Kirschning, R. Abu-Reziq, *Chem. Mater.* **2014**, *26,* 4781–4787. **DOI:**10.1021/cm501840d
24. L. Sheikhian, S. Bina, *J. Chromatogr. B* **2016**, *1008,* 34–43.

DOI:10.1016/j.jchromb.2015.11.047
25. W. Fam, J. Mansouri, H. Li, J. Hou, V. Chen, *Ind. Eng. Chem. Res.* **2019**, *58,* 3304–3313. **DOI:**10.1021/acs.iecr.8b05027
26. M. Rzelewska-Piekut, M. Regel-Rosocka, *Sep. Purif. Technol.* **2019**, *212,* 791–801. **DOI:**10.1016/j.seppur.2018.11.091
27. G. Absalan, M. Akhond, L. Sheikhian, *Talanta* **2008**, *77,* 407–411. **DOI:**10.1016/j.talanta.2008.06.049
28. S. Carda–Broch, A. Berthod, D. W. Armstrong, *Anal. Bioanal. Chem.* **2003**, *375,* 191–199. **DOI:**10.1007/s00216-002-1684-1
29. P. Bonhote, A. P. Dias, N. Papageorgion, K. Kalyanasundaram, M. Gratzel, *Inorg. Chem.* **1996**, *35,* 1168–1178. **DOI:**10.1021/ic951325x
30. J. Wang, Y. Pei, Y. Zhao, Z. Hu, *Green Chem.* **2005**, *7,* 196–202. **DOI:**10.1039/b415842c
31. J. G. Huddleston, A. E. Visser, W. M. Reichert, H. D. W. G. A. Brokers, R.D. Rogers, *Green Chem.* **2001**, *3,* 156–164. **DOI:**10.1039/b103275p
32. J. D. Holbrey, K. R. Seddon, *J. Chem. Soc. Dalton Trans.* **1999**, 2133–2139. **DOI:**10.1039/a902818h
33. S. W. Sun, Y. C. Lin, Y. M. Weng, M. J. Chen, *J. Food Compos. Anal.* **2006**, *19,* 112–117. **DOI:**10.1016/j.jfca.2005.04.006
34. G. Absalan, M. Akhond, L. Sheikhian, *Amino Acids* **2010**, *39,* 167–174. **DOI:**10.1007/s00726-009-0391-z
35. H. Tsunekawa, A. Narumi, M. Sano, A. Hiwara, M. Fujita, H. Yokoyama, *J. Phys. Chem. B* **2003**, *107,* 10962–10966. **DOI:**10.1021/jp0300546
36. A. Noda, K. Hayamizu, M. Watanabe, J. Phys. Chem. B, **2001**, *105,* 4603–4610. **DOI:**10.1021/jp004132q
37. L. Cammarata, S. G. Kazarian, P. A. Salter, T. Welton, *Phys. Chem. Chem. Phys.* **2001**, *3,* 5192–5200. **DOI:**10.1039/b106900d
38. V. V. Yaminsky, E. A. Vogler, Current Opinion in Colloid and Interface Science, **2001**, *6(4),* 342–349. **DOI:**10.1016/S1359-0294(01)00104-2
39. H. Shekaari, F. Jebali, *Fluid Phase Equilibr.* **2010**, *295,* 68–75. **DOI:**10.1016/j.fluid.2010.04.002
40. M. G. Freire, L. M. N. B. F. Santos, A. M. Fernandes, J. A. P. Coutinho, I. M. Marrucho, *Fluid Phase Equilibr.* **2007**, *26,* 449–454. **DOI:**10.1016/j.fluid.2007.07.033

Povzetek

Študirali smo porazdelitvene koeficienta glicina in *p*-amino benzojske kisline, dveh modelnih amfoternih spojin, v ionske tekočine (IL) na osnovi imidazola, to so $[C_8mim][BF_4]$, $[C_4mim][PF_6]$, and $[C_8mim][PF_6]$. Porazdelitveni koeficienti so pokazali, da ima glicin dvoionsko (zwitterionsko) strukturo, medtem ko ima *p*-amino benzojska kislina nevtralno (ne-zwitterionsko) strukturo v izoelektrični točki. Pokazali smo, da je določitev dvoionske ali neionske strukture amfoternih snovi na osnovi njihovega porazdeljevanja med vodno in IL fazo, enstavna, hitra in zanesljiva metoda v primerjavi z metodami, o katerih so poročali v preteklosti.

Except when otherwise noted, articles in this journal are published under the terms and conditions of the Creative Commons Attribution 4.0 International License

Scientific paper

Preparation of Quinoline-2,4-dione Functionalized 1,2,3-Triazol-4-ylmethanols, 1,2,3-Triazole-4-carbaldehydes and 1,2,3-Triazole-4-carboxylic Acids

David Milićević,[1] Roman Kimmel,[1] Damijana Urankar,[2] Andrej Pevec,[2] Janez Košmrlj[2,*] and Stanislav Kafka[1,*]

[1] *Faculty of Technology, Tomas Bata University in Zlin, Vavrečkova 275, 760 01 Zlin, Czech Republic*

[2] *Faculty of Chemistry and Chemical Technology, University of Ljubljana, Večna pot 113, SI-1000 Ljubljana, Slovenia*

** Corresponding author: E-mail: kafka@utb.cz; Janez.Kosmrlj@fkkt.uni-lj.si*
Tel: (+420)-576031115, (+386)-14798558

Received: 06-30-2019

Dedicated to Professor František Liška, University of Chemistry and Technology, Prague and Charles University, on the occasion of his 80th birthday.

Abstract

(1-(2,4-Dioxo-1,2,3,4-tetrahydroquinolin-3-yl)-1*H*-1,2,3-triazol-4-yl)methyl acetates substituted on nitrogen atom of quinolinedione moiety with propargyl group or (1-substituted 1*H*-1,2,3-triazol-4-yl)methyl group, which are available from the appropriate 3-(4-hydroxymethyl-1*H*-1,2,3-triazol-1-yl)quinoline-2,4(1*H*,3*H*)-diones unsubstituted on quinolone nitrogen atom by the previously described procedures, were deacetylated by acidic ethanolysis. Thus obtained primary alcohols, as well as those aforenamed unsubstituted on quinolone nitrogen atom, were oxidized to aldehydes on the one hand with pyridinium chlorochromate (PCC), on the other hand with manganese dioxide, and to carboxylic acids using Jones reagent in acetone. The structures of all prepared compounds were confirmed by ^{1}H, ^{13}C and ^{15}N NMR spectroscopy. The corresponding resonances were assigned on the basis of the standard 1D and gradient selected 2D NMR experiments (^{1}H–^{1}H gs-COSY, ^{1}H–^{13}C gs-HSQC, ^{1}H–^{13}C gs-HMBC) with ^{1}H–^{15}N gs-HMBC as a practical tool to determine ^{15}N NMR chemical shifts at the natural abundance level of ^{15}N isotope.

Keywords: 1,2,3-triazole; quinoline-2,4-dione; hydroxymethylderivatives; aldehydes; carboxylic acids

1. Introduction

1,4-Disubstituted 1,2,3-triazole is considered to be a suitable structural part of compounds that could be of interest from the point of view of various research areas. Apart from many applicable properties including coordination[1–3] and catalytic abilities,[4] as well as photophysical and electrochemical characteristics,[5–8] 1,2,3-triazoles further exhibit large variety of medical activities.[9–14] Some of us have previously dealt with preparation of pyridine appended 1,2,3-triazoles and their synthetic utilization.[15] 1,2,3-Triazolium salts prepared from them have shown an efficiency in palladium-catalyzed Suzuki–Miyaura coupling.[15] From these salts, Ru(II) complexes were prepared, which have shown a catalytic activity in the oxidation of alcohols with *tert*-butyl hydroperoxide.[16] Cp*-Ir(III) complexes with additional chelating ligands containing 1,2,3-triazole ring are useful as catalysts for oxidation of cyclooctane to cyclooctanone.[17] A bis(pyridyl-functionalized 1,2,3-triazol-5-ylidene)-palladium(II) complex $[Pd(Py\text{-}tzNHC)_2]^{2+}$ was found to catalyze the copper-, amine-, phosphine-, and additive-free aerobic Sonogashira alkynylation of (hetero)aryl bromides in water as the only reaction solvent.[18]

Similarly, quinoline-2,4-dione based compounds were also recognized as distinctively attractive species, when taking into account their versatile beneficial purposefulness.[19]

The mentioned fact inspired us to synthesize never before described 1,2,3-triazole- and quinoline-2,4(1*H*,3*H*)dione-based bis-heterocycles. In 2011, we reported the synthesis of 3-alkyl/aryl-3-(1*H*-1,2,3-triazol-1-yl)quinoline-2,4(1*H*,3*H*)-diones by the click reaction of appropri-

ate 3-azidoquinolinediones with terminal alkynes.[20] In the same year, the patent application[21] was administered, which comprised preparation of tautomeric 4-hydroxyquinolin-2-ones with 1,2,3-triazol-1-yl group in position 3 of quinolinone scaffold that are effective as adenosine monophosphate-activated protein kinase (AMPK) activators. Since then still more reports on the 4-hydroxy-quinolin-2-one derivatives, in which hydrogen atom of hydroxyl group was replaced with various substituents comprising 1,2,3-triazole pattern, have been published.[22–29] Some of these substances have been found to show some acetylcholine receptors binding affinity.[22] Recently we have reported an utilization of the above mentioned 3-(1*H*-1,2,3-triazol-1-yl)quinoline-2,4(1*H*,3*H*)-diones unsubstituted on the nitrogen atom of the quinolone moiety for the synthesis of bis(1,2,3-triazole) functionalized quinoline-2,4-diones.30 In frame of that study,[30] in place of starting materials were used, among others, derivatives of (1*H*-1,2,3-triazol-4-yl) methanol, in which hydroxyl group was protected by acetylation and their structure was subsequently modified. There was offered the idea of the removal of protecting acetyl group and the oxidative conversion of thus obtained primary alcohols as well as starting triazolylmethanols to the corresponding 1,2,3-triazole-4-carbaldehydes and 1,2,3-triazole-4-carboxylic acids.

In terms of biological effects, 1,2,3-triazole-4-carbaldehydes are particularly interesting. For example, a series of them has been found to prove tuberculostatic effect.[31] Some (1*H*-1,2,3-triazol-4-yl)methanols exhibit cytotoxic activity.[32] Some known 1-substituted 1,2,3-triazol-4-carboxylic acids have antibacterial effect against *Staphylococcus aureus*.[33]

2. Results and Discussion

Compounds **1**, **2** and **3** (Figure 1) were obtained through the multistep synthetic pathway, which we have developed recently,[30] and were utilized as starting compounds in this study.

Although acetates **1a,b** were prepared by acetylation of the corresponding primary alcohols **4a,b**,[30] we exploited them as model compounds and dealt with finding a suitable procedure for their deacetylation back to the mentioned alcohols so that we can apply it to prepare alcohols **5a,b** and **6a–f** from the more laboriously obtainable corresponding acetates **2a,b** and **3a–f**. At first, we tried processing with a methanolic solution of sodium methoxide, however, in parallel with ester methanolysis, undesirable nucleophilic quinoline-2,4-dione ring opening and successive reactions took place resulting in mixtures, from which only corresponding *N*-substituted anthranilic acids and eventually their methyl esters were isolated after neutralization with diluted hydrochloric acid. Also alkaline hydrolysis of ester group is accompanied with above mentioned ring opening; the treatment of **1b** with a solution of potassium hydroxide in aqueous ethanol afforded corresponding anthranilic acid as main product.

Finally, acidic alcoholysis (37% HCl : EtOH 1:100 v/v) has proved to be suitable. After the successful deacetyl-

Table 1. Acidic alcoholysis of acetates **1a,b**, **2a,b**, and **3a–f**.

Entry	Acetate	R^1	R^2	Time (h)	Alcohol	Yield (%)
1	**1a**	Me	–	3	**4a**	92[a]
2	**1b**	Ph	–	3	**4b**	93[a]
3	**2a**	Me	–	3	**5a**	83[b]
4	**2b**	Ph	–	3	**5b**	87[b]
5	**3a**	Me	Bn	3.5	**6a**	86[a]
6	**3b**	Me	Ph	3.5	**6b**	98[a]
7	**3c**	Me	2-Py	2.5	**6c**	80[a]
8	**3d**	Ph	Bn	4	**6d**	89[a]
9	**3e**	Ph	Ph	3	**6e**	97[a]
10	**3f**	Ph	2-Py	3	**6f**	87[a]

[a] Refers to pure (by TLC and IR) isolated product. [b] Refers to percent yield of crystallized product.

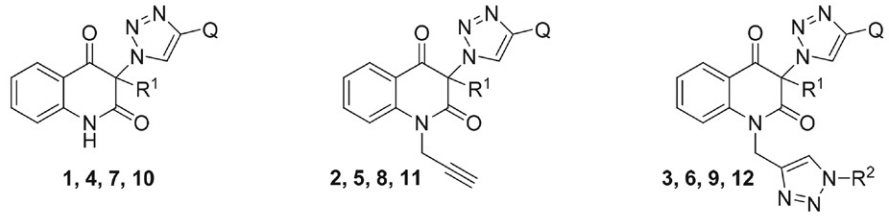

1, 2, 4, 5, 7, 8, 10, 11	a	b
R^1	Me	Ph

3, 6, 9, 12	a	b	c	d	e	f
R^1	Me	Me	Me	Ph	Ph	Ph
R^2	Bn	Ph	2-Py	Bn	Ph	2-Py

Figure 1. Subject compounds

ation of compounds **1a,b**, this method was applied also to deacetylation the acetates **2a,b** and **3a–f**. This reaction was carried out by boiling the reaction mixtures and was finished in 2.5–4 hours. The appropriate primary alcohols were obtained with yields 80–90% (see Table 1).

The reaction conditions of the conversion of prepared alcohols to the corresponding aldehydes were optimized for the oxidation of alcohols **4a,b** to aldehydes **7a,b**. The results are summarized in the Table 2. From the range of usual reagents used for these transformations, we first chose pyridinium chlorochromate (PCC). As can be found in literature,34 oxidations of primary alcohol to aldehydes can proceed smoothly with good yields using 1.2 mmol PCC per 1 mmol substrate in dichloromethane (DCM) at room temperature. However, the conversion of **4a** under these conditions is very slow, because of its low solubility in DCM. Boiling the reaction mixture, and particularly by performing the reaction in a microwave reactor in a closed vial at 40 °C, the time required to react the substrate is significantly reduced, but at the same time decreases the yield of **7a**. Higher yields of **7a** were achieved when DCM was replaced with acetone, in which **4a** is more soluble; we have achieved the best yield (36%) of **7a** by increasing the excess of PCC and allowing the reaction to proceed for 22 hours at room temperature.

Oxidation of **4b**, which is more soluble in DCM than its methyl analogue **4a**, was performed in this solvent with the best yield (44%) of **7b** using 1.2 mmol PCC per 1 mmol **4b** and boiling of the reaction mixture, whereas the reaction was finished within 1.5 hour. When the mixture of the same initial composition was heated in a microwave reactor in a closed vial to 40 °C for 10 minutes, the yield of **7b** was only slightly lower than the former. The same applies to carrying out the reaction in DCM with 1.5 mmol PCC per 1 mmol **4b** at room temperature. Further increasing of the amount of PCC results in a shorter reaction time together with a reduction of yield of **7b**. In contrast to oxidation of **4a** to **7a**, the oxidation of **4b** with PCC in acetone under the same conditions furnished the aldehyde **7b** with significantly lower yield.

Apart from oxidation with PCC, Swern reaction, i.e. oxidation with dimethylsulfoxide (DMSO) in the presence of oxalyl chloride and *N*,*N*-diisopropylethylamine (DIPEA), was also briefly examined using slightly modified synthetic procedure from the literature,[35] however obtained yields were unsatisfactory for both, phenyl and methyl mono-triazole derivatives **7a** and **7b**, respectively. While the former resulted in 33% yield of isolated product, no product was isolated in case of the latter. The main drawback of this approach is presence of hardly removable dimethyl sulfoxide that remained in our products despite the fact that they were several times washed with ice-cold water. Apparently, utilization of relatively large quantities of water also caused significant loses of target compounds that were much more obvious in the case of methyl derivative **7a**. Moreover, we have experience that our 1,2,3-triazole- and quinoline-2,4-dione-based bis-heterocycles are more or less unstable in DMSO and therefore, the use of this solvent in their preparation is not always appropriate.

As the third option, oxidation of primary alcohols **4a,b** with MnO_2 was further studied. Comparing the reaction parameters such as reaction times and quantities of reagents, acetone was recognized superior in comparison

Table 2. Oxidation of primary alcohols **4a,b** to aldehydes **7a,b**.[a]

Entry	Alcohol	R[1]	Reagent	*n* (mmol)[b]	Time (h)	Solvent	Aldehyde	Yield (%)
1	**4a**	Me	PCC	1.7	22[c]	Me_2CO	**7a**	36[d]
2	**4a**	Me	PCC	1.2	22[c]	CH_2Cl_2	**7a**	31[d]
3	**4a**	Me	PCC	1.2	0.17[e]	CH_2Cl_2	**7a**	16
4	**4a**	Me	PCC	1.2	1.5	CH_2Cl_2	**7a**	15
5	**4a**	Me	PCC	1.2	5	Me_2CO	**7a**	23[d]
6	**4b**	Ph	PCC	1.7	1.5[c]	CH_2Cl_2	**7b**	35
7	**4b**	Ph	PCC	1.7	22[c]	Me_2CO	**7b**	26[d]
8	**4b**	Ph	PCC	1.7	0.5	CH_2Cl_2	**7b**	34
9	**4b**	Ph	PCC	2.0	1[c]	CH_2Cl_2	**7b**	31
10	**4b**	Ph	PCC	1.5	4[c]	CH_2Cl_2	**7b**	41
11	**4b**	Ph	PCC	1.2	1.5	CH_2Cl_2	**7b**	44
12	**4b**	Ph	PCC	1.2	0.17[e]	CH_2Cl_2	**7b**	42
13	**4a**	Me	DMSO	2.6	3.5[f]	Me_2CO	**7a**	0
14	**4b**	Ph	DMSO	2.6	3.5[f]	CH_2Cl_2	**7b**	33
15	**4a**	Me	MnO_2	10	1.25	Me_2CO	**7a**	60
16	**4b**	Ph	MnO_2	10	1.5	Me_2CO	**7b**	58
17	**4b**	Ph	MnO_2	15[g]	3	CH_2Cl_2	**7b**	62
18	**4b**	Ph	MnO_2	10	96[c]	CH_2Cl_2	**7b**	44

[a] Reactions were carried out in boiling reaction mixtures unless indicated otherwise. [b] Amount of reagent per 1 mmol of alcohol. [c] Carried out at room temperature. [d] Complete consumption of **4** was not reached. [e] Carried out in the microwave reactor at 40 °C. [f] For the reaction conditions see Experimental. [g] Reaction was started with 10 mmol of MnO_2, additional 5 mmol of MnO_2 were added after 2 hours.

Table 3. Oxidation of primary alcohols **5a,b** and **6a–f** to aldehydes **8a,b** and **9a–f**, respectively.

Entry	Alcohol	R^1	R^2	Reagent	Time (h)	Solvent	Aldehyde	Yield (%)
1	**5a**	Me	–	PCC	1	CH_2Cl_2	**8a**	41
2	**5a**	Me	–	MnO_2	1.25	Me_2CO	**8a**	40
3	**5b**	Ph	–	PCC	0.75	CH_2Cl_2	**8b**	38
4	**5b**	Ph	–	MnO_2	2	Me_2CO	**8b**	38
5	**6a**	Me	Bn	PCC	0.5	CH_2Cl_2	**9a**	41
6	**6b**	Me	Ph	PCC	0.5	CH_2Cl_2	**9b**	40
7	**6b**	Me	Ph	MnO_2	0.75	Me_2CO	**9b**	51
8	**6c**	Me	2-Py	PCC	0.75	CH_2Cl_2	**9c**	48
9	**6d**	Ph	Bn	PCC	0.5	CH_2Cl_2	**9d**	41
10	**6e**	Ph	Ph	PCC	0.5	CH_2Cl_2	**9e**	45
11	**6f**	Ph	2-Py	PCC	0.5	CH_2Cl_2	**9f**	41

with dichloromethane, while transformation yields were practically the same (approx. 60%) in both cases.

The findings from the above experiments were used in the oxidation of primary alcohols **5a,b** and **6a–f** to aldehydes **8a,b** and **9a–f**, respectively. In all cases, oxidation was carried out using PCC under optimum conditions for the conversion of alcohol **4b** to aldehyde **7b**, *i.e.* using 1.2 mmol PCC per 1 mmol alcohol in dichloromethane at the reflux temperature. Furthermore, the aldehydes **8a,b** and **9b** were prepared from the corresponding alcohols by oxidation with MnO_2 in acetone. Due to the very similar yields of aldehydes achieved with the use of one or the other reagent and the toxicity of Cr^{VI}-containing reagents, it can be stated that MnO_2 is a more advantageous agent than PCC.

So far described oxidations of triazolyl-4-methanols to the corresponding carboxylic acids were carried out mostly with permanganate in basic medium.[36–38] In one case, the oxidation with a mixture of sodium chlorite and sodium hypochlorite with an addition of 2,2,6,6-tetramethylpiperidine *N*-oxide (TEMPO) in phosphate buffer was patented.[39] Since basic media causes destruction of quinolinedione scaffold, the choice of reagents for the oxidation of alcohols **4a,b**, **5a,b**, and **6a–f** is limited to those, for which the presence of no base is needed. For the transformation of these alcohols to carboxylic acids **10a,b**, **11a,b**, and **12a–f**, we decided to try out Jones reagent (solution of CrO_3 in diluted sulfuric acid) in acetone. While this method has long been known and its use for the preparation of carboxylic acids has been described in many cases, we have found in the literature only one report[40] on its use for the preparation of triazole-4-carboxylic acids, which were intermediates in a multistep synthesis, without giving their yields and experimental details. Although at most 9 mol of CrO_3 per one mol of primary alcohol is usually used,[41–43] in the cases provided herein, it has been shown that the most suitable ratio is 24 mol CrO_3 per 1 mol of primary alcohol (Table 4). The acid with methyl group in position 3 of quinolone scaffold **10a** was isolated in a considerably lower yield than its phenyl analogue **10b** probably due to its significantly higher solubility in water.

Table 4. Oxidation of primary alcohols **4a,b**, **5a,b**, and **6a–f** to carboxylic acids **10a,b**, **11a,b**, and **12a–f**, respectively[a].

Entry	Alcohol	R^1	R^2	Time (h)	Carboxylic acid	Yield (%)
1	**4a**	Me	–	2.75	**10a**	33
2	**4b**	Ph	–	3	**10b**	40[b]
3	**4b**	Ph	–	3.25	**10b**	71
4	**5a**	Me	–	2.5	**11a**	55
5	**5b**	Ph	–	3	**11b**	68
6	**6a**	Me	Bn	3	**12a**	88
7	**6b**	Me	Ph	2.5	**12b**	92
8	**6c**	Me	2-Py	2.5	**12c**	84
9	6**d**	Ph	Bn	2	**12d**	75
10	**6e**	Ph	Ph	2.25	**12e**	77
11	**6f**	Ph	2-Py	2.5	**12f**	69

[a] CrO_3 (2.4 g, 24mmol) in 2M H_2SO_4 (24 mL) per 1 mmol of alcohol was used, unless otherwise stated. [b] CrO_3 (600 mg, 6.0 mmol) in 2M H_2SO_4 (6 mL) per 1 mmol of alcohol **4b** was used, complete consumption of an intermediate (apparently aldehyde **7b**) was not reached according to TLC.

All compounds were characterized by ^1H and ^{13}C and, in cases of **6a–e**, **7a,b**, **9a–f**, **10a**, and **12a–f**, also by ^{15}N NMR spectroscopy. The corresponding resonances

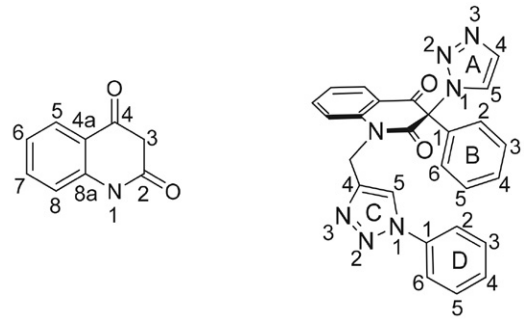

Figure 2. Designation of positions in the structure of prepared compounds.

were assigned on the basis of gradient-selected 2D NMR experiments including $^{1}H–^{1}H$ gs-COSY, $^{1}H–^{13}C$ gs-HSQC, $^{1}H–^{13}C$ gs-HMBC and $^{1}H–^{15}N$ gs-HMBC. Atoms and rings labeling scheme, which was extensively applied in the »Experimental« section is presented in Figure 2.

From the solution of **12d** in deuteriochloroform originally designed to measure NMR spectra, the crystal has grown, which we have used to corroborate the structure of this compound (Figure 3) by the single crystal X-ray structure determination. It has been found that the crystal is a solvate **12d** · $2CDCl_3$. Selected bond lengths and angles are displayed in Table 5. The X-ray diffraction study has shown that the solvate **12d** · $2CDCl_3$ crystallizes in monoclinic $P2_1/n$ space group. Intermolecular hydrogen bonds of the type O–H···N are found in the crystal structure of compound **12d** · $2CDCl_3$. Atom O2 acts as hydrogen bond donor and N5 of symmetry related molecule as acceptor and thus forming two dimensional chain extending along the *b*-axis (Figure 4, Table 6).

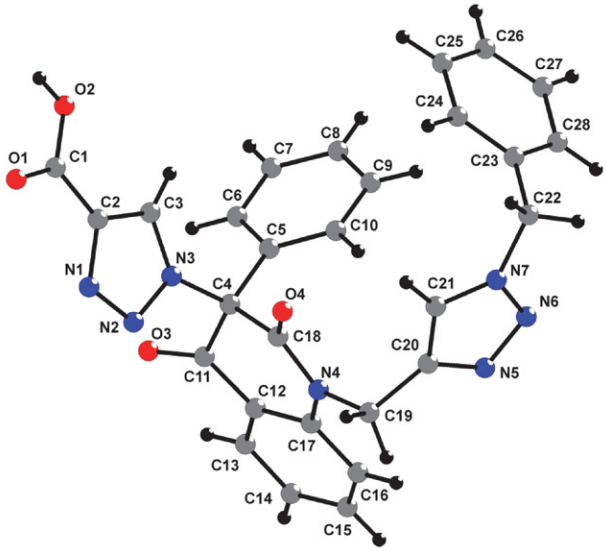

Figure 3. Crystallographic view and numbering scheme of the molecule **12d** · $2CDCl_3$. $CDCl_3$ molecules are omitted for clarity.

Table 5. Selected bond lengths (Å) and angles (°) for compound **12d** · $2CDCl_3$.

N1–N2	1.298(5)	N1–N2–N3	106.8(3)
N2–N3	1.359(5)	N5–N6–N7	106.8(4)
N5–N6	1.310(5)	N2–N3–C3	110.7(3)
N6–N7	1.328(6)	N6–N7–C21	111.2(4)
N1–C2	1.353(5)	N1–C2–C3	108.3(4)
N3–C3	1.330(5)	N3–C3–C2	104.9(3)
N3–C4	1.456(5)	N4–C17–C12	119.9(4)
N4–C17	1.424(5)	N4–C18–C4	118.0(3)
N4–C18	1.358(5)	N4–C19–C20	112.1(3)
N4–C19	1.475(5)	N5–C20–C21	107.0(4)
N5–C20	1.348(6)	N7–C21–C20	105.4(4)
N7–C21	1.328(6)	C17–N4–C18	123.2(3)
N7–C22	1.481(6)	C19–N4–C17	121.9(4)

3. Conclusions

A collection of novel 1,2,3-triazole- and quinoline-2,4(1*H*,3*H*)-dione based bis-heterocycles functional derivatives was prepared and characterized by IR, NMR and HRMS. Appropriate starting compounds with 4-(acetoxymethyl)-1*H*-1,2,3-triazole moiety were firstly deacetylated, and the obtained corresponding alcohols were further oxidized to aldehydes and carboxylic acids. Investigation of transformation approaches was carried

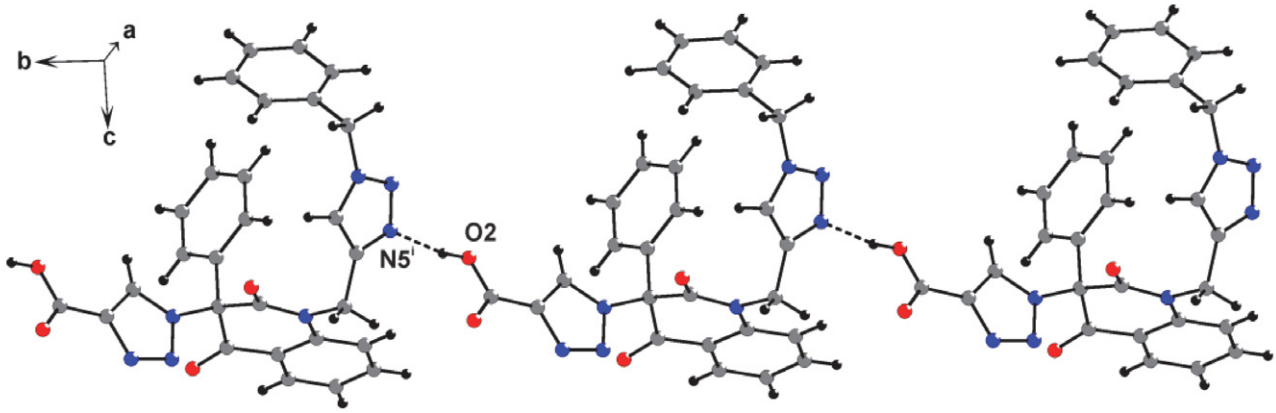

Figure 4. Hydrogen bonding interactions in the crystal structure of **12d**·$2CDCl_3$ showing the polymeric chain. Symmetry code: (i) x, y+1, z.

Table 6. Hydrogen bonding geometry for compound **12d** · $2CDCl_3$.

D–H···A	D–H (Å)	H···A (Å)	D···A (Å)	D–H···A (°)	Symmetry code
O2–H2···N5	0.82	1.90	2.700(5)	166.7	x, y+1, z

out using more accessible mono-triazoles, while optimized reaction conditions were then utilized for preparation of bis-triazole counterparts in moderate to excellent yields. Synthesized derivatives could potentially possess some desirable properties or might be exploited as precursors in further transformations.

In this article we present a group of new quinoline-2,4-dione based compounds with primary alcohol, aldehyde or carboxyl functional group on 1,2,3-triazole. Even though, the chemistry applied throughout the syntheses of our final materials is pretty elemental and straightforward, we believe that we have been handling with very promising substances and therefore, in our opinion, it was worthwhile to deal with them. Prepared compounds would not only potentially exhibit some extraordinary characteristics, but may also serve as precursors in further reactions such as esterification, peptide bond formation, nucleophilic additions to formyl group etc.

4. Experimental

The reagents and solvents were used as obtained from the commercial sources. Column chromatography was carried out on Fluka Silica gel 60 (particle size 0.063–0.2 mm, activity acc. Brockmann and Schodder 2–3). Melting points were determined on the microscope hot stage, Kofler, PolyTherm, manufacturer Helmut Hund GmbH, Wetzlar and are uncorrected. TLC was carried out on pre-coated TLC sheets ALUGRAM® SIL G/UV$_{254}$ for TLC, MACHEREY-NAGEL. NMR spectra were recorded with a Bruker Avance III 500 MHz NMR instrument operating at 500 MHz (^{1}H), 126 MHz (^{13}C) and 51 MHz (^{15}N) at 300 K, or JEOL ECZ400R/S3 instrument operating at 400 MHz (^{1}H) and 100 MHz (^{13}C). Proton spectra were referenced to TMS as internal standard, in some cases to the residual signal of DMSO-d_5 (at δ 2.50 ppm) or $CHCl_3$ (at δ 7.26 ppm). Carbon chemical shifts were determined relative to the ^{13}C signal of DMSO-d_6 (39.52 ppm) or $CDCl_3$ (77.16 ppm). ^{15}N chemical shifts were extracted from ^{1}H–^{15}N *gs*-HMBC spectra (with 20 Hz digital resolution in the indirect dimension and the parameters adjusted for a long-range ^{1}H–^{15}N coupling constant of 5 Hz) determined with respect to external nitromethane and are corrected to external ammonia by addition of 380.5 ppm. Nitrogen chemical shifts are reported to one decimal place as measured of the spectrum, however, the data should not be considered to be more accurate than ±0.5 ppm because of the digital resolution limits of the experiment. Chemical shifts are given on the δ scale (ppm). Coupling constants (*J*) are given in Hz. Multiplicities are indicated as follows: s (singlet), d (doublet), t (triplet), q (quartet), m (multiplet) or br (broadened). Infrared spectra were recorded on FT-IR spectrometer Alpha (Bruker Optik GmbH Ettlingen, Germany) using samples in potassium bromide disks and only the strongest/structurally most important peaks are listed. HRMS spectra were recorded with Agilent 6224 Accurate Mass TOF LC/MS system with electrospray ionization (ESI).

X-ray crystallography. The molecular structure of compound **12d** was determined by single-crystal X-ray diffraction methods. Crystallographic data and refinement details are given in Table 7. Diffraction data for **12d** were collected at room temperature with Agilent SuperNova dual source diffractometer using an Atlas detector and equipped with mirror-monochromated MoKα radiation (λ = 0.71073 Å). The data were processed by using CrysAlis PRO.44 All the structures were solved using SHELXS-9745 and refined against F^2 on all data by full-matrix least-squares with SHELXL–2016.[46] All non-hydrogen atoms were refined anisotropically. The C3 and C21 bonded hydrogen atoms were located in a difference map and refined with the distance restraints (DFIX) with C–H = 0.98 Å and with U_{iso}(H) = 1.2U$_{eq}$(C). All other hydrogen atoms were included in the model at geometrically calculated positions and refined using a riding model. The crystal structure **12d** contains deuterated solvent molecules ($CDCl_3$). The D and H atoms are both treated as hydrogens but the SFAC instruction for D enables the formula weight and density to be calculated correctly. The C29 and C30 bonded deuterium atoms were located in a

Table 7. Crystal data and structure refinement details for compound **12d** · 2$CDCl_3$.

	12d · 2CDCl$_3$
formula	$C_{30}H_{21}Cl_6D_2N_7O_4$
Fw (g mol^{-1})	760.29
crystal size (mm)	0.50 × 0.30 × 0.10
crystal color	colourless
crystal system	monoclinic
space group	$P\,2_1/n$
a (Å)	13.5462(6)
b (Å)	11.9884(9)
c (Å)	20.8335(10)
β (°)	92.823(4)
V (Å^3)	3379.2(3)
Z	4
calcd density (g cm^{-3})	1.494
F(000)	1544
no. of collected reflns	29191
no. of independent reflns	7754
R_{int}	0.0563
no. of reflns observed	3853
no. parameters	438
$R[I > 2\sigma(I)]^a$	0.0974
wR_2(all data)^b	0.3413
Goof, S^c	1.092
maximum/minimum residual electron density (e Å^{-3})	+0.90/–0.80

$^aR = \Sigma||F_o| - |F_c||/\Sigma|F_o|$. $^bwR_2 = \{\Sigma[w(F_o^2 - F_c^2)^2]/\Sigma[w(F_o^2)^2]\}^{1/2}$. $^cS = \{\Sigma[(F_o^2 - F_c^2)^2]/(n/p)\}^{1/2}$ where n is the number of reflections and p is the total number of parameters refined.

difference map and refined with the distance restraints (DFIX) with C–D = 0.98 Å and with $U_{iso}(D) = 1.2U_{eq}(C)$.

CCDC 1892717 (for **12d** · $2CDCl_3$) contain the supplementary crystallographic data for this paper. These data can be obtained free of charge from The Cambridge Crystallographic Data Centre *via* www.ccdc.cam.ac.uk/data_request/cif.

General procedure for the synthesis of alcohols 5a,b and 6a–f. A solution of appropriate acetate in acidified ethanol (37% HCl : EtOH 1:100 *V*/*V*) was stirred at the reflux temperature (90–100 °C in oil bath) for 2.5–4 hours. Obtained pale yellow solution was then allowed to cool to room temperature, and subsequently neutralized with saturated aqueous $NaHCO_3$. Resulting suspension was concentrated by rotary evaporation *in vacuo*, diluted with deionized water and extracted with chloroform (3–6x 50 mL). Organic phases were joined together, washed with deionized water (1x50 mL), dried over anhydrous Na_2SO_4, filtered. and volatile components were evaporated *in vacuo*. The residual oily or solid product was then purified by chromatography on silica-gel column using 5% ethanol or 30% ethyl acetate in chloroform as eluent, or crystalized from ethyl acetate.

3-(4-(Hydroxymethyl)-1H-1,2,3-triazol-1-yl)-3-methyl-1-(prop-2-ynyl)quinoline-2,4(1H,3H)-dione (5a). Colorless crystals, mp 182–188 °C (ethyl acetate); R_f = 0.12 (5% ethanol in chloroform); R_f = 0.31 (10% ethanol in chloroform); ^{1}H NMR (500 MHz, DMSO-d_6) δ 2.08 (s, 3H), 3.35-3.38 (m, 1H), 4.56 (d, 2H, *J* = 5.7 Hz), 4.84 (dd, 1H, *J* = 18.1, 2.4 Hz), 4.95 (dd, 1H, *J* = 18.1, 2.4 Hz), 5.29 (t, 1H, *J* = 5.7 Hz), 7.36 (ddd, 1H, *J* = 7.6, 7.4, 0.9 Hz), 7.57 (d, 1H, *J* = 8.4 Hz), 7.89 (ddd, 1H, *J* = 8.4, 7.4, 1.7 Hz), 7.96 (dd, 1H, *J* = 7.8, 1.6 Hz), 8.26 (s, 1H); ^{13}C NMR (126 MHz, DMSO-d_6) δ 23.3, 32.6, 55.1, 72.4, 75.3, 78.3, 116.6, 119.2, 123.9, 124.1, 128.1, 137.1, 140.8, 147.5, 167.9, 189.8; IR (cm^{-1}): ν 3270, 3134, 2126, 1709, 1677, 1600, 1465, 1385, 1301, 1180, 1022, 1011, 791, 762; HRMS (ESI+): *m/z* calcd for $C_{16}H_{15}N_4O_3^+$ [M + H]$^+$ 311.1139, found 311.1138.

3-(4-(Hydroxymethyl)-1H-1,2,3-triazol-1-yl)-3-phenyl-1-(prop-2-ynyl)quinoline-2,4(1H,3H)-dione (5b). Colorless crystals, mp 141–148 °C (ethyl acetate); R_f = 0.21 (5% ethanol in chloroform); R_f = 0.46 (10% ethanol in chloroform); ^{1}H NMR (500 MHz, $CDCl_3$) δ 2.34 (t, 1H, *J* = 2.5 Hz), 2.35–2.41 (m, 1H), 4.48 (dd, 1H, *J* = 17.8, 2.4 Hz), 4.71–4.79 (m, 2H), 5.33 (dd, 1H, *J* = 17.8, 2.4 Hz), 7.05 (s, 1H), 7.22 (ddd, 1H, *J* = 7.6, 7.5, 0.9 Hz), 7.33 (d, 1H, *J* = 8.3 Hz), 7.41–7.50 (m, 5H), 7.65 (ddd, 1H, *J* = 8.3, 7.4, 1.7 Hz), 8.03 (dd, 1H, *J* = 7.8, 1.6 Hz); ^{13}C NMR (126 MHz, $CDCl_3$) δ 33.6, 56.8, 73.6, 79.7, 115.8, 120.9, 124.6, 128.9, 129.2, 129.7, 130.1, 131.3, 136.9, 140.5, 145.8, 165.7, 187.5; IR (cm^{-1}): ν 3273, 3158, 2125, 1715, 1682, 1602, 1468, 1374, 1302, 1175, 1044, 871, 761; HRMS (ESI+): *m/z* calcd for $C_{21}H_{17}N_4O_3^+$ [M + H]$^+$ 373.1295, found 373.1291.

1-((1-Benzyl-1H-1,2,3-triazol-4-yl)methyl)-3-(4-(hydroxymethyl)-1H-1,2,3-triazol-1-yl)-3-methylquinoline-2,4(1H,3H)-dione (6a). Colorless powder, mp 69–98 °C; R_f = 0.24 (5% ethanol in chloroform), R_f = 0.11 (3% ethanol in chloroform); ^{1}H NMR (500 MHz, $CDCl_3$), δ 2.11 (s, 3H, CH_3), 2.59 (s, 1H, OH), 4.80 (s, 2H, OCH_2), 5.29 (d, 1H, *J* = 15.8 Hz, N-1–CHα), 5.33 (d, 1H, *J* = 15.8 Hz, N-1–CHβ), 5.44 (d, 1H, *J* = 14.8 Hz, N-1^C–CHα), 5.50 (d, 1H, *J* = 14.8 Hz, N-1^C–CHβ), 7.19–7.28 (m, 3H, H2^D, H-6^D, H-6), 7.29–7.38 (m, 3H, H-3^D, H-4^D, H-5^D), 7.56 (s, 1H, H-5^C), 7.67–7.74 (m, 2H, H-7, H-5^A), 7.79 (d, 1H, *J* = 8.4 Hz, H-8), 7.99 (dd, 1H, *J* = 7.8, 1.6 Hz, H-5); ^{13}C NMR (126 MHz, $CDCl_3$) δ 23.5 (CH_3), 39.5 (N-1–CH_2), 54.5 (N-1^C–CH_2), 56.9 (OCH_2), 71.7 (C-3), 116.9 (C-8), 119.2 (C-4a), 122.1 (C-5^A), 123.5 (C-5^C), 124.6 (C-6), 128.2 (C-2^D, C-6^D), 129.0 (C-5), 129.3 (C-4^D), 129.3 (C-3^D, C-5^D), 134.4 (C-1^D), 137.7 (C-7), 141.7 (C-8a), 142.9 (C-4^C), 147.3 (C-4^A), 168.3 (C-2), 189.6 (C-4); ^{15}N NMR (51 MHz, $CDCl_3$) δ 138.6 (N-1), 247.1 (N-1^A), 250.4 (N-1^C), 349.3 (N-3^C), 350.4 (N-3^A), 361.6 (N-2^C), 362.1 (N-2^A); IR (cm^{-1}): ν 3413, 3141, 1714, 1678, 1602, 1470, 1384, 1185, 1051, 793, 762, 722, 664; HRMS (ESI+): *m/z* calcd for $C_{23}H_{22}N_7O_3^+$ [M + H]$^+$ 444.1779, found 444.1773.

3-(4-(Hydroxymethyl)-1H-1,2,3-triazol-1-yl)-3-methyl-1-((1-phenyl-1H-1,2,3-triazol-4-yl)methyl)quinoline-2,4(1H,3H)-dione (6b). Colorless powder, mp 96–115 °C; R_f = 0.41 (10% ethanol in chloroform), R_f = 0.17 (5% ethanol in chloroform); ^{1}H NMR (500 MHz, $CDCl_3$) δ 2.17 (s, 3H, CH_3), 2.65 (s, 1H, OH), 4.82 (s, 2H, OCH_2), 5.37 (d, 1H, *J* = 15.8 Hz, N-1–CHα), 5.48 (d, 1H, *J* = 15.8 Hz, N-1–CHβ), 7.22–7.27 (m, 1H, H-6), 7.39-7.44 (m, 1H, H-4^D), 7.46–7.52 (m, 2H, H-3^D, H-5^D), 7.68–7.75 (m, 3H, H-2^D, H-6^D, H-7), 7.76 (s, 1H, H-5^A), 7.82 (d, 1H, *J* = 8.4 Hz, H-8), 8.01 (dd, 1H, *J* = 7.8, 1.6 Hz, H-5), 8.09 (s, 1H, H-5^C); ^{13}C NMR (126 MHz, $CDCl_3$) δ 23.4 (CH_3), 39.5 (N-1–CH_2), 56.9 (OCH_2), 71.6 (C-3), 116.8 (C-8), 119.2 (C-4a), 120.6 (C-2^D, C-6^D), 121.8 (C-5^C), 122.1 (C-5^A), 124.6 (C-6), 129.1 (C-4^D), 129.4 (C-5), 129.9 (C-3^D, C-5^D), 136.9 (C-1^D), 137.8 (C-7), 141.7 (C-8a), 143.2 (C-4^C), 147.3 (C-4^A), 168.4 (C-2), 189.5 (C-4); ^{15}N NMR (51 MHz, $CDCl_3$) δ 138.5 (N-1), 247.4 (N-1^A), 256.2 (N-1^C), 350.8 (N-3^A), 351.6 (N-3^C); IR (cm^{-1}): ν 3400, 3143, 1715, 1678, 1601, 1470, 1384, 1303, 1233, 1183, 1047, 760, 690, 663; HRMS (ESI+): *m/z* calcd for $C_{22}H_{20}N_7O_3^+$ [M + H]$^+$ 430.1622, found 430.1614.

3-(4-(Hydroxymethyl)-1H-1,2,3-triazol-1-yl)-3-methyl-1-((1-(pyridin-2-yl)-1H-1,2,3-triazol-4-yl)methyl)quinoline-2,4(1H,3H)-dione (6c). Colorless powder, mp 66–89 °C; R_f = 0.32 (10% ethanol in chloroform), R_f = 0.09 (5% ethanol in chloroform); ^{1}H NMR (500 MHz, $CDCl_3$) δ 2.19 (s, 3H, CH_3), 2.32 (s, 1H, OH), 4.83 (s, 2H, OCH_2), 5.36 (d, 1H, *J* = 15.9 Hz, N-1–CHα), 5.52 (d, 1H, *J* = 15.9 Hz, N-1–CHβ), 7.23 (ddd, 1H, *J* = 7.7, 7.3, 1.0 Hz, H-6), 7.30–7.37 (m, 1H, H-5^D), 7.71 (ddd, 1H, *J* = 8.5, 7.2, 1.6 Hz,

H-7), 7.75–7.78 (m, 2H, H-5^{A}, H-8), 7.87–7.92 (m, 1H, H-4^{D}), 8.01 (dd, 1H, *J* = 7.7, 1.6 Hz, H-5), 8.10–8.15 (m, 1H, H-3^{D}), 8.45-8.49 (m, 1H, H-6^{D}), 8.58 (s, 1H, H-5^{C}); ^{13}C NMR (126 MHz, $CDCl_3$) δ 23.7 (CH_3), 39.4 (N-1–CH_2), 56.9 (OCH_2), 72.0 (C-3), 113.9 (C-3^{D}), 116.6 (C-8), 119.3 (C-4a), 120.9 (C-5^{C}), 122.3 (C-5^{A}), 124.0 (C-5^{D}), 124.6 (C-6), 129.3 (C-5), 137.6 (C-7), 139.3 (C-4^{D}), 141.6 (C-8a), 143.0 (C-4^{C}), 147.4 (C-4^{A}), 148.8 (C-6^{D}), 149.0 (C-2^{D}), 168.3 (C-2), 189.6 (C-4); ^{15}N NMR (51 MHz, $CDCl_3$) δ 137.7 (N-1), 246.7 (N-1^{A}), 259.9 (N-1^{C}), 283.6 (N-1^{D}), 350.3 (N-3^{A}), 355.0 (N-3^{C}); IR (cm^{-1}): ν 3379, 3132, 1715, 1679, 1600, 1471, 1384, 1298, 1234, 1183, 1040, 782, 755, 658; HRMS (ESI+): *m/z* calcd for $C_{21}H_{19}N_8O_3^+$ $[M + H]^+$ 431.1575, found 431.1579.

1-((1-Benzyl-1H-1,2,3-triazol-4-yl)methyl)-3-(4-(hydroxymethyl)-1H-1,2,3-triazol-1-yl)-3-phenylquinoline-2,4(1H,3H)-dione (6d). Colorless powder, mp 93–121 °C; R_f = 0.23 (5% ethanol in chloroform); ^{1}H NMR (500 MHz, $CDCl_3$) δ 2.34 (t, 1H, *J* = 5.6 Hz, OH), 4.75 (d, 2H, *J* = 4.6 Hz, OCH_2), 5.20 (d, 1H, *J* = 15.6 Hz, N-1^{C}–CHα), 5.43 (d, 1H, *J* = 14.8 Hz, N-1–CHα), 5.49 (d, 1H, *J* = 15.6 Hz, N-1^{C}–CHβ), 5.54 (d, 1H, *J* = 14.8 Hz, N-1–CHβ), 7.03 (s, 1H, H5^{A}), 7.17 (ddd, 1H, *J* = 7.9, 7.2, 0.8 Hz, H-6), 7.23-7.28 (m, 4H, H-2^{D}, H-3^{D}, H-5^{D}, H-6^{D}), 7.29–7.32 (m, 2H, H-2^{B}, H-6^{B}), 7.34–7.42 (m, 4H, H-3^{B}, H-4^{B}, H-5^{B}, H-4^{D}), 7.59 (s, 1H, H5^{C}), 7.62 (ddd, 1H, *J* = 7.9, 7.9, 1.6 Hz, H-7), 7.74 (d, 1H, *J* = 8.4 Hz, H-8), 7.98 (dd, 1H, *J* = 7.7, 1.6 Hz, H-5); ^{13}C NMR (126 MHz, $CDCl_3$) δ ^{13}C NMR (126 MHz, $CDCl_3$) δ 39.9 (N-1^{C}–CH_2), 54.5 (N-1–CH_2), 56.9 (OCH_2), 79.6 (C-3), 116.8 (C-8), 120.9 (C-4a), 123.6 (C-5^{C}), 124.5 (C-5^{A}), 124.5 (C-6), 128.3 (C-2^{D}, C-6^{D}), 128.8 (C-2^{B}, C-6^{B}), 129.0 (C-5), 129.0 (C-4^{B}), 129.3 (C-3^{B}, C-5^{B}), 129.9 (C-1^{D}), 130.0 (C-3^{D}, C-5^{D}), 131.2 (C-4^{D}), 134.5 (C-1^{B}), 137.2 (C-7), 141.1 (C-8a), 142.9 (C-4^{C}), 145.8 (C-4^{A}), 166.6 (C-2), 188.0 (C-4); ^{15}N NMR (51 MHz, $CDCl_3$) δ 140.4 (N-1), 248.9 (N-1^{A}), 250.6 (N-1^{C}), 350.0 (N-3^{C}), 352.8 (N-3^{A}), 362.8 (N-2^{C}), 364.9 (N-2^{A}); IR (cm^{-1}): ν 3391, 3141, 1715, 1678, 1601, 1469, 1450, 1376, 1049, 1032, 871, 761, 665, 608; HRMS (ESI+): *m/z* calcd for $C_{28}H_{24}N_7O_3^+$ $[M + H]^+$ 506.1935, found 506.1937.

3-(4-(Hydroxymethyl)-1H-1,2,3-triazol-1-yl)-3-phenyl-1-((1-phenyl-1H-1,2,3-triazol-4-yl)methyl)quinoline-2,4(1H,3H)-dione (6e). Colorless powder, mp 118–131 °C; R_f = 0.35 (5% ethanol in chloroform), R_f = 0.22 (3% ethanol in chloroform); ^{1}H NMR (500 MHz, $CDCl_3$) δ 2.33 (s, 1H, OH), 4.78 (s, 2H, OCH_2), 5.41 (d, 1H, *J* = 15.7 Hz, N-1–CHα), 5.53 (d, 1H, *J* = 15.7 Hz, N-1–CHβ), 7.09 (s, 1H, H-5^{A}), 7.20 (ddd, 1H, *J* = 7.9, 7.2, 0.7 Hz, H-6), 7.38–7.48 (m, 6H, H-2^{B}, H-3^{B}, H-4^{B}, H-5^{B}, H-6^{B}, H-4^{D}), 7.49–7.55 (m, 2H, H-3^{D}, H-5^{D}), 7.65 (ddd, 1H, *J* = 8.7, 7.1, 1.7 Hz, H-7), 7.68–7.72 (m, 2H, H2^{D}, H-6^{D}), 7.75 (d, 1H, *J* = 8.4 Hz, H-8), 8.02 (dd, 1H, *J* = 7.8, 1.5 Hz, H-5), 8.07 (s, 1H, H5^{C}); ^{13}C NMR (126 MHz, $CDCl_3$) δ 39.8 (N-1–CH_2), 56.9 (OCH_2), 79.6 (C-3), 116.7 (C-8), 120.7 (C-2^{D}, C-6^{D}), 120.9 (C-4a), 121.8 (C-5^{C}), 124.6 (C-5^{A}), 124.6 (C-6), 128.9 (C-2^{B}, C-6^{B}), 129.1 (C-5), 129.2 (C-4^{D}), 130.0 (C-1^{B}), 130.0 (C-3^{D}, C-5^{D}), 130.1 (C-3^{B}, C-5^{B}), 131.3 (C-4^{B}), 136.9 (C-1^{D}), 137.3 (C-7), 140.9 (C-8a), 143.2 (C-4^{C}), 145.8 (C-4^{A}), 166.9 (C-2), 188.0 (C-4); ^{15}N NMR (51 MHz, $CDCl_3$) δ 139.5 (N-1), 249.0 (N-1^{A}), 256.2 (N-1^{C}), 352.6 (N-3^{C}), 353.0 (N-3^{A}); IR (cm^{-1}): ν 3401, 3144, 1716, 1679, 1600, 1501, 1468, 1449, 1377, 1044, 871, 760, 692; HRMS (ESI+): *m/z* calcd for $C_{27}H_{22}N_7O_3^+$ $[M + H]^+$ 492.1779, found 492.1768.

3-(4-(Hydroxymethyl)-1H-1,2,3-triazol-1-yl)-3-phenyl-1-((1-(pyridin-2-yl)-1H-1,2,3-triazol-4-yl)methyl)quinoline-2,4(1H,3H)-dione (6f). Colorless powder, mp 185–194 °C; R_f = 0.37 (5% ethanol in chloroform); ^{1}H NMR (400 MHz, $CDCl_3$) δ 2.38 (s, 1H, OH), 4.77 (s, 2H, OCH_2), 5.28 (d, 1H, *J* = 15.8 Hz, N-1–CHα), 5.69 (d, 1H, *J* = 15.8 Hz, N-1–CHβ), 7.09 (s, 1H, H-5^{A}), 7.17 (ddd, 1H, *J* = 7.7, 7.3, 1.0 Hz, H-6), 7.32–7.48 (m, 6H, H-5^{D}, H-2^{B}, H-3^{B}, H-4^{B}, H-5^{B}, H-6^{B}), 7.61 (ddd, 1H, *J* = 8.4, 7.2, 1.7 Hz, H-7), 7.68 (d, 1H, *J* = 8.3 Hz, H-8), 7.86–7.94 (m, 1H, H-4^{D}), 8.01 (dd, 1H, *J* = 7.8, 1.5 Hz, H-5), 8.11–8.16 (m, 1H, H-3^{D}), 8.47–8.51 (m, 1H, H-6^{D}), 8.61 (s, 1H, H-5^{C}); ^{13}C NMR (100 MHz, $CDCl_3$) δ 39.9 (N-1–CH_2), 56.9 (OCH_2), 79.7 (C-3), 113.9 (C-3^{D}), 116.6 (C-8), 121.0 (C-4a), 121.0 (C-5^{C}), 124.0 (C-5^{D}), 124.5 (C-6), 124.5 (C-5^{A}), 128.9 (C-2^{B}, C-6^{B}), 129.0 (C-5), 130.0 (C-1^{B}), 130.1 (C-3^{B}, C-5^{B}), 131.2 (C-4^{B}), 137.1 (C-7), 139.3 (C-4^{D}), 141.2 (C-8a), 143.0 (C-4^{C}), 145.9 (C-4^{A}), 148.9 (C-6^{D}), 149.0 (C-2^{D}), 166.7 (C-2), 188.0 (C-4); IR (cm^{-1}): ν 3401, 3156, 1716, 1680, 1599, 1469, 1375, 1313, 1034, 999, 779, 760, 695, 683; HRMS (ESI+): *m/z* calcd for $C_{26}H_{21}N_8O_3^+$ $[M + H]^+$ 493.1731, found 493.1732.

General procedure for the preparation of aldehydes 7a,b, 8a,b and 9a-f using PCC as the reagent. To a vigorously stirred solution of suitable alcohol (1 mmol) in dichloromethane or acetone (15 mL), PCC (259 mg; 1.2 mmol) was added and the reaction mixture was stirred at the reflux temperature unless otherwise stated. Obtained reaction mixture was then stirred at the reflux temperature for up to one hour. The original orange color of mixture changed to almost black. Resulting solution with the sticky sediment was poured into a narrow (1 cm in diameter) column of silica gel (13 g). The organic portion was eluted with 5% ethanol in chloroform (approximately 350 mL). Volatile components of dark yellow eluate were evaporated *in vacuo* and obtained residue was chromatographed on a column of silica-gel (35 g) using 50% or 67% ethyl acetate in petroleum ether. Some crude products were further crystalized from ethyl acetate or benzene. For the reaction conditions and yields see Table 2 or Table 3, respectively.

General procedure for the preparation of aldehydes 7a,b using Swern reaction. To a dry 25 mL evacuated flask, oxalyl chloride (155 μL; 1.8 mmol) and dry tetrahydrofurane

(THF) were added. The flask was equipped with nitrogen gas inlet and cooled to –70 °C using dry ice–ethanol bath. Afterwards, DMSO (280 μL) was added dropwise and obtained solution was stirred for 60 minutes, keeping the temperature bellow –65 °C. Then, suitable mono-triazole alcohol **4** (1.5 mmol) dissolved in dry dichloromethane or acetone (11 mL) was added and stirring was continued for 90 minutes. Finally, after addition of DIPEA (1.275 mL; 7.32 mmol), the content of the flask was stirred for additional 2 hours and tempered to the lab temperature. The reaction mixture was diluted with distilled water (10 mL) and extracted with dichloromethane (3x 20 mL). Combined organic phases were washed with ice-cold water (4x 20 mL), dried over anhydrous Na_2SO_4, filtered and volatile components were evaporated *in vacuo*. Obtained oily crude product was purified on silica-gel column, using 38% ethyl acetate in petroleum ether as mobile phase. To that way gained oily product, diethyl ether was added and it was cooled to –20 °C to provide solid compound that was filtered through the sintered glass filter and dried at 50 °C. For the yields of products see Table 2.

General procedure for the synthesis of aldehydes using MnO_2 as a reagent. To a vigorously stirred solution of suitable alcohol (1 mmol) in acetone (10 mL), MnO_2 (869 mg; 10 mmol) was added. Obtained reaction mixture was then stirred at the reflux temperature unless otherwise stated. Resulting black suspension was filtered through the filter paper and volatile components of the filtrate were evaporated *in vacuo*. Residual crude oily product was chromatographed on silica-gel column, using 50% ethyl acetate in petroleum ether as mobile phase. Some that way obtained TLC and IR pure products were further crystalized from ethyl acetate. For the reaction conditions and yields see Table 2 or Table 3, respectively.

1-(1,2,3,4-Tetrahydro-3-methyl-2,4-dioxoquinolin-3-yl)-1H-1,2,3-triazole-4-carbaldehyde (7a). Colorless crystals, mp 267–271 °C (ethyl acetate); R_f = 0.54 (10% ethanol in chloroform); ^{1}H NMR (500 MHz, DMSO-d_6) δ 2.16 (s, 3H, CH_3), 7.23 (d, 1H, J = 7.7 Hz, H-8), 7.21–7.27 (m, 1H, H-6), 7.75 (ddd, 1H, J = 7.8, 7.7, 1.5 Hz, H-7), 7.85 (dd, 1H, J = 7.8, 1.7 Hz, H-5), 9.18 (s, 1H, H-5^A), 10.08 (s, 1H, CHO), 11.50 (s, 1H, H-1); ^{13}C NMR (126 MHz, DMSO-d_6) δ 23.4 (CH_3), 73.6 (C-3), 117.0 (C-8), 117.6 (C-4a), 123.5 (C-6), 127.6 (C-5), 129.6 (C-5^A), 137.2 (C-7), 141.4 (C-8a), 146.6 (C-4^A), 168.3 (C-2), 185.1 (CHO), 190.3 (C-4); ^{15}N NMR (51 MHz, DMSO-d_6) δ 133.4 (N-1), 252.0 (N-1^A), 358.6 (N-3^A), 367.9 (N-2^A); IR (cm^{-1}): ν 3308, 3140, 2851, 1716, 1680, 1614, 1531, 1484, 1378, 1345, 1231, 1211, 816, 757, 667; HRMS (ESI+): *m/z* calcd for $C_{13}H_{11}N_4O_3^+$ [M + H]$^+$ 271.0826, found 271.0833.

1-(1,2,3,4-Tetrahydro-2,4-dioxo-3-phenylquinolin-3-yl)-1H-1,2,3-triazole-4-carbaldehyde (7b). Colorless crystals, mp 188–191 °C (ethyl acetate); R_f = 0.36 (5% ethanol in chloroform), R_f = 0.35 (30% ethyl acetate in chloroform); ^{1}H NMR (500 MHz, DMSO-d_6) δ 7.09 (d, 1H, J = 8.0 Hz, H-8), 7.17 (ddd, 1H, J = 7.6, 7.6, 1.0 Hz, H-6), 7.34–7.41 (m, 2H, H-2^B, H-6^B), 7.47–7.54 (m, 3H, H-3^B, H-4^B, H-5^B), 7.63 (ddd, 1H, J = 8.2, 7.3, 1.6 Hz, H-7), 7.85 (dd, 1H, J = 7.8, 1.4 Hz, H-5), 8.93 (s, 1H, H-5^A), 10.05 (s, 1H, CHO), 11.68 (s, 1H, H-1); ^{13}C NMR (126 MHz, DMSO-d_6) δ 80.7 (C-3), 116.7 (C-8), 119.5 (C-4a), 123.5 (C-6), 127.5 (C-5), 128.9 (C-2^B, C-6^B), 129.7 (C-3^B, C-5^B), 129.7 (C-1^B), 130.7 (C-4^B), 130.7 (C-5^A), 136.8 (C-7), 140.4 (C-8a), 146.2 (C-4^A), 166.6 (C-2), 185.1 (CHO), 188.4 (C-4); ^{15}N NMR (51 MHz, DMSO-d_6) δ 134.8 (N-1), 249.8 (N-1^A), 351.6 (N-3^A), 356.4 (N-2^A); IR (cm^{-1}): ν 3253, 2914, 2860, 1723, 1689, 1615, 1595, 1486, 1355, 1208, 1045, 857, 780, 752, 697; HRMS (ESI+): *m/z* calcd for $C_{18}H_{13}N_4O_3^+$ [M + H]$^+$ 333.0982, found 333.0988.

1-(1,2,3,4-Tetrahydro-3-methyl-2,4-dioxo-1-(prop-2-ynyl)quinolin-3-yl)-1H-1,2,3-triazole-4-carbaldehyde (8a). Colorless crystals, mp 189–194 °C (benzene); R_f = 0.40 (5% ethanol in chloroform); R_f = 0.63 (10% ethanol in chloroform); ^{1}H NMR (500 MHz, $CDCl_3$) δ 2.23 (s, 3H), 3.32–3.37 (m, 1H), 4.66 (dd, 1H, J = 17.9, 1.6 Hz), 5.11 (dd, 1H, J = 17.9, 1.6 Hz), 7.30–7.37 (m, 1H), 7.47 (d, 1H, J = 8.4 Hz), 7.81 (ddd, 1H, J = 8.4, 7.3, 1.5 Hz), 8.09 (d, 1H, J = 7.7 Hz), 8.31 (s, 1H), 10.18 (s, 1H);^{13}C NMR (126 MHz, $CDCl_3$) δ 23.9, 33.2, 72.8, 73.9, 76.7, 116.3, 119.2, 124.9, 126.3, 129.6, 137.7, 140.9, 147.1, 166.9, 185.1, 188.7; IR (cm^{-1}): ν 3282, 3150, 2125, 1704, 1673, 1601, 1528, 1470, 1444, 1381, 1306, 1206, 798, 761; HRMS (ESI+): *m/z* calcd for $C_{16}H_{13}N_4O_3^+$ [M + H]$^+$ 309.0982, found 309.0979. Anal. Calcd for $C_{16}H_{12}N_4O$ (308.29): C 62.33, H 3.92, N 18.17; found: C 62.26, H 4.22, N 17.92.

1-(1,2,3,4-Tetrahydro-2,4-dioxo-3-phenyl-1-(prop-2-ynyl)quinolin-3-yl)-1H-1,2,3-triazole-4-carbaldehyde (8b). Colorless crystals, mp 176–182 °C (benzene); R_f = 0.68 (5% ethanol in chloroform); R_f = 0.51 (30% ethyl acetate in chloroform); ^{1}H NMR (500 MHz, $CDCl_3$) δ 2.33-2.37 (m, 1H), 4.52 (dd, 1H, J = 17.8, 1.4 Hz), 5.34 (dd, 1H, J = 17.8, 1.4 Hz), 7.22–7.28 (m, 1H), 7.33-7.38 (m, 1H), 7.44–7.55 (m, 5H), 7.61 (s, 1H), 7.64–7.71 (m, 1H), 8.05 (d, 1H, J = 7.7 Hz), 10.13 (s, 1H); ^{13}C NMR (126 MHz, $CDCl_3$) δ 33.7, 73.8, 76.6, 80.2, 116.0, 120.8, 124.8, 128.5, 128.8, 129.0, 129.2, 130.5, 131.8, 137.2, 140.4, 145.8, 165.1, 185.2, 186.9; IR (cm^{-1}): ν 3237, 3151, 2124, 1716, 1682, 1603, 1469, 1373, 1301, 1200, 1170, 1042, 774, 692; HRMS (ESI+): *m/z* calcd for $C_{21}H_{15}N_4O_3^+$ [M + H]$^+$ 371.1139, found 371.1130.

1-(1-((1-Benzyl-1H-1,2,3-triazol-4-yl)methyl)-1,2,3,4-tetrahydro-3-methyl-2,4-dioxoquinolin-3-yl)-1H-1,2,3-triazole-4-carbaldehyde (9a). Colorless powder, mp 63–87 °C; R_f = 0.48 (5 % ethanol in chloroform); R_f = 0.13 (50% ethyl acetate in petroleum ether); R_f = 0.28 (33% petroleum ether in ethyl acetate); ^{1}H NMR (500 MHz,

$CDCl_3$), δ 2.16 (s, 3H, CH_3), 5.28 (d, 1H, J = 15.7 Hz, N-1–CHα), 5.37 (d, 1H, J = 15.7 Hz, N-1–CHβ), 5.45 (d, 1H, J = 14.8 Hz, N-1^C–CHα), 5.50 (d, 1H, J = 14.8 Hz, N-1^C–CHβ), 7.21–7.26 (m, 2H, H-2^D, H-6^D), 7.27 (ddd, 1H, J = 7.6, 7.5, 0.9 Hz, H-6), 7.31–7.38 (m, 3H, H-3^D, H-4^D, H-5^D), 7.53 (s, 1H, H-5^C), 7.75 (ddd, 1H, J = 8.4, 7.4, 1.7 Hz, H-7), 7.86 (d, 1H, J = 8.4 Hz, H-8), 8.02 (dd, 1H, J = 7.8, 1.6 Hz, H-5), 8.30 (s, 1H, H-5^A), 10.15 (s, 1H, CHO); ^{13}C NMR (126 MHz, $CDCl_3$) δ 23.8 (CH_3), 39.5 (N-1–CH_2), 54.5 (N-1^C–CH_2), 72.6 (C-3), 117.0 (C-8), 119.0 (C-4a), 123.4 (C-5^C), 124.8 (C-6),126.3 (C-5^A), 128.2 (C-2^D, C-6^D), 129.0 (C-4^D), 129.3 (C-3^D, C-5^D), 129.3 (C-5), 134.3 (C-1^D), 138.0 (C-7), 141.5 (C-8a), 142.7 (C-4^C), 147.0 (C-4^A), 167.7 (C-2), 185.0 (CHO), 188.9 (C-4); ^{15}N NMR (51 MHz, $CDCl_3$) δ 138.4 (N-1), 250.6 (N-1^C), 251.7 (N-1^A), 350.0 (N-3^C), 361.8 (N-2^A), 362.6 (N-2^C); IR (cm^{-1}): ν 3137, 2929, 2852, 1681, 1601, 1470, 1385, 1211, 1186, 1048, 799, 763, 721, 686, 663; HRMS (ESI+): *m/z* calcd for $C_{23}H_{20}N_7O_3^+$ $[M + H]^+$ 442.1622, found 442.1620.

1-(1,2,3,4-Tetrahydro-3-methyl-2,4-dioxo-1-((1-phenyl-1H-1,2,3-triazol-4-yl)methyl)quinolin-3-yl)-1H-1,2,3-triazole-4-carbaldehyde (9b). Colorless powder, mp 71–93 °C; R_f = 0.44 (33% petroleum ether in ethyl acetate); R_f = 0.40 (5% ethanol in chloroform); ^{1}H NMR (500 MHz, $CDCl_3$) δ 2.22 (s, 3H, CH_3), 5.45 (s, 2H, N-1–CH_2), 7.29 (ddd, 1H, J = 7.6, 7.5, 0.9 Hz, H-6), 7.41–7.46 (m, 1H, H-4^D), 7.48–7.53 (m, 2H, H-3^D, H-5^D), 7.68–7.72 (m, 2H, H-2^D, H-6^D), 7.78 (ddd, 1H, J = 8.4, 7.4, 1.7 Hz, H-7), 7.90 (d, 1H, J = 8.4 Hz, H-8), 8.04 (dd, 1H, J = 7.9, 1.6 Hz, H-5), 8.05 (s, 1H, H-5^C), 8.36 (s, 1H, H-5^A), 10.17 (s, 1H, CHO) ^{13}C NMR (126 MHz, $CDCl_3$) δ 23.8 (CH_3), 39.5 (N-1–CH_2), 72.5 (C-3), 117.0 (C-8), 119.0 (C-4a), 120.6 (C-2^D, C-6^D), 121.8 (C-5^C), 124.9 (C-6), 126.2 (C-5^A), 129.2 (C-4^D), 129.4 (C-5), 130.0 (C-3^D, C-5^D), 136.8 (C-1^D), 138.1 (C-7), 141.5 (C-8a), 143.0 (C-4^C), 147.0 (C-4^A), 167.8 (C-2), 185.0 (CHO), 188.8 (C-4); ^{15}N NMR (51 MHz, $CDCl_3$) δ 138.5 (N-1), 251.6 (N-1^A), 256.2 (N-1^C), 352.0 (N-3^C), 362.2 (N-2^A); IR (cm^{-1}): ν 3138, 2928, 2853, 1682, 1601, 1470, 1385, 1212, 1185, 1046, 760, 690, 663; HRMS (ESI+): *m/z* calcd for $C_{22}H_{18}N_7O_3^+$ $[M + H]^+$ 428.1466, found 428.1461.

1-(1,2,3,4-Tetrahydro-3-methyl-2,4-dioxo-1-((1-(pyridin-2-yl)-1H-1,2,3-triazol-4-yl)methyl)quinolin-3-yl)-1H-1,2,3-triazole-4-carbaldehyde (9c). Colorless powder, mp 47–65 °C; R_f = 0.12 (30% ethyl acetate in chloroform); R_f = 0.34 (5% ethanol in chloroform); ^{1}H NMR (500 MHz, $CDCl_3$) δ 2.24 (s, 3H, CH_3), 5.35 (d, 1H, J = 15.9 Hz, N-1–CHα), 5.58 (d, 1H, J = 15.9 Hz, N-1–CHβ), 7.24–7.31 (m, 1H, H-6), 7.32–7.38 (m, 1H, H-5^D), 7.76 (ddd, 1H, J = 8.4, 7.3, 1.7 Hz, H-7), 7.83 (d, 1H, J = 8.4 Hz, H-8), 7.88-7.93 (m, 1H, H-4^D), 8.04 (dd, 1H, J = 7.8, 1.6 Hz, H-5), 8.11-8.16 (m, 1H, H-3^D), 8.35 (s, 1H, H-5^A), 8.46-8.49 (m, 1H, H-6^D), 8.59 (s, 1H, H-5^C), 10.18 (s, 1H, CHO); ^{13}C NMR (126 MHz, $CDCl_3$) δ 24.0 (CH_3), 39.4 (N-1–CH_2), 72.9 (C-3), 113.9 (C-3^D), 116.8 (C-8), 119.1 (C-4a), 120.8 (C-5^C), 124.1 (C-5^D), 124.8 (C-6), 126.4 (C-5^A), 129.4 (C-5), 137.9 (C-7), 139.3 (C-4^D), 141.6 (C-8a), 142.8 (C-4^C), 147.1 (C-4^A), 148.8 (C-6^D), 148.9 (C-2^D), 167.7 (C-2), 185.1 (CHO), 189.0 (C-4); ^{15}N NMR (51 MHz, $CDCl_3$) δ 137.8 (N-1), 251.1 (N-1^A), 261.0 (N-1^C), 283.9 (N-1^D), 355.3 (N-3^C), 361.8 (N-2^A); IR (cm^{-1}): ν 3138, 2929, 2854, 1683, 1600, 1471, 1385, 1211, 1184, 1038, 999, 781, 760, 663; HRMS (ESI+): *m/z* calcd for $C_{21}H_{17}N_8O_3^+$ $[M + H]^+$ 429.1418, found 429.1431.

1-(1-((1-Benzyl-1H-1,2,3-triazol-4-yl)methyl)-1,2,3,4-tetrahydro-2,4-dioxo-3-phenylquinolin-3-yl)-1H-1,2,3-triazole-4-carbaldehyde (9d). Colorless powder, mp 87–113 °C; R_f = 0.58 (5% ethanol in chloroform); R_f = 0.40 (33% petroleum ether in ethyl acetate); ^{1}H NMR (500 MHz, $CDCl_3$) δ 5.20 (d, 1H, J = 15.6 Hz, N-1–CHα), 5.44 (d, 1H, J = 14.8 Hz, N-1^C–CHα), 5.53 (d, 1H, J = 15.6 Hz, N-1–CHβ), 5.56 (d, 1H, J = 14.8 Hz, N-1^C–CHβ), 7.20 (ddd, 1H, J = 7.6, 7.5, 0.8 Hz, H-6), 7.26–7.28 (m, 4H, H-3^B, H-5^B, H-3^D, H-5^D), 7.28-7.30 (m, 2H, H-2^B, H-6^B), 7.37–7.40 (m, 3H, H-2^D, H-6^D, H-4^B), 7.41–7.47 (m, 1H, H4^D), 7.58 (s, 1H, H-5^C), 7.58 (s, 1H, H-5^A), 7.65 (ddd, 1H, J = 8.4, 7.4, 1.7 Hz, H-7), 7.78 (d, 1H, J = 8.4 Hz, H-8), 8.00 (dd, 1H, J = 7.7, 1.6 Hz, H-5), 10.13 (s, 1H, CHO); ^{13}C NMR (126 MHz, $CDCl_3$) δ 40.0 (N-1–CH_2), 54.5 (N-1^C–CH_2), 80.1 (C-3), 117.0 (C-8), 120.7 (C-4a), 123.5 (C-5^C), 124.8 (C-6), 128.3 (C-3^B, C-5^B), 128.4 (C-5^A), 128.6 (C-3^D, C-5^D), 129.0 (C-5), 129.0 (C-1^B), 129.1 (C4^B), 129.4 (C-2^D, C-6^D), 130.4 (C-2^B, C-6^B), 131.7 (C-4^D), 134.4 (C-1^D), 137.5 (C-7), 141.0 (C-8a), 142.7 (C-4^C), 145.8 (C-4^A), 165.9 (C-2), 185.2 (CHO), 187.3 (C-4); ^{15}N NMR (51 MHz, $CDCl_3$) δ 140.0 (N-1), 250.6 (N-1^C), 253.7 (N-1^A), 350.8 (N-3^C), 362.5 (N-2^C); IR (cm^{-1}): ν 3138, 2850, 1701, 1680, 1601, 1469, 1376, 1044, 871, 772, 748, 724, 696; HRMS (ESI+): *m/z* calcd for $C_{28}H_{22}N_7O_3^+$ $[M + H]^+$ 504.1779, found 504.1782.

1-(1,2,3,4-Tetrahydro-2,4-dioxo-3-phenyl-1-((1-phenyl-1H-1,2,3-triazol-4-yl)methyl)quinolin-3-yl)-1H-1,2,3-triazole-4-carbaldehyde (9e). Colorless powder, mp 91–122 °C; R_f = 0.62 (5% ethanol in chloroform), R_f = 0.29 (50% ethyl acetate in petroleum ether); ^{1}H NMR (500 MHz, $CDCl_3$) δ 5.41 (d, 1H, J = 15.7 Hz, N-1–CHα), 5.58 (d, 1H, J = 15.7 Hz, N-1–CHβ), 7.23 (ddd, 1H, J = 7.6, 7.5, 0.9 Hz, H-6), 7.41–7.43 (m, 2H, H-2^B, H-6^B), 7.43–7.45 (m, 2H, H-3^B, H-5^B), 7.45–7.48 (m, 1H, H-4^D), 7.48–7.51 (m, 1H, H-4^B), 7.51–7.55 (m, 2H, H-3^D, H-5^D), 7.64 (s, 1H, H-5^A), 7.68 (ddd, 1H, J = 9.5, 7.4, 1.7 Hz, H-7), 7.69–7.72 (m, 2H, H-2^D, H-6^D), 7.79 (d, 1H, J = 8.4 Hz, H-8), 8.04 (dd, 1H, J = 7.8, 1.6 Hz, H-5), 8.06 (s, 1H, H-5^C), 10.15 (s, 1H, CHO); ^{13}C NMR (126 MHz, $CDCl_3$) δ 39.8 (N-1–CH_2), 80.1 (C-3), 116.8 (C-8), 120.7 (C-2^D, C-6^D), 120.7 (C-4a), 121.8 (C-5^C), 124.8 (C-6), 128.4 (C-5^A), 128.8 (C-2^B, C-6^B), 129.1 (C-1^B), 129.2 (C-4^D), 129.3 (C-5), 130.0 (C-3^D, C-5^D), 130.5 (C-3^B, C-5^B), 131.8 (C-4^B), 136.8

(C-1^D), 137.6 (C-7), 140.9 (C-8a), 143.0 (C-4^C), 145.8 (C-4^A), 166.2 (C-2), 185.1 (CHO), 187.2 (C-4); ^{15}N NMR (51 MHz, $CDCl_3$) δ 139.3 (N-1), 254.3 (N-1^A), 256.1 (N-1^C), 256.1 (N-2^C), 352.7 (N-3^C), 363.4 (N-2^A), IR (cm^{-1}): ν 3141, 2848, 1701, 1682, 1600, 1468, 1376, 1306, 1042, 872, 772, 691, 665; HRMS (ESI+): *m/z* calcd for $C_{27}H_{20}N_7O_3^+$ $[M + H]^+$ 490.1622, found 490.1616.

1-(1,2,3,4-Tetrahydro-2,4-dioxo-3-phenyl-1-((1-(pyridin-2-yl)-1H-1,2,3-triazol-4-yl)methyl)quinolin-3-yl)-1H-1,2,3-triazole-4-carbaldehyde (9f). Colorless powder, mp 88–114 °C; R_f = 0.44 (5% ethanol in chloroform), R_f = 0.23 (30% ethyl acetate in chloroform); ^{1}H NMR (500 MHz, $CDCl_3$) δ 5.31 (d, 1H, *J* = 15.8 Hz, N-1–CHα), 5.72 (d, 1H, *J* = 15.8 Hz, N-1–CHβ), 7.21 (ddd, 1H, *J* = 7.5, 7.5, 0.9 Hz, H-6), 7.35–7.39 (m, 1H, H-5^D), 7.40–7.51 (m, 5H, H-2^B, H-3^B, H-4^B, H-5^B, H-6^B), 7.62–7.68 (m, 2H, H-5^A, H-7), 7.72 (d, 1H, *J* = 8.4 Hz, H-8), 7.89–7.95 (m, 1H, H-4^D), 8.04 (dd, 1H, *J* = 7.8, 1.5 Hz, H-5), 8.13–8.17 (m, 1H, H-3^D), 8.48-8.52 (m, 1H, H-6^D), 8.63 (s, 1H, H-5^C), 10.15 (s, 1H, CHO); ^{13}C NMR (126 MHz, $CDCl_3$) δ 39.9 (N-1–CH_2), 80.2 (C-3), 113.9 (C-3^D), 116.7 (C-8), 120.8 (C-4a), 120.9 (C-5^C), 124.1 (C-5^D), 124.8 (C-6), 128.4 (C-5^A), 128.8 (C-2^B, C-6^B), 129.0 (C-1^B), 129.1 (C-5), 130.5 (C-3^B, C-5^B), 131.7 (C-4^B), 137.4 (C-7), 139.3 (C-4^D), 141.1 (C-8a), 142.8 (C-4^C), 145.8 (C-4^A), 148.9 (C-6^D), 149.0 (C-2^D), 165.9 (C-2), 185.2 (CHO), 187.3 (C-4); ^{15}N NMR (51 MHz, $CDCl_3$) δ 139.2 (N-1), 254.0 (N-1^A), 260.2 (N-1^C), 284.4 (N-1^D), 355.5 (N-3^C), 363.1 (N-2^A); IR (cm^{-1}): ν 3153, 2852, 1700, 1681, 1599, 1470, 1375, 1313, 1035, 999, 776, 750, 696; HRMS (ESI+): *m/z* calcd for $C_{26}H_{19}N_8O_3^+$ $[M + H]^+$ 491.1575, found 491.1578.

General procedure for the preparation of carboxylic acids 10a,b, 11a,b and 12a-f. To a vigorously stirred ice-cooled solution of appropriate alcohol (1.00 mmol) in acetone, also ice-cooled solution of chromium(VI) oxide (2.4 g, 24 mmol unless otherwise stated) in 2M H_2SO_4 (24 mL unless otherwise stated) was added during 5 minutes and stirring was continued still for the time indicated in Table 4. The original intense red color of reaction mixture changed to black. After completion of reaction (TLC), ethanol (15 mL) was added and the mixture was poured onto ice. After the ice melted, the solid phase was filtered off, washed with water and ethanol and dried at 50 °C affording the first part of product. The filtrate was extracted with chloroform (up to 7 × 50 mL, until the product was detectable in the extract by TLC), washed with water (100 mL), dried (Na_2SO_4) and filtered. From the filtrate, volatile components were evaporated *in vacuo*, whereby the second portion of crude product was obtained. In some cases, both parts of TLC and IR pure crude product were joined together and crystalized from ethyl acetate.

1-(1,2,3,4-Tetrahydro-3-methyl-2,4-dioxoquinolin-3-yl)-1H-1,2,3-triazole-4-carboxylic acid (10a). Colorless crystals, mp 198–201 °C (ethyl acetate); R_f = 0.05–0.37 (50% ethanol in chloroform); ^{1}H NMR (500 MHz, DMSO-d_6) δ 2.14 (s, 3H, CH_3), 7.22 (d, 1H, *J* = 7.9 Hz, H-8), 7.21–7.27 (m, 1H, H-6), 7.74 (ddd, 1H, *J* = 7.8, 7.7, 1.5 Hz, H-7), 7.84 (d, 1H, *J* = 7.6 Hz, H-5), 8.99 (s, 1H, H-5^A), 11.45 (s, 1H, H-1), 13.21 (br, 1H, COOH); ^{13}C NMR (126 MHz, DMSO-d_6) δ 23.4 (CH_3), 73.4 (C-3), 117.0 (C-8), 117.7 (C-4a), 123.4 (C-6), 127.6 (C-5), 130.4 (C-5^A), 137.2 (C-7), 139.5 (C-4^A), 141.5 (C-8a), 161.7 (COOH), 168.5 (C-2), 190.5 (C-4); ^{15}N NMR (51 MHz, DMSO-d_6) δ 133.2 (N-1), 250.2 (N-1^A), 357.1 (N-3^A), 367.5 (N-2^A); IR (cm^{-1}): ν 3436, 3141, 2927, 1718, 1684, 1614, 1485, 1392, 1361, 1260, 1163, 1020, 761, 665, 597; HRMS (ESI+): *m/z* calcd for $C_{13}H_{11}N_4O_4^+$ $[M + H]^+$ 287.0775, found 287.0777.

1-(1,2,3,4-Tetrahydro-2,4-dioxo-3-phenylquinolin-3-yl)-1H-1,2,3-triazole-4-carboxylic acid (10b). Colorless crystals, mp 205–209 °C (ethyl acetate); R_f = 0.00–0.19 (10% ethanol in chloroform); ^{1}H NMR (500 MHz, DMSO-d_6) δ 7.07 (d, 1H, *J* = 8.0 Hz, H-8), 7.16 (ddd, 1H, *J* = 7.7, 7.5, 1.0 Hz, H-6), 7.32–7.40 (m, 2H, H-2^B, H-6^B), 7.45–7.53 (m, 3H, H-3^B, H-4^B, H-5^B), 7.62 (ddd, 1H, *J* = 8.2, 7.3, 1.6 Hz, H-7), 7.83 (dd, 1H, *J* = 7.8, 1.4 Hz, H-5), 8.71 (s, 1H, H-5^A), 11.63 (s, 1H, H-1), 13.06 (br, 1H, COOH); ^{13}C NMR (126 MHz, DMSO-d_6) δ 80.6 (C-3), 116.7 (C-8), 119.6 (C-4a), 123.4 (C-6), 127.4 (C-5), 128.9 (C-2^B, C-6^B), 129.6 (C-3^B, C-5^B), 129.8 (C-1^B), 130.6 (C-4^B), 131.1 (C-5^A), 136.7 (C-7), 139.2 (C-4^A), 140.4 (C-8a), 161.7 (COOH), 166.8 (C-2), 188.6 (C-4); IR (cm^{-1}): ν 3364, 3157, 1740, 1724, 1679, 1613, 1594, 1485, 1201, 1183, 1039, 855, 778, 754; HRMS (ESI+): *m/z* calcd for $C_{18}H_{13}N_4O_4^+$ $[M + H]^+$ 349.0931, found 349.0927.

1-(1,2,3,4-Tetrahydro-3-methyl-2,4-dioxo-1-(prop-2-ynyl)quinolin-3-yl)-1H-1,2,3-triazole-4-carboxylic acid (11a). Colorless crystals, mp 187–190 °C (ethyl acetate); R_f = 0.15 (50% ethanol in chloroform); ^{1}H NMR (500 MHz, DMSO-d_6) δ 2.14 (s, 3H), 3.38 (dd, 1H, *J* = 2.4, 2.3 Hz), 4.84 (dd, 1H, *J* = 18.1, 2.3 Hz), 4.97 (dd, 1H, *J* = 18.1, 2.4 Hz), 7.38 (dd, 1H, *J* = 7.7, 7.3 Hz), 7.59 (d, 1H, *J* = 8.5 Hz), 7.91 (ddd, 1H, *J* = 8.5, 7.3, 1.4 Hz), 7.97 (dd, 1H, *J* = 7.7, 1.4 Hz), 8.99 (s, 1H), 13.23 (br, 1H); ^{13}C NMR (126 MHz, DMSO-d_6) δ 23.5, 32.7, 73.7, 75.4, 78.2, 116.7, 119.2, 124.2, 128.1, 130.6, 137.1, 139.6, 140.7, 161.7, 167.7, 189.5; IR (cm^{-1}): ν 3259, 3137, 2127, 1742, 1693, 1650, 1603, 1472, 1393, 1304, 1214, 1187, 1045, 781, 753; HRMS (ESI+): *m/z* calcd for $C_{16}H_{13}N_4O_4^+$ $[M + H]^+$ 325.0931, found 325.0930.

1-(1,2,3,4-Tetrahydro-2,4-dioxo-3-phenyl-1-(prop-2-ynyl)quinolin-3-yl)-1H-1,2,3-triazole-4-carboxylic acid (11b). Colorless crystals, mp 154–161 °C (ethyl acetate); R_f = 0.23 (50% ethanol in chloroform); R_f = 0.00–0.15 (10% ethanol in chloroform); ^{1}H NMR (500 MHz, DMSO-d_6) δ 3.40–3.44 (m, 1H), 4.80 (dd, 1H, *J* = 16.8, 3.3 Hz), 5.16 (dd, 1H, *J* = 16.8, 3.3 Hz), 7.23-7.32 (m, 3H),

7.39–7.53 (m, 4H), 7.75 (ddd, 1H, J = 8.4, 7.4, 1.7 Hz), 7.92 (dd, 1H, J = 7.7, 1.5 Hz), 8.79 (s, 1H), 13.23 (br, 1H); ^{13}C NMR (126 MHz, DMSO-d_6) δ 33.2, 75.5, 77.8, 80.5, 116.3, 121.0, 124.2, 127.8, 128.7, 129.5, 129.7, 130.7, 131.3, 136.7, 139.2, 139.9, 161.7, 165.7, 187.5; IR (cm^{-1}): ν 3494, 3205, 2118, 1720, 1683, 1603, 1469, 1374, 1306, 1218, 1040, 871, 764, 696; HRMS (ESI+): *m/z* calcd for $C_{21}H_{15}N_4O_4^+$ [M + H]$^+$ 387.1088, found 387.1084.

1-(1-((1-Benzyl-1H-1,2,3-triazol-4-yl)methyl)-1,2,3,4-tetrahydro-3-methyl-2,4-dioxoquinolin-3-yl)-1H-1,2,3-triazole-4-carboxylic acid (12a). Colorless solid, mp 129–148 °C; R_f = 0.00–0.35 (10% ethanol in chloroform); ^{1}H NMR (500 MHz, DMSO-d_6), δ 2.15 (s, 3H, CH_3), 5.18 (d, 1H, J = 16.2 Hz, N-1–CHα), 5.48 (d, 1H, J = 16.2 Hz, N-1–CHβ), 5.57 (s, 2H, N-1^C–CH_2), 7.24–7.28 (m, 2H, H-2^D, H-6^D), 7.28–7.38 (m, 4H, H-6, H-3^D, H-4^D, H-5^D), 7.64 (d, 1H, J = 8.5 Hz, H-8), 7.81 (ddd, 1H, J = 8.7, 7.1, 1.7 Hz, H-7), 7.93 (dd, 1H, J = 7.6, 1.2 Hz, H-5), 8.16 (s, 1H, H-5^C), 8.96 (s, 1H, H-5^A), 12.98 (br, 1H, COOH); ^{13}C NMR (126 MHz, DMSO-d_6) δ 23.6 (CH_3), 38.9 (N-1–CH_2), 52.9 (N-1^C–CH_2), 74.0 (C-3), 116.7 (C-8), 119.3 (C-4a), 123.9 (C-5^C), 123.9 (C-6), 127.9 (C-2^D, C-6^D), 128.0 (C-4^D), 128.2 (C-5),128.8 (C-3^D, C-5^D), 130.6 (C-5^A), 136.0 (C-1^D), 137.1 (C-7), 139.6 (C-4^A), 141.4 (C-8a), 142.3 (C-4^C), 161.7 (COOH), 168.2 (C-2), 189.8 (C-4); ^{15}N NMR (51 MHz, DMSO-d_6) δ 136.8 (N-1), 249.3 (N-1^A), 251.2 (N-1^C), 351.1 (N-3^C), 357.4 (N-3^A), 362.4 (N-2^C), 367.7 (N-2^A); IR (cm^{-1}): ν 3468, 3140, 2945, 1716, 1679, 1602, 1470, 1385, 1278, 1222, 1045, 784, 764, 721; HRMS (ESI+): *m/z* calcd for $C_{23}H_{20}N_7O_4^+$ [M + H]$^+$ 458.1571, found 458.1579.

1-(1,2,3,4-Tetrahydro-3-methyl-2,4-dioxo-1-((1-phenyl-1H-1,2,3-triazol-4-yl)methyl)quinolin-3-yl)-1H-1,2,3-triazole-4-carboxylic acid (12b). Colorless solid, mp 143–168 °C; R_f = 0.00–0.35 (10% ethanol in chloroform); R_f = 0.18 (50% ethanol in chloroform); ^{1}H NMR (500 MHz, DMSO-d_6) δ 2.22 (s, 3H, CH_3), 5.27 (d, 1H, J = 16.3 Hz, N-1–CHα), 5.62 (d, 1H, J = 16.3 Hz, N-1–CHβ), 7.34 (dd, 1H, J = 7.4, 7.4 Hz, H-6), 7.45–7.52 (m, 1H, H-4^D), 7.55–7.62 (m, 2H, H-3^D, H-5^D), 7.69 (d, 1H, J = 8.4 Hz, H-8), 7.81–7.91 (m, 3H, H-7, H-2^D, H-6^D), 7.96 (d, 1H, J = 7.3 Hz, H-5), 8.74 (s, 1H, H-5^C), 8.97 (s, 1H, H-5^A), 13.02 (br, 1H, COOH); ^{13}C NMR (126 MHz, DMSO-d_6) δ 23.6 (CH_3), 38.8 (N-1–CH_2), 74.1 (C-3), 116.8 (C-8), 119.4 (C-4a), 120.2 (C-2^D, C-6^D), 121.8 (C-5^C), 124.0 (C-6), 128.0 (C-5), 128.9 (C-4^D), 130.0 (C-3^D, C-5^D), 130.6 (C-5^A), 136.5 (C-1^D), 137.2 (C-7), 139.7 (C-4^A), 141.5 (C-8a), 143.3 (C-4^C), 161.7 (COOH), 168.3 (C-2), 189.9 (C-4); ^{15}N NMR (51 MHz, DMSO-d_6) δ 135.9 (N-1), 249.4 (N-1^A), 255.8 (N-1^C), 353.6 (N-3^C), 356.9 (N-3^A), 358.2 (N-2^C), 367.2 (N-2^A); IR (cm^{-1}): ν 3142, 3085, 2925, 1717, 1679, 1601, 1470, 1386, 1278, 1226, 1193, 1045, 760, 690, 663; **HRMS** (ESI+): *m/z* calcd for $C_{22}H_{18}N_7O_4^+$ [M + H]$^+$ 444.1415, found 444.1413.

1-(1,2,3,4-Tetrahydro-3-methyl-2,4-dioxo-1-((1-(pyridin-2-yl)-1H-1,2,3-triazol-4-yl)methyl)quinolin-3-yl)-1H-1,2,3-triazole-4-carboxylic acid (12c). Colorless solid, mp 152–161 °C; R_f = 0.03 (10% ethanol in chloroform); R_f = 0.14 (50% ethanol in chloroform); ^{1}H NMR (500 MHz, DMSO-d_6) δ 2.22 (s, 3H), 5.40 (d, 1H, J = 16.5 Hz), 5.55 (d, 1H, J = 16.5 Hz), 7.33 (ddd, 1H, J = 7.6, 7.4, 0.8 Hz), 7.51–7.57 (m, 1H), 7.61 (d, 1H, J = 8.5 Hz), 7.81 (ddd, 1H, J = 8.4, 7.4, 1.7 Hz), 7.96 (dd, 1H, J = 7.7, 1.6 Hz), 8.09-8.13 (m, 2H), 8.56–8.60 (m, 1H), 8.83 (s, 1H), 8.99 (s, 1H), 13.19 (br, 1H); ^{13}C NMR (126 MHz, DMSO-d_6) δ 23.6 (CH_3), 38.8 (N-1–CH_2), 74.2 (C-3), 113.7 (C-3^D) 116.6 (C-8), 119.4 (C-4a), 120.7 (C-5^C), 123.9 (C-6), 124.5 (C-5^D), 128.0 (C-5), 130.6 (C-5^A), 137.1 (C-7), 139.7 (C-4^A), 140.2 (C-4^D), 141.2 (C-8a), 143.2 (C-4^C), 148.4 (C-2^D), 149.0 (C-6^D), 161.7 (COOH), 168.5 (C-2), 189.8 (C-4); ^{15}N NMR (51 MHz, DMSO-d_6) 1 δ 249.2 (N-1^A), 260.3 (N-1^C), 284.1 (N-1^D); IR (cm^{-1}): ν 3147, 2926, 1717, 1680, 1600, 1471, 1385, 1278, 1223, 1038, 1000, 781, 755, 663; HRMS (ESI+): *m/z* calcd for $C_{21}H_{17}N_8O_4^+$ [M + H]$^+$ 445.1367, found 445.1372.

1-(1-((1-Benzyl-1H-1,2,3-triazol-4-yl)methyl)-1,2,3,4-tetrahydro-2,4-dioxo-3-phenylquinolin-3-yl)-1H-1,2,3-triazole-4-carboxylic acid (12d). Colorless solid, mp 139–162 °C; R_f = 0.12–0.46 (10% ethanol in chloroform); R_f = 0.00–0.18 (3% ethanol in chloroform); ^{1}H NMR (500 MHz, DMSO-d_6) δ 5.11 (d, 1H, J = 15.9 Hz, N-1–CHα), 5.61 (d, 1H, J = 15.9 Hz, N-1–CHβ), 5.61 (d, 2H, J = 14.8 Hz, N-1^C–CH_2), 7.13–7.20 (m, 2H, H-2^B, H-6^B), 7.21–7.29 (m, 3H, H-6, H-3^B, H-5^B), 7.29–7.44 (m, 6H, H-2^D, H-6^D, H-4^D, H-3^D, H-5^D, H-4^B), 7.66 (d, 1H, J = 8.2 Hz, H-8), 7.71 (dd, 1H, J = 8.0, 7.9 Hz, H-7), 7.90 (d, 1H, J = 7.4 Hz, H-5), 8.24 (s, 1H, H-5^C), 8.76 (s, 1H, H-5^A), 13.25 (br, 1H, COOH); ^{13}C NMR (126 MHz, DMSO-d_6) δ 39.8 (N-1–CH_2), 52.8 (N-1^C–CH_2), 80.5 (C-3), 116.6 (C-8), 121.1 (C-4a), 124.0 (C-6), 124.3 (C-5^C), 127.7 (C-5), 128.0 (C-2^D, C-6^D), 128.2 (C-4^D), 128.7 (C-2^B, C-6^B), 128.8 (C-3^D, C-5^D), 129.3 (C-3^B, C-5^B), 129.6 (C-1^B), 130.5 (C-4^B), 131.2 (C-5^A), 136.0 (C-1^D), 136.6 (C-7), 139.3 (C-4^A), 140.8 (C-8a), 141.9 (C-4^C), 161.7 (COOH), 166.1 (C-2), 187.9 (C-4); ^{15}N NMR (51 MHz, DMSO-d_6) δ 249.8 (N-1^A), 250.9 (N-1^C), 351.6 (N-3^C), 356.4 (N-3^A), 362.7 (N-2^C); IR (cm^{-1}): ν 3467, 3141, 1717, 1680, 1601, 1469, 1376, 1224, 1038, 872, 760, 724, 696, 665, 610; HRMS (ESI+): *m/z* calcd for $C_{28}H_{22}N_7O_4^+$ [M + H]$^+$ 520.1728, found 520.1730.

1-(1,2,3,4-Tetrahydro-2,4-dioxo-3-phenyl-1-((1-phenyl-1H-1,2,3-triazol-4-yl)methyl)quinolin-3-yl)-1H-1,2,3-triazole-4-carboxylic acid (12e). Colorless solid, mp 153–169 °C; R_f = 0.00–0.22 (10% ethanol in chloroform); ^{1}H NMR (500 MHz, DMSO-d_6) δ 5.28 (d, 1H, J = 16.0 Hz, N-1–CHα), 5.70 (d, 1H, J = 16.0 Hz, N-1–CHβ), 7.26 (dd, 1H, J = 7.4, 7.3 Hz, H-6), 7.28–7.34 (m, 2H, H-2^B, H-6^B), 7.35–7.41 (m, 2H, H-3^B, H-5^B), 7.41–7.46 (m, 1H, H-4^B),

7.48–7.54 (m, 1H, H-4^{D}), 7.57-7.65 (m, 2H, H-3^{D}, H-5^{D}), 7.68 (d, 1H, *J* = 8.3 Hz, H-8), 7.73 (dd, 1H, *J* = 7.6, 7.4 Hz, H-7), 7.85–7.91 (m, 2H, H2^{D}, H-6^{D}), 7.93 (d, 1H, *J* = 7.4 Hz, H-5), 8.79 (s, 1H, H-5^{A}), 8.81 (s, 1H, H-5^{C}), 13.12 (br, 1H, COOH); ^{13}C NMR (126 MHz, DMSO-d_6) δ 39.2 (N-1–CH_2), 80.7 (C-3), 116.7 (C-8), 120.2 (C-2^{D}, C-6^{D}), 121.1 (C-4a), 122.4 (C-5^{C}), 124.1 (C-6), 127.8 (C-5), 128.9 (C-4^{D}), 129.0 (C-2^{B}, C-6^{B}), 129.4 (C-3^{B}, C-5^{B}), 129.7 (C-1^{B}), 130.0 (C-3^{D}, C-5^{D}), 130.7 (C-4^{B}), 131.3 (C-5^{A}), 136.5 (C-1^{D}), 136.8 (C-7), 139.3 (C-4^{A}), 140.7 (C-8a), 142.9 (C-4^{C}), 161.8 (COOH), 166.3 (C-2), 188.0 (C-4); ^{15}N NMR (51 MHz, DMSO-d_6) δ 139.5 (N-1), 249.8 (N-1^{A}), 255.6 (N-1^{C}), 354.2 (N-3^{C}), 357.5 (N-3^{A}), 372.6 (N-2^{A}); IR (cm^{-1}): ν 3525, 3145, 3067, 1717, 1681, 1600, 1469, 1377, 1234, 1041, 872, 759, 692, 665; HRMS (ESI+): *m/z* calcd for $C_{27}H_{20}N_7O_4^+$ [M + H]$^+$ 506.1571, found 506.1567.

1-(1,2,3,4-Tetrahydro-2,4-dioxo-3-phenyl-1-((1-(pyridin-2-yl)-1H-1,2,3-triazol-4-yl)methyl)quinolin-3-yl)-1H-1,2,3-triazole-4-carboxylic acid (12f). Colorless solid, mp 116–172 °C; R_f = 0.06 (10% ethanol in chloroform), R_f = 0.00 (5% ethanol in chloroform); ^{1}H NMR (500 MHz, DMSO-d_6) δ 5.43 (d, 1H, *J* = 16.2 Hz, N-1–CHα), 5.64 (d, 1H, *J* = 16.2 Hz, N-1–CHβ), 7.25 (dd, 1H, *J* = 7.4, 7.3 Hz, H-6), 7.28–7.36 (m, 2H, H-2^{B}, H-6^{B}), 7.38–7.48 (m, 3H, H-3^{B}, H-4^{B}, H-5^{B}), 7.50–7.59 (m, 2H, H-8, H-5^{D}), 7.69 (dd, 1H, *J* = 7.6, 7.5 Hz, H-7), 7.95 (d, 1H, *J* = 7.4 Hz, H-5), 8.07-8.19 (m, 2H, H-3^{D}, H-4^{D}), 8.56–8.64 (m, 1H, H-6^{D}), 8.79-8.91 (m, 2H, H-5^{C}, H-5^{A}), 13.23 (br, 1H, COOH); ^{13}C NMR (126 MHz, DMSO-d_6) δ 39.7 (N-1–CH_2), 80.8 (C-3), 113.7 (C-3^{D}), 116.5 (C-8), 120.9 (C-5^{C}), 121.2 (C-4a), 124.0 (C-6), 124.5 (C-5^{D}), 127.9 (C-5), 128.9 (C-2^{B}, C-6^{B}), 129.5 (C-3^{B}, C-5^{B}), 129.8 (C-1^{B}), 130.7 (C-4^{B}), 131.3 (C-5^{A}), 136.7 (C-7), 139.2 (C-4^{A}), 140.3 (C-4^{D}), 140.4 (C-8a), 143.0 (C-4^{C}), 148.3 (C-2^{D}), 149.0 (C-6^{D}), 161.8 (COOH), 166.7 (C-2), 187.9 (C-4); ^{15}N NMR (51 MHz, DMSO-d_6) δ 137.8 (N-1), 249.7 (N-1^{A}), 260.4 (N-1^{C}), 284.9 (N-1^{D}), 356.8 (N-3^{A}), 357.1 (N-3^{C}); IR (cm^{-1}): ν 3435, 3157, 2927, 1718, 1682, 1600, 1470, 1375, 1313, 1189, 1035, 779, 758, 696; HRMS (ESI+): *m/z* calcd for $C_{26}H_{19}N_8O_4^+$ [M + H]$^+$ 507.1524, found 507.1527.

Acknowledgments.

This work was financed by TBU in Zlín (internal grant no. IGA/FT/2019/010, funded from the resources of specific university research). The authors acknowledge also the financial support from the Slovenian Research Agency (Research Core Funding Grant P1-0230, Project J1-8147, and Project J1-9166).

5. References

1. D. Urankar, B. Pinter, A. Pevec, F. De Proft, I. Turel, J. Košmrlj, *Inorg. Chem.* **2010**, *49*, 4820–4829. **DOI:**10.1021/ic902354e
2. K. J. Kilpin, E. L. Gavey, C. J. McAdam, C. B. Anderson, S. J. Lind, C. C. Keep, K. C. Gordon, J. D. Crowley, *Inorg Chem* **2011**, *50*, 6334–6346. **DOI:**10.1021/ic200789b
3. J. D. Crowley, D. A. McMorran, *Top. Heterocycl. Chem.* **2012**, *28*, 31–84. **DOI:**10.1007/7081_2011_67
4. R. J. Detz, S. A. Heras, R. de Gelder, P. W. N. M. Van Leeuwen, H. Hiemstra, J. N. H. Reek, J. H. Van Maarseveen, *Org. Lett.* **2006**, *8*, 3227–3230. **DOI:**10.1021/ol061015q
5. B. Beyer, C. Ulbricht, D. Escudero, C. Friebe, A. Winter, L. González, U. S. Schubert, *Organometallics* **2009**, *28*, 5478–5498. **DOI:**10.1021/om9003785
6. A. Kumar, R. K. Chhatra, P. S. Pandey, *Org. Lett.* **2010**, *12*, 24–27. **DOI:**10.1021/ol902351g
7. S. H. Kim, H. S. Choi, J. Kim, S. J. Lee, D. T. Quang, J. S. Kim, *Org. Lett.* **2010**, *12*, 560–563. **DOI:**10.1021/ol902743s
8. J. M. Fernández-Hernández, C. H. Yang, J. I. Beltrán, V. Lemaur, F. Polo, R. Fröhlich, J. Cornil, L. De Cola, *J. Am. Chem. Soc.* **2011**, *133*, 10543–10558. **DOI:**10.1021/ja201691b
9. Y. C. Duan, Y. C. Ma, E. Zhang, X. J. Shi, M. M. Wang, X. W. Ye, H. M. Liu, *Eur. J. Med. Chem.* **2013**, *62*, 11–19. **DOI:**10.1016/j.ejmech.2012.12.046
10. B. Garudachari, A. M. Isloor, M. N. Satyanarayana, H.-K. Fun, G. Hegde, *Eur. J. Med. Chem.* **2014**, *74*, 324–332. **DOI:**10.1016/j.ejmech.2014.01.008
11. Y. W. He, C. Z. Dong, J. Y. Zhao, L. L. Ma, Y. H. Li, H. A. Aisa, *Eur. J. Med. Chem.* **2014**, *76*, 245–255. **DOI:**10.1016/j.ejmech.2014.02.029
12. K. T. Petrova, T. M. Potewar, P. Correira-da-Silva, M. T. Barros, R. C. Calhelha, A. Ćiric, M. Soković, I. C. F. R. Ferreira, *Carbohydr. Res.* **2015**, *417*, 66–71. **DOI:**10.1016/j.carres.2015.09.003
13. I. Fichtali, W. Laaboudi, E. M. El Hadrami, F. El Aroussi, A. Ben-Tama, M. Benlemlih, S. E. Stiriba, *J. Mater. Environ. Sci.* **2016**, *7*, 1633–1641.
14. M. R. Jones, E. Mathieu, C. Dyrager, S. Faissner, Z. Vaillancourt, K. J. Korshavn, M. H. Lim, A. Ramamoorthy, V. W. Yong, S. Tsutsui, P. K. Stys, T. Storr, *Chem. Sci.* **2017**, *8*, 5636–5643. **DOI:**10.1039/C7SC01269A
15. A. Bolje, J. Košmrlj, *Org. Lett.* **2013**, *15*, 5084–5087. **DOI:**10.1021/ol4024584
16. A. Bolje, S. Hohloch, D. Urankar, A. Pevec, M. Gazvoda, B. Sarkar, J. Košmrlj, *Organometallics* **2014**, *33*, 2588–2598. **DOI:**10.1021/om500287t
17. S. Hohloch, S. Kaiser, F. L. Duecker, A. Bolje, R. Maity, J. Košmrlj, B. Sarkar, *Dalton Trans.* **2015**, *44*, 686–693. **DOI:**10.1039/C4DT02879A
18. M. Gazvoda, M. Virant, A. Pevec, D. Urankar, A. Bolje, M. Kočevar, J. Košmrlj, *Chem. Commun. (Cambridge, U. K.)* **2016**, *52*, 1571–1574. **DOI:**10.1039/C5CC08717A
19. K. Proisl, S. Kafka, J. Košmrlj, Curr. Org. Chem. **2017**, *21*, 1949–1975. **DOI:**10.2174/1385272821666170711155631
20. S. Kafka, S. Hauke, A. Salčinović, O. Soidinsalo, D. Urankar, J. Košmrlj, Molecules **2011**, *16*, 4070–4081. **DOI:**10.3390/molecules16054070
21. A. C.-M. Daugan, Y. Lamotte, O. Mirguet, Quinolinone de-

rivatives, PCT Int Appl WO 2012/119978, date of patent September 13, **2012**.
22. N. P. Grimster, B. Stump, J. R. Fotsing, T. Weide, T. T. Talley, J. G. Yamauchi, A. Nemecz, C. Kim, K.-Y. Ho, K. B. Sharpless, P. Taylor, V. V. Fokin, *J. Am. Chem. Soc.* **2012**, *134*, 6732–6740. **DOI:**10.1021/ja3001858
23. J. G. Yamauchi, K. Gomez, N. Grimster, M. Dufouil, A. Nemecz, J. R. Fotsing, K.-Y. Ho, T. T. Talley, K. B. Sharpless, V. V. Fokin, P. Taylor, *Mol. Pharmacol.* **2012**, *82*, 687–699. **DOI:**10.1124/mol.112.080291
24. C. D. Rillahan, E. Schwartz, R. McBride, V. V. Fokin, J. C. Paulson, *Angew. Chem. Int. Ed.* **2012**, *51*, 11014–11018. **DOI:**10.1002/anie.201205831
25. Y. Miyamoto, J. Kalisiak, K. Korthals, T. Lauwaet, D. Y. Cheung, R. Lozano, E. R. Cobo, P. Upcroft, J. A. Upcroft, D. E. Berg, F. D. Gillin, V. V. Fokin, K. B. Sharpless, L. Eckmann, *Proc. Natl. Acad. Sci. U. S. A.* **2013**, *110*, 17564–17569. **DOI:**10.1073/pnas.1302664110
26. J. S. Oakdale, R. K. Sit, V. V. Fokin, *Chem. – Eur. J.* **2014**, *20*, 11101–11110. **DOI:**10.1002/chem.201402559
27. V. Fokin, B. K. Sharpless, L. Eckmann, Y. Miyamoto, Expanded therapeutic potential in nitroheteroaryl antimicrobials, PCT Int Appl WO 2014/205414, date of patent December 24, **2014**.
28. J. Dong, K. B. Sharpless, Sulfur(VI) fluoride compounds and methods for the preparation thereof, PCT Int Appl WO 2015/188120, date of patent December 10, **2015**.
29. W. J. Kim, K. A. Korthals, S. Li, C. Le, J. Kalisiak, K. B. Sharpless, V. V. Fokin, Y. Miyamoto, L. Eckmann, *Antimicrob. Agents Chemother.* **2017**, *61*, e02397/1– e02397/12. **DOI:**10.1128/AAC.02397-16.
30. D. Milićević, R. Kimmel, M. Gazvoda, D. Urankar, S. Kafka, J. Košmrlj, *Molecules* **2018**, *23*, 2310/1–2310/21. **DOI:**10.3390/molecules23092310
31. N. Boechat, V. F. Ferreira, S. B. Ferreira, M. de L. G. Ferreira, Da F. de C. Silva, M. M. Bastos, M. dos S. Costa, M. C. S. Lourenço, A. C. Pinto, A. U. Krettli, A. C. Aguiar, B. M. Teixeira, Da N. V. Silva, P. R. C. Martins, F. A. F. M. Bezerra, A. L. S. Camilo, G. P. Da Silva, C. C. P. Costa, *J. Med. Chem.* **2011**, *54*, 5988–5999. **DOI:**10.1021/jm2003624
32. D. M. Reddy, J. Srinivas, G. Chashoo, A. K. Saxena, H. M. S. Kumar, Eur. *J. Med. Chem.* **2011**, *46*, 1983–1991. **DOI:**10.1016/j.ejmech.2011.02.016
33. M. Aufort, J. Herscovici, P. Bouhours, N. Moreau, C. Girard, *Bioorg. Med. Chem. Lett.* **2008**, *18*, 1195–1198. **DOI:**10.1016/j.bmcl.2007.11.111
34. P. R. Bagdi, R. S. Basha, A. T. Khan, *RSC Adv.* **2015**, *5*, 61337–61344. **DOI:**10.1039/C5RA09671E
35. B. Orzeszko, M. Fedoryński, A. E. Laudy, B. J. Starościak, A. Orzeszko, *Acta Pol. Pharm.* **2006**, *63*, 374–377.
36. T. Sasaki, S. Eguchi, M. Yamaguchi, T. Esaki, *J. Org. Chem.* **1981**, *46*, 1800–1804. **DOI:**10.1021/jo00322a009
37. X. Wang, Z.-C. Dai, Y.-F. Chen, L.-L. Cao, W. Yan, S.-K. Li, J.-X. Wang, Z.-G. Zhang, Y.-H. Ye, *Eur. J. Med. Chem.* **2017**, *126*, 171–182. **DOI:**10.1016/j.ejmech.2016.10.006
38. C. Han, S. Dong, W. Zhang, Z. Chen, *Synlett* **2018**, *29*, 673–677. **DOI:**10.1055/s-0036-1589157
39. M. N. Rajadhyaksha, R. Nair, P. V. Ramesan, K. Johnson, A. M. Panandikar, Process for preparation of fluorinated triazole compound, PCT Int Appl WO 2012/032540, date of patent March 15, 2012.
40. Y. Naro, N. Ankenbruck, M. Thomas, Y. Tivon, C. M. Connelly, L. Gardner, A. Deiters, *J. Med. Chem.* **2018**, *61*, 5900–5909. **DOI:**10.1021/acs.jmedchem.7b01891
41. J. M. Rieger, M. L. Brown, G. W. Sullivan, J. Linden, T. L. Macdonald, *J. Med. Chem.* **2001**, *44*, 531–539. **DOI:**10.1021/jm0003642
42. G. Abbiati, A. Contini, D. Nava, E. Rossi, *Tetrahedron* **2009**, *65*, 4664–4670. **DOI:**10.1016/j.tet.2009.04.041
43. D.-S. Kim, K. Bolla, S. Lee, J. Ham, *Tetrahedron* **2011**, *67*, 1062–1070. **DOI:**10.1016/j.tet.2010.12.049
44. Oxford Diffraction, CrysAlis PRO, Oxford Diffraction Ltd., Yarnton, England, 2009.
45. G. M. Sheldrick, *Acta Crystallogr., Sect. A: Found. Crystallogr.* **2008**, *64*, 112–122. **DOI:**10.1107/S0108767307043930
46. G. M. Sheldrick, *Acta Crystallogr., Sect. C: Struct. Chem.* **2015**, *71*, 3–8. **DOI:**10.1107/S2053229614024218

Povzetek

V prispevku je opisana kisla etanoliza (deacetiliranje) (1-(2,4-diokso-1,2,3,4-tetrahidrokinolin-3-il)-1*H*-1,2,3-triazol-4-il)metil acetatov, substituiranih na dušikovem atomu kinolindionske skupine s propargilno skupino ali pa z (1-substituirano *1H*-1,2,3-triazol-4-il)metilno skupino. Izhodni acetate so pripravili iz ustreznih 3-(4-hidroksimetil-*1H*-1,2,3-triazol-1-il)kinolin-2,4(*1H, 3H*)-dionov, ki niso substituirani na kinolonskem dušiku, po še opisanih postopkih. Tako dobljene primarne alkohole, kot tudi tiste, ki niso substituirani na kinolonskem dušiku, so oksidirali bodisi v aldehide s piridinijevim klorokromatom (PCC), ali pa z manganovim dioksidom v karboksilne kisline, ob uporabi Jones-ovega reagent v acetonu kot topilu. Strukture vseh pripravljenih spojin so potrdili z ^{1}H, ^{13}C and ^{15}N NMR spectroskopijo. Ustrezne rešitve struktur analiziranih spojin so bile narejene na podlagi standardnih 1D in izbranih gradientnih 2D NMR poskusov (^{1}H–^{1}H gs-COSY, ^{1}H–^{13}C gs-HSQC, ^{1}H–^{13}C gs-HMBC), skupaj z ^{1}H–^{15}N gs-HMBC, kot praktičnim orodjem za določitev ^{15}N NMR kemijskih premikov v spojinah, ki niso obogatene z ^{15}N izotopom.

Except when otherwise noted, articles in this journal are published under the terms and conditions of the Creative Commons Attribution 4.0 International License

Scientific paper

Demographic Characteristics of Chemistry Teachers in Croatia Affecting the Use of Pre-laboratory Activities in the Classroom

Snježana Smerdel[1,*] and Meliha Zejnilagić Hajrić[2]

[1] *University of Split, Faculty of Science, Ruđera Boškovića 33, 21000 Split, Croatia*

[2] *University of Sarajevo, Faculty of Science, Zmaja od Bosne 33-35, 71000 Sarajevo, Bosnia and Herzegovina*

* *Corresponding author: E-mail: ssmerdel@gmail.com*

Received: 07-07-2019

Abstract

Pre-laboratory activities are designed to focus the attention of students on some aspects of the experiment they are preparing to do during the week. Previous research has found that such activities reduce the cognitive load in laboratory time and tend to increase the efficiency of students' laboratory work. This research aims at comparing the importance of demographic characteristics affecting the teachers' use of pre-laboratory activities in a chemistry class. In the frame of the quantitative survey research, an online questionnaire was completed by 166 chemistry teachers from all regions in Croatia. In pre-laboratory sessions, the teachers most commonly used a pre-lab discussion and pre-lab worksheets whereas computer simulations were represented the least. Three characteristics affecting the teachers' use of pre-laboratory activities in chemistry classes were their gender, age and teaching subjects. The teachers' education, teaching experience and school types were nonsignificant characteristics.

Keywords: Cognitive load; pre-laboratory activities; pre-learning strategy; secondary chemistry education.

1. Introduction

Laboratory activities are learning experiences in which students interact with materials and/or models to observe and understand the natural world. Science educators have suggested that many benefits accrue from engaging students in science laboratory activities.[1] This includes exposing students to concrete experiences with objects and concepts mentioned in the classroom.[2] In addition, it allows the connection of macroscopic observations to the abstract representations and symbolizations used in science to be made by facilitating the understanding of chemical concepts.[3] Literature findings have indicated that the students' preparation for laboratory work should increase the chances of their understanding of what they are doing in the lab. This is intended to avoid a 'cookbook' or 'recipe-following scenario'.[4]

This research is focused on the use of various aspects of preparation for laboratory work in Croatian schools, exploring the possible influence of the teachers' demographic profile. The chemistry teachers were required to complete a survey questionnaire about the use of pre-laboratory activities (PLABs) in their teaching practice.

The next section explains the importance of preparing students for laboratory work. Information processing and knowledge building are limited to the working memory capacity but the use of PLABs leads to reducing working memory load in laboratory time.

2. Theoretical Framework

2. 1. The Importance of PLABs

The concept of PLABs is particularly based on ideas developed by Ausubel[5] (preparing the mind for learning) and Sweller, Van Merrienboer and Paas's[6] cognitive load theory (CLT). According to CLT, information processing and knowledge building are limited to the working memory capacity. The overloaded working memory capacity does not leave space for thinking and information organization, which results in cognitive overload.[7] In a laboratory, there is much more information to be processed than necessary. For a novice, all of the information (the bubble, the colour change, the smell, etc.) is potentially important and relevant, while only a limited part of this is important for an expert because of the precise filter available to them. An ex-

pert has the information held in the long-term memory as prior knowledge, theory and/or previous experience.[8]

PLABs are designed to focus the attention of students on some aspects of the experiment they are preparing to do during the week[9] in accordance with the selected objectives for experimental work.[10]

According to Johnstone et al., the aim of PLABs is to prepare students to take an intelligent interest in the experiment by knowing where they will go, why they will go there, and how they will get there.[4] The importance of preparing students for laboratory work by reducing the cognitive load in laboratory time has been highlighted by educators and psychologists, and it has also been the subject of a lot of research.[11]

According to Agustian and Seery,[12] the advantages of students' preparation in advance of a laboratory session can be classified into four categories:

- Overall – PLABs tend to have a positive impact on learning in the laboratory.[8,13]
- Experimental – PLABs tend to increase the efficiency of students' laboratory work and reduce the time spent on experimental tasks.[11]
- Conceptual – PLABs that prepare students for conceptual aspects of laboratory work tend to result in students performing better in the laboratory. PLABs that present conceptual ideas of laboratory work tend to lead students to feel more autonomous about completing their laboratory work.[8,14]
- Affective – PLABs enable students to feel more confident about laboratory work[13,15] and/or reduce students' negative feelings towards laboratory classes.[16]

The nature and purpose of PLABs depend on the context and purpose of the laboratory in question.[12] Rollnick et al.[17] concluded that the best form of preparation varies from student to student. Some students will prepare thoroughly no matter what obligatory preparation is demanded. Those who are willing in spirit but poorly organized, or those who would skip preparation because of the load of other academic work are the ones who benefit most from the obligatory preparation.[17]

2. 2. Literature Review of PLABs

In science education literature, the use of various PLABs is extensively described at an undergraduate level. Parallel experiences at a secondary school level are considerably smaller but also vital.[18] The conventional way of preparing students would be to encourage them to read their laboratory manuals, but these typically overload them with information to be held at the same time. On the other hand, only a limited number of students try to understand or do read the manuals before entering the laboratory.[19] The literature review revealed the use of various aspects of PLABs, such as pre-laboratory discussions,[20] pre-lab questionnaires,[8] pre-lab exercises with solving theoretical problems related to the experiment,[9] and pre-laboratory instructions.[21] Students can be required to prepare a laboratory notebook in advance with customary information[22] or complete pre-lab worksheets with questions relevant to a particular experiment.[4]

The results of recent studies indicate frequent use of video demonstrations and online quizzes in advance of laboratory classes,[14,15] as well as online pre-laboratory assignments.[13] The videos can consist of voice-over PowerPoints with photographs of laboratory glassware set-up, explanation/description of laboratory procedures, important safety considerations and waste disposal instructions.[15] The use of quizzes with feedback improves links between theory and practical work by providing immediate feedback to students.[13] Pre-laboratory software resources and simulations are being increasingly used as preparation for laboratory work and as a way of introducing students to the theory relevant to the experiment, as well as for introducing experimental design aspects.[11,18]

Although these previous studies have been useful, the subject of whether demographic characteristics influence the use of PLABs remains unexplored. Only by comparing them, we can determine their possibly important influence on the teaching practice.

2. 3. Demographic Characteristics in Education

The relationship between education and demographic characteristics has been described and analyzed in a considerable number of research works. Some studies have investigated of the teacher candidates' attitudes towards teaching profession according to their demographic variables,[23] then what are the effects of pre-service teachers' demographic features on their concerns about teaching in technology-integrated flipped classrooms[24] and some have focused on gender differences in mathematics and science.[25]

Recent research mostly has addressed the effects of the teachers' demographic characteristics on their information and communication technology (ICT) readiness,[26] the integration of ICT into their teaching practices[27–29] and on the teachers' perceived usefulness of ICT.[30] According to Koh, Chai and Tsai,[31] teaching level and teaching experience have significant influence on the teachers' knowledge of using constructivist teaching methods whereas age and gender are not affected.

Despite the literature related to education, any relationship between the use of teaching methods and demographic characteristics remains unclear. In this paper, we have tried to investigate a possible influence of the teachers' demographic characteristics on the use of PLABs in the chemistry classroom.

2. 4. Research Purpose

In the Croatian education system, there is a lack of relevant scientific research that refers to the importance of pre-

paring students to reduce the cognitive load during laboratory classes. In addition, beyond the context of Croatia, not much research analyses the use of PLABs in secondary chemistry education. Our study is an attempt to fill these gaps by focusing on these issues in the context of Croatia. The conducted research is the first part of a more comprehensive study within a PhD project regarding the implementation of the pre-learning strategy into chemistry education.

The main purpose of this research was to determine the frequency of using PLABs for teaching chemistry and at the same time to explore the influence of demographic characteristics on the use of PLABs within the chemistry teacher population. Six specific characteristics were analyzed: gender, age, teacher education, teaching subjects, school type and teaching experience. The research findings should provide direct insight into the actual practice of teachers and their priorities in the selection of certain aspects of PLABs in chemistry teaching. Learning more about the demographic characteristics of chemistry teachers will allow a more detailed analysis and give a more accurate view of the real current situation in Croatian chemistry education, thus preparing the way for methodological intervention strategies.

Research questions. This research intends to provide answers to the following research questions:

1. How often do chemistry teachers use PLABs in their classes?

2. Does the teachers' use of PLABs depend on their demographic characteristics (gender, age, teacher education, teaching subjects, school type and teaching experience)?

3. Methodology

This quantitative survey research enables the collection of data about the demographic characteristics of participants and can also quantify the frequency of using PLABs. A nationwide questionnaire survey was administered to the population of chemistry teachers from the whole of Croatia.

3. 1. Research Participants

The sampling frame consisted of 600 chemistry teachers from all 21 regions in Croatia whose email addresses were obtained on request from the education advisor database. A total of 166 of the targeted chemistry teachers (27.7% response rate) completed the online survey, but an ideal representation with regard to the number and gender of chemistry teachers in each region could not be achieved. Most of them were in the City of Zagreb region (24.7%) and the fewest in the Karlovac region (0.6%).

The data presented in Table 1 illustrate the profile of the participants for this research. The results revealed that the majority of the participants were female (88.6%), which presents a realistic picture of the great underrepresentation of the male gender in Croatian primary and secondary schools. Likewise, the majority of the participants' age was over 45 years (44.5%) whereas 22.3% were under 36 years old.

According to their education, a total of 69.3% of the participants were teachers whilst others were engineering educators with pedagogical knowledge. The results presented in Table 1 indicate that 63.3% of the participants had over 11 years of teaching experience. About a half of the participants (46.4%) teach in a general high school, while slightly more than one-third (37.3%) teach in a vocational school. The highest percentage belongs to those who teach only chemistry (51.2%), followed by those who teach chemistry and biology (44.0%).

An approval of the protocol by an institutional review board from the Faculty of Science of the University of

Table 1. Description of Participants' Demographic Characteristics (N = 166) by Groups

Demographic characteristic	Group	N	%
Gender	Male	19	11.4
	Female	147	88.6
Age (years)	< 36	37	22.3
	36–45	55	33.2
	> 45	74	44.5
Teacher's Education	Teacher	115	69.3
	Engineer/Educator	51	30.7
Teaching Experience	< 11	61	36.7
	11–25	78	47.0
	> 25	27	16.3
School Types	Primary	27	16.3
	Vocational	62	37.3
	High School	77	46.4
Teaching Subjects	Chemistry	85	51.2
	Chemistry/Biology	73	44.0
	Chemistry/Physics	8	4.8

Split, was obtained. The participation in this survey research was completely voluntary, and all participants were informed of the research purpose, the research content and the benefit that included their contribution to the advancement of the education research. The teachers' consent to participate in this research freely and consciously was obtained from all participants. The confidentiality and anonymity were a priority for the participants of the research.

3. 2. Research Instrument

The Using the Pre-Laboratory Activities Questionnaire (UPLAQ) (Appendix 1) as designed for the purpose of this research and based on the data obtained from a review of existing literature[4,32] was made with the free web survey tool Google Docs. The UPLAQ consists of 15 items – 14 close-ended items and 1 open-ended item. The first seven items include demographic characteristics of chemistry teachers (region, gender, age, education, teaching subjects, school type, and teaching experience). The remaining seven close-ended items relate to the research topic required the participants to estimate the frequency of the use of various forms of PLABs:

- reading the laboratory manual,
- pre-lab discussion about the most important points of an experiment,
- completing pre-lab worksheets,
- solving theoretical problems related to the experiment,
- using audiovisual materials,
- solving online pre-lab assignments,
- doing computer simulations of experiments.

In order to suit the purpose of this research and facilitate administration, the Likert six-point scale of frequency (1-never, 2-sometimes, 3-usually, 4-often, 5-very often, 6-always) was chosen. In order to avoid restricting the teachers to choose among the seven types of PLABs, the following open-ended question was included at the end of UPLAQ: "If you use other types of PLABs not mentioned here, please describe them briefly".

The credibility of the applied instrument was assured by considering the test validity and reliability. The content validity was estimated through the work of two university professors in the field of Chemistry Teaching and two high school chemistry teachers. The experts independently examined the questionnaire regarding the clarity and meaningfulness of the questionnaire's claims, the applied terminology and the diversity in pre-learning activities used, so the UPLAQ was revised according to the given recommendations.

The next step in the development of the instrument was a pilot research (March 2017) carried out with chemistry and biology teachers in primary and secondary schools in one Croatian region and focused on the quality control of the questionnaire and data collection for its optimisation.[33] Seven questionnaire items, which provide information about the frequency of the use of various PLABs, were used as a basis for determining the internal consistency. The internal consistency reliabilities using the Cronbach α coefficient was calculated .79 for all items.[34] The results indicated that the scale had an acceptable level of reliability.

3. 3. Research Context

In this research, an email invitation with a link to access the UPLAQ was distributed at the same time to 600 chemistry teachers from the whole Croatia.

Schooling in Croatia consists of eight primary grades and four secondary grades. Chemistry is a subject for 7th–8th grade primary students and 1st–4th grade secondary students, depending on the school type. Most schools hold two 45-minute chemistry lessons per week. In the first grade of general high school, general chemistry is discussed, in the second physical, in the third inorganic and in the fourth organic chemistry.

During June and July 2017, the UPLAQ was completed online by 166 chemistry teachers. Prior to filling it, the teachers had to read the introductory text explaining the research purpose, result process and instructions for completing the UPLAQ. The time frame for completing the web survey was not limited. The researchers were available via email for addressing any problems or comments regarding the survey questionnaire throughout the research.

3. 4. Data Analysis

Based on the set research questions and hypotheses, the collected data were analyzed with the statistical package IBM SPSS Statistics 21.0 where descriptive and inferential analyses were employed. Descriptive statistics such as a frequency distribution was employed to describe the general data of this research. For the purpose of revealing any differences between the selected demographic characteristics and the use of PLABs, inferential analyses such as non-parametric two-tailed Mann–Whitney U-test and Kruskal–Wallis H test were utilized. These tests were chosen since they enabled the testing of hypotheses on small and asymmetrically distributed samples.

4. Results

4. 1. Frequency of the Use of PLABs

The first research question was: *How often do chemistry teachers use PLABs in their classes?* The descriptive statistics analysis was carried out in order to calculate the frequency percentage of the teachers' responses for the UPLAQ data on the overall sample (Fig. 1). It can be seen that the teachers most commonly use *a pre-lab discussion*

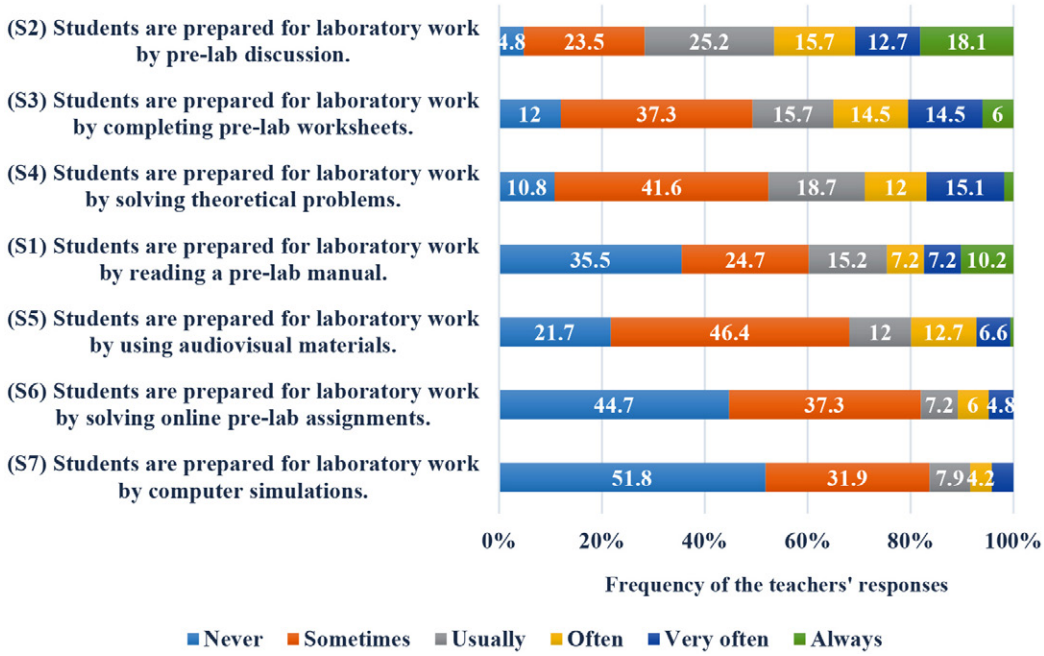

Figure 1: The frequency percentage of teachers' responses (N=166) to the online survey of Using the Pre-Laboratory Activities, by statements (S)

(S2). Almost a half of the teachers (46.5%) use the pre-lab discussion often to always.

From the results presented in Fig. 1, the second most commonly used activity is *completing pre-lab worksheets* (S3), and about one-third of the teachers (35.0%) often to always assign completing pre-lab worksheets to the students. The least use was noticed for *computer simulations* (S7). The results show that about a half of the participants never use computer simulations as PLABs, whereas almost one-third do that sometimes. A slightly higher use was obtained for *solving online pre-lab assignments* (S6). These activities are sometimes carried out by 37.3% of the participants whereas 44.7% never use them.

A smaller number of the teachers responded to the open-ended question "If you use other types of PLABs not mentioned in the questionnaire, please describe them briefly". The following responses were obtained:

"A lot of things from the survey questions are used after the experiment."

"At the end of the lesson, I always tell the students what we are going to do in the next laboratory work."

"I publish in our Facebook group some type of a riddle or questions which refer to the exercise from laboratory work which will be graded during the next lesson. Some students research it, so they have an advantage in doing laboratory work."

Other answers contemplated the technical and syllabus possibilities of teaching (e.g. "the experimental work is done in a classroom without computer equipment", "we do not have classic laboratory exercises at school as they have not been envisaged in the syllabus"). Differences in the use of PLABs are examined and discussed in detail in the following subsection.

4. 2. Differences in the Use of PLABs Regarding Demographic Characteristics

Each group of data was tested for normality with the Kolmogorov–Smirnov test with Lilliefors' significance.[35] The results (p <.05) indicated that the collected data did not satisfy the requirements of a normal distribution. The assumption of the independence of observations was met; there were two or more independent groups compared at the ordinal level.

In order to provide a complete answer to the second research question posed in this paper: *Does the teachers' use of PLABs depend on their demographic characteristics (gender, age, teacher education, teaching subjects, school type and teaching experience)* and the six null hypotheses associated with this research question, the non-parametric Mann–Whitney U test and Kruskal–Wallis H test (level of significance at p < .05) were applied. For this analysis, the teachers' uses of seven aspects of PLABs were defined as dependent variables while demographic characteristics were defined as independent variables.

4. 2. 1. Gender Differences in the Use of PLABs

For an evaluation of gender differences in the teachers' responses, the two-tailed non-parametric Mann–Whitney U test was used for two independent groups: group 1 – male (N = 19) and group 2 – female (N = 147).

Table 2 shows higher mean rank (MR) values for male participants in each of the seven statements (S). Statistically significant gender differences were obtained in S1: *Students are prepared for laboratory work by reading the pre-lab manual* (Mann–Whitney U = 1016.500, Z = –1.993,

Table 2. The results of the Mann–Whitney U test (two-tailed) of statistically significant gender differences in the chemistry teachers' use of pre-laboratory activities (N(male) = 19; N(female) = 147)

Items	Pre-laboratory Activities	Group[a]	Mean Rank	*U*	*Z*	*p*
1	Pre-lab manual	Male	103.50	1016.500	–1.993	*.046*
		Female	80.91			
2	Pre-lab discussion	Male	106.24	964.500	–2.238	*.025*
		Female	80.56			
3	Pre-lab worksheets	Male	95.55	1167.500	–1.201	.230
		Female	81.94			
4	Solving theoretical problems	Male	101.00	1064.000	–1.763	.078
		Female	81.24			
5	Audiovisual materials	Male	83.84	1390.000	–0.035	.972
		Female	83.46			
6	Online assignments	Male	85.82	1352.500	–0.241	.810
		Female	83.20			
7	Computer simulations	Male	92.11	1233.000	–0.911	.362
		Female	82.39			

[a] Grouping Variable: Gender

$N_1 = 147$, $N_2 = 19$, $p = .046$, two-tailed) and in S2: *Students are prepared for laboratory work by a pre-lab discussion* (Mann–Whitney $U = 964.500$, $Z = –2.238$, $N_1 = 147$, $N_2 = 19$, $p = .025$, two-tailed).

In order to provide a clear description of the size of the observed statistically significant influences, the effect sizes were evaluated using the r benchmarks, provided by Cohen,[36] following the formula:[37]

$$R = z/\sqrt{N} \quad (1)$$

Small effect sizes were determined for *the use of reading pre-lab manual* activity ($r = –0.15$) and for *the use of a pre-lab discussion* activity ($r = –0.17$).

4. 2. 2. Teaching Subjects Differences in the Use of PLABs

In order to evaluate teaching subjects differences in the teachers' responses, the non-parametric Kruskal–Wallis H test was used for three independent groups: group 1

Table 3. The results of the Kruskal–Wallis H test of statistically significant differences in the chemistry teachers' use of pre-laboratory activities regarding teaching subjects (N(chem) = 85; N(chem/bio) = 73; N(chem/phys) = 8)

Items	Pre-laboratory activities	Group[a]	Mean Rank	χ^2	*p*
1	Pre-lab manual	Chem	83.56	1.686	.430
		Chem/Bio	81.22		
		Chem/Phys	103.69		
2	Pre-lab discussion	Chem	88.61	5.401	.067
		Chem/Bio	74.97		
		Chem/Phys	107.06		
3	Pre-lab worksheets	Chem	81.85	1.223	.542
		Chem/Bio	83.51		
		Chem/Phys	100.88		
4	Solving theoretical problems	Chem	84.61	6.078	*.048*
		Chem/Bio	78.20		
		Chem/Phys	120.06		
5	Audiovisual materials	Chem	79.76	1.248	.536
		Chem/Bio	87.83		
		Chem/Phys	83.69		
6	Online assignments	Chem	85.18	4.729	.094
		Chem/Bio	78.27		
		Chem/Phys	113.38		
7	Computer simulations	Chem	82.02	4.502	.105
		Chem/Bio	81.72		
		Chem/Phys	115.50		

[a] Grouping Variable: Teaching Subjects

– chemistry (N = 85), group 2 – chemistry/biology (N = 73) and group 3 – chemistry/physics (N = 8).

According to Table 3, the mean rank (MR) values were the highest for chemistry/physics teachers in most statements, except in S5: *Students are prepared for laboratory work by using audiovisual materials*. The Kruskal–Wallis H test showed a statistically significant difference regarding teaching subjects in S4: *Students are prepared for laboratory work by solving theoretical problems* ($\chi^2(2)$ = 6.078, p=.048) with the highest mean rank value for chemistry/physics teachers (MR = 120.06).

The post-hoc Mann–Whitney U test was used to identify the cause of the effect in the Kruskal–Wallis H test. The results in Table 4 revealed a significant difference between *chemistry/biology* and *chemistry/physics* regarding the use of solving theoretical problems (U = –41.864, p = .044).

Table 4. Group comparison with post-hoc Mann–Whitney tests (two-tailed) in the chemistry teachers' use of pre-laboratory activities regarding teaching subjects

Pairs of Groups	*U*	*p*
Chem – Chem/Bio	6.413	1.000
Chem/Bio – Chem/Phys	–41.864	*.044*
Chem/Phys – Chem	–35.451	.111

4. 2. 3. Age Differences in the Use of PLABs

In order to evaluate age differences in the teachers' responses, the non-parametric Kruskal–Wallis H test was used. The amount of the obtained quantitative data was reduced with classification into three independent groups: 1) under 36 years (containing groups of under 30 years old and 30–35 years old); 2) 36–45 years (containing groups of 36–40 years old and 41–45 years old); 3) over 45 years (containing groups of 46–55 years old and over 55 years old).

In Table 5, the largest mean rank difference can be noted in S3: *Students are prepared for laboratory work by completing pre-lab worksheets*, with the highest MR value (101.18) for group 1 (under 36 years). The results of the Kruskal–Wallis H test ($\chi^2(2)$ = 7.494, p = 0.024) showed a statistically significant difference.

The results of the Mann–Whitney U test (p > .05) showed that there were no statistically significant differences in the overall use of PLABs regarding the *teachers' education* (teacher, engineer/educator). Likewise, the results of the Kruskal–Wallis H test (p > 0.05) showed that there were no statistically significant differences in the overall use of PLABs regarding both *teaching experience* and *school types*.

5. Discussion

The findings of the present research were obtained by a survey of chemistry teachers from all regions of Croatia about the use of various aspects of PLABs. The research sought to offer an overview of the actual practice in

Table 5. The results of the Kruskal–Wallis H test of statistically significant differences in the chemistry teachers' use of pre-laboratory activities regarding the age of teachers (N(< 36) = 37; N(36–45) = 55; N(> 45) = 74)

Items	Pre-laboratory activities	Group[a]	Mean Rank	χ^2	*p*
1	Pre-lab manual	< 36 years	88.15	0.917	.632
		36–45 years	79.02		
		> 45 years	84.51		
2	Pre-lab discussion	< 36 years	85.68	1.851	.396
		36–45 years	76.52		
		> 45 years	87.60		
3	Pre-lab worksheets	< 36 years	101.18	7.494	*.024*
		36–45 years	82.15		
		> 45 years	75.66		
4	Solving theoretical problems	< 36 years	91.59	1.539	.463
		36–45 years	79.99		
		> 45 years	82.06		
5	Audiovisual materials	< 36 years	85.18	0.543	.762
		36–45 years	79.83		
		> 45 years	85.39		
6	Online assignments	< 36 years	80.39	0.233	.890
		36–45 years	84.55		
		> 45 years	84.27		
7	Computer simulations	< 36 years	89.85	1.152	.562
		36–45 years	79.96		
		> 45 years	82.95		

[a] Grouping Variable: Age of Teachers

chemistry teaching concerning the teachers' demographic characteristics and their use of PLABs.

The teachers' demographic characteristics that affected the use of PLABs include their age, gender and the subjects they teach. The use of PLABs was shown to be greater among male teachers[26] who are relatively young[30] and teach both chemistry and physics. The results of our study indicate a significant difference between genders in the use of PLABs in chemistry practice although the influence of this variable is small. These findings are consistent with the previous study[23,24,26] that found a significant gender difference (1) in their attitude of teaching profession,[23] (2) in the pre-service teachers' concerns about teaching in technology-integrated flipped classrooms,[24] and (3) in the teachers' ICT readiness,[26] but our findings are opposite to some previous studies in education.[27–29,31] According to the presented results, in pre-laboratory sessions, male teachers most commonly use *a pre-lab discussion* by setting up questions that serve as the focus for discussion and guide inquiry in the lab as presented in the previous research.[20] The conventional way of preparing students for laboratory work is reading laboratory manuals, but Reid and Shah find that these typically overload them with information to be held at the same time.[19] The *pre-lab manual*, which contains the explanation of laboratory procedures and important safety considerations, was mostly used by male teachers.

Pre-lab worksheets, described in Johnstone et al.'s study,[4] are the second aspect of PLABs often used in chemistry teaching but vary by the teachers' age. The teachers under 36 years of age with typically less teaching experience compared to their older colleagues[29] more often use PLABs in their teaching practice, which is consistent with the previous study showing that a higher age may be associated with higher levels of perceiving the problems and obstacles of the use of ICT for teaching and learning.[30] However, our results are opposite to most of the relevant researches.[23,26,28,29,31]

Our findings revealed that the teaching subjects affect the use of PLABs in teaching practices. Chemistry/physics teachers use *solving theoretical problems* activities with a more significant frequency than chemistry/biology teachers. This result was similar to those of other studies[24,27] indicating that the subject of the teaching programs matters has to be considered in the integration of ICT into teaching practices.[27]

On the other hand, the lowest use appeared in *solving online assessments* and *doing computer simulations*, although studies show that the use of quizzes provides immediate feedback to students by improving links between theory and practical work.[13] The use of pre-lab *computer simulations*, aimed at the theory central to the laboratory exercise, reduces the cognitive load in students.[11]

Even though the responses "never" and "sometimes" were very frequent for certain questionnaire items, it cannot be claimed that the chemistry teachers used the suggested PLABs insufficiently. Perhaps every participating teacher used at least one form of PLABs for every laboratory class. An open-ended question was included at the end of the UPLAQ to allow a full picture of the teachers' use of PLABs. The teachers announced using laboratory work at the following class or posting interesting tasks on Facebook, which is in line with the affinities of today's student generations.

Regardless of the observed statistical differences by gender, age and teaching subjects, it cannot be claimed with sufficient probability that these differences exist in the entire population of teachers represented by our sample. The use of all PLABs was more frequent in male teachers and in chemistry/physics teachers (except *using audiovisual materials*) but the lack of significant differences was likely due to uneven group sizes (gender, $N_1 = 19$, $N_2 = 147$ and teaching subjects, $N_1 = 85$, $N_2 = 73$, $N_3 = 8$). The likelihood that the test correctly rejected the null hypothesis decreased as the group sizes were more uneven.

Several limitations should be taken into account when drawing conclusions from this research. First, email addresses of 600 teachers were obtained on request from the education advisor database but an unknown proportion of the entire population was not sampled. The obtained sample of 166 teachers may not represent the entire chemistry teacher population accurately. The research results cannot be used in generalizations about the entire population. However, by applying appropriate statistical tests, useful conclusions on the population could be extrapolated.

The second limitation is that all conclusions must be considered within the context of the limitations that arise from the nature of the survey research itself. Although the self-administered online questionnaire allows increased anonymity, which increases the likelihood of honest responses,[38] there was no way of telling how truthful the participants were – they could be forgetful or did not think within the full context of the situation and responded based on their own interpretation of statements of the questionnaire.

The third and largest limitation in testing possible differences in the use of PLABs was the impossibility of establishing the equivalence of samples. Very uneven sample sizes regarding gender provide a realistic picture of male underrepresentation in Croatian primary and secondary schools, and such a bias could be difficult to avoid. However, the assumption is that the groups were homogeneous in social status, profession and level of education. Despite these limitations, the present research provided a satisfactory analysis of the actual current situation in the Croatian chemistry education regarding the use of PLABs.

6. Conclusions

This survey research was aimed at examining the use of PLABs for chemistry teaching. Seven aspects of PLABs

were offered in UPLAQ to get direct insight into how often chemistry teachers use PLABs in their classes. At the same time, the influence of six demographic characteristics on the use of PLABs in the chemistry teacher population was explored.

In pre-laboratory sessions, teachers most commonly used a pre-lab discussion and pre-lab worksheets whereas PLABs with ICT (online assignment, computer simulations) were represented the least. The strongest demographic characteristic affecting the teachers' use of PLABs in chemistry lessons was their gender, followed by age and teaching subjects. The teachers' education, teaching experience and school types were nonsignificant characteristics.

Although these influences were small, a trend regarding more frequent use of PLABs can be noticed in male chemistry/physics teachers under 36 years of age, which could lead to further research to establish the equivalence of samples. To get more detailed demographic profiles, future studies can include a questionnaire with open-ended questions in items regarding age and teaching experience.

Acknowledgements

The authors would like to thank the chemistry teachers throughout Croatia who participated in this research for being willing to share their experience. The authors would also like to thank the colleagues who contributed to the development of the questionnaire.

7. References

1. A. Hofstein, V. N. Lunetta, *Sci. Educ.* **2004**, *88*, 28–54. **DOI:**10.1002/sce.10106
2. G. Tsaparlis, in: J. K. Gilbert, D. Treagust (Eds.): Multiple representations in chemical education, Springer, Dordrecht, The Netherlands, **2009**, pp. 109–136.
3. A. H. Johnstone, *J. Chem. Educ.* **1993**, *70*, 701–705. **DOI:**10.1021/ed070p701
4. A. H. Johnstone, A. Watt, T. U. Zaman, *Phys. Educ.* **1998**, *33*, 22–29. **DOI:**10.1088/0031-9120/33/1/016
5. D. P. Ausubel, *Educational psychology: A cognitive view.* Holt, Rinehart and Winston, New York, NY, **1968.**
6. J. Sweller, J. J. G. Van Merrienboer, F. G. W. C. Paas, *Educ. Psychol. Rev*. **1998**, *10*, 251–296. **DOI:**10.1023/A:1022193728205
7. A. H. Johnstone, H. El-Banna, *Stud. High. Educ.* **1989**, *14*, 159–168. **DOI:**10.1080/03075078912331377486
8. A. H. Johnstone, R. J. Sleet, J. F. Vianna, *Stud. High. Educ.* **1994**, *19*, 77–87. **DOI:**10.1080/03075079412331382163
9. D. Lair, Center for Research on Teaching Excellence. 2011, 1–12. Advance online publication, https://cloudfront.escholarship.org/dist/prd/content/qt8623f3zs/qt8623f3zs .pdf, (accessed: April 20, 2018)
10. A. Logar, C. Peklaj, V. F. Savec, *Acta Chim. Slov.* **2017**, *64*, 661–671. **DOI:**10.17344/acsi.2017.3544
11. T. M. Winberg, C. A. R. Berg, *J. Res. Sci. Teach.* **2007**, *44*, 1108–1133. **DOI:**10.1002/tea.20217
12. H. Y. Agustian, M. K. Seery, *Chem. Educ. Res. Pract.* **2017**, *18*, 518–532. **DOI:**10.1039/C7RP00140A
13. G. D. Chittleborough, M. Mocerino, D. F. Treagust, *J. Chem. Educ.* **2007**, *84*, 884–888. **DOI:**10.1021/ed084p884
14. J. Schmidt-McCormack, M. Muniz, E. Keuter, S. K. Shaw, R. Cole, *Chem. Educ. Res. Pract.* **2017**, *18*, 749–762. **DOI:**10.1039/C7RP00078B
15. J. L. Chaytor, M. Al Mughalaq, H. Butler, *J. Chem. Educ*. **2017**, *94*, 859–866. **DOI:**10.1021/acs.jchemed.6b00850
16. D. Spagnoli, L. Wong, S. Maisey, T. D. Clemons, *Chem. Educ. Res. Pract*. **2017**, *18*, 26–44. **DOI:**10.1039/C6RP00157B
17. M. Rollnick, S. Zwane, M. Staskun, S. Lotz, G. Green, *Int. J. Sci. Educ.* **2001**, *23*, 1053–1071. **DOI:**10.1080/09500690110038576
18. S. K. E. O'Sullivan, T. G. Harrison, *Acta Didact. Napocensia*. **2016**, *9*, 51–64, https://files.eric.ed.gov/fulltext/EJ1103433.pdf, (accessed: April 20, 2018)
19. N. Reid, I. Shah, *Chem. Educ. Res. Pract*. **2007**, *8*, 172–185. **DOI:**10.1039/B5RP90026C
20. S. E. Kulevich, R. S. Herrick, K. V. Mills, *J. Chem. Educ*. **2014**, *91*, 1207–1211. **DOI:**10.1021/ed400377a
21. M. D. Carter, S. S. Pierce, A. D. Dukes III, R. H. Brown, B. S. Crow, R. L. Shaner, et al., *J. Chem. Educ.* **2017**, *94*, 1094–1097. **DOI:**10.1021/acs.jchemed.6b00964
22. M. C. Roslaniec, E. M. Sanford, *J. Chem. Educ.* **2010,** *88*, 229–231. **DOI:**10.1021/ed100487a
23. E. Yildirim, *Procedia Soc. Behav. Sci*. **2012**, *46*, 2352-2355. **DOI:**10.1016/j.sbspro.2012.05.483
24. Y. Hao, K. S. Lee, *Comput. Hum. Behav*. **2016**, *57*, 250–260. **DOI:**10.1016/j.chb.2015.12.022
25. D. Reilly, D. L. Neumann, G. Andrews, *Res. Sci. Educ*. **2019**, *49*, 25–50. **DOI:**10.1007/s11165-017-9630-6
26. A. O. Alazzam, A. R. Bakar, R. Hamzah, S. Asimiran, *IES*. **2012**, *5*, 229–243. **DOI:**10.5539/ies.v5n6p229
27. A. Aslan, C. Zhu, *Br. J. Educ. Technol.* **2017**, *48*, 552-570. **DOI:**10.1111/bjet.12437
28. J. Gil-Flores, J. Rodríguez-Santero, J. J. Torres-Gordillo, *Comput. Hum. Behav.* **2017**, *68*, 441–449. **DOI:**10.1016/j.chb.2016.11.057
29. T. Teo, M. Zhou, *Interact. Learn. Environ*. **2017**, *25*, 513–527. **DOI:**10.1080/10494820.2016.1143844
30. R. Scherer, F. Siddiq, T. Teo, *Comput. Educ*. **2015**, *88*, 202–214. **DOI:**10.1016/j.compedu.2015.05.005
31. J. H. L. Koh, C. S. Chai, C. C. Tsai, *Educ. Technol. Soc*. **2014**, *17*, 185–196, https://media.proquest.com/media/hms/PFT/1/7Aml7?_s=WWZgKh5cL48aPy8nXz 8nMQdzUu0%3D, (accessed: November 15, 2019)
32. M. K. Seery, *J. Chem. Pharm. Sci.* **2010**, *3*, 1–3, http://www.dit.ie/media/ditlttc/documents/lttcresources/Using%20Pre-Lecture%20 Resources %20in%20your%20teaching.pdf, (accessed: January 24, 2017)
33. S. Smerdel, M. Zejnilagić Hajrić, *Nat. Sci. Educ*. **2017**, *14*, 90–96, https://journals.indexcopernicus.com/search/article?articleId=1883115, (accessed: November 16, 2019)

34. K. S. Taber, *Res. Sci. Educ*. **2018**, *48*, 1273–1296. **DOI:**10.1007/s11165-016-9602-2
35. H. W. Lilliefors, *J. Am. Stat. Assoc*. **1967**, *62*, 399–402. **DOI:**10.1080/01621459.1967.10482916
36. J. Cohen, *Statistical power analysis for the behavioral sciences*. Lawrence Erlbaum Associates, Hillsdale, New York, **1988.**
37. T. N. Hrin, D. D. Milenković, M. D. Segedinac, S. Horvat, *J. Serb. Chem. Soc.* **2016**, *81*, 1455–1471, https://shd-pub.org.rs/index.php/JSCS/article/view/3593/352, (accessed: April 24, 2018)
38. W. L. Neuman, *Social research methods: Qualitative and quantitative approaches* (7th ed.). Pearson Education Limited, Harlow, UK, **2013**.

Povzetek

Predlaboratorijske aktivnosti so načrtovane z namenom pritegnitve zanimanja s strani učencev do nekaterih aspektov eksperimenta, ki ga nameravajo izvesti. Predhodne raziskave so pokazale, da tovrstne aktivnosti zmanjšajo kognitivno breme v laboratoriju in izboljšujejo učinkovitost laboratorijskega dela učencev. Ta raziskava temelji na primerjavi pomembnosti demografskih karakteristik, ki vplivajo na učiteljevo uporabo predlaboratorijskih aktivnosti pri kemijskih predmetih. V okviru kvantitativne raziskovalne ankete je sodelovalo 166 učiteljev kemije iz vseh regij Hrvaške. V predlaboratorijskem pouku so se učitelji najpogosteje poslužili diskusije in uporabe predlog medtem ko so najmanj uporabljali računalniške simulacije. Tri karakteristike, ki vplivajo na učiteljevo uporabo predlaboratorijskih aktivnosti pri kemiji, so spol, starost in področje poučevanja. Izobrazba učiteljev, učne izkušnje in vrsta šole predstavljajo nepomembne karakteristike.

Except when otherwise noted, articles in this journal are published under the terms and conditions of the Creative Commons Attribution 4.0 International License

Scientific paper

Characterization of Biomolecules with Antibiotic Activity from Endophytic Fungi *Phomopsis Species*

Janko Ignjatović,[1] Nevena Maljurić,[1] Jelena Golubović,[1] Matjaž Ravnikar,[2] Miloš Petković,[3] Nika Savodnik,[4] Borut Štrukelj[2] and Biljana Otašević[1,*]

[1] *Department of Drug Analysis, University of Belgrade, Faculty of Pharmacy, Vojvode Stepe 450, 11221 Belgrade, Serbia*

[2] *Chair for Pharmaceutical Biology, Faculty of Pharmacy, University of Ljubljana, Aškerčeva cesta 7, 1000 Ljubljana, Slovenia*

[3] *Department of Organic Chemistry, University of Belgrade – Faculty of Pharmacy, Vojvode Stepe 450, 11221 Belgrade, Serbia*

[4] *Biotechnical Faculty, University of Ljubljana, Jamnikarjeva 101, 1000 Ljubljana, Slovenia*

** Corresponding author: E-mail: biljana.otasevic@pharmacy.bg.ac.rs*

Phone: +381 113951 334; Fax: +381 113972 840

Received: 07-08-2019

Abstract

Recently, growing interest is devoted to investigation of bioactive secondary metabolites of endophytic fungi. Thus, as an extension to our previous achievements related to antimicrobial potential of endophytic fungi, *Phomopsis species* isolated from conifer needles was selected as appropriately promising natural source for drug discovery. Its dichloromethane and ethanol extracts considerably inhibited growth of *Escherichia coli* and *Staphylococcus aureus*. Moreover, the individual compounds of dichloromethane extract have been separated, collected and purified using semi preparative liquid chromatographic analysis and comprehensively characterized using mass spectrometry (MS) and nuclear magnetic resonance spectroscopy (NMR). Based on their antimicrobial activity and unique structural characteristics in comparison with well-established drugs from the same therapeutic category, two dominant compounds (Z)-(Z)-2-acetoxyprop-1-en-1-yl-3-(3-((E)-3,4-dihydroxypent-1-en-1-yl)oxiran-2-yl)acrylate (denoted as 325-3) and (Z)-(Z)-2-acetoxyprop-1-en-1-yl 3-(3-((E)-4-hydroxy-3-oxopent-1-en-1-yl)oxiran-2-yl)acrylate (denoted as 325-5) were recognized as valuable leading structures for future discovery of novel antibiotics.

Keywords: Endophytic fungi; antibacterial activity; HPLC; GC-MS; NMR

1. Introduction

During evolution, plants have developed certain defending capabilities such as producing specific secondary metabolites in order to repel microorganisms, insects, or other animals that are feeding on them.[1] Moreover, plant tissues contain many types of microorganisms, which are referred to as endophytes.[2–4] During certain period of their life, endophytes colonize living internal tissues of their plant hosts without causing any symptoms.[2] Usually, an endophyte is specific for each host and is characteristic for conditions and geographical area in which its host develops.[5,6] Endophytic organisms seem to have mutualistic relation to their plant host by means that they preserve hosts from threats of pathogenic microorganisms, insects or other animals in return for their nutrition.[7,8] In order to facilitate the survival of a host plant, endophytes help host plant to overcome the invasion of pathogenic microorganisms by producing secondary metabolites.[9] There is also evidence that endophytes produce metabolites for plant growth regulation, productivity and phytoremediation.[10,11]

The literature search pointed out significant antibacterial and antimycotic activity of endophytic fungi *Phomopsis species*.[12–16] For example, secondary metabolites from fungus that was isolated from the leaves of tropical fruit tree *Garcinia dulcis* demonstrated activity on *Mycobacterium tuberculosis*.[17] Additionally, fungus isolated from marine-derived mangrove showed considerable potential for inhibition of *Candida albicans* and *Fusarium oxysporum*.[18] It is concluded that the fungus is susceptible to production of wide variety of secondary metabolites

and this fact is closely dependent on factors like type of plant host, plant organ, eventual cohabitance with other strains of microorganisms, climatic conditions, sessional fluctuations, habitat microclimate, temperature, etc.[5,19–21] Rakshith et al. state that the genus *Phomopsis* has been known to be a rich source of bioactive secondary metabolites of novel, diverse structure and function such as Phomopscichalasin, cytochalasin, convolvulanic acid, and isobenzofuranones, oblongolide, phomopsolide, Phomodiol, Phomoxanthones, and Xanthones dimer, phomoenamide, phomonitroester, deacetylphomoxanthone B, dicerandrol A, (1S,2S,4S)-p-menthane-1,2,4-triol, uridine, ethyl 2,4- dihydroxy-5,6-dimethylbenzoate and Phomopscilactone.[22] Those structures have been further tested and showed antibacterial, antifungal and antialgal activity.[23]

Thus, the main aim of this study was investigation of endophyte *Phomopsis species* isolated from conifer needles in Slovenia and its secondary metabolites responsible for the antimicrobial effect on selected representatives of G^- (*Escherichia coli*) and G^+ (*Staphylococcus aureus*) bacteria.

2. Experimental

2. 1. Chemicals and Reagents

For the purpose of executing microbiological tests, endophyte or bacterial sawing and endophyte extract preparation we have used: Potato dextrose agar – PDA, quality level 200, Sigma-Aldrich (Taufkirchen, Germany), LB broth, quality level 200, Sigma-Aldrich (Taufkirchen, Germany), Mueller-Hinton agar, quality level 100, Sigma-Aldrich (Taufkirchen, Germany), Dichloromethane, ≥ 99.0% purity, Sigma-Aldrich (Taufkirchen, Germany), Ethanol, ≥ 99.9% purity, Sigma-Aldrich (Taufkirchen, Germany), Methanol, ≥ 99.9% purity, Sigma-Aldrich (Taufkirchen, Germany) and Ampicillin USP standard substance, 99.3% purity, Sigma-Aldrich (Taufkirchen, Germany).

Furthermore, for the purpose of conducting all chromatographic analysis, GC-MS and NMR we have used: Acetonitrile, 99.99% purity, Sigma-Aldrich (Taufkirchen, Germany), Formic acid solution in water. 0.1% (v/v), Sigma-Aldrich (Taufkirchen, Germany), Helium gas, 99.999% purity, Sigma-Aldrich (Taufkirchen, Germany), Deuterochloroform, 99.9% purity, Sigma-Aldrich (Taufkirchen, Germany), Tetramethylsilane as the internal standard, > 99.99% purity, Sigma-Aldrich (Taufkirchen, Germany), DMSO, ≥ 99% purity, Sigma-Aldrich (Taufkirchen, Germany), Deuterochloroform, 99.9% purity, Sigma-Aldrich (Taufkirchen, Germany).

2. 2. Preparation of Endophytic Material

Endophytic fungi *Phomopsis species*, which is isolated from conifer needles, has been provided by the Department of Wood Science and Technology within Biotechnical Faculty, University in Ljubljana, Slovenia. Potato dextrose agar – PDA was used for fungal cultivation. PDA was prepared by dissolving 8.4 g of dry mixture in 200 mL of ultra-pure water, poured in Petri plates and left to solidify in sterile conditions. Afterwards, fungal sample was sawed on PDA plates and left to grow on room temperature (approximately 25 °C) for one month and then plate content was grinded and mixed using homogenizer Ultra Turrax (Ika, Staufen, Germany).

Two types of extraction solvents were tested. In accordance with previous literature records, dichloromethane and ethanol were selected due to their differences in polarity and ability to extract potential secondary metabolites.[24] Therefore, homogenization of fungal material was followed with the addition of 50 mL of dichloromethane and absolute ethanol separately and thorough mixing. Moreover, the mixtures were ultrasonicated for 15 minutes covered with thin foil and then left overnight at room temperature for extraction process to take place. Then, the mixtures were filtered through filter paper and solvent was removed using rotavapor set at 50 °C while the pressure was 700 mbar. Moreover, dichloromethane solution evaporated fully out of extract under reduced pressure, while ethanol extract sample had to be additionally left overnight on room temperature so that the rest of ethanol and remaining water could evaporate freely. Afterwards, both dry extracts were weighed and dissolved in approximately 5 mL of mixture of methanol and ultra-pure water (50:50, v/v) so that concentration of both extracts was approximately 8 mg/mL. This step was enhanced using ultrasonication for approximately 10 minutes. Afterwards, both samples were filtered through 0.22 μm nylon membranes (Agilent Technologies, Santa Clara, USA).

2. 3. Microdilution Assay

In order to determine antibiotic activity of prepared extracts from endophyte *Phomopsis species* that was isolated from conifer needles, cultures of *Escherichia coli* (strain DH5-α) and *Staphylococcus aureus* (strain ACTC 10788) obtained from permanent cultures, were used. LB broth for bacterial cultivation was prepared by dissolving 8 g of dry mixture in 400 mL of ultra-pure water. Bacterial suspensions were then prepared in a way that 20 mL of LB medium was added to the centrifuge container after which *E. coli* or *S. aureus* were seeded separately from the permanent culture. The centrifuge container was left over night and shaked in an incubator at 37 °C in order to multiply the bacteria.

Next, 2 mg of dichloromethane and 2 mg of ethanol dry extracts of the endophyte were dissolved separately in 1 mL of mixture of methanol and ultra-pure water (50:50, v/v) and used for initial antimicrobial activity testing within microdilution tests. Prior performing microdilution tests dissolved endophyte extract in mixture of methanol and ultra-pure water (50:50, v/v) was additionally concen-

trated using Speed Vac Plus (Savant, Waltham, MA, USA) to desired volume, required for microdilution assays.

Bacterial suspensions were diluted in LB broth in order to set the suitable optical density between 0.08 and 0.10 of the mixture by measuring the absorbance of a mixture at λ = 600 nm.[25,26] Assay was carried out on a microwell plate by executing tests in duplicates for extract activity as well as for positive and negative control. Activity of extract was tested in a mixture of 90 µL of *E. coli* or *S. aureus* suspension solution in LB broth and 10 µL of extract obtained as described above. Negative control was prepared using 90 µL of *E. coli* or *S. aureus* suspension solution in LB broth and 10 µL of mixture of methanol and ultra-pure water (50:50, v/v). As positive control, 90 µL *E. coli* or *S. aureus* suspension solution in LB broth was mixed with 1 µL of 100 mg/mL solution of ampicillin that was dissolved in 9 µL of 50% (v/v) solution of methanol in water. Plates were analysed instantly at absorbance of 600 nm and left overnight under incubation temperature of 37 °C for growing and to be measured also the next day in order to detect any changes in the bacterial growth. Changes in absorbance due to bacterial growth were used to calculate bacterial inhibition rate for each of the *Phomopsis species* extract types. The microdilution assay for determination of antibacterial activity was done for every prepared sample in duplicate and average result was calculated.

2. 4. Isolation and Chemical Structure Characterization of Components from Endophytic Fungal Material

Prior chromatographic and spectral analysis, 2 mg of dichloromethane dry endophyte extract was dissolved in 1 mL of methanol and ultra-pure water (50:50, v/v). Isolation and collection of components from endophyte extract was performed on Dionex Ultimate 3000 HPLC system (Thermo Fisher Scientific, Dreieich, Germany) equipped with DAD detector and binary pump. Separation was achieved on Hypersil Gold semi-preparative revered-phase HPLC column (C18, particle size 5 µm, length 150 mm, internal diameter 10 mm, Thermo Fisher Scientific, Dreieich, Germany) at 25 °C. Samples were maintained at 10 °C in autosampler prior analysis. Injection volume was 100 µL. A gradient elution program was composed of acetonitrile as mobile phase A and 0.1% (v/v) formic acid solution in water as mobile phase B. The gradient program started with 95% (v/v) mobile phase B. During 28 minutes, the percentage of mobile phase B was decreasing to 5% (v/v), following the return to the initial ratio in 0.05 minute. Column was then re-equilibrated, so the total run time was 40 minutes at a flow rate of 2 mL/min. Detection was performed simultaneously, by measuring the absorbance at 220 nm, 235 nm, 254 nm and 285 nm wavelength in order to assure recording of all possible components with different spectral properties.

Fraction collection procedure was performed on *Phomopsis species* dichloromethane dry extract dissolved in 50% (v/v) solution of methanol in water, using the aforementioned chromatographic method on Dionex Ultimate 3000 HPLC system with DAD detection. Five distinct peaks from the chromatogram at the retention times of approximately 12.88, 13.67, 14.40, 16.02 and 17.13 min have been manually collected in Eppendorf tubes. Solvent from separate peak fractions was removed using rotavapor set at 50 °C while the pressure was 700 mbar and dry peak residues have been used for further analytics.

Mass spectrometry (MS) analyses were done on Agilent Technologies 5975C MS system (Agilent Technologies, Santa Clara, USA) coupled with Agilent Technologies 6890N GC system (Agilent Technologies, Santa Clara, USA). Initial temperature of the oven of the GC system was 60 °C and maximum temperature was 325 °C. Front inlet of the system was set in mode to split ratio 10:1, while initial temperature was set at 200 °C, pressure was 14.47 psi and split flow was 10.0 mL/min. The method used Agilent Technologies HP-5 5% Phenyl Methyl Siloxane, Agilent 19091J-433 column, (internal diameter 0.25 mm, length 30.0 m, film thickness 0.25 mm, column format 7 inch, manufacturer Agilent Technolog Santa Clara, USA) and helium gas pumped at 1 mL/min flow rate. The fractions collected using semi-preparative HPLC analysis with the concentration of 0.1 mg/mL were introduced into GC-MS system with 1 µL injection volume and total run time was 44 minutes. The mode of ionization was electron impact operated at 70 eV. Low mass scan parameters for MS was 10, while high mass scan parameter was 550.

For acquiring nuclear magnetic resonance (NMR) spectra on Bruker Ascend 400 (400 MHz) spectrometer (Billerica, MA, USA), the fractions collected using semi-preparative HPLC analysis, were evaporated using Rotavapor R-114 (Büchi, Flawil, Switzerland) and dry content weighing about 5 mg was dissolved in 250 µL deuterochloroform. NMR spectra were recorded at 25 °C and chemical shifts were given in parts per million (δ) downfield from tetramethylsilane as the internal standard.

2. 5. Disc Diffusion Method for Determining the Antibiotic Potential

Firstly, the microbial cultures of *E. coli* and *S. Aureus* were diluted with saline solution until the density of 0.5 McFarland. Both cultures were seeded on separate Mueller-Hinton agar plates. Afterwards, 15 µL of collected peak fraction 3, 4 and 5 were added on separate places on seeded Mueller-Hinton agar plates, while 15 µL DMSO served as control on each plate. Then, plates were incubated in thermostat at 37 °C in the period from 16 to 24 h. Growth inhibition zone diameter readings are performed after incubation for each of the peak fractions.

3. Results and Discussion

3. 1. Evaluation of Endophytic Fungi Extract Antibiotic Activity

Within microdilution assay for antibiotic activity of dichloromethane extract against *E. coli* after 24 h, average absorbance value 0.4603 was for the negative control, and 0.1590 for the positive control. Dichloromethane extract of *Phomopsis species* showed absorbance value of 0.2812. Therefore, it was concluded that this extract demonstrated inhibition rate of 59.44%. The same set of microdilution test experiments were repeated using dry ethanol extract of the fungi and these also pointed out the presence of antibacterial activity. Moreover, it was observed that ethanol extract demonstrated 51.63% of inhibition rate against *E. coli*.

In order to further evaluate the relationship between extract concentration and the level of antibiotic activity on *E. coli*, a microdilution experiment was repeated using additional four lower volumetric ratios of dichloromethane extract, since better inhibition dependency was observed comparing to ethanol extract of fungus. In this experiment also negative control was used in the same volumetric ratios. Therefore, *Phomopsis species* dichloromethane extract samples were prepared so that the percentage of *Phomopsis species* dichloromethane extract solution in LB broth suspension of *E. coli* was approximately 10%, 5%, 2.5% or 1% (v/v). From the results, the concentration dependent antibiotic activity was observed. In specific, average absorbance value of 0.2812 was measured for 10% (v/v) extract, 0.3305 for 5% (v/v) extract, 0.3275 for 2.5% (v/v) extract and 0.3896 for 1% (v/v) extract. As expected, lower presence of extract or control influenced greater growth of *E. coli*. Furthermore, even the sample with the lowest ratio of *Phomopsis species* dichloromethane extract also demonstrated antibiotic effect comparing to the negative control, as can be concluded from the average absorbance value for extract (0.3896 at 1%, v/v) comparing to the average absorbance value for negative control (0.4603). Based on presented data, inhibition concentration of dichloromethane extract that eradicates 50% of bacteria (IC50) was calculated to be 6.95%.

Furthermore, the same procedure was performed once again for evaluation of antibacterial activity of endophytic fungi extracts against *S. aureus* after 24 h. It was noticed that ethanol extract has high inhibition rate of 92.80% on the growth of *S. aureus* during preliminary tests. On the other side, dichloromethane extract did not show notable antibacterial activity against *S. aureus*. Thus, we continued with microdilution assay with *Phomopsis species* ethanol extract. Samples for microdilution test were prepared so that *Phomopsis species* ethanol extract concentration in *S. aureus* final suspension was approximately 10%, 5% and 1% (v/v). From the results, the concentration dependent antibiotic activity was observed. In specific, average absorbance value of 0.1755 was measured for 10% (v/v) extract, 0.1805 for 5% (v/v) extract and 0.2010 for 1% (v/v) extract. Absorbance result for negative control was 0.4655 and for positive control 0.1530. Moreover, even sample with lowest tested dilution of 1% (v/v) of *Phomopsis species* ethanol extract has pronounced antibiotic activity comparing to both positive and negative control. Out of available data, IC50 value of *Phomopsis species* ethanol extract for *S. aureus* of 1.30% was calculated.

This data supported the hypothesis that biomolecules from investigated endophytic fungi have the potential to become candidates for new potential drugs as demonstrated bioactivity could represent valuable contribution to current antibacterial therapy with a proper chance for dealing with growing trend of bacterial resistance. Based on presented data and having in mind future industrial exploitation of prepared extracts, we have further analysed the components of *Phomopsis species* dichloromethane extract using spectral and chromatographic tools, due to its stability and facilitated dry extract preparation comparing to the ethanol one. Furthermore, based on the previous research of the group[24] we expected that more potent secondary metabolites could be extracted from the fungal material using dichloromethane as extraction solvent.

Nevertheless, *Phomopsis species* dry ethanol extract secondary metabolites could be a subject for further analytical research using proposed methods in this article, that were developed for characterization of components of *Phomopsis species* dichloromethane extract.

3. 2. Active Biomolecules Isolation and Chemical Structure Elucidation

Dichloromethane dry extract dissolved in 50% (v/v) solution of methanol in water has been further analysed using semi-preparative HPLC method. Total number of five peaks was inspected in the chromatogram at the retention times of 12.88, 13.67, 14.40, 16.02 and 17.13 min, respectively (Figure 1). The compounds related to all five peaks seemed to have relatively similar spectral properties (Figure 2), so it was possible to record all of them in a single chromatogram acquired at 235 nm detection wavelength. As expected, due to differences in chromatographic systems (e.g. the composition of mobile phase and chemistry of stationary phase, technical characteristics of used instruments) employed during sample collection and following GC-MS analysis, the previously reported retention times were different from those in recorded total ion chromatogram (Figure 3 and 8). Despite this, reliable peak-to-peak tracking was accomplished with the same elution order and all relative retention times preserved. Although there was a risk that the first two eluting peaks belong to compounds with activity that was measured for the whole extract, we deliberately omitted them in further work by means of preparative chromatography and fraction collections for chemical structure elucidation. Authors have invested effort to chromatographically resolve

all peaks for further processing. However, the purity of fractions was serious limitation as well as concentration level of a compound in a collected fraction. Due to this, background noise was too high and we could not perform accurate data analysis except for last three eluting peaks.

In line with fraction collection, we have performed disc diffusion method for determining the antibiotic potential of fractions as verification of bioactivity in order to ensure that ascribed bioactivity of whole extract could be related to all collected fractions. Tested concentration of peak fraction 3 and 4 was 1 mg/mL, while fraction of peak 5 had the concentration 3 mg/mL. The results revealed that there was no activity on any of the microorganisms tested for peak fraction 4. For peak fraction 3, a 6 mm diameter inhibition zone was observed on *S. aureus* plate, while no antimicrobial activity was observed on *E. coli* plate. Furthermore, for peak fraction 5, a 7 mm diameter of the inhibition zone was observed against *S. aureus* and 4 mm diameter of the inhibition zone was noted on *E. coli* plate. The test pointed out that only peaks with elution order 3

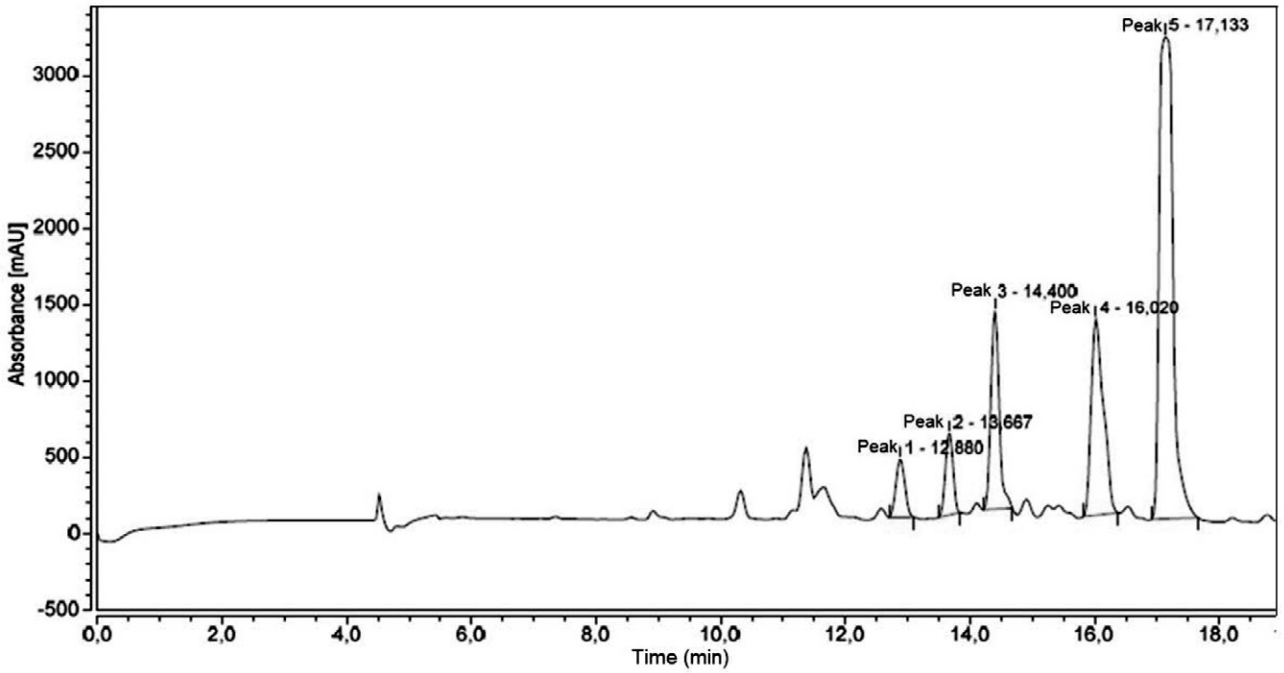

Figure 1. Chromatogram of *Phomopsis species* dichloromethane dry extract dissolved in mixture of methanol and water 50:50 (v/v) from semi-preparative HPLC analysis

Table 1. ^{1}H (400 MHz) and ^{13}C (100 MHz) spectral analysis of compounds 325-3 and 325-5

	Compound 325-3		**Compound 325-5**	
Position	δ_H (*J* in Hz)	δ_c	δ_H (J in Hz)	δ_c
1		162.33		161.95
2	6.24 (d, *J* = 9.7 Hz, 1H)	125.12	6.25 (d, *J* = 9.7 Hz, 1H)	124.12
3	7.00 (dd, *J* = 9.7, 5.5 Hz, 1H)	140.89	7.10 (dd, *J* = 9.7, 5.9 Hz, 1H)	141.00
4	5.38 (dd, *J* = 5.5, 3.0 Hz, 1H)	63.41	5.66 (dd, *J* = 5.8, 2.8 Hz, 1H)	63.20
5	5.10 (s, 1H)	78.50	5.98 (dd, *J* = 4.7, 2.8 Hz, 1H)	76.85
6	5.89 (dd, *J* = 16.0, 5.8 Hz, 1H)	124.73	H-6/H-7: 6.42 (d, *J* = 4.7 Hz, 2H) *	142.97
7	6.01 (dd, *J* = 15.5, 5.2 Hz, 1H)	134.72	H-6/H-7: 6.42 (d, *J* = 4.7 Hz, 2H) *	124.54
8	3.93 (s, 1H)	76.22		202.04
9	3.62 (s, 1H)	70.60	4.36 (q, *J* = 7.1 Hz, 1H)	73.14
10	1.17 (d, *J* = 6.3 Hz, 3H)	11.98	1.40 (d, *J* = 7.1 Hz, 3H)	19.59
1’	6.90 (d, *J* = 6.0 Hz, 1H)	140.89	6.86 (dd, *J* = 7.3, 1.7 Hz, 1H)	139.57
2’		127.60		127.53
3’	1.80 (s, 3H)*	18.84	1.79 (s, 3H)*	14.54
1”		166.74		166.50
2”	1.81 (s, 3H)*	14.54	1.80 (s, 3H)*	12.00
OH	C-8/C-9: 2.22 (bs, 1H); 2.16 (bs, 1H)		C-9: 3.36 (bs, 1H)	

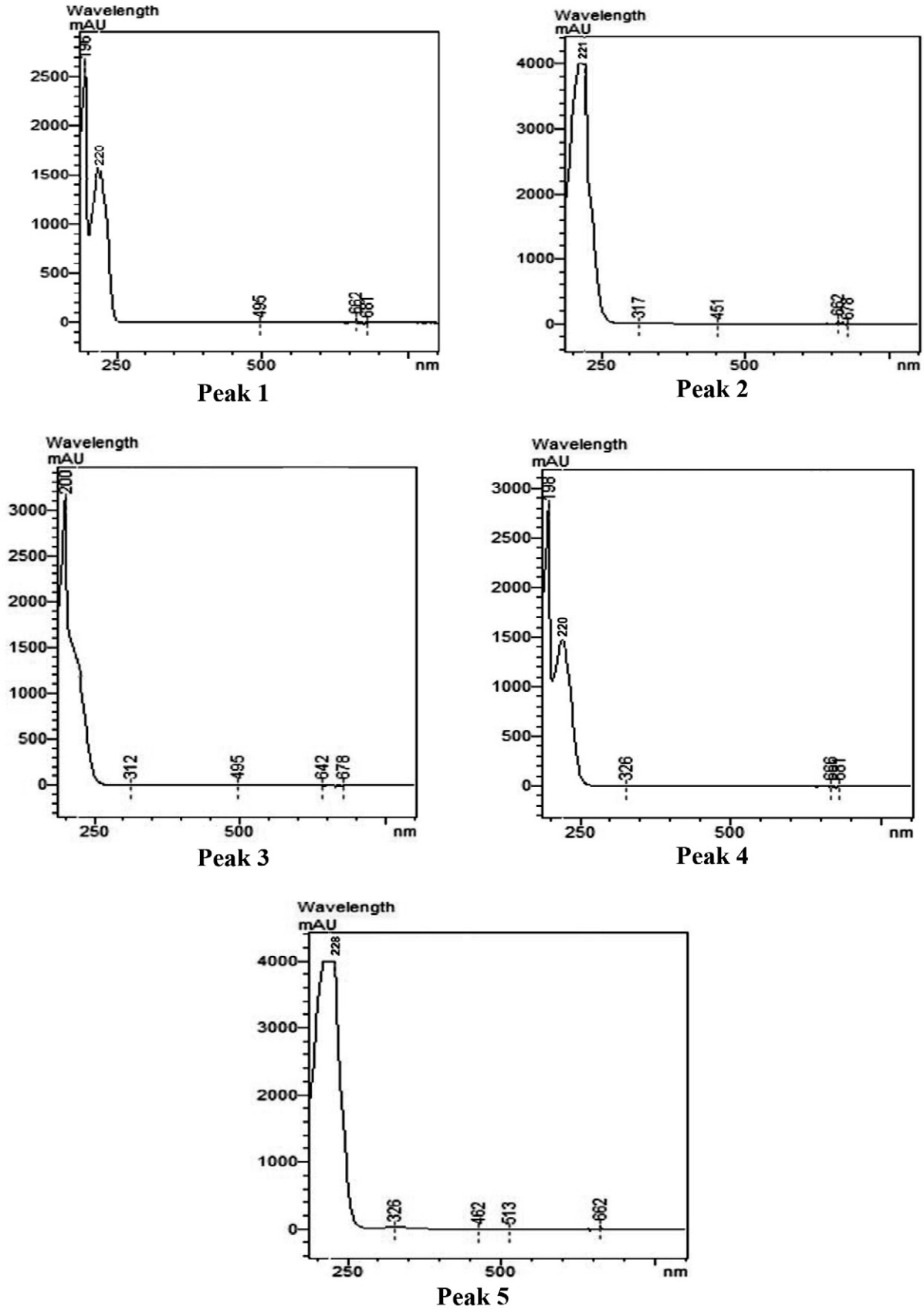

Figure 2. Absorption spectra of compounds corresponding to five peaks chromatographed using dichloromethane dry extract dissolved in methanol and water 50:50 (v/v)

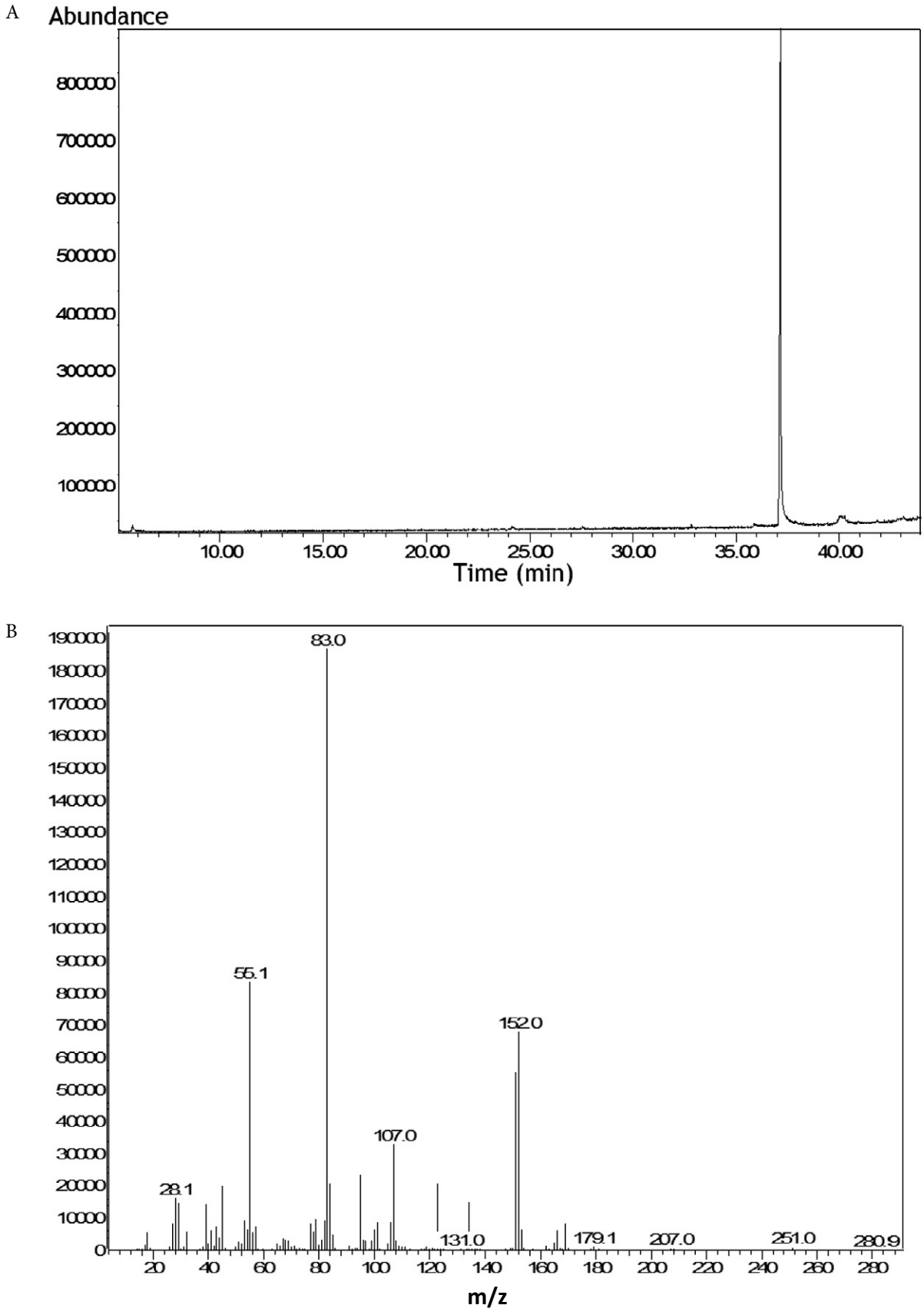

Figure 3. Total ion chromatogram (A) and GC/MS spectra (B) of compound 325-3

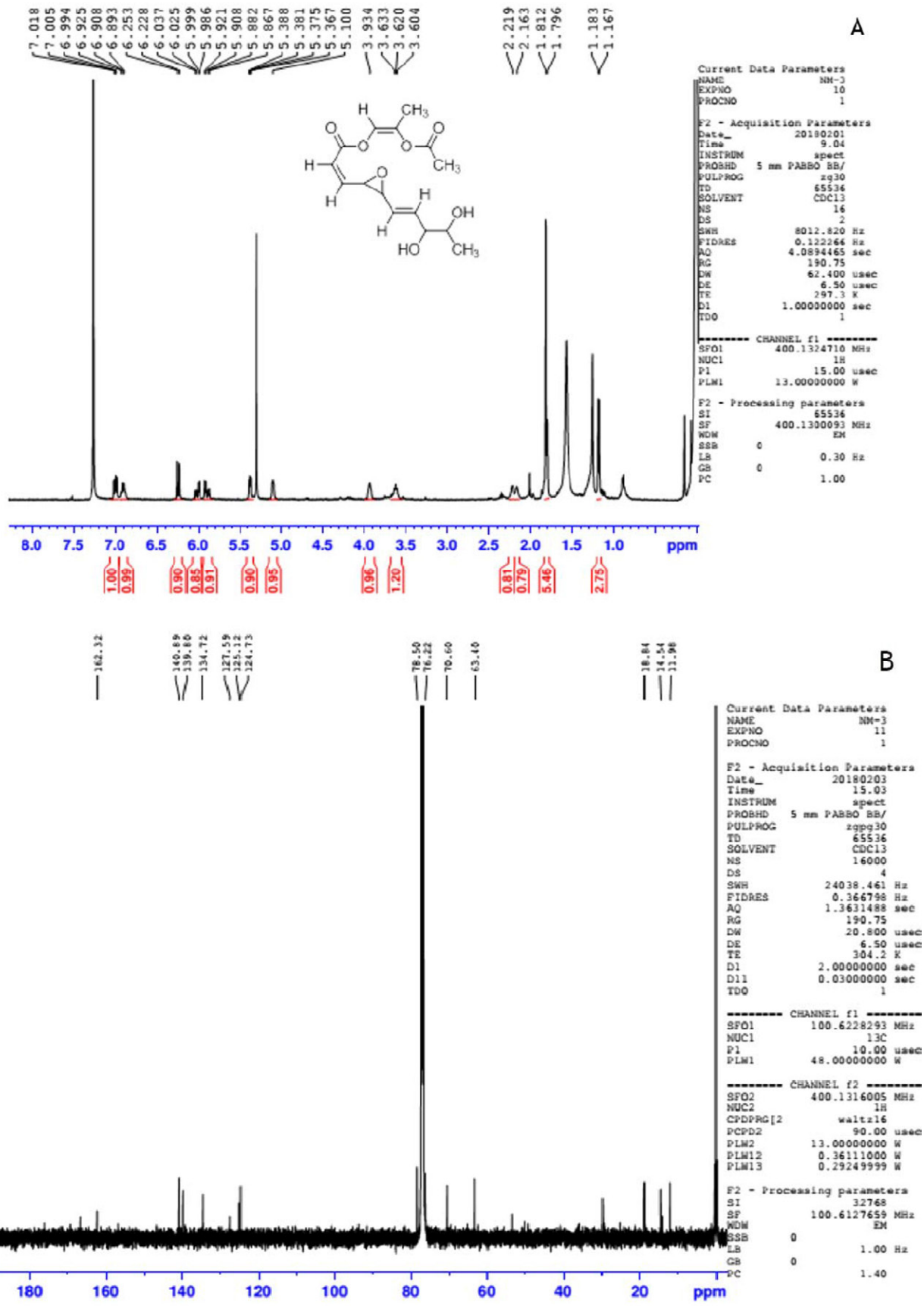

Figure 4. ^{1}H NMR spectra (A), ^{13}C NMR spectra (B) for toluene standard and compound 325-3

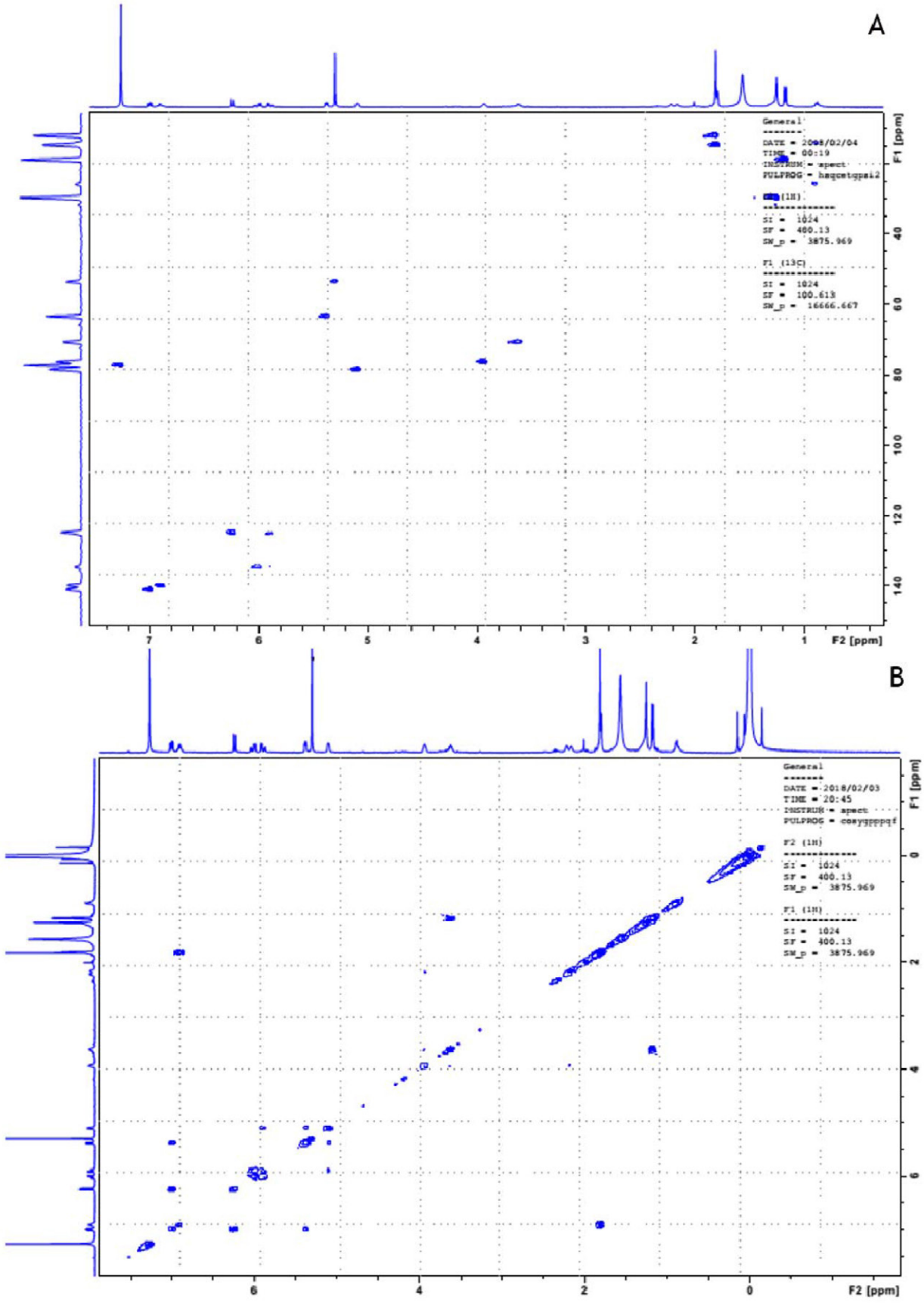

Figure 5. HSQC (A) and COSY (B) spectra of compound 325-3

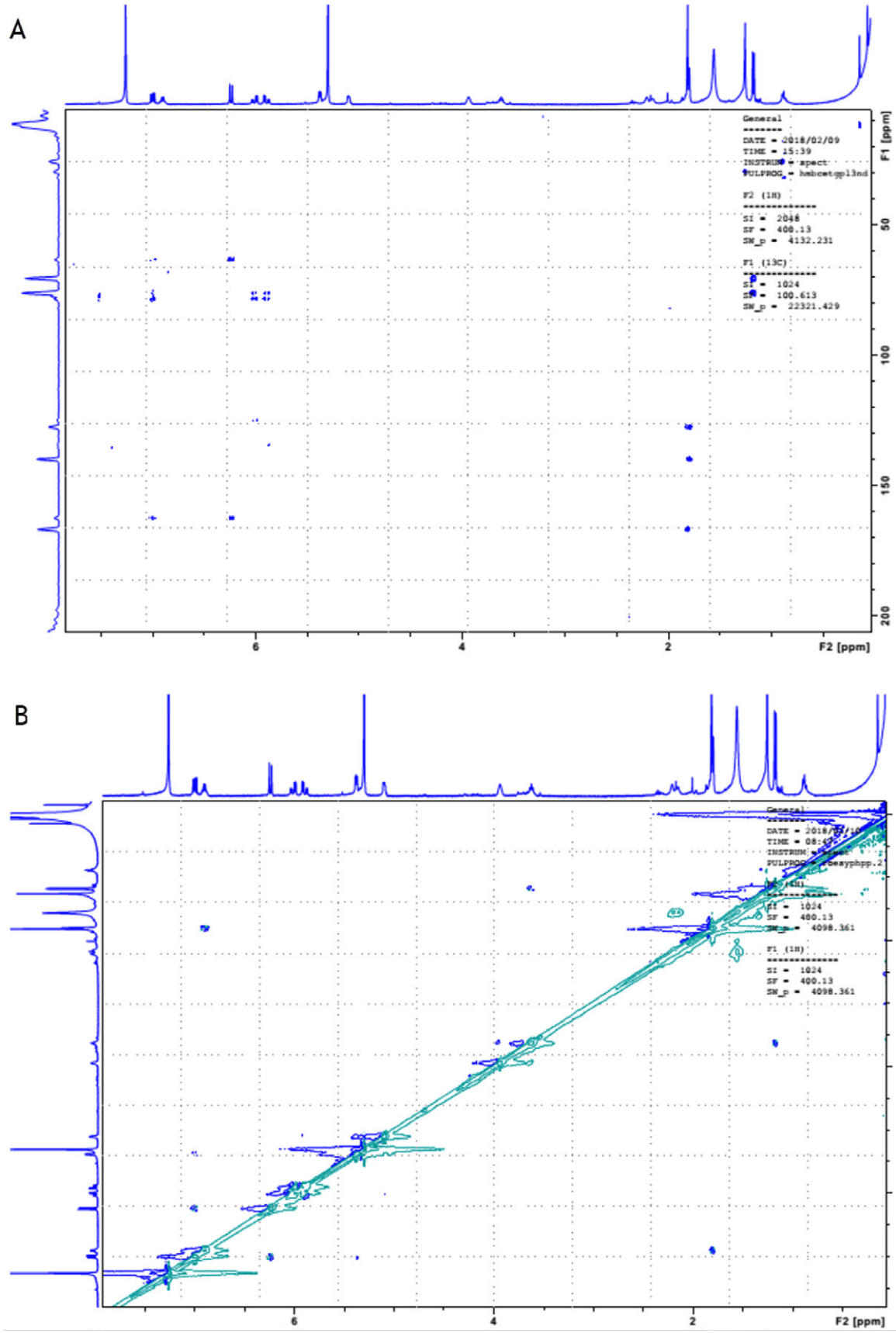

Figure 6. HMBC (A) and NOESY (B) spectra of compound 325-3

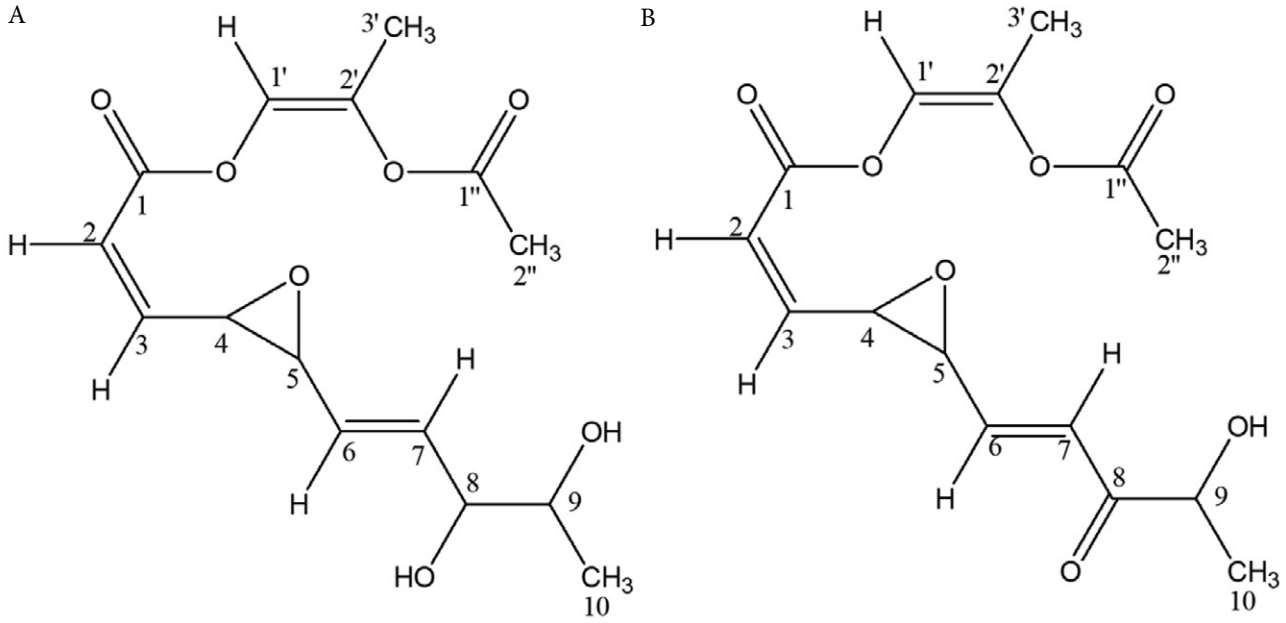

Figure 7. Molecular structures of compounds 325-3 (A) and 325-5 (B)

and 5 showed bioactivity. Therefore, after fraction collection and weighing of evaporated fractions, it has been noticed that dry mass of the collected peak fractions 3 and 5 was at least 5 mg, which was dissolved with deuterochloroform in cuvette up to volume of 250 μL. The final concentration was high enough to perform suitable NMR analysis. The compounds corresponding to peak 3 and 5 were denoted as 325-3 and 325-5 in further text, respectively.

Compound that corresponded to peak 3 in the chromatogram and denoted as 325-3, was obtained as a colourless oil with the molecular formula of $C_{15}H_{20}O_7$ (recorded by GC-MS method as ion [M+H-OH-CH_3] = 281, calc. 313.1282, Figure 3). The numbers of hydrogen and carbon atoms observed in the ^{1}H- and ^{13}C-NMR spectra recorded in $CDCl_3$ (Table 1) were in agreement with the molecular formula. The ^{1}H NMR (Figure 4A) data indicated the existence of five sp^2 methines (H-2, H-3, H-6, H-7 and H-1'), four oxygenated sp^3 methines (H-4, H-5, H-8 and H-9), two hydroxyl and three methyl groups (H-10, H-3' and H-2"). The ^{13}C NMR (Figure 4B) and HSQC spectra (Figure 5A) indicated 15 carbons, which were classified into six olefinic carbons (C-2, C-3, C-6, C-7, C-1' and C-2'), four oxygenated sp^3 methine carbons (C-4, C-5, C-8 and C-9), three sp^3 methyl carbons (C-10, C-3' and C-2") and two carbonyl carbons (C-1 and C-1"). The ^{1}H–^{1}H COSY of compound 325-3 (Figure 5B) showed all expected bonds between hydrogens on adjacent carbons from H-2 to H-10 and from H-1' to H-3'. The HMBC correlations (Figure 6A) from H-2 to C-1, H-3' to C-2' and H-2" to C-2' also proved suggested structure. The Z geometries of C-1'/C-2' and C-2/C-3 double bonds were elucidated by the NOESY cross-peaks between H-2 and H-3 and H-1′ and H-3′ (Figure 6B). Also, the absence of the NOESY cross-peak between H-6 and H-7 indicated E configuration of the C-6/C-7 double bond. Additionally, configurations of all double bonds were confirmed by magnitudes of the coupling constants in ^{1}H-NMR spectra. Thus, the structure of compound 325-3 was finally elucidated as (Z)-(Z)-2-acetoxyprop-1-en-1-yl-3-(3-((E)-3,4-dihydroxypent-1-en-1-yl)oxiran-2-yl)acrylate (Figure 7A). Geometric isomers of this compound were not detected.

Compound 325-5 was also obtained as a colourless oil, whose molecular formula was determined as $C_{15}H_{18}O_7$ (recorded by GC-MS method as ion [M+H-OH-CH3] = 279, calc. 311.1125, Figure 8). A comparison of ^{1}H spectra (Figure 9A) showed that compound 325-5 shared the same spectroscopic characteristics with compound 325-3, with one oxygenated sp^3 methine and one hydroxyl group less. In the ^{13}C NMR spectra of compound 325-5 (Figure 9B), three carbonyl carbon signals and three oxygenated sp^3 methines were detected, suggesting that compound 325-5 was oxidation product of compound 325-3. The ^{1}H–^{1}H COSY (Figure 10B) showed bonds between hydrogens on adjacent carbons from H-2 to H-7 and from H-9 to H-10 indicated carbonyl group at C-8. The HMBC correlations (Figure 11A) from H-7 to additional carbonyl group also supported this assumption. Configurations of all double bonds were found to be the same as of compound 325-3, based on the analysis of NOESY spectrum (Figure 11B) and magnitudes of the coupling constants. Based on this, the structure of compound 325-5 was determined as (Z)-(Z)-2-acetoxyprop-1-en-1-yl 3-(3-((E)-4-hydroxy-3-oxopent-1-en-1-yl)oxiran-2-yl)acrylate (Figure 7B). Geometric isomers of this compound were not detected.

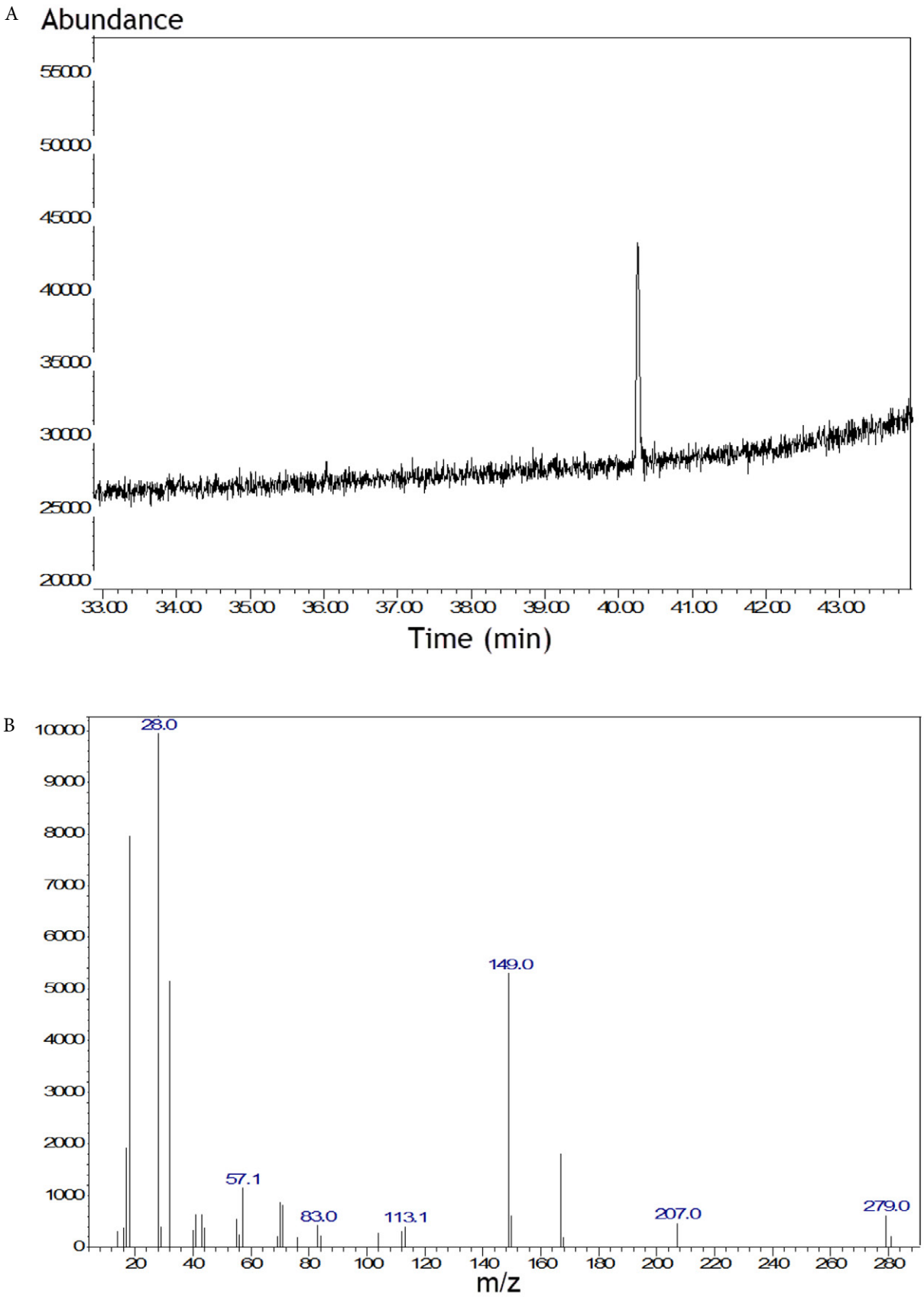

Figure 8. Total ion chromatogram (A) and GC/MS spectra (B) of compound 325-5

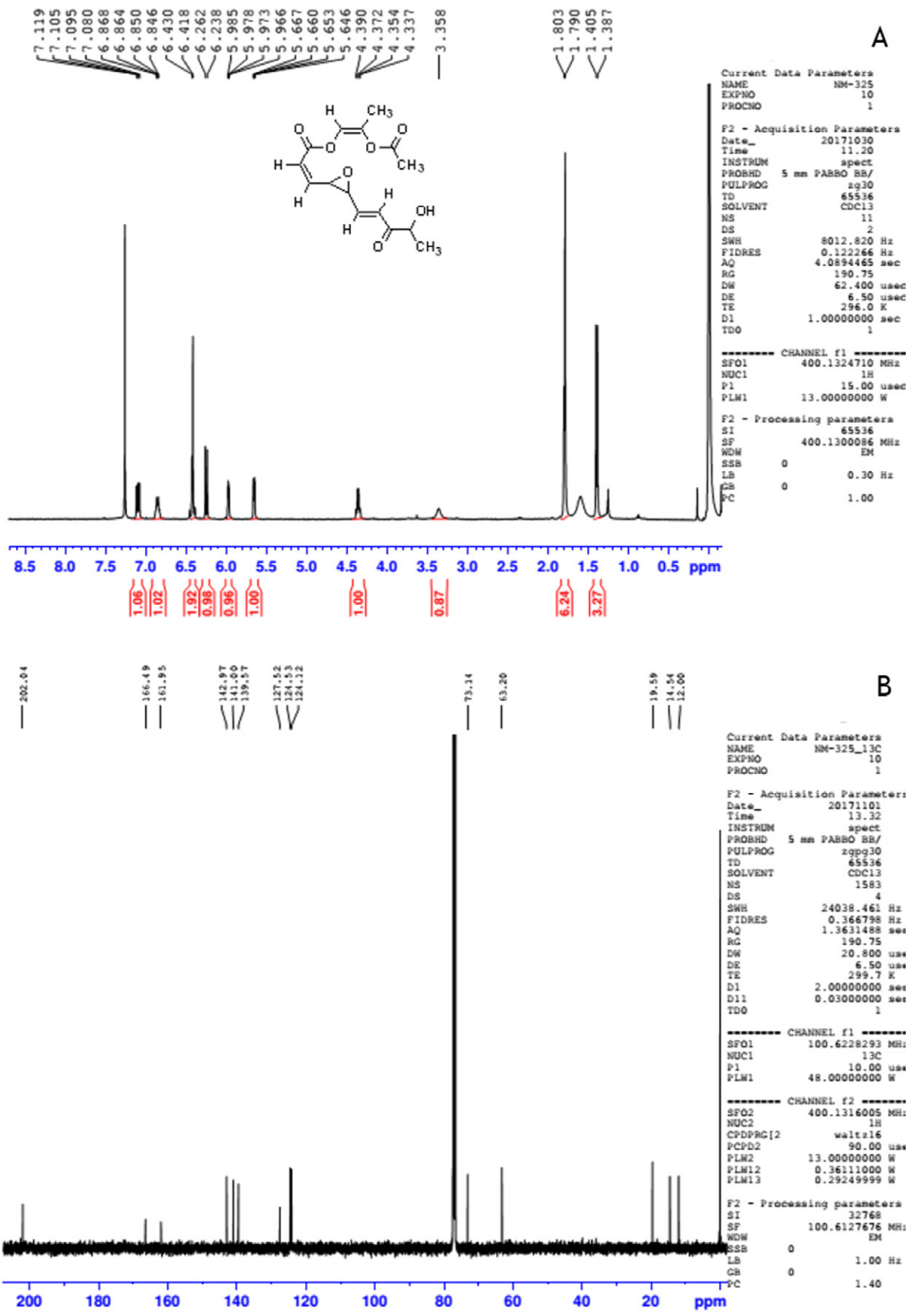

Figure 9. ^{1}H NMR spectra (A), ^{13}C NMR spectra (B) for toluene standard and compound 325-5

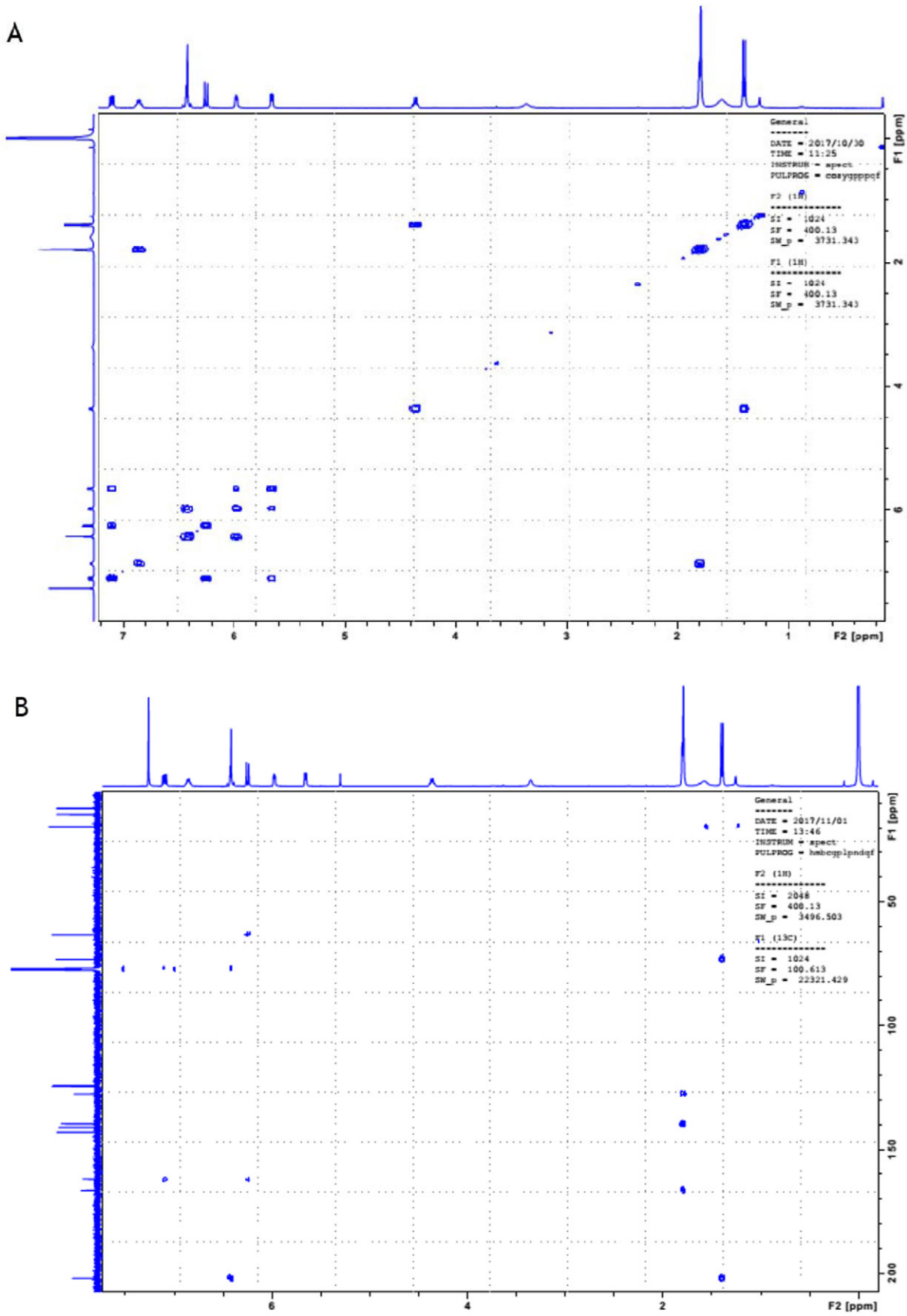

Figure 10. HSQC (A) and COSY (B) spectra of compound 325-5

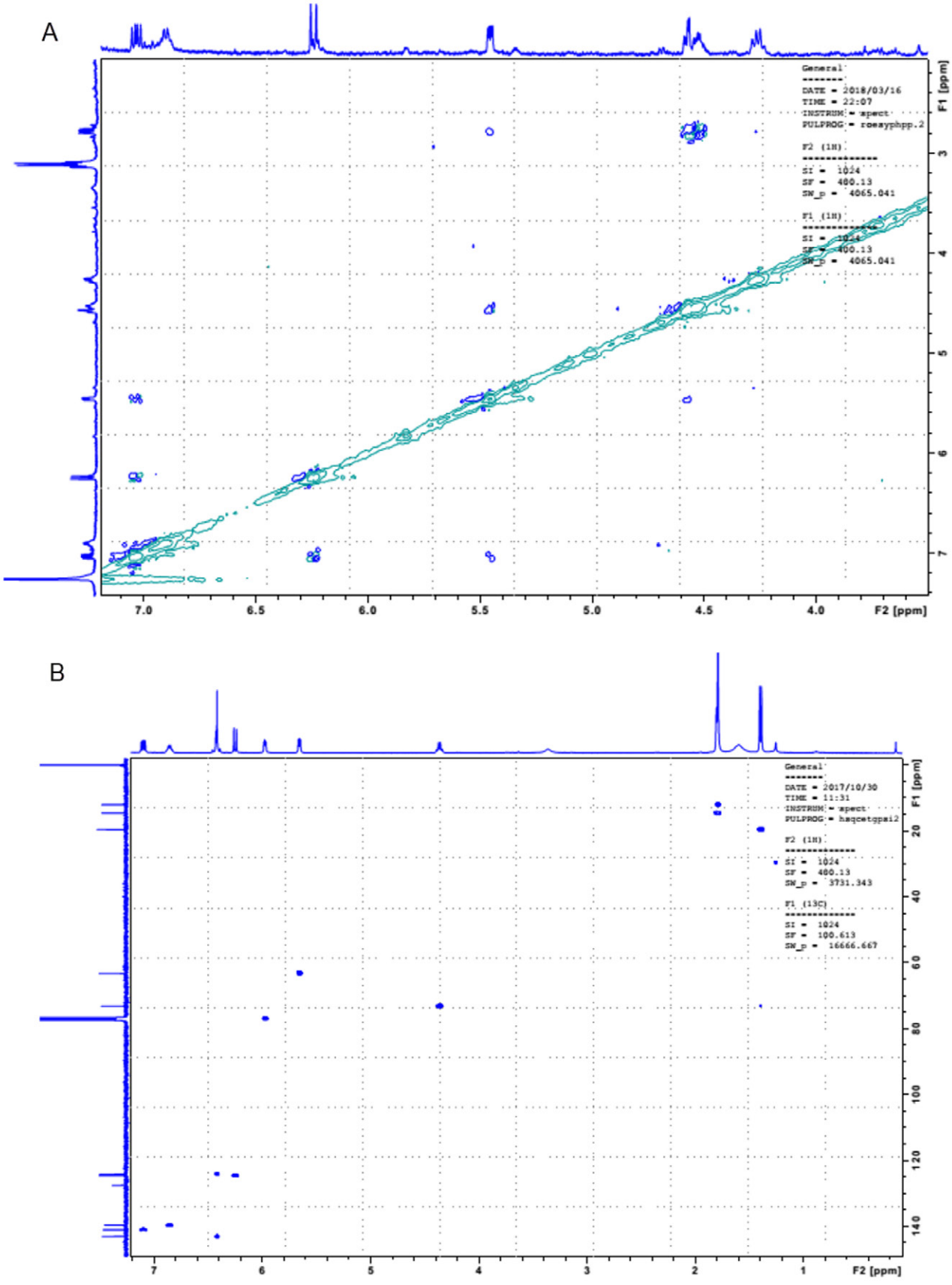

Figure 11. HMBC (A) and NOESY (B) spectra of compound 325-5

Phomopsis sp. was already recognized as potent producer of bioactive compounds. However, it can be noticed that *Phomopsis sp*. is able to produce a variety of known secondary metabolites with great differences in chemical compositions. Among them, relatively small molecule which is similar to compounds resulted from our study, is phomoenamide, a metabolite of *Phomopsis sp.* PSU-D15 isolated from leaves of *Garcinia dulcis (Roxb.) Kurz.* that has moderate activity against *M. tuberculosis*. [27] Another endophytic fungi, *Culvularia geniculate* obtained from limbs of *Catunaregam tomentosa*, produces five metabolites known as culvularides A-E, with similar structures to molecules from *Phomopsis species* we have characterized. For cuvularides A-E antifungal activity against *Candida albican*s has been determined.[28] Therefore, the authors consider that the future perspective of this research could be directed towards spreading the antimicrobial assay evaluation in accordance with mentioned indices from literature records.

4. Conclusions

Within this scientific article, antibiotic potential of endophyte *Phomopsis species* isolated from conifer needles has been determined against bacteria *Escherichia coli* and *Staphylococcus aureus*. Dominant compounds potentially responsible for antimicrobial activity have been discussed. Based on their antimicrobial activity and unique structural characteristics in comparison with well-established drugs from the same therapeutic category, two dominant compounds (Z)-(Z)-2-acetoxyprop-1-en-1-yl-3-(3-((E)-3,4-dihydroxypent-1-en-1-yl)oxiran-2-yl)acrylate (denoted as 325-3) and (Z)-(Z)-2-acetoxyprop-1-en-1-yl 3-(3-((E)-4-hydroxy-3-oxopent-1-en-1-yl)oxiran-2-yl)acrylate (denoted as 325-5) were characterized. Moreover, based on their specific properties, these biomolecules could serve as leading structures for further antibiotic drug discovery. The evaluation of relationship between the chemical structure and the intensity of antibacterial activity may provide guidelines for development of series of new derivatives and further improvement of bioactivity.

Acknowledgements

This scientific research has been funded by Ministry of Education, Science and Technological Development of Republic of Serbia (project no. 172033) and Slovenian Research Agency (grant number P4-0127) within bilateral projects between Faculty of Pharmacy, University in Belgrade, Serbia and Faculty of Pharmacy, University in Ljubljana, Slovenia, EU (project no. BI-RS/16-17-022).

6. References

1. M. Wink, *Phytochemistry*. **2003**, *64*, 3–19. **DOI:**10.1016/S0031-9422(03)00300-5
2. H. Nisa, A. N. Kamili, I. A. Nawchoo, S. Shafi, N. Shameem, S. A. Bandh, *Microb. Pathog.* **2015**, *82*, 50–59. **DOI:**10.1016/j.micpath.2015.04.001
3. B. Schulz, C. Boyle, S. Draeger, A. K. Römmert, K. Krohn, *Mycol. Res.* **2002**, *106*, 996–1004. **DOI:**10.1017/S0953756202006342
4. S. Kusari, C. Hertweck, M. Spiteller, *Chem. Biol*. **2012**, *19*, 792–798. **DOI:**10.1016/j.chembiol.2012.06.004
5. D. Udayanga, X. Liu, E. H. McKenzie, E. Chukeatirote, A. H. Bahkali, K. D. Hyde, *Fungal Diversity*. **2011**, *50*, 189–225. **DOI:**10.1007/s13225-011-0126-9
6. A. E. Arnold, L. C. Mejía, D. Kyllo, E. I. Rojas, Z. Maynard, N. Robbins, E. A. Herre. *Proc. Natl. Acad. Sci*. **2003**, *100*, 15649–15654. **DOI:**10.1073/pnas.2533483100
7. G. A. Strobel, *Microbes. Infect.* **2003**, *5*, 535–544. **DOI:**10.1016/S1286-4579(03)00073-X
8. R. P. Ryan, K. Germaine, A. Franks, D. J. Ryan, D. N. Dowling, *FEMS Microbiol. Lett*. **2008**, *278*, 1–9. **DOI:**10.1111/j.1574-6968.2007.00918.x
9. R. X. Tan, W. X. Zou, *Nat. Prod. Rep*. **2001**, *18*, 448–459. **DOI:**10.1039/b100918o
10. Z. Deng, L. Cao, *Chemosphere*. **2017**, *168*, 1100–1106. **DOI:**10.1016/j.chemosphere.2016.10.097
11. S. L. Doty, *New Phytol*. **2008**, *179*, 318–333. **DOI:**10.1111/j.1469-8137.2008.02446.x
12. H. Hussain, M. K. Tchimene, I. Ahmed, K. Meier, M. Steinert, S. Draeger, B. Schulz, K. Krohn, *Nat. Prod. Commun*. **2011**, *6*, 1905–1906. **DOI:**10.1177/1934578X1100601228
13. M. Corrado, K. F. Rodrigues, *Int. J. Biochem. Physiol. Genet. Morphol. Ecol. Microorg.* **2004**, *44*, 157–160. **DOI:**10.1002/jobm.200310341
14. M. Isaka, A. Jaturapat, K. Rukseree, K. Danwisetkanjana, M. Tanticharoen, Y. Thebtaranonth, *J. Nat. Prod*. **2001**, *64*, 1015–1018. **DOI:**10.1021/np010006h
15. G. Jayanthi, S. Kamalraj, K. Karthikeyan, J. Muthumary, *Int. J. Curr. Sci*. **2011**, *1*, 85–90.
16. D. Rakshith, P. Santosh, S. Satish, *Int. J. Chem. Anal. Sci.* **2013**, *4*, 156–160. **DOI:**10.1016/j.ijcas.2013.08.006
17. V. Rukachaisirikul, U. Sommart, S. Phongpaichit, J. Sakayaroj, K. Kirtikara, *Phytochem*. **2008**, *69*, 783–787. **DOI:**10.1016/j.phytochem.2007.09.006
18. Z. Huang, X. Cai, C. Shao, Z. She, X. Xia, Y. Chen, J. Yang, S. Zhou, Y. Lin, *Phytochem*. **2008**, *69*, 1604–1608. **DOI:**10.1016/j.phytochem.2008.02.002
19. L. Mostert, P. W. Crous, J. C. Kang, A. J. Phillips, *Mycol*. **2001**, *93*, 146–167. **DOI:**10.1080/00275514.2001.12061286
20. E. L. Diogo, J. M. Santos, A. J. Phillips, *Fungal Divers.* **2010**, *44*, 107–115. **DOI:**10.1007/s13225-010-0057-x
21. D. F. Farr, L. A. Castlebury, A. Y. Rossman, *Mycol.* **2002**, *94*, 494–504. **DOI:**10.1080/15572536.2003.11833214
22. D. Rakshith, P. Santosh, S. Satish, *Int. J. Chem. Anal. Sci.* **2013,** *4*(3), 156–160. **DOI:**10.1016/j.ijcas.2013.08.006
23. H. Hussain, M. K. Tchimene, I. Ahmed, K. Meier, M. Steinert, S. Draeger, B. Schulz, K.Krohn, *Nat. Prod. Commun.* **2011**, *6*(12), 1905–1906. **DOI:**10.1177/1934578X1100601228

24. M. Ravnikar, M. Tercelj, D. Janeš, B. Štrukelj, S. Kreft, *Afr. J. Biotechnol.* **2015**, *14*, 867-871. **DOI:**10.5897/AJB2014.14387
25. M. Friedman, P. R. Henika, C. E. Levin, R. E. Mandrell, *J. Agric. Food Chem.* **2004**, *52*(19), 6042–6048. **DOI:**10.1021/jf0495340
26. M. Godoy-Gallardo, C. Mas-Moruno, M. C. Fernández-Calderón, C. Pérez-Giraldo, J. M. Manero, F. Albericio, F., J. G. Francisco, D. Rodríguez, *Acta Biomater.* **2014,** *10*(8), 3522–3534. **DOI:**10.1016/j.actbio.2014.03.026
27. V. Rukachaisirikul, U. Sommart, S. Phongpaichit, J. Sakayaroj, K. Kirtikara, *Phytochem*. **2008**, *69*(3), 783–787. **DOI:**10.1016/j.phytochem.2007.09.006
28. P. Chomcheon, S. Wiyakrutta, T. Aree, N. Sriubolmas, N. Ngamrojanavanich, C. Mahidol, S. Ruchirawat, P. Kittakoop, *Chem. – Eur. J.* **2010**, *16*(36), 11178–11185. **DOI:**10.1002/chem.201000652

Povzetek

V zadnjem desetletju je vse več zanimanja namenjenega raziskovanju bioaktivnih sekundarnih metabolitov endofitnih gliv. Kot nadaljevanje naših predhodnih raziskav na področju endofitnih gljiv s protimikrobnim potencialom, smo izbrali in izolirali vrsto *Phomopsis sp.* iz iglic iglavcev. Diklorometanski in etanolni ekstrakt *Phomopsis sp.* sta znatno zavirala rast bakterij *Escherichia coli* in *Staphylococcus aureus*. Spojine diklorometanskega izvlečka so bile ločene, zbrane in očiščene s pomočjo tehnike semi-preparativne visoko zmogljivostne tekočinske kromatografije (HPLC) ter okarakterizirane s tehnikama masne spektrometrije (MS) in jedrske magnetne resonančne spektroskopije (NMR). Na podlagi protimikrobne aktivnosti in edinstvenih strukturnih značilnosti, v primerjavi z uveljavljenimi zdravilnimi učinkovinami iz iste terapevtske kategorije, sta bili dve prevladujoči spojini (Z)-(Z) -2-acetoksiprop-1-en-1-il-3- (3- ((E) -3,4-dihidroksipent-1-en-1-il)oksiran-2-il)akrilat (označen kot 325-3) in (Z)-(Z)-2-acetoksiprop-1-en-1-il-3-(3-((E)-4-hidroksi-3-oksopent-1-en-1-il)oksiran-2-il)akrilat (označen kot 325-5) prepoznani kot obetavni spojini za nadaljnje raziskave na področju novih naravnih antibiotičnih učinkovin.

Except when otherwise noted, articles in this journal are published under the terms and conditions of the Creative Commons Attribution 4.0 International License

DOI: 10.17344/acsi.2019.5390 *Acta Chim. Slov.* **2020,** *67,* 462–468
creative commons

Scientific paper

Facile Synthesis of Poly(DMAEMA-co-MPS)-coated Porous Silica Nanocarriers as Dual-targeting Drug Delivery Platform: Experimental and Biological Investigations

Mohammad Hegazy,[1,2,*] Pei Zhou,[3] Guangyu Wu,[4] Nadia Taloub,[1,5] Muhammad Zayed,[6] Xin Huang[1,*] and Yudong Huang[1,*]

[1] *MIIT Key Laboratory of Critical Materials Technology for New Energy Conversion and Storage, Key Laboratory of Microsystems and Microstructures Manufacturing, School of Chemistry and Chemical Engineering, Harbin Institute of Technology, Harbin 150001, China*

[2] *Department of Polymer Chemistry, Faculty of Science, Menoufia University, Shebin El-Kom 32511, Egypt*

[3] *School of Environmental and Municipal Engineering, North China University of Water Resources and Electric Power, Zhengzhou 450011, China*

[4] *College of Biology and the Environment, Co-Innovation Center for the Sustainable Forestry in Southern China, Nanjing Forestry University, Nanjing, Jiangsu 210037, China*

[5] *LIPE Laboratory, University of Constantine 3, 25000 Constantine, Algeria*

[6] *Botany and Microbiology Department, Menoufia University, Shebin El-Kom, 32511, Egypt*

** Corresponding author: E-mail: dr_hegazy2000@yahoo.com; xinhuang@hit.edu.cn; huangyd@hit.edu.cn*

Received: 07-12-2019

Abstract

Inorganic structures with functionalized polymers play essential roles in diverse biological trends. Herein, thermal and CO_2 dual-stimuli nanomaterials composed of mesoporous silica nanoparticles (MSN) anchored with two grafted copolymers: poly(3-methacryloxypropyltrimethoxysilane) "PMPS" & poly(N,N-dimethylaminoethyl methacrylate) "PDMAEMA" were synthesized via one-step reaction and characterized by BET as well as BJH methods to estimate pore sizes, pore volumes, and surface areas. The smart PDMAEMA acted as an active gatekeeper to adjust the loading or *in vitro* release processes of a fungicidal drug-loaded inside the mesopores by altering temperature or CO_2 of the tested environment. Furthermore, treating the nanomaterials by CO_2 for a few minutes was found to have a bactericidal effect with promising results as indicated by the disk diffusion technique. In general, the positive biological activity against selected strains of bacteria and fungi indicates that these particles may be helpful for engineering more efficient antifungal or antibacterial agents for pharmaceutical applications.

Keywords: CO_2-responsive release, thermal-triggered release, biopolymeric materials, antimicrobial agents

1. Introduction

Over the past two decades, smart polymeric materials have been exploited for versatile applications e.g. ion absorbance capacity,[1] wastewater treatment,[2] cargo delivery systems,[3] photodynamic or photothermal effects,[4] and enhancing the mechanical properties as well as the interfacial performance of specific fibers.[5,6] A famous example is MSN which have been used widely as drug carriers in biomedical technologies, thanks to several merits e.g. biocompatibility, easiness of surface-modification, and controllable mesopore sizes.[7] PDMAEMA was applied as a CO_2 responsive polymer in aqueous solutions as a result of protonation of the tertiary amine group which can also deprotonate reversibly by N_2 stimulation, i.e. swelling-shrinking effect.[8] Furthermore, this smart

polymer showed pretty good thermo-responsiveness, as it can form coil-to-globule states by changing temperatures degrees and showed a lower critical solution temperature (LCST) in aqueous solutions,[9] which is a similar character to the well-known thermosensitive poly(N-isopropylacrylamide) (PNIPAAm).[10,11] More interestingly, quaternization of terminal amino groups of PDMAEMA had promising antimicrobial activity against some bacterial strains.[12]

Because of the possible applications in various promising areas including material science and life science, this study aims to synthesize and characterize pharmaceutical nanocontainers with dual-sensitive character to release the loaded cargos with a response to CO_2 or temperature or both together, followed by biological evaluation against microbial strains as illustrated in Scheme 1. We exploited the alkoxysilane moiety of silicon derivative monomer 3-methacryloxypropyltrimethoxysilane (MPS) to link it (through a condensation reaction) with silanols surface of MSN from one side. In contrast, the other side (active double bond) was polymerized simultaneously with N,N-dimethylaminoethyl methacrylate (DMAEMA) monomer via thermal polymerization using AIBN as azo initiator.[13,14] The growing PDMAEMA onto the MSN surface was used as a cap to maintain or trigger anidulafungin, which utilized as a model antifungal drug. The release behavior of the cargo was investigated by the two mentioned responses and tested against some microorganisms to evaluate the biological activity. The advantages of this construction are not only for the simple synthesis via a one-step experiment, but also lie for obtaining high drug loading capacity, effective response for thermo- or CO_2-stimuli and the potential application as antifungal or antibacterial agents, especially after converting PDMAEMA into its cationic form.

2. Materials and Characterization Techniques

The chemicals and reagents were purchased with analytical grade via Sigma-Aldrich. The specific surface areas and mesoporous structures were obtained through N_2 adsorption-desorption isotherms. The cloud point for a given polymeric material solution was chosen as the corresponding inflection point of "the transmittance versus temperature curve". The LCST results of the aqueous material solutions were determined at a 50% decrease of the optical transmittance, through measuring the wavelength at 500 nm using a UV-visible spectrophotometer (Shimadzu UV-1700). The temperature degrees of the sample cells were controlled thermostatically by using an exterior constant temperature bath. Zeta potential analysis for polymeric material solutions (pH 6.8, 5.0 mM buffer PBS, 0.2 mg/mL material sample) was tested by using a ZETASIZER (Malvern Instruments, Britain) at 25 °C. Both loading and releasing contents of anidulafungin drug were studied by UV-Vis spectrophotometry at λmax of 303 nm. Random isolates from *Escherichia coli* (*E.coli*, gram-negative bacteria) as well as *Candida albicans* (*C. albicans*, fungi) were obtained from the College of Life Science, Northeast Forestry University, Harbin, China.

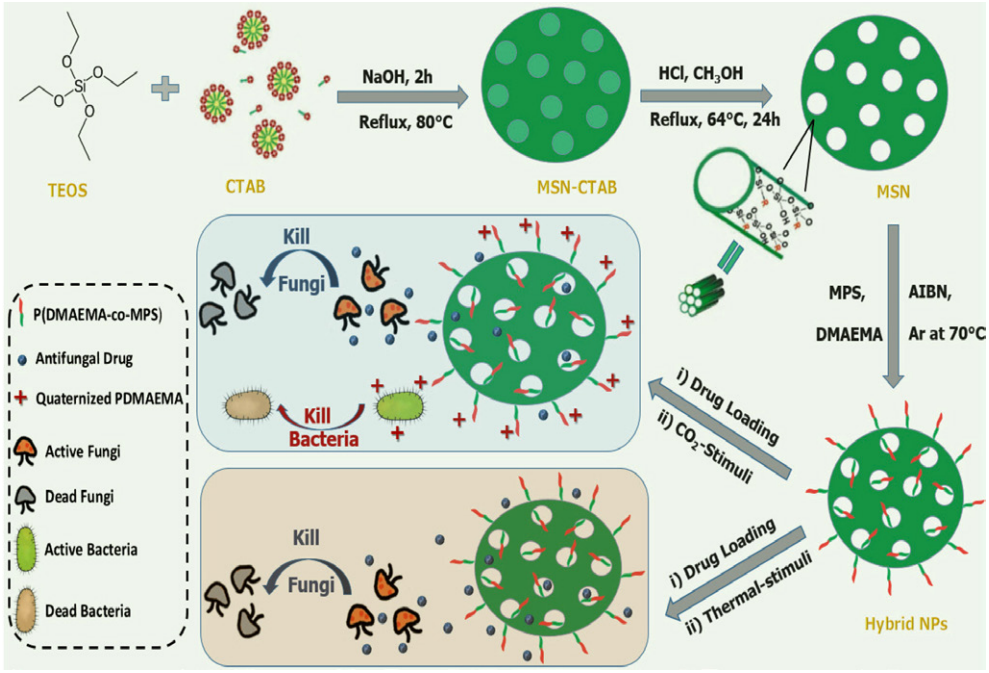

Scheme 1. Schematic illustration of MSN/P(MPS-co-DMAEMA) generation followed by drug loading, then CO_2 and hyperthermia-induced release through the dual-functional biomedical platform.

The culture medium was nutrient agar (NA) which prepared by adding agar (20 gm), beef extract (3 gm), peptone (5 gm) and sodium chloride (5 gm) then completed to one liter of deionized water.

3. Methods

MSN/P(MPS-co-DMAEMA) nanocarriers were prepared by established polymerization method,[15] and then loaded with anidulafungin drug after several purifications according to Rahoui et al.[16] The loading content of the drug was estimated from UV-Vis spectra via Eq. (1).

$$\text{Loading content (\%)} = \frac{\text{the initial amount of drug} - \text{the supernatant free amount of drug}}{\text{the weight of loaded drug nanocarriers}} \times 100 \quad (1)$$

On contrast, *in vitro* drug release experiments were tested in physiological saline solution (PSS) and estimated according to Eq. (2) at different periods (from 1h to 24h).[7,16] The release behavior in PSS (100 mM) using dialysis membrane (molecular weight cut-off: 8000–14000 Da) were calculated by detecting the corresponding absorbance peak of anidulafungin at 303 nm using different environments including; (i) temperature lower and higher LCST of PDMAEMA (i.e. 25 °C & 45 °C) and (ii) bubbling with CO_2 for 10 min at the two mentioned temperatures.

$$\text{Releasing content (\%)} = \frac{\text{the amount of drug in the release medium}}{\text{the amount of loaded drug into nanocarriers}} \times 100 \quad (2)$$

The antimicrobial activity for the nanocarriers containing anidulafungin (NCA) was tested (after the releasing process with the two stimuli) using the well diffusion technique. The inoculum density in the chosen NA plate was 10^8 CFU · ml^{-1}, which related to the 0.5 McFarland turbidity scale.[17] The seeded plates were dried in the incubator at 36 °C for 25 min. A borer of cork with 7 ml diameter was applied to cut uniform wells onto the inoculated agar surface, then around 100 µl of every sample (20 mg/ml) was added to the well. Free anidulafungin and tetracycline were used (with the same concentration as NCA) as the positive control for antifungal and antibacterial activities, respectively. Deionized water and filter paper were used as the negative control (around 100 µl of the solvent). The plates were accordingly incubated for one day at the normal body temperature (37 °C). By the end of incubation time, the biological activity was tested through inhibition zones in millimeters.[18]

4. Results and Discussion

The corresponding chemical structures of MPS monomer, DMAEMA monomer, MSN and MSN/P(MPS-co-DMAEMA) nanocarriers were represented in Fig. 1.

Both MSN and MSN/P(MPS-co-DMAEMA) nanocarriers were synthesized according to Scheme 1, then characterized by N_2 sorption isotherms (Fig. 2), using BET and BJH methods. For both materials, the isotherms were of type IV, which suggesting the mesoporous nature[19] as indicated in Fig. 2A. The high surface area of 705 m^2 g^{-1} for MSN had decreased considerably to 257 m^2 g^{-1} after coating with the copolymer layer to obtain MSN/P(MPS- co-DMAEMA) (see Table 1), which matching well with similar studies.[20,21] Similarly and from pore size distribution curves (Fig. 2B) and the same Table, there was a decrease in the pore volume (from 0.66 to 0.51 mL/g) along with the mean pore diameter (from 8.82 to 6.53 nm), when going from MSN to MSN/P(MPS-co-DMAEMA). The maintained large pore volume and high surface area for MSN/P(MPS-co-DMAEMA nanocarriers, refers to that their mesopores have not been blocked after anchoring both PMPS & PDMAEMA on the silica surface, and consequently have the opportunity to carry the drug in the next step.

The pH-dependent electro-kinetic characterizations were used to demonstrate the effect of pH changes on the obtained nanocarrier solutions, and to strengthen the understanding of the process and its usefulness. As shown in

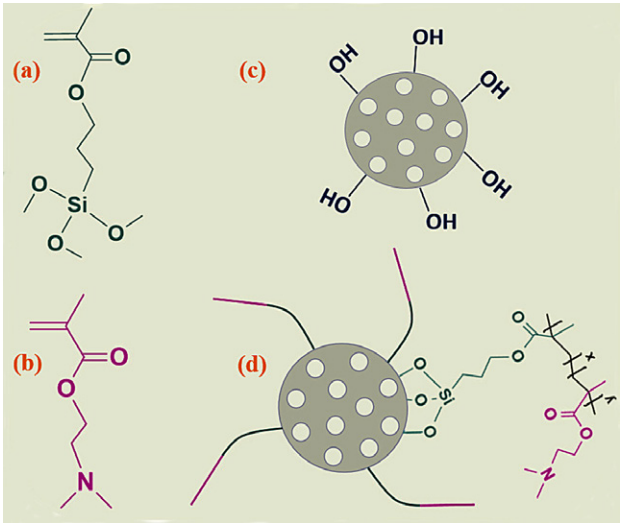

Fig. 1. Chemical structures of (a) MPS monomer, (b) DMAEMA monomer, (c) MSN and (d) MSN/P(MPS-co-DMAEMA) nanocarriers.

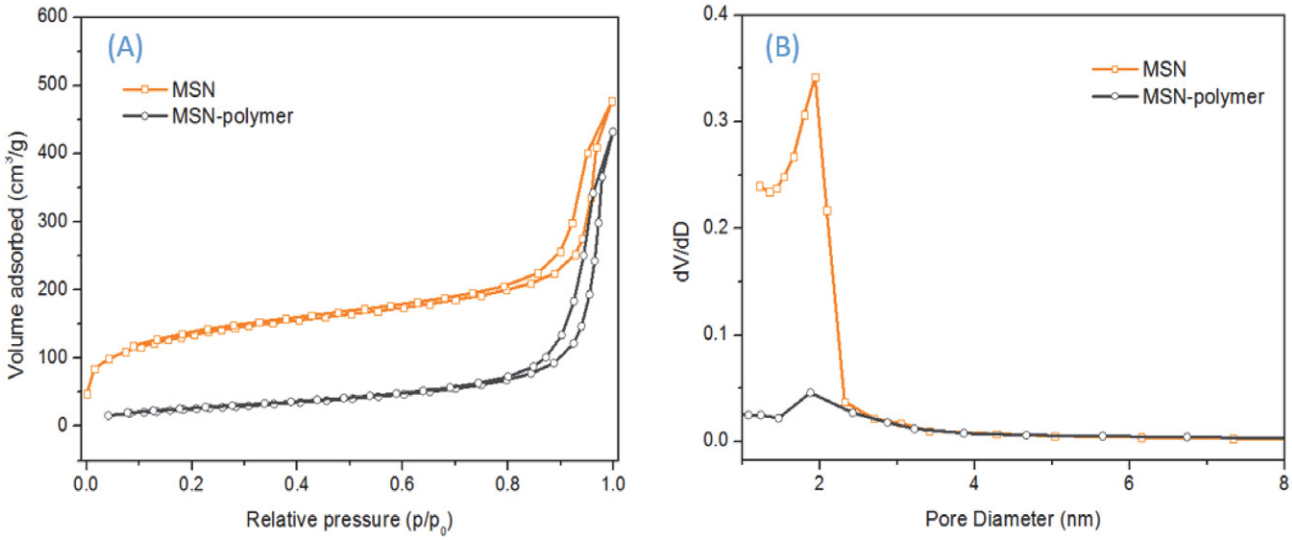

Fig. 2. (A) N_2 adsorption-desorption isotherms and (B) pore size distribution curves for MSN and MSN/P(MPS-co-DMAEMA).

Table 1. Structure parameters of MSN and MSN/P(MPS-co -DMAEMA) derived from nitrogen sorption.

Samples	BET surface area (m^2/g)	Pore volume (mL/g)	Mean pore diameter (nm)
MSN	705	0.66	8.82
MSN/P(MPS-co-DMAEMA)	257	0.51	6.53

Fig. 3, the apparent zeta-potential (ζ) decreases notably with the pH increasing, which perhaps due to protonation of tertiary-amine groups (involved within PDMAEMA backbones) by acidic media, therefore, ζ has high positive values with low pH values and vice versa. The critical pH for PDMAEMA chains needed to plug the pores of the prepared nanocarriers was measured to be pH 7.2 which is lower than 7.4 value (human blood medium). Thus, one can conclude that in case this system is used as a smart drug delivery nanocarrier, the release of any encapsulated-drug from MSN/P(MPS-co-DMAEMA) can only be noticed after reaching the desired pathological organs, where the pH values are slightly acidic (e.g. treatment of CO_2 gas in our study here).

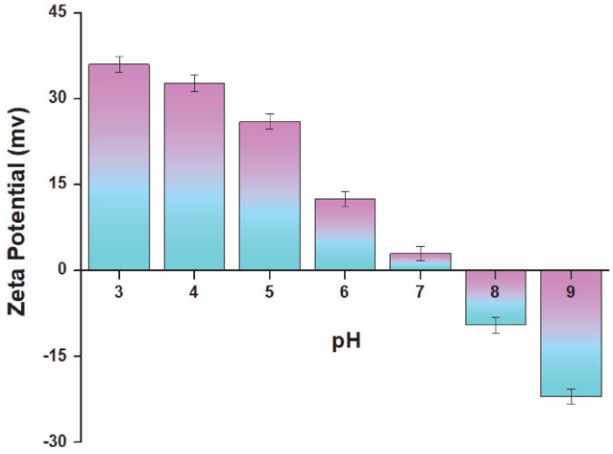

Fig. 3. Apparent zeta-potential (ζ) measurements for MSN/P(MPS-co-DMAEMA) nanocarriers determined from pH-dependent experiments.

It is widely known that thermo-sensitive polymers/copolymers can display phase separation by increasing their temperature degrees above the lower critical solution temperature (LCST). Since PDMAEMA is a typical weak polyelectrolyte and its pKa value is 7.0–7.5 (with exhibiting an LCST of 40–50 °C in the aqueous solutions[22]), we tested LCST of the obtained MSN/P(MPS-co-DMAEMA) nanocarriers in a pH-controlled environment because the LCST is pH-dependent and the solubility of CO_2 is temperature-dependent.

It is expected that MSN/P(MPS-co-DMAEMA) nanomaterials are pH-responsive as similar to PDMAEMA due to the presence of terminal dimethylamino groups. The pH-sensitive properties of these polymeric materials are shown in Fig. 4. One can notice the transmittance character (for aqueous solutions of such materials) against temperature degrees at different pH values, whereas the LCST is indicated at a pH range beginning from 3.35 to 10.92. It is clear that the aqueous solutions of MSN/P(MPS-co-DMAEMA) are soluble in low pH environments, such as 3.35 & 6.42, and no LCST is obtained within a temperature range of 20–60 °C for theses environments. This perhaps is due to the occurrence of stable polymeric nanomaterials that formed at low pH and yielding protonated PDMAEMA side chains in the

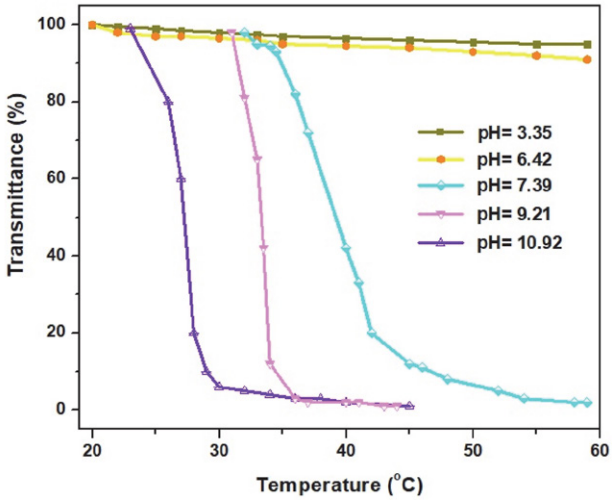

Fig. 4. Transmittance for aqueous solutions of MSN/P(MPS-co-DMAEMA) as a function of temperature degrees at various pH values.

outer shell of the nanomaterials, leading to an increase in the electrostatic repulsion force and consequently preventing the phase separation.[23] By contrast, the LCST of MSN/P(MPS-co- DMAEMA) is noticed at pH 7.39. Moreover, the cloud temperature of the polymeric nanomaterials decreases gradually by raising the pH from 7.39 to 10.92, which is similar to the situation of LCST for PDMAEMA homopolymer that discussed by Plamper et al.[24]

For drug encapsulation studies, anidulafungin was chosen as a model antifungal agent, especially for the treatment of candidemia caused by C*andida albicans* yeast. The loading content (%) was calculated by UV-Vis spectrophotometry at λmax of 303 nm according to Eq. (1) and it was 17.9 ± 0.7%, which is still higher than most surface-modified MSN previous studies (lower than 10%). This could be attributed to the hydrogen bonds and strong electrostatic interactions between the drug and nanocarriers.

The triggered release of anidulafungin from NCA was tested by the dialysis method in PSS, according to Eq. (2) under the following environments: (i) 25 °C, (ii) 45 °C, (iii) 25 °C & bubbling with CO_2 for 10 min and (iv) 45 °C & bubbling with CO_2 for 10 min. The results demonstrated that the extended copolymer could perform as a smart gatekeeper for this system according to CO_2 or temperature changes. For the gas-response, the extended PDMAEMA is hydrophobic at neutral or alkaline pH values with collapsed uncharged chains, while it can convert into the weak cationic character in acidic medium with water-soluble, protonated and extended chains (i.e. after treated with CO_2 gas).[25] On the other hand, the releasing of anidulafungin at hyperthermia state could be related to thermo-responsive features of the PDMAEMA segments. When the temperature increased (above LCST), the extended PDMAEMA units would shrink to the globular structure due to the weakening or breaking of hydrogen bonds, which resulting in collapsed PDMAEMA chains.[26]

The release process of the chosen antifungal drug at the four mentioned conditions was indicated in Fig. 5. About 13% of conjugated anidulafungin was only released from the NCA after incubation for 36 hours at room temperature, indicating that many anidulafungin molecules were still covalently incorporated inside the nanocarriers without significant release. Therefore, the release level of anidulafungin is low, which further indicates the stability of this polymeric material at room temperature. Also, there is a hydrophobic interaction between anidulafungin and PMPS chains and at the same time the anidulafungin has interactions with PDMAEMA layers in aqueous media (thanks to its unique chemical constitution).

On the other hand, the released amount of the encapsulated payload reached 25 % after bubbling with CO_2 for 10 min at room temperature and during the same number of hours, indicating that, such carbon dioxide treatment for these polymeric materials can induce the programmed release in a successful way.

Subsequently, at 45 °C (which is above the LCST), the release process increased dramatically to 35 % within only 10 h and reached 63% after 36 h. This substantial increase could be due to the copolymer layer underwent a coil-to globule change and shrank into a compact mass, which allowing pores opening and showing the significant release of the loaded drug. This situation illustrates a good agreement with most known thermoresponsive polymeric-nanomaterials which can keep their cargos at room temperature, and then deliver them within the locally heated diseased sites (~40–42 °C).

Moreover, the release behavior of the drug at 45 °C after bubbling with CO_2 for 10 min was noticed to yield around 21% after 10 h & 42 % after 36 h, which was lower than the corresponding release at 45 °C alone without CO_2 bubbling. However, the release condition of 45 °C with

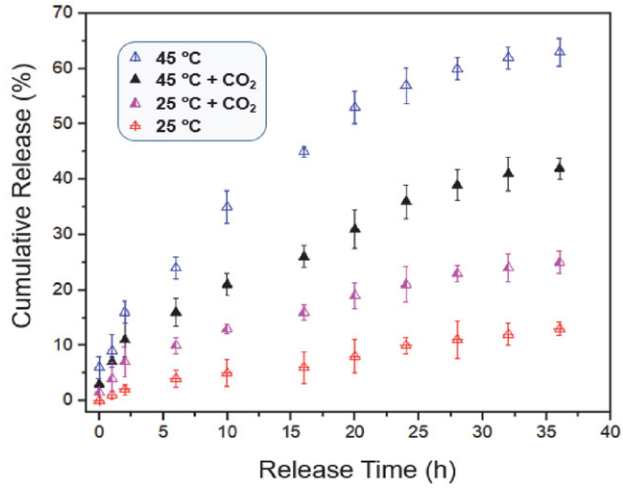

Fig. 5. Controlled release of anidulafungin from NCA at four different conditions.

CO_2 was still higher than the other previous two conditions (25 °C without CO_2 & 25 °C with CO_2). This could be attributed to the increase of thermo-motions at elevated temperature enhanced the diffusion of anidulafungin from the expanded nanoparticles.

After the releasing processes via dual stimuli from NCA, we evaluated the biological activity through antimicrobial screening using two organisms (*E.coli*, & *C. albicans*) according to Table 2. Free anidulafungin and tetracycline were used as the positive control for the antifungal and antibacterial properties, respectively. The results showed that NCA did not express the essential antimicrobial impact on these microorganisms except an exceedingly weak impact on *C. albicans*, which perhaps due to the minimal leakage of anidulafungin from NCA at room temperature (entry 1 in Table 2). Bubbling with CO_2 for 10 min at this room temperature (single CO_2 stimulus, entry 2 in Table 2), showed a moderate antifungal effect against *C. albicans*, but a very strong one against *E. coli*, which could be attributed to formation of ionene polymers (cationic polymers include positive nitrogen or phosphor in their backbones) after reacting with CO_2 gas. This result is in a good agreement with recent studies, which proved that the cationic PDMAEMA$^+$ has a strong bactericidal effect against *E. coli* and some other bacterial strains.[12,27]

On the other hand, upon heating to 45 °C (temperature stimulus alone), no antibacterial impact occurred, but a very strong antifungal effect was obtained. This effect reflects that the temperature stimulus cannot convert PDMAEMA into its quaternary ammonium salt PDMAEMA$^+$ (which is the key point for bacteria-killing), however, this stimulus can release the loaded anidulafungin extremely which inhibited the growth of the yeast considerably (entry 3 in Table 2). Bubbling with CO_2 gas at this elevated temperature reduced the loaded cargo a little bit to a strong inhibition growth of *C. albicans* and further this effect converted PDMAEMA to PDMAEMA$^+$ with strong inhibition too for *E. coli* growth (entry 4 in Table 2). It is clear that the most important steps for antifungal and antibacterial effects were for pure temperature stimulus and pure CO_2 stimulus, respectively. Using both stimuli together is also effective against the two microbes, but it is not powerful like using the individual stimulus alone.

Table 2. The cytotoxicity effect of each stimulus on two selected microbial strains *E. coli* and *C. albicans* which symbolized by +: weak, ++: medium, +++: strong and ++++: very strong.

Stimuli Type	Antimicrobial activity on *E. coli (Bacteria)*	*C. albicans (Yeast)*
25 °C	NA	+
25 °C + CO_2	++++	++
45 °C	NA	++++
45 °C + CO_2	+++	+++

5. Conclusions

In this article, a temperature- and CO_2-sensitive delivery system composed of grafted copolymer capped MSN was explained. A poly(DMAEMA)-co-poly(MPS) shell on MSN was constructed via a facile one-step reaction (condensation & polymerization) and characterized successfully. The grafted copolymer showed both temperature- and CO_2-sensitive release properties for the antifungal anidulafungin drug, which then confirmed by killing *C. albicans* yeast, with low to moderate results (high in some cases). Most importantly, the PDMAEMA coating can kill *E. coli* bacteria effectively upon converting to its cationic form through CO_2 responses. This novel strategy of designing dual-responses via particles-coating followed by evaluating the biological activity can inspire the engineering of advanced bionanomaterials.

Acknowledgments

This work was supported by the National Natural Science Foundation of China (No. 21871069) and Open Project of Key Laboratory of Microsystems and Microstructures Manufacturing (2016KM003).

Notes

The authors declare no competing financial interest.

6. References

1. P. Zhou, L. Wang, G. Wu, Y. Zhou, M. Hegazy, X. Huang, *ChemistrySelect* **2017**, *2,* 6249–6253. **DOI:**10.1002/slct.201701339
2. G. Wu, X. Liu, P. Zhou, L. Wang, M. Hegazy, X. Huang, Y. Huang, *Mater. Sci. Eng. C* **2018**, *94,* 524–533. **DOI:**10.1016/j.msec.2018.09.061
3. N. Rahoui, M. Hegazy, B. Jiang, N. Taloub, Y. D. Huang, *Am. J. Anal. Chem.* **2018**, *9,* 273–285. **DOI:**10.4236/ajac.2018.95021
4. N. Rahoui, P. Zhou, N. Taloub, M. Hegazy, Y. D. Huang, *IOP Conf. Ser.: Mater. Sci. Eng.* **2018**, *389,* 012009. **DOI:**10.1088/1757-899X/389/1/012009
5. N. Taloub, L. Liu, N. Rahoui, M. Hegazy, Y. Huang, *Polym. Test.* **2019,** *75,* 344–349. **DOI:**10.1016/j.polymertesting.2019.02.016
6. N. Taloub, A. Henniche, L. Liu, J. Li, N. Rahoui, M. Hegazy, Y. Huang, *Comp. Part B: Eng.* **2019**, *163,* 260–271. **DOI:**10.1016/j.compositesb.2018.11.007
7. M. Hegazy, P. Zhou, G. Wu, L. Wang, N. Rahoui, N. Taloub, X. Huang, Y. Huang, *Polym. Chem.* **2017**, *8,* 5852–5864. **DOI:**10.1039/C7PY01179B
8. W. Fan, X. Tong, F. Farnia, B. Yu, Y. Zhao, *Chem. Mater.* **2017**, *29,* 5693–5701. **DOI:**10.1021/acs.chemmater.7b01656
9. X. Tang, X. Liang, L. Gao, X. Fan, Q. Zhou, *J. Polym. Sci. Part A: Polym. Chem.* **2010**, *48,* 2564–2570. **DOI:**10.1002/pola.24034

10. P. Zhou, S. Wu, X. Liu, M. Hegazy, G. Wu, X. Huang, *ACS Appl. Mater. Interfaces* **2018**, *10,* 38565–38573. **DOI:**10.1021/acsami.8b11216
11. G. Wu, X. Liu, P. Zhou, Z. Xu, M. Hegazy, X. Huang, Y. Huang, *Mater. Sci. Eng. C* **2019**, *99,* 1153–1163. **DOI:**10.1016/j.msec.2019.02.069
12. Y. Xue, H. Xiao, Y. Zhang, *Int. J. Mol. Sci.* **2015**, *16,* 3626–3655. **DOI:**10.3390/ijms16023626
13. S. El-Hamouly, M. Azab, M. Hegazy *et al.*, *Asian J. Chem.* **2012**, *24,* 176-180.
14. P. Zhou, S. Wu, M. Hegazy, H. Li, X. Xu, H. Lu, Xin Huang, *Mater. Sci. Eng. C* **2019**, *104,* 109914. **DOI:**10.1016/j.msec.2019.109914
15. M. Hegazy, N. Rahoui, A. A. Elyazed, D. E. Fouad, Xin Huang, Yudong Huang, *Polym. Korea* **2019**, *43,* 387–393. **DOI:**10.7317/pk.2019.43.3.387
16. N. Rahoui, B. Jiang, N. Taloub, M. Hegazy, Y. D. Huang, *J. Biomater. Sci., Polym. Ed.* **2018**, *29,* 1482–1497. **DOI:**10.1080/09205063.2018.1466470
17. N. Longkumer, K. Richa, R. Karmaker, V. Kuotsu, A. Supong, L. Jamir, P. Bharali, U. B. Sinha, *Acta Chim. Slov.* **2019**, *66,* 276–283. **DOI:**10.17344/acsi.2018.4580
18. M. Hegazy, S. El-Hamouly, M. Azab, S. Beshir, M. Zayed, *Polym. Sci. Ser. B* **2014**, *56,* 182–190. **DOI:**10.1134/S1560090414020067
19. A. Vasile, M. Ignat, M. F. Zaltariov, L. Sacarescu, I. Stoleriu, D. Draganescu, M. Dumitras, Lacramioara Ochiuz, *Acta Chim. Slov.* **2018**, *65,* 97–107. **DOI:**10.17344/acsi.2017.3641
20. N. Rahoui, B. Jiang, M. Hegazy, N. Taloub, Y. Wang, M. Yu, Y. D. Huang, *Colloids Surf. B: Biointerf.* **2018**, *171,* 176–185. **DOI:**10.1016/j.colsurfb.2018.07.015
21. M. Hegazy, P. Zhou, N. Rahoui, G. Wu, N. Taloub, Y. Lin, X. Huang, Y. Huang, *Colloids Surf. A: Physicochem. Eng. Asp.* **2019**, 581, 123797. **DOI:**10.1016/j.colsurfa.2019.123797
22. Z. Dong, J. Mao, D. Wang, M. Yang, X. Ji, *Langmuir* **2015**, *31,* 8930–8939. **DOI:**10.1021/acs.langmuir.5b02159
23. L. Ma, R. Liu, J. Tan, D. Wang, X. Jin, H. Kang, M. Wu, Y. Huang, *Langmuir* **2010**, *26(11),* 8697–8703. **DOI:**10.1021/la904431z
24. F. A. Plamper, M. Ruppel, A. Schmalz, O. Borisov, M. Ballauff, A. H. E. Muller, *Macromolecules* **2007**, *40,* 8361. **DOI:**10.1021/ma071203b
25. H. Che, M. Huo, L. Peng, Q. Ye, J. Guo, K. Wang, Y. Wei, J. Yuan, *Polym. Chem.* **2015**, *6,* 2319–2326. **DOI:**10.1039/C4PY01800A
26. H. Zou, W. Yuan, *Polym. Chem.* **2015**, *6,* 2457–2465. **DOI:**10.1039/C5PY00024F
27. B. Wang, Q. Xu, Z. Ye, H. Liu, Q. Lin, K. Nan, Y. Li, Y. Wang, L. Qi, H. Chen, *ACS Appl. Mater. Interfaces* **2016**, *8,* 27207–27217. **DOI:**10.1021/acsami.6b08893

Povzetek

Anorganske strukture funkcionalizirane s polimeri imajo pomembno vlogo na različnih bioloških področjih. V tej raziskavi smo z enostopenjsko reakcijo sintetizirali dvojno odziven nanomaterial, pripravljen iz mezoporozne silike na katero smo graftirali dva okoljsko-odzivna polimera: poli (3-metakriloksipropiltrimetoksilan) "PMPS" in poli(N,N-dimetilaminoetil metakrilat) "PDMAEMA". Pripravljen material smo karakterizirali z BET in BJH tehnikami, da smo določili velikost por, volumen por in specifično površino. PDMAEMA je deloval kot aktivno stikalo, ki je določalo nalaganje oziroma in-vitro sproščanje protiglivičnega zdravila adsorbiranega v mezoporah materiala, glede na spremembe v temperature oziroma CO_2 koncentracije okolice. Če smo sintetiziran material izpostavili CO_2 atmosferi za nekaj minut, se je s tehniko difuzije na disku pokazal obetajoč bakteriocidni učinek. V splošnem smo pokazali pozitiven učinek proti nekaterim bakterijskim sevom in glivam kar nakazuje možnost, da bi lahko sintetizirani delci pripomogli k načrtovanju bolj učinkovitih protiglivičnih in protibakterijskih učinkovin za farmacevtske aplikacije.

Except when otherwise noted, articles in this journal are published under the terms and conditions of the Creative Commons Attribution 4.0 International License

Scientific paper

Oxidized Carbon Nanohorns as Novel Sensing Layer for Resistive Humidity Sensor

Bogdan Catalin Serban,[1,*] Octavian Buiu,[1] Nicolae Dumbravescu,[1] Cornel Cobianu,[1] Viorel Avramescu,[1] Mihai Brezeanu,[2] Marius Bumbac[3,4] and Cristina Mihaela Nicolescu[4]

[1]*National Institute for Research and Development in Microtechnologies, IMT-Bucharest, 126 A Str Erou Iancu Nicolae, 077190, Voluntari, Ilfov, Romania*

[2]*University Politehnica of Bucharest, Romania, Faculty of Electronics, Telecommunications and IT, 313 Splaiul Independentei, Sector 6, 060042, Bucharest, Romania*

[3]*Valahia University of Targoviste, Faculty of Sciences and Arts, Sciences and Advanced Technologies Department, 2 Bd. Carol I, 130024, Targoviste, Dambovita, Romania*

[4]*Valahia University of Targoviste, Institute of Multidisciplinary Research for Science Technology, 2 Bd. Carol I, 130024, Targoviste, Dambovita Romania*

** Corresponding author: E-mail: bogdan.serban@imt.ro Tel: +40 724284128*

Received: 07-16-2019

Abstract

The paper reports the relative humidity (RH) sensing response of a resistive sensor employing oxidized carbon nanohorns – based sensing layer. The sensing layer is deposited on an interdigitated (IDT) structure, comprising a Si substrate, a SiO_2 layer, and IDT electrodes. The structure exhibits good RH sensitivity when varying RH from 0% up to 90%, either in humid nitrogen or in a humid air environment. The conductivity of the sensing layer decreases, while the RH level increases. During the interaction with the water molecules (acting as electron donors), the number of holes will decrease and oxidized single-walled carbon nanohorns (SWCNHs), considered normally *p*-type semiconductor, will become more resistive. The sensing mechanism is explained in terms of the Hard Soft Acid Base (HSAB) paradigm, building on the fact that water molecules are hard bases, while oxidized carbon nanohorns can be virtually assimilated with hard acids.

Keywords: Humidity sensor; oxidized carbon nanohorns; HSAB principle

1. Introduction

Relative humidity (RH) sensors have received increasing attention in the last decades due to their high importance in various areas of environmental control, in both domestic and industrial applications:[1,2] control of the living environment in buildings, textile and paper industry, food processing, medical field (respirators, incubators, sterilizers), automotive industry (oil humidity control), pharmaceutical processing (quality control of drugs), electronics, meteorology, agriculture, chemical industry (dryers, chemical gas purification, and furnaces), etc. Since RH monitoring is required in fields with various environmental conditions, different types of humidity sensors based on a variety of sensing principles were reported in literature.[3] Besides ceramic, polymers, polyelectrolytes and semiconducting metal oxides, nanocarbonic materials[4–6] were also widely used as sensing layers in RH sensors.

Single-walled carbon nanohorns (SWCNHs), consisting of horn-shaped sheath aggregate of graphene sheets, were first reported by Iijima in 1998.[7] These carbon nanostructures exhibit outstanding properties, such as high conductivity, high dispersibility, large specific surface area, versatile synthesis process (no metal catalyst is involved in their synthesis), availability of high – purity samples, etc.[8] Thanks to these remarkable features, SWCNHs

have been widely investigated for different applications, such as catalyst support[9] or catalyst in the design of fuel cells,[10] gas storage media,[11] drug carrier for controlled release,[12] etc.

However, little information about the sensing capabilities of SWCNHs and their derivatives is available. Sano et al fabricated resistive sensor for ammonia detection at room temperature using SWCNHs as a sensing layer and it was demonstrated that the adsorption of NH_3 increases the resistance of the carbonaceous sensing layer.[13]

This study presents for the first time, to our knowledge, the RH sensing response of an oxidized SWCNHs-based sensing layer employed as a resistive sensor.

1. 1. Experimental

The testing chamber employed for this study accommodated two RH detectors: an oxidized SWCNHs-based sensing structure (depicted as DUT – Device Under Test in Figure 1) and a commercially available Sensirion® *RH* sensor. The latter was used for double-checking the RH value indicated by the mass flow controller (MFC)-system. By placing the RH detectors close to each other and to the gas inlet, the two devices were exposed to the same amount of gas flow (in order to provide identical experimental conditions, leading to reliable results). The oxidized SWCNHs (depicted in Figure 2), powder or crystals, 0% metallic compounds, 10% graphite, diameter 2–5 nm (TEM), specific surface area 1300–1400 m^2/g (BET), were purchased from Sigma Aldrich.[14] A Keithley 6620 current source was used, ensuring a current variation between 0.01–0.09 A; data was collected and analysed through a Picolog.

For obtaining the SWCNHs-based sensing layer, the following synthesis route was followed:

(i) 0.5 g of oxidized SWCNHs were dispersed in 25 mL deionized water and subjected to magnetic stirring for 14400 seconds at room temperature.

(ii) the resulted dispersion was deposited by the "drop casting" method on the sensing structure described below (after previously masking the contact area).

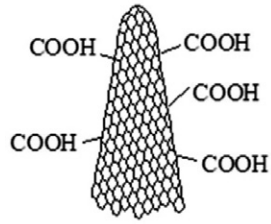

Figure 2. The structure of oxidized SWCNHs.

(iii) the sensing layer was subjected to heat treatment at 150° C, for 3600 seconds, under vacuum.

The sensing structure is an interdigitated (IDT) structure, manufactured on a Si substrate (470 μm thickness), covered by a SiO_2 layer (1 μm thickness) (Figure 3). The metal stripes of IDT comprise Cr (10 nm thickness) and Au (100 nm thickness). The width of the digit is approximately 10 microns, with a 0.6 mm separation between digits and the bus-bar. In order to avoid increasing the resistance due to the swelling effect, no hydrophilic

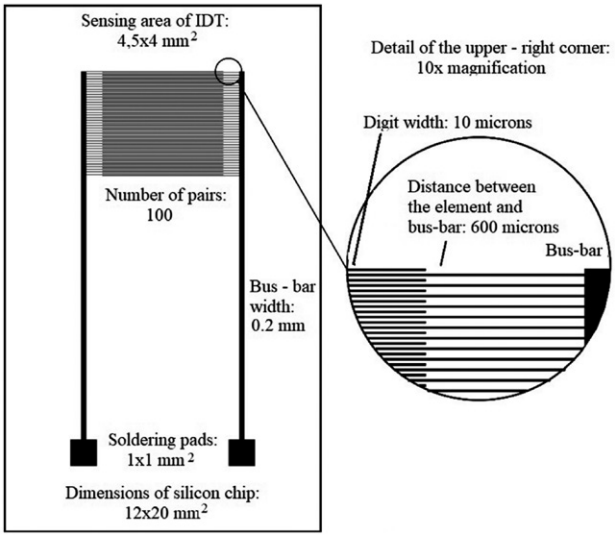

Figure 3. The metal stripes of IDT (Interdigitated structure)

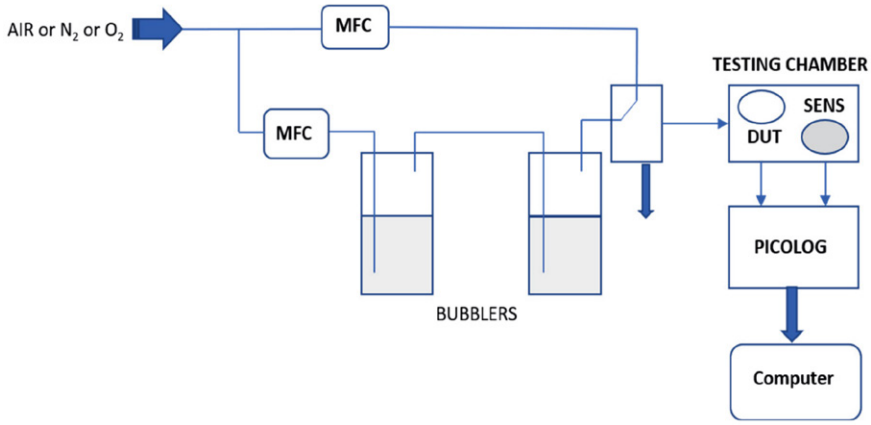

Figure 1. Experimental set-up employed for RH measurements.

polymer was employed in the composition of the sensing layer .[15,16]

The oxidized SWCNHs were chosen for RH sensing due to their outstanding properties: uniform size, high purity, no metallic compounds, high surface area and high dispersibility in water and organic solvents such as ethanol, and isopropyl alcohol.

2. Results and Discussion

The Raman spectrum of the oxidized SWCNHs samples (as purchased) measured at room conditions in two points of the surface are depicted in Figure 4. The measurements were made using a Horiba Jobin Yvone HR800 Raman Instrument, with incident light at 532 nm and using a power of 45.8 mW. The spectrum exhibits D (~1315 cm^{-1}), G (~1590 cm^{-1}) and 2D (~2616 cm^{-1}) modes, which are characteristic for sp^2 defected carbon nanomaterials. The G mode corresponds to tangential atomic vibrations of the graphite mesh, while the D mode reveals defect carbon states different from the graphite mesh. Two types of topological distorsions are responsible for the D band origination in oxidized carbon nanohorns Raman spectrum: pentagons to generate the characteristic conical-like architecture and layer folding.[17,18] Moreover, oxidation partially affects the sample and increases defectiveness.[19] Comparing the Raman spectra of oxidized SWNHs, pristine SWNHs and SWNTs, we noticed that oxidized SWNHs exhibit a D band with higher intensity which is in agreement with the literature data,[20] while the characteristic 2D band varies with the ABAB stacking of graphene layers.[21]

The RH response of the sensor was investigated by applying a current between the two electrodes and measuring the voltage drop when varying the RH from 0% up

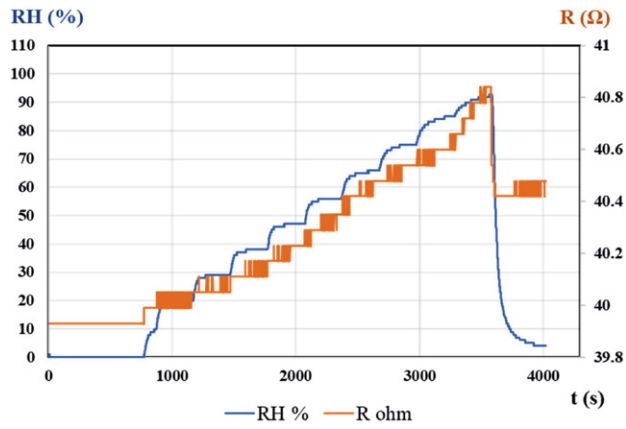

Figure 5. The RH response of the oxidized SWCNHs-based sensor in humid nitrogen (red curve) vs. the RH response of the Sensirion RH sensor (blue curve)

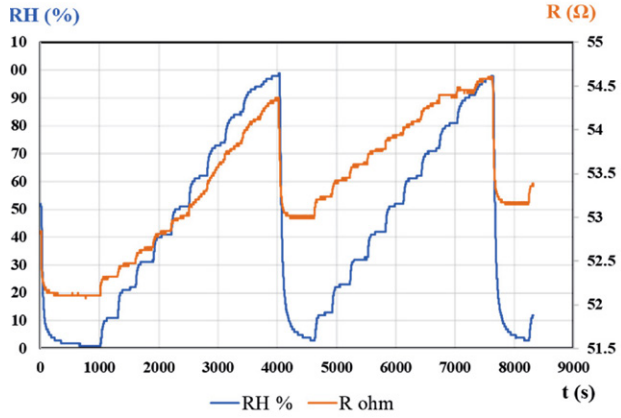

Figure 6. The RH response of the oxidized SWCNHs-based sensor in humid air (red curve) vs the RH response of the Sensirion RH sensor (blue curve)

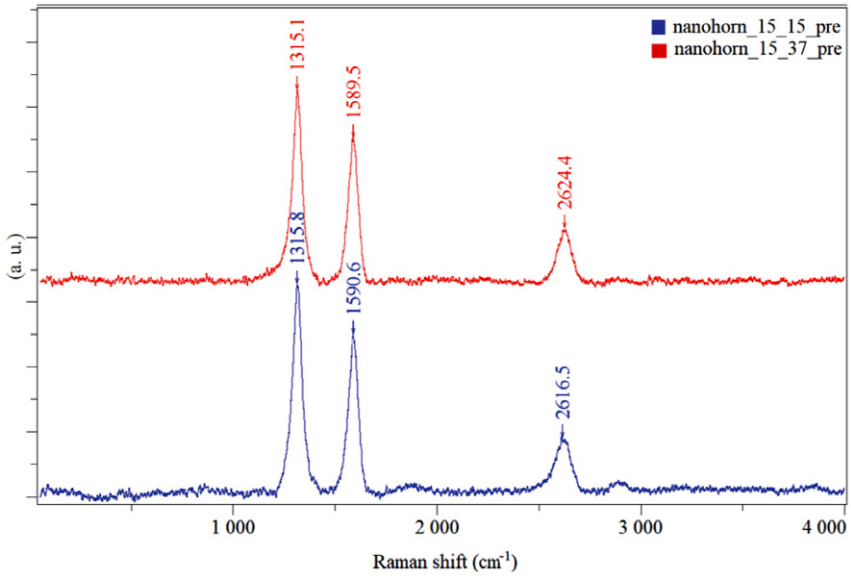

Figure 4. Raman spectra for oxidized carbon nanohorns.

to 90%, both in humid nitrogen environment (Figure 5) and in the humid air (Figure 6). The resistance of the carbonaceous sensing layer increases when RH increases.

The overall linearity of the oxidized SWCNHs-based sensor response – in both humid nitrogen and humid air, when varying RH from 10% to 90% – is very good, as shown in Figures 7 and 8.

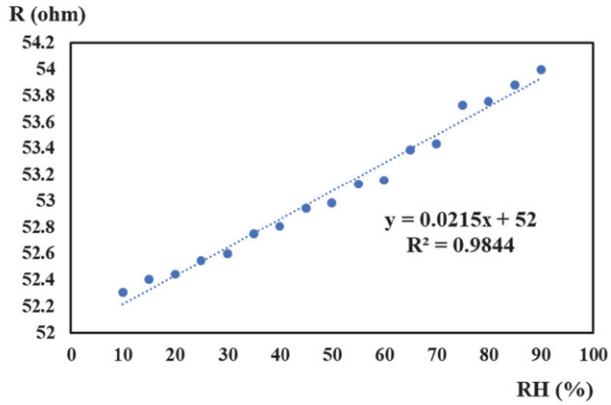

Figure 7. The transfer function of the sensor in humid air (RH = 10%–90%)

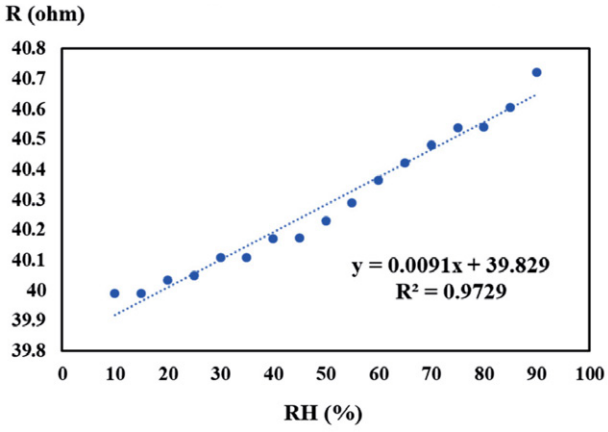

Figure 8. The transfer function of the sensor in humid nitrogen (RH = 10%–90%)w

In terms of linearity, the RH response in humid air is better than in humid nitrogen (R^2 = 0.9844 in humid air versus R^2 = 0.9729 for humid nitrogen). Sensitivity calculated when varying RH from 10% to 90%, as the slope of the trendline, is approximately two times higher in humid air compared to humid nitrogen (21 mΩ/RH unit compared to 9.1 mΩ/RH unit).

If the sensitivity (S) is evaluated by considering the variation of the sensor resistance with RH, i. e.:

$$S(x) = \frac{R_{10} - R_x}{RH_x - RH_{10}} \quad (1)$$

then it can be shown that S is, in general, increasing with RH; the lowest value of S (0.0133) is obtained at RH = 20%, while the maximum value (0.021) is reached for RH = 75%. These results are in agreement with the literatura data, comparable sensitivities being obtained using other type of carbonaceous materials as sensing layers.[22]

The response time (t_r) of the humidity sensor represents a key performance parameter; if R(t) is the response of the device in time, the t_r can be evaluated as:

$$t_r = t_{90} - t_{10} \quad (2)$$

where t_{90} and t_{10} represent the moments in time where the response R(t) is reaching 90% and 10%, respectively from the total variation of the sensor's resistance.[22] The response time of the oxidized carbon nanohorns based sensor in humid air is 3s, while in humid nitrogen is 8s. A comparison with the response times humidity sensors based on other nanocarbonic materials used as sensing layers are shown in Table 1.

In terms of drift, the performance of the novel sensor – in absolute terms – was worse that of the Sensirion® RH sensor. In the case of the novel sensor described here, the hysteresis could be attributed to the water molecules pen-

Table 1. Response times humidity sensors based on carbonaceous materials used as sensing layers

Type of sensing material	Response time(seconds)	Reference
Multi-Walled Carbon Nanotubes (MWCNTs)	120–180	[23]
Suspended Carbon Nanotubes	12	[24]
MWCNTs / Polyacrylic acid (1:4 w/w)	670	[25]
MWCNTs/Polyvinylpirrolidone	15	[26]
Single-Walled Carbon Nanotubes(SWCNTs)/ Polyvinyl alcohol (1:5 w/w)	40	[27]
3 wt% MWCNTs in a Polyimide	<5	[28]
Graphene oxide (GO)	2	[29]
GO	30 ms (fastest humidity sensor known at present)	[30]
GO/MoS_2	from 116 to 17 (depending on the specific composition)	[31]

etrating deep into the hydrophilic sensitive film at higher relative humidity. Due to the presence of hydrophilic carboxyl groups in oxidized SWCNHs and their propensity for forming hydrogen bonds with water molecules, the sensing layer could adsorb a significant number of molecules which eventually induce their condensation in the proximity of carboxylic groups.

Given the specifics of the sensing materials used, two distinct sensing mechanisms can be considered at first glance. The first one takes into account the dissociation of water. The adsorbed water molecules on oxidized carbon nanohorns surface may dissociate to H^+ and OH^- ions at the edges of carbonaceous nanomaterial, similar to what is observed for other nanocarbonic materials such as graphene oxide samples.[32] The protons generated by the water dissociation process may tunnel from one water molecule to another through hydrogen bonding, increasing the overall electrical conductivity of the sensitive film. The second mechanism takes into accounts the fact that oxidized SWCNHs are *p*-type semiconducting material. When interacting, the water molecules donate their electrons pairs, thus decreasing the number of the holes in oxidized SWCNHs. Therefore, the conductivity of the oxidized SWCNHs-based sensing layer decreases.

Without completely excluding the first mechanism, it is clear that the second effect dominates, and the tandem oxidized SWCNHs (acting as a *p*-type semiconductor) / water (electrons release) is the decisive factor for the overall decreasing resistance of the sensing layer.

Better sensitivity of oxidized SWCNHs in humid air in comparison with humid nitrogen is not surprising at all. This result is in agreement with those reported by Watts et al.[33] The vast majority of O_2 molecules present in the humid air are preferentially absorbed onto the polar carboxyl groups on the oxidized carbon nanohorns. The oxygen molecules are slightly polarizable (i.e. induced dipole) and can generate hydrogen bonding with the hydroxide (–OH) on the carboxyl group. Thus, the electron-withdrawing effect of the carboxyl group decreases and hence slightly decreases the hole carrier concentration on the oxidized SWCNHs, yielding to a minor overall increase in resistance for the oxidized SWCNHs. Even though oxygen molecules physisorption yields to an antithetical electrical response, the presence of carboxylic groups onto the backbone of SWCNHs is a key structural feature and formation of the hydrogen bond to each carboxyl group is a dominant factor.

2. 1. Extension of HSAB Concept to Oxidized Carbon Nanohorn- Based Humidity Sensor

Recently, the Hard-Soft Acid Base (HSAB) concept was used in gas sensing research and development.[34,35] Based on this theory, many sensitive films were synthesized and used for detecting different species, such as sulphur dioxide,[36] carbon dioxide,[37] nitrogen dioxide,[38] ammonia,[39] benzene.[40]

The HSAB concept operates with Lewis bases and acids; a molecular species donating a pair of electrons are classified as bases, while molecular entities accepting a pair of electrons are classified as acids. Based on different properties such as HOMO energy level, polarizability, the dimension of ionic radii, electronegativity, charge, Pearson categorizes Lewis' bases and acids into hard, borderline and soft.

The HSAB theory postulates that a hard base prefers to bind to a hard acid, whereas a soft base tends to interact with a soft acid. Correspondingly, a borderline base tends to bond to a borderline acid. From the HSAB theory point of view, water is classified as a hard base, while oxidized SWCNHs are hard acids.

Considering, on one hand, the electronic interaction between water molecules and hard acid species and, on the other hand, the conductive properties of carbon nanomaterials, the following question arises: can the HSAB concept explain the moisture sensing capabilities by oxidized SWCNHs-based sensing layers?

If one changes the paradigm and considers that, by analogy, the holes in various carbon nanomaterials are Lewis sites, then one can conclude that their exposure to hard bases (such as water) could change their electrical resistance. Thus, in the case of p-type nanocarbonic layers (such as oxidized SWCNHs), water molecules are adsorbed on their surface and donate electrons to them. As a consequence, the number of holes in oxidized SWCNHs decreases, a phenomenon which leads to increasing the difference between its Fermi level and its valence band. This determines an increase of the electrical resistance, which is exactly the result reported in this paper.

Several results reported in the literature are also in agreement with this statement. RH sensors based on multi-walled carbon nanotubes thin films,[41] CMOS ink-jet-printed graphene,[42] reduced graphene oxide/polymer nanocomposite film[43] are just a few examples.

3. Conclusions

A resistive sensor for RH monitoring employing oxidized SWCNHs as a novel sensing layer was fabricated. The sensing capability of the sensitive film was investigated when varying between 10% up to 90% in both humid nitrogen environment and humid air. It was demonstrated that the conductivity of the sensing layer decreases, while RH increases. The sensitivity of oxidized SWCNHs as sensing layer is approximately two times higher in humid air compared to humid nitrogen and this result was explained through the presence of the carboxylic groups. From the sensing mechanism point of view, interaction with the water molecules (which act as electron donors) decreases the number of holes and oxidized SWCNHs (*p*-type semiconductor) becomes more resistive. The sens-

ing mechanism was discussed, also, in terms of HSAB concept based on the fact that water molecules are hard bases and considering the holes as hard acids. Due to its excellent sensitivity and fast response time, oxidized SWCNHs is a promising material for resistive RH monitoring. It is clear that optimized degree of hydrophilicity (an "ideal" number of carboxylic groups onto the surface of SWCNHs) is a key factor in order to obtain a sensor with better sensitivity, high response time and low hysteresis.

These types of oxidized carbon nanohorns can be synthesized by heat treatment in air,[44] acid treatment,[45] and H_2O_2 treatment of pristine SWCNHs.[46] Last but not least, hydrophilization of carbon nanohorns, as -grown, can be performed using different treatment in plasma oxygen, plasma water by adjusting the exposure time and/or power source.

Regarding the future work, It is expected that composites of the oxidized carbon nanohorns with different polymers will increase the overall performance of the sensor. The interfacial heterojunctions between oxidized carbonaceous material and a hydrophilic polymer such as polyvinylpirrolidone (PVP) can strongly influence the sensitivity and response/recovery times of the sensors.

Acknowledgment

Authors from IMT Bucharest do acknowledge the financial support of Romanian Ministry for Research and Innovation through contracts 14N/2019 – MICRO-NANO-SIS PLUS and 42/2019 (PCCDI) – NANOCARBON+. Also, the support of Dr. Florin Comanescu in performing the Raman spectroscopy measurements is greatly acknowledged.

4. References

1. Z. Chen, C. Lu, C., *Sensors Letters*, **2005**, *3*, 274–295. **DOI:**10.1166/sl.2005.045
2. E. Traversa, *Sensors & Actuators B: Chemical*, **1995**, *23*, 135–156. **DOI:**10.1016/0925-4005(94)01268-M
3. C. Y. Lee, G. B. Lee, *Sensors Letters*, **2005**, *3*, 1–15.
4. Z. M. Rittersma, *Sensors & Actuators A: Physical*, **2002**, *96*, 196–210. **DOI:**10.1016/S0924-4247(01)00788-9
5. C. Cobianu, B. C. Serban, M. Mihaila, US Patent Number 8,479,560, date of patent July 9, **2013**.
6. H. Bi, K. Yin, X. Xie, J. Ji, S. Wan, L. Sun, L., M. S. Dresselhaus, *Sci. Rep*., **2013**, *3*, 2714.
7. S. Iijima, M. Yudasaka, R. Yamada, S. Bandow, K. Suenaga, F. Kokai, K. Takahashi, *Chem. Phys. Lett.*, **1999**, 309, 165–170. **DOI:**10.1016/S0009-2614(99)00642-9
8. N. Karousis, I. Suarez-Martinez, C. P. Ewels, N. Tagmatarchis, *Chem. Rev*., **2016**, *116*, 4850–4883. **DOI:**10.1021/acs.chemrev.5b00611
9. T. Yoshitake, Y. Shimakawa, S. Kuroshima, H. Kimura, T. Ichihashi, Y. Kubo, S. Iijima, *Physica B*, **2002**, *323*, 124–126. **DOI:**10.1016/S0921-4526(02)00871-2
10. L. Zhang, N. Zheng, A. Gao, C. Zhu, Z. Wang, Y. Wang, Y. Liu, *J. Power Sources*, **2012**, *220*, 449–454. **DOI:**10.1016/j.jpowsour.2012.08.009
11. E. Bekyarova, K. Murata, M. Yudasaka, D. Kasuya, S. Iijima, H. Tanaka, K. Kaneko, *J. Phys. Chem. B*, **2003**, *107,* 4681–4684. **DOI:**10.1021/jp0278263
12. J. Xu, M. Yudasaka, S. Kouraba, M. Sekido, Y. Yamamoto, S. Iijima, *Chem. Phys. Lett*., **2008**, *461*, 189–192. **DOI:**10.1016/j.cplett.2008.06.077
13. N. Sano, M. Kinugasa, F. Otsuki, J. Suehiro, *Adv. Powder Technol*., **2007**, *18*, 455–466. **DOI:**10.1163/156855207781389447
14. Sigma-Aldrich, Carbon nanohorns, oxidized, 804126, https://www.sigmaaldrich.com/catalog/product/aldrich/804126?lang=en&region=CZ, accessed June 2019.
15. W. Li, F. Xu, L. Sun, W. Liu, Y. Qiu, *Sensors & Actuators B: Chemical*, **2016**, *230*, 528 – 535. **DOI:**10.1016/j.snb.2016.02.108
16. T. Fei, K. Jiang, F. Jiang, R. Mu, T. Zhang, *J. of Appl. Polymer Sci.*, **2014,** *131*, 39726. **DOI:**10.1002/app.39726
17. T. Yamaguchi, S. Bandow and S. Iijima, *Chem. Phys. Lett.,* **2004**, 389, 181–185. **DOI:**10.1016/j.cplett.2004.03.068
18. A. C. Ferrari and J. Robertson, *Phys. Rev. B*, **2000**, 61, 14095–14107. **DOI:**10.1103/PhysRevB.61.14095
19. M. Peña-Álvarez, E del Corro, F. Langa, V.G. Baonza, M. Taravillo, *RSC Advances*, **2016,** *6*(55), 49543–49550. **DOI:**10.1039/C5RA27162B
20. C. T. Cioffi, *Functionalization and application of carbon nanohorns and carbon onions*, PhD thesis (**2008**). https://www.openstarts.units.it/handle/10077/2614
21. N. Larouche and B. L. Stansfield, *Carbon*, **2010**, 48, 620–629. **DOI:**10.1016/j.carbon.2009.10.002
22. J.M Tulliani, B. Inserra, and D. Ziegler. *Micromachines* 10.4, **2019**, 232. **DOI:**10.3390/mi10040232
23. O. K.Varghese, P. D. Kichambre, D. Gong, K. G. Ong, E. C. Dickey, C. A. Grimes, *Sensors & Actuators B: Chemical* **2001**, 81, 32–41. **DOI:**10.1016/S0925-4005(01)00923-6
24. S. Arunachalam, R. Izquierdo, F. Nabki, *Sensors* **2019**, 19(3), 680. **DOI:**10.3390/s19030680
25. J. Lee, D. Cho, Y. Jeong, *Solid-State Electronics* **2013**, 87, 80–84. **DOI:**10.1016/j.sse.2013.05.001
26. X. Pan , Q. Xue J. Zhang, Q. Guo , Y. Jin, W. Lu, X. Li , C. Ling. *Adv. Mater. Interfaces*. **2016**, 3, 1–7. **DOI:**10.1002/admi.201600153
27. G. Zhou , J. H. Byun , Y. Oh, B. -M. Jung, H. -J. Cha, D. G. Seong, M. K. Um, S. Hyun, T. W. Chou, *ACS Appl. Mater. Interfaces*. **2017**, 9, 4788–4797. **DOI:**10.1021/acsami.6b12448
28. Q. Y. Tang, Y. C. Chan , K. Zhang, *Sens. Actuators B Chem*. **2011**, 152, 99–106. **DOI:**10.1016/j.snb.2010.09.016
29. L. Guo ,H. -B. Jiang, R. -Q. Shao, Y. -L. Zhang, S. -Q. Xie,J. -N. Wang, X.-B. Li, F. Jiang, Q. -D. Chen, T. Zhang, *Carbon* **2012**, 50, 1667–1673. **DOI:**10.1016/j.carbon.2011.12.011
30. S. Borini, R. White, M. Astly, R. White, D. Wei, S. Haque, E. Spigone, N. Harris, *ACS Nano* **2013**, 12, 11166–11173. **DOI:**10.1021/nn404889b
31. S. Y. Park, J. E. Lee , Y. H. Kim, J. J.Kim , Y. -S. Shim , S. Y.

Kim , M. H. Lee, H. W. Jang, *Sensors & Actuators B: Chemical* **2018**, 258, 775–782. **DOI:**10.1016/j.snb.2017.11.176
32. H. Bi, K. Yin, X. Xie, J. Ji, S. Wan, L. Sun, M. S. Dresselhaus, *Scientific Reports*, 2013, 3, 2714.
33. P. C. P. Watts, N. Mureau, Z. Tang, Y. Miyajima, J. D. Carey, S. R. P. Silva, *Nanotechnology*, **2007**, *18*, 175701. **DOI:**10.1088/0957-4484/18/17/175701
34. R. G. Pearson, *J. Am. Chem. Soc*., **1963**, *85*, 3533–3539. **DOI:**10.1021/ja00905a001
35. R. G. Pearson, *J. Am. Chem. Soc*., **1988**, *110*, 7684–7690. **DOI:**10.1021/ja00231a017
36. B. C. Serban, C. P. Cobianu, M. N. Mihaila, V. G. Dumitru, U.S. Patent Number 8,609,427, date of patent December 17, **2013**.
37. B. C. Serban, A. K. Sarin Kumar, M. Brezeanu, C. P. Cobianu, O. Buiu, C. Bostan, N. Varachiu, S. Costea, *Romanian Journal of Inf. Sci. and Tech.*, **2011**, *14*, 222 –231.
38. B. C. Serban, C. P. Cobianu, M. N. Mihaila, V. G. Dumitru, O. Buiu, U.S. Patent Number 8,563,319, date of patent October 22, **2013**.
39. B. C. Serban, O. Buiu, C. P. Cobianu, M. Brezeanu, M. Bumbac, C. M. Nicolescu, *Acta Chim. Slov.*, **2018**, *65*, 1014 – 1021. **DOI:**10.17344/acsi.2018.4564
40. B. C. Serban, O. Buiu, M. Brezeanu, C. P. Cobianu, C. G. Bostan, C. Diaconu, US Patent Number 10,254,217, date of patent April 9, **2019**.
41. C. L. Cao, C. G. Hu, L. Fang, S. X. Wang, Y. S. Tian, and C. Y. Pan, *Journal of Nanomaterials* **2011** (2011): 5.
42. S. Santra, G. Hu, R. C. T. Howe, A. De Luca, S. Z Ali, F. Udrea, J. W. Gardner, S. K. Ray, P. K. Guha, T. Hasan, *Sci. Rep*., **2015**, *5*, 17374. **DOI:**10.1038/srep17374
43. D. Zhang, J. Tong, B. Xia, *Sensors & Actuators B: Chemical*, **2014**, *197*, 66–72. **DOI:**10.1016/j.snb.2014.02.078
44. J. Fan, M. Yudasaka, J. Miyawaki, K. Ajima, K. Murata, S. Iijima, *J. Phys. Chem. B* **2006**, *110*, 1587–1591. **DOI:**10.1021/jp0538870
45. R. Yuge, T. Ichihashi, Y. Shimakawa, Y. Kubo, M. Yudasaka, S. Iijima, *Adv. Mater.* **2004**, *16*, 1420. **DOI:**10.1002/adma.200400130
46. M. Zhang, M. Yudasaka, K. Ajima, J. Miyawaki, S. Iijima, *ACS Nano* **2007**, *1*, 265. **DOI:**10.1021/nn700130f

Povzetek

V prispevku predstavljamo odziv senzorja relativne vlažnosti, ki uporablja senzorsko plast na osnovi oksidiranih ogljikovih nanorogov (single-walled carbon nanohorns, SWCNH). Senzorska plast je nanesena na interdigitalno (IDT) strukturo, ki vsebuje substrat Si, plast SiO_2 in IDT elektrode. Senzor ima dobro občutljivost za merjenje relativne vlažnosti v območju od 0 % do 90 %, bodisi v vlažnem dušiku, bodisi v okolju vlažnega zraka. Prevodnost senzorske plasti se zmanjšuje, medtem ko se raven relativne vlažnosti povečuje. Med interakcijo z molekulami vode, ki delujejo kot donorji elektronov, se bo število odprtin zmanjšalo in upornost oksidiranih ogljikovih nanorogov, ki jih običajno uvrščamo med polprevodnike tipa p, se bo povečala. Mehanizem zaznavanja smo razložili s teorijo trdih in mehkih kislin in baz (HSAB), ki temelji na dejstvu, da so molekule vode trde baze, oksidirane ogljikove nanorogove pa lahko ponazorimo s trdimi kislinami.

Except when otherwise noted, articles in this journal are published under the terms and conditions of the Creative Commons Attribution 4.0 International License

DOI: 10.17344/acsi.2019.5466 *Acta Chim. Slov.* **2020,** *67,* 476–486
creative commons

Scientific paper

Immobilized VO–Schiff Base Complex on Modified Graphene Oxide Nanosheets as an Efficient and Recyclable Heterogeneous Catalyst in Deep Desulfurization of Model Oil

Maryam Abdi,[1] Abdollah Fallah Shojaei,[2,*] Mohammad Ghadermazi[1] and Zeinab Moradi-Shoeili[2]

[1] *Department of Chemistry, Faculty of Science, University of Kurdistan, Sanandaj, Iran*

[2] *Department of Chemistry, Faculty of Sciences, University of Guilan, P.O. Box 41335–1914, Rasht, Iran.*

* *Corresponding author: E-mail: a.f.shojaie@guilan.ac.ir, shoja47@gmail.com*

Received: 08-04-2019

Abstract

New heterogeneous catalyst was synthesized via covalent anchoring of oxovanadium(IV) complex of 5,5'-dibromo-bis(salicyledene)diethylenetriamine (VO[5-Br(Saldien)]) on the surface of chloro-modified graphene oxide (GO@CTS). The structure of the catalyst was investigated using different characterization techniques such as XRD, SEM, EDX, FT-IR, TG, DTA and ICP-AES analyses. The synthesized heterogeneous oxovanadium(IV) was an efficient catalyst for high yield and selective oxidation desulfurization (ODS) of dibenzothiophene (DBT) as a model oil using H_2O_2 as oxidant and formic acid as a promoter. The effects of the catalyst mass, reaction temperature and time, formic acid/H_2O_2 ratio and molar ratio of H_2O_2 to the total amount of sulfur (O/S) on oxidation desulfurization activity were investigated. Moreover, the prepared catalyst can be easily separated from the reaction mixture and reused six times without a significant loss of catalytic activity and selectivity.

Keywords: Vanadium; desulfurization; graphene oxide; heterogeneous catalyst.

1. Introduction

Growing energy demand will be accompanied by growing greenhouse gas (GHG) emissions e.g. CO_2 with an impact on climate change and non-GHG emissions e.g. NO_x, SO_2, volatile organic compounds and particulate materials with an impact on local air quality.[1] In addition to environmental pollution, these emissions have been threatening human health.[2] The combustion of transportation fuels contaminated by sulfur compounds results in the emission of SO_x, which is responsible for the photochemical smog, acid rain, corrosion, etc. And also contributes to global warming.[3] These concerns have driven the need to reduce sulfur emissions to the atmosphere through the regulation of sulfur in transportation fuels.[4] Thus desulfurization of fuels has attracted much attention due to the environmental pressures to reduce the sulfur content in recent years.[5] Petroleum fractions contain considerable amounts of benzothiophene (BT), dibenzothiophene (DBT), and their alkyl-substituted derivatives. These polyaromatic sulfur molecules are low reactive toward the hydrogenolysis of the C–S bond and, as a consequence, are difficult to remove by conventional hydrodesulfurization reactions (HDS).[6,7] To overcome the disadvantages of HDS, various methods, such as adsorptive desulfurization,[8] extractive desulfurization, oxidative desulfurization (ODS)[9–11] and biodesulfurization[12] were investigated to produce ultra clean fuels. Among these techniques, ODS is regarded as a promising method to obtain low levels of sulfur in fuel oils.[13–17] The ODS processes usually include two successive steps: oxidation of organosulfur compounds to less harmful polar derivatives (sulfoxides and sulfones) and elimination of these compounds by extraction into a polar solvent or onto a sorbent.[18,19] Homogeneous and heterogeneous catalysis systems using molecular oxygen, hydrogen peroxide, *tert*-butyl hydroperoxide, and peroxyorganic acids as oxidants are capable of desulfurizing diesel fuels under mild reaction condi-

tions (50–90 °C).[16,18–22] However, the commercialization of these processes will need optimization of the oxidant, the catalyst, and the method for isolating the oxidized products of heterocyclic sulfur compounds from the petroleum fractions.[22] The oxidation of organosulfur compounds occurs in the presence of metal catalysts, mostly transition metals, in high oxidation states, such as Mo (IV), Ti (IV), V (V),W (IV) and Re.[23–25]Vanadium, among transition metals, is relatively cheap and readily available. Moreover, due to the interesting chemical properties of vanadium such as selectivity, reactivity and stereoselectivity, oxidovanadium complexes are of special interest as a catalyst in oxidation of several organic compounds.[20] A. Coletti et al. reported the application of oxovanadium(V) species, ligated with substituted salicylaldehyde Schiff bases and o-phenylendiamine or 1,2-ethanediamine, as catalysts for oxidation of sulfides in the presence of H_2O_2.[21] However, because of their homogeneous nature, these catalysts are difficult to separate from the reaction mixture and thus, cannot be recycled. Covalent attachment is known as the most effective method for anchoring the homogeneous metal complexes on the surface of various supports. Maurya et al. reported two oxidovanadium(IV) and dioxidovanadium(V) complexes grafted on polymer support for the oxidation of thiophene derivatives present in model fuel diesel. Results showed that the immobilization of homogeneous complexes onto the polystyrene support enhances their stability and catalytic reactions are heterogeneous in nature.[26] Ogunlaja and coworkers reported a continuous flow system for oxidative desulfurization of refractory organosulfur compounds by two oxovanadium(IV) polymer supported catalysts.[23] Graphene oxide (GO) has attracted considerable attention as one of the most promising supports to immobilize homogeneous vanadium complexes.[27] Mungse et al. reported the covalent anchoring of an oxovanadium Schiff base complex onto GO nanosheets for the oxidation of various alcohols, diols, and α-hydroxyketones to carbonyl compounds using *tert*-butylhydroperoxide (TBHP) as an oxidant.[28] Verma et al. reported that oxovanadium Schiff base supported graphene oxide exhibited a higher catalytic efficiency than the homogeneous vanadyl acetylacetonate for epoxidation of fatty acids and esters.[29] Moreover, Hajjar and coworkers reported the application of nano-graphene sheet supported Co and Mo species in the HDS process. They clearly showed that Co–Mo/graphene catalysts were more active than the industrial Co–Mo/γ-Al_2O_3 catalysts.[30] In the present work, the synthesis of heterogeneous catalyst by immobilization of VO[5-Br(Saldien)] complex on the modified graphene oxide as support (GO@5-Br(Saldien)VO) is described. In addition, this report includes the results of the investigation of the catalytic performance of GO@5-Br(Saldien)VO in ODS reactions. The heterogeneous catalyst proved to be efficient for the selective oxidation of DBT with H_2O_2 promoted by formic acid. The effects of the catalyst mass, reaction temperature and time, formic acid/H_2O_2 ratio, and the O/S ratio (molar ratio of H_2O_2 to the total amount of sulfur in an initial solution of DBT) on ODS activity was investigated. Moreover, the prepared catalyst was successfully reused for six runs without a significant loss in catalytic activity.

2. Experimental

2. 1. Materials and Characterization

All reagents and materials used in this work were obtained from Fluka, Aldrich or Merck and were used without further purification. All solvents were reagent grade and dried and distilled before use, according to the standard procedures. X-ray diffraction (XRD) patterns were recorded on a MPD diffractometer of X'pert with Cu–Kα radiation (l = 1.5418 Å) under the conditions of 40 kV and 30 mA. SEM images were recorded using FESEM-TESCAN MIRA3. Fourier transforms infrared (FT-IR) spectra of KBr disks were measured on a VERTEX70 model BRUKER FT-IR spectrophotometer. Thermogravimetric analysis (TGA) was carried out under N_2 flow while gradually increasing the temperature with a rate of 10 °C min^{-1}, using a STA PT-1000 LINSEIS. The elemental analysis of the samples was done by energy dispersive X-ray spectroscopy (EDX, TSCAN). The progress of model reactions was recorded on a CARY 100 Bio VARIAN UV–vis spectrophotometer. For determining vanadium loading in the synthesized catalyst, ICP-AES analysis was carried out by an inductively coupled plasma atomic emission spectroscopy (ICP-AES) on a Perkin-Elmer AA-300 spectrophotometer.

2. 2. Synthesis of 5,5`-Br-Bissalicylidendiethyl Enetriamine Ligand 5-Br(Saldien)

In a typical procedure, one molecular equivalent of diethylenetriamine (dien) (0.1 mL, 1 mmol) was added to two molecular equivalents of 5-bromosalicylaldehyde (0.402 g, 2 mmol) dissolved in absolute ethanol at room temperature. After stirring for 15 min, the volume of the solution was reduced until only an oil remained which was identified via FT-IR spectroscopy.[31]

2. 3. Synthesis of Chloro-Functionalized Graphene Oxide (GO@CTS)

In a typical procedure, 250 mL dry toluene was added into a two-necked flask and then 1.0 g GO was dispersed using ultrasound. Afterward, 3 mL 3-chlorooropropyltrimethoxysilane (CTS) diluted in 20 mL dry toluene was added to the stirred solution. The reaction mixture was refluxed at 110 °C under N_2 atmosphere for 48 h. The mixture was filtered and washed with a large amount of toluene and ethanol to remove excess CTS and then dried in the oven at 70 °C.[32]

2. 4. Immobilization of VO[5-Br(Saldien)] Complex onto the GO@CTS

To a suspension of freshly dried GO@CTS (2 g) in dry toluene (40 mL), a solution of 5-Br(saldien) ligand (1 g) in dry toluene (10 mL) and triethylamine (0.5 mL) was added and the resulting solution was refluxed for 12 h. After this step, the resulted product was separated and then washed with anhydrous toluene several times to remove the unreacted 5-Br(saldien) ligand adsorbed on the surface of GO@CTS and dried under vacuum at 70 °C. Then, 5-Br(saldien)-functionalized GO@CTS (1 g) was dispersed in 250 mL dry ethanol by using ultrasonication. In the subsequent step, $VO(acac)_2$ (0.1 g) was added to the stirring mixture. This mixture was refluxed for 3 h. The final product was filtered and washed with dry ethanol and dried under vacuum overnight.

2. 5. Catalytic Activity Tests (Oxidation of DBT)

The oxidative desulfurization experiments were optimized using the model oil, 500 ppm DBT in n-heptane. The desired amounts of catalyst and 5mL acetonitrile were added into 5mL model oil containing 500 ppm DBT in a two-necked flask, equipped with a condenser, agitator and thermometer. Prior to the catalytic reaction the mixture was magnetic stirring at a constant speed for 30 min to ensure an adsorption-desorption equilibration of the system. Afterward, a specific amount of H_2O_2 was added to the system. The system was continuously stirred at a constant temperature using a water bath at atmospheric pressure.

3. Results and Discussion

The schematic representation for the synthesis of heterogeneous GO@5-Br(Saldien)VO complex is shown in Fig.1. Heterogeneous catalyst was successfully obtained in a three-step procedure. The first step involves the functionalization GO by 3-chloropropyltrimethoxysilane. Then the ligand was attached to GO@CTS using nucleophilic displacement of cholorine by the basic amino group of the ligand. Finally, $VO(acac)_2$ was added to the stirring mixture of 5-Brsaldien functionalized GO@CTS which affords GO@5-Br(Saldien)VO.

3. 1. Spectroscopic Characterization of GO@5-Br(Saldien)VO Heterogeneous Catalyst

Fig. 2 shows the FT-IR spectra of the GO, GO@CTS, GO@5-Br(Saldien) and covalently attached salen complex catalyst, GO@5-Br(Saldien)VO. Characteristic bands of

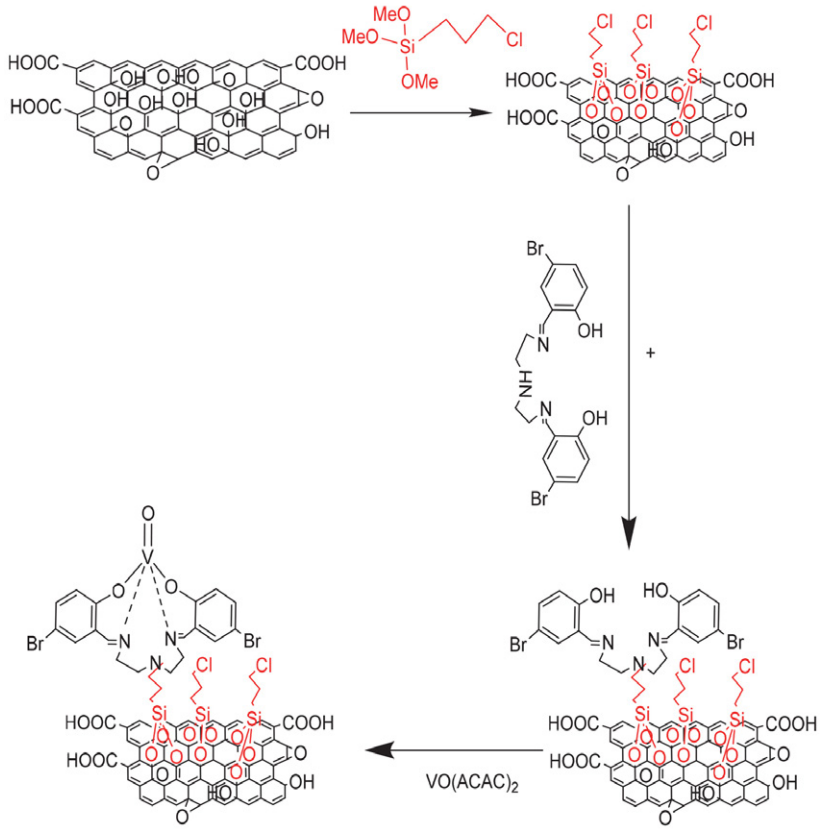

Fig. 1. Schematic representation for the synthesis of GO@5-Br(Saldien)VO heterogeneous catalyst.

the pure GO support (Fig. 2a) appeared in a. 3421, 1723, 1623, 1033 cm^{-1} corresponding to the stretching modes of O–H, C=O, C=C, and C–O–C moieties, respectively.[33] The presence of numerous hydroxyl groups on the GO provides active sites for the bonding between GO sheets and CTS. The FT-IR spectrum of GO@CTS has been exhibited in Fig. 2b. The absorption peak at 1032 cm^{-1} represents the Si–O–C stretching vibration and the vibrational bands at 2926 cm^{-1} and 2854 cm^{-1} are attributed to CH_2 groups. Also, the presence of a peak at 695 cm^{-1} represents the C–Cl bond stretching, which indicated the successful coating of CTS onto the graphene oxide through chemical bonding.[34] Comparing the FT-IR spectra of the covalently attached GO@5-Br(Saldien)VO on the choloro-modified graphene oxide with that of the graphene oxide and GO@CTS revealed some new weak peaks in the range of 1600–1200 cm^{-1} due to C–O, C–N and aromatic ring vibrations. The FT-IR spectrum of GO@5-Br(Saldien) shows a new peak at around 1611 cm^{-1}, attributed to C=N stretching due to the Schiff base indicating that the salen ligand was successfully immobilized on GO. The sharp band at 1611 cm^{-1} (Fig. 2c) which was assigned to γ(C=N) has shifted to the 1605 cm^{-1} range (Fig. 2d) in the spectra of the complex. This observation indicates the coordination of nitrogen to the vanadium, which is in agreement with the literature values.[35] Furthermore ICP-AES analysis of the covalent attachment of the oxovanadium(IV) complex on modified graphene oxide also indicates the successful introduction of the metal ion. The loading of vanadium in the synthesized catalyst was found to be 0.39 mmol g^{-1}.

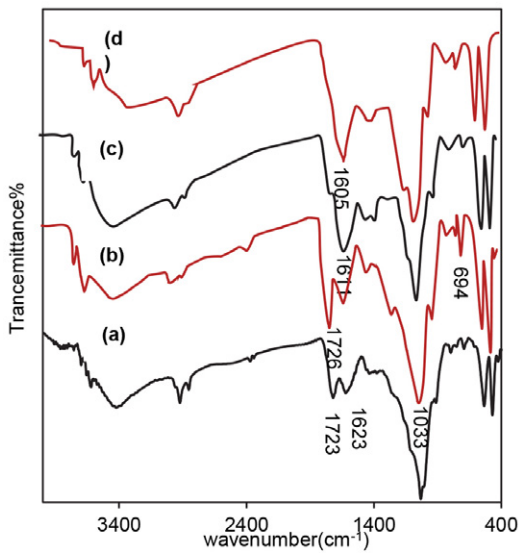

Fig. 2. FT-IR spectra of: (a) GO; (b) GO@CTS; (c) GO@5-Br(Saldien) (d) GO@5-Br(Saldien)VO.

Fig. 3 shows the XRD patterns of GO and GO@5-Br(Saldien)VO. The peak at around 11.8° can be attributed to the (001) reflection of graphene oxide, indicating the oxygen species inserted into the graphitic layers. After the surface covalent functionalization of GO with CTS, coupling process and final production of the GO@5-Br(Saldien)VO catalyst, the diffraction peak at 2θ = 11.8° was disappeared compared to GO and another broad diffraction peak of graphite at 2θ = 23.77° (002) appeared, indicating that the major oxygen containing groups of GO have been successfully functionalized with oxovanadium complex.[29]

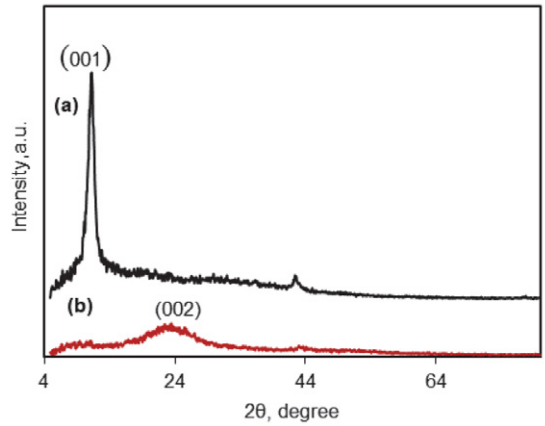

Fig. 3. XRD pattern of (a) GO (b) GO@5-Br(Saldien)VO.

The SEM images of GO and GO@5-Br(Saldien)VO are shown in Fig. 4a and 4b, respectively. It can be seen that GO and GO@5-Br(Saldien)VO have a similar morphology composed of two-dimensional nanosheets with a wavelike flexible and ultrathin sheet structure.[36] To provide further information about the elemental composition of the GO@5-Br(Saldien)VO, the product was characterized by energy dispersive X-Ray (EDX) analysis (Fig. 5). The results clearly demonstrated the presence of vanadium in the synthesized heterogeneous catalyst, GO@5-Br(Saldien)VO.

The TG/DTA curves of GO and GO@5-Br(Saldien)VO are depicted in Fig. 6. The TG curve corresponding to the graphene oxide exhibited a typical three-step weight loss processes in the range of 31 to 700 °C under N_2 flow (Fig. 6a), which can be assigned to the loss of physically adsorbed water and the decomposition of oxygen carrying functionalities, respectively.[28] In a first endothermic stage, GO started to decompose below 150 °C which can be ascribed by the removal of adsorbed water. The GO showed major weight losses within the temperature range from 150 °C to 250 °C which can be attributed to CO, CO_2, and steam release from the most labile functional groups.[37] Further increase of the temperature leads to weight loss for material, which ascribed to the bulk pyrolysis of the carbon skeleton.[38] For GO@5-Br(Saldien)VO catalyst, the first weight loss at temperatures below 250 °C is due to the loss of physically adsorbed water and the decomposition of unused oxygen carrying functionalities, which have not interacted with CTS.[28] The weight loss within the tempera-

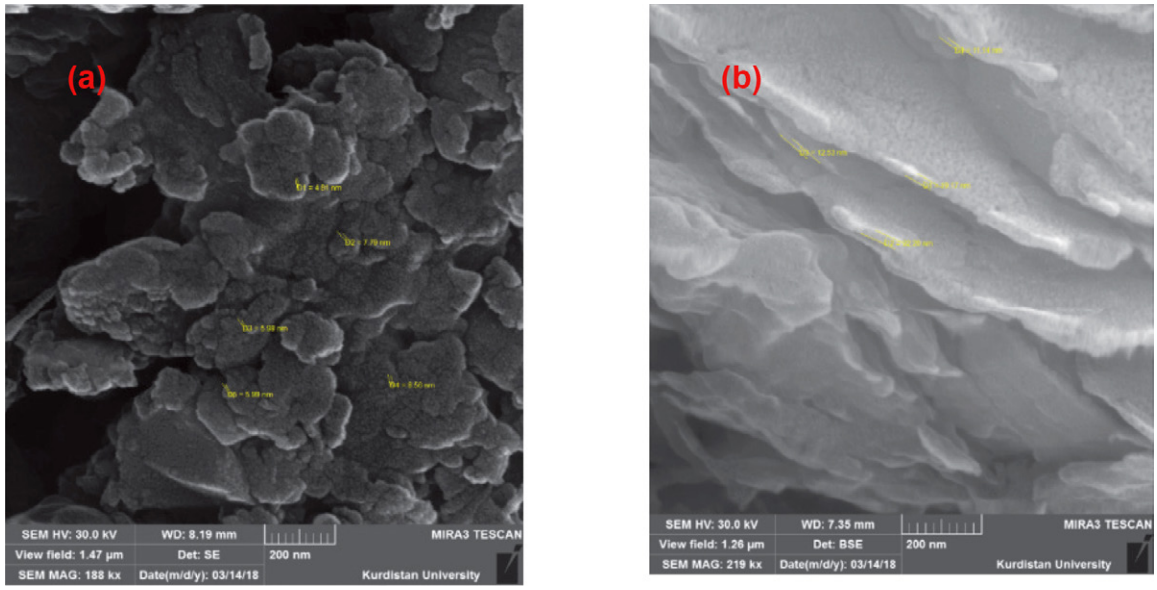

Fig. 4. SEM image of (a) GO, (b) GO@5-Br(Saldien)VO

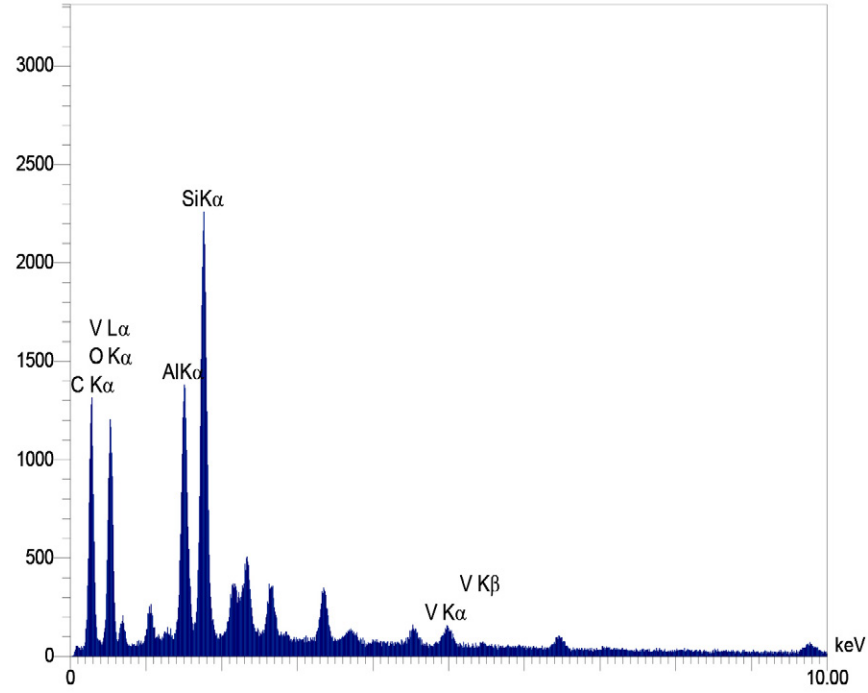

Fig. 5. EDX of GO@5-Br(Saldien)VO.

ture range of 250 to 450 °C is due to undigested oxygen carrying functionalities. Weight loss between 450–670 °C can probably be attributed to the decomposition of the Schiff base ligand.[39]

3. 2. Evaluation of Catalytic Activity

The progress of the model reactions was monitored by UV-vis spectroscopy. The absorption at 286 nm was used to monitor the DBT concentration in the n-heptane phase.[40] Fig. 7 shows the variations intensity of the UV–vis bands corresponding to DBT concentration, using GO@(5-Br, Saldien)VO as catalyst and H_2O_2 as oxidant under acidic condition. DBT concentration gradually decreases as the reaction time increases. Samples (100 µL) were taken out from the n-heptane phase every 5 minutes during the first half hour of the experiment and every ten minutes afterward. In a typical analysis, 100 µL of samples were di-

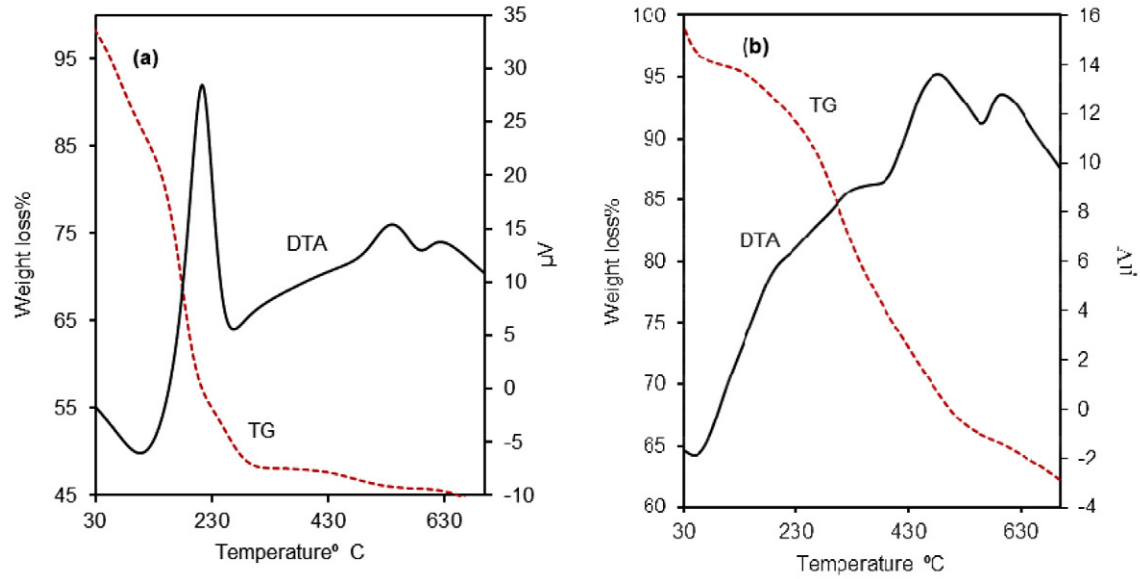

Fig. 6. TG and DTA curves of (a) GO (b) GO@5-Br(Saldien)VO.

luted with 5 ml of absolute *n*-hexane (99.85%). The DBT oxidation versus reaction time was determined according to the following equation:

$$C_{DBT}(\%) = \frac{(C_0 - C_t)}{C_0} \quad (1)$$

The absorption was converted to the concentration through the standard curve, where C_0 is the concentration at time zero and C_t is the DBT concentration at time t.

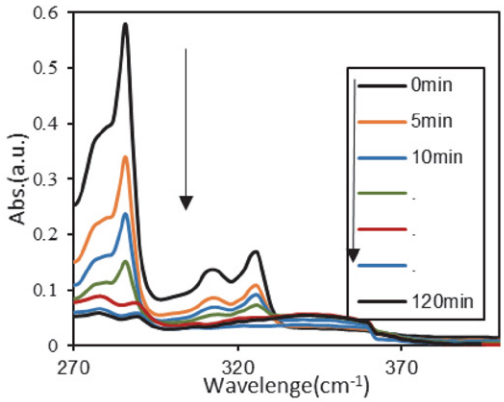

Fig. 7. Time dependent UV–visible spectral changes for oxidation of DBT (500ppm) using GO@(5-Br,Saldien)VO as catalyst, H_2O_2 as oxidant and 5ml acetonitrile, under acidic condition at 60 °C.

3. 3. Influence of the Reaction Temperature on Catalytic Activity

The reaction temperature greatly influences the activity of the catalyst and it is one of the greatest factors that could not be ignored in the desulfurization process.[41] The effect of the temperature on the kinetics of oxidation of DBT was investigated in the temperature range of 30–70 °C.

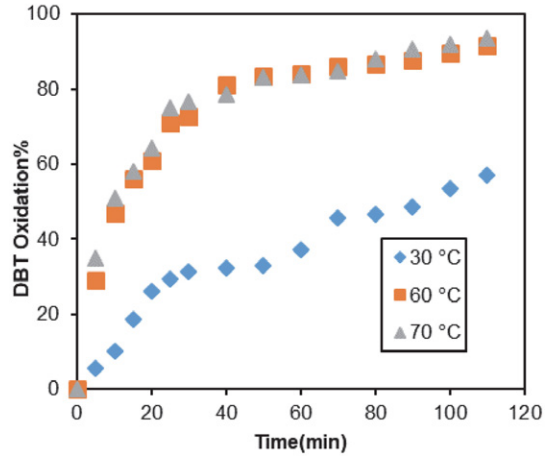

Fig. 8. Influence of the reaction temperature on DBT oxidation. The reaction conditions are as follows: reaction time: 120 min, a catalyst mass 2.4 g/l, O/S= 6 and acetonitrile = 5mL, a mixture of formic acid and hydrogen peroxide was added in the reaction mixture (formic acid/H_2O_2 = 1).

According to Fig. 8, the catalytic performance improved significantly when the reaction temperature was raised. The DBT conversion is only 57% at 30 °C and increased to around 92% and 93% in 60 °C and 70 °C, respectively. A rise in the reaction temperature from 30 to 60 °C led to a remarkable increase in the reaction rate at every time of the reaction. However, this increase in the temperature from 60 to 70 °C was less marked. Thus, 60 °C is chosen as an optimum temperature for the catalytic system.

3. 4. Effect of Catalyst Mass on DBT Oxidation

The effect of the catalyst mass was evaluated over the range from 1.2 g/L to 7.2 g/L of the catalyst. Fig. 9 shows

the effect of the catalyst mass in the oxidation of DBT. When the catalyst mass increases from 1.2 to 2.4 g/l, the DBT conversion increases, Increasing the catalyst mass lead to the increase in active sites which causes more amounts of DBT to be converted to dibenzothophene sulfone ($DBTO_2$).[42] According to the Fig. 9, under identical conditions, only 33% of DBT is removed from the reaction by pure experiment. When 2.4g/l catalyst is employed, sulfur removal of DBT reaches 92% within 120 min. However, increasing the catalyst mass to 7.2g/L apparently led to a decrease in activity. The decreased activity might be attributed to the poor dispersion of the catalyst solids within the reaction system.[40] Therefore, the lower value of 2.4 g/L was selected as the catalyst mass in the experiments.

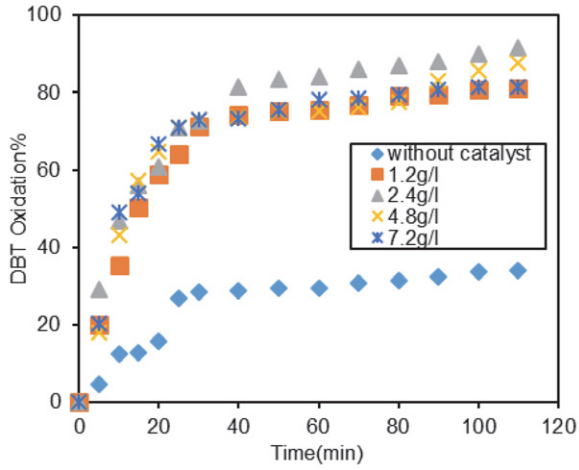

Fig. 9. Effect of catalyst mass on DBT oxidation, temperature 60 °C, reaction time 120 min, and O/S = 6, formic acid/ H_2O_2 = www1 and acetonitrile = 5ml.

3. 5. Effect of the Amount of Hydrogen Peroxide in the Oxidation Process

Detection of an optimum excess amount of H_2O_2 is an important agent that affects the efficiency and economy of the process.[42] Theoretically, 2 moles of H_2O_2 are needed to completely oxidize 1 mole of the sulfur compound.[43] However, usually, a bit higher amount of H_2O_2 is used in oxidative reaction because the undesirable thermal decomposition of H_2O_2 takes place simultaneously with the catalytic oxidation.[44] With a lower O/S molar ratio, sufficient intermediate active species is not available during the reaction and a more portion of DBT will remain unoxidized in the solvent. On the other hand, a high O/S molar ratio is unfavorable because of wasting the oxidant and safety risks.[44] Fig. 10 shows that the O/S molar ratio also had a significant influence on the oxidation DBT. An increase in O/S ratio from 2 to 6 results in a sharp increase in the overall desulfurization yield while the further increase from 8 to 10 has a slight effect. The current optimum value of 10 for the O/S ratio seems to be ideal achieving a complete oxidative desulfurization yield.

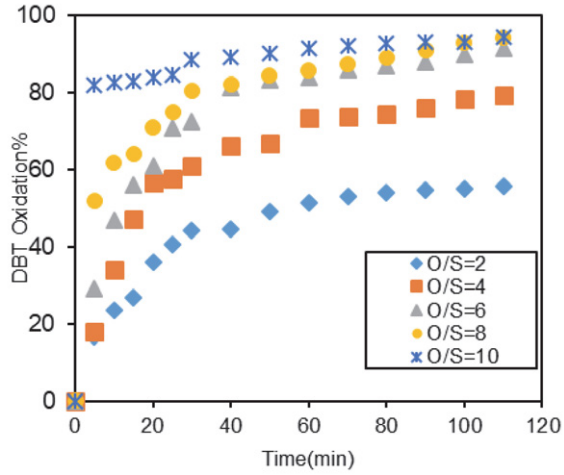

Fig. 10. Effect of the amount of hydrogen peroxide in the oxidation process. The reaction conditions are as follows: reaction time: 120 min, a catalyst Mass 2.4g/l, acetonitrile = 5ml, a mixture of formic acid and hydrogen peroxide was added in the reaction mixture (formic acid/H_2O_2 = 1) and reaction temperature 60 °C.

3. 6. Role of Formic Acid Promoter in the Oxidation Process

It should be noted that during the ODS process, aliphatic peroxyacid as an oxygen supplier is obtained by the oxidation of the corresponding carboxylic acid with aqueous hydrogen peroxide.[45] In turn, the interaction of peroxyformic acid with GO@5-Br(Saldien)VO generates active oxidizing species like peroxometallics and superoxometallics.[46] This electrophilic active oxygen in oxo-peroxo metal species attacks the sulfur atom at a high electron density to form sulfones.[47] They were also more stable than H_2O_2 as connecting to the surface metallic sites.[48] Formation of peroxometallic complexes effectively inhibited the H_2O_2 decomposition to release gaseous oxygen before the reaction and thus improved the ODS efficien-

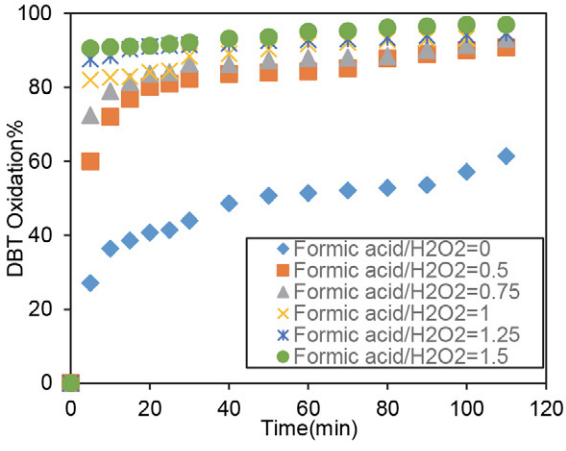

Fig. 11. Role of formic acid promoter in oxidation DBT, reaction time: 120 min, a catalyst mass 2.4g/l, O/S=10, acetonitrile = 5ml, a mixture of formic acid and hydrogen peroxide was added in the reaction mixture (formic acid/H_2O_2 = 0, 0.5, 0.75, 1, 1.25, 1.5) and reaction temperature 60 °C.

Table 1. oxidation DBT under various reaction conditions in the presence of GO@5-Br(Saldien)VO.

Entry	Catalyt amount(g/l)	Temperature(°C)	Molar ratio of O/S	Formic acid/ H_2O_2	Time(h)	Conversion%	TON
1	2.4	30	6	1	2	57%	343.342
2	2.4	60	6	1	2	92%	554.167
3	2.4	70	6	1	2	93%	560.19
4	Without catalyst	60	6	1	2	33.99%	
5	1.2	60	6	1	2	81.01%	975.85
6	4.8	60	6	1	2	87.57%	263.717
7	7.2	60	6	1	2	81.3%	162.96
8	2.4	60	2	1	2	55.92%	335.594
9	2.4	60	4	1	2	79.34%	476.145
10	2.4	60	6	1	2	91.54%	549.362
11	2.4	60	8	1	2	94.37%	568.443
12	2.4	60	10	1	2	94.56%	569.587
13	2.4	60	10	0	2	61.43%	368.661
14	2.4	60	10	0.5	2	90.78%	544.801
15	2.4	60	10	0.75	2	93.11%	558.784
16	2.4	60	10	1.25	2	94.6%	567.726
17	2.4	60	10	1.5	2	96.92%	581.649

TON = (% conv) × (substrate moles) / catalyst (vanadium) moles.

cy.[49] As shown in Fig. 11, when formic acid (formic acid/ H_2O_2 = 1.5) is added to the reaction, in the first 5 min of the reaction, more than 90% of the DBT was oxidized, but in the other reaction without the presence of formic acid, in the first 5 min of the reaction only 27% of DBT was oxidized. Table 1 shows the DBT oxidation under various reaction conditions in the presence of GO@5-Br(Saldien) VO.

Table 2 shows the comparison of the catalytic activity of GO@5-Br(Saldien)VO with that of other reported catalysts. The results indicated that of GO@5-Br(Saldien)VO was quite reliable for ODS in comparison with other catalysts.

Table 2. Effect of different catalysts in oxidation desulfurization of dibenzothiophene compound.

Entry	Catalyst	Conversion%	Reaction condition	Ref
1	GO@ (5-Br, Saldien) VO	96.92%	5ml of model fuel (500 ppm of DBT in n-heptane), 2.4 g/l of catalyst, O/S = 10, formic acid/ H_2O_2=1.5, acetonitrile = 5ml at 60°C for 2 h	This work
2	PS-[$V^{IV}O$(fsal-dmen)(MeO)]*	87.9%	DBT(500 ppm) in n-heptane, O/S=3, catalyst: 0.0715 mmol, at 60°C, for 2h	26
3	PS-[$V^{V}O_2$(fsal-dmen)]**	98.4%		
4	poly[VO-(allylSB-co-EGDMA)]***	99%	Flow rate of 1 ml/h, t-BuOOH/S= 6.8, an aqueous solution of tert-butylhydroperoxide (t-BuOOH) and dibenzothiophene (DBT), were dissolved in 10 ml solution of toluene/hexane (1:4). at 40°C	23
5	poly[VO(sal-AHBPD)]****	88%	TBHP] = 0.5 g (5.5 mmol), [dibenzothiophene]= 0.15 g (0.814 mmol), catalyst = 0.015 g (0.0135 mmol). Temp. = 40 °C. Toluene–hexane (1 : 4) = 10 ml for 2h.	50

*: PS-[$V^{IV}O$(fsal-dmen)(MeO)]= 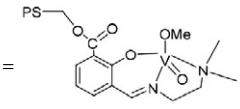

**: PS-[$V^{V}O_2$(fsal-dmen)]=. 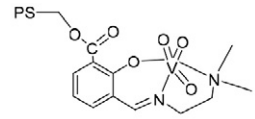

***: poly[VO-(allylSB-co-EGDMA)]= 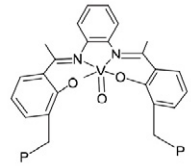

****: poly[VO(sal-AHBPD)]= 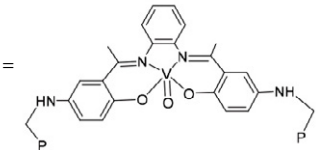

3. 7. Catalyst Reusability

The graphene oxide bounded oxovanadium Schiff base catalyst was reused six times for the oxidative desulfurization of DBT under similar oxidation conditions. After each catalytic run, the reaction mixture centrifuged and the used catalyst was recovered by washing with fresh acetonitrile and dried. The fresh model fuel, H_2O_2, and formic acid were then added to start a new cycle. At the end of each cycle, samples were taken and analyzed by UV-vis and DBT removal is observed. Results showed that the catalytic activity is nearly maintained during the recycling performance.

The results of the ODS reactions using the reused GO@ (5-Br, Saldien)VO after six reuse presented in Table 3. The FT-IR spectrum of the recovered GO@ (5-Br, Saldien)VO after the sixth run confirmed no significant change in the structure of the catalyst (Fig. 12).

To determine whether the reaction is truly carried out in a heterogeneous way or not, hot filtration test was investigated.[51] The result is as follows. In the 15 min of the reaction process the reaction media were filtered in hot condition. The catalyst remained on the filter paper and the filtrate came through. In the next step the reaction was continued. It was found that the conversion remained the same of the filtrate. This showed that there was no leaching of the immobilized Schiff base complex. Thus, this confirms that the synthesized catalyst acts heterogeneously.

Table 3. Reuse of the synthesized catalyst for ODS reaction

Run	DBT oxidation%
1	96.92%
2	93.23%
3	91.30%
4	91.08%
5	91.04%
6	86.83%

Conditions of ODS: 5ml of model fuel (500 ppm of DBT), 2.4 g /l of catalyst, O/S = 10, formic acid/ H_2O_2 = 1.5, acetonitrile = 5ml for 2 h at 60°C.

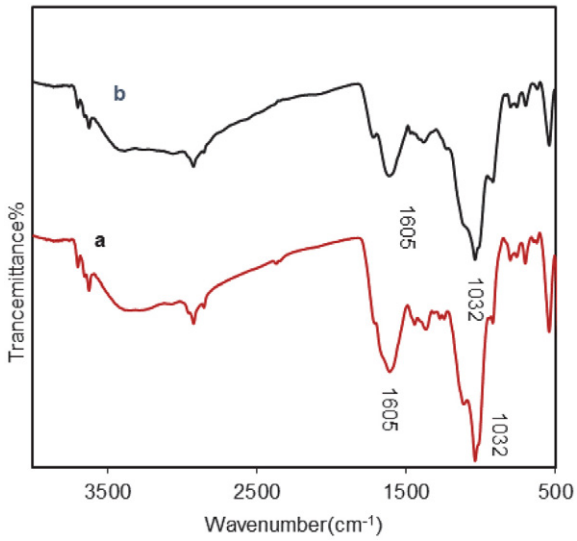

Fig. 12. FT-IR spectrum of (a) GO@5-Br(Saldien)VO and (b) sixth recovered GO@5-Br(Saldien)VO, 5ml of model fuel (500 ppm of DBT), 2.4 g/l of catalyst, O/S = 10, formic acid/ H_2O_2 = 1.5, acetonitrile = 5ml, for 2 h at 60 °C.

3. 8. Product Characterization

Oxidative desulfurization reaction in the presence of an oxidant occurs through two consecutive stages.[52] At the first stage, DBT is oxidized to dibenzothiophene sulfoxide (DBTO), and then, the formed DBTO is rapidly converted to $DBTO_2$.[53] The FT-IR spectrum of the produced crystal is shown in Fig. 13. The oxidation product was further proven to be the dibenzothiophene sulfone ($DBTO_2$) by FT-IR (characteristic peaks at 1288 and 1165 cm^{-1}) that can be attributed to the asymmetrical and symmetrical stretching vibration modes of O=S=O, respectively.[54]

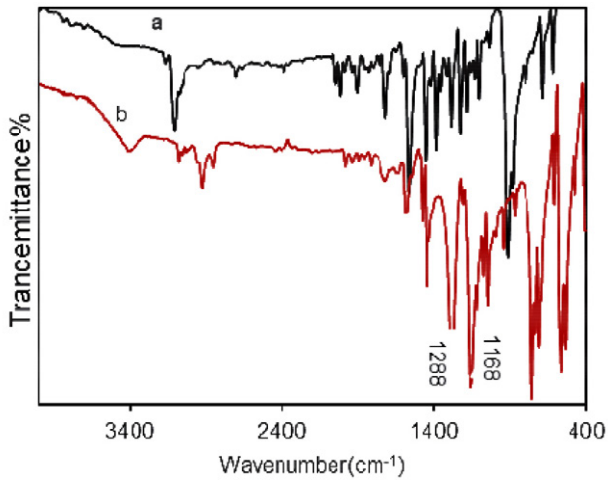

Fig. 13. FT-IR spectrum of the sulfur compound (a) before and (b) after desulfurization reaction.

4. Conclusions

New heterogeneous catalyst was synthesized by covalent anchoring of the oxovanadium Schiff base on the graphene oxide support previously functionalized with 3-chloropropyltrimethoxysilane. XRD, FTIR, TG, DTA, SEM, EDX and ICP-AES analyses revealed well loading of the oxovanadium Schiff base complex on the functionalized graphene oxide. The developed catalyst was found to be highly efficient for oxidation desulfurization of model oil using H_2O_2 as an oxidant and formic acid as a promoter. The effects of the main process variables such as temperature, catalyst mass, oxygen to sulfur ratio (O/S) and formic acid/H_2O_2 ratio were inspected using experimental

design. As a result, a nearly complete oxidative desulfurization was obtained in the optimum condition of 60 °C, an O/S ratio of 10, and a formic acid/H_2O_2 ratio of 1.5 in a 120 min and low catalyst loading (2.4 g/L). Moreover, the developed catalyst was found to be easily recoverable and recyclable and could be reused for five subsequent runs.

Acknowledgments

The authors are grateful to the Research Council of the University of Kurdistan and the University of Guilan for the partial support of this study.

5. References

1. X. Xiao, H. Zhong, C. Zheng, M. Lu, X. Zuo, J. Nan, *Chem. Eng. J.* **2016**, *304*, 908–916. **DOI:**10.1016/j.cej.2016.07.022
2. M. I. S. de Mello, E. V. Sobrinho, V. Teixeira da Silva, S. B. C. Pergher, *Ind. Eng. Chem. Res.* **2018**, *57*, 15663–15669. **DOI:**10.1021/acs.iecr.8b03232
3. C. Song, X. Ma, *Appl Catal B.* **2003**, *41*, 207–238. **DOI:**10.1016/S0926-3373(02)00212-6
4. B. Pawelec, R. M. Navarro, J. M. Campos-Martin, J. L. G. Fierro, *Catal. Sci. Technol* **2011**, *1*, 23–42. **DOI:**10.1039/c0cy00049c
5. A. F. Shojaei, M. A. Rezvani, M. H. Loghmani, *Fuel Process. Technol.* **2014**, *118*, 1–6. **DOI:**10.1016/j.fuproc.2013.08.004
6. S. Otsuki, T. Nonaka, N. Takashima, W. Qian, A. Ishihara, T. Imai, T. Kabe, *Energy Fuels* **2000**, *14*, 1232–1239. **DOI:**10.1021/ef000096i
7. Y. Shiraishi, K. Tachibana, T. Hirai, I. Komasawa, *Ind. Eng. Chem. Res.* **2002**, *41*, 4362–4375. **DOI:**10.1021/ie010618x
8. A. Srivastav, V. C. Srivastava, *J. Hazard. Mater.* **2009**, *170*, 1133–1140. **DOI:**10.1016/j.jhazmat.2009.05.088
9. Z. Hasan, J. Jeon, S. H. Jhung, *J. Hazard. Mater.* **2012**, *205–206*, 216–221. **DOI:**10.1016/j.jhazmat.2011.12.059
10. C. Song, *Catal. Today* **2003**, *86*, 211–263. **DOI:**10.1016/S0920-5861(03)00412-7
11. S. Dhir, R. Uppaluri, M. K. Purkait, *J. Hazard. Mater.* **2009**, *161*, 1360–1368. **DOI:**10.1016/j.jhazmat.2008.04.099
12. C. Shen, Y. Wang, J. Xu, G. Luo, *Green Chem.* **2016**, *18*, 771–781. **DOI:**10.1039/C5GC01653C
13. L. A. Gonzalez, P. Kracke, W. H. Green, J. W. Tester, L. M. Shafer, M. T. Timko, *Energy Fuels* **2012**, *26*, 5164–5176. **DOI:**10.1021/ef201289r
14. D. Huang, Z. Zhai, Y. C. Lu, L. M. Yang, G. S. Luo, *Ind. Eng. Chem. Res.* **2007**, *46*, 1447–1451. **DOI:**10.1021/ie0611857
15. J. Luis García-Gutiérrez, G. A. Fuentes, M. Eugenia Hernández-Terán, P. García-Gutiérrez, F. Murrieta-Guevara, J. L. Garcia-Gutierrez, *Appl. Catal., A* **2008**, *334*, 366–373. **DOI:**10.1016/j.apcata.2007.10.024
16. W. Zhu, G. Zhu, H. Li, Y. Chao, M. Zhang, D. Du, Q. Wang, Z. Zhao, *Fuel Process. Technol.* **2013**, *106*, 70–76. **DOI:**10.1016/j.fuproc.2012.07.003
17. A. Chica, A. Corma, M. E. Dómine, *J. Catal.* **2006**, *242*, 299–308. **DOI:**10.1016/j.jcat.2006.06.013
18. K. Yazu, M. Makino, K. Ukegawa, *Chem. Lett.* **2004**, *33*, 1306–1307. **DOI:**10.1246/cl.2004.1306
19. W. Zhang, H. Liu, Q. Xia, Z. Li, *Chem. Eng. J.* **2012**, *209*, 597–600. **DOI:**10.1016/j.cej.2012.08.050
20. J. A. L. da Silva, J. J. R. F. da Silva, A. J. L. Pombeiro, *Coordin Chem Rev* **2011**, *255*, 2232–2248. **DOI:**10.1016/j.ccr.2011.05.009
21. A. Coletti, P. Galloni, A. Sartorel, V. Conte, B. Floris, *Catal. Today* **2012**, *192*, 44–55. **DOI:**10.1016/j.cattod.2012.03.032
22. L. Kuznetsova, L. Detusheva, N. Kuznetsov, V. Duplyakin, V. Likholobov, *Kinet. Catal.* **2008**, *49*, 644–652. **DOI:**10.1134/S002315840805008X
23. A. S. Ogunlaja, R. S. Walmsley, C. du Sautoy, N. Torto, Z. R. Tshentu, *Energy Fuels* **2013**, *27*, 7714–7723. **DOI:**10.1021/ef401708f
24. M. Zhou, W. Meng, Y. Li, Q. Wang, X. Li, S. Zang, *Energy Fuels* **2013**, *28*, 516–521. **DOI:**10.1021/ef402103e
25. D. Piccinino, I. Abdalghani, G. Botta, M. Crucianelli, M. Passacantando, M. L. Di Vacri, R. Saladino, *Appl Catal B-Environ.* **2017**, *200*, 392–401. **DOI:**10.1016/j.apcatb.2016.07.037
26. M. R. Maurya, A. Arya, A. Kumar, M. L. Kuznetsov, F. Avecilla, J. Costa Pessoa, *Inorg. Chem.* **2010**, *49*, 6586–6600. **DOI:**10.1021/ic1004209
27. S. Guo, S. Sun, *J. Am. Chem. Soc.* **2012**, *134*, 2492–2495. **DOI:**10.1021/ja2104334
28. H. P. Mungse, S. Verma, N. Kumar, B. Sain, O. P. Khatri, *J. Mater. Chem.* **2012**, *22*, 5427–5433. **DOI:**10.1039/c2jm15644j
29. S. Verma, M. Aila, S. Kaul, S. L. Jain, *RSC Adv.* **2014**, *4*, 30598–30604. **DOI:**10.1039/C4RA03454F
30. Z. Hajjar, M. Kazemeini, A. Rashidi, M. Bazmi, *Fuel* **2016**, *165*, 468–476. **DOI:**10.1016/j.fuel.2015.10.040
31. W. Coleman, L. Taylor, *Inorg. Chem* **1971**, *10*, 2195–2199. **DOI:**10.1021/ic50104a021
32. M. A. Nasseri, A. Allahresani, H. Raissi, *RSC Adv.* **2014**, *4*, 26087–26093. **DOI:**10.1039/c4ra03047h
33. K. Krishnamoorthy, M. Veerapandian, K. Yun, S.-J. Kim, *Carbon* **2013**, *53*, 38–49. **DOI:**10.1016/j.carbon.2012.10.013
34. H. Naeimi, Z. Ansarian, *Appl. Organomet. Chem.* **2017**, *31*, e3796. **DOI:**10.1002/aoc.3796
35. Z. Li, S. Wu, H. Ding, H. Lu, J. Liu, Q. Huo, J. Guan, Q. Kan, *New J. Chem.* **2013**, *37*, 4220–4229. **DOI:**10.1039/c3nj00982c
36. D. C. Marcano, D. V. Kosynkin, J. M. Berlin, A. Sinitskii, Z. Sun, A. Slesarev, L. B. Alemany, W. Lu, J. M. Tour, *ACS nano* **2010**, *4*, 4806–4814. **DOI:**10.1021/nn1006368
37. A. M. Rodriguez, P. V. Jiménez, *Thermochim Acta* **1984**, *78*, 113–122. **DOI:**10.1016/0040-6031(84)87138-5
38. H. Raghubanshi, S. M. Ngobeni, A. O. Osikoya, N. D. Shooto, C. W. Dikio, E. B. Naidoo, E. D. Dikio, R. K. Pandey, R. Prakash, *Ind Eng Chem* **2017**, *47*, 169–178. **DOI:**10.1016/j.jiec.2016.11.028
39. H. Su, Z. Li, Q. Huo, J. Guan, Q. Kan, *RSC Adv.* **2014**, *4*, 9990–9996. **DOI:**10.1039/C4RA01812E

40. U. Arellano, J. Wang, M. Timko, L. Chen, S. P. Carrera, M. Asomoza, O. G. Vargas, M. Llanos, *Fuel* **2014**, *126*, 16–25. **DOI:**10.1016/j.fuel.2014.02.028
41. H. Yang, B. Jiang, Y. Sun, L. Zhang, Z. Sun, J. Wang, X. Tantai, *Chem. Eng. J.* **2017**, *317*, 32–41. **DOI:**10.1016/j.cej.2017.01.135
42. A. K. Dizaji, H. R. Mortaheb, B. Mokhtarani, *Chem. Eng. J.* **2018**, *335*, 362–372. **DOI:**10.1016/j.cej.2017.10.129
43. M. d. C. Capel-Sanchez, P. Perez-Presas, J. M. Campos-Martin, J. Fierro, *Catal. Today* **2010**, *157*, 390–396. **DOI:**10.1016/j.cattod.2010.01.047
44. J. Zhang, A. Wang, X. Li, X. Ma, *J. Catal.* **2011**, *279*, 269–275. **DOI:**10.1016/j.jcat.2011.01.016
45. V. Mošovský, Z. Cvengrošová, A. Kaszonyi, M. Králik, M. Hronec, *Collect. Czech. Chem. Commun.* **1996**, *61*, 1457–1463. **DOI:**10.1135/cccc19961457
46. M. A. Rezvani, S. Khandan, *Appl. Organomet. Chem.* **2018**, *32*, e4524. **DOI:**10.1002/aoc.4524
47. J. Xiong, W. Zhu, W. Ding, L. Yang, M. Zhang, W. Jiang, Z. Zhao, H. Li, *RSC Adv.* **2015**, *5*, 16847–16855. **DOI:**10.1039/C4RA14382E
48. I. Arends, R. Sheldon, *Appl. Catal., A* **2001**, *212*, 175–187. **DOI:**10.1016/S0926-860X(00)00855-3
49. U. Arellano, Z. Wang, L. Chen, J. A. Wang, M. Asomoza, A. Estrella, *Ind. Eng. Chem. Res.* **2017**, *56*, 12080–12091. **DOI:**10.1021/acs.iecr.7b02787
50. A. S. Ogunlaja, W. Chidawanyika, E. Antunes, M. A. Fernandes, T. Nyokong, N. Torto, Z. R. Tshentu, *Dalton Trans.* **2012**, *41*, 13908–13918. **DOI:**10.1039/c2dt31433a
51. H. Lempers, R. Sheldon, *J. Catal.* **1998**, *175*, 62–69. **DOI:**10.1006/jcat.1998.1979
52. E. Torres-García, A. Galano, G. Rodriguez-Gattorno, *J. Catal.* **2011**, *282*, 201–208. **DOI:**10.1016/j.jcat.2011.06.010
53. M. Y. Masoomi, M. Bagheri, A. Morsali, *Inorg. Chem.* **2015**, *54*, 11269–11275. **DOI:**10.1021/acs.inorgchem.5b01850
54. L. Hao, L. Sun, T. Su, D. Hao, W. Liao, C. Deng, W. Ren, Y. Zhang, H. Lü, *Chem. Eng. J.* **2019**, *358*, 419–426. **DOI:**10.1016/j.cej.2018.10.006

Povzetek

Sintetizirali smo nov heterogeni katalizator preko kovalentnega sidranja oksovanadijevega(IV) kompleksa s 5,5'-dibromobis(salicileden)dietilenetriaminom (VO[5-Br(Saldien)]) na površino kloro-modificiranega grafen oksida (GO@CTS). Strukturo katalizatorja smo proučevali z uporabo različnih karakterizacijskih tehnik, kot so XRD, SEM, EDX, FT-IR, TG, DTA in ICP-AES analize. Sintetiziran heterogeni oksovanadijev(IV) katalizator je učinkovit katalizator za selektivno oksidacijo in desulfurizacijo (ODS) dibenzotiofena (DBT) kot modela z uporabo H_2O_2 kot oksidanta in mravljinčno kislino kot promotorja. Proučili smo tudi vpliv mase katalizatorja, reakcijske temperature in časa, razmerja HCOOH/H_2O_2 in molskega razmerja H_2O_2 glede na celokupno količino žvepla (O/S) na učinkovitost oksidacije in desulfurizacije. Pripravljeni katalizator je enostavno ločiti iz reakcijske zmesi in ponovno uporabiti šestkrat brez opaznega zmanjšanja katalitske aktivnosti in selektivnosti.

Except when otherwise noted, articles in this journal are published under the terms and conditions of the Creative Commons Attribution 4.0 International License

Scientific paper

Encapsulation of Dirhenium(III) Carboxylates into Zirconium Phosphate

Anastasiia Slipkan,[1,2] Nataliia Shtemenko,[1,2] Dina Kytova[1,2] and Alexander Shtemenko*[,1]

[1] *Ukrainian State University of Chemical Technology, Gagarin Ave. 8, Dnipro, Ukraine, 49005*

[2] *Dnipro University of Technology, Dmytro Yavornytskiy Ave. 19, Dnipro, Ukraine,49005*

** Corresponding author: E-mail: shtemenko@ukr.net*
Tel.+380 (97) 392 91 52

Received: 08-27-2019

Abstract

Present work reports the synthesis of zirconium phosphate nanoparticles containing dirhenium(III) substance bis-dimethylsulfoxide-cis-tetrachlorodi-μ-pivalatodirhenium(III) with formula *cis*-$Re_2(C(CH_3)_3COO)_2Cl_4 \cdot 2DMSO$ (**I**) and θ-zirconium phosphate with formula θ-$Zr(HPO_4)_2 \cdot 6H_2O$ (ZrP). The intercalation process was monitored by EAS. Due to the spectral characteristics of the quadruple bond the conclusion was made that the obtained intercalated compounds had *cis*-configuration of ligands around cluster dirhenium fragment. The proposed mechanism of intercalation includes the substitution of the axial ligands of **I** by phosphate groups of ZrP first on the surface of ZrP, than in the inner layers. Two received products of the intercalation were characterized by SEM, XRPD, FT-IR, TGA analysis witnessing about successful intercalation process. The formation of new phases with interlayer distances of 10.53–16.6 Å was found, the average size of obtained platelets was 100–200 nm.

Keywords: Dirhenium(III) carboxylates, zirconium phosphate, nanoparticles, intercalation.

1. Introduction

Layered Zr(IV) phosphates ZrP with α, β, γ and θ-structures, α-$Zr(HPO_4)_2 \cdot H_2O$, β-$Zr(HPO_4)_2 \cdot 2H_2O$, θ-$Zr(HPO_4)_2 \cdot 6H_2O$ and γ-$ZrPO_4 \cdot H_2PO_4 \cdot 2H_2O$ are well known as convenient, long storing and non-toxic preparations, that due to labile protons of POH groups can be used for many chemical processes. [1,2,3] ZrP is one of the most studied inorganic cation exchange material with high thermal stability, solid-state ion conductivity, resistance to ionizing radiation and is known as a host capable to incorporate different types of guest molecules.[4]

Crystal structure of ZrP presents a lattice with Zr^{4+} ions bonding to oxygen atoms from three different phosphate groups producing covalently connected three-dimensional cross-linked planes. The fourth oxygen atom of the tetrahedral phosphate group is protonated and points towards the interlayer space. Water molecules in the interlayer space form hydrogen bonds with hydroxyl groups and are perpendicular to the layer. θ-ZrP is a hydrated phase of α-ZrP and has a similar structure to the α-ZrP with five additional water molecules in the interlaminar space, thus the distance between the layers increases up to 10.3 Å (Fig. 1A). (Fig. 1A)

Upon dehydration, θ-ZrP is converted to α-ZrP (the distance between the layers is 7.6 Å) without the formation of any other intermediate phase.[5] The efficiency of intercalation to all types of ZrP depends on the distance between the layers and the size of intercalated molecules.[6] Cations (less than 2.63 Å) or small molecules can be intercalated within the layers of α-ZrP. However, the intercalation of large cations here was very low. Due to the larger interlaminar space θ-ZrP can include large molecules and cations, such as insulin and others[6,7]. That is why among the described modification of ZrP we chose θ-ZrP for our study. It was shown that differences in properties (solubility, charge, polarity) substances such as doxorubicin, insulin, amino acids and various organometallic complexes could be intercalated into ZrP layers.[5,6,8–13]

Dirhenium(III) carboxylates with the unique quadruple bond were described as anticancer, anti-anemic, nephro- and hepato-protecting substances, possessing mighty antioxidant properties due to δ-bond unsaturation.[14–17] Being nontoxic, these compounds present a perspective platform

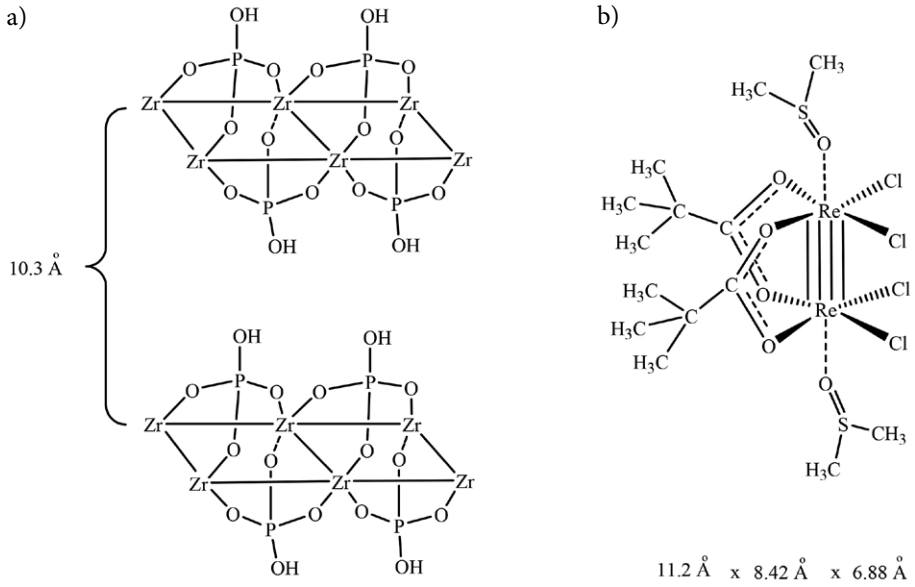

Fig. 1 Structure of $Zr(HPO_4)_2 \cdot 6H_2O$ (θ-ZrP) (a) and *cis*-$Re_2(C(CH_3)_3COO)_2Cl_4 \cdot 2DMSO$ (**I**) (b) with linear dimensions.

for the creation of a new class of Re-containing medicines. Bis-dimethylsulfoxide-cis-tetrachlorodi-μ-pivalatodirhenium(III) of common formula *cis*-$Re_2(C(CH_3)_3COO)_2Cl_4 \cdot 2DMSO$ (**I**) and structure shown on the Fig.1B was studied in the model of tumor-growth and showed essential antioxidant and anticancer activities as a component of the antitumor rhenium-platinum antitumor system.[18,19] Among them the substances with superoxide dismutase activity and abilities to interact with proteins were found. The valuable biological properties of these compounds were better realized in the forms of liposomes, than in water solutions,[20,21] that occurred due to lipid layer protection of dirhenium substances from hydrolysis and also by existing of the equilibrium inside the liposome, that enhanced chemical potential of the preparations. Thus, the approach to create nanocarriers for delivery of the quadruple-bonded complexes is very promising.

The ZrP nanoplatelets may be prepared by methods of intercalation or exfoliation [22]. The last method had some disadvantages, for example, the necessity of the preintercalator, which may be toxic. That's why we consider it reasonable to use the intercalation procedure.

Thus, taking into account all the above, the aim of the present work was to investigate the process of intercalation of *cis*-$Re_2(C(CH_3)_3COO)_2Cl_4 \cdot 2DMSO$ (**I**) into θ-ZrP and to obtain **I**/ZrP nanoplatelets by intercalation method.

2. Experimental Section

2. 1. Materials and Methods

All used chemicals were of analytical grade purity. θ-ZrP was obtained according to [5] with some modifications (see below). *cis*-$Re_2(C(CH_3)_3COO)_2Cl_4 \cdot 2DMSO$ (**I**) was obtained according to.[16]

2. 2. Synthetic Methods

Synthesis of θ-ZrP: 200 ml of 0.05 M water solution of $ZrOCl_2 \cdot 8H_2O$ was added to preheated up to 94 °C 200 ml of 6 M H_3PO_4 in a 500 ml round bottom flask. The resulting solution was constantly stirred at 94°C for 48 h. The product was a crystalline precipitate centrifuged and washed several times with water.

*Synthesis of **I**/θ-ZrP composites*. The process of intercalation of **I** in θ-ZrP was conducted in isopropyl alcohol (IPA), not in the water, to avoid possible hydrolytic processes of dirhenium(III) complexes. First, the suspension of **I** and θ-ZrP in IPA in the molar ratios of **I** and θ-ZrP 1:5 and 1:30 was prepared: the required amount of θ-ZrP was suspended in $5.0 \cdot 10^{-3}$ M solution of **I.** The molar ratios of **I**/θ-ZrP 1:5 and 1:30 were taken according to the similar investigations of the intercalation process between θ-ZrP and platinides.[23] Then the suspension was stirred vigorously at 60 °C for 5 days. The intercalation process was controlled by each day measurements of pH and UV-Vis absorption spectra (EAS) of the supernatant of a centrifuged aliquot. Constant pH and UV-Vis absorbance indicated the end of the intercalation process. The reaction mixture was cooled, centrifuged (micro-centrifuge type 320; Mechanika Precyzyjna, Poland) at 14000xg, filtered, washed three times with IPA, dried and weighted. As a result of the intercalation, the mass of the I/θ-ZrP of 1:5 and 1:30 molar ratio increased on 0.57 g (26% of the substance was intercalated) and 1.45 g (66% of the substance was intercalated) correspondingly.

2. 3. Measurements

pH was controlled by pH-meter-millivoltmeter pH-150 MA. UV-vis absorption spectra were measured

in IPA using spectrophotometer "Specord M-40" (Germany).

Calculations of three-dimension structures and linear dimensions were made with the help of the Mercury (Mercury for Windows, version 3.6 using the crystal structure of **I** [16]) program for crystal structure visualization, exploration and analysis.

Scanning electron micrographs (SEM) of the samples were performed using a Tescan Mira 3 LMU scanning electron microscope at an acceleration voltage of 30 kV. Samples were prepared using Digiprep 251 and MicraCut 151 (Metkon). The speed of rotation of the disk – 50–600 rpm, the speed of rotation of the samples 50–150 rpm.

Zeta potentials of ZrP nanoplatelets were determined using Zeta Sizer Nano S (Malvern, UK) at 25 °C at pH 7.4.

X-ray diffraction (XRPD) measurements were performed from 5 to 60 °C using X-ray diffractometer PANalytical X'Pert High Score with a copper anode source ($K_{\alpha 1}$, λ = 1.5406 Å).

IR spectra were recorded in the range of the 4000–400 cm^{-1} in dehydrated KBr tablets in infrared spectrophotometer FT-IR Spectrum BX, (Perkin Elmer).

Thermogravimetric analysis (TGA analysis) was conducted on the derivatograph Q-1500D Paulik-Paulik-Erday on the air in the interval 20–1000 °C with the speed 10 °C/min of temperature changing. α-Al_2O_3 served as an etalon. The error in determined temperature intervals was not more than 5%. After that, another modification of thermal destruction investigation, i.e. method of thermal exposures was used. The weighted sample of the substance was placed in the glass reactor for thermal exposures and was heated in an inert atmosphere under the temperatures of earlier determined temperatures of the weight losses during 4 h. After each exposure, the sample was weighed and the weight loss was determined.

The drug encapsulation efficiency (EE) of the composites was measured by spectrophotometric method according to[2] at different time intervals at 14900 cm^{-1} using Eq. (1):

$$EE(\%) = [(\text{Total } \mathbf{I} - \mathbf{I} \text{ in supernatant}) / \text{Total } \mathbf{I}] \times 100\% \quad (1)$$

3. Results and Discussion

3. 1. Spectral Investigation of Intercalation I with ZrP.

Spectral analysis was used by us to investigate interactions of different types of dirhenium cluster compounds with 1-palmitoyl-2-oleylphosphatidylcholin (POPC) preparation of liposomes,[20,24] proteins[25] and zirconium phosphate[26,27] due to ability of the quadruple bond to absorb in the visible area.

Different structural types of Re_2^{6+} derivatives had the characteristic absorption maxima in the visible area, the position of which were dependent from the quantity of hyperconjugated cycles around Re_2^{6+} center. The effect of hyperconjugation was realized due to the interaction of the delocalized π-bond of μ-carboxylic ligands group and the δ-component of the quadruple Re-Re bond. If dichlorotetra-μ-isobutiratodirhenium(III) $Re_2(i\text{-}PrCOO)_4Cl_2$ had

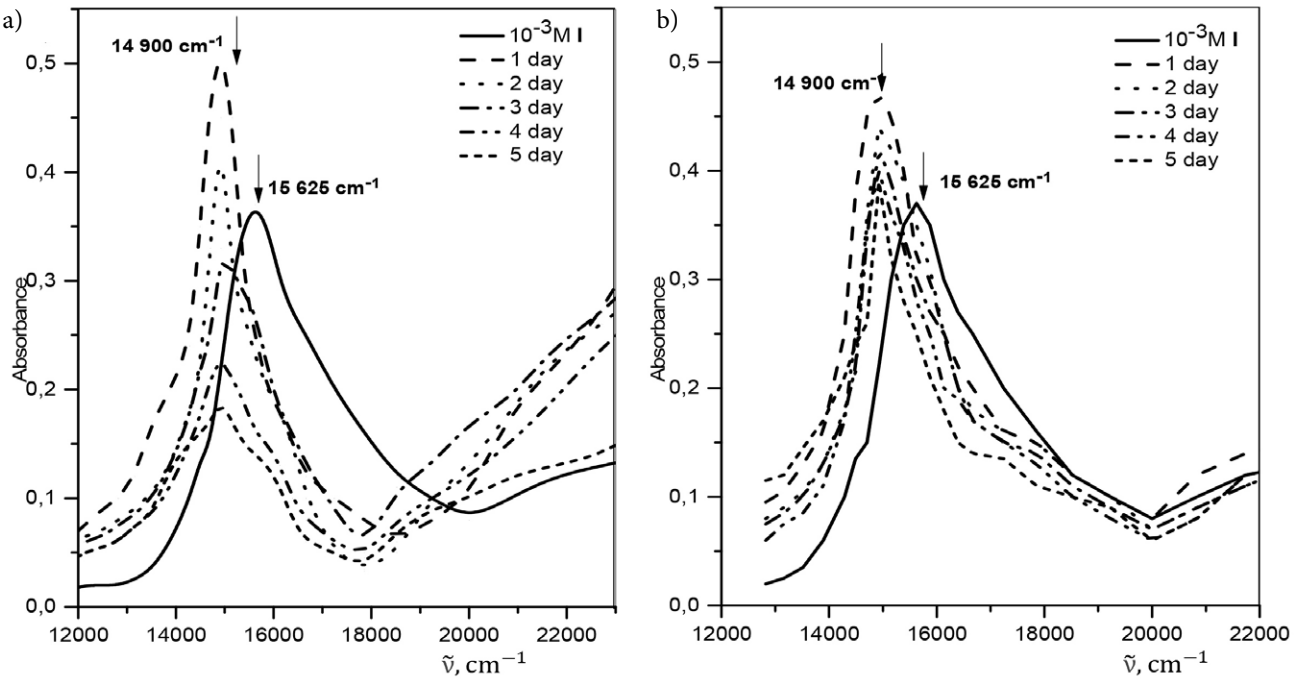

Fig. 2 EAS of the reaction mixture of **I** (10^{-3}M) and ZrP in IPA: a) at 1:30 ratio over time; b) at 1:5 ratio over time; control – IPA

maximum absorption in the area 20000 cm^{-1}, the bidentate coordinated tetra-μ-phosphates $[Re_2(HPO_4)_4(H_2O)_2]^{2-}$ and $[Re_2(HPO_4)_2(H_2PO_4)_2(H_2O)_2] \cdot 4H_2O$ had the δ→δ* absorption band at 15625 cm^{-1}. The replacement of carboxylic ligands on phosphate or chlorine groups would shift the absorption band δ→δ* to low energy region (bathochromic shift). So, the analogical spectral picture was expected to be seen in the present experiment.

Before starting the experiment, two important measurements were done: 1. The spectrum of ZrP in IPA was investigated, and no absorption in the area 12000–22000 cm^{-1} was detected; 2. The solution of **I** in IPA in concentration 10^{-3}M was heated at 60 °C during 5 days with spectral investigations and it was found that the intensity of the characteristic band of **I** (15625 cm^{-1}) was not changed. These measurements supported the idea, that any changes in the investigated area of the spectrum should be the reason of **I** and ZrP interactions.

On figure 2, EAS of the reaction mixtures of **I** with ZrP at 1:30 and 1:5 molar ratio over time are presented.

In both variants of the experiment, the sharp increase of intensity of the characteristic bond was noticed together with the shift from 15625 cm^{-1} to 14900 cm^{-1} that definitely indicated that there was an interaction of **I** with ZrP and formation of new complexes of **I** with phosphate groups from ZrP (**I**/ZrP) on the surface layers. Then the decrease of the intensity of the band 14900 cm^{-1} took place. To our mind, during the following process of intercalation, the concentration of **I** decreased due to penetration of **I** to interlayer space of ZrP. As more molecules of **I** penetrated to interlayer space and formed new complexes, as more the equilibrium **I** + ZrP ↔ **I**/ZrP was shifted to the side of the intercalation and formation of new complexes and accordingly we watched the decreasing of the characteristic band 14900 cm^{-1}.

Earlier it was shown by us, that dicarboxylates of dirhenium(III) reacted with POPC by substitution of axial chlorine groups on phosphate groups.[20,24] In our experiment we investigated the little bathochromic shift in the area of quadruple bond absorption that may propose the substitution of the carboxylic groups by phosphate from ZrP. But, it was proved, that dicarboxylates reacted with POPC by another type, i.e. by substitution of chlorine atoms on phosphate groups.[20,24]

The interaction of dicarboxylates with POPC was followed by a decrease of the bands 15400–15700 cm^{-1} and concomitant appearance of a new band at 12133 cm^{-1}, the intensity of which increased dramatically with time.[24] These two features are characteristics of a $Re_2(\delta) \rightarrow Re_2(\delta^*)$ electron transition for trans-dicarboxylates.[15] The process possibly involves the substitution of the chloride groups of dicarboxylates by POPC via oxygen atoms from the phosphate groups which initiates a cis-trans rearrangement of the bridging carboxylate ligand.

In our experiments, we did not detect the appearance of absorption in the area 12000 cm^{-1} that confirmed another mechanism of interaction without the formation of *trans*-product. Thus, the possible explanation of the spectral characteristic of the reaction mixture is the substitution of the DMSO in **I** by phosphate groups of ZrP without the formation of trans-derivatives and the only obtained product is the presented one on the Fig. 3 with remained *cis*-configuration.

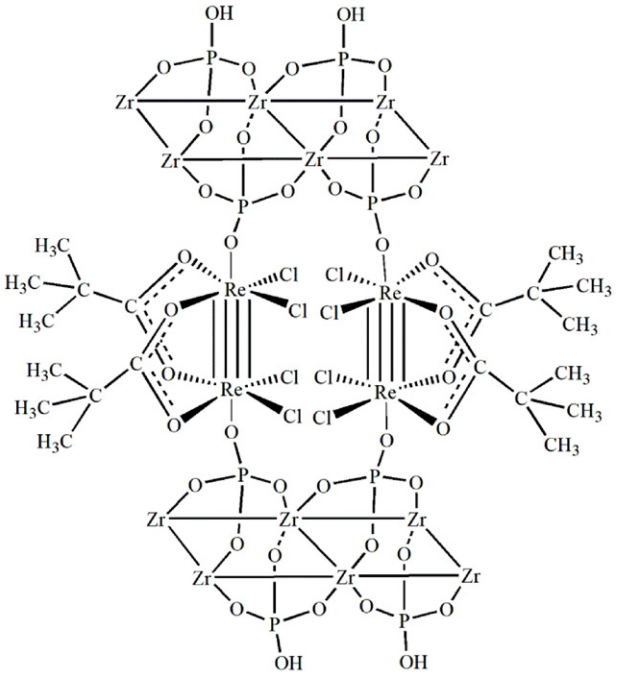

Fig. 3 The proposed formula of the product of the reaction between **I** and phosphate groups on the surface layers of ZrP

It is necessary to note, that the quadruple bond between two rhenium atoms has unique spectral properties: first to absorb in the visible area due to the δ→δ* transition of the spectrum, where no other organic molecules can absorb; second very important property of the band is the dependence of absorption from the number of organic ligands around cluster Re_2^{6+} fragment and their orientation. These two facts make it possible to demonstrate the mechanism of intercalation of the dirhenium(III) compound, which includes the modification of ZrP surface due to the coordination of its phosphate groups to the Re-Re core at first. Then the intercalation took place in ZrP inner layers. As to our knowledge, such mechanisms have not been shown yet for any intercalated substance.

3. 2. SEM

The SEM images of **I**/ZrP intercalation product 1:30 and 1:5 showed that hexagonal like shape of initial ZrP was stored (Fig. 4).

The average diameter of platelets is 104 nm for 1:30 adduct (Fig. 4A) and 120 nm for 1:5 adduct (Fig. 4B). The thickness for them is approximately 15.7 nm and 24.5 nm accordingly (Fig.4 C, D).

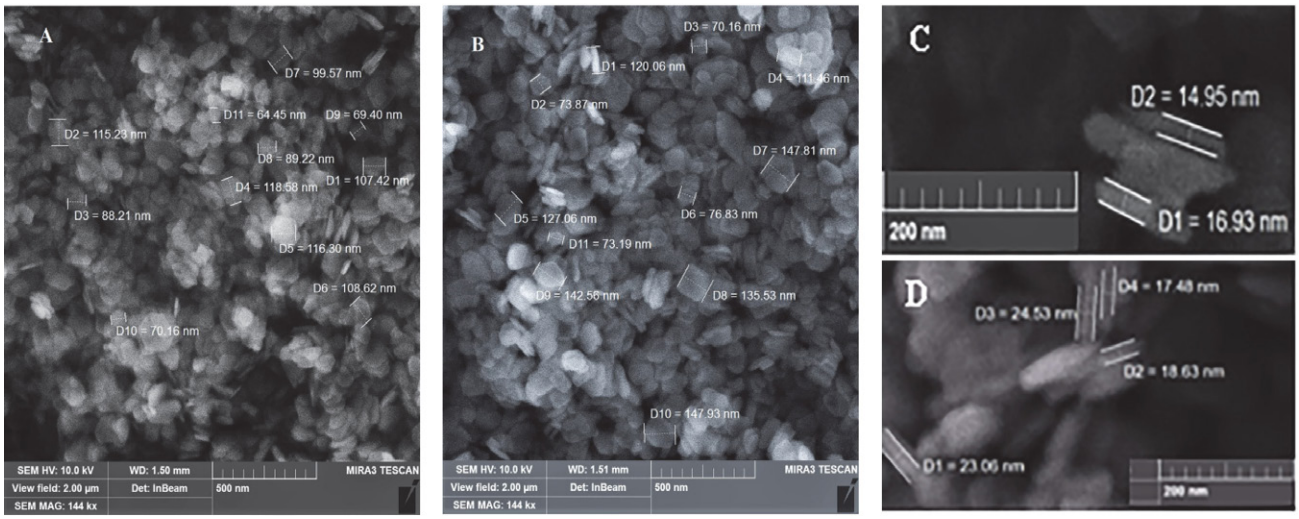

Fig. 4 The SEM images of the **I**/ZrP: A, C – 1:30, B,D – 1:5

Since the phosphate groups of ZrP are directed down and up relative to the plane, the rhenium(III) complex can coordinate on the surface of the nanoparticles as well. Such surface modification of ZrP with I was proved by EDX of intercalated material. Fig. 5 shows that the EDX spectrum for the I/ZrP intercalated product includes the characteristic peak indicating the presence of Re (8.1%) on the surface of the nanoparticles.

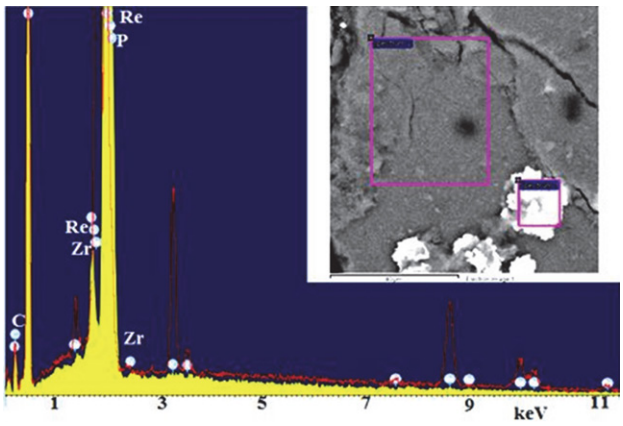

Fig. 5 EDX spectrum of I/ZrP 1:5

Zeta potential of both preparations **I**/ZrP is –37±2 mV showing that obtained nanoplatelets are stable in an aqueous medium.[12] The obtained nanoparticles have a platelet-like shape. Such shapes were shown to have some advances in comparison to spherical ones due to better adhesion, margination and binding properties. For example, the binding probability of nanorods was found to be three times higher than that of nanospheres with the same volume.[28] The obtained SEM data together with spectral investigations point that ZrP can be used as a matrix for cluster rhenium(III) with *cis*-configuration of carboxylate ligands.

3. 3. X-ray Powder Diffraction

The reaction of intercalation of **I** into interlayers is topotactic,[6] i.e. solid-phase reaction during which the packaging of atoms in the crystal of the reagent is practically the same, only distances between some atoms in several directions are changing. The diffraction peaks at the lowest 2θ angle correspond to the interlayer distance which depends on the intercalated substance.[29] The XRPD patterns of **I**/ZrP for molar ratios 1:30 and 1:5 show the appearance of new peaks (Fig. 6 B, C), indicating the formation of new phases.

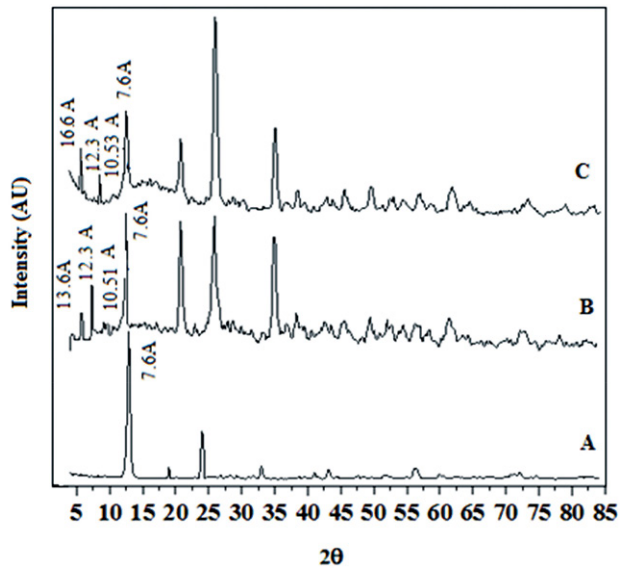

Fig. 6 X-ray diffraction α-ZrP (A), **I**/ZrP 1:30 (B) and **I**/ZrP = 1:5 (C)

In the absence of intercalated substances, the distance between layers of α-ZrP corresponds to 7.6 Å (Fig. 6A). The presence of this peak in the diffraction patterns of the intercalation products indicates that formed phases are

mixed. The intensity of this peak is lower in patterns B and C than in A, pointing to the reduction of this phase with increasing concentration of **I**.

Formations of new phases are followed with appearance of first-order diffraction peak 13.59 Å for **I**/ZrP 1:30 (Fig. 6B) and 16.6 Å for **I**/ZrP = 1:5 (Fig. 6C); besides, both composites show the second and the third peaks: 12.28 Å and 10.53 Å for **I**/ZrP 1:30 (Fig. 6B); 12.3 Å and 10.51 Å for **I**/ZrP = 1:5 (Fig. 6C).

Three-dimensional structure and lineal dimensions of **I** are presented on Fig. 7.

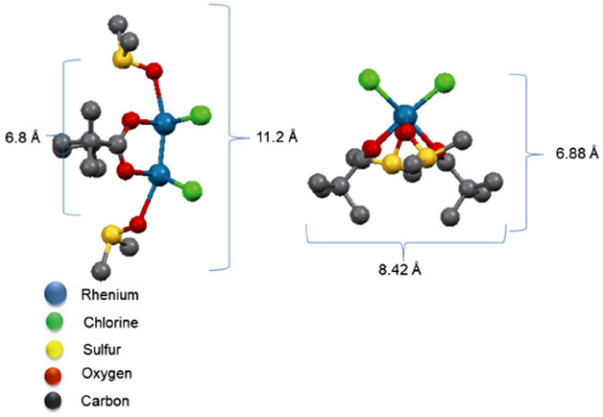

Fig. 7 Structure of **I** showing its dimensions as calculated by Mercury

If lineal dimensions for **I** molecule are known 11.2 x 8.42 x 6.88 Å3 and are presented on the Fig. 7, and interlayer distance in ZrP is also known to be 6.6 Å, this allows us to predict the interlayer distances in the newly formed phases and approximate coordination of the **I** molecules between ZrP layers. For instance, for **I**/ZrP 1:30 the shown interlayer distance 13.59 Å may correspond to disposition of **I** molecules parallel to ZrP layers (6.88 Å + 6.6 Å = 13.48 Å); accordingly the diffraction peak 16.6 Å may correspond to perpendicular disposition of **I** to ZrP layers (11.2 Å + 6.6 Å = 17.8 Å). A little decrease between calculated and real distances may be explained by compressing of ZrP layers and/or by hiding (interaction) of branched ligands of **I** into so-called "pockets" of ZrP.[6]

Thus, the analysis of XRPD patterns of newly synthesized **I**/ZrP products gives confirmation about the formation of new intercalated products and imagination about a possible disposition of **I** between layers of ZrP.

3. 4. FT-IR Data.

The obtained FT-IR data for **I**/ZrP 1:30 and 1:5 were identical, so we demonstrate data only for the first one in comparison with primary substances (Fig. 8).

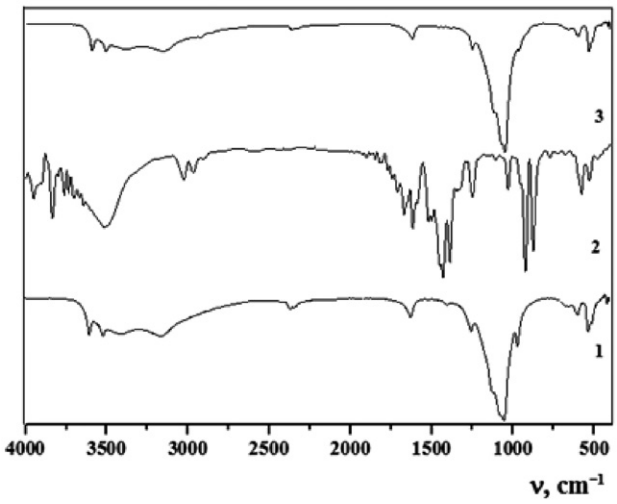

Fig. 8 FT-IR spectra of ZrP (1); **I** (2); **I**/ZrP 1:30 (3)

The data presented in the table and in the Fig.8 show the disappearance of the absorption bands in **I**/ZrP 1:30 characteristic for **I** structure, indicating that **I** is absent on the surface of the composite and support the earlier speculations about successful intercalation procedure. The only difference in spectra of initial ZrP and the complex **I**/ZrP is the absence of the band 1100–940 cm^{-1} in the last one referred to fluctuations of phosphate groups that may occur due to involvement of phosphate groups in the reaction.

3. 5. TGA Analysis.

Thermograms of both intercalation products show three weight losses (Fig.9).

First weight loss under 120°C corresponds to the loss of coordinated water in zirconium phosphate; the second

Table 1: Characteristic frequencies (cm^{-1}) and their correspondence in the FT-IR spectra of **I**, ZrP and **I**/ZrP 1:30

Substance	$\nu_s(CO)$	δ_{as}, ν_s $(C(CH_3)_3COO-)$	$\nu_s(H_2O)$, $\nu_s(OH-)$	ν_s *(DMSO)*	$\nu_s(P-O)$, $\nu_s(P-OH)$	$\nu_s(M-O)$
I	1420	2800 1470–1430	3500	1225–980	–	390–480
ZrP	–	–	1620 3500	– –	1200 1100–940	522
I/ZrP 1:30	–	–	1620 3500	–	1200	522

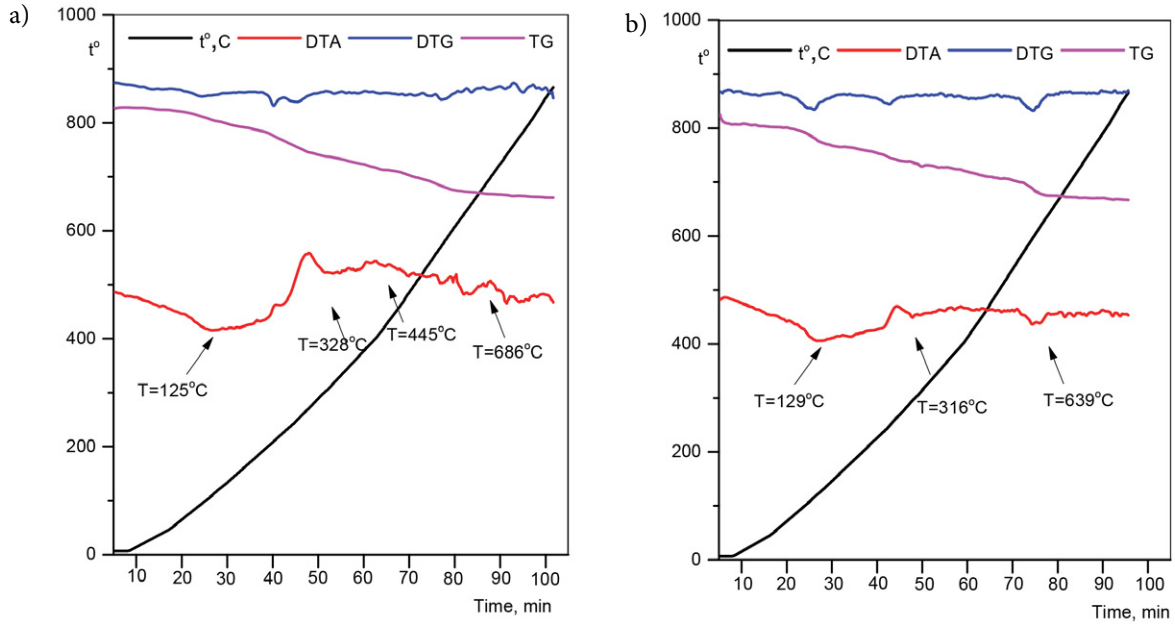

Fig. 9 Thermograms of **I**/ZrP: a) **I**/ZrP 1:5; b) **I**/ZrP 1:30.

under 250–350 °C – to the thermo destruction of **I** with the formation of the trans-isomer;[30] and the third – to condensation of phosphate groups and the formation of zirconium pyrophosphate. [31]

The weight losses in the first and second stages of thermograms for the **I**/ZrP 1:5 were: 9%; 13.2% (Fig. 9A) and for the **I**/ZrP 1:30 9%; 10% (Fig. 9B). Low levels of weight loss could be the result of quickly temperature increasing, so we decided to undertake another modification of thermal destruction investigation (see Materials and methods), i.e. method of thermal exposures. In this modification method following weight losses for the **I**/ZrP 1:5 were: 8.87% under 120 °C; 29.89% under 250–350 °C of heating and for **I**/ZrP 1:30 9.8% and 10.9% accordingly.

3. 6. Drug Loading Studies.

The time-depending drug encapsulation efficiency (EE) studies of **I**/ZrP 1:5 and **I**/ZrP 1:30 (Fig. 10) showed not so rapid uptake of **I** as it was found for example for curcumin (120 min).[2]

This may be explained by more necessary time for the reaction of substitution in comparison with time for the formation of hydrogen bonds between the hydroxyl groups of curcumin and negatively charged phosphate groups of ZrP. The maximum EE (66%) was reached only on the 5th day for **I**/ZrP 1:30 and 26% for **I**/ZrP 1:5.

Our further investigations are aimed at obtaining the mixed composites (for example **I** + cisplatin, or **I** + doxorubicin) and on studying their biological activities. This direction is very promising due to the following reasons: anticancer properties of solely introduced **I** and some alkyl carboxylates were not very essential, as it is known about introduction of other cytostatics; the group of Prof. A. Clearfield recently have shown good perspectives of ZrP composites as medicines[31,32] as in several biological models ZrP-composites were shown to be more active than free substances.

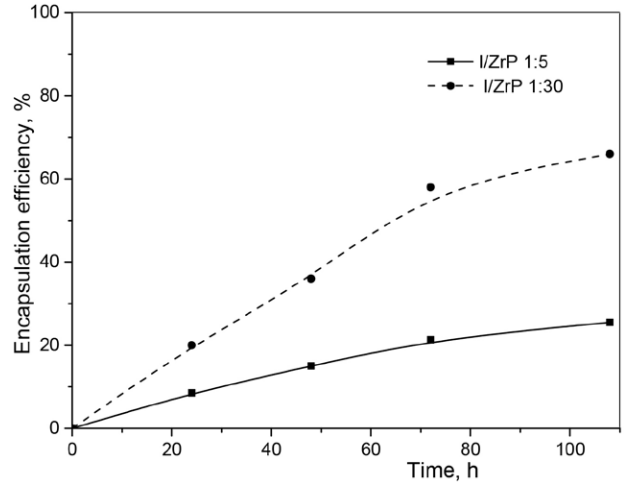

Fig. 10 Time-dependent **I** encapsulation efficiency of ZrP nanoplatelets

4. Conclusions

The method of intercalation of **I**, the representative of cis-carboxylate of dirhenium(III) compounds, into θ-ZrP was elaborated. The possible mechanism of intercalation is the substitution of the axial ligands by the layers phosphate groups to the cluster center Re_2^{6+} producing new phases with interlayer distances of 10.53–16.6 Å and the average size of platelets 100–200 nm. Two received

products of the intercalation process were characterized by appropriate methods. The existence of the quadruple bond in the structure of **I** made it possible to demonstrate the mechanism of intercalation of the dirhenium(III) compound. The obtained result is the starting point for the synthesis of mixed ZrP nanocarriers on the base of quadruple-bonding compounds with promising biological properties.

Acknowledgments

We are grateful to the Ministry of Education and Science of Ukraine (Grants 0107U000528 and 0111U000111) the studies were supported by.

5. References

1. W. J. Roth, B. Gil, W. Makowski, B. Marszaleka and P. Eliasova, *Chem. Soc. Rev.* **2016**, *45*, 3400–3438. **DOI:**10.1039/C5CS00508F
2. H. Kalita, B. N. Prashanth Kumar, S. Konar, S. Tantubay, M. Kr. Mahto and M. Mandal, *Mater. Sci. Eng: C.* **2016,** *60,* 84–91**.** **DOI:**10.1016/j.msec.2015.11.010
3. J. Gonzalez-Villegas, Y. Kan, V. I. Bakhmutov, A. Garcia-Vargas, M. Martinez, A. Clearfield and J. L. Colon, *Inorg. Chim. Acta*. **2017**, *468*, 270–279. **DOI:**10.1016/j.ica.2017.05.057
4. A. Diaz, V. Saxena, J. Gonzalez, A. David, B. Casanas, C. Carpenter, J. D. Batteas, J. L. Colon, A. Clearfield and M. D. Hussain, *Chem. Commun*. **2012**, *48*, 1754–1756. **DOI:**10.1039/c2cc16218k
5. A. A. Marti and J. L. Colon, *Inorg. Chem*. **2003**, *42***,** 2830–2832. **DOI:**10.1021/ic025548g
6. A. Diaz, A. David, R. Perez, M. L. Gonzalez, A. Baez, S. E. Wark, P. Zhang, A. Clearfield and J. L. Colon, *Biomacromolecules*. **2010**, *11***,** 2465–2470. **DOI:**10.1021/bm100659p
7. A. A. Marti, N. Rivera, K. Soto, L. Maldonado and J. L. Colon, *Dalton Trans.* **2007**, *17*, 1713–1718. **DOI:**10.1039/B618802H
8. A. Clearfield, R. H. Blessingt and J. A. Stynes, *J. Inorg, nucl. Chem*. **1968**, *30*, 2249–2258. **DOI:**10.1016/0022-1902(68)80224-6
9. U. Costantino, *J. Chem. Soc., Dalton Trans.* **1979**, *2*, 402–405. **DOI:**10.1039/dt9790000402
10. R. Backov, D. J. Jones and J. Roziere, *Chem. Commun*. **1996**, *1*, 599–600. **DOI:**10.1039/CC9960000599
11. F. Carn, A. Derre, W. Neri, O. Babot, H. Deleuze and R. Backov, *New J. Chem.* **2005**, *29*, 1346–1350. **DOI:**10.1039/b507960h
12. V. Saxena, A. Diaz, A. Clearfield and J. D. Batteas, M. D. Hussain, *Nanoscale*. **2013**, *5*, 2328–2336. **DOI:**10.1039/c3nr34242e
13. S. Shakshooki, B. E. Ali, S. El-Rais and M. El-Rais, *Am. J. Chem*. **2014**, *4*, 22–28.
14. N. Shtemenko, A. Shtemenko *Ukr. Biochem. J.*. **2017**, *89*, 5–26. **DOI:**10.15407/ubj89.02.005
15. N. Shtemenko, K. Domasevich, E. Zabitskaya and A. Golichenko, *J. Chem. Soc., Dalton Trans.* **2009**, *26*, 5132–5136. **DOI:**10.1039/b821041a
16. N. I. Shtemenko, H. T. Chifotides, K. V. Domasevich, A. A. Golichenko, S. A. Babiy, Z. Li, K. V. Paramonova, A. V. Shtemenko and K. R. Dunbar, *J. Inorg. Biochem.* **2013**, *129*, 127–134. **DOI:**10.1016/j.jinorgbio.2013.09.001
17. A. A. Golichenko, K. V. Domasevitch, D. E. Kytova and A. V. Shtemenko, *Acta Cryst.* **2015**, *71*, 45–47. **DOI:**10.1107/S2056989014026620
18. I. V. Leus, I. A. Klenina, K. A. Zablocka, A. A. Golichenko, A. V. Shtemenko and N. I. Shtemenko, *Biopolymers and Cell.* **2011**, *27*, 465–471. **DOI:**10.7124/bc.000119
19. K. L. Shamelashvili, N. I. Shtemenko, I. V. Leus, S. O. Babiy and O. V. Shtemenko, *Ukr. Biochem. J*. **2016**, *88*, 29–39. **DOI:**10.15407/ubj88.04.029
20. N. Shtemenko, O. Berzenina, D. Yegorova and A. Shtemenko, *Chem. Biodivers*. **2008**, *5*, 1660–1667. **DOI:**10.1002/cbdv.200890153
21. Y. Zhu, T. Shimizu, T. Kitajima, K. Morisato, N. Moitra, N. Brun, T. Kiyomura, K. Kanamori, K. Takeda, H. Kurata, M. Tafu and K. Nakanishi, *New J. Chem.* **2015**, *39*, 2444–2450. **DOI:**10.1039/C4NJ01749H
22. F. Xia, H. Yong, X. Han and D. Sun, *Nanoscale Res. Lett.* **2016**, 11, 1–7. **DOI:**10.1186/s11671-016-1559-6
23. E. J. Rivera, C. Figueroa, J. L. Colon, L. Grove and W. B. Connick, *Inorg.Chem.*, **2007**, *46*, 8569–8576. **DOI:**10.1021/ic7006183
24. Z. Li, N. I. Shtemenko, D. Y. Yegorova, S. O. Babiy, A. J. Brown, T. Yang, A. V. Shtemenko and K. R. Dunbar *J Liposome Res*. **2015**, *25*, 78–87. **DOI:**10.3109/08982104.2014.954127
25. I. V. Leus, I. O. Klenina, K. A. Zablotska, O. A. Golichenko, O. V. Shtemenko, N. I. Shtemenko *Biopolymers and Cell*. **2011**, *27*, 465–471 (In Ukrainian). **DOI:**10.7124/bc.000119
26. A.V. Slipkan, D.E. Kytova, A.V. Shtemenko, *Ukr.* Chem. *J.* **2017**, *83*, 35–41 (In Ukrainian).
27. A.V. Slipkan, D.E. Kytova, A.V. Shtemenko, *Voprosy khimii i khimicheskoi tekhnologii*. **2018**, *2*, 39–45 (In Ukrainian).
28. S. Shah, Y. Liu, W. Hu and J. Gao, *J. Nanosci. Nanotechnol.* **2011**, *11*, 919–928. **DOI:**10.1166/jnn.2011.3536
29. H. Maeda and Y. Matsumura, *Adv. Drug. Deliv. Rev.* **2011**, *63*, 129–130. **DOI:**10.1016/j.addr.2010.05.001
30. M. Iziumskyi, S. Melnyk and A. V. Shtemenko *Chem. Met. Alloys*. **2013**, *6*, 121–124. **DOI:**10.30970/cma6.0246
31. B. M. Mosby, A. Diaz, V. Bakhmutov and A. Clierfield, *ACS Appl. Mater. Interfaces*. **2014**, *6*, 585–592. **DOI:**10.1021/am4046553
32. A. Diaz, M. L. Gonzalez, R. J. Perez, A. David, A. Mukherjee, A. Baez, A. Clearfield and J. L. Colon, *Nanoscale,* **2013**, *5*, 11456–1146. **DOI:**10.1039/c3nr02206d

Povzetek

V prispevku poročamo o sintezi kompozita nanodelcev cirkonijevega fosfata (θ-$Zr(HPO_4)_2 \cdot 6H_2O$ (ZrP)), ki vsebujejo spojino renija(III) (*cis*-$Re_2(C(CH_3)_3COO)_2Cl_4 \cdot 2DMSO$ (**I**)). Proces interkalacije smo spremljali z elektronsko absorpcijsko spektroskopijo (EAS). Na osnovi spektroskopskih podatkov smo sklepali, da so ligandi v okolici klastra direnijevega(III) fragmenta razporejeni v *cis* konfiguraciji. V predlaganem mehanizmu interkalacije smo predvideli substitucijo aksialnih ligandov **I** s fosfatnimi skupinami ZrP najprej na površini nanodelcev ZrP, kasneje pa tudi v notranjih plasteh. Dva produkta procesa interkalacije smo karakterizirali z naslednjimi metodami: vrstično elektronsko mikroskopijo (SEM), rentgensko praškovno difrakcijo (XRPD), infrardečo spektroskopijo (FT-IR) in termogravimetrično analizo (TGA). V produktih je bila razdalja med plastmi od 10,53 Å do 16,6 Å, povprečna velikost ploščič pa od 100 nm do 200 nm.

Except when otherwise noted, articles in this journal are published under the terms and conditions of the Creative Commons Attribution 4.0 International License

DOI: 10.17344/acsi.2019.5513 *Acta Chim. Slov.* **2020,** *67,* 496–506
creative commons

Scientific paper

Effective Adsorption of Doxorubicin Hydrochloride on the Green Targeted Nanocomposite

Omid Arjmand,[1] Mehdi Ardjmand,[1,*] Ali Mohammad Amani[2] and Mohmmad Hasan Eikani[3]

[1] *Department of Chemical Engineering, South Tehran Branch, Islamic Azad University, Tehran, Iran.*

[2] *Department of Medical Nanotechnology, School of Advanced Medical Sciences and Technologies, Shiraz University of Medical Sciences, Shiraz, Iran.*

[3] *Department of Chemical Technologies, Iranian Research organization of Science and Technology (IROST), P.O. Box 33535111, Tehran, Iran.*

* *Corresponding author: E-mail: m_arjmand@azad.ac.ir*

Received: 08-22-2019

Abstract

This study examined the adsorption properties of the doxorubicin anticancer drug on a designed and fabricated system. A novel nanocomposite based on green magnetic – *Graphene* Oxide – Chitosan – Allium Sativum – Quercus was successfully fabricated. To evaluate the doxorubicin adsorption, the effectiveness parameters on the adsorption process were investigated including the contact time, pH value, concentration, the adsorbent dosage, and temperature. The results indicated that the maximum adsorption of doxorubicin on the fabricated nanocomposite occurred at pH 6.3, concentration 3.6 mg/1.8 ml, contact time 10 minutes, and the adsorbent dosage 1.4 g/L. This designed system not only increased the drug adsorption up to 100%, but it also can absorb low concentrations of doxorubicin. This suggests that the current challenge in using the higher concentrations of doxorubicin could be essentially minimized thanks to the excellent components used in the nanocomposite structure. The developed system has greatly improved DOX adsorption, confirming that the fabricated nanocomposite could be applied for a drug delivery.

Keywords: Adsorption, Doxorubicin, Nanocomposite, Natural Components, Functional Groups

1. Introduction

Graphene oxide (GO) with various functional groups including hydroxyl, epoxy, and carboxyl is gaining popularity in different areas such as chemistry, materials, physics, and medicine.[1] Modified GO has been explored via covalent or non-covalent bands as a desired carrier for targeted drug delivery.[2] As hydrophobic drugs can be loaded on graphene sheets by π–π starching, so nanocomposite design based on graphene for targeted drug delivery have been explored.[3] Doxorubicin (DOX) as a strong anticancer agent belongs to the Adriamycin (ADM) groups which is widely utilized in the free form or combined with other drugs for cancer treatment. During the DOX injection the normal cells are also damaged and the unwanted serious side effects such as myelotoxicity and the cumulative cardiotoxicity limits its therapeutic index. Nanoparticle drug delivery system (NDDS) has attracted great attention by binding a functional ligand to reduce the side effects on normal organs.[4] To reach the best therapeutic outcomes, several nanoparticles in combination with DOX have been designed to overcome this challenge. An electrostatic interaction between the positively charged amine moiety of DOX and the negatively charged of nanoparticles facilitates the DOX adsorption on the surface.[5] During a reversible process on the carbon nanotube (CNT), the adsorbed and encapsulated DOX in the inner space CNT can easily cross through the cell membrane.[6] The molecular interaction between the carboxylate groups and amino groups of the adjoined DOX with Fe_3O_4@SiO_2-Glu cause DOX to be strongly adsorbed via the chemisorptions process without any degradation.[7] The molecular dynamics (MD) simulation of the adsorbed doxorubicin (DOX) drug on covalent functionalized carbon nanotubes (CNTs) revealed that the molecular interactions of DOX with f-CNTs can provide the drug release as well.[8] The release kinetics of DOX load-

ed on mesoporous silica nanoparticle and the desired dosage of the active ingredient is associated with the initial drug adsorption and affects the extent of the adsorbed ingredien.[9] Protein competition, lower pH values, and the short adsorption time significantly facilitate doxorubicin desorption on oxidized carbon nanotubes.[10] As reported in the literature the electrostatic interactions between the negatively charged nanoferrite surface and the positively charged DOX molecules, leaded to an enhanced and effective adsorption of the drug.[11] The adsorption rate of DOX on poly (methyl methacrylate) – chitosan-heparin-coated with the activated carbon was significantly reduced with an increase in the loaded heparin content.[12] In this study, to illustrate the mechanism of interaction between DOX molecules and a designed biocompatible nanocomposite, adsorption analysis has been studied. The adsorption of doxorubicin, as a strong anticancer agent on the carrier surface, plays an important role in targeted treatment. Hence, a novel system based on the strong and more effective components is absolutely necessary for the drug adsorption. A novel targeted composite was designed and fabricated based on various functional groups used in its structure for further adsorption of DOX. The literature has not reported DOX adsorption on a nanocomposite based on chitosan and the natural components. The more effective functional groups existing at the natural component of allium sativum such as the hydroxyl, amino, and carboxyl groups be effectively interacted with amino group and the phenolic structure of DOX. Allium sativum used at the nanocomposite structure owing to its much effective components such as polyphones is leaded that the further functional groups of OH be formed and the surface charge of nanocomposite be essentially promoted, resulting the positively charged surface of the DOX molecule to be rapidly adsorbed on the fabricated nanocomposite. Indeed, the more effective functional groups existing at natural component of allium sativum and quercus such as the hydroxyl, amino, and carboxyl groups is effectively interacted with the phenol structure and aromatic ring of the DOX molecule. Chitosan as a natural polymer play an important role at the nanocomposite structure and it can help to adjoined all nonocomposite components effectively; therefore it acts as cross linker especially in the solution while the phenol group of DOX could be adsorbed onto the gel like-structure of chitosan. In addition, due to the physicochemical characterization of tumor tissue and existing of the polysaccharide receptors, chitosan will increase the cellular adsorption and further amount of the loaded drug could be released at the targeted sites. The polyphenolic molecules of the natural component as one of the most important targeted ligands could blind with amino group of the DOX molecule, resulting the drug adsorption on the designed nanocomposite be increased. Amino group of chitosan with the negative charge interact with the negative active functional groups. Taking it on consideration and investigation of the research works in literature this novel system due to the used superior components could absorb further concentration of DOX.

2. Experimental Section

2. 1. Chemical & Reagents

Iron (III) chloride hexahydrate, iron(II) chloride tetrahydrate (99%), natural graphite flakes with average particle size of 150 μm and purity of > 98%, doxorubicin hydrochloride, hydrogen peroxide (H_2O_2), potassium permanganate ($KMNO_4$), phosphoric acid (H_3PO_4), $FeCl_3$ $6H_2O$, $FeSO_4$ $7H_2O$, phosphate buffer solution (PBS), ammonia (NH_3), acid clohidric (HCl), hydroxide sodium (NaOH), n-hexane, chitosan. The all chemical components used at this research were purchased from the Sigma-Aldrich Company.

2. 2. Natural Components

Allium sativum from Hamadan province in western Iran, Quercus brantii and Alhagi maurorum from Fars province in southwestern Iran were obtained as natural components.

2. 3. Methodology

To evaluate and determine the DOX adsorption on the fabricated nanocomposite, the batch experiments at different temperature, pH, dosage, contact time, and the concentration of DOX were conducted. The pH value of the samples was adjusted using the diluted solutions of NaOH and HCl (0.1 M). In order to evaluate the adsorbed amounts of the DOX drug, the related experiments were accomplished at ranges from 190 to 800 nm by ultraviolet visible (UV-Vis) absorption spectrometer (Agilent technologies Cary Series UV/VIS Spectrometer model). For this case, the related experiments were conducted under the batch condition by dispersing the fabricated nanocomposite in 25 ml solution containing the DOX drug at various conditions such as alteration of temperature, pH, the nanocomposite dosage and the drug concentration. Subsequently, the prepared solution including the determined concentration of DOX and nanocomposite was sonicated as well at speed 4500 rpm for 5 minutes.

2. 4. Synthesis of Graphene Oxide (GO)

The modified Hummers method was used to synthesize the GO nanosheets as reported in the literature.[13,14]

2. 5. Preparation of Alhagi Maurorum Essential Oil

The essential oil of Alhagi Maurorum using the clevenger apparatus was extracted according to the literature.[14,15]

2. 6. Preparation of Allium Sativum and Quercus Powder

Allium sativum species belong to Hamadan province located in the west of Iran was prepared. It is peeled, chopped and washed with the deionized water and then allowed to be dried in the oven (50 °C) for 24 h. The dried allium sativum particles was crushed and mixed in a ball mill for 24 h and the prepared powder stored at 4 °C. Quercus (oak) powder was also prepared according to mentioned approach.[14]

2. 7. Preparation of Green Magnetic/ Graphene Oxide / Chitosan / Allium Sativum / Quercus Nanocomposite

The green magnetic – graphene oxide (GO) – chitosan (CS) – allium sativum – quercus nanocomposite was successfully fabricated as reported in the literature. [14, 16]

3 Results and Discussion

3. 1. Analysis of the Adsorption and Observations

To better understand the interaction mechanism between the DOX molecular and the fabricated nanocomposite, the surface adsorption analysis was performed. The adsorption peak of drug on the nanocomposite surface at wavelengths 290 and 482 nm as λ max value was shaped.

3. 2. Characterization

The functional groups and the surface morphology of the fabricated nanocomposite were analyzed by FTIR and SEM techniques, respectively and reported in our previous work.[14]

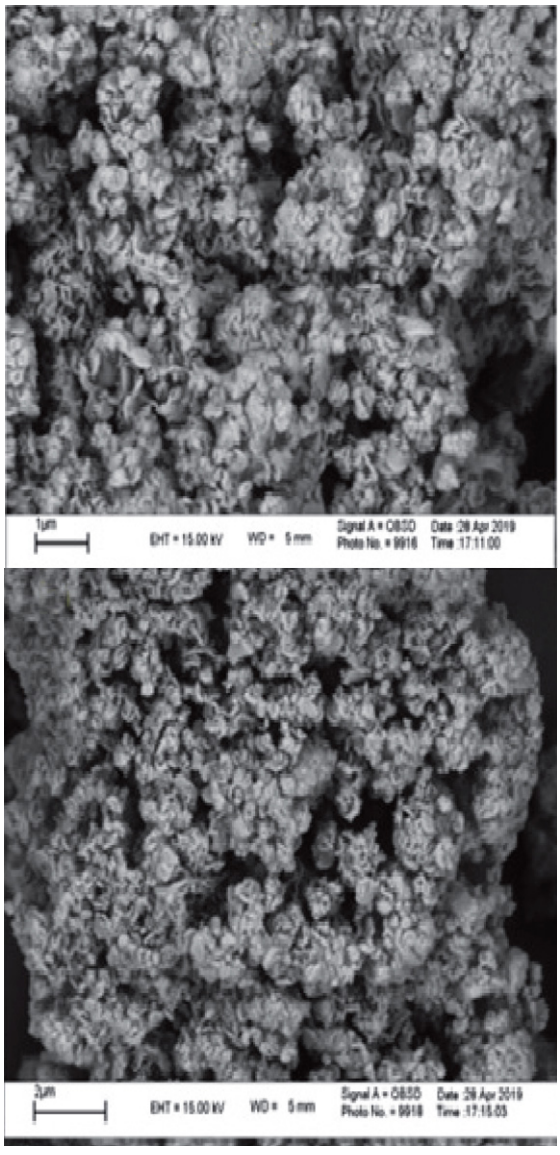

Figure 2. SEM image of fabricated nanocomposite

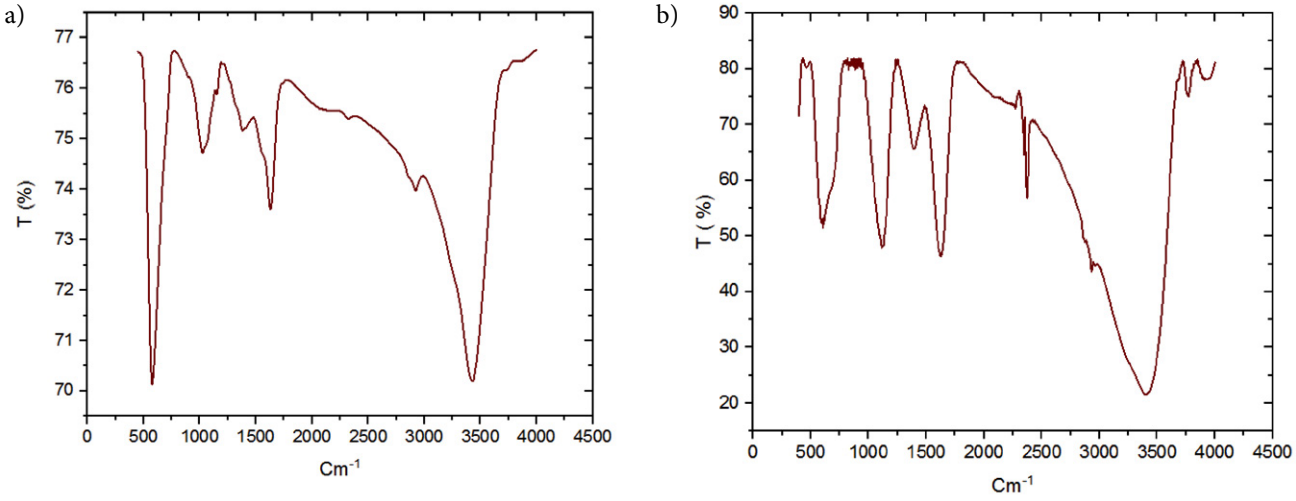

Figure 1. Fourier transform infrared spectroscopy (FTIR) spectra of a (Mn / GO / CS/ A. sativum / Que) b (GrMn / GO / CS / A. sativum / Que)

The surface morphology of the designed nanocomposite was analyzed by scanning electronic microscopy (SEM). SEM image shows a high density surface with the active sites, revealing that the magnetic chitosan particles and natural components have been assembled on the GO layers (Figure 2). The observed roughness on the agglomerated and compacted regions is associated with magnetic iron oxide particles. As it can be seen, the GO layers have been basically covered with the uniform coverage of particles leading that leaded to the development of the spherical spiral structure.[14] The combination and interactions between the chitosan active sites and the functional groups of the natural ingredients in the nanocomposite structure resulted in the formation of the non-uniform pores at the nanocomposite bulk and also further liquid phase accumulation occurred in the pores created between the active sites on the nanocomposite surface. Moreover, it is observed that the accumulated particles have been formed due to the strong interaction between CS and the natural ingredients used on the chemically improved GO surface. The observed multilayer structure has been formed from the combination of non-uniform porous cavity and the stacked and agglomerated particles resulting in creation of more active sites.

3. 3. Effect of pH

As the pH of the aqueous solution impacts on both surface charge and ionization degree of the adsorbent, pH of the supernatant and its effect as key parameter at adsorption process using the stock concentration 3.6 mg / 1.8 ml of DOX was analyzed and investigated. Figures 3 and 4 display the pH effect of initial solution on the adsorbed doxorubicin. As seen in Figure 3, the adsorption maximum was observed at pH 6.3 for green magnetic - graphene oxide – chitosan – allium sativum – oak (quercus) (Gr Mn - GO - CS - A. sativum - Que) nanocomposite and by increasing the initial pH from 2.87 to 6.3, the adsorption capacity was increased and the maximum amount of adsorption was observed at pH 6.3. As observed, the drug adsorption in the pH value above 6.3 is reduced, which may be attributed to the surface charge alteration and the formed bounds related to the functional groups. Regarding the colure alteration of DOX in the pH above 8.5 the adsorption capacity decreased basically, so can be concluded that at this range the DOX drug has strongly reacted with the nanocomposite. As observed for magnetic - graphene oxide – chitosan – allium sativum quercus nanocomposite without using the more effective component of the alhagi maurorum, the pH alterations has less effect on the adsorption and the adsorption maximum was seen at the higher acidity of solution, while chemically improved Gr Mn-GO-CS- A. sativum, Que nanocomposite because of the alhagi maurorum essential oil used at nanocomposite structure created the more effective functional groups with further negatively-charged and it depends basically on pH. It has not been reported the adsorption process of DOX on GO-CS and nanocomposite based on them, but reportedly[17] that the maximum of DOX adsorption on graphene oxide take place at pH = 8.5, considering that the DOX stability by increasing pH decreases, consequently the made nanocomposite for the DOX adsorption is very suitable and in comparison with GO the adsorbed drug can be better released.[18] The adsorbed DOX on glutaric anhydride functionalized Fe_3O_4@SiO_2 magnetic nanoparticles at acidity condition is much less than the fabricated nanocomposite.[7]

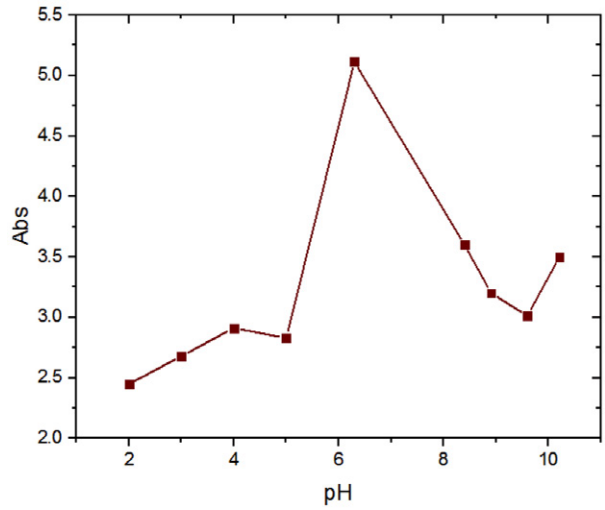

Figure 3. Effect of pH alterations of (Gr Mn / GO / CS / A. sativum / Que) on drug adsorption

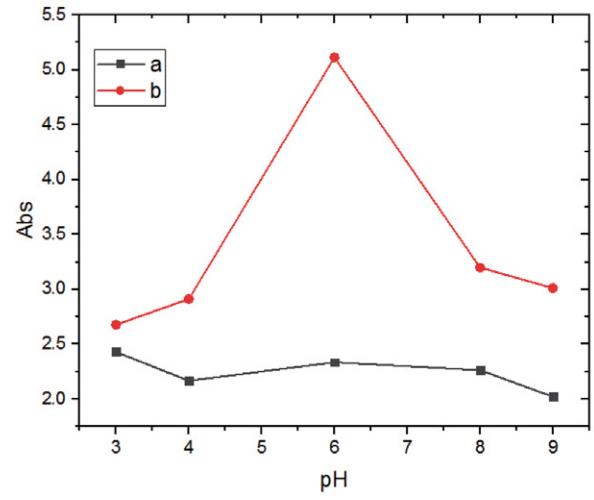

Figure 4. Effect of pH on the drug adsorption a (Gr Mn / GO / CS / A. sativum / Que), b (Mn / GO / CS / A. sativum / Que)

3. 4. Effect of Contact Time

The contact time effect of the DOX drug on the made nanocomposite surface at concentration 3.6 mg/1.8 ml, pH 6.3 and temperature 298 °K was studied. As seen in

Figure 5, the adsorption process takes place rapidly and after 20 minutes the adsorption capacity reaches its equilibrium state. Meanwhile, the maximum amount of adsorption after 10 minutes of the contact time was observed. The achieved results showed that by increasing the contact time up to 10 minutes, the maximum drug adsorption took place on the nanocomposite surface. Therefore, 10 minutes of the stirring time was considered as the optimal mixing time. After 10 minutes by increasing the contact time, adsorption become constant and after 20 minutes be gradually decreased which may be due to a decrease of the active sites and the driving force. Further, after 5 minutes of mixing the adsorption peak at the lower wavelength 290 nm shies to 300 nm and the higher peak of adsorption (482 nm) is prolonged to 300 nm. This designed system in comparison with GO / vitamin C with 24 h of contact time has very higher potential for DOX adsorption. [19]

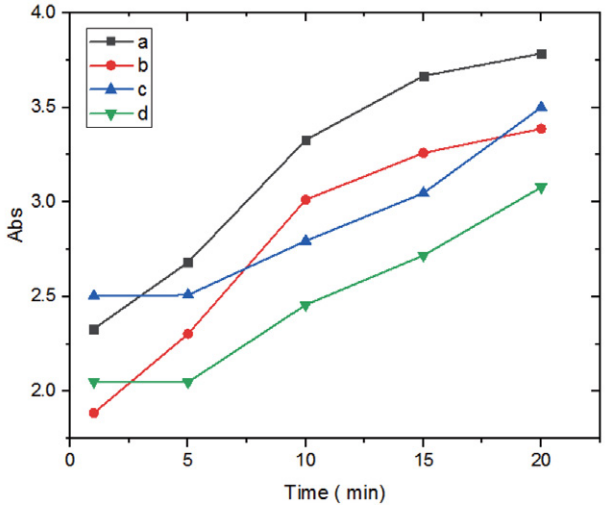

Figure 5. The effect of contact time on drug adsorption a, (Dosage = 1.6 gr / L, λ max = 482) b (Dosage = 1.6 gr / L, λ max = 290) c (Dosage = 0.8 gr / L, λ max = 482) d (Dosage = 0.8 gr / L, λ max = 290)

3. 5. Effect of Nanocomposite Dosage

The effect of nanocomposite dosage on the DOX adsorption at pH 6.3, was investigated. As observed from Figure 6, by increasing the nanocomposite amount from 0.8 gr / L to 1.6 gr / L, the drug adsorption has essentially increased and at 1.6 gr / L the DOX adsorption reached its maximum amount. As expected, by increasing the nanocomposite dosage due to the more availability of the active sites, the drug adsorption be increased. With further increase at nanocomposite dosage from 2 gr / L to 2.4 gr / L the adsorption capacity has been significantly increased. Indeed, increase of the drug adsorption at this range is due to the saturated concentration of nanocomposite and instability of the aqueous solution at the higher dosage from 2 gr / L. The optimum dosage for the DOX adsorption was 1.4 gr / L and the adsorption capacity reached the maximum taking in to consideration all conditions. Indeed, with alteration of the other parameters such as the contact time, the drug adsorption could be increased. Considering the dosages used, the optimum dosage 1.4 gr / L was found and selected. The effect of the CS, GO-CS amount as the adsorbent on the drug adsorption was also investigated and they were compared to the used nanocomposite. As illustrated in Figure 7, the made nanocomposite toward CS, GO-CS has the higher adsorption capacity and in comparison with CS, GO-CS has increased the DOX adsorption around 40%, 20%, respectively. Regarding the used CS, GO at the nanocomposite structure, it is indicated that the natural components such as allium sativum, quercus, alhagi maurorum chemically have improved the designed system and their much effective molecules such as polyphones is leaded that the drug adsorption be significantly increased.

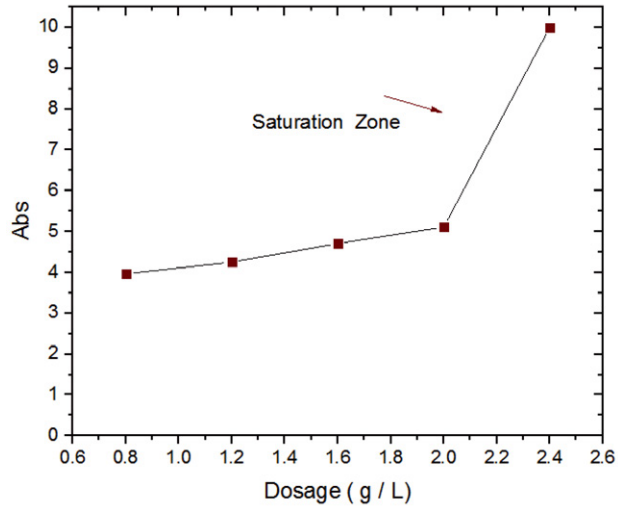

Figure 6. Effect of used dosage of nanocomposite on the DOX adsorption

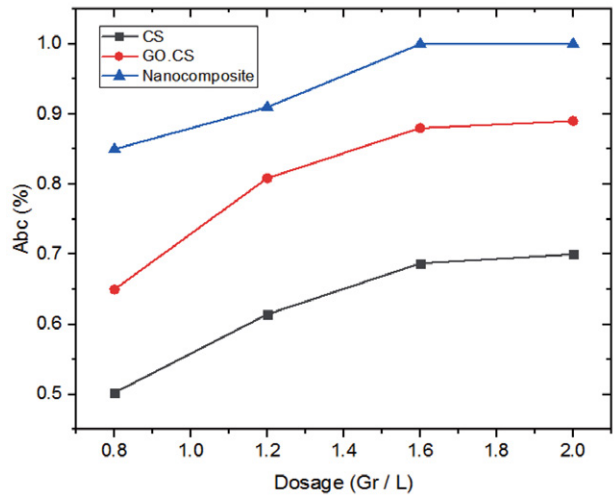

Figure 7. The effect of the used CS, GO-CS, fabricated nanocomposite adsorbent on the DOX adsorption

3. 6. Effect of Drug Concentration

The effect of drug concentration on the adsorption efficiency with various concentrations at pH 6.3 for Gr Mn - GO - CS - A. sativum - Que nanocomposite was investigated. As shown from Figure 8, with increase in the drug concentration, the amount of the drug adsorption increased. By increasing the drug concentration further molecules of drug are contacted to the nanocomposite surface, resulting the amount of DOX adsorption be essentially increased. At pH 6.3 and temperature 298° k, the maximum of adsorption at concentration 3.6 mg / 1.8 ml was observed. Designed and fabricated nanocomposite with the superior properties can absorb further concentrations of drug and reduce the side effects of the used drug at high concentration. The results were compared with the fabricated nanocomposite without the green alhagi maurorum essential oil, (Mn - GO - CS - A. sativum - Que)

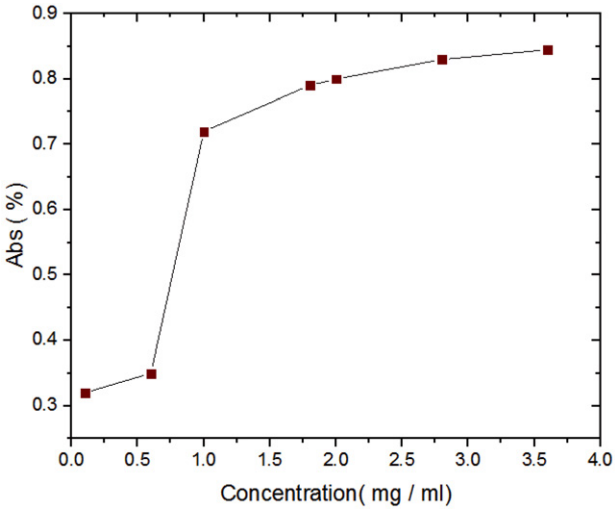

Figure 8. The effect of DOX concentration on adsorption efficiency of Gr Mn / GO / CS / A. sativum / Que

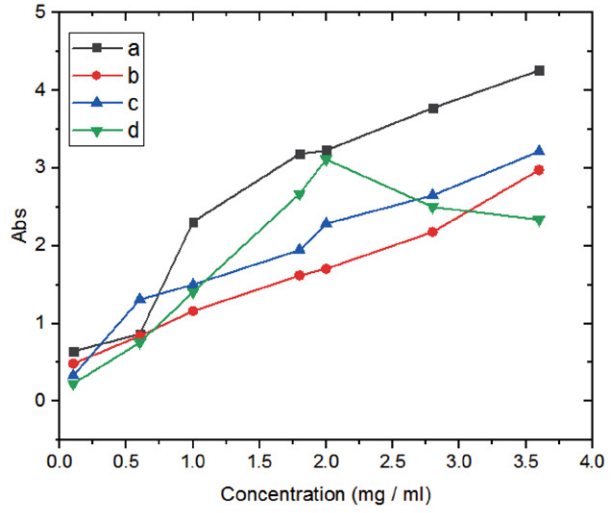

Figure 9. The DOX adsorption at different concentrations using, a (Gr Mn / GO / CS / A. sativum / Que) b (Free DOX) C (Mn CS) d (Mn / GO / CS / A. sativum / Que)

nanocomposite and free DOX. The calibration cure related to DOX at wavelength 490 nm was drawn and the second peak was observed at 294 nm. The results indicated that by increasing the DOX concentration from its initial concentration the adsorption capacity at dosage 0.8 gr / L reaches 85% and at higher dosage of drug adsorption reaches 100%. Compared to the magnesium oxide nanoparticles, graphene oxide, this nanocomposite could adsorb further concentrations of DOX.[20,16]

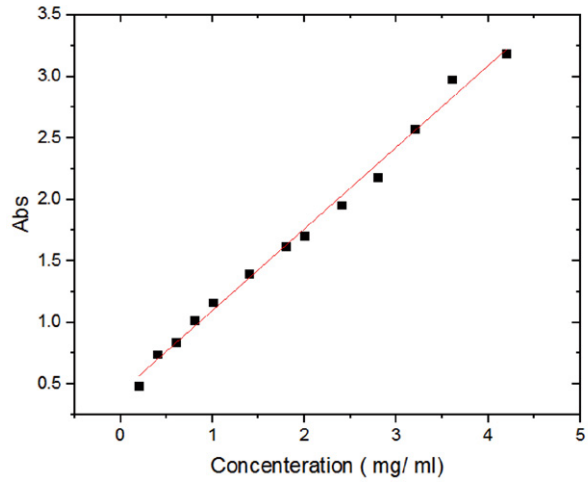

Figure 10. The calibration carve of DOX adsorption

3. 7. Effect of Temperature on the Drug Adsorption

The drug adsorption on the made nanocomposite at the various temperatures was evaluated. The obtained results demonstrated that increasing the temperature to more than 30 °C decreased the drug adsorption basically and at this range the drug adsorption is rapidly destroyed. At temperature 30 °C, the drug adsorption was suddenly increased that resulting of further molecular motion and

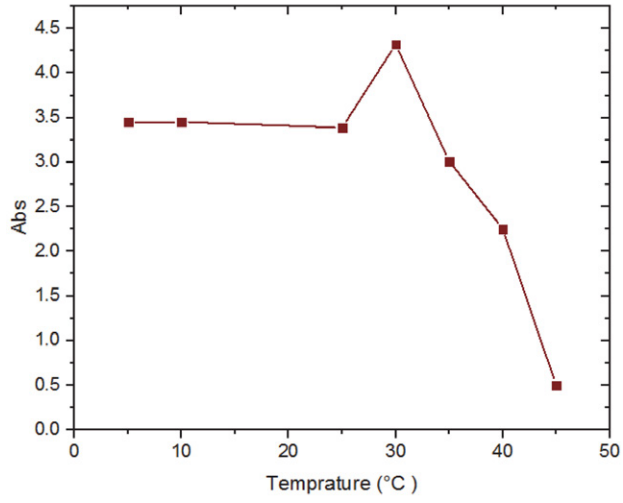

Figure 11. Effect of temperature on drug adsorption

high competitiveness to the occupied active sites on the nanocomposite surface. At lower temperatures the adsorbed drug has high stability and affective drug loading at this range must be considered.

3. 8. Absorption Isotherm

The adsorption isotherms study describes the nature of the formed adsorption and interaction pathway of adsorbate with adsorbents. Somehow monolayer sorption process onto the adsorbent surface with a finite number of the uniform adsorption sites without transmigration of adsorbate and adsorption on the heterogeneous surface are associated with Langmuir and Freundlich models respectively. Thus, as illustrated in Figure 12, the obtained results using Langmuir and Freundlich models were modeled for better understanding of the adsorption process.

$$\frac{c_e}{q_e} = \frac{1}{bq_{max}} + \frac{c_e}{q_{max}} \quad \text{Langmuir equation:} \quad (1)$$

$$lnq_e = lnk_f + \frac{1}{n} lnc_e \quad \text{Freundlich equation:} \quad (2)$$

For Freundlich isotherm q_e, C_e, are concentrations of the adsorbed drug toward the adsorbent amount at the equilibrium state (mg /g), equilibrium concentration (mg / L), as well as the model constants of K_f and n represent the relationship between the adsorption capacity and the adsorption intensity, respectively. By plotting log qe vs. log C_e the amounts of K_f and n from the intercept and the slope, are determined respectively. For Langmuir model, C_e /q_e, C_e, constant b and q max as index of the adsorption specification, equilibrium concentration of adsorption, adsorption energy and the maximum adsorption capacity, are expressed respectively. Furthermore, by plotting (C_e / q_e) versus the equilibrium concentration (C_e), adsorption energy and the maximum adsorption capacity from Langmuir isotherm are measured. The obtained parameters associated with adsorption isotherms have been summarized in Table (1).

Table 1. Parameters related to the adsorption isotherm.

Model	Kf	b(L/mg)	qm(mg/g)	R^2	n
Langmuir		0.99	4.44	0.91	
Freundlich	2.13			0.96	0.79

The results indicate that the Freundlich adsorption model according to the gained optimum conditions has the higher correlation coefficient (R^2 = 0.9613) and compared to the Langmuir model it can better describe DOX adsorption. As value of the correlation coefficient for both isotherm is close to unique and as it was found at low concentration of drug the Langmuir model shows appropriate behavior, revealing that the drug adsorption is monolayer, whereas at the higher concentration of drug the Freundlich isotherm better fits the experiment results consequently, it can be concluded that adsorption process follows both isotherms but according to further concentration of drug for targeted therapy is considered, indicating that the Freundlich isotherm has more advantage and better describes the drug adsorption process.

3. 9. The Kinetic Study of Adsorption

As the kinetic study of adsorption reveals the better understanding of the took place process and considering that the speed of molecular interaction into supernatant has a potential influence on the physicochemical adsorption, therefore the mechanism of adsorption in terms of the kinetic alterations must be basically considered and investigated. Indeed, with accurate assessment of the adsorption kinetics could monitor and adjust the effective parameter, resulting that the adsorption efficiency be promoted. For current research the experimental date with four selected models was adapted and investigated. Figure13 illustrates the used kinetic models related to the experimental date of the DOX adsorption. The kinetic models are described according to following equations:

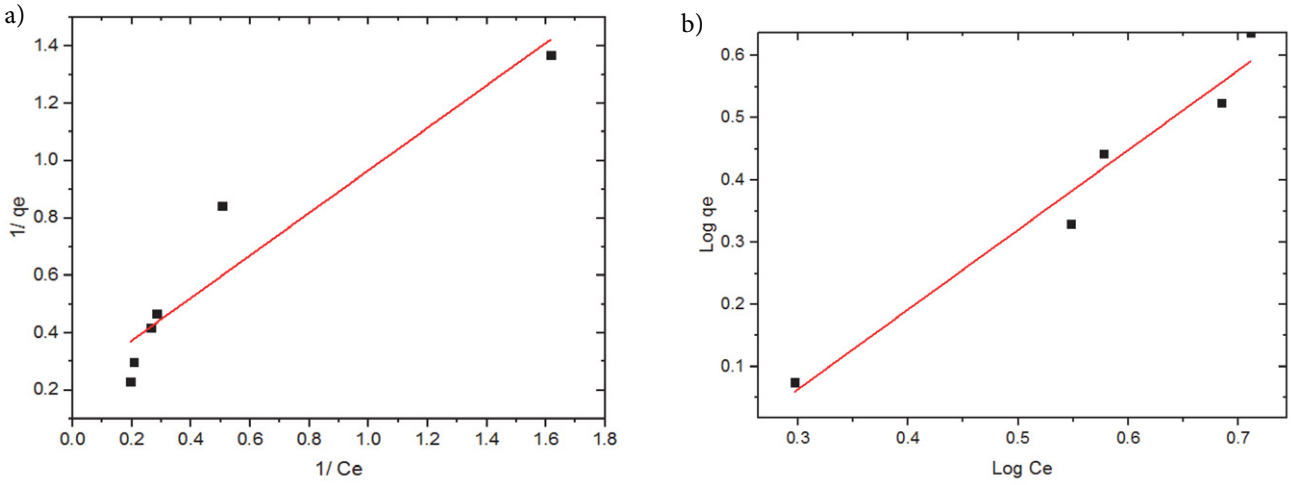

Figure 12. Langmuir curve of adsorption (a) Freundlich curve of adsorption (b)

$$log(q_e - q_t) = logq_e - k_{ad}\frac{t}{2.303} \quad (3)$$

The pseudo-first-order equation

$$\frac{t}{q_t} = \frac{1}{k_2 q_{e2}} + \frac{t}{q_e} \quad (4)$$

The pseudo-second-order equation

$$q_t = k_i t^{1/2} + C \quad (5)$$

The intra-particle diffusion model

$$q_t = \frac{1}{\beta} ln\alpha\beta + \frac{1}{\beta} lnt \quad (6)$$

The Elovich model

Where q_e and q_t, are the adsorption capacities of DOX at time t and equilibrium, also K_1, K_2, K_i min^{-1} are the equilibrium rate constant of pseudo-second kinetic model, pseudo-first kinetic model, intra-particle diffusion (ki) at stage i, respectively. The constants α and β by plotting qt versus ln t from the slope and intercept were determined. The kinetics parameters have been summarized at Table 2.

The kinetic studies demonstrated an enhanced drug adsorption due to the further contact of DOX molecules with the designed and fabricated system. It was also found that by increasing the contact time up to 5 minutes, the maximum adsorption wavelength from 482 nm shifted to 290 nm possibly due to the higher competitiveness between molecules in the supernatant. The experimental data fitting the kinetics models indicated that the simultaneous increase of the nanocomposite dosage and the contact time caused enhanced drug adsorption. As observed in Figure 14, the pseudo-second-order kinetic model compared to the other kinetic models used has fitted the experimental results as well, and considering the same conditions higher accordance is observed.

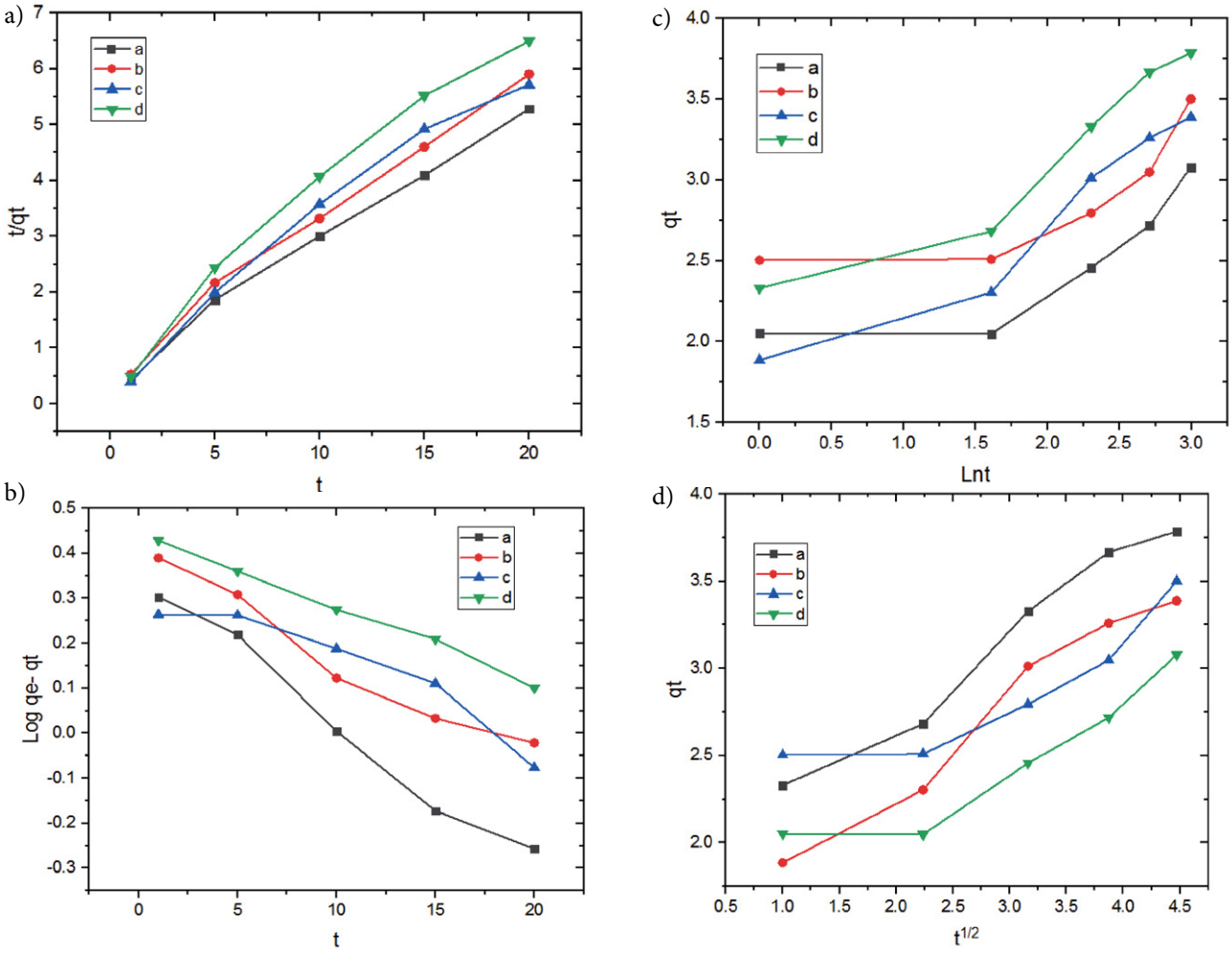

Figure 13. The kinetics models plot for DOX adsorption a (Dosage =1.6 gr / L, λ max = 482) b (Dosage =1.6 gr / L, λ max = 292) c (Dosage = 0.8 gr / L, λ max = 482) d (Dosage = 0.8 gr / L, λ max = 290) A, B, C, D pseudo-second kinetic model, pseudo-first kinetic model, intra-particle diffusion model, Elovich model, respectively

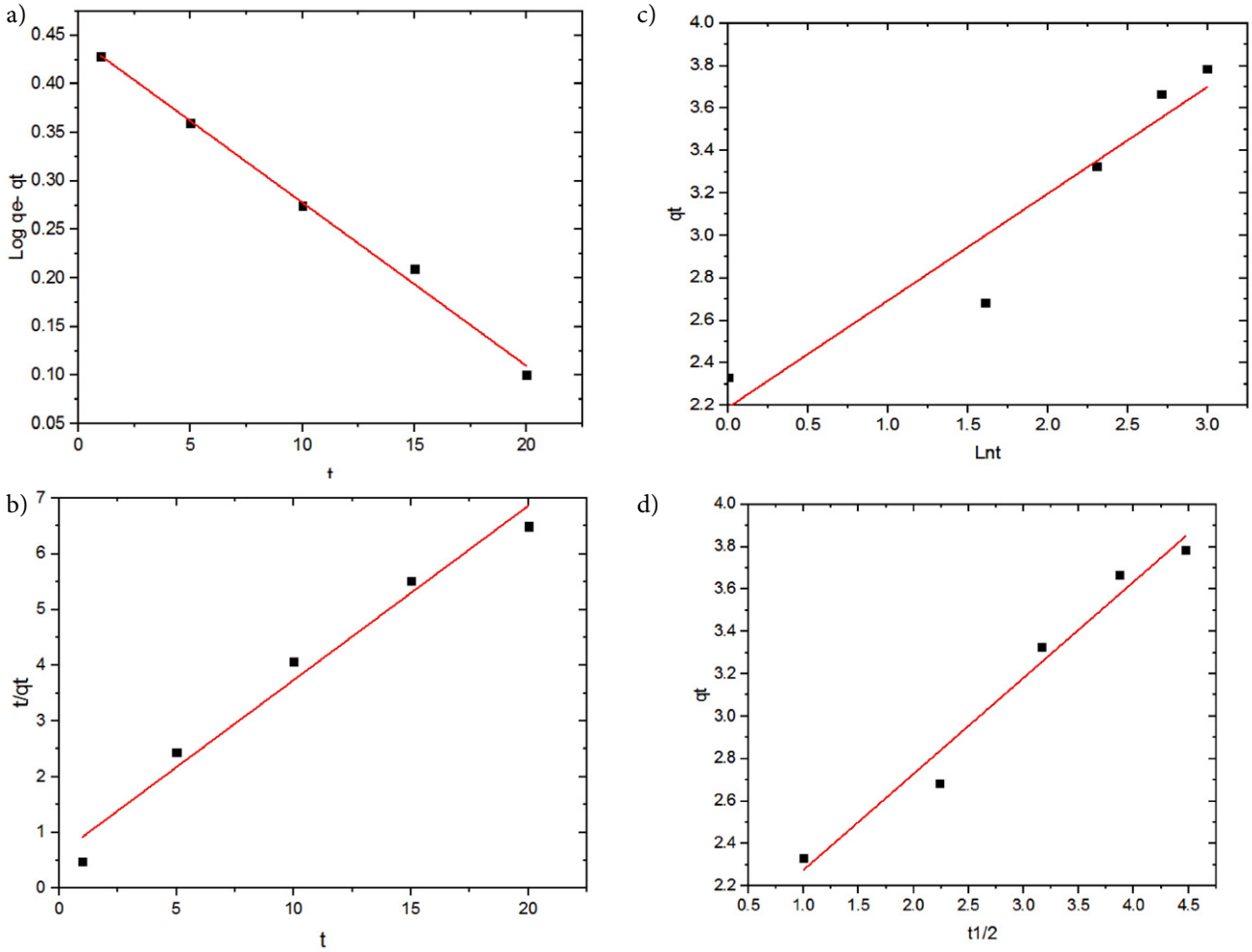

Figure 14. Kinetics analysis of the drug adsorption on fabricated nanocomposite (a) fitting by the first-second-order model (b) fitting by the pseudo-second-order model; (c) fitting by Elovich model; (d) fitting by the intraparticle diffusion model

Table 2. The kinetic parameters of adsorption

	R^2	qe	qt	K_1	K_2	K_i	α	β
Pseudo-First order kinetic model	0.976	4.31	4.73	0.056				
Pseudo-second order kinetc model	0.995	3.56	3.51		0.174			
Intra-particle diffusion	0.973		2.028			0.5324		
Elovich model	0.94		3.50				4.1	18.87

3. 10. Thermodynamic of Adsorption

The thermodynamic parameters related to the drug adsorption including the alterations of Gibbs free energy (ΔG°), enthalpy (ΔH°) and entropy (ΔS°), via the van't Hoff equation were evaluated and measured.

$$K_d = \frac{q_e}{C_e} \quad (7)$$

$$\Delta G^o = -RTlnK_d \quad (8)$$

$$lnK_d = -\frac{\Delta H^o}{RT} + \frac{\Delta S^o}{R} \quad (9)$$

$$\Delta S^o = \frac{\Delta G^o - \Delta H^o}{T} \quad (10)$$

In addition, ΔH° (kJ mol^{-1}), ΔG° (kJ mol^{-1}), ΔS° (J mol^{-1} K^{-1}) as the important thermodynamic qualities, the other appeared parameter at above equation are the known universal gas constant and the absolute temperature (K°). Where K_d represents the ratio of the adsorbed drug on the surface of fabricated nanocomposite at equilibrium (q_e) to the residual concentration of DOX drug into supernatant at equilibrium (C_e). By plotting ln (q_e / C_e) vs. q_e and determination of the intercept K_d be obtained (Figure 15).

Further, isosteric heat of adsorption according to Clausius – Clapeyron equation was calculated (Figure 16). The thermodynamic parameters of drug adsorption have been summerized in Table 3.

$$\frac{d(\ln Ce)}{dT} = \frac{\Delta Hx}{RT^2} \quad (7)$$

Clausius- Clapeyron equation

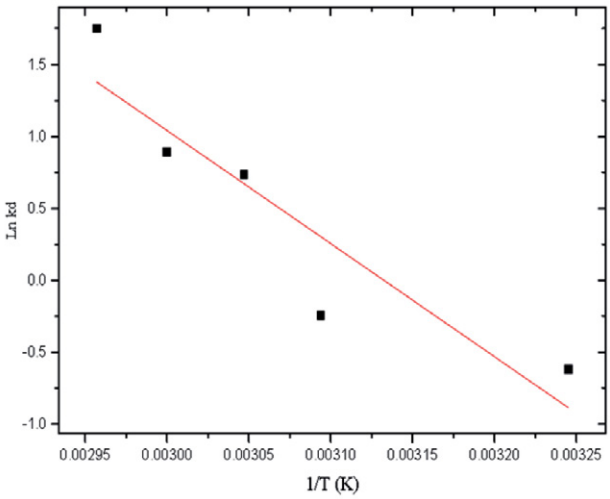

Figure 15. Ln k vs temperature for calculation of thermodynamic properties.

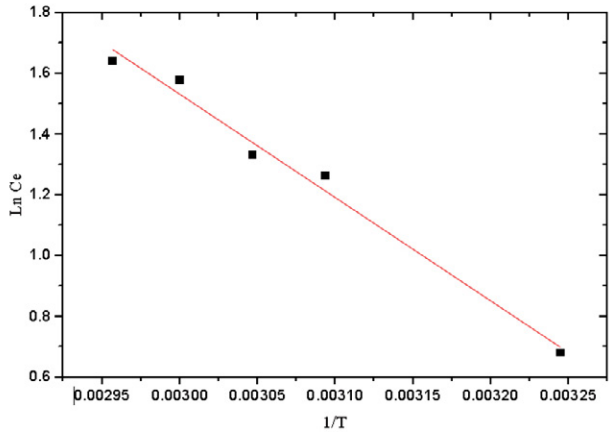

Figure 16. Ln Ce vs temperature for calculation isosteric heat of adsorption

Table 3. Thermodynamic parameters of adsorption

Thermodynamic parameter	ΔH° kJ mol^{-1}	ΔS° kJ mol^{-1}	ΔG° (kJ mol^{-1})	ΔHx (Isosteric heat) kJ mol^{-1}
	62.512	2.023	–4.004	28.267

3. 11. Surface Excess

Surface excess is defined as a concentration in a small volume near the surface nanocomposite.

$$\Gamma = \frac{(C\ initial - C\ after\ adsorption)\ .Volume}{Surface\ area}$$

The results indicated that at range concentration up to 1 mg / ml the surface excess has increased, while by increasing the concentration from 1 mg / ml the surface excess has basically increased. Meanwhile at concentration 3.6 it reached its minimum amount, resulting at concentration 3.6 the maximum amount of DOX has been adsorbed on the nanocomposite surface (Figure 17).

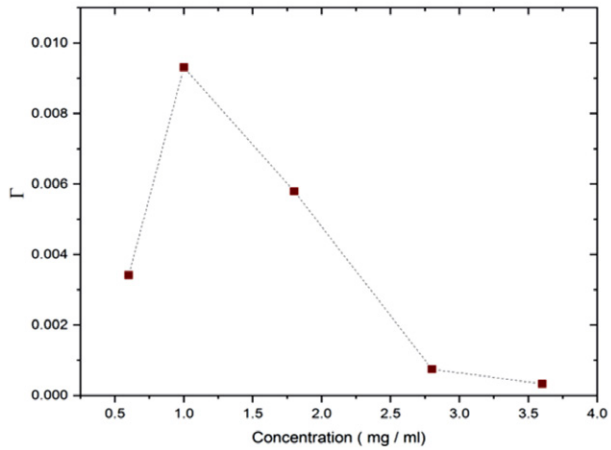

Figure 17. The alteration of surface excess with drug concentration.

4. Conclusion

As the physical interactions between doxorubicin and the fabricated nanocomposite plays an important role in the drug loading and release, thus by adjusting the effective parameters, the best clinical therapy state can be achieved. The obtained results revealed that by increasing the drug concentration and the nanocomposite dosage, the DOX adsorption increased. Under acidity conditions, more adsorption of DOX was observed with the maximum adsorption capacity occurring at pH 6.3. The drug adsorption satisfactorily followed both Langmuir and Freundlich isotherms at lower and higher concentrations of the drug, respectively. Our findings indicated that the obtained experimental data of the drug adsorption results in compression with the other kinetic model was further consisted with the pseudo-second kinetic model. The obtained thermodynamic parameters revealed that the adsorption process of DOX on the nanocomposite surface was endothermic and spontaneous. This designed nanocomposite had a high efficiency of DOX adsorption thanks to the excellent component used in its structure; so it can essentially be considered and used in targeted drug deliv-

ery. Indeed, since the current challenge in using higher concentrations of DOX during clinical treatment of cancer limits its efficiency, the design of an effective system with a high performance of adsorption is a necessity for medical applications. This drug system with high adsorption properties in the field of chemotherapy and targeted drug delivery could load the further amount of drug, resulting the encapsulated drug efficiency be essentially improved. Furthermore, the nanocomposite made with a unique component could act as anticancer agent.

5. References

1. H. Zh. Tifeng, J. E. Lexin, Zh. Jingxin. Zh. Qingrui, Zh. Email, Q. P. Xuehai Yan *Sci China Mater* **2015**, *10,* 811–818. **DOI:**10.1007/s40843-015-0090-x
2. J. Liu L. Cui, D. Osic *Acta Biomaterialia* **2013,** *9,* 9243–9257. **DOI:**10.1016/j.actbio.2013.08.016
3. Xi. Zhang, W. Cai, Li Hao, S. Feng, Qi. Lin, W. Jiang *Journal of Nanomaterials* **2017**, *2017*, 1–10. **DOI:**10.1155/2017/6702890
4. D. Bi, L. Zhao, R. Yu, H. Li, Yi. Guo, Xi. Wang, M. Han *Drug Delivery* **2018,** *25*, 564–575. **DOI:**10.1080/10717544.2018.1440447
5. D. Curry, A. Cameron, B. MacDonald, C. Nganou, H. Scheller, J. Marsh, S. Beale, M. Lu, Zh. Shan, R. Kaliaperumal, H. Xu, M. Servos, C. Bennett, S. MacQuarrie, K. D. Oakes, M. Mkandawirea, X. Zhang *Nanoscale* **2015,** *7*, 19611–19619. **DOI:**10.1039/C5NR05826K
6. Sh. Sadaf, L. Walder *Adv. Mater. Interfaces* **2017**, *4*, 1–10. **DOI:**10.1002/admi.201700649
7. W. Caia, M. Guoa, Xi. Wenga, W. Zhangb, Zu. Chen *Materials Science & Engineering C* **2019,** *98*, 65–73. **DOI:**10.1016/j.msec.2018.12.145
8. A. Kordzadeh, S. A. -Iranagh, M. Zarif, H. Modarress *Journal of Molecular Graphics and Modeling* **2019,** *88*, 11–22. **DOI:**10.1016/j.jmgm.2018.12.009
9. N. V. Roik, Lyudmila A. Belyakova, M. O. Dziazko *Adsorption Science & Technology* **2016,** *35*, 86–101. **DOI:**10.1177/0263617416669504
10. Y. Wanga, Sh. Yanga, Y. Wanga, Y. Liua, H. Wang *Colloids and Surfaces B: Biointerfaces* **2012,** *97,* 62–69. **DOI:**10.1016/j.colsurfb.2012.04.013
11. K. Nawara, J. Romiszewski, K. Kijewska, J. Szczytko, A. Twardowski, M. Mazur, P. Krysinsk *J. Phys. Chem. C* **2012**, *116*, 5598–5609. **DOI:**10.1021/jp2095278
12. J. Miao, F. Zhang, M. Takieddin Sh. Mousa, R.J. Linhardt *Langmuir* **2012,** *28*, 4396–4403. **DOI:**10.1021/la3000137
13. N. I. Zaabaa, K. L. Fooa, U. Hashima, S. J. Tanb, Wei-Wen Liua, C. H. Voon *Procedia Engineering* **2017,** *184*, 469–477. **DOI:**10.1016/j.proeng.2017.04.118
14 O. Arjmand, M. Ardjmand, A. M. Amani M. H. Eikani *Anti-Cancer Agents in Medicinal Chemistry* **2020,** *20 (1).* **DOI:**10.2174/1871520620666200213105203
15 J. F. Clevenger *The Journal of the American Pharmaceutical Association* **1912,** *17*, 345–349. **DOI:**10.1002/jps.3080170407
16. Y. Wei, B. Han, X. Hu, Y. Lin, X. Wang, X. Deng *Procedia Engineering* **2012**, *27*, 632–637. **DOI:**10.1016/j.proeng.2011.12.498
17. B. KartickS. K. Srivastava, I. Srivastava *Journal of Nanoscience and Nanotechnology* **2013,** *13*, 4320–4324. **DOI:**10.1166/jnn.2013.7461
18. Sh. Wu, X. Zhao, Y. Li, Q. Du, J. Sun, Y. Wang, X. Wang, Y. Xia, Z. Wang, L. Xia *Materials* **2013**, *6*, 2026–2042. **DOI:**10.3390/ma6052026
19. Z. Liu, J. Liu, T. Wang, Q. Li, P. S. Francis, C. J. Barrow, W. Duan, W.Yang *J. Mater. Chem. B.* **2018**, *6*, 1251–1259. **DOI:**10.1039/C7TB03063K
20. T. Somanathan1, V. M. Krishna, V. Saravanan, R. Kumar, R. Kumar, *Journal of Nanoscience and Nanotechnology* **2016**, *16,* 9421–9431. **DOI:**10.1166/jnn.2016.12164

Povzetek

V tej študiji smo preučevali adsorpcijo zdravila proti raku doksorubicina na ciljno načrtovan in izdelan material. Gre za nov nanokompozit pripravljen iz zelenega magneta, grafen oksida, hitozana ter česnovega in hrastovega prahu. Za ovrednotenje adsorpcije doksorubicina smo spreminjali različne parametre kot so kontaktni čas, pH vrednost, koncentracija, količina adsorbenta in temperatura. Rezultati so pokazali, da je adsorpcijski maksimum pripravljenega kompozita dosežen pri pH vrednosti 6.3, koncentraciji 3.6 mg/1.8 ml, kontaktnem času 10 min in količini adsorbenta 1.4 g/L. Pripravljen sistem kaže preko 100 % boljše adsorpcijske lastnosti, adsorpcija pa je učinkovita tudi pri nizkih koncentracijah. Zaradi tega so potrebne nižje količine adsorbenta, tudi pri višjih koncentracijah doksorubicina. Pripravljen kompozit torej kaže superiorne adsorpcijske lastnosti in bi ga lahko uporabili kot dostavni sistem za zdravilo.

Except when otherwise noted, articles in this journal are published under the terms and conditions of the Creative Commons Attribution 4.0 International License

Scientific paper

Hydrothermal Preparation, Crystal Structure, Photoluminescence and UV-Visible Diffuse Reflectance Spectroscopic Properties of a Novel Mononuclear Zinc Complex

Xiu-Guang Yi,[1,*] Xiao-Niu Fang,[1] Jin Guo,[1] Jia Li[1,3] and Zhen-Ping Xie[2]

[1] *School of Chemistry and Chemical Engineering, Jinggangshan University, Institute of Applied Chemistry, Ji'an Jiangxi 343009, China*

[2] *Ji'an Academy of Forestry Sciences, Ji'an Jiangxi 343009, China*

[3] *State Key Laboratory of Molecular Reaction Dynamics, Dalian Institute of Chemical Physics, Chinese Academy of Sciences, Dalian 116023, China*

* *Corresponding author: E-mail: jayxgggchem@163.com*
Tel: +86(796)8100490; fax: +86(796)8100490

Received: 08-29-2019

Abstract

A novel mononuclear zinc complex $[ZnL(Phen)(H_2O)] \cdot H_2O$ containing the mixed ligands of Phen (Phen = 1,10-phenanthroline) and 3-hydroxy-2-methylquinoline-4-carboxylic acid (HL) was prepared by hydrothermal synthesis and its crystal structure was characterized by X-ray single-crystal diffraction method. The title complex crystallizes in the orthorhombic systems and forms monomeric units. The molecules in the title complex are connected through the interactions of hydrogen-bonding and π···π interactions to give a three-dimensional (3*D*) supramolecular structure. The fluorescence result discovers a wide emission band in the violet blue region. Time-dependent density functional theory (TDDFT) calculations reveal that this emission can be attributed to ligand-to-ligand charge transfer (LLCT). Solid-state diffuse reflectance shows there is a wide optical band gap.

Keywords: Hydrothermal preparation; photoluminescence; band gap; zinc.

1. Introduction

In recent years, metal complexes have attracted increased attention due to their numerous properties, as well as their potential application in the fields of catalysis, medicine, photoluminescence, semiconductor materials, and so on.[1–4] So far, researchers have been engaged in a large number of studies on the properties of lanthanide and transition metal complexes.[5–7] In these characteristics, photoluminescence is particularly attractive to us. The interesting photoluminescence properties of transition metal complexes mainly come from the d^{10} orbital electron configuration in transition metal elements. As far as we know, as long as the d^{10} electrons of transition metals can be excited effectively, zinc complexes usually exhibit strong photoluminescence. Up to date, extended research affords have been devoted to the design, preparation and characterization of novel transition photoluminescence materials.[8–13]

Despite of a large number of studies on photoluminescence properties, semiconductor properties of zinc complexes have rarely been reported.[14–17] Semiconductor materials are attractive because they are potential photocatalysts for helping to solve some of the environmental problems of the 21th century. So far, some transition metal-organic semiconductor complexes have been documented, such as, $[Ln(IA)_3(H_2O)_2]_n(Hg_3Cl_9)_n4n(H_2O)$, (IA = isonicotinic acid),[18] $Zn(O_2CCH_3)_2(H_2O)_2$,[19] NiL_2 (L = 2-ethoxy-6-(N-methyliminomethyl)phenolate).[20] As the result, transition metal-organic semiconductor complexes are worthy to exploring.

In order to synthesize metal coordination compounds, it is crucial to consider appropriate organic ligands

since the composition of organic ligands can determine the crystal structure and function of metal complexes. Many organic ligands, such as aromatic sulfonic acid, aromatic carboxylic acid and N-heterocyclic derivatives,[21,22] are used in the preparation of metal complexes. Hydroxyquinoline carboxylic acid is an interesting organic ligand with multiple bonding sites, which contains not only phenolic hydroxyl group, carboxyl group, but also nitrogen atom. As a well-known rigid and rod-like molecule, 1,10-phenanthroline (Phen) is an interesting secondary building unit (SBU) for the construction of a supramolecular or an extended structural motif, because Phen possesses a delocalized π-electron system, which allows it to be a useful candidate in preparing new fluorescence compounds with potential applications.

Based on this, we are interested in the crystal engineering of Zn(II) complexes with 3-hydroxy-2-methylquinoline-4-carboxylic acid (HL) and Phen as the mixed ligands. In this article, we report the hydrothermal synthesis, X-ray crystal structure, photoluminescent and UV-visible diffuse reflectance spectroscopic properties, as well as time-dependent density functional theory (TDDFT) calculations for the novel zinc(II) complex, $[ZnL(Phen)(H_2O)] \cdot H_2O$, (Phen = 1,10-phenanthroline, HL = 3-hydroxy-2-methylquinoline-4-carboxylic acid), with a mononuclear structure.

2. Experimental

2. 1. Materials and Instrumentation

The reagents and chemicals for the synthesis of the title compound were analytical reagent grade, commercially available and applied without further purification. Infrared spectra were recorded in the Nicolet iS10 spectrometer using KBr pellets. The photoluminescence study with solid state samples was performed on the FX-97XP fluorescence spectrometer. The solid state UV/Vis diffuse reflectance spectroscopy was carried out TU-1901 UV/Vis spectrometer with an integrating sphere in the wavelength range of 190-900 nm. $BaSO_4$ power was used as a reference, on which the finely ground powder sample was coated as a 100% reflectance. ^{1}H NMR spectra were measured on Bruker Avance 400 MHz instrument with dimethyl sulfoxide (DMSO) as solvent. TDDFT investigations were carried out by means of the Gaussian 09 suite of program packages.

2. 2. Synthesis of 3-hydroxy-2-methylquinoline-4-carboxylic acid (HL)

Synthesis of isatin: indigo (131 g, 0.5 mol), $K_2Cr_2O_7$ (74 g, 1.0 mol) and distilled water (200 mL) were added into the flask with three necks of 500 mL and stirred. After cooling, dilute H_2SO_4 (10%, 250 mL) was added and kept stirring at 43 °C for 1.5 h. The mixture was diluted with twice its volume of distilled water, filtered off, dissolved in 10% NaOH solution, filtered again and neutralized with 10% HCl to pH = 7. Yield: 116 g (90%); m.p. 210 °C; HRMS *m*/*z* (ESI): calcd. for $C_8H_5NO_2$ ($[M+H]^+$ 147.0320, found 147.0826.

Synthesis of HL: isatin (73.5 g, 0.5 mol) and NaOH (20 g, 0.5 mol) were dissolved in distilled water (200 mL) and filtered. The filtrate and NaOH (20 g, 0.5 mol) were added into chloroacetone (92 g, 1.0 mol), and hydrochloric acid was added dropwise to adjust pH = 7, and then the mixture was filtered. Yield: 96 g (95%); m.p. 225°C; HRMS *m*/*z* (ESI): calcd. for $C_{11}H_9NO_3$ ($[M+H]^+$ 203.0582, found 203.0548. ^{1}H NMR (400MHz, DMSO) δ 9.15 (s, 1H), 7.93 (d, *J* = 8.0 Hz, 1H), 7.64 (t, *J* = 8.0 Hz, 1H), 7.60–7.52 (m, 2H), 2.70 (s, 3H).

2. 3. Synthesis of $[ZnL(Phen)(H_2O)]\cdot(H_2O)$

The title compound was prepared by mixing $Zn(CH_3COO)_2 \cdot 2H_2O$ (1.0 mmol, 219.5 mg), HL (1.0 mmol, 203 mg), Phen (1.0 mmol, 180 mg), 1 mL triethylamine and 10 mL distilled water in a 25 mL Teflon lined stainless steel autoclave. The mixture was heated to 120 °C and kept at this temperature for 7 days. When the mixture was cooled slowly down to room temperature, yellow crystals suitable for X-ray analysis were collected and washed. Yield 411 mg (85% based on zinc). IR (KBr, cm^{-1}): 3424(vs), 1624(w), 1580(w), 1518(m), 1483(s), 1446(m), 1351(vs), 1320(s), 851(vs), 821(w), 773(w), 726(s); Anal. Calcd for $C_{23}H_{19}N_3O_5Zn$: C, 57.22; H, 3.97; N, 8.70; found: C, 57.30; H, 3.95; N, 8.75%.

2. 4. Crystal Structure Determination

The single crystal X-ray diffraction data of the title complex was collected on a SuperNova CCD X-ray diffrac-

Table 1. Crystal data and structure refinement details for the title complex

Formula	$C_{23}H_{19}N_3O_5Zn$
Fw	482.78
Color	yellow
Crystal system	orthorhombic
Space group	*Pbca*
a (Å)	9.5869(3)
b (Å)	18.6505(7)
c (Å)	23.2010(9)
V (Å^3)	4148.3(3)
Z	8
Reflections collected	12374
Independent, observed Reflections (R_{int})	4878(0.0212)
$d_{calcd.}$ (g/cm^3)	1.546
μ (mm^{-1})	1.226
T (K)	293(2)
F (0 0 0)	1984
R_1, wR_2	0.0353, 0.083
S	1.04
Δρ (max, min) (e/Å^3)	0.29, –0.40

tometer with graphite monochromated Mo-*Kα* radiation (λ = 0.71073Å) by means of a ω scan method. The data reduction and empirical absorption corrections were performed with CrystalClear software.[24] Using Olex2,[25] the structure for the title complex was solved with the ShelXT,[26] the structure solution program using Intrinsic Phasing and refined with the ShelXL refinement package using Least Squares minimization.[27] All of the non-hydrogen atoms and the hydrogen atoms of water were generated based on the subsequent Fourier difference maps and refined anisotropically. The other hydrogen atoms were located theoretically and ride on their parent atoms. Crystallographic data and structural refinements for the title complex are summarized in Table **1**. Selected bond lengths and bond angles for the crystal structure are displayed in Table **2**. The hydrogen bonding interactions are presented in Table **3**.

3. Results and Discussion

3. 1. Preparation of Ligand and the Title Complex

The ligand HL was prepared according to the literature,[23] as shown in Scheme 1. At the first, indigo was oxidized by potassium dichromate to form the intermediate isatin. Then the isatin is hydrolyzed, cyclized by nucleophilic addition, and finally dehydrated to form the ligand, 3-hydroxy-2-methylquinoline-4-carboxylic acid. Finally, the title complex was prepared by hydrothermal synthesis of the ligand with zinc acetate, phenanthrene and water in the presence of triethylamine. By the infrared spectrum of the title complex, the strong broad band at 3424 cm^{-1} indicates the presence of water, the absorption at 1624 cm^{-1} was assigned to the contribution of C=N, the absorptions at 1580 cm^{-1} and 1351 cm^{-1} are regarded as the presence of monodentated carboxylate in the title complex.

3. 2. Structural Description

Single crystal X-ray diffraction analysis reveals that the title complex is a neutral molecule and it crystallizes in the space group *Pbca* of the orthorhombic system. The Zn^{2+} ion is sitting at the inversion center and is pentacoordinated by the HL, Phen and water molecule, yielding a rectangular pyramid geometry. The Zn^{2+} ion is coordinated by three oxygen atoms and two nitrogen atoms, of which two oxygen atoms are from HL ligand, one oxygen atom is from coordinated water molecule, two nitrogen atoms are from Phen ligand. Quinolinecarboxylate (L^-) and Phen act as the bidentate ligand, water molecule acts as the monodentate ligand coordinated to the zinc metal center, as presented in Fig. 1. The bond distance of Zn1–O2 is 2.013(2) Å, Zn1–O3 is 1.932(2) Å, Zn1–O4 is 1.988(2) Å, while that Zn1–N1 is 2.105(2) Å, Zn1–N2 is 2.193(2) Å. These are comparable with that reported in the references.[28–30] A intramolecular hydrogen bond can be found between the C–H bond and carbonyl oxygen atom (C8–H8···O1). A lots of intermolecular hydrogen bonds can be found in the crystal structure form O–H···O or O–H···N, such as O4–H4A···O1^{i} (Symmetry code (i): ½ + *x*, $^3/_2$ – *y*, 1 – *z*), O4-H4B···O5, O5–H5D···O1^{ii} (Symmetry code (ii): 1 + *x*, *y*, *z*), O5–H5E···N3^{iii} (Symmetry code (iii): ½ + *x*, *y*, ½ – *z*), and thus formed a three-dimensional supramolecular structure, as presented in Fig. 2. and Fig. 3. Additionally, there are abundant offset face-to-face π···π stacking interaction between *Cg*2···*Cg*5^{iv}, *Cg*1···*Cg*5^{v}, *Cg*4···*Cg*3^{vi} (Symmetry codes (iv): 2 – *x*, 1 – *y*, 1 – *z*; v: 1 – *x*, 1 – *y*, 1– *z*; (vi): –½ + *x*, *y*, ½ – *z*), as present in Fig. 4 (The *Cg*1 is ring of N1-C19-C20-C21-C22-C23, *Cg*2 is N2-C12-C13-C14-C15-C16, *Cg*3 is N3-C2-C3-C4-C6-C7, *Cg*4 is C6 to C11 and *Cg*5 is C15 to C20). The centroid-centroid distance of *Cg*2···*Cg*5^{iv} is 3.753(2) Å, with the slippage distance 1.290 Å and the dihedral angle of 0.5(2)°, for the *Cg*1···*Cg*5^{v} is 3.767(2) Å, 1.637 Å and 1.9(2)°; for the *Cg*4···*Cg*3^{vi} is 3.883(2) Å, 1.436 Å and 3.6(2)°.

Table 2. Selected bond lengths (Å) and bond angles (°)

Distance	(Å)	Distance	(Å)
Zn1–O3	1.932(2)	Zn1–N1	2.105(2)
Zn1–O4	1.988(2)	Zn1–N2	2.193(2)
Zn1–O2	2.013(2)		
Angle	**(°)**	**Angle**	**(°)**
O3–Zn1–O4	122.76(7)	O2–Zn1–N2	169.03(7)
O3–Zn1–O2	90.11(6)	N1–Zn1–N2	77.48(7)
O4–Zn1–O2	93.91(7)	C1–O2–Zn1	128.2(2)
O3–Zn1–N1	126.71(7)	C3–O3–Zn1	125.0(2)
O4–Zn1–N1	109.73(7)	C23–N1–Zn1	126.5(2)
O2–Zn1–N1	95.21(7)	C20–N1–Zn1	115.1(2)
O3–Zn1–N2	87.85(6)	C12–N2–Zn1	128.6(2)
O4–Zn1–N2	96.25(7)	C16–N2–Zn1	112.5(2)

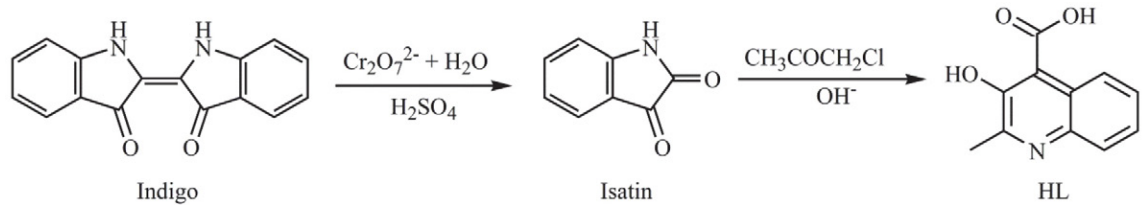

Scheme 1: Synthetic route of ligand HL

Table 3. Hydrogen bonds for the title complex

D–H···*A*	*D*–H, Å	H···*A*, Å	*D*···*A*, Å	*D*–H···*A*, °
O4–H4A···O1^{i}	0.76(3)	1.96(3)	2.716(2)	171(3)
C8–H8···O1	0.93	2.26	2.852(3)	120.6
O5–H5D···O1^{ii}	0.86(3)	1.95(3)	2.787(3)	163(3)
O5–H5E···O1^{iii}	0.80(3)	1.95(3)	2.825(3)	170(3)
O4–H4B···O1	0.86(3)	1.80(3)	2.639(3)	168(3)

Symmetry codes: (i) ½ + *x*, $^{3}/_{2}$ – *y*, 1 – *z*; (ii) 1 + *x*, *y*, *z*; (iii) ½ + *x*, *y*, ½ – *z*.

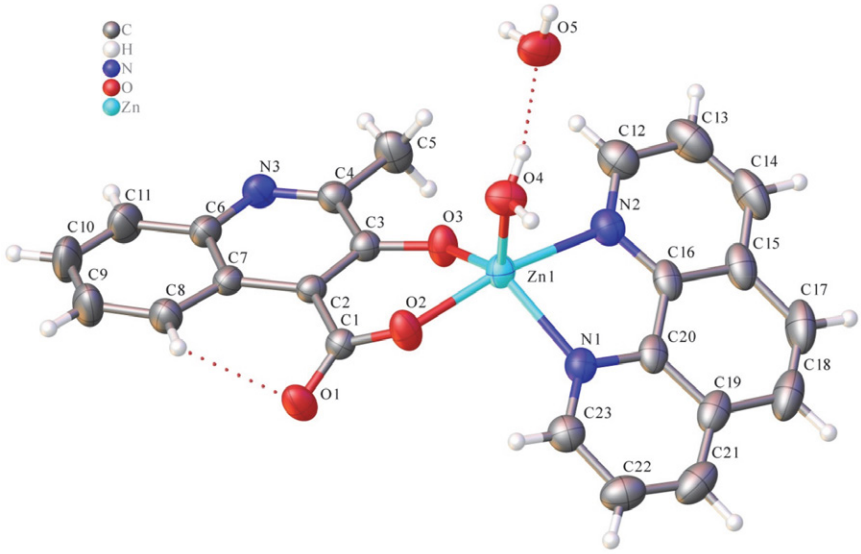

Fig. 1. The molecular structure of the title complex

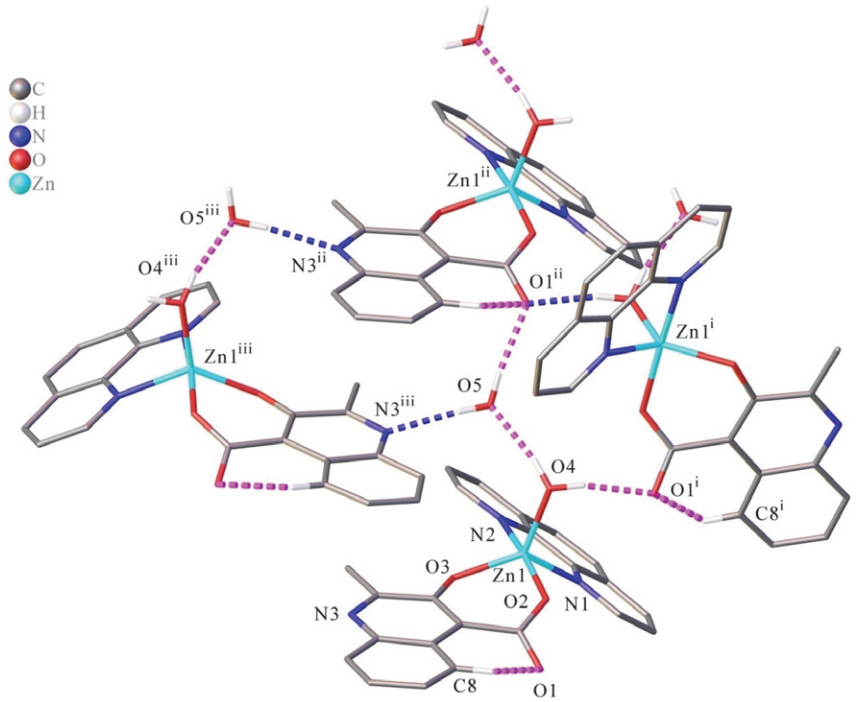

Fig. 2. The hydrogen bonds of the title complex. Hydrogen atoms not involved in the motif shown were removed for clarity. Symmetry codes: (i) ½ + *x*, $^{3}/_{2}$ – *y*, 1 – *z*; (ii) 1 + *x*, *y*, *z*; (iii) ½ + *x*, *y*, ½ – *z*.

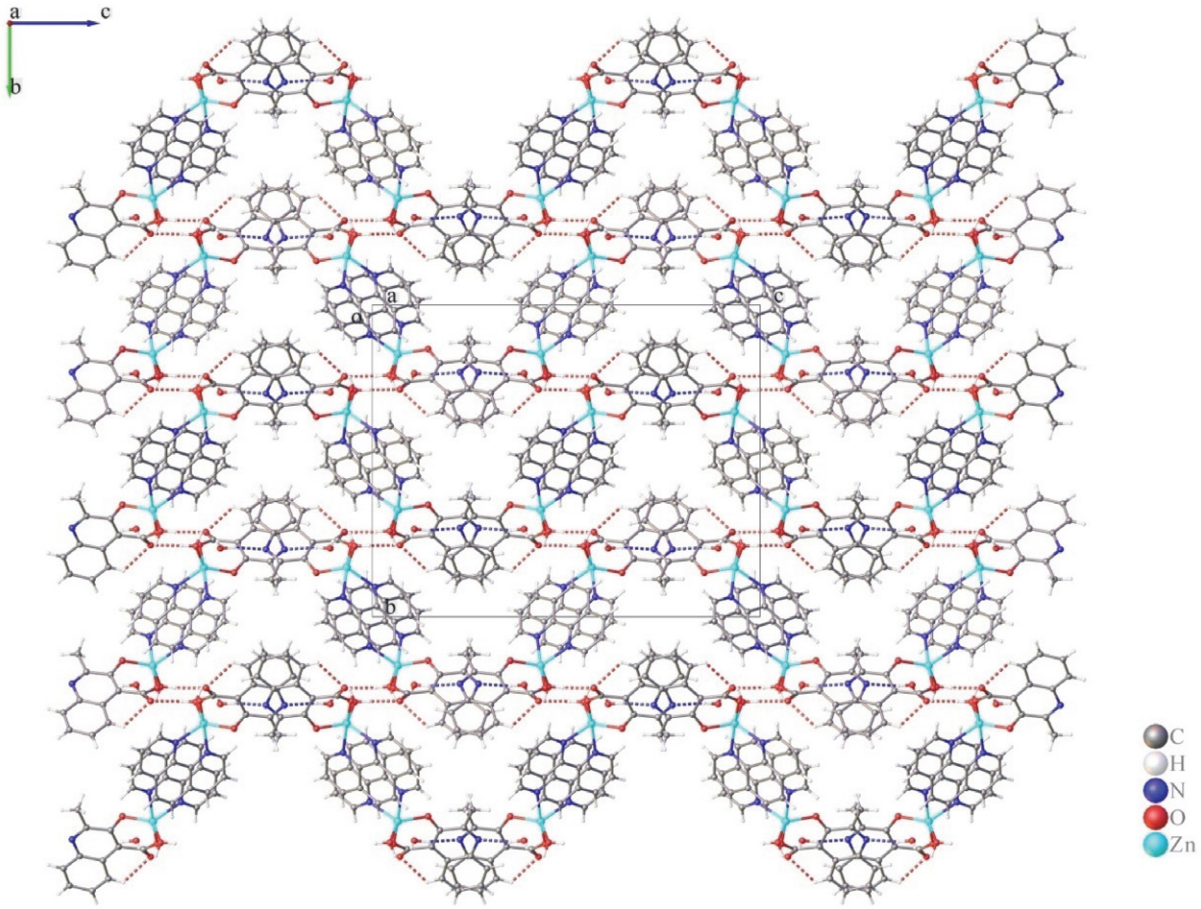

Fig. 3. The packing diagram of the title complex with the dashed lines representing the hydrogen bonding interactions. Symmetric code: (i) ½ + *x*, $^3/_2$ – *y*, 1 – *z*; (ii) 1 + *x*, *y*, *z*; (iii) ½ + *x*, *y*, ½ – *z*.

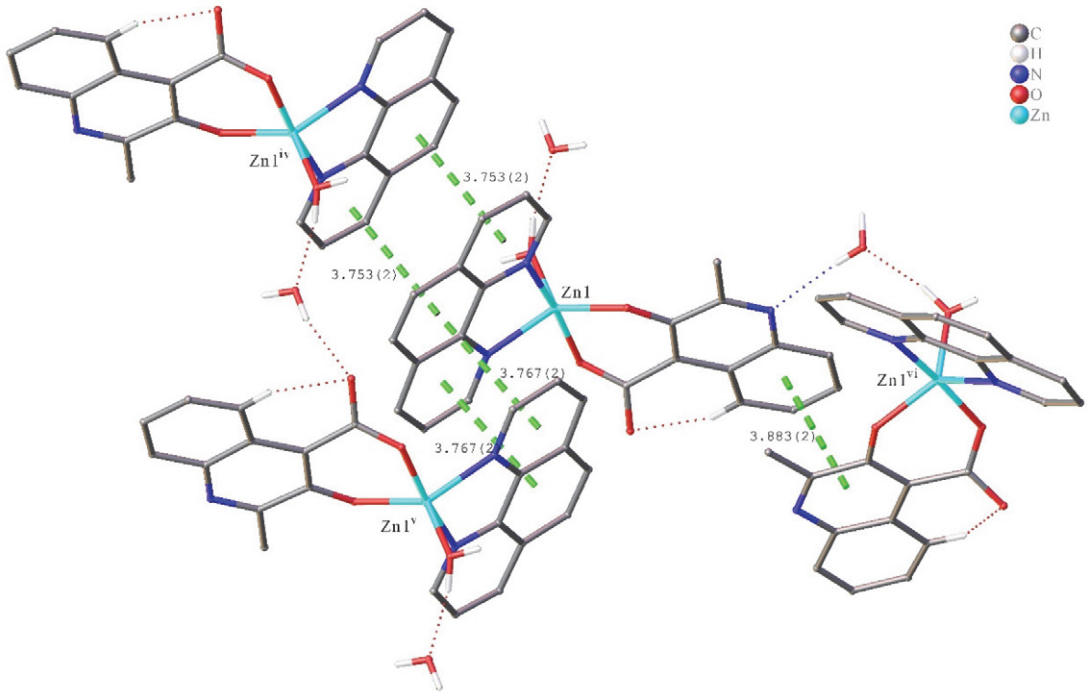

Fig. 4. The π···π stacking interactions of the title complex. Symmetric codes (iv): 2 – *x*, 1 – *y*, 1 – *z*; (v): 1 – *x*, 1 – *y*, 1 –*z*; (vi): –½ + *x*, *y*, ½ – *z*.

3. 2. Photoluminescence

In recent years, the photoluminescence of coordination compounds has gained increasing interest.[31–33] Generally, coordination compounds containing lanthanide and transition elements can exhibit photoluminescence behavior because they possess rich 4*f*-orbit and 3/4*d*-orbit electron configurations. Many studies about the photoluminescence performance of lanthanide and transition compounds have been conducted so far.[34,35] The title complex contains Zn^{2+} ions, therefore, we deemed that zinc and HL complexes can possibly exhibit interesting photoluminescence performance. Based on the above considerations and in order to reveal its potential photoluminescent properties, we carried out the photoluminescence spectra with solid state samples at room temperature and the result is presented in Fig. 5. It is obvious that the photoluminescent spectrum of the title complex displays an effective energy absorption residing in the wavelength range 240–325 nm. Upon the emission of 462 nm, the excitation spectrum shows a band at 288 nm. We further measured the corresponding photoluminescence emission spectrum of the title compound. Upon excitation at 288 nm, the emission spectrum is characterized by a sharp band at 462 nm in the blue purple region of the spectrum. The emission band of the title complex is located in the blue purple light region with the CIE (Commission Internationale de l'Éclairage) chromaticity coordinate (0.1731, 0.0048) (Fig. 6), As a result, the title complex is a potential blue purple photoluminescent material.

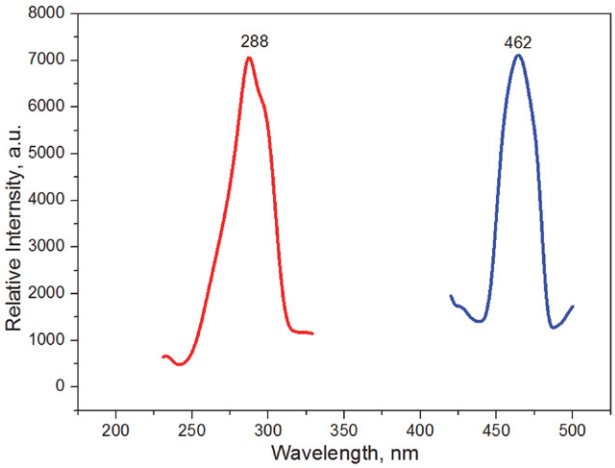

Fig. 5. The solid-state excitation (red) and emission (blue) spectra of the title complex at room temperature (color figure available online)

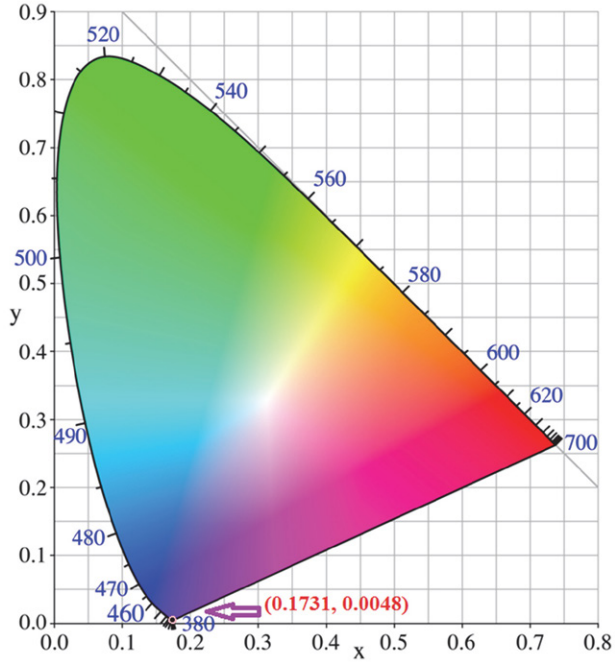

Fig. 6. CIE chromaticity diagram and chromaticity coordinates of the emission spectrum of the title complex

3. 3. TDDFT Calculations

In order to investigate the fluorescence essentiality of the title complex, we performed its theoretical calculation in light of the time-dependent density functional theory (TDDFT) based on the B3LYP function with basis set of SDD for Zn and 6-31G* for C, H, O, N and carried out by means of the Gaussian09 program.[36–38] The ground state geometry was truncated from its single crystal X-ray data (without optimization). The characteristics of the highest occupied molecular orbital (HOMO) and the lowest unoc-

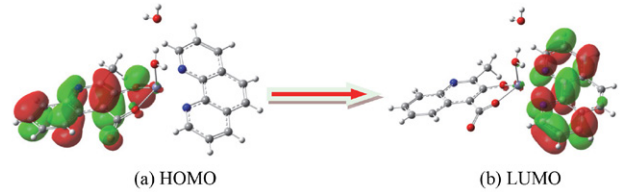

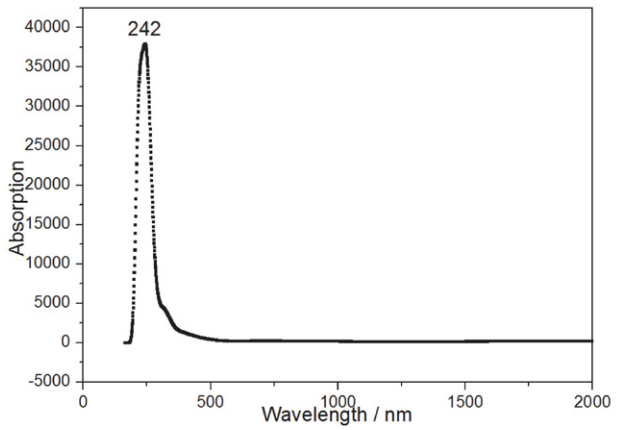

(c) Simulated fluorescent emission spectra

Fig. 7. (a) HOMO and (b) LUMO (with isosurface of 0.003) and TD-DFT simulated fluorescent emission spectra of the title complex

cupied molecular orbital (LUMO) as well as simulated fluorescent emission spectra of the title complex are given in Fig. 7. It is easy to find out that the electron population of the singlet state of HOMO is dominantly located at the HL ligand with an energy of –0.14331 Hartree. However, the electron density of the LUMO is largely distributed on the Phen ligand with an energy of –0.10413 Hartree. The energy difference between LUMO and HOMO is 0.03918 Hartree, and this is small enough to allow the charge transfer from HOMO to LUMO. In light of this observation, it is proposed that the essence of the photoluminescence of the title complex could be assigned to the ligand-to-ligand charge transfer (LLCT; from the HOMO of the π-orbital of ligand HL to the LUMO of the π-orbital of ligand Phen). This calculation result is in good agreement with the experimental observations.

3. 4. Solid State UV/Vis Diffuse Reflectance Spectroscopy

To investigate the semiconductive properties of the title complex, the solid-state UV/Vis diffuse reflectance spectra of powder sample of the title complex was measured at room temperature, using barium sulfate as the reference for 100% reflectivity. After measuring the solid-state diffuse reflectance spectra, the data was treated with the Kubelka-Munk function that is known as $\alpha/S = (1 - R)^2/(2R)$. With regard to this function, the parameter α means the absorption coefficient, *S* means the scattering coefficient, and *R* means the reflectance, which is actually wavelength independent when the size of the particle is larger than 5 μm. From the α/S vs. energy gap diagram, we can obtain the value the optical band gap, which can be extrapolated from the linear portion of the absorption edges. The solid-state UV-Vis diffuse reflectance spectrum reveals that the complex has a wide optical energy band gap of 3.22 eV, as shown in Fig. 8. As a result, the complex is a possible candidate for wide band gap semiconductors. The energy band gap of 3.22 eV of the complex is obviously larger than those of reported organic semiconductors,[39–41] which are well known as highly efficient band gap photovoltaic materials.

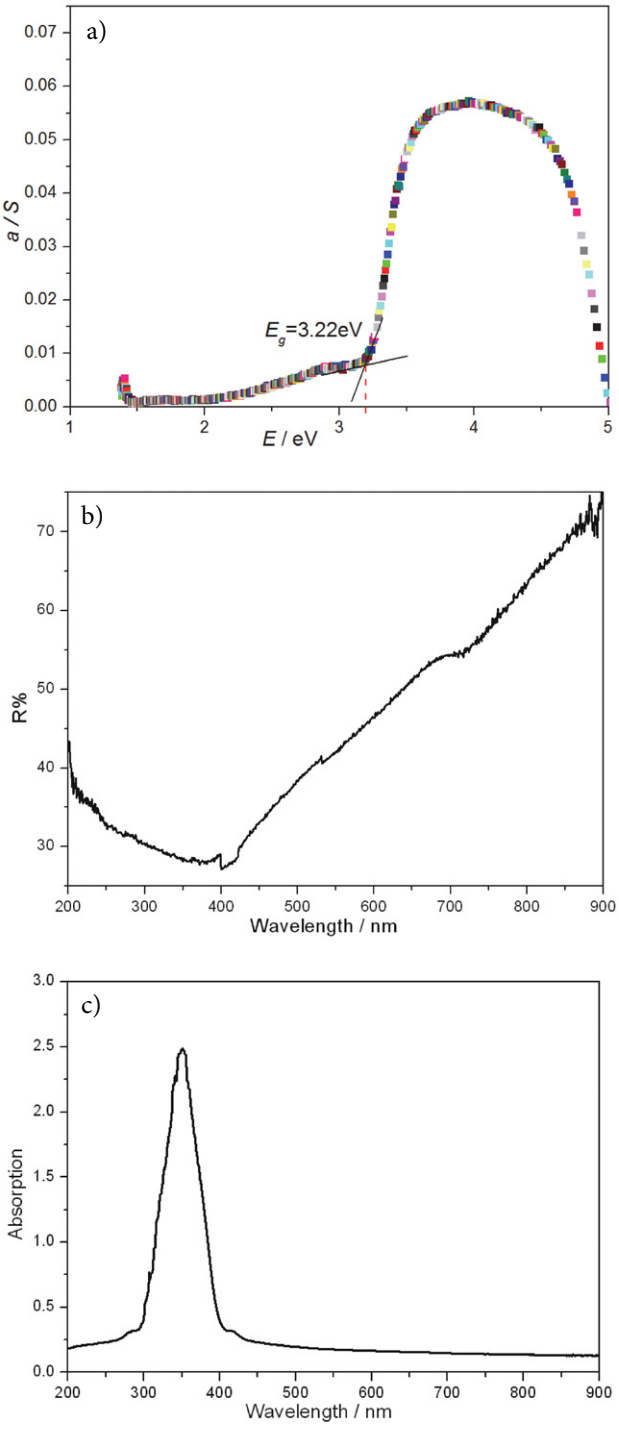

Fig. 8. (a) the solid–state UV-Vis diffuse reflectance spectrum of the title complex; (b) normal UV-vis diffuse reflectance spectra; (c) normal UV-vis absorption spectra measured in DMF solution.

4. Conclusions

In summary, a novel zinc complex with mixed ligands was prepared by using a hydrothermal method. The crystal structure of title complex shows that it is a mononuclear isolated structure of the orthorhombic *Pbca* spatial system, and a three-dimensional superstructure was constructed by intermolecular hydrogen bonds and intermolecular π···π interactions. The title complex displays blue purple light photoluminescence, which is due to the ligand-to-ligand charge transfer (LLCT; from the HOMO of the HL to the LUMO of the Phen) as shown by the TDDFT calculation. Solid-state UV/Vis diffuse reflectance spectroscopy measurements reveal that the title complex is a candidate used for wide optical band gap organic semiconductors. Our interest is to synthesize more transition metal complexes containing hydroxyquinoline carboxylates and to reveal the intrinsic relationship among the synthesis methods, crystal structures and properties.

Acknowledgements

This work was supported by the NSF of China (51363009), Jiangxi Provincial Department of Education's Item of Science and Technology (GJJ190550), Doctoral Research Startup Foundation of Jinggangshan University (JZB1905), and Natural Science Foundation Project of Jinggangshan University (JZ1901).

Appendix A. Supplementary Material

Crystallographic data for the structural analysis have been deposited with the Cambridge Crystallographic Data Centre, CCDC No. 1913492 for the title complex. Copies of this information may be obtained free of charge from the Director, CCDC, 12 Union Road, Cambridge, CBZ 1EZ, UK (Fax: +44-1223-336033; email: deposit@ccdc.cam.ac.uk or http://www.ccdc.cam.ac.uk).

5. References

1. W. H. Zhao, V. Ferro, M. V. Baker, *Coord. Chem. Rev.* **2017**, *339*, 1–16. **DOI:**10.1016/j.ccr.2017.03.005
2. M. Hu, X. Z. Ai, Z. M. Wang, Z. J. Zhang, H. L. Chong, W. M. Zhang, J. Lin, H. H. Yang, B. G. Xing, *Nano Res.* **2018**, *11*, 5474–5498. **DOI:**10.1007/s12274-018-2138-1
3. H. J. Chen, G. Y. Lyu, Y. F. Yue, T. W. Wang, D. P. Li, H. Shi, J. N. Xing, J. Y. Shao, R. Zhang, J. Liu, *J. Mater. Chem. C* **2019**, *7*, 7249–7258. **DOI:**10.1039/C9TC01520E
4. L. H. Abdel-Rahman, A. M. Abu-Dief, R. M. Shehata, F. M. Atlam, *Appl. Organomet. Chem.* **2019**, *33*, E4699–4700. **DOI:**10.1002/aoc.4699
5. D. Lionetti, V. W. Day, J. D. Blakemore, *Dalton Trans.***2017**, *46*, 11779–11789. **DOI:**10.1039/C7DT02577G
6. X. Yang, Q. Zhang, H. Peng, Z. Zuo, D. Yuan, Y. Chen, Q. Chen, G. Chen, Z. Niu, G. Li, *Acta Chim. Slov*. **2019**, *66*, 378–384. **DOI:**10.17344/acsi.2018.4876
7. T. Husch, L. Freitaq, M. Reiher, *J. Chem. Theory Comput.* **2018**, *14*, 2456–2468. **DOI:**10.1021/acs.jctc.8b00061
8. W. Lin, W. Chen, H. Kuang, H. Luo, *Acta Chim. Slov*. **2018**, *65*, 1008–1013. **DOI:**10.17344/acsi.2017.4833
9. J. Hou, X. Wang, D. Fu, C. Ko, Y. Chen, Y. Sun, K. X. Wang, K. Dong, S. Tongay, J. Yao, K. Liu, J. Wu, *Small* **2016**, *12*, 3976–3984. **DOI:**10.1002/smll.201601021
10. K. M. Mccreary, M. Currie, A. T. Hanbicki, H. J. Chuang, B. T. Jonker, *ACS Nano.* **2018**, *11*, 7988–7994. **DOI:**10.1021/acsnano.7b02554
11. X. D. Ma, B. T. Diroll, W. Cho, I. Fedin, R. D. Schaller, D. V. Talapin, G.-P. Wiederecht, *Nano Lett.* **2018**, *18*, 4647–4652. **DOI:**10.1021/acs.nanolett.8b00347
12. L. Z. Lin, Q. X. Zhong, J. T. Hong, H. L. Chen, W. T. Chen, *Inorg. Acta.* **2018**, *479*, 30–35. **DOI:**10.1016/j.ica.2018.04.039
13. M. Hamer, J. Zultak, A. V. Tyurnina, D. Terry, A. Barinov, A. Garrner, J. Donoghue, A. P. Rooney, V. Kandyba, A. Giampietri, A. J. Graham, N. R. Wilson, *Mater. Science* **2019**, *13*, 2136–2142. **DOI:** 10.1021/acsnano.8b08726.
14. T. Dietl, H. Ohno, F. Matsukura, J. Cibert, D. Ferrand, *Science* **2000**, *287*, 1019–1022. **DOI:**10.1126/science.287.5455.1019
15. W. K. Hyoun, J. K. Yong, M. Ali, Y. K. Sung, S. K. Myung, H.-B. Jae, S. K. Sang, *Sensor. Acturat. B:Chem.* **2017**, *249*, 590–601. **DOI:** 10.1016/j.snb.2017.03.149.
16. K. Makoto, S. Tohru, H. Yukiko, S. Katsuaki, A. Yoshio, *Sci. Rep.* **2018**, 8, 10839. **DOI:** 10.1038/s41598-018-27953-6.
17. J. G. Kang, K. Taekim, S. Piljeon, A. Facchetti, J. Kim, S. K. Park, *RSC Adv.* **2019**, *9*, 6193–6198. **DOI:**10.1039/C8RA09917K
18. X. G. Yi, Z. X. Zhang, W. T. Chen, L. Z. Lin, H. L. Chen, *J. Solid State Chem.* **2018**, *266*, 16–22. **DOI:**10.1016/j.jssc.2018.07.004
19. D. L. Reger, A. Debreczeni, M. D. Smith, *Inorg. Chem.* **2011**, *50*, 11754–11764. **DOI:**10.1021/ic201830h
20. Y. F. Wu, S. Zhao, H. X. Na, P. Y. Yang, H. B. Xu, Y. X. Zhang, Y. L. Chen, M. H. Zeng, *Inorg. Chem.* **2018**, *57*, 12683–12689. **DOI:**10.1021/acs.inorgchem.8b01841
21. S. Tripathi, S. Sachan, G. Anantharaman, *Polyhedron* **2016**, *119*, 55–70. **DOI:**10.1016/j.poly.2016.08.009
22. D. Dhara, P. Kalita, S. Mondal, R. S. Narayanan, K. R. Mote, V. Huch, M. Zimmer, C. B. Yildiz, D. Scheschkewitz, V. Chandrasekhar, A. Jana, *Chem. Sci.* **2018**, *9*, 4235–4243. **DOI:**10.1039/C8SC00348C
23. X. G. Yi, Y. Z. Liu, X. N. Fang, X. Y. Zhou, Y. X. Li, *Chinese Struct. Chem.* **2019**, *38*, 325–330. **DOI:**10.14102/j.cnki.0254-5861.2011-2065.
24. Rigaku, CrystalClear Version 1.35, *Rigaku Corporation*, **2002**.
25. O. V. Dolomanov, L. J. Bourhis, R. J. Gildea, *J. Appl. Cryst.***2009**, *42*, 339–341. **DOI:**10.1107/S0021889808042726
26. G. M. Sheldrick, *Acta Cryst. A* **2015**, *71*, 3–8. **DOI:**10.1107/S2053229614024218
27. G. M. Sheldrick, *Acta Cryst. C* **2015**, *71*, 3–8. **DOI:**10.1107/S2053229614024218
28. I. D. Brown, D. Altermat, *Acta Cryst. B* **1985**, *41*, 240–244. **DOI:**10.1107/S0108768185002051
29. L. Tian, N. Yang, G. Zhao, *Inorg. Chem. Commun.* **2010**, *13*, 1497–1500. **DOI:**10.1016/j.inoche.2010.08.026
30. O. Kozachuk, K. Khaletskaya, M. Halbherr, *Eurjin. Org. Chem.* **2012**, *10*, 1688–1695. **DOI:**10.1002/ejic.201101295
31. G. Gheno, M. Bortoluzzi, R. Ganzerla, F. Enrichi, *J. Lumin.* **2014**, *145*, 963–969. **DOI:**10.1016/j.jlumin.2013.09.027
32. S. S. Zhang, H. F. Su, Z. Wang, X. P. Wang, W. X. Chen, Q. Q. Zhao, C. H. Tung, D. Sun, L. S. Zheng, *Chem. Eur. J.* **2018**, *24*, 1998–2003. **DOI:**10.1002/chem.201705264
33. Y. Wang, Y. Y. Li, J. Han, X. Tang, L. Ni, L. Wang, *RSC Adv.* **2016**, *6*, 82309–82320. **DOI:**10.1039/C6RA16327K
34. F. Q. Huang, K. Mitchell, J. A. Ibers, *Inorg. Chem.* **2001**, *40*, 5123–5126. **DOI:**10.1021/ic0104353
35. M. D. Allendorf, C. A. Bauer, R. K. Bhakta, R. J. T. Houk, *Chem. Soc. Rev.* **2009**, *38*, 1330–1352. **DOI:**10.1039/b802352m
36. A. D. Becke, *J. Chem. Phys.* **1993**, *98*, 5648–5652. **DOI:**10.1063/1.464913
37. C. Lee, W. Yang, R. G. Parr, *Phys. Rev. B* **1988**, *37*, 785–789. **DOI:**10.1103/PhysRevB.37.785

38. M. J. Frish, *et al*., Gaussian 09, Revision A.02, *Gausian, Inc.*, Wallingford CT, **2009**.
39. R. Agneeswari, M. Kong, J. Lee, J.H. Kwon, V. Tamilavan, S.S. Park, S.H. Park, Y. Jin, *Mol. Cryst. Liq. Cryst.* **2019**, *685*, 29–39. **DOI:**10.1080/15421406.2019.1645458
40. H.-M. Kuang, J.-G. Huang, L.-Z. Lin, Q.-X. Zhong, W.-T. Chen, *Inorg. Chim. Acta* **2019**, *489*, 48–53. **DOI:**10.1016/j.ica.2019.02.006
41. Q. Luo, H. Luo, H. Kuang, W. Chen, Y. Wen, *J. Solid State Chem.* **2019**, *270*, 200–204. **DOI:**10.1016/j.jssc.2018.09.040

Povzetek

S hidrotermalno sintezo smo pripravili nov enojedrni cinkov kompleks [ZnL(Phen)(H_2O)] · H_2O, ki vsebuje liganda Phen (Phen = 1,10-fenantrolin) in 3-hidroksi-2-metilkinolin-4-karboksilno kislino (HL). Določili smo strukturo z monokristalno rentgensko difrakcijo. Kompleks kristalizira v ortorombskem kristalnem sistemu in tvori enojedrne enote. Molekule so povezane preko vodikovih vezi in π···π interakciji in tvorijo tridimenzionalno (3*D*) supramolekularno strukturo. Pri fluorescenci je razviden širok emisijski pas v vijolično-modrem območju. Izračuni z uporabo časovno odvisne teorije gostotnostnega funkcionala (TDDFT) kažejo, da lahko emisijo pripišemo prenosu naboja ligand-ligand (LLCT). Difuzna reflektanca v trdnem stanju kaže na širok optični pasovni razmik.

Except when otherwise noted, articles in this journal are published under the terms and conditions of the Creative Commons Attribution 4.0 International License

DOI: 10.17344/acsi.2019.5539 *Acta Chim. Slov.* **2020,** *67,* 516–521
creative commons

Scientific paper

Nickel(II) Complex with a Flexidentate Ligand Derived from Acetohydrazide: Synthesis, Structural Characterization and Hirshfeld Surface Analysis

Rasoul Vafazadeh,[1,*] Zahra Mansouri[1] and Anthony C. Willis[2]

[1] *Department of Chemistry, Yazd University, Yazd, Iran.*

[2] *Research School of Chemistry, Australian National University, Canberra, ACT 2601, Australia.*

** Corresponding author: E-mail: e-mail address: rvafazadeh@yazd.ac.ir*
Tel: +98 351 8214778; Fax: +98 351 7250110

Received: 09-02-2019

Abstract

The mononuclear Ni(II) complex $[Ni(L^P)_2(CH_3OH)_2]Cl_2$ has been synthesized by reacting 1-(5-hydroxy-3-methyl-5-phenyl-4,5-dihydro-1*H*-pyrazol-1-yl)ethan-1-one ligand (HL) with $NiCl_2{\cdot}6H_2O$ in methanol solution. In the reaction, the tridentate ligand, HL, was converted *in situ* into 4-hydroxy-4-phenylbut-3-en-2-ylidene)acetohydrazid ligand, (pyrazole, L^P). The pyrazole ligand acts as bidentate neutral ligand and the hydroxyl group is left uncoordinated. The structure of the Ni(II) complex has been established by X-ray crystallography. The Ni(II) is six-coordinate and has a distorted octahedral geometry. It is bonded by two nitrogen and by two oxygen atoms of the two pyrazole ligands and two oxygen atoms of methanol molecules. The Hirshfeld surface analysis and the 2D the fingerprint plot are used to analyses all of the intermolecular contacts in the crystal structures. The main intermolecular contacts are H/H and Cl/H interactions.

Keyword: Flexidentate ligand; pyrazole ligand; Hirshfeld surface; fingerprint plot; hydroxyl group

1. Introduction

The complexation of transition metal ions with multidentate Schiff base ligands has been studied extensively as their structures can be divers and they can have versatile properties.[1–3] The hydrazone ligands which are formed by condensation reactions between hydrazide derivatives and relevant aldehyde or ketones, are a signification class of such multidentate ligands. Metal complexes with these ligands can have a wide range of structures with significant variations in geometry.[3–7] Also, the cyclization reaction of hydrazide precursors may take place and lead to the formation of pyrazole ligands.[8–10] The pyrazole compounds themselves are hydrolytically and thermally stable and can act as a mono- or bidentate ligands. The pyrazoles and their complexes can have interesting structural features, properties and biologically actives.[11–14]

In our previous work, we reported the synthesis of CuLX complexes where HL is 1-(5-hydroxy-3-methyl-5-phenyl-4,5-dihydro-1*H*-pyrazol-1-yl)ethan-1-one ligand

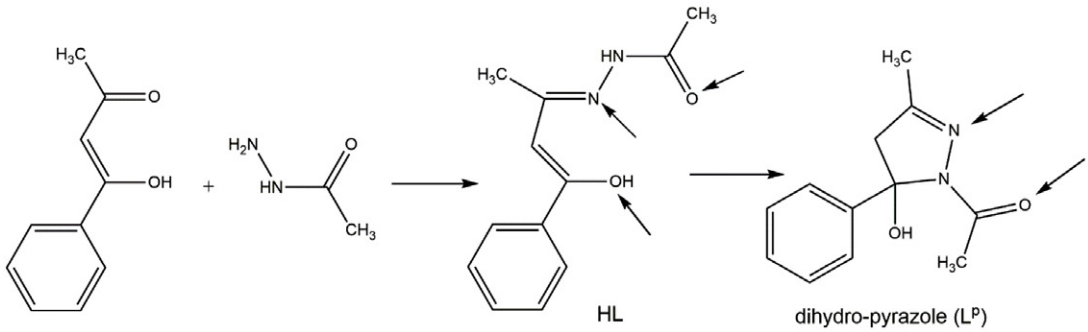

Scheme 1. Preparation of HL and L^P ligands with potential ligating sites

(Scheme 1).[15] In these complexes, the hydrazone ligand was in the keto form and acted as a tridentate monoanionic. In order to investigate the effect of the metal on the coordination behavior of the hydrazone ligand, we report here the reaction of Ni(II) salts with HL. *In situ,* the ligand is converted into the 4-hydroxy-4-phenylbut-3-en-2-ylidene)acetohydrazide ligand, (pyrazole, L^p) by the self-cyclization reaction of HL in the presence $NiCl_2$. The pyrazole coordinates to Ni(II) and act as bidentate neutral ligand and the hydroxyl group is left uncoordinated (Scheme 1).

A search of the literature revealed that the pyrazole had been reported previously by Wang *et al.* and Alberola *et al.* and crystal structure has also been determined.[16,17] Pyrazole has been prepared by the reaction of 1-phenylbutane-1,3-dione and acetohydrazide in the presence of a catalytic amount of acid under solventless conditions[16] or in solvent.[17]

2. Experimental Section

2. 1. Starting Materials

All chemicals were of analytical reagent grade and were used without further purification.

Caution! Transition-metal complex perchlorate salts are known to be hazardous and must be treated with care, especially in the presence of organic solvents.

2. 2. Physical Measurements

Infrared spectra were taken with an Equinox 55 Bruker FT-IR spectrometer using KBr pellets in the 400–4000 cm^{-1} range. Absorption spectra were determined using methanol and dimethylformamide (DMF) solutions in a GBC UV-Visible Cintra 101 spectrophotometer with a 1 cm quartz cell, in the range 200–800 nm. Elemental analyses (C, H, N) were performed by using a CHNS-O 2400II PERKIN-ELMER elemental analyzer.

2. 3. X-ray Crystallography and Hirshfeld Surfaces Analyses

Single-crystal X-ray diffraction data were collected at 150 K on an Agilent SuperNova diffractometer using Cu Kα (λ = 1.54180 Å) radiation. Data were extracted using the CrysAlis PRO package.[17] The structures were solved by direct methods with the use of SIR92.[19] The structures were refined on F^2 by full matrix last-squares techniques using the CRYSTALS program package.[20] The H atoms were initially refined with soft restraints on the bond lengths and angles to regularize their geometry (C–H in the range 0.93–0.98 Å, O–H = 0.83 Å) and with U_{iso}(H) in the range 1.2–1.5 times U_{eq} of the parent atom. After this, the positions of the H atoms bonded to O and N were refined without constraints whereas those bonded to C ride on the atoms to which they are bonded. Crystallographic data and refinement details for the complex is given in Table 1.

Table 1. Crystallographic data of the complex **1**

Compound	$[Ni(L^p)_2(CH_3OH)_2]Cl_2$
Chemical formula	$C_{26}H_{36}Cl_2N_4NiO_6$
Formula weight	630.21
Temperature (K)	150
Space group	Orthorhombic, *Pbca*,
a (Å)	7.3033 (1)
b (Å)	19.2677 (1)
c (Å)	20.4218 (1)
Z	4
F(000)	1320
D_{Calc} (g cm^{-3})	1.457
Crystal size (mm)	0.22 × 0.12 × 0.11
μ (mm^{-1})	3.08
GOF on F^2	1.020
$R[F^2 > 2\sigma(F^2)]$	0.029
$wR(F^2)$ (all data)	0.072*

*$w = 1/[\sigma^2(F^2) + (0.04P)^2 + 2.1P]$, where $P = (\max(F_o^2,0) + 2F_c^2)/3$

Hirshfeld surfaces analysis and the associated two-dimensional fingerprint plots for the complexes were calculated with CrystalExplorer 3.1 program.[21] The d_{norm} surface and 2D fingerprint were used to analyses intermolecular interaction in the crystal packing.

2. 4. Syntheses of HL Ligand

The Schiff base ligand, HL, was prepared as previously reported elsewhere by us.[15] Briefly, the ligand was obtained by condensation of equimolar amounts of benzoylacetone (20 mmol, 3.24 g) and acetohydrazide (20 mmol, 1.48 g) in methanol (30 mL). The mixture was refluxed for 2 h during which a light-yellow precipitate was formed. The reaction mixture was then cooled to room temperature and the solid compound formed was filtered. The compound was recrystallized from warm acetone. Yield 67%. IR (KBr, cm^{-1}): υC=N = 1610, υC=O = 1650. Electronic spectra in acetone: λ_{max}(nm), (log ε): 333 (2.66), 232 (4.29).

2. 5. Synthesis of Ni(II) Complex, $[Ni(L^p)_2(CH_3OH)2]Cl_2$, 1.

This complex was obtained as an unexpected product from following reaction: $NiCl_2{\cdot}6H_2O$ (2 mmol, 0.475 g) was added to a stirred solution of the ligand HL (2 mmol, 0.434 g) in methanol (30 mL) and the resulting solution was stirred at room temperature for 2 h. The solution's color turned green. After two days, blue block-shaped crystals of the $[Ni(L^p)_2(CH_3OH)_2]Cl_2$ complex suitable for X–ray analysis appeared at the bottom of the vessel. They were filtered off and dried in air. Yield: 61% based on HL. Anal. Calc. for $C_{26}H_{36}C_{l2}N_2NiO_6$: C, 49.55; H, 5.76; N, 8.89%. Found: C, 49.47; H, 5.62; N, 8.84%. IR (KBr, ν_{max}/cm^{-1}): υC=N = 1587, υC=O = 1605. UV-Vis, λ_{max}(methanol)/nm: 784 (log ε, 0.93), 371 (3.50) and 207 (4.54).

By comparison, the corresponding reactions of NiX_2 ($X = NO_3^-$ and ClO_4^-) with HL were undertaken under the same conditions, but it was found that new Ni(II) complexes were not formed and the sole product isolated from the preparative mixtures were the initial salt, *i.e.* NiX_2.

3. Results and Discussion

3. 1. Synthesis and Characterization of the Complexes

Complex **1** was obtained by the reactions of $NiCl_2 \cdot 6H_2O$ with an equimolar amount of the ligand HL in methanol solution at room temperature. The reaction of $NiCl_2$ with HL ligand did not lead to formation of the NiL-Cl complex. The ligand instead was converted *in situ* into the pyrazole ligand, L^P under the reaction conditions. L^P coordinates to the Ni(II) center, acting as a neutral bidentate ligand and leading to an unexpected product, $(Ni(L^P)_2(CH_3OH)_2]Cl_2$. In contrast, the reaction of copper(II) salts with this ligand did not lead to a cyclization reaction, and the copper complexes which were formed have the ligand acting as a monoanionic tridentate species, *i.e.* [CuLX].[15] The cyclization reactions in the Ni(II) case may occur due to formation of an unstable Ni(II) complex with HL or Ni(II) may have catalyzed the cyclization reaction.

The IR spectrum of the free HL ligand shows bands at 1610 and 1650 cm^{-1}, which is assigned as νC=N and νC=O, respectively.[3,22,23] In the IR spectra of complex, these bands were shifted toward lower energy in comparison with the free ligand, which indicates coordination of the imine nitrogen atom and the carbonyl group to the nickel ion.[23–25] The fairly broad band of medium intensity appearing at around 3400 cm^{-1} corresponds to the intramolecular hydrogen bonding in the free ligand, this band in the complex is observed in around the 3050 cm^{-1} region, which indicates that the hydroxyl group remains as an uncoordinated OH group.[26–28]

3. 2. Description of Crystal Structure of the Complex 1

The structural fragment of the complex **1** is shown in Fig. 1. The complex crystallizes in orthorhombic space group *Pbca* and there are four molecules in the unit cell (Z = 4). As shown by Fig. 1, the crystallographic asymmetric unit is one-half of the structural fragment and consists of a Ni(II) atom, one L^P ligand, a coordinated methanol and a chloride counter anion. The remainder of the cation is generated by a crystallographic inversion symmetry operation centered on the metal.

The Ni(II) is sixcoordinate (N2O4 donor atoms) and has a distorted octahedral geometry. The equatorial plane is formed by two nitrogen and two oxygen atoms from two L^P ligands coordinates to the metal center. The ligands with Ni(II) atom formed five-membered chelate rings. The two axial positions are occupied by oxygen atoms of the two methanol molecules.

The Ni–N bond length in the complex is 2.067(1) Å. The Ni–O bond length at the axial position (2.061(1) Å) is slightly longer than the corresponding bond in the equatorial plane (2.037(1) Å). The Ni–O and Ni–N bond lengths of the complex are in good agreement with Ni(II) complexes previously reported.[29–31] The chelating N–Ni–O angle is 79.37(4)°, whereas the non-chelating N–Ni–O angles is 100.63(4)°. The O3–Ni1–O1 and O3–Ni1–N1 angles are 88.20(4)° and 89.47(5)°, respectively. The C4-O1 bond distance of 1.232(3) Å agrees well with the value of C=O bond as already observed in similar compounds.[32] This bond length is similar to the carbonyl group bond length in uncoordinated pyrazole (1.241 and 1.229 Å).[16,17] The C3–O2 bond length of the alcohol group (1.391(2) Å) is longer than the bond length of the carbonyl group (C4–O1) and similar to C–O(hydroxyl) bond length in uncoor-

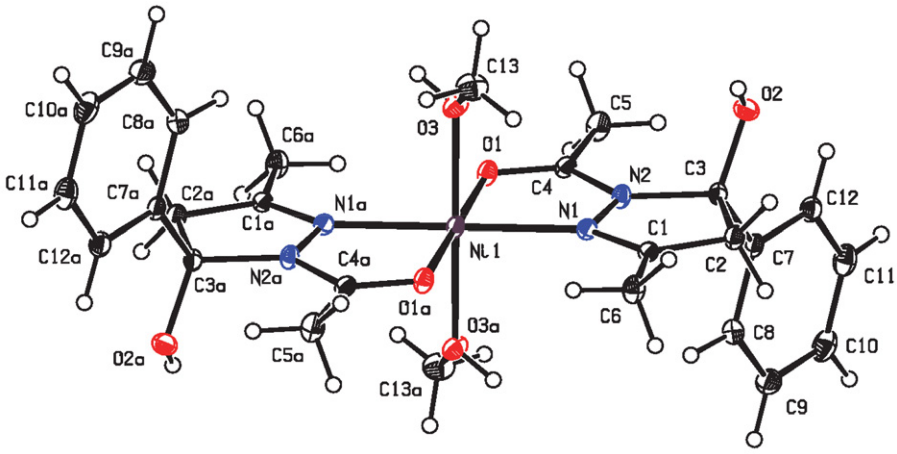

Fig. 1. The molecular structure of complex **1** with labelling of selected atoms, ellipsoids show 30% probability levels (symmetry code: (a) $-x + 1, -y + 1, -z + 1$).

dinated pyrazole (1.413 and 1.395 Å).[16,17] Selected bond lengths and angles, are summarized in Table 2.

The sum of the internal angles of the pyrazole ring in complex **1** [N1–N2–C1–C2–C3 = 539.78°] shows the planarity of this ring since it is very close to the ideal value of 540°. The value is also close to the internal angles of the uncoordinated pyrazole ring uncoordinated (549.78 and 539.61°). The planarity is also illustrated by the small deviations of the atoms of the pyrazole ring from the corresponding mean plane (0.008–0.028 Å). In the uncoordinated pyrazole which was synthesized by Wang et al. and Alberola et al., the deviate from the plane are in the 0.006–0.028 Å and 0.009–0.032 Å rang, respectively.[16,17]

Table 2. Selected bond lengths (Å) and angles (°) in the Ni(II) complex

Ni1–O1	2.0372(10)	O1–Ni1–N1	79.37(4)
Ni1–O3	2.0606(11)	O1–Ni1–O3	88.20(4)
Ni1–N1	2.0674(12)	O1–Ni1–N1[a]	100.63(4)
C4–O1	1.2476(18)	N1–Ni1–O3	89.47(5)
C3–O2	1.3914(18)	C3–N2–N1	112.21(10)
C4–N2	1.3434(18)	N2–N1–C1	109.12(11)
C3–N2	1.5160(17)	O1–C4–N2	120.44(13)
C1–N1	1.2814(18)	C3–O2–H2	107.90(17)

Symmetry code: (a) $-x + 1, -y + 1, -z + 1$.

The mean planes of the pyrazole and aromatic rings in complex **1** are almost perpendicular. The dihedral angle is ca. 87.66° which is similar to the values found in uncoordinated pyrazole previously reported (85.73 and 85.79°).[16,17]

The chloride counter anions are involved in intermolecular and intramolecular hydrogen bonding interaction with the OH groups of the uncoordinated hydroxyl of the ligand and coordinated methanol molecule, which build a 1D chain structure running through the *a* axis (Fig. 2). The Ni···Ni distance is 7.303 Å, which is much longer than the van der Waals radii sum for nickel (3.26 Å), showing that there is no interaction between the nickel atoms. The distance between Cl and the center of aromatic ring from adjacent complex and centers of aromatic rings are 6.489 and 7.303 Å, showing that there are no Cl···π and π···π interactions in the packing for complex **1**.

Full details of the hydrogen bonding are given in Table 3.

3. 3. Hirshfeld Surface Analyses

The Hirshfeld surface analyses and the fingerprint plots provide some useful quantitative information about the strength and role of the intermolecular contacts, and to estimate their importance in the in the crystal packing stability.[1,26,33,34] In Fig. 3, the 3D Hirshfeld surface mapped are shown over a d_{norm} (normalized contact distance) range of –0.705–1.148 Å. The value of the d_{norm} can be

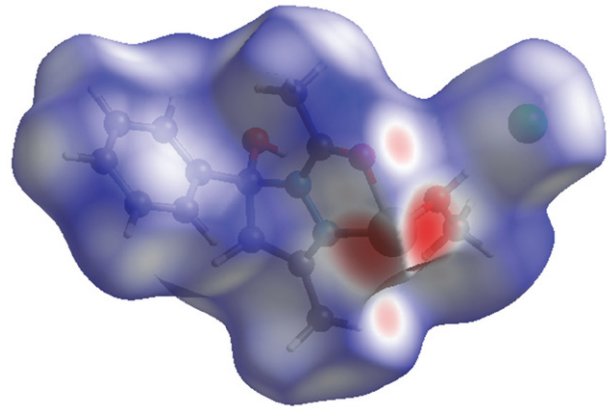

Fig. 3. Hirshfeld surface mapped with d_{norm} for complex **1**.

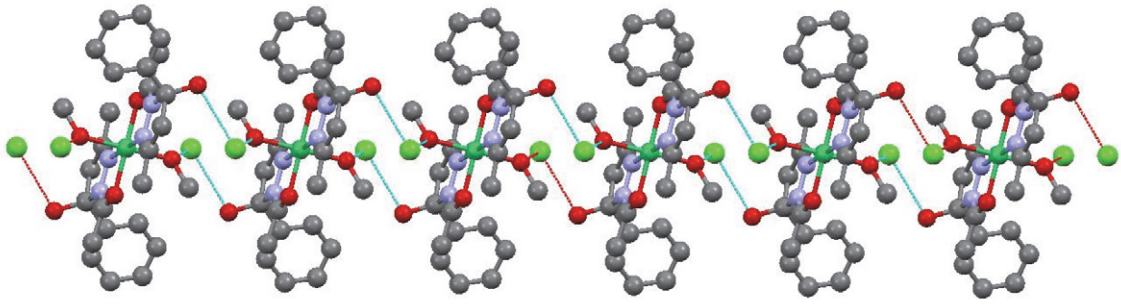

Fig. 2. The hydrogen bonding interactions between uncoordinated hydroxyl group of ligand and the chloride counter anions in complex **1** along *b* axis.

Table 3. Hydrogen bonding (Å) and angles (°) in complex **1**

D–H···*A*	D–H	H···*A*	D…*A*	D–H···*A*	Symmetry code
O2–H2···Cl1	0.77(2)	2.33(2)	3.093(1)	174.9(19)	$-x, -y + 1, -z + 1$
O3–H3···Cl1	0.83(2)	2.16(2)	2.987(1)	173.0(20)	

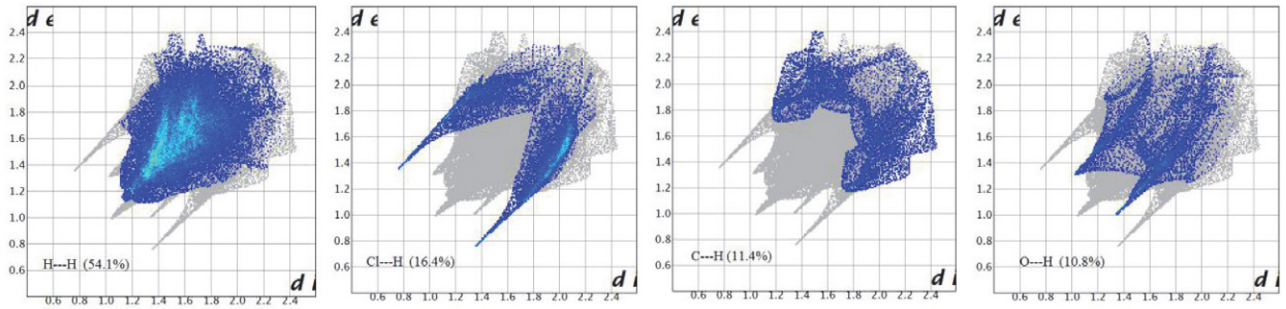

Fig. 4. The 2D fingerprint plots and relative contributions to the percentage of Hirshfeld surface for various interactions in complex **1**.

positive or negative when intermolecular contacts are longer or shorter than the sum van der Waals radii of the atoms (vdW), respectively. The d_{norm} values are mapped onto the Hirshfeld surface using a red–blue–white color scheme. Red regions correspond to closer contacts and negative d_{norm} value, the blue regions correspond to longer contacts and positive d_{norm} value. The white-colored regions correspond to weak contacts and the distance of contacts is around the vdW separation ($d_{norm} \approx 0$).[33–35]

The 2D fingerprint plot and the contribution of each type of interaction are describe in Fig. 4. The H···H interaction (54.1%) appears as wide and blunt spikes in the region 1.15 Å < (de + di) < 1.70 Å. The Cl···H/H···Cl interaction (16.4%) also appears as two distinct spikes, the lower spike corresponding to the acceptor spike represents the Cl···H interactions (di = 1.35 Å and de = 0.75 Å) and the upper spike being a donor spike represents the H···O interactions (de = 1.35 Å and di = 0.9 Å) in the fingerprint plots. Further, the C···H/H···C interaction which comprise 10.2% of the total Hirshfeld surfaces were appeared as two distinct spikes, the C···H interaction with de = 1.17 Å and di = 1.70 Å and H···C interaction with de = 1.70 Å and di = 1.17 Å. The O···H/H···O interactions comprise 10.8% of the total Hirshfeld surfaces with de = 1.17 Å and di = 1.70 Å and de = 1.70 Å and di = 1.17 Å for O···H and H···O interactions, respectively.

4. Conclusion

The $Ni(L^P)_2(CH_3OH)_2]Cl_2$ complex was obtained as an unexpected product from reaction of $NiCl_2$ with HL at room temperature. In the Ni(II) complex, metal center is hexacoordinated with a distorted octahedral geometry. The ligand coordinates to the metal center as a neutral bidentate ligand, while in the reaction of copper(II) salts with this ligand, as previously reported, the ligand acts as a monoanionic tridentate ligand. In the reaction with $NiCl_2$, the ligand was converted *in situ* into the pyrazole ligand, L^P in a cyclization reaction. The Hirshfeld surface analyses and the fingerprint plots provide some useful quantitative information about the role of intermolecular contacts in the crystal packing.

Supplementary material

The deposition numbers of the studied complex is CCDC 1949210. This data can be obtained free-of-charge via www.ccdc.cam.ac.uk/data_request/cif, by emailing data-request@ccdc.cam.ac.uk, or by contacting The Cambridge Crystallographic Data Centre, 12 Union Road, Cambridge CB2 1EZ, UK; fax +44 1223 336033.

Acknowledgments

The authors are grateful to the Yazd University and the Australian National University for partial support of this work.

5. References

1. R. Vafazadeh, M. Ehsani1, A. C. Willis, *J. Iran. Chem. Soc.* **2019**, *16,* 2509–2518. **DOI:**10.1007/s13738-019-01721-3
2. T. Ghosh, S. Pal, *Inorg. Chim. Acta* **2010**, *363,* 3632–3636. **DOI:**10.1016/j.ica.2010.07.007
3. R. Vafazadeh, R. Esteghamat-Panah, A. C. Willis, A. F. Hill, Polyhedron, 2012, 48, 51–57. **DOI:**10.1016/j.poly.2012.08.057
4. R. Vafazadeh, Z. Moghadas, A.C. Willis, *J. Coord. Chem.,* **2015**, *68,* 4255–5271. **DOI:**10.1080/00958972.2015.1096349
5. R. Vafazadeh, N. Abdollahi, A.C. Willis, *Acta Chim. Slov.* **2017**, *64,* 409–414. **DOI:**10.17344/acsi.2017.3263
6. A. Mukhopadhyay, S. Pal, *Polyhedron* **2004**, 23, 1997–2004. **DOI:**10.1016/j.poly.2004.05.002
7. A. Mukhopadhyay, S. Pal, *Eur. J. Inorg. Chem.* **2009**, 4141–4148. **DOI:**10.1002/ejic.200900472
8. R. Vafazadeh, N. Hasanzade, M. M. Heidari, A. C. Willis, *Acta Chim. Slov.* **2015**, *62,* 122–129. **DOI:**10.17344/acsi.2014.797
9. R. Vafazadeh, A. C. Willis, *Acta Chim. Slov.* **2016**, *63,* 186–192.
10. K. Sancak, M. Er, Y. Unver, M. Yildirim, I. Degirmencioglu, *Transit. Met. Chem.* **2007**, *32,* 16–22.
11. P. P. Devi, F. A.S. Chipem, C. B. Singh, R. K. Lonibala, *J. Mol. Struct.* **2019**, *1176,* 7–18. **DOI:**10.1016/j.molstruc.2018.08.070
12. G. He, X. Hua, N. Yang, L. Li, J. Xu, L. Yang, Q. Wang, L. Ji, *Bioorg. Chem.* **2019**, *91,* 103176–103178. **DOI:**10.1016/j.bioorg.2019.103176

13. G. A. Gamov, M. N. Zavalishin, A. Y. Khokhlova, A. V. Gashnikova, V. V. Aleksandriiskii, V. A. Sharnin, *J. Coord. Chem.* **2018**, *71,* 3304–3314. **DOI:**10.1080/00958972.2018.1512708
14. P. Tyagi, M. Tyagi, S. Agrawal, S. Chandra, H. Ojha, M. Pathak, *Spectrochim. Acta A.* **2017**, *171,* 246–257. **DOI:**10.1016/j.saa.2016.08.008
15. R. Vafazadeh, M. Alinaghi, A. C. Willis, A. Benvidi, *Acta Chim. Slov.,* **2014**, *61,* 121–125.
16. Z.-X. Wang, H.-L. Qin, *Green Chem.* **2004**, *6,* 90–92. **DOI:**10.1039/b312833d
17. A. Alberola, L. Calvo, A. G. Ortega, M. L. Sidaba, M. C. Saiiudo, S. G. Granda, E. G. Rodriguezt, *Heterocycles* **1999**, *51,* 2675–2686. **DOI:**10.3987/COM-99-8683
18. Z. Otwinowski, W. Minor. Methods in Enzymology, edited by C. W. Carter Jr & R. M.W. Sweet, New York: Academic Press, **1997**, 276, pp. 307–326. **DOI:**10.1016/S0076-6879(97)76066-X
19. A. Altomare, G. Cascarano, G. Giacovazzo, A. Guagliardi, M. C. Burla, G. Polidori, M. Camalli, *J. Appl. Cryst.* **1994**, *27,* 435–436. **DOI:**10.1107/S0021889894000221
20. P. W. Betteridge, J. R. Carruthers, R. I. Cooper, K. Prout, D. J. Watkin, *J. Appl. Cryst.* **2003**, *36,* 1487–1487. **DOI:**10.1107/S0021889803021800
21. K. Wolff, D. J. Grimwood, J. J. McKinnon, M. J. Turner, D. Jayatilaka, M. A. Spackman. CrystalExplorer, Version 3.0. University of Western Australia, **2012**.
22. K. Nakamoto, Infrared and Raman Spectra of Inorganic and Coordination Compounds, fourth ed., Wiley, New York, **1986**.
23. R. Vafazadeh, F. Jafari, M. M. Heidari, A.C. Willis, *J. Coord. Chem.* **2016**, *69,* 1313–1325. **DOI:**10.1080/00958972.2016.1163547
24. M. Shebl, S. M. E. Khalil, *Monatsh Chem.* **2015**, *146,* 15–33. **DOI:**10.1007/s00706-014-1302-x
25. R. Vafazadeh, B. Khaledi, A. C Willis, *Acta Chim. Slov.* **2012**,*59,* 954–958.
26. R. Vafazadeh, A. Kazemi-nasab, A. C. Willis, *Acta Chim. Slov.* **2019**, *66,* 1010–1018. **DOI:**10.17344/acsi.2019.5333
27. M. Barwiolek, E. Szlyk, A. Berg, A. Wojtczak, T. Muziol, J. Jezierska, *Dalton Trans.,* **2014**, *43,* 9924–9933. **DOI:**10.1039/C4DT00654B
28. M. Dolai, T. Mistri, A. Panja, M. Ali, *Inorg. Chim. Acta* **2013**, *399,* 95–104. **DOI:**10.1016/j.ica.2013.01.006
29. R. Vafazadeh, M. Namazian, B. Shahpoori-Arani, A. C. Willis, P. D. Carr, *Acta Chim. Slov.* **2018,** *65,* 372–379. **DOI:**10.17344/acsi.2017.4096
30. L. Radovanović, J. Rogan, D. Poleti, M. V. Rodić, Z. Jagličić, *Acta Chim. Slov.* **2018**, *65,* 191–198. **DOI:**10.17344/acsi.2017.3813
31. R. Vafazadeh, A. Gorji, S. Ansari, A. C. Willis, *Acta Chim. Slov.* **2012**, *59,* 897–903.
32. P. M. V. Kumar, P. K. Radhakrishnan, *Inorg. Chim. Acta* **2011**, *375,* 84–92. **DOI:**10.1016/j.ica.2011.04.034
33. M. A. Spackman, D. Jayatilaka, *CrystEngComm* **2009**, *11,* 19–32. **DOI:**10.1039/B818330A
34. Y. X. Sun, L. Z. Liu, F. Wang, X. Y. Shang, L. Chen, W. K. Dong, *Crystals* **2018**, *8,* 227–239. **DOI:**10.3390/cryst8050227
35. N. Khelloul, K. Toubal, N. Benhalima, R. Rahmani, A. Chouaih, A. Djafri, F. Hamzaoui, *Acta Chim. Slov.* **2016**, *63,* 619–626. **DOI:**10.17344/acsi.2016.2362

Povzetek

Sintetizirali smo enojedrni Ni(II) kompleks $[Ni(L^p)_2(CH_3OH)_2]Cl_2$ z reakcijo 1-(5-hidroksi-3-metil-5-fenil-4,5-dihidro-1*H*-pirazol-1-il)etan-1-ona (HL) z $NiCl_2{\cdot}6H_2O$ v metanolu. Tekom reakcije se je trovezni ligand HL *in situ* pretvoril v 4-hidroksi-4-fenilbut-3-en-2-iliden)acetohidrazidni ligand, (pirazol, L^p). Pirazolni ligand je dvovezni nevtralni ligand katerega hidroksilna skupina se ne koordinira. Struktura Ni(II) kompleksa je bila določena z rentgensko kristalografijo. Ni(II) ima popačeno oktaedrično geometrijo. Nanj sta vezana dva dušikova atoma in dva kisikova atoma z dveh pirazolskih ligandov ter dve molekuli metanola. Intermolekularni kontakti v kristalni strukturi so bili študirani z Hirshfeldovo analizo površine in 2D diagrami prstnih odtisov. Glavni intermolekularni kontakti so H/H in Cl/H interakcije.

Except when otherwise noted, articles in this journal are published under the terms and conditions of the Creative Commons Attribution 4.0 International License

DOI: 10.17344/acsi.2019.5551 *Acta Chim. Slov.* **2020,** *67,* 522–529
creative commons

Scientific paper

Formation of Cobalt Ferrites Investigated by Transmission and Emission Mössbauer Spectroscopy

Vit Prochazka, Anezka Burvalova, Vlastimil Vrba, Josef Kopp and Petr Novak*

Department of Experimental Physics, Faculty of Science, Palacký University, 17. listopadu 1192/12, 77 146 Olomouc, Czech Republic

** Corresponding author: E-mail: petr.novak@upol.cz*

Received: 09-06-2019

Abstract

This study focuses on cobalt and iron ordering within a ferrite structure $Co_xFe_{3-x}O_4$, formed during a solid-state reaction of α-Fe_2O_3 and $CoCl_2$. A unique combination of transmission and emission Mössbauer spectroscopy was employed to inspect selectively the positions of iron and cobalt atoms in the structure. The comparison of transmission and emission spectra allowed the determination of tetrahedral and octahedral positions occupation. The presented method of combining the two Mössbauer spectroscopy techniques is suitable for any compounds containing both iron and cobalt atoms. Additional information concerning the samples composition and morphology were obtained by X-ray powder diffraction and scanning electron microscopy. An increased level of Co atoms incorporation into the structure of ferrite was revealed when higher amounts of Co entered the reaction.

Keywords: Cobalt ferrite, Mössbauer spectroscopy, degree of inversion, solid state reaction

1. Introduction

Cobalt ferrites are thoroughly investigated because of their magnetic, optical and electrical properties and their wide range of technological applications such as transformer cores, batteries, recording heads, ferrofluids, biomedical applications including biosensors and cellular therapy, catalysis and sensors.[1–10] Cobalt ferrite is a magnetically hard material with a high positive magnetic anisotropy constant, good chemical stability, high mechanical hardness and high level of magnetization. Furthermore, it does not pose a risk to the biological environment.[1,11] Most of the physical properties of this ferrite strongly depend on the size and shape of the particles.[12] Cobalt ferrite nanoparticles are also photomagnetic materials which demonstrate an interesting change in coercivity induced by light.[13]

The specific properties of cobalt ferrites are governed by their microstructural arrangement that is formed during their synthesis. Therefore, it is important to understand the mechanisms of their formation and the dynamics of their synthesis. Ferrites form the spinel structure (AB_2O_4). The basic cell of $MeFe_2O_4$ spinel ferrite, where Me refers to the metal atom, is a cubic close-packed structure containing 32 anions.[14] Cations occupy two different crystallographic sites, namely A and B positions. Cations localized at A positions are surrounded by 4 oxygen atoms forming a tetrahedron, thus this position is also referred to as tetrahedral. Cations in B positions are enclosed by six oxygen atoms forming octahedron. Therefore, the B position is called octahedral. Each basic cell contains 8 tetrahedral (A) positions and 16 octahedral (B) positions.[1,14,15]

Cobalt ferrites can be prepared by a number of different methods such as solid-state reaction,[16–18] mechanochemical synthesis,[12] combustion method,[19–21] co-precipitation,[22–24] hydrothermal synthesis,[25–27] sol-gel method[28,29] or reverse micelle technique.[30,31]

Ferrites are divided into several groups according to their cations distribution.[14,32] For the normal structure the formula $(Me)[Fe_2]O_4$ is usually used. Square and round brackets denote the cations´ association to the octahedral and tetrahedral positions respectively. In the normal structure all the non-iron cations are located in tetrahedral positions. The opposite extreme, the inverse structure, has all the non-iron cations in octahedral positions according to the formula $(Fe)[MeFe]O_4$. The transition state between these two extremes can be represented as $(Me_{1-\delta}Fe_\delta)[Me_\delta Fe_{2-\delta}]O_4$, where δ is called the degree of inversion. It is equal to 0 for the normal spinel structure and to 1 for the inverse spinel structure.

The degree of inversion expresses the ratio of cations at different crystallographic positions. Nevertheless, its determination in cobalt ferrites is rather challenging task because Fe and Co atoms have similar atomic scattering factors and their identification by X-ray powder diffraction is limited. Cobalt ferrites usually form the inverse structure, where Co^{2+} ions are located only in B positions and Fe^{3+} ions are situated in both A and B positions. However, the degree of inversion might not be constant and it can depend on the previous heat treatment.[33–36]

Within this study we utilized emission Mössbauer spectroscopy and transmission Mössbauer spectroscopy for investigation of the local surroundings of Co and Fe atoms. The transmission arrangement inspects the local surroundings of iron atoms. On the contrary, the emission arrangement offers information selectively on the local structure around the ^{57}Co atoms. The combination of these two complementary information allows to determine the degree of inversion. Moreover, the correlation of cobalt and iron Mössbauer spectra could bring new enlightenment to the problem of cobalt ferrite structure formation.

2. Experimental Section

Samples with different composition were prepared by solid phase synthesis from hematite (prepared at Regional Centre of Advanced Technologies and Materials in Olomouc) and cobalt chloride (prepared at Merck KGaA, Darmstadt, Germany). The required amount of cobalt chloride and hematite (Table 1) was mixed and crushed for approximately 10 minutes in an agate mortar. After adding 30 µl of 0.1 M HCl 50 mg of homogeneous mixture was placed into a laboratory furnace. To guarantee the same thermal treatment conditions, all the samples were placed into the furnace simultaneously. After being dried for one hour at 90 °C the samples were heated up to the temperature of 1000 °C with a rate of 30 °C per minute and annealed in static air atmosphere for 5 hours. In respect to radiation safety two sample series were prepared. The first series contained a radioactive ^{57}Co, while the other was prepared with the use of a non-radioactive Co. In the case of radioactive samples, the HCl solution contained small amount of dissolved ^{57}CoCl with radionuclide purity of 99.8 %. Namely 10^{17} of radioactive atoms per 30 µl of solution were incorporated inside the resulting material during the synthesis. The resulting activity of the samples was 1.1 MBq. The radioactive samples were used in transmission and emission Mössbauer experiments. Non-radioactive samples were used for other techniques, i.e. scanning electron microscopy and X-ray powder diffraction.

The studied samples, listed in Table 1, follow the notation S*x* where *x* denotes the amount of cobalt in the formula $Co_xFe_{3-x}O_4$ assuming that all Fe and Co atoms are incorporated into the resulting ferrite. Samples prepared with radioactive cobalt are labelled by *. Sample S1.00^{168} was prepared using an annealing time of 168 h. Observing only small differences between the sample S1.00^{168} and S1.00 we can state that annealing time of 5 h was sufficient for incorporation of Co atoms to the structure and formation of ferrite.

The morphology of the samples was examined by Tescan VEGA3 LMU scanning electron microscope (SEM). The pictures were achieved using accelerating voltage of 20 kV. The crystal structure and phase composition of the samples were analysed by X-ray powder diffraction (XRD). Diffractometer with a cobalt X-ray lamp (Co Kα radiation λ = 1.79031 Å) operated in the Bragg-Brentano geometry in the 2θ angle range of 10–105 °.

Mössbauer spectroscopy measurements were performed on MS96 virtual spectrometer[37,38] in a constant acceleration regime. The used scintillation detector contained a crystal of sodium iodide activated by thallium. In transmission measurement, ^{57}Co in a rhodium matrix was utilized as a radiation source. In the emission arrangement, $K_2MgFe(CN)_6$ with 0.25 mg/cm^2 of ^{57}Fe was employed as a reference absorber. The measuring time in the transmission and emission modes was approximately five and eleven days, respectively.

3. Results and Discussion

The morphology of the studied samples is shown in the SEM images in Figure 1. The S0.33 sample consisted of

Table 1. List of samples, cobalt and iron atomic ratios and the quantities of cobalt chloride and hematite used for the synthesis. The nominal amount of Co in the formula $Co_xFe_{3-x}O_4$ is denoted by x. The samples prepared with radioactive ^{57}Co are labelled with *.

x	Sample	A_X (Co) : A_X (Fe)	Weight of Fe_2O_3(mg)	Weight of $CoCl_2$ (mg)
0.33	S0.33, S0.33*	0.25:2.00	100.0	20.3
0.66	S0.66, S0.66*	0.50:2.00	90.0	36.5
0.82	S0.82, S0.82*	0.75:2.00	80.0	48.7
1.00	S1.00, S1.00*, S1.00^{168}	1.00:2.00	79.8	64.9
1.15	S1.15, S1.15*	1.25:2.00	60.0	60.9
1.29	S1.29, S1.29*	1.50:2.00	50.0	60.9
1.40	S1.40, S1.40*	1.75:2.00	50.0	71.1

spherical particles of 200 nm, see Figure 1a. There is a wide particle size distribution from 0.1 to 1 μm for the sample S0.66 (Figure 1b). The further increase in the overall particle size was observed with rising concentration of Co in the samples (Figure 1c-f). The size of particles overcomes even 2 μm. Particles forming natural octahedrons typical for spinel structure can be seen in the SEM images (Figure 1d-h).

Figure 2 shows the diffraction patterns of all the samples. The structures belonging to cobalt ferrites, Fe_2O_3 and Co_3O_4 were identified in the diffraction patterns and their amounts were estimated using Rietveld analysis. The development of the individual phases can be observed in the range of diffraction patterns containing the cobalt ferrite (220), cobalt oxide (220) and hematite (104) reflections. The reflections show the gradual rise in the amount of cobalt ferrite with the increase of cobalt ratio inside the samples (2θ = 35.2 °). Similarly, the slight increase in the peak corresponding to cobalt oxide could be observed as well (2θ = 36.5 °). On the other hand, the amount of hematite followed the opposite trend and decreased (2θ = 38.7 °). For the samples S1.29 and 1.40 the broadening of reflections corresponding to the ferrite structure and their shift to higher angles may indicate lattice defects.

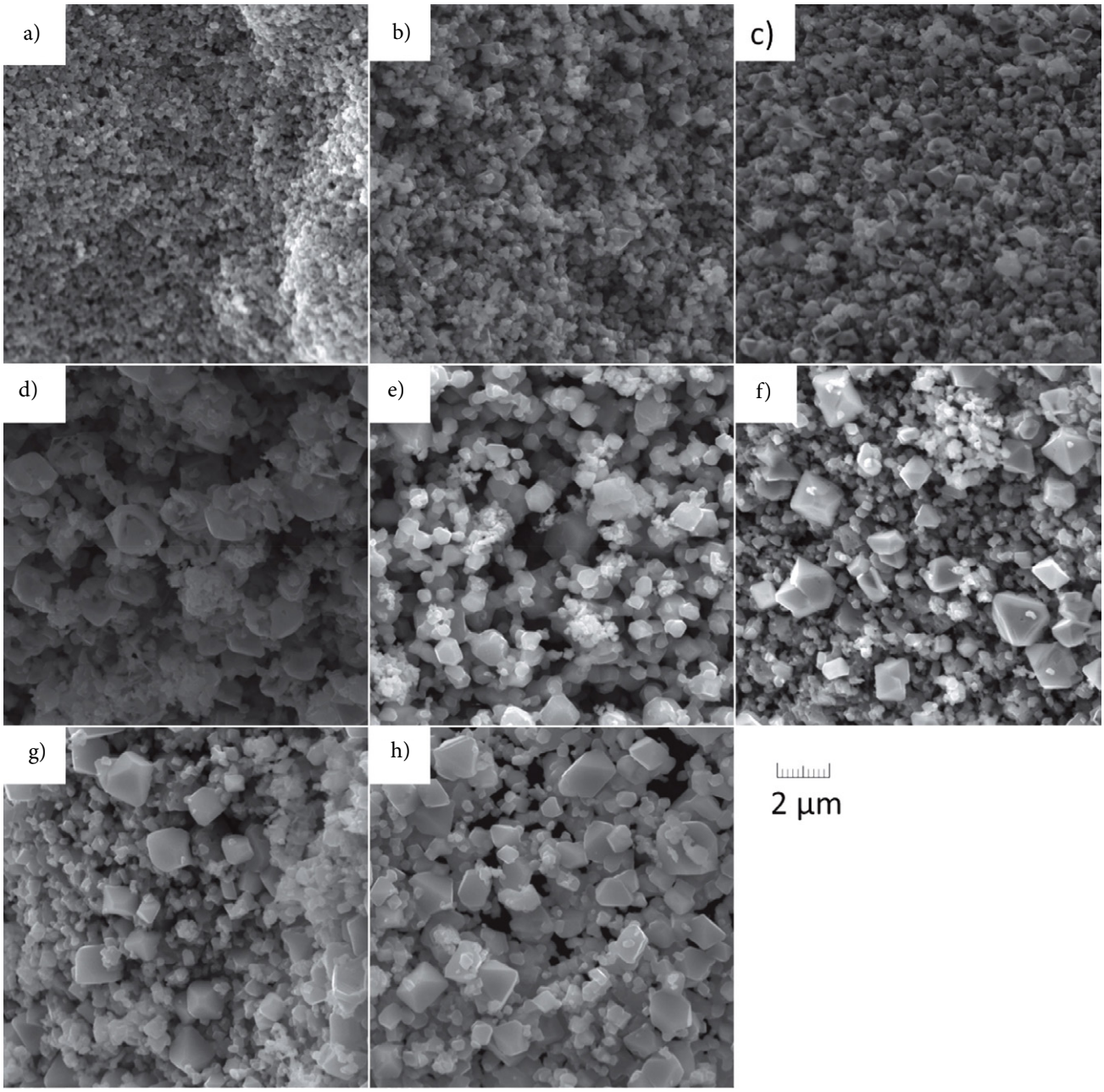

Figure 1. SEM images a) S0.33, b) S0.66, c) S0.82, d) S1.00, e) S1.00[168], f) S1.15, g) S1.29, h) S1.40.

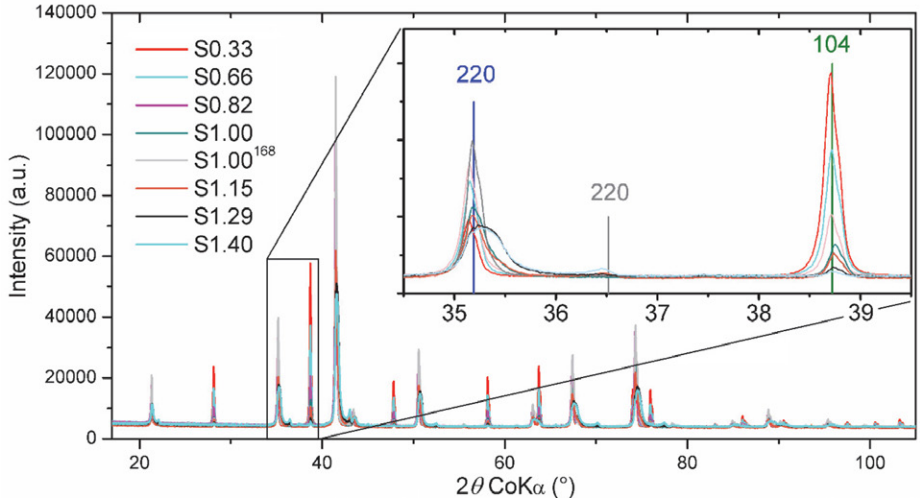

Figure 2. X-ray powder diffraction patterns for samples S0.33, S0.66, S0.82, S1.00, S1.00[168], S1.15, S1.29 and S1.40. The cobalt ferrite (220), cobalt oxide (220) and hematite (104) reflections are shown in detail in the upper-right corner. The positions of these reflections are marked by blue, grey and green vertical lines, respectively.

Figure 3 shows the dependence of the phase composition on cobalt concentration in the samples. The amount of cobalt ferrites rose with the increasing nominal Co concentration *x*, while the amount of hematite decreased. In addition to the shown samples, 7.5 % of Fe_2O_3 and 92.5 % of cobalt ferrites were determined for the sample S1.00[168].

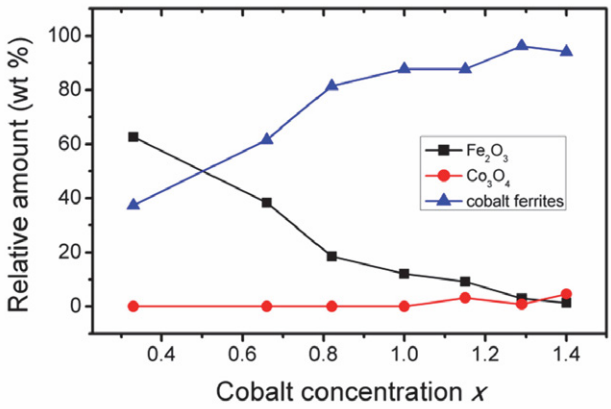

Figure 3. Mass percentage of individual phases in samples.

As can be seen in Figure 3, not all the Co atoms from $CoCl_2$ were incorporated into the cobalt ferrite structure. Therefore, the nominal amount *x* differs from the actual amount of Co in ferrite, denoted as *y*. The values of *y* in $Co_yFe_{3-y}O_4$ were determined from mass ratios of cobalt ferrite, hematite and cobalt oxide obtained by XRD and from the inputs of the reaction. The resulting *y* with respect to the nominal *x* is shown in Figure 4. It can be seen that for lower amounts of Co entering the reaction relatively low amount of ferrite with higher concentration of

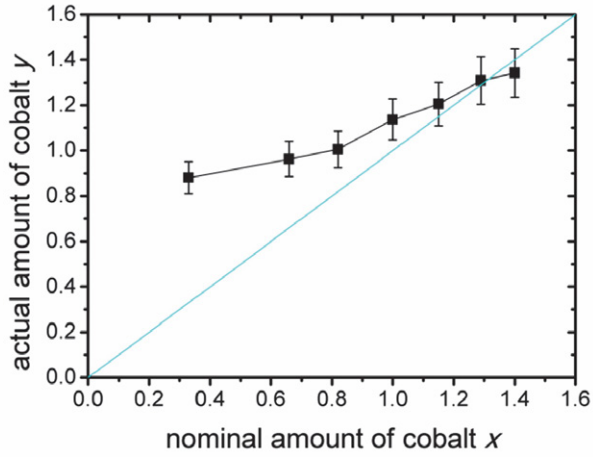

Figure 4. The actual amount of cobalt *y* in ferrite $Co_yFe_{3-y}O_4$ versus the nominal amount of cobalt *x*.

Co is formed. With increasing amount of Co entering the reaction the actual *y* reaches the nominal *x*.

Figure 5 shows emission and transmission spectra of the samples S0.33*, S0.66*, S0.82*, S1.00*, S1.15*, S1.29* and S1.40*. All the spectra were normalized to unit area absorbed. The arrows in the figure 5 indicate the lines positions of $CoFe_2O_4$ and Fe_2O_3. They were calculated according to the hyperfine parameters listed in Table 2.[11] The

Table 2. Hyperfine parameters of $CoFe_2O_4$ A and B site and hematite.[11]

	Δ (mm/s)	ΔE_Q (mm/s)	B_{hf} (T)
$CoFe_2O_4$ (A)	0.29	-0.01	48.78
$CoFe_2O_4$ (B)	0.36	0.01	51.64
Hematite	0.37	-0.19	51.75

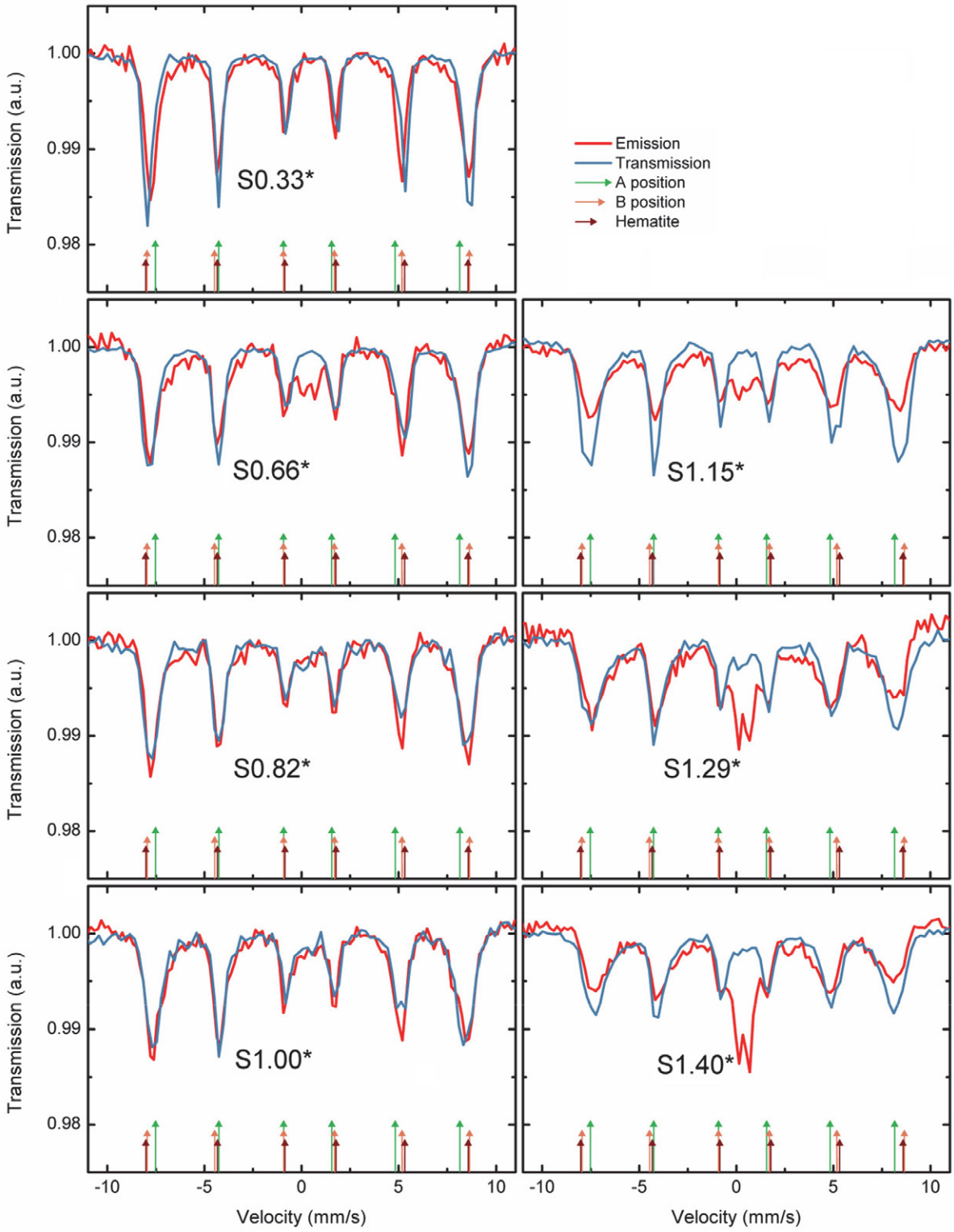

Figure 5. Emission and transmission spectra of samples S0.33*, S0.66*, S0.82*, S1.00*, S1.15*, S1.29* and S1.40*. The arrows indicate the lines positions of $CoFe_2O_4$ (A and B positions) and Fe_2O_3.

difference between emission and transmission spectrum of sample S0.33* is caused by the presence of excess hematite in the sample. Hematite contributed only to a transmission spectrum because it contains no ^{57}Co.

The doublet in the emission spectra, positioned at the centre of the measured area, was ascribed to ^{57}Co atoms incorporated into the structure of cobalt oxide. There was also an evident line broadening in the case of samples

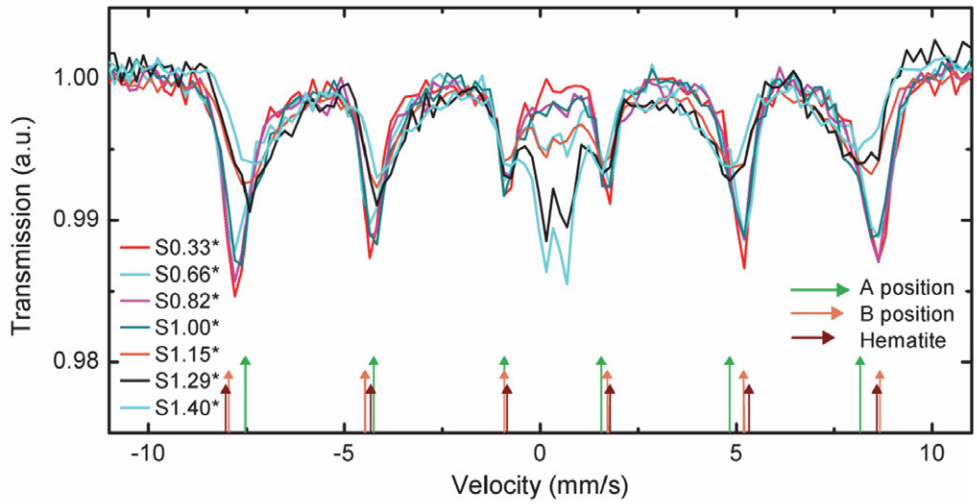

Figure 6. Emission spectra of S0.33*, S0.66*, S0.82*, S1.00*, S1.15*, S1.29* and S1.40* samples.

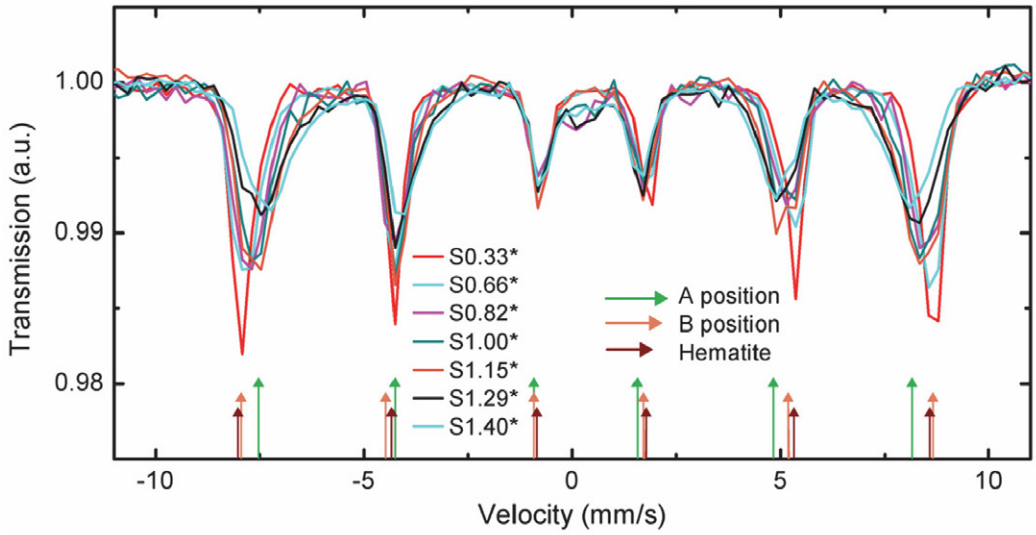

Figure 7. Transmission spectra of S0.33*, S0.66*, S0.82*, S1.00*, S1.15*, S1.29* and S1.40* samples.

S1.29* and S1.40* which indicates an occurrence of a distribution of hyperfine magnetic field. That is in accordance with the observation of line broadening in X-ray powder diffraction patterns for samples S1.29 and S1.40. Likely, the higher amount of Co caused higher disorder in the ferrite lattice.

Figure 6 compares the emission spectra of samples S0.33*, S0.66*, S0.82*, S1.00*, S1.15*, S1.29*, and S1.40*. One could clearly see a change in the distribution of hyperfine magnetic field with the increasing Co concentration. The spectral lines get broader and shift to lower energies.

Figure 7 shows transmission Mössbauer spectra of S0.33*, S0.66*, S0.82*, S1.00*, S1.15*, S1.29* and S1.40* samples. Similarly to the emission spectra, there was a shift in the positions of the spectral lines as well as the change in their shape with the increasing concentration of cobalt.

Comparing the transmission and emission spectra, it can be concluded that the formed cobalt ferrites did not exhibit the inverse spinel structure. In the case of the inverse spinel structure the Co atoms would occupy only the B positions. This would cause an observable difference between the magnetic contribution to the emission and transmission Mössbauer spectra as only the B position spectral lines would occur in the former. However, in our case the line positions of emission and transmission spectra for individual samples did not exhibit any significant differences. This is typical for a uniform distribution of cobalt and iron atoms in the A and B positions, leading to a mixed spinel structure described by a formula $(Co_{0.33y}Fe_{1-0.33y})[Co_{0.66y}Fe_{2-0.66y}]O_4$. Therefore, the measured data suggest that the A and B positions occupation approaches the uniform distribution. For samples with the cobalt concentration y close to 1 this would lead to a classic

formula $(Co_{1-\delta}Fe_{\delta})[Co_{\delta}Fe_{2-\delta}]O_4$, where the degree of inversion δ equals 0.66. Small differences between the emission and transmission spectra can be ascribed to the presence of hematite (samples S0.33* and S0.66*) or cobalt oxide (samples S0.66*, S1.15*, S1.29* and S1.40*).

4. Conclusion

In this work, the samples of cobalt ferrites containing various amount of Co atoms were prepared by a solid-state reaction of hematite and cobalt chloride. The relative amount of cobalt in the ferrite structure was obtained by XRD. The relatively small amount of cobalt ferrite with higher concentration of Co was observed for lower number of Co atoms entering the reaction. A novel approach of comparing the results from transmission and emission Mössbauer spectroscopy allows to follow the formation of cobalt ferrites in more detail. Namely, it suggests that cations distribution in the ferrite structure approaches the uniform distribution according to the formula $(Co_{0.33y}Fe_{1-0.33y})[Co_{0.66y}Fe_{2-0.66y}]O_4$. For samples whose relative ratios of cobalt and iron atoms were close to 1:2 the degree of inversion was close to $\delta = 0.66$.

Acknowledgement

The authors gratefully acknowledge the financial support from the internal IGA grant of Palacký University (IGA_PrF_2019_002 and IGA_PrF_2019_023). Authors would also like to thank Ivo Medřík for preparation of hematite powder, Josef Kaslik for XRD measurements and Helena Sedláčková for her help with the paper.

5. References

1. D. S. Mathew, R. Juang, *Chem. Eng. J.* **2007**, *129*, 51–65. **DOI:**10.1016/j.cej.2006.11.001
2. P. Lavela, J. L. Tirado, *J. Power Sources* **2007**, *172*, 379–387. **DOI:**10.1016/j.jpowsour.2007.07.055
3. I. Sharifi, H. Shokrollahi, S. Amiri, *J. Magn. Magn. Mater.* **2012**, *324*, 903–915. **DOI:**10.1016/j.jmmm.2011.10.017
4. S. Amiri, H. Shokrollahi, *Mater. Sci. Eng. C* **2013**, *33*, 1–8. **DOI:**10.1016/j.msec.2012.09.003
5. A. Manikandan, R. Sridhar, S. A. Antony, S. Ramakrishna, *J. Mol. Struct.* **2014**, *1076*, 188–200. **DOI:**10.1016/j.molstruc.2014.07.054
6. P. D. Prasad, J. Hemalatha, *J. Magn. Magn. Mater.* **2019**, *484*, 225–233. **DOI:**10.1016/j.jmmm.2019.04.026
7. O. Caltun, I. Dumitru, M. Feder, N. Lupu, H. Chiriac, *J. Magn. Magn. Mater.* **2008**, *320*, 869–873. **DOI:**10.1016/j.jmmm.2008.04.067
8. M. Gharibshahian, O. Mirzaee, M. S. Nourbakhsh, *J. Magn. Magn. Mater.* **2017**, *425*, 48–56. **DOI:**10.1016/j.jmmm.2016.10.116
9. A. B. Salunkhe, V. M. Khot, N. D. Thorat, M. R. Phadatare, C. I. Sathish, D. S. Dhawale, S. H. Pawar, *Appl. Surf. Sci.* **2013**, *264*, 598–604. **DOI:**10.1016/j.apsusc.2012.10.073
10. M. Kooti, S. Gharineh, M. Mehrkhah, A. Shaker, H. Motamedi, *Chem. Eng. J.* **2015**, *259*, 34–42. **DOI:**10.1016/j.cej.2014.07.139
11. Z. P. Niu, Y. Wang, F. S. Li, *Phys. Status Solidi B* **2010**, *247*, 198–201. **DOI:**10.1002/pssb.200945455
12. M. Eshraghi, P. Kameli, *Curr. Appl. Phys.* **2011**, *11*, 476–481. **DOI:**10.1016/j.cap.2010.08.032
13. J. Wang, T. Deng, Y. Lin, C. Yang, W. Zhan, *J. Alloys Compd.* **2008**, *450*, 532–539. **DOI:**10.1016/j.jallcom.2007.02.099
14. R. J. Hill, J. R. Craig, G. V Gibbs, *Phys. Chem. Miner.* **1979**, *4*, 317–339. **DOI:**10.1007/BF00307535
15. D. Carta, M. F. Casula, A. Falqui, D. Loche, G. Mountjoy, C. Sangregorio, A. Corrias, *J. Phys. Chem. C* **2009**, *4*, 8606–8615. **DOI:**10.1021/jp901077c
16. V. G. Patil, S. E. Shirsath, S. D. More, S. J. Shukla, K. M. Jadhav, *J. Alloys Compd.* **2009**, *488*, 199–203. **DOI:**10.1016/j.jallcom.2009.08.078
17. R. Pandit, K. K. Sharma, P. Kaur, R. Kumar, *Mater. Chem. Phys.* **2014**, *148*, 988–999. **DOI:**10.1016/j.matchemphys.2014.09.009
18. P. C. R. Varma, R. Sekhar, D. Banerjee, M. Raama, K. G. Suresh, A. K. Nigam, *J. Alloys Compd.* **2008**, *453*, 298–303. **DOI:**10.1016/j.jallcom.2006.11.058
19. A. J. Franco, E. C. de O. Lima, M. A. Novak, P. R. J. Wells, *J. Magn. Magn. Mater.* **2007**, *308*, 198–202. **DOI:**10.1016/j.jmmm.2006.05.022
20. M. S. Khandekar, R. C. Kambale, J. Y. Patil, Y. D. Kolekar, S. S. Suryavanshi, *J. Alloys Compd.* **2011**, *509*, 1861–1865. **DOI:**10.1016/j.jallcom.2010.10.073
21. R. C. Kambale, P. A. Shaikh, N. S. Harale, V. A. Bilur, Y. D. Kolekar, C. H. Bhosale, K. Y. Rajpure, *J. Alloys Compd.* **2010**, *490*, 568–571. **DOI:**10.1016/j.jallcom.2009.10.082
22. Y. Zhang, Z. Yang, D. Yin, Y. Liu, C. Fei, R. Xiong, J. Shi, G. Yan, *J. Magn. Magn. Mater.* **2010**, *322*, 3470–3475. **DOI:**10.1016/j.jmmm.2010.06.047
23. E. Mendelovici, R. Villalba, A. Sagarzazu, *Thermochim. Acta* **1998**, *318*, 51–56. **DOI:**10.1016/S0040-6031(98)00329-3
24. Z. Karimi, Y. Mohammadifar, H. Shokrollahi, S. Khameneh, G. Youse, L. Karimi, *J. Magn. Magn. Mater.* **2014**, *361*, 150–156. **DOI:**10.1016/j.jmmm.2014.01.016
25. A. Repko, J. Vejpravová, T. Vacková, D. Zákutná, D. Nižňanský, *J. Magn. Magn. Mater.* **2015**, *390*, 142–151. **DOI:**10.1016/j.jmmm.2015.04.090
26. X. Li, C. Xu, X. Han, L. Quiao, T. Wang, F.-S. Li, *Nanoscale Res. Lett.* **2010**, *5*, 1039–1044. **DOI:**10.1007/s11671-010-9599-9
27. L. J. Cote, A. S. Teja, A. P. Wilkinson, Z. J. Zhang, *Fluid Phase Equilib.* **2003**, *210*, 307–317. **DOI:**10.1016/S0378-3812(03)00168-7
28. T. Dippong, E. A. Levei, O. Cadar, F. Goga, L. Barbu-Tudoran, *J. Anal. Appl. Pyrolysis* **2017**, *128*, 121–130. **DOI:**10.1016/j.jaap.2017.10.018

29. T. Dippong, E. A. Levei, O. Cadar, F. Goga, L. Barbu-Tudoran, G. Borodi, *J. Therm. Anal. Calorim.* **2017**, *128*, 39–52. **DOI:**10.1007/s10973-016-5930-8
30. I. Sharifi, H. Shokrollahi, M. Mahdi, R. Safi, *J. Magn. Magn. Mater.* **2012**, *324*, 1854–1861. **DOI:**10.1016/j.jmmm.2012.01.015
31. S. Rana, J. Philip, B. Raj, *Mater. Chem. Phys.* **2010**, *124*, 264–269. **DOI:**10.1016/j.matchemphys.2010.06.029
32. H. S. C. O´Neill, A. Navrotsky, *Am. Mineral.* **1983**, *68*, 181–194.
33. G. A. Petitt, D. W. Forester, *Phys. L Rev. B* **1971**, *4*, 3912–3923. **DOI:**10.1103/PhysRevB.4.3912
34. G. A. Sawatzky, F. Van Der Woude, A. H. Morrish, *Phys. Rev.* **1969**, *187*, 747–757. **DOI:**10.1103/PhysRev.187.747
35. Z. Szotek, W. M. Temmerman, D. Ködderitzsch, A. Svane, L. Petit, H. Winter, *Phys. Rev. B* **2006**, *74*, 1–12. **DOI:**10.1103/PhysRevB.74.174431
36. Y. H. Hou, Y. J. Zhao, Z. W. Liu, H. Y. Yu, X. C. Zhong, W. Q. Qiu, D. C. Zeng, L. S. Wen, *J. Phys. D. Appl. Phys.* **2010**, *43*, 445003. **DOI:**10.1088/0022-3727/43/44/445003
37. J. Pechoušek, D. Jančík, J. Frydrych, J. Navařík, P. Novák, *AIP Conf. Proc.* **2012**, *1489*, 186–193.
38. J. Pechousek, R. Prochazka, D. Jancik, J. Frydrych, M. Mashlan, *J. Phys. Conf. Ser.* **2010**, *217*, 012006 (4). **DOI:**10.1088/1742-6596/217/1/012006

Povzetek

V študiji se osredotočamo na urejanje kobalta in železa znotraj feritne strukture $Co_xFe_{3-x}O_4$. Spojine smo pripravili z reakcijami v trdnem stanju med α-Fe_2O_3 and $CoCl_2$. Za selektivno preverjanje položaja železovih in kobaltovih atomov v strukturi smo uporabili kombinacijo transmisijske in emisijske Mössbauerjeve spektroskopije. S primerjavo transmisijskih in emisijskih spektrov smo lahko določili zasedenost tetraedrskih in oktaedrskih položajev. Predstavljena metoda združevanja teh dveh tehnik Mössbauerjeve spektroskopije je primerna za katero koli spojino, ki vsebuje železove in kobaltove atome. Dodatne informacije glede sestave in morfologije vzorcev smo dobili z rentgensko prašno difrakcijo in z vrstično elektronsko mikroskopijo (SEM). Ob uporabi večje množine Co v reakciji, se je povečala tudi stopnja vgradnje atomov Co v strukturo ferita.

Except when otherwise noted, articles in this journal are published under the terms and conditions of the Creative Commons Attribution 4.0 International License

DOI: 10.17344/acsi.2019.5553 *Acta Chim. Slov.* **2020,** *67,* 530–536
creative commons

Scientific paper

FT-IR Spectroscopy for the Detection of Diethylene Glycol (DEG) Contaminant in Glycerin-Based Pharmaceutical Products and Food Supplements

Ayman Y. Hammoudeh, Safwan M. Obeidat,* Eman Kh. Abboushi and Amal M. Mahmoud

Chemistry Department, Faculty of Science, Yarmouk University, Irbid, Jordan.

** Corresponding author: E-mail: Safwan@yu.edu.jo; Safobeidat@yahoo.com*
Tel: 962-27211111

Received: 10-10-2019

Abstract

Identification and determination of diethylene glycol (DEG) in glycerin-based products was successfully achieved using FT-IR spectroscopy. Studied samples included 0.5% to 20% by mass DEG spiked into cough syrup, two paracetamol syrup formulations, and two food supplements. The characteristic DEG wavenumbers at 881 cm^{-1} and 1083 cm^{-1} were used for its quantitative determination in the studied samples. A very good accuracy in determining the DEG fraction was achieved with a mean error% of ±2.02% to ±7.69% upon using the corrected absorbance at 881 cm^{-1}. The corrected absorbance at 1083 cm^{-1} band was used in the case of paracetamol formulations and resulted in a mean error% ranging from ±2.50% to ±10.28%. The values of limit of detection of the current method ranged from 0.051% to 0.068% DEG for all studied samples.

Keywords: FT-IR; diethylene glycol (DEG); glycerin; pharmaceutical products; food supplements.

1. Introduction

Glycerin (or glycerol) is a popular alcohol with a wide range of applications in pharmaceutical, food, and personal care products industries. Glycerin acts as a humectant, preservative, and lubricant; it can be found in more than 2,000 products, including toothpaste, mouthwash, and pain relief medications.[1,2] Usually, it is prepared from fats and oils and may also be obtained as a by-product from some biofuel production reactions.[3] The global demand for glycerin is continuously increasing. This encouraged greedy sellers to adulterate glycerin with diethylene glycol (DEG) that is less expensive and has similar physical properties. However, DEG is toxic to humans. Adulterating glycerin with DEG has caused many fatalities in a number of countries around the world.[4] For example, it was reported that many death cases among children in Nigeria in 2008 were due to DEG poisoning.[5] In 2006, cough syrups in Panama were manufactured with DEG instead of glycerine, resulting in 51 death cases.[2] In 1996, in Haiti, at least 59 children died of acute kidney failure caused by contaminated paracetamol syrup containing up to 26% DEG.[6,7] More poisoning cases around the world were reported in much detail in reference[2]. Recommended Food and Drug Administration (FDA) limits of potential DEG contamination are 0.1% to 12.7% in pharmaceutical formulations of liquid excipients and 0.1% in sorbitol and other excipient solutions.[8] Therefore, many analytical methods of identifying and determining DEG in contaminated glycerin were reported. Gas chromatography (GC) was used for DEG quantitation in some food products, human sera, and pharmaceutical products.[9–11] GC combined with mass spectrometry (GC-MS) was also reported for confirming the identity of different glycols and DEG in bait fish, human plasma, and electronic cigarettes.[12–14] Thin layer chromatography (TLC) was also employed to detect the presence of DEG in toothpastes.[15] A combination of GC, IR spectroscopy, and TLC was used to test the purity of glycerin.[6] Fourier transform infrared (FT-IR) and near-infrared (NIR) spectroscopic techniques were reported as viable, simple, cost effective, and rapid methods for the identification and quantification of DEG in glycerin-based cough syrups.[5] In a recent study, mid-IR spectroscopy has been shown to be a simple and rapid technique to determine possible DEG contamination in glycerin raw materials.[16] The current work addresses the

applicability of mid-IR spectroscopy for determining possible DEG contamination in more complex glycerin-containing commercial products whose other constituents may also interfere and absorb in the spectroscopic range of interest; these include a cough syrup, two paracetamol syrup formulations, and two food supplements.

2. Experimental

2. 1. Materials and Methods

The cough syrup Hederal (product of Delass, Jordan) was purchased from a local pharmacy in the City of Irbid in Jordan. It consists of the dried leaf of *Hedera helix* (an ivy leaf) as expectorant, in addition to glycerin, sorbitol, propylene glycol, polysorbate (tween 80), sucrose syrup, strawberry flavor, and water. Two glycerin-based food supplements were also studied; a natural plant based glycerite sweetener that consists of stevia plant extract, glycerin, and water (brand name: Better Stevia, NOW Foods, USA), and a liquid herbal extract claimed to support healthy nervous system and consists of glycerin, water, and a lemon balm extract (brand name: Lemon Balm, Herb Pharm, USA). Both supplements were purchased from local markets in USA. Two paracetamol syrup formulations were prepared according to the procedure described in reference[17]. All studied samples were spiked with known amounts of DEG ranging from about 0.5% to 20% by mass. Glycerin (99.5%) and DEG (99%) were purchased from Tedia (USA) and Vickerings (UK), respectively.

2. 2. Instrumentation and Data Acquisition

All infra-red measurements were performed in attenuated total reflection (ATR) mode using a Bruker Alpha FT-IR spectrometer equipped with a deuterated triglycine sulfate (DTGS) detector and a zinc selenide window. All IR spectra in this study were collected in triplicate (i.e. three IR spectra were taken and averaged for each solution) in the range 700–4000 cm^{-1} with a resolution of 4 cm^{-1} against air as a background. For each test product investigated in this work, calibration curves were constructed by plotting the absorbance (peak intensity without baseline correction) at selected wavenumbers versus the percentage of DEG spiked in the tested samples. Spiking the test solutions with DEG leads however to decreased percentages of the original constituents in the test solutions. A correction for this behavior was undertaken, subtracting thereby the expected absorbance contribution of the original constituents of the test product from the actually measured absorbance. This contribution has been estimated to be the mass percent of test product in the final solution (i.e. after spiking with DEG) multiplied by the absorbance of the original test product at the wavenumbers of interest in this study (881 and 1083 cm^{-1}). The correction is shown in equations (1)-(3) for the absorbance at 881 cm^{-1}; *A* stands for the actually measured absorbance, product% is the percentage of tested product in the final solution after spiking with DEG, A_{DEG} is the magnitude of absorbance associated with DEG:

$$A(881\ cm^{-1}) = A_{DEG}(881\ cm^{-1}) + \\ + A_{product}(881\ cm^{-1}) \quad (1)$$

$$A(881\ cm^{-1}) = A_{DEG}(881\ cm^{-1}) + \frac{product\%}{100} \times \\ \times A_{unspiked\ product}(881\ cm^{-1}) \quad (2)$$

$$A_{DEG} = A(881\ cm^{-1}) - \frac{product\%}{100} \times \\ \times A_{unspiked\ product}(881\ cm^{-1}) \quad (3)$$

3. Results and Discussion

The IR spectrum of DEG is rich in bands, but only those below 1200 cm^{-1} are useful in the quantification of DEG in glycerin-containing systems.[16] Figure 1 represents the IR spectra of neat DEG and neat glycerin in the spectral range 810–1170 cm^{-1}. The band around 1030 cm^{-1} is assigned to the C-O stretching vibration of primary alcohol,[18] and is found both in glycerin and DEG. In glycerin, the band at 1110 cm^{-1} is attributed to the C-O stretching vibration of the secondary alcohol group. This band is absent in DEG due to the lack of secondary OH groups. Instead, a DEG characteristic band is observed at 1085 cm^{-1} which is attributed to the asymmetric C-O-C stretch mode, whereas the DEG bands at 881 cm^{-1} and 860 cm^{-1} are attributed to the CH_2 rocking mode.[16] In a previous study,[16] the DEG characteristic bands at 1085 cm^{-1} and 881 cm^{-1} were used successfully to quantify DEG in a glycerin raw material. Hence, these bands may hold the poten-

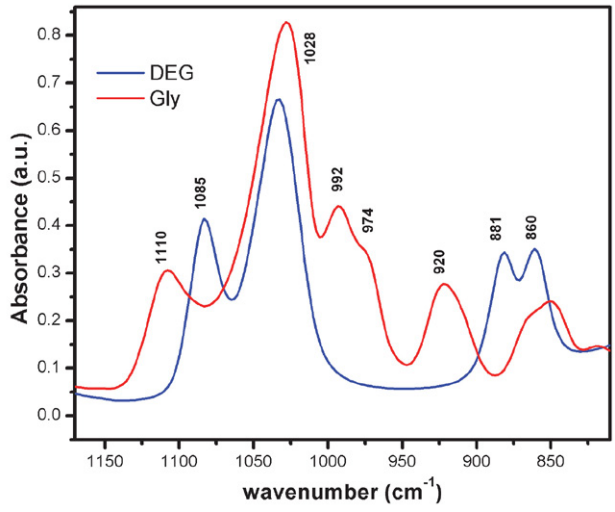

Figure 1: IR spectra of neat glycerin (red) and DEG (blue) in the spectral range 810–1170 cm^{-1}. The characteristic bands are labeled by the wavenumbers at band maxima.

tial for determining DEG in real glycerin-based products. These bands were tested in the current study to quantify spiked DEG in pharmaceutical products and food supplements which contain not only glycerin and water, but also other constituents that may also absorb in the IR range of interest and make the analysis more difficult.

3. 1. Cough Syrup Hederal

Seventeen syrup samples were spiked with different amounts of DEG resulting in different DEG weight percentages in the samples, ranging from approximately 1% to 16%. Figure 2 shows how the intensity of the IR bands at 1083, 1036, 881, and 860 cm^{-1} increases with increased DEG%. All these bands belong to DEG but may also have contributions from other constituents. Sorbitol, for example, shows an IR band at 1078 cm^{-1}, glycerin at 1036 cm^{-1}, sucrose has a wide absorption profile from 960 cm^{-1} to 1095 cm^{-1}. The absorption at 881 cm^{-1} is mostly due to DEG with minimum contribution from the other constituents. Figure 2 shows also that for certain bands, e.g. the glycerin characteristic bands at 1110 cm^{-1} and 994 cm^{-1}, the intensity drops in general with increased amounts of spiked DEG, apparently due to sample dilution with DEG.

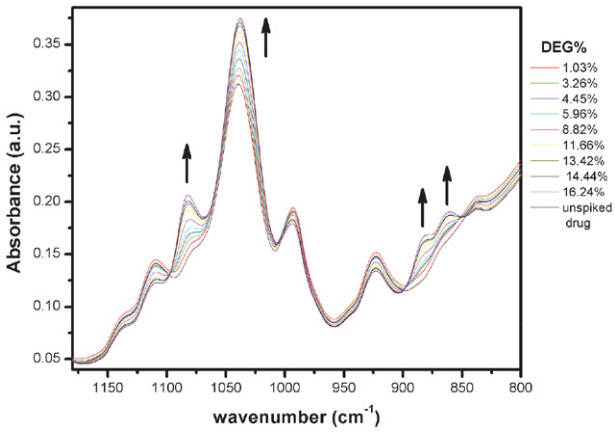

Figure 2: FT-IR spectra of Hederal unspiked and spiked with different DEG%.

correlation coefficients of the obtained linear relations were improved, reading 0.9985 for DEG absorbance at 881 cm^{-1} and 0.9992 for that at 1083 cm^{-1}.

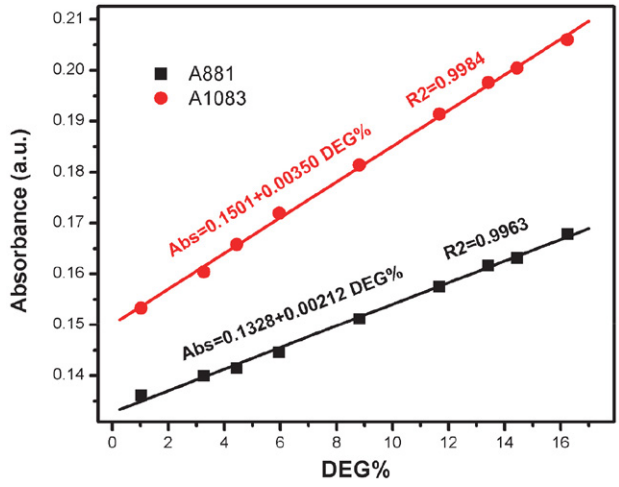

Figure 3. The intensity of the IR bands at 881 cm^{-1} and 1083 cm^{-1} versus DEG% in spiked Hederal samples.

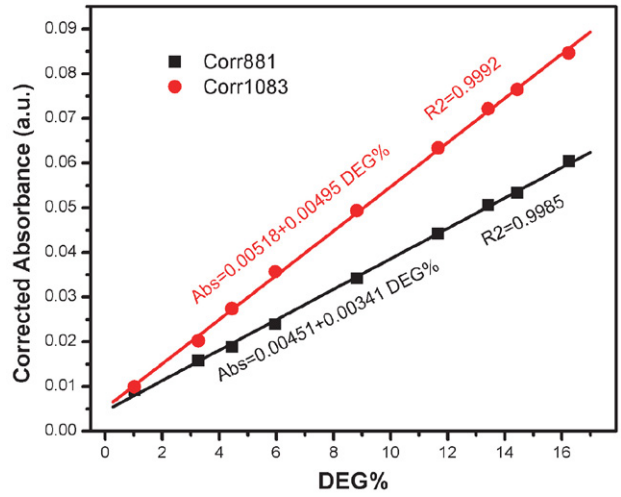

Figure 4. Corrected DEG absorbance at 881 cm^{-1} and 1083 cm^{-1} versus its percentage in spiked Hederal samples.

The two DEG characteristic bands at 881 cm^{-1} and 1083 cm^{-1} were further investigated for the quantitative determination of spiked DEG in Hederal. The intensity of the DEG spiked samples at 881 cm^{-1} and 1083 cm^{-1} was plotted in the calibration curves shown in Figure 3. For both wavenumbers, a straight line was obtained with R^2 values of 0.9963 and 0.9984, respectively. In order to find the absorbance contribution due to DEG only, the absorbance measured at 881 cm^{-1} or 1083 cm^{-1} was corrected according to equation (3) as explained in the experimental part. The corrected absorbance (i.e. of DEG) at 881 cm^{-1} and 1083 cm^{-1} is plotted in Figure 4 versus DEG%. The

The equations describing the linearity of the calibration model were then used to determine the concentration of DEG in a validation set of seven samples of spiked Hederal. A very good agreement between the actual and the predicted DEG concentrations in the validation samples was obtained as displayed in Table 1. From this table, it is quite clear that the calibration curve of corrected absorbance gives more accurate values than that without correction (an average error% of ±2.0% for the absorbance at 881 cm^{-1} compared to ±3.3% when no correction was undertaken). In addition, the absorbance at 881 cm^{-1} is a better measure of DEG% than that at 1083 cm^{-1} (average er-

ror% of ±2.02% for corrected absorbance at 881 cm^{-1} compared to ±4.38% at 1083 cm^{-1}) as listed in Table 1. The limit of detection (LOD) for this drug was calculated based on the 881 cm^{-1} band and found to be 0.051 DEG%.

Table 1: Actual and predicted DEG% in Hederal and associated errors from IR absorbance at 881 cm^{-1} and 1083 cm^{-1}.

881 cm^{-1}	Predicted DEG%		Error%	
DEG% actual	without correction	after correction	without correction	after correction
1.90	2.06	1.99	8.11	4.68
3.72	3.66	3.67	1.75	1.37
5.38	4.99	5.13	7.30	4.80
7.62	7.68	7.63	0.83	0.27
10.02	9.76	9.84	2.63	1.87
12.63	12.67	12.63	0.37	0.01
14.27	14.58	14.43	2.18	1.13
		Mean	**3.31**	**2.02**

1083 cm^{-1}	Predicted DEG%		Error%	
DEG% actual	without correction	after correction	without correction	after correction
1.90	1.63	1.71	14.54	9.88
3.72	3.93	3.88	5.66	4.20
5.38	5.17	5.24	3.94	2.66
7.62	8.71	8.40	14.39	10.25
10.02	10.29	10.22	2.65	1.93
12.63	12.77	12.73	1.13	0.84
14.27	14.31	14.30	0.26	0.22
		Mean	**6.08**	**4.28**

3. 2. Formulations of Paracetamol Syrup

In a study of pharmaceutical solution formulations for paracetamol,[17] six paracetamol syrup formulations were tested for the stability of active ingredient. Two of these formulations (A and B) were investigated in this work for the identification of possible contamination with DEG by means of FT-IR. The approximate solvent composition of these formulations is given in Table 2.

Table 2: Approximate solvent composition of two formulations for paracetamol syrup.

	Glycerin/%	Sorbitol/%	Ethanol/%	Water/%
Formulation A	33.1	30.2	6.7	30.0
Formulation B	36.7	9.6	26.9	26.8

Both formulations have comparable amounts of glycerin. Formulation B is four times richer in ethanol (26.9%) with only 9.6% of sorbitol, while formulation A contains small amounts of ethanol (6.7%) with sorbitol being a major constituent (30.2%). DEG was spiked in these formulations with a mass percent ranging from 0.8% to 16%. The collected IR spectra as well as the correlation between DEG% and corrected absorbance at 1083 cm^{-1} and 881 cm^{-1} are presented in Figure 5. Obviously, the presence of ethanol and sorbitol complicates the absorbance behavior at 881 cm^{-1}. The effect of ethanol seems greater as it can be recognized in Figure 5 that a large absorption band appears around 880 cm^{-1} in the unspiked formulation B, due to the presence of large amounts of ethanol. The absorbance at 1083 cm^{-1} is also affected by the presence of sorbitol and ethanol; it is higher in unspiked formulation A than in unspiked formulation B, but the band shape experiences in general no significant change. The above example of paracetamol syrup formulations shows that the absorbance behavior in the IR region of interest for DEG determination is very sensitive to the formulation composition, but good estimates for DEG can still be made after correcting the absorbance for the contribution of unspiked reference formulation (Figure 5). In formulation B, however, DEG% below 1% are not well reflected by the linear correlation given in Figure 5, suggesting that the uncertainty in the determination of such low amounts of DEG (<1%) becomes large if the original formulation shows strong IR absorption especially at 881 cm^{-1}.

Similar findings were also noticed upon studying a validation set that contains five DEG-spiked paracetamol samples from each formulation of DEG ranging from about 2.5% to 13.0%. The results of DEG analysis at 1083 cm^{-1} are displayed in Table 3. Once more, the error% calculations showed that a better accuracy is obtained in case of formulation A, with mean error% value of ±2.86%, versus ±10.28% for formulation B. More specifically, Table 3 shows a much larger error% for DEG percentages smaller than 5% in formulation B than in formulation A. We find for example for the DEG% of 2.5% and ~5% an error% of ±34.5% and ±9.66% in the case of formulation B compared to only ±3.11% and ±1.66%, respectively, in the case of formulation A. This large uncertainty in the DEG% below 5% in formulation B is obviously associated with the presence of high amounts of ethanol (26.9%) and not sorbitol which is present in formulation A in almost the same percentage (30.2%) as ethanol in formulation B. Apparently, the presence of high percentages of ethanol in test product presents a limitation for the spectral analytical technique suggested in this work, especially at DEG% < 5%. The DEG% LOD values for both formulations were calculated based on the 1083 cm^{-1} band and found to be 0.058% and 0.067% for formulation A and B, respectively.

3. 3. Food Supplements (Better Stevia and Lemon Balm)

Better Stevia and *Lemon Balm* samples were spiked with DEG in the range 2–20%. The absorbance at

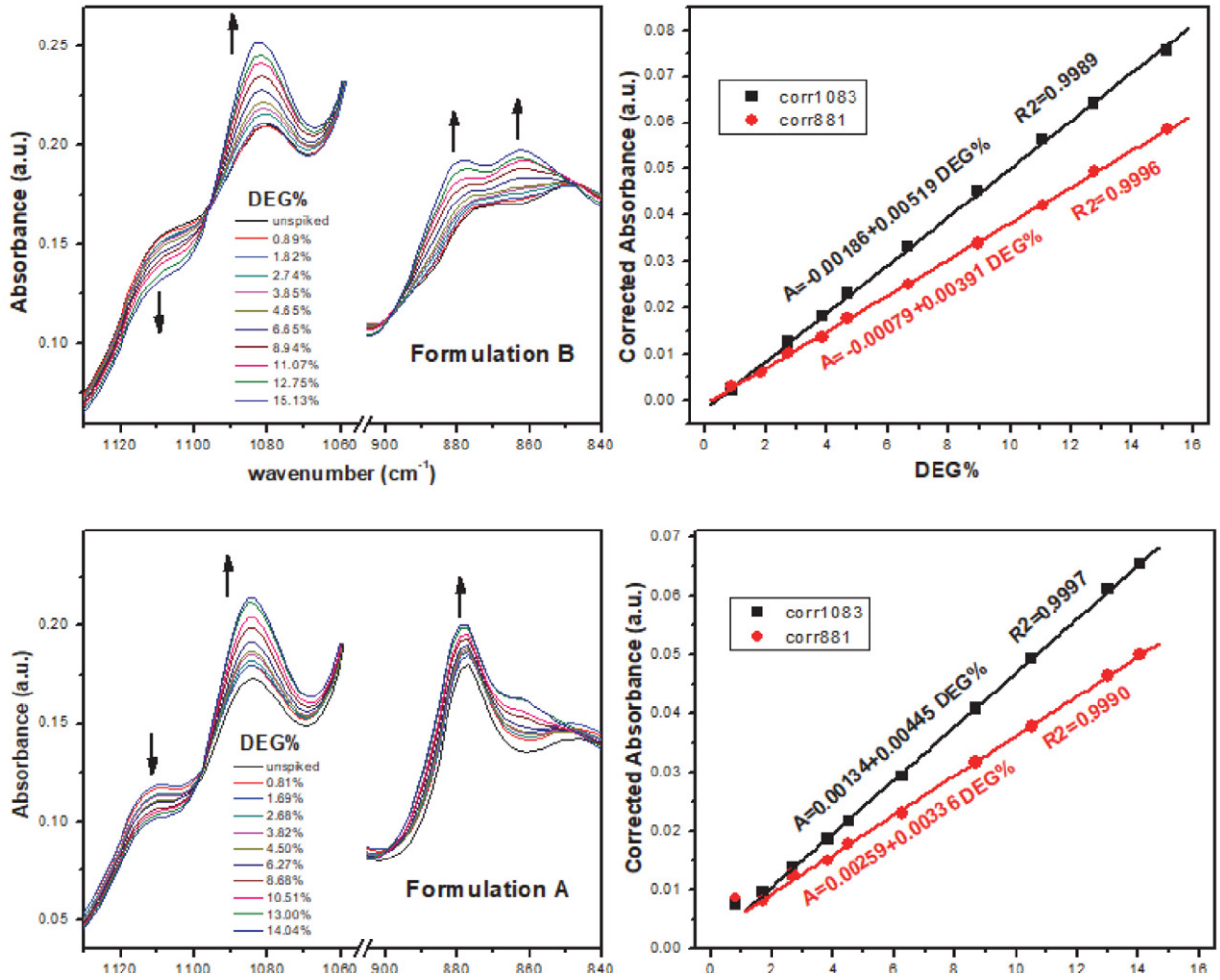

Figure 5: FT-IR spectra of paracetamol formulations (A and B) unspiked and spiked with different DEG% (left). Corrected DEG absorbance at 881 cm^{-1} and 1083 cm^{-1} versus its percentage in spiked samples of each formulation (right).

Table 3: Actual and predicted DEG percentages from corrected absorbance at 1083 cm^{-1} of two formulations for paracetamol syrup

Formulation A			Formulation B		
DEG% actual	**Calculated DEG%**	**Error%**	**DEG% actual**	**Calculated DEG%**	**Error%**
2.52	2.44	3.11	2.50	3.36	34.50
4.94	4.85	1.68	4.58	5.020	9.66
6.95	6.58	5.26	6.10	7.32	4.66
11.07	10.66	3.65	11.052	10.86	1.77
13.14	13.05	0.63	12.77	12.88	0.80
	Mean	**2.86**			**10.28**

881 cm^{-1} as well as that at 1083 cm^{-1} were used to quantify DEG in the spiked samples. Like DEG quantification in Hederal cough syrup, the absorbance at 881 cm^{-1} gave better results, as shown below, the reason why in the following text, and for the sake of clarity, only the results based on the absorbance at 881 cm^{-1} are presented. Figure 6 shows the corrected absorbance calibration curves for the absorbance only at 881 cm^{-1}. Straight lines of R^2 values of 0.9985 and 0.9989 were obtained for Better Stevia and Lemon Balm, respectively. The obtained calibration equations shown in Figure 6 were then used to determine the DEG% in two validation sets consisting of 11 samples each. Tables 4 and 5 show the real and predicted DEG% for all samples of the validation sets. Obviously, the current method represents a reliable method for determining the DEG% in the studied food supplements based on the very good agreement of the DEG% in actual and predicted concentrations. The good accuracy of the current work is evidenced by the low mean error% values, which were ±3.34% and ±7.69% for Better Stevia and Lemon Balm, respectively. These values are smaller than those obtained when the absorbance at 1083 cm^{-1} is used to quantify spiked DEG where mean error% of ±7.77% and ±9.46% were obtained for Better Stevia and Lemon Balm, respectively. LOD values based on the absorbance at 881 cm^{-1} were computed for both products and were found to be 0.055% for Better Stevia and 0.068% for Lemon Balm.

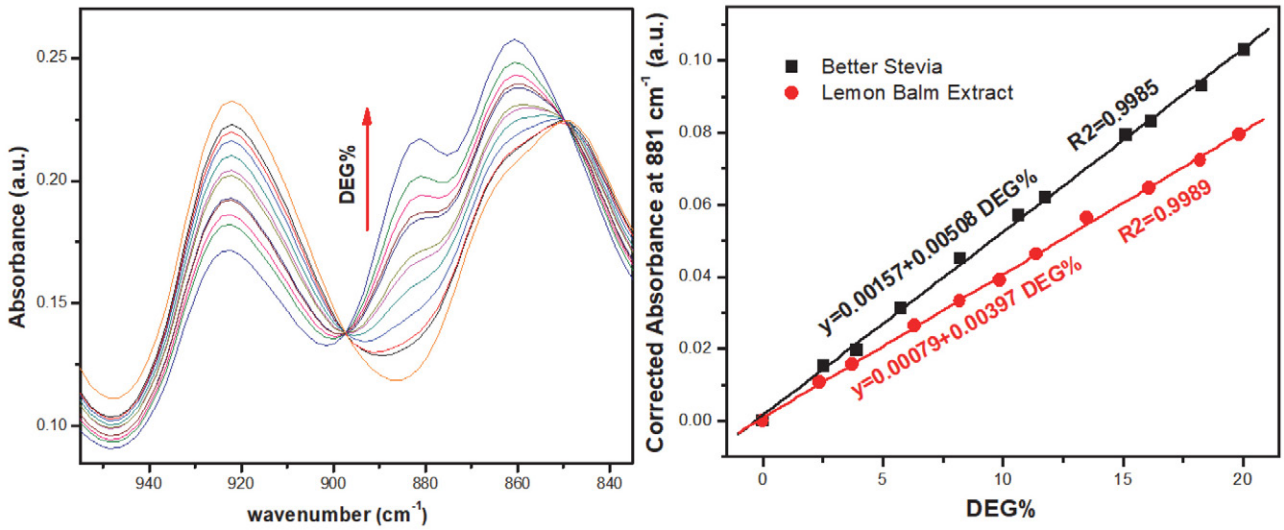

Figure 6: FT-IR spectra of Better Stevia spiked with DEG (left) and corrected absorbance at 881 cm^{-1} for DEG-spiked Better Stevia and Lemon Balm Extract (right).

Table 4: Actual and predicted DEG percentages from corrected absorbance at 881 cm^{-1} for Better Stevia.

Actual DEG%	Calculated DEG%	Error%
2.61	2.93	12.14
4.12	4.25	3.16
6.43	6.47	0.52
8.64	8.23	4.82
9.75	9.91	1.67
11.94	11.85	0.78
14.01	14.06	0.29
15.66	15.33	2.11
20.30	19.38	4.56
Mean	3.34	

Table 5: Actual and predicted DEG percentages from corrected absorbance at 881 cm^{-1} for Lemon Balm Extract

Actual DEG%	Calculated DEG%	Error%
2.30	2.74	18.90
3.63	3.17	12.71
6.08	6.56	7.76
8.07	8.48	5.03
9.92	10.44	5.28
13.29	14.02	5.49
13.79	14.67	6.40
16.16	17.17	6.25
18.36	19.53	6.36
19.66	20.19	2.76
–	mean	7.69

4. Conclusions

In the current work, IR spectroscopy is shown to be a relatively simple, fast and accurate method for determining DEG in spiked glycerin-based cough syrup, drug formulations, and food supplements. From test sets of spiked samples, two main characteristic DEG bands (881 and 1083 cm^{-1}) were found to be, for this purpose, the best. Hence, a linear regression analysis based on these test sets was employed for DEG determination in validation sets of samples of each studied product. The results showed a very good agreement of the real and predicted DEG values in all samples. Accuracy has also been improved upon using corrected absorbance values where the absorbance before adding DEG was subtracted from the total absorbance after spiking with DEG. This result was evidenced by the decreased mean error% values. For the studied cough syrup and food supplements, the mean error% is smaller when the absorbance at 881 cm^{-1} is considered for DEG quantification in comparison to quantification based on the absorbance at 1083 cm^{-1}, reflecting the better accuracy associated with the band at 881 cm^{-1} for DEG determination in these products. However, in the case of paracetamol formulations, the band at 1083 cm^{-1} was found to be better than the band at 881 cm^{-1} for DEG determination due to the presence of high ethanol concentrations in these samples that disturb and complicate the absorbance behavior around 880 cm^{-1}.

Conflict of Interest

The authors declare no conflict of interest.

5. References

1. S. Alfred, P. Coleman, D. Harris, T. Wigmore, E. Stachowski, A. Graudins, *Clin. Toxicol.*, **2005**, *43*(3), 155–159. **DOI:**10.1081/CLT-200057875
2. B. D. Barr, et al., *J. Anal. Toxicol.*, **2007**, *31*(6), 295–303.

3. A. B. Leoneti, V. Aragão-Leoneti, Sonia, V. W. B. Oliveira, *Renew. Energy,* **2012**, 45, 138–145. **DOI:**10.1016/j.renene.2012.02.032
4. L. A. Ferrari, L. Giannuzzi, *Forensic Sci Int.*, **2005**, *153*, 45–51. **DOI:**10.1016/j.forsciint.2005.04.038
5. M. K. Ahmed, M. P. McLeod, J. Nézivar, A. W. Giuliani, *Spectroscopy,* **2010**, *24*, 601–608. **DOI:**10.1155/2010/608749
6. M. T. S. R. Gomes, M. I. S. Veriâ ssimo, J. A. B. P. Oliveira, *J. Pharm. Pharmacol.,* **1999**, *51*, 233–236.
7. L. Blecher, A. Mercill, *Pharm. Technol*., **1998**, *22*, 50–54.
8. G. Holloway, R. Maheswaran, A. Leeks, S. Bradby, S. Wahab, *J. Pharm. Biomed. Anal.,* **2009**, *51*, 507–511. **DOI:**10.1016/j.jpba.2009.08.025
9. L. Castle, H. R. Cloke, J. R. Startin, J. Gilbert, *J AOAC Int.*, **1988**, *71*, 499–502.
10. J. B. Brooks, M. T. Basta, C. C. Alley, J. S. Holley, A. M. El Kholy, *J. Chromatogr*. **1984**, *309*, 269–272. **DOI:**10.1016/0378-4347(84)80034-1
11. P. Baffi, S. Elneser, M. Baffi, M. Demelin, *J. AOAC Int.* **2000**, *83*, 793–801.
12. J. E. Matusik, P. P. Eilers, E. M. Waldron, S. M. Conrad, J. A. Sphon, *J. AOAC Int.*, 1993, *76*, 1344–1347.
13. J. E. Maurer, C. Kessler, *Arch. Toxicol*., 1988, *62*, 66–69. **DOI:**10.1007/BF00316260
14. V. Varlet, K. Farsalinos, M. Augsburger, A. Thomas, J. Etter, *Int. J. Environ. Res. Public. Health*, **2015**, *12*(5), 4796–4815. **DOI:**10.3390/ijerph120504796
15. A. S. Kenyon, S. Xiaoye, W. Yan, N.G. Wai Har, R. Prestidge, K. Sharp, *J. AOAC Int.***1988**, *81*, 44–49.
16. S. M. Obeidat, A. Y. Hammoudeh, A. Mahmoud, *Spectroscopy Lett.,* **2019**, *52* (1), 60–65. **DOI:**10.1080/00387010.2018.1556220
17. A. Bedri, S. Vehbi, L. Azem, I. Hilmi, Med. Arh., **2012**, *66* (1), 5–8.
18. P. Harder, M. Grunze, R, Dahint, G. M. Whitesides, P. E. Laibinis, *J. Phys. Chem. B*, **1998**, *102*, 426–436. **DOI:**10.1021/jp972635z

Povzetek

S pomočjo FT-IR spektroskopije smo uspešno identificirali in določili dietilen glikol (DEG) v proizvodih na osnovi glicerina. Preiskovani vzorci so vsebovali od 0,5 % do 20 % (*m*/*m*) DEG, dodanega sirupu proti kašlju, dvema pripravkoma sirupa s paracetamolom in dvema prehranskima dopolniloma. Za kvantitativno določitev DEG v preiskovanih vzorcih smo uporabili karakteristični valovni števili za DEG pri 881 cm^{-1} in 1083 cm^{-1}. Z uporabo korigirane absorbance pri 881 cm^{-1} smo dosegli zelo dobro točnost pri določitvi deleža DEG s povprečno napako ±2,02 % do ±7,69 %. Korigirano absorbanco pri traku 1083 cm^{-1} smo uporabili za paracetamolne pripravke in dobili povprečno napako v območju ±2,50 % do ±10,28 %. Vrednosti meje zaznave pri predstavljeni metodi so bile v območju 0,051 % do 0,068 % DEG za vse preiskovane vzorce.

Except when otherwise noted, articles in this journal are published under the terms and conditions of the Creative Commons Attribution 4.0 International License

Scientific paper

Selective Colorimetric Detection of Mn^{2+} and Cr^{2+} Ions using Silver Nanoparticles Modified with Sodium Dodecyl Sulfonate and β-Cyclodextrin

Maryam Akhondi[1,*] and Effat Jamalizadeh[2]

[1] *Department of Chemistry, University of Shahid Bahonar , Kerman, Iran.*

[2] *Department of Chemistry, University of Shahid Bahonar , Kerman, Iran.*

* *Corresponding author: E-mail: m.akhondi67@gmail.com*

Received: 09-07-2019

Abstract

The present study was conducted to determine manganese (Mn^{2+}) and chromium (Cr^{2+}) ions in aqueous systems with a simple, rapid, sensitive, selective and cost-effective colorimetric approach. Sodium dodecyl sulfonate (SDS) and β-cyclodextrin (CD) were used as both stabilizer and surface functionalizing agents for the synthesis of silver nanoparticles (AgNPs). Synthesized AgNPs were characterized by FT-IR spectroscopy, UV-visible spectroscopy, scanning electron microscopy (SEM), transmission electron microscopy (TEM), X-ray diffraction (XRD) and dynamic light scattering (DLS) techniques. The effect of pH on the stability of nanoparticles was investigated. SDS modified silver nanoparticles (SDS-AgNPs) and SDS with **β**-cyclodextrin modified silver nanoparticles (SDS-CD-AgNPs) demonstrated sensitive and selective colorimetric detection of Mn^{2+} and Cr^{2+} ions at ppm level, respectively. The prepared SDS-AgNPs and SDS-CD-AgNPs solution showed a color change visible to the naked eye from yellow to orange upon adding Mn^{2+} and Cr^{2+} ions, respectively; however, other metal ions did not induce such a change. In addition, the results of SEM TEM and DLS" for both sensors showed the aggregation of nanoparticles after adding Mn^{2+} or Cr^{2+}. Overall, the results of this study show the successful synthesis of AgNPs, SDS-AgNPs, and SDS-CD-AgNPs as simple, rapid, sensitive, selective colorimetric sensors with high potential for rapid and on-site detection of Mn^{2+}.

Keywords: Silver nanoparticles; Sodium dodecyl sulfonate; β-cyclodextrin; Colorimetric sensor

1. Introduction

Manganese (Mn) and Chromium (Cr) are essential trace elements for many life processes of the human body such as enzyme activity, bone growth, and fat metabolism.[1,2] However, excessive levels of these elements in biological activities can be toxic for health and may lead to fatal diseases.[3,4] Essential quality standards for Mn (0.05 mg/L) and Cr (0.1 mg/L) have been adopted at the EU level.[5,6] Therefore, the determination of these ions has become inevitable for remedial processes. In this regard, many efforts have been done to detect Mn and Cr ions with high selectivity and sensitivity.

Conventional methods for detecting metal ions are mostly spectroscopy-based techniques such as fluorescent probes,[7,8] atomic absorption,[9,10] surface-enhanced Raman spectroscopy,[11] inductively coupled plasma atomic emission,[12] and inductively coupled plasma mass spectroscopies.[13–15] However, some of these methods are not widely used due to high cost, multi-step sample Pretreatments, and time-intensiveness.[16,17] The attempts to overcome these limitations led to the development of alternative colorimetric sensors. Several colorimetric assays for detecting metal ions in aqueous solutions based on the use of sensitive chromophores or fluorophores,[18] polymers,[19,20] oligonucleotides,[21] DNA,[22,23] and metal nanoparticles[24,25] have been developed. These assays have advantages such as high sensitivity, simplicity, speed and ease of use without the need of any special apparatus.[26] Nanostructured materials have extensive applications in biosensors and ecosensors, especially for detecting metal ions.[27–32] Noble metal nanoparticles, especially gold and AgNPs, have attracted considerable attention in preparing metal ion sensors because of their size and morphology dependent optical properties, strong surface plasmon resonance properties, high extinction coefficient at the visible region, highly stable dispersions, good biocompatibility and chemical inert-

ness.[33,34] Notably, AgNPs have attracted much attention because of lower prices and higher extinction coefficients than those of gold nanoparticles.[16,35,36] The performance of these sensors is based on the surface plasmon resonance (SPR)-induced color variance of nanoparticles, as a result of signal-analyte interaction.[37–40]

Nanoparticles surface functionalization affects the interaction between nanoparticles and metal ions,[38,41] which is critical in the development of noble nanoparticles as a colorimetric sensor for metal ions. For example, among the works conducted in this regard, one can name Ag nanoparticles surface functionalization by octamethoxy resorcin[4]arene tetrahydrazide as a reducing and stabilizing agent for colorimetric detection of cadmium,[42] synthesized AgNPs by cysteic acid as a capping agent for detection of manganese ions,[17] Glutathione-stabilized AgNPs as a colorimetric sensor for nickel ions,[43] thiodisuccinic acid-functionalized AgNPs as a sensor for lead ions,[38] β-cyclodextrin-functionalized AgNPs for detection of mercury and sulfide ions,[44] glutathione-modified AgNPs as a sensor for cobalt ions,[45] dopamine-AgNPs as a sensor for copper ions,[46] AgNPs without any surface modification as a sensor for copper ions,[47] and N-acetyl-L-cysteine-stabilized AgNPs for detection of iron ions.[48]

The purpose of this study is to develop a simple, rapid, efficient and cost-effective method for the determination of some metal ions by functionalized AgNPs. Two new AgNPs based colorimetric sensors were prepared with SDS and SDS-CD as the stabilizing agents without further modification and investigated as colorimetric sensors for Mn^{2+} and Cr^{2+} ions, respectively. There are many published works on colorimetric detection of Mn^{2+} ion based on functionalized AgNPs system; e.g., Pyrophosphate capped AgNPs ($Na_4P_2O_7$),[49] Sodium pyrophosphate (Na4P2O7) and hydroxy propyl methyl cellulose-stabilized AgNPs,[50] 5-sulfoanthranilic acid dithiocarbamate-stabilized AgNPs,[51] L-tyrosine stabilized AgNPs,[52] l-arginine-stabilized AgNPs[16] and alginate-stabilized AgNPs.[53] Although several efforts have been devoted to the development of colorimetric detection of both Cr^{3+} and Cr^{6+} cations,[54–57] based on the functionalized AgNPs system, the detection of Cr^{2+} species has been overlooked. To the best of authors' knowledge, only, Rull-Barrull et al. reported a selective rhodamine-based chemosensor for colorimetric and fluorimetric detection of Cr^{2+} under aqueous conditions.[58]

Herein, the SDS was chosen as a candidate for modifying the AgNPs to design a selective and sensitive colorimetric sensor for detecting Mn^{2+} in the wide range pH (3–13) with a suitable response rate. Also, SDS and CD were chosen to modify the AgNPs to design a selective and sensitive colorimetric sensor for detecting Cr^{2+} in a wide range of pH (i.e., 3–13) with a suitable response rate. Consequently, simple, rapid colorimetric assays for detecting Mn^{2+} and Cr^{2+} were established. These detection methods showed successful detection under various pH conditions. The colorimetric detection mechanism of two sensors, which is based on the accumulation of AgNPs, is illustrated in Figure 1.

2. Experimental

2. 1. Materials

Silver nitrate ($AgNO_3$ ≥ 99%) and β-cyclodextrin (CD ≥ 97%), sodium borohydride ($NaBH_4$, 98%), Hydrochloric acid (HCl, 37%), sodium hydroxide (NaOH, 97%), and Sodium dodecyl sulfonate (SDS ≥ 99.0%) were purchased from Sigma-Aldrich.

2. 2. Instrumentation

UV-vis spectra were recorded on a spectrophotometer (Varian, Cary50), using a 1 cm of quartz cell. Scanning

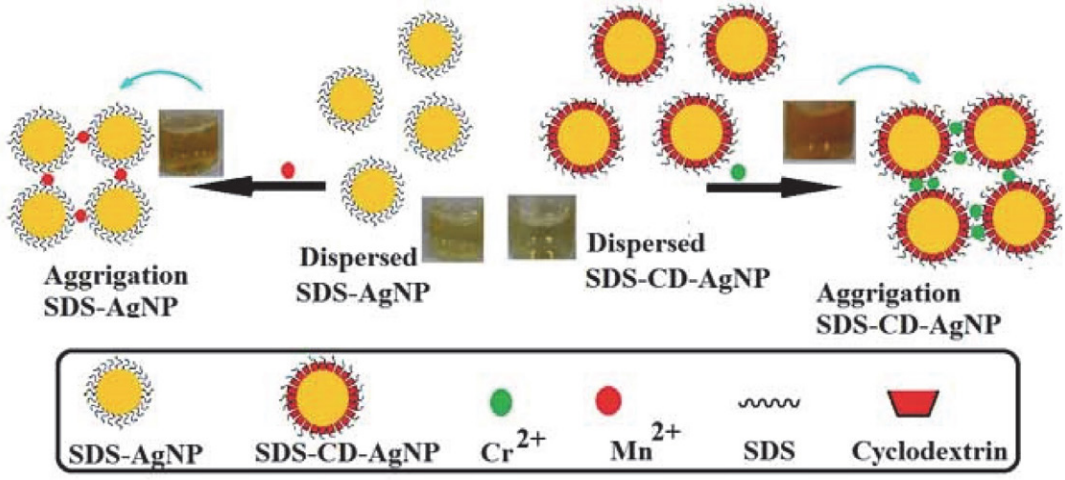

Figure 1. Schematic illustration of detecting mechanism of Mn^{2+} and Cr^{2+} ions based on the aggregation of SDS-AgNPs and SDS-CD-AgNPs, respectively

electron microscopy (SEM) images were obtained using a field-emission scanning electron microscope (KYKT, model EM-3200). Transmission Electron Microscope (TEM) images were recorded from JEOL 2100F TEM. XRD patterns were obtained in reflection mode using a powder X-ray diffractometer (X′ Pert Pro MPD Philips X-ray diffractometer, Ni-filtered Cu-Kα radiation, λ = 0.154 nm). The FT-IR spectra were recorded using the FT-IR spectrometer (Brucker, model Tensor 27) in the region 4,000–400 cm^{-1} using KBr pellets. To determine the mean hydrodynamic diameter (d_H) of the AgNPs in aqueous solution, dynamic light scattering (DLS) investigations were performed without filtering AgNPs solutions at 25 °C using the new non-invasive back-scatter (NIBS) technology by a 1-cm quartz cell. The pH measurements were performed using a pH-meter (METROHM, Model 713).

2. 3. Synthesis of AgNPs

AgNPs were prepared by reducing $AgNO_3$ with $NaBH_4$ in the presence of SDS or mixture of CD and SDS as stabilizing agents. Briefly, 0.1 g of the stabilizing agent was dissolved in 50 ml deionized water. Then, 1.0 mL of $AgNO_3$ aqueous solution (0.001M) was slowly added into the above solution under vigorous stirring for 30 min. Finally, 0.001 g $NaBH_4$ was added into the solution, which caused the color change from yellow to orange.

2. 4. pH-Dependent Stability Study of AgNPs

There are several important factors that affect the stability of the AgNPs.[59] In this section, we will investigate the effect of pH on the stability of AgNPs by monitoring the color variation and UV-vis intensity changes of the AgNPs solution upon the addition of HCl or NaOH solution (0.1 M). In order to study the effect of pH on the stability of AgNPs, the absorption spectra were recorded after 30 min of mixing.

2. 5. Cation-Sensing Studies

The AgNPs sensor behavior in a solution containing various metal ions such as Na^+, K^+, Mg^{2+}, Ca^{2+}, Al^{3+}, As^{3+}, Co^{2+}, Cu^{2+}, Ni^{2+}, Zn^{2+}, Cd^{2+}, Fe^{2+}, Hg^{2+}, Mn^{2+}, and Cr^{2+} ions was studied by recording the UV-vis absorption spectra upon their addition. Thus, 1 ml of each ion solution (10 μM) was added into 1 ml of the freshly prepared AgNPs solution.

For all samples, after 2 min of mixing, some photographs were taken using a digital camera under daytime light and absorption spectra were recorded using a spectrophotometer. The limit of detection (LOD) and limit of quantitation (LOQ) were determined from the standard deviation of the slope of the calibration curve using the following expressions: LOD = 3.3 σ_a /b and LOQ = 10 σ_a /b; where σ_a is the standard deviation of the blank signals and b is the slope of the calibration curve.

To investigate anti-interferential capability of SDS-AgNPs sensors, a mixture of each ion solution (Na^+, K^+, Mg^{2+}, Ca^{2+}, Al^{3+}, As^{3+}, Co^{2+}, Cu^{2+}, Ni^{2+}, Zn^{2+}, Cd^{2+}, Fe^{2+}, Hg^{2+}, and Cr^{2+}) with Mn^{2+} ions was prepared by adding 1 ml of each ion solution (10 μM) into 1 ml 10 μM Mn^{2+} ion solution. Afterward, 1 ml of each solution was mixed with 1 mL SDS-AgNPs solution. This procces was repeated for the SDS-CD-AgNPs with a mixture of each ion solution (Na^+, K^+, Mg^{2+}, Ca^{2+}, Al^{3+}, As^{3+}, Cr^{2+}, Co^{2+}, Cu^{2+}, Ni^{2+}, Zn^{2+}, Cd^{2+}, Fe^{2+}, Hg^{2+}, and Mn^{2+}) with Cr^{2+} ions.

3. Results and Discussion

3. 1. Characterization of Silver Nanoparticles

The synthesized AgNPs were characterized by UV-visible spectroscopy, FT-IR spectroscopy, SEM, TEM, TEM, XRD and DLS techniques. AgNPs absorption spectra in the UV-visible region show a specific absorbance band due to the excitation mode of their surface plasmons by incident light.[60] Based on Mie's theory, spherical nanoparticles have only one SPR band depending on their size.[61,62] Thus, the UV spectrum was used to confirm the synthesis of AgNPs (Figure S1).[61,62] The UV-Visible spectrum shows an absorption maximum that appears at 410 and 400 nm for SDS-AgNPs and SDS-CD-AgNPs, respectively. These values are in good agreement with the literature values for AgNPs.[60] The difference in UV-vis absorption spectra between the SDS-AgNPs and SDS-CD-AgNPs spectrums is due to the variation in the size distribution of the AgNPs as confirmed using SEM and TEM (Figures S2 and 2). The results of SEM and TEM images show that both nanoparticles are polygonal. But, compering these nanoparticles show that SDS-AgNPs have a smaller size with a narrower size distribution than SDS-CD-AgNPs. Based on the TEM results, the average diameter of SDS-AgNPs and SDS-CD-AgNPs are 8 nm and 15 nm, respectively. According to the lectures, using the same reduction reagent, nanoparticle size can be varied by changing the synthesis conditions.[63,64] Probably, the size difference is due to the different rates of diffusion of silver ions into the seed of SDS-AgNPs and SDS-CD-AgNPs. According to previous studies, it is very likely that for both types of nanoparticles (i.e., SDS-AgNPs and SDS-CD-AgNPs), the anionic SDS was adsorbed on the surface of nanoparticles through hydrophobic bonding with a tail surface/headwater orientation. Furthermore, in the presence of cyclodextrin, the hydrophobic carbon chain of SDS was wrapped into the CD cavity-forming host-guest molecules complex.[65] Based on these results for the SDS-CD-AgNPs, the AgNPs were capped by the host-guest inclusion of SDS-CD. And it can be stated that the diffusion of silver ions into the primary seed coated with SDS is more difficult than penetration of silver ions into the primary seed coated with SDS-CD. As a result, the size of SDS-AgNPs is smaller than the size of SDS-CD-AgNPs. In addition, based on the TEM results

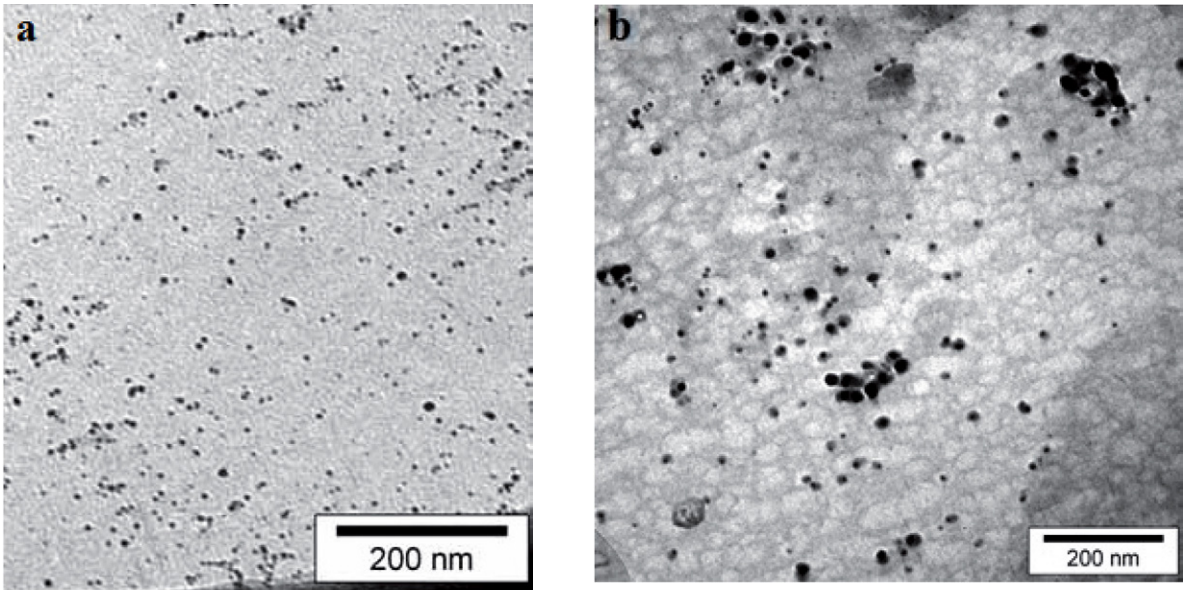

Figure 2. TEM images of the synthesized AgNPs: (a) SDS-AgNPs and (b) SDS-CD-AgNPs.

SDS-CD-AgNPs are more agglomerate than SDS-AgNps. According to the pka values, the SDS surface groups are more deprotonated than the CD groups at neutral pH, consequently, more electrostatic repulsions between the negatively charged groups of SDS-AgNPs, leading to more dispersion of SDS-AgNPs than SDS-CD-AgNPs.[66] In addition, the binding affinity (hydrogen and hydrophobic interactions) between cyclodextrin molecules on the surface of AgNPs leads to some agglomeration of SDS-CD-AgNPs. These agglomeration structures for SDS-CD-AgNPs can be seen in the TEM image.

The effective diameter of the AgNPs in the aqueous solution (pH = 7) was measured by DLS (Figure S3). Unlike the results of TEM, the hydrodynamic diameter of SDS-CD-AgNPs was significantly larger than the hydrodynamic diameter in DLS analysis. Indeed, this analysis shows how a particle diffuses within a fluid while TEM just shows the shape and size of AgNPs.[67]

The FTIR spectra of the SDS-AgNPs and SDS-CD-AgNPs are also recorded to identify the functional groups of the SDS and CD involved in the synthesis of the AgNPs. According to the FTIR spectrums in Figures 3a and 3b, the sharp peaks belonging to the SDS and CD were observed in the spectrum of the AgNPs. In Figure 3a, the FTIR spectra of the SDS-AgNPs and SDS-CD-AgNPs show the peaks at 2943, 2915, 2848, and 1465 cm^{-1} corresponding to the CH_2 stretching and bending modes, the 1220 cm^{-1} peak corresponding to skeletal vibration involving the bridge S–O stretch, and the 1075 cm^{-1} peak corresponding to C–C band stretching of SDS. Also, the peaks at 827 and 579 cm^{-1} correspond to asymmetric C–H bending of the CH_2 group of SDS.[68] The FTIR results are in good agreement with the values reported in literature for SDS. In addition, the spectra of SDS-CD-AgNPs in Figure 3b shows such peaks at 3400 cm^{-1}, 2930 cm^{-1}, and 1155 cm^{-1} corresponding to O–H, C–H, C–O–C bands of CD, respectively; which are in good agreement with the literature values.[69] These results indicate the presence of β-cyclodextrin and SDS as a capping agent of AgNPs.

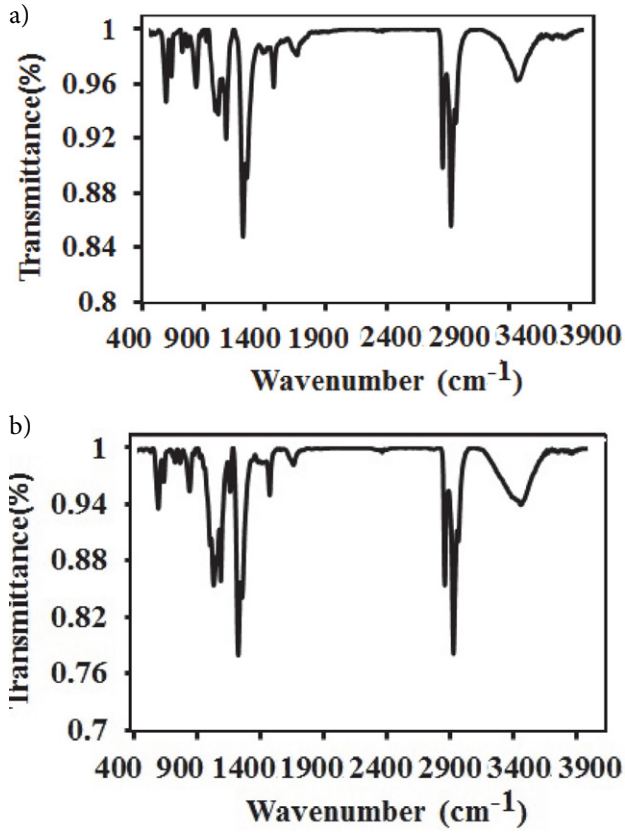

Figure 3 FTIR spectrum of the synthesized AgNPs (a) SDS-AgNP (b) SDS-CD-AgNP.

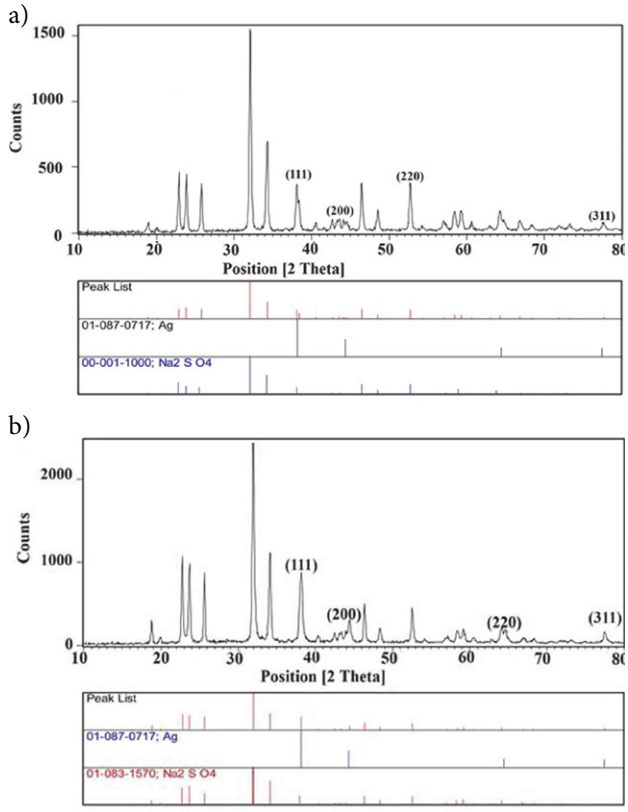

Figure 4. The XRD pattern of (a) SDS-AgNPs and (b) SDS-CD-AgNPs.

Figure 4 shows the XRD spectra of the SDS-AgNPs and SDS-CD-AgNPs after calcination at 500 °C. The XRD pattern of SDS-AgNPs is shown in Figure 4a. The prominent diffraction peaks at 2θ = 38.19°, 44.49°, 64.26° and 77.64° are indexed to the (111), (200), (220), and (311) crystalline planes, respectively. All diffraction peaks indicated that the AgNPs possess a face-centered-cubic (fcc) structure (JCPDS card number 01-087-0717).[70,71] Similarly, the XRD pattern of SDS-CD-AgNPs shows well defined peaks at 2θ = 38.19°, 44.43°, 64.09° and 77.48° are due to the (111), (200), (220), and (311) crystal planes in accordance with a fcc structure of AgNPs (JCPDS card number 01-087-0717).[70, 71]

Moreover, the spectrums of AgNPs contain the XRD characteristic peaks of Na_2SO_4 that corresponded well with those of the standard spectrum. As reported in the literature,[72] SDS undergoes hydrolysis to yield dodecanol and sodium hydrogen sulfate when heated and then it is converted to Na_2SO_4.

3. 2. pH-Dependent Stability Study of AgNPs

As the pH of the solution may influence the surface charge and aggregation of NPs, the pH-dependent stability of SDS-AgNps and SDS-CD-AgNps were studied by UV-visible absorption measurements at the pH range of 1–13 Figure S4. The results show that the SDS-AgNPs are stable in the pH range of 3–11. However, according to

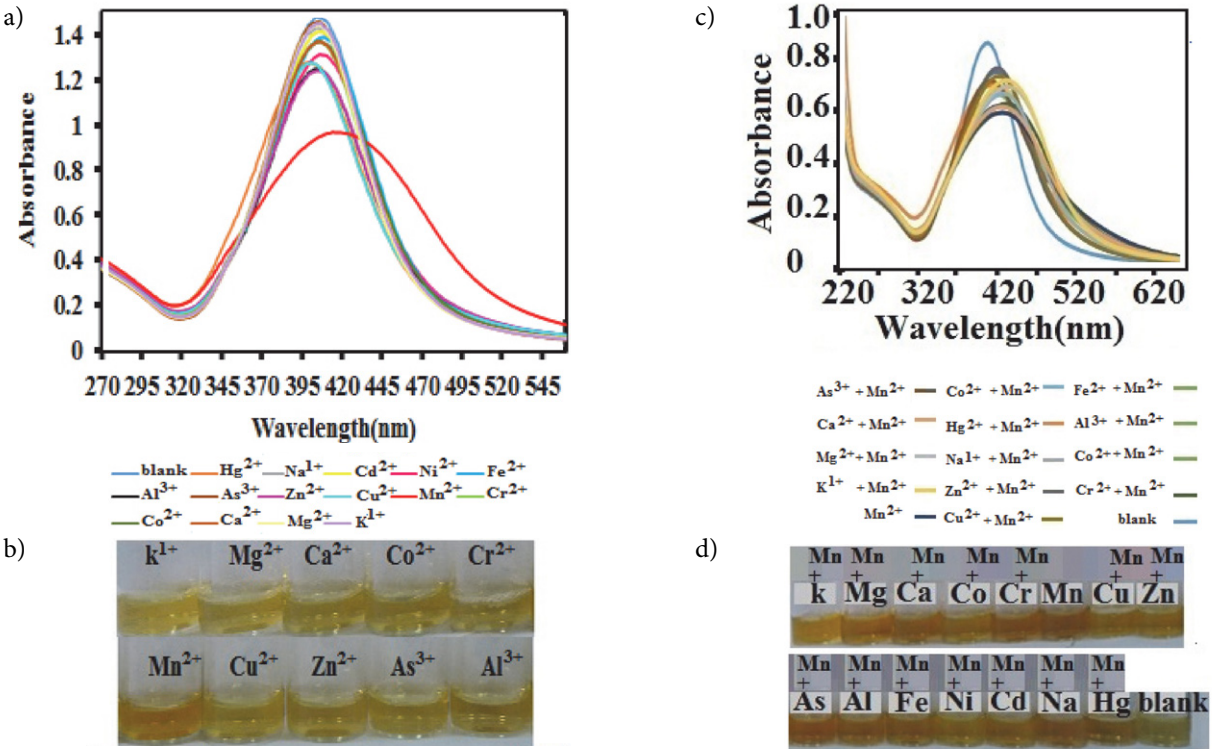

Figure 5. Selectivity of the SDS-AgNPs for Mn^{2+} compared with other ions: (a) UV-vis spectra; (b) photographic images for detecting AgNPs incubated with K^+ (50 μM), Cu^{2+} (50 μM), Hg^{2+} (50 μM), or other ions (50 μM) at pH 7; (c) UV-vis spectra; and (d) Photographic image of detecting SDS-AgNPs incubated with mixture of Mn^{2+} (5 μM) and other ions (5 μM) at pH 7.

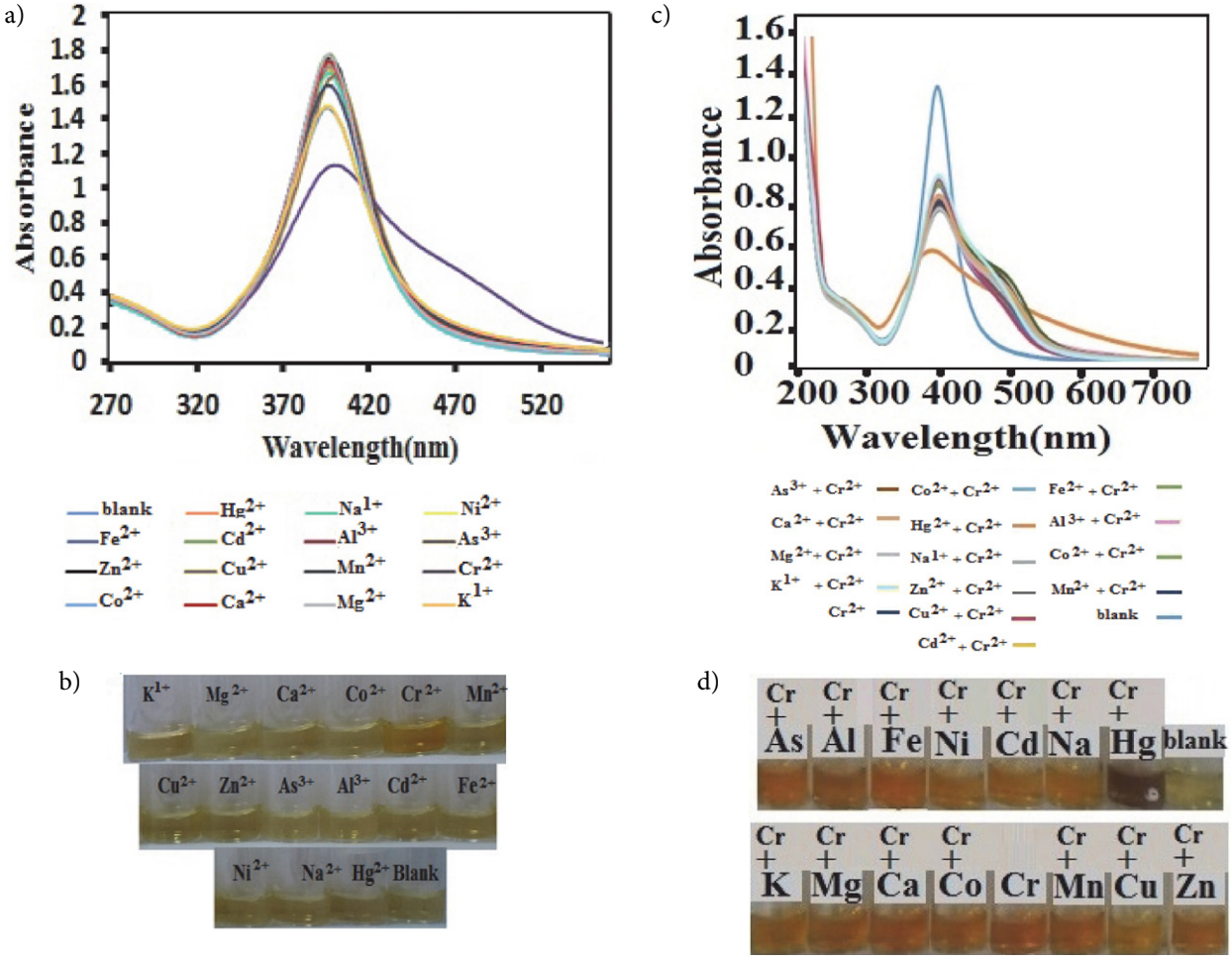

Figure 5. Selectivity of the SDS-AgNPs for Mn^{2+} compared with other ions: (a) UV-vis spectra; (b) photographic images for detecting AgNPs incubated with K^+ (50 μM), Cu^{2+} (50 μM), Hg^{2+} (50 μM), or other ions (50 μM) at pH 7; (c) UV-vis spectra; and (d) Photographic image of detecting SDS-AgNPs incubated with mixture of Mn^{2+} (5 μM) and other ions (5 μM) at pH 7.

significant changes in the SPR absorption intensity and color of solutions, nanoparticles are unstable at pH < 3 and pH > 11. At higher pH values (> 11), SDS-AgNPs aggregate shows a sudden change in the solution color from yellow to orange, a decrease in SPR absorption intensity, and a new peak at 547 nm. According to Mie's theory,[73] due to the exhibition of two bands, SDS-AgNPs may not be spherical and have an anisotropic shape at this range of pH.

From absorption spectra and image of the SDS-CD-AgNPs, it is seen that the particles are stable when pH value changes from 3 to 13. In addition, according to significant changes in the SPR absorption intensity and color of solutions, nanoparticles are unstable at pH < 3.

3. 3. Selectivity Assay of AgNPs

Figures 5 and 6 present that SDS-AgNPs and SDS-CD-AgNPs, when tested against a range of other physiologically and environmentally important cations, have remarkable selectivity for Mn^{2+} and Cr^{2+} ions, respectively. Figures 5(a) and 5(b) show that the other metal ions have no clear effect on the color or UV absorption. Moreover, these Figures show that SDS-AgNPs is efficiently selective for Mn^{2+} ions. Figures 5 (c) and 5 (d) depict the UV-vis spectra of detecting of SDS-AgNPs incubated with a mixture of Mn^{2+} and other metal ions (such as Na^+, K^+, Mg^{2+}, Ca^{2+}, Al^{3+}, As^{3+}, Co^{2+}, Cu^{2+}, Ni^{2+}, Zn^{2+}, Cd^{2+}, Fe^{2+}, Hg^{2+}, and Cr^{2+}) at pH = 7. According to the UV-vis spectra and photographic image, the SDS-AgNPs possess high detection ability and selectivity toward Mn^{2+} in the presence of other cations.

Similarly, Figures 6 (a) and 6 (b) show that SDS-CD-AgNPs have substantial selectivity power for Cr^{2+} ions when tested against a range of other cations. Moreover, these Figures show that the other metal ions have no obvious effect on the color or UV absorption, proving that SDS-CD-AgNPs are sufficiently selective for the Cr^{2+} ions. The UV-vis spectra (Figure 6 (c)) and photographic image (Figure 6 (d)) show the anti-interferential capability of the SDS-CD-AgNPs toward Cr^{2+} in the presence of other competitive ions (e.g., Na^+, K^+, Mg^{2+}, Ca^{2+}, Al^{3+}, As^{3+},

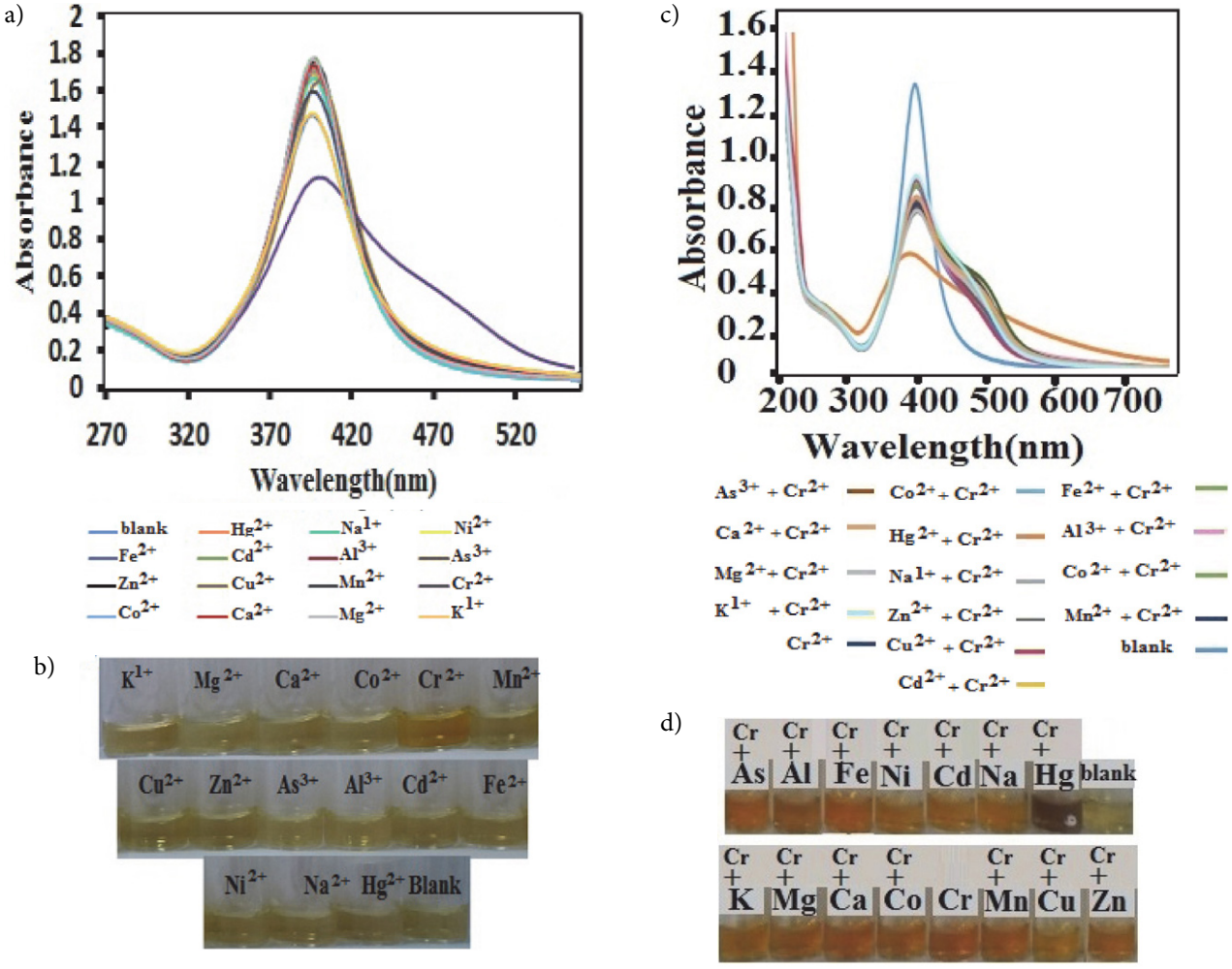

Figure 6. Selectivity of the SDS-CD-AgNPs for Cr^{2+} compared with other ions: (a) UV-vis spectra; (b) photographic images of detecting SDS-CD-AgNPs incubated with K^{+} (5 μM), Cu^{2+} (5 μM), Hg^{2+} (5 μM), or other ions (5 μM) at pH 7; (c) UV-vis spectra; and (d) Photographic image of detecting SDS-CD-AgNPs incubated with the mixture of Cr^{2+} (5 μM) and other ions (5 μM) at pH 7

Co^{2+}, Cu^{2+}, Ni^{2+}, Zn^{2+}, Cd^{2+}, Fe^{2+}, Hg^{2+}, and Mn^{2+} ions) at pH 7. In addition, the results indicate that the solution contacting both Cr^{2+} and Hg^{+} ions changes from yellow to brown. Also, a change in the SPR band was observed (Figure S5). In addition, the absorption ratios of this solution are much lower than the other solutions. These results show that the sensing of Cr^{2+} ions is also possible in the presence of other metal ions and SDS-CD-AgNPs has a good selectivity to Cr^{2+} ions. Furthermore, it is possible to use the SDS-CD-AgNPs solution containing Cr^{2+} ions as an Hg^{2+} sensor. Similar research has been done in this regard.[11, 35]

The sensitivity of SDS-AgNPs toward Mn^{2+} was evaluated by varying the concentration of Mn^{2+} ions (Figure 7). According to this Figure S6, by adding Mn^{2+} ions (1.0 mM to 6.0 μM) to SDS-AgNPs solution, the color of SDS-AgNPs solution changed, which was detected by the naked eye. But, based on the UV-vis spectrum (Figure 7), the changes in the absorption intensity at the maximum wavelength (λ_{410}) showed a linear relationship only in the concentration range from 6.0 μM to 9.0 μM. And in this concentration range the color of the solutions changed from yellow to orange, Figure S6. The LOD and LOQ for Mn^{2+} were 0.02 μM and 0.04 μM, respectively. Similarly, as can be seen from Figure S7, by adding Cr^{2+} ions (1.0 mM to 3.0 μM) to SDS-CD-AgNPs solution, the color of solution changed. But, the changes in the absorption intensity showed a linear relationship with the concentration of Cr^{2+} only in the range from 3.0 μM to 9.0 μM. As Figure 8a Shows, by increasing Cr^{2+} concentration from 3.0 μM to 9.0 μM, the UV-vis absorption peak intensity at 400 nm decreased and the color of the solutions changed from yellow to orange (Figure S7). The LOD and LOQ for Cr^{2+} were 0.01 μM and 0.03 μM, respectively.

3. 4. Real-Time UV-vis Response of AgNP Sensors Toward Desired Ions

Figure S8 shows the changes in the SDS-AgNPs absorbance spectrum after the addition of Mn^{2+} ions. As can be seen, after about 1 min, the colorimetric response of the sensor is observed. Also, after 14 min, the aggre-

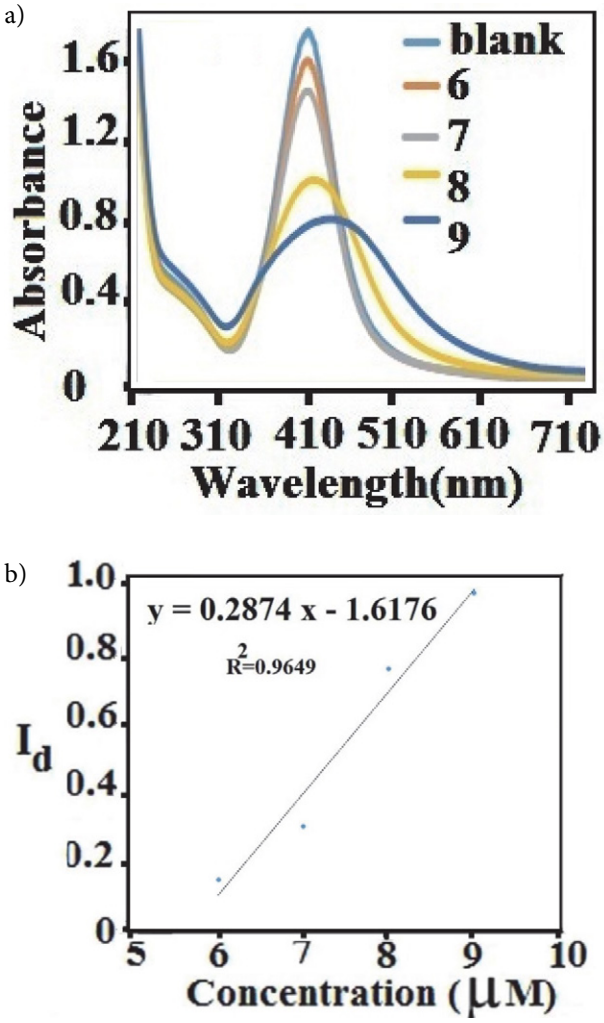

Figure 7. (a) absorption spectral changes observed for SDS-AgNPs after addition of Mn^{2+} ions at a concentration range from 6.0 μM to 9.0 μM and plot of changes in the value of the absorption intensity at the maximum wavelength (λ410) of SDS-AgNPs against Mn^{2+} ion concentration from 6.0 μM to 9.0 μM

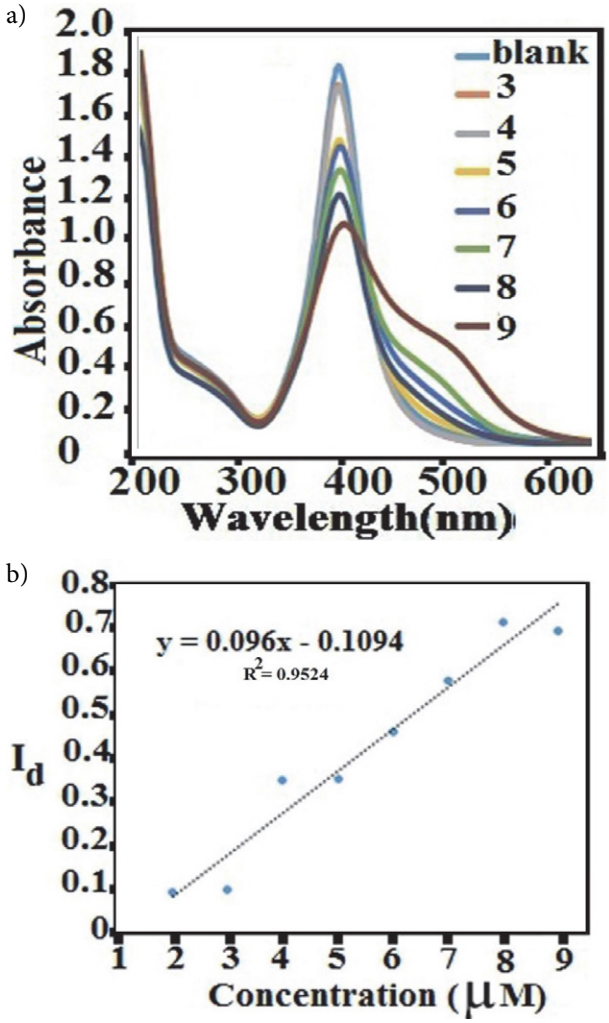

Figure 8. (a) absorption spectral changes observed for SDS-CD-AgNPs after the addition of Cr^{2+} ions at a concentration range from 3 μM to 9.0 μM and (b). The plot of changes in the value of the absorption intensity at the maximum wavelength (λ400) of SDS-CD-AgNPs against Cr^{2+} ions concentration from 3.0 μM to 9.0 μM

gation is completed and there is no change in the absorbance signals.

Similarly, Figure S9 shows that after the addition of Cr^{2+} to the SDS-CD-AgNPs solution, first, there is a decrease in the SPR peak intensity and then it reaches relatively constant values within 4 min.

3. 5. Optimization of the Conditions for the Mn^{2+} or Cr^{2+} Measurement

In the following, the effect of the concentration of the AgNps and pH on the detection of Mn^{2+} or Cr^{2+} ions was investigated.

3. 5. 1. Effect of the Concentration of the AgNps

The effect of the dosage of AgNps on their colorimetric sensing ability is examined as follows: First, different concentrations of AgNPs were prepared with diluting AgNPs solutions in different volumes of deionized water as blank solutions (2:1, 1:1, and 1:2 V:V). Then, different volume ratios of AgNPs solutions to the desired ion solution are prepared (2:1, 1:1, and 1:2).

The absorption spectra and image of Figure 9 reveal that by varying the dosage of AgNps, the colorimetric sensing ability of AgNPs was preserved; however, by increasing the volume ratio of AgNPs solutions to the desired ion solution, a decrease in analytical signal occurs. This reduction could be due to the complexing action of SDS or CD-SDS surface functionality with metal ions (Mn^{2+} or Cr^{2+}), leading to the aggregation of NPs. Also, the Figure shows that by increasing the volume ratio of the AgNPs to the desired ion solution, a higher red shift in the AgNPs SPR band occurred. Since desired ions could complex with surface functionality of several nanoparticles, it can be stated that the presence of more nanoparticles

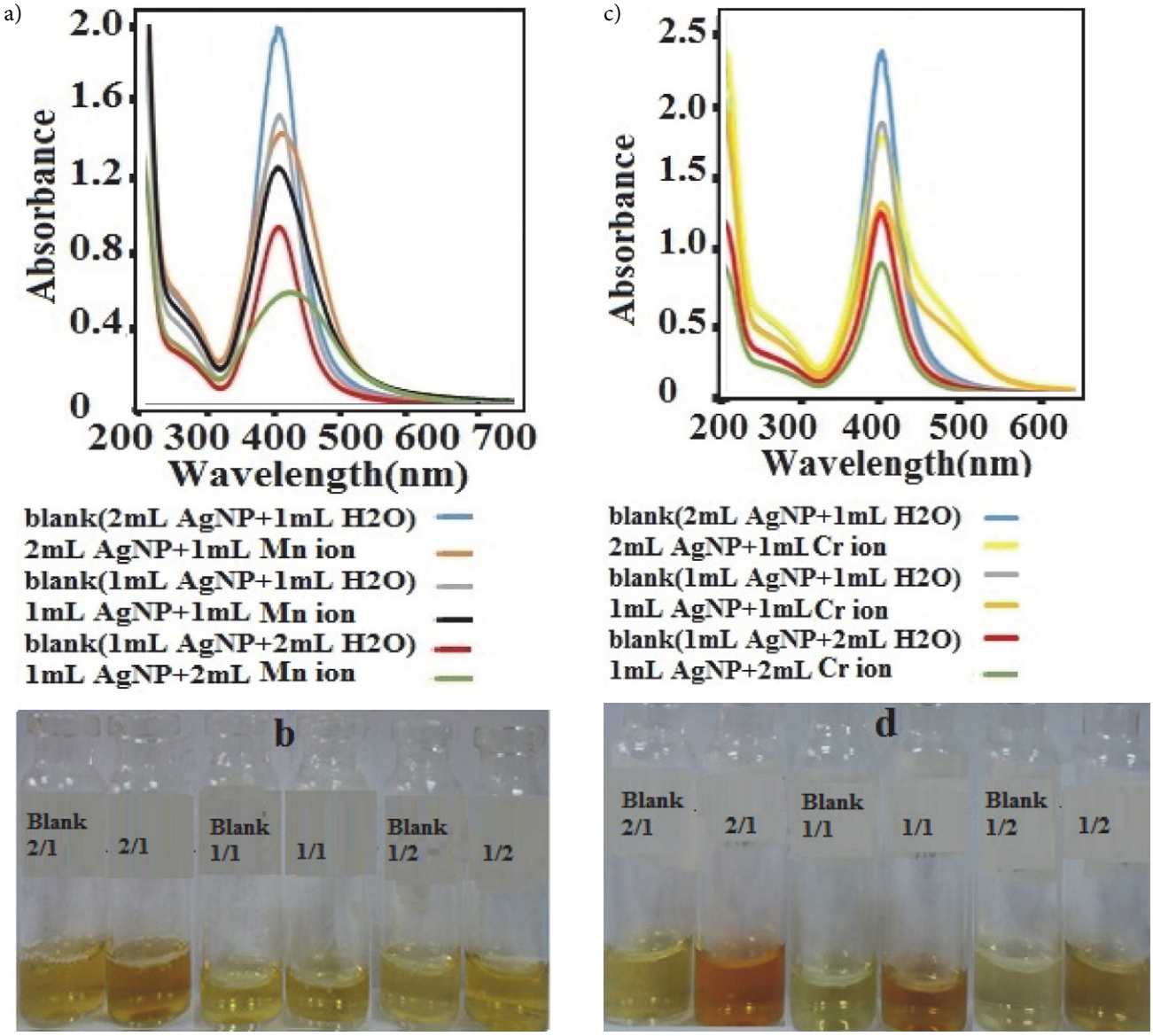

Figure 9. The UV–vis spectra and the photographic images of 2:1, 1:1, and 1:2 volume ratio of (a and b) SDS-AgNPs solutions to Mn^{2+} ions solution and (c and d) SDS-CD-AgNPs solutions to Cr^{2+} ions solution.

around the desired ions in the solution results in agglomeration of more nanoparticle, forming bigger agglomerates, and a higher redshift in the AgNPs SPR band. Thus, the volume ratio of AgNPs to ion solution was selected to be 2:1 with maximal changes in SPR peaks and the color of the solution was selected as the optimal ratio for detecting desired ions by both sensors.

3. 5. 2. Effect of pH on the Detection of Mn^{2+} or Cr^{2+} Ions

The effect of pH on the performance of the sensors was tested as follows. About 1 mL AgNPs solution was mixed with 0.1 ml HCl or NaOH solutions with different concentrations. Next, 1 mL 10 μM Mn^{2+} or Cr^{2+} ions solution was added to the AgNPs solutions. Figure 10 present the effect of pH (1 to 13) on the colorimetric response of the sensors. According to Figure, by adding desired ions to all solutions, a color change and a decrease in the absorbance ratio is clearly observed. These results indicate that both sensors keep their sensing capability at a pH range of 3 to 13. The results show that at the investigated pH range (1–13), pH values of 5 and 11 have more UV-vis intensity changes of the AgNPs solution toward Mn^{2+} detection than the other pHs. Thus, the pHs of 5 and 11 were selected as the best values for detecting manganese ion by SDS-AgNPs in acidic and basic media, receptively. Meanwhile, the pHs of 3 and 9 showed more UV-vis intensity changes toward Cr^{2+} detection than the other pHs. The effect of pH on the colorimetric response of AgNPs can be ascribed to the four factors: (I) AgNPs dissolution (II) forming hydroxide for metal ions, (III) size of AgNPs, and (IV) the effect of electrostatic inter-

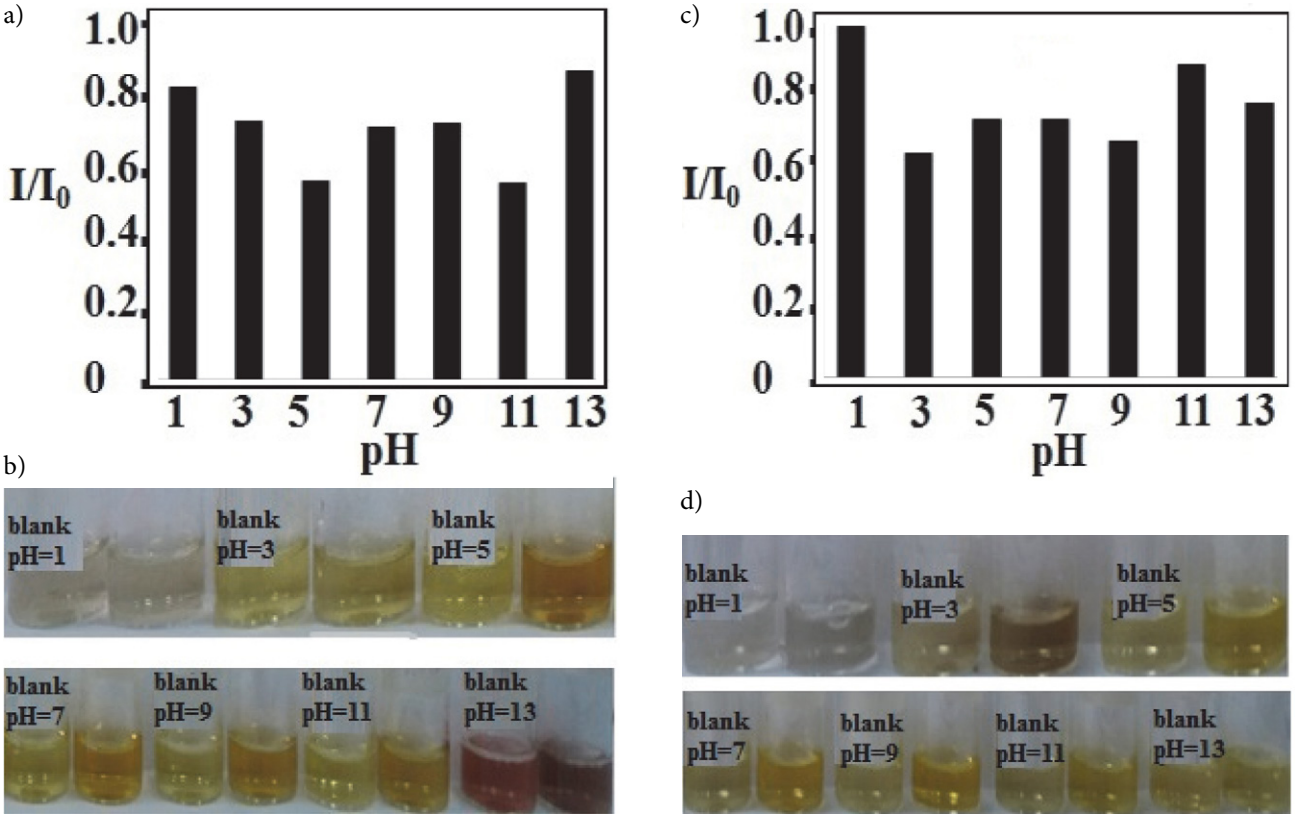

Figure 10. Bar graphs of UV-vis intensity changes and photographic images of (a and b) SDS-CD-AgNPs at different pH levels (c and d) SDS-CD-AgNPs at different pH levels.

action between the negatively charged groups of the surface-bonded SDS or CD and positively charged metal ions.

The results reported in the literature show that particle size has generally an inverse effect on AgNPs dissolution: small AgNPs release more Ag^+ than large ones because smaller particles are energetically unfavorable due to higher surface-to-volume ratio and consequently are more soluble[76]. Based on the TEM results, SDS-AgNPs have a smaller size and a narrower size distribution than SDS-CD-AgNPs. Thus, SDS-CD-AgNPs are more stable than SDS-AgNPs. It was shown at low pH values, AgNPs are dissolved.[76] As can be seen in Figure 10, at pH = 1, both AgNPs are dissolved and no colorimetric response was observed for them. Also, at pH = 3, the SDS-AgNPs have less UV-vis intensity changes toward Mn^{2+} detection than the pH = 5, which could be due to the lower concentration of SDS-AgNPs at pH = 3 than pH = 5. However, at pH = 3, the SDS-CD-AgNPs have the best UV-vis intensity changes toward Cr^{2+} detection, which is due to the larger size of SDS-CD-AgNPs than SDS-AgNPs and their more stability at this pH.

Overall, it can be stated that the performance of SDS-AgNPs and SDS-CD-AgNPs between pH = 5–11 and pH = 3–9 is influenced by two factors, which compete with each other: (I) the size of AgNPs and (II) the electrostatic interaction between the negatively charged groups of AgNPs and positively charged matal ions. Thus, at lower pH, size may control the sensing ability of AgNPs, so that by decreasing pH, the size of particles decreased, as well. And at upper pH, the negative charge of the SDS or CD groups of AgNPs is a more effective factor. So, by increasing pH, SDS surface groups are more deprotonated and, consequently, the electrostatic repulsions between the negatively charged groups increased, leading to an increase in the dispersion of AgNPs. Thus, the desired ions could complex more with surface functionality of nanoparticles than lower pH. Although proper dispersion of nanoparticles enhances the responsiveness of the sensors under alkaline conditions, at pH = 11 for Mn^{2+} and pH = 10 for Cr^{2+}, the sensor performance is reduced due to the formation of manganese hydroxide and chromium hydroxide and, consequently, a decrease in the concentration of Mn^{2+} and Cr^{2+} ions.[50, 52] However, the results indicate that the colorimetric response of SDS-CD-AgNPs at pH = 13 is higher than pH = 11, probably due to the deprotonation of hydroxyl groups of CD bound at the surface of nanoparticles at pH > 12. Therefore, dihydroxylation of OH-groups of cyclodextrin molecules plays a key role in enhancing the formation of Cr^{2+}–CD complex and agglomeration of the nanoparticles.[66]

3. 6. SEM, TEM and DLS Analysis

To explain the mechanism of sensing of the AgNPs to detect desired ions, the nanoparticles were examined

before and after desired exposure using UV-vis, TEM, SEM, and DLS observations. According to the above results, the color of both nanoparticles changes from yellow to orange in the presence of desired ions. The results of TEM, SEM, and DLS for SDS-AgNPs sensor show that SDS-AgNPs are dispersed with small size (Figures 2a, S2a and S3a); but, after adding Mn^{2+} ions, a significant aggregation of nanoparticles is observed (Figures 11a, S 10a and S 11a). Similarly, Figures (2b, S2b and S3b) present the TEM image and SEM and DLS of the SDS-CD-AgNPs sensor. The Figures show the dispersion of the SDS-CD-AgNPs, but adding Cr^{2+} ions resulted in the aggregation of nanoparticles (Figures 11 b, S 10b and S 11b). According to the UV-vis results, with increasing the metal ions concentration (Mn^{2+} or Cr^{2+}), a red shift in the AgNPs SPR band appears. This shift, which could be due to the complexing action of SDS or CD-SDS surface functionality with metal ions (Mn^{2+} or Cr^{2+}), leads to the aggregation of NPs. Thus, for both sensors, the aggregation resulted in reflecting the ion-induced aggregation of the functional AgNPs. As mentioned, according to the information obtained from previous studies,[68,77] it is very likely that the SDS was adsorbed on the surface of nanoparticles through hydrophobic bonding with a tail surface/headwater orientation. The high selectivity of the SDS-AgNP toward Mn^{2+} can be attributed to two phenomena: (I) the cooperative effect of electrostatic interaction between the negatively charged SO^{4-} groups of SDS and positively charged Mn^{2+} ions and (II) the complexation of Mn^{2+} ions as hard acids with oxygen donors of SDS. Accordingly, the SDS-AgNPs tend to come closer, which decreases the interparticle distance and makes them aggregated. According to the lectures,[78, 79] cyclodextrin stabilizes the surface of AgNPs through chemisorption of hydroxyl groups and the hydrophobic-hydrophobic interactions. Thus, the CD has been applied as both stabilizer and surface functionalizing agents for AgNPs synthesis. Furthermore, as mentioned earlier, in the SDS-CD-AgNPs, the AgNPs are capped by the host-guest inclusion of SDS-CD. According to the obtained results, SDS-AgNPs do not respond to the Cr^{2+} ions. In comparison, the SDS-CD-AgNPs demonstrates sensitive and selective colorimetric detection of Cr^{2+} ions. Probably, Cr^{2+} ion as a harder acid than Mn^{2+} ion in addition to bind sulfate groups and oxygen donors of SDS, has tendency to bind ether and hydroxyl groups of cyclodextrin. Thus, selectivity of the SDS-CD-AgNPs toward Cr^{2+} can be ascribed to the three facators: (I) The cooperative effect of electrostatic interaction between the negatively charged SO_4^- groups of SDS and positively charged Cr^{2+} ions; (II) The complexation of Cr^{2+} ions as hard acids with oxygen donors of SDS; and (III) The complexation of Cr^{2+} ions as hard acids with ether and hydroxyl groups of cyclodextrin as hard base. Owning to these reasons, the SDS-CD-AgNPs tend to keep closer, decreasing the interparticle distance and gets aggregated. Based on TEM results, the aggregates of the SDS-CD-AgNPs in the presence of Cr^{2+} ions are larger than those of the SDS-AgNPs in the presence of Mn^{2+} ions. This can be attributed that the SDS-CD-AgNPs are more agglomerate than SDS-AgNps, Figure 2. In addition, as mentioned, the interaction between SDS and CD surface groups with desired ions are different.

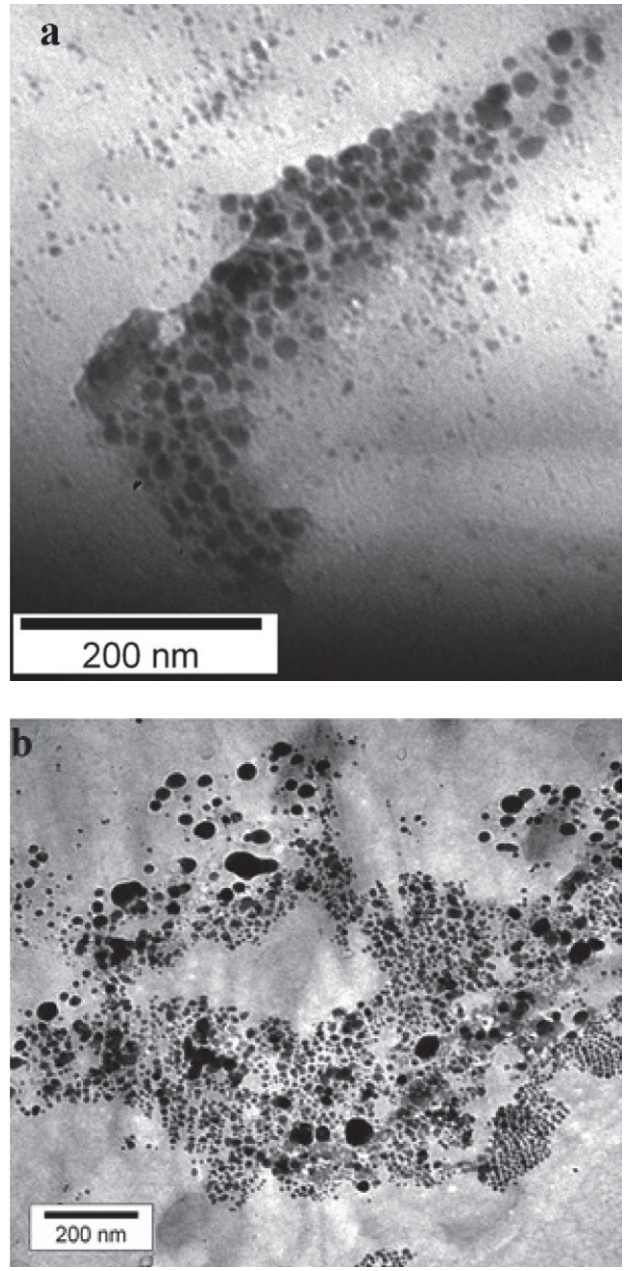

Figure 11. TEM images (a) of SDS-AgNPs after the addition of 0.5 μM of Mn^{2+} ions (b) of SDS-CD-AgNPs after the addition of 0.5 μM of Cr^{2+} ions.

Table 1 summarizes information of various Mn^{2+} detection methods based on AgNPs as a colorimetric sensor. In contrast to some studies [49,80,81] reported in the table, SDS-AgNPs have much lower detection level for Mn^{2+} ions. As shown in Table 1, although the sensing ability of sensors reported in this Table is suitable, compared to our

Table 1. Comparison of different methods using AgNPs as a colorimetric sensor for Mn^{2+} detection.

No	Time of preparation	Capping agents	pH range	Detection time (min)	Selectivity	LOD	Ref
1	2.5 h	B-cyclodextrin and Adamantine	–	5	Selective μM	0.5	80
2	24.5 h	Sodium pyrophosphate and hydroxyl propyl methyl cellulose	12	10	selective	2 nM	50
3	5 min	L-tyrosine	7–12	–	Responsive for Hd^{2+} and Mn^{2+}	16 nM	52
4	1.20 h with sonicate	5-sulfoanthranilic acid di thiocarbamate	2–12	1	Responsive to Cd^{2+} and Mn^{2+}	3 nM	51
6	1 h	Pyrophosphate	More than pH 9.0	–	Selective	0.03 μM	49
7	0.5 h	l-arginine	9.4	40	Selective	20 nM	16
8	1 h	alginate	10	30	Selective	2 μM	53
9	5 min	tripolyphosphate	Lower than 11.5		Selective	0.1 μM,	81
10	2 h	Sodium dodecyl sulfonate	3–11	14	Selective	0.02 μM	This work

Table 2. Comparison of colorimetric sensing probe for Cr^{2+}detection.

No	Time of preparation (hour)	Capping agents	pH range	Detection time	Selectivity	LOD (μM)	Ref
1	75	Rhodamine B, Umbelliferone	–	–	Selective	64	58
2	2	Sodium dodecyl sulfonate and β-cyclodextrin	3–11	4 min	Selective	0.01	This work

study, each of them has some limitations. For example, colorimetric sensors reported by Wu et al.[50] Chen et al.[49], He et al.[16] and Badri et al.[53] had a detection limitation with respect to pH conditions for Mn^{2+} ions. Compared with these reports for the colorimetric detection of Mn^{2+}, our method provided a good detection performance of Mn^{2+} for the pH range of 1 to 13. Moreover, according to Table 1, the sensors reported by Annadhasan et al.[52] and Vaibhavkumar et al.[51] suffered from selectivity limitations of detecting Mn^{2+} ions. Compared with these works, the sensors in our work are selective only for Mn^{2+} detection. In some studies reported by Wu et al.[50] and Vaibhavkumar et al,[51] the AgNPs sensor preparation process is complicated. Our approach to synthesize SDS-AgNPs is not time-consuming and costly. Table 2 summarizes information of Cr^{2+} detection method based on the colorimetric sensing probe. According to Table 2, our method provided a better sensing ability for detecting Cr^{2+} for the pH range of 1 to 13 and a good response rate. Compared to Rull-Barrull's work, our sensor has a higher sensitivity. As well as, in Rull-Barrull's study, the AgNPs sensor preparation process is complicated.[58]

4. Conclusion

In summary, two types of stable silver nanoparticles (AgNPs) were synthesized with SDS and a combination of SDS and CD, which were successfully utilized as a colorimetric sensor for Mn^{2+} and Cr^{2+} ions at ppm level, respectively. Upon adding desired ions, both AgNPs solutions changed from yellow to orange, which was detected by the naked eye and UV-vis spectroscopy. Indeed, the desired ions can be detected rapidly based on the color change of the system, due to the aggregation of Ag nanoparticles by adsorbing metal ions on their surface.

5. References

1. J. L. Aschner and M. Aschner, *Mol Aspects med* **2005**, *26*, 353–362. **DOI:**10.1016/j.mam.2005.07.003
2. R. T. Achmad and E. I. Auerkari, *Annu Rev Plant BioL.* **2017**, 1–8. **DOI:**10.9734/ARRB/2017/33462
3. M. Faisal and S. Hasnain, *J. Pharmacol. Toxicol* **2006**, *1*, 248–258.
4. S. L. O'Neal and W. Zheng, *Current environmental health reports* **2015**, *2*, 315–328. **DOI:**10.1007/s40572-015-0056-x
5. S. H. Frisbie, E. J. Mitchell, H. Dustin, D. M. Maynard and B. Sarkar, *Environ Health Perspect.* **2012**, *120*, 775–778. **DOI:**10.1289/ehp.1104693
6. M. Deveau, J Toxicol Environ *Health. Part A* **2010**, *73*, 235–241. **DOI:**10.1080/15287390903340880
7. J. Mao, Q. He and W. Liu, *Anal Bioanal Chem* **2010**, *396*, 1197–1203. **DOI:**10.1007/s00216-009-3161-6

8. K. Dutta, R. C. Deka and D. K. Das, *J. Fluoresc.* **2013**, *23*, 1173–1178. **DOI:**10.1007/s10895-013-1248-0
9. U. Divrikli, M. Soylak and L. Elci, *Environ Monit Assess.* **2008**, *138*, 167–172. **DOI:**10.1007/s10661-007-9754-7
10. V. Doroschuk, S. Lelyushok, V. Ishchenko and S. Kulichenko, *Talanta* **2004**, *64*, 853–856. **DOI:**10.1016/j.talanta.2004.03.056
11. W. Zhou, B.-C. Yin and B.-C. Ye, *Biosens Bioelectron* **2017**, *87*, 187–194.
12. A. Ramesh, B. A. Devi, H. Hasegsawa, T. Maki and K. Ueda, *MicrocheM J.* **2007**, *86*, 124–130. **DOI:**10.1016/j.microc.2007.01.002
13. A. Milne, W. Landing, M. Bizimis and P. Morton, *Anal. Chim. Acta* **2010**, *665*, 200–207. **DOI:**10.1016/j.aca.2010.03.027
14. H. Gürleyük and D. Wallschläger, *J. Anal. At. Spectrom.* **2001**, *16*, 926–930. **DOI:**10.1039/B102740A
15. E. Grygo-Szymanko, A. Tobiasz, N. Miliszkiewicz, D. Dudek-Adamska and S. Walas, *Analytical Letters* **2017**, *50*, 2147–2160. **DOI:**10.1080/00032719.2016.1267185
16. Y. He and X. Zhang, *Sensors and Actuators B: Chemical* **2016**, *222*, 320–324. **DOI:**10.1016/j.snb.2015.08.089
17. Y.-X. Qi, Z.-b. Qu, Q.-X. Wang, M. Zhang and G. Shi, *Anal. Chim. Acta* **2017**, *980*, 65–71. **DOI:**10.1016/j.aca.2017.05.018
18. Y. Zhao and Z. Zhong, *J. Am.Chem. Soc* **2006**, *128*, 9988–9989. **DOI:**10.1021/ja062001i
19. X. Liu, Y. Tang, L. Wang, J. Zhang, S. Song, C. Fan and S. Wang, *Advanced Materials* **2007**, *19*, 1471–1474. **DOI:**10.1002/adma.200602578
20. I.-B. Kim and U. H. Bunz, *J. Am.Chem. Soc* **2006**, *128*, 2818–2819. **DOI:**10.1021/ja058431a
21. X. Xu, J. Wang, K. Jiao and X. Yang, *Biosensors and Bioelectronics* **2009**, *24*, 3153–3158. **DOI:**10.1016/j.bios.2009.03.025
22. D. Zhang, M. Deng, L. Xu, Y. Zhou, J. Yuwen and X. Zhou, *Chemistry–A European Journal* **2009**, *15*, 8117–8120. **DOI:**10.1002/chem.200901268
23. M. Hollenstein, C. Hipolito, C. Lam, D. Dietrich and D. M. Perrin, *Angewandte Chemie International Edition* **2008**, *47*, 4346–4350. **DOI:**10.1002/anie.200800960
24. M. Rex, F. E. Hernandez and A. D. Campiglia, *Anal Lett.* **2006**, *78*, 445–451. **DOI:**10.1021/ac051166r
25. Y.-R. Kim, R. K. Mahajan, J. S. Kim and H. Kim, *ACS Appl Mater Inter.* **2009**, *2*, 292–295. **DOI:**10.1021/am9006963
26. P. Vasileva, T. Alexandrova and I. Karadjova, *J Chem* **2017**, *2017*. **DOI:**10.1155/2017/6897960
27. S. S. J. Xavier, G. Siva, J. Annaraj, A. R. Kim and D. J. Yoo, *Sens Actuators B Chem* **2018**, *259*, 1133–1143. **DOI:**10.1016/j.snb.2017.12.046
28. K. Ramachandran and K. J. Babu, *Sci Rep* **2016**, *6*, 36583. **DOI:**10.1038/srep36583
29. K. J. Babu, N. Senthilkumar and A. R. Kim, *Sens Actuators B Chem* **2017**, *241*, 541–551. **DOI:**10.1016/j.snb.2016.10.069
30. P. Wuamprakhon, A. Krittayavathananon, N. Ma, N. Phattharasupakun, T. Maihom, J. Limtrakul and M. Sawangphruk, *J Electroanal Chem.* **2018**, *808*, 124–132. **DOI:**10.1016/j.jelechem.2017.12.003
31. K. J. Babu, D. J. Yoo and A. R. Kim, *RSC Adv.* **2015**, *5*, 41457–41467. **DOI:**10.1039/C5RA03305E
32. K. J. Babu, T. Raj Kumar, D. J. Yoo, S.-M. Phang and G. Gnana kumar, *ACS Sustain Chem Eng.* **2018**, *6*, 16982–16989. **DOI:**10.1021/acssuschemeng.8b04340
33. C. Burda, X. Chen, R. Narayanan and M. A. El-Sayed, *Chem Rev.* **2005**, *105*, 1025–1102. **DOI:**10.1021/cr030063a
34. R. Shukla, V. Bansal, M. Chaudhary, A. Basu, R. R. Bhonde and M. Sastry, *Langmuir* **2005**, *21*, 10644–10654. **DOI:**10.1021/la0513712
35. V. V. Kumar and S. P. Anthony, *Sens Actuators B Chem* **2014**, *191*, 31–36. **DOI:**10.1016/j.snb.2013.09.089
36. W. Leesutthiphonchai, W. Dungchai, W. Siangproh, N. Ngamrojnavanich and O. Chailapakul, *Talanta* **2011**, *85*, 870–876. **DOI:**10.1016/j.talanta.2011.04.041
37. T. Kim, C.-H. Lee, S.-W. Joo and K. Lee, *J colloid interf sci* **2008**, *318*, 238–243. **DOI:**10.1016/j.jcis.2007.10.029
38. L. Wei, Z. Yuping, C. Chengxing, C. Wentao, L. Runqiang and Q. Lingbo: 2011 Third International Conference on Measuring Technology and Mechatronics Automation, IEEE, 2011, pp. 1013–1016.
39. K. Aslan, J. R. Lakowicz and C. D. Geddes, *Anal. Biochem.* **2004**, *330*, 145–155. **DOI:**10.1016/j.ab.2004.03.032
40. B. Paul and A. Tiwari, *IOSR J. Environ. Sci. Toxicol. Food Technol.(Iosr-Jestft)* **2015**, *1*, 1–7.
41. E. Priyadarshini and N. Pradhan, *Sens Actuators B Chem* **2017**, *238*, 888–902. **DOI:**10.1016/j.snb.2016.06.081
42. B. A. Makwana, D. J. Vyas, K. D. Bhatt, S. Darji and V. K. Jain, *Appl. Nanosci.* **2016**, *6*, 555–566. **DOI:**10.1007/s13204-015-0459-x
43. H. Li, Z. Cui and C. Han, *Sens Actuators B Chem* **2009**, *143*, 87–92. **DOI:**10.1016/j.snb.2009.09.013
44. R. Rajamanikandan and M. Ilanchelian, *Mater Today Commun.* **2018**, *15*, 61–69. **DOI:**10.1016/j.mtcomm.2018.02.024
45. H. K. Sung, S. Y. Oh, C. Park and Y. Kim, *Langmuir* **2013**, *29*, 8978–8982. **DOI:**10.1021/la401408f
46. Y.-r. Ma, H.-y. Niu and Y.-q. Cai, *Chem Comm* **2011**, *47*, 12643–12645. **DOI:**10.1039/c1cc15048k
47. C. J. Kirubaharan, D. Kalpana, Y. S. Lee, A. Kim, D. J. Yoo, K. S. Nahm and G. G. Kumar, *Ind Eng Chem Res.* **2012**, *51*, 7441–7446. **DOI:**10.1021/ie3003232
48. X. Gao, Y. Lu, S. He, X. Li and W. Chen, *Anal. Chim. Acta* **2015**, *879*, 118–125. **DOI:**10.1016/j.aca.2015.04.002
49. L. Chen, Y. Ye, H. Tan and Y. Wang, *Colloid Surface A.* **2015**, *478*, 1–6.
50. G. Wu, C. Dong, Y. Li, Z. Wang, Y. Gao, Z. Shen and A. Wu, *RSC Adv.* **2015**, *5*, 20595–20602. **DOI:**10.1039/C5RA00001G
51. V. N. Mehta, J. V. Rohit and S. K. Kailasa, *New J Chem.* **2016**, *40*, 4566–4574. **DOI:**10.1039/C5NJ03454J

52. M. Annadhasan, T. Muthukumarasamyvel, V. Sankar Babu and N. Rajendiran, *ACS Sustain Chem Eng.* **2014**, *2*, 887–896. **DOI:**10.1021/sc400500z
53. K. B. Narayanan and S. S. Han, *Res Chem Intermediat.* **2017**, *43*, 5665–5674. **DOI:**10.1007/s11164-017-2954-z
54. A. Ravindran, M. Elavarasi, T. Prathna, A. M. Raichur, N. Chandrasekaran and A. Mukherjee, *Sensor Actuat B-Chem.* **2012**, *166*, 365–371. **DOI:**10.1016/j.snb.2012.02.073
55. A. Ravindran, V. Mani, N. Chandrasekaran and A. Mukherjee, *Talanta* **2011**, *85*, 533–540. **DOI:**10.1016/j.talanta.2011.04.031
56. M. Elavarasi, A. Rajeshwari, S. A. Alex, D. N. Kumar, N. Chandrasekaran and A. Mukherjee, *Anal Methods.* **2014**, *6*, 5161–5167. **DOI:**10.1039/c4ay00877d
57. R. P. Modi, V. N. Mehta and S. K. Kailasa, *Sensor Actuat B-Chem.* **2014**, *195*, 562–571. **DOI:**10.1016/j.snb.2014.01.059
58. J. Rull-Barrull, M. d'Halluin, E. Le Grognec and F.-X. Felpin, *Tetrahedron Lett.* **2017**, *58*, 505–508. **DOI:**10.1016/j.tetlet.2016.12.038
59. J. K. Patra and K.-H. Baek, *J. Nanomater.* **2014**, *2014*, 219. **DOI:**10.1155/2014/417305
60. S. Agnihotri, S. Mukherji and S. Mukherji, *RSC Adv.* **2014**, *4*, 3974–3983. **DOI:**10.1039/C3RA44507K
61. G. Mie, *Ann. Phys* **1908**, *25*, 377–442. **DOI:**10.1002/andp.19083300302
62. H. Wang, Y. Wang, J. Jin and R. Yang, *Anal. Chem.* **2008**, *80*, 9021–9028. **DOI:**10.1021/ac801382k
63. E.-J. Bae, H.-J. Park, J.-S. Park, J.-Y. Yoon, Y.-H. Kim, K.-H. Choi and J.-H. Yi, *Bull. Korean Chem. Soc.* **2011**, *32*, 613–619. **DOI:**10.5012/bkcs.2011.32.2.613
64. H. Zhang and C. Zhang, *J. Mater. Environ. Sci.* **2014**, *5*, 231–236.
65. Z. Li, H. Li, C. Wang, J. Xu, V. Singh, D. Chen and J. Zhang, *Acta Pharm. Sin. B.* **2016**, *6*, 344–351. **DOI:**10.1016/j.apsb.2016.03.003
66. E. Gaidamauskas, E. Norkus, E. Butkus, D. C. Crans and G. Grincienė, *Carbohydr. Res.* **2009**, *344*, 250–254. **DOI:**10.1016/j.carres.2008.10.025
67. I. Niskanen, V. Forsberg, D. Zakrisson, S. Reza, M. Hummelgård, B. Andres, I. Fedorov, T. Suopajärvi, H. Liimatainen and G. Thungström, *Chem. Eng. Sci.* **2019**, *201*, 222–229. **DOI:**10.1016/j.ces.2019.02.020
68. S. A. Ghoto, M. Y. Khuhawar and T. M. Jahangir, *Anal Sci* **2019**, 18P417.
69. C. Yuan, B. Liu and H. Liu, *Carbohydr. Polym.* **2015**, *118*, 36–40. **DOI:**10.1016/j.carbpol.2014.10.070
70. R. Azimpanah, Z. Solati and M. Hashemi, *Iet Nanobiotechnol.* **2018**, *12*, 673–677. **DOI:**10.1049/iet-nbt.2017.0236
71. A. Alam, A. Ravindran, P. Chandran and S. S. Khan, *Spectrochim Acta A Mol Biomol* Spectrosc. **2015**, *137*, 503–508. **DOI:**10.1016/j.saa.2014.09.004
72. B. Qiao, Y. Liang, T.-J. Wang and Y. Jiang, *Appl Surf Sci.* **2016**, *364*, 103–109. **DOI:**10.1016/j.apsusc.2015.12.116
73. V. Amendola, S. Polizzi and M. Meneghetti, *Langmuir* **2007**, *23*, 6766–6770. **DOI:**10.1021/la0637061
74. D. V. Leff, P. C. Ohara, J. R. Heath and W. M. Gelbart, *Am. J. Phys. Chem.* **1995**, *99*, 7036–7041. **DOI:**10.1021/j100018a041
75. G. Mie, *Ann. Phys* **1908**, *25*, 377–442. **DOI:**10.1002/andp.19083300302
76. B. Molleman and T. Hiemstra, *Environ. Sci. Nano* **2017**, *4*, 1314–1327. **DOI:**10.1039/C6EN00564K
77. A. López-Miranda, A. López-Valdivieso and G. Viramontes-Gamboa, *J Nanopart Res.* **2012**, *14*, 1101. **DOI:**10.1007/s11051-012-1101-4
78. S. S. J. Xavier, C. Karthikeyan, A. R. Kim and D. J. Yoo, *Anal Methods.* **2014**, *6*, 8165–8172. **DOI:**10.1039/C4AY01183J
79. Q. Ma, J. Song, S. Zhang, M. Wang, Y. Guo and C. Dong, *Colloids Surf B Biointerfaces* **2016**, *148*, 66–72. **DOI:**10.1016/j.colsurfb.2016.08.040
80. R. Hu, L. Zhang and H. Li, *New J Chem* **2014**, *38*, 2237–2240. **DOI:**10.1039/C3NJ01593A
81. Y.-X. Gao, J.-W. Xin, Z.-Y. Shen, W. Pan, X. Li and A.-G. Wu, *Sens Actuators B Chem* **2013**, *181*, 288–293. **DOI:**10.1016/j.snb.2013.01.079

Povzetek

V študiji smo razvili preprosto, hitro, občutljivo, selektivno in poceni kolorimetrično metodo za določanje magnezijevih (Mn^{2+}) in kromovih (Cr^{2+}) ionov v vodnih raztopinah. Natrijev dodecil sulfat (SDS) in β-ciklodekstrin (CD) sta bila uporabljena kot stabilizatorja in površinsko aktivni snovi za sintezo srebrovih nanodelcev (AgNPs). Sintetizirane AgNPs smo okarakterizirali s FT-IR spektroskopijo, UV-vis spektroskopijo, vrstično elektronsko mikroskopijo (SEM) in dinamičnim sipanjem svetlobe (DLS). Preučili smo tudi vpliv pH vrednosti na stabilnost AgNPs. Srebrovi nanodelci modificirani z SDS (SDS-AgNPs) in z SDS ter β-ciklodekstrinom (SDS-CD-AgNPs) izkazujejo občutljivost in so uporabni za kolorimetrično detekcijo Mn^{2+} in Cr^{2+} ionov v ppm koncentracijah. SDS-AgNPs in SDS-CD-AgNPs povzročijo barvno spremembo vidno s prostim očesom iz rumene v oranžno po dodatku Mn^{2+} in Cr^{2+} ionov medtem ko ostali ioni tega ne povzročijo. Rezultati SEM in DLS kažejo, da dodatek Mn^{2+} ali Cr^{2+} ionov povzroči agregacijo delcev. Tekom študije smo tako uspeli sintetizirati AgNPs, SDS-AgNPs in SDS-CD-AgNPs, ki lahko služijo kot preprost, hiter, občutljiv in selektivni kolorimetrični senzor z znatnim potencialom za hitro detekcijo Mn^{2+} in Cr^{2+} ionov na terenu.

Except when otherwise noted, articles in this journal are published under the terms and conditions of the Creative Commons Attribution 4.0 International License

Scientific paper

Synthesis and Characterization of Cross Linked Acetoguanamine Polymer Complexes: Investigation of their Thermal and Magnetic Properties

Gurkan Guney,[1] Saban Uysal[2,*] and Ziya Erdem Koc[3]

[1] *University of Karabuk, Institue of Natural and Applied Sciences, Department of Polymer Engineering, 78050 Karabuk, Turkey*

[2] *University of Karabuk, Faculty of Science, Department of Chemistry, 78050 Karabuk, Turkey*

[3] *University of Selcuk, Faculty of Science, Department of Chemistry, 42075 Konya, Turkey*

** Corresponding author: E-mail: sabanuysal@karabuk.edu.tr*
Tel +9 (0532) 303 30 35

Received: 09-12-2019

Abstract

In this study, 2,4-diamino-6-methyl-1,3,5-triazine (acetoguanamine) was used as the starting material. 2,4-diamino-6-methyl-1,3,5-triazine was boiled under reflux with glutaraldehyde and terephthaldehyde in acetonitrile. And, s-triazine-containing polymer ligands (IV and V) were obtained by these condensation reactions. These target s-triazin containing polymer ligands we obtained were analyzed by ^{1}H-NMR, FT-IR and elemental analysis. Then, polymeric metal (Co^{2+}, Ni^{2+} and Cu^{2+}) complexes of the polymeric ligands (VI-XI) were obtained from the interaction with $CoCl_2{\cdot}6H_2O$, $NiCl_2{\cdot}6H_2O$ and $CuCl_2{\cdot}2H_2O$ at 60 °C in ethyl alcohol. The structures of these complexes were also illuminated and elucidated using FT-IR, elemental analysis and magnetic susceptibility analysis. The polymerization degrees of the polymeric ligands were determined by the molecular weight determination study with the viscometer.

Keywords: Acetoguanamine; s-triazine; Schiff bases; cross-linked polymeric complexes; thermal decomposition; magnetic properties.

1. Introduction

In recent years, an important class of compounds consisting of substituted s-triazine derivatives has been a growing interest in the using of s-triazine derivatives in different fields.[1,2] The remarkable reactivity and unique structure of the s-triazine moiety attracted the researchers to utilize it in the modification and construction of new materials.[3] s-Triazine based polymers have a high transparency and an enormous thermal and mechanical stability.[4,5] They have been widely used as matrixes for advanced composites or as resins in their own right for structural applications, especially for automotive, aerospace and microelectronic utilities.[6] Acetoguanamine (2,4-diamino-6-methyl-1,3,5-triazine) is one of the most widely used s-triazine derivatives, because it is a commercially available, inexpensive material and it has an excellent ability to undergoes nucleophilic substitution reaction under controlled temperature,[7,8] which allow it to be useful in many material and pharmaceutical,[9,10] and industrial applications.[11–13]

The design and synthesis of supramolecular polynuclear metal complexes have been an area of rapid growth for the past 20 years.[14] During the last decade, a remarkable development in the preparation of self-assembled architecture through metal ion coordination has been observed.[8] The motivation behind much of the studies related with polynuclear metal complexes has been provided by the prospect of producing a wide range of purpose-built materials with predetermined structures and potential applications in separation, gas storage, molecular recognition, and catalysis.[8,14,15] The preparation of polymetallic complexes can be achieved using rationally designed polydentate ligands.[16] On the other hand, it has been demonstrated that the 1,3,5-triazine ring is a suitable structural element to be incorporated into thermotropic liquid crystals.[17]

Schiff base chemistry, formed by the reversible condensation of amines and aldehydes has been made available in biomedicine as a result of its high efficiency and inoffensive by-product (only water).[18–20] The Schiff-base cross-linked injectable hydrogels were reported to have tunable gelation kinetics, biodegradability, and self-repair functions.[21–23]

We now report the synthesis and characterization of polymeric Schiff base including two imin groups as new templates. The condensation reaction of acetoguanamine (2,4-diamino-6-methyl-1,3,5-triazine) with glutaraldehyde and terephthaldehyde in acetonitrile gave the desired polynuclear metal complexes moieties in a single step.[24] The NH_2 groups were then modified with dimeric acetoguanamine (2,4-diamino-6-methyl-1,3,5-triazine) as a single-directional linker,[6–10] followed by treatment with Co(II), Ni(II) and Cu(II)[11–20] to give the mentioned new cross linked polymeric Schiff bases metal complexes IV and V.

2. Experimental

2. 1. Reagents and Solvents

Both of solvents (acetonitrile and ethanol), acetoguanamine (**1**), glutaraldehyde, tereftaldehyde and *o*-phenylenediamine, acetic acid, $CoCl_2 \cdot 6H_2O$, $NiCl_2 \cdot 6H_2O$, $CuCl_2 \cdot 2H_2O$ and sodium hydroxide were bought from Sigma and they were used without further purification. The ^{1}H NMR spectra of the polymers were taken with an Agilent NMR VNMRS spectrometer at 400 MHz, through their dimethyl sulfoxide (DMSO-d_6) solutions. The internal standard of the NMR measurements was tetramethylsilane (TMS). FT-IR spectra were taken by Perkin Elmer 1600 Spectrum 100 ATR Polarization (4000–440 cm^{-1}). Thermogravimetric Analysis (TGA) were performed using Hitachi STA7300 instrument. Elemental analyses were realized on a Leco 932 CHNS device where the results were in good harmony with the theoretical values. The metal contents of each complex were defined on a Varian, Vista AX CCD Simultaneous model ICP-AES. The pH values of all solutions were measured from a Milwaukee Mi 150 pH meter. Magnetic moment values of the metal complexes were determined with a Sherwood Scientific MX Gouy magnetic susceptibility apparatus using the Gouy method with $Hg[Co(SCN)_4]$ as calibrant. The effective magnetic moments per metal atom, μ_{eff}, were calculated using the well-known formula $\mu_{eff} = 2.84\sqrt{X_M T}$ B.M., where χ_M is the molar susceptibility.

2. 2. Synthesis of Polymeric Ligands

2. 2. 1. Synthesis of IV

Acetoguanamine (0.125 g, 1.00 mmol) was solved in 25 mL acetonitrile under reflux for an hour. Equivalent amount of glutaraldehyde solution (%2) was added to this solution drop by drop. Then, 5-6 drops of acetic acid were dropped as catalyst. This mixture was boiled under reflux for 3 hrs. The resulting precipitate was filtered off and dried under vacuum at 60 °C.

^{1}H NMR (ppm) data for IV: 7.50 (2H, triplet), 2.40 (3H, singlet), 2.20–2.05 (6H, multiplet); FT-IR (cm^{-1}) data for **IV** = 2926, 2854 ($CH_{aliphatic}$), 1655 (CH=N), 1537 ($CH{=}N_{triazine}$).

2. 2. 2. Synthesis of V

Acetoguanamine (0.125 g, 1.00 mmol) was solved in 25 mL acetonitrile under reflux for an hour. Then, teraftalaldehyde (0,134 g, 1.00 mmol) was added to this solution portionwise. And then, 2 mL of acetic acid were dropped as catalyst. This mixture was boiled under reflux for 2 hrs. The resulting precipitate was filtered off and dried under vacuum at 60 °C.

^{1}H NMR (ppm) data for **V**: 8.80 (2H, singlet), 8.05–7.70 (4H, multiplet), 2.40 (3H, singlet); FT-IR (cm^{-1}) data for **V**: 1633 (CH=N), 1556 (CH=N triazine).

2. 3. Synthesis of Cross-Linked Polymeric Complexes (VI–XI)

IV or **V** (0.44 g or 0.51 g, 1.00 mmol) were solved in 50 mL of 0.1 M HCl solution. Then, equivalent amount of 0.001 M $CoCl_2{\cdot}6H_2O$, $NiCl_2{\cdot}6H_2O$, $CuCl_2{\cdot}2H_2O$ in ethanol were added to these solutions drop by drop. These mixtures were heated under reflux at 60 °C. Finally, the pH of the system was adjusted to around 6.00 with NaOH 5%. The resulting precipitate (the Co(II), Ni(II), Cu(II) cross-linked polymeric complexes of AGGA and AGTA) were filtered off and dried under vacuum at 60 °C.

FT-IR (cm^{-1}) data for **VI**: 2926, 2854 ($CH_{alifatic}$), 1662 (CH=N), 1545 ($CH{=}N_{triazine}$), 540 (Co-N); FT-IR (cm^{-1}) data for **VII**: 2926, 2854 ($CH_{alifatic}$), 1662 (CH=N), 1545 ($CH{=}N_{triazine}$), 541 (Ni-N); FT-IR (cm^{-1}) data for **VIII**: 2926, 2854 ($CH_{alifatic}$), 1662 (CH=N), 1545 ($CH{=}N_{triazine}$), 540 (Cu-N); FT-IR (cm^{-1}) data for **IX**: 1648 (CH=N), 1568 (CH=N triazine), 545 (Co-N); FT-IR (cm^{-1}) data for **X**: 1648 (CH=N), 1568 (CH=N triazine), 546 (Ni-N); FT-IR (cm^{-1}) data for **XI**: 1648 (CH=N), 1568 (CH=N triazine), 545 (Cu-N).

2. 4. Determination of The Average Molecular Weight of IV and V by Measuring Intrinsic Viscosity

In order to determine the average molecular weights of the IV and V polymers we synthesized here, we measured their solution viscosity using the Ostwald viscometer. The average molecular weight of polymeric ligands **IV** and **V** was then determined from the Mark Houwink's relation ($[\eta] = KM^{\alpha}$, where M is the molecular weight and $[\eta]$ is the intrinsic viscosity). The value of $[\eta]$ was deter-

mined by using the Huggins relationship $\eta_{sp}= [\eta]c + k'[\eta]^2c^2$ + (or $\eta_{sp}/c= [\eta] + k'[\eta]^2c$), where c is the concentration, η_{sp} is the specific viscosity $\eta_{sp} (= \eta_{rel} -1 = (\eta - \eta_0)/\eta_0)$, and $\eta_{rel} (= \eta/\eta_0 = t/t_0)$ is the relative viscosity that was obtained from the measured viscosities of solvent (η_0) and polymer solution (η); t and t_0 are flow times of the solution and the solvent. The specific viscosity is affected by the solution concentration and its dependence on c is given by the Huggins relation. The intrinsic viscosity [η] is determined by extrapolation of η_{sp}/c to $c = 0$. According to this, dilute solutions of IV and V were prepared at different concentrations in toluene at 30 °C. Intrinsic viscosity values obtained are [η] = 1.494 kg s m^{-1} (for **IV**), η = 1.985 kg s m^{-1} (for **V**).

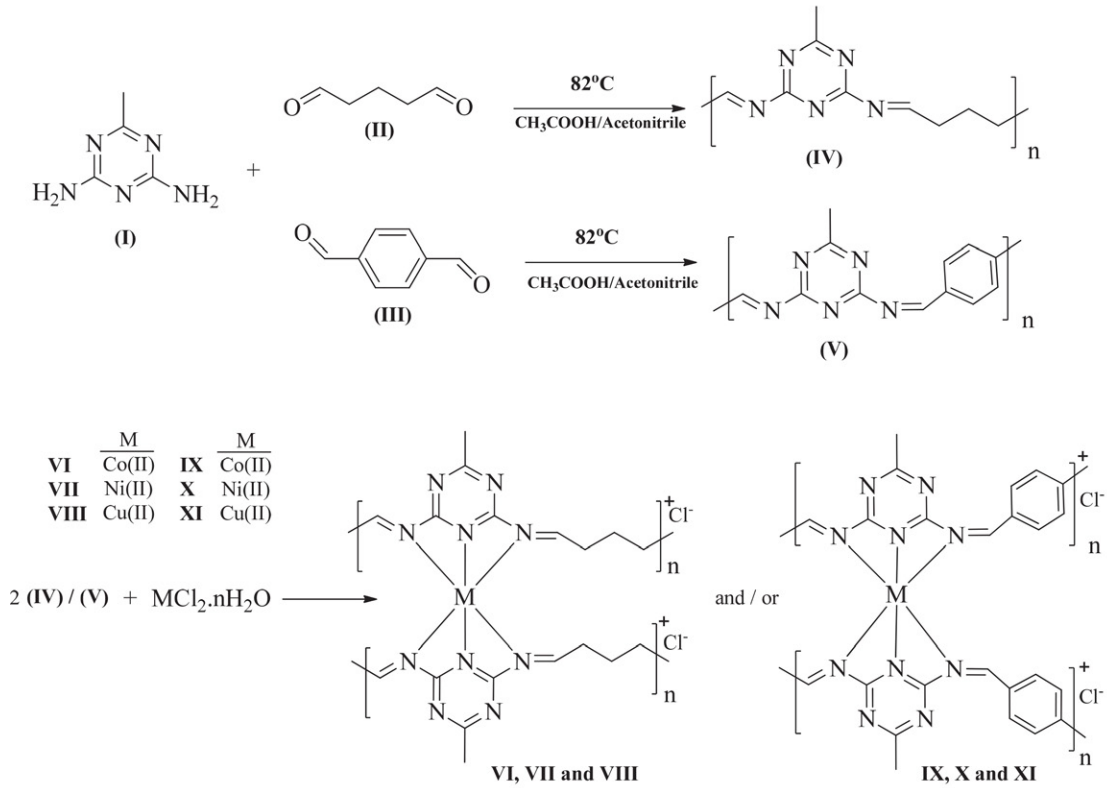

Scheme 1: The synthetic route of polymeric ligands and their cross linked polymeric complexes.

Table 1. The elemental analysis data and physical properties of all ligands and complexes.

[Empirical Formula] (Compound Codes)	μeff (B.M.) 296 K	M.P °C	Color	[Mw]	Yield %	Contents (%) Calculated/**Found** C	H	N	M**
$C_9H_{11}N_5$ (IV)	Dia	106	White	$[189]_n$	68	57.14	5.82	37.04	–
						56.70	**5.75**	**36.91**	
$C_{12}H_9N_5$ (V)	Dia	108	Yellow	$[223]_n$	65	64.57	4.04	31.39	–
						64.15	**3.85**	**29.13**	
$C_{18}H_{22}N_{10}CoCl_2$ (VI)	3.76	>400*	Orange	$[507.93]_n$	58	42.53	4.31	27.56	11.60
						41.78	**3.85**	**26.82**	**10.98**
$C_{18}H_{22}N_{10}NiCl_2$ (VII)	2.81	>400*	Brown	$[507.69]_n$	60	42.55	4.33	27.56	11.56
						41.90	**3.98**	**27.18**	**11.17**
$C_{18}H_{22}N_{10}CuCl_2$ (VIII)	1.76	>400*	Claret Red	$[512.55]_n$	55	42.14	4.29	27.31	12.40
						41.78	**3.82**	**27.06**	**12.02**
$C_{24}H_{18}N_{10}CoCl_2$ (IX)	3.75	>400*	Violet	$[575.93]_n$	62	50.01	3.13	24.31	10.23
						49.73	**2.97**	**24.11**	**10.01**
$C_{24}H_{18}N_{10}NiCl_2$ (X)	2.79	>400*	Dark Green	$[575.69]_n$	65	50.02	3.13	24.32	10.19
						49.55	**3.12**	**23.77**	**09.38**
$C_{24}H_{18}N_{10}CuCl_2$ (XI)	1.75	>400*	Light Green	$[580.55]_n$	67	49.61	3.10	24.12	10.95
						49.08	**3.04**	**24.01**	**10.16**

* Decomposition point, ** M = Co(II), Ni(II) ve Cu(II), μ_{eff} = Effective magnetic moment

3. Results and Discussions

In this study, 2,4-diamino-6-methyl-1,3,5-triazine (acetoguanamine) was used as the starting material. 2,4-diamino-6-methyl-1,3,5-triazine was boiled under reflux with glutaraldehyde and terephthaldehyde in acetonitrile using acetic acid as catalyst. And, s-triazine-containing polymer ligands codded as IV and V were obtained by these condensation reactions. These target s-triazin containing polymer ligands obtained were analyzed by ^{1}H NMR, FT-IR, TGA and elemental analysis. Then, polymeric metal (Co^{2+}, Ni^{2+} and Cu^{2+}) complexes of the polymeric ligands codded as (**VI**–**XI**) were obtained from the interaction with $CoCl_2 \cdot 6H_2O$, $NiCl_2 \cdot 6H_2O$ and $CuCl_2 \cdot 2H_2O$ at 60 °C in ethyl alcohol. The structures of these complexes were also illuminated and elucidated using FT-IR, elemental analysis, thermogravimetric analysis and magnetic susceptibility analysis. The polymerization degrees of the polymeric ligands were determined by the molecular weight determination study with the viscometer. Based on the elemental analysis, spectral studies and the coordination geometry has been assigned and is shown in Scheme 1 and Table 1.

3. 1. Interpretation of ^{1}H NMR Spectra

In the ^{1}H-NMR spectrum of the resulting s-triazine-containing polymer **IV**, the triplet for two protons at 7.50 ppm, the singlet for three protons at 2.40 ppm and the multiplet for six protons in the range of 2.20–2.05 ppm were observed and attributed to CH=N group, CH_3 group on triazine and aliphatic CH/CH_2 groups, respectively. As for the polymer **V**, the singlet for two protons at 8.80 ppm, the multiplet for four protons in the range of 8.05–7.70 ppm and the singlet for three protons at 2.40 ppm were observed and attributed to CH=N group, aromatic CH and CH_3 group on triazine, respectively. These peaks observed in the ^{1}H NMR spectra proved that both structures were successfully obtained.[25–28]

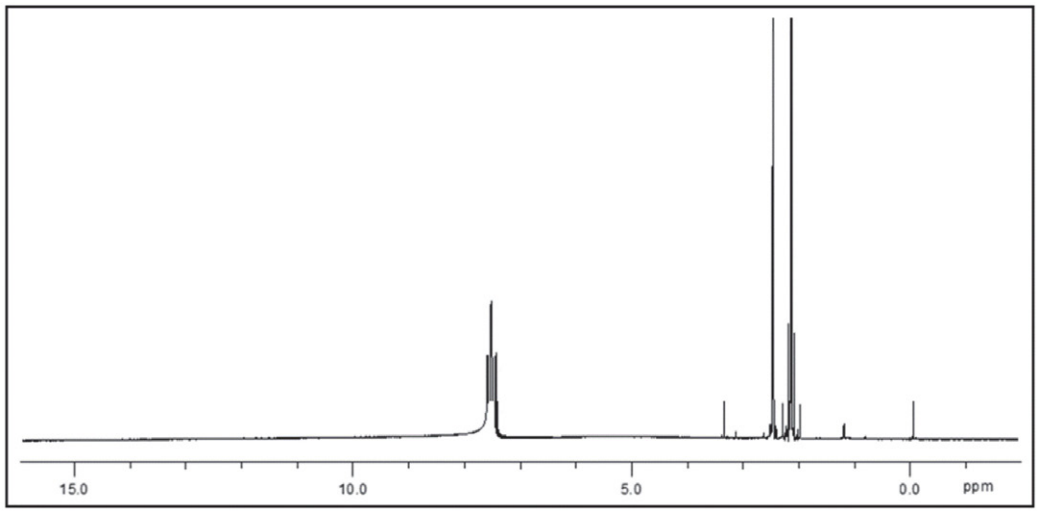

Figure 1. ^{1}H NMR spectrum of **IV**.

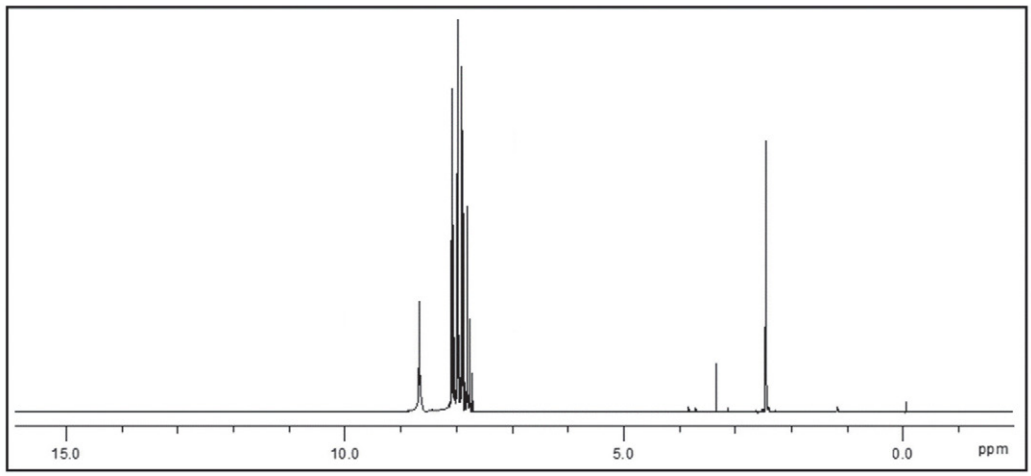

Figure 2. ^{1}H NMR spectrum of **V**.

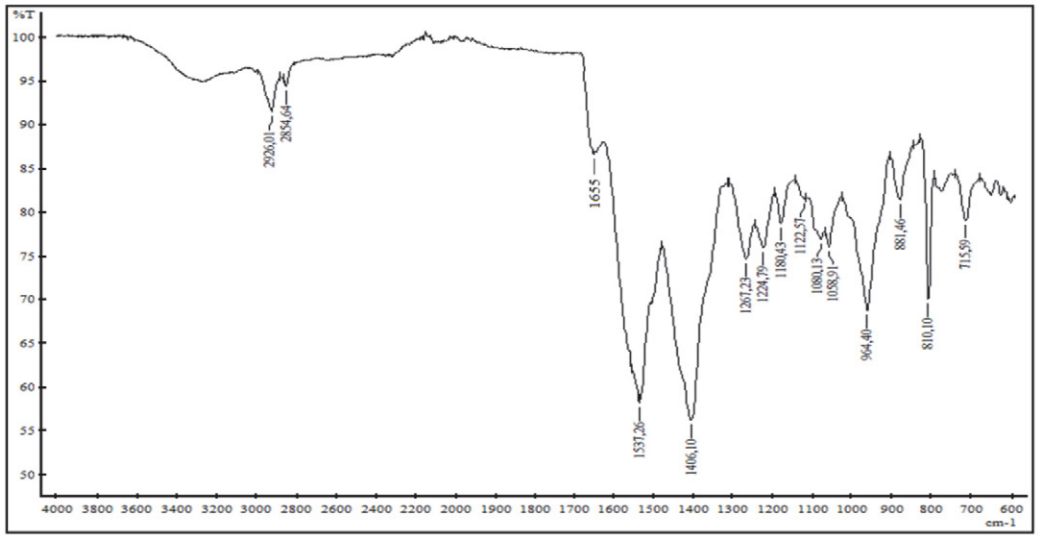

Figure 3: FT-IR spectrum of **IV**.

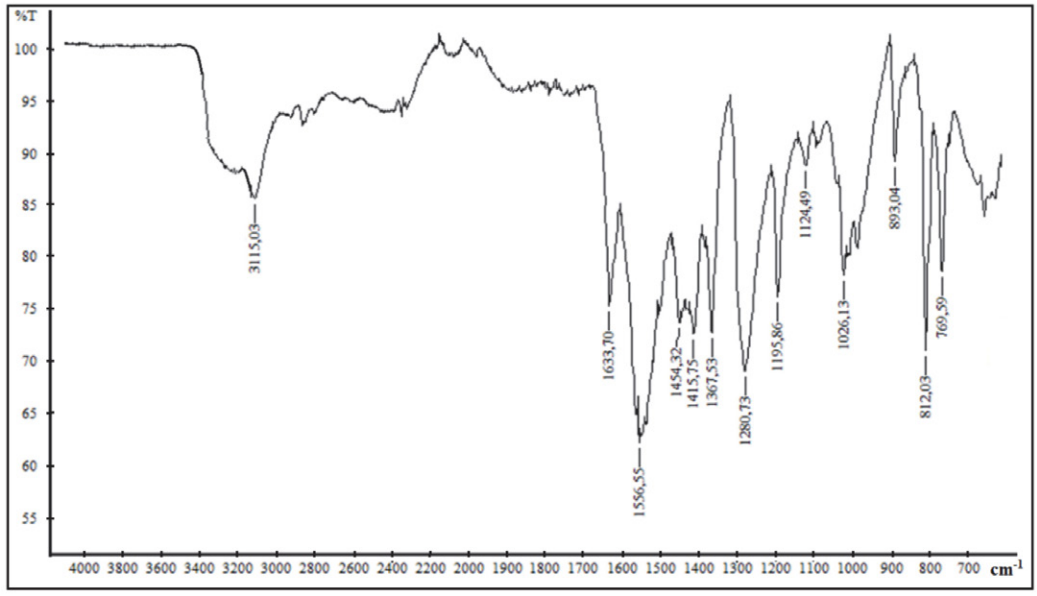

Figure 4: FT-IR spectrum of **V**.

3. 2. Interpretation of FT-IR Spectra

The FT-IR spectra of the polymer ligands and their complexes we synthesized were recorded and the bands we observed were summarized in the experimental section. Firstly, when we look at the FT-IR spectra of the polymer ligands we synthesized, C=N bands from the central s-triazine groups were observed at 1537 cm^{-1} and 1556 cm^{-1} for **IV** and **V**, respectively. Disappearance of N–H bending band at 3391 cm^{-1} and N-H bending band at 1510 cm^{-1} for acetoguanamine and instead, appearance of C=N stretching bands at 1655 cm^{-1} and 1633 cm^{-1} for **IV** and **V**, respectively, aliphatic C–H stretching bands at 2926 cm^{-1} and 2854 cm^{-1} for **IV** proves that glutaraldehyde and tereftalaldehyde linked to the s-triazine ring of acetoguanamine.[5,29,30]

Schiff base polymeric complexes were obtained from the reaction of polymer Schiff base ligands (**IV** and **V**) with metal salts of $CoCl_2{\cdot}6H_2O$, $NiCl_2{\cdot}6H_2O$ and $CuCl_2{\cdot}\ 2H_2O$ under reflux in ethanol. In order to study the binding mode of the ligand to the metal in complexes, the FT-IR spectrum of the free ligand was compared with the spectra of the metal(II) complexes. In the FT-IR spectra of the obtained complexes, bands of C=N Schiff base and s-triazine C=N groups were observed to shift to 12–15 cm^{-1} higher wave number after complex formation. The FT-IR spectra of the ligands show strong bands at 1537 cm^{-1} and 1556 cm^{-1} for **IV** and **V**, respectively assigned to C=N group of s-triazine. These bands are shifted to higher wave number in the spectra of all the complexes indicate the coordination of triazine ring nitrogen to the metal. In addition, M–N stretching bands

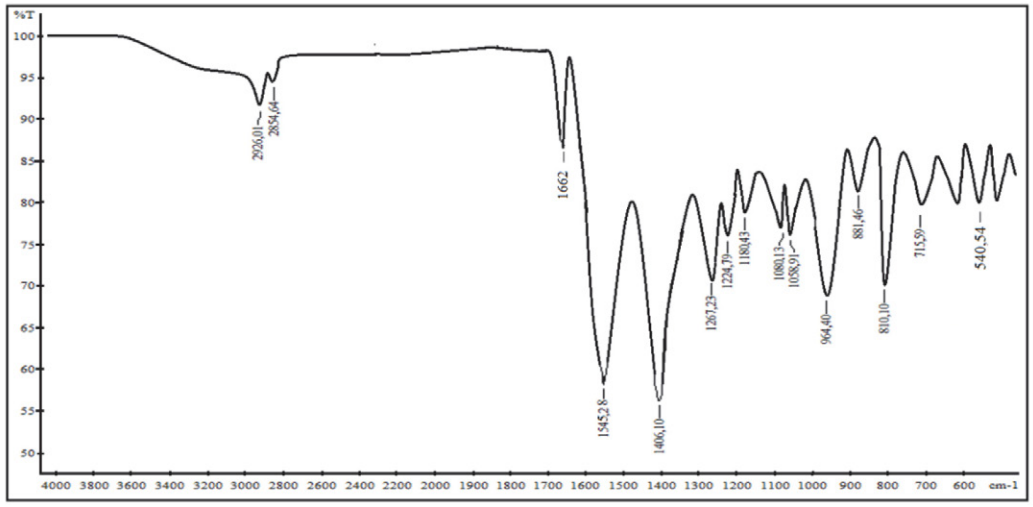

Figure 5. FT-IR spectrum of Co(II) cross polymer complex of **IV**.

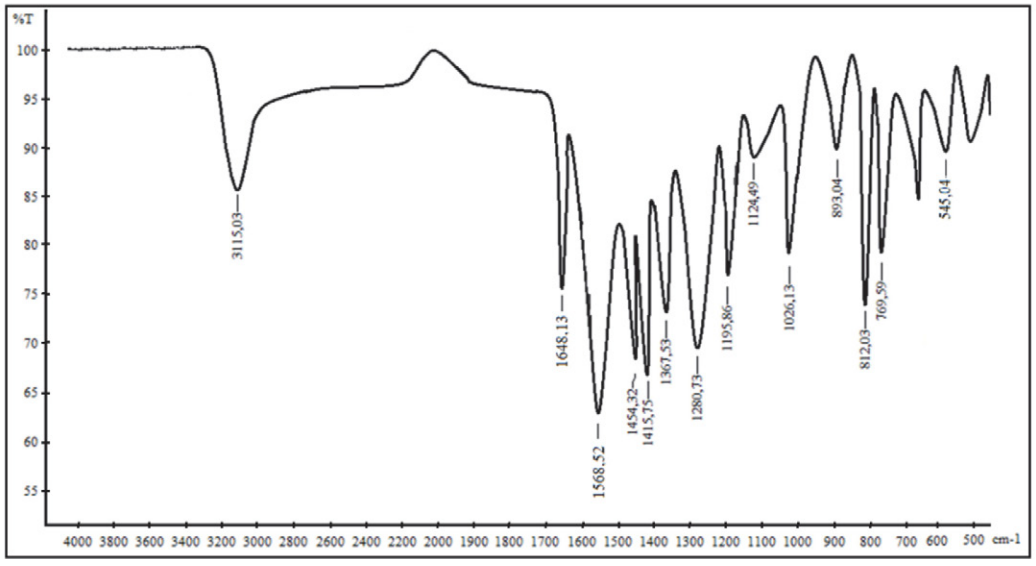

Figure 6: FT-IR spectrum of Co(II) cross polymer complex of **V**.

were observed at 540 cm^{-1} and 545 cm^{-1}, respectively.[5,28,29,31–34]

3. 3. Interpretation of Magnetic Data

In order to obtain information about the magnetic characters and geometries of s-triazine-containing polymeric complexes, effective magnetic moment (μ_{eff}) values were measured at 25 °C. μ_{eff} values of all complexes are given in Table 1. All polymeric complexes were determined as paramagnetic with d^7, d^7, d^8, d^8, d^9 and d^9 metal ions electron arrangement for VI-XI, respectively. Their effective magnetic moment (μ_{eff}) values were determined as follows: 3.76, 3.75, 2.81, 2.79, 1.76 and 1.75 B.M for each Co(II), Ni(II) and Cu(II) ions in $[(b_{2g})^2(e_g)^3(b_{1g})^1(a_{1g})^1]$, $[(b_{2g})^2(e_g)^4(b_{1g})^1(a_{1g})^1]$ and $[(b_{2g})^2(e_g)^4(b_{1g})^2(a_{1g})^1]$ electronic arrangement, respectively. The magnetic moments of the complexes are lower than the theoretical spin-only values for three, two and one unpaired electrons, respectively. According to our results, it was concluded that these complexes have distorted octahedral geometry (flat tetragonal distortion).[5,32,35–39] These results also support the proposed geometry. In other words, the fact that the s-triazine ring acts as a three-dentate ligand has forced geometry into distorted (flat tetragonal distortion) octahedral geometry. There are some examples in the literature supporting this geometry.[40,41]

3. 4. Interpretation of Thermal Analyses Curves

In order to determine the thermal behavior of the ligands and complexes we obtained, the ligands and complexes were heated in a nitrogen atmosphere at a temper-

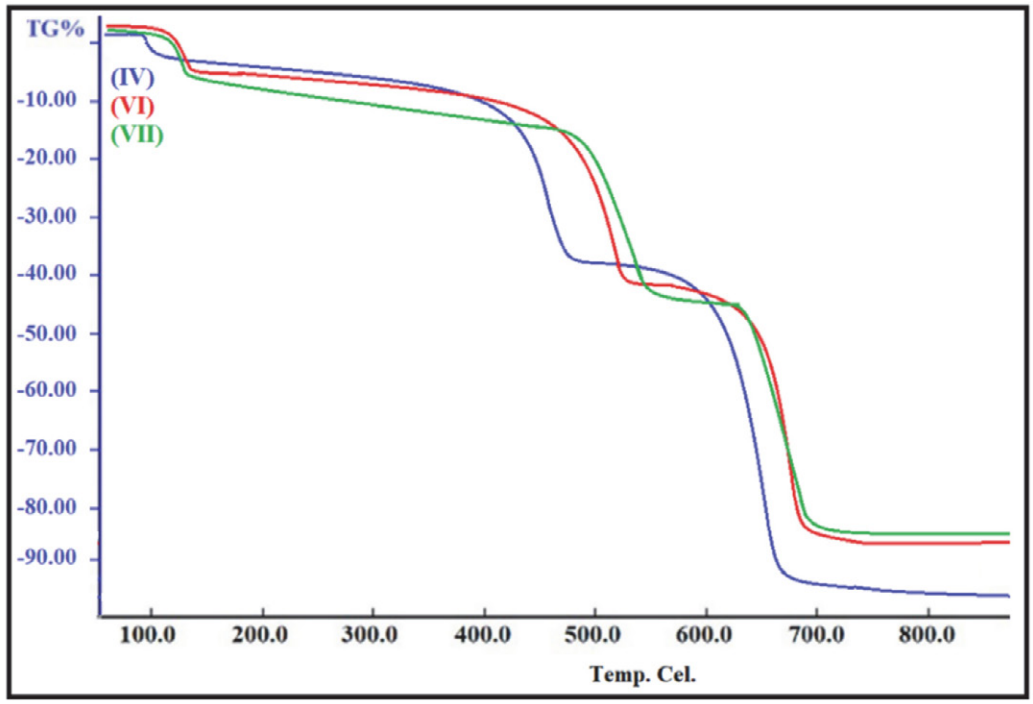

Figure 7. TGA curves of **IV**, **VI** and **VII**

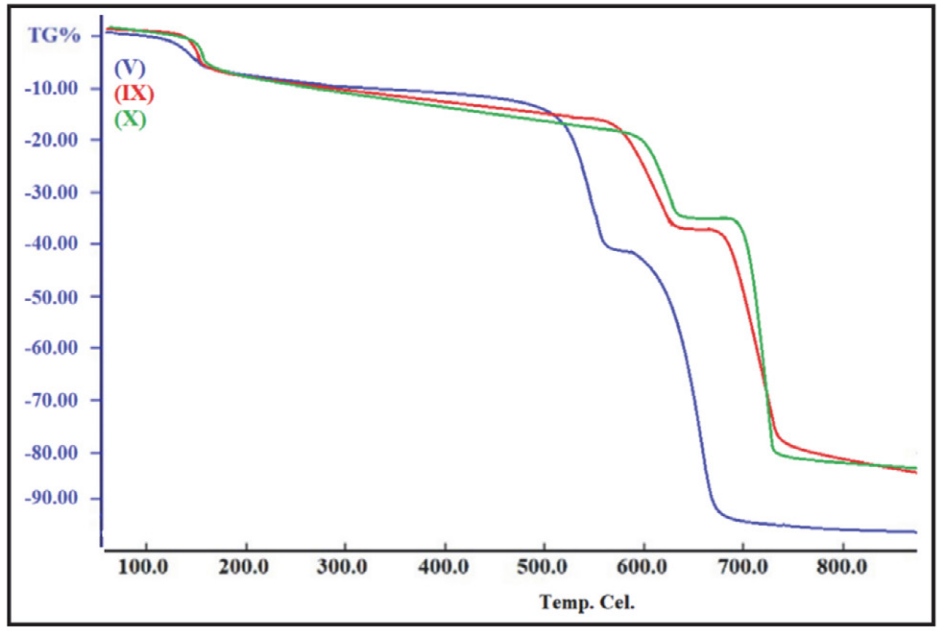

Figure 8. TGA curves of **V**, **IX** and **X**

ature of 50–1000 °C at a rate of 10 °C/min. When we interpret the TGA graphs obtained as a result of thermal analysis, we observed that the ligands and complexes decompose in two steps. However, we observed that the ligand **V** begins to decompose at a temperature of about 65 °C higher than the ligand **IV** that the main skeleton is degraded immediately after both ligands begin to decompose. The experimentally observed mass loss corresponds approximately to the mass of glutaraldehyde for the ligand **IV** and tereftaldehyde for the ligand **V**. After 5.5% moisture loss of the ligand **IV** in the temperature range of 90–105 °C, the weight loss in the first step began at 480 °C and was completed at 485 °C. The weight loss in this step is about 33%. After 4.5% moisture loss of the ligand **V** in the temperature range of 90–105 °C, the weight loss in the first step began at 545 °C and was completed at 550 °C. The weight loss in this step is about 40%. It was calculated that the weight losses in the last steps observed around

650 °C were equal to the mass of the remaining s-triazine ring.[5,42]

When we examined the TGA curves of the Co(II), Ni(II) and Cu(II) complexes of these ligands, we observed that the decomposition temperature shifted to about 40 °C higher. When we look at the rate of decomposition, we observed that there is not much difference compared to ligands. That is, while these polymeric complexes using metal ions as crosslinkers decompose, the 5-membered aliphatic chain from glutaraldehyde, and the aromatic ring from terephthaldehyde, which are the polymerizing groups, appear to decompose, firstly. It was calculated that the weight losses in the last steps observed in the temperature range of 680–720 °C were equal to the mass of the remaining s-triazine ring. The metal halide salts remain in the complexes without decomposition.[5,42]

3. 5. Interpretation of Average Molecular Weight of Polymer Ligands

The average molecular weights of the polymers **IV** and **V** were determined from the measured intrinsic viscosities: $\eta = 1.494$ kg s m^{-1} (for IV), $\eta = 1.985$ kg s m^{-1} (for V). Using the equation $\eta = KM\alpha$ (with polystyrene as standard,[5] $K = 1.7 \times 10^{-4}$ and $\alpha = 0.78$), the average molecular weights of these polymers are 9800 g/mol (IV) and 14200 g/mol (V). Using these data, it is concluded that these polymers consist of an average of 48 and 56 monomer units, respectively.[5,43,44] Because of the usage of polystyrene as standard, the actual molecular weight values might be slightly higher than observed. The reason of the detected values to be lower is the fact that the polymers have a spherical type structure, also supported by other studies.[5]

4. Conclusion

In this work, we synthesized two novel s-triazine-cored Schiff base polymeric ligands including acetoguanamine group and their six-novel cross-linked polynuclear complexes. These complexes are the first examples of these s-triazine-cored Schiff base polymeric complexes coordinated by imine groups to the Co(II), Ni(II) or Cu(II) centers. The magnetic data for the complexes show good harmony with the d^7 (S = 3/2) (for Co(II) complexes), the d^8 (S = 1) (for Ni(II) complexes) and d^9 (S = 1/2) (for both Cu(II) complexes) metal ion in distorted octahedral geometry (flat tetragonal distortion). When we interpret the TGA graphs obtained as a result of thermal analysis, we observed that the ligands and complexes decompose in two steps. It has been observed that these polymeric complexes are thermally stable complexes until 480 °C. According to the results of viscosity measurement, it can be concluded that polymeric ligands (**IV** and **V**) have average 48 and 56 monomer units, respectively.

Conflict of Interest

The authors declare that there is no conflict of interest related to this work.

5. Acknowledgement

We acknowledge that this study was financially supported by the Karabuk University Scientific Research Projects Coordinatorship (Project No: KBÜBAP-17-YL-036).

6. References

1. S. M. Osman, S. N. Khattab, E. A. Aly, E. Kenawy, A. El-Faham, *J. Polym. Res.* **2017**, *24*, 231–244. **DOI:**10.1007/s10965-017-1385-2
2. Z. E. Koc, H. Bingol, A. O. Saf, E. Torlak, A. Coskun, *J. Hazard. Mater.* **2010**, *183*, 251–255.
3. G. Blotny, *Tetrahedron* **2006**, *62*, 9507–9522. **DOI:**10.1016/j.tet.2006.07.039
4. S. Uysal, Z. E. Koc, S. Celikbilek, H. I. Ucan, *Synthetic Commun.* **2012**, *42*, 1033–1044. **DOI:**10.1080/00397911.2010.535635
5. S. Uysal, *J. Incl. Phenom. Macro.* **2013**, *76*, 223-230. **DOI:**10.1007/s10847-012-0194-9
6. G. P. Yu, C. Liu, J. Y. Wang, X. P. Li, X. G. Jian, *Polym. Degrad. Stabil.* **2010**, *95*, 2445–2452. **DOI:**10.1016/j.polymdegradstab.2010.08.011
7. A. El-Faham, S. M. Soliman, H. A. Ghabbour, Y. A. El-nakady, T. A. Mohaya, M. R. H. Siddiqui, F. Albericio, *J. Mol. Struct.* **2016**, *1125*, 121–135. **DOI:**10.1016/j.molstruc.2016.06.061
8. Z. E. Koc, *J. Heterocyclic Chem.* **2011**, *48*, 769–775. **DOI:**10.1002/jhet.577
9. M. Xie, W. Wei, Z. F. Jiang, Y. G. Xu, J. M. Xie, *Ceram. Int.* **2016**, *42*, 4158–4170. **DOI:**10.1016/j.ceramint.2015.11.089
10. H. S. Patel, S. N. Desai, *J. Polym. Mater*. **2008**, *25*, 519–527.
11. J. W. Grate, K. F. Mo, M. D. Daily, *Angew. Chem. Int. Ed.* **2016**, *55*, 3925–3930. **DOI:**10.1002/anie.201509864
12. C. A. Figg, T. Kubo, B. S. Sumerlin, *ACS Macro Lett.* **2015**, *4*, 1114–1118. **DOI:**10.1021/acsmacrolett.5b00634
13. J. F. Zhou, J. J. Wang, K. K. Jin, J. Sun, Q. Fang, *Polymer* **2016**, *102*, 301–307. **DOI:**10.1016/j.polymer.2016.09.027
14. P. Gamez, P. de Hoog, M. Lutz, A. L. Spek, J. Reedijk, *Inorg. Chim. Acta* **2003**, *351*, 319–325. **DOI:**10.1016/S0020-1693(03)00203-2
15. P. Gamez, P. de Hoog, M. Lutz, W. L. Driessen, A. L. Spek, J. Reedijk, *Polyhedron* **2003**, *22*, 205–210. **DOI:**10.1016/S0277-5387(02)01326-8
16. P. de Hoog, P. Gamez, W. L. Driessen, J. Reedijk, *Tetrahedron Lett.* **2002**, *43*, 6783–6786. **DOI:**10.1016/S0040-4039(02)01498-3
17. D. Goldmann, D. Janietz, C. Schmidt, J. H. Wendorff, *Liq. Cryst.* **1998**, *25*, 711–719. **DOI:**10.1080/026782998205723

18. M. E. Belowich, J. F. Stoddart, *Chem. Soc. Rev.* **2012**, *41*, 2003–2024. **DOI:**10.1039/c2cs15305j
19. C. D. Meyer, C. S. Joiner, J. F. Stoddart, *Chem. Soc. Rev.* **2007**, *36*, 1705–1723. **DOI:**10.1039/b513441m
20. Y. Xin, J. Y. Yuan, *Polym. Chem.* **2012**, *3*, 3045-3055. **DOI:**10.1039/c2py20290e
21. G. H. Deng, C. M. Tang, F. Y. Li, H. F. Jiang, Y. M. Chen, *Macromolecules* **2010**, *43*, 1191–1194. **DOI:**10.1021/ma9022197
22. F. Y. Liu, F. Y. Li, G. H. Deng, Y. M. Chen, B. Q. Zhang, J. Zhang, C. Y. Liu, *Macromolecules* **2012**, *45*, 1636–1645. **DOI:**10.1021/ma202461e
23. X. L. Wu, C. L. He, Y. D. Wu, X. S. Chen, *Biomaterials* **2016**, *75*, 148–162. **DOI:**10.1016/j.biomaterials.2015.10.016
24. S. Uysal, Z. E. Koc, *J. Mol. Struct.* **2016**, *1109*, 119–126. **DOI:**10.1016/j.molstruc.2015.12.080
25. Z. E. Koc, H. I. Ucan, *Transit. Metal. Chem.* **2007**, *32*, 597–602.
26. Z. E. Koc, S. Uysal, *Helv. Chim. Acta* **2010**, *93*, 910–919. **DOI:**10.1002/hlca.200900294
27. S. Uysal, Z. E. Koc, *J. Hazard. Mater.* **2010**, *175*, 532–539. **DOI:**10.1016/j.jhazmat.2009.10.038
28. B. Therrien, *J. Organomet. Chem.* **2011**, *696*, 637–651. **DOI:**10.3109/9781841848372-20
29. S. Uysal, H. I. Ucan, *J. Incl. Phenom. Macro.* **2010**, *68*, 165–173. **DOI:**10.1007/s10847-010-9762-z
30. I. T. Ahmed, A. A. A. Boraei, *Spectrosc. Lett.* **2005**, *38*, 47–59. **DOI:**10.1081/SL-200045464
31. R. Shanmugakala, P. Tharmaraj, C. D. Sheela, *J. Mol. Struct.* **2014**, *1076*, 606–613. **DOI:**10.1016/j.molstruc.2014.08.012
32. D. J. Reid, J. E. W. Cull, K. D. S. Chisholm, A. Langlois, P. H. Lin, J. Long, O. Lebel, I. Korobkov, R. Y. Wang, J. D. Wuest, M. Murugesu, J. Scott, *Dalton Trans.* **2011**, *40*, 5009–5017. **DOI:**10.1039/c1dt00018g
33. M. Shao, M. X. Li, Z. X. Wang, X. He, H. H. Zhang, *Cryst. Growth Des.* **2017**, *17*, 6281–6290. **DOI:**10.1021/acs.cgd.7b00967
34. Q. L. Zhu, C. B. Tian, C. J. Shen, T. L. Sheng, S. M. Hu, X. T. Wu, *Crystengcomm* **2013**, *15*, 2120–2126. **DOI:**10.1039/c2ce26461g
35. B. Isci, S. Uysal, *J. Incl. Phenom. Macro.* **2018**, *92*, 281–299. **DOI:**10.1007/s10847-018-0844-7
36. N. K. Chaudhary, P. Mishra, *Bioinorg. Chem. Appl.* **2017**, Article ID 6927675, 1–13. **DOI:**10.1155/2017/6927675
37. F. Mendizabal, C. Olea-Azar, G. Zapata-Torres, F. Eisner, *J. Mol. Struc. Theochem* **2001**, *543*, 23–37. **DOI:**10.1016/S0166-1280(00)00828-9
38. R. A. Polunin, N. P. Burkovskaya, S. V. Kolotilov, M. A. Kiskin, A. S. Bogomyakov, S. A. Sotnik, I. L. Eremenko, *Russ. Chem. Bull.* **2014**, *63*, 252–266. **DOI:**10.1007/s11172-014-0421-1
39. R. A. Polunin, N. P. Burkovskaya, J. A. Satska, S. V. Kolotilov, M. A. Kiskin, G. G. Aleksandrov, O. Cador, L. Ouahab, I. L. Eremenko, V. V. Pavlishchuk, *Inorg. Chem.* **2015**, *54*, 5232–5238. **DOI:**10.1021/acs.inorgchem.5b00179
40. R. Shanmugakala, P. Tharmaraj, C. D. Sheela, N. Chidambaranathan, *Med. Chem. Res.* **2014**, *23*, 329–342. **DOI:**10.1007/s00044-013-0634-0
41. B. Kebede, N. Retta, V. J. T. Raju, Y. Chebude, *Transit. Metal Chem.* **2006**, *31*, 19–26. **DOI:**10.1007/s11243-005-6301-7
42. Z. E. Koc, S. Uysal, *J. Inorg. Organomet. Polym.* **2011**, *21*, 400–406.
43. C. Gao, D. Yan, *Prog. Polym. Sci.* **2004**, *29*, 183–275. **DOI:**10.1016/j.progpolymsci.2003.12.002
44. S. S. Mahapatra, N. Karak, *Polym. Degrad. Stabil.* **2007**, *92*, 947–955. **DOI:**10.1016/j.polymdegradstab.2007.03.012

Povzetek

2,4-diamino-6-metil-1,3,5-triazin (acetogvanamin) smo uporabili kot izhodno spojino. 2,4-diamino-6-metil-1,3,5-triazin smo refluktirali z glutaraldehidom in tereftalaldehidom v acetonitrilu. S to kondenzacijsko reakcijo smo pripravili polimerne ligande, ki vsebujejo s-triazin (**IV** in **V**). Te polimere smo analizirali z ^{1}H NMR, FT-IR in elementno analizo. V naslednji stopnji smo pripravili polimerne kovinske komplekse (Co^{2+}, Ni^{2+} in Cu^{2+}) (**VI**–**XI**) z reakcijo z $CoCl_2 \cdot 6H_2O$, $NiCl_2 \cdot 6H_2O$ in $CuCl_2 \cdot 2H_2O$ pri 60 °C v etanolu. Strukture teh polimerov smo določili z uporabo FT-IR, elementne analize in analize magnetne susceptibilnosti. Stopnjo polimerizacije polimernih ligandov smo določili z molekulsko maso določeno z viskozimetrijo.

Except when otherwise noted, articles in this journal are published under the terms and conditions of the Creative Commons Attribution 4.0 International License

DOI: 10.17344/acsi.2019.5571 *Acta Chim. Slov.* **2020,** *67,* 560–569
creative commons

Scientific paper

Synthesis and *in vitro* Anticancer Activity of Novel Heterocycles Utilizing Thiophene Incorporated Thioureido Substituent as Precursors

Marwa Abdel-Motaal,[1,2*] Asmaa L. Alanzy[2] and Medhat Asem[3]

[1] *Department of chemistry, College of Science, Qassim university, Buridah, Qassim, Saudi Arabia*

[2] *Department of Chemistry, Faculty of Science, Mansoura University, ET-35516 Mansoura, Egypt.*

[3] *PhD of biochemistry, Faculty of Science, Menoufia University, Menoufia, Egypt.*

* *Corresponding author: E-mail: dr_maroochem@yahoo.com*

Received: 09-15-2019

Abstract

Abstract: Ethyl 2-(3-allylthioureido)-4,5,6,7-tetrahydrobenzo[*b*]thiophene-3-carboxylate (**1**) was used as a building block for synthesis of new heterocycles. Pyrimidine and thiazole moieties were achieved upon condensation of compound **1** with various reagents such as chloroacetic acid, dietyl malonate, ninhydrin, 2,3-epoxy-2,3-dihydro-1,4-naphthoquinone, and hydrazine hydrate. The structures of the newly synthesized compounds were confirmed using spectral measurements. The prepared products were evaluated for their anticancer activity against colon HCT-116 human cancer cell line. Compounds **6**, **9**, **10a**, **11**, **12**, **15** have displayed potent activity.

Keywords: Tetrahydrobenzo[*b*]thiophene; thiourea substituent; heterocycles; anticancer activity

1. Introduction

Heterocyclic compounds containing thiophene ring have been widely reported to have numerous pharmaceutical importance. For example, such compounds exhibited anticancer,[1–4] antibacterial,[5] antifungal,[6] anti-inflammatory,[7] anti-ulcer,[8] anti-diabetic,[9] antileishmanial,[10] antimicrobial,[11,12] antitubercular,[13] COX-2 selective inhibition,[14] antiproliferative[15] activities. Thiophene derivatives were utilized as inhibitors for hepatitis C virus polymerase,[16] novel BACE1,[17] alkaline phosphatases,[18] and kinesin spindle protein[19] and they are more effective in the treatment of Alzheimer's disease.[20] Moreover, thiophene derivatives have acquired great importance in drug discovery studies[21–23] which are available in markets, such as methaphenilene that acts as antiallergic agent; tiagabine acts as anticonvulsant agent; Sertaconazole acts as anti-fungal drug and is available as a cream for treatment of skin infections, such as athlete's foot, and the important drug biotin which is used for treating the deficiency of biotin related to pregnancy. The interest in these heterocycles has been attributed to their promising utilization as dye-sensitized solar cells,[24] organic semiconductors,[25] potential light-emitting materials for OLEDs[26] and in textile dyeing.[27, 28] Accordingly, several methods for the synthesis of thiophene and related heterocycles earn great attention. Normally, the most important method for their preparation is Gewald method involving the reaction of an equimolar amount of elemental sulfur with α-methylene ketones and acetonitrile in a basic medium.[29,30] Polyfunctionalized thiophenes were synthesized via the multicomponent reactions from starting materials, such as β-ketodithioesters with cyclohexylisocyanide and α-haloketones.[31] Two-step synthesis of benzothiophene derivatives using iodocyclization followed by etherification reaction sequence has been reported.[32] On the other hand, incorporation of thiourea chain residues was used to obtain key intermediates necessary to produce important heterocyclic compounds.[33–35] It has been reported that compounds containing pyrimidine[36–37] and thiazole[38–39] moieties have potent anticancer activity. According to these facts, we decided to develop the synthesis of new heterocycles utilizing thiophene moiety bearing thioureido chain substituent as a building block and to characterize the prepared products by spectral and analytical techniques. The activity of the newly synthesized heterocyclic compounds against HCT-116 cell lines was tested.

2. Experimental

2. 1. General

Most reagents and chemicals were purchased, utilized without additional purification, and bought from Sigma-Aldrich. Melting points are uncorrected and an electrothermal apparatus was used for their measurements. The purity of reagents and reaction validation were checked by thin-layer chromatography (TLC) technique on silica gel plates and the spots were imagined under UV light (254 nm) using mobile phase (pethroleum ether - ethyl acetate). Infrared spectra were detected using KBr discs on Shimadzu FT-IR 8201 PC spectrophotometer. ^{1}H NMR and ^{13}C NMR spectra were recorded on a Bruker instrument at 850 MHz spectrometer using tetramethylsilane (TMS) as an internal standard in $CDCl_3$ or DMSO-d_6 as solvents; chemical shifts are expressed in δ (ppm); spectroscopic measurements were carried out in the Microanalysis unit at the Universities of Qassim and Abdul-Aziz (KSA). Mass spectra were recorded on a GCMS-QP1000 EX spectrometer at 70 eV. Anticancer analysis was performed at the National cancer institute (NCl), Cairo, Egypt. Starting materials were already prepared according to the reported method.[39]"

2. 2. Synthetic Procedures

Synthesis of 2-((3-Allyl-2-((3-(ethoxycarbonyl)-4,5,6,7-tetrahydrobenzo[*b*]thiophen-2-yl)imino)-2,3-dihydrothiazol-4-yl)oxy)acetic acid (4)

A mixture of substitueted thiourea **1** (5 mmol), monochloroacetic acid (5 mmol) and potassium hydroxide (5 mmol) in methanol (15 mL) was refluxed at water bath for 8 h. The mixture was left to cool and then poured into ice-water, then acidified with acetic acid. The precipitate that formed was filtered off and recrystallized from methanol to afford **4** as white crystals with yield 88%; mp 152–153 °C. IR (KBr) (ν_{max}, cm^{-1}): 1640, 1680 (2C=O). ^{1}H NMR ($CDCl_3$): δ 1.32 (t, 3H, CH_3), 1.75–1.79 (m, 4H, $2CH_2$), 2.61–2.76 (m, 4H, $2CH_2$), 3.77 (s, 2H, $\underline{CH_2}$-COOH), 3.89 (s, 2H, CH_2 allyl), 4.14 (s, 1H, =CH-S), 4.24 (q, 2H, CH_2), 4.80 (m, 1H, =CH trans allyl), 5.26–5.29 (m, 1H, =CH cis allyl), 5.92–5.98 (m, 1H, =$\underline{CH}$-CH_2 allyl), 11.94 (s, 1H, COOH).^{13}C NMR ($CHCl_3$): δ 14.32, 14.41, 22.86, 22.99, 23.73, 24.36, 26.38, 60.46, 111.27, 111.26, 126.65, 130.67, 147.65, 166.69, 166.91. MS: *m/z* (%) 422 (M^+, 5), 381 (M^+ – allyl, 20), 365 (100), 223 (60)."

Synthesis of Ethyl 2-(3-Allyl-5-benzylidene)-4-oxothiazolidin-2-ylidene)amino)-4,5,6,7-tetrahydrobenzo[*b*]thiophene-3-carboxylate (5)

To a solution of compound **1** (5 mmol), benzaldehyde (5 mmol) and monochloroacetic acid (5 mmol) in a mixture of acetic anhydride (5 mL) and acetic acid (15 mL), fused sodium acetate (5 mmol) was added. The reaction mixture was heated under reflux for 8 h. The mixture was cooled and poured onto crushed ice, the produced solid was filtered off and recrystallized from methanol to afford compound **5** as a yellow powder in yield 75%; mp 115 °C. IR (KBr) (ν_{max}, cm^{-1}): 1651, 1690 (2C=O). ^{1}H NMR ($CDCl_3$): δ 1.40 (t, 3H, CH_3), 1.76 (m, 4H, $2CH_2$), 2.63–2.75 (m, 2H, $2CH_2$), 5.70 (s, 2H, CH_2 allyl), 4.31 (q, 2H, CH_2), 5.20–5.39 (m, 1H, =CH trans allyl), 4.45–4.50 (m, 1H, =CH cis allyl), 5.92–5.99 (m, 1H, =$\underline{CH}$-CH_2 allyl), 7.29–7.51 (m, 6H, Ar-H).^{13}C NMR ($CDCl_3$): δ 14.3, 22.8, 24.4, 26.3, 34.5, 46.4, 52.9, 60.4, 112.3, 119.4, 130.12, 130.93, 131.2, 132.3, 134.5, 146.7, 151.8, 155.8, 161.6, 164.6, 166.2, 169.05, 171,01. MS: *m/z* (%) 453 (M^+, 3), 365 (M^+, 22), 268 (100)."

Synthesis of Ethyl 2-(3-Allyl-4,6-dioxo-2-thioxotetrahydropyrimidin-1(2*H*)-yl)-4,5,6,7-tetrahydrobenzo[*b*]thiophene-3-carboxylate (6)

A solution of compound **1** (2 mmol) and diethyl malonate in sodium ethoxide solution (2 mmol) in 15 mL of abs. ethanol was heated under reflux for 2 h. After cooling, the formed precipitate was filtered off and dissolved in water and then in ice bath neutralized with hydrochloric acid. The solid product was filtered off, washed with water, and recrystallized from ethanol to give **6** as a white precipitate with 85% yield; mp 215–218 °C. IR (KBr) (ν_{max}, cm^{-1}): 1640, 1701 (3C=O). ^{1}H NMR ($CDCl_3$): δ 1.25 (t, 3H, CH_3), 1.80–1.93 (m, 4H, $2CH_2$), 2.60–2.90 (m, 2H, $2CH_2$), 3.88 (s, 2H, CO-$\underline{CH_2}$-CO), 4.31 (q, 2H, CH_2), 5.17–5.27 (m, 1H, =CH trans allyl), 5.32–5.39 (m, 1H, =CH cis allyl), 5.78 (s, 2H, CH_2 allyl), 5.92–5.99 (m, 1H, =$\underline{CH}$-CH_2 allyl). ^{13}C NMR ($CHCl_3$): δ 14.32, 22.86, 22.99, 23.73, 24.36, 26.38, 60.46, 111.27, 126.65, 130.67, 147.65, 166.69, 166.91. MS: *m/z* (%) 392 (M^+, 4), 279 (80), 223 (100)."

General Procedure for the Synthesis of Compounds 7a, 7b and 8.

A mixture of compound **1** (2 mmol) and appropriate aromatic aldehyde, namely: furfural and benzaldehyde or isatin (2 mmol) was heated at reflux in EtOH (15 mL) containing a few drops of piperidine for 7 h. The solvent was evaporated till half of its volume. The solid that formed was filtered off and recrystallized from appropriate solvent to give the corresponding final products **7a, 7b** and **8**."

Ethyl 2-(3-Allyl-5-(furan-2-ylmethylene)-4,6-dioxo-2-thioxotetrahydropyrimidin-1(2*H*)-yl)-4,5,6, 7-tetrahydrobenzo[*b*]thiophene-3-carboxylate (7a)

Brown powder, yield 58%; mp155–156 °C (EtOH); IR (KBr) (ν_{max}, cm^{-1}): 1642, 1670 (2C=O). ^{1}H NMR ($CDCl_3$): δ 1.80 (m, 7H, CH_3, $2CH_2$), 2.68 (t, 2H, CH_2), 2.92 (t, 2H, CH_2), 3.90 (s, 2H, CH_2 allyl), 4.38 (q, 2H, CH_2), 5.24–5.28 (m, 1H, =CH trans allyl), 5.34–5.36 (m, 1H, =CH cis allyl), 5.96–6.013 (m, 1H, =$\underline{CH}$-CH_2 allyl), 7.01 (m,3H, H-Ar), 8.22 (s, 1H, CH=). ^{13}C NMR ($CHCl_3$): δ 21.8, 22.9, 24.6, 25.25, 48.24, 48.47, 117.04, 118.69, 129.02, 130.71, 131.6, 132.52, 137.9, 144.1, 147.75, 157.68,

159.96, 161.56, 173.88. MS: *m/z* (%) 476 (M^++5, 15), 289 (48), 210 (50), 139 (22), 86 (100)."

Ethyl 2-(3-Allyl-5-benzylidene-4,6-dioxo-2-thioxotetrahydropyrimidin-1(2*H*)-yl)-4,5,6,7-tetrahydrobenzo[*b*]thiophene-3-carboxylate (7b)

Yellow crystals; yield 66%; mp 205–208 °C (dil. EtOH), IR (KBr) (ν_{max}, cm^{-1}): 1640, 1710 (2C=O). ^{1}H NMR ($CDCl_3$): δ 0.86 (t, 3H, CH_3), 1.79–1.90 (m, 4H, $2CH_2$), 2.67 (t, 2H, CH_2), 2.91 (t, 2H, CH_2), 4.07 (q, 2H, CH_2), 4.16–4.30 (m, 1H, =CH trans allyl), 5.10 (s, 2H, CH_2 allyl), 5.20–5.35 (m, 1H, =CH cis allyl), 5.93–6.00 (m, 1H, =CH-CH_2 allyl), 7.40–7.80 (m, 5H, Ar-H), 8.10 (s, 1H). ^{13}C NMR ($CHCl_3$): δ 20.6, 22.09, 22.9, 24.6, 25.22, 29.7, 48.4, 117.04, 118.62, 128.4, 129.11, 130.7, 130.2, 131.17, 132.3,133.6, 136.4, 147.95, 156.58, 169.85, 173.83. MS: *m/z* (%) 481 (M^+, 3), 454 (M^+-CH=CH_2, 8), 275 (95), 68 (100), 324 (40)."

Ethyl 2-(3-Allyl-4,6-dioxo-5-(2-oxoindolin-3-ylidene)-2-thioxotetrahydropyrimidin-1(2*H*)-yl)-4,5,6,7-tetrahydrobenzo[*b*]thiophene-3-carboxylate (8)

Deep yellow powder; yield 55%; mp 170–173 °C (dil. EtOH); IR (KBr) (ν_{max}, cm^{-1}): 3234 (NH), 1655, 1645, 1634 (4C=O). ^{1}H NMR ($CDCl_3$): δ 1.20 (t, 3H, CH_3), 1.80 (m, 4H, $2CH_2$), 2.96 (t, 2H, CH_2), 2.73 (t, 2H, CH_2), 4.36 (q, 2H, CH_2), 4.40–4.70 (m, 1H, =CH trans allyl), 4.80 (s, 2H, CH_2 allyl), 5.09–5.34 (m, 1H, =CH cis allyl), 5.90–5.99 (m, 1H, =CH-CH_2 allyl), 6.90–7.60 (m, 4H, Ar-H), 8.10 (s, 1H, NH). ^{13}C NMR ($CHCl_3$): δ 112.25, 116.88, 118.39, 123.11 125.8, 128.7, 131.2, 132.5, 138.6, 144.12, 147.8, 149.09, 157.7, 158.9, 159.99,161.62, 174.15. MS: *m/z* (%) 521 (M^+, 20), 365 (30), 268 (100)."

Synthesis of Ethyl 2-(3-Allyl-4,6-dioxo-2-thioxo-5-((*para*-tolylamino)methyl)tetrahydropyrimidin-1(2*H*)-yl)-4,5,6,7-tetrahydrobenzo[*b*]thiophene-3-carboxylate (9)

A mixture of **6** (0.01 mol) and HCHO (2 mL) in EtOH (10 mL) was warmed for 10 min; after the addition of *para*-toluidine (0.01 mol), the mixture was refluxed for 3 h and cooled. The solid that formed was filtered off and then recrystallized from ethanol to give white crystals of **9** in 72% yield; mp 223–225 °C; IR (KBr) (ν_{max}, cm^{-1}): 1640, 1710 (2C=O). ^{1}H NMR ($CDCl_3$): δ 0.86 (t, 3H, CH_3), 1.79–1.90 (m, 4H, $2CH_2$), 2.67 (t, 2H, CH_2), 2.91 (t, 2H, CH_2), 4.07 (q, 2H, CH_2), 4.16–4.30 (m, 1H, =CH trans allyl), 5.10 (s, 2H, CH_2 allyl), 5.20–5.35 (m, 1H, =CH cis allyl), 5.93–6.00 (m, 1H, =CH-CH_2 allyl), 7.40–7.80 (m, 5H, Ar-H), 8.10 (s, 1H, NH).^{13}C NMR ($CHCl_3$): δ 13.98, 18.44, 21.9, 22.9, 24.68, 25.24, 25.48, 48.46, 85.54, 68.32, 117.06, 118.6, 129.08, 130.73, 132.47, 147.81, 156.53, 173.83. MS: *m/z* (%) 438 (M^+ – COOEt, 20), 263 (100), 278 (34)."

General Procedure for the Synthesis of Compounds 10a and 10b

A diazonium solution was prepared by dissolving (0.02 mol) of *para*-toluidine or 4-aminobenzophenone in 30 mL water and 6 mL concentrated HCl; this solution was cooled to 0 °C. The solution was then treated with 0.02 mol sodium nitrite in 20 mL of water, were added gradually with stirring for 30 min with cooling in an ice bath to complete the diazotization. The formed diazonium chloride was slowly added to compound **6** in pyridine with stirring at 0–5 °C for 2 h. The mixture was added with stirring to ice-cold water. The resulting solid was filtered off, dried and recrystallized from methanol."

Ethyl (*Z*)-2-(3-Allyl-4,6-dioxo-2-thioxo-5-(2-(*para*-tolyl)hydrazono)tetrahydropyrimidin-1(2*H*)-yl)-4,5,6,7-tetrahydrobenzo[*b*]thiophene-3-carboxylate (10a)

Reddish brown powder; yield 85%; mp 206–208 °C; IR (KBr) (ν_{max}, cm^{-1}): 3246 (NH), 1640 (C=O). ^{1}H NMR ($CDCl_3$): δ 1.20 (t, 3H, CH_3), 1.80 (m, 4H, $2CH_2$), 2.96 (t, 2H, CH_2), 2.73 (t, 2H, CH_2), 4.36 (q, 2H, CH_2), 4.40–4.70 (m, 1H, =CH trans allyl), 4.80 (s, 2H, CH_2 allyl), 5.09–5.34 (m, 1H, =CH cis allyl), 5.90–5.99 (m, 1H, =CH-CH_2 allyl), 6.90–7.60 (m, 4H, Ar-H), 8.10 (s, 1H, NH). ^{13}C NMR ($CHCl_3$): δ 21.95, 22.2, 22.9, 24.6, 29.71, 48.92, 62.2, 64.14, 77.04, 116.9, 118.3, 129.03, 129.56, 130.02, 130.4, 130.7, 131.18, 132.2, 135.56, 148.38, 156.7, 161.7, 171.5, 172.3, 173.9. MS: *m/z* (%) 521 (M^+, 20), 365 (30), 268 (100)."

Ethyl (*Z*)-2-(3-Allyl-5-(2-(4-benzoylphenyl)hydrazono)-4,6-dioxo-2-thioxotetrahydropyrimidin-1(2*H*)-yl)-4,5,6,7-tetrahydrobenzo[*b*]thiophene-3-carboxylate (10b)

Reddish brown powder; yield 82%; mp 160–161 °C; IR (KBr) (ν_{max}, cm^{-1}): 3247 (NH), 1716, 1639 (C=O). ^{1}H NMR ($CDCl_3$): δ 1.42 (t, 3H, CH_3), 1.76–1.82 (m, 4H, $2CH_2$), 2.63–2.90 (m, 4H, $2CH_2$), 4.43 (q, 2H, CH_2), 4.86 (s, 2H, CH_2 allyl), 5.079–5.22 (m, 1H, =CH trans allyl), 5.92–6.00 (m, 1H, =CH cis allyl), 5.20 (m, 1H, =CH-CH_2 allyl), 7.42–7.90 (m, 7H, Ar-H), 8.40 (s, 1H, Ar-H), 8.90 (s, 1H, Ar-H), 12.70 (s, 1H, broad NH). ^{13}C NMR ($CHCl_3$): δ 14.13, 22.2, 22.9, 25.4, 29.7, 62.03, 46.3, 118.16, 116.8, 126.9–134.69 (Ar-C), 163.4, 172.6, 173.79, 195.9, 196.8. MS: *m/z* (%) 600 (M^+, 13), 554 (10), 406 (8), 278 (34), 263 (100)."

Synthesis of Ethyl (*Z*)-2-((1-Allyl-4,5-dioxo-4,5-dihydronaphtho[1,2-*d*]thiazol-2(1*H*)-ylidene)amino)-4,5,6,7-tetrahydrobenzo[*b*]thiophene-3-carboxylate (12)

A mixture of compound **1** (0.01 mol) and 2,3-dihydro-2,3-epoxy-1,4-naphthoquinone (0.01 mol) in ethanol (20 mL) was refluxed for 5 h in water bath. After cooling, the precipitate that formed was isolated, dryed and then dissolved in 15 mL of water. The formed solution was neutralized with dil. HCl with stirring in ice bath. The resulted solid was filtered off and recrystallized from methanol to afford **12** as a reddish brown powder in 93% yield; mp 258–260 °C. IR (KBr) (ν_{max}, cm^{-1}): 1689, 1680, 1668 (3C=O). ^{1}H NMR ($CDCl_3$): δ 1.24 (t, 3H, CH_3), 1.20–1.30 (m, 4H, $2CH_2$), 1.60–1.70 (m, 4H, $2CH_2$), 4.27 (q, 2H,

CH_2), 4.12–4.25 (m, 1H, =CH trans allyl), 5.08–5.22 (m, 3H, =CH trans allyl, CH_2 allyl), 5.80–5.90 (m, 1H, =CH cis allyl), 7.80–8.50 (m, 4H, Ar-H). ^{13}C NMR ($CHCl_3$): δ 14.1, 22.4, 118.5, 125.9, 126.2, 125.4, 125.99, 126.24, 129.97, 130.6, 131.9, 133.62, 134.5, 134.64, 156.3, 178.7, 180.8, 181.3. MS: *m/z* (%) 478 (M^+, 4), 353 (20), 226 (100)."

Synthesis of Ethyl (*Z*)-2-((3-Allyl-3a,8a-dihydroxy-8-oxo-3,3a,8,8a-tetrahydro-2*H*-indeno[1,2-*d*]thiazol-2-ylidene)amino)-4,5,6,7-tetrahydrobenzo[*b*]thiophene-3-carboxylate (13)

A mixture of compound **1** (0.01 mol) and ninhydrin (0.01 mol) in AcOH (15 mL) was refluxed with stirring at 85 °C for 5 h. After cooling, the mixture was poured into cold water. The precipitate that formed was filtered off, dried and crystallized from ethanol to afford **13** as a reddish brown powder in 66% yield; mp 170–172 °C. IR (KBr) (ν_{max}, cm^{-1}): 1640, 1680 (2C=O). ^{1}H NMR ($CDCl_3$): δ 1.38 (t, 3H, CH_3), 1.81–1.86 (m, 4H, $2CH_2$), 2.70–2.73 (m, 4H, $2CH_2$), 4.34 (m, 1H, =CH-S), 4.39 (q, 2H, CH_2), 4.50–4.70 (m, 1H, =CH trans allyl), 5.17–5.30 (m, 1H, =CH cis allyl), 5.95–5.98 (m, 1H, =CH-CH_2 allyl), 7.50 (s, 2H, 2OH), 7.62–7.93 (m, 4H, Ar-H).^{13}C NMR ($CHCl_3$): δ11.45, 14.12, 22.4, 25.3, 26.2, 46.3, 62.52, 89.4, 93.01, 117.3, 125.01, 125.34, 126.46, 131.23, 131.55, 132.72, 136.6, 137.09, 137.63, 147.6, 166.2, 166.5, 180.4, 180.7, 193.2, 193.9. MS: *m/z* (%) 484 (M^+, 2), 322.9 (M^+, 58), 260 (13), 277 (100)."

Synthesis of 4-Allyl-1-phenyl-6,7,8,9-tetrahydrobenzo[4,5]thieno[3,2-*e*][1,2,4]triazolo[4,3-*a*]pyrimidin-5(4*H*)-one (14)

A mixture of compound **1** (0.01 mol) and the benzoyl hydrazide (0.01 mol) was heated under reflux for 12 h in ethanol (15 mL) in the presence of a few drops of AcOH. The mixture was left to cool. The precipitate that formed was filtered off and then recrystallized from EtOH to give **14** as white needles in 93% yield; mp 267–270 °C. IR (KBr) (ν_{max}, cm^{-1}): 1641, 1735 (2 C=O). ^{1}H NMR ($CDCl_3$): δ 1.79–1.87 (m, 4H, $2CH_2$), 2.68 (t, 2H, CH_2), 2.92 (t, 2H, CH_2), 4.80 (m, 2H, CH_2 allyl), 5.10 (m, 1H, =CH trans allyl), 5.24–5.36 (m, 1H, =CH cis allyl), 5.96–6.01 (m, 1H, =CH-CH_2 allyl), 7.20–7.80 (m, 5H, Ar-H). ^{13}C NMR ($CHCl_3$): δ 21.89, 22.9, 24.6, 25.25, 48.48, 117.03, 118.67, 125.8, 129.0, 130.72, 131.81, 132.52, 147.7, 156.5, 173.88. MS: *m/z* (%) 362 (M^+, 5), 324 (M^+, 22), 263 (92), 179 (100)."

Synthesis of 3-Allyl-2-mercapto-5,6,7,8-tetrahydrobenzo[4,5]thieno[2,3-*d*]pyrimidin-4(3*H*)-one (15)

A solution of compound **1** (0.01 mol) in DMF (15 mL) in the presence of KOH (0.01 mol) was stirred overnight. The mixture was poured onto crushed ice with stirring. The precipitate that formed was filtered off, dried and recrystallized from EtOH to give **15** as white crystals in 85% yield 85%; mp 235–236 °C."

Synthesis of *N*'-(3-Allyl-4-oxo-3,4,5,6,7,8-hexahydrobenzo[4,5]thieno[2,3-*d*]pyrimidin-2-yl)benzohydrazide (16)

Thienopyrimidine derivative **15** (0.01 mol) was heated under reflux with benzoyl hydrazide (0.01 mol) in ethanol for 28 h. After cooling, the resulted solid was isolated, dried and recrystallized from ethanol to afford **16** as white crystals in 65% yield; mp 177–178 °C. IR (KBr) (ν_{max}, cm^{-1}): 3251, 3397 (2NH), 1689, 1670, 1642 (4C=O). ^{1}H NMR ($CDCl_3$): δ 1.76–1.81 (m, 4H, $2CH_2$), 2.60–2.92 (m, 4H, $2CH_2$), 4.89 (m, 2H, CH_2 allyl), 4.08 (S,1H, NH), 5.10 (m, 1H, =CH trans allyl), 5.26–5.34 (m, 1H, =CH cis allyl), 5.96–6.01 (m, 1H, =CH-CH_2 allyl), 7.40–7.90 (m, 7H, Ar-H, NH_2). ^{13}C NMR ($CHCl_3$): δ 21.8, 22.9, 24.6, 48.2, 48.48, 117.05, 118.65, 129.02, 130.4, 130.7, 131.62, 132.31, 132.52, 137.92, 144.11, 147.75, 156.52, 157.68, 159.97, 161.56, 173.88. MS: *m/z* (%) 408 (M^++28, 0.18), 278 (30), 263 (100)."

General Method for Synthesis of 17 and 18

Compound **1** (0.01 mol) was mixed with hydrazine hydrate (0.015 mol) in ethanol (30 mL). The resulting solution was refluxed for 8 h. After cooling, the precipitate that formed was filtered off and crystallized to give **18** as bright white needles; yield 90%; mp 280–283 °C. The filtrate was evaporated till 10 mL and then was left overnight to cool. The formed solid was filtered off, dried and crystallized from EtOH to give **17** as white crystals; yield 82%; mp 198–199 °C (EtOH)."

3-Allyl-2-hydrazinyl-5,6,7,8-tetrahydrobenzo[4,5]thieno[2,3-*d*]pyrimidin-4(3*H*)-one (17)[43] and 3-Methyl-1,2,3,4,7,8,9,10-octahydro-6*H*-benzo[4',5']thieno[2',3':4,5]pyrimido[2,1-*c*][1,2,4]triazin-6-one (18)

IR (KBr) (ν_{max}, cm^{-1}): 3239 (NH), 1638 (C=O). ^{1}H NMR ($CDCl_3$): δ 1.02 (m, 2H, CH_2-3), 1.79–1.80 (m, 4H, $2CH_2$), 2.68 (t, 2H, CH_2), 2.92 (t, 2H, CH_2), 4.17 (t, 2H, CH_2-2), 4.37 (t, 2H, CH_2-4), 8.80 (s, 2H, NH_2). ^{13}C NMR ($CHCl_3$): δ 11.3, 21.9, 22.9, 24.7, 25.2, 25.4, 48.3, 123.2, 137.6, 143.9, 157.8, 159.8, 161.5. MS: *m/z* (%) 280 (M^++2, 100), 278 (M^+, 30), 263 (62), 179 (71).

2. 3. Cytotoxic Activity

Cytotoxicity of the synthesized compounds was evaluated against HCT-116 (colon adenocarcinoma) using MTT assay.[44] The prepared compounds were dissolved in DMSO (dimethylsulfoxide) and diluted 1000-times during the test. It is essential to enable cells to be attached to the wall of the plate. Prior to the treatment with the tested compounds, these cell lines were plated in 96-multi well plate (10^4 cells/well) for 24 h. Each well was supplemented with 100 μg/mL of the tested compounds. Under a 5% CO_2 atmosphere, the monolayer cells were incubated with the samples at 37 °C for 72 h. Then, 20 μL of MTT solution at 5 mg/mL has been added and incubated for 4 h after 24 h

of drug treatment. The colorimetric assay is evaluated and registered using a plate reader at 570 nm absorbance. Determination of IC_{50} (the half-maximal inhibitory concentration) for three samples of the most potent inhibitions. Calculation of IC_{50} values along with the respective 95% confidence intervals by plotting the relationship between the surviving fraction and the sample concentration to obtain the cancer cell line survival curve.

3. Results and Discussion

3. 1. Chemistry

Our target was to convert the open-chain thiourea substituent **1** into heterocycles to enhance their biological activity. The building block thiourea derivative **1** was synthesized through multicomponent synthetic route starting by Gewald reaction of ethyl cyanoacetate with cyclohexanone in the presence of elemental sulfur and then subsequent treatment of **1** with allyl thiocyanate.[40] Spectral and analytical data of the synthesized thiourea intermediate were compatible with reported results. Refluxing of **1** with chloroacetic acid in the presence of potassium hydroxide has unexpectedly afforded the corresponding thiazole derivative **4** rather than the thiazolidinone derivative **2**[40] while it was expected that the formation of **2** through the reaction as the intermediate would be possible.

The mechanism suggested for the creation of **4** begins with the electronegative sulfur attack on the active methylene group which is an electron-deficient carbon, followed by cyclization to form thiazolidinone intermediate **2**. Keto-enol tautomerism leads to enol form and then *O*-alkylation with another molecule of chloroacetic acid takes place. The spectral data of **4** supported our explanations (Scheme 1). IR spectrum of **4** revealed the disappearance of NH absorption band. ^{1}H NMR spectrum confirmed the structure while it showed the presence of a singlet signal at 11.9 ppm due to –COOH group beside the other signals of the compound. Also, its ^{13}C NMR spectral data revealed the presence of 19 signals. Mass spectrum showed molecular ion peak at *m/z* M^+ $-CO_2$ 381 (20%) with a base peak at *m/z* 365 due to $M^+ - CH_2COOH$ fragment. One-pot reaction of **1** by cyclocondensation with chloroacetic acid and benzaldehyde in boiling acetic acid and acetic anhydride in the presence of sodium acetate produced the benzylidene-thiazolidinone **5** in good yield. Spectral data have confirmed its structure. ^{1}H NMR spectrum revealed the appearance of multiplet signals at 7.29–7.51 ppm due to the phenyl ring protons.

Cyclocondesation of the thiourea derivative **1** with diethyl malonate in the presence of sodium ethoxide in ethanol formed the pyrimidinone derivative **6**. Structure of **6** was confirmed using IR, NMR and mass spectra. IR spectrum showed significant stretching bands at 1639 cm^{-1} due to the amidic carbonyls beside the lack of NH absorption bands. Its ^{1}H NMR spectrum accentuated the presence of singlet signal at 3.88 ppm due to the methylene protons in addition to the other expected signals.

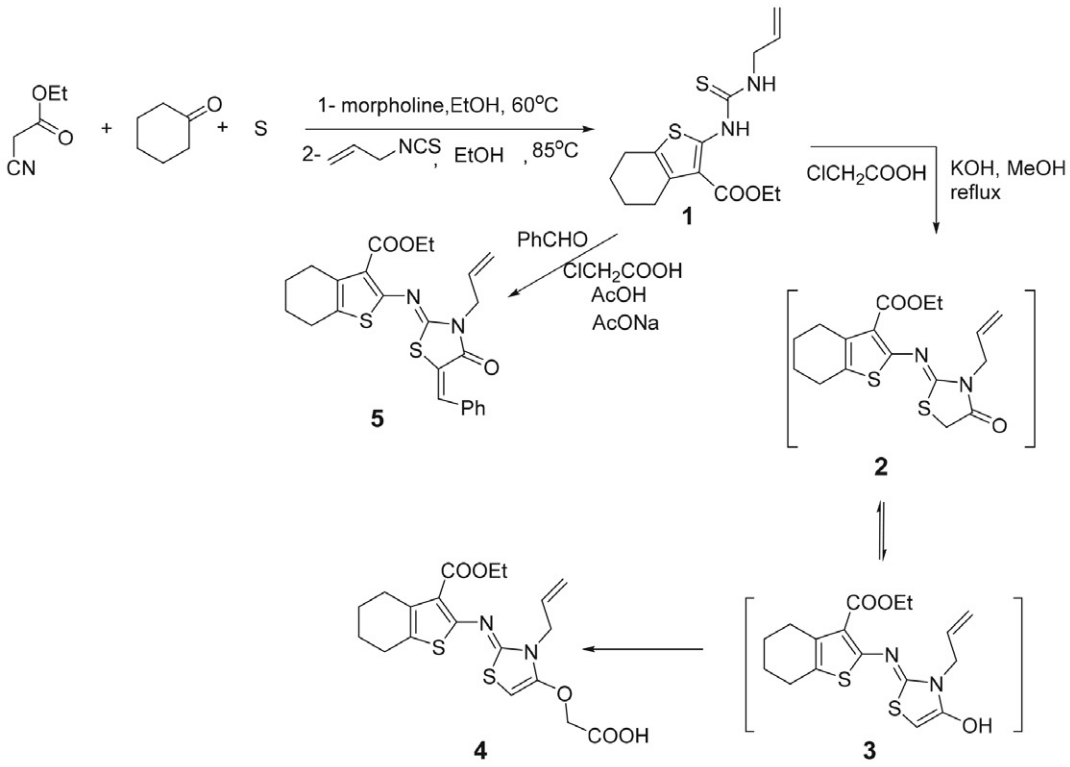

Scheme 1. Synthesis of thiazole derivatives **4** and **5** by reaction of thiourea derivative **1** with monochloroacetic acid under different conditions.

The resulting pyrimidinone **6** underwent subsequent condensation with corresponding aromatic aldehydes, namely furfural and benzaldehyde and isatin in refluxing ethanol in the presence of piperidine yielding the arylidene derivatives **7a**,**b** and **8**, respectively. Mannich base **9** was formed in good yield via Mannich reaction of **6** by amino alkylation of its acidic protons which are placed between the two carbonyl groups with *para*-anisidine and formaldehyde. Further treatment of **6** with aryl diazonium chloride obtained from the suitable aromatic amines (*para*-toluidine and 4-aminobenzophenone) in pyridine furnished the corresponding hydrazones **10a**,**b** (Scheme 2). The spectral and analytical data for compounds **7a**,**b**–**10a**,**b** were matching with their expected structures. Their IR and NMR spectra revealed the absence of methylene bands and new bands appeared in accordance with the proposed structures. As well, mass spectra of these synthesized compounds showed molecular ion peaks compatible with their molecular mass.

Ethyl (*Z*)-2-((1-allyl-4,5-dioxo-4,5-dihydronaphtho[1,2-*d*]thiazol-2(1*H*)-ylidene)amino) -4,5,6,7-tetrahydrobenzo[*b*]thiophene-3-carboxylate (**11**) was synthesized by the treatment of **1** with an equimolar amount of epoxynaphthoquinone derivative **11** in boiling acetonitrile. The mechanism of its formation is expected to be similar to the one described in previous work.[41] Condensation of **1** with ninhydrin in acetic acid yielded the corresponding imidazole derivative **13** (Scheme 3). Structures of **12** and **13** were spectroscopically elucidated. IR spectrum of **12** showed stretching bands at 1689, 1680 and 1668 cm^{-1} due to the carbonyl of –COOEt and 2C=O of 1,2-quinone. Moreover, its ^1H NMR spectrum revealed the presence of aromatic protons at 7.8–8.5 ppm with the other expected signals.

Further reaction of thiourea intermediate **1** with benzoyl hydrazide in sodium ethoxide in boiling ethanol afforded the unexpected triazolopyrimidinone **14** in very good yield. The general mechanism suggested that this reaction proceeds via the formation of the thienopyrimidine **15** followed by condensation and cyclization after the removal of H_2S gas. Isolation of **14** was confirmed; its synthesis utilizing an alternative route by cyclization of compound **1** to give **15** in DMF and in the presence of KOH with stirring **15** was synthesized previously[42] with a different method. All spectral and analytical data were compatible with the reported results. Further reaction of **15** with

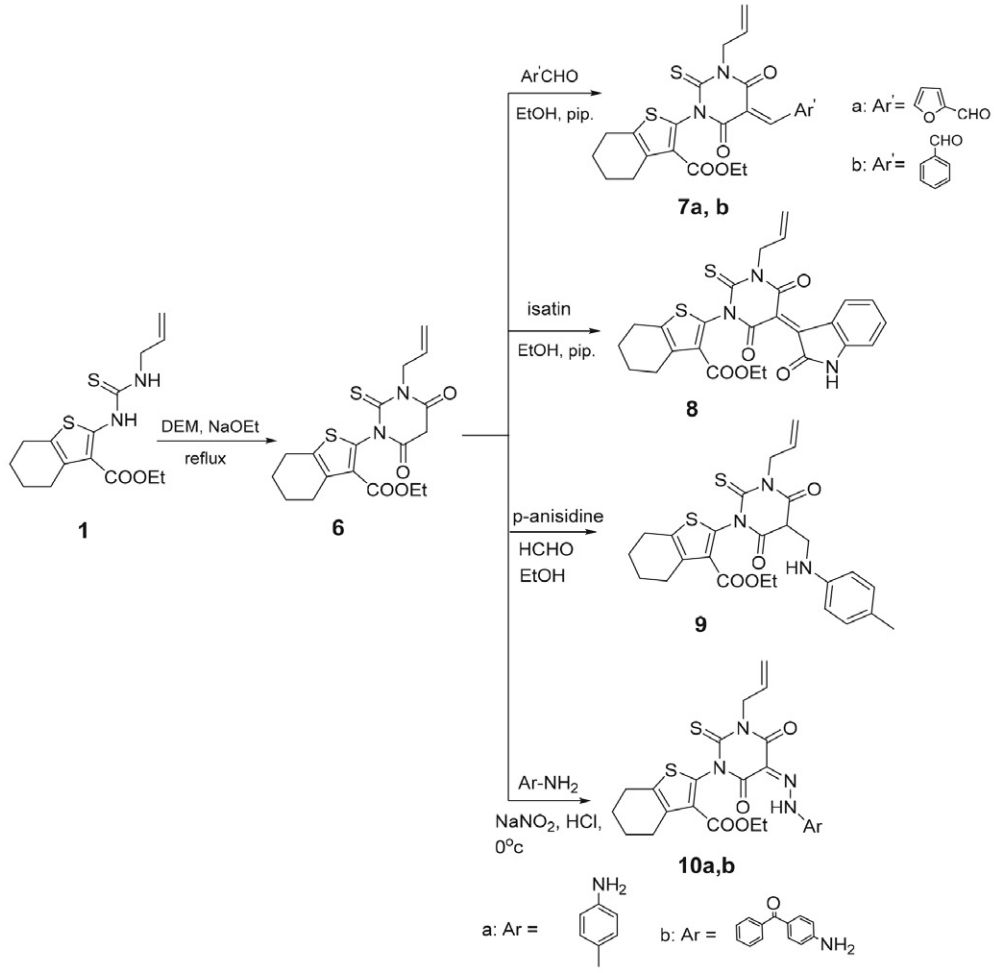

Scheme 2. Synthesis of various pyrimidine derivatives **6**–**10a**,**b**.

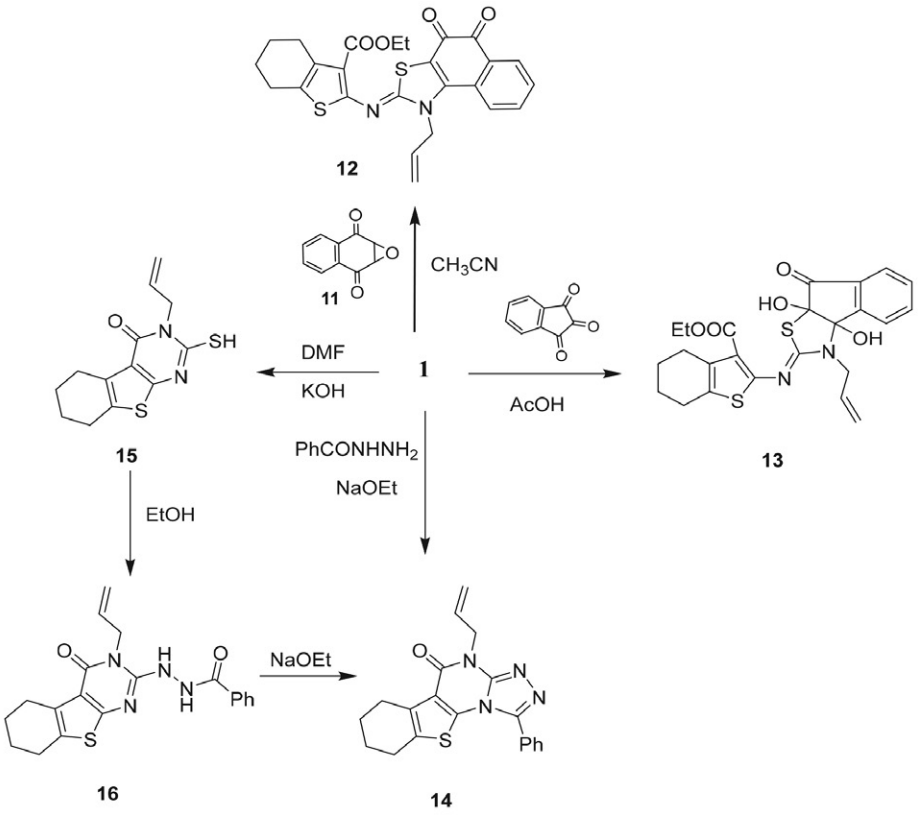

Scheme 3. Synthesis of condensed thiazoles and thienopyrimidine derivatives by treatment of the thiourea dderivative **1** with epoxy naphthoquinone, ninhydrin and benzoyl hydrazine, respectively.

benzoyl hydrazide in boiling ethanol led to the formation of **16** followed by intramolecular cyclization in sodium ethoxide. Structural conformations of compounds **14** and **16** were obtained by their IR, mass and NMR spectra. IR spectra of **14** and **16** lacked the stretching band of ester group and presence of 2NH stretching bands at 3251, 3397 cm^{-1} for compound **16** and disappearance of this band for compound **14**. While their ^1H NMR spectra affirmed multiplet signals at 7.2–7.8 owing to aromatic protons and the disappearance of –COOEt protons.

Finally, the starting compound **1** contains many active sites that led to expect various products. Accordingly, unexpected products were synthesized by treatment of **1** with hydrazine hydrate. However, it was observed that when compound **1** was treated with hydrazine hydrate in ethanol this resulted in the formation of the thienopyrimidine derivatives **17** and **18** which were separated easily from ethanol (Scheme 4). Compound **17** was prepared previously from the reaction of **15** with hydrazine hydrate in EtOH. The spectral and analytical data of the synthesized thienopyrimidine **17** were compatible with the reported ones. Evidence of thienopyrimidine **18** was gained from its spectral measurements. Its IR spectrum revealed the presence of NH stretching band 3239 cm^{-1} and demised of the ester band. ^1H NMR spectrum lacked the signals of –COOEt and allyl protons, in addition, it showed signals at 1.02, 4.17 and 4.37 ppm due to 3 CH_2 protons.

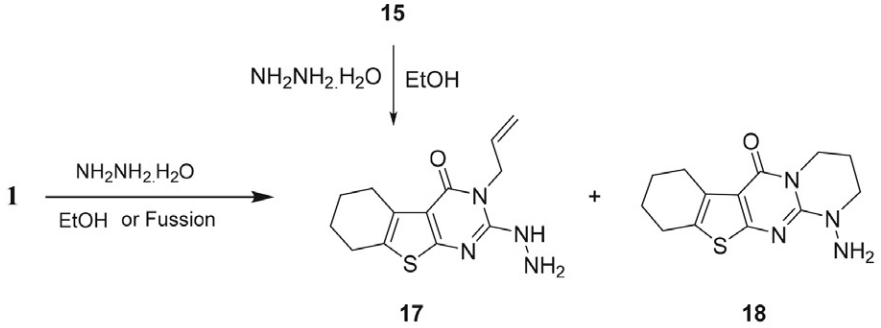

Scheme 4. Treatment of **1** with hydrazine hydrate to afford thienopyrimidines **17** and **18**.

3. 2. Anticancer Activity

The newly synthesized compounds **1**–**18** were preliminarily screened via *in vitro* anticancer screening in a single high dose (100 μg/mL) concentration against colorectal carcinoma (HCT-116) human cancer cell lines. The efficacy of anticancer activity in comparison to the standard drug 5-fluorouracil and the results of cytotoxic activity are in Table 1. As shown in the table, the majority of the synthesized compounds have low to good anticancer activity versus HCT116 cell line. The obtained results revealed that compounds **6**, **9**, **11**, **12**, and **15** showed the highest activity against the cell line; so these compounds were chosen to test at inhibitory concentration 50% (IC_{50}). The structure–activity relationship according to the results obtained, indicates that incorporation of pyrimidine moieties enhances the anticancer activity of the tested compounds. Compound **6** showed the most potent activity, indicating that the presence of the pyrimidinone ring increases the anticancer activity in comparison with pyrimidine moiety. While results for compounds **9** and **10a** indicate that the introduction of *para*-tolyl substituent with the pyrimidine moiety will increase their anticancer activity. The highest activity of compounds **11** and **12** is expected to be due to the presence of 1,2-naphthoquinone moieties and two OH groups, respectively. It is known that introducing amidic group with pyrimidine moiety enhances the anticancer activity in which its structure is similar to the most important anticancer drugs, such as Imatinib; based on that, compounds **12** and **15** showed higher activity."

Table 1. Growth inhibition (%) of Single Dose Experiment on HCT-116 (colon adenocarcinoma) cell line (100 μg/mL) of the synthesized compounds after 72 h of incubation.

Compound.	Surviving %	Inhibition %
4	56.2948	43.7052
5	53.02419	46.97581
6	51.07527	48.92473
7a	43.21237	56.78763
7b	43.6828	56.3172
8	44.89247	55.10753
9	35.9543	64.0457
10a	57.7957	42.2043
10b	36.96237	63.03763
12	38.44086	61.55914
13	32.25806	67.74194
14	43.6828	56.3172
15	53.0914	46.9086
16	34.27419	65.72581
17	53.76344	46.23656
18	48.3871	51.6129

Table 2 IC_{50} (μg/mL) of the more potent tested compounds on HCT-116 (colon adenocarcinoma) cell line.

Compound	IC_{50}
9	44 ±1.39
13	9.5 ± 2.81
16	21 ± 3.03

4. Conclusion

In conclusion, a new series of pyrimidines and thiazoles bearing thiophene ring systems were synthesized. Their structures were characterized by spectral data (IR, NMR and mass spectra). Our products were assessed for their anticancer activity against colon HCT-116 human cancer cell line. Among all the synthesized compounds, compounds **6**, **9**, **10a**, **12**, **13**, **16** displayed potent anticancer activity. The rest of compounds showed a moderate to weak activity against the tested tumor cell lines.

5. References

1. M. S. A. El-Gaby, Z. H. Ismail, S. M. Abdel-Gawad, H. M. Aly, M. M. Ghorab, *Phosphorus Sulfur Silicon Relat. Elem.* **2009**, *184*, 2645–2654. **DOI:**10.1080/10426500802561096
2. M. M. Ghorab, M. S. Bashandy, M. S. Alsaid, *Acta Pharmaceut.* **2014**, *64*, 419–431. **DOI:**10.2478/acph-2014-0035
3. F. A. Dos Santos, M. C. Pereira, T. B. de Oliveira, F. J. B. Mendonça Junior, M. do C. A. de Lima, M. G. da R. Pitta, I. da R. Pitta, M. J. B. de Melo Rêgo, M. G. da Rocha Pitta, *Anti-Cancer Drug.* **2017**, 1–10. **DOI:**10.1097/CAD.0000000000000581
4. M. M. Fouad, E. R. El-Bendary, G. M. Suddek, I. A. Shehata, M. M. El-Kerdawy, *Bioorg. Chem.* **2018**, *81*, 587–598. **DOI:**10.1016/j.bioorg.2018.09.022
5. A. M. Isloor, B. Kalluraya, K. Sridhar Pai, *Eur. J. Med. Chem.* **2010**, *45*, 825–830. **DOI:**10.1016/j.ejmech.2009.11.015
6. L. S. Ming, J. Jamalis, M.Sankaranarayanan, S. Chander, *Chem. Data Collect.* **2017**, *9–10,* 104–113. **DOI:**10.1016/j.cdc.2017.04.004
7. M. H. Helal, M. A. Salem, M. A. Gouda, N. S. Ahmed, A. A. El-Sherif, *Spectrochim. Acta A* **2015**, *147*, 73–83. **DOI:**10.1016/j.saa.2015.03.070
8. N. N. E. El-sayed, M. A. Abdelaziz, W. W. Wardakhan, R. M. Mohareb, *Steroids* **2016**, *107,* 98–111. **DOI:**10.1016/j.steroids.2015.12.023
9. C. Gopi, M. D. Dhanaraju, *Beni-Suef University Journal of Basic and Applied Sciences,* **2018**, *7,* 291–298. **DOI:**10.1016/j.bjbas.2018.02.004
10. M. B. Félix, E. R. de Souza, M. do C. A. de Lima, D. K. G. Frade, V. D. L. Serafim, K. A. da F. Rodrigues, P. L. do N. Néris, F. F. Ribeiro, L. Scotti, M. T. Scotti, T. M. de Aquino, F. J. B. Mendonça Jr., M. R. de Oliveira, *Bioorg. Med. Chem.* **2016**, *24*, 3972–3977. **DOI:**10.1016/j.bmc.2016.04.057
11. N. Süleymanoğlu, R. Ustabaş, Y. Ünver, Y. B. Alpaslan, Ş. Direkel, Ü. Karaman, *J. Mol. Struct.* **2019**, *1182*, 36–46. **DOI:**10.1016/j.molstruc.2019.01.005

12. T. Harit, R. Bellaouchi, A. Asehraou, M. Rahal, I. Bouabdallah, F. Malek, *J. Mol. Struct.* **2017**, *1133*, 74–79. **DOI:**10.1016/j.molstruc.2016.11.051
13. L. Pulipati, J. P. Sridevi, P.Yogeeswari, D. Sriram, S. Kantevari, *Bioorg. Med. Chem. Lett.* **2016**, *26*, 3135–3140. **DOI:**10.1016/j.bmcl.2016.04.088
14. M. S. E l-Shoukrofy, H. A. Abd El Razik, O. M. AboulWafa, A. E. Bayad, I. M. El-Ashmawy, *Bioorg. Chem.* **2019**, *85*, 541–557. **DOI:**10.1016/j.bioorg.2019.02.036
15. C. Viet, A. Faouzi, C. Barette, A. Farce, M. Fauvarque, T. Lomberget, *Bioorg. Med. Chem. Lett.* **2016**, *26*, 174–180. **DOI:**10.1016/j.bmcl.2015.11.010
16. D. Barnes-Seeman, C. Boiselle, C. Capacci-Daniel, R. Chopra, K. Hoffmaster, C. T. Jones, M. Kato, K. Lin, S. Ma, G. Pan, L. Shu, J. Wang, L. Whiteman, M. Xu, R. Zheng, J. Fu, *Bioorg. Med. Chem. Lett.* **2014**, *24,* 3979–3985. **DOI:**10.1016/j.bmcl.2014.06.031
17. Y. Xu, S. Yuan, S. Bowers, R. K. Hom, W. Chan, H. L. Sham, Y. L. Zhu, P. Beroza, H. Pan, E. Brecht, N. Yao, J. Lougheed, J. Yan, D. Tam, Z. Ren, L. Ruslim, M. P. Bova, D. R. Artis, *Bioorg. Med. Chem. Lett.* **2013**, *23*, 3075–3080. **DOI:**10.1016/j.bmcl.2013.03.009
18. L. Li, L. Chang, S. Pellet-Rostaing, F. Liger, *Bioorg. Med. Chem.* **2009**, *17*, 7290–7300. **DOI:**10.1016/j.bmc.2009.08.048
19. A. B. Pinkerton, T. T. Lee, T. Z. Hoffman, Y. Wang, M. Kahraman, T. G. Cook, D. Severance, T. C. Gahman, S. A. Noble, A. K. Shiau, R. L. Davis, *Bioorg. Med. Chem. Lett.* **2007**, *17*, 3562–3569. **DOI:**10.1016/j.bmcl.2007.04.076
20. S. S. Darwish, M. M. Abdel-Halim, Salah, A. H. Abadi, W. Becker, M. Engel, *Eur. J. Med. Chem.* **2018**, *157*, 1031–1050. **DOI:**10.1016/j.ejmech.2018.07.050
21. R. S. Keri, K. Chand, S. Budagumpi, S. B. Somappa, S. A. Patil, B. M. Nagaraja, *Eur. J. Med. Chem.* **2017**, *183,* 1002–1033. **DOI:**10.1016/j.ejmech.2017.07.038
22. Y. Mabkhot, F. Alatibi, N. El-Sayed, S. Al-Showiman, N. Kheder, A.Wadood, A. Rauf, S. Bawazeer, T. Hadda, *Molecules* **2016**, *21*, 222–238. **DOI:**10.3390/molecules21020222
23. D. Gramec, L. Peterlin Mašič, M. S. Dolenc, *Chem. Res. Toxicol.* **2014**, *27*, 1344–1358. **DOI:**10.1021/tx500134g
24. A. V. Medved'ko, V. K. Ivanov, M. A. Kiskin, A. A. Sadovnikov, E. S. Apostolova, V. A.Grinberg, V. V. Emets, A. O. Chizhov, O. M. Nikitin, T. V. Magdesieva, S. A. Kozyukhin, *Dyes Pigm.* **2017**, *140*, 169–178. **DOI:**10.1016/j.dyepig.2017.01.030
25. D. K. Sagdullina, I. E. Kuznetsov, A. V. Akkuratov, L. I. Kuznetsova, *Synth. Met.* **2019**, *250*, 7–11. **DOI:**10.1016/j.synthmet.2019.01.019
26. B. Chen, J. Zeng, Y. Xiong, H. Nie, W. Luo, Z. Zhao, B. Z. S. Tang, *Dyes Pigm.* **2018**, *159*, 275–282. **DOI:**10.1016/j.dyepig.2018.04.069
27. H. S. Nassar, *Fibers* **2015**, *4*, 102–112. **DOI**: 10.5923/j.textile.20150405.02
28. S. Al-Mousawi, M. El-Apasery, H. Mahmoud, *Molecules* **2013**, *18*, 7081–7092. **DOI:**10.3390/molecules18067081
29. M. S. Abaee, S. Cheraghi, *J. Sulfur Chem.* **2014**, *35*, 261–291. **DOI:**10.1080/17415993.2013.860141
30. M. A. A. Elneairy, A. E. M.Mekky, A. A. M. Ahmed, *J. Sulfur Chem.* **2012**, *33*, 373–383. **DOI:**10.1080/17415993.2012.683433
31. F. M. Moghaddam, M. R. Khodabakhshi, A. A. Latifkar, *Tetrahedron Lett.* **2014**, *55*, 1251–1254. **DOI:**10.1016/j.tetlet.2014.01.014
32. T. Kesharwani, J. Craig, C. Del. Rosario, R. Shavnore, C. Kornman, *Tetrahedron Lett.* **2014**, *55*, 6812–6816. **DOI:**10.1016/j.tetlet.2014.10.064
33. M. A. Ameen, E. K. Ahmed, *J. Sulfur Chem.* **2015**, *36*, 293–299. **DOI:**10.1080/17415993.2015.1020494
34. A. Doregiraee, K. E. Tavakolinejad, H. Khabazzadeh, B. S. Pouramiri, *J. Chil. Chem. Soc.* **2015**, *60*, 3021–3023. **DOI:**10.4067/S0717-97072015000300009
35. A. S. Pankova, P. R. Golubev, A. F. Khlebnikov, A. Y. Ivanov, M. A. Kuznetsov, *Beilstein J. Org. Chem.* **2016**, *12*, 2563–2569. **DOI:**10.3762/bjoc.12.251
36. R. Pingaew, S. Prachayasittikul, N. Sinthupoom, V. Prachayasittikul, A.Worachartcheewan, S. Ruchirawat, *Mini-Rev. Med. Chem.* **2016**, *17*, 869–901. **DOI:***10.2174/1389557516666160923125801*
37. R. Dudhe, P. K. Sharma, P. K. Verma, *Org. Med. Chem. Lett.* **2014**, *4*, 3. **DOI:**10.1186/s13588-014-0003-0
38. T. I. de Santana, M. de O. Barbosa, P. A. T. de M. Gomes, A. C. N. da Cruz, T. G. da Silva, A. C. L. Leite, *Eur. J. Med. Chem.* **2018**, *144*, 874–886. **DOI:**10.1016/j.ejmech.2017.12.040
39. Z. M. Nofal, E. A. Soliman, S. S. Abd El-Karim, M. I. El-Zahar, A. M. Srour, S.Sethumadhavan, T. J. Maher, *J. Heterocycl. Chem.* **2014**, *51*, 1797–1806. **DOI:**10.1002/jhet.1886
40. E. F.Silva-Júnior, E. P. S. Silva, P. H. B. França, J. P. N. Silva, E. O. Barreto, E. B. Silva, R. S. Ferreira, C. C. Gatto, D. R. M. Moreira, J. L.Siqueira-Neto, F. J. B. Mendonça-Júnior, M. C. A. Lima; J. H. Bortoluzzi; M. T. Scotti; L. Scotti, M. R. Meneghetti, T. M. Aquino, J. X. Araújo-Júnior, *Bioorg. Med. Chem.* **2016**, *24*, 4228–4240. **DOI:**10.1016/j.bmc.2016.07.013
41. A. H. Abdel-Rahman, E. M. Kandeel, M. A. Berghot, M. Abdel-Motaal, *J. Heterocycl. Chem.* **2013**, *50,* 298–303. **DOI:**10.1002/jhet.1061
42. M. Kut, M. Onysko, V. Lendel, *Heterocycl. Commun.* **2016**, *22*, 347–350. **DOI:**10.1515/hc-2016-0169
43. A. L. Alanzy, H. H. El-Ganzory, *J. Chem. Pharm. Res.* **2017**, *9,* 195–234.
44. T. Mosmann, *J. Immunol. Methods* **1983**, *65*, 55–63.

Povzetek

Spojino etil 2-(3-aliltioureido)-4,5,6,7-tetrahidrobenzo[*b*]tiofen-3-karboksilat (**1**) smo uporabili kot gradnik za sintezo novih heterociklov. Vključitev pirimidinskih in tiazolnih fragmentov smo dosegli s pomočjo kondenzacije spojine **1** z različnimi reagenti, kot so kloroocetna kislina, dietil malonat, ninhidrin, 2,3-epoksi-2,3-dihidro-1,4-naftokinon in hidrazin hidrat. Strukture novih produktov smo potrdili s pomočjo spektroskopskih meritev. Za pripravljene produkte smo določili aktivnost proti celični liniji HCT-116 človeškega raka debelega črevesja. Spojine **6**, **9**, **10a**, **11**, **12**, **15** so izkazale močno aktivnost.

Except when otherwise noted, articles in this journal are published under the terms and conditions of the Creative Commons Attribution 4.0 International License

DOI: 10.17344/acsi.2019.5572 *Acta Chim. Slov.* **2020,** *67,* 570–580
creative commons

Scientific paper

Adsorption Kinetics for CO_2 Capture using Cerium Oxide Impregnated on Activated Carbon

Azizul Hakim Lahuri,[1,*] Michael Ling Nguang Khai,[2] Afidah Abdul Rahim[2] and Norazzizi Nordin[2]

[1]*Department of Science and Technology, Faculty of Agriculture, Science and Technology, Universiti Putra Malaysia Bintulu Campus, P.O Box 396, Nyabau Road, 97008 Bintulu, Sarawak, Malaysia.*

[2]*School of Chemical Sciences, Universiti Sains Malaysia, 11800 Gelugor, Pulau Pinang, Malaysia.*

** Corresponding author: E-mail: azizulhakim@upm.edu.my*

Received: 09-16-2019

Abstract

Various metal oxides of CeO_2, ZnO, and Co_3O_4 impregnated on activated carbon (AC) were synthesized to determine the CO_2 capture efficiency and analyse with adsorption kinetics model. Batch kinetic studies showed that CeO_2/AC is the most efficient adsorbent with an equilibrium time of 10 minutes that was needed to obtain adsorption capacity of 52.68 mg/g. CO_2 adsorption at 30 °C exhibits the optimum temperature with only 6.53% loss in adsorption capacity after 5 cycles of CO_2 adsorption-desorption. The CeO_2 on AC was detected through X-ray diffraction and the scanning electron microscope image shows well-distributed CeO_2 particles on AC surfaces. CO_2 adsorption at 30 °C is best fitted with the pseudo-second-order kinetics with $R^2 = 0.9994$ and the relative error between calculated and experimental adsorption capacity only 1.32%. The adsorption considering chemisorption is responsible for improving adsorption capacity. The addition of CeO_2 on AC enhanced the adsorption capacity by providing active sites to attract CO_2.

Keywords: CO_2 capture; adsorption kinetics; cerium (IV) oxide; activated carbon; recyclability

1. Introduction

Growing global populations lead to an increasing demand for energy consumption. The same is true for CO_2 gas production resulting from transportation and industrial activities. CO_2 is one of the major greenhouse gases (GHG) that often becomes key environmental concern among policy advocates due to its environmental effects. Based on the National Oceanic and Atmospheric Administration (NOAA),[1] the global CO_2 concentration in the Earth's atmosphere during January 2020 was reported to be 413.40 ppm or which accounts for an increas of 0.63% compared to 410.83 ppm in January 2019. The current annual mean global CO_2 growth rate at approximately 2.94 ppm in 2019 may cause severe climatic change e.g. global warming and rising level of seawater.[2]

In order to reduce the CO_2 emission from a large point source, a process known as Carbon Capture and Storage (CCS) was introduced to fossil fuel power plants.[3] In September 2008, an integrated pilot-scale CCS power plant was commissioned and proven effective to reduce CO_2 emission up to approximately 80% compared to power plants without CCS.[4] In order to sustain a better environment for future generations, several approaches to sorption-based technologies were developed to reduce environmental pollution caused by the massive emission of CO_2 gas.

Amongst the sorption-based technologies developed, adsorption technologies were seen as an alternative to the most mature amine-based solvent processes[5] in the early 1990s.[6] Liquid amine-based absorbent suffers from multiple unfavorable conditions including the corrosive nature of amines, high cost and high regeneration energy.[7] Therefore, the attention has shifted to producing a solid adsorbent which possesses a wider temperature range of regeneration, yields less waste during recycling, and is easier to discard the spent adsorbent.[8] Among these technologies, adsorption-based is preferred over absorption-based due to the drawbacks of absorption with aqueous alkanolamine solutions, such as high equipment corrosion rate, high energy consumption in regeneration and a large requirement for absorbent volume. Adsorbents e.g. amine-based chemical adsorbents with large surface area, large CO_2 adsorption capacity, high adsorption and desorption

rates, high tolerance to moisture, and high selectivity towards CO_2.[9] Furthermore, Yu *et al.* also reported that 60% of total energy is consumed for the regeneration of CO_2-rich chemical absorbents.[9]

CO_2 adsorption on solid sorbents can be classified into two mechanisms namely physical adsorption which involves intermolecular forces and chemical adsorption which involve the sharing of electrons by the adsorbent and the adsorbate.[10] The emerging research in solid CO_2 adsorbents along with their properties and performances provides good insights towards developing the progress in this field. Among the adsorption-based sorbents, it includes the low-temperature solid adsorbents (< 200 °C) such as carbon-based adsorbents,[11] zeolite-based adsorbents,[12] metal-organic framework based adsorbents,[13] alkali metal carbonate-based adsorbents,[14] amine-based solid adsorbents,[15] the intermediate-temperature solid adsorbents (200–400 °C) and high-temperature solid adsorbents (> 400 °C) such as calcium-based adsorbents[16] and alkali ceramic-based adsorbents.[7] Hence, a further modification to obtain easy handling in comparison to liquid absorbent by using support materials to impregnate the amine-based sorbent is being sought. Several amine-based adsorbents were reported such as monoethanolamine (MEA) on activated carbon (AC) that exhibit low adsorption capacity (15.40 mg/g) due to the large molecule coating the AC microporous surfaces.[17] Kamarudin *et al.*[18] reported various types of amine-functionalized kenaf with tetraethylenepentamine (TEPA), which showed higher adsorption capacity (40.22 mg/g) than MEA on kenaf and raw kenaf. A larger molecule of octadecylamine (ODA) on silica gel (SG) pre-treated at 600 °C was found to have similarly adsorption capacity (15.61 mg/g)[15] as MEA on AC.

The calcium-based adsorbent is a classically used metal oxide adsorbent for capturing CO_2 due to its high reactivity with CO_2 and low-cost material. The reversible reaction between CaO and CO_2 is shown in Equation 1. The forward reaction shows the adsorption of CO_2 at a temperature between 600 to 700 °C[7] to form $CaCO_3$ while backward reaction depicts the regeneration of CO_2 but requires high heat supply between 900 and 950 °C for the next cycle of CO_2 adsorption.[19–21]

$$CaO\ (s) + CO_2\ (g) \rightleftarrows CaCO_3 \quad (1)$$

Therefore, an alternative metal oxide was used as adsorbent of CO_2 e.g. iron oxides (FeO, Fe_2O_3, and Fe_3O_4),[22] TiO_2,[23] γ-Al_2O_3,[23] CeO_2,[24] SiO_2,[24] ZrO_2,[24] and ZnO.[25] According to Chanapattharapol *et al.*,[10] iron oxide doped MCM-41 adsorbent prepared by impregnation reported higher CO_2 adsorption than the undoped MCM-41 partly due to increased surface area and electron transfer from metal to CO_2. Numerous studies were reported on the CO_2 adsorption on AC due to its wide availability, low cost, and green production. However, AC only offers a weak interaction by physisorption.[22] Thus, surface modification on the carbonaceous support can contribute to higher selectivity towards CO_2 and increase the adsorption capacity of the porous material. AC surface modification by adding metal oxide of alkali metal, alkaline earth metal, and transition metal provides basicity sites on the AC surfaces. A study reported a successful surface modification of AC loaded with Fe_2O_3 with 103.7 mg/g adsorbent with physisorption mainly contributed by AC and chemisorption contributed by Fe_2O_3.[26] Other studies reported using NiO,[27] MgO[28] and CuO[29] to modify the AC surfaces and enhance its adsorption capacity. It is notable to highlight that metal oxide load-

Table 1. Adsorption capacities of various adsorbents.

Adsorbent	Adsorption Capacity (mg/g)	Adsorption Temperature (°C)	CO_2 Purity	Sources
35%ODA/SG600	15.61	25	99%	15
MEA/AC	15.40	25	15%	16
Raw kenaf	27.46	30	99.99%	17
50%MEA-Kenaf	34.36	30	99.99%	17
50%TEPA-Kenaf	40.22	30	99.99%	17
MCM-41	35.00	25	n.a	10
Fe_2O_3/MCM-41	38.40	25	n.a	10
NiO	14.14	25	99%	25
CeO_2	48.00	25	≥ 99.5%	30
Fe_2O_3	17.00	25	99%	31
SiO_2	33.73	25	99%	32
1%[bmim][CF_3SO_3]/SiO_2	66.71	25	99%	32
10%NiO/[emim][HSO_4]/SiO_2	48.80	25	99%	33
10%[emim][HSO_4]/SiO_2	26.70	25	99%	33
10%ChCl:U/SG200	22.30	30	99%	34
ChCl:U/AC	39.40	25	15% in N_2	35

n.a is not available

ing on AC increases the adsorption capacity because it attracts significantly more CO_2 to be chemically bonded and provide better chemisorption properties for the adsorbent.

Recently, ionic liquid-based and deep eutectic solvent (DES)-based materials were applied to the CO_2 capture. Marliza *et al.* reported that ionic liquid functionalized SiO_2 shows highest adsorption capacity for 1-butyl-3-methylimidazolium trifluoromethanesulfonate, [bmim][CF_3SO_3]/SiO_2 than SiO_2 alone.[32] Addition of NiO to the 1-ethyl-3-methylimidazolium hydrogensulfate, [emim][HSO_4] functionalized SiO_2 shows enhanced adsorption capacity due to higher surface area than 10%[emim][HSO_4]/SiO_2.[33] Green technology application through the DES of Choline chloride: urea (ChCl:U) is biocompatible, non-toxic, biodegradable, inexpensive and easy to prepare.[34] The ChCl:U functionalized silica gel was found to have lower adsorption capacity (22.30 mg/g) due to lower surface area (317.50 m^2/g)[34] of the adsorbent rather than ChCl:U functionalized AC,[35] which exhibits higher surface area (581.23 m^2/g) and adsorption capacity. Nonetheless, the significance of desorption properties for the adsorbents are not reported for these works. The performance of various adsorbents is reported in Table 1.

In the present work, double activation will be performed on AC to reactivate the surfaces. The metal oxides of ZnO, CeO_2, and Co_3O_4 were added to the modified AC. These metal oxides were chosen based on the previous study which the metal oxides on AC are not yet discovered its adsorption capacity and adsorption kinetics. Hence, the specific aim of this work is to measure the adsorption capacity, evaluate the desorption properties, identify the most efficient metal loaded on AC, and determine optimum adsorption temperature with adsorption kinetics analysis for CO_2 capture.

2. Experimental

2. 1. Sample Preparation

Charcoal activated carbon (Qrec), cobalt (II) sulfate heptahydrate (Hamburg), cerium (III) nitrate hexahydrate (Nacalai Tesque), and zinc sulfate heptahydrate (R&M) were used as precursors. Moisture removal was conducted by drying the AC in an oven for 2 hours at 110 °C. Double activation of AC was performed by using readily purchased AC to reactivate by using $KMnO_4$. For the support treatment, AC was weighed to 5 g and was added into a solution of 0.1 M $KMnO_4$. The mixture was shaken for 20 minutes at 200 rpm and followed by filtering and rinsing with 200 mL distilled water. The AC was dried in an oven overnight at 110 °C. The adsorbents were prepared by a conventional wet impregnation method. Generally, 0.1 M metal salt was prepared in a 50 mL volumetric flask. AC was subsequently added into the metal salt solution and shaken for 8 hours at 200 rpm. The mixture was filtered and rinsed with 400 mL of 1% $NaHCO_3$ solution, followed by soaking overnight in 600 mL of 1% $NaHCO_3$ solution. Soaked samples were filtered and rinsed with distilled water and allowed to air dry for 2 hours. The samples were dried overnight in an oven at 110 °C. The resultant adsorbents were denoted as metal oxide/activated carbon (MO/AC) where MO represents Co_3O_4, CeO_2, ZnO.

2. 2. CO_2 Adsorption and Desorption

The CO_2 adsorption was measured by using thermogravimetric analysis-derivative thermogravimetry (TGA-DTG) from a Simultaneous Thermal Analyzer (STA) 6000, Perkin Elmer. Approximately 10 mg of each sample was cleaned at 350 °C in the N_2 atmosphere prior to adsorption measurement. The adsorbent was heated from 30 to 350 °C at 30 °C/min and was cooled to 30 °C. The CO_2 adsorption was conducted at 30 °C for 20 minutes. Then, the adsorption capacity was measured from the weight gained after the saturation exposure. Finally, the gas feed was switched to the N_2 atmosphere and was heated again up to 900 °C for the desorption process. The carbonate dissociation temperature was determined to perform the recyclability test at different adsorption temperature.

2. 3. Adsorbent Characterization

The infrared spectra of various metal oxides supported on AC were recorded between 400 and 4000 cm^{-1} using FTIR (PerkinElmer) with KBr pellet method for sample preparation. N_2 adsorption-desorption isotherms were measured on a static volumetric technique instrument (Micromeritics ASAP 2020) for determination of the Brunauer-Emmett-Teller (BET) surface area, mesopore surface area, micropore surface area, total pore volume, micropore volume, and the average pore diameter. The pore size distribution was computed using density functional theory (DFT) method. Approximately 0.5 g of each adsorbent was degassed at 350 °C under vacuum prior to the measurement for the elimination of humidity gases trapped in the adsorbents. In this regard, a water circulating bath was used to control the temperature. The N_2 adsorption-desorption isotherms were recorded at liquid nitrogen temperature of 77 K, and applied in a relative pressure (P/Po) ranging from 0 to 1.0. The surface area (S_{BET}) was calculated by using a commonly used method called Brunauer-Emmett-Teller (BET) method. All surface area measurements were calculated from the nitrogen adsorption-desorption isotherms by assuming the N_2 molecule to be 0.162 nm^2. The t-plot method was used to calculate the mesopore surface area (S_{meso}), micropore surface area (S_{micro}) and micropore volume (V_{micro}). The total pore volume (V_{tot}) was obtained by converting the amount of N_2 gas adsorbed (in cm^3/g at STP) at relative pressure to the volume of gas adsorbate.

The most efficient adsorbent was characterized by its phase composition and surface morphology. X-ray Dif-

fraction (XRD) pattern was obtained by using XRD diffractometer (Bruker D8 Advance). The crystal structures were verified by recording 2θ diffraction angle from 10° to 70° and matched with the standard diffraction data (JCPDS) file for interpretation of the crystalline phase. The surface micrograph of the most efficient adsorbent was observed using a scanning electron microscope (SEM, Quanta 650 field emission gun).

2. 4. Adsorption Optimization and Recyclability Test

The most efficient adsorbent was optimized with different adsorption temperatures of 30 and 50 °C. The recyclability test was performed for 5 cycles of CO_2 adsorption and desorption by using the aforementioned TGA-DTG analysis. Generally, for the first cycle, the adsorbent will start with the cleaning process, cooled to desirable adsorption temperature (30 or 50 °C), CO_2 adsorption, and CO_2 desorption process. After cooling to the desirable adsorption temperature, the second cycle CO_2 adsorption starts again and followed by the desorption process. These methods were repeated up to 5 times to determine the regeneration properties of selected adsorbents.

2. 5. Adsorption Kinetics Study

The experimental data for CO_2 adsorption of the most efficient adsorbent at different adsorption temperatures were analyzed with kinetic models such as the pseudo-first-order kinetic model and pseudo-second-order kinetic model. The adsorption kinetics describes CO_2 uptake rate controls with adsorption time of adsorbate uptake at the solid and gas interface.

3. Results and Discussion

3. 1. Adsorbent Characterization

FTIR spectra were recorded to investigate the functional groups of activated carbon before and after impregnation with various metal oxides as it offers the properties of molecules and characteristics of chemical bonds. The IR spectra and absorption bands are shown in Figure 1 and Table 2, respectively. A typical band at 3406 cm^{-1} is indicative of O-H stretching due to the hydrogen bond caused by moisture content in the sample.[22] The intensity of the strong band decreased after impregnating the metal oxide onto the activated carbon. The decrease in the moisture content was due to the metal oxides deposited on the AC, thus, trapped the the moisture.

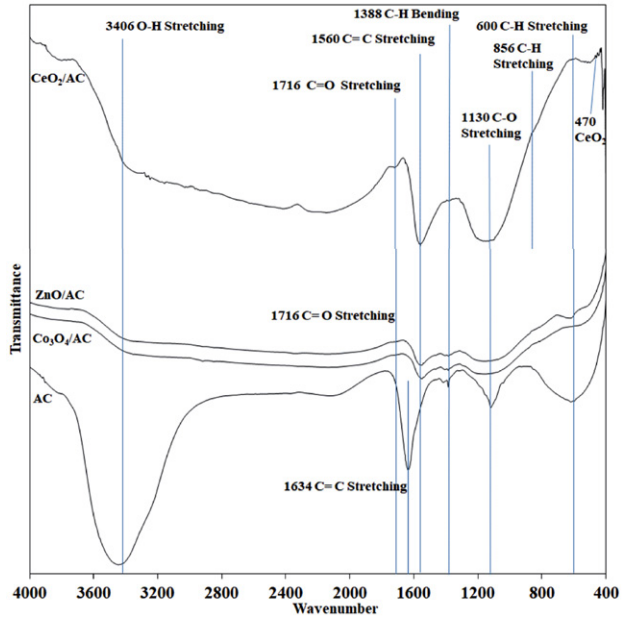

Figure 1. IR spectra of AC and various MO/AC.

Table 2. Vibrational frequencies IR spectroscopy of various MO/AC.

Vibrational modes	This study (cm^{-1})	Reference (cm^{-1})
O-H Stretching	3406	3412
C=O stretching	1716	1716
C=C Stretching	1634	1633
C=C Stretching	1560	1550
C-H Bending	1388	1390
C-O Stretching	1130	1130
C-H Stretching	600	600
Ce-O	470	459

The bands at 1643, 1388 and 600 cm^{-1} are reported to be characteristic absorption bands of activated carbon corresponding to C=C stretching, C-H bending and C-H stretching, respectively.[36] The decrease of intensities in these bands after impregnation with metal oxides indicates that the deposition of metal oxides has reduced the absorption bands for AC.[37] Nonetheless, reactivating the AC for the MO/AC adsorbents contribute to the alteration of surface nature by introducing oxygen-containing functional groups of C=O at 1716 $cm^{-1}$and changing intensities for C-O stretching at 1130 cm^{-1}. This explains $KMnO_4$ oxidizing the surface of AC, besides forming pores structure, which is in agreement with Zhang *et al.*[38] The peak at 1634 cm^{-1} shows a large redshift of 74 cm^{-1} compared to 1560 cm^{-1}, after loading of metal oxides which also occurred when using silver loaded on activated carbon by Zhao *et al.*[39]. In addition, the bands at 470 cm^{-1} are ascribed to the characteristic bands of metal oxides CeO_2,[40] respectively.

The N_2 adsorption-desorption isotherms are shown in Figure 2. According to the International Union of Pure and Applied Chemistry (IUPAC) classification, all of the isotherms exhibit Type I isotherm.[41] The initial steep region is attributed to strong adsorption by a typical microporous material. Hysteresis loop closing at around relative pressure of 0.4 can be observed in all isotherms, indicating

Table 3. The textural characteristics of the adsorbents.

Adsorbent		AC	CeO_2/AC	ZnO/AC	Co_3O_4 /AC
Surface area	S_{BET} (m^2/g)	1043.6	763.4	792.9	838.5
	S_{meso} (m^2/g)	171.0	254.1	280.4	302.2
	S_{micro} (m^2/g)	872.6	509.4	512.5	536.3
Pore Volume	V_{total} (cm^3/g)	0.46	0.42	0.45	0.47
	V_{micro} (cm^3/g)	0.35	0.21	0.21	0.22
Average pore diameter (nm)		1.8	2.2	2.3	2.2

S_{BET} is surface area by BET method; S_{mic} is the micropore surface area by t-plot method; V_{total} is single point total pore volume; V_{micro} is micropore volume obtained by the t-plot method

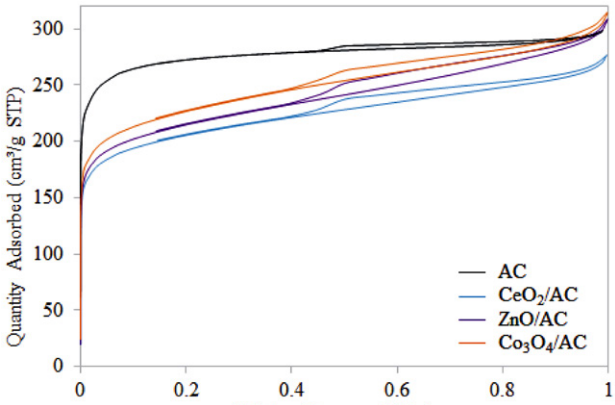

Figure 2. N_2 adsorption-desorption isotherms of the adsorbents.

that the mesoporosity of slit-shaped pores is present in the samples.[26] The adsorbents show H4 hysteresis which is associated with porous materials and indicates a narrow slit-shaped pore.[42] The N_2 adsorption-desorption isotherm for AC has the highest steep initial region ascribed from high micropore structure that easily occupied. The hysteresis of metal oxides loaded AC shows a larger area indicating of high mesopore structure. These are correlated with the textural properties as indicated in Table 3. The formation of mesopores may be explained by the metal oxide burning off carbon wall and enlarging pore sizes during thermal treatment.

The BET surface area decreased with the loading of metal oxides onto AC samples (Table 3). This also suggests that the pores of the AC are blocked or covered.[26] However, an increase in micropore surface area and mesopore surface area ascribed to reactivation of ACs by chemical treatment with $KMnO_4$ prior to metal oxide impregnation. It is notable that Co_3O_4/AC has a higher surface area compared to CeO_2/AC and ZnO/AC. We presume that the Co_3O_4 particles are deposited on AC surfaces instead of pores due to larger particle size. Thus, the pores generated from Co_3O_4 also contribute to the increment of the adsorbent's surface area. The reduction in micropore volume after impregnation with metal oxides is mainly attributed to the addition of metal oxides particles which tend to deposit on the AC surface. In other words, the deposited metal oxides particles fill in the pores of AC surface.

Next, the DFT method was used to compute pore size distribution (Figure 3) of the microporous AC containing various metal oxides. Although AC has a lower intensity of distribution at the region of 9–12 Å (0.9–1.2 nm) as shown in the inset of Figure 3, the AC possessed the highest pore distribution in the region of 16–20 Å (1.6–2.0 nm). Thus, it has a high distribution of micropore structure in which the diameter of the pores is below 2 nm. Most of the metal oxides generated are unable to enter the pores below 12 Å (1.2 nm) because the distribution in the region is less affected. Nonetheless, the distribution in the region of 16-20 Å (1.6–2.0 nm) was diminished, possibly be due to the fine particle metal oxides capable to enter the AC pores, or deposited on the AC pores. Above 21 Å (2.1 nm), higher pore size distribution compared to AC alone attributed by the pores generated from metal oxides themselves.

Thermal stability of various metal oxides impregnated on AC was later computed using the TGA-DTG by heating up to 900 °C (Figure 4). The initial steep region of weight loss was explained by moisture removal. No distinct peak of derivative weight loss was observed at higher

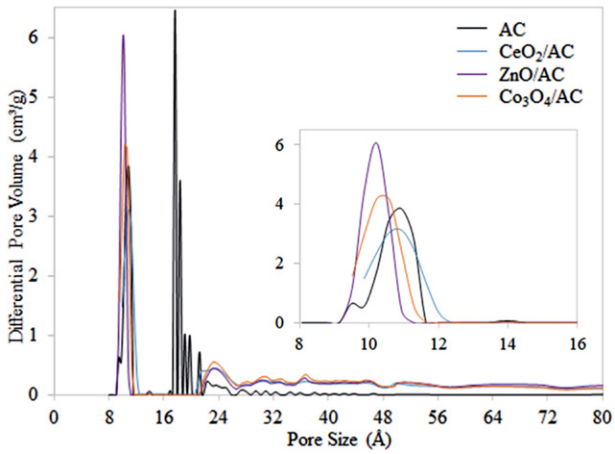

Figure 3. Pore size distribution with the inset image shows clearer pore size distribution at the range of 8-12 Å (0.8–1.2 nm).

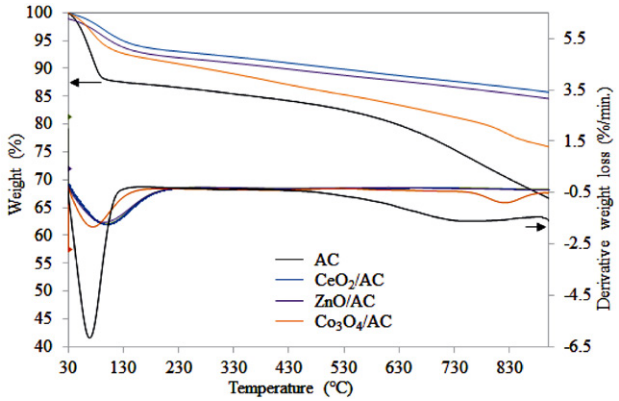

Figure 4. Thermal stability of the adsorbents.

temperature. This implies the samples were resistant to heat. The Co_3O_4/AC shows a derivative weight loss peak at a temperature of 830 °C which corresponded to the decomposing temperature of Co_3O_4.[43]

3. 2. CO_2 Capture

CO_2 capture was performed using TGA and the wide-angle of the thermograms was plotted as shown in Figure 5. The CO_2 adsorption and desorption processes which equalize to its origin were plotted as depicted in Figures 6a and 6b, respectively. The adsorption capacity was obtained from the weight gain shown in Figure 6a. At the beginning of the adsorption, it is observed that the initial steep increase indicates the amount of CO_2 adsorbed on CeO_2/AC and AC is faster than ZnO/AC and Co_3O_4/AC. Eventually, the adsorption gradually decreases when the progress of the adsorption process reaches equilibrium. Figure 6a demonstrates that the adsorption process has reached equilibrium state at the time of 5 minutes for AC and Co_3O_4/AC; 10 minutes for CeO_2/AC; 13 minutes for ZnO/AC. Steep initial region corresponds to stronger binding force between CO_2 with metal oxides and CO_2 with micropores of AC. At the knee-shaped region, the multilayer CO_2 adsorption on the adsorbent formed by occupying CO_2 adsorbate on the uneven bonded CO_2 surface and creating CO_2-CO_2 interaction. It is noteworthy to observe that CeO_2/AC and ZnO/AC show higher adsorption capacity at equilibrium state compared to AC only. This is indicative of CeO_2 and ZnO to possess higher basic properties compared to Co_3O_4. Whereas AC was unable to hold CO_2 strongly compared to those with the presence of metal oxides on AC. Although AC only exhibits the highest surface area, the adsorption capacity was observed to be lower than with CeO_2/AC. Reactivating the AC by using chemical activation of $KMnO_4$ may improve AC surface nature, changing the properties of AC, including pore structure and purity. The significance of double activation increasing the oxygen functional group results in enhancement of AC surfaces and adsorption capacity.

Furthermore, the AC surface modification by impregnation of CeO_2 provides basic active sites that are mainly responsible for the formation of carbonate species and enhancing adsorption capacity. The formation of carbonate species by CO_2 chemisorption reaction pathway can be simplified as in Equation 2.

$$CO_2\ (\text{adsorbate}) + O\ (\text{surface of } CeO_2) \rightarrow \rightarrow [CO_2\text{-}O] \rightarrow CO_3\ (\text{chemisorption}) \quad (2)$$

The chemisorption allows the active sites from the oxygen surface of CeO_2 to exchange electron with CO_2 forming carbonate species product. This could be the reason for the presence of metal oxides that may hold the CO_2 firmly at equilibrium state compared to AC only. Lower in adsorption capacity for Co_3O_4/AC compared to AC only might also be attributed to the weakly adsorbed CO species by cobalt ion which can be fully desorbed at 230K (–43 °C) as reported by Ferstl *et al.*[44]

The thermograms for the desorption process (Figure 6b) shows CeO_2/AC has the highest weight loss up to around 400 °C for CO_2 regeneration. It has a relatively lower CO_2 desorption temperature of 160-280 °C.[45] Hence, the carbonate product will be dissociated to regenerate as CO_2 and leaving the adsorbent that is suitably reused for the next cycle. The desorption temperature above 400 °C resulting in greater weight loss for all adsorbents. Thus, the desorption temperature up to 400 °C will be deployed for the recyclability test.

The adsorption capacity for all adsorbents and similar works are tabulated in Table 4. Among the synthesized adsorbents, CeO_2/AC shows the highest adsorption capacity of 52.78 mg/g at equilibrium. Therefore, CeO_2/AC was chosen as the most efficient adsorbent for further performance optimization through the recyclability test at different adsorption temperature. In comparison, the unmodified AC, which was used to load with 10% CeO_2 (ACCe-HT) and CuO (ACCu-HT) separately by using hydrothermal treatment,[46] shows lower adsorption capacity than this work (Table 4). Meanwhile, Heo *et al.*[28] deployed a slightly complicated method than the one of this work but obtained a comparable CO_2 adsorption capacity through 12 minutes microwave radiated synthesis of MgO on microporous carbon (MC).

Several common activating agents were reported such as zinc chloride ($ZnCl_2$), potassium hydroxide (KOH), hydrochloric acid (HCl), nitric acid (HNO_3) and phosphoric acid (H_3PO_4).[47] This study reported double activation of AC by reactivating with $KMnO_4$. The significance of chemical activation over physical activation was reported in which chemical activation by using $ZnCl_2$ is a promising method to obtain better textural properties for AC derived from palm kernel shell (PCAC).[48] By loading BaO on PCAC, it was observed to be the best adsorbent for CO_2 capture ascribed from the highest BET surface area. Meanwhile, Plaza *et al.*[49] reported AC from the

Table 4. Adsorption capacities of various sorbents.

Adsorbent	Adsorption Capacity (mg/g)	Adsorption Temperature (°C)	CO_2 Purity	Sources
AC	52.01	30	99%	This study
CeO_2/AC	52.78	30	99%	This study
ZnO/AC	52.06	30	99%	This study
Co_3O_4/AC	43.17	30	99%	This study
ACCe-HT	37.66	30	20%	47
ACCu-HT	25.74	30	20%	47
Mg-MCs-12	53.68	40	15% in N_2	28

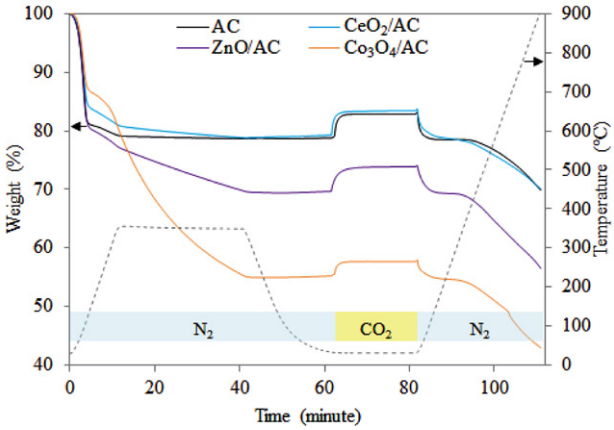

Figure 5. Simultaneous CO_2 adsorption and desorption for all adsorbents with adsorption temperature of 30 °C.

spent coffee ground to show higher CO_2 adsorption capacity by chemical activation using KOH than physical activation.

The phase composition of CeO_2/AC was determined by XRD diffractograms as shown in Figure 7. Typical graphitic structure for AC with broad amorphous diffraction peaks at 2θ values of 26° and 43°. After loading with CeO_2, the amorphous peaks decreased and shifted from 26° and 43° toward 29° and 48° respectively. Another new diffraction peak was observed at 56°. These three diffraction peaks are the reflections of the (111), (220) and (311) crystallographic planes of the cubic CeO_2 phase.[50] The CeO_2/AC surface morphology (Figure 8) shows the well-distributed of fine particles CeO_2 on AC surfaces. Reactivating the AC results in scavenging effect to the AC surface and

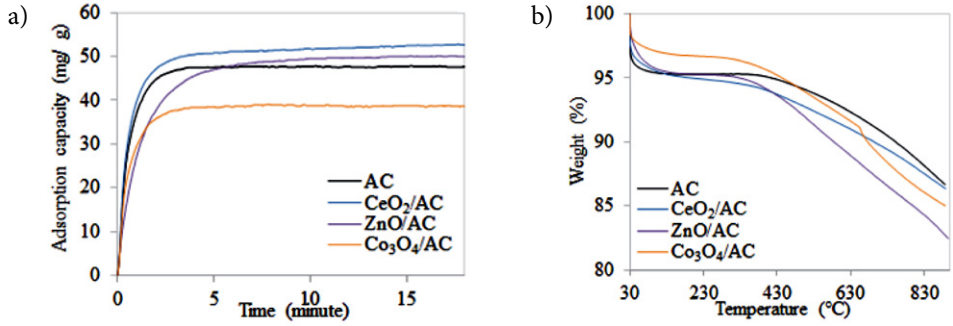

Figure 6. a) CO_2 adsorption at 30 °C and b) desorption process until 400 °C.

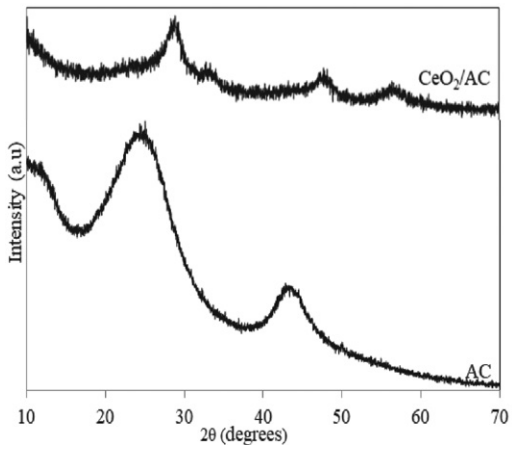

Figure 7. XRD diffractograms.

slightly enlarged pore structure. The SEM image supports the prediction from the textural properties with a possible ability of the CeO_2 to enter the pores of AC and deposit on the AC surfaces.

3. 3. Recyclability Test

Five cycles of CO_2 adsorption-desorption was conducted to optimize the performance for CeO_2/AC at different adsorption temperature of 30 and 50 °C (Figure 9). It is interesting to note that the adsorption capacity is higher for the adsorption temperature of 30 °C than 50 °C. At adsorption temperature of 30 °C, the loss in adsorption capacity was only 6.53% with a decrease from first to fifth cycles is 52.50 mg CO_2/ g adsorbent to 49.07 mg CO_2/g

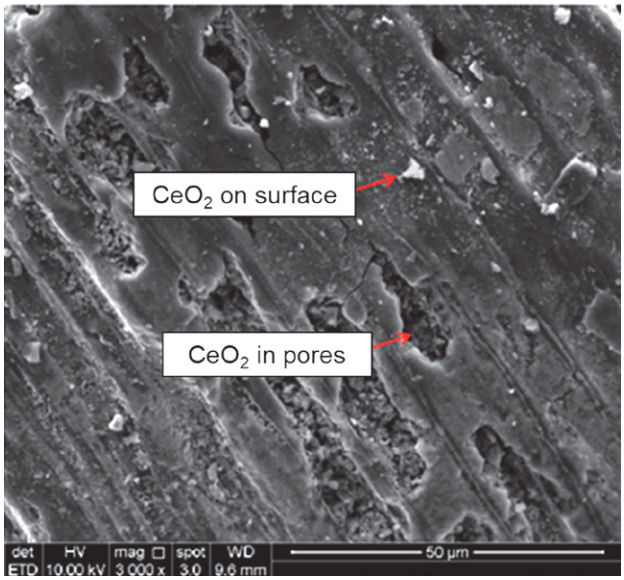

Figure 8. SEM image of CeO_2/AC.

adsorbent, respectively. At adsorption temperature of 50 °C, there was a 7.86% loss in adsorption capacity with a decrease from the first to fifth cycles is 40.56 mg CO_2/ g adsorbent to 37.37 mg CO_2/ g adsorbent, respectively. These observations may suggest that adsorption capacity decreases as the adsorption temperature increases. According to Rashidi *et al.*,[51] an exothermic process where physisorption is favored at lower temperature implies the existence of physisorption throughout the process of adsorption. Thus, at a temperature above 30 °C, the adsorbate of CO_2 has the tendency to desorb during the adsorption period reaching its equilibrium which eventually leads to lower adsorption capacity.

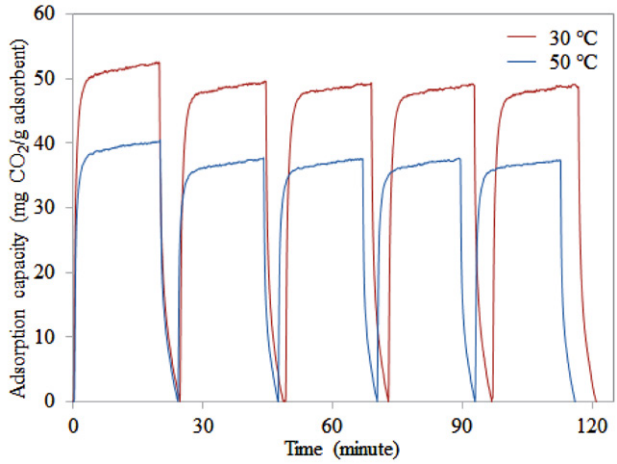

Figure 9. Five cycles of CO_2 capture at adsorption temperature of 30 and 50 °C.

3. 4. Kinetic Analysis

The CO_2 adsorption kinetics data for CeO_2/AC at different operating adsorption temperatures from the first cycle was adjusted by using two kinetic models, namely pseudo-first-order (Equation 3) and pseudo-second-order kinetic model (Equation 4).

$$\log(q_e - q_t) = \log q_e - \left(\frac{k_1}{2.303}\right) t \quad (3)$$

$$\frac{t}{q_t} = \frac{1}{k_2 q_e^2} + \left(\frac{1}{q_e}\right) t \quad (4)$$

where q_t and q_e are the adsorption capacity at any particular time t and at equilibrium, respectively, and k_1 is the pseudo-first-order kinetic constant, k_2 is the pseudo-second-order kinetic constant and ($k_2 \cdot q_e^2$) is initial adsorption rate. The kinetic linear plot using the two equations for evaluating the mechanism of the adsorption process is shown in Figure 10. The kinetic parameters are tabulated in Table 5.

The pseudo-first-order kinetic model describes the initial phase and the progress of adsorption. The value of $\log(q_e - q_t)$ were calculated from the kinetic data. The graph was plotted for $\log(q_e - q_t)$ against t based on the calculations (Figure 10 a). Next, k_1 was calculated from the slope of the plotted graph. It is clear that calculated adsorption capacity also significantly deviates from the actual adsorption capacity, which is similar to findings for this model with Rashidi *et al.*[51] and Gopal *et al.*[52] Thus, this study does not support pseudo-first-order kinetic model, in addition to the low R^2 value at 0.9178 and 0.8777 for CO_2 adsorption at 30 and 50 °C, respectively. The kinetic data obtained in this study failed to fit this model, which appears to be invalid for this work.

In the case of pseudo-second-order kinetic model, it describes the control of the chemisorption in the speed of progress. A graph was plotted for t/q_t against t as shown in Figure 10 b). Next, k_2 was calculated from the slope of the plot. Based on the Table 5, it shows high correlation coefficient values of R^2 are 0.9994 and 0.9622 for both adsorption temperatures of 30 and 50 °C, respectively, which support the adsorption capacity of CO_2 toward the CeO_2/AC. The relative error between actual and calculated adsorption capacity were comparatively lower than that of pseudo-first-order kinetic model. It has the relative error calculated for adsorption temperatures of 30 and 50 °C at 1.32 and 2.74%, respectively.

Based on these R^2 values and relative errors, the pseudo-second-order kinetic model is indeed the most suitable model for the CO_2 adsorption kinetic profiles at both adsorption temperatures of 30 and 50 °C. This suggests the CO_2 adsorption is inclined towards chemisorption in the existence of both physisorption and chemisorption. It might be the limiting step involving the exchange of electron between CeO_2 and CO_2 adsorbate resulting in the adsorption process mainly governed by monolayer adsorption referring to chemical phenomena. However, the presence of physisorption remains undeniable due to the fact that adsorbent is AC based material which may form

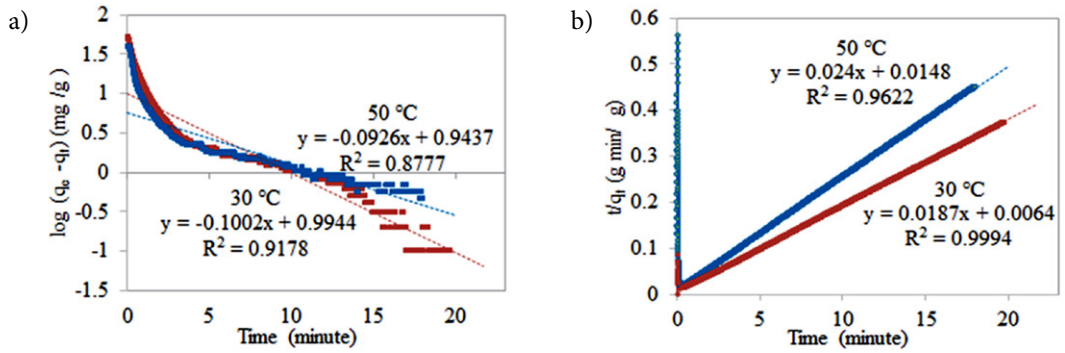

Figure 10. Kinetic plot a) pseudo-first-order kinetic model and b) pseudo-second-order kinetic model at different adsorption temperatures for CeO_2/AC.

Table 5. Kinetic parameters of CO_2 adsorption onto CeO_2/AC.

Kinetic model	Parameter	Temperature (°C) 30	50
	$q_{e(act)}$ (mg/g)	52.78	40.56
Pseudo-first order kinetic	$q_{e(cal)}$ (mg/g)	9.87	8.78
	k_1(1/min)	0.2308	0.2132
	R^2	0.9178	0.8777
	Relative error (%)	81.29	78.34
Pseudo-second-order kinetic	$q_{e(cal)}$ (mg/g)	53.47	41.67
	k_2 (g/mg min)	0.0546	0.0389
	h (mg/g min)	156.14	67.57
	R^2	0.9994	0.9622
	Relative error (%)	1.32	2.74

where $q_{e(act)}$ = actual adsorption capacity; $q_{e(cal)}$ = calculated adsorption capacity

Van der Waals forces with CO_2. This proves that AC surface reactivation with the addition of CeO_2 could enhance the adsorption capacity by chemisorption.

4. Conclusion

Various metal oxides impregnated on chemically reactivated AC were successfully synthesized. SEM images and XRD pattern confirmed that CeO_2 is highly dispersed on the AC surface. FTIR showed the characteristic peaks for the increased oxygen-containing functional group on activated carbon. All the MO/AC showed great thermal stability with high resistance toward heat up to 900 °C except for Co_3O_4/AC. The CeO_2/AC exhibits the most efficient adsorbent with an adsorption capacity of 52.78 mg/g at the equilibrium state of 10 minutes. It showed only a 6.53% loss in adsorption capacity after five cycles with adsorption temperature at 30 °C and a relatively lower desorption temperature of 160–280 °C, which requires less energy consumption. The pseudo-second-order kinetic model was best fitted compared to the pseudo-first-order kinetic model with a higher correlation coefficient. Besides, the pseudo-second-order-kinetic model yields the closest values for calculated adsorption quantity to the actual adsorption quantity. This significantly implies both physisorption and chemisorption for CeO_2/AC.

Acknowledgement

The authors are grateful to the Department of Science and Technology, Universiti Putra Malaysia Kampus Bintulu and School of Chemical Sciences, Univerisiti Sains Malaysia for the research facilities. The authors wish to thanks the Ministry of Higher Education for the financial support for grant numbers of GP-IPM-9657200, GP-IPM-9559000, 1001.PKIMIA.811333 and 1001.PKIMIA.822215.

5. References

1. National Oceanic and Atmospheric Administration (NOAA), Recent Global CO_2, https://www.esrl.noaa.gov/gmd/ccgg/trends/global.html (accessed: March 3rd, 2020)
2. N. Mimura, *P. Jpn. Acad. B Phys. Bio. Sci.* **2013,** 89(6), 281–301. **DOI:**10.2183/pjab.89.281
3. J. R. Fanchi, C. J. Fanchi, Energy in the 21st Century, Fourth Edition, World Scientific, Singapore, Singapore, **2016.** **DOI:**10.1142/10160
4. B. Metz, O. Davidson, H. D. Coninck, M. Loos, L. Meyer, IPCC special report on carbon dioxide capture and storage, Cambridge University Press, New York, United States, **2005**.
5. W. Yuan, Z. Li, A. Otto, M. Robinius, D. Stolten, *Energy Procedia.* **2017**, *114*, 650–665. **DOI:**10.1016/j.egypro.2017.03.1209
6. E. S. Kikkinides, R. T. Yang, S. H. Cho, *Ind. Eng. Chem. Res.* **1993**, *32*, 2714–2720. **DOI:**10.1021/ie00023a038
7. Q. Wang, Q. J. Luo, Z. Zhong, A. Borgna, *Energ. Environ. Sci.* **2011**, *4*(1), 42–55. **DOI:**10.1039/C0EE00064G
8. J. Gale, Y. Kaya, Greenhouse Gas Control Technologies, Pergamon, New York, United States, **2003**.
9. C. H. Yu, C. H. Huang, C. S. Tan, *Aerosol Air Qual. Res.* **2012**, *12*(5), 745–769. **DOI:**10.4209/aaqr.2012.05.0132

10. K. C. Chanapattharapol, S. Krachuamram, S. Youngme, *Micropor. Mesopor. Mat*. **2017**, *245*, 8–15. **DOI:**10.1016/j.micromeso.2017.02.072
11. A. E. Ogungbenro, D. V. Quang, K. Al-Ali, M. R. M. Abu-Zahra, *Energy Procedia*. **2017**, *114*, 2313–2321. **DOI:**10.1016/j.egypro.2017.03.1370
12. R. Kodasma, J. Fermoso, A. Sanna, *Chem. Eng. J.* **2018**, *358*, 1351–1362. **DOI:**10.1016/j.cej.2018.10.063
13. C. E. Bien, K. K. Chen, S. C. Chien, B. R. Reiner, L. C. Lin, C. R. Wade, W. S. W. Ho, *J. Am. Chem. Soc.* **2018,** *140*(40), 12662–12666. **DOI:**10.1021/jacs.8b06109
14. S. S. Shang, A. Hanif, M. Z Sun, Y. M. Tian, Y. S. Ok, I. K. M.Yud, D. C.W. Tsang, Q. F. Gue, J. Shang, *J. Hazard, Mater*. **2019,** *373*, 285–293. **DOI:**10.1016/j.jhazmat.2019.03.077
15. M. N. Abu Tahari, A. Hakim, T. S. Marliza, N. H. Mohd, M. A. Yarmo, *Mater. Sci. Forum* **2017,** *888*, 529–533. **DOI:**10.4028/www.scientific.net/MSF.888.529
16. M. A. Naeem, A. Armutlulu, Q. Imtiaz, C. R. Meller, *ChemPhysChem*. **2017,** *18*, 3280–3285. **DOI:**10.1002/cphc.201700695
17. A. Boonpoke, S. Chiarakorn, N. Laosiripojana, S. Towprayoon, *Korean J. Chem. Eng.* **2012**, *29*, 89–94. **DOI:**10.1007/s11814-011-0143-0
18. K. S. N. Kamarudin, N. Zaini, N. E. A. Khairuddin, *J. Environ. Chem. Eng.* **2018,** *6*, 549–559. **DOI:**10.1016/j.jece.2017.12.040
19. S. Lin, T. Kiga, Y. Wang, K. Nakayama, *Energy Procedia* **2011,** *4*, 356–361. **DOI:**10.1016/j.egypro.2011.01.062
20. S. C. Tian, J. G. Jiang, F. Yan, K. M. Li, X. J. Chen, V. Manovic, *Green Chem*. **2016,** *18*, 4022–4031. **DOI:**10.1039/C6GC00400H
21. S. Wongsakulphasatch, K. Sukchoknamchai, N. Suthapot, W. Praikaew, C. Chaisuk, W. Kiatkittipong, N. Laosiripojana, S. Assabumrungrat, S. *MATEC Web of Conferences* **2018,** 192, 03057. **DOI:**10.1051/matecconf/201819203057
22. A. Hakim, T. S. Marliza, M. N. Abu Tahari, W. N. R. Wan Isahak, M. R. Yusop, M. W. Mohamed Hisham, M. A. Yarmo, *Ind. Eng. Chem. Res.* **2016,** *55*(29), 7888–7897. **DOI:**10.1021/acs.iecr.5b04091
23. J. Baltrusaitis, J. Schuttlefield, E. Zeitler, V. H. Grassian, 2011. *Chem. Eng. J.* 2011, *170*, 471–481. **DOI:**10.1016/j.cej.2010.12.041
24. K. Yoshikawa, H. Sato, M. Kaneeda, J. N. Kondo, *J. CO_2 Util.* **2014,** *8*, 34–38. **DOI:**10.1016/j.jcou.2014.10.001
25. Y. M. Wang, R. Kováčik, B. Meyer, K. Kotsis, D. Stodt, V. Staemmler, H. S. Qiu, F. Traeger, D. Langenberg, M. Muhler, C. Wöll, *Angew. Chem. Int. Edit*. **2007,** *46*, 5624–5627. **DOI:**10.1002/anie.200700564
26. A. Hakim, M. N. Abu Tahari, T. S. Marliza, W. N. R. Wan Isahak, M. R. Yusop, M. W. M. Hisham, M. A. Yarmo, *J. Teknol. (Sci. Eng.)*. **2015,** 77(33), 75–84. **DOI:**10.11113/jt.v77.7010
27. A. Hakim, W. N. R. Wan Isahak, M. N. Abu Tahari, M. R. Yusop, M. H. Mohamed Wahab, M. A. Yarmo, *Adv. Mat. Res.* **2015,** *1087*, 45–49. **DOI:**10.4028/www.scientific.net/AMR.1087.45
28. Y. J. Heo, S. J. Park, *Sci. Rep.* **2017,** *5653*, 1–9.
29. W. N. R. Wan Isahak, Z. A. Che Ramli, A. Z. Lahuri, M. R. Yusop, M. H. Mohamed Wahab, M. A. Yarmo, *Adv. Mat. Res.* **2015,** *1087*, 111–115. **DOI:**10.4028/www.scientific.net/AMR.1087.111
30. C. Slotowski, S. Marre, P. Dagault, O, Babot, T. Toupance, C. Aymonier, *J. CO_2 Uti.*, **2017**, *20*, 52–58. **DOI:**10.1016/j.jcou.2017.03.023
31. A. Hakim, M. A. Yarmo, T. S. Marliza, M. N. A. Tahari, W. Z. Samad, M. R. Yusop,M. W. M. Hisham, N. Dzakaria, *Malaysian J. Anal. Sci.* **2016**, *20(6)*, 1286–1298. **DOI:**10.4028/www.scientific.net/MSF.888.485
32. T. S. Marliza, M. A. Yarmo, A. Hakim, M. N. A. Tahari, Y. H. Taufiq-Yap, *Mater. Sci. Forum*, **2017**, *888*, 485–490.
33. T. S. Marliza, M. A. Yarmo, A. Hakim, M. N. A. Tahari, M. W. M. Hisham, Y. H. Taufiq-Yap, *AIP.* **2017,** *20008*, 1–8.
34. Z. Ghazali, N. H. Hassan, M. A. Yarmo, L. P. Teh, R. Othaman, *Sains Malays.* **2019**, *48(5)*, 1025–1033. **DOI:**10.17576/jsm-2019-4805-11
35. N. Z. Zulkurnai, U. F. Md. Ali, N. Ibrahim, N. S. Abdul Manan, *E3S Web Conf.* **2018**, *34*, 02030. **DOI:**10.1051/e3sconf/20183402030
36. S. Ge, Z. Liu, Y. Furuta, W. Peng, *Saudi J. Biol. Sci*. **2017**, *24*(6), 1370–1374. **DOI:**10.1016/j.sjbs.2016.12.016
37. G. Zhang, J. Qu, H. Liu, A. T. Cooper, R. Wu, *Chemosphere* **2007,** *68*(6), 1058–1066. **DOI:**10.1016/j.chemosphere.2007.01.081
38. G. Zhang, Y. Sun, P. Zhao, Y. Xu, A. Su, J. Qu, *J. CO_2 Util.* **2017,** *20*, 129–140. **DOI:**10.1016/j.jcou.2017.05.013
39. H. Zhao, F. Wang, Y. Ning, B. Zhao, F. Yin, Y. Lai, K. Hu, *Sci. Rep*. **2013,** *3*, 1511. **DOI:**10.1038/srep01511
40. G. H. Hara Priya, N. Sunganya, V. Jaisankar, *Int. J. Adv. Chem. Sci. Appl.* **2015,** *3*, 6–14.
41. K. S. W. Sing, D. H. Everett, R. A. W. Haul, L. Moscou, R. A. Pierotti, J. Rouquerol, *Pure & Appl. Chem.* **1985,** *57*(4), 603–619.
42. J. B. Condon, Surface Area and Porosity Determinations by Physisorption: Measurements and Theory, first ed., Oxford, United Kingdom, Elsevier B. V., **2006.**
43. G. A. El-Shobaky, A. S. Ahmad, A. N. Al-Noaimi, H. G. El-Shobaky, *J. Therm. Anal.* **1996,** *46*(6), 1801–1808. **DOI:**10.1007/BF01980784
44. P. Ferstl, S. Mehl, M. A. Arman, M. Schuler, A. Toghan, B. Laszlo, J. Knudsen, *J. Phys. Chem. C* **2015,** *119*(29), 16688–16699. **DOI:**10.1021/acs.jpcc.5b04145
45. V. Savin, V. Sobolev, Z. Eremenko, Z. Grigor'eva, *J. Anal. Chem.-USSR.* **1985,** *59*(3), 571–575.
46. H. Madzaki, W. A. W. A. K. Ghani, S. Y. Thomas Choong, U. Rashid, N. Muda, *J. Kejuruteraan.* **2018,** *30(1)*, 31–38. **DOI:**10.17576/jkukm-2018-30(1)-05
47. I. Senturk, M. Alzein, *Acta Chim. Slov.* **2020,** 67, 1–15. **DOI:**10.17344/acsi.2019.5195
48. A. R. Hidayu, N. Muda, *Procedia Eng.* **2016,** 148, 106–113. **DOI:**10.1016/j.proeng.2016.06.463
49. M. G. Plaza, A. S. Gonzalez, C. Pevida, J. J. Pis, F. Rubiera, *Appl. Energy*. **2012,** 99, 272–279. **DOI:**10.1016/j.apenergy.2012.05.028

50. H. Qin, H. Chen, X. Zhang, G. Yang, Y. Feng, *J. Chem. Technol. Biot.* **2014,** *89*(9), 1402–1409. **DOI:**10.1002/jctb.4222
51. N. A. Rashidi, S. Yusup, B. H. Hameed, *Energy.* **2013**, *61*, 440–446. **DOI:**10.1016/j.energy.2013.08.050
52. K. Gopal, N. I. Mohd, M. Raoov, F. B. M. Suah, N. Yahaya, N. N. M. Zain, *RSC. Adv*. **2019**, *9*, 36915–36930. **DOI:**10.1039/C9RA07151B

Povzetek

Za določitev učinkovitosti zajemanja (adsorpcije) CO_2 in analizo adsorpcije z raznimi kinetičnimi modeli so bili sintetizirani različni kovinski oksidi (CeO_2, ZnO in Co_3O_4), ki smo jih impregnirali na aktivnem oglju (AC). Šaržne kinetične študije so pokazale, da je CeO_2/AC najučinkovitejši adsorbent, kjer je bil čas do vzpostavitve ravnotežja le 10 minut in adsorpcijska zmogljivost 52,68 mg/g. Adsorpcija CO_2 je optimalna pri temperaturi 30° C z le 6,53% izgubo adsorpcijske zmogljivosti po 5 ciklih adsorpcije in desorpcije CO_2. CeO_2 na AC je bil karakteriziran z rentgensko difrakcijo in vrstično elektronsko mikroskopijo, ki kažeta dobro razporejene delce CeO_2 na AC površinah. Kinetika adsorpcije CO_2 pri 30 ° C se najbolje ujema s kinetičnim modelom psevdo drugega reda z R^2 = 0,9994 in relativno napako med izračunano in eksperimentalno adsorpcijsko zmogljivostjo le 1,32%. Za izboljšanje adsorpcijske sposobnosti je odgovorna kemisorpcija. Dodatek CeO_2 na AC je povečal adsorpcijsko sposobnost z zagotavljanjem aktivnih mest, ki privlačijo CO_2.

Except when otherwise noted, articles in this journal are published under the terms and conditions of the Creative Commons Attribution 4.0 International License

Scientific paper

Two Zinc(II) Complexes with Similar Hydrazone Ligands: Syntheses, Crystal Structures and Antibacterial Activities

Ya-Li Sang,* Xue-Song Lin and Wei-Dong Sun

Department of Chemistry and Chemical Engineering, Chifeng University, Chifeng 024000, P. R. China

** Corresponding author: E-mail: sangyali0814@126.com*

Received: 09-20-2019

Abstract

A pair of new mononuclear zinc(II) complexes with hydrazone ligands 4-methoxybenzoic acid (1-pyridin-2-yl-methylidene)hydrazide (HL^a) and benzoic acid (1-pyridin-2-ylethylidene)hydrazide (HL^b) were prepared. They are $[Zn(L^a)_2]$ (**1**) and $[Zn(L^b)_2]$ (**2**). The complexes were characterized by physico-chemical methods and single crystal X-ray determination. The tridentate hydrazone ligands coordinate to the Zn atoms through the pyridine nitrogen, imino nitrogen and enolate oxygen atoms. The Zn atom in each complex is six coordinated by two hydrazone ligands, to form octahedral coordination. The complexes have effective activities against the bacteria *Bacillus subtilis*, *Staphylococcus aureus*, *Escherichia coli* and *Pseudomonas fluorescens*.

Keywords: Schiff base; Zinc complex; Crystal structure; Antibacterial activity

1. Introduction

Schiff bases are readily synthesized by the condensation reaction of aldehydes with primary amines, which have been widely investigated for their antibacterial and antitumor activities.[1] The metal complexes of Schiff bases have also received much attention due to their contribution to the development of coordination chemistry related to catalysis and enzymatic reactions, magnetism and molecular architectures,[2] as well as biological activities.[3] The Schiff bases 4-methoxybenzoic acid (1-pyridin-2-yl-methylidene)hydrazide (HL^a; Scheme 1) and benzoic acid (1-pyridin-2-ylethylidene)hydrazide (HL^b; Scheme 1) are interesting tridentate hydrazone-type ligands, which possess potential antibacterial activities.[4] In this paper, two new mononuclear zinc(II) complexes, $[Zn(L^a)_2]$ (**1**) and $[Zn(L^b)_2]$ (**2**), have been synthesized and structurally characterized. The antibacterial activities against *Bacillus subtilis*, *Staphylococcus aureus*, *Escherichia coli*, and *Pseudomonas fluorescens*, were evaluated for the complexes.

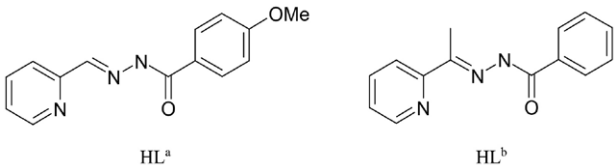

HL^a HL^b

Scheme 1. The Schiff bases, HL^a and HL^b.

2. Experimental

2. 1. Materials and Measurements

Pyridine-2-carbaldehyde, pyridine-2-ethanone, 4-methoxybenzohydrazide, and benzohydrazide with AR grade were obtained from Aldrich and used as received. Elemental analyses (C, H, N) were performed using a Perkin-Elmer 240C analytical instrument. Infrared spectra were recorded on a Nicolet 5DX FT-IR spectrophotometer with KBr pellets. UV–vis spectra were recorded on a Lambda 900 spectrophotometer.

2. 2. Synthesis of Complex 1

Pyrdine-2-ethanone (1.21 g, 0.01 mol) and 4-methoxybenzohydrazide (1.66 g, 0.01 mol) were stirred in 30 mL methanol at room temperature for 20 min. Then, zinc nitrate hexahydrate (2.97 g, 0.01 mol) dissolved in 30 mL methanol was added dropwise to the solution. The mixture was further stirred for 30 min and filtered. The filtrate was evaporated slowly in air to give colorless block-like single crystals, which were washed three times with methanol and dried in open air. Yield: 55%. Found: C, 59.72; H, 4.71; N, 14.13. Anal. Calcd. for $C_{30}H_{28}N_6O_4Zn$: C, 59.86; H, 4.69; N, 13.96%. IR data (cm^{-1}, KBr pellet): 1602, 1585, 1562, 1511, 1495, 1455, 1407, 1361, 1317, 1300, 1289, 1247, 1171, 1097, 1063, 1042, 1027, 905, 840, 765, 680, 635, 618.

UV-Vis data (λ_{max} (nm), ε (L mol^{-1} cm^{-1})): 276 (1.23 × 10^3), 325 (1.38 × 10^3), 370 (1.45 × 10^3).

2. 3. Synthesis of Complex 2

Pyrdine-2-ethanone (1.21 g, 0.01 mol) and benzohydrazide (1.36 g, 0.01 mol) were stirred in 30 mL methanol at room temperature for 20 min. Then, zinc nitrate hexahydrate (2.97 g, 0.01 mol) dissolved in 30 mL methanol was added dropwise to the solution. The mixture was further stirred for 30 min and filtered. The filtrate was evaporated slowly in air to give colorless block-like single crystals, which were washed three times with methanol and dried in open air. Yield: 61%. Found: C, 26.21; H, 4.53; N, 15.40. Anal. Calcd. for $C_{28}H_{24}N_6O_2Zn$: C, 62.06; H, 4.46; N, 15.51%. IR data (cm^{-1}, KBr pellet): 1595, 1587, 1562, 1498, 1460, 1431, 1357, 1316, 1293, 1169, 1160, 1095, 1060, 1041, 903, 776, 746, 708, 683, 637. UV-Vis data (λ_{max} (nm), ε (L mol^{-1} cm^{-1})): 270 (1.12 × 10^3), 310 (1.29 × 10^3), 365 (1.30 × 10^2).

2. 4. X-ray Crystallography

Single crystal structural diffraction was performed on a Bruker Smart 1000 CCD area-detector diffractometer with graphite monochromatized Mo-Kα radiation (λ = 0.71073 Å). Diffraction data for the complexes were collected by ω scan mode at 298(2) K. Data reduction and cell refinement were performed by the SMART and SAINT programs.[5] Empirical absorption correction was applied by using SADABS.[6] Structures of the complexes were solved by direct method and refined with the full-matrix least-squares technique using SHELXL97.[7] The non-H atoms in the structures were subjected to refined anisotropic refinement. All hydrogen atoms were located in geometrically and treated with the riding mode. Crystallographic data and experimental details for the complexes are summarized in Table 1. Selected bond lengths and angles for the complexes are listed in Table 2.

2. 5. Antibacterial Test

Antibacterial activities of the Schiff bases and the complexes were tested *in vitro* against *Bacillus subtilis*, *Staphylococcus aureus*, *Escherichia coli*, and *Pseudomonas fluorescens* using MH medium (Mueller–Hinton medium: casein hydrolysate 17.5 g, soluble starch 1.5 g, beef extract 1000 mL) in triplicate. The minimum inhibitory concentrations (MIC) of the test compounds were determined by a colorimetric method using the dye MTT (3-(4,5-dimethylthiazol-2-yl)-2,5-diphenyltetrazolium bromide). A solution of the compound (50 μg mL^{-1}) in DMSO was prepared and graded quantities of the test compounds were incorporated in specified quantity of sterilized liquid MH medium. A specified quantity of the medium containing the compound was poured into microtitration plates. Sus-

Table 1. Crystallographic and experimental data for the complexes.

	1	2
Chemical formula	$C_{30}H_{28}N_6O_4Zn$	
$C_{28}H_{24}N_6O_2Zn$		
Formula weight	601.95	541.90
T (K)	298(2)	298(2)
crystal system	orthorhombic	monoclinic
space group	*Pbca*	*Cc*
a (Å)	11.9317(7)	10.3526(13)
b (Å)	10.1046(6)	19.287(2)
c (Å)	47.2193(18)	12.3879(19)
β (°)	90	90.536(2)
V (Å^3)	5693.0(5)	2473.3(6)
Z	8	4
ρ (g/cm^3)	1.405	1.455
μ(Mo-Kα) (mm^{-1})	0.909	1.032
F(000)	2496	1120
No. of measured reflections	32450	7154
No. of unique reflections	5299	3379
No. of observed reflections	3633	3003
Parameters	374	337
R_{int}	0.0500	0.0372
Goodness of fit on F^2	1.136	1.045
R_1, wR_2 [$I \geq 2\sigma(I)$][a]	0.0490, 0.0962	0.0771, 0.2050
R_1, wR_2 (all data)[a]	0.0801, 0.1078	0.0847, 0.2118
Highest peak and deepest hole (e Å^{-3})	0.250, –0.321	0.745, –0.490

[a] $R_1 = \text{å}|F_o| - |F_c|/\text{å}|F_o|$, $wR_2 = [\text{å}w(F_o^2 - F_c^2)^2/\text{å}w(F_o^2)^2]^{1/2}$.

Table 2. Selected bond lengths (Å) and angles (°) for the complexes.

	1		
Bond lengths			
Zn1–N2	2.055(2)	Zn1–N5	2.058(2)
Zn1–O1	2.099(2)	Zn1–O3	2.136(2)
Zn1–N4	2.197(3)	Zn1–N1	2.212(3)
Bond angles			
N2–Zn1–N5	174.18(10)	N2–Zn1–O1	75.79(9)
N5–Zn1–O1	109.85(9)	N2–Zn1–O3	103.22(9)
N5–Zn1–O3	74.85(9)	O1–Zn1–O3	99.04(10)
N2–Zn1–N4	106.59(10)	N5–Zn1–N4	75.12(10)
O1–Zn1–N4	91.76(10)	O3–Zn1–N4	149.97(9)
N2–Zn1–N1	74.44(10)	N5–Zn1–N1	100.09(10)
O1–Zn1–N1	149.59(9)	O3–Zn1–N1	93.62(10)
N4–Zn1–N1	90.86(11)		
	2		
Bond lengths			
Zn1–N2	2.030(9)	Zn1–N5	2.062(8)
Zn1–O2	2.106(7)	Zn1–O1	2.137(7)
Zn1–N1	2.184(9)	Zn1–N4	2.199(8)
Bond angles			
N2–Zn1–N5	173.0(3)	N2–Zn1–O2	102.9(3)
N5–Zn1–O2	73.4(3)	N2–Zn1–O1	74.9(3)
N5–Zn1–O1	99.6(3)	O2–Zn1–O1	99.7(3)
N2–Zn1–N1	74.9(4)	N5–Zn1–N1	110.9(4)
O2–Zn1–N1	92.7(4)	O1–Zn1–N1	149.2(3)
N2–Zn1–N4	108.5(3)	N5–Zn1–N4	75.9(4)
O2–Zn1–N4	147.9(3)	O1–Zn1–N4	94.6(3)
N1–Zn1–N4	89.3(4)		

pension of the microorganism was prepared to contain about 10^5 colony forming units cfu mL^{-1} and applied to microtitration plates with serially diluted compounds in DMSO to be tested and incubated at 37 °C for 24 h. After the MICs were visually determined on each of the microtitration plates, 50 μL of PBS (Phosphate Buffered Saline 0.01 mol L^{-1}, pH 7.4: $Na_2HPO_4 \cdot 12H_2O$ 2.9 g, KH_2PO_4 0.2 g, NaCl 8.0 g, KCl 0.2 g, distilled water 1000 mL) containing 2 mg of MTT was added to each well. Incubation was continued at room temperature for 4–5 h. The content of each well was removed, and 100 μL of isopropyl alcohol containing 5% 1.0 mol L^{-1} HCl was added to extract the dye. After 12 h of incubation at room temperature, the optical density (OD) was measured with a microplate reader at 550 nm.

3. Results and Discussion

The complexes were readily prepared by the reaction of the Schiff bases and zinc nitrate in methanol (Scheme 2).

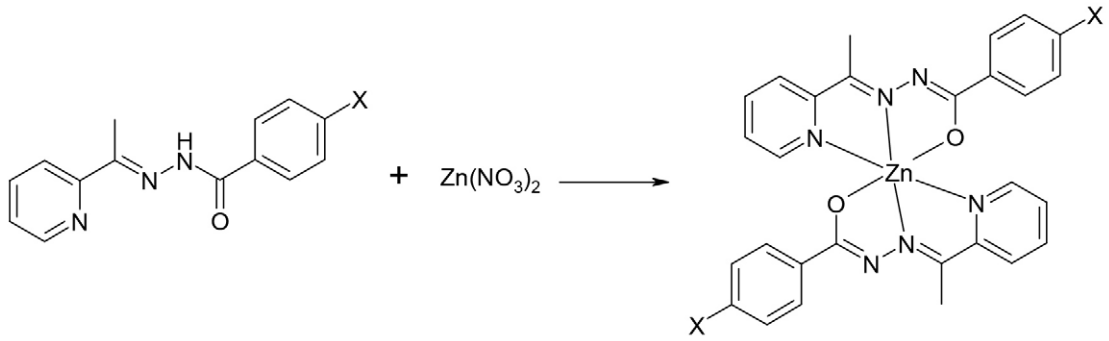

Scheme 2. Synthetic procedure of the complexes. X = OCH_3 for **1**, and H for **2**.

3. 1. Crystal Structure Description

Molecular structures of complexes **1** and **2** are shown in Figures 1 and 2, respectively. The Zn atom in each complex is coordinated by two hydrazone ligands, to form octahedral coordination geometry. The hydrazone ligand coordinates to the Zn atom through the pyridine nitrogen, imino nitrogen and enolate oxygen atoms. The coordinate bond lengths in the two complexes are comparable to each other, and also similar to those observed in zinc complexes with similar ligands.[8] The hydrazone ligands adopt *trans* configuration with respect to the methylidene unit. The shorter distances of the C–N bonds and the longer distances of the C–O bonds for the –C(O)–NH– units than usual, suggest conjugation effect in the hydrazone molecules. The dihedral angles among the benzene rings and the pyridine rings of the hydrazone ligands are 3.4(5)° and 20.9(5)° for **1**, and 7.4(3)° and 19.5(3)° for **2**.

3. 2. IR and Electronic Spectra

In the spectra of the complexes, the characteristic absorption of the ν(C=N) vibrations are located at 1602 cm^{-1} for **1** and 1595 cm^{-1} for **2**.[9] In the UV–Vis spectra of the complexes, the absorptions centered about 270 nm and 320 nm are attributed to the π–π^* and n–π^* transitions of the azomethine chromophores.[10] The absorptions cen-

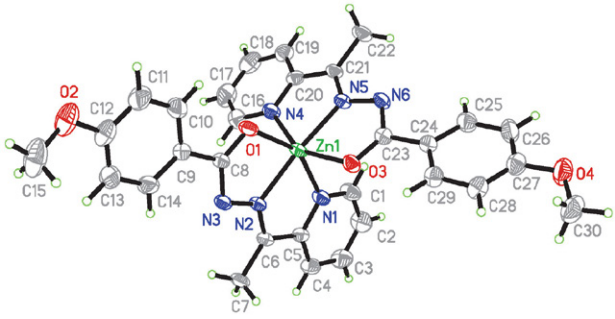

Figure 1. Molecular structures of complex **1** with ellipsoids at 30% probability.

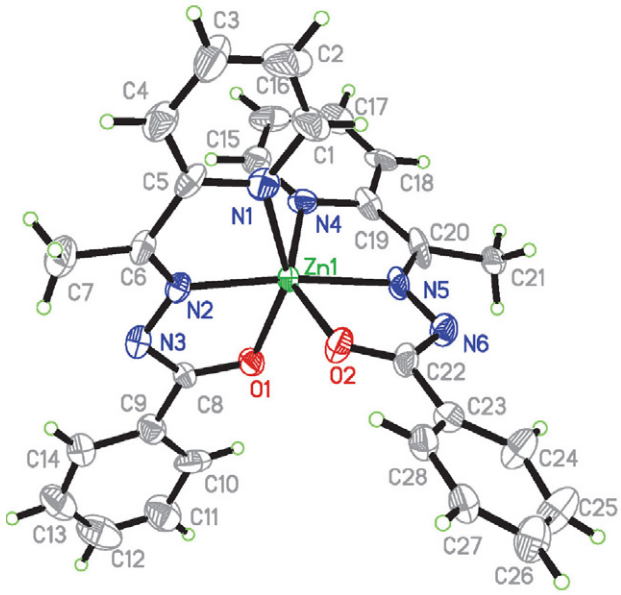

Figure 2. Molecular structures of complex **2** with ellipsoids at 30% probability.

tered about 370 nm may attribute to the ligand to metal charge transfer.

3. 3. Antibacterial Activity

The Schiff bases and the two complexes were screened *in vitro* for antibacterial activities against *Bacillus subtilis*, *Staphylococcus aureus*, *Escherichia coli*, and *Pseudomonas fluorescens* by the MTT method. The MICs of the compounds against the bacteria are presented in Table 3. Penicillin was used as reference drug.

Table 3. Antibacterial results (MIC (μg mL^{-1})).

Compound	*Bacillus subtilis*	*Staphylococcus aureus*	*Escherichia coli*	*Pseudomonas fluorescens*
HL^1	43.1	18.5	32.6	> 100
HL^2	63.7	32.8	51.2	> 100
1	10.2	7.8	15.4	28.5
2	17.8	19.2	27.5	45.3
Penicillin	1.3	2.1	> 100	> 100

The Schiff base HL^1 shows medium antibacterial activities against *Staphylococcus aureus*, weak activities against *Bacillus subtilis* and *Escherichia coli*, and no activity against *Pseudomonas fluorescens*. The Schiff base HL^2 shows weak activities against *Bacillus subtilis*, *Staphylococcus aureus* and *Escherichia coli*, and no activity against *Pseudomonas fluorescens*. In general, the zinc complexes have stronger activities against all bacteria than the free Schiff bases. The antibacterial activities of complex **1** are better than those of complex **2**. Complex **1** shows strong activities against *Bacillus subtilis* and *Staphylococcus aureus*, medium activity against *Escherichia coli*, and weak activities against *Pseudomonas fluorescens*. Complex **2** shows medium activities against *Bacillus subtilis*, *Staphylococcus aureus* and *Escherichia coli*, and weak activity against *Pseudomonas fluorescens*. As for *Escherichia coli* and *Pseudomonas fluorescens*, both complexes have more activities than Penicillin, which deserves further investigation.

4. Conclusion

We report the syntheses and crystal structures of two new mononuclear zinc(II) complexes with tridentate hydrazone ligands. The Zn atoms are in octahedral coordination. Both complexes have effective activities against the bacteria *Bacillus subtilis*, *Staphylococcus aureus*, *Escherichia coli* and *Pseudomonas fluorescens*.

Supplementary material

CCDC reference numbers 1578771 (**1**) and 1578772 (**2**) contain the supplementary crystallographic data for this paper. These data can be obtained free of charge at www.ccdc.cam.ac.uk, or from Cambridge Crystallographic Data Center, 12, Union Road, Cambridge CB2 1EZ, UK; Fax: +44 1223 336 033; e-mail: deposit@ccdc.cam.ac.uk.

Acknowledgments

We gratefully acknowledge the financial support by the Research Program of Science and Technology at Universities of Inner Mongolia Autonomous Region (NJZY239) and Inner Mongolia Key Laboratory of Photoelectric Functional Materials.

5. References

1. (a) Z. H. Chohan, M. ul-Hassan, K. M. Khan, C. T. Supuran. *J. Enzyme Inhib. Med. Chem.* **2005**, *20*, 183–188; **DOI:**10.1080/14756360500043257
(b) J. Zhang, F. Pan, H. Cheng, W. Du. *Russ. J. Coord. Chem.* **2010**, *36*, 514–519; **DOI:**10.1134/S1070328410070067
(c) A. Iqbal, H. L. Siddiqui, C. M. Ashraf, M. H. Bukhari, C. M. Akram. *Chem. Pharm. Bull.* **2007**, *55*, 1070–1072. **DOI:**10.1248/cpb.55.1070
2. (a) A. Lalehzari, J. Desper, C. J. Levy. *Inorg. Chem.* **2008**, *47*, 1120–1126; **DOI:**10.1021/ic702015u
(b) L. Xu, Y. Li, M. Duan, Y. Li, M. Han, J. Wu, Y. Wang, K. Dong, Z. You. *Polyhedron* **2019**, *165*, 138–142; **DOI:**10.1016/j.poly.2019.03.016
(c) Y. Li, L. Xu, M. Duan, B. Zhang, Y. Wang, Y. Guan, J. Wu, C. Jing, Z. You. *Polyhedron* **2019**, *166*, 146–152; **DOI:**10.1016/j.poly.2019.03.051
(d) M. Duan, Y. Li, L. Xu, H. Yang, F. Luo, Y. Guan, B. Zhang, C. Jing, Z. You. *Inorg. Chem. Commun.* **2019**, *100*, 27–31. **DOI:**10.1016/j.inoche.2018.12.009
3. (a) G. B. Bagihalli, P. G. Avaji, S. A. Patil, P. S. Badami. *Eur. J. Med. Chem.* **2008**, *43*, 2639–2649; **DOI:**10.1016/j.ejmech.2008.02.013
(b) Z. H. Chohan, M. Arif, A. Rashid. *J. Enzyme Inhib. Med. Chem.* **2008**, *23*, 785–796; **DOI:**10.1080/14756360701450145
(c) Z. H. Chohan, M. Arif, Z. Shafiq, M. Yaqub, C. T. Supuran. *J. Enzyme Inhib. Med. Chem.* **2006**, *21*, 95–103; **DOI:**10.1080/14756360500456806
(d) Y. Li, L. Xu, M. Duan, J. Wu, Y. Wang, K. Dong, M. Han, Z. You. *Inorg. Chem. Commun.* **2019**, *105*, 212–216; **DOI:**10.1016/j.inoche.2019.05.011

(e) Z. You, H. Yu, B. Zheng, C. Zhang, C. Lv, K. Li, L. Pan. *Inorg. Chim. Acta* **2018**, *469*, 44–50; **DOI:**10.1016/j.ica.2017.09.011
(f) H.-L. Zhu, X.-Z. Zhang, Y. Gu, A. Liu, F. Liu, Z. You, Y. Li. *Acta Chim. Slov.* **2016**, *63*, 721–725.
4. (a) M. Zhang, D.-M. Xian, H.-H. Li, J.-C. Zhang, Z.-L. You. *Aust. J. Chem.* **2012**, *65*, 343–350; **DOI:**10.1071/CH11424
(b) P. G. Avaji, C. H. V. Kumar, S. A. Patil, K. N. Shivananda, C. Nagaraju. *Eur. J. Med. Chem.* **2009**, *44*, 3552–3559; **DOI:**10.1016/j.ejmech.2009.03.032
(c) M. J. Hearn, M. H. Cynamon, M. F. Chen, R. Coppins, J. Davis, H. J.-O. Kang, A. Noble, B. Tu-Sekine, M. S. Terrot, D. Trombino, M. Thai, E. R. Webster, R. Wilson. *Eur. J. Med. Chem.* **2009**, *44*, 4169–4178. **DOI:**10.1016/j.ejmech.2009.05.009
5. Bruker. *SMART and SAINT.* Bruker AXS, Madison, WI, 2002.
6. G. M. Sheldrick. *SADABS. Program for Empirical Absorption Correction of Area Detector;* University of Göttingen, Germany, 1996.
7. G. M. Sheldrick. *SHELXTL V5.1 Software Reference Manual*; Bruker AXS, Inc., Madison, WI, 1997.
8. (a) H.-H. Li, Z.-L. You, C.-L. Zhang, M. Yang, L.-N. Gao, L. Wang. *Inorg. Chem. Commun.* **2013**, *29*, 118–122; **DOI:**10.1016/j.inoche.2012.12.023
(b) Z.-L. You, M. Zhang, D.-M. Xian. *Dalton Trans.* **2012**, *41*, 2515–2524; **DOI:**10.1039/c1dt11566a
(c) S. Basak, S. Sen, S. Banerjee, S. Mitra, G. Rosair, M. T. G. Rodriguez. *Polyhedron* **2007**, *26*, 5104–5112. **DOI:**10.1016/j.poly.2007.07.025
9. X.-M. Hu, L.-W. Xue, G.-Q. Zhao, Y.-J. Han. *Synth. React. Inorg. Met.-Org. Nano-Met. Chem.* **2012**, *42*, 557-562. **DOI:**10.1080/15533174.2011.613884
10. L.-W. Xue, X. Wang, G.-Q. Zhao. *Synth. React. Inorg. Met.-Org. Nano-Met. Chem.* **2012**, *42*, 1334-1338. **DOI:**10.1080/15533174.2012.680139

Povzetek

Sintetizirali smo dva nova enojedrna cinkova(II) kompleksa s hidrazonskima ligandoma 4-metoksibenzojsko kislino (1-piridin-2-ilmetiliden)hidrazidom (HL^a) in benzojsko kislino (1-piridin-2-iletiliden)hidrazidom (HL^b), $[Zn(L^a)_2]$ (**1**) in $[Zn(L^b)_2]$ (**2**). Kompleksa sta bila okarakterizirana s fiziko-kemijskimi metodami in monokristalno rentgensko difrakcijo. Tridentatna hidrazonska liganda se koordinirata na Zn atom preko piridinskega dušikovega atoma, iminskega dušikovega atoma in enolatnega kisikovega atoma. Zn atom v obeh kompleksih ima koordinacijsko število šest in je koordiniran z dvema hidrazonskima ligandoma v oktaedrični geometriji. Kompleksa sta učinkovita proti bakterijam *Bacillus subtilis*, *Staphylococcus aureus*, *Escherichia coli* in *Pseudomonas fluorescens*.

Except when otherwise noted, articles in this journal are published under the terms and conditions of the Creative Commons Attribution 4.0 International License

DOI: 10.17344/acsi.2019.5601 *Acta Chim. Slov.* **2020,** *67,* 586–593
creative commons

Scientific paper

A Simple and Convenient Method for the Synthesis of 1-Methyl-7-arylfuro[3,2-*g*]pteridine-2,4(1*H*,3*H*)-diones and Their Substituted Derivatives

Maxim Stanislavovich Kazunin,[1] Oleksii Yurievich Voskoboynik,[1] Svetlana Valentynivna Shishkina,[2] Oleksii Mykolayovych Antypenko[1] and Sergey Ivanovich Kovalenko[1,*]

[1] *The Department of Organic and Bioorganic Chemistry, Zaporizhzhia State Medical University, 26 Maiakovski Ave., Zaporizhzhia, 69035, Ukraine*

[2] *State Scientific Institution «Institute for Single Crystals» of National Academy of Sciences of Ukraine, 60 Nauki Ave., Kharkov, 61000, Ukraine*

* *Corresponding author: E-mail: kovalenkosergiy@gmail.com*

Received: 09-23-2019

Abstract

A simple and effective method for the synthesis of unknown 1-methyl-7-arylfuro[3,2-*g*]pteridine-2,4(1*H*,3*H*)-diones by dehydration of the corresponding 1-methyl-6-phenacyl-pteridine-2,4,7(1*H*,3*H*,8*H*)-triones is reported in the article. It was shown that their alkylation by butyl chloroacetate in basic medium proceeded by the N_3-atom of the heterocycle. The structure and purity of the synthesized compounds were confirmed by IR, ^{1}H, ^{13}C NMR spectroscopy, gas chromatography-mass spectrometry, mass spectrometry, as well as X-ray diffraction analysis. The proposed mechanism of the dehydration reaction was discussed.

Keywords: 1-methyl-6-(2-oxo-2-arylethyl)pteridine-2,4,7(1*H*,3*H*,8*H*)-triones; dehydration; 1-methyl-7-arylfuro[3,2-*g*]pteridine-2,4(1*H*,3*H*)-diones; alkylation; X-ray diffraction analysis

1. Introduction

Condensed heterocyclic derivatives of pteridines belong to the important, but insufficiently studied group of organic substances. Although, the methods for the synthesis of annelated pteridines were systematized in few monographs[1,2] and reviews,[3–5] research devoted to the synthesis of condensed pteridines continues due to their high biological activity. Antimicrobial,[6,7] anticancer,[8–10] anti-inflammatory and analgesic activities[11,12] of condensed pteridines as well as their ability to inhibit PLK1 kinase[13,14] have been described. Besides, these substances could be used as functional materials as shown in previous reports.[15–17] The furo[3,2-*g*]pteridine system was not mentioned in the scientific literature, however methods for the isomeric furo[2,3-*g*]pteridines synthesis are known.[3]

Based on the above, the purpose of this work consists in developing a simple and convenient method for the synthesis of 1-methyl-7-arylfuro[3,2-*g*]pteridine-2,4(1*H*,3*H*)-diones by dehydration of 1-methyl-6-(2-oxo-2-arylethyl)pteridine-2,4,7(1*H*,3*H*,8*H*)-triones.

2. Experimental Part

2. 1. Chemistry

Melting points were determined in open capillary tubes in a Mettler Toledo MP 50 apparatus and are uncorrected. The elemental analyses (C, H, N) were performed using the ELEMENTAR vario EL cube analyzer (USA) and are within ±0.3% of the theoretical values. IR spectra (4000–600 cm^{-1}) were recorded on a Bruker ALPHA FT-IR spectrometer (Bruker Bioscience, Germany) using a module for measuring attenuated total reflection (ATR). ^{1}H NMR spectra (400 MHz) were recorded on a Varian-Mercury 400 (Varian Inc., Palo Alto, CA, USA) spectrometers with TMS as internal standard in DMSO-d_6 solution. ^{13}C NMR spectra of compounds (**3b–e**, **3g–j**, 100 MHz) were recorded in TFA-d_1 solution. LC-MS were re-

corded using chromatography/mass spectrometric system which consists of high performance liquid chromatography Agilent 1100 Series (Agilent, Palo Alto, CA, USA) equipped with diode-matrix and mass-selective detector Agilent LC/MSD SL (atmospheric pressure chemical ionization – APCI). Electron impact mass spectra (EI-MS) were recorded on a Varian 1200 L instrument at 70 eV (Varian, USA).

Compounds **1a–k** (1-methyl-6-(2-oxo-2-arylethyl) pteridine-2,4,7(1*H*,3*H*,8*H*)-triones) were obtained according to the previously described method.[18] For the experiment commercially available reagents from Merck (Darmstadt, Germany), Sigma-Aldrich (Missouri, USA) and Enamine (Kyiv, Ukraine) were used.

General Method for the Synthesis of 1-Methyl-7-arylfuro[3,2-*g*]pteridine-2,4(1*H*,3*H*)-diones 2a–k. A suspension of 10 mmol of the corresponding 1-methyl-6-(2-oxo-2-arylethyl)pteridine-2,4,7(1*H*,3*H*,8*H*)-trione **1a–k** in 20 mL of polyphosphoric acid was heated to 130 °C and stirred for 1 hour. Afterwards, the reaction mixture was cooled, poured into 100 mL of water and stirred. The precipitate formed was filtered off, washed with water and dried.

1-Methyl-7-phenylfuro[3,2-*g*]pteridine-2,4(1*H*,3*H*)-dione (2a). Yield: 2.35 g (75%), light yellow compound, mp > 300 °C; IR (cm^{-1}): 1698, 1504, 1340, 1274, 1178, 1058, 1010, 895, 831, 781, 761, 694, 670; ^{1}H NMR δ (ppm): 11.75 (s, 1H, 3-NH), 8.01 (d, *J* = 7.3 Hz, 2H, Ar H-2,6), 7.67 (s, 1H, H-6), 7.56–7.12 (m, 3H, Ar H-3,4,5), 3.60 (s, 3H, 1-N-CH_3); EI-MS *m/z* (*I*% rel): 295 (13.6), 294 ($M^{+\bullet}$, 66.8), 251 (12.6), 224 (18.2), 223 (100), 222 (11.5), 196 (11.9), 180 (5.6), 168 (5.2), 167 (5.9), 154 (16.9), 153 (8.3), 140 (24.8), 139 (9.8), 129 (8.4), 128 (11.0), 127 (24.5), 126 (9.6), 105 (27.6), 103 (12.7), 102 (21.8), 92 (10.1), 77 (25.3), 76 (6.9), 70 (12.6), 67 (16.8), 63 (5.0), 44 (76.2), 43 (15.9), 42 (6.9), 41 (10.6), 40 (7.0); LC-MS *m/z* = 294 $[M+H]^+$. Anal. Calcd. for $C_{15}H_{10}N_4O_3$: C, 61.22; H, 3.43; N, 19.04; found: C, 61.27; H, 3.48; N, 19.09.

1-Methyl-7-(*para*-tolyl)-furo[3,2-*g*]pteridine-2,4(1*H*,3*H*)-dione (2b). Yield: 2.49 g (81%), light yellow compound, mp > 300 °C; IR (cm^{-1}): 1681, 1506, 1342, 1274, 1179, 1060, 894, 863, 822, 804, 752, 670, 612; ^{1}H NMR δ (ppm): 11.74 (s, 1H, 3-NH), 7.89 (d, *J* = 7.5 Hz, 2H, Ar H-2,6), 7.57 (s, 1H, H-6), 7.34 (d, *J* = 7.4 Hz, 2H, Ar H-3,5), 3.59 (s, 3H, 1-N-CH_3), 2.44 (s, 3H, $ArCH_3$); LC-MS *m/z* = 308 $[M+H]^+$. Anal. Calcd. for $C_{16}H_{12}N_4O_3$: C, 62.33; H, 3.92; N, 18.17; found: C, 62.39; H, 3.98; N, 18.22.

7-(4-Isopropylphenyl)-1-methylfuro[3,2-*g*]pteridine-2,4(1*H*,3*H*)-dione (2c). Yield: 2.75 g (82%), light yellow compound, mp > 300 °C; IR (cm^{-1}): 1680, 1503, 1339, 1270, 1059, 801, 746; ^{1}H NMR δ (ppm): 11.88 (s, 1H, 3-NH), 7.91 (d, *J* = 7.5 Hz, 2H, Ar-H-2,6), 7.62 (s, 1H, H-6), 7.38 (d, *J* = 7.5 Hz, 2H, Ar H-3,5), 3.58 (s, 3H, 1-N-CH_3), 3.07–2.88 (m, 1H, $\underline{CH}(CH_3)_2$), 1.30 (d, *J* = 6.4 Hz, 6H, $CH(\underline{CH_3})_2$); LC-MS *m/z* = 336 $[M+H]^+$. Anal. Calcd. for $C_{18}H_{16}N_4O_3$: C, 64.28; H, 4.79; N, 16.66; found: C, 64.33; H, 4.84; N, 16.71.

1-Methyl-7-(2-fluorophenyl)furo[3,2-*g*]pteridine-2,4(1*H*,3*H*)-dione (2d). Yield: 2.41 g (77%), light yellow compound, mp > 300 °C; IR (cm^{-1}): 1696, 1488, 1338, 1263, 1175, 1056, 1008, 895, 808, 777, 762, 745, 652; ^{1}H NMR δ (ppm): 11.96 (s, 1H, 3-NH), 8.24–8.02 (m, 1H, Ar H-6), 7.70–7.50 (m, 2H, H-6, Ar H-4), 7.47–7.28 (m, 2H, Ar H-3,5), 3.60 (s, 3H, 1-N-CH_3); LC-MS *m/z* = 312 $[M+H]^+$. Anal. Calcd. for $C_{15}H_9FN_4O_3$: C, 57.70; H, 2.91; N, 17.94; found: C, 57.76; H, 2.30; N, 17.99.

1-Methyl-7-(4-fluorophenyl)furo[3,2-*g*]pteridine-2,4(1*H*,3*H*)-dione (2e). Yield: 2.55 g (82%), light yellow compound, mp > 300 °C; IR (cm^{-1}): 3048, 1713, 1683, 1603, 1505, 1435, 1345, 1274, 1236, 1162, 1059, 893, 843, 805, 747, 611; ^{1}H NMR δ (ppm): 11.91 (s, 1H, 3-NH), 8.10–8.02 (m, 2H, Ar H-2,6), 7.73 (s, 1H, H-6), 7.37–7.21 (m, 2H, Ar H-3,5), 3.57 (s, 3H, 1-N-CH_3); LC-MS *m/z* = 312 $[M+H]^+$. Anal. Calcd. for $C_{15}H_9FN_4O_3$: C 57.70; H, 2.91; N, 17.94; found: C, 57.76; H, 2.97; N, 17.98.

7-(2,4-Difluorophenyl)-1-methylfuro[3,2-*g*]pteridine-2,4 (1*H*,3*H*)-dione (2f). Yield: 2.57 g (78%), light yellow compound, mp > 300 °C; ^{1}H NMR δ (ppm): 11.83 (s, 1H, 3-NH), 8.18–7.96 (m, 2H, Ar H-6), 7.49 (s, 1H, H-6), 7.33–7.08 (m, 2H, Ar 3,5), 3.58 (s, 3H, 1-N-CH_3); LC-MS *m/z* = 330 $[M+H]^+$. Anal. Calcd. for $C_{15}H_8F_2N_4O_3$: C, 54.55; H, 2.44; N, 16.97; found: C, 54.61; H, 2.50; N, 17.02.

1-Methyl-7-(4-chlorophenyl)-furo[3,2-*g*]pteridine-2,4(1*H*,3*H*)-dione (2g). Yield: 2.59 g (79%), light yellow compound, mp > 300 °C; IR (cm^{-1}): 3047, 1716, 1689, 1504, 1433, 1342, 1288, 1177, 1090, 1059, 1003, 893, 841, 826, 805, 751; ^{1}H NMR δ (ppm): 11.86 (s, 1H, 3-NH), 8.03 (d, *J* = 8.9 Hz, 2H, Ar H-2,6), 7.78 (s, 1H, H-6), 7.54 (d, *J* = 9.3 Hz, 2H, Ar H-3,5), 3.58 (s, 3H, 1-N-CH_3); LC-MS *m/z* = 328 $[M+H]^+$. Anal. Calcd. for $C_{15}H_9ClN_4O_3$: C, 54.81; H, 2.76; N, 17.04; found: C, 54.88; H, 2.81; N, 17.09.

7-(4-Bromophenyl)-1-methylfuro[3,2-*g*]pteridine-2,4(1*H*,3*H*)-dione (2h). Yield: 3.09 g (83%), light yellow compound, mp > 300 °C; IR (cm^{-1}): 3054, 1691, 1503, 1340, 1286, 1059, 1001, 893, 837, 822, 803, 749; ^{1}H NMR δ (ppm): 11.44 (s, 1H, 3-NH), 7.98 (d, *J* = 7.3 Hz, 2H, Ar H-2,6), 7.84 (s, 1H, H-6), 7.71 (d, *J* = 7.4 Hz, 2H, Ar H-3,5), 3.59 (s, 3H, 1-N-CH_3); LC-MS *m/z* = 373 $[M+H]^+$. Anal. Calcd. for $C_{15}H_9BrN_4O_3$: C, 48.28; H, 2.43; N, 15.01; found: C, 48.32; H, 2.49; N, 15.08.

1-Methyl-7-(3-nitrophenyl)furo[3,2-*g*]pteridine-2,4(1*H*,3*H*)-dione (2i). Yield: 2.74 g (81%), light brown com-

pound, mp > 300 °C; IR (cm^{-1}): 1681, 1527, 1503, 1342, 1291, 1270, 1187, 1059, 914, 850, 807, 740, 725, 681; ^{1}H NMR δ (ppm): 11.98 (s, 1H, 3-NH), 8.86 (s, 1H, Ar H-2), 8.48 (d, *J* = 8.6 Hz, 1H, Ar H-6), 8.33 (d, *J* = 7.4 Hz, 1H, Ar H-4), 8.14 (s, 1H, H-6), 7.86 (t, *J* = 8.8 Hz, 1H, Ar H-5), 3.60 (s, 3H, 1-N-CH_3); LC-MS *m/z* = 339 $[M+H]^+$. Anal. Calcd. for $C_{15}H_9N_5O_5$: C, 53.10; H, 2.67; N, 20.64; found C, 53.17; H, 2.73; N, 20.69.

1-Methyl-7-(naphthalen-2-yl)-furo[3,2-*g*]pteridine-2,4(1*H*,3*H*)-dione (2j). Yield: 2.85 g (83%), light orange substance, mp > 300 °C; IR (cm^{-1}): 3047, 1728, 1674, 1507, 1468, 1346, 1283, 1266, 1215, 1060, 947, 833, 748, 711, 662; ^{1}H NMR δ (ppm): 12.03 (s, 1H, 3-NH), 8.80 (s, 1H, naphthalene H-1), 8.11–7.14 (m, 7H, H-6, naphthalene H-3,4,5,6,7,8), 3.61 (s, 3H, 1-N-CH_3); LC-MS *m/z* = 344 $[M+H]^+$. Anal. Calcd. for $C_{19}H_{12}N_4O_3$: C, 66.28; H, 3.51; N, 16.2; found: C, 66.34; H, 3.58; N, 16.32.

7-(4-Methoxyphenyl)-1-methylfuro[3,2-*g*]pteridine-2,4(1*H*,3*H*)-dione (2k). Yield: 2.65 g (82%), light yellow compound, mp > 300 °C; IR (cm^{-1}): 1714, 1681, 1600, 1504, 1340, 1286, 1259, 1175, 1057, 1014, 893, 843, 798, 748, 614; ^{1}H NMR δ (ppm): 11.86 (s, 1H, 3-NH), 7.95 (d, *J* = 7.3 Hz, 2H, Ar H-2,6), 7.53 (s, 1H, H-6), 7.06 (d, *J* = 8.8 Hz, 2H, Ar H-3,5), 3.88 (s, 3H, OCH_3), 3.57 (s, 3H, 1-N-CH_3); LC-MS *m/z* = 324 $[M+H]^+$. Anal. Calcd. for $C_{16}H_{12}N_4O_4$: C, 59.26; H, 3.73; N, 17.28; found: C, 59.31; H, 3.79; N, 17.32.

General Method for the Synthesis of Butyl 2-(7-Aryl-2,4-dioxo-1-methyl-1,4-dihydrofuro[3,2-*g*]pteridine-3(2*H*)-yl)acetates 3a–j. To a suspension of 10 mmol of the corresponding 1-methyl-7-arylfuro[3,2-*g*]pteridine-2,4(1*H*,3*H*)-dione **2a–k** and 10 mmol of K_2CO_3 in 30 mL of dimethylformamide, 10 mmol of butyl chloroacetate was added and refluxed for 2 hours. The reaction mixture was cooled, poured into 100 mL of water and stirred. The precipitate formed was filtered off, washed with water, dried and crystallized from dimethylformamide.

Butyl 2-(2,4-Dioxo-1-methyl-7-phenyl-1,4-dihydrofuro[3,2-*g*]pteridine-3(2*H*)-yl)acetate (3a). Yield: 3.34 g (81%), light yellow compound, mp: 297–299 °C; IR (cm^{-1}): 1750, 1715, 1675, 1562, 1508, 1360, 1279, 1200, 1008, 931, 893, 803, 770, 755, 688; ^{1}H NMR δ (ppm): 8.03 (d, *J* = 7.3 Hz, 2H, Ar H-2,6), 7.78 (s, 1H, H-6), 7.62–7.46 (m, 3H, Ar H-3,4,5), 4.73 (s, 2H, NCH_2), 4.15 (t, *J* = 6.5 Hz, 2H, O$\underline{CH_2}$ $CH_2CH_2CH_3$), 3.69 (s, 3H, 1-N-CH_3), 1.78–1.52 (m, 2H, $OCH_2\underline{CH_2}CH_2CH_3$), 1.52–1.20 (m, 2H, $OCH_2CH_2\underline{CH_2}$ CH_3), 0.95 (t, *J* = 7.3 Hz, 3H, $OCH_2CH_2CH_2\underline{CH_3}$); EI-MS *m/z* (*I*% rel): 409 (11.6), 408 (46.6), 352 (10.6), 309 (8.0), 308 (31.9), 307 (30.2), 279 (8.7), 251 (9.5), 249 (5.3), 224 (60), 223 (23.9), 167 (6.4), 140 (10.2), 105 (8.8), 86 (34.3), 84 (49.5), 83 (8.9), 57 (17.3), 56 (18.4), 51 (29.5), 50 (6.8), 49 (100), 48 (11.8), 47 (15.6), 44 (8.9), 43 (6.8), 42 (5.9), 41 (36.4); LC-MS *m/z* = 408 $[M+H]^+$. Anal. Calcd. for $C_{21}H_{20}N_4O_5$: C, 61.76; H, 4.94; N, 13.72; found C, 61.81; H, 5.01; N, 13.77.

Butyl 2-(2,4-Dioxo-1-methyl-7-(*p*-tolyl)-1,4-dihydrofuro[3,2-*g*]pteridine-3(2*H*)-yl)acetate (3b). Yield: 3.21 g (76%), light yellow compound, mp: 295–297 °C; IR (cm^{-1}): 1754, 1714, 1674, 1505, 1453, 1360, 1279, 1195, 1000, 932, 892, 818, 801, 756; ^{1}H NMR δ (ppm): 7.93 (d, *J* = 7.5 Hz, 2H, Ar H-2,6), 7.69 (s, 1H, H-6), 7.36 (d, *J* = 6.9 Hz, 2H, Ar H-3,5), 4.74 (s, 2H, NCH_2), 4.17 (t, *J* = 6.4 Hz, 2H, O$\underline{CH_2}$ $CH_2CH_2CH_3$), 3.70 (s, 3H, 1-N-CH_3), 2.46 (s, 3H, $ArCH_3$), 1.86–1.55 (m, 2H, $OCH_2\underline{CH_2}CH_2CH_3$), 1.46–1.36 (m, 2H, $OCH_2CH_2\underline{CH_2}CH_3$), 0.97 (t, *J* = 6.8 Hz, 3H, OCH_2CH_2 $CH_2\underline{CH_3}$); ^{13}C NMR δ (ppm): 172.7 (COO), 170.1 (C-8a), 157.5 (C-4), 150.3 (C-7), 148.3 (C-2), 145.7 (C-9a), 135.5 (C-5a), 130.4 (Ar C-2,6), 127.8 (Ar C-3,5), 122.5 (Ar C-1), 117.6 (C-4a), 113.8 (Ar C-4), 95.1 (C-6), 68.2 (O$\underline{CH_2}CH_2$ CH_2CH_3), 43.5 (NCH_2CO), 30.0 (N-CH_3), 29.7 (OCH_2 $\underline{CH_2}CH_2CH_3$), 20.2 (Ar-CH_3), 18.2 ($OCH_2CH_2\underline{CH_2}CH_3$), 11.7 ($OCH_2CH_2CH_2\underline{CH_3}$); LC-MS *m/z* = 422 $[M+H]^+$. Anal. Calcd. for $C_{22}H_{22}N_4O_5$: C, 62.55; H, 5.25; N, 13.26; found: C, 62.59; H, 5.29; N, 13.31.

Butyl 2-(2,4-Dioxo-7-(4-isopropylphenyl)-1-methyl-1,4-dihydrofuro[3,2-*g*]pteridine-3(2*H*)-yl)acetate (3c). Yield: 3.46 g (77%), light yellow compound, mp: 288–291 °C; IR (cm^{-1}): 2957, 1761, 1724, 1667, 1512, 1455, 1362, 1282, 1157, 1006, 894, 843, 805, 755; ^{1}H NMR δ (ppm): 7.95 (d, *J* = 8.1 Hz, 2H, Ar H-2,6), 7.69 (s, 1H, H-6), 7.40 (d, *J* = 8.1 Hz, 2H, Ar H-3,5), 4.74 (s, 2H, NCH_2), 4.16 (t, *J* = 6.6 Hz, 2H, O$\underline{CH_2}CH_2CH_2CH_3$), 3.70 (s, 3H, 1-N-$CH_3$), 3.16–2.62 (m, 1H, $\underline{CH}(CH_3)_2$), 1.66 (m, 2H, $OCH_2\underline{CH_2}$ CH_2CH_3), 1.41 (m, 2H, $OCH_2CH_2\underline{CH_2}CH_3$), 1.31 (d, *J* = 6.8 Hz, 6H, $CH(\underline{CH_3})_2$), 0.97 (t, *J* = 7.3 Hz, 3H, OCH_2CH_2 $CH_2\underline{CH_3}$); ^{13}C NMR δ (ppm): 168.1 (COO, C-8a), 161.4 (C-4), 159.1 (C-7), 155.7 (Ar C-4), 152.2 (C-2), 150.1 (C-9a), 145.6 (C-5a), 139.0 (C-4a), 127.7 (Ar C-2,6), 125.9 (Ar C-3,5), 125.0 (Ar C-1), 116.0 (C-4a), 101.4 (C-6), 65.3 (O$\underline{CH_2}CH_2CH_2CH_3$), 43.2 ($NCH_2CO$), 33.9 ($\underline{CH}(CH_3)_2$), 30.5 ($OCH_2\underline{CH_2}CH_2CH_3$), 30.0 (N-$CH_3$), 23.9 (CH $(\underline{CH_3})_2$), 18.9 ($OCH_2CH_2\underline{CH_2}CH_3$), 13.9 ($OCH_2CH_2CH_2$ $\underline{CH_3}$); LC-MS *m/z* = 450 $[M+H]^+$. Anal. Calcd. for $C_{24}H_{26}N_4O_5$: C, 63.99; H, 5.82; N, 12.44; found: C, 64.04; H, 5.87; N, 12.49.

Butyl 2-(2,4-Dioxo-1-methyl-7-(2-fluorophenyl)-1,4-dihydrofuro[3,2-*g*]pteridine-3(2*H*)-yl)acetate (3d). Yield: 3.24 g (76%), light yellow compound, mp > 300 °C; IR (cm^{-1}): 1752, 1720, 1676, 1504, 1456, 1361, 1276, 1199, 894, 772, 752; ^{1}H NMR δ (ppm): 8.22–7.84 (m, 1H, Ar H-6), 7.63–7.49 (m, 2H, H-6, Ar H-4), 7.46–7.23 (m, 2H, Ar H-3,5), 4.74 (s, 2H, NCH_2), 4.17 (t, *J* = 6.6 Hz, 2H, O$\underline{CH_2}CH_2CH_2CH_3$), 3.69 (s, 3H, 1-N-$CH_3$), 1.67 (quintet, *J* = 6.9 Hz, 2H, $OCH_2\underline{CH_2}CH_2CH_3$), 1.42 (sextet, *J* = 7.3 Hz, 2H, $OCH_2CH_2\underline{CH_2}CH_3$), 0.97 (t, *J* = 7.3 Hz, 3H, OCH_2

$CH_2CH_2\underline{CH_3}$); ^{13}C NMR δ (ppm): 168.1 (COO, C-8a), 159.7 (d, *J* = 254.1 Hz, Ar C-2), 159.0 (C-4), 155.3 (d, *J* = 18.2 Hz, C-7), 150.1 (C-2), 146.0 (C-9a), 138.3 (C-5a), 133.1 (d, *J* = 8.9 Hz, Ar C-5), 127.5 (Ar C-6), 125.7 (d, *J* = 21.2 Hz, Ar C-1), 125.6 (C-4a), 117.1 (d, *J* = 20.7 Hz, Ar C-3), 116.4 (d, *J* = 11.0 Hz, Ar C-4), 106.4 (d, *J* = 12.2 Hz, C-6), 65.29 ($OCH_2CH_2CH_2CH_3$), 43.22 (NCH_2CO), 30.55 ($N\text{-}CH_3$), 30.12 ($OCH_2CH_2CH_2CH_3$), 18.94 ($OCH_2CH_2CH_2CH_3$), 13.95 ($OCH_2CH_2CH_2CH_3$); LC-MS *m/z* = 426 $[M+H]^+$. Anal. Calcd. for $C_{21}H_{19}FN_4O_5$: C, 59.15; H, 4.49; N, 13.14; found: C, 59.21; H, 4.53; N, 13.19.

Butyl 2-(2,4-Dioxo-1-methyl-7-(4-fluorophenyl)-1,4-dihydrofuro[3,2-*g*]pteridine-3(2*H*)-yl)acetate (3e). Yield: 3.36 g (79%), light yellow compound, mp > 300 °C; IR (cm^{-1}): 1719, 1679, 1603, 1502, 1359, 1279, 1194, 1157, 1007, 895, 833, 800, 755; ^{1}H NMR δ (ppm): 8.12 (d, *J* = 7.6 Hz, 2H, Ar H-2,6), 7.79 (s, 1H, H-6), 7.33 (t, *J* = 7.9 Hz, 2H, Ar H-3,5), 4.75 (s, 2H, NCH_2), 4.17 (t, *J* = 6.5 Hz, 2H, $O\underline{CH_2}CH_2CH_2CH_3$), 3.71 (s, 3H, 1-N-$CH_3$), 1.66 (quintet, *J* = 7.2 Hz, 2H, $OCH_2\underline{CH_2}CH_2CH_3$), 1.42 (m, 2H, $OCH_2CH_2\underline{CH_2}CH_3$), 0.97 (t, *J* = 7.2 Hz, 3H, $OCH_2CH_2CH_2\underline{CH_3}$); ^{13}C NMR δ (ppm): 170.4 (COO), 169.2(C-8a), 166.7 (d, *J* = 258.7 Hz, Ar C-4), 160.0 (C-4), 158.4 (C-7), 150.6 (C-2), 145.9 (C-9a), 136.6 (C-5a), 129.8 (d, *J* = 9.6 Hz, Ar C-2,6), 122.2 (d, *J* = 2.3 Hz, Ar C-1), 117.0 (C-4a), 116.9 (d, *J* = 23.1 Hz, Ar C-3,5), 96.6 (C-6), 68.2 ($O\underline{CH_2}CH_2CH_2CH_3$), 43.5 ($NCH_2CO$), 30.0 ($N\text{-}CH_3$), 29.7 ($OCH_2\underline{CH_2}CH_2CH_3$), 18.2 ($OCH_2CH_2\underline{CH_2}CH_3$), 11.7 ($OCH_2CH_2CH_2\underline{CH_3}$); LC-MS *m/z* = 426 $[M+H]^+$. Anal. Calcd. for $C_{21}H_{19}FN_4O_5$: C, 59.15; H, 4.49; N, 13.14; found: C, 59.20; H, 4.53; N, 13.19.

Butyl 2-(2,4-Dioxo-7-(2,4-difluorophenyl)-1-methyl-1,4-dihydrofuro[3,2-*g*]pteridine-3(2*H*)-yl)acetate (3f). Yield: 3.55 g (80%), light yellow compound, mp > 300 °C; IR (cm^{-1}): 1750, 1722, 1677, 1601, 1501, 1453, 1362, 1278, 1198, 893, 803, 774, 753; ^{1}H NMR δ (ppm): 8.32–8.05 (m, 1H, Ar H-6), 7.71 (s, 1H, H-6), 7.58–7.49 (m, 2H, Ar H-3,5), 4.76 (s, 2H, NCH_2), 4.21 (t, *J* = 6.6 Hz, 2H, $O\underline{CH_2}CH_2CH_2CH_3$), 3.70 (s, 3H, 1-N-$CH_3$), 1.71 (quintet, *J* = 6.9 Hz, 2H, $OCH_2\underline{CH_2}CH_2CH_3$), 1.44 (sextet, *J* = 7.3 Hz, 2H, $OCH_2CH_2\underline{CH_2}CH_3$), 1.00 (t, *J* = 7.3 Hz, 3H, $OCH_2CH_2CH_2\underline{CH_3}$); LC-MS *m/z* = 444 $[M+H]^+$. Anal. Calcd. for $C_{21}H_{18}F_2N_4O_5$: C, 56.76; H, 4.08; N, 12.61; found: C, 56.81; H, 4.13; N, 12.66.

Butyl 2-(2,4-Dioxo-1-methyl-7-(4-chlorophenyl)-1,4-dihydrofuro[3,2-*g*]pteridine-3(2*H*)-yl)acetate (3g). Yield: 3.44 g (78%), light yellow compound, mp > 300 °C; IR (cm^{-1}): 1751, 1719, 1679, 1509, 1361, 1275, 1198, 1019, 928, 893, 830, 802, 756; ^{1}H NMR δ (ppm): 8.08 (d, *J* = 9.2 Hz, 2H, Ar H-2,6), 7.87 (s, 1H, H-6), 7.58 (d, *J* = 9.4 Hz, 2H, Ar H-3,5), 4.75 (s, 2H, NCH_2), 4.47–4.03 (m, 2H, $O\underline{CH_2}CH_2CH_2CH_3$), 3.71 (s, 3H, 1-N-$CH_3$), 1.73–1.55 (m, 2H, $OCH_2\underline{CH_2}CH_2CH_3$), 1.50–1.36 (m, 2H, $OCH_2CH_2\underline{CH_2}CH_3$), 0.97 (t, 3H, $OCH_2CH_2CH_2\underline{CH_3}$); ^{13}C NMR δ (ppm): 170.5 (COO), 167.5 (C-8a), 159.3 (C-4), 159.1 (C-7), 150.7 (C-2), 145.9 (C-9a), 140.4 (Ar C-4), 137.4 (C-5a), 129.7 (Ar C-2,6), 127.8 (Ar C-3,5), 124.5 (Ar C-1), 118.3 (C-4a), 97.9 (C-6), 68.2 ($O\underline{CH_2}CH_2CH_2CH_3$), 43.5 ($NCH_2CO$), 29.9 ($N\text{-}CH_3$), 29.7 ($OCH_2\underline{CH_2}CH_2CH_3$), 18.2 ($OCH_2CH_2\underline{CH_2}CH_3$), 11.7 ($OCH_2CH_2CH_2\underline{CH_3}$); LC-MS *m/z* = 442 $[M+H]^+$. Anal. Calcd. for $C_{21}H_{19}ClN_4O_5$: C, 56.96; H, 4.32; N, 12.65; found: C, 57.01; H, 4.37; N, 12.69.

Butyl 2-(7-(4-Bromophenyl)-2,4-dioxo-1-methyl-1,4-dihydrofuro[3,2-*g*]pteridine-3(2*H*)-yl)acetate (3h). Yield: 3.79 g (78%), light yellow compound, mp > 300 °C; IR (cm^{-1}): 1748, 1718, 1678, 1505, 1453, 1361, 1275, 1203, 1058, 1005, 929, 894, 817, 801, 756; ^{1}H NMR δ (ppm): 8.01 (d, *J* = 9.0 Hz, 2H, Ar H-2,6), 7.89 (s, 1H, H-6), 7.73 (d, *J* = 7.9 Hz, 2H, Ar H-3,5), 4.75 (s, 2H, NCH_2), 4.21–4.07 (m, 2H, $O\underline{CH_2}CH_2CH_2CH_3$), 3.71 (s, 3H, 1-N-$CH_3$), 1.75–1.55 (m, 2H, $OCH_2\underline{CH_2}CH_2CH_3$), 1.52–1.36 (m, 2H, $OCH_2CH_2\underline{CH_2}CH_3$), 1.02–0.92 (m, 3H, $OCH_2CH_2CH_2\underline{CH_3}$); ^{13}C NMR δ (ppm): 170.4 (COO), 166.9 (C-8a), 159.5 (C-4), 159.0 (C-7), 150.8 (C-2), 145.9 (C-9a), 137.7 (C-5a), 132.7 (Ar C-2,6), 128.3 (C-1), 127.6 (Ar C-3,5), 125.1 (C-4), 119.4 (C-4a), 98.3 (C-6), 68.2 ($O\underline{CH_2}CH_2CH_2CH_3$), 43.6 ($NCH_2CO$), 29.9 ($N\text{-}CH_3$), 29.7 ($OCH_2\underline{CH_2}CH_2CH_3$), 18.2 ($OCH_2CH_2\underline{CH_2}CH_3$), 11.8 ($OCH_2CH_2CH_2\underline{CH_3}$); LC-MS *m/z* = 487 $[M+H]^+$. Anal. Calcd. for $C_{21}H_{19}BrN_4O_5$: C, 51.76; H, 3.93; N, 11.50; found: C, 51.82; H, 3.98; N, 11.57.

Butyl 2-(2,4-Dioxo-1-methyl-7-(3-nitropheny)-1,4-dihydrofuro[3,2-*g*]pteridine-3(2*H*)-yl)acetate (3i). Yield: 3.53 g (78%), light brown compound, mp: 287–289 °C; IR (cm^{-1}): 1713, 1674, 1505, 1349, 1315, 1282, 1211, 918, 857, 804, 756, 740, 723, 684; ^{1}H NMR δ (ppm): 8.89 (s, 1H, Ar H-2), 8.50 (d, *J* = 8.0 Hz, 1H, Ar H-6), 8.35 (d, *J* = 8.4 Hz, 1H, Ar H-4), 8.19 (s, 1H, H-6), 7.87 (t, *J* = 7.1 Hz, 1H, Ar H-5), 4.76 (s, 2H, NCH_2), 4.18 (t, *J* = 6.7 Hz, 2H, $O\underline{CH_2}CH_2CH_2CH_3$), 3.72 (s, 3H, 1-N-$CH_3$), 1.81–1.53 (m, 2H, $OCH_2\underline{CH_2}CH_2CH_3$), 1.54–1.34 (m, 2H, $OCH_2CH_2\underline{CH_2}CH_3$), 0.98 (t, *J* = 6.5 Hz, 3H, $OCH_2CH_2CH_2\underline{CH_3}$); ^{13}C NMR δ (ppm): 170.8 (COO, C-8a), 158.1 (C-4, C-7), 151.2 (C-2), 148.5 (C-9a), 146.3 (Ar C-3), 138.8 (C-5a), 132.2 (Ar C-6), 130.6 (Ar C-5), 129.1 (Ar C-1), 126.1 (Ar C-4), 122.3 (Ar C-2), 120.8 (C-4a), 101.4 (C-6), 68.2 ($O\underline{CH_2}CH_2CH_2CH_3$), 43.6 ($NCH_2CO$), 29.8 ($OCH_2\underline{CH_2}CH_2CH_3$), 29.8 (N-$CH_3$), 18.2 ($OCH_2CH_2\underline{CH_2}CH_3$), 11.73 ($OCH_2CH_2CH_2\underline{CH_3}$); LC-MS *m/z* = 453 $[M+H]^+$. Anal. Calcd. for $C_{21}H_{19}N_5O_7$: C, 55.63; H, 4.22; N, 15.45; found: C, 55.69; H, 4.28; N, 15.48.

Butyl 2-(2,4-Dioxo-1-methyl-7-(naphthalen-2-yl)-1,4-dihydrofuro[3,2-*g*]pteridine-3(2*H*)-yl)acetate (3j). Yield: 3.43 g (75%), light orange compound, mp > 300 °C; IR (cm^{-1}): 1716, 1673, 1554, 1503, 1455, 1363, 1282, 1196,

945, 906, 800, 748; ^{1}H NMR δ (ppm): 8.59 (s, 1H, naphthalene H-1), 8.11 (d, J = 8.7 Hz, 1H, naphthalene H-4), 8.06–8.00 (m, 2H, naphthalene H-3,8), 7.95–7.83 (m, 2H, H-6, naphthalene H-5), 7.59 (d, J = 5.2 Hz, 2H, naphthalene H-6,7), 4.76 (s, 2H, NCH_2), 4.18 (t, J = 7.4 Hz, 2H, $O\underline{CH_2}CH_2CH_2CH_3$), 3.71 (s, 3H, 1-N-$CH_3$), 1.78–1.56 (m, 2H, $OCH_2\underline{CH_2}CH_2CH_3$), 1.52–1.34 (m, 2H, $OCH_2CH_2\underline{CH_2}CH_3$), 0.98 (t, J = 7.8 Hz, 3H, $OCH_2CH_2CH_2\underline{CH_3}$); ^{13}C NMR δ (ppm): 170.2 (COO), 166.6 (C-8a), 158.8 (C-4), 158.3 (C-7), 150.4 (C-2), 145.0 (C-9a), 137.2 (naphthalene C-5a), 134.8 (C-5a), 132.2 (naphthalene C-4a), 129.2 (naphthalene C-4), 128.9 (naphthalene C-8), 128.8 (naphthalene C-5), 127.4 (naphthalene C-6), 127.3 (naphthalene C-3), 127.1 (naphthalene C-7), 123.1 (naphthalene C-2), 121.7 (naphthalene C-1), 118.4 (C-4a), 98.3 (C-6), 68.1 ($O\underline{CH_2}CH_2CH_2CH_3$), 43.5 ($NCH_2CO$), 29.8 (N-$CH_3$), 29.7 ($OCH_2\underline{CH_2}CH_2CH_3$), 18.3 ($OCH_2CH_2\underline{CH_2}CH_3$), 11.8 ($OCH_2CH_2CH_2\underline{CH_3}$); LC-MS m/z = 458 $[M+H]^+$. Anal. Calcd. for $C_{25}H_{22}N_4O_5$: C, 65.49; H, 4.84; N, 12.22; found: C, 65.52; H, 4.87; N, 12.25.

2. 2. X-Ray Diffraction Analysis

Crystals of compound **2a** were monoclinic, $C_{15}H_{10}N_4O_3$, at 20 °C, a = 7.7443(6) Å, b = 6.4905(4) Å, c = 12.7022(8) Å, β = 105.371(7)°, V = 615.63(7) Å^3, M_r = 294.27, Z = 2, space group P21, $d_{calc.}$ = 1.587 g/cm^3, μ(MoKα) = 0.115 mm^{-1}, F(000) = 304. Unit cell parameters and intensities of 5928 reflections (3081 independent, R_{int} = 0.022) were measured on a Xcalibur-3 diffractometer (MoKα) radiation, a CCD detector, a graphite monochromator, ω-scanning, $2\theta_{max}$ = 60°). The structure was deciphered by the direct method using the SHELXTL software package.[19] The positions of the hydrogen atoms were revealed from the difference synthesis of electron density and refined using the rider model with U_{iso} = nU_{eq} non-hydrogen atom associated with this hydrogen atom (n = 1.5 for the methyl group and n = 1.2 for the remaining hydrogen atoms). The hydrogen atom of the amino group was refined in the isotropic approximation. The structure was refined by F2 by full-matrix least squares in the anisotropic approximation for non-hydrogen atoms up to $wR2$ = 0.090 by 3021 reflections (R_1 = 0.035 by 2646 reflections with F > 4σ (F), S = 0.998). The atomic coordinates, as well as the complete tables of bond lengths and bond angles, were deposited with the Cambridge Structural Data Bank (e-mail: deposit@ccdc.cam.ac.uk) under the number CCDC 1940140.

3. Results and Discussion

The Paal–Knorr synthesis, despite more than a century of experience in use, remains to be one of the most

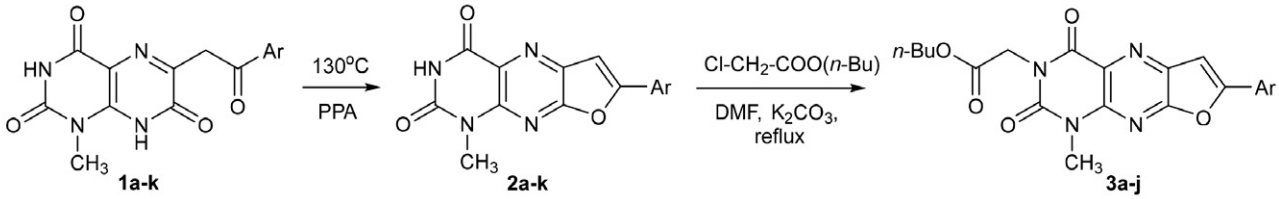

a:Ar = -C_6H_5; **b**:Ar = -(4-CH_3)C_6H_4; **c**:Ar = -(4-*i*-C_3H_7)C_6H_4; **d**:Ar = -(2-F)C_6H_4; **e**:Ar = -(4-F)C_6H_4; **f**:Ar = -(2,4-F)C_6H_3; **g**:Ar = -(4-Cl)C_6H_4; **h**:Ar = -(4-Br)C_6H_4; **i**:Ar = -(3-NO_2)C_6H_4; **j**:Ar = naphtalene-2-yl; **k**:Ar = -(4-CH_3O)C_6H_4.

Scheme 1. The dehydration of 1-methyl-6-(2-oxo-2-arylethyl)pteridine-2,4,7(1*H*,3*H*,8*H*)-triones and the alkylation of 1-methyl-7-arylfuro[3,2-*g*]pteridine-2,4(1*H*,3*H*)-diones

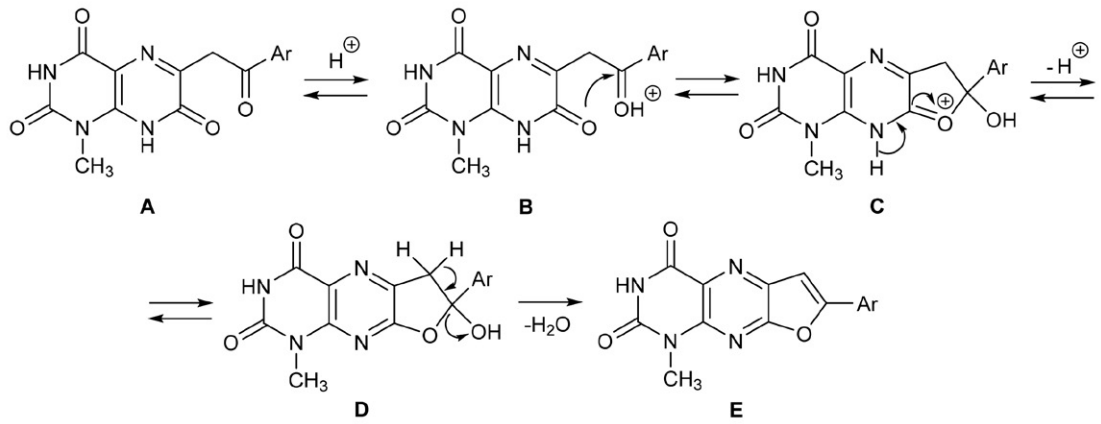

Scheme 2. The supposed mechanism of 1-methyl-6-(2-oxo-2-arylethyl)pteridine-2,4,7-(1*H*,3*H*,8*H*)-triones dehydration

effective methods for the formation of five-membered heterocycles with one heteroatom.[20] Considering the structural similarity of 1-methyl-6-(2-oxo-2-arylethyl)pteridine-2,4,7(1*H*,3*H*,8*H*)-triones **1a**–**k** with 1,4-dicarbonyl compounds and in the continuation of modification studies of pteridines their dehydration was investigated. It was found that dehydration of compounds **1a**–**k** in concentrated sulfuric acid both at room temperature and during heating proceeded doubtfully. In this case, either a mixture of substances difficult to identify was formed, or its tarring occurred. The dehydration reaction was carried out by heating of the starting materials in polyphosphoric acid (Scheme 1). Pure 1-methyl-7-arylfuro[3,2-*g*]pteridine-2,4(1*H*,3*H*)-diones **2a**–**k** were formed with high yields.

It should be noted that dehydration of compounds **1a**–**k** (**A** in Scheme 2) in the solution of polyphosphoric acid proceeded according to the Paal–Knorr synthesis.[21] The mechanism of this reaction assumes the nucleophilic attack of the amide fragment oxygen atom of the molecule at the carbon atom of the protonated carbonyl group (**B**). The oxonium cation **C** became aromatic in the result of deprotonation and dehydration with the formation of the final product **E**.

To increase the solubility of 1-methyl-7-arylfuro[3,2-*g*]pteridin-2,4(1*H*,3*H*)-diones **2a**–**k** in organic solvents (DMSO, DMF), the next step was to study their alkylation. It was found that alkylation of compounds **2a**–**k** by butyl chloroacetate in DMF in the presence of K_2CO_3 proceeded by the N_3-atom of the heterocycle. Corresponding esters **3a**–**j** were formed with satisfactory yields (Scheme 1). In this cases, compounds **3a**–**j** have higher solubility in organic solvents.

The formation of compounds **2a**–**k** was indicated by ^{1}H NMR spectra. Such singlet signals of proton at the 6th position were recorded in the region of 8.14–7.49 ppm. However, these protons were in some cases (compounds **2f** and **2h**) recorded as multiplets together with the signals of protons of the substituent at the 7thposition. Protons at the 3rd position of compounds **2a**–**k** were found in the range of 12.03–11.44 ppm in the low-field part of the ^{1}H NMR spectra. Speaking about compounds **3a**–**j**, the characteristic signal of the proton at the 6th position was recorded at 8.19–7.69 ppm. At once, in the ^{1}H NMR spectra of compounds **3a**–**j**, unlike compounds **2a**–**k**, there were singlet signals of protons of the NCH_2 group at 4.74–4.76 ppm and a series of proton signals of a butoxycarbonyl fragment. Also, in the spectra of compounds **2a**–**k** and **3a**–**j** there were singlet signals of methyl group protons at 3.57–3.72 ppm and a set of signals corresponding to the substituent at the 7th position.[22] Additionally, the formation of furo[3,2-*g*]pteridine-2,4(1*H*,3*H*)-diones **2a**–**k** was confirmed by the ^{13}C NMR spectrometry when studying their more soluble esters **3**. The characteristic signals in the ^{13}C NMR spectra of compounds **3a**–**j** were: signals of carbon atom at the 6th position at 106.4–95.1 ppm, signals of carbon atoms of the COO– group at 168.1–172.7 ppm and signals of NCH_2CO-fragment at 43.2–43.6 ppm. The positions of other signals in the ^{13}C NMR spectra correspond to the proposed structures.[23]

The analysis of the data of the chromato-mass spectra confirmed structure and purity of the compounds **2a**–**k** and **3a**–**j**. An additional analysis of the mass spectra (EI) of compounds **2a** and **3a** showed the fragmentation of the furo[3,2-*g*]pteridine system. Thus, the high stability of the molecular ion of compound **2a** ($[M]^{\bullet+}$, m/z = 294, I_{rel} = 66.8%), determined its fragmentation along the less aromatic dihydropyrimidine cycle with a step-by-step release of HNCO molecules (F_1, m/z = 251, I_{rel} = 12.6%), CO (F_2, m/z = 223, I_{rel} = 100%) and the $NCH_3^{\bullet}$ ion (F_3, m/z = 194, I_{rel} = 10.5%). Formed 6-phenylfuro[2,3-*b*]pyrazine ion (F_3) eliminated two HCN molecules with formation of ions with F_4 (m/z = 167, I_{rel} = 5.9%) and F_5 (m/z = 140, I_{rel} = 24.8%), while for F_5 formation of two alternative fragmentation ions $[C_6H_5]^{\bullet+}$ (m/z = 77, I_{rel} = 25.3%) and $[C_4H_3O]^{\bullet+}$ (m/z = 67, I_{rel} = 16.8%) was characteristic. Whereas, the molecular ion of ether **3a** was less stable ($[M]^{\bullet+}$, m/z = 408, I_{rel} = 46.6%). The main ways of its fragmentation were associated with the initial elimination of $C_4H_9^+$ (F_1, m/z = 352, I_{rel} = 10.6%) and CO_2 (F_2, m/z = 308, I_{rel} = 31.9%). Further degradation of the fragmented ion (F_2) proceeded similarly to the path described for compound **2a**, which led to the appearance of signals with m/z = 251 (I_{rel} = 9.5%), m/z = 223 (I_{rel} = 23.9%) and m/z = 140 (I_{rel} = 10.2%).

The final structure of compound **2a** was confirmed by X-ray diffraction study (Fig. 1). It was found that it

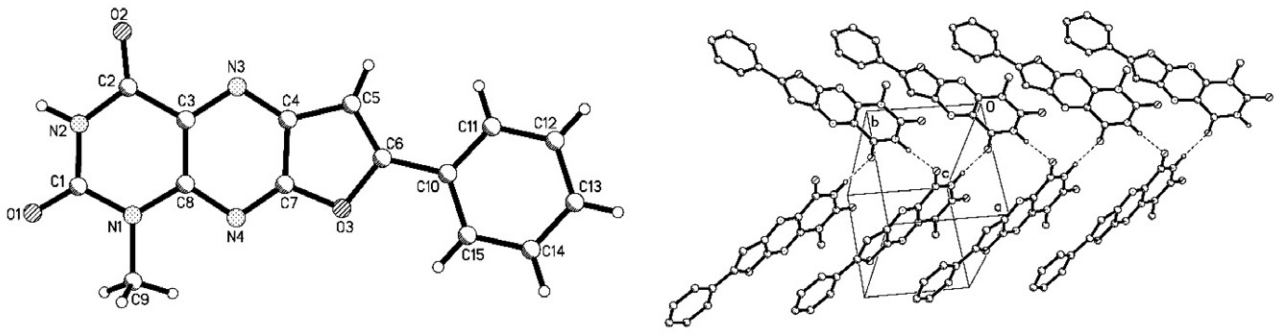

Fig. 1. Molecular structure and packing of molecules in a crystal of compound **2a**.

crystallized in the non-centrosymmetric space group P21, despite the absence of chiral centers in the molecule (Fig. 1).

All non-hydrogen atoms in the molecule lie in the plane with an accuracy of 0.05 Å, despite the presence of slight steric repulsion between the atoms of the tricyclic fragment and the phenyl substituent (shortened intramolecular contacts H(11)···C(5) 2.79 Å with the sum of the van der Waals radii[24] 2.87 Å and H(15)···O(3)2.43 Å (2.46 Å). In the crystal of molecule **2a** double chains along the crystallographic direction [0 1 0] were formed due to the intermolecular hydrogen bond N(2)–H···O(2)' (–*x*, –0.5 + *y*, –*z*), H···O 1.94 Å, N–H···O 175° and stacking interactions (the distance between the π-systems of neighboring molecules was 3.37 Å).

4. Conclusion

Using spectral methods and X-ray diffraction studies, it was found that the dehydration of 1-methyl-6-(2-oxo-2-arylethyl)pteridine-2,4,7(1*H*,3*H*,8*H*)-triones proceeded according to the Paal–Knorr synthesis with the formation of the original 1-methyl-7-arylfuro[3,2-*g*]pteridine-2,4(1*H*,3*H*)-diones. For these molecules, the alkylation reaction was studied.

Acknowledgements

The work was performed with the financial support of «Enamine Ltd» (Kyiv, Ukraine).

5. References

1. W. Pfleiderer, *Compr. Heterocycl. Chem. II, Bicyclic 6-6 Systems: Pteridines*; A. R. Katritzky, C. W. Rees, E. F. V. Scriven, (Eds.): Pergamon Press, **1996,** pp. 679–736. **DOI:**10.1016/B978-008096518-5.00162-3
2. C. Suckling, C. Gibson, J. Huggan, *Compr. Heterocycl. Chem. III, Bicyclic 6-6 Systems: Pteridines;* Katritzky, A. R.; Ramsden, C. A.; Taylor, R. J. K. Eds.; Elsevier, **2008,** pp. 915–975. **DOI:**10.1016/B978-008044992-0.00918-4
3. A. V. Gulevskaya, A. F. Pozharskii, *Russ. Chem. Rev.* **2011,** *80(6)*, 495–529. **DOI:**10.1070/RC2011v080n06ABEH004168
4. A. A. Sayed, A. H. Elghandour, H. S. Elgendy, *Pharma Chem.* **2014,** *6(3)*, 194–219
5. C. Suckling, *IUBMB Life* **2013,** *65(4)*, 283–299. **DOI:**10.1002/iub.1148
6. A. Fadda, N. Bayoumy, I. El-Sherbiny, *Drug Dev. Ind. Pharm.* **2015,** *42(7)*, 1–16. **DOI:**10.3109/03639045.2015.1108331
7. I. H. El Azab, M. E. Khalifa, A. A. Gobouri, T. A. Altalhi, *J. Heterocycl. Chem.* **2019,** *56*, 1352–1361. **DOI:**10.1002/jhet.3509
8. M. Mokaber-Esfahani, H. Eshghi, A. Shiri, M. Akbarzadeh, M. Mirzaei, *J. Chem. Res.* **2015,** *39*, 216–219. **DOI:**10.3184/174751915X14271341601550
9. S. El Kalyoubi, E. Fayed, *J. Chem. Res.* **2016,** *40*, 771–777. **DOI:**10.3184/174751916X14798125870610
10. X. Bi, J. Li, J. Li, W. Shi, Y. Dai, Q. Li, W. Zhang, W. Huang, H. Qian, C. Jiang, *Bioorg. Med. Chem.* **2019,** *27*, 2813–2821. **DOI:**10.1016/j.bmc. 2019.05.006
11. A. Abu-Hashema, M. El-Shazly, *Med. Chem*. 2018, *14*, 356–371. **DOI:**10.2174/1573406414666180112110947
12. A. A. Ghoneim, N. Ali, A. Elkanzi, R. B. Bakr, *J. Taibah. Univ. Sci.* **2018,** *12(6)*, 774–782. **DOI:**10.1080/16583655.2018.1510163
13. A. Kiryanov, S. Natala, B. Jones, C. McBride, V. Feher, B. Lam, Y. Liu, K. Honda, N. Uchiyama, T. Kawamoto, Y. Hikichi, L. Zhang, D. Hosfield, R. Skene, H. Zou, J. Stafford, X. Cao, T. Ichikawa, *Bioorg. Med. Chem. Lett.* **2017,** *27*, 1311–1315. **DOI:**10.1016/j.bmcl.2016.10.009
14. K. Ishimoto, K. Nakaoka, O. Yabe, A. Nishiguchi, T. Ikemoto, *Tetrahedron* **2018,** *74*, 5779–5790. **DOI:**10.1016/j.tet.2018.08.020
15. A. A. Wiles, B. Fitzpatrick, N. A. McDonald, M. M. Westwater, De-L. B. Long, Ebenhoch, V. M. I. D. Rotello, W. Samuel, G. Cooke, *RSC Adv.* **2016,** *6*, 7999–8005. **DOI:**10.1039/C5RA22402K
16. I. H. El Azab, N. A. A. Elkanzi, A. A. Gobouri, *J. Heterocycl. Chem.* **2018,** *55*, 65–76. **DOI:**10.1002/jhet.2978
17. V. A. Mamedov, N. A. Zhukova, A. T. Gubaidullin, V. V. Syakaev, M. S. Kadyrova, T. N. Beschastnova, O. B. Bazanova, I. Kh. Rizvanov, S. K. Latypov, *J. Org. Chem.* **2018,** *83*, 14942–14964. **DOI:**10.1021/acs.joc.8b02161
18. M. S. Kazunin, O. Yu. Voskoboynik, I. S. Nosulenko, G. G. Berest, T. Sergeieva, S. Okovytyy, O. V. Karpenko, B. O. Priimenko, S. I. Kovalenko, *J. Heterocycl. Chem*. **2018,** *4*, 1033–1041. **DOI:**10.1002/jhet.3135
19. G. M. Sheldrick *Acta Cryst.* **2008,** *A64*, 112–122. **DOI:**10.1107/S0108767307043930
20. A. R. Katritzky, C. W. Rees, In Comprehensive Heterocyclic Chem*i*stry; (Eds.): Pergamon Press, Oxford, 1984, 4, p. 705.
21. A. Venkateraman, A. Kalyani, *J. Org. Chem.* **1995,** *60*, 301–307. **DOI:**10.1021/jo00107a006
22. O. I. El-Sabbagh, M. E. El-Sadek, S. El-Kalyoubi, I. Ismail, *Arch. Pharm. Chem. Life Sci*. **2007,** *340*, 26–31. **DOI:**10.1002/ardp.200600149
23. N. E. Jacobsen, NMR spectroscopy explained: simplified theory, applications and examples for organic chemistry and structural biology; John Wiley & Sons, Inc., **2007,** p. 688.
24. Yu. V. Zefirov, *Crystallography* **1997,** *42(5)*, 936–958.

Povzetek

V članku predstavljamo enostavno in učinkovito metodo sinteze doslej neopisanih 1-metil-7-arilfuro[3,2-*g*]pteridin-2,4(1*H*,3*H*)-dionov s pomočjo dehidratacije ustreznih 1-metil-6-fenacilpteridin-2,4,7(1*H*,3*H*,8*H*)-trionov. Pokazali smo, da njihovo alkiliranje z butil kloroacetatom v bazičnem poteka na N_3-atomu heterocikla. Strukturo in čistočo pripravljenih produktov smo dokazali z IR, ^{1}H in ^{13}C NMR spektroskopijo, plinsko kromatografijo-masno spektrometrijo, masno spektrometrijo in tudi z rentgensko difrakcijsko analizo. Opisujemo tudi predlagani mehanizem dehidratacije.

Except when otherwise noted, articles in this journal are published under the terms and conditions of the Creative Commons Attribution 4.0 International License

DOI: 10.17344/acsi.2019.5612 *Acta Chim. Slov.* **2020,** *67,* 594–601
creative commons

Scientific paper

Study on the Complex Formation and the Ion-Association of Anionic Chelate of Molybdenum(VI) with Bidentate Ligand and the Cation of 2,3,5-Triphenyl-2*H*-tetrazolium Chloride

Kirila Stojnova,[1] Petya Racheva,[2] Vidka Divarova,[2] Pavel Yanev[1] and Vanya Lekova[1,*]

[1] *Department of General and Inorganic Chemistry with Methodology of Chemistry Education, Faculty of Chemistry, Plovdiv University "Paisii Hilendarski", 24 Tsar Assen Street, Plovdiv 4000, Bulgaria*

[2] *Department of Chemical Sciences, Faculty of Pharmacy, Medical University-Plovdiv, 15A Vasil Aprilov Boulevard, Plovdiv 4002, Bulgaria*

* *Corresponding author: E-mail: vanlek@uni-plovdiv.bg tel.:+35932261420*

Received: 10-01-2019

Abstract

The complex formation between the anionic chelate of molybdenum(VI) with the bidentate ligand of 3,5-dinitrocatechol (3,5-DNC) and its ion-association with the cation of 2,3,5-triphenyl-2*H*-tetrazolium chloride (TTC) in the liquid-liquid extraction system Mo(VI)–3,5-DNC–TTC–H_2O–$CHCl_3$ were studied by spectrophotometry. The validity of Beer's law was checked and some analytical characteristics of the system were calculated under the optimum conditions for the chelate formation and extraction. The effect of various co-existing ions and reagents on the process of chelate formation and ion-association was investigated. The molar ratio of the components in the ion-associated complex Mo(VI)–3,5-DNC–TTC was determined by independent methods. The association process in aqueous phase and the extraction equilibria were investigated and quantitatively characterized by the following equilibrium constants: association constant, distribution constant, extraction constant and recovery factor. Based on this, a reaction scheme, a general formula and a structural formula of the complex were suggested.

Keywords: Molybdenum(VI); bidentate ligand; chelate formation; extraction equilibriums

1. Introduction

The molybdenum is a transition metal with rich coordination chemistry, it occurs in various oxidation states, coordination numbers and geometries.[1–3] Molybdenum(VI) forms complexes with various organic ligands, such as polyphenols and their functional derivatives, polyhydroxycarboxylic acids, aminopolycarboxylic acids, hydroxamic acids, amines (primary, secondary and ternary), 8-hydroxyquinoline and its derivatives, aldehyde hydrazones, oximes, β-diketones, fluorones, hydroxyazodyes, biomolecules (chitosan, chitin, D-glucosamine, L-alanine, L-phenylalanine).[4–17] Molybdenum(VI) complexes with bidentate ligands, containing [S,S], [S,O], [S,N] donor atoms, like toluene-3,4-dithiol, 2-mercaptophenol, 2-aminothiophenol, ethane-1,2-dithiol, dithiooxamide, 2-thiopheno-carboxamide, were obtained and structurally characterized.[18] Molybdenum(VI) gives colored anionic chelates with bidentate ligands of aromatic compounds, containing two or more hydroxyl groups in *o*-position relative to each other. 1,2-Dihydroxybenzene, 1,2,3,-trihydroxybenzene and 3,4,5-trihydroxybenzoic acid form colored bidentate chelates, while phenol, 1,3-dihydroxybenzene and 1,4-dihydroxybenzene do not form colored chelates in the pH range 1.1–10.9.[4] The colored anionic chelates of molybdenum(VI) form ion-associated complexes with bulky organic cations, like methyltrioctylammonium, cetylpyridinium, cetyltrimethylammonium, tetraphenylphosphonium.[4,19–21]

The ion-associated complexes of anionic chelates of metals with various natural organic and inorganic ligands

with N-, S- and O-containing donor atoms and with the participation of mono- and ditetrazolium cations are a special scientific research field of the chemistry of the coordination compounds. It is up-to-date topic, not only as a theoretical background for the preparation of novel ion-associated complexes, but mainly due to the possibility for their application in the Analytical Chemistry for determination of various metals in natural, industrial, pharmaceutical and biological samples, addressing in such a way a number of ecological issues. Tetrazolium salts are used as reagents for the preparation of various ion-associated complexes of metals, e.g. W(VI), Ge(IV), Tl(III), Nb(V), V(V), Ga(III), Co(II), Ge(IV).[22–31] The structure and properties of mono- and ditetrazolium salts, the bulky hydrophobic organic substituents in their molecules, determine their ability to form ion-associated complexes, increasing the extractability in non-polar solvents. The presence of a quaternary nitrogen atom in the molecules of the tetrazolium salts determines the ability to form ionic associates in the aqueous phase without protonation, as opposed to the amines.[22,32,33]

The liquid-liquid extraction is a part of the chemistry of the solutions and the coordination compounds. It is applied to study the processes of complex formation and the extraction equilibria. The extraction spectrophotometry is a relatively simple, convenient, rapid to perform and inexpensive method for preparation and characterization of new complex compounds as well as for their application in the chemical analysis.[34–40]

The aim of our current investigation was to synthesize molybdenum(VI) ion-associated complex in liquid-liquid extraction system and estimate its feasibility in analytical chemistry of Mo(VI), in order to evaluate the possible applications of the system for determination of traces of molybdenum(VI) in alloys, biological, medical and pharmaceutical samples. The extraction equilibria of the chelate formation between molybdenum(VI) with the bidentate ligand of 3,5-dinitrocatechol (3,5-DNC) and the cation of 2,3,5-triphenyl-2H-tetrazolium chloride (TTC) in the liquid-liquid system Mo(VI)–3,5-DNC–TTC–H_2O–$CHCl_3$ was study spectrophotometrically.

2. Experimental

2. 1. Reagents and Apparatus

$Na_2MoO_4 \cdot 2H_2O$ (Fluka AG, p.a.): an aqueous 1.6×10^{-2} mol L^{-1} solution was prepared.

3,5-Dinitrocatechol (3,5-DNC) (Sigma-Aldrich, p.a.): 3,5-DNC was dissolved in $CHCl_3$ to give a 1.0×10^{-2} mol L^{-1} solution. 2,3,5-triphenyl-2H-tetrazolium chloride (TTC) (Loba Feinchemie, p.a.): an aqueous 3.0×10^{-3} mol L^{-1} solution was prepared. H_2SO_4 (95–97% for analysis, Merck): 9 mol L^{-1} solution was prepared. The concentration of H_2SO_4 was determined titrimetrically. A Camspec M508 spectrophotometer (UK), equipped with 10 mm path length cells, was employed for measurement of the absorbance. The organic solvent $CHCl_3$ was additionally distilled.

2. 2. Procedure for Establishment of the Optimum Conditions for Chelate Formation and Ion-Association

The required aliquots of the solutions of Mo(VI), TTC and H_2SO_4 were introduced into 250 mL separatory funnels. The resulting solutions were diluted with distilled water to a total volume of 10 mL. A required aliquot of a chloroform solution of 3,5-DNC was added and then the organic phase was adjusted to a volume of 10 mL with chloroform. The funnels were shaken for a fixed time (up to 300 s). A portion of the organic extract was filtered through a filter paper into a 1 cm cell and the absorbance was measured against a blank. The blank extraction was performed in the same manner in the absence of molybdenum.[29]

2. 3. Procedure for Determination of the Distribution Constant

The distribution constant (K_D) can be calculated according to the ratio $K_D = A_1/(A_3–A_1)$, where A_1 and A_3 are respectively the light absorbance after a single extraction in chloroform under optimum operating conditions and after a triple extraction performed under the same conditions. Single extraction: the single extraction was performed under the optimum conditions for chelate formation (Table 1, column 1). The organic layer was transferred into 25 mL calibrated flask and the flask was brought to volume with chloroform. The measurement of the light absorbance A_1 is done against a blank sample, prepared under the same conditions. Triple extraction: the first stage of the triple extraction is performed with 10 mL of chloroform and the extract is transferred into a 25 mL calibrated flask. During the second stage of the extraction, 8 mL of chloroform are added to the aqueous phase remaining after the first stage. The organic layer is added to that from the first stage. For the third stage of extraction, 7 mL of chloroform are added to the aqueous phase remaining after the second stage and for the third time an extraction is performed. The organic layer is transferred to the previous two. The calibrated flask is brought to volume with chloroform. The measurement of A_3 is performed against a blank sample prepared in the same way.[41]

3. Results and Discussion

3. 1. Optimum Extraction-Spectrophotometric Conditions for Chelate Formation and Ion-Association

The colored anionic chelate of molybdenum(VI) with the bidentate ligand of 3,5-dinitrocatrchol (3,5-

DNC) was extracted in chloroform in the presence of the bulky hydrophobic monotetrazolium cation of 2,3,5-triphenyl-2H-tetrazolium chloride (TTC). The absorption spectrum of the extract of the studied ion-associated complex Mo(VI)-3,5-DNC-TTC in $CHCl_3$ was characterized by an absorption maximum in the visible range (λ_{max} = 410 nm) (Figure 1). The acidity of the aqueous phase influences the extraction of the anionic chelate Mo(VI)-3,5-DNC into the organic phase in the form of ion-associate with the tetrazolium cation of TTC. The maximum and constant extraction of the ion-associated complex is achieved in strongly acidic solution of H_2SO_4 ((0.9-7.2) × 10^{-1} mol L^{-1}) (Figure 2). The results from the experiments showed that the extraction equilibrium cannot be achieved within less than 120 s. The prolonged shaking does not have an impact on the absorbance. The next experiments were performed for 3 min. The concentrations of the reagents are the most important factor, influencing the extraction equilibrium. The chelate formation of Mo(VI)-3,5-DNC requires 6.25–fold excess of 3,5-DNC (≥1.0 × 10^{-3} mol L^{-1}) and 1.13–fold excess of TTC (≥1.8 × 10^{-4} mol L^{-1}) for maximum association and extraction.

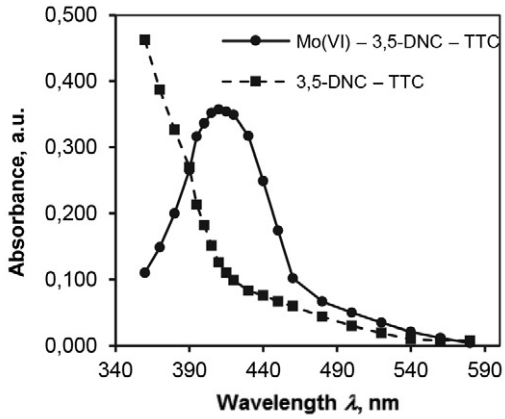

Figure 1. Absorption spectra of the complex Mo(VI)-3,5-DNC-TTC and of the blank sample 3,5-DNC-TTC in $CHCl_3$ $C_{Mo(VI)}$ = 1.6 × 10^{-5} mol L^{-1}; $C_{3,5\text{-}DNC}$ = 1.2 × 10^{-3} mol L^{-1}, C_{TTC} = 2.4 × 10^{-4} mol L^{-1}; C_{H2SO4} = 4.5 × 10^{-1} mol L^{-1}; λ = 410 nm; τ = 3 min

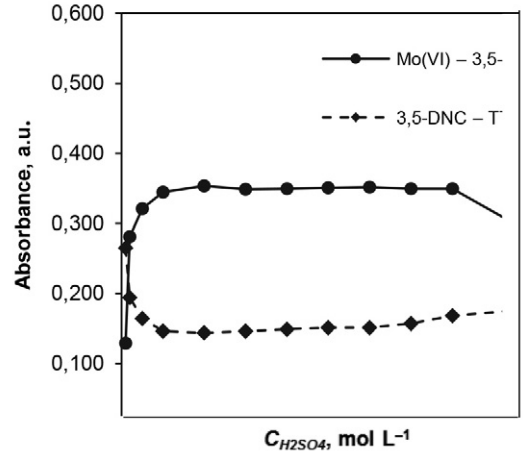

Figure 2. Absorption spectra of the complex Mo(VI)-3,5-DNC-TTC in $CHCl_3$ against 3,5-DNC-TTC extract vs. acidity of the aqueous phase: $C_{Mo(VI)}$ = 1.6 × 10^{-5} mol L^{-1}; $C_{3,5\text{-}DNC}$ = 1.2 × 10^{-3} mol L^{-1}, C_{TTC} = 2.4 × 10^{-4} mol L^{-1}; λ = 410 nm; τ = 3 min

The optimum experimental conditions for the extraction of the ion-associated complex Mo(VI)-3,5-DNC-TTC are summarized in Table 1, column 1.

3. 2. Beer's Law, Apparent Molar Absorptivity and other Analytical Characteristics

The range of agreement with Beer's law, i.e. the linear relationship between the molybdenum concentration in the aqueous phase ($C_{Mo(VI)}$, μg mL^{-1}) and the absorbance of the ion-association complex in the organic phase after extraction regression analysis under the optimum conditions for complex formation was used. The equation of a straight line was found to be Y = 0.1806 X + 0.0022 with a correlation coefficient squared 0.9994. Under the optimum conditions for complex formation, the linearity is observed for concentrations up to 6.72 μg mL^{-1} Mo(VI). Further analytical characteristics, e.g. apparent molar absorptivity ε', Sandell's sensitivity, limit of detection and limit of quantification, are shown in Table 1, column 2.

From the analytical characteristics of the extraction system Mo(VI)-3,5-DNC-TTC-H_2O-$CHCl_3$, it can be

Table 1. Optimum extraction-spectrophotometric conditions and analytical characteristics of the system Mo(VI)–3,5-DNC–TTC–H_2O–$CHCl_3$

Optimum conditions	Analytical characteristic
Absorption maximum (λ_{max}) 410 nm	Apparent molar absorptivity (ε') (2.16 ± 0.03) × 10^4 L mol^{-1} cm^{-1}
Volume of the aqueous phase 10 mL	True molar absorptivity (ε) (2.01 ± 0.04) × 10^4 L mol^{-1} cm^{-1}
Volume of the organic phase 10 mL	Sandell's sensitivity (SS) 4.45 ng cm^{-2}
Concentration of H_2SO_4 in the aqueous phase (0.9÷7.2) × 10^{-1} mol L^{-1}	Adherence to Beer's law up to 6.72 μg cm^{-3}
Shaking time (τ) 3 min	Relative standard deviation (RSD) 1.17%
Concentration of 3,5-DNC ≥ 1.0 × 10^{-3} mol L^{-1}	Limit of detection (LOD) 0.19 μg mL^{-1}
Concentration of TTC ≥ 1.8 × 10^{-4} mol L^{-1}	Limit of quantification (LOQ) 0.62 μg mL^{-1}

concluded that the ion-associate formed between the anionic chelate of Mo(VI) with the bidentate ligand of 3,5-DNC and the monotetrazolium cation allows determination of Mo(VI) with a high sensitivity.

3. 3. Effect of Co-Existing Ions and Reagents on the Complex Formation

The effect of various co-existing ions and reagents on the process of the association in aqueous phase and the extraction equilibria was studied under optimum extraction conditions (Table 1, column 1). The concentration of Mo(VI) in the presence of the co-existing ions and reagents was determined from the sequence of Beer's law. A deviation of ±3% from the absorbance of the complex in the absence of co-existing ions was accepted as an interfering effect. The results are presented in Table 2. From them, it can be concluded that most of the ions studied do not interfere, but some of them, like Al(III), Fe(II) and Cr(VI) in concentrations higher than the indicated ones, hinder the extraction of Mo(VI) as an associated complex with 3,5-DNC and TTC. The extraction equilibrium is severely interfered by Fe(III), V(V) and W(VI) ions at very low concentrations. The interfering ions can be masked or removed from the extraction system to avoid this. Our investigations as well as the studies published in the literature show that same of the co-existing ions, like Al(III), Fe(II) and Fe(III) can be removed by their pre-precipitation with OH^- at pH = 11.[42] Vanadium(V) can be co-precipitated with Fe(III) in alkali medium.[43] The co-existing ions, like Fe(II), Fe(III) and Al(III) can be masked with added Complexone III, Complexone IV or L-ascorbic acid in concentrations lower than the indicated.

Table 2. Effect of co-existing ions and reagents on the complex formation of the ion-associate Mo(VI)–3,5-DNC–TTC for extraction in the presence of 20 μg Mo(VI)

Co-existing ion and reagent	Co-existing ion and reagent, μg/10 cm^3 aqueous phase	Mo(VI) found, μg	R, %
Na^+	10000	20.19	100.95
K^+	10000	20.24	101.20
Mg^{2+}	10000	19.87	99.35
Ca^{2+}	10000	19.77	98.85
Cu^{2+}	10000	19.95	99.75
Zn^{2+}	10000	19.63	98.15
Cd^{2+}	10000	20.46	102.30
Ni^{2+}	10000	20.29	101.45
Mn^{2+}	10000	20.01	100.05
Co^{2+}	10000	19.92	99.60
Al^{3+}	4000	20.32	101.61
Cr^{3+}	10000	19.97	99.83
Fe^{2+}	750	20.20	101.02
Fe^{3+}	100	17.59	87.95
V(V)	100	21.17	105.87
Nb(V)	50	15.94	79.68
Cr(VI)	100	19.91	99.56
W(VI)	50	25.06	125.32
F^-	10000	19.96	99.79
Br^-	10000	20.22	101.08
NO_3^-	2500	20.82	104.09
PO_4^{3-}	10000	20.42	102.10
$P_2O_7^{4-}$	10000	20.37	101.83
CH_3COO^-	10000	20.43	102.16
$C_4H_4O_6^{2-}$	10000	19.94	99.69
$C_6H_5O_7^{3-}$	10000	20.20	101.02
Complexone III	10000	20.03	100.15
Complexone IV	10000	20.10	100.52
L-Ascorbic acid	1000	20.21	101.05

3. 4. Molar Ratios of the Ion-Associated Complex

The molar ratios of the ion-associated complex were determined by three independent methods: the mobile equilibrium method, the straight-line method of Asmus and the method of continuous variations.[44]

The mobile equilibrium method and the straight-line method of Asmus were applied to prove the molar ratios Mo(VI):3,5-DNC and Mo(VI):TTC. The results from the application of these methods are shown in Figures 3–5, respectively.

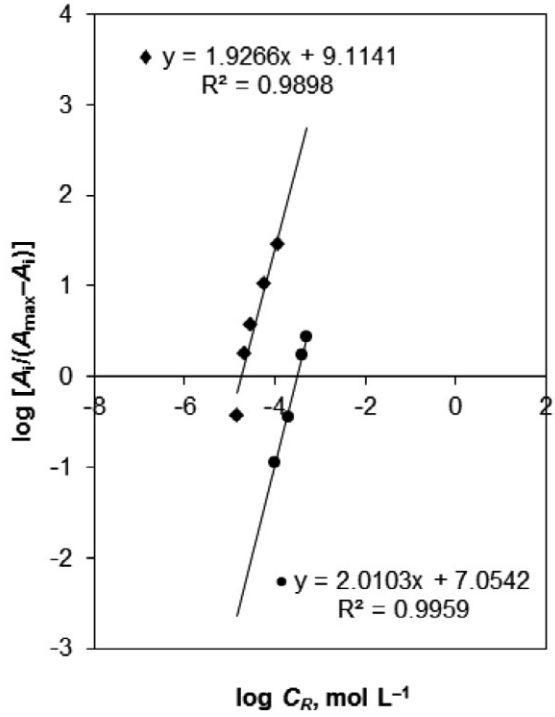

Figure 3. Straight lines by the mobile equilibrium method for determination of the molar ratios Mo(VI):3,5-DTC and Mo(VI):TTC $C_{Mo(VI)} = 1.6 \times 10^{-5}$ mol L^{-1}; $C_{H2SO4} = 4.5 \times 10^{-1}$ mol L^{-1}; $\lambda = 410$ nm; $\tau = 3$ min
• Mo(VI) : 3,5-DNC, $C_{TTC} = 2.4 \times 10^{-4}$ mol L^{-1};
♦ Mo(VI) : TTC, $C_{3,5\text{-}DNC} = 1.2 \times 10^{-3}$ mol L^{-1}

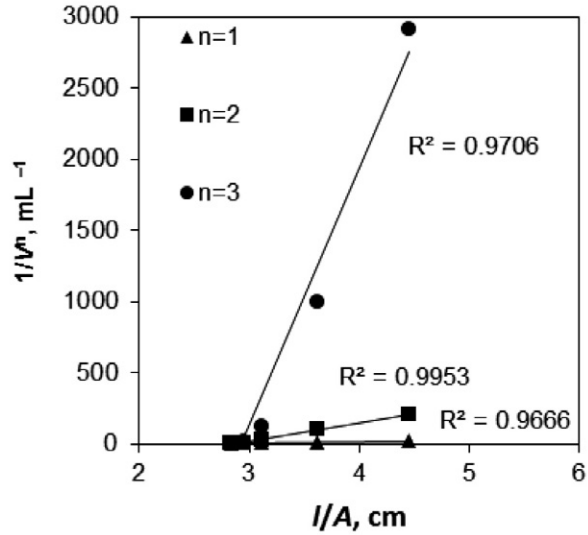

Figure 4. Determination of the molar ratio (n) Mo(VI):TTC by the method of Asmus $C_{Mo(VI)} = 1.6 \times 10^{-5}$ mol L^{-1}; $C_{3,5\text{-DNC}} = 1.2 \times 10^{-3}$ mol L^{-1}; $C_{H2SO4} = 4.5 \times 10^{-1}$ mol L^{-1}; $\lambda = 410$ nm; $\tau = 3$ min

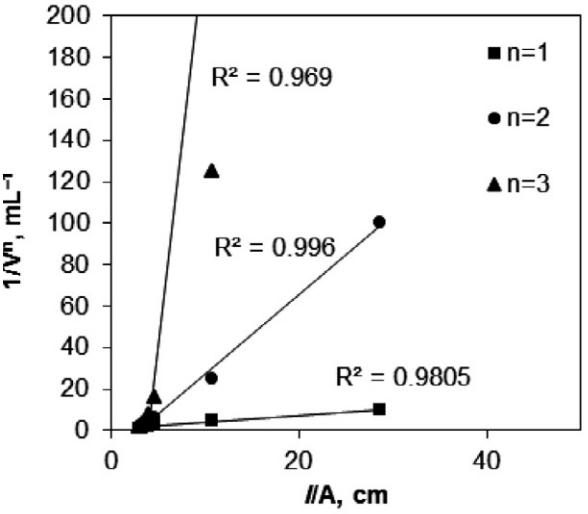

Figure 5. Determination of the molar ratio (n) Mo(VI):3,5-DNC by the method of Asmus $C_{Mo(VI)} = 1.6 \times 10^{-5}$ mol L^{-1}; $C_{TTC} = 2.4 \times 10^{-4}$ mol L^{-1}; $C_{H2SO4} = 4{,}5 \times 10^{-1}$ mol L^{-1}; $\lambda = 410$ nm; $\tau = 3$ min

On the basis of the results it can be concluded that Mo(VI), 3,5-DNC and TTC interact in molar ratio 1:2:2. The application of the method of continuous variations confirmed the molar ratio Mo(VI):TTC = 1:2 (Figure 6).

3. 5. Reaction Scheme and Suggested General Formula

The carried out experiments showed that the chelate formation and the extraction of the ion-associated complex occurred in strongly acidic solution. Under these conditions, the chelate formation between molybdenum(VI) and the bidentate ligand 3,5-dinitrocatechol (3,5-DNC) is given by the equation (1):

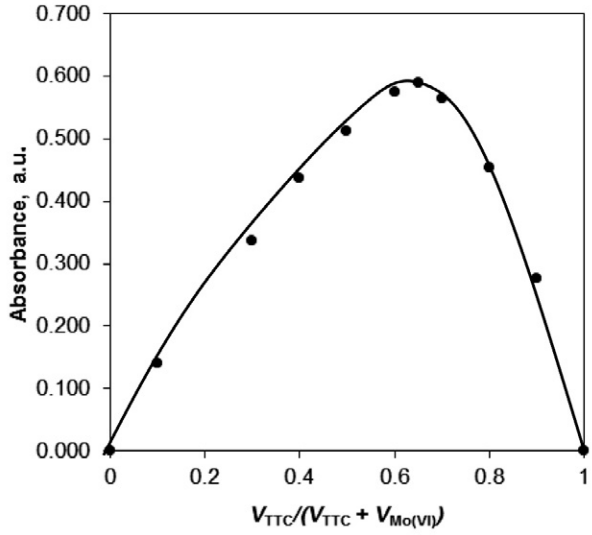

Figure 6. Determination of the molar ratio (n) Mo(VI):TTC by the method of continuous variations $C_{Mo(VI)} + C_{TTC} = 8.0 \times 10^{-5}$ mol L^{-1}; $C_{3,5\text{-DNC}} = 1.2 \times 10^{-3}$ mol L^{-1}; $C_{H2SO4} = 4.5 \times 10^{-1}$ mol L^{-1}; $\lambda = 410$ nm; $\tau = 3$ min

$$MoO_4^{2-} + 2\ (HO)_2C_6H_2(NO_2)_2 \rightleftharpoons \{MoO_2[O_2C_6H_2(NO_2)_2]_2\}^{2-} + 2\ H_2O \quad (1)$$

Having in mind the reaction of chelate formation of Mo(VI)–3,5-DNC and the molar ratio indicated above, it can be suggested that the formation of the ion-associate in the aqueous phase, its distribution between the aqueous and the organic phases and its extraction in chloroform can be given by the following equations (2–4).

$$2(TTC)^+_{(aq)} + \{MoO_2[O_2C_6H_2(NO_2)_2]_2\}^{2-}_{(aq)} \rightleftharpoons (TTC)_2\{MoO_2[O_2C_6H_2(NO_2)_2]_2\}_{(aq)} \quad (2)$$

$$(TTC)_2\{MoO_2[O_2C_6H_2(NO_2)_2]_2\}_{(aq)} \rightleftharpoons (TTC)_2\{MoO_2[O_2C_6H_2(NO_2)_2]_2\}_{(org)} \quad (3)$$

$$2(TTC)^+_{(aq)} + \{MoO_2[O_2C_6H_2(NO_2)_2]_2\}^{2-}_{(aq)} \rightleftharpoons (TTC)_2\{MoO_2[O_2C_6H_2(NO_2)_2]_2\}_{(org)} \quad (4)$$

Therefore, the ion-associated chelate of Mo(VI)–3,5-DNC with the cation of the monotetrazolium salt 2,3,5-triphenyl-2H-tetrazolium chloride (TTC) can be represented by the general formula $(TTC)_2\{MoO_2[O_2C_6H_2(NO_2)_2]_2\}$.

3. 6. Extraction Equilibria, True Molar Absorptivity, Recovery Factor and Structural Formula of the Ion-Associated Complex

The association process in aqueous phase and the extraction equilibria were investigated and quantitatively characterized with respect to the following key constants: association constant β, distribution constant K_D, extraction constant K_{ex} and recovery factor $R\%$.

The association constant β and the true molar absorptivity ε were determined by the method of Komar-Tolmachev from equation (5):[44]

$$\beta = (l/n)^n / [\varepsilon (tg\ \alpha)^{n+1}] \quad (5)$$

where l is the cuvette thickness (l = 1 cm); n – the molar ratio between the components independently determined (e.g. by the mobile equilibrium method, the straight-line method of Asmus or the method of continuous variations) (n = 2), ε – the true molar absorptivity.

The true molar absorptivity ε was determined by the method of Komar-Tolmachev (Figure 7) from the equation of a straight line Y = 1.6762 X + 4.9692 ((ε = 1/ (4.9692 × 10^{-5}, L mol^{-1} cm^{-1})) and its value is given in Table 1, column 2.

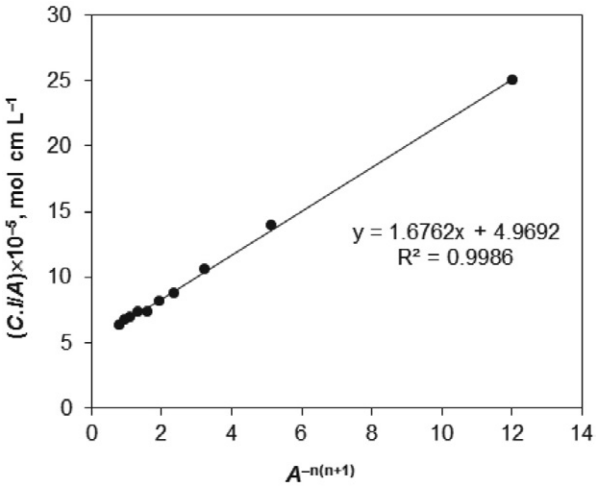

Figure 7. Dependency of $(C.l/A)$ on $A^{-n/(n+1)}$ (method of Komar–Tolmachev) $C = C_{Mo(VI)}$ mol L^{-1}; $C_{TTC} = 2\ C_{Mo(VI)}$ mol L^{-1}; $C_{3,5\text{-DNC}}$ = 1.2×10^{-3} mol L^{-1}; A – absorbance; l – cell thickness, l = 1 cm; n = 2

The distribution constant (K_D) was determined by the equation (6), where A_1 and A_3 are the absorbance (measured against blanks) obtained after a single and triple extraction, respectively.

$$K_D = \{(TTC)_2\{MoO_2[O_2C_6H_2(NO_2)_2]_2\}\}_{(org)} / \{(TTC)_2\{MoO_2[O_2C_6H_2(NO_2)_2]_2\}\}_{(aq)} = A_1 / (A_3 - A_1) \quad (6)$$

The recovery factor was determined from the equation (7):

$$R\% = 100\ K_D / (K_D + 1) \quad (7)$$

The extraction constant K_{ex} was calculated by two independent methods:

$$\text{(i)}\ \log K_{ex} = \log K_D + \log \beta \quad (8)$$

where β was determined by the method of Komar-Tolmachev.

(ii) the method of Likussar-Boltz:[45]

The method uses the data from the method of continuous variations (Figure 6). The extraction constant K_{ex} was calculated by the equation of Likussar-Boltz for molar ratio 1:2 (equation 9):

$$\log K_{ex} = 0.3522 - 2 \log K + \log Y_{max} - 3 \log (1 - Y_{max}) \quad (9)$$

where K is the total concentration of reagents –($K = C_{Mo(VI)} + C_{TTC} = 8.0 \times 10^{-5}$ mol L^{-1}); Y_{max} and $(1-Y_{max})$ are determined by additionally plotted normalized absorption curve (Y_{max} = 0.689; $(1 - Y_{max})$ = 0.311) (Figure 6).

The values of the equilibrium constants and the recovery factor, describing quantitatively the equilibrium in the aqueous phase and the extraction of the ion-associated complex in the organic phase are presented in Table 3.

The results obtained by independent methods are statistically similar and confirm the proposed scheme of the process of complex formation of the ion-associated complex in the aqueous phase, its distribution between the aqueous and the organic phases and its extraction in chloroform. Based on this, the proposed structural formula of the ion-associated complex is represented in Figure 8.

Table 3. Values of the equilibrium constants and the recovery factor

Equilibrium constant and recovery factor	**Value**
Equilibrium (Eq. 2) – Association constant b $b = (TTC)_2\{MoO_2[O_2C_6H_2(NO_2)_2]_2\}_{(aq)} / \{[(TTC)^+]^2_{(aq)}\ \{MoO_2[O_2C_6H_2(NO_2)_2]_2\}^{2-}\}_{(aq)}$	$\log b = (9.42 \pm 1.08)^a$
Equilibrium (Eq. 3) – Distribution constant K_D $K_D = \{(TTC)_2\{MoO_2[O_2C_6H_2(NO_2)_2]_2\}\}_{(org)} / \{(TTC)_2\{MoO_2[O_2C_6H_2(NO_2)_2]_2\}\}_{(aq)}$	$\log K_D = (1.15 \pm 0.01)^b$
Equilibrium (Eq. 4) – Extraction constant K_{ex} $K_{ex} = \{(TTC)_2\{MoO_2[O_2C_6H_2(NO_2)_2]_2\}\}_{(org)} / \{\{[TTC]^+\}^2_{(aq)}\ ' \{MoO_2[O_2C_6H_2(NO_2)_2]_2\}^{2-}\}_{(aq)}$ $\log K_{ex} = (9.86 \pm 0.06)^d$	$\log K_{ex} = (10.57 \pm 1.09)^c$
Recovery factor R%	$R = (93.39 \pm 0.05)\%^e$

[a] Calculated by Komar–Tolmachev method (equation 5); [b] Calculated by equation (6); [c] Calculated by equation (8), where β is determined by the Komar–Tolmachev method; [d] Calculated by Likussar–Boltz method (equation (9)); [e] Calculated by equation (7).

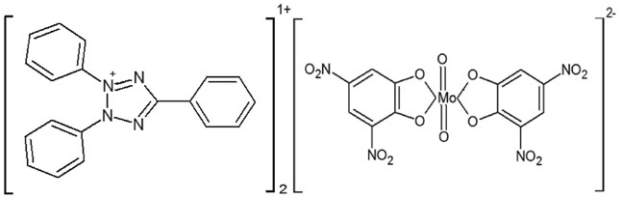

Figure 8. Structural formula of the ion-associated complex Mo(VI)-3,5-DNC-TTC

4. Conclusion

The equilibria of the complex formation of the anionic chelate of molybdenum(VI) with the bidentate ligand of 3,5-dinitrocatechol (3,5-DNC) and its extraction with the cation of 2,3,5-triphenyl-2H-tetrazolium chloride (TTC) in the form of an ion-associated complex in the liquid-liquid extraction system Mo(VI)-3,5-DNC-TTC-H_2O-$CHCl_3$ was studied by spectrophotometry. In the presence of the monotetrazolium cation, the yellow-colored anionic chelate of Mo(VI)-3,5-DNC forms an ion-associated complex well soluble in chloroform. The bulky organic molecule of the tetrazolium salt determined the extractability of the ion-associate in the organic phase. The optimum conditions for the association in aqueous phase and for extraction of the ion-associated complex Mo(VI)-3,5-DNC-TTC into chloroform were established. The effect of co-existing ions and reagents on the process of chelate formation and ion-association was studied. The validity of Beer's law was checked and the following analytical characteristics were calculated: the apparent molar absorptivity (ε'), the true molar absorptivity (ε), the limit of detection (*LOD*), the limit of quantification (*LOQ*) and the Sandell's sensitivity (*SS*). From the analytical characteristics of the extraction system Mo(VI)-3,5-DNC-TTC-H_2O-$CHCl_3$, it can be concluded that the ion-associate formed between the anionic chelate of Mo(VI)-3,5-DNC and the monotetrazolium cation allows determinations of Mo(VI) with a high sensitivity. The equilibrium constants needed for the quantitative assessment of the extraction equilibrium were also calculated, i.e. the association constant (β), the distribution constant (K_D), the extraction constant (K_{ex}) and the recovery factor (*R%*). The molar ratio of the components, determined by independent methods, shows that the ion-associated complex could be represented with the general formula $(TTC)_2\{MoO_2[O_2C_6H_2(NO_2)_2]_2\}$. A corresponding reaction scheme and a structural formula of the ion-associated complex were also suggested.

Acknowledgements

The authors would like to thank the Research Fund of the University of Plovdiv for the financial support of the current research.

5. References

1. Y. D. Tretyakov, L. I. Martinenko, A. N. Grigorev: Inorganic Chemistry, Moscow University, Moscow, Russia, **2007**, pp. 309-369
2. F. A. Cotton, G. Wilkinson, C. A. Murillo, M. Bochmann: Advanced Inorganic Chemistry, sixth ed., Wiley Publishers, New Jersey, **1999**, pp. 844-883.
3. V. V. Skopenko, A. Y. Tsivadze, L. I. Sabranskiy, A. D. Garnovskiy: Coordination Chemistry, Akademkniga, Moscow, Russia, **2007**, pp. 76-81.
4. A. P. Vinogradov: Analytical Chemistry of Elements - Molybdenum, Nauka, Moscow, Russia, **1962**, pp. 25-97.
5. V. M. Ivanov, G. A. Kochelaeva, *J. Anal. Chem.* **2003**, *58*, 31-37. **DOI:**10.1023/A:1021830013973
6. M. L. Harikumaran Nair, Anju. S. Appukuttan, *J. Korean Chem. Soc.* **2012**, *56*, 217-227. **DOI:**10.5012/jkcs.2012.56.2.217
7. T. Nakamura, S. Nishihama, K. Yoshizuka, *Solvent Extr. Res. Dev.* **2009**, *16*, 47-56.
8. L. Xue, D. Deng, Y. Xu, Q. Wang, *Russ. J. Coord. Chem.* **2016**, *42*, 137-142. **DOI:**10.1134/S1070328416020093
9. V. M. Ivanov, G. A. Kochelaeva, G. V. Prokhorova, *J. Anal. Chem.* **2002**, *57*, 758-772. **DOI:**10.1023/A:1020015521584
10. P. A. Petrov, M. Y. Afonin, D. Y. Naumov, S. N. Konchenko, A. V. Piskunov, *Russ. J. Coord. Chem.* **2015**, *41*, 31-36. **DOI:**10.1134/S1070328415010078
11. W. X. Xu, W. H. Li, *Russ. J. Coord. Chem.* **2012**, *38*, 92-98. **DOI:**10.1134/S107032841202011X
12. F. L. Fan, F. A. Lei, L. N. Zhang, J. Bai, M. S. Lin, H. J. Ding, X. L. Wu, D. Nayak, Z. Qin, *Solvent Extr. Ion Exch.* **2009**, *27*, 395-407. **DOI:**10.1080/07366290902821305
13. S. Tascioglu, E. Kaki, S. Tascioglu, *J. Appl. Spectrosc.* **2012**, *79*, 540-546. **DOI:**10.1007/s10812-012-9637-8
14. S. J. Kokake, A. A. Gavande, V. K. Vikhe, H. R. Aher, S.R. Kuchekar, *Indian J. Chem. Techn.* **2010**, *17*, 154–157.
15. J. Y. Lee, J. R.Kumar, H. S. Jeon, J. S. Kim, *Chem. Eng.* **2010**, *54*, 27-31. **DOI:**10.3311/pp.ch.2010-1.04
16. P. K. Parhi, Kyung-Ho Park, H. Kim, J. Park, *Hydrometallurgy* **2011**, *105*, 195-200. **DOI:**10.1016/j.hydromet.2010.09.004
17. J. Kim, S. Park, S. Kim, *Fluid Phase Equilib.* **2010**, *295*, 172-176. **DOI:**10.1016/j.fluid.2010.04.016
18. R. Colopado-Peralta, M. Sanches-Vazquez, I. F. Hernandes-Ahuactzi, S. A., Sanchez-Ruiz, R. Contreras, A. Flores-Parra, S. E. Castillo-Blum, *Polyhedron* **2012**, *48*, 72–79. **DOI:**10.1016/j.poly.2012.09.013
19. A. T. Pilipenko, M. M. Tananayko: Mixed Ligands and Mixed Metal Complexes and their Application in Analytical Chemistry, Khimiya, Moscow, Russia, **1983**, pp. 101-125.
20. J. L. Martinez-Vidal, A. R. Fernandez-Alba, F. Salinas, *Analyst* **1990**, *3*, 329-331. **DOI:**10.1039/an9901500329
21. M. L. C. Passos, M. Lucia M. F. S. Saraiva, J. F. C. Lima, *Anal. Sci.* **2005**, *12*, 1509-1515. **DOI:**10.2116/analsci.21.1509
22. K. Gavazov, A. Dimitrov, V. Lekova, *Russ. Chem. Rev.* **2007**, *76*, 169-179. **DOI:**10.1070/RC2007v076n02ABEH003655
23. K. B. Gavazov, V. D. Lekova, G. I. Patrovov, *Acta Chim. Slov.* **2006**, *53*, 506-511.
24. V. Divarova, V. Lekova, P. Racheva, K. Stojnova, A. Dimitrov,

Acta Chim. Slov. **2014**, *61*, 813–818.
25. V. V. Divarova, K. T. Stojnova P. V. Racheva, V. D. Lekova, *J. Appl. Spectrosc.* **2017**, *84*, 231–236. **DOI:**10.1007/s10812-017-0456-9
26. V. Divarova, K. Stojnova, P. Racheva, V. Lekova, *Acta Chim. Slov.* **2016**, *63*, 97–103. **DOI:**10.17344/acsi.2015.1987
27. P. Racheva, K. Stojnova, V. Divarova, V. Lekova, *Acta Chim. Slov.* **2017**, *64*, 365–372. **DOI:**10.17344/acsi.2017.3214
28. K. Stojnova, P. Racheva, V. Divarova, K. Bozhinova, V. Lekova, *Russ. J. Inorg. Chem.* **2017**, *62*, 249–256. **DOI:**10.1134/S0036023617020188
29. K. Stojnova, V. Divarova, P. Racheva, K. Bozhinova, V. Lekova, *Acta Chim. Slov.* **2018**, *65*, 213–220. **DOI:**10.17344/acsi.2017.3860
30. K. Stojnova, V. Lekova, *Acta Chim. Slov.* **2019**, *66*, 360–366. **DOI:**10.17344/acsi.2018.4862
31. K. T. Stojnova, V. D. Lekova, *Russ. J. Inorg. Chem.* **2019**, *64*, 1235–1241. **DOI:**10.1134/S0036023619100152
32. A. W. Nineham, *Chem. Rev.* **1955**, *55*, 355–483. **DOI:**10.1021/cr50002a004
33. H. Şenöz, *Hacettepe J. Biol. & Chem.* **2012**, *40*, 293–301.
34. A. K. Babko, A. T. Pilipenko: Photometric Analysis, Khimiya, Moscow, Russia, **1968**, pp. 159–164.
35. J. Inczédy: Analytical Applications of Complex Equilibria, Mir, Moscow, Russia, **1979**, pp. 225–242.
36. T. P. Rao, M. L. P. Reddy, A. R. Pillai, *Talanta* **1998**, *46*, 765–813. **DOI:**10.1016/S0039-9140(97)00262-2
37. A. N. Turanov, V. K. Karandashev, V. E. Baulin, E. V. Kirillov, S. V. Kirillov, V. N. Rychkov, A. Yu. Tsivadze, *Russ. J. Inorg. Chem.* **2016**, *61*, 1335–1338. **DOI:**10.1134/S0036023616100211
38. A. N. Turanov, V. K. Karandashev, O. I. Artyushin, E. V. Sharova, *Solvent Extr. Ion Exch.* **2015**, *33*, 540–553. **DOI:**10.1080/07366299.2015.1067052
39. V. A. Mikhaylov: Extraction Chemistry, Nauka, Novosibirsk, Russia, **1984**, pp. 194–249.
40. G. Kristian: Analytical Chemistry, BINOM, Moscow, Russia, **2009**, pp. 414–426.
41. K. Stojnova, V. Divarova, P. Racheva, K. Bozhinova, V. Lekova, *Acta Chim. Slov.* **2016**, *63*, 654–660. **DOI:**10.17344/acsi.2016.2513
42. Z. Marczenko, M. Baltcerzak: UV-Vis Spectrophotometric Methods Applied to the Inorganic Analysis, BINOM, Moscow, Russia, **2009**, pp. 169-174.
43. B. F. Quin, R. R. Brooks, *Anal. Chim. Acta* **1975**, *74*, 75–84. **DOI:**10.1016/S0003-2670(01)82781-1
44. M. I. Bulatov, I. P. Kalinkin: Practical Handbook on Photometric Methods of Analysis, Khimiya, Leningrad, Russia, **1986**, pp. 174–264.
45. W. Likussar, D. F. Boltz, *Anal. Chem.* **1971**, *43*, 1265–1272. **DOI:**10.1021/ac60304a006

Povzetek

S spektrofotometričnimi metodami smo raziskali tvorbo kompleksa med anionskim kelatom molibdena(VI) z dvoveznim ligandom 3,5-dinitrokateholom (3,5-DNC) in ionski asociat s kationom 2,3,5-trifenil-2*H*-tetrazolijevim kloridom (TTC) v tekoče-tekoče ekstrakcijskem sistemu Mo(VI)-3,5-DNC-TTC-H_2O-$CHCl_3$. Preverili smo veljavnost Beerovega zakona ter izračunali nekatere analizne karakteristike pri optimalnih pogojih za tvorbo kelata in ekstrakcijo. Raziskali smo vpliv različnih prisotnih ionov in reagentov na proces tvorbe kelata in ionskega asociata. Molsko razmerje komponent v ionsko asociiranem kompleksu Mo(VI)–3,5-DNC–TTC smo določili na podlagi neodvisnih metod. Asociacijski proces v vodni fazi in ekstrakcijsko ravnotežje smo proučili ter kvantitativno karakterizirali sledeče ključne konstante: konstanto asociacije, porazdelitveno in ekstrakcijsko konstanto ter izkoristek ekstrakcije. Na podlagi dobljenih podatkov je predlagana reakcijska shema, splošna formula in struktura kompleksa.

Except when otherwise noted, articles in this journal are published under the terms and conditions of the Creative Commons Attribution 4.0 International License

DOI: 10.17344/acsi.2019.5616 *Acta Chim. Slov.* **2020,** *67,* 602–608
creative commons

Scientific paper

Enhanced Adsorption of Lead (II) Ions from Aqueous Solution by a Chemically Modified Polyurethane

Mangaleshwaran Lakshmipathy,[1] Muthukumaran Chandrasekaran[2] and Rasappan Kulanthasamy[3]

[1] *Department of Civil Engineering, Government College of Technology, Coimbatore-641013, Tamilnadu, India*

[2] *Department of Industrial Biotechnology, Government College of Technology, Coimbatore-641013, Tamilnadu, India*

[3] *Department of Civil Engineering, Coimbatore Institute of Technology, Coimbatore-641014, Tamilnadu, India*

* *Corresponding author: E-mail: iitmangal@yahoo.com*
Tel.: +91 9442051988

Received: 10-04-2019

Abstract

Heavy metal pollution is a major threat to living systems due to increase in the industrial development worldwide. In this study, the adsorption of lead (II) ions by chemically modified polyurethane was reported. Polyurethane (PU) was chemically modified by sulphonation and chlorination to obtain sulphonated PU (SPU) and chlorinated PU (CPU). The adsorption parameters such as pH, contact time, adsorbent loading and initial metal ion concentration were optimized in batch experiments for both the adsorbents. Maximum Pb (II) ion adsorption of 90 and 85% was observed for SPU and CPU respectively at optimal conditions. Isotherms results showed that the equilibrium data was fitted with Freundlich isotherm and followed multilayer adsorption mechanism. Adsorption of Pb (II) ions by both SPU and CPU followed pseudo second order kinetics. The outcome of this study showed that chemical modification of PU is effective for efficient removal of Pb (II) ions from effluent.

Keywords: lead; isotherm; chemical modification; polyurethane, kinetics.

1. Introduction

Heavy metal pollution in the environment was mainly caused by the industrial waste discharge to water bodies.[1] Unlike organic pollutants, heavy metal ions are stable and persistent environmental contaminants which are non biodegradable. Water contaminated by toxic metal ions remains a serious public health problem for human health.[2] Unique properties of lead like high ductility, flexibility, softness, resistance to corrosion and low melting point have resulted in its widespread usage in different industries like ceramics, plastics, automobiles, paint, etc. This in turn has led to a manifold rise in the occurrence of free lead in biological systems and environment. Human exposure to lead occurs through various sources like battery recycling, coal combustion, leaded gasoline and industrial processes etc. Lead toxicity is particularly insidious hazard with the potential of causing irreversible health effects. It was known to interfere with numerous body functions and it primarily affects hematopoietic, central nervous, renal and hepatic system producing serious disorders.[3] Chronic toxicity, on the other hand was much more common and occurs at blood Lead levels of about 40–60 μg/dL. It could be much more severe, if not treated in time resulted by encephalopathy, persistent vomiting, delirium, lethargy, convulsions and coma.[4,5]

Several methods commonly employed for Pb (II) removal from aqueous solution include biosorption,[6–7] nanofiltration,[8] ion exchange[9] and reverse osmosis.[10] But these methods have the disadvantages like less removal efficiency, require high energy, generation of toxic end products which need further treatments made these processes costly for heavy metal removal at lower concentration. Adsorption is an effective technique with many advantages like convenience, simplicity, efficiency including cost-effectiveness and minimization of secondary wastes. Polyurethane foam (PU) is a cheaper and thermodynamically favorable adsorbent material for heavy metal removal from industrial wastewaters.[11] Previously, PU was reported as an effective

adsorbent for removal of nickel, mercury, cadmium etc.[12–14] The porosity and high surface of PU make it suitable as efficient adsorbent for heavy metal removal.[15] Mangaleshwaran et al. reported that the efficiency of adsorption can be enhanced by chemical modification of PU.[12]

The aim of the present study was to evaluate the adsorption efficiency of chemically modified polyurethane for Pb (II) ion removal from aqueous solution. The batch optimization of adsorption parameters (pH, contact time, adsorbent loading and initial metal ion concentration) was investigated. Adsorption isotherms and kinetics of Pb (II) ion adsorption were also reported.

2. Experimental

2. 1. Synthesis and Chemical Modification of PU

25 mL of toluene diisocyanate (Merck, India) and 25 mL of tetra methylene ether glycol (Merck, India) was added in acidic condition and form homogenous mixture to initiate polymerization. In the polymerization reaction, initially toluene diisocyanate in acidic medium reacts initially with free available H^+ ions and then reacts with tetra methylene ether glycol to form PU. After completion of foaming, solid structured open cellular PU was cut into small cubes (1 cm) and used for further studies. The synthesized PUF was chemically modified by two methods (i) sulphonation and (ii) chlorination. To obtain sulphonated PU (SPU), 25 mL of 4N H_2SO_4 (Merck, India) added to 2 g of PUF and agitated for 45 min at 60 °C at 100 rpm. After this treatment, the cubes were dried at 105–110 °C for 3 h. In chlorination reaction, 50 mL of 0.5% bleaching powder (Sigma Aldrich, India) solution was added to 2 g of PUF and agitated for 45 min at 60 °C at 100 rpm. After this step, the cubes were dried at 105–110 °C for 3 hrs to get chlorinated PU (CPU) [12]. The chemically modified SPU and CPU were used for further Pb (II) ion adsorption in batch mode.

2. 2. Preparation of Pb (II) Adsorbate Solution

Pb (II) stock solution was prepared by dissolving 1.6 grams of lead nitrate in a 1000 mL volumetric flask and diluted using double distilled water to get a 1000 (mg/L) concentration. The sample solution concentrations 10-50 (mg/L) were prepared from stock solution by dilution using double distilled water and the pH of the samples were adjusted using 0.1N HCl and 0.1N NaOH.

2. 3. Batch Adsorption Studies Using SPU and CPU

The adsorption efficiency of SPU and CPU were studied in a batch mode by varying the adsorption parameters such as pH (2–6), contact time (5–150 min), adsorbent dosage (0.25–3g/50 mL) and initial adsorbate concentration (10–50 mg/L). At the end of each batch experiment, remaining Pb (II) ion concentration was determined by measuring absorbance in UV-Vis spectrophotometer at 520 nm as per IS 3025 (Part 47): 2003 procedure. The adsorption efficiency was calculated using following Eq.1

$$\text{Pb(II)adsorption efficiency} = = \frac{(Initial\ absorbance - final\ absorbance)}{Initial\ absorbance} x\ 100 \quad (1)$$

2. 4. Desorption and Reusability Studies

For desorption studies, NaOH was chosen as regenerant since the adsorption was carried out in acidic environment. 50 mL of 0.2, 0.4, 0.6, 0.8 and 1.0N NaOH was taken in 250 mL Erlenmeyer flask and 1 g of adsorbents (SPU, CPU after adsorption) was added separately in each flask, agitated at 100 rpm, 120 minutes for Pb (II) ions desorption. After desorption, the adsorbents were taken out and dried. The dried adsorbents were employed for adsorption of 50 mL of Pb (II) solution (10 mg/L) and their removal efficiency was calculated by measuring the absorbance after adsorption. A plot between maximum removal efficiency and concentration of regenerant was plotted and optimum dose of regenerant was selected. The adsorption and desorption process were repeated for 5 cycles and the Pb (II) removal efficiency were calculated.

3. Results and Discussion

3. 1. Batch Adsorption Studies Using SPU and CPU on Pb (II) ion Adorption

Batch experiments were carried out to study the factors affecting the adsorption process such as pH, contact time, adsorbent dosage and initial adsorbate concentration on Pb (II) ion adsorption by SPU and CPU.

3. 1. 1 Effect of pH

In order to study the effect of pH on Pb (II) adsorption, experiments were carried out for SPU and CPU at the pH range (2 to 6) keeping the contact time constant as 150 min. For SPU, the Pb (II) ion adsorption efficiency was observed increase with increase in pH from 2 to 4 and above pH 4, Pb (II) ion removal efficiency was declined (Fig.1a). The maximum Pb (II) ion removal efficiency of 90 % was obtained at pH 4 for SPU. Similar to SPU, the maximum Pb (II) adsorption efficiency (79%) was obtained at pH 4 for CPU whereas the adsorption efficiency was observed lesser than SPU (Fig.1a). The optimal pH for maximum Pb (II) absorption by both the adsorbent was found to be 4

and it was correlated with the results published previously.[16–17] The results revealed that the optimum pH at which the maximum Pb (II) ions removed by SPU and CPU were in the acidic range. At acidic pH, H^+ ions compete with Pb (II) ions at the adsorbent surface which would hinder Pb (II) ions reaching the bonding sites of adsorbate caused by the repulsive forces. At higher pH > 6, the Pb (II) ions get precipitated due to hydroxide anions forming lead hydroxide precipitate. This hydroxylated form metals can also compete with metal ions at the active sites of the adsorbent thereby decreasing the adsorption.[16]

3. 1. 2 Effect of Contact Time

The effect of contact time on the Pb (II) ion removal efficiency using SPU and CPU at optimized pH 4 was represented in Fig.1b. The Pb (II) ion removal efficiency of SPU was increased from 18 to 90% as the contact time was increased from 5 to 90 min and beyond 90 min, the adsorption of Pb (II) ion attained equilibrium. Khan et al.[18] obtained 87.6 % of Pb (II) ion removal using 0.1 g/L of multiwalled carbon nanotubes with the contact time of 90 min which was comparable to the present study. For CPU, Pb (II) ion adsorption efficiency was initially rapid and increased till 120 min. Further increase in contact time beyond 120 min to 180 min showed that adsorption attained equilibrium. The maximum Pb (II) ion removal efficiency (80%) by CPU was observed at 120 min. Nordiana and Siti[16] also reported similar contact time for maximum Pb (II) ions removal using activated charcoal and peanut shell. The Pb (II) ion removal efficiency by SPU and CPU increases rapidly during the initial stage which may be due to that adsorbent sites at the surface were empty and the adsorbate concentration gradient was high. Later, the adsorbate uptake rate was decreased mainly due to the unavailability of adsorption sites in the adsorbent surface.[19]

3. 1. 3 Effect of Adsorbent Dosage

Absorbent dosage is a critical parameter in the adsorption process to identify the optimal amount of adsorbent required for maximum adsorbate removal. The effect of adsorbent dosage (0.25–3 g/50 mL) on the adsorption of Pb (II) ion by SPU and CPU were studied at pH 4 and contact time 90 min and 120 min respectively. Fig.1c represents the Pb (II) ion removal efficiency by SPU and CPU at different adsorbent dosage. The optimal adsorbent dosage of SPU and CPU was found to be 0.75 g in 50 mL and 1 g in 50 mL and

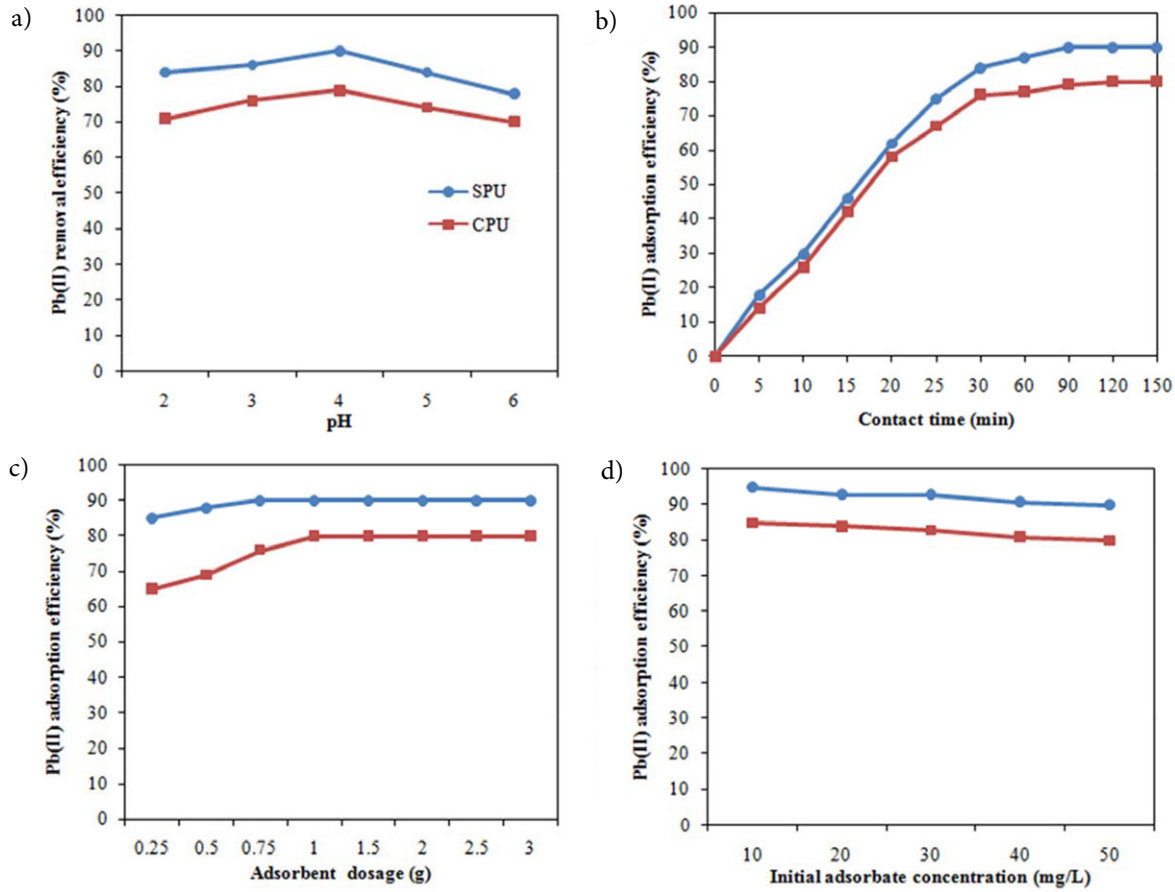

Figure 1. Effect of (a) pH, (b) contact time, (c) adsorbent dosage and (d) initial adsorbate concentration on Pb (II) ion removal efficiency using SPU and CPU

the maximum Pb (II) ion removal of 90% and 80% respectively. The increase in removal efficiency with the increase of adsorbent dosage was mainly attributed to the presence of more vacant active sites in the adsorbent surface.[20]

3. 1. 4 Effect of Initial Adsorbate Concentration

Experiments were carried out to study the effect of initial adsorbate concentration (10–50 mg/L) on Pb (II) adsorption by SPU and CPU with optimized pH 4, optimized contact time (SPU 90 min, CPU 120 min) and optimized adsorbent dosage (SPU 0.75 g/50 mL, CPU 1 g/50 mL).The trend of Pb (II) removal efficiency by SPU and CPU was shown in Fig.1d.At the initial Pb (II) ion concentration of 10 (mg/L), higher Pb (II) removal efficiency was expected than the other studied concentrations for both SPU and CPU. At lower concentration, the numbers of Pb (II) ions available in the solution are less as compared to the available sites on the adsorbent. However, at higher concentrations, the available sites for adsorption become fewer, and the percentage removal of lead ions depends on the initial concentration.[21]

3. 2. Adsorption Isotherms

The mechanism of Pb (II) ion adsorption onto the adsorbent surface was studied by fitting equilibrium data with Langmuir[22] and Freundlich[23] isotherm models represented in Eq.2 and 3.

$$\frac{C_e}{q_e} = \frac{C_e}{q_0} + \frac{1}{q_0 b} \quad (2)$$

$$\ln q_e = \ln K + \frac{1}{n \ln C_e} \quad (3)$$

where *q*e (mg/g) is metal adsorbed per mass of adsorbent, q_0 (mg/g) is maximum adsorption capacity, *b* (L/mg) adsorption energy constant, *C*e (mg/L) is equilibrium metal ion concentration, *K* and *n* were Freundlich isotherm constants.

Langmuir and Freundlich plots for SPU and CPU on Pb (II) adsorption were represented in Fig. 2a–d and the estimated isotherm model constant values were given in Table.1. Based on the R^2 value, both the adsorbents fitted well with both the isotherm models and are highly correlated with Freundlich model than Langmuir model (Table.1). The characteristic equilibrium separation factor R_L of Langmuir isotherm SPU and CPU were calculated as 0.299 and 0.640 respectively, which indicates the favorable adsorption of Pb (II) ion on the adsorbent.

The maximum adsorption capacity (q_0) for SPU and CPU were estimated from Langmuir plot as 5.435 and 5.495 mg/g respectively and the obtained results was compared with other adsorbents reported in the previous studies on Pb (II) ion adsorption (Table.2).The Freundlich isotherm

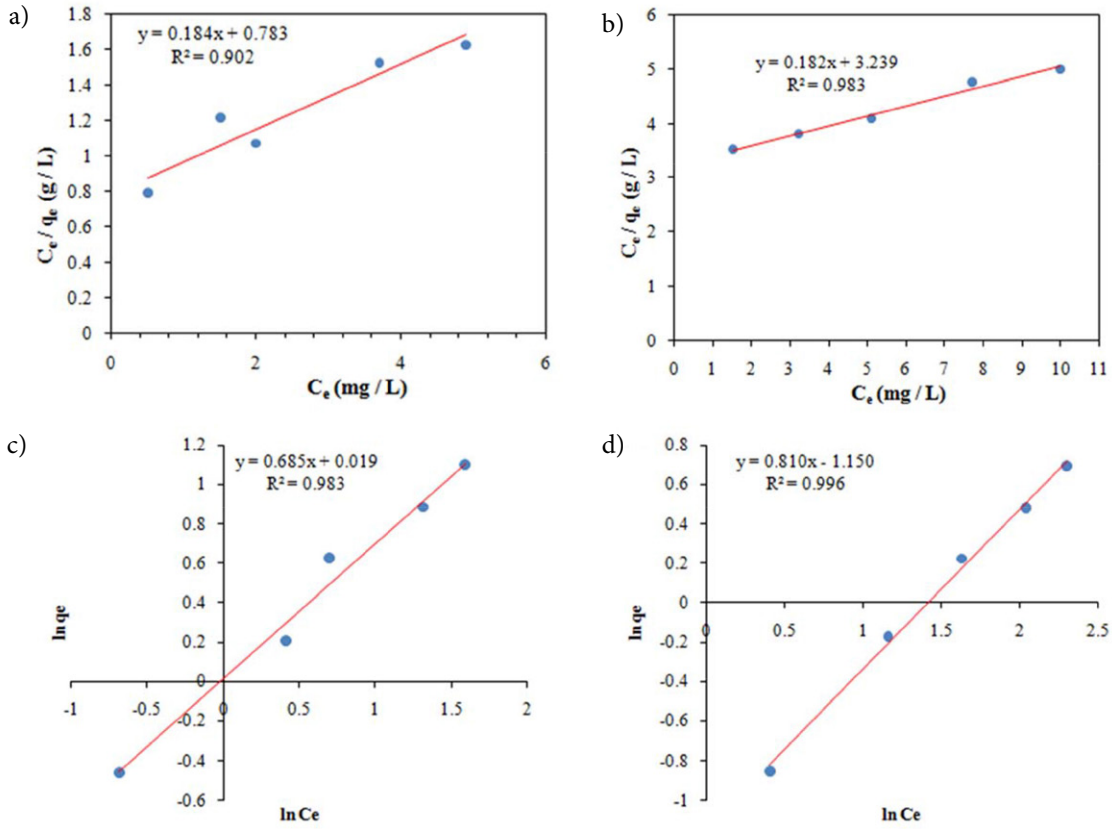

Figure 2. (a &b) Langmuir isotherms and (c & d) Freundlich isotherm for the adsorbents SPU and CPU.

Table 1. Estimated constants for Langmuir and Freundlich isotherm models for the adsorption of Pb (II) ion using SPU and CPU

Adsorbent	Langmuir model				Freundlich model		
	b (L / mg)	q_0 (mg / g)	$R_L = \frac{1}{1+bC_0}$	R^2	K_f (mg/g)	n (L / mg)	R^2
SPU	0.235	5.435	0.299	0.902	1.019	1.460	0.983
CPU	0.056	5.495	0.640	0.983	0.316	1.235	0.996

parameter 'n' measures adsorption intensity of adsorbent and the value of 'n' between 1 to 10 indicates favorable multilayer adsorption. Based on the obtained 'n' values for SPU and CPU, this study revealed that the adsorption of Pb (II) ion for SPU and CPU favored by multilayer mechanism.

3. 3. Adsorption Kinetics

The adsorption data were used to fit the pseudo first order[24] and pseudo second order[25] kinetic models to predict the controlling mechanism of adsorption.

Table 2. Comparison of Langmuir isotherm model parameters for Pb (II) ion adsorption using various adsorbents

Absorbent	Langmuir isotherm model parameters			Reference
	q_o (mg / g)	b (L / mg)	R^2	
Sesame leaf activated carbon	279.860	0.123	0.994	Liu et al.[31]
CS-Fe_2O_3 nanocomposite	214.92	0.077	0.991	Ahmad and Mirza,[32]
2,2'- Ethylenedithio diethanol immobilized amberlite XAD 16	107.52	11.625	0.999	Khalil et al. [33]
Maize green algae activated carbon	24.154	0.350	0.982	Suresh and Chandrasekaran, [21]
CPU	5.495	0.056	0.983	Present study
SPU	5.435	0.235	0.902	Present study
Maize leaf activated carbon	3.713	0.627	0.998	Uzma, [17]
Chitosan -G- Polyacrylonitrile	3.080	0.019	0.984	Shanmugapriya et al.[34]

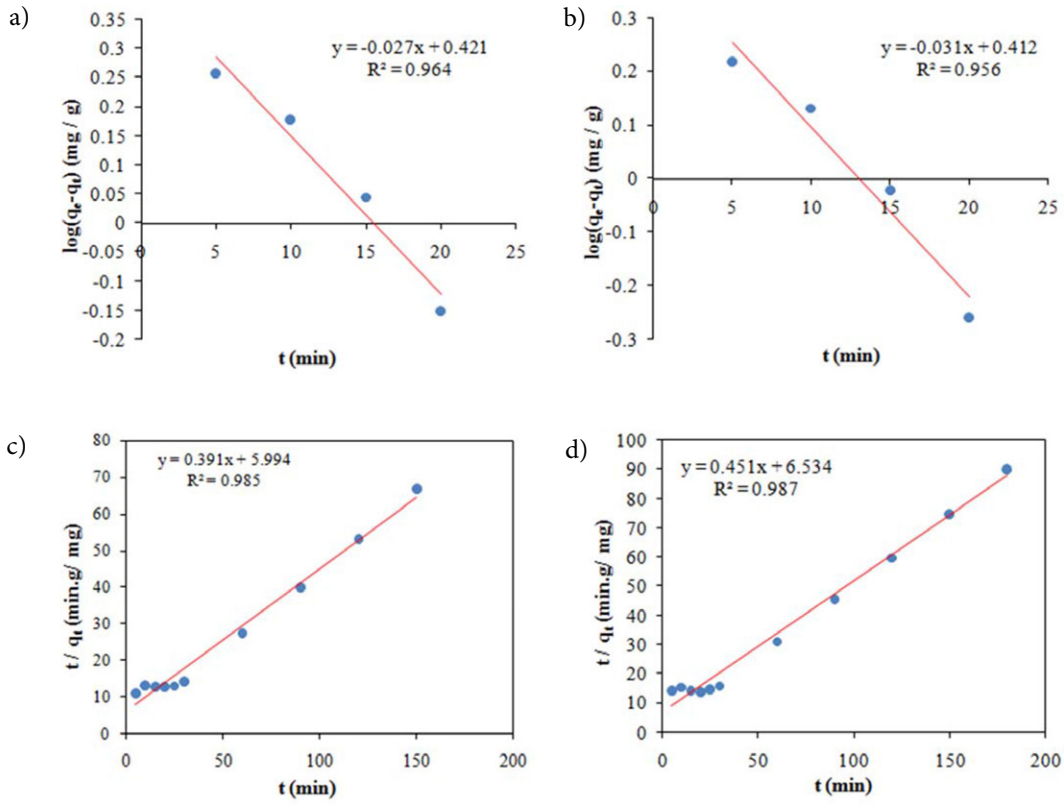

Figure 3. (a & b) Pseudo first order and (c & d) Pseudo second order kinetics plot for Pb (II) ion adsorption by SPU and CPU

$$\log(q_e - q_t) = \log q_e - \frac{k_1}{2.303} t \quad (4)$$

$$\frac{t}{q_t} = \frac{1}{k_2 q_e^2} + \frac{t}{q_e} \quad (5)$$

where q_e and q_t are the amount of metal ion adsorbed (mg/g) at equilibrium and at time t, k_1 is pseudo first order rate constant (min^{-1}) and k_2 is pseudo second order rate constant (min^{-1}).

The graphs were plotted between log (q_e–q_t) versus t and t/q_t versus t to estimate the rate constants for pseudo first order and pseudo second order kinetic model respectively. The kinetic plots for SPU and CPU on Pb (II) adsorption were shown below (Fig.3a–d). The estimated kinetic constants were given in Table.3 and observed that the pseudo second order model have good agreement with the experimental data since the R^2 values are closer to unity for both SPU and CPU. Similar results were reported for Pb (II) ions adsorption using different adsorbents.[26–27] The higher consistency of q_e experimental with q_e calculated from pseudo second order model indicates that the adsorption process was controlled by chemisorption.[28]

Table 3. Pseudo first order and pseudo second order kinetic constant for Pb (II) ion adsorption by SPU and CPU

Adsorbent	Pseudo first order constants			Pseudo Second order constants		
	$q_{e,cal}$ (mg . g^{-1})	K_1 (min^{-1})	R^2	$q_{e,cal}$ (mg . $g^{-1)}$	K_2 (min^{-1})	R^2
SPU	2.636	0.0621	0.964	2.558	0.0255	0.985
CPU	2.582	0.0713	0.956	2.217	0.2060	0.987

3. 4. Desorption and Reusability Studies

The recycling and regeneration of adsorbent was useful for making the process cost effective by reutilizing the adsorbent for several cycles.[29] Table.4 represented the maximum adsorption of Pb (II) ions using SPU and CPU as adsorbent for five adsorption – desorption cycles. From the adsorption- desorption cycles of Pb (II) adsorption by SPU and CPU revealed that the adsorption was reversible. However the removal efficiency of each adsorbent (SPU and CPU) was decreasing for each cycles. About 15–22% of reduction in adsorption efficiency was observed in SPU and 26 to 32 % reduction in adsorption efficiency was observed in CPU after 5 cycles. Similar results were obtained by Lingamdinne et al.[30] for Pb (II) ions using graphene oxide based nickel ferrite nano composite for 5 cycles.

4. Conclusions

The present study revealed that the efficiency of SPU and CPU for the removal of Pb (II) ions from the aqueous solution was highly depends on pH, contact time, adsorbent dosage and initial adsorbate concentration. 15 g /L of SPU effectively removed 95% of Pb (II) ion from 10 mg/L concentrated aqueous solutions at pH 4 for 90 minutes contact time. 20 g/L of CPU effectively removed 85 % of Pb (II) ion from 10 mg / L concentrated aqueous solutions at pH 4 for 120 min contact time.Adsorption data fitted with Langmuir and Freundlich isotherm model. Based on R^2 value, Freundlich isotherm model fitted well than Langmuir adsorption isotherm model. The Langmuir isotherm parameters such as adsorption capacity and adsorption intensity of SPU on Pb (II) ion adsorption was obtained as 5.435 mg/g and 0.235 L/ mg respectively. The adsorption capacity and adsorption intensity of CPU on Pb (II) ion adsorption was obtained as 5.495 mg/g and 0.056 L/mg respectively. Kinetic modeling studies revealed that Pb (II) ion adsorption process onto SPU and CPU followed pseudo second order kinetics. Chemically Modified PU can be utilized as a cheap adsorbent for Pb (II) ion removal for waste water.

Table 4. Maximum Pb (II) ion adsorption in adsorption-desorption cycles by SPU and CPU

Adsorbent	Adsorption- desorption cycles				
	1	2	3	4	5
SPU	93	89	86	82	78
CPU	84	81	78	73	68

Acknowledgement

Authors wish to thank The Principal and Head, Department of Civil Engineering, Government College of Technology, Coimbatore for providing facilities to carry out this study.

5. References

1. A. Demirbas, A. Sari, O. Isildak, *J. Hazard. Mater.* **2006,** *135*, 226–231. **DOI:**10.1016/j.jhazmat.2005.11.056
2. A. Demirbas, *J. Hazard. Mater.* **2008**, *157*, 220–229. **DOI:**10.1016/j.jhazmat.2008.01.024
3. K. Kalia, S. J. Flora, *J. Occup. Health*. **2005**, *47*, 1–21. **DOI:**10.1539/joh.47.1
4. S. J. S. Flora, G. Flora, G. Saxena, in: S. C. José, S. José (Eds.), Lead: Amsterdam, Elsevier, **2006**, pp 158–228. **DOI:**10.1016/B978-044452945-9/50004-X
5. J. M. Pearce, *European Neurol.* **2007**, *57*, 118–119. **DOI:**10.1159/000098100
6. Y. Zhu, Y. Jiang, Z. Zhu, H. Deng, H. Ding, Y. Li, L. Zhang, J. Lin, J. Clean. Prod. **2018**, *187*, 650–661. **DOI:**10.1016/j.jclepro.2018.03.275
7. M. Ziati, S. Hazourli, *Microchem. J.* **2019**, *146*, 164–169. **DOI:**10.1016/j.microc.2018.12.041

8. A. Otero-Fernández, J. A. Otero, A. Maroto-Valiente, J. I. Calvo, L. Palacio, P. Pradanos, A. Hernandez, *Clean Technol. Environ. Pol*. **2018**, *20*, 329–343. **DOI:**10.1007/s10098-017-1474-2
9. Q. Dong, X. Guo, X. Huang, L. Liu, R. Tallon, B. Taylor, J. Chen, *Chem. Eng. J.* **2019**, *361*, 1535–1542. **DOI:**10.1016/j.cej.2018.10.208
10. K. Jainaea, K. Sanuwong, J. Nuangjamnong, N. Sukpirom, F. Unob, *Chem. Eng. J.* **2010**, *160*, 586–593. **DOI:**10.1016/j.cej.2010.03.080
11. C. Yong, G. Yu, G. Zeng, H. Yang, F. Chen, C. Jin, J. Environ. Sci. **2011**, *23*, 1325–1333. **DOI:**10.1016/S1001-0742(10)60565-7
12. L. Mangaleshwaran, A. Thirulogachandar, V. Rajasekar, C. Muthukumaran, K. Rasappan, J. *Taiwan Inst. Chem. Eng.* **2015**, *55*,112–118. **DOI:**10.1016/j.jtice.2015.03.034
13. J. F. Flores-Aguilar, C. A. Galán-Vidal, J. A. Rodríguez, J. G. Alvarado-Rodríguez, M. E. Páez-Hernández , *Int. J. Environ. Sci. Technol.* **2019**, *16*, 1005–1014. **DOI:**10.1007/s13762-018-1723-x
14. M. Sayed, N. Burham, *Int. J. Environ. Sci. Technol.* **2018**, *15*, 105–118. **DOI:**10.1007/s13762-017-1369-0
15. M. Abbas, M. L. Moslem, B. Mehdi, *React. Function. Polym.* **2014,** *83,*14–23.
16. S. M. T. Nordiana, Z. A. R. Siti, *World J. Sci. Technol. Res.* **2013**, *1*, 102–109.
17. N. Uzma, *European Chem. Bull.* **2013**, *2*, 927–931.
18. T. A. Khan, N. Momina, E. A. Khan, R. Ufana, *J. Mol. Liq.* **2015**, *212*, 467–479.
19. A. A. Farghali, M. Bahgat, A. A. Enaiet, M. H. Khedr, *Beni-Suef Univ. J. Basic Appl. Sci.* **2013**, *2*, 61–71. **DOI:**10.1016/j.bjbas.2013.01.001
20. M. Kumar, J. S. Chung, S. H. Hur, *Appl. Sci*. **2019**, *9*, 2925. **DOI:**10.3390/app9142925
21. J. R. P. Suresh, V. Chandrasekaran, *Int. J. Ind. Chem*. **2014**, *4*, 1–10.
22. I. Langmuir, *J. Am. Chem. Soc*. **1918**, *40*, 1361–1403. **DOI:**10.1021/ja02242a004
23. H. Freundlich, Z. Phys. Chem. **1906**, *57*, 385–470.
24. S. Lagergren, KSven. Vetenskapsakad. Handl. **1898**, *24*, 1–39.
25. Y. S. Ho, G. McKay, *Process Biochem*. **1999**, *34*, 451–465. **DOI:**10.1016/S0032-9592(98)00112-5
26. K. Tomasz, K. Anna, C. Ryszard, *Microchem. J*. **2019**, *145*, 1011–1025. **DOI:**10.1016/j.microc.2018.12.005
27. C. Xiong, S.Wang, W. Sun, Y. Li, *Microchem. J*. **2019**, *146*, 270–278. **DOI:**10.1016/j.microc.2019.01.005
28. L. I. Hui, D. L. Xiao, H. E. Hua, L. I. N. Rui, P. L. Zuo, *Trans. Nonferrous Metal Soc. China*. **2013**, *23*, 2657–2665. **DOI:**10.1016/S1003-6326(13)62782-X
29. A. Rashid, N. B. Haq, I. Munawar, N. Saima, Ecol. Eng. **2016**, *91*, 459–471. **DOI:**10.1016/j.ecoleng.2016.03.014
30. L. P. Lingamdinne, J. R. Koduru, Y. L. Choi, Y. Y. Chang, J. K. Yang, *Hydrometallurgy* **2016**,*165*, 64–72. **DOI:**10.1016/j.hydromet.2015.11.005
31. L. E. Liu, J. Liu, H. Li, H. Zhang, J. Liu, H. Zhang, *BioResources,* **2012**, *7*, 3555–3572.
32. R. Ahmad, A. Mirza, *J. Clean. Prod*. **2018**, *186*, 342–352. **DOI:**10.1016/j.jclepro.2018.03.075
33. T. E. Khalil, A. E. Dissouky, S. Rizk, *J. Mol. Liq*. **2016**, *219*, 533–546. **DOI:**10.1016/j.molliq.2016.03.063
34. A. Shanmugapriya, M. Hemalatha, B. Scholastica, A.P.D. Agustine, Der Pharma Chemica. **2013**, *5*, 141–155.

Povzetek

Zaradi vsesplošne industrializacije predstavlja onesnaženje s težkimi kovinami resno grožnjo vsem živim bitjem. V tej študiji smo preučevali adsorpcijo svinčevih (II) ionov na modificiran poliuretan. Poliuretan (PU) smo kemijsko modificirali s sulfonacijo in kloriranjem, s čimer smo pridobili sulfoniran PU (SPU) in kloriran PU (CPU). Pri obeh adsorbentih smo optimirali parametre adsorpcije kot so pH vrednost, kontaktni čas, količina adsorbenta in začetna koncentracija kovinskih ionov. Pod optimalnimi pogoji smo dosegli 90% in 85% adsorpcijo ionov na SPU oziroma CPU. Ravnotežni rezultati adsorpcije so pokazali, da gre za večplastno adsorpcijo, ki jo lahko opišemo s Freundlich-ovo izotermo. Hitrost adsorpcije na oba nosilca je sledila kinetiki pseudo-drugega reda. Rezultati študije so pokazali, da lahko kemijsko modificiran PU učinkovito odstranjuje Pb (II) ione iz odplak.

Except when otherwise noted, articles in this journal are published under the terms and conditions of the Creative Commons Attribution 4.0 International License

Scientific paper

Enhanced Catalytic Degradation of Acid Orange 7 Dye by Peroxymonosulfate on Co_3O_4 Promoted by Bi_2O_3

Vanina Ivanova-Kolcheva,[1] Labrini Sygellou[2] and Maria Stoyanova[2,*]

[1] *Department of Physical Chemistry, University of Plovdiv 24, Tsar Asen Str., 4000 Plovdiv, Bulgaria*

[2] *Foundation for Research and Technology, Institute of Chemical Engineering Sciences (FORTH/ICE-HT), Patras, GR-26504, Greece*

** Corresponding author: E-mail: marianas@uni-plovdiv.bg*
tel: +35 932 261248 fax: +35 932 261403

Received: 10-16-2019

Abstract

In this study, Bi_2O_3-Co_3O_4 composite oxides were prepared and their catalytic efficiency to activate peroxymonosulfate (PMS) towards the degradation of Acid Orange 7 dye (AO7) was evaluated. The characterization of the synthesized catalysts was carried out by XRD, TEM, XPS, FT-IR, and ICP-OES analyses. The increased basicity of the Bi_2O_3-Co_3O_4 hybrids contributed to the much better catalytic activity in PMS activation resulting in a considerably higher rate of AO7 degradation compared to that obtained with bare Co_3O_4. The sample with 50 wt.% Bi_2O_3 showed the best performance under a broad pH range with very low Co leaching of 72 μg/L even under acidic conditions. Degradation of 50 mg/L AO7 reached almost 100% within a short duration of 12 min by using very low catalysts concentration of 0.1 g/L and [PMS]/[AO7] = 6. The influence of the Bi_2O_3 content, catalyst dosage, molar ratio of [PMS]/[AO7], initial pH, and temperature on AO7 degradation were studied. Surface-bound sulfate radicals generated in the Bi_2O_3-Co_3O_4/PMS oxidation system were proved as the predominant radical species through radical quenching experiments.

Keywords: Acid orange 7 degradation; Bi_2O_3-Co_3O_4 catalyst; peroxymonosulfate; sulfate radicals

1. Introduction

Azo dyes represent one of the largest groups of organic pollutants in wastewaters, generally released from textile, leather, paper, printing, plastic, food, pharmaceutical and cosmetic industries.[1,2] Dyes are not only highly visible, but also toxic, mutagenic, carcinogenic and low biodegradable.[3–5] Therefore, these contaminants must be removed from wastewater prior to discharge into natural water bodies to prevent their detrimental effect to the natural ecosystem and human health. Due to the complex aromatic molecular structures of azo dyes, most of them are persistent and recalcitrant in the environment and therefore cannot easily be degraded by the conventional wastewater treatment processes.[6–8] In the recent decade, the application of peroxymonosulfate (PMS) based catalytic oxidation processes for the degradation of several refractory organic contaminants in water including dyes has attracted increasing interest.[9–13] PMS is capable of generating highly reactive radicals, such as sulfate radicals ($SO_4^{\bullet-}$, E^o = 2.5–3.1 V) and hydroxyl radicals (•OH, E^o = 1.9–2.7 V), by activation through transition metals and their oxides,[9–16] ultrasound,[17,18] anions,[19,20] and base.[21,22] Compared to the •OH, $SO_4^{\bullet-}$ has a longer lifetime (30–40 ms vs 20 ns) thus allowing it to react effectively with the target organic pollutant.[23] Among the PMS activation methods, the most feasible route for production of $SO_4^{\bullet-}$ radicals is catalytic activation by transition metal ions, with cobalt ions (Co^{2+}) being the best activator.[14] Anipsitakis and Dionysiou showed that Co^{2+}/PMS could be an alternative method for degradation of organic compounds with excellent performance in neutral pH, which is an applicable benefit of this system compared to the Fenton reagent.[9] However, the difficult recovery of the homogeneous catalyst and especially the problem related to the potential environmental and health impact of cobalt in aquatic environment limit the practical-scale application of the homogeneous Co^{2+}/PMS system. Therefore, the development of

heterogeneous cobalt-based catalysts to activate PMS with low cobalt leaching is highly desirable. Among cobalt oxides, Co_3O_4 has been thoroughly investigated to activate PMS for degradation of various organic pollutants in water such as 2,4-dichlorophenol,[24] phenol,[25,26] antibiotics,[16,27] and dyes.[28,29] In order to enhance the catalytic performance and reduce cobalt leaching of Co_3O_4, several supports such as common oxide materials (Al_2O_3, TiO_2, MgO, SBA-15), activated carbon, carbon nanofibers, zeolite, etc. have been used for hosting Co_3O_4 particles and tested for oxidative degradation of contaminants in the presence of PMS.[10,30–35] Zhang et al. reported for a much better performance of Co/MgO catalyst than bulk Co_3O_4 for degradation of methylene blue dye via heterogeneous PMS activation.[30] The abundance of surface hydroxyl groups on the MgO support facilitate the formation of surface Co–OH complexes, which is considered as the rate-limiting step for PMS activation.[31] Co_3O_4 supported on graphene oxide was prepared and used in the degradation of azo dye AO7 by advanced oxidation technology based on sulfate radicals.[36] The Co_3O_4/GO nanocomposite exhibits a markedly better efficiency for PMS activation than both the homogeneous Co^{2+} and the heterogeneous unsupported Co_3O_4 catalyst due to the Co–OH complexes formed on the surface of the GO sheet through the direct interaction of Co species with nearby hydroxyl groups. As the presence of surface basic sites can promote the formation of the surface Co–OH complex, doping of Co_3O_4 with basic metal oxides would have a promotional effect on its PMS activation ability. Due to the high density of surface hydroxyl groups of the Bi-based materials, their synergistic coupling with Co_3O_4 can enhance its catalytic performance for PMS activation.[37] The bimetallic Co-Bi oxide catalyst synthesized using a microwave-assisted method showed a much higher bisphenol A degradation and TOC removal efficiency via PMS activation than those of Co_3O_4/PMS and Bi_2O_3/PMS systems.[38]

Herein, a performance evaluation of Bi_2O_3-Co_3O_4 catalysts as PMS activator for oxidative degradation of azo dye Acid Orange 7 is investigated. The kinetics of the oxidation process and the effects of various operational parameters, namely Bi_2O_3 content, catalyst dosage, molar ratio of [PMS]/[AO7], initial pH, and reaction temperature on the catalytic efficiencies in Bi_2O_3-Co_3O_4 /PMS system were studied in detail. Specific quenching studies were also carried out to identify the primary radical species formed from the catalyst-mediated decomposition of PMS.

2. Experimental

2. 1. Chemicals

Cobalt nitrate ($Co(NO_3)_2 \times 6H_2O$), bismuth nitrate ($Bi(NO_3)_3 \times 5H_2O$), magnesium nitrate ($Mg(NO_3)_2 \times 6H_2O$), Acid Orange 7 (AO7) and methylene blue (MB) were provided by Sigma-Aldrich (St. Louis, MO, USA). Oxone ($2KHSO_5 \cdot KHSO_4 \cdot K_2SO_4$, 4.7% active oxygen) was obtained from Sigma-Aldrich (St. Louis, MO, USA) and used as an oxidant. Other reagents were of analytical grade and were purchased as reagent grade. All chemicals were used as received without any further purification. Double distilled water was used to prepare solutions.

2. 2. Preparation of Bi_2O_3-Co_3O_4 Composite Catalysts

The x-Bi_2O_3-Co_3O_4 (x presenting the weight ratio of Bi_2O_3 to Bi_2O_3-Co_3O_4 composite, x = 20%, 50%, and 80%) were prepared by co-precipitation method and subsequent annealing of the co-precipitated precursors. For the co-precipitation process, 0.8 mol/L NaOH was added dropwise at 333 K into a solution of metal nitrates containing Co^{2+} and Bi^{3+}, taken in the specified stoichiometric ratio, under vigorous stirring until the solution pH reached 10. The initially formed precipitate was kept under continuous stirring for 30 minutes at 333 K. After filtration, the black product was washed with deionized water and ethanol several times to neutral pH, dried at 378 K overnight, and finally calcined at 773 K for 3 h in static air. For comparison, pristine Co_3O_4 and Bi_2O_3 were also prepared by the same synthetic procedure.

2. 3. Characterization

The Co and Bi contents in the composites as well as the concentration of leached Co ions after the reaction were determined by ICP-OES analysis on an iCAP 6300 instrument (ThermoFisher, MA, USA). The crystal structures of the synthesized catalysts were analyzed by X-ray diffraction. The powder XRD patterns were collected on a Bruker D8 Advance diffractometer (Bruker AXS, Billerica, MA, USA) equipped with Cu Kα radiation and LynxEye detector. Phase identification was performed with the Diffracplus EVA using ICDD-PDF2 Database. The morphology of the catalysts was characterized by a JEM 2100 high-resolution transmission electron microscope (JEOL, Tokyo, Japan) using an accelerating voltage of 200 kV. Two basic regimes of microscope mode were used – bright-field transmission microscopy (TEM) and selected area electron diffraction (SAED). The surface elemental composition and chemical oxidation state were investigated by an X-ray photoelectron spectroscopy (XPS) on a UHV chamber ($P < 10^{-9}$ mbar) equipped with a dual Mg/Al X-Ray gun and a SPECS LHS-10 hemispherical electron analyzer, using an MgKα ($h\nu$ = 1253.6 eV) X-ray source operated at 10 mA and 12 kV. The XPS spectra were analyzed with ECLIPSE using a Shirley background. The binding energies (BEs) obtained from the XPS analysis were calibrated with a reference BE of C 1s (284.8 eV). Fourier transform infrared (FT-IR) spectra were collected with a Vertex 70 spectrophotometer (Bruker Optics) using KBr pellets. The BET specific surface area of the samples was determined from the nitrogen adsorp-

tion-desorption using a Tristar 3000 porosimeter (Micromeritics, Aachen, Germany) at the liquid nitrogen temperature. The pH of the point of zero charge (pH_{PZC}) of the catalysts was determined by pH drift method.[39]

2. 4. Catalytic Degradation Procedure

Batch experiments were carried out in a 400 mL glass reactor with constant stirring at around 400 rpm at 293 K. Typically, a certain dose of solid PMS (in the form of Oxone, $2KHSO_5 \cdot KHSO_4 \cdot K_2SO_4$) was added into a 200 mL 50 mg/L AO7 aqueous solution to attain the predefined PMS/AO7 molar ratio and stirred until dissolved. Degradation reaction was initiated by addition of a specified amount of catalyst. At the given time intervals, 4.0 mL of suspension was taken and quenched by 1 mL methanol to stop the reaction, and then centrifuged at 4000 rpm for 1 min to remove the catalyst.

The concentration of AO7 was analyzed by UV–vis spectroscopy (Cintra 101, GBC Scientific Equipment Ltd., Australia) at a maximum wavelength of 486 nm. All tests were conducted in triplicate to ensure the reproducibility of experimental results. For the quenching experiments, prior to the addition of oxidant and catalyst, a specified amount of radical scavengers was added into the AO7 solution to obtain a required scavenger/PMS molar ratio.

3. Results and Discussion

3. 1. Characterization of Bi_2O_3-Co_3O_4 Catalysts

The Bi_2O_3 content in the synthesized composite materials calculated on the basis of ICP-OES results was close to preparation settings (25.7, 52.9, and 78.4 wt.% for the 20%, 50%, and 80% Bi_2O_3-Co_3O_4 samples, respectively).

The crystal structure of Bi_2O_3-Co_3O_4 catalysts was analyzed by XRD and compared to that of pure Bi_2O_3 and

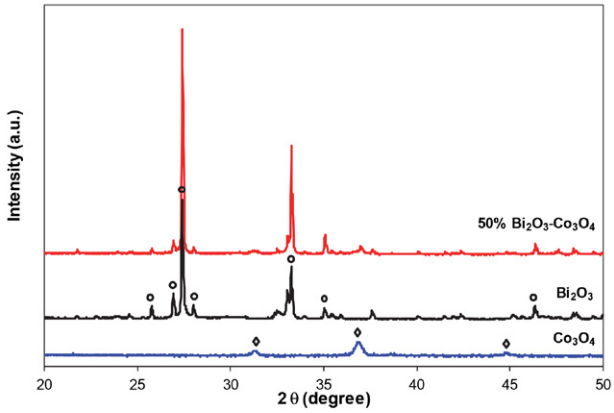

Fig. 1. XRD patterns of 50% Bi_2O_3-Co_3O_4, Co_3O_4, and Bi_2O_3

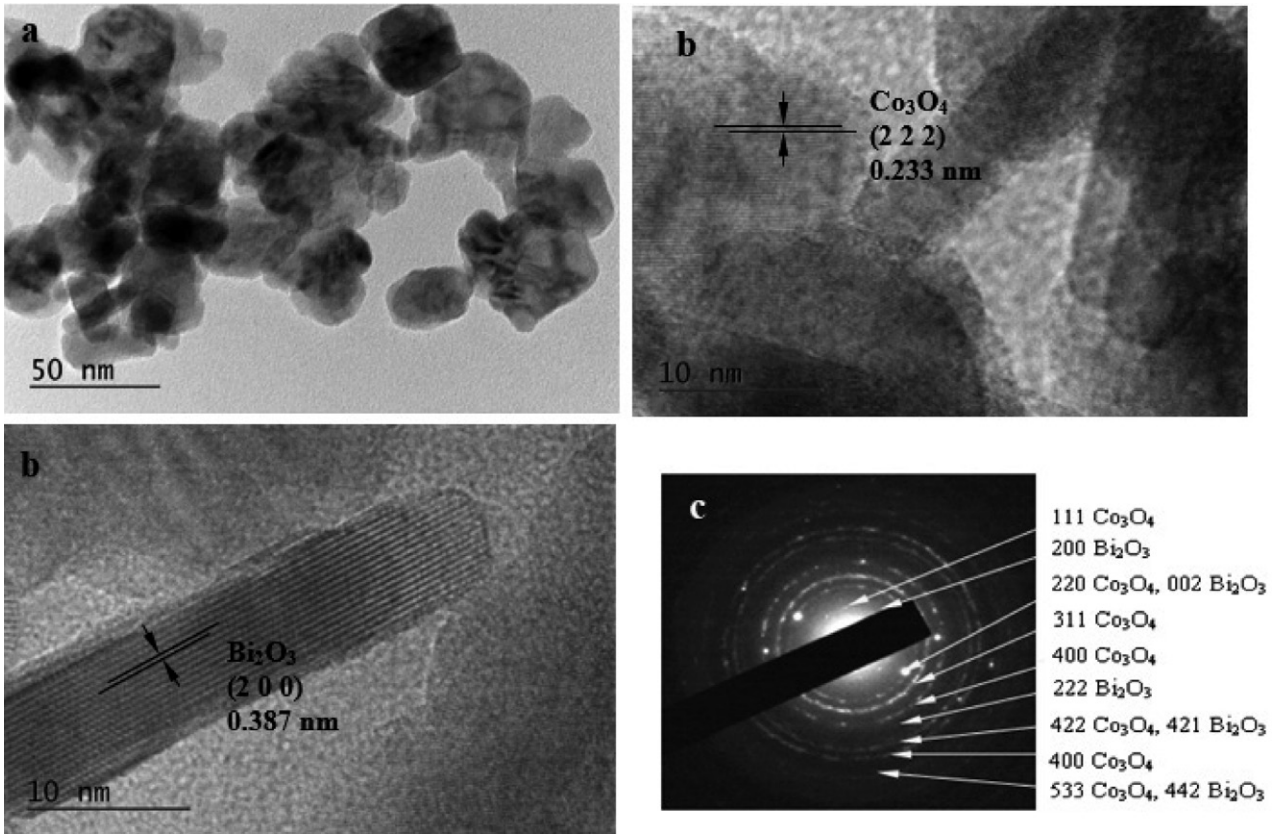

Fig. 2. (a) Bright-field TEM image, (b) HRTEM images and (c) SAED pattern of 50% Bi_2O_3-Co_3O_4.

Co_3O_4 (Fig. 1). The crystallographic phases of the prepared pristine oxides were confirmed as monoclinic α-Bi_2O_3, (JCPDS 41-1449) and cubic spinel-type Co_3O_4 (JCPDS 42-1467), respectively. For the composite catalysts, the characteristic peaks of Bi_2O_3 were observed at about 2 Θ values 26.93º (1 1 1), 27.40° (1 2 0) and 33.26° (2 0 0). The diffraction peaks at 31.2°, 36.9° and 44.7° can be indexed to (220), (311) and (400) planes of Co_3O_4 crystal (JCPDS 42-1467). As seen in Fig. 1, reflections associated with cobalt species in Bi_2O_3-Co_3O_4 were too weak, suggesting good dispersion of the Co_3O_4 particles in the resulting product. Moreover, no positive shift of the diffraction peaks of Bi_2O_3 was registered in the composite catalyst, which suggests that Co species are not incorporated into Bi_2O_3 lattice and Co_3O_4 and Bi_2O_3 coexist in the composite.

The coexistence of Co_3O_4 and Bi_2O_3 phases in the composite catalysts was confirmed through TEM and HR-TEM analysis. As observed in Fig. 2a, the 50 wt.% Bi_2O_3-Co_3O_4 sample was composed of predominantly flat particles with a near-rectangular shape and size in the range of 30–50 nm. The HRTEM image of the sample (Fig. 2b) showed well-defined lattice fringes, which indicates that it was highly crystallized. The fringes of d = 0.233 nm matched the (2 2 2) plane of Co_3O_4 nanoparticles, while the fringes of d = 0.387 nm corresponded to the (2 0 0) plane of α-Bi_2O_3, respectively. This confirmed that both Bi_2O_3 and Co_3O_4 phases coexisted in the Bi_2O_3-Co_3O_4 samples. The SAED pattern (Fig. 2c) obtained from the TEM showed well-defined rings and spots characteristic of well crystalline materials. Indexations of the diffraction pattern confirm the presence of both oxide phases in the catalyst.

The functional groups on the 50 wt.% Bi_2O_3-Co_3O_4 composite and bare Co_3O_4 and Bi_2O_3 were analyzed by FTIR technique and the obtained FTIR spectra are shown in Fig. 3. The formation of Co_3O_4 spinel oxide in the composite catalyst was confirmed by the presence of two distinct absorption bands at 573 and 665 cm^{-1} which originate from the stretching vibrations of the cobalt-oxygen bonds. The low frequency band represents the vibrations of octahedrally coordinated Co^{3+} with oxygen in the spinel lattice, while the high frequency band at 665 cm^{-1} can be assigned to the tetrahedral Co^{2+}.[37,40] The band at 847 cm^{-1} registered in the FTIR spectra of Bi_2O_3-Co_3O_4 and pure Bi_2O_3 is related to the vibration of Bi-O bonds and the existence of α-Bi_2O_3.[41] In all samples, the absorption peaks at around 3445 and 1630 cm^{-1} correspond to the stretching and bending vibrations of hydroxyl groups and the adsorbed water molecules, respectively.[42]

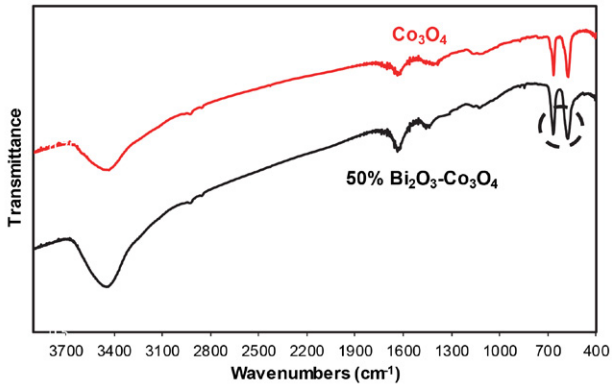

Fig. 3. FTIR spectra of the 50% Bi_2O_3-Co_3O_4, Co_3O_4 and Bi_2O_3

XPS measurements were conducted to elucidate the surface characteristics of the prepared composite catalysts. Obvious photoelectron peaks due to Co, Bi and O elements were detected in the survey spectrum of 50 wt.% Bi_2O_3-Co_3O_4 sample (Fig. 4a), confirming the presence of these elements on the surface of the catalyst. The curve fitting of Co 2p spectrum is shown in Fig. 4b. The Co 2p peaks at binding energies of 779.5 eV and 794.2 eV with satellite peak at 789.2 eV are characteristics of Co^{3+} located at octahedral sites in the cubic spinel structure of Co_3O_4, while the peaks at 781.4 eV and 796.4 eV with satellite signal at 787.7 eV are assigned to tetrahedral Co^{2+}. The calculated atomic ratio of Co^{3+} to Co^{2+} was 1.93, which is typical for Co_3O_4. The spin-orbit splitting of the Co $2p_{3/2}$ and Co $2p_{1/2}$ peaks signals was 15.1 eV, which is well consistent with the literature data of spinel Co_3O_4 and further confirmed that Co is present in the form of Co_3O_4 in composite catalysts.[43] Two evident peaks observed at 162.7 eV and 156.9 eV in Bi 4f XPS spectrum of (Fig. 4c) are assigned to Bi 4f 5/2 and Bi 4f 7/2 of Bi_2O_3, respectively.[44] The high-resolution XPS spectrum of O 1s (Fig. 4d) shows two different peaks at 529.7 and 531.5 eV, which were assigned to the lattice oxide oxygen and surface hydroxyl groups, respectively.[45] Quantitative analysis of the O 1s spectra reveals that the relative content of the surface hydroxyl oxygen in the Co-Bi composite (22% of the total oxygen) was twice higher than calculated for pure Co_3O_4. The availability of more hydroxyl groups on the surface of composite catalysts can promote the formation of surface Co-OH complexes, which may favour the enhancement of the catalytic activity of Co catalysts for PMS activation.

3. 2. Catalytic Performance of Bi_2O_3-Co_3O_4 /PMS System on AO7 Oxidative Degradation

The AO7 oxidative degradation was selected to evaluate the catalytic performance of the Co-Bi composite oxides for PMS activation. Initially, to confirm the occurrence of a catalytic reaction in the catalyst/PMS system, control experiments including adsorption tests and no catalyst addition were conducted. In comparison, the Co_3O_4, Bi_2O_3 and Co(II) ions (dissolved $Co(NO_3)_2$) were employed as references. Fig. 5 shows that no noticeable removal of AO7 was observed in the single use of PMS after 30 min, indicating that PMS alone cannot produce free radicals to induce AO7 degradation. The as-prepared composite catalyst had no obvious adsorption toward AO7

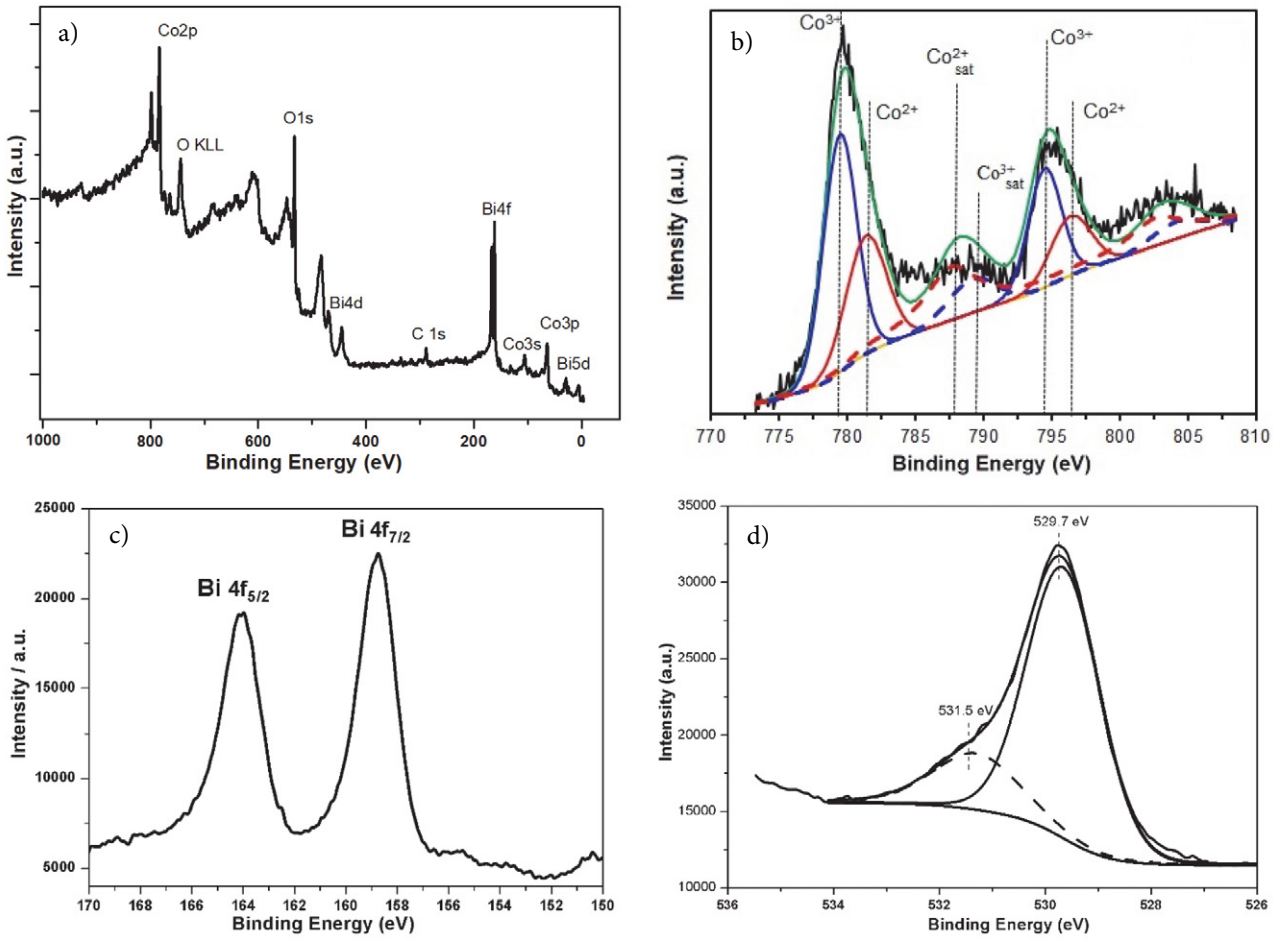

Fig. 4. XPS spectra of 50% Bi_2O_3-Co_3O_4 sample: (a) wide survey, (b) Co 2p, (c) Bi 4f and (d) O1s

and only less than 5% of the dye was removed in 30 min. PMS also did not cause any decrease in the AO7 concentration when it was combined with pristine Bi_2O_3, indicating that Bi_2O_3 had low reactivity for PMS activation to degrade the dye. When bare Co_3O_4 was used as the catalyst for the activation of PMS to generate the active radicals, only 39% decolorization efficiency could be achieved within 12 min, while a complete discoloration of the solution was attained for 90 min. However, doping of Bi_2O_3 on Co_3O_4 greatly improved its catalytic performance for PMS activation and catalytic degradation of AO7. Specifically, after the addition of PMS, AO7 was completely degraded in 12 min using Co_3O_4 doped with 50 wt.% Bi_2O_3, which should be attributed to the fast running radical-involved process. Since the contributions of adsorption and direct PMS oxidation on the AO7 removal are negligible, the catalytic oxidation over the composite catalyst can be considered as the main AO7 removal pathway. Furthermore, given that PMS is inefficient for AO7 degradation alone, the observed rapid first degradation stage in the degradation curve of 50% Bi_2O_3-Co_3O_4 indicates that a large number of free radicals are generated upon the contact of the oxidant with the catalyst surface.

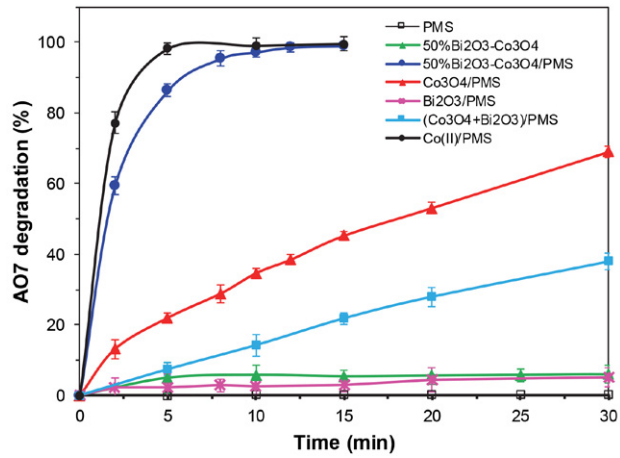

Fig. 5. Removal profiles of AO7 in different systems. Reaction conditions: $[AO7]_o$ = 50 mg/L; [PMS]/[AO7] = 6; [Catalyst]= 0.1 g/L; $[Co^{2+}]$ = 0.39 mg/L; initial pH = 3.04; T = 293 K.

The superior catalytic activity of Co-Bi composite oxides relative to either Co_3O_4 or Bi_2O_3 suggests a synergistic effect of both oxides in the catalysts towards PMS activation for AO7 degradation. This synergetic coupling

effect was further proved by degradation test conducted using the mechanical mixture of Co_3O_4 and Bi_2O_3 with a weight ratio of 1:1 as a catalyst. The results indicated that the catalytic performance of this mixture was evidently inferior to that of 50% Bi_2O_3-Co_3O_4 composite under identical conditions. In fact, only 22% AO7 removal in 15 min was achieved in the presence of the mechanical mixture, which is close to the average degradation value by Co_3O_4 and Bi_2O_3. Furthermore, a linear AO7 removal profile in a mechanical mixture/PMS system further evidences that activation of oxidant is the rate-limiting step of the oxidation process rather than the destruction of the dye molecules by radicals formed.

The catalytic performance of the most active composite 50% Bi_2O_3-Co_3O_4 was slightly inferior to the Co(II) ions, used as a homogeneous catalyst for the activation of PMS at the same molar concentration of the solid catalyst. It could be speculated that the high weight percent of cobalt oxide in the catalyst may lead to significant leaching of Co ions in the solution. However, though the leaching process occurred during the degradation reaction, the amount of dissolved Co ions was detected to be up to 72 μg/L (Co leaching percent of 0.21%) after the reaction was completed even in acidic conditions. This gives a reason to suggest that the homogeneous activation of PMS by leached Co(II) ions would be negligible and the heterogeneous pathway of PMS activation dominated in the Bi_2O_3-Co_3O_4/PMS system. The insignificant contribution of the homogeneous catalytic reaction promoted by dissolved Co ions was also confirmed by comparative experiments, in which leaching solution obtained upon complete removal of AO7 and filtering the catalyst was used to activate PMS for the oxidation of dye again. Less than 4% AO7 was degraded in the leaching solution by PMS addition, which was much lower compared to the Bi_2O_3-Co_3O_4/PMS oxidation system, indicating that the main catalytic contribution is from the composite catalyst, not dissolved cobalt ions.

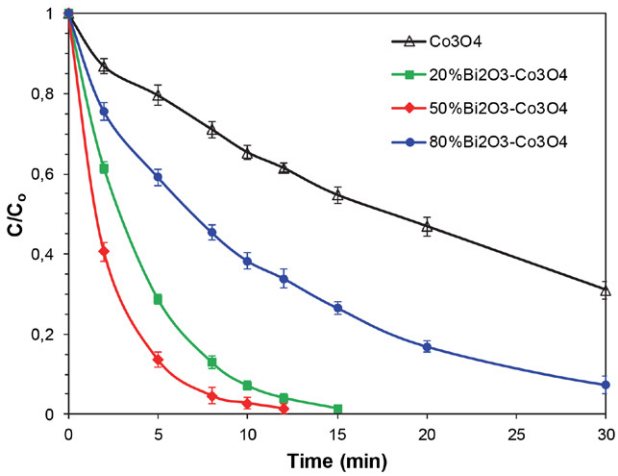

Fig. 6. AO7 catalytic degradation in x-Bi_2O_3-Co_3O_4 composite/PMS systems. Reaction conditions: $[AO7]_o$ = 50 mg/L; [PMS]/[AO7] = 6; [Catalyst]= 0.1 g/L; initial pH = 3.04; T = 293 K.

The Bi_2O_3 mass content in the composite catalysts had a noticeable influence on the catalytic activity of Co_3O_4 resulting in different AO7 degradation profiles. As seen from Fig. 6, the AO7 degradation efficiency considerably increased with the increase of Bi_2O_3 content up to 50%. However, as the Co_3O_4 particles in the composites determined the PMS activation, the excessive amount of Bi_2O_3 (80 wt.%) did not further promote the catalytic activity of Co_3O_4 and only 66% of dye was degraded for 12 min. Nevertheless, the catalytic efficiency of all Bi_2O_3-Co_3O_4 composites was higher than that of bare Co_3O_4.

Data of AO7 degradation with various catalysts in the PMS oxidation system were fitted well with the pseudo-first-order kinetic model (Fig. 7), indicating that the catalytic process is not controlled by the PMS activation step and radical generation. As seen from the inserted figure, the reaction rate constant (k) of AO7 degradation increased considerably upon doping of Co_3O_4 with Bi_2O_3, demonstrating the positive effect of Bi_2O_3 addition for the faster PMS activation. Specifically, the kinetic constant for 50% Bi_2O_3-Co_3O_4 is *ca.* 9.5 times higher than those of Co_3O_4 although the specific surface area of the composite (28.12 m^2/g) was only slightly lower than that of the pure cobalt oxide (30.1 m^2/g). This result indicates that some other factors besides the specific surface area played much more important roles in the activation process.

The much better performance for PMS activation ex-

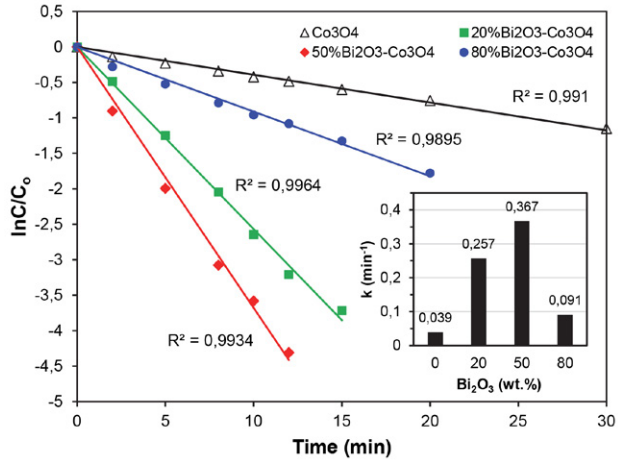

Fig. 7. First-order kinetic fitting of the AO7 degradation curves. Reaction conditions: $[AO7]_o$ = 50 mg/L; [PMS]/[AO7] = 6; [Catalyst] = 0.1 g/L; initial pH = 3.04; T = 293 K.

hibited by Bi_2O_3-Co_3O_4 hybrids than the bare cobalt oxide could be attributed to the increased basicity of the Co_3O_4 surface after Bi_2O_3 modification resulting in a more hydroxylated surface that facilitates the decomposition of PMS to reactive radicals. This suggestion was well in accordance with the point of zero charge (pH_{pzc}) measurements. The pH at which the curve pH(final) = pH(initial) crosses the dashed line, obtained without the addition of a catalyst (see Fig. 8) is taken as the pH_{pzc} of the given cata-

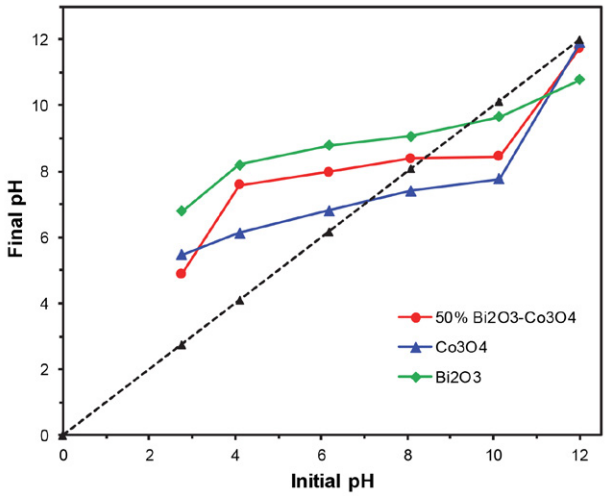

Fig. 8. pH drift method to obtain the pH_{pzc} of the as-prepared oxide systems. The dashed line applies to the system without added catalyst

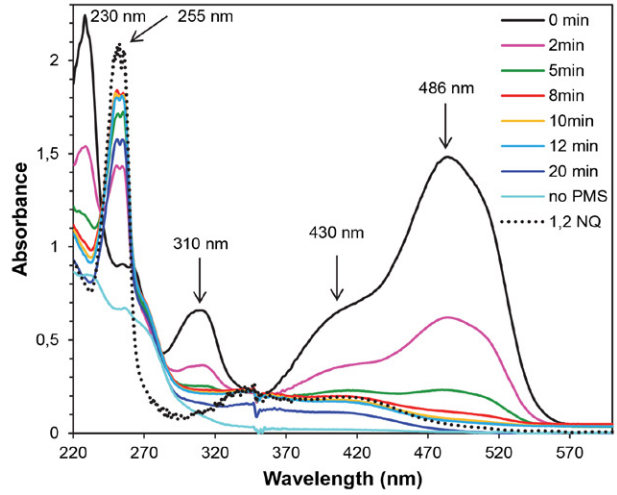

Fig. 9. UV–vis spectra of AO7 catalytic degradation on 50% Bi_2O_3-Co_3O_4. Reaction conditions: $[AO7]_o$ = 50 mg/L; [PMS]/[AO7] = 6; [Catalyst] = 0.1 g/L; initial pH = 3.04; T = 293 K.

lyst. As given in Fig. 8, the pH_{pzc} value of Co_3O_4 increased from 7.1 to 8.4 after the doping with Bi_2O_3, indicating for the enhanced content of hydroxyl groups on the surface of the composite catalyst. Such difference between the surface charge of the Co_3O_4 and Bi_2O_3-Co_3O_4 is consistent with the XPS results that show a higher content of the surface hydroxyl oxygen in the Co-Bi composite than that in Co_3O_4.

Fig. 9 depicts the UV-vis spectral changes of AO7 in solution during the catalytic degradation in the presence of most active 50% Bi_2O_3-Co_3O_4 composite. In the visible region, the spectrum of initial AO7 solution exhibits a main band with a maximum located at 486 nm and a shoulder at 430 nm, corresponding to the n–π* transitions of the hydrazone form and azo form of the dye, respectively, and are due to the chromophore-containing azo-linkage.[46] The other two bands in the ultraviolet region, located at 230 and 310 nm, are ascribed to the π–π* transitions in the benzene and naphthalene rings of AO7, respectively. It is apparent that the major band at 486 nm declined rapidly as the reaction progressed and finally disappeared after 12 min, indicating the facile break-up of the azo-linkage. In parallel, the intensity of the absorbance bands in the UV region is also reduced, implying for concomitant destruction of the conjugated p-system of the dye molecule. Meanwhile, a new absorption band around 255 nm appeared concurrently with the decay in the visible region, indicating that a new structure unit is formed from chromophore cleavage. This band was generated at the very beginning of reaction (even at 2 min) and after discoloration of the solution at 12 min, its intensity starts to drop slowly, which proves that an intermediate formed is further also degraded. 1,2-naphthoquinone was identified to contribute to the peak at 255 nm by comparing the spectra of the reaction mixture and a standard solution of 1,2-naphthoquinone.

The degradation intermediates of AO7 were also monitored by HPLC analysis. Fig. 10 shows chromatograms of the AO7 solution before and in the course of degradation catalyzed by the 50% Bi_2O_3-Co_3O_4 together with the chromatogram of a standard solution, containing the expected main intermediates from AO7 degradation. The chromatogram of the initial AO7 solution shows a single peak with a retention time t_R at 12.75 min, whose intensity dramatically declined when the reaction proceeded and almost disappeared after 10 min. Concurrently, six intermediates were generated, identified as 4-hydroxybenzenesulfonic acid (t_R at 2.6 min), phthalic anhydride (t_R at 7.08 min), phthalimide (t_R at 8.1 min), 1,2-naphthoquinone (t_R at 12.3 min), coumarin (t_R at 13.3 min), and unidentified product with t_R at 11.2 min. The intermediate product 1,2-naphthoquinone distinguished from the other ones by its highest intensity during the whole process, as well as by

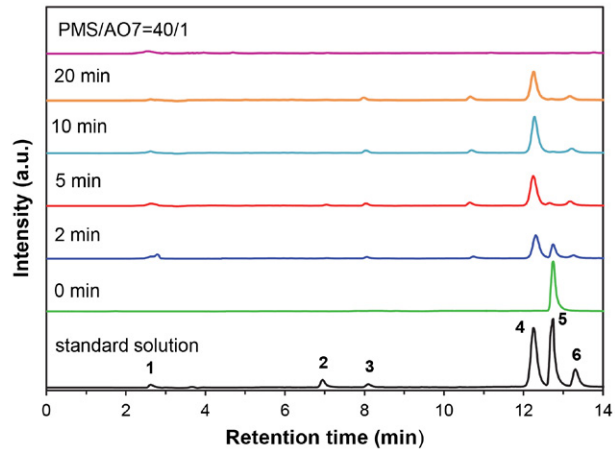

Fig. 10. HPLC chromatograms of AO7 during catalytic oxidation on 50% Bi_2O_3-Co_3O_4 and standard solution [(1) 4-hydroxybenzenesulfonic acid, (2) phthalic anhydride, (3) phthalimide, (4) 1,2-naphthoquinone, (5) AO7, (6) coumarin]. Reaction conditions: $[AO7]_o$ = 50 mg/L; [PMS]/[AO7] = 6; [Catalyst] = 0.1 g/L; initial pH = 3.04; T = 293 K.

the most well-defined intensity changes. It gradually accumulated up to 10 min and then starts to decrease as evidenced by UV-vis analysis as well. However, the disappearance of all peaks when raising the PMS/AO7 molar ratio to 40:1, corresponding to the stoichiometric one for mineralization of AO7, suggests that the generated intermediates were finally mineralized.

3. 3. Effect of Reaction Variables on AO7 Degradation

Further kinetic studies were carried out using the most active 50% Bi_2O_3-Co_3O_4 catalyst to investigate the effects of several key parameters, namely the catalyst dosage, PMS concentration, initial solution pH, and temperature on the AO7 degradation.

3. 2. 1. Effect of Catalyst Amount

Fig.11a depicts the degradation kinetics of AO7 by PMS with different Bi_2O_3-Co_3O_4 dosages in the range of 0.05 g/L – 0.3 g/L. Apparently, increasing the amount of catalyst resulted in an increased degradation rate for AO7, confirming the crucial role of the catalyst for the generation of the radicals as well as indicating that the surface reaction is the rate-limiting step. In comparison, at catalyst loading of 0.05 g/L,[3] AO7 removal efficiency could reach 100% after 20 min, whereas only 5 minutes are needed for complete dye degradation in the presence of 0.3 g/L catalyst. Accordingly, the first-order rate constant *k* increased from 0.1804 to 0.839 min^{-1} as observed in Fig 11b. Besides, the degradation rate constants present a linear trend as a function of catalyst dosage at the same PMS concentration, thereby implying that there is no competition between the dye and PMS for the active sites on the catalyst surface. The inset in Fig. 11 presenting the kinetic fitting curves confirms that the AO7 degradation follows a first-order kinetics model. The continuous increase of the AO7 degradation rate with catalyst load can be attributed to the more surface active sites for PMS activation, thereby resulting in a faster generation of reactive radical species and consequently in an enhancement of the reaction rate.

3. 2. 2. Effect of PMS Concentration

As illustrated in Fig. 12, the AO7 catalytic degradation on Bi_2O_3-Co_3O_4 also showed a positive dependence on the PMS dosage (in terms of PMS/AO7 molar ratio). At the lowest [PMS/AO7] ratio of 1:1 complete removal of AO7 was not achieved due to a lack of sufficient oxidant amount. However, as the [PMS]/[AO7] ratio was increased from 1:1 to 6:1, the AO7 removal efficiency significantly increased from 66.5% to 100% and the degradation rate constant rapidly rises from 0.113 to 0.367 min^{-1} (inset of Fig. 12). However, further increase of the [PMS]/[AO7] molar ratio to 12:1 induced only a slight enhancement in

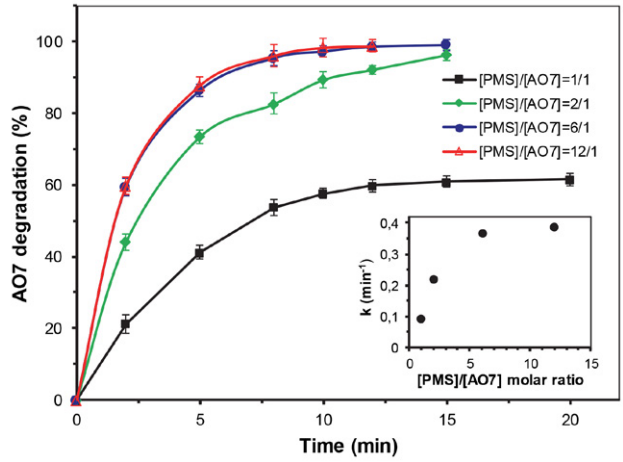

Fig. 12. Effect of PMS dosages on AO7 degradation and AO7 degradation kinetics (inset) by 50% Bi_2O_3-Co_3O_4/PMS oxidation system. Reaction conditions: 50 mg/L; [Catalyst] = 0.1 g/L; initial pH = 3.04; T = 293 K.

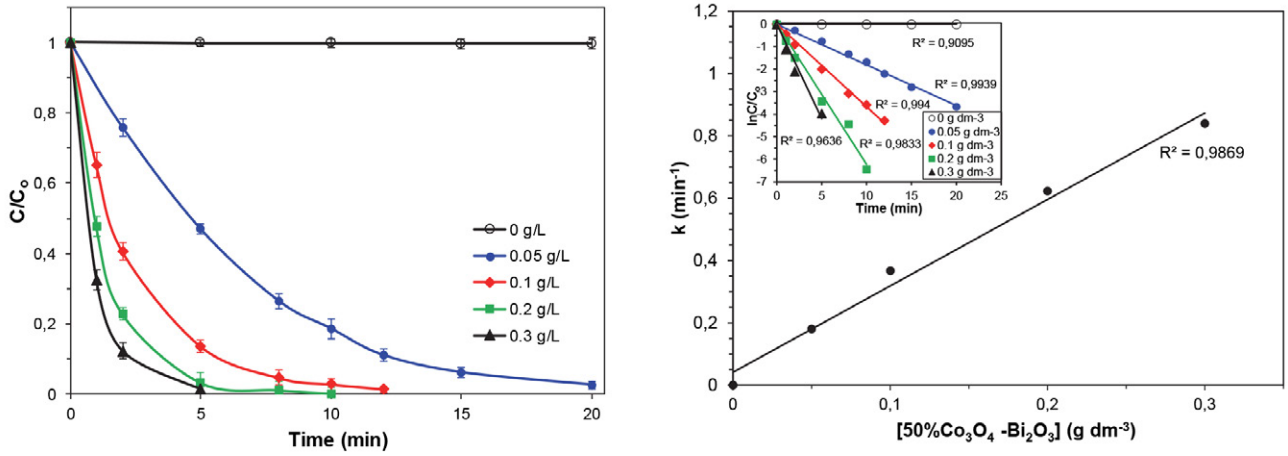

Fig. 11. Catalytic performance of 50%Bi_2O_3-Co_3O_4 at various dossages in the presence of PMS and AO7: (a) AO7 degradation; (b) AO7 degradation kinetics. Reaction conditions: $[AO7]_o$ = 50 mg/L; [PMS]/[AO7] = 6; initial pH = 3.04; T = 293 K.

the AO7 degradation rate. Being the source of active radicals, an increase of the PMS dosage promotes the generation of more radicals, which accounts for the rapid AO7 degradation. However, at high PMS concentrations, the fixed amount of catalyst gradually became the limiting factor controlling the generation of radicals so that the radical yield was almost independent of PMS dosage. Furthermore, the unreacted PMS behaves as the quencher of active radicals according to the following reactions: [47]

$$SO_4^{\cdot-} + HSO_5^- \rightarrow SO_5^{\cdot-} + HSO_4^- \quad (1)$$

$$^{\cdot}OH + HSO_5^- \rightarrow SO_5^{\cdot-} + H_2O \quad (2)$$

3. 2. 3. Effect of pH

Solution pH plays a significant role in the degradation process due to its influence on the surface charge of the catalyst as well as the existing form of PMS in solution. As the natural wastewater has variable acidity, it is important to investigate the influence of pH on the degradation efficiency of AO7 in 50% Bi_2O_3-Co_3O_4/PMS system. Fig. 13a shows that the efficient catalytic degradation of AO7 in this system is applicable to a wide pH range of 3.04 to 9.3, which covers the common pH of natural water and wastewater. Moreover, the discoloration of AO7 solution was complete in a short period of time (12 min) even at alkaline conditions. The surface of Bi_2O_3-Co_3O_4 particles is positively charged when the solution pH is less than 8.4 (pH_{pzc} of the sample). According to the pK_a values of PMS ($pK_{a1} < 0$, $pK_{a2} = 9.4$[47]), PMS mainly exists in the form of HSO_5^- in the solution pH range of 4.0 to 8.5. Therefore, PMS and catalyst surface were oppositely charged within this pH range, which facilitates their interaction through the electrostatic attractive forces. Although electrostatic repelling forces between the negatively-charged catalyst's surface and HSO_5^- are prominent at pH 9.3, slightly faster initial discoloration kinetics was observed at this pH, suggesting that base activation of PMS by NaOH (used to adjust pH to 9.3) may also take effect in basic conditions. Furthermore, the different UV-vis absorption spectrum of the solution after the degradation process at pH 9.3 imply for a different AO7 degradation mechanism (Fig. 13b). Specifically, the new peak at 255 nm did not appear in the spectra as well as a residual absorbance at 228 and 310 nm was still observed even when the reaction was completed, indicating that some intermediates generated from the fragmentation of the azo links still contain benzoic and naphthalene rings.

Meanwhile, pH variation during the AO7 degradation process was also monitored. As shown in Fig. 13c, the solution pH with an initial value of 3.04 maintained almost unchanged over time but decreased when the initial pH was 7.06 and reached around pH 3.4 within 8 min reaction. This phenomenon could be attributed to the release of protons along with PMS decomposition and the formation of acidic intermediate products during the AO7 degradation process. However, under basic conditions, the pH value only slightly decreased as the reaction went on

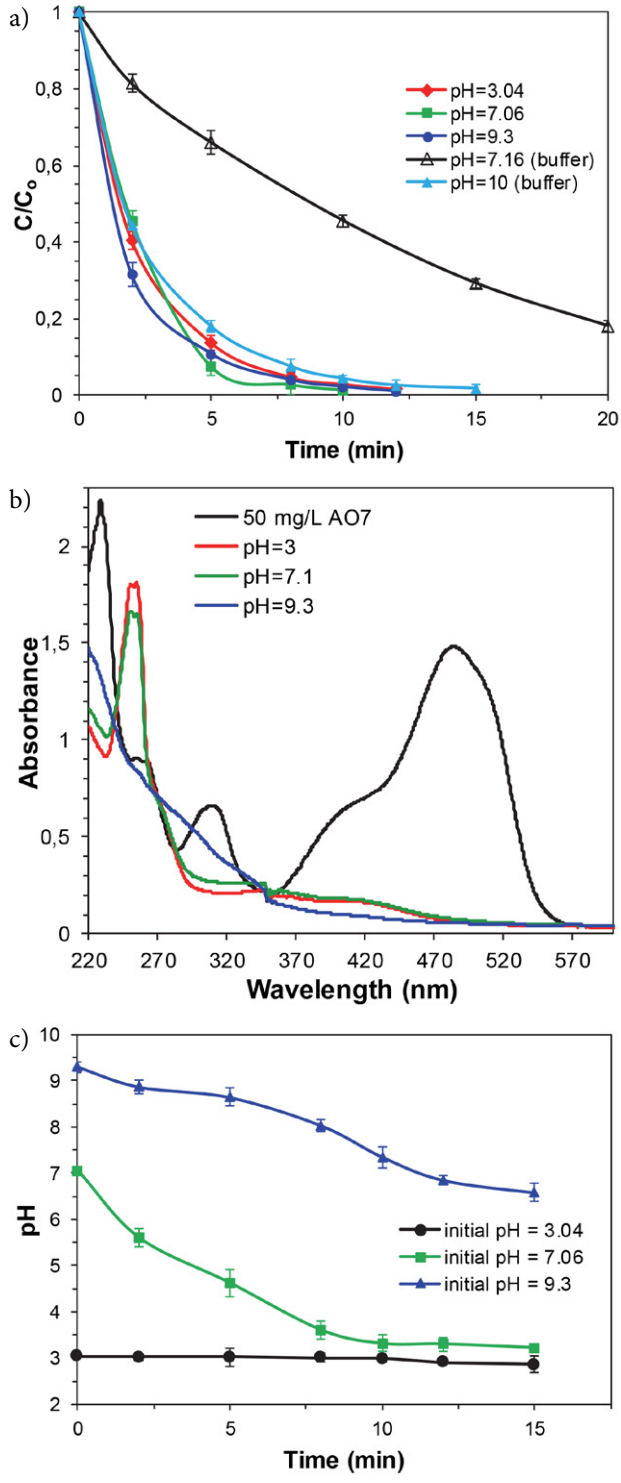

Fig. 13. Performance of 50% Bi_2O_3-Co_3O_4 for AO7 degradation with PMS at different initial pHs: (a) AO7 degradation; (b) UV–vis spectra of the AO7 aqueous solution at 12 min ; (c) Changes of pH over time in the case of different initial pH values. Reaction conditions : $[AO7]_o$ = 50 mg/L; [PMS]/[AO7] = 6; [Catalyst] = 0.1 g/L; T = 293 K.

and finally kept to nearly neutral probably due to the high initial concentration of OH^- (2.0 mM) which prevented a significant decrease in the pH.

The effect of buffer solutions on the AO7 removal efficiency was also evaluated. Accordingly with Fig. 13a, the degradation rate of AO7 was considerably decreased when the initial solution was buffered to 7.16 using 0.004 M phosphate buffer (in the forms of $H_2PO_4^-$ and HPO_4^{2-}). In the buffered system, complete AO7 degradation was achieved in 50 min and the rate constant decreased 5.3 times compared with the experiment at an initial pH of 7.06 adjusted with NaOH. The observed retarding effect could be due to the quenching of active radicals generated from PMS catalytic decomposition by phosphate anions in the solution.[48,49] In contrast, the oxidation of AO7 was quite significant when $NaHCO_3$/NaOH buffer used to adjust the initial pH to 10 (Fig. 13a). Although the surface of Bi_2O_3-Co_3O_4 is negatively charged at pH higher than 8.4 and PMS existed mostly in the form of SO_5^{2-} at pH range of 9.5–10.5, the AO7 degradation rate and efficiency were comparable to that attained in an acidic medium. Therefore, it could be speculated that along with heterogeneous activation of PMS, the active species may also be generated as a result of anion decomposition of PMS which, due to its unsymmetric structure, can easily be attacked by nucleophile such as HCO_3^-.[50] Besides, base activation of PMS by NaOH was also enhanced at pH 10.

3. 2. 4. Effect of Temperature

The effect of reaction temperature on PMS activation by 50%Bi_2O_3-Co_3O_4 for AO7 degradation was also studied. Considering the observations in Fig. 14, an increase in temperature had a positive effect on AO7 removal rate due to accelerating the decomposition of PMS into active radicals under thermal activation.[51] As the temperature increased from 18 to 38 °C, the decolorization kinetics was remarkably enhanced and the rate constant value increased from 0.283 to 0.530 min^{-1}. At 18 °C, AO7 was completely destroyed within 15 min, whereas removal reached up to 100% at 38 °C in just 7 min. The temperature dependence of the rate constant was further used to determine activation energy (E_a) by plotting ln$k$ against $1/T$ according to the Arrhenius equation (inset of Fig. 14). The calculated E_a value for AO7 degradation with 50% Bi_2O_3-Co_3O_4 as a catalyst was 22.7kJ mol^{-1}, whereas that obtained in the presence of pristine Co_3O_4 was 35.5kJ mol^{-1}. Both E_a values are higher than the activation energy of diffusion-controlled reactions (10–13 kJ mol^{-1}), revealing that the AO7 catalytic degradation process was controlled by the rate of chemical reaction on the catalyst surface rather than mass transfer rate. The lower E_a value obtained for the 50% Bi_2O_3-Co_3O_4 /PMS system was in agreement with its best AO7 degradation efficiency and confirmed that Bi_2O_3 had a great influence on the Co_3O_4 catalytic reactivity for PMS activation.

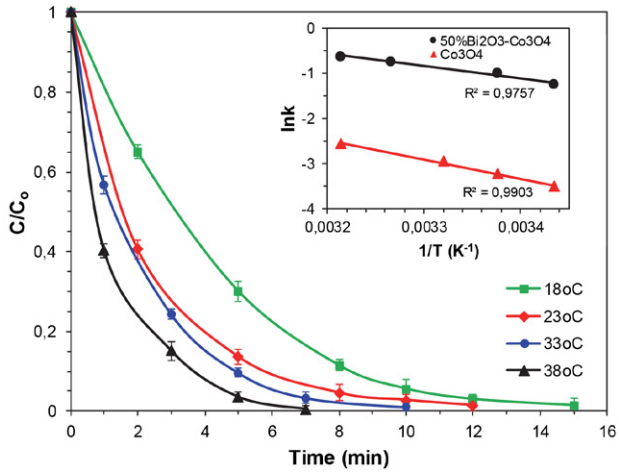

Fig. 14. Effect of reaction temperature on AO7 degradation by 50% Bi_2O_3-Co_3O_4/PMS oxidation system. Reaction conditions: $[AO7]_o$ = 50 mg/L; [PMS]/[AO7] = 6; [Catalyst] = 0.1 g/L; initial pH = 3.04.

3. 2. 5. Identification of Reactive Species

Selective radical quenching tests were performed to identify the dominating radical species formed during PMS activation by the catalyst and accounting for the AO7 degradation. The activation of PMS by metal-containing catalysts might produce sulfate ($SO_4^{\bullet-}$), hydroxyl (•OH), and peroxy-sulfate ($SO_5^{\bullet-}$) radicals.[52] The AO7 degradation by $SO_5^{\bullet-}$ could be neglected because of its much lower oxidation potential (E^o = 0.81 V).[53]

Various radical scavengers were tested in the reaction solution including ethanol (EtOH), tert-butyl alcohol (TBA), KI, and ascorbic acid and the results are presented in Fig. 15. With the addition of 0.02 M ascorbic acid, the degradation of AO7 is almost completely inhibited and the degradation rate is the same as observed by the removal of dye without PMS. Since the ascorbic acid is considered to be a strong radical scavenger, it can be concluded that the radical pathway mechanism of AO7 degradation is involved in the 50% Bi_2O_3-Co_3O_4 activated PMS system. To evaluate the contribution of $SO_4^{\bullet-}$ and •OH to AO7 degradation, EtOH and TBA were used as radical scavengers. EtOH (containing α-hydrogen) can readily react with both radicals at high and comparable rates ($k_{\bullet OH}$:1.2–2.8 × 10^9 mol L^{-1} s^{-1}; $k_{SO4\bullet-}$:1.6–7.7 × 10^7 mol L^{-1} s^{-1}), whereas the scavenging of •OH by TBA (without a-hydrogen) is much faster than $SO_4^{\bullet-}$ ($k_{\bullet OH}$:3.8–7.6 × 10^8 mol L^{-1} s^{-1}; $k_{SO4\bullet-}$:4–9.1 × 10^5 mol L^{-1} s^{-1}).[14,53,54] As observed in Fig. 15, the AO7 removal kinetics was slightly affected by the presence of TBA, and the kinetic constant of AO7 degradation decreased from 0.367 min^{-1} (with no scavenger) to 0.271 min^{-1} at a TBA/PMS ratio of 2000/1. On the other hand, the addition of EtOH resulted in decreasing AO7 removal to 76.4% at 12 min and reaching final removal efficiency of 85.2% at 20 min when the PMS was exhausted. Accordingly, around a 3-fold decrease of the reaction rate constant value was observed due to the inhibitory effect of ethanol.

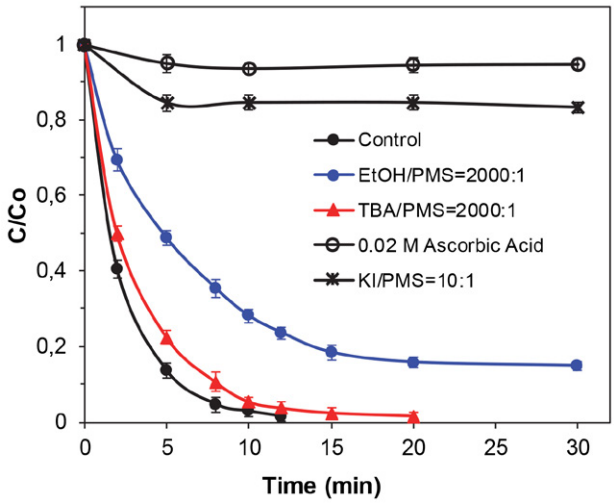

Fig. 15. Effect of radical scavengers on AO7 degradation. Reaction conditions: $[AO7]_o$ = 50 mg/L; [PMS]/[AO7] = 6; [Catalyst] = 0.1 g/L; initial pH = 3.04; T = 293 K.

These results suggest that in the Bi_2O_3-Co_3O_4/PMS system the major radical species involved in the attack of AO7 are sulfate radicals. A probable reason for the relative slight inhibitory effects of both alcohols might be that EtOH and TBA being highly hydrophilic prefer to quench free radicals in solution rather than reacting radicals in catalyst surface.[55] Furthermore, a complete suppression of the AO7 degradation was observed upon the addition of KI even at a KI/PMS ratio of 10/1. Since iodine ions are considered as scavenging agents for surface-bound radicals in advanced oxidation processes, it may be concluded that $SO_4^{\bullet-}$ radicals on the surface play a dominant role in the AO7 degradation in Bi_2O_3-Co_3O_4 /PMS oxidation system.

4. Conclusions

In this work, Bi_2O_3-Co_3O_4 composites with different content were synthesized using a facile co-precipitation method and applied as catalysts for the degradation of AO7 dye by activating PMS via a radical pathway. The XRD and HRTM characterization confirmed the coexistence of Bi_2O_3 and Co_3O_4 phases in the Bi_2O_3-Co_3O_4 composites. Compared to bare Co_3O_4, the as-prepared composite catalysts exhibited superior performance in the heterogeneous activation of PMS to generate radical species and thus induced the rapid degradation of AO7 over a wide pH range (pH 3-10). In the presence of the most active 50 wt.% Bi_2O_3-Co_3O_4, an initial AO7 concentration of 50 mg/L was completely removed within 12 min, and the rate constant is around 9.5 – fold as compared with bare Co_3O_4. The enhanced PMS-activating ability of the Bi_2O_3-Co_3O_4 composites was attributed to the increased hydroxyl oxygen content on their surface due to the presence of basic Bi oxide, which facilitates the formation of surface Co-OH complexes and promotes the activation of PMS. The increase of catalyst dosage, PMS concentration and temperature leads to enhancement of the AO7 removal efficiency, however increasing the catalyst loading is most beneficial. Based on the chemical scavenger study, sulfate radicals were identified as the major reactive species formed by the catalyst/PMS interaction and responsible for AO7 degradation. The synthesized catalytic systems could be regarded as promising heterogeneous catalysts for the degradation of organic pollutants in water through a sulfate radical approach.

Acknowledgements

Authors gratefully acknowledge financial support by the Centre for Competence»Personalized Innovative Medicine, PERIMED (EU Programme "Science and Education for Smart Growth" grant BG05M2OP001-1.002-0005-C01).

5. References

1. B. D. Tony, D. Goyal, S. Khanna, *Int. Biodeter. Biodegr.* **2009**, *63*, 462–469. **DOI:**10.1016/j.ibiod.2009.01.003
2. R. D. Ambashta, M. Sillanpää, *J. Hazard. Mater.* **2010**, *180*, 38–49. **DOI:**10.1016/j.jhazmat.2010.04.105
3. S. Eftekthari, A. Habibi-Yangjeh, Sh. Sohrabnezhad, *J. Hazard. Mater.* **2010**, *178*, 349–355. **DOI:**10.1016/j.jhazmat.2010.01.086
4. R. D. Ambashta and M. Sillanpaa, *J. Hazard. Mater.*, **2010**, *180*, 38–49. **DOI:**10.1016/j.jhazmat.2010.04.105
5. S. H. Chen, J. Zhang, C. L. Zhang, Q. Y. Yue, Y. Li and C. Li, *Desalination*, **2010**, *252*, 149–156. **DOI:**10.1016/j.desal.2009.10.010
6. M. Cai, J. Su, G. Lian, X. Wei, C. Dong, H. Zhang, M. Jin, Z. Wei, *Ultrason. Sonochem.* **2016**, *31*, 193–200. **DOI:**10.1016/j.ultsonch.2015.12.017
7. N. Riaz, F. K. Chong, B. K. Dutta, Z. B. Man, M. S. Khan, E. Nurlaela, *Chem. Eng. J.* **2012**, *185–186*, 108–119. **DOI:**10.1016/j.cej.2012.01.052
8. N. Inchaurrondo, J. Font, C. P. Ramos, P. Haure, *Appl. Catal. B: Environ.* **2016**, *181*, 481–494. **DOI:**10.1016/j.apcatb.2015.08.022
9. G. P. Anipsitakis, D.D. Dionysiou, *Environ. Sci. Technol.* **2003**, *37*, 4790–4797. **DOI:**10.1021/es0263792
10. Q. Yang, H. Choi, Y. Chen, D. D. Dionysiou, *Appl. Catal. B: Environ.* **2008**, *77*, 300–307. **DOI:**10.1016/j.apcatb.2007.07.020
11. H. Liang, H. Sun, A. Patel, P. Shukla, Z. H. Zhu, Sh. Wang, *Appl. Catal. B: Environ.* **2012,** *127*, 330–335. **DOI:**10.1016/j.apcatb.2012.09.001
11. Y. B. Ding, L. H. Zhu, N. Wang, H. Tang, *Appl. Catal. B: Environ.* **2013**, *129*, 153–162. **DOI:**10.1016/j.apcatb.2012.09.015
12. G. Nie, J. Huang, Y. Hu, Y. Ding, X. Han, H. Tang, *Chin. J. Catal.* 2017, 38, 227–239. **DOI:**10.1016/S1872-2067(16)62566-4
13. X. Dong, B. Ren, Z. Sun, Ch. Li, X. Zhang, M. Kong, S. Zheng,

D. D. Dionysiou, *Appl. Catal. B: Environ.* **2019**, *253*, 2016 – 217. **DOI:**10.1016/j.apcatb.2019.04.052
14. G. P. Anipsitakis, D. D. Dionysiou, *Environ. Sci. Technol.*, **2004**, 38, 3705–3712. **DOI:**10.1021/es035121o
15. J. Deng, S. Feng, X. Ma, Ch. Tan, Sh. Zhou, J. Li, *Sep. Purif. Technol.*, **2016**, 167, 181–189. **DOI:**10.1016/j.seppur.2016.04.035
16. J. Deng, S. Feng, K. Zhang, J. Li, H. Wang, T. Zhang, X. Ma, *Chem. Eng. J.* **2017**, *308*, 505–515. **DOI:**10.1016/j.cej.2016.09.075
17. S. N. Su, W. L. Guo, C. L. Yi, Y. Leng, Zh. Ma, *Ultrason. Sonochem.* **2012**, *19*, 469–474. **DOI:**10.1016/j.ultsonch.2011.10.005
18. J. Liu, J. Zhou, Z. Ding, Z. Zhao, X. Xu, Z. Fang, *Ultrason. Sonochem.* **2017**, *34*, 953–959. **DOI:**10.1016/j.ultsonch.2016.08.005
19. X. Y. Lou, L. X. Wu, Y. G. Guo, C. Chen, Z. Wang, D. Xiao, C. Fang, J. Liu, J. Zhao, S. Lu, *Chemosphere* 117 (2014) 582–585. **DOI:**10.1016/j.chemosphere.2014.09.046
20. K. H. Chan, W. Chu, *Water Res.* **2009**, *43*, 2513–2521. **DOI:**10.1016/j.watres.2009.02.029
21. O. S. Furman, A. L. Teel, R. J. Watts, *Environ. Sci. Technol.*, **2010**, 44, 6423–6428. **DOI:**10.1021/es1013714
22. C. D. Qi, X. T. Liu, J. Ma, C. Y. Lin, X. W. Li, H. J. Zhang, *Chemosphere*, **2016**, *151*, 280–288. **DOI:**10.1016/j.chemosphere.2016.02.089
23. B.-T. Zhang, Y. Zhang, Y. Teng, M. Fan, *Crit. Rev. Environ. Sci. Technol.* **2015**, *45*, 1756–1800.
24. G. P. Anipsitakis, E. Stathatos, D. D. Dionysiou, *J. Phys. Chem. B* **2005**, *109*, 13052–13055. **DOI:**10.1021/jp052166y
25. Y. Wang, L. Zhou, X. Duan, H. Sun, E. L. Tin, W. Jin, S. Wang, *Catal. Today* **2015**, *258*, 576–584. **DOI:**10.1016/j.cattod.2014.12.020
26. E. Saputra, S. Muhammad, H. Sun, H-M. Ang, M. O. Tade´, S. Wang, *J Colloid Interface Sci* **2013**, *407*, 467–473. **DOI:**10.1016/j.jcis.2013.06.061
27. W. Guo, S. Su, C. Yi, Z. Ma, *Environ. Prog. Sustain.* **2013**, *32*, 193–197. **DOI:**10.1002/ep.10633
28. X. Chen, J. Chen, X. Qiao, D. Wang, X. Cai, *Appl. Catal. B: Environ.* **2008**, *80*, 116–121. **DOI:**10.1016/j.apcatb.2007.11.009
29. B.-T. Zhang, Y. Zhang, W. Xiang, Y. Teng, Y. Wang, *Chem. Res. Chin. Univ.* **2017**, *33 (5)*, 822–827. **DOI:**10.1007/s40242-017-6413-6
30. W. Zhang, H. L. Tay, S. S. Lim, Y. S. Wang, Z. Y. Zhong, R. Xu, *Appl. Catal. B: Environ.* **2010**, *95*, 93–99. **DOI:**10.1016/j.apcatb.2009.12.014
31. Q. Yang, H. Choi, D. D. Dionysiou, *Appl. Catal. B: Environ.* **2007**, *74*, 170–178. **DOI:**10.1016/j.apcatb.2007.02.001
32. P. R. Shukla, Sh. Wang, H. Sun, H. M. Ang, M. O. Tadé, *Appl. Catal. B: Environ.* **2010**, *100*, 529–534. **DOI:**10.1016/j.apcatb.2010.09.006
33. P. R. Shukla, H. Sun, S.B. Wang, H. M. Ang, M. O. Tade´, *Sep. Purif. Technol.*, **2011**, 77, 230–236. **DOI:**10.1016/j.seppur.2010.12.011
34. L. Hu, X. Yang, S. Dang, *Appl. Catal. B: Environ.* **2011**, *102*, 19–26. **DOI:**10.1016/j.apcatb.2010.11.019
35. B.-T. Zhang, Y. Zhang, Y. Teng, Appl. Surf. Sci. **2018**, *452*, 443–450. **DOI:**10.1016/j.apsusc.2018.05.065
36. P. Shi, R. Su, F. Wan, M. Zhu, D. Li, S. Xua, *Appl. Catal. B: Environ.* **2012**, *123-124*, 265–272. **DOI:**10.1016/j.apcatb.2012.04.043
37. M. Kosmulski, *Adv. Colloid Interface Sci.* **2009**, *152*, 14–25. **DOI:**10.1016/j.cis.2009.08.003
38. L. Hu, G. Zhang, M. Liu, Q. Wang, P. Wang *Chem. Eng. J.* **2018**, *338*, 300–310. **DOI:**10.1016/j.cej.2018.01.016
39. M.V. Lopez-Ramon, F. Stoeckli, C. Moreno-Castilla, F. Carrasco-Marin *Carbon* **1999**, *37*, 1215–1221. **DOI:**10.1016/S0008-6223(98)00317-0
40. Z. S. Wu, W. C. Ren, L. Wen, L. Gao, J. Zhao, Z. Chen, G. Zhou, F. Li, H.-M. Cheng, *ACS Nano* **2010**, *4 (6)*, 3187–3194. **DOI:**10.1021/nn100740x
41. Z. Ai, Y. Huang, S. Lee, L. Zhang, *J. Alloys Compd.* **2011**, *509*, 2044–2049. **DOI:**10.1016/j.jallcom.2010.10.132
42. T. Tsoncheva, L. Ivanova, J. Rosenholm, M. Linden, *Appl. Catal. B: Environ.* **2009**, *89*, 365–374. **DOI:**10.1016/j.apcatb.2008.12.015
43. J. Yang, H. Liu, W. N. Martens, R. L. Frost, *J. Phys. Chem. C* **2010**, *114*, 111–119. **DOI:**10.1021/jp908548f
44. H. T. Fan, S. S. Pan, X. M. Teng, C. Ye, G. H. Li, L. D. Zhang, *Thin Solid Films* **2006**, *513*, 142–147. **DOI:**10.1016/j.tsf.2006.01.074
45. B. Y. Bai, H. Arandiyan, J. H. Li, *Appl. Catal. B: Environ.* **2013**, *142–143*, 677–683. **DOI:**10.1016/j.apcatb.2013.05.056
46. M. Stylidi, D. I. Kondarides, X. E. Verykios, *Appl. Catal. B: Environ.* **2004**, *47*, 189–201.
47. Y. H. Guan, J. Ma, X. C. Li, J. Y. Fang, L. W. Chen, *Environ. Sci. Technol.* **2011,** *45*, (21), 9308–9314. **DOI:**10.1021/es2017363
48. W. D. Oh, Z. Dong, T. T. Lim, *Appl. Catal. B: Environ.* **2016**, *194*, 169–201. **DOI:**10.1016/j.apcatb.2016.04.003
49. P. Hu, M. Long, *Appl. Catal. B: Environ.* **2016**, *181*, 103–117. **DOI:**10.1016/j.apcatb.2015.07.024
50. S. Yang, P. Wang, X. Yang, L. Shan, W. Zhang, X. Shao, R. Niu, *J. Hazard. Mater.* **2010**, *179*, 552–558. **DOI:**10.1016/j.jhazmat.2010.03.039
51. Y. J. Yao, Y. M. Cai, G. D. Wu, F. Wei, X. Li, H. hen, S. Wang, *J. Hazard. Mater.* **2015**, *296*, 128–137. **DOI:**10.1016/j.jhazmat.2015.04.014
52. G. P. Anipsitakis, D. D. Dionysiou, *Appl. Catal. B: Environ.* **2004**, *54*, 155–163. **DOI:**10.1016/j.apcatb.2004.05.025
53. P. Neta, R .E. Huie, A. B. Ross, *J. Phys. Chem. Ref. Data* **1988**, *17*, 1027–1284. **DOI:**10.1063/1.555808
54. Y. Yao, H. Chen, C. Lian, F. Wei, D. Zhang, G. Wu, B. Chen, S. Wang, *J. Hazard. Mater.* **2016**, *314*, 129–139. **DOI:**10.1016/j.jhazmat.2016.03.089
55. Y. Xu, J. Ai, H. Zhang, *J. Hazard. Mater.* **2016**, *309*, 87–96. **DOI:**10.1016/j.jhazmat.2016.01.023

Povzetek

V tej študiji smo pripravili sestavljene okside Bi_2O_3-Co_3O_4 in ocenili njihovo katalitično učinkovitost za aktiviranje peroksimonosulfata (PMS) proti razgradnji barvila Acid Orange 7 (AO7). Karakterizacijo sintetiziranih katalizatorjev smo izvedli z analizami XRD, TEM, XPS, FT-IR in ICP-OES. Povečana bazičnost hibridov Bi_2O_3-Co_3O_4 je prispevala k veliko boljši katalitični aktivnosti pri aktivaciji PMS, kar je povzročilo znatno višjo stopnjo razgradnje AO7 v primerjavi s tisto, ki jo dobimo s samim Co_3O_4. Vzorec s 50 mas. % Bi_2O_3 je pokazal najboljše rezultate v širokem območju pH z zelo majhnim uhajanjem Co (72 μg/L) tudi v kislih pogojih. Razgradnja 50 mg/L AO7 je dosegla skoraj 100 % v kratkem času (12 minut) z uporabo zelo nizke koncentracije katalizatorjev (0,1 g/L) in z razmerjem [PMS]/[AO7] = 6. Proučevali smo vpliv vsebnosti Bi_2O_3, količine katalizatorja, molskega razmerja [PMS]/[AO7], začetnega pH in temperature na razgradnjo AO7. S poskusi na osnovi kaljenja radikalov so bili površinsko vezani sulfatni ostanki, ki nastajajo v oksidacijskem sistemu Bi_2O_3-Co_3O_4/PMS, dokazani kot prevladujoča vrsta radikalov.

Except when otherwise noted, articles in this journal are published under the terms and conditions of the Creative Commons Attribution 4.0 International License

DOI: 10.17344/acsi.2019.5630 *Acta Chim. Slov.* **2020,** *67,* 622–628
creative commons

Scientific paper

Magnetic, Photoluminescent and Semiconductor Properties of a 4*f*-5*d* Bromide Compound

Wen-Tong Chen*

[1] *Institute of Applied Chemistry, School of Chemistry and Chemical Engineering, Jinggangshan University, Ji'an, Jiangxi 343009, China*

[2] *Department of Ecological and Resources Engineering, Fujian Key laboratory of Eco-Industrial Green Technology, Wuyi University, Wuyishan, Fujian 354300, China*

[3] *State Key Laboratory of Structural Chemistry, Fujian Institute of Research on the Structure of Matter, Chinese Academy of Sciences, Fuzhou, Fujian 350002, China*

** Corresponding author: E-mail: wtchen_2000@aliyun.com Tel.: +86(796)8100490; fax +86(796)8100490*

Received: 10-14-2019

Dedicated to Professor Jin-Shun Huang on the occasion of his 80th birthday.

Abstract

A novel 4*f*–5*d* material ($HgDy_6Br_{12}$)Hg_8Br_{24} (**1**) is prepared by hydrothermal reactions and structurally characterized by single crystal X-ray diffraction. Compound **1** is characterized by a two-dimensional (2*D*) layered structure. A photoluminescence measurement with solid-state samples shows that this compound exhibits a strong emission in the blue region. A narrow optical band gap of 1.97 eV is revealed by a solid-state UV/Vis diffuse reflectance spectrum. The variable-temperature magnetic susceptibility obeys the Curie-Weiss law ($\chi_m = c/(T-\theta)$) with $C = 0.78$ K and a Weiss constant $\theta = -0.38$ K as revealed by the magnetic measurements, suggesting the existence of an antiferromagnetic interaction.

Keywords: Lanthanide; mercury; magnetism; photoluminescence; semiconductor

1. Introduction

Lanthanide compounds have recently gained more and more attention because of their attractive photoluminescent, magnetic, catalytic and other performances.[1–9] Nowadays, scientists from chemistry and material domains have completed a large number of explorations on different lanthanide compounds, in order to find out their application potentials in luminescent probes, light-emitting diodes (LEDs), electrochemical displays, and magnetic materials and so on.[10–14] The attractive photoluminescent and magnetic performances of lanthanide compounds mainly come from the abundant 4f electrons of lanthanide (LN) ions. Generally speaking, lanthanide compounds may show strong photoluminescence only when the electronic transitions of the 4f electron of the lanthanide ion can efficiently happen. Moreover, a number of lanthanide compounds are interesting due to their fascinating magnetic and magneto-optical performances.[15–20] As a result, a great number of researchers have devoted themselves into the exploration of design, preparation and characterization of new lanthanide-containing magnetic compounds. However, the semiconductor performances of lanthanide compounds are rarely explored yet in comparison with the studies on the photoluminescent and magnetic properties of the lanthanide materials.[21]

Group 12 (IIB) metals are zinc, cadmium and mercury and they have drawn much attention due to the following aspects: various coordination modes, photoluminescent and photoelectric properties, as well as the vital role played in the biosystem by zinc.[22,23] The IIB metals are also very important components in semiconductor compounds and, up to date, many semiconductor compounds containing IIB metals have so far been reported.[24–27] Since many years ago, photoluminescent, magnetic and semiconductor compounds have become one of research hotspots. The LN-IIB-VIIA (LN = lanthanide, VIIA = halogen) compounds have become one of research hotspots

due to the attractive crystal structure, photoluminescence, magnetism and semiconductor performances. In this work, the synthesis, crystal structure, gas adsorption, magnetism, photoluminescence, and semiconductor performances of a 4*f*–5*d* material ($HgDy_6Br_{12}$)Hg_8Br_{24} (**1**) with a 2-D layered structure are reported. It should be pointed out that some ternary LN-IIB-VIIA compounds have thus far been reported,[28–32] but most of them are fluorides and an iodide with cadmium or zinc.

2. Experimental Section

2. 1. Materials and Characterization

The chemicals were purchased via commercial sources and directly used. The photoluminescence experiments were carried out on a F97XP photoluminescent spectrometer. A solid-state UV/vis diffuse reflectance spectrum was measured at room temperature on a computer-controlled TU1901 UV/vis spectrometer equipped with an integrating sphere in the wavelength range of 190–900 nm. The barium sulfate powder was applied as a reference of 100% reflectance, on which the finely ground powder sample was daubed. Variable-temperature magnetic susceptibility and field dependence magnetization measurements of the title compound on polycrystalline samples were carried out on a PPMS 9T Quantum Design SQUID magnetometer and the diamagnetism correction of the magnetic data was calculated from the Pascal's constants.

2. 2. Synthesis of 1

A mixture of $Dy(NO_3)_3 \cdot 6H_2O$ (1 mmol, 458 mg), $HgBr_2$ (1 mmol, 360 mg) and distilled water (10 mL) was sealed into a 23 mL Teflon-lined stainless steel vessel. The vessel was heated to 473 K and kept there for one week under autogenous pressure. When the vessel was slowly cooled to room temperature, colorless block-like crystals were obtained. The yield was 21% based on $HgBr_2$.

2. 3. Crystal Structure Determination and Refinement

A carefully selected single crystal (0.08 × 0.07 × 0.06 mm^3) was adhered onto the tip of a glass fiber and then mounted to a SuperNova CCD diffractometer. The X-ray source is graphite monochromated Mo-*Kα* radiation with the λ = 0.71073 Å. The intensity data were obtained at 293(2) K with the ω scan mode. For data reduction and empirical absorption correction, CrystalClear software was applied. The crystal structure of the title compound was solved by using the direct methods. The final structure was refined on F^2 by full-matrix least-squares using the Siemens SHELXTL^{TM} V5 crystallographic software package. All of the atoms were generated on the difference Fourier maps and refined anisotropically. The high max./min. residual electron density is ghost peak around the heavy atom. The crystal data as well as the details of the data collection and refinement are given in Table 1, while the selected bond lengths and bond angles are listed in Table 2.

Table 1. Crystal data and structure refinement details.

Formula	$Br_{36}Dy_6Hg_9$
Mr	5656.71
Crystal system	orthorhombic
Space group	*Pbam*
a (Å)	13.0997(11)
b (Å)	13.6459(13)
c (Å)	27.906(3)
V (Å^3)	4988.4(8)
Z	2
$2\theta_{max}$ (°)	50
Reflections collected	12182
Independent, observed reflections (R_{int})	3855, 2167 (0.0437)
$d_{calcd.}$ (g/cm^3)	3.741
μ (mm^{-1})	31.850
F(000)	4722
R_1, wR_2	0.1122, 0.3031
S	1.032
$\Delta\rho$ (max, min) (e/Å^3)	1.956, –2.820

Table 2. Selected bond lengths (Å) and bond angles (°).

Hg1-Br5	2.400(4)	Dy2-Br4	3.349(3)
Hg1-Br6	2.748(4)	Dy2-Br4#4	3.349(3)
Hg1-Br7	2.617(5)	Dy3-Br4	2.417(3)
Hg1-Br8	2.767(6)	Dy3-Br4#7	2.417(3)
Hg2-Dy2#1	2.961(2)	Dy3-Br5	3.278(4)
Hg2-Dy2	2.961(2)	Dy3-Br5#7	3.278(4)
Hg2-Dy1#2	3.037(2)	Dy1-Dy2	3.468(3)
Hg2-Dy1#3	3.037(2)		
Hg2-Dy3	3.431(2)	Br5-Hg1-Br7	124.2(2)
Hg2-Dy3#1	3.431(2)	Br5-Hg1-Br8	114.7(2)
Hg3-Br10	2.370(4)	Br7-Hg1-Br8	102.60(18)
Hg3-Br11	2.397(4)	Br5-Hg1-Br6	121.91(18)
Dy1-Br1#4	2.390(3)	Br7-Hg1-Br6	94.15(14)
Dy1-Br1	2.390(3)	Br8-Hg1-Br6	93.27(16)
Dy1-Br2#5	3.425(6)	Br10-Hg3-Br11	174.89(19)
Dy1-Br3#6	3.310(6)	Br2-Dy2-Br3	163.63(19)
Dy2-Br2	2.420(5)	Br4-Dy3-Br4#7	173.99(19)
Dy2-Br3	2.398(5)	Br4-Dy3-Br5	90.74(13)

Symmetry transformations used to generate equivalent atoms: #1 $-x+3, -y-2, -z-1$; #2 $-x+7/2, y+½, z$; #3 $x-½, -y-5/2, -z-1$; #4 $x, y, -z-1$; #5 $x+½, -y-5/2, -z-1$; #6 $-x+7/2, y-½, z$; #7 $-x+3, -y-2, z$.

3. Results and Discussion

As revealed by the single crystal X-ray diffraction, the title compound crystallizes in the space group *Pbam* of the orthorhombic system with two formula units in one cell. The asymmetric unit of compound **1** includes

three mercury ions (Hg1 in full occupancy, Hg2 in 0.25 occupancies, Hg3 in full occupancy), three dysprosium ions (Dy1, Dy2, Dy3; all in 0.5 occupancies) and eleven bromine ions (from Br1 to Br11; Br2, Br3, Br6, Br9 in 0.5 occupancies, while others in full occupancy), as depicted in Fig. 1. Most of the crystallographically independent ions are located in the general positions, but all dysprosium ions as well as Hg2, Br2, Br3, Br6, and Br9 ions are resided at the special positions. Results of the bond valence calculations indicate that all dysprosium ions are in +3 oxidation state (Dy1: 3.395, Dy2: 3.246, Dy3: 3.231), while mercury ions Hg1 and Hg3 are in +2 oxidation state (Hg1: 2.318, Hg3: 2.093).[33,34] The bond valence of Hg2 is not available because it contains only metal-metal bonds.

The Hg1 ion is coordinated by four bromine atoms and yields a slightly distorted $HgBr_4$ tetrahedron with the bond angles of Br-Hg1-Br locating in the span of 93.27(16)° to 124.2(2)° and the bond lengths of Hg-Br locating in the range of 2.400(4) Å to 2.767(6) Å, which is comparable with those reported previously.[35–37] Differently, the Hg2 ion is surrounded by six dysprosium ions and forms a $HgDy_6$ octahedron. The distances of Hg-Dy are in the range of 2.961(2) Å to 3.431(2) Å. The Hg3 ion, however, is coordinated by two bromine ions to give an almost linear geometry of $HgBr_2$ with the bond angle of Br10-Hg3-Br11 being of 174.89(19)° and the bond lengths of Hg-Br being of 2.370(4) Å and 2.397(4) Å. All dysprosium ions are surrounded by four bromine ions. The bond distance of Dy-Br is located in the range of 2.390(3) Å to 3.425(6) Å. The bond angle of Br-Dy-Br is in the span of 90.74(13)° to 173.99(19)°. Two $HgBr_4$ tetrahedra connect together via a corner-sharing bromide ion to yield a dimer, as shown in Fig. 2a. The dimers then interconnect together via the bromide ions to form a one-dimensional (1-D) chain running along the *a* axis. The chains and $HgBr_2$ moieties are in the same plane and form an Hg-Br layer (Fig. 2a and the purple layers in Fig. 3). The $HgDy_6$ octahedra interconnect together via Dy-Dy interactions to yield a two-dimensional (2-D) Hg-Dy-Br layer extending parallel to the *ab* plane. The Dy-Dy distance is 3.468(3) Å, which is comparable with those reported in the literature.[38,39] These Hg-Br layers and Hg-Dy-Br layers stack along the *c* axis in the number of 2-1-2 to yield a crystal packing structure of compound **1**, as presented in Fig. 3.

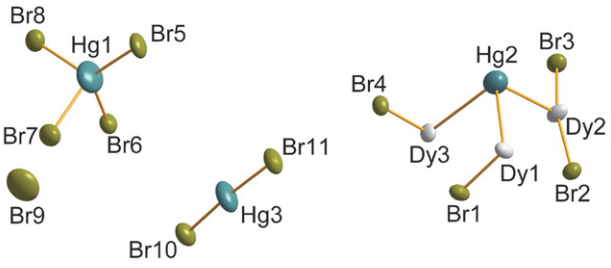

Figure 1. An ORTEP drawing of the asymmetric unit of **1** with 30% thermal ellipsoids.

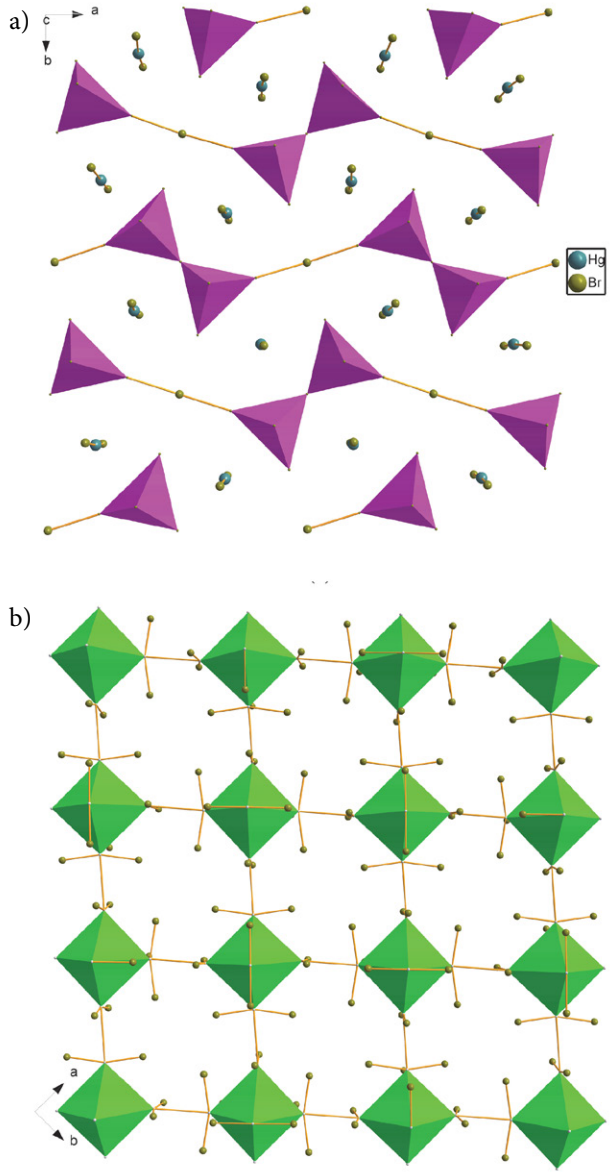

Figure 2. (a) The Hg-Br layer with the purple polyhedra representing the $HgBr_4$ tetrahedra and (b) the Hg-Dy-Br layer with the green polyhedra representing the $HgDy_6$ octahedra.

Lanthanide materials can usually exhibit photoluminescence and, nowadays, a large number of lanthanide materials have been reported for the photoluminescent performance and for potential applications as photoluminescent emitting materials like electrochemical displays, LEDs, chemical sensors and so on.[40–42] As a dysprosium-containing compound, the title compound is possible to display photoluminescence. The photoluminescence property of compound **1** was explored in the solid state at room temperature. The results of the photoluminescence experiments are given in Fig. 4. The photoluminescence spectrum of compound **1** obviously shows an effective energy absorption residing in the wavelength span of 400 to 430 nm. The photoluminescence excitation spectrum using the emission wavelength of 445 nm yields one sharp

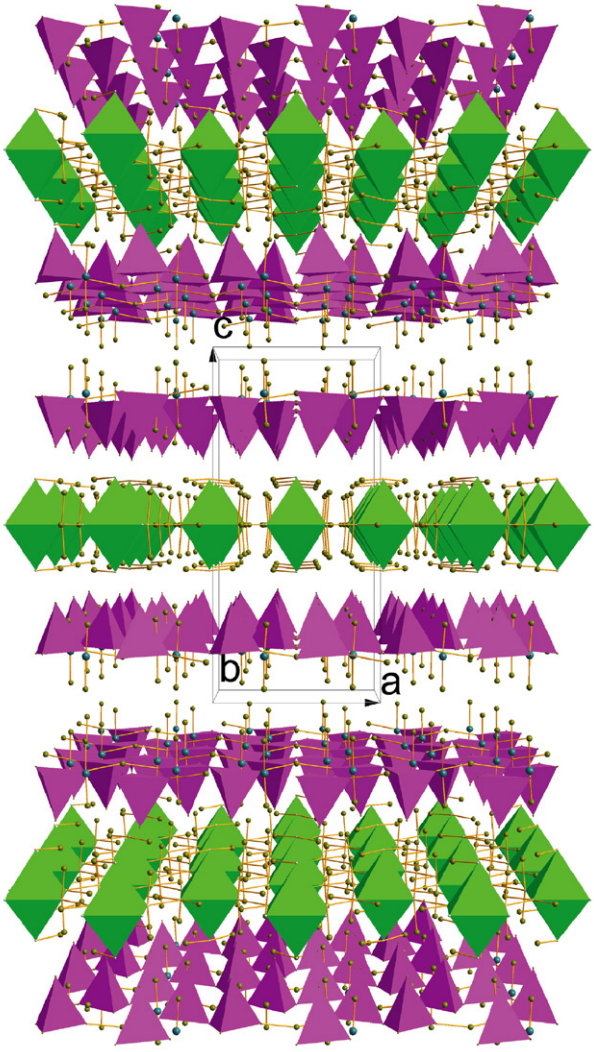

Figure 3. A packing diagram of compound **1**.

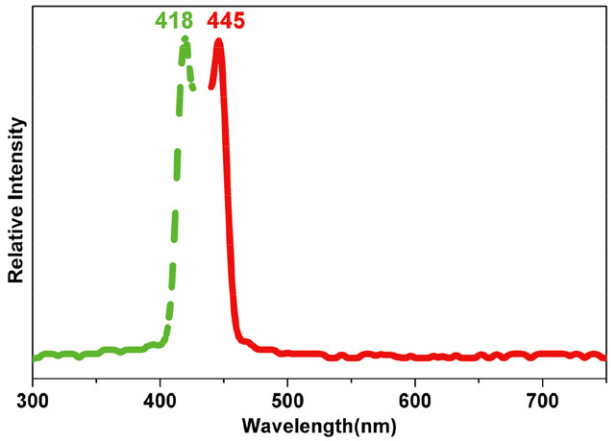

Figure 4. The solid state photoluminescence spectra of compound **1**. Green dashed line: excitation; red solid line: emission.

excitation peak at 418 nm. The corresponding photoluminescence emission spectrum of compound **1** is also measured, with the irradiation wavelength at 418 nm. The photoluminescence emission spectrum is characteristic of one sharp peak residing at 445 nm of blue region. Therefore, the title compound can be a candidate for potential blue photoluminescence materials.

Mercury is well-known as an important component of semiconductor materials. The title compound contains mercury and it is supposed to display semiconductor property. So, the solid-state UV/Vis diffuse reflectance spectrum is explored with solid state samples at room temperature and the data of the diffuse reflectance spectrum were treated using the Kubelka-Munk function, namely, $\alpha/S = (1\text{-}R)^2/2R$. In this function, α means the absorption coefficient, S is the scattering coefficient that is practically wavelength independent when the particle size is larger than 5 μm, while R is the reflectance. The optical band gap value can be determined by extrapolating from the linear part of the absorption edges of the α/S vs. energy diagram, as presented in Fig. 5. The solid-state diffuse reflectance spectrum shows that compound **1** has a narrow optical band gap of 1.97 eV and, therefore, compound **1** can be a candidate for narrow band gap semiconductor materials. The solid-state diffuse reflectance spectrum displays a slow slope of the optical absorption edge that indicates an indirect transition process.[43] The optical band gap value of 1.97 eV of compound **1** is larger than that of $CuInS_2$ (1.55 eV), CdTe (1.5 eV) and GaAs (1.4 eV) which are efficient photovoltaic materials.[44,45]

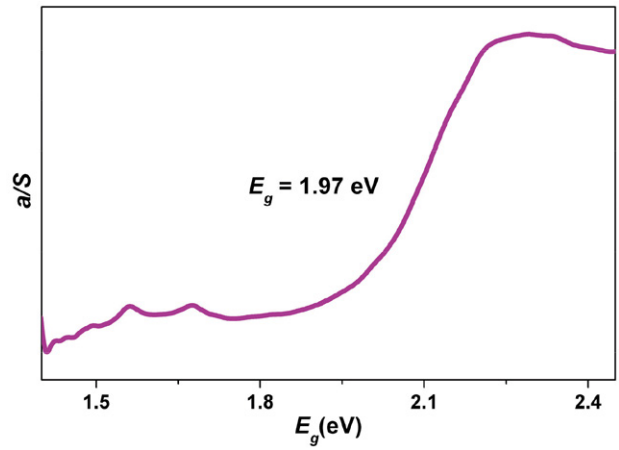

Figure 5. A solid-state diffuse reflectance spectrum for compound **1**.

Trivalent lanthanide ions-containing compounds can generally display magnetic performance.[46–48] Therefore, the title compound is supposed to exhibit magnetic behaviors. The χ_M vs. T and μ_{eff} vs. T curves for the title compound are presented in Fig. 6. The χ_M is the magnetic susceptibility per Dy-containing molecule. When the temperature is decreased, the χ_M vs. T diagram continuously increases from 0.06 emu mol^{-1} at 300 K to 0.39 emu mol^{-1} at 2 K. Such a χ_M vs. T diagram of compound **1** indicates an antiferromagnetic-like performance. The essence of this antiferromagnetic-like performance is not clear yet, but it

is supposed to be originated from the gradual thermal depopulation of the Stark components of the dysprosium ions. The magnetic susceptibility diagram agrees well with the Curie-Weiss law, namely, $\chi_m = c/(T-\theta)$. The data of the magnetic susceptibility is fitted from 300 K to 2 K using this Curie-Weiss law and it results in the value of C being of 0.78 K and a Weiss constant θ being of –0.38 K, as presented in Fig. 6. The negative Weiss constant confirms the presence of the antiferromagnetic-like performance in compound **1**. When the temperature was decreased, the μ_{eff} vs. T diagram continuously decreases from 11.89 μ_B at 300 K to 2.45 μ_B at 2 K, which also confirms the presence of the antiferromagnetic-like performance in compound **1**, as shown in Fig. 6. The field dependence of the magnetization of compound **1** was carried out at 2 K, as given in Fig. 7. This diagram shows a very small coercive field of about 40 Oe and a remnant magnetization of around 0.002 $N\beta$. The magnetization diagram increases fast with the increased field from –80 kOe to 80 kOe. A saturation value cannot be obtained even at 80 kOe. The value is 0.49 Nβ at 80 kOe.

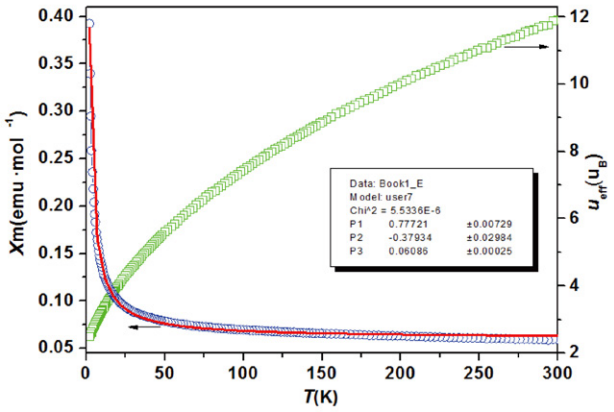

Figure 6. Thermal dependence of χ_M and μ_{eff} for **1** with the red line representing the best fitting curve

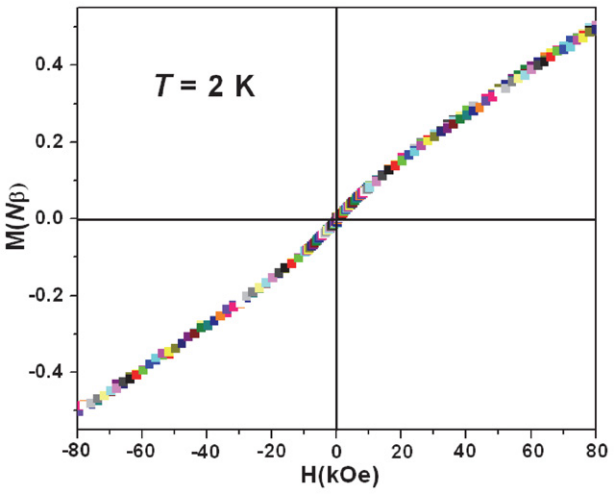

Figure 7. A curve of magnetization vs H.

4. Conclusions

A novel 4*f*-5*d* bromide compound $(HgDy_6Br_{12})Hg_8B_{r24}$ has been synthesized and structurally characterized by single crystal X-ray diffraction. This compound is characteristic of a 2-D layered structure. The solid-state photoluminescence measurement shows that it displays a strong emission in the blue region. A solid-state UV/Vis diffuse reflectance spectrum shows that this compound has a narrow optical band gap of 1.97 eV. This compound exhibits an antiferromagnetic interaction with C = 0.78 K and a Weiss constant θ = –0.38 K. As a result, this compound is probably a candidate of photoluminescence, semiconductive or magnetic materials.

Acknowledgments

Author thanks the financial support of the NSF of China (21361013), Jiangxi Provincial Department of Education's Item of Science and Technology (GJJ170637), and the open foundation (20180008) of the State Key Laboratory of Structural Chemistry, Fujian Institute of Research on the Structure of Matter, Chinese Academy of Sciences.

Supplementary Material

Crystallographic data in CIF format have been deposited with FIZ Karlsruhe with the following CSD numbers: 1947021. These data can be obtained from the Fachinformationszentrum Karlsruhe, 76344 Eggenstein-Leopoldshafen, Germany, (fax: (49) 7247-808-666; e-mail: crysdata@fiz.karlsruhe.de).

5. References

1. T. Zheng, C. Cao, P. Dong, S. Liu, F. Wang, X. Tong, J. Liao, J. Chen, H. Wen, *Polyhedron* **2016**, *113*, 96–101. **DOI:**10.1016/j.poly.2016.04.011
2. R. F. Mendes, D. Ananias, L. D. Carlos, J. Rocha, F. A. A. Paz, *Cryst. Growth Des.* **2017**, *17*, 5191–5199. **DOI:**10.1021/acs.cgd.7b00667
3. S.-J. Liu, T.-F. Zheng, J. Bao, P.-P. Dong, J.-S. Liao, J.-L. Chen, H.-R. Wen, J. Xu, X.-H. Bu, *New J. Chem.* **2015**, *39*, 6970–6975. **DOI:**10.1039/C5NJ01229E
4. P. Zhang, L. Zhang, C. Wang, S. Xue, S.-Y. Lin, J. Tang, *J. Am. Chem. Soc.* **2014**, *136*, 4484–4487. **DOI:**10.1021/ja500793x
5. S.-L. Yao, C. Cao, X.-M. Tian, T.-F. Zheng, S.-J. Liu, X.-L. Tong, J.-S. Liao, J.-L. Chen, H.-R. Wen, *ChemistrySelect* **2017**, *2*, 10673–10677. **DOI:**10.1002/slct.201702223
6. S. Han, R. Deng, X. Xie, X. Liu, *Angew. Chem. Int. Edit.* **2014**, *53*, 11702–11715. **DOI:**10.1002/anie.201403408
7. S. Liu, Y. Cui, W. Song, Q. Wang, X. Bu, *Chinese J. Inorg. Chem.* **2015**, *31*, 1894–1902.

8. B. Zhou, L. Tao, Y. Chai, S. P. Lau, Q. Zhang, Y. H. Tsang, *Angew. Chem. Int. Edit*. **2016**, *55*, 12356–12360. **DOI:**10.1002/anie.201604682
9. S.-J. Liu, S.-L. Yao, C. Cao, T.-F. Zheng, C. Liu, Z.-X. Wang, Q. Zhao, J.-S. Liao, J.-L. Chen, H.-R. Wen, *Polyhedron* **2017**, *121*, 180–184. **DOI:**10.1016/j.poly.2016.09.040
10. F. Pointillart, O. Cador, B. Le Guennic, L. Ouahab, *Coord. Chem. Rev*. **2017**, *346*, 150–175. **DOI:**10.1016/j.ccr.2016.12.017
11. H. Kuang, Z. Zhang, L. Lin, H. Chen, W. Chen, *Chinese J. Struct. Chem*. **2019**, *38*, 337–344. **DOI:**10.1016/j.ccr.2017.01.012
12. J. A. Kitchen, *Coord. Chem. Rev*. **2017**, *340*, 232–246.
13. S.-D. Han, S.-J. Liu, Q.-L. Wang, X.-H. Miao, T.-L. Hu, X.-H. Bu, *Cryst. Growth Des*. **2015**, *15*, 2253–2259. **DOI:**10.1021/acs.cgd.5b00024
14. I. A. Shkrob, M. D. Kaminski, C. J. Mertz, P. G. Rickert, M. S. Derzon, K. Rahimian, *J. Am. Chem. Soc*. **2009**, *131*, 15705–15710. **DOI:**10.1021/ja9035253
15. T.-F. Zheng, X.-M. Tian, S.-L. Yao, C. Cao, J.-B. Cai, S.-J. Liu, *J. Mol. Struct*. **2018**, *1165*, 326–331. **DOI:**10.1016/j.molstruc.2018.03.112
16. O. Ofer, J. Sugiyama, J. H. Brewer, E. J. Ansaldo, M. Mansson, K. H. Chow, K. Kamazawa, Y. Doi, Y. Hinatsu, *Phys. Rev. B* **2011**, *84*, 054428/1–054428/5. **DOI:**10.1103/PhysRevB.84.054430
17. S. Liu, X. Xie, T. Zheng, J. Bao, J. Liao, J. Chen, H. Wen, *CrystEngComm* **2015**, *17*, 7270–7275. **DOI:**10.1039/C5CE00997A
18. G. Abbas, Y. Lan, G. Kostakis, C. E. Anson, A. K. Powell, *Inorg. Chim. Acta* **2008**, *361*, 3494–3499. **DOI:**10.1016/j.ica.2008.03.024
19. A. Kirste, N. P. Kolmakova, S. Hansel, H.-U. Mueller, M. Von Ortenberg, *Physica B* **2004**, *346-347*, 191–195. **DOI:**10.1016/j.physb.2004.01.048
20. S.-J. Liu, C. Cao, S.-L. Yao, T.-F. Zheng, Z.-X. Wang, C. Liu, J.-S. Liao, J.-L. Chen, Y.-W. Li, H.-R. Wen, *Dalton Trans*. **2017**, *46*, 64–70. **DOI:**10.1039/C6DT03589B
21. N. Ahmed, J. Nisar, R. Kouser, A. G Nabi, S. Mukhtar, Y. Saeed, M. H. Nasim, *Mater. Res. Express* **2017**, *4*, 065903/1–065903/8. **DOI:**10.1088/2053-1591/aa75fc
22. J. B. Waters, R. S. P. Turbervill, J. M. Goicoechea, *Organometallics* **2013**, *32*, 5190–5200. **DOI:**10.1021/om400728u
23. B. Mohapatra, S. Verma, *Cryst. Growth Des*. **2013**, *13*, 2716–2721. **DOI:**10.1021/cg4006168
24. Y. Yoshida, H. Ito, Y. Nakamura, M. Ishikawa, A. Otsuka, H. Hayama, M. Maesato, H. Yamochi, H. Kishida, G. Saito, *Cryst. Growth Des*. **2016**, *16*, 6613–6630. **DOI:**10.1021/acs.cgd.6b01294
25. L. Zhang, H. Lin, Y. Wu, S. Zhuo, *Chem. Phys. Lett*. **2016**, *661*, 224–227. **DOI:**10.1016/j.cplett.2016.08.079
26. Y. Zeng, D. F. Kelley, *J. Phys. Chem. C* **2016**, *120*, 17853–17862. **DOI:**10.1021/acs.jpcc.6b06282
27. T. Uematsu, E. Shimomura, T. Torimoto, S. Kuwabata, *J. Phys. Chem. C* **2016**, *120*, 16012–16023. **DOI:**10.1021/acs.jpcc.5b12698
28. A. F. Konstantinova, E. A. Krivandina, D. N. Karimov, B. P. Sobolev, *Crystallogr. Rep*. **2010**, *55*, 990–994. **DOI:**10.1134/S1063774510060143
29. N. I. Sorokin, E. A. Krivandina, Z. I. Zhmurova, *Crystallogr. Rep*. **2013**, *58*, 948–952. **DOI:**10.1134/S1063774513060217
30. S. V. Kuznetsov, P. P. Fedorov, *Inorg. Mater*. **2008**, *44*, 1434–1458. **DOI:**10.1134/S0020168508130037
31. A. F. Konstantinova, T. M. Glushkova, I. I. Buchinskaya, E. A. Krivandina, B. P. Sobolev, *Crystallogr. Rep*. **2009**, *54*, 609–612. **DOI:**10.1134/S1063774509040117
32. M. Lukachuk, L. Kienle, C. Zheng, H. Mattausch, A. Simon, *Inorg. Chem*. **2008**, *47*, 4656–4660. **DOI:**10.1021/ic800024n
33. M. Kasunič, S. D. Škapin, D. Suvorov, A. Golobič, *Acta Chim. Slov*. **2012**, *59*, 117–123.
34. I. D. Brown, D. Altermat, *Acta Crystallogr. B* **1985**, *41*, 244. **DOI:**10.1107/S0108768185002063
35. S. J. Sabounchei, M. Ahmadianpoor, A. Hashemi, F. Mohsenzadeh, R. W. Gable, *Inorg. Chim. Acta* **2017**, *458*, 77–83. **DOI:**10.1016/j.ica.2016.12.023
36. J. Vallejos, I. Brito, A. Cardenas, J. Llanos, M. Bolte, M. *J. Solid State Chem.* **2015**, *223*, 17–22. **DOI:**10.1016/j.jssc.2014.03.022
37. G. Mahmoudi, A. A. Khandar, J. K. Zareba, M. J. Bialek, M. S. Gargari, M. Abedi, G. Barandika, D. Van Derveer, J. Mague, A. Masoumi, *Inorg. Chim. Acta* **2015**, *429*, 1–14. **DOI:**10.1016/j.ica.2014.12.027
38. T. Stewart, M. Nishiura, Y. Konno, Z. Hou, G. J. McIntyre, R. Bau, *Inorg. Chim. Acta* **2010**, *363*, 562–566. **DOI:**10.1016/j.ica.2009.03.024
39. K. Daub, G. Meyer, *Z. Anorg. Allg. Chem.* **2010**, *636*, 1716–1719.
40. J. J. Joos, D. Poelman, P. F. Smet, *Phys. Chem. Chem. Phys.* **2015**, *17*, 19058–19078. **DOI:**10.1039/C5CP02156A
41. Y. Zhang, W. Wei, G. K. Das, T. Yang, T. Timothy, *J. Photoch. Photobio. C.* **2014**, *20*, 71–96. **DOI:**10.1016/j.jphotochemrev.2014.06.001
42. W. G. J. H. M. van Sark, J. de Wild, J. K. Rath, A. Meijerink, R. El Schropp, *Nanoscale Res. Lett.* **2013**, *8*, 81/1–81/10.
43. F. Q. Huang, K. Mitchell, J. A. Ibers, *Inorg. Chem.* **2001**, *40*, 5123–5126. **DOI:**10.1021/ic0104353
44. P. Dürichen, W. Bensch, *Eur. J. Solid State Inorg. Chem.* **1997**, *34*, 1187–1198.
45. R. Tillinski, C. Rumpf, C. Näther, P. Duerichen, I. Jess, S. A. Schunk, W. Bensch, *Z. Anorg. Allg. Chem.* **1998**, *624*, 1285–1290. **DOI:**10.1002/(SICI)1521-3749(199808)624:8<1285::AID-ZAAC1285>3.0.CO;2-5
46. S.-J. Liu, C. Cao, C.-C. Xie, T.-F. Zheng, X.-L. Tong, J.-S. Liao, J.-L. Chen, H.-R. Wen, Z. Chang, X.-H. Bu, *Dalton Trans*. **2016**, *45*, 9209–9215. **DOI:**10.1039/C6DT01349J
47. R.-P. Li, Q.-Y. Liu, Y.-L. Wang, C.-M. Liu, S.-J. Liu, *Inorg. Chem. Front.* **2017**, *4*, 1149–1156. **DOI:**10.1039/C7QI00178A
48. T.-F. Zheng, S.-L. Yao, C. Cao, S.-J. Liu, H.-K. Hu, T. Zhang, H.-P. Huang, J.-S. Liao, J.-L. Chen, H.-R. Wen, *New J. Chem*. **2017**, *41*, 8598–8603. **DOI:**10.1039/C7NJ01463E

Povzetek

S hidrotermalno sintezo smo pripravili 4*f*–5*d* material ($HgDy_6Br_{12}$)Hg_8Br_{24} (**1**) in ga strukturno okarakterizirali z rentgensko monokristalno analizo. Spojine **1** ima dvodimenzionalno plastovito strukturo. Fotoluminiscenca v trdnem stanju kaže močno emisijo v modrem območju. Ozek optični pasovni razmik 1.97 eV je bil določen z UV/Vis difuzno refleksijo v trdnem. Magnetna susceptibilnost pri različnih temperaturah je v skladu z Curie-Weissovim zakonom ($c_m = c/(T-q)$) z C = 0.78 K in z Weissovo konstanto θ = –0.38 K, kar kaže na obstoj antiferomagnetnih interakcij.

Except when otherwise noted, articles in this journal are published under the terms and conditions of the Creative Commons Attribution 4.0 International License

Scientific paper

Study of Quinizarin Interaction with SDS Micelles as a Model System for Biological Membranes

Ana Maria Toader,[1] Petruta Oancea[2] and Mirela Enache[1,*]

[1]*Institute of Physical Chemistry Ilie Murgulescu, Romanian Academy, Splaiul Independentei 202, Bucharest 060021, Romania*

[2]*Department of Physical Chemistry, University of Bucharest, Blvd. Elisabeta 4-12, Bucharest 030018, Romania*

* *Corresponding author: E-mail: enachemir@yahoo.com*

Received: 10-21-2019

Abstract

Investigation of the interaction of quinizarin (Q), an analogue of the core unit of different anticancer drugs, with anionic SDS micelles has been performed by absorption and conductance measurements in 0.1 M phosphate buffer, pH 7.4 and over the temperature range of 293.15–323.15 K. The values of binding constant (K_b), partition coefficient (K_x) and the corresponding thermodynamic parameters (Gibbs free energy, enthalpy, entropy) for the binding and distribution of quinizarin between the bulk aqueous solution and surfactant micelles have been determined and discussed in terms of possible intermolecular interactions. Values of critical micelle concentration (CMC) and degree of ionization (α) for SDS in the absence and the presence of quinizarin have been evaluated from conductometric study. Comparing the absorption spectra of quinizarin in SDS micelles with the spectra in different solvents revealed that quinizarin molecules are located in the hydrophilic region of SDS micelles. The trend of changes in Gibbs free energy, enthalpy and entropy with temperature shows that both binding and partition processes are spontaneous and entropy driven. In addition, the hydrophobic interactions are the main forces involved in binding and partition processes.

Keywords: Quinizarin; SDS micelles; binding constant; partition coefficient

Introduction

Quinizarin (1,4-dihydroxy-9,10-anthraquinone, Q) belongs to the synthetic anthraquinones which are known for their antifungal, antibacterial and antioxidant properties.[1,2] Quinizarin is also an interesting molecule from a pharmaceutical point of view; this chromophore framework is the main part in the structure of anticancer drugs such as doxorubicin, daunorubicin, and mitoxantrone which are widely used in clinical practice. These drugs exhibit their antitumor activity by intercalation of the aromatic moiety between the DNA base pairs, resulting in the inhibition of both DNA replication and RNA transcription.[3–8] Because the biological activity of these drugs is governed by the planar anthraquinone moiety, the interaction of different anthraquinones (quinizarin, danthron, purpurin) with DNA has been already investigated and compared with the established drugs. These studies revealed the different types of binding modes as partial intercalation and hydrogen binding, and binding constants values similar with anthracyclines.[9–12] In addition to affinity of anthraquinone chromophore toward DNA, the quinone functionality is involved in generation of reactive oxygen species responsible for the cardiotoxicity of these drugs.[13,14] Also, quinizarine is commonly used as fuel marker to distinguish the origin and quality of fuels.[15]

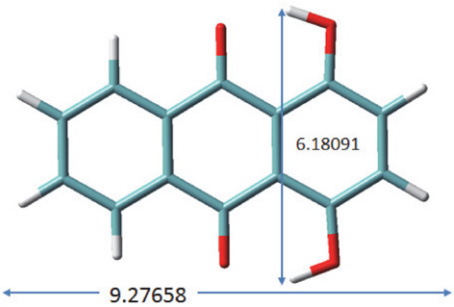

Figure 1. Optimized molecular structure of quinizarin using B3LYP/6-311G* basis set.

As DNA, the main target of anthracycline anticancer drugs is localized in the nucleus of cells they must cross the cell membrane as well the nuclear envelope to obtain pharmacological activity. Also, in eukaryotic cells the drug

molecules may interact with membranes of organelles such as the endoplasmic reticulum, the Golgi and the mitochondria once they are released into the cytosol. Therefore, the understanding of the interactions between anticancer drugs and cellular membranes is of primary importance because these interactions are related with drug transport, accumulation and pharmacological activity.[16] Although the cellular and nuclear membranes are not the primary target of the anthraquinone anticancer drugs, interactions between drug molecules and membrane lipids may induce profound alterations in cell functions like transient increase in membrane fluidity, correlated with ceramide generation and the fusion of membrane lipid rafts leading to activation of the apoptotic cascade.[17] As the anthraquinone chromophore of quinizarin is the major part in the structure of these anticancer drugs, it can be inferred that the similar major effects are expected to be induced by quinizarin at the level of biological membranes. These interactions are very difficult to investigate because of the complexity of structure and functions of biological membranes. Therefore, different simplified model membranes composed by a hydrophobic core and hydrophilic surface have gained a significant role in research as alternatives for biological membranes. Micelles are colloidal-sized aggregates of surfactants at concentrations higher than critical micelle concentration (CMC). The structural similarity of micelles with biological membranes allows them to be used as simple model system to conduct in vitro study of drug-membrane interactions.[18–23] Besides, the micelles can solubilize poorly soluble drugs and can be used as drug carriers in different drug delivery systems.[24] Micelles with their hydrophobic core and hydrophilic interface region mimic biological membranes and are able to account for both hydrophobic and hydrophilic (hydrogen bonds, electrostatic and dipole-dipole) interactions, which occur during the interaction of different drugs with biological membranes.[25,26]

Taking into account that the planar anthraquinone unit of quinizarin plays a key role in pharmacological activity of different anticancer drugs and that the surfactant micelles are accepted as simple model systems for studying different aspects of drug molecules interactions with biological membranes, in the present paper the interaction of quinizarin with SDS micelles was studied by employing absorption and conductometric techniques. The binding constant, partition coefficient and thermodynamic parameters for both binding and partition processes were calculated. These quantitative results would further help as a basic knowledge for the design of more efficient drug delivery systems.

2. Material and Methods

2. 1. Materials

Quinizarin (96% purity), SDS and other chemicals were purchased from Sigma Aldrich and employed as received without further purification. Experiments were performed in 0.1 M phosphate buffer (pH 7.4) and deionized water (Mili-Q water purification system) was used for the preparation of solutions. A concentrated (2mM) stock solution of quinizarin was prepared by dissolving appropriate amount of compound in methanol. Then, a small aliquot of that stock was diluted with phosphate buffer. Methanol content in the investigated solutions was always below 1%. The solutions were kept in the dark due to quinone moiety being sensitive to light.

2. 2. Apparatus and Methods

Spectrophotometric measurements were made on a JASCO V-630 spectrophotometer equipped with a Peltier-controlled ETCR-762 model accessory (JASCO Corporation, Tokyo, Japan) using a matched pair of quartz cuvettes with a path length of 1 cm. The absorption spectra of pure quinizarin in 0.1 M phosphate buffer (pH 7.4) and in the presence of different concentrations of SDS have been recorded in the temperature range of 293.15–323.15 K with an increment of 10 K interval, in the wavelength range of 350–700 nm. The absorption titration experiments were performed by successive additions of concentrated surfactant stock solution directly into a cuvette containing 2 ml of quinizarin solution. After addition of surfactant aliquots, the mixtures were gentle shaken and the absorption spectra were registered after 3 minutes of equilibration.

Specific conductivities were measured with Consort K912 conductivity meter (Parklaan 36, B-2300 Turnhout, Belgium). This instrument has auto ranging from 0 to 1000 mS/cm and conductivity control with accuracy of ±0.5%. The electrodes used have a cell constant of 0.98 cm^{-1}. The conductivity runs were carried out by gradually adding small amounts (20 μl) of a concentrated solution of SDS into 0.1 M phosphate buffer (pH 7.4), in the absence and the presence of quinizarin.

3. Results and Discussion

3. 1. Absorption Spectral Characteristics of Quinizarin in the Presence of SDS

The absorption spectra of quinizarin in the absence and in the presence of various concentrations of SDS in 0.1 M phosphate buffer (pH 7.4) at 293.15 K and 313.15 K are given in Fig. 2. The pK_a values of quinizarin are reported to be $pK_1 = 10.15$ and $pK_2 = 13.19$, therefore quinizarin can exist in neutral, monodeprotonated and dideprotonated forms as a function of pH. Also, the deprotonation produces significant changes in the visible absorption spectrum of quinizarin.[27] At pH 7.4, quinizarin exists in neutral form and the visible absorption spectrum shows a broad absorption maximum at ~ 470 nm and a shoulder at about 520 nm. It can be seen from Fig. 2 that the absorption

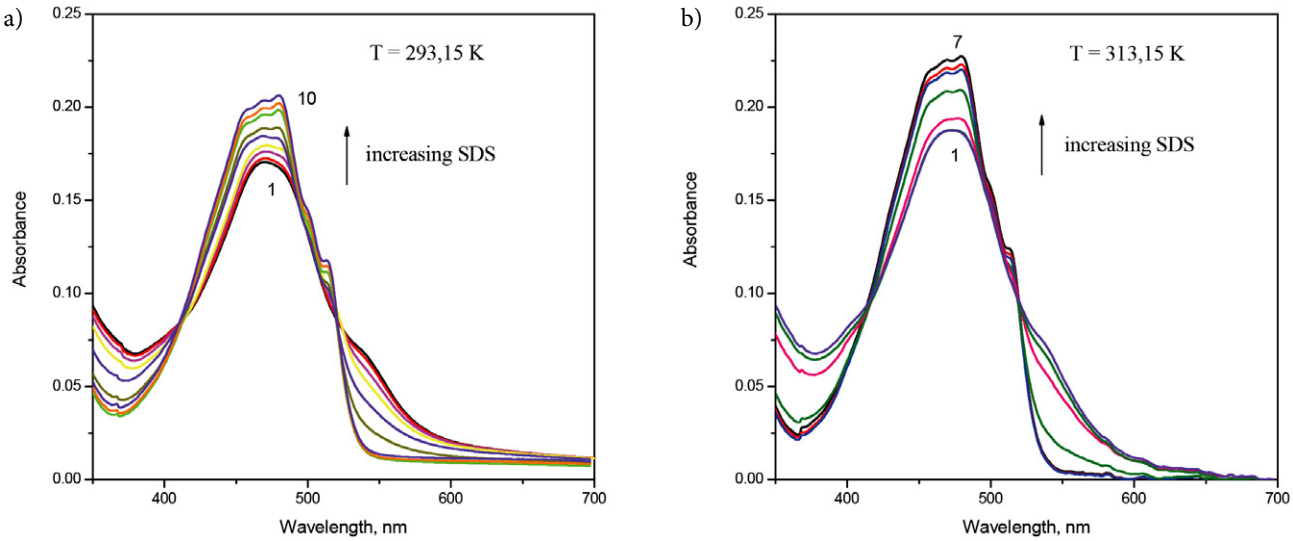

Figure 2. Absorption spectra of 1.80×10^{-5} M quinizarin in 0.1 M phosphate buffer (pH 7.4) in the absence (spectrum 1) and in the presence of increasing amounts of SDS: (a) T = 293.15 K; (b) T = 313.15 K.

maximum of quinizarin increases as the SDS concentration enhances. Moreover, with increasing SDS concentrations the absorption maximum is split in three peaks, a new peak appeared around 515 nm and the shoulder at about 535 nm disappeared. Also, the addition of SDS yields two isobestic points at 416 nm and 524 nm. These spectral changes clearly suggest the occurrence of interaction between quinizarin and SDS micelles and the gradual incorporation of quinizarin molecule in SDS micelles. Also, the environment around quinizarin molecules in surfactant micelles is different from bulk aqueous solution as the absorption maxima are red shifted (for about 10 nm).

The effect of temperature on the absorption spectra of quinizarin alone and in the presence of SDS micelles is shown in Fig. 3. As seen from Fig. 3(a), the absorbance value of quinizarin increases with increasing temperature from 298.15 K to 323.15 K and the absorption maximum is red shifted. In the presence of SDS micelles, the shape of the absorption spectrum is similar for all investigated temperature and the absorption maximum (483 nm) decreases with increasing temperature (Fig. 3(b)).

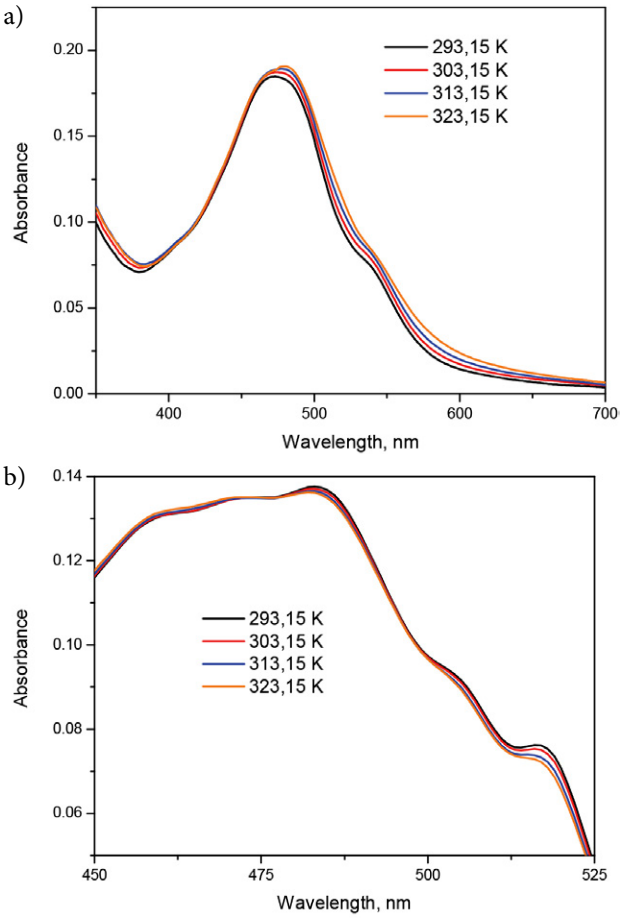

Figure 3. The influence of temperature on: (a) the absorption spectrum of quinizarin and (b) the absorption spectrum of quinizarin incorporated in SDS micelles.

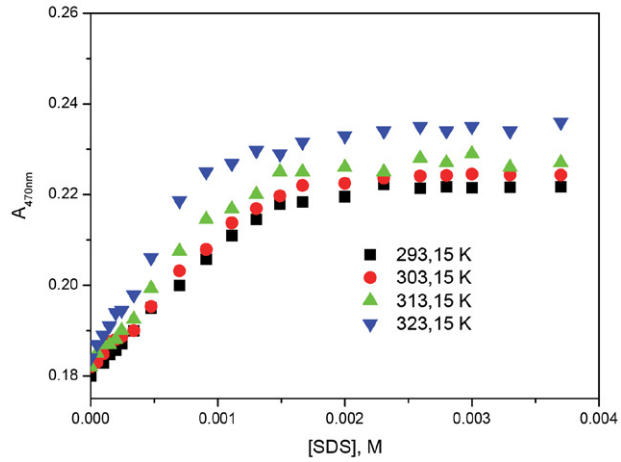

Figure 4. The variation of absorbance with SDS concentration at different temperatures.

The absorbance of quinizarin in the presence of SDS increases rapidly for SDS concentrations lower than CMC, while in post micellar region the absorbance increases very slowly and becomes almost constant because of the maximum incorporation of drug molecules into micelles (Fig. 4). This spectral behavior is observed for all investigated temperatures but the maximum absorbance increases as the temperature increases for the same SDS concentration.

The CMC of pure SDS in 0.1 M phosphate buffer (pH 7.4) at 293.15 K was determined from conductivity measurements (see Conductivity studies paragraph) and it is 9.28×10^{-4} M. This value is smaller than the CMC of SDS in water (8.08×10^{-3} M) and is an agreement with literature data, which indicate that the CMC value decreases in phosphate buffer as the concentration of electrolyte increases (from 6.09×10^{-3} M in 5 mM electrolyte concentration to 1.99×10^{-3} M in 50 mM electrolyte concentration).[28]

3. 2. Determination of Binding Constant

The quantification of the degree of the interaction of quinizarin with SDS micelles was made by determination of the binding constant (K_b) and micelle-water partition coefficient (K_x) at different temperatures. These parameters were determined from the absorbance values at 470 nm of series of solutions containing a fixed quinizarin concentration and increasing surfactant concentrations.

The binding constant (K_b) was estimated from the Benesi-Hildebrand equation:[29,30]

$$\frac{1}{A - A_0} = \frac{1}{K_b (A_1 - A_0)[SDS]_m} + \frac{1}{A_1 - A_0} \quad (1)$$

where $[SDS]_m$ is the concentration of the micellized SDS ($[SDS]_m = [SDS] - CMC$), A_0, A, A_{max} are the absorbance in the absence of, at intermediate concentration, and at high concentration of SDS, respectively. The plot of $1/(A - A_0)$ vs. $1/[SDS]$ gives straight lines for all investigated temperatures (Fig. 5), which further indicates the formation of a 1:1 complex between quinizarin and SDS micelles. The values of the binding constant obtained from the ratio of the intercept to the slope of the Benesi–Hildebrand plots (Fig. 5) are presented in Table 1. It can be observed that the binding constant increases with increasing temperatures.

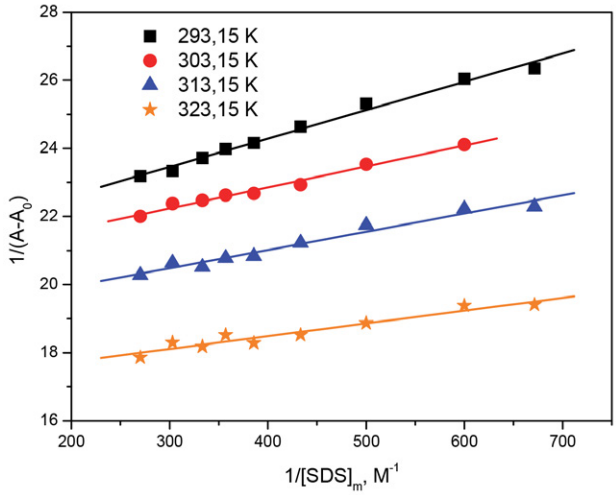

Figure 5. Plot of $1/(A-A_0)$ versus $1/[SDS]_m$ for the interaction of quinizarin with SDS micelles at various temperatures.

Comparing the values of the binding constants at 293.15 K for the interaction of quinizarin with SDS micelles with those for the interaction of mitoxantrone[25,31] or epirubicin[21] with SDS micelles, it is clear that the interaction of quinizarin with SDS micelles is stronger than the interaction of mitoxantrone or epirubicin with SDS micelles. Mitoxantrone is a synthetic anthracenedione anticancer drug, which at pH 7.4 exists as di-cation with two positive charges on the nitrogen atoms from the side chains, while epirubicin has one positive charge localized at protonated amino nitrogen on the sugar moiety. In spite of positive charges of mitoxantrone and epirubicin and electrostatic attractions for negatively charged SDS micelles, these drugs exhibit smaller binding constants than neutral quinizarin. A possible explanation for the stronger interaction of quinizarin with SDS micelles than that of mitoxantrone or epirubicin could be the smaller size of quinizarin which leads to a better accommodation of quinizarin molecules into SDS micelles. This explanation is supported by our previous results which indicate higher binding constants for the interaction of mitoxantrone with SDS micelles at pH 10 (when mitoxantrone molecule is uncharged) in comparison with pH 7.4 when mitoxantrone is positively charged.[31]

Table 1. Binding constant, partition coefficient and corresponding standard thermodynamic parameters for the interaction of quinizarin with SDS micelles.

T (K)	K_b (M^{-1})	ΔG_b^0 (kJ mol^{-1})	ΔH_b^0 (kJ mol^{-1})	ΔS_b^0 (J mol^{-1} K^{-1})	$K_x / 10^5$ (M^{-1})	ΔG_x^0 (kJ mol^{-1})	ΔH_x^0 (kJ mol^{-1})	ΔS_x^0 (J mol^{-1} K^{-1})
293.15	2524 ± 0.05	−19.08	14.34	114.00	3.44 ± 0.08	−31.06	16.84	163.40
303.15	3290 ± 0.09	−20.40		114.60	4.74 ± 0.07	−32.92		164.14
313.15	3520 ± 0.09	−21.25		113.65	5.26 ± 0.08	−34.28		163.24
323.15	4530 ± 0.08	−22.61		114.34	6.77 ± 0.09	−36.05		163.67

Based on these results, we can say that the hydrophobic interactions play a major role in the binding of quinizarin to SDS micelles. Studies performed by Das and co-workers established that the hydrophobic interaction plays a crucial role in the binding of 2-amino-3-hydroxy-anthraquinone to SDS micelles, while the hydrophilic interaction plays an important role in its interaction with CTAB micelles.[32]

3. 3. Determination of Partition Coefficient

Partition coefficient (K_x) was evaluated from the following equation, according to the pseudo-phase model:[33,34]

$$\frac{1}{\Delta A} = \frac{1}{\Delta A_\infty} + \frac{n_W}{K_x \Delta A_\infty ([SDS] + C_T - CMC)} \quad (2)$$

where $\Delta A = A - A_0$, $\Delta A_\infty = A_1 - A_0$, C_T is the total drug concentration and n_w = 55.5 M is the molarity of water. The value of K_x is obtained from the slope of the plot of $1/\Delta A$ versus $1/(C_T + [SDS] - CMC)$ as shown in Fig. 6 for different temperatures. This relation is linear for very high surfactant concentrations and the curve tends to bend upwards for decreasing surfactant concentrations.[34]

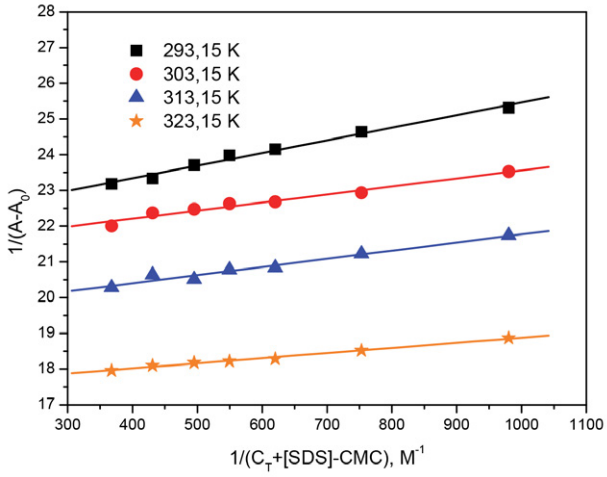

Figure 6. Plot of $1/(A-A_0)$ versus $1/(C_T + [SDS]-CMC)$ for the interaction of quinizarin with SDS micelles at various temperatures.

From Table 1 it follows that quinizarin presents large positive values of K_x indicating that quinizarin molecules prefer to move from aqueous environment to SDS micelles. Moreover, the results show that the partition coefficient increases with the increase in temperature. The values of K_x obtained for quinizarin are higher than those obtained for the distribution of mitoxantrone in SDS micelles.[31] This indicates that quinizarin molecules are partitioned in SDS micelles to much greater extent than mitoxantrone. The smaller molecular size of quinizarin molecule in comparison with mitoxantrone allows them to be accommodated in palisade layer close to the micelle surface where large space is available and can fit larger number of molecules.

3. 4. Thermodynamic Parameters for the Binding and Partition Processes

The binding and partition processes for the interaction of quinizarin with SDS micelles were characterized thermodynamically by determining the standard Gibbs free energy of interaction (ΔG_b^0) and the standard Gibbs free energy of the transfer of drug from bulk aqueous phase to micellar phase(ΔG_x^0), and the corresponding standard enthalpy (ΔH^0) and the standard entropy (ΔS^0) changes. These parameters, summarized in Table 1, were calculated from the values obtained for K_b and K_x at different temperatures from the spectral studies using the following equations:

$$\Delta G^0 = -RT\ln K \quad (3)$$

$$\Delta H^0 = \frac{\partial(\Delta G^0/T)}{\partial(1/T)} \quad (4)$$

$$\Delta S^0 = \frac{\Delta H^0 - \Delta G^0}{T} \quad (5)$$

A plot of $\Delta G^0/T$ versus 1/T yields a straight line (Fig. 7) and the slope of this line is equal to ΔH^0 according to Eq. 4.

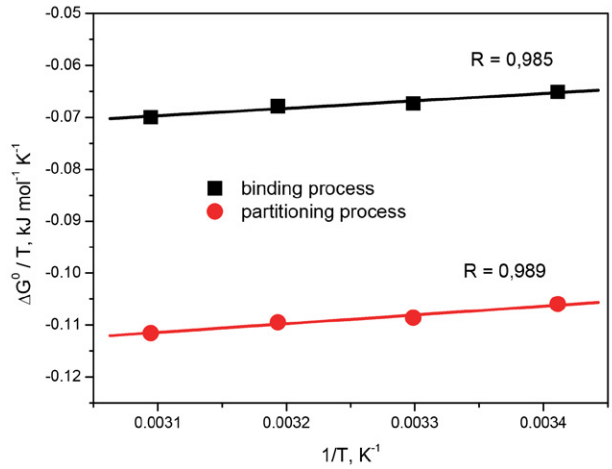

Figure 7. Plot of $\Delta G^0/T$ versus 1/T for the binding and partitioning of quinizarin to SDS micelles.

As seen in Table 1, ΔG^0 values are negative at each investigated temperature and for both binding and partition processes. These negative values of ΔG^0 indicate the spontaneity of the binding process of quinizarin to SDS micelles and the partition process of qunizarin between the micellar and the bulk aqueous phases. Besides, the ΔG^0 values become more negative with the increase in temperature for

both binding and partition processes indicating that both processes are more spontaneous at higher temperatures.

The values of ΔH^0 were found to be positive suggesting the endothermic nature of both binding and partition processes. The net ΔH^0 is the sum of the change in enthalpies resulting from hydrophobic interactions, electrostatic interactions, hydration of polar head groups, and counterion binding to micelles.[35–37] Positive values of ΔH^0 suggest that the hydrophobic interactions are the main forces involved in both binding and partitioning processes. The values of ΔS^0 are positive and constant for all investigated temperatures and for both binding and partition processes. The positive values of ΔS^0 and ΔH^0 indicate that both binding and partition processes are entropy controlled over the range of studied temperatures. The endothermic nature of both binding and partition processes accompanied with a strong favorable entropic contribution suggests dominant hydrophobic interactions.

3. 5. Conductometric Studies

The electrical conductivity measurement was used to determine CMC of SDS in the absence and the presence of quinizarin at 293.15 K. Figure 8 shows the conductance (κ) versus surfactant concentration plot obtained for SDS in the absence and in the presence of quinizarin. The values of CMC were estimated as the intersection point between the two straight lines obtained for low and high concentrations of SDS. The results are summarized in Table 2.

It can be observed that the presence of quinizarin increases the CMC of SDS in 0.1 M phosphate buffer from 9.28×10^{-4} M to 1.06×10^{-3} M. The increase of the CMC of surfactants was also reported for other different drugs or dyes and it was explained by the possibility of hydrogen bonding between hydrophilic parts of drug and water, as the localization of drug molecules is more probable in the outer portion of micelle close to micelle water interface. This kind of drug solubilization leads to decrease in entropy thus making process of micellization less convenient and increases the CMC.[20,35,38]

The degree of ionization (α) of the micelles can be estimated from the ratio of the slopes of the two straight lines above and below the CMC, when the specific conductivity is plotted versus concentration. The degree of counterion association (β) is given as $\beta = 1 - \alpha$.[39] The reported values for the degree ionization for SDS micelles in aqueous medium are in the range 0.29-0.86, depending on the experimental technique employed.[40,41] In our study, the degree of ionization of SDS is 0.23 in 0.1 M phosphate buffer (Table 2) and this value is smaller than the reported values in aqueous solution. In phosphate buffer, the salts of phosphates ionize in solution and the sodium ions tend to condense onto the micelle surface. This leads to a decrease of the ionization degree and an increase in the aggregation number and microviscosity.[42] The presence of quinizarin leads to an increase of the degree of ionization. This can be explained by the location of quinizarin in the palisade layer of the micelles leading to a steric hindrance to the binding of counterions to the micelles, facilitating the dissociation of the counterions, which yields higher degree of ionization.[43] Also, the solubilization of quinizarin in the palisade layer of SDS micelles decreases the surface charge density, facilitating the ionization of the counterions from the head groups of surfactant, and, thereby, yielding higher degree of ionization in the presence of quinizarin.[43]

Table 2. Critical micelle concentration (CMC), degree of ionization (α) and degree of counterion binding (β) for SDS in 0.1 M phosphate buffer (pH 7.4) and in the presence of 2.15×10^{-5} M quinizarin at 293.15 K.

	CMC, M	α	β
SDS	$(9.28 \pm 0.11) \times 10^{-4}$	0.230 ± 0.020	0.770 ± 0.020
SDS + quinizarin	$(1.06 \pm 0.08) \times 10^{-3}$	0.380 ± 0.016	0.620 ± 0.016

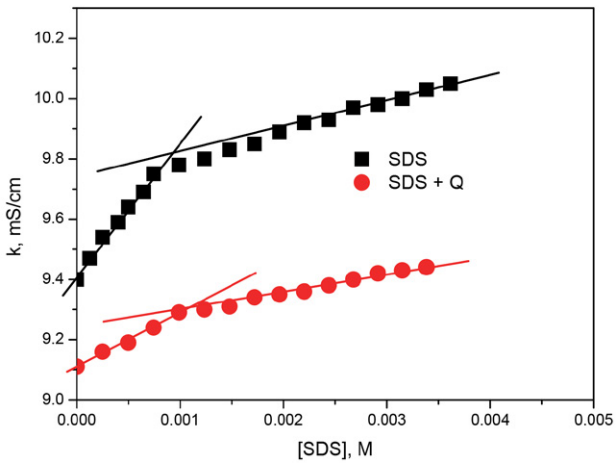

Figure 8. Plots of electrical conductivity versus SDS concentration in the absence and the presence of quinizarin at 293.15 K.

3. 6. Location of Quinizarin in SDS Micelles

Drug molecules can interact with surfactant micelles in distinct ways, depending on the hydrophobic character of drugs. They can be adsorbed on the surface of micelles (hydrophilic molecules), entrapped into the hydrocarbon core (hydrophobic molecules) showing a deep penetration) or oriented near the surface in the palisade layer displaying a short penetration.[30,44–46] The position of incor-

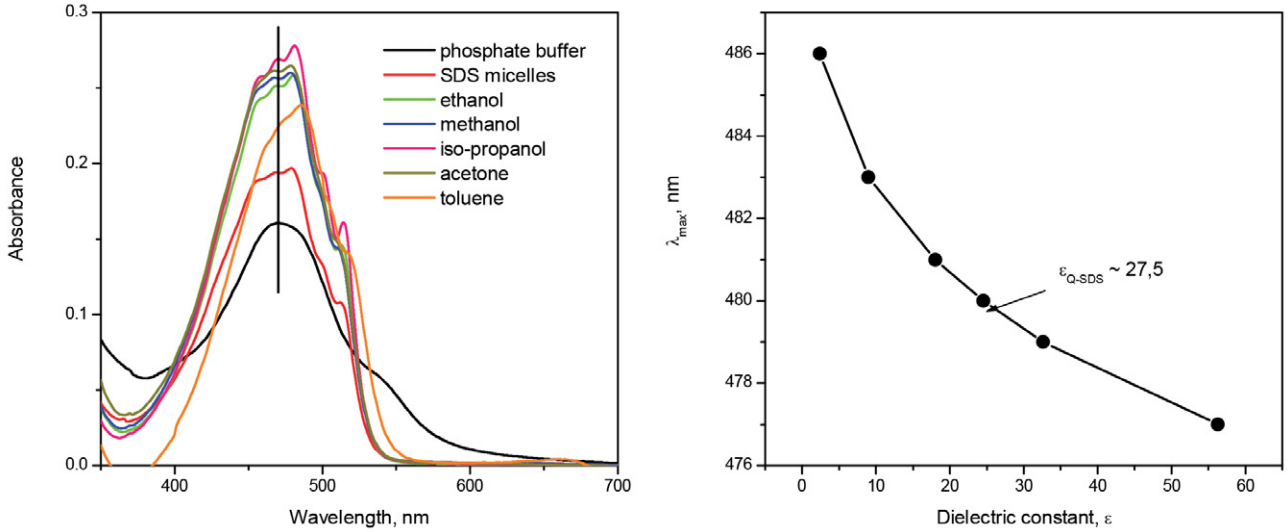

Figure 9. (a) Absorption spectra of quinizarin in different solvents and SDS micelles; (b) Absorption maxima of quinizarin in different solvents as a function of the dielectric constant.

porated molecules into micelles determines the extent of solubilization, the chemical reactivity of the solubilized molecules, and the rate of their release from the micelles and is also a measure of the strength of specific interactions between the solubilized molecules and the micelle (electrostatic or hydrophobic interactions, hydrogen bonds, etc).[47]

Information about the position of quinizarin molecule into SDS micelles was obtained indirectly by comparing the absorption spectrum of the drug in surfactant micelles with the adsorption spectra in solvents with different polarities which mimic the polarity of different parts of the micelles. The spectra of quinizarin in different solvents and SDS micelles are shown in Fig. 9a.

It can be observed that the absorption spectra of quinizarin in phosphate buffer present a maximum at 470 nm. As the polarity of the solvents decreases, the shape of quinizarin spectrum changes and new peaks and / or shoulders appears. Also, the absorption maximum is shifted to higher wavelength with the decrease of the solvents polarity (Fig. 9b). The absorption spectrum of quinizarin in SDS micelles is quite similar with the spectra in polar solvents like methanol and ethanol and different from the spectra in a non-polar solvent such as toluene. Also, the relative polarity of quinizarin molecule in SDS micelles has a value ($\varepsilon_{Q\text{-}SDS}$ ~ 27.5) characteristic for polar solvents, such as methanol and ethanol. It is well known that micelles present an increasing polarity gradient from the core to the surface of the micelles.[48] As the absorption spectrum of quinizarin in SDS micelles reproduces the characteristics of the spectra in polar solvents, we can say that quinizarin molecules are located in an aqueous microenvironment similar to methanol and ethanol. Hence, it can be deduced that quinizarin molecules are solubilized in the hydrophilic region rather than the hydrophobic region of micelles. This location in the outer portion of micelle close to micelle water interface can be explained by the structure of quinizarin molecule: a rigid, planar anthraquinone substituted by uncharged hydrophilic groups, which can be involved in hydrogen bonds with water molecules.[49,50] Studies regarding the solubilization of quinizarin in anionic, cationic, nonionic and cationic gemini surfactants indicated that the straight chain surfactants were better solubilizers than alkyl aryl surfactants, the solubilization increases with the temperature and is higher for gemini surfactants than that of DTAB and quinizarin molecules are located just below the head group region of the surfactant micelles.[49,50]

4. Conclusions

This paper presents the results regarding the interaction of quinizarin with SDS micelles using spectrophotometric and conductometric techniques. The binding constant and partition coefficient values indicate a strong interaction between quinizarin and SDS micelles. The positive values of ΔS^0 and ΔH^0 indicate that both binding and partition processes are entropy controlled over the range of studied temperatures and the hydrophobic interactions are dominant. Regarding the position of quinizarin molecule in SDS micelles, the changes of absorption spectra of quinizarin in solvents with different polarities suggest that quinizarin molecule are located in a comparatively polar environment at the outer hydrophilic region of micelles.

The anthraquinone chromophore of quinizarin is present in the structure of widely used drugs in the treatment of different types of cancers. Even if the prevailing mechanism is the interaction with DNA, these drug molecules must pass the cell and nuclear membranes before interacting with DNA. The understanding of molecular interactions between drugs and biological membranes are

important for medical research because these interactions are connected with the pharmacological activity of drugs. The present results using simple surfactant micelles as biomimetic model membranes give useful information regarding the interaction of drug molecules with biological membranes which will allow the rational design of new more efficient therapeutic agents and drug delivery systems. However, further more detailed investigations using distinct model membranes (i.e., liposomes with different lipid composition, supported lipid bilayers) are necessary for better understanding of the interaction mechanism.

5. References

1. G. Zengin, N.S. Degirmenci, L. Alpsoy, A. Aktumsek, *Hum. Exp. Toxicol.* **2016**, *35*, 544–553. **DOI:**10.1177/0960327115595687
2. S. Rossi, C. Tabolacci, A. Lentini, B. Provenzano, F. Carlomosti, S. Frezzotti, S. Beninati, *Anticancer Res.* **2010**, *30*, 445–450.
3. Agudelo D, Bourassa P, Bérubé G, Tajmir-Riahi HA, *J. Photochem. Photobiol. B* **2016**, *158*, 274–279. **DOI:**10.1016/j.jphotobiol.2016.02.032
4. G. Minotti, P. Menna, E. Salvatorelli, G. Cairo, L. Gianni, *Pharmacol. Rev.* **2004**, *56*, 185–229. **DOI:**10.1124/pr.56.2.6
5. C. Pérez-Arnaiz, N. Busto, J. M. Leal, B. Garcia, *J.* Phys. Chem. B **2014**, *118*, 1288–1295. **DOI:**10.1021/jp411429g
6. S. Agarwal, D. K. Jangir, R. Mehrotra, *J. Photochem. Photobiol. B* **2013**, *120*, 177–182. **DOI:**10.1016/j.jphotobiol.2012.11.001
7. M. Enache, E. Volanschi, *Rev. Roumaine Chim.* **2005**, *50*, 131–140.
8. J. Bhattacharyya, A. Basu, G. S. Kumar, *J. Chem. Thermodynamics* **2014**, *75*, 45–51. **DOI:**10.1016/j.jct.2014.04.015
9. P. S. Guin, S. Das, P. C. Mandal, *J. Solution Chem.* **2011**, *40*, 492–501. **DOI:**10.1007/s10953-011-9654-x
10. M. B. Gholivand, S. Kashanian, H. Peyman, H. Roshanfekr, *Eur. J. Med. Chem.* **2011**, *46*, 2630–2638. **DOI:**10.1016/j.ejmech.2011.03.034
11. V. Verebova, J. Adamcik, P. Danko, D. Podhradsky, P. Mišk-ovsky, J. Stanicova, *Biochem. Biophys. Res. Commun.* **2014**, *444*, 50–55. **DOI:**10.1016/j.bbrc.2014.01.007
12. P. Das, D. Bhattacharya, P. Karmakar, S. Das, *RSC Adv.* **2015**, *5*, 73099–73111. **DOI:**10.1039/C5RA07805A
13. C. Batchelor-McAuley, I. B. Dimov, L. Aldous, R. G. Compton, *Proc. Natl. Acad. Sci. U.S.A* **2011**, *108*, 19891–19895. **DOI:**10.1073/pnas.1113615108
14. M. Enache, C. Bendic, E. Volanschi, *Bioelectrochemistry* **2008**, *72*, 10–20. **DOI:**10.1016/j.bioelechem.2007.10.001
15. M. A. G. Trindade, U. Bilibio, M. V. B. Zanoni, *Fuel* **2014**, *136*, 201–207. **DOI:**10.1016/j.fuel.2014.07.044
16. C. Bourgaux, P. Couvreur, *J. Control. Release* **2014**, *190*, 127–138. **DOI:**10.1016/j.jconrel.2014.05.012
17. M.-T. Dimanche-Boitrel, O. Meurette, A. Rebillard, S. Lacour, *Drug Resist. Updat.* **2005**, *8*, 5–14. **DOI:**10.1016/j.drup.2005.02.003
18. S. Roy, P. S. Sengupta, P. S. Guin, *Chem. Phys. Lett.* **2018**, *694*, 7–13. **DOI:**10.1016/j.cplett.2018.01.029
19. A. D. Saraf, S. Sharma, S. Sachar, *Langmuir* **2018**, *34*, 14624–14632. **DOI:**10.1021/acs.langmuir.8b02814
20. T. S. Banipal, R. Kaur, P. K. Banipal, *J. Mol. Liq.* **2018**, *255*, 113–121. **DOI:**10.1016/j.molliq.2018.01.089
21. N. Erdinc¸ S. Gokturk, M. Tuncay, *J. Pharm. Sci.* **2004**, *93*, 1566–1576. **DOI:**10.1002/jps.20056
22. A. Datta, S. Roy, P. Mondal, P. S. Guin, *J. Mol. Liq.* **2016**, *219*, 1058–1064. **DOI:**10.1016/j.molliq.2016.04.049
23. O. Cudina, J. Brboric, I. Jankovic, K. Karljikovic-Rajic, S. Vladimirov, *Colloids Surf. B: Biointerfaces* **2008**, *65*, 80–84. **DOI:**10.1016/j.colsurfb.2008.03.002
24. Zahari Vinarov , V. Katev, D. Radeva, S. Tcholakova and N. D. Denkov, *Drug Dev. Ind. Pharm.* **2017**, *44*, 677–686. **DOI:**10.1080/03639045.2017.1408642
25. M. Enache, A. M. Toader, M. I. Enache, Molecules **2016**, 21, 1356. **DOI:**10.3390/molecules21101356
26. M. Enache, S. Ionescu, E. Volanschi, *J. Mol. Liq.* **2015**, *208*, 333–341. **DOI:**10.1016/j.molliq.2015.05.006
27. M. Savko, S. Kascakova, P. Gbur, P. Miskovsky, J. Ulicny, *J. Mol. Struct. THEOCHEM* **2007**, *823*, 78–86. **DOI:**10.1016/j.theochem.2007.08.032
28. E. Fuguet, C. Rafols, M. Roses, E. Bosch, *Anal. Chim. Acta* **2005**, *548*, 95–100. **DOI:**10.1016/j.aca.2005.05.069
29. H. A. Benesi, J. H. Hildebrand, *J. Am. Chem. Soc.* **1949**, *71*, 2703–2707. **DOI:**10.1021/ja01176a030
30. Y. Shiraishi, S. Sumiya, Y. Kohno, T. Hirai, *J. Org. Chem.* **2008**, *73*, 8571–8574. **DOI:**10.1021/jo8012447
31. M. Enache, A. M. Toader, *J. Surfact. Deterg.* **2018**, *21*, 31–41. **DOI:**10.1002/jsde.12014
32. A. Das, S. Roy, P. Mondal, A. Datta, K. Mahali, G. Loganathan, D. Dharumadurai, P.S. Sengupta, M.A. Akbarsha, P.S. Guin, *RSC Adv.* **2016**, *6*, 28200–28212. **DOI:**10.1039/C6RA00062B
33. L. Sepulveda, E. Lissi, F. Quina, *Adv. Colloid Int. Sci.* **1986**, *25*, 1–57. **DOI:**10.1016/0001-8686(86)80001-X
34. H. Kawamura, M. Manabe, Y. Miyamoto, Y. Fujita, S. Tokunaga, *J. Phys. Chem.* **1989**, *93*, 5536–5540. **DOI:**10.1021/j100351a042
35. M. Usman, M. A. Rashid, A. Mansha, M. Siddiq, *Thermochim. Acta* **2013**, *573*, 18–24. **DOI:**10.1016/j.tca.2013.08.014
36. F. Akhtar, M. A. Hoque, M. A. Khan, *J. Chem. Thermodyn.* **2008**, *40*, 1082–1086. **DOI:**10.1016/j.jct.2008.03.001
37. M.A. Hoque, M. A. Khan, M. D. Hossain, *J. Chem. Thermodyn.* **2013**, *60*, 71–75. **DOI:**10.1016/j.jct.2013.01.001
38. M. Usman, M. Siddiq, *Spectrochim. Acta A: Mol. Biomol. Spectrosc.* **2013**, *113*, 182–190. **DOI:**10.1016/j.saa.2013.04.089
39. M. Rahman, M. A. Khan, M. A. Rubb, M. A. Hoque, *J. Mol. Liq.* **2016**, *223*, 716–724. **DOI:**10.1016/j.molliq.2016.08.049
40. A. D. Mudawadkar, T. J. Patil, *Chem. Sci. Trans.* **2016**, *5*, 149–162.
41. T. Sasaki, H. Michihiro, S. Jun, N. Kenji, *Bull. Chem. Soc. Jpn.* **1975**, *48*, 1397–1403. **DOI:**10.1246/bcsj.48.1397
42. M. A. Bahri, M. Hoebeke, A. Grammenosb, L. Delanaye, N.

Vandewalle, A. Seret, *Colloids Surf. A Physicochem. Eng. Asp.* **2006**, *290*, 206–212. **DOI:**10.1016/j.colsurfa.2006.05.021
43. A. Ali, S. Uzair, N. A. Malik, M. Ali, *J. Mol. Liq.* **2014**, *196*, 395–403. **DOI:**10.1016/j.molliq.2014.04.013
44 C. O. Rangel-Yagui, A. Pessoa Jr., L. C. Tavares, *J. Pharm. Pharm. Sci.* **2005**, *8*, 147–165.
45. J. Oakes, P. Gratton, *Color. Technol.* **2003**, *119*, 91–99. **DOI:**10.1111/j.1478-4408.2003.tb00156.x
46. A. R. Tehrani-Bagha, K. Holmberg, *Materials* **2013**, *6*, 580–608. **DOI:**10.3390/ma6020580
47. A. Choucair, A.Eisenberg, *J. Am. Chem. Soc.* **2003**, *125*, 11993– 2000. **DOI:**10.1021/ja036667d
48 E. Blatt, K. P. Ghiggin, *J. Chem. Soc. Faraday Trans.* I **1981**, 77, 2551–2558. **DOI:**10.1039/f19817702551
49. A. R. Tehrani-Bagha, R. G. Singh, K. Holmberg, *J. Colloid Interface Sci.* **2012**, *376*, 112–118. **DOI:**10.1016/j.jcis.2012.02.016
50. A. R. Tehrani-Bagha, R. G. Singh, K. Holmberg, *Colloids Surf. A Physicochem. Eng. Asp.* **2013**, *417*, 133–139. **DOI:**10.1016/j.colsurfa.2012.10.006

Povzetek

Preiskava medsebojnega delovanja kvinizarina (Q), ki je podoben osrednji enoti različnih zdravil proti raku, in anionskih micel natrijevega dodecil sulfata (SDS), je bila izvedena z meritvami absorpcije in prevodnosti v 0,1 M fosfatnem pufru s pH 7,4 in v temperaturnem območju 293.15–323,15 K. Vrednosti vezavne konstante (K_b), porazdelitvenega koeficienta (K_x) in ustrezni termodinamični parametri (Gibbsova prosta energija, entalpija, entropija) za vezavo in porazdelitev kvinizarina med vodno raztopino in micelami površinsko aktivne snovi so bile določene in obravnavane v smislu možnih medmolekulskih interakcij. Vrednosti kritične micelne koncentracije (CMC) in stopnje ionizacije (α) za SDS v odsotnosti in prisotnosti kvinizarina so bile določene iz kondometrične študije. Primerjava absorpcijskih spektrov kvinizarina v micelah SDS s spektri v različnih topilih je pokazala, da se molekule kvinizarina nahajajo v hidrofilnem območju SDS micel. Trend sprememb Gibbsove proste energije, entalpije in entropije s temperaturo kaže, da sta oba procesa,vezava in porazdelitev, spontana in entropijsko vodena. Poleg tega so hidrofobne interakcije glavne gonilne sile, ki sodelujejo v procesih vezave in porazdeljevanja.

Except when otherwise noted, articles in this journal are published under the terms and conditions of the Creative Commons Attribution 4.0 International License

DOI: 10.17344/acsi.2019.5644 *Acta Chim. Slov.* **2020,** *67,* 638–643
creative commons

Scientific paper

N'-(2-Hydroxybenzylidene)-3-Methylbenzohydrazide and its Copper(II) Complex: Syntheses, Characterization, Crystal Structures and Biological Activity

Hui Zhao,[1,2] Xiang-Peng Tan,[1,2] Qi-An Peng,[1,2] Cong-Zhong Shi,[3] Yi-Fei Zhao[3] and Yong-Ming Cui[3,*]

[1] *School of Environmental Engineering, Wuhan Textile University, Wuhan 430073, P. R. China*

[2] *Engineering Research Center for Clean Production of Textile Dyeing and Printing, Ministry of Education, Wuhan 430200, P. R. China*

[3] *National Local Joint Engineering Laboratory for Advanced Textile Processing and Clean Production, Wuhan Textile University, Wuhan 430200, P. R. China*

** Corresponding author: E-mail: cuiym981248@163.com*

Received: 10-23-2019

Abstract

The hydrazone compound *N*'-(2-hydroxybenzylidene)-3-methylbenzohydrazide (H_2L) was prepared. With H_2L and copper acetate a new copper complex [Cu(HL)(NCS)]·CH_3OH was synthesized. Both the hydrazone and the copper complex were characterized by physico-chemical methods and single crystal X-ray diffraction techniques. The complex is a thiocyanato-coordinated copper(II) species. The Cu atom in the complex is in square planar geometry. The complex is a promising urease inhibitor.

Keywords: Hydrazone; copper complex; crystal structure; biological activity

1. Introduction

In recent years, much efforts have been focused on Schiff bases because they have a wide range of biological activities such as antibacterial,[1] antitumor,[2] anti-inflammatory[3] and cytotoxic,[4] *etc*. Some chloro, fluoro, iodo, and bromo-substituted compounds have remarkable antimicrobial activities.[5] Some hydrazones have strong urease inhibitory activities.[6] In addition, hydrazones are a kind of versatile ligands during the coordination with metal ions.[7] Vanadium complexes derived from hydrazides show interesting urease inhibitory activities.[8] You and coworkers have found that some Schiff base complexes are effective urease inhibitors,[9] and some hydrazones have various biological properties.[10] In pursuit of new urease inhibitors, in this work, a new copper(II) complex, [Cu(HL)(NCS)]·CH_3OH, derived from *N*'-(2-hydroxybenzylidene)-3- methylbenzohydrazide (H_2L, Scheme 1), was presented.

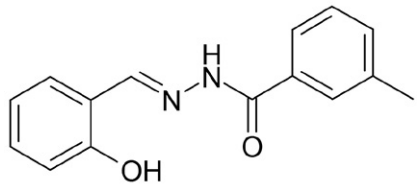

Scheme 1. H_2L

2. Experimental

2. 1. Materials and Methods

Salicylaldehyde and 3-methylbenzohydrazide were purchased from Sigma-Aldrich Co. Ltd, and were used as received. Other reagents were obtained from commercial suppliers with AR grade. Elemental analyses for C, H and N were performed on a Perkin-Elmer 240C elemental analyzer. IR spectra were recorded on a Jasco FT/IR-4000 spectrometer as KBr pellets in the 4000–400 cm^{-1} region. UV-Vis spectra were recorded on a Lambda 35 spectrometer. ^1H NMR spectrum for the hydrazone was recorded

on a Bruker 300 MHz spectrometer. Single crystal X-ray diffraction was carried out on a Bruker SMART 1000 CCD diffractometer.

2. 2. Synthesis of H_2L

Salicylaldehyde (1.22 g, 0.01 mol) and 3-methylbenzohydrazide (1.50 g, 0.01 mol) were dissolved in methanol (70 mL). The mixture was heated under reflux for 30 min, and the solvent removed under reduced pressure. The solid was re-crystallized from methanol to give colorless single crystals. Yield 2.12 g (83%). Anal. Calc. for $C_{15}H_{14}N_2O_2$: C, 70.8; H, 5.5; N, 11.0. Found: C, 71.0; H, 5.6; N, 10.9%. IR data (cm^{-1}): 3413 ν(OH), 3257 ν(NH), 3055, 2961, 2925, 2852, 1690 ν(C=O), 1612 ν(C=N), 1534, 1457, 1437, 1282, 1234, 1208, 1139, 1040, 901, 786, 752, 532, 507. UV–Vis data (methanol, λ/nm (ε/M^{-1} cm^{-1})): 205 (18,320), 235 (10,125), 286 (15,516), 300 (15,670), 325 (8,737), 387 (2,210). ^{1}H NMR (300 MHz, d^6-DMSO, ppm) δ 12.95 (s, 1H, O*H*), 8.72 (s, 1H, C*H*=N), 7.82 (d, 1H, Ar*H*), 7.76 (s, 1H, Ar*H*), 7.65–7.35 (m, 4H, Ar*H*), 7.10 (t, 1H, Ar*H*), 6.97 (d, 1H, Ar*H*), 2.31 (s, 3H, CH_3).

2. 3. Synthesis of $[Cu(HL)(NCS)]\cdot CH_3OH$

H_2L (1.0 mmol, 0.25 g), $Cu(CH_3COO)_2\cdot H_2O$ (1.0 mmol, 0.20 g) and NH_4NCS (1.0 mmol, 0.076 g) were dissolved in methanol. The mixture was stirred for 30 min at room temperature and filtered. The filtrate was kept in air for a few days, to form deep blue single crystals. Yield: 157 mg (39%). Anal. Calc. for $C_{17}H_{17}CuN_3O_3S$: C, 50.2; H, 4.2; N, 10.3. Found: C, 50.0; H, 4.3; N, 10.5%. IR data (KBr, cm^{-1}): 3370 ν(NH), 2027 ν(NCS), 1648 ν(C=O), 1610 ν(C=N), 1434, 1386, 1363, 1160, 1072, 950, 860, 701, 682, 620, 546, 523, 466. UV–Vis data (methanol, λ/nm (ε/L mol^{-1} cm^{-1})): 269 (13,770), 290 (15,382), 310 (14,710), 323 (11,620), 390 (12,325). Λ_M (10^{-3} mol L^{-1} in methanol): 35 Ω^{-1} cm^2 mol^{-1}.

2. 4. X-ray Crystallography

Diffraction intensities for the compounds were collected at 298(2) K with MoKα radiation (λ = 0.71073 Å). The collected data were reduced with SAINT,[11] and multi-scan absorption correction was performed with SADABS.[12] Structures of the hydrazone and the copper complex were solved by direct methods and refined against F^2 by full-matrix least-squares method with SHELXTL.[13] All of the non-hydrogen atoms were refined anisotropically. The amino H atoms in H_2L and the complex were located from difference Fourier maps and refined isotropically. The N–H distances are restrained to 0.90(1) Å, and the remaining hydrogens were placed in calculated positions and constrained to ride on their parent atoms. Crystallographic data for the hydrazone and the copper complex are summarized in Table 1.

Table 1. Crystal data for H_2L and the copper complex

	H_2L	**the copper complex**
Formula	$C_{15}H_{14}N_2O_2$	$C_{17}H_{17}CuN_3O_3S$
FW	254.28	406.94
Crystal system	Orthorhombic	Orthorhombic
Space group	$Pna2_1$	$P2_12_12_1$
a (Å)	22.1876(18)	5.7269(15)
b (Å)	5.0760(13)	13.087(2)
c (Å)	11.0325(19)	23.720(2)
V (Å^3)	1242.5(4)	1777.8(6)
Z	4	4
l (MoKa) (Å)	0.71073	0.71073
m (Mo*K*a) (cm^{-1})	0.092	1.367
Reflections/parameters	6791/177	9105/232
Unique reflections	2119	3211
Observed reflections [I ³ 2s(I)]	1789	2940
Restraints	2	1
Goodness of fit on F^2	1.033	1.046
R_1, wR_2 [I ³ 2s(I)]	0.0462, 0.1054	0.0274, 0.0649
R_1, wR_2 (all data)	0.0578, 0.1148	0.0321, 0.0667

3. Results and Discussion

3. 1. Chemistry

The hydrazone compound *N*'-(2-hydroxybenzylidene)-3-methylbenzohydrazide was obtained by the reaction of 1:1 molar ratio of salicylaldehyde and 3-methylbenzohydrazide in methanol solution. The copper complex was obtained by the reaction of 1:1:1 molar ratio of H_2L, copper acetate and ammonium thiocyanate in methanol solution. The complex in methanol is of non-electrolytic nature, as evidenced by low molar conductivity value.[14]

3. 2. Structure Description of the Hydrazone H_2L

The molecular structure of the hydrazone H_2L is shown in Fig. 1. Selected bond lengths and angles are given in Table 2. The molecule is in an *E* configuration about the methylidene group. The methylidene bond, with the distance of 1.278(4) Å, indicates a definitely double bond. In the –C(O)–NH– group, the C–N bond is shorter and the C=O bond is longer than usual, which is caused by the conjugation character in the hydrazone molecule. All the bond distances of the compound are within normal ranges.[10c] The two benzene rings form a dihedral angle of 28.7(5)°. In the crystal structure, the hydrazone molecules are linked *via* C–H···O and N–H···O hydrogen bonds (Table 3), to form two-dimensional layers along the *bc* plane (Fig. 2).

Table 2. Selected bond lengths (Å) and angles (°) for H_2L and the copper complex

H_2L			
C7–N1	1.278(4)	N1–N2	1.376(3)
N2–C8	1.364(4)	C8–O2	1.2219(3)
Complex			
Cu1–O1	1.0996(16)	Cu1–O2	1.9955(17)
Cu1–N1	1.921(2)	Cu1–N3	1.921(3)
O1–Cu1–N3	93.00(9)	O1–Cu1–N1	91.07(8)
N3–Cu1–N1	168.67(10)	O1–Cu1–O2	167.02(8)
N3–Cu1–O2	93.47(9)	N1–Cu1–O2	80.58(8)

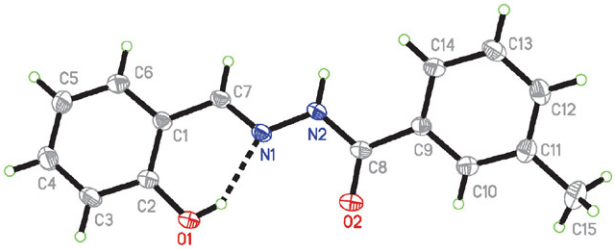

Fig. 1. Molecular structure of the hydrazone H_2L. Displacement ellipsoids for non-hydrogen atoms are drawn at the 30% probability level.

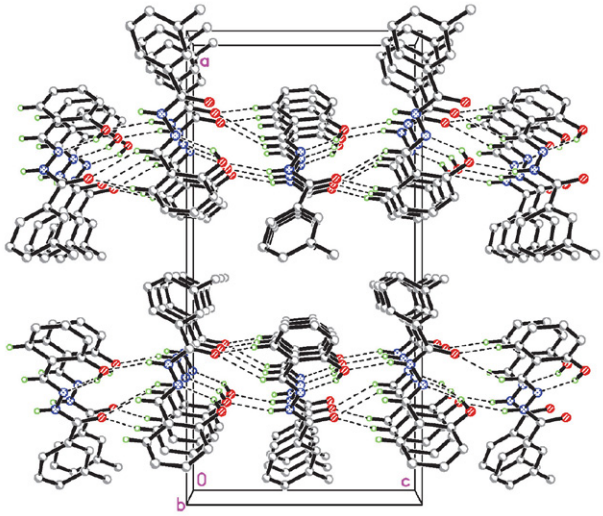

Fig. 2. Molecular packing structure of the hydrazone H_2L, viewed along the *b* axis. Hydrogen bonds are shown as dashed lines.

3. 3. Structure Description of the Copper Complex

The molecular structure of the copper complex is shown in Fig. 3. The asymmetric unit contains a [Cu(HL)(NCS)] complex molecule and a methanol molecule. The complex is linked to the methanol solvate molecule through N2–H2···O4 hydrogen bond (Table 3). The Cu atom is in a square planar geometry. The four donor atoms come from the phenolate O, imino N and carbonyl O atoms of the hydrazone ligand, and the thiocyanate N atom. The Cu atom deviates by 0.175(2) Å from the least squares plane defined by the donor atoms. The Cu–O bond lengths of 1.90-2.00 Å and Cu–N bond lengths of 1.92 Å are similar to the copper(II) complexes with square planar geometry.[9b] The *cis* and *trans* bond angles of the Cu atom in the basal plane are 80.58(8)–93.47(9)° and 167.02(8)–168.67(10)°, respectively. The two benzene rings of the hydrazone ligand form a dihedral angle of 6.2(5)°.

In the crystal structure, the complex molecules are linked by methanol molecules through O–H···O and N–H···O hydrogen bonds (Table 3), to form one-dimensional chains along the *b* axis (Fig. 4).

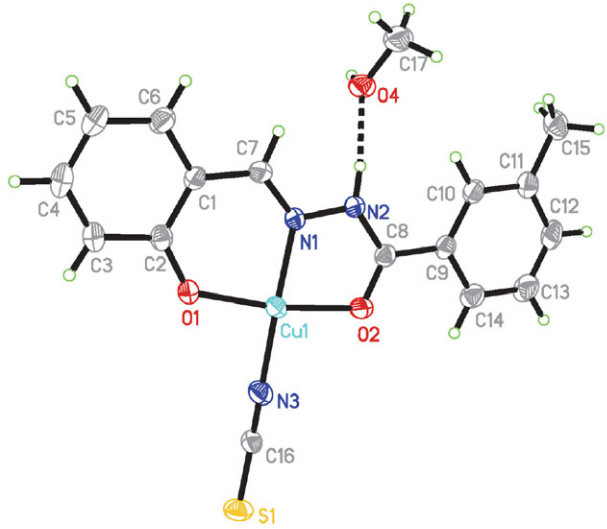

Fig. 3. Molecular structure of the copper complex. Displacement ellipsoids for non-hydrogen atoms are drawn at the 30% probability level.

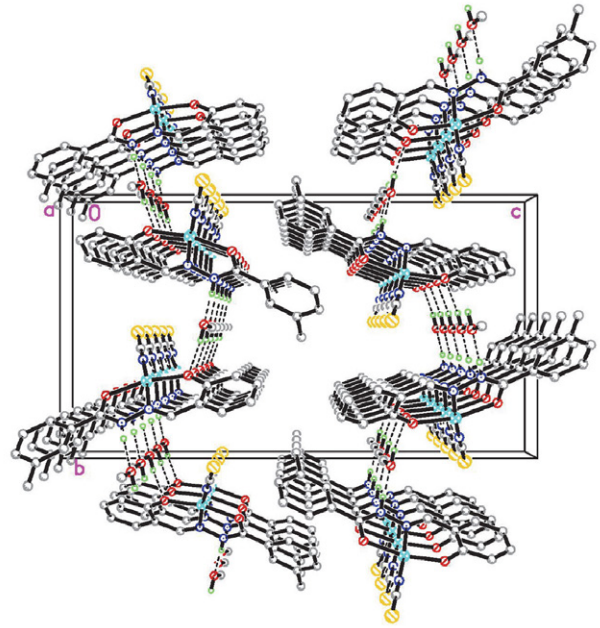

Fig. 4. Molecular packing structure of the copper complex, viewed along the *a* axis. Hydrogen bonds are shown as dashed lines.

Table 3. Hydrogen bond distances (Å) and bond angles (°) for H_2L and the complex

D–H···*A*	*d*(*D*–H)	*d*(H···*A*)	*d*(*D*···*A*)	Angle (*D*–H···*A*)
H_2L				
O1–H1···N1	0.82	1.88	2.597(3)	146(4)
N2–H2···O1^{i}	0.90(1)	2.16(2)	3.032(3)	164(4)
C6–H6···O2^{ii}	0.93	2.38	3.216(3)	150(4)
C7–H7···O2^{ii}	0.93	2.53	3.327(3)	143(4)
Complex				
O4–H4···O1^{iii}	0.82	1.90	2.719(3)	173(3)
N2–H2···O4	0.90(1)	1.80(1)	2.690(3)	173(3)

Symmetry codes: i: ½ – *x*, –½ + *y*, –½ + *z*; ii: ½ – *x*, ½ + *y*, –½ + *z*; iii: – *x*, –½ + *y*, 3/2 – *z*.

3. 4. IR and UV-Vis Spectra

The weak absorption centered at 3413 cm^{-1} in the IR spectrum of the hydrazone is attributed to the phenol group. The sharp bands observed at 3257 and 3370 cm^{-1} for H_2L and the complex, respectively, are due to the N–H vibrations. The intense absorptions at 1690 cm^{-1} for H_2L and 1648 cm^{-1} for the copper complex are due to the carbonyl groups.[16] The typical absorption for the azomethine groups, C=N, are located at 1612–1610 cm^{-1}.[15b] The strong band at 2027 cm^{-1} for the copper complex is assigned to the NCS ligand.[15b]

In the electronic spectra of H_2L and the copper complex, the bands centered at 260-290 nm are assigned to the intra-ligand π–π^* transition of the aromatic groups. The charge transfer LMCT band of the copper complex is located at 390 nm. The complex has weak *d-d* electronic transition centered at 640 nm, which is assigned to $^2E_{g(D)} \rightarrow {}^2T_{2g(D)}$.[17]

3. 5. Biological Activity

The assay of the urease inhibitory activity was carried out according to the literature method.[18] The urease inhibitory activity of the hydrazone and the copper complex is given in Table 4. The hydrazone has obvious weak activity on the urease. While the copper complex has remarkable activity (IC_{50} = 2.8 μmol L^{-1}). Inorganic copper salts are known urease inhibitors. Copper perchlorate was used as a reference with IC_{50} value of 8.5 μmol L^{-1}, which is higher than the copper complex. Acetohydroxamic acid is a commercial urease inhibitor, which was used as a reference with IC_{50} value of 28.1 μmol L^{-1}. The urease inhibitory activity of the copper complex is similar to the bromido- and thiocyanato-coordinated copper complexes with pyridine based hydrazone ligands, and stronger than the other copper complex with the above mentioned hydrazone ligand.[19] In general, the copper complexes have much better activity than the complexes with other metals.[9a,10a,10b] Thus, the present copper complex is a promising urease inhibitor.

Table 4. Inhibition of urease by the tested materials

Tested materials	Inhibition rate (%)[a]	IC_{50} (μmol L^{-1})
H_2L	8.3 ± 1.6	> 100
the copper complex	89.8 ± 2.7	2.8 ± 1.3
Copper perchlorate	70.2 ± 3.3	8.5 ± 1.7
Acetohydroxamic acid	85.5 ± 3.9	28.1 ± 3.6

[a] The concentration of the tested material is 100 μmol L^{-1}.

4. Conclusion

A new hydrazone *N*'-(2-hydroxybenzylidene)-3-methylbenzohydrazide was prepared and structurally characterized. With the hydrazone compound, a new copper(II) complex was synthesized and characterized. Single crystal structures of the hydrazone compound and the oxidovanadium(V) complex were determined. The hydrazone compound coordinate to the Cu atom through the NOO donor set. The complex is a thiocyanato-coordinated copper(II) species. The Cu atom in the complex is in square planar geometry. The complex shows remarkable urease inhibitory activity.

5. Supplementary Data

CCDC 1887945 for H_2L, and 1445986 for the copper complex contain the supplementary crystallographic data for this paper. These data can be obtained free of charge *via* http://www.ccdc.cam.ac.uk/conts/retrieving.html, or from the Cambridge Crystallographic Data Centre, 12 Union Road, Cambridge CB2 1EZ, UK; fax: (+44) 1223-336-033; or e-mail: deposit@ccdc.cam.ac.uk.

Acknowledgments

This work was supported by the Science and Technology Research Project of Hubei Provincial Department of Education (Project No. B2018061), the Hubei Provincial University Teaching Team "Environmental Control and Energy Resource Utilization Teaching Team" (Project No. 109), and the Environmental Engineering and Science Major Course Teaching Team of Wuhan Textile University (Project No. B2018061).

6. References

1. (a) M. V. Angelusiu, S. F. Barbuceanu, C. Draghici, G. L. Almajan, *Eur. J. Med. Chem.* **2010**, *45*, 2055–2062; **DOI:**10.1016/j.ejmech.2010.01.033
(b) H. Y. Qian, *Russ. J. Coord. Chem.* **2018**, *44*, 32–38; **DOI:**10.1134/S1070328418010074
(c) O. O. Ajani, C. A. Obafemi, O. C. Nwinyi, D. A. Akinpelu, *Bioorg. Med. Chem.* **2010**, *18*, 214–221; **DOI:**10.1016/j.bmc.2009.10.064

(d) H. Y. Qian, *Transit. Met. Chem.* **2019**, *44*, 501–506; **DOI:**10.1007/s11243-018-00296-x
(e) H.-Y. Qian, *Acta Chim. Slov.* **2019**, *66*, 995–1001; **DOI:**10.4149/neo_2019_190112N36
(f) Y. Tan, *Acta Chim. Slov.* **2019**, *66*, 1002–1009; **DOI:**10.17344/acsi.2019.5297
(g) L.-H. Wang, X.-Y. Qiu, S.-J. Liu, *Acta Chim. Slov.* **2019**, *66*, 675–680. **DOI:**10.17344/acsi.2019.5117

2. (a) Y. H. Zhang, L. Zhang, L. Liu, J. X. Guo, D. L. Wu, G. C. Xu, X. H. Wang, D. Z. Jia, *Inorg. Chim. Acta* **2010**, *363*, 289–293; **DOI:**10.1016/j.ica.2009.08.017
(b) T. Horiuchi, J. Chiba, K. Uoto, T. Soga, *Bioorg. Med. Chem. Lett.* **2009**, *19*, 305–308. **DOI:**10.1016/j.bmcl.2008.11.090

3. (a) M. A. A. El-Sayed, N. I. Abdel-Aziz, A. A. M. Abdel-Aziz, A. S. El-Azab, Y. A. Asiri, K. E. H. ElTahir, *Bioorg. Med. Chem.* **2011**, *19*, 3416–3424; **DOI:**10.1016/j.bmc.2011.04.027
(b) S. M. Sondhi, M. Dinodia, A. Kumar, *Bioorg. Med. Chem.* **2006**, *14*, 4657–4663. **DOI:**10.1016/j.bmc.2006.02.014

4. (a) P. Krishnamoorthy, P. Sathyadevi, A. H. Cowley, R. R. Butorac, N. Dharmaraj, *Eur. J. Med. Chem.* **2011**, *46*, 3376–3387; **DOI:**10.1016/j.ejmech.2011.05.001
(b) P. G. Avaji, C. H. V. Kumar, S. A. Patil, K. N. Shivananda, C. Nagaraju, *Eur. J. Med. Chem.* **2009**, *44*, 3552–3559. **DOI:**10.1016/j.ejmech.2009.03.032

5. (a) N. P. Rai, V. K. Narayanaswamy, T. Govender, B. K. Manuprasad, S. Shashikanth, P. N. Arunachalam, *Eur. J. Med. Chem.* **2010**, *45*, 2677–2682; **DOI:**10.1016/j.ejmech.2010.02.021
(b) N. P. Rai, V. K. Narayanaswamy, S. Shashikanth, P. N. Arunachalam, *Eur. J. Med. Chem.* **2009**, *44*, 4522–4527;
(c) H. Y. Qian, *Inorg. Nano-Met. Chem.* **2018**, *48*, 615–619. **DOI:**10.1080/24701556.2019.1567542

6. (a) K. M. Khan, F. Rahim, A. Khan, S. Ali, M. Taha, S. M. Saad, M. Khan, Najeebullah, A. Shaikh, S. Perveen, M. I. Choudhary, *J. Chem. Soc. Pak.* **2015**, *37*, 479–483;
(b) E.-C. Liu, W. Li, X.-S. Cheng, *Acta Chim. Slov.* **2019**, *66*, 971–977.

7. (a) S. P. Dash, S. Roy, M. Mohanty, M. Fernanda, N. N. Carvalho, M. L. Kuznetsov, J. C. Pessoa, A. Kumar, Y. P. Patil, A. Crochet, R. Dinda, *Inorg. Chem.* **2016**, *55*, 8407–8421; **DOI:**10.1021/acs.inorgchem.6b01001
(b) M. Sutradhar, E. C. B. A. Alegria, K. T. Mahmudov, M. Fatima, C. Guedes da Silva, A. J. L. Pombeiro, *RSC Advances* **2016**, *6*, 8079–8088; **DOI:**10.1039/C5RA25774C
(c) S. Anbu, R. Ravishankaran, M. Fatima, C. Guedes da Silva, A. A. Karande, A. J. L. Pombeiro, *Inorg. Chem.* **2014**, *53*, 6655–6664; **DOI:**10.1021/ic500313m
(d) H. Y. Qian, *Inorg. Nano-Met. Chem.* **2018**, *48*, 461–466; **DOI:**10.1080/24701556.2019.1569689
(e) H. Y. Qian, *Russ. J. Coord. Chem.* **2017**, *43*, 780–786. **DOI:**10.1134/S1070328417110070

8. R. Ara, U. Ashiq, M. Mahroof-Tahir, Z. T. Maqsood, K. M. Khan, M. A. Lodhi, M. I. Choudhary, *Chem. Biodiversity* **2007**, *4*, 58–71. **DOI:**10.1002/cbdv.200790007

9. (a) Y. T. Li, J. W. Dong, Y. Lu, Y. T. Gu, C. N. Shang, F. Y. Liu, Y. Xin, C. L. Jing, Z. L. You, *Chinese J. Inorg. Chem.* **2018**, *34*, 1192–1198;
(b) L. Pan, C. Wang, K. Yan, K. Zhao, G. Sheng, H. Zhu, X. Zhao, D. Qu, F. Niu, Z. You, *J. Inorg. Biochem.* **2016**, *159*, 22–28; **DOI:**10.1016/j.jinorgbio.2016.02.017
(c) Z. You, M. Liu, C. Wang, G. Sheng, X. Zhao, D. Qu, F. Niu, *RSC Advances* **2016**, *6*, 16679–16690; **DOI:**10.1039/C6RA00500D
(d) K. Cheng, Z. L. You, H. L. Zhu, *Aust. J. Chem.* **2007**, *60*, 375–379; **DOI:**10.1071/CH06479
(e) Z. L. You, P. Zhou, *Inorg. Chem. Commun.* **2007**, *10*, 1273–1275. **DOI:**10.1016/j.inoche.2007.08.007

10. (a) X. S. Cheng, J. C. Zhang, Z. L. You, X. Wang, H. H. Li, *Transition Met. Chem.* **2014**, *39*, 291–297; **DOI:**10.1007/s11243-014-9802-4
(b) D. Qu, F. Niu, X. L. Zhao, K. X. Yan, Y. T. Ye, J. Wang, M. Zhang, Z. You, *Bioorg. Med. Chem.* **2015**, *23*, 1944–1949; **DOI:**10.1016/j.bmc.2015.03.036
(c) M. Zhang, D. M. Xian, H. H. Li, J. C. Zhang, Z. L. You, *Aust. J. Chem.* **2012**, *65*, 343–350. **DOI:**10.1071/CH11424

11. Bruker, SMART (Version 5.628) and SAINT (Version 6.02); Bruker AXS: Madison, Wisconsin, USA, 1998.

12. G. M. Sheldrick, SADABS Program for Empirical Absorption Correction of Area Detector; University of Göttingen, Germany, 1996.

13. G. M. Sheldrick, *Acta Crystallogr.* **2008**, *A64*, 112–122. **DOI:**10.1107/S0108767307043930

14. W. J. Geary, *Coord. Chem. Rev.* **1971**, *7*, 81–122. **DOI:**10.1016/S0010-8545(00)80009-0

15. (a) D. S. Badiger, R. S. Hunoor, B. R. Patil, R. S. Vadavi, C. V. Mangannavar, I. S. Muchchandi, Y. P. Patil, M. Nethaji, K. B. Gudasi, *Inorg. Chim. Acta* **2012**, *384*, 197–203; **DOI:**10.1016/j.ica.2011.11.063
(b) J. Wang, D. Qu, J. X. Lei, Z. L. You, *J. Coord. Chem.* **2017**, *70*, 544–555. **DOI:**10.1080/00958972.2016.1262538

16. S. Guo, T. Wang, J. Xin, Q. Hu, S. Ren, G. Sheng, L. Pan, C. Zhang, K. Li, Z. You, *J. Coord. Chem.* **2017**, *70*, 3449–3458. **DOI:**10.1080/00958972.2017.1390569

17. A. A. Alhadi, S. A. Shaker, W. A. Yehye, H. M. Ali, M. A. Abdullah, *Bull. Chem. Soc. Ethiopia* **2012**, *25*, 95–101.

18. W. J. Mao, P. C. Lv, L. Shi, H. Q. Li, H. L. Zhu, *Bioorg. Med. Chem.* **2009**, *17*, 7531–7536. **DOI:**10.1016/j.bmc.2009.09.018

19. (a) Z. You, H. Yu, B. Zheng, C. Zhang, C. Lv, K. Li, L. Pan, *Inorg. Chim. Acta* **2018**, *469*, 44–50; **DOI:**10.1016/j.ica.2017.09.011
(b) Z. You, H. Yu, Z. Li, W. Zhai, Y. Jiang, A. Li, S. Guo, K. Li, C. Lv, C. Zhang, *Inorg. Chim. Acta* **2018**, *480*, 120–126. **DOI:**10.1016/j.ica.2018.05.020

Povzetek

Sintetizirali smo hidrazon *N*'-(2-hidroksibenziliden)-3-metilbenzohidrazid (H_2L). Z H_2L in bakrovim acetatom smo sintetizirali nov bakrov kompleks [Cu(HL)(NCS)]·CH_3OH. Hidrazon in bakrov kompleks smo okarakterizirali s fiziko-kemijskimi metodami in monokristalno rentgensko difrakcijo. Kompleks je bakrova(II) zvrst koordinirana s tiocianato ligandom. Cu atom ima kvadratno planarno geometrijo. Kompleks ima obetavne lastnosti kot inhibitor ureaze.

Except when otherwise noted, articles in this journal are published under the terms and conditions of the Creative Commons Attribution 4.0 International License

DOI: 10.17344/acsi.2019.5650 *Acta Chim. Slov.* **2020,** *67,* 644–650
creative commons

Scientific paper

Synthesis, X-Ray Crystal Structure of Oxidovanadium(V) Complex Derived from 4-Bromo-*N*'-(2-hydroxybenzylidene) benzohydrazide with Catalytic Epoxidation Property

Qi-An Peng,[1] Xiang-Peng Tan,[1] Yi-Di Wang,[1] Si-Huan Wang,[1] You-Xin Jiang[1] and Yong-Ming Cui[1,2,3,*]

[1] *School of Environmental Engineering, Wuhan Textile University, Wuhan 430073, P. R. China*

[2] *National Local Joint Engineering Laboratory for Advanced Textile Processing and Clean Production, Wuhan Textile University, Wuhan 430073, P. R. China*

[3] *Hubei Provincial Engineering Laboratory for Clean Production and High Value Utilization of Bio-Based Textile Materials, Wuhan Textile University, Wuhan 430073, P. R. China*

** Corresponding author: E-mail: cuiym981248@163.com*

Received: 10-28-2019

Abstract

A new oxidovanadium(V) complex, [VOL(OCH_3)(CH_3OH)], where H_2L = 4-bromo-*N*'-(2-hydroxybenzylidene)benzohydrazide, has been synthesized and fully characterized on the basis of CHN elemental analysis, FT-IR, UV-Vis, ^1H and ^{13}C NMR spectroscopy. Structures of the free hydrazone and the complex were further characterized by single crystal X-ray diffraction, which indicates that the V atom in the complex adopts octahedral coordination, and the hydrazone ligand behaves as a tridentate ligand. The catalytic epoxidation property of the complex was investigated.

Keywords: Hydrazone; oxidovanadium complex; crystal structure; catalytic epoxidation

1. Introduction

Schiff bases are a kind of interesting ligands in coordination chemistry.[1] The metal complexes with Schiff bases have attracted remarkable attention due to their facile synthesis and special biological, catalytic and industrial applications.[2] Catalytic epoxidation of olefins is an important reaction in chemistry. Many transition metal complexes are active catalysts for this process.[3] However, among the complexes, vanadium and molybdenum complexes seem more interesting because of their excellent catalytic ability in the oxidation of olefins and sulfides.[4] In this paper, a new vanadium(V) complex derived from 4-bromo-*N*'-(2-hydroxybenzylidene)benzohydrazide (H_2L, Scheme 1) was prepared and studied for its catalytic epoxidation property on cyclooctene.

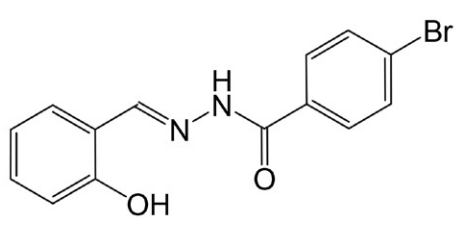

Scheme 1. The hydrazone H_2L.

2. Experimental

2. 1. Materials and Methods

4-Bromobenzohydrazide, salicylaldehyde and VO(acac)$_2$ were purchased from Alfa Aesar and used as received. Reagent grade solvents were used as received. Microanalyses of the complexes were performed with a Vario EL III CHNOS elemental analyzer. Infrared spectra were recorded as KBr pellets with an FTS-40 spectrophotometer. Electronic spectra were recorded on a Lambda 900 spectrometer. ^1H and ^{13}C NMR spectra were recorded on a Bruker spectrometer at 500 MHz. The catalytic reactions were followed by gas chromatography on an Agilent 6890A

chromatograph equipped with an FID detector and a DB5-MS capillary column (30 m × 0.32 mm, 0.25 μm). Molar conductance measurements were made by means of a Metrohm 712 conductometer in acetonitrile.

2. 2. Synthesis of 4-Bromo-*N*'-(2-Hydroxybenzylidene)benzohydrazide (H_2L)

4-Bromobenzohydrazide (10 mmol, 2.15 g) and salicylaldehyde (10 mmol, 1.22 g) were refluxed in methanol (50 mL). The reaction was continued for 1 h in oil bath during which a solid compound separated. It was filtered and washed with cold methanol. The crude product was recrystallized from methanol and dried over anhydrous $CaCl_2$. Yield: 2.36 g (74%). IR data (KBr pellet, cm^{-1}): 3445 ν(O–H), 3220 ν(N–H), 1643 ν(C=O), 1612 ν(C=N). UV-Vis data in methanol (nm): 287, 298, 327, 388. Analysis: Found: C 52.55, H 3.56, N 8.71%. Calculated for $C_{14}H_{11}BrN_2O_2$: C 52.69, H 3.47, N 8.78%. ^{1}H NMR (500 MHz, d^6-DMSO): δ 12.18 (s, 1H, O*H*), 11.22 (s, 1H, N*H*), 8.65 (s, 1H, C*H*=N), 7.90 (d, 2H, Ar*H*), 7.78 (d, 2H, Ar*H*), 7.57 (d, 1H, Ar*H*), 7.33 (t, 1H, Ar*H*), 6.93 (t, 2H, Ar*H*). ^{13}C NMR (126 MHz, d^6-DMSO) δ 162.72, 158.59, 143.07, 133.15, 130.79, 129.43, 129.39, 128.55, 128.49, 127.97, 127.69, 119.53, 118.15, 116.48.

2. 3. Synthesis of the Complex [VOL(OCH_3)(CH_3OH)]

The hydrazone compound H_2L (1.0 mmol, 0.32 g) and $VO(acac)_2$ (1.0 mmol, 0.26 g) were refluxed in methanol (30 mL). The reaction was continued for 1 h in oil bath to give a deep brown solution. Single crystals of the complex were formed during slow evaporation of the reaction mixture in air. The crystals were isolated by filtration, washed with cold methanol and dried over anhydrous $CaCl_2$. Yield: 0.23 g (51%). IR data (KBr pellet, cm^{-1}): 3438 ν(O–H), 1607 ν(C=N), 1390 ν(C–$O_{phenolate}$), 1157 ν(N–N), 953 ν(V=O). UV-Vis data in methanol (nm): 268, 323, 400. Molar conductance (10^{-3} mol L^{-1}, methanol): 27 Ω^{-1} cm^2 mol^{-1}. Analysis: Found: C 43.12, H 3.75, N 6.17%. Calculated for $C_{16}H_{16}BrN_2O_5V$: C 42.98, H 3.61, N 6.26%. ^{1}H NMR (500 MHz, d^6-DMSO): δ 13.93 (s, 1H, O*H*), 9.11 (s, 1H, C*H*=N), 7.78 (d, 1H, Ar*H*), 7.72 (t, 2H, Ar*H*), 7.58 (t, 1H, Ar*H*), 7.47 (t, 1H, Ar*H*), 7.42 (t, 1H, Ar*H*), 7.01 (t, 1H, Ar*H*), 6.90 (d, 1H, Ar*H*), 3.45 (s, 3H, CH_3), 2.12 (d, 3H, CH_3OH). ^{13}C NMR (126 MHz, d^6-DMSO) δ 167.40, 163.44, 156.14, 135.46, 133.70, 133.23, 132.25, 131.96, 131.11, 127.58, 120.87, 120.03, 119.07, 116.06, 40.02, 16.41.

2. 4. Crystal Structure Determination

Data were collected on a Bruker SMART 1000 CCD area diffractometer using a graphite monochromator Mo Kα radiation (λ = 0.71073 Å) at 298(2) K. The data were corrected with SADABS programs and refined on F^2 with Siemens SHELXL software.[5] The structures of H_2L and the complex were solved by direct methods and difference Fourier syntheses. All non-hydrogen atoms were refined anisotropically. The amino H atom (H2) in H_2L and the methanol H atom (H5) in the complex were located from difference Fourier maps and refined isotropically. The remaining hydrogen atoms were placed in calculated positions and included in the last cycles of refinement. Crystal data and details of the data collection and refinement are listed in Table 1.

Table 1. Crystallographic Data for H_2L and the Complex

Parameters	H_2L	The complex
Empirical formula	$C_{14}H_{11}BrN_2O_2$	$C_{16}H_{16}BrN_2O_5V$
Formula weight	319.16	447.16
Crystal system	Monoclinic	Triclinic
Space group	$P2_1/n$	P –1
a [Å]	5.9246(9)	7.7967(11)
b [Å]	29.6219(12)	11.1240(13)
c [Å]	7.5728(11)	11.6316(12)
α [°]	90	66.901(1)
β [°]	92.303(1)	83.748(1)
γ [°]	90	71.652(1)
V [Å^3]	1327.9(3)	880.6(2)
Z	4	2
$\rho_{calcd.}$ [g cm^{-3}]	1.596	1.686
μ [mm^{-1}]	3.094	2.861
F(000)	640	448
Measured reflections	7903	5279
Independent reflections	2468	3274
Observed reflections ($I > 2\sigma(I)$)	1661	1677
Parameters	176	229
Restraints	1	1
Final R indices [$I > 2\sigma(I)$]	0.0384, 0.0729	0.0581, 0.0856
R indices (all data)	0.0732, 0.0845	0.1438, 0.1140
Goodness-of-fit on F^2	1.013	1.005
Largest difference in peak and hole (e Å^{-3})	0.266 and –0.207	0.422 and –0.463

2. 5. Catalytic Epoxidation Process

A mixture of cyclooctene (2.76 mL, 20 mmol), acetophenone (internal reference) and the complex as the catalyst (0.05 mmol) was stirred and heated up to 80 °C before addition of aqueous *tert*-butyl hydroperoxide (TBHP; 70% w/w, 5.48 mL, 40 mmol). The mixture is initially an emulsion, but two phases become clearly visible as the reaction progresses, a colorless aqueous one and a yellowish organic one. The reaction was monitored for 5 h with withdrawal and analysis of organic phase aliquots (0.1 mL) at required times. Each withdrawn sample was mixed with 2 mL of diethylether, treated with a small quantity of MnO_2 and then filtered through silica and analyzed by GC.

3. Results and Discussion

3. 1. Synthesis

The hydrazone compound H_2L and the complex were synthesized in a facile and analogous way (Scheme 2).

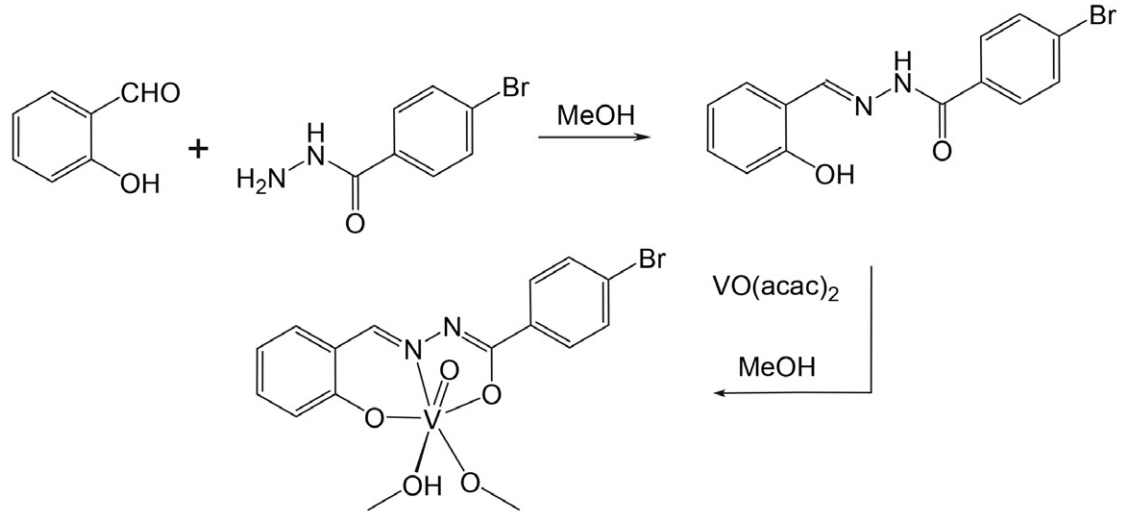

Scheme 2. The synthesis of the hydrazone H_2L and the complex

The hydrazone H_2L acts as a tridentate dianionic ONO donor ligands toward the VO^{2+} core. The vanadium complex was obtained from a refluxing mixture of the hydrazone and $VO(acac)_2$ in 1:1 molar proportion in methanol. The complex was isolated as brown single crystals from the reaction mixture by slow evaporation at room temperature. Crystals of the complex are stable at room temperature and are found to be fairly soluble in most of the common organic solvents such as methanol, ethanol, acetonitrile, DMF and DMSO. The low molar solution conductance of the complex in methanol indicates its non-electrolyte behavior.

3. 2. IR and Electronic Spectra

The IR spectrum of the hydrazone H_2L shows bands centered at 3220 cm^{-1} for ν(N–H), 3445 cm^{-1} for ν(O–H), and 1643 cm^{-1} for ν(C=O).[6] The peaks attributed to ν(N–H) and ν(C=O) are absent in the spectrum of the complex as the ligand binds in dianionic form resulting in losing proton from carbohydrazide group. Strong band observed at 1607 cm^{-1} for the complex is attributed to ν(C=N), which is located at lower frequencies as compared to the free hydrazone ligand, *viz.* 1612 cm^{-1}.[7] The complex exhibits characteristic band at 953 cm^{-1} for the stretching of V=O bond.[8] Based on the IR absorption, it is obvious that the hydrazone ligand exists in the uncoordinated form in *keto*-amino tautomer form and in the complex in imino-enol tautomeric form. This is not uncommon in the coordination of the hydrazone compounds.[9]

Electronic spectrum of the complex recorded in methanol displays strong absorption band centered at 400 nm, which is assigned as charge transfer transitions of N($p\pi$)–Mo($d\pi$) LMCT. The medium absorption band centered at 323 nm for the complex is assigned as charge transfer transitions of O($p\pi$)–Mo($d\pi$) LMCT.[10]

3. 3. Description of the Structure of H_2L

The perspective view of H_2L together with the atom numbering scheme is shown in Figure 1. Selected bond lengths and angles are given in Table 2. The molecule adopts an *E* configuration with respect to the methylidene unit. The methylidene bond, with the distance of 1.264(4) Å, confirms it a typical double bond. The shorter distance of the C8–N2 bond (1.343(4) Å) and the longer distance of the C8–O2 bond (1.225(4) Å) for the amide group than usual, suggests the presence of conjugation effects in the hydrazone molecule. The presence of intramolecular O1–H1···N1 hydrogen bond, as well as the conjugation effects, result in the two benzene rings form a dihedral angle of 6.8(5)°. In the crystal structure of the compound, the hydrazone molecules are linked by intermolecular

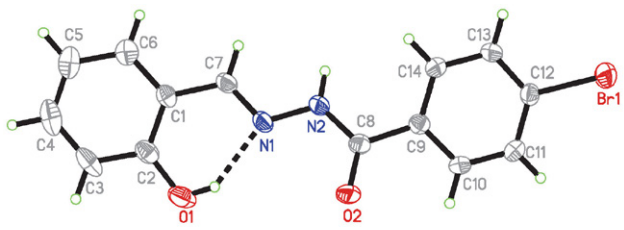

Figure 1. ORTEP plots (30% probability level) and numbering scheme for H_2L.

Table 2. Selected Bond Lengths (Å) and Angles (°) for H_2L and the Complex

H2L			
C7–N1	1.264(4)	N1–N2	1.386(3)
C8–N2	1.343(4)	C8–O2	1.225(4)
Complex			
V1–O1	1.849(4)	V1–O2	1.948(4)
V1–O3	1.582(4)	V1–O4	1.757(4)
V1–O5	2.358(5)	V1–N1	2.119(5)
O3–V1–O4	103.4(2)	O3–V1–O1	99.7(2)
O4–V1–O1	101.1(2)	O3–V1–O2	96.2(2)
O4–V1–O2	94.8(2)	O1–V1–O2	154.2(2)
O3–V1–N1	97.0(2)	O4–V1–N1	157.9(2)
O1–V1–N1	83.5(2)	O2–V1–N1	74.5(2)
O3–V1–O5	173.7(2)	O4–V1–O5	81.3(2)
O1–V1–O5	83.3(2)	O2–V1–O5	79.0(2)
N1–V1–O5	77.7(2)		

Table 3 Hydrogen bond distances (Å) and bond angles (°) for H_2L and the complex

D*–H···*A	***d*(*D*–H)**	***d*(H···*A*)**	***d*(*D*···*A*)**	**Angle (*D*–H···*A*)**
H_2L				
O1–H1···N1	0.82	1.92	2.627(3)	144(5)
N2–H2···O2^{i}	0.90(1)	1.97(1)	2.851(3)	168(3)
C7–H7···O2^{i}	0.93	2.55(2)	3.261(3)	134(3)
Complex				
O5–H5···N2^{ii}	0.85(1)	2.01(2)	2.828(6)	163(7)

Symmetry codes: (i) –½ + x, ½ – y, –½ + z; (ii) – x, 1 – y, 1 – z.

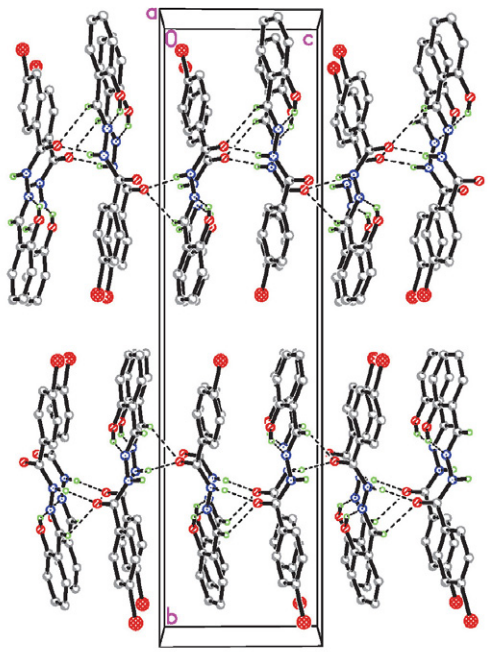

Figure 2. The molecular packing diagram of H_2L, viewed down the *a* axis. Hydrogen bonds are shown as dashed lines.

N2–H2···O2 and C7–H7···O2 hydrogen bonds, to form 1D chains running along the *c* axis (Table 3, Figure 2).

3. 4. Description of the Structure of the Complex

The perspective view of the complex together with the atom numbering scheme is shown in Figure 3. The coordination geometry around the V atom reveals a distorted octahedral environment with NO_5 chromophore. The hydrazone ligand behaves as a dianionic tridentate ligand binding through the phenolate oxygen, the enolate oxygen and the imine nitrogen, and occupies three positions in the equatorial plane. The fourth position of the equatorial plane is occupied by the deprotonated methanol ligand. The neutral methanol ligand occupies one axial position of the octahedral coordination, and the other axial position is defined by the oxido group. The vanadium atom is found to be deviated from the mean equatorial planes defined by the four donor atoms by 0.310(2) Å. The V1–O5 bond length is longer than the normal single bond lengths (2.358(5) Å against 1.9–2.0 Å). This shows that the neutral methanol ligand is loosely attached to the V center. This is due to the *trans* effect generated by the oxido group. The remaining V–O bond lengths of 1.58–1.95 Å and the V–N bond length of 2.12 Å are similar to the corresponding bond values observed in other vanadium(V) complexes.[11] The C8–O2 bond length in the complex is 1.311(7) Å, which is closer to single bond length rather than C=O double bond length. However, the shorter length compared to C–O single bond may be attributed to extended electron delocalization in the ligand.[12] Similarly shortening of C8–N2 bond length (1.308(7) Å instead of normal 1.38 Å) together with the elongation of N1–N2 bond length (1.398(6) Å) also supports the electron cloud delocalization in the ligand system. The hydrazone ligand forms a five-membered and a six-membered chelate rings with the V center. The five-membered metallacycle ring is thus rather planar, but the six-membered metallacycle ring is clearly distorted. The two benzene rings form a dihedral angle of 4.3(5)°. The *trans* angles are in the range 154.2(2)–173.7(2)°, indicating considerable

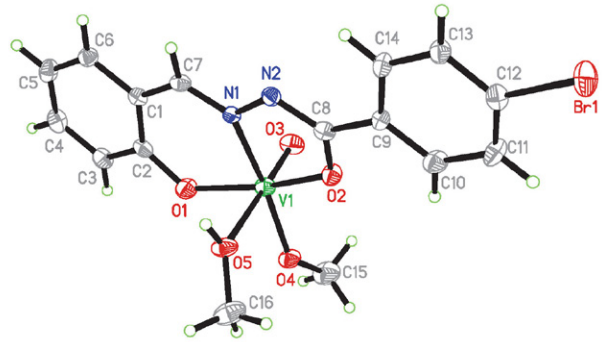

Figure 3. ORTEP plots (30% probability level) and numbering scheme for the complex.

distortion of the coordination octahedron around the V center.

In the crystal structure of the complex, adjacent two complex molecules are linked by intermolecular O5–H5···N2 hydrogen bonds (Table 3), to form dimers (Table 3, Figure 4).

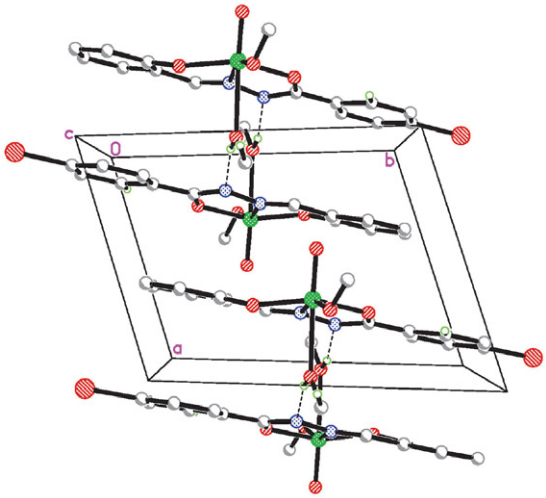

Figure 4. The molecular packing diagram of the complex, viewed down the *c* axis. Hydrogen bonds are shown as dashed lines.

3. 5. Catalytic Epoxidation Results

Before addition of aqueous TBHP at 80 °C, the complex dissolved completely in the organic phase. The aqueous phase of the solution was colorless and the organic phase was brown, indicating that the catalyst is mainly confined in the organic phase. TBHP is mainly transferred into the organic phase under those conditions, and for that reason the reactant and products in the organic layer were analyzed. Cyclooctene and cyclooctene oxide are not significantly soluble in water, therefore the determination of the epoxide selectivity (epoxide formation/cyclooctene conversion) is expected to be accurate. For the cyclooctene epoxidation by using aqueous TBHP, with no extra addition of organic solvents, the present study shows effective activity. Kinetic profiles of the complex as catalyst are presented in Figure 5. No induction time was observed. The cyclooctene conversion for the complex is 93% after 5 h, and the selectivity towards cyclooctene oxide is 67%. Possible mechanistic consideration involves coordination of TBHP as a neutral molecule, with the hydrogen bond O–H···O (Scheme 3).

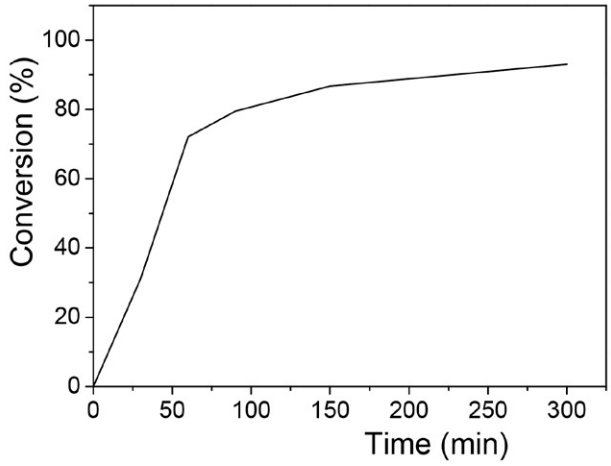

Figure 5. Kinetic monitoring of *cis*-cyclooctene epoxidation with TBHP–H_2O in the presence of the complex.

4. Conclusion

In summary, a new hydrazone compound 4-bromo-*N*'-(2-hydroxybenzylidene)benzohydrazide was prepared and structurally characterized. With the hydrazone

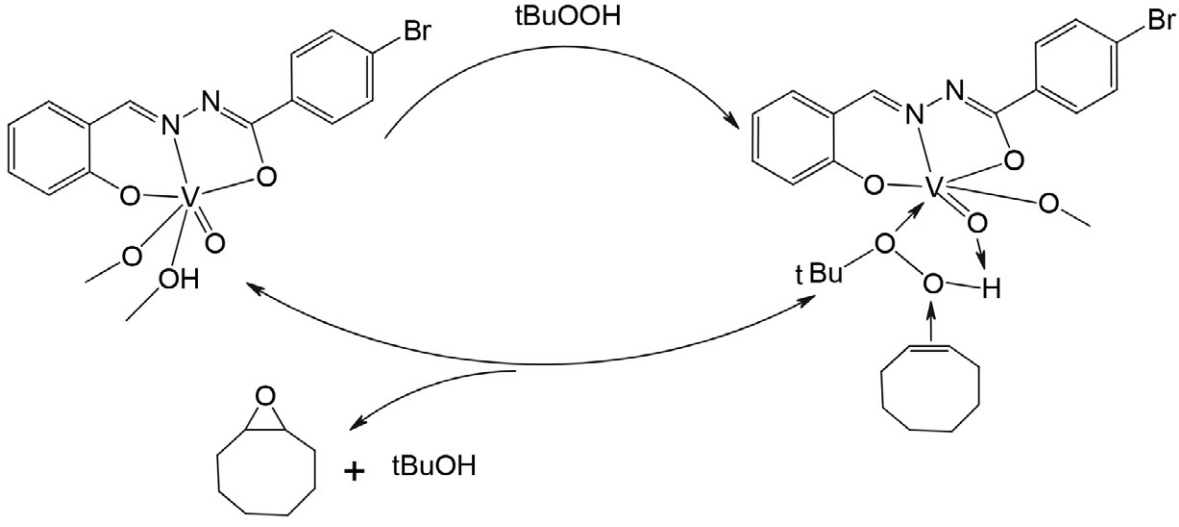

Scheme 3. Proposed mechanism for the catalytic process of the complex.

compound, a new oxidovanadium(V) complex was synthesized and characterized. Single crystal structures of the hydrazone compound and the oxidovanadium(V) complex were determined. The hydrazone compound coordinate to the V atom through the NNO donor set. The V atom of the complex is in octahedral coordination. The complex can catalyze the epoxidation of cyclooctene, with high conversion and selectivity.

5. Supplementary Data

CCDC numbers 1916011 for H_2L and 1916013 for the complex contain the supplementary crystallographic data. These data can be obtained free of charge *via* http://www.ccdc.cam.ac.uk/conts/retrieving.html, or from the Cambridge Crystallographic Data Center, 12, Union Road, Cambridge CB2 1EZ, UK; fax: +44 1223 336 033; or e-mail: deposit@ccdc.cam.ac.uk.

Acknowledgments

This work was supported by the Collaborative Innovation Plan of Hubei Province for Key Technology of Eco-Ramie Industry.

6. References

1. (a) R. Dhiman, C. M. Nagaraja, *New J. Chem.* **2019**, *43*, 13662–13669; **DOI:**10.1039/C9NJ02281C
(b) J. E. Baumeister, A. W. Mitchell, S. P. Kelley, C. L. Barnes, S. S. Jurisson, *Dalton Trans.* **2019**, *48*, 12943–12955; **DOI:**10.1039/C9DT02630D
(c) A. Najafian, T. R. Cundari, *Inorg. Chem.* **2019**, *58*, 12254–12263; **DOI:**10.1021/acs.inorgchem.9b01696
(d) H.-Y. Qian, N. Sun, *Transition Met. Chem.* **2019**, *44*, 501–506; **DOI:**10.1007/s11243-018-00296-x
(e) L. Pogany, B. Brachnakova, P. Masarova, J. Moncol, J. Pavlik, M. Gal, M. Mazur, R. Herchel, I. Nemec, I. Salitros, *New J. Chem.* **2019**, *43*, 13916–13928; **DOI:**10.1039/C9NJ03087E
(f) H.-Y. Qian, *Inorg. Nano-Met. Chem.* **2018**, *48*, 615–619. **DOI:**10.1080/24701556.2019.1567542
2. (a) R. Ogawa, T. Suzuki, M. Hirotsu, N. Nishi, Y. Shimizu, Y. Sunatsuki, Y. Teki, I. Kinoshita, *Dalton Trans.* **2019**, *48*, 13622–13629; **DOI:**10.1039/C9DT03007G
(b) H.-Y. Qian, *Inorg. Nano-Met. Chem.* **2018**, *48*, 461–466; **DOI:**10.1080/24701556.2019.1569689
(c) H. Y. Qian, *Russ. J. Coord. Chem.* **2017**, *43*, 780–786; **DOI:**10.1134/S1070328417110070
(d) I. Mondal, K. Ghosh, S. Chattopadhyay, *Inorg. Chim. Acta* **2019**, *494*, 123–131; **DOI:**10.1016/j.ica.2019.05.003
(e) M. H. Esfahani, H. Iranmanesh, J. E. Beves, M. Kaur, J. P. Jasinski, M. Behzad, *J. Coord. Chem.* **2019**, *72*, 2326–2336; **DOI:**10.1080/00958972.2019.1643846
(f) H. Y. Qian, *Russ. J. Coord. Chem.* **2018**, *44*, 32–38. **DOI:**10.1134/S1070328418010074
3. (a) L. S. Neira, M. M. Antunes, A. C. Gomes, L. Cunha-Silva, M. Pillinger, A. D. Lopes, A. A. Valente, I. S. Goncalves, *Dalton Trans.* **2019**, *48*, 11508–11519; **DOI:**10.1039/C9DT02127B
(b) H. Albright, P. S. Riehl, C. C. McAtee, J. P. Reid, J. R. Ludwig, L. A. Karp, P. M. Zimmerman, M. S. Sigman, C. S. Schindler, *J. Am. Chem. Soc.* **2019**, *141*, 1690–1700. **DOI:**10.1021/jacs.8b11840
4. (a) G. Romanowski, J. Kira, M. Wera, *Polyhedron* **2014**, *67*, 529–539; **DOI:**10.1016/j.poly.2013.10.008
(b) J.-Q. Wu, Y.-S. Li, *Coord. Chem. Rev.* **2011**, *255*, 2303–2314; **DOI:**10.1016/j.ccr.2011.01.048
(c) K. Nomura, S. Zhang, *Chem. Rev.* **2011**, *111*, 2342–2362; **DOI:**10.1021/cr100207h
(d) A. V. Chuchuryukin, R. B. Huang, E. E. van Faassen, G. P. M. van Klink, M. Lutz, J. C. Chadwick, A. L. Spek, G. van Koten, *Dalton Trans.* **2011**, *40*, 8887–8895; **DOI:**10.1039/c1dt10482a
(e) M. L. Kuznetsov, J. C. Pessoa, *Dalton Trans.* **2009**, *28*, 5460–5468; **DOI:**10.1039/b902424g
(f) X.-W. Zhu, *Acta Chim. Slov.* **2018**, *65*, 939–945; **DOI:**10.17344/acsi.2018.4607
(g) M. Liang, N. Sun, D.-H. Zou, *Acta Chim. Slov.* **2018**, *65*, 964–969; **DOI:**10.17344/acsi.2018.4625
(h) L.-W. Xue, Q.-L. Peng, P.-P. Wang, H.-J. Zhang, *Acta Chim. Slov.* **2019**, *66*, 694–700. **DOI:**10.17344/acsi.2019.5151
5. G. M. Sheldrick, SHELXS97 Program for solution of crystal structures, University of Göttingen, Germany, **1997**.
6. (a) Y.-T. Ye, F. Niu, Y. Sun, D. Qu, X.-L. Zhao, J. Wang, D.-M. Xian, H. Jurg, Z.-L. You, *Chinese J. Inorg. Chem.* **2015**, *31*, 1019–1026;
(b) Z.-L. You, D.-M. Xian, M. Zhang, *CrystEngComm* **2012**, *14*, 7133–7136. **DOI:**10.1039/c2ce26201k
7. (a) R. A. Lal, M. Chakrabarty, S. Choudhury, A. Ahmed, R. Borthakur, A. Kumar, *J. Coord. Chem.* **2010**, *63*, 163–175; **DOI:**10.1080/00958970903259451
(b) T. Glowiak, L. Jerzykiewicz, J. A. Sobczak, J. J. Ziolkowski, *Inorg. Chim. Acta* **2003**, *356*, 387–392. **DOI:**10.1016/S0020-1693(03)00301-3
8. C. A. Koellner, N. A. Piro, W. S. Kassel, C. R. Goldsmith, C. R. Graves, *Inorg. Chem.* **2015**, *54*, 7139–7141. **DOI:**10.1021/acs.inorgchem.5b01136
9. (a) L.-X. Li, Y. Sun, Q. Xie, Y.-B. Sun, K.-H. Li, W. Li, Z.-L. You, *Chinese J. Inorg. Chem.* **2016**, *32*, 369–376;
(b) L. Pan, C. Wang, K. Yan, K.-D. Zhao, G.-H. Sheng, H.-L. Zhu, X.-L. Zhao, D. Qu, F. Niu, Z.-L. You, *J. Inorg. Biochem.* **2016**, *159*, 22–28; **DOI:**10.1016/j.jinorgbio.2016.02.017
(c) D. Qu, F. Niu, X. Zhao, K.-X. Yan, Y.-T. Ye, J. Wang, M. Zhang, Z. You, *Bioorg. Med. Chem.* **2015**, *23*, 1944–1949. **DOI:**10.1016/j.bmc.2015.03.036
10. (a) R. Hahn, U. Kusthardt, W. Scherer, *Inorg. Chim. Acta* **1993**, *210*, 177–182; **DOI:**10.1016/S0020-1693(00)83325-3
(b) S. Gupta, A. K. Barik, S. Pal, A. Hazra, S. Roy, R. J. Butcher, S. K. Kar, *Polyhedron* **2007**, *26*, 133–141. **DOI:**10.1016/j.poly.2006.08.001

11. (a) M. R. Maurya, S. Agarwal, C. Bader, M. Ebel, D. Rehder, *Dalton Trans.* **2005**, 537-544;
(b) H.-Y. Qian, *Acta Chim. Slov.* **2019**, *66*, 995–1001.
DOI:10.4149/neo_2019_190112N36

12. H. H. Monfared, S. Alavi, R. Bikas, M. Vahedpour, P. Mayer, *Polyhedron* **2010**, *29*, 3355–3362.
DOI:10.1016/j.poly.2010.09.029

Povzetek

Sintetizirali smo nov oksidovanadijev(V) kompleks, [VOL(OCH_3)(CH_3OH)], kjer je H_2L = 4-bromo-*N*'-(2-hidroksibenziliden)benzohidrazid, in ga okarakterizirali z CHN elementno analizo, FT-IR, UV-Vis, ^1H in ^{13}C NMR spektroskopijo. Strukturi prostega hidrazona in kompleksa smo okarakterizirali tudi z monokristalno rentgensko difrakcijo, ki je razkrila, da ima V atom oktaedrično koordinacijo ter da je hidrazon trovezni ligand. Raziskali smo tudi katalitične lastnosti pri epoksidaciji.

Except when otherwise noted, articles in this journal are published under the terms and conditions of the Creative Commons Attribution 4.0 International License

Scientific paper

Kinetic Analysis of Poly(ε-caprolactone)/poly(lactic acid) Blends with Low-cost Natural Thermoplastic Starch

Vesna Ocelić Bulatović,[1] Miće Jakić*,[2] and Dajana Kučić Grgić[3]

[1] *Faculty of Metallurgy, University of Zagreb, Sisak, Aleja narodnih heroja 3, HR-44000 Sisak, Croatia*

[2] *Faculty of Chemistry and Technology, Department of Organic Technology, University of Split, Ruđera Boškovića 35, HR-21000 Split, Croatia*

[3] *Faculty of Chemical Engineering and Technology, University of Zagreb, Marulićev trg 19, HR-10000 Zagreb, Croatia*

** Corresponding author: E-mail: mjakic@ktf-split.hr*

Received: 11-04-2019

Abstract

Non-isothermal thermogravimetry in an inert atmosphere was used to investigate the thermal stability of poly(e-caprolactone) (PCL), polylactide (PLA), thermoplastic starch (TPS) and their binary (PCL/PLA, PCL/TPS and PLA/TPS) and ternary (PCL/PLA/TPS) blends. All investigated blends were prepared by Brabender kneading chamber. A two-stage degradation pattern is seen in the case of PCL, while PLA exhibits only single stage degradation. On the other hand, the degradation of neat TPS proceeds through three degradation stages. It was found that addition of PLA affects the degradation of PCL/PLA blends indicating PLA's destabilising effect on PCL. TPS addition thermally destabilizes both, PCL and PLA, but notably the PCL sample. Likewise, that addition of TPS thermally destabilized all investigated ternary blends. The obtained data were used for the kinetic analysis of the degradation process. By using the isoconversional Friedman method and the multivariate nonlinear regression method kinetic analysis was performed. Kinetic analysis revealed the complexity of the thermal degradation process for neat samples and all investigated blends. Kinetic parameters (activation energy, pre-exponential factor and kinetic model) for each degradation stage of neat samples and all investigated blends were calculated.

Keywords: Kinetic analysis, poly(ε-caprolactone), polylactide, Thermogravimetric analysis, thermoplastic starch

1. Introduction

In recent decades, the growing environmental awareness has encouraged the development of biodegradable materials from renewable resources to replace conventional non-biodegradable materials in many applications. Therefore, additional approaches, such as using biodegradable plastics, are sought to enforce the reduction of using petroleum-based plastic packaging that ends in landfills, especially in food packaging applications where recycling is difficult or prohibited due to contamination. Similarly to other areas, the plastics industry started looking for alternative sources of raw materials in the last few decades, and considerable interest is shown in natural, renewable solutions. Biopolymers, i.e. polymers produced from renewable feedstock might replace fossil sources and also have considerable environmental benefits like decreased carbon-dioxide emission.[1] In spite of increasing production capacity, biopolymers are still quite expensive compared to commodity polymers and their properties are also often inferior, or at least do not correspond to the expectation of users. To meet market expectations, the properties of biopolymers must be altered and constantly adapted. Timely, biopolymer modification is at the center of scientific research. In contrast to the development of novel polymeric materials and new polymerization routes, blending is a relatively cheap and fast method to tailor the properties of plastics. The modification of biopolymers by blending with other biopolymers and/or biodegradable materials has many advantages, since it offers an option to adjust properties in a wide range, while legislation also favors completely compostable materials with minimal already mentioned carbon-dioxide emission. Polysaccharides such as starches stand out as a promising replacement of synthetic polymers in plastics industries due to their low cost, non-toxicity, biodegradability and availability.[2–4] A large number

of researches are focused on incorporations of starch in the polyester matrix to reduce production costs and maintain the biodegradability.[5–7] A variety of biodegradable polyesters can be obtained from renewable sources, and of these poly(lactic acid) (PLA) is a material of particular interest due to its exquisite and enviable mechanical properties.[5,8] Polycaprolactone (PCL) is another polymer which seems to be promising synthetic biodegradable material due to its encouraging properties and its compatibility with many types of polymers. PCL is a good candidate to supplement the shortcomings of PLA. A clear upward trend in PCL and PLA usage in research over the past decade signifies the recognition of these highly versatile resorbable polymers, particularly in the field of biomaterials.[9–10] PLA/PCL blends offers an interesting and unobtrusive characteristic because of its wide variety of physical property and biodegradability, in which the glassy PLA with high degradation rate shows better tensile strength, while the rubbery PCL with much slower degradation rate shows better toughness.[11] However, they are extremely costly to be widely used as required by the packaging application. This is the reason why they are blended with lower-cost natural biopolymers such as thermoplastic starch.[8,12–14] The blending also causes the changes kinetics of decomposition of as individuals' polymers in the blends. The more components in the blend, the process of thermal decomposition of such material is more complex. Because of the thermal degradation of individual polymers in the blends due to their intrinsic chemical reaction processes the investigation of their thermal properties and degradation kinetics of the decomposition is crucial for an accurate prediction of the materials behavior under different working conditions and as well as to optimize the process conditions.[15,16] In addition, thermal degradation of starch is important to conduct comprehensive studies on their thermal properties and stability of their application in food and pharmaceutical industries and to facilitate their use, since starch undergo thermal processes during their preparation, processing and consumption and on the other hand are poorly researched.[17] Thermogravimetry (TG) has proved to be reliable method which results can be used for determination of thermal stability of biopolymers and kinetic analysis.[15,16] On the other hand, the goal of the kinetic analysis is to provide kinetic parameters of the degradation process, i.e. the activation energy (E), the pre-exponential factor (A) and a kinetic model ($f(\alpha)$), the so called "kinetic triplet". Kinetic analysis of the non-isothermal degradation of individual polymer materials and their binary blends has already been studied but from the point of view of ternary blends with starch is a very poor overview of the literature. The thermal degradation of PCL has already been investigated in the literature,[18–20] but the conclusion is debatable. Persenaire et al.[18] proposed a two-stage degradation mechanism of random cleavage through cis-elimination and specific chain end scission by unzipping from the hydroxyl end of the polymer chain. Contrary, Aoyagi et al.[20] proposed a single step degradation mechanism, where the polymer degrades by specific removal of monomer from the end groups. On the other hand, according to the literature,[20–23] PLA thermal degradation is caused by intramolecular transesterification reactions leading to cyclic oligomers of lactic acid and lactide. Simultaneously, there is a recombination of the cyclic oligomers with linear polyesters through insertion reactions, whereas molecules with longer chains lengths are favoured. Moreover, beside above mentioned, the main decomposition products are acetaldehyde, carbon monoxide, carbon dioxide and methylketene.[24] The thermo-oxidative degradation of TPS has already been investigated in the literature by several authors.[25,26] They all concluded that TPS degrades through three or four stages, respectively. Janković[25] determinated that degradation process of the TPS is very complex and proceeds through three main degradation stages with one additional substage attached to the second degradation stage. Futhermore, he concluded that most important degradation stage consist of simultaneously attack of the free radicals on linear and branched molecular forms of the starch. Wahyuningtiyas et al.[26] utilized TG analysis to obtain the decomposition process mechanism of starch based bioplastic and concluded that decomposition process occurs through four main degradation stages. First stage is the result of the release of moisture or water, while the second one is the main thermal decomposition stage; hence this stage triggers the rapid thermal decomposition with a large mass loss. On the other hand, Guaras et al.[27] characterized TPS/PCL blends by means of TG analysis under nitrogen atmosphere. Authors confirmed that thermal degradation process of native starch proceeds through three-step reaction; first step corresponds to the water loss, the second between 260 and 330 °C to starch decomposition and the third between 500 and 600 °C to the oxidation of partially decomposed starch. In the second step they observed the shoulder on the DTG curve probably due to the degradation events of the main peak through the series of competitive reactions, which includes depolymerization (which can be explained by the chain scission of the glycosidic linkage of polysaccharide). But in the case of TPS they observed a four-step reaction where fourth step corresponds to ethylene glycol degradation.

Altghouh PCL/TPS and PLA/TPS blends have already been investigated in the literature,[28–32] information about the thermogravimetric and kinetic analysis of the non-isothermal degradation of ternary PCL/PLA/TPS blends couldn't be found. Acordingly, in this work the non-isothermal thermogravimetry in an inert atmosphere and its results were used for determination of thermal stability of PCL, PLA, TPS and their binary (PCL/PLA, PCL/TPS and PLA/TPS) and ternary (PCL/PLA/TPS) blends. Finnally, by using isoconversional Friedman method[33] in

combination with the multivariate non-linear regression method, these results were utilized for determination of the true kinetic triplets of the non-isothermal degradation of neat polymers and their investigated blends.

2. Material and Methods

2. 1. Materials

The polylactide used in this study was a comercial grade Ingeo™ Biopolymer4043D supplied by NatureWorks (Minnetonka, MN, USA). Its main properties are a density of 1.24 g cm^{-3} at 25 °C, a glass transition temperature in the 50–70 °C range, and a melt peak temperature range between 145–160 °C. Regarding to poly(e-caprolactone) (PCL), a commercial grade Polycaprolactone 440744 (MFI = 2.01–4.03 g/10 min at 160 °C) was supplied by Sigma-Aldrich (Taufkirchen, Germany) in pellet form with a density of 1.145 g cm^{-3}. Their average molecular weights are respectively 70 000 and 90 000 g mol^{-1} by GPC with M_w / M_n < 2. The samples were previously dried and used in the experiments in as received pellet form. Wheat varieties "Srpanjka" (harvest 2008) were obtained from Agricultural Institute, Osijek, Croatia. According to the data provided with samples, "Srpanjka" variety contained 68.73 % d.m. starch, 12.57 % d.m. protein and 12.20 % moisture. Isolation of starch from wheat and characterization of starch was described in research by our colleagues.[34] Wheat starch (WS) contains 22.49 ± 2.01 wt %. amylose. WS was modified to obtain thermoplastic starch (TPS) by using glycerol. Glycerol was supplied by Gram Mol (Zagreb, Croatia).

2. 2. Sample Preparation

Preparation of blends, binary and ternary, was carried out in two different stages. Prior to further processing, all materials were dried to avoid moisture, which could affect hydrolysis during manufacturing. PLA were dried at 60 °C for 24 h, while PCL was dried at 45 °C for 24 h. The first stages were preparation of thermoplastic starch (TPS). TPS was prepared from a manual mixture of the following components: 70 wt % native wheat starch and 30 wt % glycerol. The appropriate amounts of each component were weighed and mechanically pre-mixed in a zipper bag until homogenization. Then, the TPS were extruded in a laboratory single-screw extruder (Model 19/20DN; Brabender GmbH, Germany). The extrusion parameters were as follows: screw 1: 1 and die 4 mm. A rotating speed of 40 rpm was used with a temperature profile of 130 °C (ejection zone), 100 °C (compression zone), and 100 °C (feeding hopper) and with dosing speed of 15 rpm. These conditions provide good processing in terms of viscosity and avoid thermal degradation. After extrusion the samples were air-dried overnight and then stored in sealed plastic bags at room temperature until further analysis. The next stage was prepared binary and ternary blends using a Brabender kneading chamber. The components were put in the chamber preheated up to 170 °C with a rotor speed of 50 rpm, and kneaded for 6 min. After homogenization the blends was pelletized and subsequently moulded in laboratory hydraulic press Fontune, Holland (SRB 140, EC 320x320NB) at 180 °C under a pressure of 25 bar for 5 min, and then kept at room temperature. Throughout this paper the designation for example PCL30/PLA70 refers to 30 wt % of PCL and 70 wt % of PLA in the blend. After preparation of the binary PCL/PLA blends, TPS was then blended with blends in a weight composition of 30 wt %. The amount of TPS in all ternary blends was maintained constant.

2. 3. Thermogravimetric Analysis

The thermal degradation of the PCL/PLA/TPS blends (sample mass approximately 10 mg) was performed by using PerkinElmer Pyris 1 TGA thermobalance at the heating rates of 2.5, 5, 10 and 20 °C min^{-1} in a temperature range 50–550 °C under a steady flow of nitrogen (20 cm^3 min^{-1}). In order to estimate the thermal stability of the investigated polymers and their blends different criteria was used. From thermogravimetric curves (TG) (mass versus degradation temperature), and corresponding derivative thermogravimetric curves (DTG) (mass loss rate versus temperature) the following characteristics were determined: the onset temperature (T_{onset}), the temperature at 5% mass loss ($T_{5\%}$), the temperature at the maximum degradation rate (T_{max}), the maximum degradation rate (R_{max}), the final mass (m_f) and the mass loss (Δm) for the corresponding degradation steps.

2. 4. Kinetic Analysis

The non-isothermal TG data can be used for the kinetic analysis of the investigated process. Kinetic analysis of the solid-state reactions that are ruled by a single process is based on Eq. (1):

$$\frac{d\alpha}{dt} \cong \beta \frac{d\alpha}{dT} = A \cdot \exp\left(-\frac{E}{RT}\right) \cdot f(\alpha) \qquad (1)$$

where α is the degree of conversion, β is the linear heating rate (°C min^{-1}), T is the absolute temperature (K), R is the general gas constant (J mol^{-1} K^{-1}) and t is the time (min). It is suggested that prior to any kinetic analysis one should investigate the complexity of the process by determining the dependence of E on α by isoconversional methods. Based on the recommendations of ICTAC Kinetics Committee for performing kinetic computations on thermal analysis data and other reliable literature,[35–38] the principle, basic equations of the solid-state reactions and isoconversional Friedman method and the experimental procedure of kinetic analysis were described in detail in already

published papers.[39–41] The Netzsch Thermokinetic 3.1 software[42] was utilized for determination of the true kinetic triplets of the non-isothermal degradation of neat polymers and their investigated blends.

3. Results and Discussion

3. 1. Thermogravimetric Analysis

In Fig. 1 TG and corresponding DTG curves of PCL/PLA blends obtained at 2.5 °C min^{-1} are shown and from them derived data (Table 1) were used to obtain information of the thermal stabilty of PCL and PLA, respectively. Neat PCL showed a two-stage degradation pattern, where its degradation starts at 374 °C (T_{onset1}) and ends at 475 °C with a peak temperature at 383 °C (T_{max1}) and 431 °C (T_{max2}). Thermal degradation of PCL proceeds almoust totally without residue which is supported by the fact that total weight loss through two degradation stages is 99.0%. Contrary, thermal degradation of the neat PLA is characterized by only a single stage degradation stage that unrolls between 319 °C (T_{onset}) and 400 °C confirming its inferior thermal stability to PCL. The peak temperature is observed at 339 °C and as in the case of PCL the total weight loss is found to be 99.2 %.

As predicted, a two-stage degradation pattern can be seen in the case of the PCL/PLA blends 50/50 and 30/70, while for blend 70/30 degradation proceeds through three stages. From the dependence of the characteristics of TG and DTG curves on the blend composition (Table 1) it can be concluded that the degradation of PCL/PLA blends is affected by addition of PLA and consequently degradation process starts at lower temperatures. This could be an indication of PLA destabilising effect on PCL. The mass loss in the first degradation stage

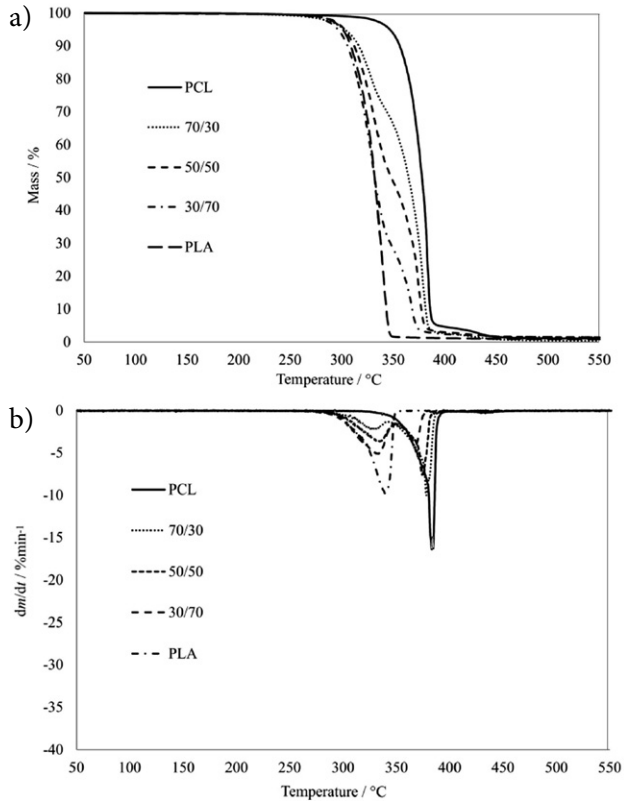

Fig. 1. TG (a) and DTG (b) curves of the thermal degradation of the PCL/PLA blends at the heating rate of 2.5 °C min^{-1}.

Table 1. The characteristics of thermal degradation curves of PCL/PLA blends (heating rate 2.5 °C min^{-1})

PCL/PLA	$T_{5\%}$ (°C)	T_{onset} (°C)	T_{max} (°C)	R_{max} (%min^{-1})	Δm(%)	m_f(%)
			First stage			
100/0	347	374	383	16.4	95.5	4.5
70/30	303	306	330	2.2	29.4	70.6
50/50	303	310	334	3.6	50.7	49.3
30/70	296	307	332	5.1	71.3	28.7
0/100	301	319	339	9.7	99.2	0.8
			Second stage			
100/0	–	422	431	0.2	3.5	1.0
70/30	–	365	378	10.1	67,9	2.7
50/50	–	366	374	7.6	47.9	1.4
30/70	–	361	368	4.1	27.3	1.4
0/100	–	–	–	–	–	–
			Third stage			
100/0	–	–	–	–	–	–
70/30		411	425	0.1	1,6	1.1
50/50	–	–	–	–	–	–
30/70	–	–	–	–	–	–
0/100	–	–	–	–	–	–

increased, while mass loss in the second degradation stage decreased linearly as the PLA content increased in the blend. The final mass at the end of the degradation is around 1% and practically independent on blend composition. Unexpectedly, PCL/PLA 30/70 blend showed the worst thermal stability, even than the neat PLA (Fig. 1, Table 1).

The TG/DTG curves of PCL/TPS and PLA/TPS blends obtained at 2.5 °C min^{-1} are shown in Fig. 2. Derived data are tabulated in Table 2 and used to indicate the effect of TPS addition on the degradation process of PCL and PLA, respectively. The PCL/TPS blend showed a three-stage degradation pattern while PLA/TPS blend degrades through two-stage degradation process. However, the degradation of neat TPS proceeds through three degradation stages starting from 91 °C (T_{onset1}) to 500 °C with a peak temperature at 128 °C (T_{max1}), 271 °C (T_{max2}) and 301 °C (T_{max3}) with total weight loss of 88.5 %. From data tabulated in Table 1 and 2 it can be seen that addition of TPS affects the degradation of neat PCL and PLA and consequently their degradation starts at lower temperatures. Unexpectedly, investigated PLA/TPS blend if compared with PCL/TPS blend showed superior thermal stability. Finnally, from Fig. 2 it can be concluded that TPS addition thermally destabilizes both, PCL and PLA, but notably the PCL sample.

The resulting TG/DTG curves of the non-isothermal thermogravimetry degradation of investigated ternary PCL/PLA/TPS blends obtained at 2.5 °C min^{-1} are showed in Fig. 3. Obtained data (Table 3) were used to evaluate the effect of TPS addition on the degradation pattern of PCL/PLA blends.

All investigated PCL/PLA/TPS blends revealed a four-stage degradation pattern, except the blend 30/70/30 which degradation proceeds through three stages. If temperature areas of thermal degradation of neat polymers are compared it can be concluded that

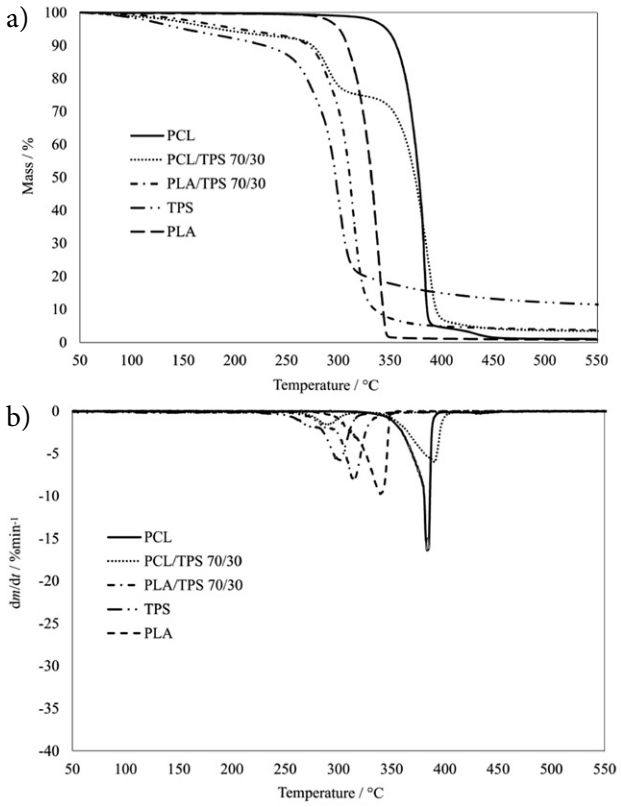

Fig. 2. TG (a) and DTG (b) curves of the thermal degradation of the PCL/TPS and PLA/TPS blends at the heating rate of 2.5 °C min^{-1}.

first and second degradation stages correspond to thermal degradation of TPS, while the third and fourth ones correspond to thermal degradation of PLA and PCL (Fig. 3), respectively.

It is evident, as well in the case of above mentioned blends, that addition of TPS thermally destabilized all investigated samples. However, addition of PLA hasn't affected the thermal stability of investigated blends (Table

Table 2. The characteristics of thermal degradation curves of PCL/TPS and PLA/TPS blends (heating rate 2.5 °C min^{-1})

Sample	$T_{5\%}$ (°C)	T_{onset} (°C)	T_{max} (°C)	R_{max} (%min^{-1})	Δm(%)	m_f(%)
			First stage			
PCL/TPS	185	105	157	0.2	7.7	92.3
PLA/TPS	204	115	174	0.1	6.3	93.7
TPS	151	91	128	0.2	8.0	92.0
			Second stage			
PCL/TPS	–	276	289	1.6	17.4	74.9
PLA/TPS	–	298	315	8.0	89.9	3.8
TPS	–	256	271	1.8	16.3	75.7
			Third stage			
PCL/TPS	–	364	390	6.1	71.4	3.5
PLA/TPS	–	–	–	–	–	–
TPS	–	292	301	5.8	64.2	11.5

3). Contrary to the PCL/PLA blends, the blend with increased PLA content showed better thermal stability. This fact is consistent with above mentioned conclusion that, if compared with PCL/TPS blend, investigated PLA/TPS blend showed superior thermal stability.

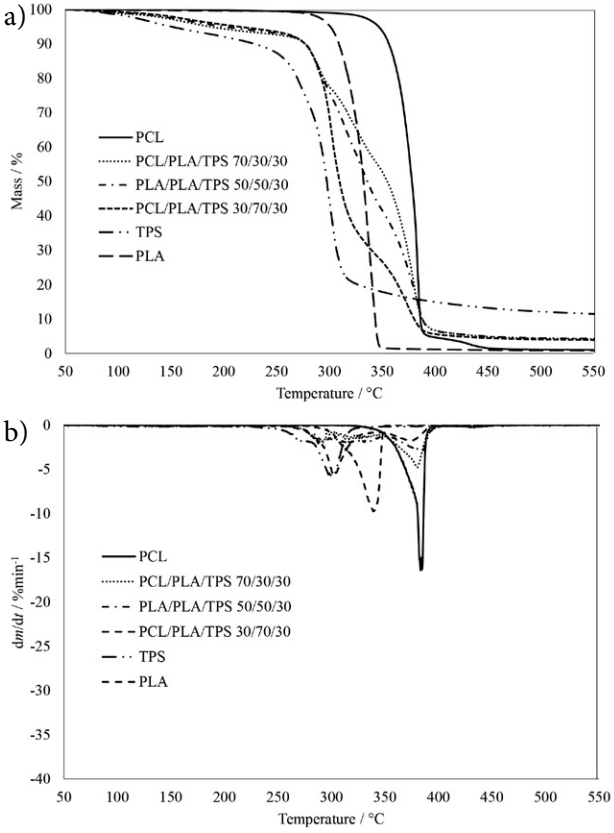

Fig. 3. TG (a) and DTG (b) curves of the thermal degradation of the PCL/PLA/TPS blends at the heating rate of 2.5 °Cmin^{-1}.

The TG/DTG curves of PCL, PLA, TPS and their binary (PCL/PLA, PCL/TPS and PLA/TPS) and ternary (PCL/PLA/TPS) blends gained at higher heating rates (5, 10 and 20 °C min^{-1}) are similar by pattern to those at 2.5 °C min^{-1} and shifted to higher temperatures and higher maximum rates od degradation, respectively.

3. 2. Kinetic Analysis

In order to obtain the valuable information about the degradation kinetics of PCL, PLA and their blends with TPS, raw data extracted from non-isothermal thermogravimetric analysis were utilized. Firstly, by using classical linear "model-free" Friedman kinetic method, the dependence of the activation energy (E) in function of the conversion degree (α) was evaluated. From Fig. 4 it can be undoubtedly concluded that in a whole conversion range E depends on α for all investigated samples, indicating complex multi-step degradation mechanism. Therefore, it is necessary to carry out a multi-step kinetic analysis which can be achieved by using the model fitting multivariate non-linear regression method.[37,38] This will provide a true kinetic triplet for each reaction step. Apparent activation energy of neat PCL sample showed two or more inflection points or maximums (Fig. 4) indicating that degradation takes place at least in two main steps.

This fact can be confirmed by reviewing DTG curves (Fig. 1). Sivalingam et al.[19] investigated kinetics of thermal degradation of PCL under non-isothermal and isothermal heating by TG in a nitrogen environment. Au-

Table 3. The characteristics of thermal degradation curves of PCL/PLA/TPS blends (heating rate 2.5 °C min^{-1})

Sample	$T_{5\%}$ (°C)	T_{onset} (°C)	T_{max} (°C)	R_{max} (% min^{-1})	Δm(%)	m_f (%)
			First stage			
70/30/30		113	169	0.2	6.9	93.1
50/50/30		101	170	0.2	6.0	94.0
30/70/30		110	165	0.1	4.9	95.1
			Second stage			
70/30/30	–	277	291	1.8	16.6	76.4
50/50/30	–	276	292	2.0	19.0	75.0
30/70/30	–	288	302	1.7	66.2	28.9
			Third stage			
70/30/30	–	310	316	1.6	20.6	55.8
50/50/30	–	307	315	2.0	33.9	41.1
30/70/30	–	360	375	5.7	25.0	3.9
			Fourth stage			
70/30/30	–	364	380	4.8	51.6	4.2
50/50/30	–	367	384	2.9	36.8	4.3
30/70/30	–	–	–	–	–	–

thors suggested that PCL undergoes two degradation stages by a parallel mechanism including random chain scission and specific chain end scission for non-isothermal heating. Hence, with detailed insight into apparent activation energy of degradation of PCL calculated by Friedman method three areas with different *E* values can be observed.

On the other hand, PLA exhibits three stage degradation mechanisms. Badia et al.[23] investigated thermal decomposition kinetics of PLA in argon atmosphere. Authors concluded that PLA degrades under only one degradation stage which can be described by two competitive different decomposition models: on the one hand, a Nucleation model (A2), which gives importance to specific decomposition sites; and on the other hand, a Reaction Contracting model (R3), which represents a particles release generalized on the whole polymer surface. Since the main mass loss decomposition process occured in the narrow conversion range (0.2–0.7), authors focused on that range. The Netzsch Thermokinetic 3.1 software allows calculation in the much wider conversion range; therefore, in this work kinetic analysis was done in a whole conversion range (0.0–1.0).

Accordingly, PLA sample showed three different areas of apparent activation energy. As expected, PCL/PLA blends showed even four different areas of apparent activation energy, except for PCL/PLA 30/70 blend which showed five different areas.

Kinetic model of thermal degradation of investigated samples can be determined by the multivariate non-linear regression analysis incorporated in Netzsch Thermokinetic 3.1software. This analysis was based on the results of the activation energy as well as on the shape and slope of experimental points and isoconversional lines from Friedman plots. More details can be found in our previous works.[39–41] F-test, correlation coefficient and especially the similarity of obtained *E* values with those calculated by FR method enabled to find the best fit of the model function that reasonably describes a kinetic model of degradation. Apparent activation energy values obtained by the FR method for each degradation stage, as well as the results of calculations for the most probable kinetic models on the basis of F-test and correlation coefficient are summarized in Table 4. Fig. 5a shows the comparison of experimental data (points) and best fitted kinetic models (solid lines) calculated from multivariate non-linear regression for the PCL sample.

Three-stage degradation mechanism, in this case with consecutive reactions A → B → C → D, proved to be appropiate for fitting the experimental data and the as-

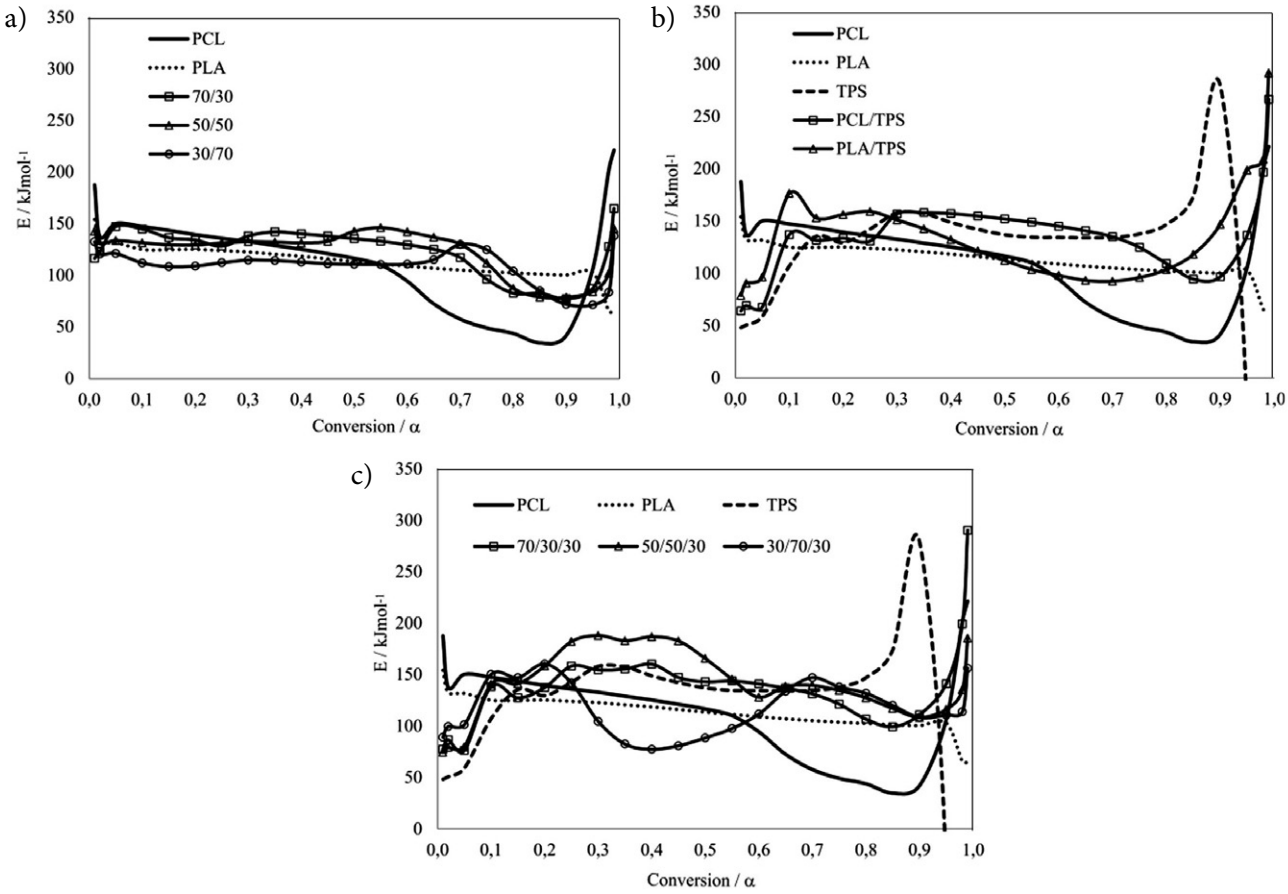

Fig. 4. Dependence of *E* on α determined by Friedman method of PCL/PLA (a), PCL/TPS and PLA/TPS (b) and PCL/PLA/TPS (c) blends.

Table 4. The most probable kinetic models of thermal degradation of PCL/PLA blends according to F-test and correlation coefficient obtained by using multivariate non-linear regression analysis

Stage of reaction	Parameter	PCL/PLA 100/0	70/30	50/50	30/70	0/100
	E_1 / kJmol^{-1}	148.7	122.6	130.0	128.1	154.0
Stage I	log A_1	8.6	7.5	8.8	8.3	10.1
	n	0.4	1.0	1.3	0.7	0.4
	Model	Cn	Cn	An	Cn	Cn
Friedman	kJmol^{-1}	128.8–150.0	116.4–147.1	130.0–142.5	108.3–132.5	125.1–153.9
	E_2 / kJ mol^{-1}	73.9.0	139.9	131.3	104.6	112.0
Stage II	log A_2	3.0	8.3	8.9	6.3	7.7
	n	5.1	3.8	0.9	0.4	4.3
	Model	An	An	An	Cn	An
Friedman	kJmol^{-1}	34.4–121.0	117.0–140.1	129.3–132.1	110.3–115.1	101.1–120.4
	E_3 / kJmol^{-1}	219.0	87.2	132.1	131.5	65.1
Stage III	log A_3	13.6	4.5	7.8	8.1	2.8
	n	1.1	0.3	0.2	0.1	5.0
	Model	Fn	Cn	Cn	Cn	An
Friedman	kJmol^{-1}	106.1–221.2	77.2–96.1	132.8–146.1	104.0–129.9	64.5–100.3
	E_4 / kJmol^{-1}	–	127.1	139.5	81.2	–
Stage IV	log A_4	–	7.8	9.6	4.8	–
	n	–	1.7	1.8	2.0	–
	Model	–	Fn	Fn	An	–
Friedman	kJmol^{-1}	–	127.8–164.8	87.3–145.1	71.7–84.9	-
	E_5 / kJmol^{-1}	–	–	–	131.6	–
Stage V	log A_5	–	–	–	8.2	–
	n	–	–	–	0.9	–
	Model	–	–	–	Fn	–
Friedman	kJmol^{-1}	–	–	–	83.5–137.9	–
Correlation coefficient,	r^2	0.99986	0.99963	0.99958	0.99952	0.99977

sumed kinetic models for PCL sample. The first stage of thermal degradation of PCL can be described by the reaction of n-th order with autocatalysis (Cn). This is partially in accordance with the work of Sivalingam et al.[19] where thermal degradation of PCL is described by a parallel mechanism including random chain scission and specific chain end scission. The second stage of thermal degradation of PCL sample may be described by the reaction of An kinetic model with a lower *E* value. This is not in accordance with the literature and ultimately with the features of fast autocatalytic random chain scission reaction. However, this divergence may be attributed to different sample preparation conditions, i.e. it may suffer thermal degradation when kept at temperatures higher than its melting point. In the final third stage, thermal degradation of investigated PCL sample can be described by the reaction of nth order (Fn). Considering the previous stages, this stage showed the highest apparent activation energy values which could be accounted by the higher collision frequencies at the higher degradation temperatures.[43]

Likewise, three-stage degradation mechanism (A → B → C → D) proved to be appropiate for fitting the experimental data and the assumed kinetic models for PLA sample as well (Fig. 5b). One again, the *E* obtained by Friedman method indicated that the first stage of degradation of PLA also might occur by the Cn kinetic model.

Although this conclusion is contrary to the literature data, in our opinion, Cn kinetic model reasonably describes first stage of the thermal degradation of PLA, both mathematically and functionally. The second stage of thermal degradation of PLA sample was also described by the reaction of An kinetic model, with the apparent activation energy which is lower than the one in the first stage. This is in accordance with the work of Badia et al.[23] where degradation of PLA was described by nucleation model (A2). Authors focused on the narrow conversion range (0.2–0.7), which corresponds to the second stage of the degradation of PLA sample in this work. On the other hand, the final third stage of degradation of PLA sample occurs by the An reaction type. This stage can be considered as the continuation of the degradation process from second stage of degradation of PLA sample. This fact would support the assumption that thermal degradation of PLA takes place through a mechanism of nucleation and growth of nuclei by a diffusion-controlled process which is considered to be

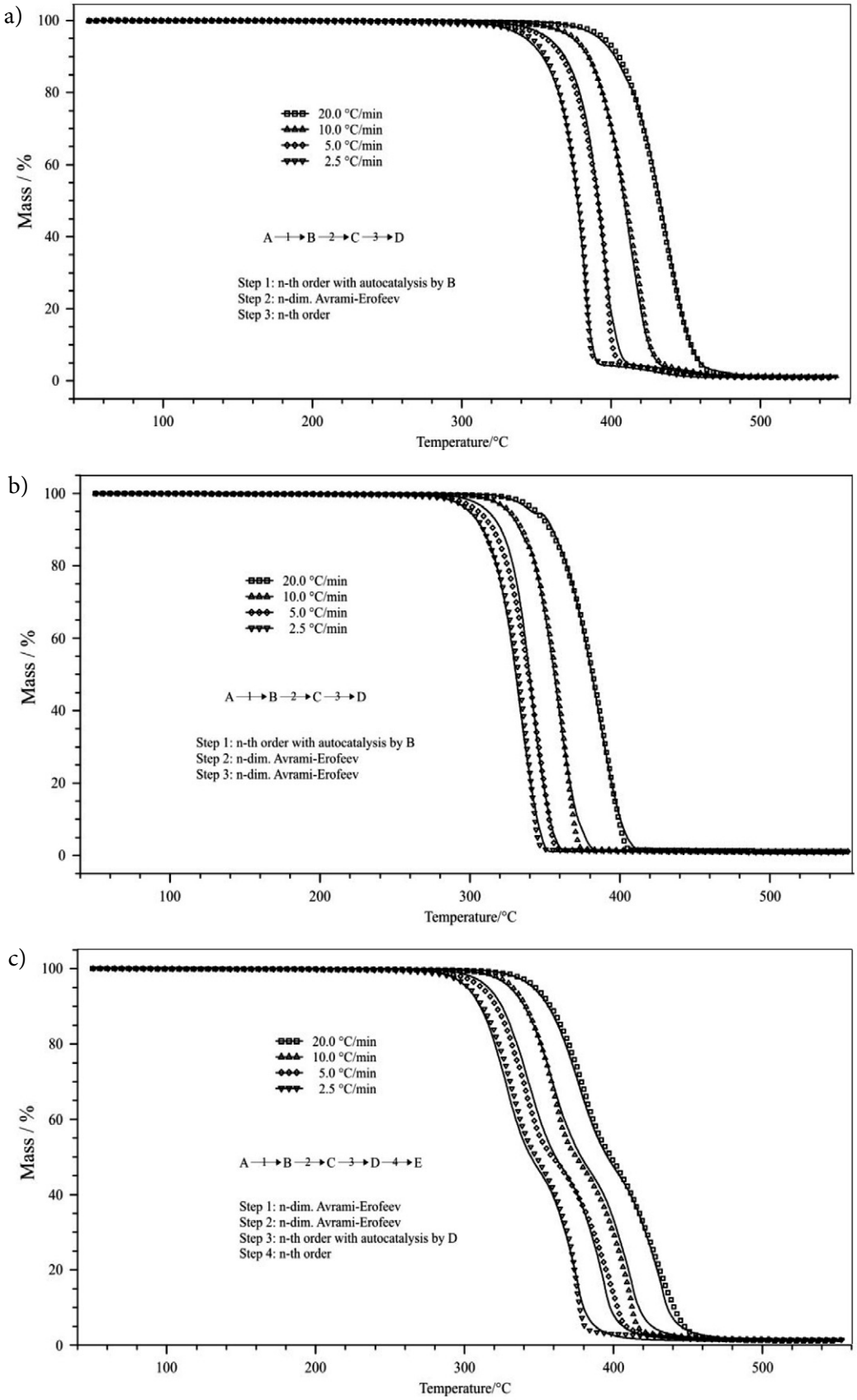

Fig. 5. Comparison of experimental data (points) and best fitted kinetic models (solid lines) calculated from multivariate nonlinear regression method for the PCL (a), PLA (b) and PCL/PLA (50/50) (c).

the best suited kinetic model for description of thermal degradation of PLA.[23]

However, a four-stage degradation mechanism (A → B → C → D →E) is seen in the case of the PCL/PLA blends 70/30 and 50/50 (Fig. 5c), while for PCL/PLA 30/70 blend degradation proceeds through five stages. These conclusions can be verified by the high correlation coefficient above 0.999. In order to eliminate complications and simplify discussion, it can be summarized that all stages of degradation for all PCL/PLA blends can be described alternately with either Cn or An kinetic model (Table 4). These results clearly indicate that the addition of PLA has negligible effect on the degradation kinetics of PCL and vice versa. These models belong to the same accelerating reaction type[42] and by this work proved to be the main kinetic models for characterization of the degradation process of the PCL/PLA blends. As mentioned before, contrary to the neat samples (PCL and PLA), PCL/PLA blends showed two more degradation stages, a fourth stage in the case of the blends 70/30 and 50/50 and fifth stage for blend 30/70. Finnally, Fn model denotes the end of the investigated degradation process, as in the case of neat PCL.

Based on the result of TG analysis (*section 3.1.*) it was concluded that degradation of natural biopolymer TPS takes place at least in three main steps. Hence, Fig. 4(b) clearly indicates four different areas of apparent activation energy for TPS sample. Contrary to other samples, in case of TPS the remaining mass of the sample depends on the heating rate (Fig. 6(a)) indicating a multi-step branched reaction path.[42]

Therefore, the best fit for TPS sample was obtained for the four-stage degradation mechanisms with branching reaction (Table 5). The apparent E of the first stage of thermal degradation of TPS obtained by Friedman method indicated that this stage might occur by diffusion mechanism (three-dimensional diffusion Ginstling–Brounstein type) (D4). At the first stage, at low conversion degrees on Friedman plot the experimental points showed a lower slope than the isoconversional lines,[39–42] which is in accordance with results of nonlinear regression. At the beginning of thermal degradation, a solid or a highly viscous melt system occurs and the mass transfer processes became rate determining. Hence, the decomposition products must diffuse to the surface to be evaporated, and diffusion of the volatile products toward the surface is the rate-controlling process in the first stage.[44] This is in accordance with the literature[27] and ultimately proves that the first stage consists of the release of moisture or water (rate-controlling process) from the TPS melt. The second stage of thermal degradation of TPS sample may be described by the Cn kinetic model with a higher E value. The second one is the main thermal decomposition stage and this stage triggers the rapid thermal decomposition with a large mass loss.[26] The second stage continues through two competitive processes, which represent the third and fourth stages. This is in accordance with the work of the Guaras et al.[27] where the main degradation process proceeded through the series of competitive reactions, which includes depolymerization (by the chain scission of the glycosidic linkage of polysaccharide). In this case the chain scission is described with An kinetic model through the third and fourth stage of TPS degradation.

Contrary, in case of the PLA/TPS and PCL/TPS (Fig. 6b) blends the remaining mass of the samples does not depend on the heating rate indicating a multi-step unbranched reactions with a four-stage and five-stage degradation mechanism, respectively. Likewise, the apparent E of thermal degradation of investigated PCL/TPS and PLA/TPS blends in the first stage are quite lower than in the case of the neat polymers (Table 4) and reveal diffusion character (D4) (Table 5). These results prove that the addition of TPS influences the thermal degradation and kinetics of PCL and PLA, respectively. However, the folowing stages of degradation for PCL/TPS and PLA/TPS blends can be described with either An or Cn kinetic model which is more-less consistent with the degradation mechanisms of the neat polymers (Table 4).

It can be concluded that TPS delays chain scission of PCL described with An kinetic model to higher conversions compared to neat PCL. Likewise, TPS addition also affects the PLA sample degradation pattern by shifting its nucleation process to higher conversion range.

Taking into account the above PLA/TPS and PCL/TPS blends could practically be described with three and four-stage process.

One of the main objectives of this work was to study non-isothermal degradation mechanisms and kinetics of the ternary PCL/PLA/TPS blends. The dependences of E on α evaluated at whole conversion range by means of FR method are shown in Fig. 4(c). The presence of four or more inflection points or maximums for investigated samples (Fig. 4(c)) indicates that degradation takes place at least in four main steps, which is consistent with TG and DTG results (Fig. 3). The remaining mass of all investigated ternary PCL/PLA/TPS blends does not depend on the heating rate indicating multi-step unbranched reactions,[42] in this case five-stage degradation mechanisms with consecutive reactions A → B → C → D → E → F (Fig. 6c and Table 6). The apparent activation energy of the first stage of thermal degradation of all investigated PCL/PLA/TPS samples reveals diffusion character (D4). Evidently, these results prove that the addition of TPS influences the thermal degradation and kinetics of PCL/PLA blends, at least in the first stage. However, the following stages of degradation for PCL/PLA/TPS blends can be described with either An or Cn kinetic model which is more-less consistent with the degradation mechanisms of the PCL/PLA blends (Table 4). However, one can notice that the third stage of degradation of PCL/PLA/TPS blend 30/70/30 was described by another (different) kinetic model known as expanded Prout-Tompkins equation (Bna). This shouldn't be suprissing since kinetic model

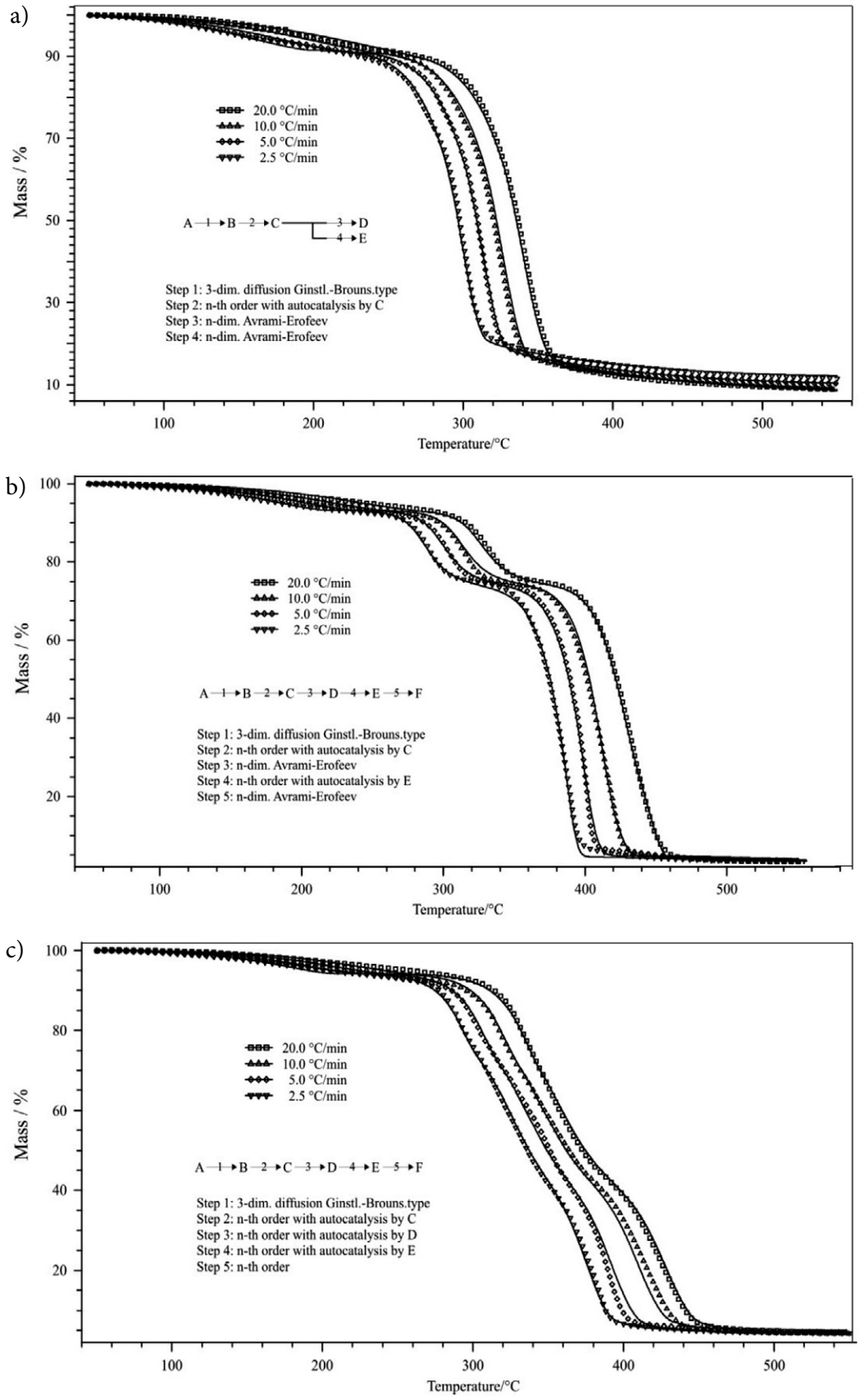

Fig. 6. Comparison of experimental data (points) and best fitted kinetic models (solid lines) calculated from multivariate nonlinear regression method for the TPS (a), PCL/TPS (b) and PCL/PLA/TPS (50/50/30) (c).

Table 5. The most probable kinetic models of thermal degradation of PCL/TPS and PLA/TPS blends according to F-test and correlation coefficient obtained by using multivariate non-linear regression analysis

Stage of reaction	Parameter	Sample PCL/TPS	PLA/TPS	TPS
Stage I	E_1 / kJmol^{-1}	64.1	78.1	56.3
	log A_1	3.5	5.1	2.9
	n	–	–	–
	Model	D4	D4	D4
Friedman	kJmol^{-1}	63.9–69.0	78.0–176.4	48.0–107.1
Stage II	E_2 / kJmol^{-1}	137.0	155.3	137.5
	log A_2	9.3	11.3	9.9
	n	2.3	0.6	0.6
	Model	Cn	Cn	Cn
Friedman	kJmol^{-1}	131.4–136.9	132.1–159.1	129.4–157.9
Stage III	E_3 / kJmol^{-1}	142.0	109.3	173.5
	log A_3	8.7	6.5	13.0
	n	1.8	0.6	0.1
	Model	An	Cn	An
Friedman	kJmol^{-1}	140.6–157.9	92.4–121.3	146.8–173.9
Stage IV	E_4 / kJmol^{-1}	101.0	147.8	65.4
	log A_4	5.4	12.5	1.6
	n	0.4	3.1	0.1
	Model	Cn	Fn	An
Friedman	kJmol^{-1}	94.5–134.9	146.7–291.4	0.0–279.2
Stage V	E_5 / kJmol^{-1}	216.3	–	–
	log A_5	14.1	–	–
	n	5.9	–	–
	Model	An	–	–
Friedman	kJmol^{-1}	136.4 – 266.4	–	–
Correlation coefficient, r^2		0.99986	0.99949	0.99985

Bna together with An and Cn models belongs to the same reaction types: accelerating one.[42] Moreover, Prout-Tompkins model belong to the autocatalysis reaction type as well as Cn model. The final stage of thermal degradation of all PCL/PLA/TPS blends occurs by the reaction of nth order (Fn). Based on the TG analysis, PCL/PLA 30/70 blend and PCL/PLA/TPS 30/70 blend showed the worst thermal stability. These results are perfectly consistent and prove that TPS addition did not affected thermal degradation and kinetics of PCL/PLA blends at higher conversion range.

Netzsch Thermokinetics 3.1 as a software module, used for the kinetic evaluation of the thermal measurements, in this case thermogravimetry, contains the isoconversional analysis, linear regression and multi-variate nonlinear regression method with advanced statistical analysis.[42] The basic principle consists of fitting a series of reaction model types[39–42] to experimental data. As a mean of verification, a method of least squares and F test method are used. However, one need to be aware of that softwares like Netzsch Thermokinetics used in this work give advantage to the quality of fit at the expense of the physical meaning of calculated kinetic models. It is possible and can be expected to happen that the mechanism with the best fit does not represent the real degradation process.[45] Hence, the apparent activation energy values obtained by isoconversional Friedman method correspond to ones calculated by a multivariate nonlinear regression method for all degradation stages confirming the fit of most probable kinetic models (Tables 4–6). The majority kinetic models can be forced to fit experimental data with a very high correlation coefficient, but only in case of *true* kinetic model *E* values similar to those obtained with isoconversional methods will be obtained. Hence, this criterion of similarity with isoconversional *E* values is crucial for selection of correct kinetic models.[45]

5. Conclusions

The main goal of this work was to provide new insights into kinetic analysis of the non-isothermal degradation of neat PCL, PLA and TPS and their investigated blends prepared by Brabender kneading chamber. For this purpose isoconversional Friedman method in combination with the multivariate nonlinear regression method,

Table 6. The most probable kinetic models of thermal degradation of PCL/PLA/TPS blends according to F-test and correlation coefficient obtained by using multivariate non-linear regression analysis

Stage of reaction	Parameter	PCL/PLA/TPS 70/30/30	PCL/PLA/TPS 50/50/30	PCL/PLA/TPS 30/70/30
Stage I	E_1 / kJmol^{-1}	76.2	74.1	88.0
	log A_1	5.2	4.8	6.5
	n	–	–	–
	Model	D4	D4	D4
Friedman	kJmol^{-1}	77.3–127.1	74.1–140.5	88.8–101.1
Stage II	E_2 / kJmol^{-1}	143.3	141.4	145.6
	log A_2	10.6	10.2	10.9
	n	1.4	0.6	1.4
	Model	An	Cn	An
Friedman	kJmol^{-1}	137.1–158.0	140.8–187.8	146.0–150.0
Stage III	E_3 / kJmol^{-1}	157.0	184.2	119.6
	log A_3	10.7	13.5	8.5
	n	2.0	1.6	1.5
	Model	Cn	Cn	Bna
Friedman	kJmol^{-1}	140.7–160.0	127.2–186.6	77.2 –160.2
Stage IV	E_4 / kJmol^{-1}	135.1	136.8	139.6
	log A_4	7.9	8.1	9.6
	n	4.4	0.6	1.4
	Model	An	Cn	An
Friedman	kJmol^{-1}	99.1–140.9	116.8–138.3	88.3–146.8
Stage V	E_5 / kJmol^{-1}	154.8	143.4	133.6
	log A_5	10.7	9.7	8.1
	n	1.2	2.5	0.6
	Model	Fn	Fn	Fn
Friedman	kJmol^{-1}	110.7–290.1	108.2–185.2	108.0–156.0
Correlation coefficient, r^2		0.99967	0.99979	0.99922

incorporated in Netzsch Thermokinetic 3.1 software, was utilized. Experimental data for kinetic computations was obtained by non-isothermal thermogravimetry in an inert atmosphere. Thermogravimetric analysis showed that thermal degradation of neat PCL sample proceed through two-stage degradation pattern, while neat PLA exhibited only single stage degradation. However, the degradation of low-cost natural TPS proceeds through three degradation stages. The addition of TPS affects the degradation of PCL and PLA and consequently their degradation starts at lower temperatures. Hence, TPS addition thermally destabilizes both, PCL and PLA, but notably the PCL sample. Likewise, binary blends are affected by TPS addition in the same manner.

Kinetic analysis was performed in a whole conversion range (0.0–1.0). Three-stage degradation mechanism, with consecutive reactions A → B → C → D, proved to be appropiate for fitting the experimental data and the assumed kinetic models for neat PCL and PLA samples. As expected, a four-stage and five-stage degradation mechanism is seen in the case of the PCL/PLA blends. It can be summarized that Cn and An kinetic model proved to be the main kinetic models, while Fn occured at the end of degradation process of all investigated PCL/PLA blends. Contrary to all others samples, TPS sample showed four-stage degradation mechanisms with branching reaction. The apparent activation energy of the first stage of thermal degradation of TPS revealed diffusion character followed by Cn and An reaction types. On the other hand, in case of the PLA/TPS and PCL/TPS blends four-stage and five-stage degradation mechanism with consecutive reactions is seen, respectively. The diffusion is the rate controlling process at the beginning of degradation process indicating that the addition of TPS influences the thermal degradation and kinetics of PCL and PLA, respectively. However, the following stages of degradation for PCL/TPS and PLA/TPS blends can be described with either An or Cn kinetic model which is more-less consistent with the degradation mechanisms of the neat polymers. In case of investigated ternary PCL/PLA/TPS samples, obtained five-stage degradation mechanisms with consecutive reactions proved to be the best option. Once again, at the beginning of degradation the addition of TPS influences the thermal degradation and kinetics of PCL/PLA binary blends. The following stages of degradation for PCL/PLA/TPS blends can be described with either An

or Cn kinetic model except for the third stage of degradation of blend 30/70/30 which was described by Bna kinetic model. Similarity of activation energies calculated by model fitting multivariate nonlinear regression method with those calculated by the isoconversional Friedman method together with statistical F test and correlation coefficient confirmed the accuracy of calculated kinetic models.

6. References

1. B. Imre, B. Pukánszky, *Eur. Polym. J*. **2013**, *49*, 1215–33. **DOI:**10.1016/j.eurpolymj.2013.01.019
2. P. Fajardo, J. T. Martins, C. Fuciños, L. Pastrana, J.A. Teixeira, A. A. Vicente, *J. Food. Eng.* **2010**, *101*, 349–56. **DOI:**10.1016/j.jfoodeng.2010.06.029
3. I. Simkovic, *J. Carb. Pol.* **2013**, *95*, 697–715. **DOI:**10.1016/j.carbpol.2013.03.040
4. J. F. Mendes, R. T. Paschoalin, V. B. Carmona, A. R. Sena Neto, A. C. P. Marques, J. M. Marconcini, L. H. C. Mattoso, E. S. Medeiros, J. E. Oliveira, *J. Carb. Pol.* **2016**, *137*, 452–58. **DOI:**10.1016/j.carbpol.2015.10.093
5. C. M. O. Müller, A. T. N. Pires, F. Yamashita, *J. Braz. Chem. Soc*. **2012**, *23*, 426–434.
6. R. Jayasekara, I. Harding, I. Bowater, G. B. Y. Christie, G. T. Lonergan, *Polym. Test.* **2004**, *23*, 17–27. **DOI:**10.1016/S0142-9418(03)00049-7
7. L. Yu, K. Dean, L. Li, *Prog. Polym. Sci.* **2006**, *31,* 576–602. **DOI:**10.1016/j.progpolymsci.2006.03.002
8. K. Van de Velde, P. Kiekens, *Polym. Test.* **2002**, *21*, 433–442. **DOI:**10.1016/S0142-9418(01)00107-6
9. M. A. Woodruff, D. W. Hutmacher, *Prog. Polym. Sci*. **2010**, *35*, 1217–1256. **DOI:**10.1016/j.progpolymsci.2010.04.002
10. L. S. Nair, C. T. Laurencin, *Progr. Polym. Sci.* **2007**, *32*, 762–798. **DOI:**10.1016/j.progpolymsci.2007.05.017
11. K. Chavalitpanya, S. Phattanarudee, *J. Egy. Pro.* **2013**, *34*, 542–48. **DOI:**10.1016/j.egypro.2013.06.783
12. J. W. Park, S. S. Im, S. H. Kim, Y. H. Kim, *Polym. Eng. Sci*. **2004**, *40*, 2539–2550. **DOI:**10.1002/pen.11384
13. U. Trommsdorff, I. Tomka, *Macromolecules* **1995**, *28*, 6138–6150. **DOI:**10.1021/ma00122a022
14. H. Li, M. A. Huneault, *J. Appl. Polym. Sci.* **2011**, *119*, 2439–4248. **DOI:**10.1002/app.32956
15. Z. Katančić, I. Grčić, Z. Hrnjak-Murgić, *Croat. Chem. Acta*. **2017**, *90*, 401–411. **DOI:**10.5562/cca3110
16. Z. Katančić, J. Travaš-Sejdić, Z. Hrnjak-Murgić, J. Jelenčić, *J. Elast. Plast*. **2014**, *46*, 233–252. **DOI:**10.1177/0095244312465301
17. D. Y. Wang, U. Gohs, N. J. Kang, A. Leuteritz, R. Boldt, U. Wagenknecht, G. Hinrich, *Langmuir* **2012**, *28*, 12601–12608. **DOI:**10.1021/la3025099
18. O. Persenaire, M. Alexandre, P. Degée, P. Dubois, *Biomacromolecules* **2001**, *2*, 288–294. **DOI:**10.1021/bm0056310
19. G. Sivalingam, G. Madras, *Polym. Degrad. Stab.* **2003**, *80*, 11–16. **DOI:**10.1016/S0141-3910(02)00376-2
20. Y. Aoyagia, K. Yamashita, Y. Doi, *Polym. Degrad. Stab*. **2002**, *76*, 53–59. **DOI:**10.1016/S0141-3910(01)00265-8
21. M. Hakkarainen, *Advan. Polym. Sci.* **2002**, *157*, 113–138. **DOI:**10.1007/3-540-45734-8_4
22. K. G. L. Ho, A. L. Pometto, P. N. Hinz, *J. Environ. Polym. Degrad*. **1999**, *83*, 83–92.
23. J. D. Badía, L. Santonja-Blasco, R. Moriana, A. Ribes-Greus, *Polym. Degrad. Stab*. **2010**, *95*, 2192–2199. **DOI:**10.1016/j.polymdegradstab.2010.06.002
24. I. C. McNeill, H. A. Leiper, *Polym. Degrad. Stab.* **1985**, *11*, 309–326. **DOI:**10.1016/0141-3910(85)90035-7
25. B. Janković, *Carbohydr. Polym*. **2013**, *95*, 621–629. **DOI:**10.1016/j.carbpol.2013.03.038
26. N. E. Wahyuningtiyas, H. Suryanto, E. Rudiyanto, S. Sukarni, P. Puspitasari, *JMES* **2017**, *1*, 69–77. **DOI:**10.17977/um016v1i22017p069
27. M. P. Guarás, V. A. Alvarez, L. N. Ludueña, *J. Polym. Res*. **2015**, *22*, 165. **DOI:**10.1007/s10965-015-0817-0
28. V. B. Carmona, A. C. Correa, L. H. Marconcini, C. Mattoso, *J. Polym. Environ*. **2015**, *23*, 83–89. **DOI:**10.1007/s10924-014-0666-7
29. J. Su, L. Chen, L. Li, *Afr. J. Biotechnol*. **2012**, *11*, 694–701. **DOI:**10.5897/AJB12.979
30. T. Ke, X. Sun, *Cereal. Chem*. **2000**, *77*, 761–768. **DOI:**10.1094/CCHEM.2000.77.6.761
31. B.Y. Shin, S. H. Jang, B. S. Kim, *Polym. Degrad. Stab.* **2011**, *51*, 826–834. **DOI:**10.1002/pen.21896
32. P. Sarazin, G. Li, W. J. Orts, B. D. Favis, *Polymer* **2008**, *49*, 599–609. **DOI:**10.1016/j.polymer.2007.11.029
33. H. L. Friedman, *J. Polym. Sci. C* **1963**, *6*, 183–195. **DOI:**10.1001/jama.1963.03700110135108
34. Đ. Ačkar, J. Babić, D. Šubarić, M. Kopjar, B. Miličević, *Carbohydr. Polym*. **2010**, *81*, 76–82. **DOI:**10.1016/j.carbpol.2010.01.058
35. S. Vyazovkin, A.I. Lesnikovich, *Thermochim. Acta*. **1990**, *165*, 273–280. **DOI:**10.1016/0040-6031(90)80227-P
36. S. Vyazovkin, N. Sbirrazzuoli, *Macromol. Rapid. Commun*. **2006**, *27*, 1515–1532. **DOI:**10.1002/marc.200600404
37. S. Vyazovkin, A.K. Burnham, J. M. Criado, L. A. Pérez-Maqueda, C. Popescu, N. Sbirrazzuoli, *Thermochim. Acta*. **2011**, *520*, 1–19. **DOI:**10.1016/j.tca.2011.03.034
38. S. Vyazovkin, K. Chrissafis, M. L. Di Lorenzo, N. Koga, M. Pijolat, B. Roduit, N. Sbirrazzuoli, J.J. Suñol, *Thermochim. Acta*. **2014**, *590*, 1–23. **DOI:**10.1016/j.tca.2014.05.036
39. M. Jakić, N. Stipanleov Vrandečić, M. Erceg, *J. Therm. Anal. Calorim*. **2016**, *123*, 1513–1522. **DOI:**10.1007/s10973-015-5096-9
40. M. Jakić, N. Stipanleov Vrandečić, M. Erceg, *J. Therm. Anal. Calorim*. **2017**, *127,* 663–674. **DOI:**10.1007/s10973-016-5768-0
41. M. Jakić, N. Stipanleov Vrandečić, M. Erceg, *Eur. Polym. J*. **2016**, *81*, 376–385. **DOI:**10.1016/j.eurpolymj.2016.06.024
42. NETZSCH Thermokinetics 3.1, Netzsch-Geraeteban GbmH, Software Manual.
43. N. M. N. Radhakrishnan, G. V. Thomas, N. M. R. Gopinathan, *Polym. Degrad. Stab*. **2007**, *92*, 189–196.

DOI:10.1016/j.polymdegradstab.2006.11.014
44. L. Byczynski, *Thermochim. Acta*. **2014**, *592*, 58–66.
DOI:10.1016/j.tca.2014.08.018
45. M. Erceg, I. Krešić, M. Jakić, B. Andričić, *J. Therm. Anal. Calorim*. **2017**, *127*, 789–797. **DOI:**10.1007/s10973-016-5413-y

Povzetek

Z uporabe neizotermične termogravimetrije v inertni atmosferi smo preučevali termično stabilnost poli(e-kaprolaktona) (PCL), polilaktične kisline (PLA), termoplastičnega škroba (TPS) in njihovih binarnih (PCL/PLA, PCL/TPS and PLA/TPS) ter ternarnih (PCL/PLA/TPS) mešanic. Vse preučevane mešanice smo pripravili z Brabender mešalnikom. PCL izkazuje dvostopenjsko termično razgradnjo, medtem ko je razgradnja PLA le enostopenjska. Po drugi strani pa poteka razgradnja samega TPS v treh stopnjah. Izkazalo se je, da dodatek PLA vpliva na razgradnjo PCL/PLA mešanic, kar kaže, da PLA destabilizira PCL. Dodatek TPS prav tako destabilizira oba, PCL in PLA, a še posebej PCL. Prav tako dodatek TPS destabilizira vse ternarne mešanice. Z uporabo izokonverzijske Friedman-ove metode in multivariante nelinearne regresije smo analizirali kinetiko. Analiza je pokazala kompleksnost termične razgradnje procesa posameznih polimerov pa tudi njihovih mešanic. Izračunali smo kinetične parametre (aktivacijsko energijo, predeksponentni faktor in kinetični model) vsake faze razgradnje za posamezne polimere in njihove mešanice.

Except when otherwise noted, articles in this journal are published under the terms and conditions of the Creative Commons Attribution 4.0 International License

DOI: 10.17344/acsi.2019.5677 *Acta Chim. Slov.* **2020,** *67,* 666–673
creative commons

Scientific paper

The c.3140-26A>G Variant of the *CFTR* Gene in Homozygous State Causes Mild Cystic Fibrosis – Overview of Longitudinal Clinical Data of the Patient Managed in our CF Center and Review of the Literature

Ana Kotnik Pirš,[1,2,*] Uroš Krivec[1] and Katarina Trebušak Podkrajšek[3,4]

[1] *Unit for Pulmonary Diseases, University Children's Hospital, University Medical Centre Ljubljana, Bohoričeva 20, 1000 Ljubljana, Slovenia*

[2] *Department for Pediatrics, Faculty of Medicine, University of Ljubljana, Bohoričeva 20, 1000 Ljubljana, Slovenia*

[3] *Institute of Biochemistry, Faculty of Medicine, University of Ljubljana, Vrazov trg 2, 1000 Ljubljana, Slovenia*

[4] *Clinical Institute for Special Laboratory Diagnostics, University Children's Hospital, University Medical Centre Ljubljana, Vrazov trg 1, 1000 Ljubljana, Slovenia*

** Corresponding author: E-mail: ana.kotnikpirs@kclj.si Tel.: +386 1 522 9257; Fax: + 386 1 522 4073.*

Received: 11-40-2019

Abstract

There are over 70.000 patients with cystic fibrosis (CF) in the world and numerous sequence variations in the *CFTR* gene have been reported but the clinical significance of all of them is still not known. There are currently 195 patients with the c.3140-26A>G (legacy name 3272-26A>G) variant in the *CFTR* gene listed in the European Cystic Fibrosis Society Patient Registry (ECFSPR) and only 4 are homozygous. We present longitudinal clinical data of one of these patients who is managed in our CF Center at the University Children's Hospital in Ljubljana and compare it with the patient data from the ECFSPR and the CFTR2 database in which additional 3 homozygous patients are described.

Moreover, the effect of the detected variant in the described patient was evaluated on the RNA level in nasal epithelial cells. The variant was shown to result in aberrant splicing introducing a frameshift and a premature termination codon while normal transcript was not detected. Alternative spliced mutant transcripts in other tissues or the presence of spliceosome-mediated RNA trans-splicing could explain the mild clinical presentation of patients with this variant in homozygous state.

1. Introduction

1. 1. Cystic Fibrosis

Cystic fibrosis (CF) is one of the most common inherited diseases in Caucasians. The incidence of the disease differs between populations with the highest incidence in Ireland 1:1.800 and the lowest in Finland with 1:20.000.[1] The incidence of CF in Slovenia is 1:4.500.[2] CF affects many organs. The lungs, gastrointestinal system, pancreas, liver, nose and sweat glands are most commonly involved. In 1989 the *CFTR* gene was discovered and variants of this gene were shown to be causative of CF.[3] In 2016 De Boeck and Amaral[4] updated the 1995 Zielinski and Tsui[5] classification of *CFTR* variants from 5 classes to 7 according to the mechanism by which they disrupt the synthesis, trafficking and function of the CFTR protein.

CF is diagnosed on the basis of clinical presentation, sweat testing and genetic confirmation.[6] To date there are over 44.000 sequence variants listed in the Ensembl genome browser 98 (https://www.ensembl.org/index.html; accessed in October 2019) in the *CFTR* gene, but not all of them are disease causing. In October 2019, more than 1800 CF causing variants located in the coding region, splice sites and the regulatory regions of the *CFTR* gene have been reported in the professional version of the Human Gene Mutation Database.[7]

Incredible progress has been made in the past 10 years in the treatment of CF. Regular therapy that improves

the symptoms which are a consequence of CFTR dysfunction has been a cornerstone of CF therapy since the implementation of pancreatic enzyme replacement therapy (PERT) shortly after the first description of CF by Dorothy Hansine Andersen in 1938.[8] New medications that influence the CFTR directly have been developed and implemented into regular therapy in 2014. New drugs named CFTR modulators work in two ways – as potentiators they enhance the function of the CFTR on the apical cell membrane in patients with milder *CFTR* variants in which the number or the function of the CFTR is affected. The second class are CFTR correctors – they influence the translation, folding and transport of the CFTR to the apical membrane in patients with severe variants in which there is only a small number of dysfunctional CFTR on the apical membrane or none at all. Potentiators (ivacaftor) are beneficial in patients with splicing variants as are the patients presented in our review, while a combination of potentiators and correctors, such as the recently approved triple combination of elexacaftor/ivacaftor/tezacaftor, is needed in patients with the classic severe *CFTR* variants such as the common p.Phe508del variant.[9]

Even with all the progress that has been made, most leading authorities in the field of CF believe that only close follow-up of patients can show the effect of a particular variant on a particular patient. It is widely accepted that two patients with the same disease causing variant can have an entirely different clinical progress of CF.[10,11]

1. 2. The c.3140-26A>G *CFTR* Variant

According to the CFTR1 and CFTR2 mutation databases and the so far published literature, the c.3140-26A>G variant (legacy name 3272-26A>G) is considered to be a mild variant of the *CFTR* gene.[12,13] Based on the combination of clinical and functional evaluation it is listed as a disease causing variant. According to CFTR1 and CFTR2, this variant does not need functional testing.[12–14] Most of the patients in the European Cystic Fibrosis Society Patient Registry (ECFSPR) and the CFTR2 database are compound heterozygotes, only 7 patients altogether are homozygotes. Therefore, it is believed that the variant is clinically important especially when in combination with another disease causing variant. Patients with this variant are likely to be pancreatic sufficient.[13] According to the published literature patients have mild signs of pulmonary disease. Some authors report that nasal polyps and chronic rhinosinusitis are more common.[15–17] After a thorough search through the National center for biotechnology information (NCBI) databases on this variant up to October 2019 no comprehensive clinical reports on homozygous patients with this variant have been published so far. We describe 12 year longitudinal clinical data on a homozygous patient with this variant managed in our CF Center.

2. Methods

All existing medical records were analyzed and clinical examinations were performed as recommended by the ECFS DNWG.[6] Evaluations were performed at the University Children's Hospital, University Medical Centre Ljubljana, Slovenia, where written informed consent was obtained from the parents prior to the study and Declaration of Helsinki protocols were followed.

Genomic DNA was isolated from blood leucocytes using the FlexiGene DNA Kit 250 (Qiagen, Germany) according to an established laboratory protocol. Initial mutation screening with Oligonucleotide Ligation Cystic Fibrosis Assay (Abbott, Germany) did not detect any of the 32 analyzed variants. Therefore, the *CFTR* coding region together with exon-intron boundaries were PCR amplified using in-house designed primers (Table 1) and sequenced with the BigDye Terminator v.3.1 Cycle Sequencing Kit and the 3500 Genetic Analyzer capillary electrophoresis system (Life Technologies, USA). Identified sequence variants were confirmed by sequencing of the additional independent PCR amplicon.

To demonstrate the effect of the identified c.3140-26A>G variant *in vivo*, total RNA of the patient, her mother and two unrelated healthy control subjects was purified from nasal epithelial cells using QIAzol Lysis Reagent and

Table 1. Primers used for the sequencing of the *CFTR* gene coding region and cDNA.

Exon nr.	Exon nr.	sequence 5'-3' (legacy)	Amplicon length (bp)	Cycling conditions
1	1	cagcactcggcttttaacct catacacacgccctcctctt	336	Annealing temperature:59 °C;
2	2	ttccatatgccagaaaagttga gccaccatacttggctccta	328	
3	3	ccttggatatacttgtgtgaatcaa tttggagttggattcatccttt	332	
4	4	aaacttgtctcccactgttgct ttaatttcagcatttatcccttacttg	543	

Exon nr.	Exon nr.	sequence 5'-3' (legacy)	Amplicon length (bp)	Cycling conditions
5	5	gcctagatgctgggaaataaaac ttactattatctgacccaggaaaactc	411	
6	6a	ttgttagtttctaggggtggaaga gcagtcctggttttactaaagtgg	305	
7	6b	gggatagagatagcatatggaatgag acaaacatcaaatatgaggtggaag	449	
8	7	catgctcagatcttccattcc ttttctatcttttcgcacattttt	431	
9	8	cattagtgggtaattcagggttg ggatgaaatccatattcacaaaga	497	
10	9	ggccatgtgcttttcaaact ctccaaaaataccttccagcac	389	
11	10	caagtgaatcctgagcgtga tccattcacagtagcttacccata	387	
12	11	tgaatttgtaaaatggacctatgga caattccagaaacagaatataaagca	533	
13	12	gtaatgcatgtagtgaactgtttaagg tttagcatgaggcggtgag	398	
16	14b	gcatgggaggaataggtgaa gcctgtggaggagctagga	305	
17	15	ccatttacatgtattggaaattcag acaaaaccacaggccctatt	398	
18	16	aatgcgtctactgtgatccaaac gacaggacttcaaccctcaatc	288	
19	17a	caatgtgaaaatgtttactcaccaac ttgggaacccagagaaacct	542	
20	17b	caaagaatggcaccagtgtg aaacaatggaaattcaaagaaatca	387	
21	18	tgatatgtgccctaggagaagtg cagtgaccctcaatttatctgtaatg	329	
22	19	aaagcccgacaaataaccaa tcaggctactgggattcacttac	443	
23	20	ttccactggtgacaggataaaa aaaaagacagcaatgcataacaaa	399	
24	21	tgatggtaagtacatgggtgtttc aaaatcatttcagttaggggtaggt	411	
27	24	ccagtttctgtccctgctct gtgtcctcaattccccttacc	439	
14	13	gagagaccccgaggataaatg tgcattctgtggggtgaaa	1066	Annealing temperature: 59 °C; elongation 1'
15	14a	accacaatggtggcatgaa ctccccactcagtctcctaaaa	791	
25, 26	22, 23	gaatgtcaactgcttgagtgtttt tgagtaaagctggatggctgt	1081	
cDNA: 18, 19, 20	cDNA: 16, 17a, 17b	ccaaacctcacagcaactca tggctaaagtcaggataataccaa	308	Annealing temperature: 58 °C

Qiagen RNAEasyMini Kit (Qiagen, Germany) according to the manufacturer's instructions. Reverse transcription of the total RNA was performed with random hexamers (Applied Biosystem, Foster City, CA, USA) and Super-Script II Reverse Transcriptase (Invitrogen, USA). *CFTR* cDNA was amplified with primer pair aligning exon 16 (forward primer) and exon 17B (reverse primer) (Table 1) and sequenced. Additionally, control amplification of the *TP53* gene was performed.

3. Results

3. 1. Clinical Characteristics

In 2007 a 12-year-old girl with unrelated parents and no family history of chronic disease was referred to our pediatric pulmonologist clinic because of persistent dry cough. The girl was born at term as the second child after a second uneventful pregnancy and birth. She was gaining weight and height well. At the age of 4 years she had a viral pneumonia without any complications. From the age of 9 she had nasal discharge, tearing and sneezing especially in the spring. From the age of 11 she was coughing almost persistently particularly when in contact with dust mite, after exertion and while laughing. She had no history of diarrhea, bulky, fatty feces, stomach discomfort or distention.

At the time of her first visit, the girl had a healthy appearance. Her weight, height and body mass index were on the 75th, 99th and 34th percentile for age and gender respectively. The clinical examination was normal beside a partially blocked nose. On spirometry the forced vital capacity (FVC) was 80% of predicted values for age, height and gender, the forced expiratory volume in one second (FEV1) 72% and the Tiffenau index 89. Asthma was excluded with a negative Metacholine Challenge Test. She had normal levels of exhaled and nasal nitric oxide (FeNO). Allergies were excluded with skin prick testing and blood IgE evaluation and her chest X-ray was normal.

She returned to our outpatient clinic after 3 years because of persistent and worsening cough. She had no other signs or symptoms of CF. Sweat testing was performed using the Gibson-Cooke method. The sweat chloride levels were elevated on two separate examinations: 56 and 57.7 mmol/l – the high end of intermediate levels. In concordance with the European recommendations for molecular genetic diagnosis of CF and CFTR-related disorders[17] molecular diagnostic testing was issued confirming the diagnosis of CF with identification of the c.3140-26A>G variant in homozygous state.

For the last 12 years, since the diagnosis was confirmed, the patient has been managed in our center for children and adolescents with CF according to the standards of care.[18] She is pancreatic sufficient with normal fecal elastase levels, has normal liver function tests and abdominal ultrasound, normal levels of A, D, E, K vitamins without supplementation, glucose metabolism and bone density. She has chronic rhinitis, but no nasal polyps. Her chest x-ray is normal therefore a chest CT has not been done yet. Her FEV1 is currently 70% predicted, with a yearly decline of 0.6% despite regular adherence to inhalatory hypertonic saline therapy and respiratory physiotherapy. *Pseudomonas aeruginosa* (Pa) has never been isolated from her sputum and her serum anti-Pseudomonas aeruginosa IgG antibodies are low.

3. 2. Genetic Analyses

Sequencing in the patient revealed the c.3140-26A>G *CFTR* variant (reference sequence NM_000492.3) in homozygous state; no additional disease causing variants were identified in the coding region or in the exon/intron boundaries. Parents were shown to be carriers of the same variant in heterozygous state. *CFTR* mRNA analysis showed an aberrant splicing pattern with 25 nucleotides inserted between exons 17A in 17B in the patient but not in her mother nor in healthy control subjects. The 25-nucleotide insertion was matching the last 25 nucleotides of intron 17a (namely TGTTTTCTATGGAAATATTTCACAG) as previously reported.[15]

3. 3. Comparison of Clinical Data of Patients with the c.3140-26A>G *CFTR* Variant Listed in the ECFSPR and the CFTR2 Database and Our Patient

After the c.3140-26A>G variant was confirmed in our patient, clinical data on patients with this variant was requested from the ECFSPR according to standard regulations. There are 195 patients with the c.3140-26A>G mutation currently listed in the ECFSPR. 191 (97.95%) are heterozygous and 4 (2.05%) homozygous for this variant. At the last data review, all 4 ECFSPR patients were alive. 2 were younger and 2 older than 18 years of age. Their mean age was 20 years, the youngest 3.3 and oldest 34.3 years old. Their mean age at diagnosis was 6 years, the earliest at 3 months and the latest at almost 13 years of age. 2 were diagnosed before the first year of life, none before the first month.

Their lung function described as mean percent of predicted FEV1 was 77.23% for the patient younger than 18 years and 89.77% for the 2 patients older than 18 years. The lung function of the 3 year old could not be measured yet by standard spirometry.

Patients over 18 years of age had a mean BMI of 26.22 kg/m2 and the BMI expressed with the mean Z score for the two patients under 18 was –0.18, with a minimum of -1.13 and maximum of 0.76.

Only one patient needed pancreatic enzyme replacement therapy, the other 3 were pancreatic sufficient. 1 patient was chronically colonized with *S. aureus* and proba-

Table 2. Comparison of clinical data of patients with the c.3140-26A>G *CFTR* variant in homozygous state listed in the ECFSPR with the data of our patient.

Clinical variable	ECFSPR patients (Total number: 4)			Our patient
	mean	minimum	maximum	
Age (years)	20	3.3	34.4	24
Age at diagnosis (years)	6	0.25	12.91	16
FEV1 (percent predicted) <18 years	77.23	77.23	77.23	/
FEV1 (percent predicted) >18 years	89.77	85.25	94.3	88
BMI (Z score) < 18 years	–0.18	–1.13	0.76	
BMI (kg/m2) > 18 years	26.22	22.77	29.67	20
	no	yes	missing data	
Use of pancreatic enzymes	3	1	0	no
Chronic *Pseudomonas aeruginosa*	3	0	1	no
Chronic *Staphylococcus aureus*	3	1	3	yes

Table 3. Clinical features of the c.3140-26A>G homozygous patients as listed in the CFTR2 mutation database, compared to all listed CF patients with 2 disease causing mutations and to our patient.

Clinical Feature	Average of all patients homozygous for c.3140-26A>G	Our patient	Average of all patients with 2 disease causing mutations in the database
Sweat chloride value (mmol/l)	90	57	96
Lung function (FEV1% predicted)	<10 years: insufficient data 10–20 years: insufficient data >20 years: insufficient data	70%	<10 years: 63-124% 10–20 years: 42–118% >20 years: 25–104%
Pancreatic status	33% (2 patients) insufficient	sufficient	85% (66.394 patients) insufficient
Pseudomonas aeruginosa chronic colonization	33% (2 patients)	No	55% (34.460 patients) chronically colonized
Average age in years	16	24	20

bly none with *P. aeruginosa*, but the information on Pa is missing for one patient. The clinical data are summarized in Table 2.

Clinical features of homozygous patients with the c.3140-26A>G variant were compared to all the other CF patients with 2 CF causing variants listed in the CFTR2 mutation database and to the here reported patient. The data are presented in Table 3.

4. Discussion with Review of the Published Literature

A review of the literature in search for the variants characteristics in terms of disease severity was done. A PubMed search using keywords 3272-26A>G or c.3140-26A>G and cystic fibrosis yielded 6 articles. References of relevant articles were analyzed and further 7 articles that mention the mutation were identified. The found references in chronological order are shown in Table 4.

To our knowledge, this is the first longitudinal clinical report on a patient with this variant in homozygous state. According to the so far published literature, c.3140-26A>G is a rare variant so far detected mostly in compound heterozygosity with other disease causing variants. Patients usually have mild disease even when this mutation is paired with a severe disease causing variant. The patients are mostly pancreatic sufficient, have good lung function are on average older and diagnosed at an older age than patients with classic CF variants, but have elevated sweat chloride levels and a higher incidence of nasal polyps.[15–17, 20–23]

The largest number of patients with c.3140-26A>G in heterozygous state was presented in a European study by Amaral et al in 2001.[14] The study included 60 patients from 6 European countries: France, Spain, Greece, Germany, Portugal and Belgium. The mean age of the patients at the time of the study was 20.5 (SD 17.5) years. 44 of the patients had the c.3140-6A>G and the p. Phe508del (c.1521_1523delCTT) combination of disease causing alleles and 16 had c.3140-26A>G in combination with another CF causing variant. Their mean age at diagnosis was 8 (SD 20) years, sweat test chlorides 99.5 (SD 24.7) mEq/l and FEV1 87 (SD 47) % predicted. 19 had nasal polyposis

Table 4. Clinical characteristics of the in the published literature found reports of patients with the c.3140-26A>G mutation and chronological characterization of the variant.[14-16, 20-23]

First author, year of publication	Number of patients with c.3140-26A>G	Genotype: c.3140-26A>G in combination with	Phenotype						Variant characterization
			Mean age	Mean age at diagnosis	Mean sweat chloride test	Pancreatic function	Nasal polyps	Mean FEV1	
Fanen et al, 1992 [23]	1	p.W846X	No data	No data	No data	Sufficient	No data	Mild pulmonary disease	
Kanavakis et al, 1995 [16]	3	2: p.Phe508del 1: unknown	11 years (SD 7)	9.5 years (SD 5)	105mEq/l (SD 7.6)	All pancreatic sufficient	2/3	108% (SD 22.6)	Proposition of the splicing defect.
Beck et al 1999 [15]	5	5: p. Phe508del	18 years (SD 10.4)	9 years (SD 13.9)	103mEq/l (SD 7.3)	4/5 sufficient, 1/4 mild insufficiency	4/5	68% (SD 24.5)	mRNA confirmation of the splicing defect. Mutated protein detected on the epithelial cell membrane.
Amaral et al, 2001 [14]	60	44: p. Phe508del 16: other disease causing	20,5 years (SD 17.5)	8 years (SD 20)	99,5mEq/l (SD 47)	39 sufficient, 16 insufficient	19/60	87% (SD 47)	Additional report of the mutation.
Feldmann et al, 2003 [20]	2	2: p. Phe508del	27 years (SD 10)	No data	62.5mEq/l (SD 2)	No data	No data	No data	Additional report of the mutation.
Storm et al, 2007 [21]	11	10: p. Phe508del 1: c.1717-1G>A	Clinical phenotypes milder than p. Phe508del homozygotes						Additional report of the mutation.
Jung et al, 2011 [22]	1	1: p.Phe508del	No data						Additional report of the

and 18 Pa colonization.[14] The other authors reported patients from individual countries or centers and therefore had lower numbers of described patients, all patients were heterozygotes for the c.3140-26A>G variant.

There are two ways to assess the severity of a mutation – on the basis of a patient's clinical status and on a molecular basis. The first is the most reliable but requires long term follow-up. The second can be used as a prediction tool for an approximate evaluation of the probable clinical findings to come. Based on the found data in the literature and the clinical status of our patient we were interested if there is a difference in mutated mRNA translation between hetero and homozygotes for the c.3140-26A>G mutation compared to healthy controls.

On the molecular level, the effect of a gene variant can be studied by observing its influence on RNA translation and protein synthesis. Splicing is a process in which a premature mRNA transcript is formed into mature mRNA. In this process introns are removed and exons which are the coding nucleotide sections within a gene are joined together into mature mRNA which is then translated into a protein.[24] Errors can occur in splicing, as in all processes. There are presumed to be three classes of variants that effect splicing: variants of a splice site that cause loss of function of that site, variants that cause a disruption of the reading frame and displacement of a splice site that causes shorter or longer exons to be formed.[24] The HGMD professional 2019.3 currently reports more than 240 different intronic disease causing variants in the *CFTR* gene. 6 of them are located in the 3' splice site of intron 17A, among them 4 including the here reported c.3140-26A>G in a polypyrimidine tract located between the branch site and the basic acceptor splice site.[7] The c.3140-26A>G *CFTR* variant was first described by Fanen et al in 1992 and was suspected to be a variant that effects mRNA splicing.[23] Additional reports followed in 1995 by Kanavakis et al and in 1999 by Beck et al where aberrant splicing was demonstrated on the mRNA level.[16,15] The c.3140-26A>G variant

results in an insertion of 25 nucleotides of intron 17a of the *CFTR* gene as confirmed in our patient and causes a frameshift and a premature stop codon in exon 17b.[15] The same insertion in mRNA was present in here reported patient with, They proposed that some of the alternative transcript reaches the cell membrane as a modified CFTR protein. Because of the location of the insertion the alternative protein retains the wild-type CFTR sequence until amino acid residue 1046 which could enable it to have some single chloride conductance remaining. It was proposed that the 36 amino acid extension caused by the insertion can have three different effects on CFTR folding, trafficking and function: a change in stability, missed interaction with PDZ-domain proteins with a probable influence on CFTR stability, chloride conductance regulation and its localization or that the protein would not fold correctly.[16]

In 2001 Amaral et al reported that the alternative acceptor splicing site in intron 17a competes with normal *CFTR* mRNA.[14] Therefore, the remaining normal mRNA is normally processed and leads to some remaining normal protein at the cell membrane. It was postulated that the remaining normal *CFTR* mRNA still existing in patients with the c.3140-26A>G variant even when paired with a severe disease causing mutation lessens the severity of CF disease. It was hypothesized that the c.3140-26A>G variation on both alleles would avoid CF totally.[15] This was not confirmed in our study, since the homozygous patient had only mutated splicing pattern present in nasal epithelial cells and normal transcript was not detected. Furthermore, in the analysed heterozygous mother, only normal splicing was present, probably due to preferential transcription of the normal allele. Of course, *CFTR* expression is tissue specific and the splicing pattern was analysed in nasal epithelial cells, where *CFTR* gene is known to be expressed in lower levels.[25,26] A mild disease presentation in patients carrying nonsense mutations was previously explained by the presence of alternative spliced mutant transcripts.[26] This could also be the case in the c.3140-26A>G variant, since we have studied only a selected part of the mRNA transcript in nasal epithelial cells. The other possibility is a presence of spliceosome-mediated RNA trans-splicing already proven to functionally correct endogenous CFTR mutant protein.[28]

5. Conclusions

Incredible progress has been made in the past 5 years in the treatment of CF. New gene variant specific medication with CFTR modulators has improved the life and outcome of patients with specific gene defects. Currently numerous *CFTR* variants are known, but the clinical significance of most of them remains trivial. Case reports on patients with rare *CFTR* variants are therefore beneficial for the prediction of the clinical course of the disease in other patients with the same variant. 12 year longitudinal data on a CF patient with the c.3140-26A>G variant in homozygous state that is presented in this report adds new knowledge. In our study, aberrant splicing of the mRNA due to the c.3140-26A>G variant was shown, probably resulting in the mild clinical presentation of the disease. Only speculations can be made on the future quality of life of our patient, but based on the current data we might predict a good outcome especially with the implementation of new variant specific therapy into everyday patient care.

Acknowledgements

We would like to thank the people with CF and their families for consenting to their data being included in the European Cystic Fibrosis Society Patient Registry, the ECFSPR for providing access to patient data and the individual country representatives for allowing the use of data for publication (www.ecfs.eu/projects/ecfs-patient-registry/steering-committee).

6. References

1. P. M. Farrell, B. J. Rosenstein, T. B. White, F. J. Accurso, C. Castellani, G. R. Cutting, et al, *The Journal of Pediatrics*. **2008**, *2:* S4–S14. **DOI:**10.1016/j.jpeds.2008.05.005
2. A. Kotnik Pirs, M. Praprotnik, K. Trebusak Podkrajsek, K. Seme, M. Aldeco, D. Lepej, J. Brecelj, N. Bratanic, U. Krivec, *Slov. Pediatr.* **2014**, *21*: 164–171.
3. B. Kerem, J. M. Rommens, J. A. Buchanan, D. Markiewicz, T. K. Cox, A. Chakravarti, M. Buchwald, L. C. Tsui, *Science.* **1989**, *245*: 1073–1080. **DOI:**10.1126/science.2570460
4. K. De Boeck, M. D. Amaral. *Lancet Respir. Med*. **2016**, 4(8): 662-674. **DOI:**10.1016/S2213-2600(16)00023-0
5. J. Zielinski, L. C. Tsui. *Annu. Rev. Genet*. **1995**, 29: 777–807. **DOI:**10.1146/annurev.ge.29.120195.004021
6. K. De Boeck, M. Wilschanski, C. Castellani, C. Taylor, H. Cuppens, J. Dodge, M. Sinaasappel, Diagnostic Working Group, *Thorax*. **2006**, *61*: 627–635. **DOI:**10.1136/thx.2005.043539
7. HGMD professional 2019.3, http://www.hgmd.cf.ac.uk/ac/index.php
8. D. H. Andersen. *Am. J. Dis. Childhood*. **1938**, 56, 344–399. **DOI:**10.1001/archpedi.1938.01980140114013
9. R. S. Pettit, C. Fellner. *P T.* **2014**, 39(7), 500–511. **DOI:**10.1038/nj7510-500a
10. K. De Boeck, N. Derichs, I. Fajae, H. R. de Jonge, I. Bronsveld, I. Sermet, F. Vermeulen, D. N. Sheppard, H. Cuppens, M. Hug, P. Melotti, P. G. Middleton, M. Wilschanski on behalf of the ECFS Diagnostic Working Group and EuroCareCF WP3 Group on CF diagnosis. *J Cyst. Fibros.* **2011**, *10(Suppl 2),* S53–S66. **DOI:**10.1016/S1569-1993(11)60009-X
11. C. Castellani, H. Cuppens, M. Macek Jr, J. J. Cassiman, E. Kerem, P. Durie, et al. *J Cyst. Fibros.* **2008**, *7*, 179–196.
12. Cystic Fibrosis Mutation Database. Available at http:// www.genet.sickkids.on.ca

13. The Clinical and Functional Translation of CFTR (CFTR2); Available at http://cftr2.org
14. M. D. Amaral, P. Pacheco, S. Beck, et al. *J Med. Genet.* **2001**, 38, 777–782.
15. S. Beck, D. Penque, D. Garcia, A. Gomes, C. Farinha, L. Mata, S. Gulbenkian, K. Gil-Ferreira, A. Duarte, P. Pacheco, C. Barreto, B. Lopes, J. Cavaco, J. Lavinha, M. D. Amaral. *Human mutation* **1999**, *14*, 133–144. **DOI:**10.1002/(SICI)1098-1004(1999)14:2<133::AID-HUMU5>3.0.CO;2-T
16. E. Kanavakis, M. Tzetis, T. Antoniadi, J. Trager-Synodinos, C. Kattamis, S. Doudounakis, G. Adam. *J Med. Genet.* **1995**, *32*, 406–407. **DOI:**10.1136/jmg.32.5.406
17. P. R. Sosnay, K. R. Siklosi, F. Van Goor, K. Kaniecki, H. Yu, N. Sharma, A. S. Ramalho, M. D. Amaral, R. Dorfman, J. Zielenski, D. L. Masica, R. Karchin, L. Millen, P. J. Thomas, G. P. Patrinos, M. Corey, M. H. Lewis, J. M. Rommens, C. Castellani, C. M. Penland, G. R. Cutting. *Nat. Genet.* **2013**, *45*, 1160–1167. **DOI:**10.1038/ng.2745
18. E. Dequeker, M. Stuhrmann, M. A. Morris, T. Casals, C. Castellani, M. Claustres, H. Cuppens, M. des Georges, C. Ferec, M. Macek, P. F. Pignatti, H. Scheffer, M. Schwartz, M. Witt, M. Schwarz, E. Girodon. *Eur J Hum. Genet*. **2009**, *17*, 51–65. **DOI:**10.1038/ejhg.2008.136
19. A. R. Smyth, S. C. Bell, S. Bojcin, M. Bryon, A. Duff, P. Flume, N. Kashirskaya, A. Munck, F. Ratjen, S. J. Schwarzenberg, I. Sermet-Gaudelus, K. W. Southern, G. Taccetti, G. Ullrich, S. Wolfe. *J Cyst. Fibros*. **2014**, *13 (Suppl 1),* S23–S42. **DOI:**10.1016/j.jcf.2014.03.010
20. D. Feldman, R. Couderc, M. P. Audrezet, C. Ferec, T. Bienvenu, M. Desgeorges, M. Clusters, H. Mittre, M. Blayau, D. Bozon, et al. *Hum. Mutat*. **2003**, *22*, 340. **DOI:**10.1002/humu.9183
21. K. Storm, E. Moens, L. Vits, H. De Vlieger, G. Delaere, M. D'Hollander, W. Wuyts, M. Biervliet, L. Van Schil, K. Desager, M. M. Nothen. *J Cyst. Fibros*. **2007**, *6*, 371–375. **DOI:**10.1016/j.jcf.2006.10.013
22. H. Jung, C. S. Ki, W. J. Koh, K. M. Aho, S. I. Lee, J. H. Kim, J. S. Ko, J. K. Seo, S. L. Cha, E. S. Lee, J. W. Kim. *KJLM*. **2011**, *31*, 21924. **DOI:**10.3343/kjlm.2011.31.3.219
23. P. Fanen, N. Ghanem, M. Vidaud, C. Besmond, J. Martin, B. Costes, F. Plassa, M. Goossens. *Genomics*. **1992**, *13*, 770–776. **DOI:**10.1016/0888-7543(92)90152-I
24. K. H. Lim, L. Ferraris, M. E. Filloux, B. J. Raphael, W. G. Fairbrother. *Proc. Natl. Acad. Sci. USA*. **2011**, *108*, 11093–11098. **DOI:**10.1073/pnas.1101135108
25. B. C. Trapnell, C. S. Chu, P. K. Paakko, et al. *Proc. Natl. Acad. Sci. USA*. **1991**, *88*, 6565–6569.
26. N. L. White, C. F. Higgins, A. E. Trezise. *Hum. Mol. Genet*. **1998**, *7*, 363–369.
27. A. Hinzpeter, A. Aissat, E. Sondo, C. Costa, N. Arous, C. Gameiro, N. Martin, A. Tarze, L. Weiss, A de Becdelievre, et al. *PLoS Genet*. **2010**; 6. pii: e1001153. **DOI:**10.1371/journal.pgen.1001153
28. X. Liu, Q. Jiang, S. G. Mansfield, M. Puttaraju, Y. Zhang, W. Zhou, J. A. Cohn, M. A. Garcia-Blanco, L. G. Mitchell, J. F. Engelhardt. *Nat. Biotechnol*. **2002**, *20*, 47–52. **DOI:**10.1038/nbt0102-47

Povzetek

Na svetu ima več kot 70.000 bolnikov cistično fibrozo (CF). Znane so številne variante v genu *CFTR*, vendar klinični pomen vseh še ni jasen. Trenutno je v Registru bolnikov Evropskega združenja za cistično fibrozo (ECFS Register) 195 bolnikov z varianto c.3140-26A>G (tradicionalna oznaka 3272-26A>G), med njimi so samo 4 homozigoti. V prispevku predstavljamo 12 letne longitudinalne podatke enega izmed njih in sicer bolnice, ki se vodi v Centru za CF na Pediatrični kliniki, UKC Ljubljana, in njihovo primerjavo s podatki bolnikov s to varianto iz ECFS Registra in baze podatkov CFTR2. Vpliv spremembe, opredeljene pri tej bolnici, smo ocenili tudi na nivoju RNA v celicah nosnega epitela. Varianta povzroči spremenjeno izrezovanje intronov, kar vodi v premik bralnega okvirja in uvedbo prezgodnjega terminacijskega kodona. Pri tem normalen prepis pri bolnici ni bil prisoten. Vzrok za blago klinično sliko CF pri bolnikih homozigotnih za opisano varianto bi lahko bilo alternativno izrezovanje intronov v drugih tkivih.

Except when otherwise noted, articles in this journal are published under the terms and conditions of the Creative Commons Attribution 4.0 International License

DOI: 10.17344/acsi.2020.5863 *Acta Chim. Slov.* **2020,** *67,* 674–681
creative commons

Scientific paper

Active Forces of Myosin Motors May Control Endovesiculation of Red Blood Cells

Samo Penič,[1,*] Miha Fošnarič,[2] Luka Mesarec,[1] Aleš Iglič[1,3,4] and Veronika Kralj-Iglič[2,4]

[1] *Faculty of Electrical Engineering, University of Ljubljana, Tržaška cesta 25, SI-1000 Ljubljana*

[2] *Faculty of Health Sciences, University of Ljubljana, Zdravstvena pot 5, SI-1000 Ljubljana*

[3] *Faculty of Medicine, University of Ljubljana, Zaloška 9, SI-1000 Ljubljana, Slovenia*

[4] *Institute of Biosciences and Bioresources, National Research Council, Pietro Castellino 111, 80131 Napoli, Italy*

** Corresponding author: E-mail: samo.penic@fe.uni-lj.si, Tel: +386 14768 822*

Received: 01-27-2020

Abstract

By using Monte Carlo (MC) simulations, we have shown that the active forces generated by (NMIIA) motor domains bound to F-actin may partially control the endovesiculation of the red blood cell (RBC) membrane. The myosin generated active forces favor pancake-like (torocyte) RBC endovesicles with a large flat central membrane region and a bulby periphery. We suggest that the myosin generated active forces acting on the RBC membrane in the direction perpendicular to the membrane surface towards the interior of the RBC may influence also other RBC shape transformations and the stability of different types of RBC shapes and should be therefore considered in the future theoretical studies of the RBC vesiculation and shape transformations.

Keywords: Myosin generated active forces; Monte Carlo simulations; endovesiclulation; intrinsic curvature; red blood cell

1. Introduction

A biological membrane forms a physical boundary between the inner volume of a biological cell and the external medium, as well as, within the cell, between the lumens of intracellular organelles and cytosol. The main building block of the biological membrane lipid bilayer consists of two monolayers of phospholipid molecules.[1] In the lipid bilayer, other constituents like membrane proteins are intercalated.[2,3] The transmembrane proteins are the pining points for membrane skeleton or/and cytoskeleton.[4] Furthermore, some of the inclusions in the lipid bilayer, like proteins or nanoparticles, can impose local curvature of the membrane,[5–9] forcing the membrane to locally and/or globally adapt its shape.[10–17] The phase separation of membrane inclusions (nanodomains) is an important mechanism that may induce the local changes of membrane curvature and is therefore the driving force for transformations of the cell shape.[17–19] The spontaneous phase separation of membrane proteins, driven by the forces of actin polymerization and cell-substrate adhesion, was in a quantitative manner predicted for the first time by Veksler and Gov.[20]

Besides the membrane inclusions' driven membrane shape changes, other mechanisms also determine the membrane cell shape. Among them, constant energy consuming forces are acting in the living cell.[17] In experiments, the cells or lipid bilayer vesicles (as model systems) may also be deformed by extracellular forces due to pressure differences,[21] stretching[22] and fluid flow.[23–25] An external force to the membrane surface can also be experimentally generated, for example by a cantilever of the atomic force microscope.[26]

The cell membrane resistance to the shape changes depends on its mechanical properties[27] mainly governed by the composition of the membrane. The dynamic response of the cell membrane shape to the force[17] is important for different cell functions that range from adhesion

and migration to division, differentiation, and cell death.[28] Therefore, the membrane mechanical properties are of great scientific interest. Consequently, new theoretical approaches for deeper understanding of the mechanisms that rule the cell's functions are constantly being developed.

In red blood cells (RBC), besides the lipid bilayer also the membrane skeleton (spectrin-F-actin network attached to the inner lipid layer)[29] plays an important role in cell shape determination and cell transformations.[30–32] It has been shown that equilibrium RBC shapes that correspond to the minimal membrane elastic energy, should take into account the local and non-local bending energy[27,33,34] and the elastic energy of the membrane skeleton.[30–32,35] The shear deformation of the membrane skeleton plays an essential role in the stability of echinocytic RBC shapes.[30,31] Additionally, cytoskeleton induced protrusions in lipid membranes has been theoretically explained by the interplay between the elasticity of the membrane lipid bilayer and the membrane skeleton – firstly for axisymmetric shapes[36,37] and later also for non-axisymmetric shapes.[38]

Non-local bending energy[27,33,39,40] depends on the change in the relaxed areas of the two lipid layers of the membrane bilayer.[41] Decreasing the difference between the relaxed areas of the outer layer and the inner lipid layer, favors the concave local membrane shape, i.e. the inward bending of the membrane.[32,35,41] On the other hand, increasing the difference between the relaxed areas of the outer and inner membrane layers promotes the formation of convex local shape, i.e. the outward bending.[31,35,42]

It was shown that exogenously added amphiphiles predominantly bound in the outer lipid layer induce the transformation of the discoid RBC into the spiculated echinocytic RBC, while amphiphiles predominantly bound in the inner lipid layer induce the transformation into invaginated stomatocytic shapes.[43] When RBCs are incubated with high sublytic concentrations of amphiphiles, the microexovesiculation starts.[42,44,45] The amphiphile induced RBC microexovesicles are highly depleted in the membrane skeleton[37] suggesting that a local disruption of the interactions between the membrane skeleton and the membrane bilayer occurred prior to micro- or nano-exovesiculation.[45]

In RBCs, most types of amphiphiles induce spherical microexovesicles that are formed from sphere-like membrane buds and are free of the membrane skeleton. On the other hand, there are also anisotropic amphiphiles which induce the growing of tubular membrane buds and the release of stable tubular microexovesicles.[44,45] The tubular budding and vesiculation of the RBC membrane can be theoretically explained by deviatoric membrane properties due to the in-plane orientational ordering of the anisotropic membrane inclusions induced by intercalated anisotropic amphiphiles.[44,45] The deviatoric properties of the membrane[12,15,42,45–52] may explain the experimentally observed tubular membrane protrusion without the application of the local force.[16,42,45,51,53,54] For isotropic membrane, the application of the local force is necessary to theoretically predict the tubular membrane protrusions.[16,54,55]

It was reported[44,56] that some amphiphilic molecules can induce large membrane invaginations (i.e. stomatocyte RBC shape) as shown in Figure 1C and endovesicles in RBCs. By means of transmission electron microscopy (TEM) and confocal laser scanning microscopy using fluorescent markers, it was also observed that many stomatocytogenic amphiphiles (for example chlorpromazine hydrochloride) can induce in RBCs with large concentrations of amphiphiles small spherical endovesicles (Figure 1D).[44,56,57] On the other hand, the stomatocytogenic detergent polyethyleneglycol dodecylether ($C_{12}E_8$) induces large endovesicles with a unique ring-like toroidal shape joined with a central flat membrane segment, i.e. flat membrane structures with a bulby periphery called also torocyte endovesicles (Figure 1 A,B and E)[57] with the shape very similar to the shape of Golgi bodies.[58] It was proposed that the observed RBC torocyte endovesicles were formed in a process in which an initially stomatocytic RBC invagination loses volume while maintaining a large surface area.[57,59]

The results of theoretical modeling indicated that torocyte RBC endovesicles can be mechanically stabilized by non-homogeneous lateral distribution of laterally mobile anisotropic membrane inclusions, like for example by anisotropic detergent-membrane component complexes.[58,59] It was further shown in 2019 that the mechanical stability of torocyte (pancake-like) closed membrane vesicle shapes can be explained also by the coupling of the curved isotropic membrane inclusions and active (cytoskeletal) forces.[55] Until recently,[60] it was believed that the active forces are absent in the mechanisms of the determination of the RBC shape and vesiculation, as discussed above. It has been shown in 2018 that nonmuscle myosin IIA (NMIIA) motor domains may generate tension in spectrin-F-actin also in a 2-dimensional RBC membrane skeleton and in this way partially control the RBC shape.[60] The role of NMIIA contractility in generating tension in the RBC network and partially controlling the RBC shape was thus in the past completely neglected, until recently.[60] The length of NMIIA filament is around 200 nm.[60]

The influence of NMIIA bipolar filaments, associated with a 2-dimensional RBC membrane skeleton can be thus described by the local force acting on the RBC membrane in the direction to the interior of the RBC. In the present paper, we shall study the interplay between the laterally mobile membrane inclusions and the inward-oriented local forces of the NMIIA bipolar filaments in the formation of torocyte endovesicles (flat membrane structures with a bulby periphery). The present study was motivated by the results presented in references 44, 56, 57, 59, 60, but it is not entirely/directly connected to the experimental and theoretical results presented in these articles. For the sake

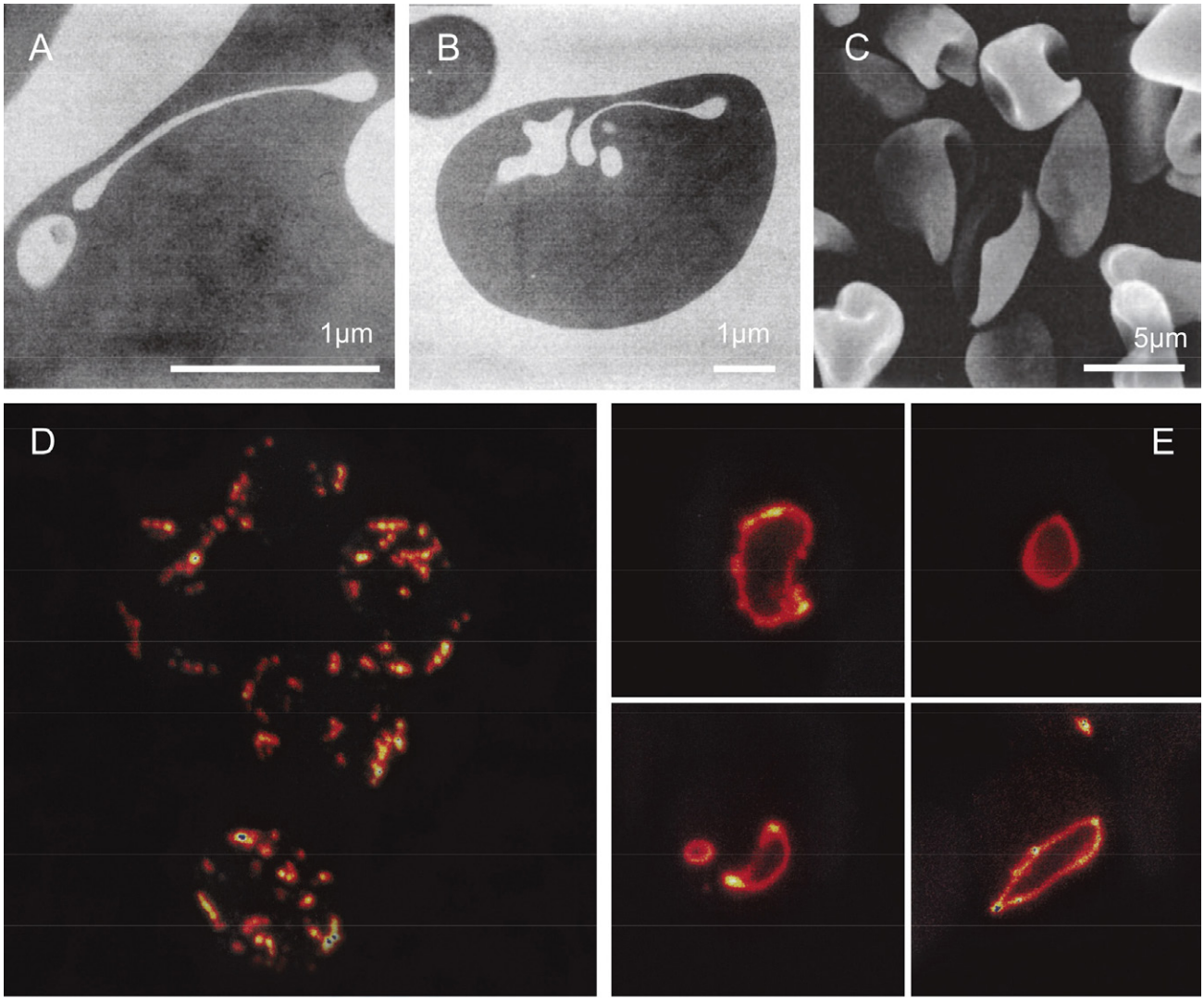

Figure 1: TEM and SEM micrographs showing stomatocytic human RBC with plate-like torocytic invaginations/endovesicles with a bulby periphery (panels A and B) formed in a process in which initially stomatocytic RBC invaginations (panel C) loose volume while maintaining a large surface area. RBCs were incubated by amphiphilic molecules octaethyleneglycol dodecylether ($C_{12}E_8$). Panels D and E show confocal laser scanning microscopy of RBCs incubated with amphiphilic molecules chlorpromazine inducing small spherical endovesicles (panel D) and with $C_{12}E_8$ inducing toroidal endovesicles (panel E) as presented also in panels A and B. Adapted from.[57]

of simplicity, we shall consider the closed lipid bilayer membrane with one type of inclusions only. In our model, the single inclusion can induce local membrane bending due to its negative intrinsic curvature and also because of inward-oriented active forces. This means that we have joined the effect of the intrinsic curvature of the membrane inclusions (nanodomains) and the effect of the local active forces of NMIIA bipolar filament domains in a single type of membrane inclusions (nanodomains).

2. Monte Carlo Simulations

Monte Carlo (MC) triangulated mesh was used to numerically model and investigate the vesicle shape and the lateral distribution of membrane inclusions by means of computer simulation.[55] Phospholipid bilayer membranes can be treated due to their small thickness in the first approximation as a two dimensional surface, allowing the continuum approach in the theoretical description of membrane surfaces.[61] In the model we discretize the membrane into patches consisting of many molecules (Figure 2). A single patch is represented by a vertex in a triangulated surface model. The main model parameter that defines mechanical bilayer properties is bending stiffness.

The vesicle is represented by a set of N vertices that are linked by bonds of flexible length d to form a closed, randomly triangulated, self-avoiding network.[62,63] The lengths of the tethers can vary between a minimal (d_{min}) and a maximal (d_{max}) value. The self-avoidance of the network can be implemented by ensuring that no vertex can penetrate through the triangular network. The maximal

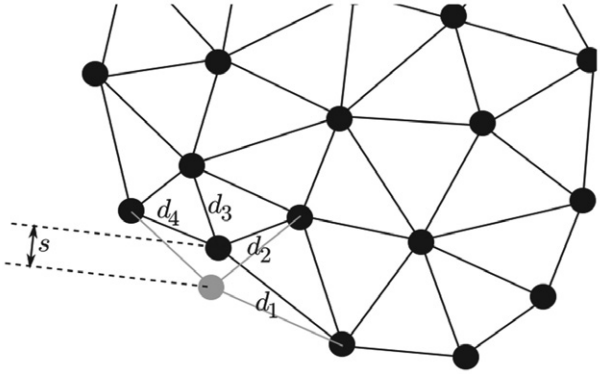

Figure 2: Schematic figure of the triangulated membrane surface in our MC model of the RBC membrane. The links between vertices are bonds, forming triangulated mesh. Lengths of all bonds must satisfy the bond length constraint so that the bond lengths are always in the range between d_{min} and d_{max}. The grayed out vertex is displaced by step size s to a new position. After the move, the lengths of bonds d_1, d_2, d_3 and d_4 are calculated and it is verified that they are between d_{min} and d_{max}.

possible random displacement of the vertex in a single step (s) should be small enough so that the fourth vertex cannot move through the plane of the other three to the minimal allowed distance, d_{min}, from the three vertices. In our scenario, we use s=0.15 d_{min} and d_{max}=1.7 d_{min}. For details about the expressions to calculate self-avoidance constraint d_{max}, see.[64]

The initial state of triangulated surface is a pentagonal bipyramid with all the edges divided into equilateral bonds so that the network is composed of 3(N-2) bonds forming 2(N-2) triangles. N_c randomly selected vertices are given non-zero isotropic intrinsic curvature of c_0, thus they become the model of the membrane inclusion. The rest of the vertices have zero intrinsic curvature. Positive curvature means that the membrane will locally bulge towards the exterior, negative curvature will force the membrane to bulge towards the interior compartment of the vesicle.

The system is developed into the thermal equilibrium state. The evolution of the system is measured in Monte Carlo sweeps (mcs). One mcs consists of individual attempts to displace each of the N vertices by a random increment in the sphere with radius s – the action we will refer to as a vertex move. Membrane fluidity is maintained by flipping bonds within the triangulated network. In each mcs, the vertex move attempts are followed by a 3N attempts to flip a randomly chosen bond. A single bond flip involves the four vertices of two neighboring triangles. The tether between the two vertices is cut and re-established between the other two, previously unconnected vertices (a detailed description was published elsewhere).[65] Each individual Monte Carlo step (vertex move or bond flip) is accepted with probability according to Metropolis Hastings algorithm, based on free energy change due to the Monte Carlo step.

The energy W in simulation consists of three parts:

$$W = W_b + W_d + W_F, \tag{1}$$

where W_b is the bending energy of the membrane, W_d is the energy of the direct interaction between vertices with intrinsic curvature and W_F is the energy due to myosin forces acting on the membrane.

For the bending energy W_b of the membrane, we use the standard Helfrich expression for a tensionless membrane with a term that represents intrinsic curvature.[66] The membrane keeps fixed topology, thus the contribution of the Gaussian curvature to the change of bending energy is cancelled out.

$$W_b = \frac{\kappa}{2}\oint_A (c_1 + c_2 - c_0)^2 \, \mathrm{d}A, \tag{2}$$

where κ is the bending stiffness of the membrane, c_1, c_2 and c_0 are the two principal curvatures and the intrinsic curvature of the vesicle membrane at the point under consideration. Note that only points where inclusions are located have non-zero intrinsic curvature c_0, whereas all other points on the membrane have intrinsic curvature c_0 set to zero. The integration is performed over the membrane area A.

For modelling attraction force between the vertices with intrinsic curvature energy term:[55]

$$W_d = -w \sum_{i<j} H\left(r_0 - r_{ij}\right), \tag{3}$$

where w is a direct interaction constant. The energy is summed over all inclusion pairs with their in-plane distance r_{ij} , r_0 is the range of direct interaction and H is a Heaviside step function with (r_0-r_{ij}) being function's argument.

The energy contribution of the local protrusive forces due to the myosin motor domains/inclusions:[55]

$$W_F = -F \sum_i \hat{n}_i \cdot x_i, \tag{4}$$

where F is the magnitude of the force, the sum runs over all proteins, is the outwards facing normal to the membrane at the location of the vertex with the inclusion i and $\boldsymbol{x_i}$ is the position vector of the vertex with the inclusion i.

3. Results and Discussion

Figure 3 shows the MC simulations of RBC shape transformations induced by laterally mobile membrane inclusions (nanodomains) with negative intrinsic curvature. It can be seen in Figure 3 that the non-homogeneous lateral redistribution of the mobile inclusions with negative intrinsic shape causes the RBC membrane to locally change the curvature resulting in the global transformation of the RBC shape. The MC predicted RBC shapes presented in

Figure 3 depend on the inclusion concentration, the inclusion intrinsic curvature, the strength of the direct attractive interaction between inclusions and on the active forces exerted by the inclusions.

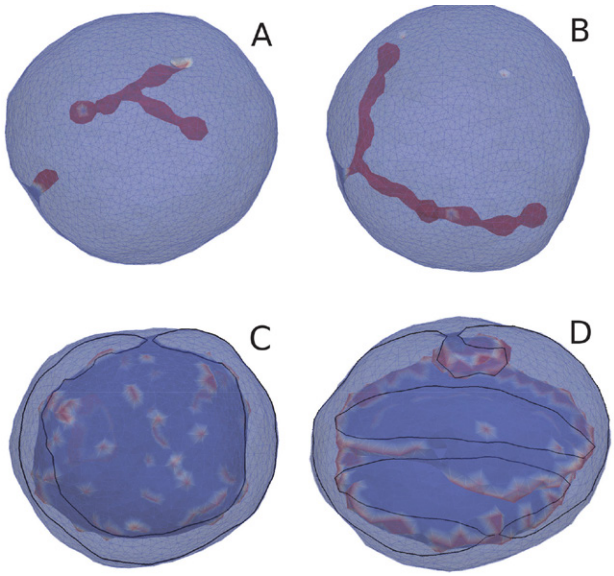

Figure 3: Monte Carlo simulation of the RBC membrane transformation induced by mobile membrane inclusions with intrinsic curvature $c_0 = -1\ l_{min}^{-1}$. Two different membrane inclusion concentrations p are considered. The upper figures A and B shows the MC results in the absence of myosin generated actin acting forces ($F = 0$), while in the lower panels C and D the myosin generated actin active forces $F = -1\ kT/l_{min}$ are taken into account. The negative sign of F denotes that the myosin generated forces points into the vesicle interior (perpendicular to the local membrane surface). The triangulated membrane surface is drawn semitransparent to uncover its interior shape. Red vertices on the mesh represents the locations of the membrane inclusions. In the panels C and D black and white outlines are added to better visualize the shape of endovesicles and membrane necks. The values of other model parameters are: bending rigidity $\kappa = 25\ kT$ and direct interaction parameter $w = 1.25\ kT$.

Figures 3A and B show that the lateral accumulation of membrane inclusions (nanodomains) can induce the formation of long undulated thin inward membrane protrusions (buds). Long undulated membrane protrusions may be further transformed into small independent spherical endovesicles, as observed in Figure 1D, due to the frustrations in the orientational ordering of membrane components in the highly curved membrane necks.[67] The same mechanism can also be responsible for the detachment of the complete inward membrane protrusion from the parent membrane[67] and the consequent formation of the endovesicles as shown in experimental Figure 1.

In calculations presented in Figures 3C and D, it is taken into account that the membrane inclusions (nanodomains) exert also active forces in the direction perpendicular to the membrane surface towards the interior of the RBC. As already discussed above, the active forces in the RBC membrane are generated by myosin (NMIIA) motor domains (inclusions) bound to F-actin of the RBC membrane skeleton.[60] It can be seen in panels of Figure 3 that at a smaller concentration of membrane inclusions exerting force on the membrane, the MC predicted RBC shape has one large invagination (Fig. 3C) as can be observed in some experiments (see refs. 44,56 and the references therein). Large invaginations can be separated from the parent cell due to the frustrations in the orientational ordering of membrane components in the highly curved membrane necks connecting the invagination and the parent cell,[67] resulting in the formation of a large endovesicle.

Furthermore, Figure 3 shows that a larger concentration of membrane inclusions exerting force on the membrane, the MC predicted RBC shape has one small and two large pancake-like torocyte membrane invaginations (Figure 3D) as can also be observed in the experiments (Figure 1, panels A, B and E). Again, the necks connecting the torocyte structures as well as the neck connecting the complete invagination to the parents cell are supposed to be ruptured due to the frustrations in the orientational ordering of membrane components in the highly curved membrane necks.[67] Note that in the torocytic membrane invaginations (Figure 3D), the myosin motor domains generated active forces that acted in the outward direction with respect to the torocyte invagination, i.e. in the direction towards the inner RBC solution. It is also important to point out that the myosin motor domains/inclusions are mainly accumulated at the bulby rim of the torocyte membrane invaginations (Figure 3D).

The stability of torocyte RBC endovesicles can be theoretically explained also by anisotropic membrane inclusions which exhibit orientational ordering in a highly curved bulby periphery.[57,59] In this work we have shown that the stability of torocyte endovesicles may be additionally favored also by active forces on the RBC membrane, generated by myosin motor nanodomains (i.e. membrane inclusions/nanodomains composed of myosin-actin-spectrin-lipids complex, see also references 7, 19, 68, 69).

Note that in the present work the total number of myosin motor nanodomains (inclusions) in Figures 3C and D is larger than the actual number of myosin motor nanodomains found in the RBC membrane.[60] Therefore, the proposed mechanisms of myosin inclusions/nanodomains driven formation and stabilization of torocyte invaginations and torocyte endovesicles in RBCs can be considered as an additional and complementary mechanism to the non-homogeneous lateral distribution and the orientational ordering of anisotropic membrane inclusions/nanodomains in the RBCs membrane.[57,59]

In accordance with experimental observations (Figure 1) we have predicted in this work the invaginated stomatocyte RBC shapes having different shapes of invaginations, like torocytic, spherical, undulated necklace-like, etc. This is an extension of the previously theoretically predicted shape classes of the invaginated stomatocytic

shapes which were mostly limited to the simple (axisymmetric) stomatocytic shape with only one large invagination (Figure 3C) (see for example ref. 32), experimentally observed also in a giant unilamellar lipid vesicle.[70]

4. Conclusions

Numerical computer modelling of the cell membrane shapes and shape transformations is a widely used method to investigate physical models of various phenomena found experimentally in cellular systems. In the present work, we used MC simulations to theoretically study the influence of active forces on the red blood cell (RBC) shape and vesiculation. We have shown that the active forces, generated by myosin motor domains, may partially control endovesiculation of the RBC membrane and also the RBC shape changes in general. Among others the myosin domains generated forces on the RBC membrane favor experimentally observed pancake-like (torocyte) RBC endovesicles with a large flat central membrane and a bulby periphery which were also experimentally observed.[57] These theoretically predicted shapes (Figure 3D) are very similar to the shapes of Golgi bodies, so the theoretical study presented in this work may be relevant also for better understanding of the physical mechanisms determining the shape of Golgi body.[58]

In conclusion, by using MC simulations, it is shown in this work that the recently discovered myosin motor domains generated active forces on the RBC membrane[60] may partially control the endovesiculation of the red blood cells and the RBC shape changes in general. We conclude that the myosin generated active forces acting on the RBC membrane should be therefore necessarily considered in the future relevant theoretical studies of the RBC vesiculation and shape transformations.

Acknowledgments

This project has received funding from the European Union's Horizon 2020 research and innovation program under grant agreement No. 801338 (VES4US project). The authors also acknowledge the financial support from the grants No. P2-0232, P3-0388 and J2-8166 from the Slovenian Research Agency (ARRS).

Conflict of Interests

The authors declare that there is no conflict of interests.

5. References

1. G. Cevc and D. Marsh, *Phospholipid Bilayers: Physical Principles and Models*, Wiley, **1987**.
2. J. N. Israelachvili, *Intermolecular and Surface Forces*, Academic Press, **1997**.
3. S. A. Safran, *Statistical Thermodynamics of Surfaces, Interfaces, and Membranes*, Addison-Wesley Publishing Company, Colorado, USA, **1994**.
4. Z. Peng, R. J. Asaro and Q. Zhu, *Phys. Rev. E*, **2010**, *81,* 031904. **DOI:**10.1103/PhysRevE.81.031904
5. I. Szleifer, D. Kramer, A. Ben-Shaul, W. M. Gelbart and S. A. Safran, *J. Chem. Phys.*, **1990**, *92,* 6800–6817. **DOI:**10.1063/1.458267
6. C. Nielsen, M. Goulian and O. S. Andersen, *Biophys. J.*, **1998**, *74,* 1966–1983. **DOI:**10.1016/S0006-3495(98)77904-4
7. M. Fošnaric, K. Bohinc, D. R. Gauger, A. Iglic, V. Kralj-Iglic and S. May, *J. Chem. Inf. Model.*, **2005**, *45,* 1652–1661. **DOI:**10.1021/ci050171t
8. S. May, *Langmuir*, **2002**, *18,* 6356–6364. **DOI:**10.1021/la025747c
9. M. Daniel, J. Řezníčková, M. Handl, A. Iglič and V. Kralj-Iglič, *Sci. Rep.*, **2018**, *8,* 10810. **DOI:**10.1038/s41598-018-28965-y
10. V. Markin, *Biophys. J.*, **1981**, *36,* 1–19. **DOI:**10.1016/S0006-3495(81)84713-3
11. S. Leibler, *J. Phys.*, **1986**, *47,* 507–516. **DOI:**10.1051/jphys:01986004703050700
12. V. Kralj-Iglič, S. Svetina and B. Žekž, *Eur. Biophys. J.*, **1996**, *24,* 311–321. **DOI:**10.1007/BF00180372
13. B. Božič, V. Kralj-Iglič and S. Svetina, *Phys. Rev. E*, **2006**, *73,* 041915. **DOI:**10.1103/PhysRevE.73.041915
14. A. Iglič, B. Babnik, K. Bohinc, M. Fošnarič, H. Hägerstrand and V. Kralj-Iglič, *J. Biomech.*, **2007**, *40,* 579–585. **DOI:**10.1016/j.jbiomech.2006.02.006
15. N. Walani, J. Torres and A. Agrawal, *Proc. Natl. Acad. Sci. USA*, **2015**, *112,* E1423–E1432. **DOI:**10.1073/pnas.1418491112
16. L. Mesarec, W. Góźdź, V. K. Iglič, S. Kralj and A. Iglič, *Coll. Surf. B*, **2016**, *141*, 132–140. **DOI:**10.1016/j.colsurfb.2016.01.010
17. N. Gov, *Philos. Trans. R. Soc. B Biol. Sci.*, **2018**, *373,* 20170115. **DOI:**10.1098/rstb.2017.0115
18. H. Hägerstrand, L. Mrówczyńska, U. Salzer, R. Prohaska, K. A. Michelsen, V. Kralj-Iglič and A. Iglič, *Mol. Membr. Biol.*, **2006**, *23,* 277–288. **DOI:**10.1080/09687860600682536
19. A. Iglič, M. Lokar, B. Babnik, T. Slivnik, P. Veranič, H. Hägerstrand and V. Kralj-Iglič, *Blood Cells. Mol. Dis.*, **2007**, *39,* 14–23. **DOI:**10.1016/j.bcmd.2007.02.013
20. A. Veksler and N. S. Gov, *Biophys. J.*, **2007**, *93,* 3798–3810. **DOI:**10.1529/biophysj.107.113282
21. D. Hunter and B. Frisken, *Biophys. J.*, **1998**, *74,* 2996–3002. **DOI:**10.1016/S0006-3495(98)78006-3
22. E. Karatekin, O. Sandre, H. Guitouni, N. Borghi, P.-H. Puech and F. Brochard-Wyart, *Biophys. J.*, **2003**, *84,* 1734–1749. **DOI:**10.1016/S0006-3495(03)74981-9
23. R. Bruinsma, *Physica A*, **1996**, *234,* 249–270. **DOI:**10.1016/S0378-4371(96)00358-5
24. V. Vitkova, M. Mader and T. Podgorski, *EPL Europhys. Lett.*, **2004**, *68,* 398. **DOI:**10.1209/epl/i2004-10211-9
25. M. M. Kozlov, F. Campelo, N. Liska, L. V. Chernomordik, S. J. Marrink and H. T. McMahon, *Curr. Opin. Cell Biol.*, **2014**, *29,*

53–60. **DOI:**10.1016/j.ceb.2014.03.006
26. A. Boulbitch, *Phys. Rev. E*, **1998**, *57,* 2123. **DOI:**10.1103/PhysRevE.57.2123
27. E. Evans and R. Skalak, *Mechanics and Thermodynamics of Biomembranes.*, Boca Raton FL CRC, **1980**. **DOI:**10.1115/1.3138234
28. D. E. Discher, in *Physics of Biological Membranes*, Springer, **2018**, pp. 263–285. **DOI:**10.1007/978-3-030-00630-3_11
29. N. Mohandas and E. Evans, *Annu. Rev. Biophys. Biomol. Struct.*, **1994**, *23,* 787–818. **DOI:**10.1146/annurev.bb.23.060194.004035
30. A. Iglič, *J. Biomech.*, **1997**, *30,* 35–40. **DOI:**10.1016/S0021-9290(96)00100-5
31. A. Iglič, V. Kralj-Iglič and H. Hägerstrand, *Eur. Biophys. J.*, **1998**, *27,* 335–339. **DOI:**10.1007/s002490050140
32. G. Lim H. W., M. Wortis and R. Mukhopadhyay, *Proc. Natl. Acad. Sci. USA*, **2002**, *99,* 16766–16769. **DOI:**10.1073/pnas.202617299
33. W. Helfrich, *Z. Naturforsch. C*, **1974**, *29,* 510–515. **DOI:**10.1515/znc-1974-9-1010
34. B. Stokke, A. Mikkelsen and A. Elgsaeter, *Eur. Biophys. J.*, **1986**, *13,* 203–218. **DOI:**10.1007/BF00260368
35. R. Mukhopadhyay, H. G. Lim and M. Wortis, *Biophys. J.*, **2002**, *82,* 1756–1772. **DOI:**10.1016/S0006-3495(02)75527-6
36. A. Iglič, S. Svetina and B. Žekš, *Biophys. J.*, **1995**, *69,* 274–279. **DOI:**10.1016/S0006-3495(95)79899-X
37. H. Hägerstrand, V. Kralj-Iglič, M. Bobrowska- Hägerstrand and A. Iglič, *Bull. Math. Biol.*, **1999**, *61,* 1019–1030. **DOI:**10.1103/PhysRevE.61.4230
38. E. J. Spangler, C. W. Harvey, J. D. Revalee, P. B. S. Kumar and M. Laradji, *Phys. Rev. E*, **2011**, *84,* 051906. **DOI:**10.1103/PhysRevE.84.051906
39. E. A. Evans, *Biophys. J.*, **1974**, *14,* 923–931. **DOI:**10.1016/S0006-3495(74)85959-X
40. L. Miao, U. Seifert, M. Wortis and H.-G. Döbereiner, *Phys. Rev. E*, **1994**, *49,* 5389. **DOI:**10.1103/PhysRevE.49.5389
41. M. P. Sheetz and S. Singer, *Proc. Natl. Acad. Sci. USA*, **1974**, *71,* 4457–4461. **DOI:**10.1073/pnas.71.11.4457
42. V. Kralj-Iglič, H. Hägerstrand, P. Veranič, K. Jezernik, B. Babnik, D. R. Gauger and A. Iglič, *Eur. Biophys. J.*, **2005**, *34,* 1066–1070. **DOI:**10.1007/s00249-005-0481-0
43. B. Deuticke, *Biochim. Biophys. Acta - Biomembranes*, **1968**, *163,* 494–500. **DOI:**10.1016/0005-2736(68)90078-3
44. H. Hägerstrand and B. Isomaa, *Biochim. Biophys. Acta - Biomembranes*, **1992**, *1109,* 117–126. **DOI:**10.1016/0005-2736(92)90074-V
45. V. Kralj-Iglič, A. Iglič, H. Hägerstrand and P. Peterlin, *Phys. Rev. E*, **2000**, *61,* 4230. **DOI:**10.1103/PhysRevE.61.4230
46. T. M. Fischer, *J. Phys. II*, **1992**, *2,* 337–343. **DOI:**10.1051/jp2:1992137
47. T. M. Fischer, *J. Phys. II*, **1993**, *3*, 1795–1805. **DOI:**10.1051/jp2:1993230
48. J. Fournier, *Phys. Rev. Lett.*, **1996**, *76,* 4436–4439. **DOI:**10.1103/PhysRevLett.76.4436
49. C. Safinya, *Coll. Surf. A*, **1997**, *128,* 183–195. **DOI:**10.1016/S0927-7757(96)03914-3
50. J.-B. Fournier and P. Galatola, *Braz. J. Phys.*, **1998**, *28,* 00–00. **DOI:**10.1590/S0103-97331998000400008
51. V. Kralj-Iglič, *Int. J. Nanomed.*, **2012**, *7,* 3579. **DOI:**10.2147/IJN.S29076
52. L. Mesarec, W. Góźdź, A. Iglič, V. Kralj-Iglič, E. Virga and S. Kralj, *Sci. Rep.*, **2019**, *9,* 1–11. **DOI:**10.1038/s41598-019-56128-0
53. N. Bobrovska, W. Góźdź, V. Kralj-Iglič and A. Iglič, *PloS One*, **2013**, *8,* e73941. **DOI:**10.1371/journal.pone.0073941
54. L. Mesarec, W. Góźdź, S. Kralj, M. Fošnarič, S. Penič, V. Kralj-Iglič and A. Iglič, *Eur. Biophys. J.*, **2017**, *46,* 705–718. **DOI:**10.1007/s00249-017-1212-z
55. M. Fosnarič, S. Penič, A. Iglič, V. Kralj-Iglič, M. Drab and N. Gov, *Soft Matter*, **2019**. *15,* 5319–5330. DOI: 10.1039/C8SM02356E
56. H. Hägerstrand and B. Isomaa, *Biochim. Biophys. Acta – Biomembranes*, **1989**, *982,* 179–186. **DOI:**10.1016/0005-2736(89)90053-9
57. M. Bobrowska-Hägerstrand, V. Kralj-Iglič, A. Iglič, K. Bialkowska, B. Isomaa and H. Hägerstrand, *Biophys. J.*, **1999**, *77,* 3356–3362. **DOI:**10.1016/S0006-3495(99)77167-5
58. A. Iglič, M. Fošnarič, H. Hägerstrand and V. Kralj-Iglič, *FEBS Lett.*, **2004**, *574,* 9–12. **DOI:**10.1016/j.febslet.2004.07.085
59. H. Hägerstrand, V. Kralj-Iglič, M. Fošnarič, M. Bobrowska-Hägerstrand, A. Wróbel, L. Mrówczyńska, T. Söderström and A. Iglič, *Biochim. Biophys. Acta - Biomembranes*, **2004**, *1665,* 191–200. **DOI:**10.1016/j.bbamem.2004.08.010
60. A. S. Smith, R. B. Nowak, S. Zhou, M. Giannetto, D. S. Gokhin, J. Papoin, I. C. Ghiran, L. Blanc, J. Wan and V. M. Fowler, *Proc. Natl. Acad. Sci. USA*, **2018**, *115,* E4377–E4385. **DOI:**10.1073/pnas.1718285115
61. H. Noguchi, *J. Phys. Soc. Jpn.*, **2009**, *78,* 041007. **DOI:**10.1143/JPSJ.78.041007
62. G. Gompper and D. M. Kroll, in *Statistical Mechanics of Membranes and Surfaces*, eds. D. Nelson, T. Piran and S. Weinberg, World Scientific, Singapore, **2004**, pp. 359–426. **DOI:**10.1142/9789812565518_0012
63. G. Gompper and D. M. Kroll, *J. Phys. I*, **1996**, *6,* 1305–1320. **DOI:**10.1051/jp1:1996246
64. M. Fošnarič, S. Penič, A. Iglič and I. Bivas, in *Advances in Planar Lipid Bilayers and Liposomes*, ed. A. Iglič & J. Genova, Elsevier, **2013**, *vol. 17,* pp. 331–357. **DOI:**10.1016/B978-0-12-411516-3.00012-7
65. S. Penič, A. Iglič, I. Bivas and M. Fošnarič, *Soft Matter*, **2015,** *11,* 5004–5009. **DOI:** 10.1039/C5SM00431D.
66. W. Helfrich, *Z. Naturforsch. C*, **1973**, *28,* 693–703. **DOI:**10.1515/znc-1973-11-1209
67. D. Jesenek, S. Perutková, W. Góźdź, V. Kralj-Iglič, A. Iglič and S. Kralj, *Int. J. Nanomed.*, **2013**, **8,** 677–687. **DOI:**10.2147/IJN.S38314
68. M. Fošnarič, A. Iglič and S. May, *Phys. Rev. E*, **2006**, *74,* 051503. **DOI:**10.1103/PhysRevE.74.051503
69. A. Iglič, T. Slivnik and V. Kralj-Iglič, *J. Biomech.*, **2007**, *40,* 2492–2500. **DOI:**10.1016/j.jbiomech.2006.11.005
70. J. Käs and E. Sackmann, *Biophys. J.*, **1991**, *60,* 825–844. **DOI:**10.1016/S0006-3495(91)82117-8

Povzetek

Z uporabo Monte Carlo (MC) simulacij stomatocitnih oblik eritrocita smo pokazali, da lahko aktivne sile miozinskih domen, pripetih na F-aktinske molekule na notranji strani membrane eritrocita, delno kontrolirajo endovezikulacijo membrane eritrocita. Miozinsko-aktinsko generirane aktivne sile, ki delujejo na membrano eritrocita, tako med drugim vplivajo tudi na nastanek ploščatih torocitnih endoveziklov eritrocitov. Na osnovi dobljenih rezultatov MC simulacij vezikulazije eritrocitov zaključujemo, da lahko miozinsko-aktinsko generirane aktivne sile, ki delujejo v smeri pravokotno na površino membrane eritrocita proti notranjosti eritrocita, pomembno vplivajo tudi na ostale transformacije oblik eritrocita ter na stabilnost različnih oblik eritrocita in bi jih bilo zato potrebno upoštevati pri bodočih teoretičnih študijah transformacije oblik in vezikulacije eritrocitov.

Except when otherwise noted, articles in this journal are published under the terms and conditions of the Creative Commons Attribution 4.0 International License

682

DRUŠTVENE VESTI IN DRUGE AKTIVNOSTI
SOCIETY NEWS, ANNOUNCEMENTS, ACTIVITIES

Vsebina

Richard Klemen, prvi učitelj encimatike na Univerzi v Ljubljani S49
Poročilo o delu v letu 2019 ..... S63
Navodila za avtorje S70

Contents

Richard Klemen, the First Lecturer of Enzymology at the University of Ljubljana S49
Report for 2019 ..... S63
Instructions for authors S70

Edicational Chemistry

Richard Klemen, the First Lecturer of Enzymology at the University of Ljubljana

Marko Dolinar

University of Ljubljana, Faculty of Chemistry and Chemical Technology, Chair of Biochemistry, Večna pot 113, 1000 Ljubljana, Slovenia

** Corresponding author: E-mail: marko.dolinar@fkkt.uni-lj.si*

Received: 05-28-2020

Abstract

Richard Klemen was the first teacher of enzymology at the University of Ljubljana. His early career in Ljubljana ended in January 1942 when he moved to Vienna, Austria. During the war he conducted experiments that led him to describe the so-called Hofmann-Klemen effect in clay. Later he was a research assistant and titular associate professor in the field of biochemical technology at the Vienna Technical University and finally a lecturer at the University of Natural Resources in Vienna. His life is an interesting example of a scientist and educator whose Gottscheer German origin would probably prevent him from continuing his career in post-war Yugoslavia. At the same time, he did not achieve in Austria the positions and status that his former colleagues and students had achieved in Slovenia. Although he was almost forgotten, he remains important as the first trained enzymologist and teacher of enzymology in Slovenia. This article also presents his full bibliography.

Keywords: enzymology education; University of Ljubljana; biochemistry

1. Introduction

Since its foundation in 1919, the University of Ljubljana (UL), Slovenia, has offered the study of chemistry. The first appointed professor of chemistry was Maks Samec (1881–1964), who graduated from the University of Vienna, Austria, in 1904. He was a versatile researcher with broad interests, who after joining UL concentrated on the study of biological polymers, mainly starch. The major part of this research today would fit into the field of physical chemistry, but also analytical, organic chemistry and biochemistry.

A hallmark of the first decades of chemical education at the University of Ljubljana was the duality of an academically-oriented and a technically-oriented chemistry programme, which were essentially divided between the Faculty of Arts (Slov.: Filozofska fakulteta) and the Faculty of Technical Sciences (Slov.: Tehniška fakulteta). This duality probably reflects the arrangement of chemistry studies in Vienna at the time, as chemistry courses were offered by both the University of Vienna and Vienna College of Technology (Ger.: Technische Hochschulle; later Vienna University of Technology, TU Wien).

With the expansion of the understanding of enzyme function and structure in the late 1920s, it became clear that a course on enzyme chemistry should be included in the chemistry curriculum of the University of Ljubljana. At about the same time, as Slovenia was still largely dependent on its own agriculture, the need arose to impart specific knowledge about agricultural chemistry.

It is remarkable that the development of biochemistry as an independent scientific discipline is even reflected in educational guidelines at the state level. Biochemical content in higher education has been officially requested by the General University Decree[1] (Slov.: Obča univerzitetna uredba) of 1932, which prescribed the organisation of state universities in the Kingdom of Yugoslavia. In this decree, 35 chairs were defined for the faculties of the arts, including a chair in chemistry (Article 96). It should cover topics of inorganic, organic and physical chemistry as well as biochemistry. For the faculties of agriculture and forestry (Article 102), agricultural chemistry was prescribed, among other fields. At that time the University of Ljubljana did not yet have a faculty specifically devoted to agriculture, which probably played an important role in the decision to include agrochemistry in the chemistry programme of the Faculty of Technical Sciences.

A pioneering role in biochemistry education in Slovenia belongs to Richard Klemen, one of the early students of Maks Samec. Klemen was the first lecturer in enzymol-

ogy and agricultural chemistry in Slovenia. The circumstances led him to move from Ljubljana to Vienna, where he was actively involved in biochemical and food technology research and teaching. Nevertheless, his work and career are almost forgotten, both in Slovenia and in Austria, where he spent most of his life.

2. Training and First Employment of Richard Klemen

Richard Klemen belonged to the German minority in Slovenia, the so-called Gottcheers (Slov.: Kočevarji). Since the 14th century they were settled in about 170 villages in the wooded south of Slovenia, with the town of Gottchee (Slov.: Kočevje) as their cultural and administrative centre. Richard's parents lived in Tschermoschnitz (Slov.: Črmošnjice), where Richard was born on 24 January 1902 and where he attended primary school. At the age of 10 he enrolled at a grammar school in Ljubljana[2] (Ger.: Kaiserlich-königliche Staats-Oberrealschule, Slov.: Cesarsko-kraljeva državna višja realka; Engl.: Imperial and royal secondary school) with German as the school language. He was an excellent student who in July 1920 graduated from the Realschule with distinction[3]. This falls into the post-war period, when the Austro-Hungarian Empire was dissolved and a new state – the Kingdom of Serbs, Croats and Slovenes – was founded. Accordingly, the language of school education changed from German to Slovenian.

At the age of 18, Richard Klemen was enrolled with the second generation of chemistry students (1920) at the newly founded University of Ljubljana (UL). He graduated on 18 July 1925 with an engineering degree (B. Eng.) in chemistry and was thus the 8th student to complete chemistry studies at the University of Ljubljana. The diploma thesis, which he completed under the mentorship of Maks Samec, dealt with the staining of starch with iodine[4]. The results of this work were published by Maks Samec in Kolloidchemische Beihefte shortly afterwards[5].

In 1925/26 Richard Klemen attended a military school for reserve officers in Maribor where he spent 8 months. After completion, he was ranked as second lieutenant in reserve pioneer troops. Immediately thereafter, he returned to Ljubljana to join the group of Maks Samec at the University of Ljubljana as a research assistant, but only for a relatively short period (1 July 1926 to 31 May 1927). This is certainly a consequence of the university's financial problems and years of discussions with the Belgrade administration about the need to maintain a technology-oriented faculty in Ljubljana[6]. Namely, for the last two months at the university, he had to agree to work as laboratory operator for a considerably lower salary.

Richard Klemen appeared on the list of members of the newly-established Yugoslav Chemical Society[7], with his home address Črmošnjice near Semič, Dolenjska region, not the university address as would be expected for a faculty member. In the years 1927–29 Klemen worked as an expert in a sugar factory in North Croatia. In the first edition of the Index Biologorum almanac[8], Richard Klemen was listed as an assistant to Professor Samec at the UL Institute of Chemistry, working in the field of physical chemistry, but this probably reflected his status in mid-1927.

3. Klemen's Connection to Agrochemistry

A part of the Klemen family lived in Gonobitz (after 1918: Konjice, today Slovenske Konjice) in northern Slovenia, where Richard's uncle Ferdinand was town councillor, deputy mayor and mayor in several mandates. He was one of the pro-German local politicians[9]. Richard was very close to his uncle Ferdinand and they visited regularly. In addition, Richard's parents bought a considerable plot of land with vines in a place named Škalce not far from the town of Gonobitz as early as 1900. Apparently the funds for the purchase of vineyards came from wood sold from forests in South Slovenia that were premarital assets of Richard's mother Maria. They still owned a farm in Tschermoschnitz and a vineyard in the Bela Krajina region, and Richard's father Franz was a merchant who, anecdotally, represented the Bavarian coffee substitute factory Kathreiner in the Duchy of Carniola, so that the family could be regarded as well-off (Ulrich Klemen, personal communication).

The connection to family and land in Gonobitz could be the reason Richard was attracted to agriculture. His stage in the state sugar factory in Beli Manastir (September 1927 to January 1929) was the first obvious step in this direction, followed by employment (in 1929) at the agricultural experimental and control station in Maribor (Slov.: Laboratorij državne poskusne in kontrolne postaje v Mariboru) where he held an assistant position. It was during his Maribor stage that he was also adjunct professor (Slov.: pomožni učitelj) of chemistry with agricultural chemistry[10] at the winemaking and fruit-growing secondary school (Slov.: Vinarska in sadjarska šola v Mariboru).

In addition to the routine work in the agricultural station, Klemen was also interested in the basic and applied chemistry. In 1930 his first professional article appeared in the Austrian journal Das Weinland. The subject of the article[11] was a comparative chemical analysis of the leaves of selected grape varieties. His work mainly referred to some earlier publications by German and French authors who suggested that the nutritional status of vines could be determined quantitatively by chemical analysis of individual leaves. Klemen has improved this approach by combining three leaves per vine and determining the average values for the chemical composition. Soil samples were analysed for comparison. Klemen discovered no obvious difference between well- and poorly-fed vines from the Maribor and Konjice vineyards, respectively. The elemental analysis of

the vine leaves did not seem to be prognostic for the condition of the vines, and the analysis of the soil could indicate the condition of the vines much better.

4. Doctorate and Habilitation

After years of financial crisis and the uncertainty to keep the Faculty of Technical Sciences as a constitutive part of the University of Ljubljana, a new law on universities was passed in 1930, according to which all faculties at the then renamed University King Alexander I in Ljubljana were retained[6]. This could be one of the reasons for Klemen's return to the faculty (Figure 1), where he worked as a teaching assistant between 1930 and 1933. His first research topic in Ljubljana had nothing to do with his other scientific activities. He worked with his colleague Janko Kavčič (a future professor of inorganic chemical technology) on a study of coal from various Slovenian mines. The aim of this study was to determine which coal was best suited for heating in the so-called Celus heaters and what is the best practice for heating different types of coal[12].

Figure 1: Identity photograph of Richard Klemen from 1930. Photographed from his civil servant folder from University of Ljubljana Archives with permission.

Richard Klemen concluded his doctoral studies on 8 October 1931 with a dissertation on the characterisation of individual starches in connection with their systematization into groups[13] under the mentorship of Maks Samec. In the same year, Samec and Klemen published an article in the journal Kolloid-Beihefte in which they described properties of different starch types[14] which obviously summarized the results of the doctoral thesis.

From May 1931 until June 1932 Richard Klemen was a visiting scholar in Prague, Czechoslovakia, in the group of Ernst Waldschmidt-Leitz. He was a productive German enzymologist who graduated in Munich in 1920 under the supervision of Richard Willstätter (1915 Nobel Prize Laureate). Waldschmidt-Leitz wrote a book[15] on enzyme activity and properties as early as 1926, which was one of the first extensive monographs on enzymes. In 1927 Waldschmidt-Leitz became head of the Institute of Biochemistry in the German Technical College (Ger.: Deutsche Technische Hochschule) in Prague where his research on various enzymes and their substrates continued.

In Ljubljana, Maks Samec' interest in enzymes may have increased as a result of working with Waldschmidt-Leitz, with whom he published the first paper on the enzymatic degradation of starch in 1931. In addition, colloid chemistry, which was at the forefront of chemical research in Ljubljana, was considered to be closely related to enzyme chemistry[16]. The fact that the 1929 Nobel Prize for chemistry was awarded to Arthur Harden and Hans von Euler-Chelpin for their investigations of fermentative enzymes could be important as well. On the part of UL, starch degradation by enzymes was first investigated by Zvonimir Čanić as part of his B. Eng. degree[17], for which the experiments were carried out in the Waldschmidt-Leitz laboratory in Prague. Next, Richard Klemen joined the Czech group to complete his postdoctoral training in enzymatic techniques. It is easy to see that one year in Prague paved Klemen's way to enzymes, which he studied over the next almost 10 years.

On 20 November 1931 Richard Klemen was appointed a Privatdozent for colloid chemistry and enzyme chemistry at the Faculty of Technical Sciences in Ljubljana (Fig. 2), and on 29 March 1933, by a royal decree, a University Assistant Professor of chemical technology. He appeared in 1934 in the compendium on Education in the Drava Banate (Slov.: Dravska banovina; the administrative province of the Kingdom of Yugoslavia, to which Slovenia largely belonged between 1929 and 1941) as university assistant professor at the Faculty of Technical Sciences responsible for 'agricultural chemistry and work instructions in the analytical and physical laboratory'[18]. It was not until 27 February 1936 that he was appointed honorary lecturer at the Faculty of Arts, although he held lectures and practical courses for students of this faculty since 1934.

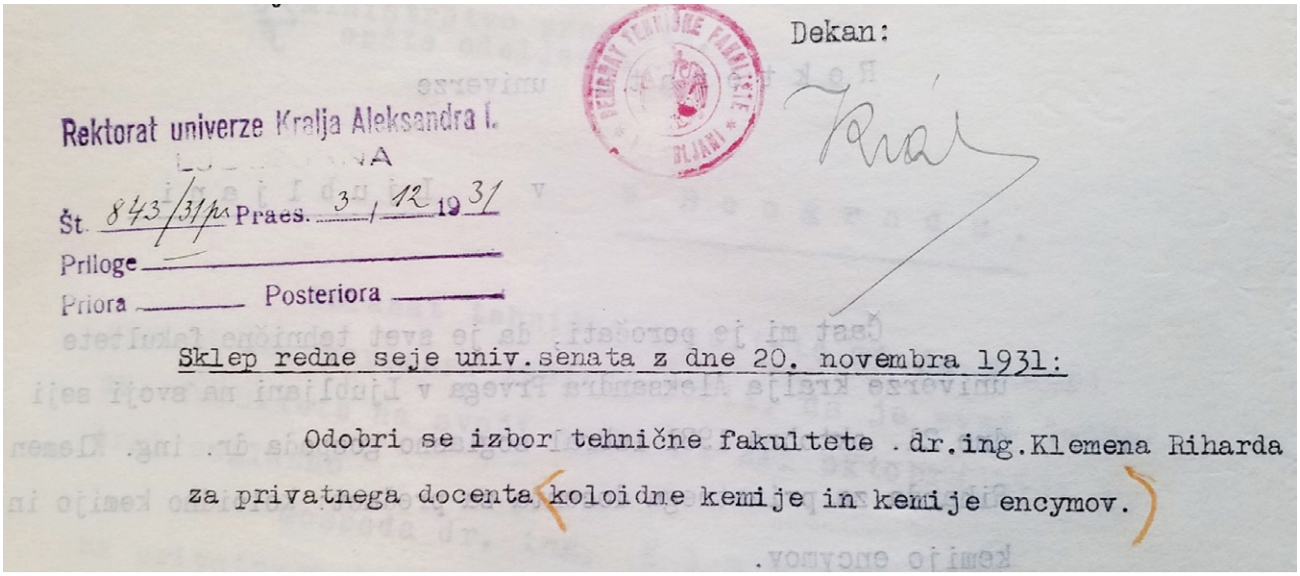
Dekan:

Rektorat univerze Kralja Aleksandra I.

Št. 843/31/pr. Praes. 3/12 1931

Priloge

Priora Posteriora

Sklep redne seje univ.senata z dne 20. novembra 1931:

Odobri se izbor tehnične fakultete dr.ing.Klemena Riharda za privatnega docenta koloidne kemije in kemije encymov.

Figure 2: Decision of the university senate dated 20 November 1931 approving election of Richard Klemen as Privatdozent for colloid chemistry and enzyme chemistry at the Faculty of Technical Sciences. Photographed from civil servant folder preserved at the University of Ljubljana Archives with permission.

At first, Richard Klemen continued to supervise students who were completing their degrees under the mentorship of professor Maks Samec, but soon he took on some practical and his own theoretical courses. In Table 1, Klemen's tasks per semester are summarized for the period 1933 to 1942.

Interestingly, Richard Klemen was leading several practical courses in the analytical laboratory, which was located in the premises of the 1st State Real Gymnasium (essentially the same school he attended from the age of ten to eighteen), which housed several chemical laboratories that belonged to the Faculty of Technical Sciences in the basement. Faculty actually arranged laboratories in this building in the year Richard completed his secondary education, so that this might have played a role in the choice of chemistry studies.

As shown in Table 1, enzymology has been part of chemical education at the University of Ljubljana since 1933. In the first three years of Klemen's teaching there seems to have been little interest in the Chemistry of Ferments course, as neither the time nor the place were fixed in the course description. The same applied to his newly established course on Agricultural Chemistry.

Klemen's teaching and research initially remained largely associated with starch, but soon turned to enzyme biochemistry, as his published works show. He was a co-mentor (mentor M. Samec) for the B.Eng. dissertation by Anton Tepež on pancreatic amylolysis[20], the results of which were published in the journal of the Yugoslav Chemical Society under the authorship of M. Samec and R. Klemen (1934) under the title A trisaccharide observed in pancreatic amylolysis of erythroamyloses[21]. Although today obsolete, the starch subspecies were divided in the 1930s into amyloamylose and erythroamylose, based on iodine staining[22].

In the mid-1930s there was a gap in the published articles, but from 1938 the publications began to take on a new dynamic. Klemen's next article came from the field of analytical biochemistry and appeared in 1938 in the journal Biochemische Zeitschrift. It dealt with influence of nitrogenous compounds on the determination of maltose by two established methods[23]. This work was also presented at the natural science conference in Ljubljana in February 1938 and published in conference proceedings[24] a year later in Slovenian language.

In continuing his early work on amylolysis with the help of his student Dušan Stucin, whom he supervised for his B.Eng. dissertation entitled Contribution to kinetics of amylolysis in wheat autolysates[25], an accompanying work on yeast autolysates was published[26] in Biochemische Zeitschrift in 1939. Another enzymes-related contribution from the late 1930s was Klemen's supervision of a B.Eng. thesis of Karel Andreč on amylase[27].

In memory of the work of the late Johan Rudolf Katz (1880–1938), an important Dutch colloid chemist, a special edition of Kolloid-Beihefte was published in March 1939. In this issue an article appeared[28] which contained results of Richard Klemen and Zvonimir Čanić. A detailed analysis of the temporal changes (aging) of the starch solution was described in this paper. The collaboration with J. R. Katz probably begun in early 1930s, since in 1932 a joint article[29] with M. Samec appeared in the January issue of the Zeitschrift für physikalische Chemie, followed by three further articles in the following years.

Richard Klemen not only worked as a university teacher. In 1939 he co-authored two textbooks[30,31] on mineralogy and chemistry for secondary schools (3rd and 4th grade) together with Vladimir Žitko, another former student of Maks Samec initially working on starch chemistry who later taught chemistry at various grammar schools in Slovenia and Croatia. In addition, in 1940 he wrote an article[32] on chemistry of fertilization for the Slovenian popular science magazine Proteus. In this article Klemen described the activity of extremely highly diluted saffron crocin-type molecules onto gamete mating in green algae as previously reported by Kuhn and co-workers[33].

5. Emigration and Early Career in Vienna

With the death of Richard's father in 1936, his land in Konjice was inherited by Richard. As assistant professor he was not able to be personally involved in grapevine cultivation and wine production. Instead, in their Konjice house lived two families of vintners who worked in the Klemen vineyards[34]. In April 1941 World War II began in Yugoslavia. The Slovenian territory was divided between Italy, Germany and Hungary. The Province of Ljubljana was integrated into the Kingdom of Italy and the work at the university was significantly impeded[35].

For the winter semester 1941/42, which ended on 15 February, Richard Klemen was still listed as a lecturer, but he received permission from the Italian provincial authorities to quit his position at the UL and emigrate to Germany after 31 January 1942. His enzymology course was later appointed to honorary lecturer Marta Blinc, who was advertised for the summer semester 1942/43 as lecturer for the course Selected Topics in Biochemistry and Enzymology (Slov.: Izbrana poglavja iz biokemije in enzimologije). Strangely enough, Richard Klemen still appeared in the course catalogue[19] for the winter semester 1942/43, which indicates that these lists are to be regarded as a historical source with care.

It could only be speculated about the reasons for Klemen's decision to leave the Italy-occupied Ljubljana, but there were probably several of them: German language ties, family property in the north of the country, which were now part of the German Reich, constantly growing teaching duties (reflected in the number of courses he delivered, see Table 1), rumours that resistance troops were hostile to people of German origin, and perhaps the fact that he appeared on the list of Kočevje Germans to be moved from the Kočevje area[36] to the plains along the Sava river on the then German side of the border to the Slovenian territories occupied by Italy. In this exodus almost all members (about 12,000, i.e. 95%) of the German minority left their villages[37]. The inability to conduct competitive research under Italian occupation in Ljubljana could also be important. The difference between the highly productive years of 1938–9 and the war situation must have been considerable. At that time Austria seemed isolated from war activities and thus offered itself as a comfortable refuge with perspectives for further research in the field of chemistry. Last but not least, Vienna was regarded as the centre of chemical education and he might have used some connections to colleagues of his former mentor, Maks Samec.

It seems obvious that Klemen's emigration to Germany (actually Austria, which was annexed to Germany in 1938) was well planned, as he was already working as a research assistant at the Vienna College of Technology on April 1, 1942. He was a member of the Institute of Inorganic and Analytical Chemistry led by Ulrich Hofmann and later by Robert Strebinger.

Essentially from the wartime comes Klemen's research, which was published only in 1950 in Zeitschrift für anorganische Chemie[38] with double authorship of Ulrich Hofmann and Richard Klemen. This is certainly the most frequently cited work of Richard Klemen. It describes an important observation in clay chemistry that is still referred to as the Hofmann-Klemen Effect. Ulrich Hofmann (1903–1986) is a well-known German chemist who (between 1942 and 1945) headed the institute in Vienna, where Klemen began as a research assistant after leaving Ljubljana. Hofmann's earlier position was that of a university professor in Rostock, Germany, from where he received one of the then rare and valuable electronic microscopes. In addition to basic research, he conducted several military projects[39]. Due to his involvement in German army-linked research and his membership in the paramilitary SA (Sturmabteilung) forces where he hold the title of Scharführer[40], he had to leave Austria in 1945. Since it was not possible for him to work in an exposed position after the war, he was first engaged as a gardener in a chemical production plant in Bavaria. Then, in 1948, he was asked to establish chemistry courses at the Regensburg university (then Philosophisch-Theologische Hochschule), where he first had to set up laboratories and start up courses[41]. For this reason, Klemen's research was probably published only in 1950 and with affiliation to the Regensburg university. However, Klemen remained bound to Vienna College of Technology and belonged to the minority of researchers who were not removed from their positions during the so-called "denazification" in post-war Austria. Only 35% of the researchers were allowed to remain[42].

In their 1950 paper, Hofmann and Klemen presented results that had already been achieved in Vienna in 1944[41]. Experimental data indicated that in clay (bentonite, more precisely montmorillonite) suspension with lithium, swelling and cation exchange capacity were lost when heated to 125°C. The proposed explanation was that lithium ions diffused into the octahedral sheet of the montmorillonite layer. This effect was later studied by several authors and the 1950 paper is still occasionally quoted.

Klemen's habilitation obtained at the University of Ljubljana in 1933 was recognized in January 1946 as proof

Table 1: List of courses assigned to Richard Klemen, sorted by semester. The two newly established Klemen's courses at the University of Ljubljana are presented in red. R. Klemen was the first university teacher at the University of Ljubljana with a habilitation in enzyme chemistry. If defined, the number of hours per week is shown in brackets next to the planned times. Slovenian course titles are only listed in brackets where they first appear. All data from the published lists of lectures at the University of Ljubljana[19]. n.d. – Data not available.

Semester	Course 1	Course 2	Course 3	Course 4	Course 5	Course 6
Winter 1933/34	Instructions for research work (Navodila za znanstveno delo), together with Prof. Samec; (20 h; Mo-Sa 8^h-18^h)	Instructions for work in analytical and physical-chemistry laboratory (Navodila k delu v analitskem in fiziko-kemičnem laboratoriju) (8 h)	Chemistry of ferments (Kemija fermentov) (1 h)			
Summer 1933/34	Instructions for work in analytical and physical* laboratory (Navodila k delu v analiznem in fizikalnem laboratoriju) (6 h)	Agricultural chemistry (Agrikulturna kemija) (2 h)				
Winter 1934/35	Experimental chemistry practical course (Vaje iz eksperimentalne kemije) for chemistry students enrolled at the Faculty of Arts (4 h)	Chemistry of ferments (2 h)				
Summer 1934/35	Experimental chemistry practical course for chemistry students (enrolled at the Faculty of Arts; 4 h)	Agricultural chemistry (2 h)	Instructions for work in analytical laboratory (2 h)			
Winter 1935/36	Experimental chemistry practical course for philosophers** (Faculty of Arts; 4 h)	Chemistry of ferments (2 h)	Instructions for research work (2 h)			
Summer 1935/36	Experimental chemistry practical course for philosophers – natural scientists (Faculty of Arts; 4 h)	Instructions for practical course on experimental chemistry for philosophers – natural scientists (Faculty of Arts; 1 h)	Agricultural chemistry (2 h; Mondays 7:15 to 9:00)	Instructions for work in analytical laboratory (2 h)		
Winter 1936/37	Experimental chemistry practical course for philosophers – natural scientists (Faculty of Arts; 4 h)	Instructions for practical course on experimental chemistry for philosophers – natural scientists (Faculty of Arts; 1 h)	Chemistry of ferments (2 h; Mondays 7:15 to 9:00)	Instructions for work in analytical laboratory (2 h)	Instructions for research work (20 h)	

Semester	Course 1	Course 2	Course 3	Course 4	Course 5	Course 6
Summer 1936/37	Experimental chemistry practical course for philosophers – natural scientists (4 h; Thursdays 14^h-18^h)	Instructions for practical course on experimental chemistry for philosophers – natural scientists (Faculty of Arts; 1 h)	Agricultural chemistry (2 h; Saturdays 7:15 to 9:00)	Instructions for work in analytical laboratory (2 h)	Instructions for research work (20 h; Mo-Fr 8^h-18^h)	
Winter 1937/38	Experimental chemistry practical course for philosophers – natural scientists (4 h; Thursdays 14^h-18^h)	Instructions for practical course on experimental chemistry for philosophers – natural scientists (1 h; Wednesdays 17^h-18^h)	Chemistry of ferments (2 h; Saturdays 7:15-9:00)	Instructions for work in analytical laboratory (2 h)	Instructions for research work (20 h; Mo-Fr 8^h-18^h)	
Summer 1937/38	Experimental chemistry practical course for philosophers – natural scientists (4 h; Thursdays 14^h-18^h)	Instructions for practical course on experimental chemistry for philosophers – natural scientists (1 h; Wednesdays 17^h-18^h)	Agricultural chemistry (2 h; Saturdays 7:15 to 9:00)	Instructions for work in analytical laboratory (2 h)	Instructions for research work (20 h; Mo-Fr 8^h-18^h)	
Winter 1938/39	n.d.					
Summer 1938/39	Experimental chemistry practical course for philosophers – natural scientists (4 h; Thursdays 14^h-18^h)	Instructions for practical course on experimental chemistry for philosophers – natural scientists (1 h; Wednesdays 17^h-18^h)	Agricultural chemistry (2 h; 7:15 to 9:00)	Instructions for work in analytical laboratory (2 h)	Instructions for research work (20 h; Mo-Fr 8^h-18^h)	
Winter 1939/40	n.d.					
Summer 1939/40	Experimental chemistry practical course for philosophers – natural scientists (4 h; Thursdays 14^h-18^h)	Instructions for practical course on experimental chemistry for philosophers – natural scientists (1 h; Tuesdays 14^h-15^h)	Agricultural chemistry (2 h; Saturdays 7:15 to 9:00)	Instructions for work in analytical laboratory (2 h)	Instructions for research work (20 h; Mo-Fr 8^h-18^h)	
Winter 1940/41	n.d.					
Summer 1940/41	Experimental chemistry practical course for philosophers – natural scientists (4 h; Thursdays 14^h-18^h)	Instructions for practical course on experimental chemistry for philosophers – natural scientists (1 h; Tuesdays 14^h-15^h)	Agricultural chemistry (2 h; Saturdays 7:15 to 9:00)	Instructions for research work (20 h; Mo-Fr 8^h-18^h)	Practical course in physical chemistry (Vaje iz fizikalne kemije) (10 h)	
Winter 1941/42	Experimental chemistry practical course for philosophers – natural scientists (4 h; Thursdays 14^h-18^h)	Instructions for practical course on experimental chemistry for philosophers – natural scientists (1 h; Tuesdays 14^h-15^h)	Chemistry of ferments (2 h; Saturdays 7^h-9^h)	Physical chemistry (Fizikalna kemija) (2 h)	Practical course in physical chemistry	Instructions for research work (20 h, Mo-Fr 8^h-18^h)

* With 'physical laboratory' physical chemistry laboratory is meant

** With 'philosophers' chemistry students who enrolled at the Faculty of Arts (Slov.: Filozofska fakulteta) are meant

of competence for teaching in Austria, but it seems that he was not regularly involved in teaching over the next few years. In June 1950 Richard Klemen moved from the Institute of Inorganic and Analytical Chemistry to the Institute of Biochemical Technology and Microbiology under the direction of Armin von Szilvinyi. Between 1953 and 1955 Klemen was acting head of this institute before appointment of Alexander Janke and during his illness. On 1 October 1954 Richard Klemen was appointed permanent university assistant.

While employed at the Vienna College of Technology, Richard Klemen contributed the biographical outline of Max Bamberger[43] for volume 1 of Neue Deutsche Biographie. Max Georg Matthias Bamberger (1861–1927) was an Austrian chemist, professor of organic and technical chemistry, associated with the Vienna College of Technology. He investigated natural compounds which is a connecting point to Klemen's interest. In addition, Bamberger was supervisor of the doctoral thesis of Margarete Garzuly (1923), who later married Alexander Janke, head of the Institute of Biochemical Technology and Microbiology[44]. One can imagine that A. Janke was originally supposed to write the text, but either because of his illness or perhaps because of a conflict of interest, the biography was finally prepared by Klemen.

The list of publications from Klemen's Vienna period is unexpectedly short, which is likely due to the fact that he was not in the role of project leader but rather assisted in various research and applied projects. Nevertheless, he was co-author of some of the publications in the field of food technology. In 1957, together with Alexander Janke he published a professional paper on the biological stabilization of grape juice with an ion-exchange resin[45]. Two years later, together with E. Seitz, he published an article on paper chromatographic analysis of the Maillard reaction[46]. This paper was dedicated to Professor Janke on the occasion of his 70th birthday.

6. Klemen's Late Career in Vienna

In April 1964 Richard Klemen was appointed "Titular Associate Professor", which is an honorary professional title in Austria. In 1967 he retired from the Vienna College of Technology, but continued to teach at the University of Agriculture in Vienna (BOKU), from 1966 as an external lecturer. He was in charge of the course on operational and quality control (Ger.: Betriebs- und Qualitätskontrolle), appointed to the Institute of Food Technology and Chair (Ger.: Lehrkanzel) of Biochemical Technology. In 1964, Klemen was actually among the candidates for the head of the newly founded BOKU's Institute of Food Technology as the second choice after Hans Klaushofer, who was later appointed to this office[47].

The appointment of Klemen to BOKU coincided with the retirement of Professor Armin von Szilvinyi in 1966. Interestingly, von Szilvinyi held two positions: he was head of the Institute of Biochemical Technology and Microbiology (where Klemen was employed from 1950 to 1967) at the Vienna College of Technology and professor at the Chair for Applied Biochemistry and Microbiological Research Methods at BOKU, where Klemen from 1966 was finally offered the opportunity to give his own lectures.

In each semester Klemen gave 3 h lectures per week, while the practical course was not under his direct supervision. In the academic year 1976/77 this course was taken over by Helmut Zenz, the later head of the Institute of Food Technology. In parallel to his assignments at the BOKU, Klemen also worked with the Experimental Station for Fermentation Professionals (Ger.: Experimentalstation für Gärungsgewerbe)[48] which was closely associated with BOKU[47], but later developed into an independent school for professional education. From his late career, Klemen's contribution at a seminar on sensory analysis in milk production was published[49].

On the occasion of his 85th birthday, Alfred Lechner, head of archives at TU Wien, assembled a curriculum vitae[50] summarizing Richard Klemen's achievements. This summary was an important source of information for the present article.

7. Richard Klemen's Private Life

In his young years, especially when he attended schools with German as language of instruction, Klemen's first name was written with a 'ch' (Ri*ch*ard), while as student and until 1942 his first name was written with an 'h' only (Ri*h*ard). After his move to Austria he adopted the German form of his first name again.

During the outbreak of World War II in Yugoslavia in April 1941, Richard Klemen was mobilized to Serbia where he was captured by German troops and sent as a prisoner to Essen, Germany. After several weeks of imprisonment[a], he was allowed to return to Ljubljana, where he continued his work at the university.

Richard's mother (aged 82) and his younger brother Toussaint and his family were part of the 1942 organized Gottscheer move from their home villages to the German-occupied lowlands along the Sava River, from which the local population had previously been expelled. Toussaint worked on a farm, but after partisans attacked the area he decided to move to Konjice. There, Richard's mother died in 1943. Toussaint and his family were expelled[51] to Austria in January 1946. They initially lived as war refugees in Austria, but later settled in Germany.

[a] UL archives keep a letter from the Italian chemical supplier Eigenmann e Veronelli dated 3 July 1941, which was replied in written on 12 July 1941. The Italian company inquired about the current address of Richard Klemen. UL rectorate replied as follows: »We have the honour to inform you that Dr. Richard Klemen is prisoner of war in Germany«.

After Richard Klemen obtained his research assistant position in Vienna in 1942, he refused to join the National Socialist German Lecturers League (Ger.: NationalsozialistischerDeutscher Dozentenbund), a division of the Nazi Party. This could be the reason why he was not allowed to work as a lecturer, which was his previous position at the University of Ljubljana. It is known that until 1945 the 'Lecturers League' was giving opinion about all candidates for teaching positions at German (and also Austrian) universities[52].

After World War II Richard Klemen was visited several times by strangers, who inquired about his possible return to Yugoslavia. On 17 September 1947 he was granted Austrian citizenship. Richard married to Gertrud Steindl, a chemist by profession. Their son Ulrich was born in 1948. During his stay in Vienna, Richard Klemen occasionally hosted colleagues from Slovenia, among others Friderik Gerl (a chemical engineer who received his B.Eng. from UL in 1926, later Associate Professor of Economics and Organization of the Chemical Industry at the University of Ljubljana, retired in 1972) and his former student Dušan Stucin (who died in 1976 as Professor of Biochemistry and head of the Institute of Biochemistry at the UL Medical Faculty).

Richard Klemen was not particularly satisfied with his career in Austria and often spoke with sympathy about Slovenia and his land in Konjice (U. Klemen, personal communication). Their family land and house were confiscated by the state in November 1945 (registered in Land Registry in January 1946) and declared 'general people's property' in 1948. Since 1951 it has been managed by the local agricultural enterprise (Kmetijsko gospodarstvo v Slovenskih Konjicah), later by the company Zlati grič[34]. Attempts by the family to recover possession of the confiscated property were unsuccessful.

Richard Klemen died on 19 May 1998 at the age of 96. He is buried in Vienna Central Cemetery. He is survived by his son Ulrich, who studied medicine and specialized in ophthalmology. He became chief physician and associate professor of ophthalmology. His wife Christine is also an ophthalmologist.

8. Bibliography

English translations of original titles are in square brackets. Richard Klemen as (co-)author is underlined in all entries.

R. Klemen (1925) Kako se spreminja jodova barva ter množina adsorbiranega joda pri spremembi koloidnega stanja škrobovih sestavin. Univerza Kraljevine Srbov, Hrvatov in Slovencev v Ljubljani, Tehniška fakulteta. Engineer degree thesis, mentor: Maks Samec [How iodine stain and amount of adsorbed iodine change with changing colloidal state of starch compounds]

M. Samec (1925) Studien über Pflanzenkolloide XVI. Verhalten der Stärkekomponenten zu Jod und ihre kolloide Schutzwirkung / nach Versuchen von R. Klemen. Kolloidchemische Beihefte 21(3–6), 55–77[Studies of plant colloids XVI. Behaviour of starch components against iodine and their colloid protection activity / Based on experiments of R. Klemen]

R. Klemen (1930) Ueber vergleichende Rebblattanalysen in verschiedenen Weinbergslagen zu bestimmten Zeiträumen. Das Weinland, Zeitschrift für Kellertechnik und Weinbau 2, 90–92 [On the comparative analysis of grapevine leaves in different vineyards at selected timepoints]

M. Samec (1931) Ugljevi Dravske banovine kao gorivo u Celus peći. Rad izveden uz sudelovanje J. Kavčiča i R. Klemena. Rudarski i Topionički Vesnik 3(1–2), 3 pp. (in Serbian language) [Coals of Drava Banate as fuel for Celsus heaters. With cooperation of J. Kavčič and R. Klemen.]

R. Klemen (1931) Koloidno kemijska karakterizacija posameznih škrobov v zvezi z njihovo razvrstitvijo v skupine. Univerza Kralja Aleksandra I. v Ljubljani, Tehniška fakulteta. Doctoral Degree thesis, mentor: Maks Samec [Colloid-chemical characterization of individual starches in connection to their systemisation into groups]

M. Samec, R. Klemen (1931) Studien über Pflanzenkolloide XXVIII. Eigenschaften verschiedener Stärkearten. Kolloid-Beihefte 33(5–8), 254–268. [Studies of plant colloids XXVIII. Properties of various types of starches]

A. Tepež (1934) K spoznavanju pankreatične amilolise. Univerza Kralja Aleksandra I. v Ljubljani, Tehniška fakulteta. B.Eng. thesis, mentor M. Samec, co-mentor R. Klemen [Towards understanding of pancreatic amylolysis]

M.Samec, R. Klemen (1934) Trisaccharid pri pankreantični amilolizi Eritroamiloz (po poizkusih A. Tepeža). Glasnik Hemijskog društva Kraljevine Jugoslavije 5(1), 25–30 [A trisaccharide observed in pancreatic amylolysis of erythroamyloses]

R. Klemen (1938) Über den Einfluss stickstoffhaltiger Stoffe auf die Maltosebestimmung nach Bertrand, Willstätter-Schudel und Auerbach-Bodländer. Biochemische Zeitschrift 299, 58–62 [Effect of nitrogenous compounds on the determination of maltose by the methods of Bertrand, Willstätter and Schudel, and Auerbach and Bodländer]

R. Klemen (1939) Doprinosi k določevanju maltoze po Bertrandu. In: Pavel Grošelj (ed.) Zbornik Prirodoslovnega društva, 1. zvezek. Prirodoslovno društvo, Ljubljana. Referatni sestanek (Ljubljana, February 25–26, 1938), pp. 28–31 [Contribution to maltose determination by Bertrand]

D. Stucin (1939) Doprinos h kinetiki amilolize v pšeničnih avtolizatih. Univerza Kralja Aleksandra I. v Ljubljani, Tehniška fakulteta. B.Eng. thesis, mentor R. Klemen [A contribution to kinetics of amylolysis in wheat autolysates]

R. Klemen, D. Stucin (1939) Über den mittels verschiedener Methoden bestimmten zeitlichen Verlauf der Zuckerbildung in Weizenautolysaten. Biochemische Zeitschrift 300(5), 338–342 [About the temporal course of sugar formation in yeast autolysates determined by means of various methods]

K. Andreč (1939): Poizkus karakterizacije elektrolitne občutljivosti amilaze neklitega pšeničnega zrna. Univerza Kralja Aleksandra I. v Ljubljani, Tehniška fakulteta. B.Eng. thesis, mentor R. Klemen [An experiment for characterization of electrolytic susceptibility of amylase from non-germinated wheat grain]

J. R. Katz, M. Samec (1939) Studien über Pflanzenkolloide XLVI. Die Alterung der Stärkelösungen, betrachtet vom kolloidchemischen, enzymatischen und röntgenspektrographischen Standpunkt aus (nach Versuchungen von Z. Čanić und R. Klemen). Kolloid-Beihefte 49 (9–12), 455–470 [Studies of plant colloids XLVI. Aging of starch solutions as observed from colloid-chemical, enzymatic and X-ray spectrographic points of view (based on experiments of Z. Čanić and R. Klemen)]

V. Žitko, R. Klemen (1939) Mineralogija in kemija s tehnologijo za 3. razred meščanskih šol. Ljubljana: Banovinska zaloga šolskih knjig in učil. [Mineralogy and chemistry with technology for 3rd classes of citizen schools]

V. Žitko, R. Klemen (1939) Mineralogija in kemija s tehnologijo za 4. razred meščanskih šol. Ljubljana: Banovinska zaloga šolskih knjig in učil. [Mineralogy and chemistry with technology for 4th classes of citizen schools]

R. Klemen (1940) Oploditev z vidika kemije. Proteus 7(2–3), 43–45 [Fertilization from the chemical point of view]

U. Hofmann, R. Klemen (1950) Verlust der Austauschfähigkeit von Lithiumionen an Bentonit durch Erhitzung. Zeitschrift für anorganische Chemie 262(1–5) 95–99 [Lost exchange capability of lithium ions on betontite upon heating]

R. Klemen (1953) Bamberger, Max. In: Neue Deutsche Biographie 1, p. 574 [Online-Version]; URL: https://www.deutsche-biographie.de/pnd116047607.html#ndbcontent (accessed October 3, 2019)

A. Janke, R. Klemen (1957) Weitere Untersuchungen über die biologische Stabilisierung von Traubensäften mittels eines Ionenaustauschers. Fruchtsaft-Industrie 2, 224–227 [Further examination on biological stabilization of grape juices using an ion-exchanger]

R. Klemen, E. Seitz (1959) Ein papierchromatographischer Beitrag zur „Maillard-Reaktion". Zeitschrift für Lebensmittel-Untersuchung und –Forschung 109 (5), 386–390. [A paper chromatography contribution to Maillard Reaction]

R. Klemen (1970) Einführung in die Qualitätsprüfung von Lebensmitteln unter besonderer Berücksichtigung der sensorischen Analyse. Presented at INTERLAB-Seminar »Sensorik in der Milchwirtschaft« (Wolfpassing, 24.–25.6.1970). Milchwirtschaftliche Berichte aus den Bundesanstalten Wolfpassing und Rotholz 25, 245–249 [Introduction to quality testing of foodstuffs with special emphasis on sensory analysis]

9. Acknowledgement

I wish to thank Dr. Tatjana Peterlin-Neumaier for her first contacts with the Archives of the Vienna University of Technology and for her interest in the progress of my research on Richard Klemen's life. This article would not be possible without the information provided by Dr. Paulus Ebner, head of TU Wien Archives, and Mag. Peter Wiltsche, head of the Archives at the University of Natural Resources and Life Sciences, Vienna. I would also like to thank the Archives of the University of Ljubljana for providing access to their historic materials, especially the civil servant folder of Richard Klemen. Insight into Richard Klemen's background and private life was given by his son, Prof. Dr. Ulrich Klemen, whom I was able to reach through the community of Gottscheer Germans with the help of Mag. Herman Leustik from the Klagenfurt section of the Gottscheer Hometown Society (Gottscheer Landsmannschaft) and the president of its Vienna section, Mr. Karl Hönigmann. Information about the Versuchsstation für das Gärungsgewerbe was received from Dr. Günther Seeleitner and Dr. Hans-Joachim Schmidt, the director of the Oesterreichisches Getraenke Institut. I would also like

to thank Mr. Branko Škrinjar, head of the UL FRI-FCCT faculty library, for checking several bibliographic records on works of Richard Klemen published in his Ljubljana period.

10. Literature

1. Obča univerzitetna uredba, in: *Službeni list kraljevske banske uprave Dravske banovine* **1932**, *3*, 365–392.
2. Jahresbericht der k. k. Staats-Oberrealschule (1912/1913). Laibach: Verlag der k. k. Oberrealschule, **1913**.
3. *Večerni list* (newspaper). July 14, **1920**. p. 4. Ljubljana: Konzorcij Večernega lista.
4. R. Klemen, Kako se spreminja jodova barva ter množina adsorbiranega joda pri spremembi koloidnega stanja škrobovih sestavin. Ljubljana: Univerza Kraljevine Srbov, Hrvatov in Slovencev v Ljubljani, Tehniška fakulteta, **1925**.
5. M. Samec, Studien über Pflanzenkolloide XVI. Verhalten der Stärkekomponenten zu Jod und ihre kolloide Schutzwirkung / nach Versuchen von R. Klemen. *Kolloidchemische Beihefte* **1925**, *21*, 55–77.
6. T. Dekleva, The Faculty of technical sciences, University of Ljubljana, in: J. Ciperle (Ed.): Tehniška fakulteta Univerze v Ljubljani 1919–1957. Ljubljana: University of Ljubljana, **2010**, pp. 91–201.
7. V. Njegovan, R. Podhorsky, Jugoslovensko hemijsko društvo, Sekcija Zagreb, *Arhiv za hemiju i farmaciju* **1927**, *1*, 41–47.
8. G.C. Hirsch, Index Biologorum: Investigatores, Laboratoria, Periodica. Editio Prima. Berlin: Julius Springer **1928**.
9. *Straža* (newspaper), January 8, **1909**. Maribor: Konzorcij. p. 4.
10. J. Priol (Ed.) Izvestje za šolsko leto 1928/29 ter gospodarski leti 1928 in 1929. Maribor: Vinarska in sadjarska šola v Mariboru, **1930**.
11. R. Klemen, Ueber vergleichende Rebblattanalysen in verschiedenen Weinbergslagen zu bestimmten Zeiträumen. *Das Weinland, Zeitschrift für Kellertechnik und Weinbau* **1930**, *2*, 90–92.
12. M. Samec, Ugljevi Dravske banovine kao gorivo u Celus peći, *Rudarski i topionički vestnik* **1931**, *3*, 3 pp.
13. R. Klemen, Koloidno kemijska karakterizacija posameznih škrobov v zvezi z njihovo razvrstitvijo v skupine. Ljubljana: Univerza Kralja Aleksandra I. v Ljubljani, Tehniška fakulteta, **1931**.
14. M. Samec, R. Klemen, Studien über Pflanzenkolloide XXVIII. Eigenschaften verschiedener Stärkearten. *Kolloid-Beihefte* **1931**, *33*, 254–268.
15. E. Waldschmidt-Leitz, Die Enzyme – Wirkungen und Eigenschaften, Braunschweig: F. Wieweg & Sohn, **1926**, 235 pp. **DOI:**10.1007/978-3-322-99074-7
16. E. Nordenskiöld, The history of biology – A survey. London: Taylor & Francis, **1929**. Republished 2018 under the title Revival: The history of biology – A survey. Abingdon: Routledge.
17. Z.F. Čanić, Prilog diferencijaciji amilo i eritro-amiloze pomoću encima pankreasa, ječma i slada, Ljubljana: Univerza kralja Aleksandra I. v Ljubljani, Tehniška fakulteta, **1931.**
18. Stalež šolstva in učiteljstva ter prosvetnih in kulturnih ustanov v Dravski banovini, Ljubljana: Prosvetni oddelek kr. banske uprave, **1934**.
19. Seznam predavanj na Univerzi kralja Aleksandra I. Ljubljana: Univerza kralja Aleksandra I. v Ljubljani, **1930 –1942**.
20. A. Tepež, K spoznavanju pankreatične amilolise. Ljubljana: Univerza kralja Aleksandra I. v Ljubljani, Tehniška fakulteta, **1934**.
21. M. Samec, R. Klemen (1934) Trisaccharid pri pankreantični amilolizi Eritroamiloz (po poizkusih A. Tepeža). *Glasnik Hemijskog društva Kraljevine Jugoslavije* **1934**, *5*, 25–30.
22. H. Kraut, M. Rohdewald, Carbohydrasen, in: G.M. Schwab (Ed.), Handbuch der Katalyse, Band 3: Biokatalyse. Wien: Springer Verlag, **1941**.
23. R. Klemen, Über den Einfluss stickstoffhaltiger Stoffe auf die Maltosebestimmung nach Bertrand, Willstätter-Schudel und Auerbach-Bodländer. *Biochemische Zeitschrift* **1938**, *299*, 58–62.
24. R. Klemen, Doprinosi k določevanju maltoze po Bertrandu, in: Pavel Grošelj (Ed.), Zbornik Prirodoslovnega društva, 1. zvezek. Ljubljana: Prirodoslovno društvo. Referatni sestanek (Ljubljana, February 25–26, 1938), **1939**, pp. 28–31.
25. D. Stucin, Doprinos h kinetiki amilolize v pšeničnih avtolizatih. Ljubljana: Univerza Kralja Aleksandra I. v Ljubljani, Tehniška fakulteta, **1939**.
26. R. Klemen, D. Stucin, Über den mittels verschiedener Methoden bestimmten zeitlichen Verlauf der Zuckerbildung in Weizenautolysaten. *Biochemische Zeitschrift* **1939**, *300*, 338–342.
27. K. Andreč, Poizkus karakterizacije elektrolitne občutljivosti amilaze neklitega pšeničnega zrna, Ljubljana: Univerza kralja Aleksandra I. v Ljubljani, Tehniška fakulteta, **1939**.
28. J.R. Katz, M. Samec, Studien über Pflanzenkolloide XLVI. Die Alterung der Stärkelösungen, betrachtet vom kolloidchemischen, enzymatischen und röntgenspektrographischen Standpunkt aus (nach Versuchungen von Z. Čanić und R. Klemen). *Kolloid-Beihefte* **1939**, *49*, 455–470.
29. M. Samec, J. R. Katz, J. C. Derksen, Abhandlungen zur physikalischen Chemie der Stärke und der Brotbereitung, VIII. Inwieweit bestehen Verkleistern und Retrogradieren bei den mit nativer Stärke verwandten Substanzen? *Zeitschrift für physikalische Chemie* **1932**, *158A*, 321–336. **DOI:**10.1515/zpch-1932-15823
30. V. Žitko, R. Klemen, Mineralogija in kemija s tehnologijo za 3. razred meščanskih šol. Ljubljana: Banovinska zaloga šolskih knjig in učil, **1939**.
31. V. Žitko, R. Klemen, Mineralogija in kemija s tehnologijo za 4. razred meščanskih šol. Ljubljana: Banovinska zaloga šolskih knjig in učil, **1939**.
32. R. Klemen, Oploditev z vidika kemije. *Proteus* **1940**, *7*, 43–45.
33. R. Kuhn, F. Moewus, C. Jerchel, Chemische Natur der Stoffe, welche die Kopulation der männlichen und weiblichen Gameten von *Chlamydomonas eugametos* im Lichte bewirken. *Berichte der deutschen chemischen Gesellschaft* **1938**, *71*, 1541–1547. **DOI:**10.1002/cber.19380710733
34. V. Hazler, Kulturna dediščina – izziv sodobnemu podjetništvu; Ljubljana: Univerza v Ljubljani, Filozofska fakulteta, Zbir-

ka kulturna dediščina, 9. zvezek, **2013**.
35. T. Peterlin-Neumeier, Življenjepis Maksa Samca (1881–1964), in: B. Stanovnik (Ed.), Maks Samec (1881–1964): življenje in delo. Ljubljana: Slovensko kemijsko društvo, **2015**, pp. 17–70.
36. Verzeichnis der Volks- und Reichsdeutschen Umsiedler, die auf Grund des Abkommens vom 31. August 1941 aus der Provinz Laibach umgesiedelt wurden, **1941**. Available online at http://gottschee.de/Dateien/Dokumente/Web%20Deutsch/Umsiedlungsverzeichnis/nachname.php (Accessed October 16, 2019).
37. M. Ferenc, Kočevska, bleak and empty. Lecture at the "Bridging Our Worlds" conference, Ljubljana, Sept. 10–12, **2001**. Published on-line at http://www2.arnes.si/~krsrd1/conference/Speeches/Ferenc_eng.htm (Accessed October 16, 2019).
38. U. Hofmann, R. Klemen (1950) Verlust der Austauschfähigkeit von Lithiumionen an Bentonit durch Erhitzung. *Zeitschrift für anorganische Chemie,* **1950**, *262*, 95–99. **DOI:**10.1002/zaac.19502620114
39. J. Mikoletzky, Researching for the "ultimate victory": The TH in Vienna as part of the wartime economy, in: Die Technische Hochschule in Wien 1914–1955 / The Technische Hochschule in Vienna 1914–1955, Teil 2: Nationalsozialismus – Krieg – Rekonstruktion (1938–1955) / Part 2: National Socialism – War – Reconstruction (1938–1955). Vienna: Böhlau Verlag, **2016**, pp. 121–141. **DOI:**10.7767/9783205202219-011
40. H. Maier, Chemiker im "Dritten Reich": Die Deutsche Chemische Gesellschaft und der Verein Deutscher Chemiker im NS-Herrschaftsapparat. Berlin: WILEY-VCH Verlag, **2015**. **DOI:**10.1002/9783527694631
41. K. Beneke, G. Lagaly, Curriculum vitae and scientific research of Ulrich Hofmann (1903 – 1986). *ECGA (European Clay Group Association)* Newsletter **2002**, *5*, 13–23.
42. J. Mikoletzky, ‚Säuberungen' im Zuge der nationalsozialistischen Machtergreifung 1938 an der Technischen Hochschule in Wien, in: J. Koll (Ed.), "Säuberungen" an österreichischen Hochschulen 1934–1945: Voraussetzungen, Prozesse, Folgen. Vienna: Böhlau Verlag, **2017**, pp. 243–266. **DOI:**10.7767/9783205205845-008
43. R. Klemen, Bamberger, Max, in: Neue Deutsche Biographie 1, **1953**, p. 574 [Online-Version]; URL: https://www.deutsche-biographie.de/pnd116047607.html#ndbcontent (Accessed October 3, 2019)
44. J. Mikoletzky, Margarete (Rita) Janke-Garzuly – Viele „Firsts" und eine gebrochene Karriere, in: Frauenspuren an der TU Wien, **2012**. Available at https://www.frauenspuren.at/frauenspuren_gestern/pionierinnen/margarete_janke_garzuly/ (Accessed November 18, 2019).
45. A. Janke, R. Klemen, Weitere Untersuchungen über die biologische Stabilisierung von Traubensäften mittels eines Ionenaustauschers. Fruchtsaft-Industrie, **1957**, *2*, 224–227.
46. R. Klemen, E. Seitz, Ein papierchromatographischer Beitrag zur „Maillard-Reaktion". *Zeitschrift für Lebensmittel-Untersuchung und Forschung* **1959**, *109*, 386–390. **DOI:**10.1007/BF01885012
47. H. Klaushofer, Geschichte der Studienrichtung Lebensmittel- und Biotechnologie, in: D. Mattanovich (Ed.), 50 Jahre Lebensmittel- und Biotechnologie an der Universität für Bodenkultur Wien, Vienna: Fachgruppe Lebensmittel- und Biotechnologie der Universität für Bodenkultur Wien, **1995**, pp. 10–50.
48. Mitteilungen der Versuchsstation für das Gärungsgewerbe in Wien, Vol. 21–23 (**1967–69**) to Vol. 30–31 (**1976–1977**).
49. R. Klemen, Einführung in die Qualitätsprüfung von Lebensmitteln unter besonderer Berücksichtigung der sensorischen Analyse. Presented at INTERLAB-Seminar »Sensorik in der Milchwirtschaft« (Wolfpassing, 24.–25.6.1970). *Milchwirtschaftliche Berichte aus den Bundesanstalten Wolfpassing und Rotholz* **1970**, *25*, 245–249.
50. A. Lechner, Titl. A.O. Univ.-Prof. Univ.-Doz. Dipl.-Ing. Dr. techn. Richard Klemen; Persönliche Daten, zusammengestellt für die Laudatio anläßlich des 85. Geburtstages am 24. Jänner 1987. Vienna: Technische Universität Wien, Universitätsarchiv, **1987** (unpublished).
51. International Refugee Organization, Decision of the review board, Geneva. Act Nr. 16636, referring to Linz District case 998.602/4, **1949**. Obtained through Arolsen Archives.
52. A. C. Nagel, "Er ist der Schrecken überhaupt der Hochschule". Der Nationalsozialistische Deutsche Dozentenbund in der Wissenschaftspolitik des Dritten Reichs, in: J. Scholtyseck, C. Studt (Eds.), Universitäten und Studenten im Dritten Reich: Bejahung, Anpassung, Widerstand. Proceedings of the XIX. Königswinterer Tagung (17.–19. February 2006). Berlin: LIT Verlag, **2008**, pp. 115–132.

Povzetek

Richard Klemen (1902–1998) je bil prvi učitelj encimatike na ljubljanski univerzi. Za privatnega docenta za področje koloidne kemije in kemije encimov je bil izvoljen takoj po doktoratu leta 1931, poleg predavanj iz encimatike in kmetijske kemije pa je vodil tudi kemijski praktikum. Doktoriral je pod mentorstvom Maksa Samca na temo sistemizacije škrobov, nato pa se je eno leto izpopolnjeval iz encimatike na Nemški tehniški visoki šoli v Pragi. Z raziskovalnim delom na področju encimatike je nadaljeval do italijanske okupacije, nato pa januarja 1942 z dovoljenjem takratne oblasti emigriral v Avstrijo. Na Dunaju se je že aprila istega leta zaposlil kot raziskovalni asistent na Inštitutu za anorgansko in analizno kemijo Tehniške visoke šole. Iz medvojnega obdobja je njegovo najbolj citirano delo, ki je sicer izšlo šele leta 1950 z afiliacijo regensburške univerze, kjer se je kasneje zaposlil Klemnov nekdanji predstojnik Ulrich Hofmann. Po njima se imenuje tudi Hofmann-Klemnov pojav v kemiji gline. Leta 1950 se je Klemen zaposlil na Inštitutu za biokemijsko tehnologijo in mikrobiologijo Tehniške visoke šole na Dunaju, kjer je ostal kot raziskovalni sodelavec in občasno učitelj do upokojitve leta 1967. Tri leta pred upokojitvijo je bil imenovan za nazivnega izrednega profesorja in v letih 1966 do 1976 predaval na dunajski kmetijski univerzi predmet Nadzor obratovanja in kakovosti. Njegova znanstvena bibliografija je sorazmerno kratka in je v tem sestavku prvič zbrana. Ob stoletnici ljubljanske univerze in bližnji 60-letnici katedre za biokemijo na Fakulteti za kemijo in kemijsko tehnologijo je poznavanje začetkov biokemije na Slovenskem za stroko še posebej pomembno.

POROČILO PREDSEDNIKA SLOVENSKEGA KEMIJSKEGA DRUŠTVA O DELU DRUŠTVA V LETU 2019

V letu 2019 je bilo društvo aktivno na številnih področjih. Izvajali smo redne letne aktivnosti, pri katerih je bil glavni poudarek na rednem izdajanju društvene revije *Acta Chimica Slovenica* (ACSi) ter organizaciji največjega letnega dogodka društva, konference "Slovenski kemijski dnevi 2019".

Slovenski kemijski dnevi 2019 (jubilejna, 25. izvedba dogodka) so bili organizirani v Mariboru, v Kongresnem centru hotela Habakuk, in sicer v dneh od 25. do 27. septembra 2019. Programskemu in organizacijskemu odboru je predsedoval predsednik društva, dr. Albin Pintar, skupaj s člani odbora v zasedbi prof. dr. Romana Cerc-Korošec, prof. dr. Zorka Novak Pintarič, prof. dr. Darja Lisjak, dr. Matic Lozinšek, prof. dr. Matjaž Valant in dr. Silvo Zupančič. Na posvetovanju je bilo predstavljenih več kot 120 prispevkov v obliki predavanj in posterjev. Delo je potekalo plenarno in v dveh oziroma občasno treh vzporednih sekcijah. V okviru konference je bil v sodelovanju z American Chemical Society organiziran dogodek »ACS on Campus«. Udeleženci konference so bili zelo zadovoljni s kakovostjo znanstvenih in strokovnih prispevkov ter spremljevalnim programom srečanja. Na konferenci je sodelovalo 16 razstavljalcev. Sponzorji dogodka so bili Cinkarna Celje, AquafilSLO, Kemomed, Krka, Labtim, Mettler Toledo, Silkem, Donau Lab Ljubljana in Helios TBLUS. Objavili smo Zbornik povzetkov konference, ki je dostopen na USB ključu ter na voljo v NUK-u in strokovnih knjižnicah po Sloveniji. Uvodni predavatelj je bil **zasl. prof. dr. Peter Glavič** (Fakulteta za kemijo in kemijsko tehnologijo, Univerza v Mariboru). Plenarni predavatelji so bili **dr. Peter Gölitz** (Wiley-VCH, Weinheim, Nemčija), **prof. dr. Judith A.K. Howard** (Durham University, Velika Britanija) in **prof. dr. Robert Dominko** (Kemijski inštitut, Ljubljana). Poleg treh plenarnih predavanj so udeleženci poslušali šest ¨keynote¨ vabljenih predavanj, ki so jih izvedli **doc. dr. Anton Kokalj** (Inštitut »Jožef Stefan«, Ljubljana), **prof. dr. Janez Košmrlj** (Fakulteta za kemijo in kemijsko tehnologijo, Univerza v Ljubljani), **prof. dr. Silvia Marchesan** (University of Trieste, Italija), **prof. dr. Sandra Gardonio** (Univerza v Novi Gorici), **prof. dr. Marija Bešter-Rogač** (Fakulteta za kemijo in kemijsko tehnologijo, Univerza v Ljubljani) in **prof. dr. Darko Goričanec** (Fakulteta za kemijo in kemijsko tehnologijo, Univerza v Mariboru). Podelili smo nagrade študentom za najboljša predavanja in posterske predstavitve; nagrade sta sosponzorirala založbi Wiley-VCH in ChemPubSoc Europe.

V letniku ***Acta Chimica Slovenica* 2019 (vol. 66)** so izšle štiri številke s skupno 114 originalnimi znanstvenimi članki, 3 tematskimi članki in 3 preglednimi članki na skupno 1037 straneh z dvokolonskim tiskom. Ena od številk revije je bila posvečena prof. dr. Ivanu Kregarju. V slovenskem delu revije so bila na 83 straneh kot društvene vesti objavljena sekcijska poročila, seznami diplomskih, magistrskih in doktorskih del s področja kemije v letu 2019. V uredništvo je prispelo preko 1200 prispevkov, vendar smo jih zaradi neustrezne tehnične priprave in dokumentacije zavrnili več kot 80 % brez recenzije. Slaba polovica recenziranih člankov je bila pozitivno ocenjenih. Objavljeni članki pokrivajo aktualna področja organske, anorganske, fizikalne in analizne kemije, kemije materialov, kemijskega, biokemijskega in okoljskega inženirstva ter splošne, uporabne in biomedicinske kemije. Pisani so v angleškem jeziku s slovenskim povzetkom. Faktor vpliva (Impact Factor) ACSi za leto 2018 znaša IF = 1,076 in je primerljiv s faktorjem vpliva revije v letu 2017 (IF = 1,104). Na internetni strani http://acta.chem-soc.si objavljamo elektronsko verzijo revije *Acta Chimica Slovenica*, kar povečuje branost ter mednarodno odmevnost revije. Članki, objavljeni v ACSi, so povzeti tudi v Chemical Abstracts Plus, Current Contents (Physical, Chemical and Earth Sciences), Science Citation Index Expanded in Scopus. Revija *Acta Chimica Slovenica* je leta 2019 kot prva slovenska revija dobila pečat DOAJ (Directory of Open Access Journals), tako imenovani DOAJ Seal.

Konec leta 2019 sta z delom v uredniškem odboru revije ACSi zaključili dr. Melita Tramšek in prof. dr. Damjana Rozman. Glavni odbor društva je v uredniški odbor s 1. januarjem 2020 za mandatno obdobje štirih let imenoval dr. Mirelo Dragomir in prof. dr. Matjaža Kristla (področje Anorganska kemija in materiali) ter dr. Aleša Berleca (področje Biokemija in molekularna biologija v biomedicinskih aplikacijah).

Slovensko kemijsko društvo je v letu 2019 kot mednarodnem letu periodnega sistema izdalo digitalno publikacijo z naslovom »Periodni sistem elementov praznuje 150 let«. V publikaciji je objavljenih več tematskih prispevkov slovenskih avtorjev. Vsebinsko sta jo uredila dr. Albin Pintar in dr. Matic Lozinšek, tehnični urednik publikacije je bil Stanislav Oražem.

Društvo je bilo konec leta 2018 uspešno pri prijavi na Javni razpis za sofinanciranje izdajanja domačih znanstvenih periodičnih publikacij v letu 2019 in 2020. Dobili smo odobrena sredstva v višini 35.944,96 EUR za obe leti, kar je letno 17.972,48 EUR. V primerjavi s preteklim razpisom (za leti 2017 in 2018) je višina odobrenih sredstev primerljiva. V letu 2019 smo prejeli finančna sredstva v dveh obrokih.

Zahvaljujem se tudi vsem inštitucijam, ki so v letu 2019 finančno podprle izdajanje revije *Acta Chimica Slovenica*. Te so Fakulteta za kemijo in kemijsko tehnologijo Univerze v Ljubljani, Fakulteta za kemijo in kemijsko tehnologijo Univerze v Mariboru, Kemijski inštitut in Inštitut »Jožef Stefan«. Sponzorji revije so bili z objavo oglasa Krka

d.d., Novo mesto, Donau Lab d.o.o. Ljubljana in Helios Domžale, d.o.o.

V letu 2019 smo nadaljevali z aktivnostmi za pridobivanje novih članov. Medse smo jih privabili 19, od tega 10 študentov. Za ta namen smo že konec leta 2017 pričeli s prenovo grafične podobe društva ter s pomočjo grafične oblikovalke izdelali plakate, ki nagovarjajo nove člane k vpisu. Plakate smo že razobesili po številnih inštitucijah, s to aktivnostjo bomo nadaljevali tudi v letu 2020. Za nove člane smo uvedli simbolno darilo (reprezentančne kemične svinčnike) ob njihovem vpisu v društvo. Člane smo o aktivnostih v letu 2019 še pogosteje obveščali preko elektronske pošte in preko spletne strani društva, za namene promocije in obveščanja pa prav tako tudi preko vzpostavljenih Facebook in Twitter profilov društva, ki sta hitro in dobro zaživela.

Člani Slovenskega kemijskega društva so bili dejavni tudi **na področju mednarodnega sodelovanja.** Predvsem je potrebno omeniti članstvo društva v mednarodnih združenjih IUPAC, ECTN, IUCr, EURACHEM, EuCheMS, EFCE, EPF, ECA in EFCATS.

Člani društva so bili aktivni pri organizaciji mednarodne znanstvene konference, ki je potekala leta 2019, tj. konferenca EAAOP-6 (6th European Conference on Environmental Applications of Advanced Oxidation Processes, 26.-30. junij 2019, Portorož). V letu 2019 smo pridobili tudi organizacijo poletne šole Evropske federacije katalitskih združenj (EFCATS), ki bo izvedena septembra letos sočasno s konferenco »Slovenski kemijski dnevi 2020« v Portorožu.

Društvo se je v letu 2019 uspešno prijavilo na Javni razpis ARRS za sofinanciranje delovanja v mednarodnih znanstvenih združenjih v letu 2019, kjer smo bili uspešni pri vseh oddanih vlogah.

V Ljubljani, dne 2. aprila 2020

znan. svet. dr. Albin Pintar
predsednik društva

Poročilo Sekcije za kristalografijo za leto 2019

Sekcija za kristalografijo pri Slovenskem kemijskem društvu je v letu 2019 delovala po ustaljenem programu. Spremljali smo delo in IUCr (mednarodne kristalografske zveze) in ECA (evropske kristalografske zveze), katerih člani smo. Sodelovali smo pri aktivnostih, ki jih promovirata obe organizaciji (letos na primer je nekaj naših članov, ki so tudi člani SKD, sodelovalo pri postavitvi razstave ob mednarodnem letu periodnega sistema. Z obema organizacijama smo v rednem stiku po e-pošti.

Delovanje v Sloveniji je bilo osredotočeno na organizacijo tradicionalne kristalografske konference. Skupaj s hrvaškim kristalografskim društvom iz Zagreba smo organizirala 27. zaporedno srečanje slovenskih in hrvaških kristalografov. Srečanje je potekalo v Rogaški Slatini med 19. in 23 junijem 2019 (https://slocro27.fkkt.uni-lj.si/). Kot vsako leto je bila tudi tokrat udeležba mednarodna, zato je bil uradni jezik srečanja angleščina. S sredstvi donatorjev in sponzorjev ter veliko prostovoljnega dela članov sekcije smo uspeli organizirati srečanje tako, da smo obdržali tradicijo in udeležencem ni bilo treba plačati kotizacije. Velika zahvala za to gre sponzorjem, ki so bili: Renacon, Rigaku, Bruker, Crystal Impact, Dectris, Optik Instruments, Aparatura, Lek-Sandoz, Krka in Scan.

Podobno kot na prejšnjih konferencah, so se tudi tokrat povabilu za sodelovanje odzvali ugledni, mednarodno uveljavljeni plenarni predavatelji. Petra Bombicz iz raziskovalnega centra za naravoslovno znanosti pri madžarski akademiji znanosti in umetnosti iz Budmpešte je predstavila predavanje *Synthon/property-engineering of calixarenes (supramolecular interactions, shape and symmetries)*, prof. Piero Macchi z universe v Bernu v Švici je imel predavanje *Are there molecules in crystals?,* Martina Vrankić z inštituta Ruđer Bošković iz Zagreba je predstavila temo *Ambient and non-ambient driven X-ray powder diffraction: insights into the structure–property relationship in powders, Matic Lozinšek z UL Fakultete z kemijo in kemijsko tehnologijo in Inštituta Jožef Stefan pa je predaval o Noble-gas chemistry in the 21st century.*

Konferenca je bila uspešna, udeležilo se je je 55 prijavljenih udeležencev iz 8 držav (Avstrija, Madžarska, Indija, Italija, Švica, Ukrajina, Hrvaška in Slovenija. Poleg plenarnih predavanj so udeleženci 38 prispevkov v obliki kratkih predavanj, kar je ena od prednosti teh konferenc. Pretežno mladi raziskovalci imajo možnost predavati pred strokovno zahtevnim, vendar naklonjenim občinstvom, kar je dragocena izkušnja. Predavanja so pokrivala sodobne vidike kristalografije kot so: strukturna analiza organskih, bioloških, anorganskih in koordinacijskih spojin, arhitektura in načrtovanje struktur, fazni prehodi, trdne raztopine, povezava med lastnostmi in strukturo, sinergija med kristalografskimi in drugimi metodami karakterizacije, predstavljenih pa je bilo tud nekaj zanimivih utrinkov iz zgodovine kristalografije.

Tudi družabni dogodki, vključeni v program (vodena ekskurzija po muzeju na prostem in Steklarni Rogaška, konferenčna večerja) so bili spet priložnost za izmenjavo spoznanj, navezavo stikov in intenzivno učenje mlajših kolegov.

Že letos pa potekajo tui priprave na tri dogodke, ki bodo v naslednjem letu in jih podpirata IUCr in ECA, to so svetovni kongres IUCr v Pragi avgusta 2020, evropska konferenca o praškovni difrakciji v Šibeniku v maju in 28. Hrvaško-Slovensko kristalografsko srečanje v juniju v Rabcu na Hrvaškem.

prof. dr. Anton Meden

Poročilo sekcije za polimere

Predsednik Sekcije za polimere dr. David Pahovnik, se je 8. februarja in 9. junija 2019 udeležil generalnih skupščin Evropske polimerne federacije (EPF), ki sta potekali v Grčiji, kjer so med drugim izvolili prof. dr. Jirija Koteka (Inštituta za makromolekularno kemijo, Češka) za novega predsednika EPF. Sekcija za polimere je avgusta 2019 za člane sekcije organizirala tudi predavanji prof. dr. Guangzhao Zhanga in prof. dr. Junpeng Zhaoa iz South China University of Technology, Kitajska.

Dr. David Pahovnik

Poročilo Sekcije za analizno kemijo v okviru Slovenskega kemijskega društva za leto 2019

Delo Sekcije za analizno kemijo v okviru Slovenskega kemijskega društva je v letu 2019 potekalo kot načrtovano, vodenje sekcijo je prevzel izr. prof. dr. Mitja Kolar s Fakultete za kemijo in kemijsko tehnologijo Univerze v Ljubljani. Sekcija združuje kemike – analitike iz znanstveno-raziskovalnih, univerzitetnih in industrijskih laboratorijev. Osnovna dejavnost Sekcije je organiziranje mednarodnih in domačih znanstvenih ter strokovnih srečanj, predavanj domačih in tujih strokovnjakov ter izvedba različnih delavnic in izobraževanj.

Leto 2019 je nedvomno najbolj zaznamovala 100-letnica Univerze v Ljubljani, ki sovpada s 100-letnico poučevanja kemije. Prav analizna kemija se lahko ponaša s prvim visokošolskim učbenikom z naslovom »Kvalitativna analyza« prof. dr. Marija Rebka (1889–1982). Ob tej priložnosti je Fakulteta za kemijo in kemijsko tehnologijo izdala zbornik, ki popisuje zgodovino, razvoj in poučevanje kemije na Univerze v Ljubljani.

V okviru Sekcije poteka mednarodno srečanje podiplomskih študentov in njihovih mentorjev YISAC (Young Investigators Seminar on Analytical Chemistry), ki je junija 2019 potekalo na Univerzi v Pardubicah (https://yisac2019.upce.cz/). Srečanje YISAC 2019 je bilo 26. zaporedno srečanje in je bilo posvečeno spominu na dva prehitro preminula kolega - analitika in prijatelja prof. dr. Karla Vytřasa iz Univerze v Pardubicah ter prof. dr. Valério Guzsvány iz Univerze v Novem Sadu. Na srečanju je sodelovalo 25 študentov, ki so predstavili svoje znanstveno-raziskovalno delo, od tega štirje iz Slovenije.

Med drugimi pomembnimi aktivnostmi Sekcije v letu 2019 velja posebej izpostaviti sodelovanje pri izvedbi 25. jubilejne konference »Slovenski kemijski dnevi 2019« septembra 2019 v Mariboru. Dogodek je bil poseben še zato, ker je konferenca potekala v znamenju sodelovanja Slovenskega kemijskega društva in Ameriškega kemijskega društva. Konferenca je potekala v sproščenem vzdušju ob druženju in izmenjavi izkušenj, so pa Slovenski kemijski dnevi 2019 ponovno potrdili, da imamo v Sloveniji zelo veliko perspektivnih mladih kemikov, tako da je imela komisija za oceno in izbor najboljših predstavitev res veliko dela.

Člani sekcije sodelujejo tudi znotraj delovnih skupin Eurachem-a in drugih združenj v evropskem prostoru (DAC, FECS) in tako pomembno prispevajo k prepoznavnosti in promociji Slovenskega kemijskega društva.

V prihodnje želimo aktivneje vključiti mlajše kolege v delovanje Sekcije za analizno kemijo, povezati industrijske in izobraževalne laboratorije ter tako zagotoviti dober prenos znanja in izkušenj. Nadaljevali bomo z organizacijo in so-organizacijo tako domačih kot tujih srečanj, ki bodo vključevala eminentne strokovnjake in raziskovalce iz različnih držav in področij analizne kemije.

Ljubljana, 4. 6. 2020

izr. prof. dr. Mitja Kolar

Sekcija za katalizo poročilo o delu v letu 2019

Člani Sekcije za katalizo pri Slovenskem kemijskem društvu so bili v letu 2019 zelo angažirani pri izvedbi in pridobivanju organizacije mednarodnih znanstvenih dogodkov.

V dneh od 26. do 30. junija 2019 je v kongresnem centru Grand hotela Bernardin v Portorožu potekala potekala mednarodna znanstvena konferenca z naslovom »6th European Conference on Environmental Applications of Advanced Oxidation Processes« (EAAOP-6; http://eaaop6.ki.si/), ki sta jo organizirala Sekcija za katalizo in Laboratorij za okoljske vede in inženirstvo s Kemijskega inštituta v Ljubljani. Konference se je udeležilo preko 300 udeležencev iz 51 držav širom po svetu. Program konference je bil precej obsežen, saj je vseboval veliko različnih tem, zajetih v štirih plenarnih predavanjih, štirih vabljenih (keynote) predavanjih, 131 krajših predavanjih in 223 postrih. Študentsko tekmovanje je bilo organizirano kot sestavni del prireditve. Obravnavane teme so med drugim vključevale nove katalitične materiale za uporabo v okolju, *in situ* in *operando* meritve, napredne oksidacijske procese (čiščenje vode in zraka, sanacija tal, proizvodnja energije in kemikalij z dodano vrednostjo), fotokatalizo, Fentonove postopke, elektrokemijske procese in pilotne študije ter aplikacije na terenu. Izbrana znanstvena dela so bila v obliki recenziranih člankov objavljena v revijah *Catalysis Today*, *Journal of Environmental Management* in *Environmental Science and Pollution Research*. Znanstvenemu in organizacijskemu odboru konference je predsedoval znan. svet. dr. Albin Pintar.

Članom Sekcije za katalizo je bila decembra 2019 zaupana izvedba poletne šole Evropske federacije katalitskih združenj (EFCATS). Dogodek (https://skd2020.chem-soc.si/2020-efcats-summer-school/), katerega tematika je inženiring materialov na področju heterogene katalize, bo organiziran v sodelovanju z Avstrijskim združenjem za katalizo v dneh od 15. do 19. septembra 2020 v kongresnem centru Grand hotela Bernardin v Portorožu, sočasno s konferenco »Slovenski kemijski dnevi 2020«.

Na sestanku EFCATS sveta, ki je avgusta 2019 potekal ob robu EuropaCat kongresa, je bila prof. dr. Nataša Novak Tušar s Kemijskega inštituta v Ljubljani izvoljena za blagajničarko EFCATS federacije za naslednje mandatno obdobje.

V Ljubljani, dne 5. junija 2020

Albin Pintar

Komisija za Kemijsko izobraževanje

V letu 2019 so bili člani Komisije za kemijsko izobraževanje pri SKD vključeni v vrsto dejavnosti, ki so tradicionalno v domeni delovanja komisije, hkrati pa so bile nekatere aktivnosti na novo zasnovane.

V sklopu **Mednarodnega leta periodnega sistema** so člani komisije sodelovali s Kemijskim inštitutom in Centrom KemikUm Univerze v Ljubljani, Pedagoške fakultete. Z **natečajem Periodni sistem elementov – včeraj, danes, jutri** so učenci in dijaki pripravili izdelke, ki so bili razstavljeni na Pedagoški fakulteti in na Kemijskem inštitutu v okviru tedna Kemijskega inštituta. Prav tako so člani komisije sodelovali pri različnih **delavnicah** za učence in dijake, kot so npr.: KemikUm raziskuje: *grelne blazinice, barvila za izdelavo tatujev*, *eterična olja*, k*emijsko zgradbo gob, plastiko,* pa tudi KemikUm vozi na metan, KemikUm molekularni gastronom, in KemikUm rešuje zločin, ter delavnico Učenje z raziskovanjem pri naravoslovju – voda za učitelje. V prvi polovici leta so bile na žalost vse KemikUm delavnice zaradi stanja v Sloveniji povezanega z virusom SARS-CoV-2 do nadaljnjega odpovedane.

Člani komisije so tudi skupaj s Kemijskim inštitutom, Uradom za Unesco, Univerzo v Ljubljani Fakulteto za kemijo in kemijsko tehnologijo, Slovenskim kemijskim društvom ter Hišo eksperimentov sodelovali pri pripravi razstave z naslovom »**Elementi vsepovsod okoli nas**«, ki je bila od 18. julija do 19. avgusta 2019 na ogled na Krakovskem nasipu in od 11. do 20. novembra 2019 v predverju velike dvorane Državnega zbora Republike Slovenije. Obiskovalci razstave, so se lahko seznanili z izbranimi kemijskimi elementi ter z ustanovami, ki so sodelovale pri pripravi razstave.

20. september 2019 je bila Univerzi v Ljubljani Pedagoški fakulteti organizirana tudi **mednarodna konferenca »PERIODNI SISTEM VČERAJ, DANES, JUTRI«,** ki je predstavljala zaključek dejavnosti povezanih z mednarodnim letom periodnega sistema.

Člani komisije so kot mentorji sodelovali z magistrskimi študenti dvopredmetnega študija kemije in je bila na osnovi magistrskih del izdana znanstvena monografija z naslovom **Učitelj raziskovalec – za prenos raziskovalnih spoznanj v pouk kemije** dostopna na *https://www.pef.uni-lj.si/fileadmin/Datoteke/Kemikum/Dokumenti/monografija_kemikum_2_2019__2_.pdf).*

Člani komisije so v letu 2019 sodelovali tudi pri organizaciji kemijskih tekmovanj za osnovnošolce (Preglova priznanja) in dijake (Preglove plakete) skupaj z ZOTKS. Državno tekmovanje iz znanja kemije organiziramo že od leta 1967. Tekmovanje je dvostopenjsko, kar pomeni, da učenci in dijaki tekmujejo najprej na šolski ravni, najboljši pa se uvrstijo še na državno tekmovanje. V januarju je potekalo **šolsk**o tekmovanje za osnovnošolce, ki se ga je udeležilo 6771 učencev s 443 šol, podeljenih je bilo 1456 bronastih Preglovih priznanj. Na državnem tekmovanju za učence osnovnih šol je sodelovalo 1697 učencev in so skupaj prejeli 153 srebrnih in 68 zlatih Preglovih priznanj. Šolskega tekmovanja iz znanja kemije za dijake se je udeležilo 3217 dijakov iz 80 srednjih šol. Osvojili so 684 bronastih Preglovih plaket. Za srednješolce je 53. državno tekmovanje iz znanja kemije za Preglove plakete potekalo na Fakulteti za kemijo in kemijsko tehnologijo Univerze v Ljubljani. Tekmovalo je 524 dijakov. Osvojili so 134 srebrnih in 69 zlatih Preglovih plaket.

Člani komisije so tudi aktivno z več prispevki (posterske in ustne predstavitve) sodelovali na jubilejnih Slovenskih kemijskih dnevih 2019 v Mariboru ter na mednarodni konferenci ESERA v Bologni, Italija in EUROVARIETY 19 (European Variety in University Chemistry Education) v Pratu, Italija.

Člani komisije intenzivno pripravljajo 9. EUROVARIETY2021 (European Variety in University Chemistry Education) mednarodno konferenco, ki bo potekala med 7. in 9. julijem 2021 na Univerzi v Ljubljani, Pedagoški fakulteti.

Načrt za leto 2020 je bil podoben, vendar bo, zaradi pandemije z novim koronavirusom SARS-CoV-2, močno okrnjen.

Prof. dr. Iztok Devetak

Poročilo Sekcije za keramiko za leto 2019

Odsek za raziskave sodobnih materialov in Odsek za nanostrukturne materiale Instituta »Jožef Stefan« sta v okviru Strateško razvojno-inovacijskega partnerstva Tovarne prihodnosti (SRIP ToP) in Sekcije za keramiko Slovenskega kemijskega društva v letu 2019 organizirala dve strokovni delavnici, namenjeni povezovanju industrijskih partnerjev z raziskovalnimi organizacijami na ključnih raziskovalno-razvojnih področjih.

– Delavnica »Sodobne tehnike karakterizacije materialov« je potekala 18. 4. 2019 na Institute »Jožef Stefan« v Ljubljani, udeležilo se jo je 47 udeležencev, industrijskim partnerjem pa se je predstavil nabor pomembnih tehnik karakterizacije materialov, ki jih ponujajo različne javne raziskovalne organizacije v Sloveniji. Osem predavateljev je predstavilo tehnike, kot so rentgenska analiza, ramanska spektroskopija in FTIR, rentgenska fotoelektronska spektroskopija in masna spektrometrija površin, vrstična in presevna elektronska mikroskopija, termična analiza, delavnica pa se je zaključila s predavanjema o električni in magnetni karakterizaciji materialov.
– Delavnica »Kemijska in strukturna analiza materialov« je potekala 28. 11. 2019 na Reaktorskem centeru Instituta »Jožef Stefan« v Podgorici, udeležilo pa se jo je 41 udeležencev iz različnih organizacij. Šest predavateljev je podrobneje predstavili značilnosti različnih karakterizacijskih tehnik, zadnje trende na področju in možnosti merjenja v Sloveniji. Tematike so med drugim vključevale uporabo rentgenske mikrotomografije v industriji in raziskavah, BET analizo, DLS meritve in elementno masno spektrometrijo za analizo materialov.

Obe delavnici je finančno omogočil SRIP ToP, ki na področju keramičnih materialov povezuje akterje preko vertikalne verige vrednosti Novi materiali in horizontalne mreže Sodobne proizvodne tehnologije.

V letu 2019 je bila okviru Evropskega keramičnega združenja (ECerS) Prof. dr. Barbara Malič iz Odseka za elektronsko keramiko Instituta »Jožef Stefan« izvoljena za častno članico društva, kar predstavlja priznanje njenemu prispevku k raziskavam fero- in piezoelektrične keramike in tankih plasti. Prof. Malič je leta 2019 postala tudi članica uredniškega odbora revije Journal of the European Ceramic Society, ki ima med znanstvenimi revijami na področju raziskav keramičnih materialov največji faktor vpliva.

Društvo ECerS je v letu 2019 doc. dr. Andražu Kocjanu iz Odseka za nanostrukturne materiale Instituta »Jožef Stefan« podelilo prestižno nagrado »Young Scientist Award«, za izjemne prispevke znanstvenikov na začetku kariere. Nagrada je bila podeljena na 16. konferenci ECerS v Torinu, Italija, ki se je odvila med 16. in 20. junijem 2019. Na slovesnosti je imel dr. Kocjan vabljeno predavanje z naslovom »*From unusual to innovative and sustainable processing of ceramics*«. Na konferenci je dr. Kocjan, kot vodja delovne skupine društva »Young Ceramists and Training« (YCT), organiziral tudi tekmovanje študentov, za katero tekmovalce iz posamezne države predlaga matično keramično združenje. Slovenijo je predstavljal Aleksander Matavž iz Odseka za fiziko trdne snovi Instituta »Jožef Stefan«, ki je na tekmovanju zasedel odlično 4. mesto. V okviru konference se je doc. dr. Matjaž Spreitzer iz Odseka za raziskave sodobnih materialov Instituta »Jožef Stefan« kot predstavnik Sekcije za keramiko Slovenskega kemijskega društva udeležil seje sveta društva, kjer je bilo podano poročilo o njenem delovanju, finančnem poslovanju ter o aktivnostih posameznih delovnih skupin.

Na 27. konferenci o Materialih in tehnologijah je Hermina Hudelja iz Odseka za nanostrukturne materiale Instituta »Jožef Stefan« zasedla 2. mesto na tekmovanju mladih raziskovalcev s predavanjem z naslovom "Featherlight, cellulose-nanofiber-reinforced γ-Al2O3 foams" in bo tako ena izmed kandidatk za udeležitev tekmovanja študentov na prihodnji konferenci ECerS, ki bo potekala leta 2021 v Nemčiji.

Doc. dr. Matjaž Spreitzer

Acta Chimica Slovenica

Author Guidelines

Submissions

Submission to ACSi is made with the implicit understanding that neither the manuscript nor the essence of its content has been published in whole or in part and that it is not being considered for publication elsewhere. All the listed authors should have agreed on the content and the corresponding (submitting) author is responsible for having ensured that this agreement has been reached. The acceptance of an article is based entirely on its scientific merit, as judged by peer review. There are no page charges for publishing articles in ACSi. The authors are asked to read the Author Guidelines carefully to gain an overview and assess if their manuscript is suitable for ACSi.

Additional information

- Citing spectral and analytical data
- Depositing X-ray data

Submission material

Typical submission consists of:

- full manuscript (PDF file, with title, authors, abstract, keywords, figures and tables embedded, and references)
- supplementary files
  - ***Full manuscript*** (original Word file)
  - ***Statement of novelty*** (Word file)
  - ***List of suggested reviewers*** (Word file)
  - ***ZIP file containing graphics*** (figures, illustrations, images, photographs)
  - ***Graphical abstract*** (single graphics file)
  - ***Proposed cover picture*** (optional, single graphics file)
  - ***Appendices*** (optional, Word files, graphics files)

Incomplete or not properly prepared submissions will be rejected.

Submission process

Before submission, authors should go through the checklist at the bottom of the page and prepare for submission.

Submission process consists of 5 steps.

Step 1: Starting the submission

- Choose one of the journal sections.
- Confirm all the requirements of the ***checklist.***
- Additional plain text comments for the editor can be provided in the relevant text field.

Step 2: Upload submission

- Upload full manuscript in the form of a Word file (with title, authors, abstract, keywords, figures and tables embedded, and references).

Step 3: Enter metadata

- First name, last name, contact email and affiliation for all authors, in relevant order, must be provided. Corresponding author has to be selected. Full postal address and phone number of the corresponding author has to be provided.
- ***Title and abstract*** must be provided in plain text.
- Keywords must be provided (max. 6, separated by semicolons).
- Data about contributors and supporting agencies may be entered.
- ***References*** in plain text must be provided in the relevant text filed.

Step 4: Upload supplementary files

- Original Word file (original of the PDF uploaded in the step 2)
- ***Statement of novelty*** in a Word file must be uploaded
- All ***graphics*** have to be uploaded in a single ZIP file. Graphics should be named Figure 1.jpg, Figure 2.eps, etc.
- ***Graphical abstract image*** must be uploaded separately
- ***Proposed cover picture*** (optional) should be uploaded separately.
- Any additional ***appendices*** (optional) to the paper may be uploaded. Appendices may be published as a supplementary material to the paper, if accepted.
- For each uploaded file the author is asked for additional metadata which may be provided. Depending of the type of the file please provide the relevant title (Statement of novelty, List of suggested reviewers, Figures, Graphical abstract, Proposed cover picture, Appendix).

Step 5: Confirmation

- Final confirmation is required.

Article Types

Feature Articles are contributions that are written on editor's invitation. They should be clear and concise summaries of the most recent activity of the author and his/her research group written with the broad scope of ACSi in mind. They are intended to be general overviews of the authors' subfield of research but should be written in a way that engages and informs scientists in other areas. They should contain the following (see also general directions for article structure in ACSi below): (1) an introduction that acquaints readers with the authors' research field and outlines the important questions to which answers are being sought; (2) interesting, new, and recent contributions of the author(s) to the field; and (3) a summary that presents possible future directions. Manuscripts normally should not exceed 40 pages of one column format (letter size 12, 33 lines per page). Generally, experts in a field who have made important contribution to a specific topic in recent years will be invited by an editor to contribute such an **Invited Feature Article**. Individuals may, however, send a proposal (one-page maximum) for an Invited Feature Article to the Editor-in-Chief for consideration.

Scientific articles should report significant and innovative achievements in chemistry and related sciences and should exhibit a high level of originality. They

should have the following structure:

1. Title (max. 150 characters),
2. Authors and affiliations,
3. Abstract (max. 1000 characters),
4. Keywords (max. 6),
5. Introduction,
6. Experimental,
7. Results and Discussion,
8. Conclusions,
9. Acknowledgements,
10. References.

The sections should be arranged in the sequence generally accepted for publications in the respective fields and should be successively numbered.

Short communications generally follow the same order of sections as Scientific articles, but should be short (max. 2500 words) and report a significant aspect of research work meriting separate publication. Editors may decide that a Scientific paper is categorized as a Short Communication if its length is short.

Technical articles report applications of an already described innovation. Typically, technical articles are not based on new experiments.

Preparation of Submissions

Text of the submitted articles must be prepared with Microsoft Word. Normal style set to single column, 1.5 line spacing, and 12 pt Times New Roman font is recommended. Line numbering (continuous, for the whole document) must be enabled to simplify the reviewing process. For any other format, please consult the editor. Articles should be written in English. Correct spelling and grammar are the sole responsibility of the author(s). Papers should be written in a concise and succinct manner. The authors shall respect the ISO 80000 standard [1], and IUPAC Green Book [2] rules on the names and symbols of quantities and units. The Système International d'Unités (SI) must be used for all dimensional quantities.

Graphics (figures, graphs, illustrations, digital images, photographs) should be inserted in the text where appropriate. The captions should be self-explanatory. Lettering should be readable (suggested 8 point Arial font) with equal size in all figures. Use common programs such as MS Excel or similar to prepare figures (graphs) and ChemDraw to prepare structures in their final size. Width of graphs in the manuscript should be 8 cm. Only in special cases (in case of numerous data, visibility issues) graphs can be 17 cm wide. All graphs in the manuscript should be inserted in relevant places and **aligned left**. The same graphs should be provided separately as images of appropriate resolution (see below) and submitted together in a ZIP file (Graphics ZIP). Please do not submit figures as a Word file. In **graphs**, only the graph area determined by both axes should be in the frame, while a frame around the whole graph should be omitted. The graph area should be white. The legend should be inside the graph area. The style of all graphs should be the same. **Figures and illustrations** should be of sufficient quality for the printed version, i.e. 300 dpi minimum. **Digital images and photographs** should be of high quality (minimum 250 dpi resolution). On submission, figures should be of good enough resolution to be assessed by the referees, ideally as JPEGs. High-resolution figures (in JPEG, TIFF, or EPS format) might be required if the paper is accepted for publication.

Tables should be prepared in the Word file of the paper as usual Word tables. The captions should appear above the table and should be self-explanatory.

References should be numbered and ordered sequentially as they appear in the text, likewise methods, tables, figure captions. When cited in the text, reference numbers should be superscripted, following punctuation marks. It is the sole responsibility of authors to cite articles that have been submitted to a journal or were in print at the time of submission to ACSi. Formatting of references to published work should follow the journal style; please also consult a recent issue:

1. J. W. Smith, A. G. White, *Acta Chim. Slov.* **2008**, *55*, 1055–1059.
2. M. F. Kemmere, T. F. Keurentjes, in: S. P. Nunes, K. V. Peinemann (Ed.): Membrane Technology in the Chemical Industry, Wiley-VCH, Weinheim, Germany, **2008**, pp. 229–255.
3. J. Levec, Arrangement and process for oxidizing an aqueous medium, US Patent Number 5,928,521, date of patent July 27, **1999**.
4. L. A. Bursill, J. M. Thomas, in: R. Sersale, C. Collela, R. Aiello (Eds.), Recent Progress Report and Discussions: 5th International Zeolite Conference, Naples, Italy, 1980, Gianini, Naples, **1981**, pp. 25–30.
5. J. Szegezdi, F. Csizmadia, Prediction of dissociation constant using microconstants, http://www. chemaxon.com/conf/Prediction_of_dissociation _constant_using_microco nstants.pdf, (assessed: March 31, 2008)

Titles of journals should be abbreviated according to Chemical Abstracts Service Source Index (CASSI).

Special Notes

- Complete characterization, **including crystal structure**, should be given when the synthesis of new compounds in crystal form is reported.
- Numerical **data should be reported with the number of significant digits corresponding to the magnitude** of experimental uncertainty.
- **The SI system of units and IUPAC recommendations** for nomenclature, symbols and abbreviations should be followed closely. Additionally, the authors should follow the general guidelines when citing spectral and analytical data, and depositing crystallographic data.
- **Characters** should be correctly represented throughout the manuscript: for example, 1 (one) and l (ell), 0 (zero) and O (oh), x (ex), D7 (times sign), B0 (degree sign). Use Symbol font for all Greek letters and mathematical symbols.
- The rules and recommendations of the **IUBMB** and the **International Union of Pure and Applied Chemistry (IUPAC)** should be used for abbreviation of chemical names, nomenclature of chemical compounds, enzyme nomenclature, isotopic compounds, optically active isomers, and spectroscopic data.
- **A conflict of interest** occurs when an individual (author, reviewer, editor) or its organization is involved in multiple interests, one of which could possibly corrupt the motivation for an act in the

other. Financial relationships are the most easily identifiable conflicts of interest, while conflicts can occur also as personal relationships, academic competition, etc. **The Editors** will make effort to ensure that conflicts of interest will not compromise the evaluation process; potential editors and reviewers will be asked to exempt themselves from review process when such conflict of interest exists. When the manuscript is submitted for publication, **the authors** are expected to disclose any relationships that might pose potential conflict of interest with respect to results reported in that manuscript. In the Acknowledgement section the source of funding support should be mentioned. The statement of disclosure must be provided as Comments to Editor during the submission process.

- **Published statement of Informed Consent.** Research described in papers submitted to ACSi must adhere to the principles of the Declaration of Helsinki (***http://www.wma.net/e/policy/b3.htm***). These studies must be approved by an appropriate institutional review board or committee, and informed consent must be obtained from subjects. The Methods section of the paper must include: 1) a statement of protocol approval from an institutional review board or committee and 2), a statement that informed consent was obtained from the human subjects or their representatives.
- **Published Statement of Human and Animal Rights.**When reporting experiments on human subjects, authors should indicate whether the procedures followed were in accordance with the ethical standards of the responsible committee on human experimentation (institutional and national) and with the Helsinki Declaration of 1975, as revised in 2008. If doubt exists whether the research was conducted in accordance with the Helsinki Declaration, the authors must explain the rationale for their approach and demonstrate that the institutional review body explicitly approved the doubtful aspects of the study. When reporting experiments on animals, authors should indicate whether the institutional and national guide for the care and use of laboratory animals was followed.
- To avoid conflict of interest between authors and referees we expect that not more than one referee is from the same country as the corresponding author(s), however, not from the same institution.
- Contributions authored by **Slovenian scientists** are evaluated by non-Slovenian referees.
- Papers describing **microwave-assisted reactions** performed in domestic microwave ovens are not considered for publication in *Acta Chimica Slovenica.*
- *Manuscripts that are **not prepared and submitted** in accord with the instructions for authors are not considered for publication.*

Appendices

Authors are encouraged to make use of supporting information for publication, which is supplementary material (appendices) that is submitted at the same time as the manuscript. It is made available on the Journal's web site and is linked to the article in the Journal's Web edition. The use of supporting information is particularly appropriate for presenting additional graphs, spectra, tables and discussion and is more likely to be of interest to specialists than to general readers. When preparing supporting information, authors should keep in mind that the supporting information files will not be edited by the editorial staff. In addition, the files should be not too large (upper limit 10 MB) and should be provided in common widely known file formats to be accessible to readers without difficulty. All files of supplementary materials are loaded separately during the submission process as supplementary files.

Proposed Cover Picture and Graphical Abstract Image

Graphical content: an ideally full-colour illustration of resolution 300 dpi from the manuscript must be proposed with the submission. Graphical abstract pictures are printed in size 6.5 x 4 cm (hence minimal resolution of 770 x 470 pixels). Cover picture is printed in size 11 x 9.5 cm (hence minimal resolution of 1300 x 1130 pixels)

Authors are encouraged to submit illustrations as candidates for the journal Cover Picture*. The illustration must be related to the subject matter of the paper. Usually both proposed cover picture and graphical abstract are the same, but authors may provide different pictures as well.

* The authors will be asked to contribute to the costs of the cover picture production.

Statement of novelty

Statement of novelty is provided in a Word file and submitted as a supplementary file in step 4 of submission process. Authors should in no more than 100 words emphasize the scientific novelty of the presented research. Do not repeat for this purpose the content of your abstract.

List of suggested reviewers

List of suggested reviewers is a Word file submitted as a supplementary file in step 4 of submission process. Authors should propose the names, full affiliation (department, institution, city and country) and e-mail addresses of three potential referees. Field of expertise and at least two references relevant to the scientific field of the submitted manuscript must be provided for each of the suggested reviewers. The referees should be knowledgeable about the subject but have no close connection with any of the authors. In addition, referees should be from institutions other than (and preferably countries other than) those of any of the authors.

How to Submit

Users registered in the role of author can start submission by choosing USER HOME link on the top of the page, then choosing the role of the Author and follow the relevant link for starting the submission process.

Prior to submission we strongly recommend that you familiarize yourself with the ACSi style by browsing the journal, particularly if you have not submitted to the ACSi before or recently.

Correspondence

All correspondence with the ACSi editor regarding the paper goes through this web site and emails. Emails are sent and recorded in the web site database. In the correspondence with the editorial office please provide ID number of your manuscript. All emails you receive from the system contain relevant links. **Please do not answer the emails directly but use the embedded links in the emails for carrying out relevant actions.** Alternatively, you can carry out all the actions and correspondence through the online system by logging in and selecting relevant options.

Proofs

Proofs will be dispatched via e-mail and corrections should be returned to the editor by e-mail as quickly as possible, normally within 48 hours of receipt. Typing errors should be corrected; other changes of contents will be treated as new submissions.

Submission Preparation Checklist

As part of the submission process, authors are required to check off their submission's compliance with all of the following items, and submissions may be returned to authors that do not adhere to these guidelines.

1. The submission has not been previously published, nor is it under consideration for publication in any other journal (or an explanation has been provided in Comments to the Editor).
2. All the listed authors have agreed on the content and the corresponding (submitting) author is responsible for having ensured that this agreement has been reached.
3. The submission files are in the correct format: manuscript is created in MS Word but will be **submitted in PDF** (for reviewers) as well as in original MS Word format (as a supplementary file for technical editing); diagrams and graphs are created in Excel and saved in one of the file formats: TIFF, EPS or JPG; illustrations are also saved in one of these formats. The preferred position of graphic files in a document is to embed them close to the place where they are mentioned in the text (See ***Author guidelines*** for details).
4. The manuscript has been examined for spelling and grammar (spell checked).
5. The ***title*** (maximum 150 characters) briefly explains the contents of the manuscript.
6. Full names (first and last) of all authors together with the affiliation address are provided. Name of author(s) denoted as the corresponding author(s), together with their e-mail address, full postal address and telephone/fax numbers are given.
7. The ***abstract*** states the objective and conclusions of the research concisely in no more than 150 words.
8. Keywords (minimum three, maximum six) are provided.
9. ***Statement of novelty*** (maximum 100 words) clearly explaining new findings reported in the manuscript should be prepared as a separate Word file.
10. The text adheres to the stylistic and bibliographic requirements outlined in the ***Author guidelines***.
11. Text in normal style is set to single column, 1.5 line spacing, and 12 pt. Times New Roman font is recommended. All tables, figures and illustrations have appropriate captions and are placed within the text at the appropriate points.
12. Mathematical and chemical equations are provided in separate lines and numbered (Arabic numbers) consecutively in parenthesis at the end of the line. All equation numbers are (if necessary) appropriately included in the text. Corresponding numbers are checked.
13. Tables, Figures, illustrations, are prepared in correct format and resolution (see ***Author guidelines***).
14. The lettering used in the figures and graphs do not vary greatly in size. The recommended lettering size is 8 point Arial.
15. Separate files for each figure and illustration are prepared. The names (numbers) of the separate files are the same as they appear in the text. All the figure files are packed for uploading in a single ZIP file.
16. Authors have read ***special notes*** and have accordingly prepared their manuscript (if necessary).
17. References in the text and in the References are correctly cited. (see ***Author guidelines***). All references mentioned in the Reference list are cited in the text, and vice versa.
18. Permission has been obtained for use of copyrighted material from other sources (including the Web).
19. The names, full affiliation (department, institution, city and country), e-mail addresses and references of three potential referees from institutions other than (and preferably countries other than) those of any of the authors are prepared in the word file. At least two relevant references (important papers with high impact factor, head positions of departments, labs, research groups, etc.) for each suggested reviewer must be provided.
20. Full-colour illustration or graph from the manuscript is proposed for graphical abstract.
21. ***Appendices*** (if appropriate) as supplementary material are prepared and will be submitted at the same time as the manuscript.

Privacy Statement

The names and email addresses entered in this journal site will be used exclusively for the stated purposes of this journal and will not be made available for any other purpose or to any other party.

ISSN: 1580-3155

Koristni naslovi

Slovensko kemijsko društvo
www.chem-soc.si
e-mail: chem.soc@ki.si

Wessex Institute of Technology
www.wessex.ac.uk

SETAC
www.setac.org

European Water Association
http://www.ewa-online.eu/

European Science Foundation
www.esf.org

European Federation of Chemical Engineering
https://efce.info/

International Union of Pure and Applied Chemistry
https://iupac.org/

Novice europske zveze kemijskih društev EuChemS najdete na:

Brussels News Updates
http://www.euchems.eu/newsletters/

Sistemi za čisto in ultračisto vodo

Kvaliteta vode 1 do 3*

***v skladu s standardom ISO 3696 in ustreznimi ASTM ter CLSI**

DONAU LAB Ljubljana
Member of LPPgroup

Donau Lab d.o.o., Ljubljana
Tbilisijska 85
SI-1000 Ljubljana
www.donaulab.si
office-si@donaulab.com

Že od
3.214€ +DDV
(B30 Trace s 25 L Pro rezerv.
Slika je simbolična)

adrona

Napredek, obarvan v zeleno

V Heliosu načela trajnostnega razvoja in skrbi za okolje vpeljujemo na vsa področja našega delovanja. Nove rešitve in proizvode razvijamo tudi z namenom, da bi zmanjšali porabo vseh vrst virov in ogljični odtis produktov.

Part of KANSAI PAINT

www.helios-group.eu

HELIOS

Designing Excellence

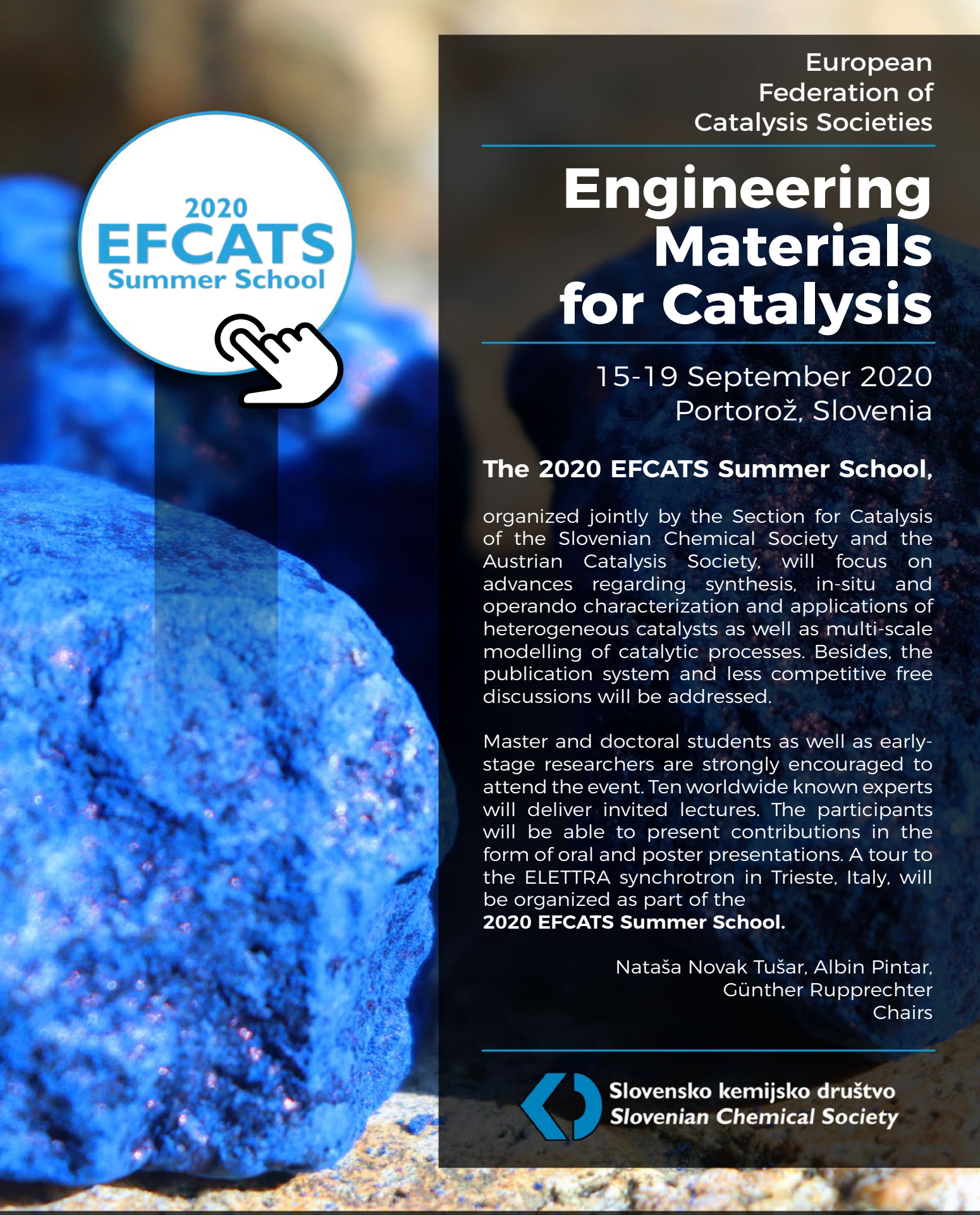

European
Federation of
Catalysis Societies

Engineering Materials for Catalysis

15-19 September 2020
Portorož, Slovenia

The 2020 EFCATS Summer School,

organized jointly by the Section for Catalysis of the Slovenian Chemical Society and the Austrian Catalysis Society, will focus on advances regarding synthesis, in-situ and operando characterization and applications of heterogeneous catalysts as well as multi-scale modelling of catalytic processes. Besides, the publication system and less competitive free discussions will be addressed.

Master and doctoral students as well as early-stage researchers are strongly encouraged to attend the event. Ten worldwide known experts will deliver invited lectures. The participants will be able to present contributions in the form of oral and poster presentations. A tour to the ELETTRA synchrotron in Trieste, Italy, will be organized as part of the
2020 EFCATS Summer School.

Nataša Novak Tušar, Albin Pintar,
Günther Rupprechter
Chairs

Slovensko kemijsko društvo
Slovenian Chemical Society

2020 EFCATS Summer School

https://skd2020.chem-soc.si/en/2020-efcats-summer-school/

Acta Chimica Slovenica

Porous polymers are an increasingly important class of materials offering tailored characteristics for numerous applications. Use of emulsions with monomers in the continuous phase results in polymers with a unique cellular morphology- polyHIPEs of which porous structure is determined by the precursor emulsion. Further functionalization od polyHIPEs with hypercrosslnking yields multi-level porous polymers with pores in both nano and macro domains (see page 349).

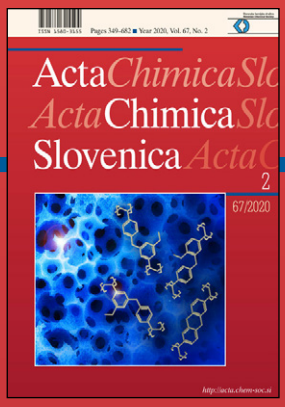

Year 2020, Vol. 67, No. 2